



supporting partners



49th INTERNATIONAL CONGRESS ON SCIENCE TECHNOLOGY AND TECHNOLOGY-BASED INNOVATION

“SDGs FOR THE BENEFIT OF MANKIND”

~PROCEEDING BOOK~



TABLE OF CONTENT

Title	Page
ORAL PRESENTATION	
SESSION A-PHYSICS / APPLIED PHYSICS	
A Study of Post-Weld Laser Cleaning on 304 Stainless Steel	1
A Toner-Print Removal From Paper Using Long Pulsed Lasers	6
Application of Low Cost and Low Precision Laser-Scribed Capacitor Sensors	15
Assessing the Influence of Physical Distancing and Face Mask Usage on Respiratory Virus Transmission: A Mathematical Modeling Study	21
Design of Divergent Beam-Based Surface Plasmon Resonance Sensor for Monitoring Bacterial Biofilm Formations	30
Evaluation of Eliashberg Gap Equations From Analytic Summations and Big Data From Independent Dft Works	36
Invention of Bone Density Measuring Instrument Using Stress Waves for Assisting in Osteoporosis Diagnosis	45
Modification of the Pump Field for Enhanced Spontaneous Parametric Down Conversion in Quantum Key Distribution	55
Optimization of Link-Level Quantum Network Using Genetic Algorithm	61
Scientific Literacy Learning Activities in the Modulus of Elasticity for Science High School Students Using an Experimental Setup to Measure Tensile Stress and Strain of Solid Wires With a Dial Gauge	71
Simple Protocol to Create a Single Photon Source by Using BBO from Spontaneous Parametric Down-Conversion Process in BBO	81
The Effect of Pouring Temperature and Stirring Speed Onto Mechanical Behaviour of Al-MMCs Composite Alloys	89
SESSION B-BIOLOGICAL SCIENCES	
Antibiofilm Effects of Biosurfactants from Lactobacillus fermentum on Escherichia coli Biofilm and Remineralization of Hydroxyapatite	95
Developing Prediction Model for the Preoperative Diagnosis of Ovarian Cancer Using Tumor Marker, Complete Blood Count and Liver Function Tests	105
Efficacy of Royal Jelly for Inhibition of Free Radical and Herpes Simplex Virus Type 1 Infection	113
In Vitro Anti-Cancer Effects of Pharmacological Ascorbate Against Glioblastoma	121
Study the Combination Effects of Ursolic Acid Encapsulation in PLGA/CS Nanoparticles in Breast Cancer Cells	131
Synthesis, Characterization, And in Vitro Study of Riboflavin-Functionalized Superparamagnetic Iron Oxide Nanoparticles in Breast Cancer Cells	139

Title	Page
The Expression of Wuhan and XBB.1.5 N-Terminal Domain (NTD) and Receptor Binding Domain (RBD) Proteins in Escherichia coli (E. coli)	149
The First Record of Multi-Male Mating Behavior of Ornate Flying Snake, Chrysopelea Ornate at Pha-Gnan and Samui Islands, Thailand	156
The Investigation of 'Phatumthani 1' Rice Rhizosphere-fungal Composition Under Commercial Organic Fertilizer and Chemical Fertilizer Treatments	164
SESSION C-CHEMISTRY (ORGANIC & MEDICINAL CHEMISTRY)	
Design and Synthesis of Novel Benzimidazole-Triazole Derivatives for Evaluation of Antioxidant Activity	174
Structural Modification of Chrysin and Their Alpha-Glucosidase Inhibitory Activity	180
Synthesis of Rhinacanthin Related Derivatives as Alpha-Glucosidase Inhibitors	188
SESSION D-MATHEMATICS / STATISTICS / COMPUTER SCIENCE / DATA SCIENCE / AI	
A Note on Fuzzy Semibipolar Soft Ideals in Ordered Groupoids	195
Application of Line Chatbots to Support It Maintenance Tasks	206
Mathematical Model for Heat Transfer in Corrugated Box With Bc Flute.	215
The Development of Program for Determining the Optimal Route for Taking the Phothong Bus in Phuket	221
The Probability Distribution of Flight Departure Delays at Chiang Mai International Airport	230
The Study of Awareness of Child Car Restraint Compliance and the Prediction of Parents' Intention to Use in Thailand	241
Using Augmented Reality Technology in Learning Statues Depicting a Thai Massage (Nuad Boran) in Wat Pho	248
Utilizing Cloud Computing for Efficient Management of Blockchain-Based Judging Competitions in Taekwondo Poomsae	258
SESSION E-ENERGY / ENVIRONMENTAL & EARTH SCIENCE / MATERIALS SCIENCE / CHEMICAL TECHNOLOGY	
Application of the XRF Core Scanner to Assess the Environmental Changes in Southern Thailand	269
Caffeine Removal From Wastewater Using Copper/Carbon/Silica Nanocomposite as Adsorbent	275
Enhancing Ocean Literacy Through Whale Watching: A Case Study of the Gulf of Thailand	282
Petrography and Geochemistry Characteristics of Limestone, Ban Dan Chang Sub-District, Na Klang District, Nong Bua Lamphu Province	294
Strength Reduction Factor of Block in Matrix and Weathered Sandstone Slopes	302
Survey of Information on the Management of Agricultural Waste From Oil Palm Gardent and the Use of Palm Oil Branch as an Alternative Fuel for Clay Brick Burning	311

Title	Page
SESSION F-FOOD SCIENCE AND TECHNOLOGY/AGRICULTURAL SCIENCE	
Development of a Healthy Spread With Riceberry Rice and Black Garlic	319
The Antihyperglycemic Effects of Microencapsulated Kluai Tani (<i>Musa balbisiana</i>) Fruit Extract in the Instant Drink Powder	330
SESSION SP5: ENVIRONMENTALLY FRIENDLY RUBBER AND ITS FUTURE	
Piezoresistive Behavior of Flexible Strain Sensors Based on Natural Rubber Composites: Effects of Sensor Shapes and Dimensions	339
POSTER PRESENTATION	
SESSION A-PHYSICS / APPLIED PHYSICS	
Developing an Experimental Instrument to Measure the Apparent Magnitude of Stars	348
Modeling Gas Detection Utilizing One-Dimensional Photonic	357
The Fabrication and Refractive Index Measurement of Diy Acrylic Convex Lenses	363
SESSION B-BIOLOGICAL SCIENCES	
A Comparative Bioinformatics Study of Pila Protein From <i>Burkholderia mallei</i>	372
Antibacterial Green Synthesized Silver Nanoparticles and Transdermal Patch Applications	379
Characterization of a Dihydrofolate reductase From <i>Leptospira interrogans</i>	385
Combined Toxicity of Imidacloprid and Glyphosate on Aquatic Oligochaetes (<i>Tubifex tubifex</i> Muller, 1774)	392
In Silico Drug Repurposing for Satellite Cell Differentiation Promoting Drug(s) Targetting Activin Type II B Receptor	403
In Silico Screening of Novel GSK3B Inhibitors for Promoting Cell Proliferation	410
Isolation and Characterization of Bacteriophage Against Antibiotic Resistant <i>Campylobacter jejuni</i>	417
Lichens Family Physciaceae and Caliciaceae the Public Parks in Bangkok Thailand	428
Morphological and Molecular Identification of Pathogenic <i>Acanthamoeba</i> spp. in Water and Soil Sources Associated With Human Activities in 3 Provinces of Southern Thailand	434
N, N, N-trimethyl Chitosan Nanoparticle (TMC NP) is an Effective Vehicle in Delivery of SARS-CoV-2 Protein into Lung Cells	443
Partial Purification and Characterization of Canthaxanthin From Green Alga <i>Tetraspora</i> sp. CU2551	452
Phylogenetic Analysis of <i>Plasmodium knowlesi</i> Isolates From Clinical Samples in Southern Thailand: Perspective From Mitochondrial Cytochrome B and Merozoite Surface Protein-1 Gene	460

Title	Page
Plasmid and Host Identification for Cloning and Expression of CD163 SRCR5-6	468
Screening of Compounds That Can Alleviate Toxicity of Alpha-Syn Using the Developed Yeast-Based Assay	477
Searching for Peptides With Mushroom Tyrosinase Inhibition Activity in the Fermented Unpolished Black Rice Sap	484
Sequencing Analysis of Indel Marker in Local Rice Varieties From South Thailand	492
Short Chain Fatty Acids Derived from Probiotic Lactobacillus Strains Inhibit the Accumulation of Lipids in 3T3-L1 Adipocytes	497
Structure Determination and Kinetic Properties of ATP sulfurylase From Durian Durio zibethinus	504
The Role of Lectin Domain in Spike Proteins of SARS-CoV-2 and SARS-like CoV	509
SESSION C-CHEMISTRY (ANALYTICAL CHEMISTRY)	
Preparation and Application of Intelligent Films Incorporated With Natural Anthocyanin Extract for Tracing Sea Food Spoilage	519
SESSION C-CHEMISTRY (INORGANIC CHEMISTRY)	
Efficient Magnetic Composite: AC, NiAl-LDO and Fe ₃ O ₄ for Removing Malachite Green and Eriochrome Black T Dyes in Water	528
Iron(III) Oxide Photocatalyst Supported on Silica Derived From Rice Husk for Degradation of Methylene Blue Dye Under Visible Light	537
Photo-Fenton Degradation of Rhodamine B Dye Solution by Fe(IO ₃) ₃ /FeOOH Under Visible Light Irradiation	543
SESSION C-CHEMISTRY (ORGANIC & MEDICINAL CHEMISTRY)	
Aporphine Alkaloids From the Leaves of Alphonsea elliptica	550
Coumarin and Acridone Alkaloid Derivatives From the Stems of Citrus hystrix	557
One-Pot Synthesis of 4-aryl-1,2-naphthoquinones and 2-aryl-1,4-naphthoquinones	562
Total Phenolic Content, Free Radical Scavenging Activities and Cytotoxicity of a Leaf Extract and Its Fractions From Chrysophyllum cainito	569
Utilization of Fruit Peel Extracts From Punica granatum and Nephelium lappaceum for Green Synthesis of Silver Nanoparticles and Their Impact on Staphylococcus Epidermidis Inhibition	576
Alpha-Glucosidase Inhibitory Activity of Extracts From Mitragyna speciosa Leave	586
SESSION C-CHEMISTRY (PHYSICAL & THEORETICAL CHEMISTRY)	
Crystal Violet Adsorption by Modified Surface Coffee Grounds Activated Carbon	591
Screening Potential Compounds From Mitragyna speciosa (Korth.) for Inhibition Acetylcholinesterase and COX-2 by Molecular Docking Technique	598

Title	Page
SESSION D-MATHEMATICS / STATISTICS / COMPUTER SCIENCE / DATA SCIENCE / AI	
Graceful Labeling of Some the Ring Sum Graphs and the Bistar Related Graphs	606
Recording Water Consumption and Dental Fluorosis Among Children in High Fluoride Areas in Northern Part of Thailand by Geographic Information Technology	612
The Center Coloring of Corona Product of Paths	618
SESSION E-ENERGY / ENVIRONMENTAL & EARTH SCIENCE / MATERIALS SCIENCE / CHEMICAL TECHNOLOGY	
Adsorption of Hydrogen Sulfide Contained in Biogas Using Biomass Power Plant Ash as an Adsorbent	625
Adsorption Study of Amoxycillin by Surface Modification of Granular Activated Carbon	630
CaCu ₃ Ti ₄ O ₁₂ Ceramic: High Dielectric Permittivity and Extrinsic and Intrinsic Origins	637
Dam Leakage Detection Using Electrical Resistivity Survey at Huai Fang Noi Reservoir, Chom Thong, Chiang Mai, Thailand	644
Experimental Heat Treating of Amethyst From Uruguay	651
Geology and Geochemistry of the Ban Nong Khrok Hot Spring Touristic Attraction, Phrao District, Chiang Mai Province for Sustainable Geotourism Potential Evaluation	659
Groundwater Characteristics and Chemistry of the Saline Area in Ban Thum, Khon Kaen Province	669
Hydrogen Sulfide Removal of Durian Peel Biochar for Biogas Cleaning	679
Mineralogy and Alteration of Pak Pat Volcanic Rocks in Nam Pat District, Uttaradit Province, Northern Thailand	686
One-Step Synthesis of Sugarcane Bagasse Ground-Based Microporous Carbon Using KOH as an Activation Agent for CO ₂ Adsorption.	694
SESSION F-FOOD SCIENCE AND TECHNOLOGY/AGRICULTURAL SCIENCE	
Characterization of Pectin From Durian Rind Using Steam Exposure	701
Microwave-assisted Extraction of Carotenoids in Palmyra Palm Meat by Using Different Vegetable Oils as Solvent	708
SESSION SP2-2: THAI TRADITIONAL MEDICINE: FROM TRADITIONAL USE TO COMMERCIALIZATION RHODOMYRTUS TOMENTOSA (AITON) HASSK AND MITRAGYNA SPECIOSA (KORTH) HAVIL	
Evaluation of Antioxidant Activity and Total Phenolic Content of Different Mitragyna Speciosa Strains in Thailand	715

ORAL PRESENTATION



SESSION A-PHYSICS / APPLIED PHYSICS

A STUDY OF POST-WELD LASER CLEANING ON 304 STAINLESS STEEL

Khanittha Sawaddee,^{1,*} Phumiphat Kittiboonanan,⁴ Polsin Taechamaneesatit,⁴ Phil Marinier,^{2,3} Amarin Ratanavis^{1,3}

¹Department of Industrial Physics and Medical Instrumentation, Faculty of Applied Science,

²International College,

³Lasers and Optics Research Center, Science and Technology Research Institute, King Mongkut's University of Technology North Bangkok

⁴Pondpol Group of Companies

*e-mail: khanittha.sawaddee@gmail.com

Abstract:

Post-weld laser cleaning on 304 stainless steel is demonstrated by using a pulse fiber laser operating at 1064 nm with pulse duration of 100 ns. The laser fluences were varied to examine the performance of the laser cleaning. Laser fluences between 0.88 J/cm² and 3.5 J/cm² can remove oxides and contaminants. A laser surface structuring process was observed at laser fluences higher than 3.5 J/cm².

Introduction:

Laser cleaning for industry applications is well known as a promising technological advance that is capable to improve production output.¹ Laser systems offer an advantage that can be integrated into production lines. Laser cleaning can be considered as an alternative to the traditional cleaning methods such as mechanical cleaning and the use of chemical solvents, reducing the cost and minimizing environmental impact of toxic or hazardous materials.² Laser cleaning can therefore facilitate the reuse of products or materials, which has additional beneficial environmental implications.

Laser cleaning in welding applications has been an area of interest.^{3,4} The pre-weld laser cleaning is a promising process to achieve excellent welding quality.⁵ This pre-weld cleaning process eliminates contamination that would result in the formation of porosities in the welds.⁶

During the welding process, an oxide layer and surface contaminants are produced.⁷ These can introduce problems with coating adhesion for painted parts.^{8,9} Therefore, a post-weld laser cleaning can be an excellent candidate to provide the surface preparation.

This work reports our study in laser cleaning of a post-welding surface, 304 stainless steel, using a nanosecond pulse laser. The 304 stainless steel is widely used in industrial, household, equipment production, and architectural paneling applications.¹⁰ This study aims to investigate the laser fluences and laser pulse repetition rates that will be suitable for laser removal of the oxide layer and contaminants generated by the Metal Inert Gas welding (MIG) process.

Methodology:

Samples of 304 stainless steel with dimensions of 1 cm x 2 cm x 0.1 cm (thickness) are welded together by MIG welding. MIG welding uses Carbon Dioxide (CO₂) gas as shielding. **Figure 1.** shows the experimental setup with welded samples. The post-weld samples are then cleaned using a fiber laser system, cleanLASER, CL50 model. This laser system provides a laser wavelength of 1064 nm with a laser pulse duration of 100 ns. The laser powers are varied from 10-50 W. The laser repetition rates are varied between 50 and 200 kHz. The images of the sample surface were recorded using an optical microscope and a

Scanning Electron Microscope (SEM) both before and after laser treatment. It should be mentioned that the laser treatments were performed with a suction unit consisting of High Efficiency Particulate Air (HEPA) and carbon filters.

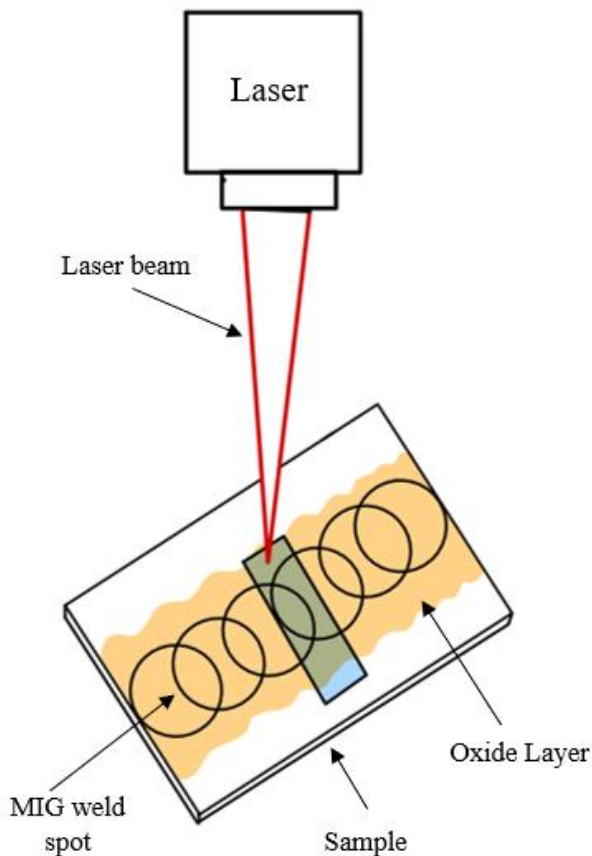


Figure 1.
Experimental setup

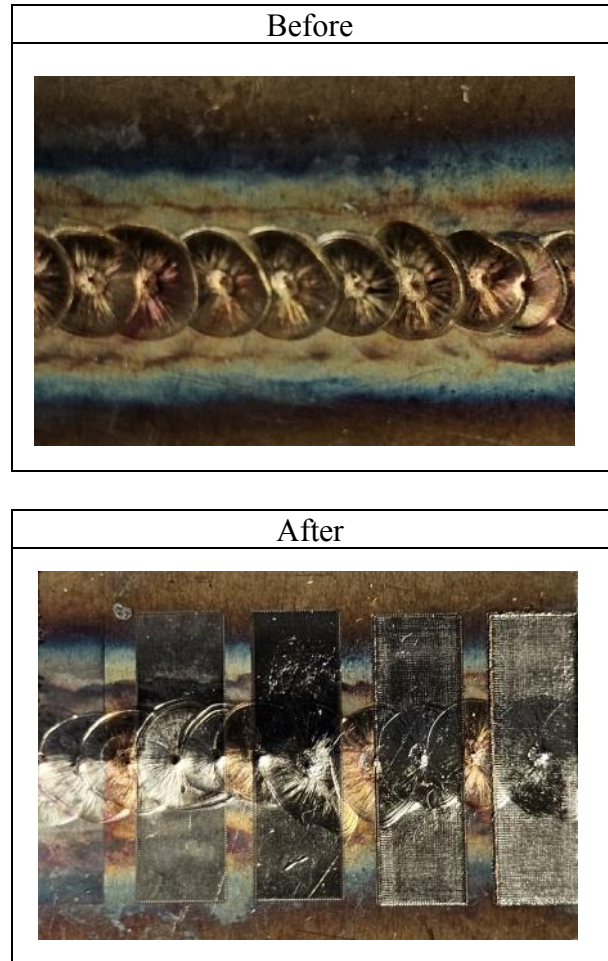
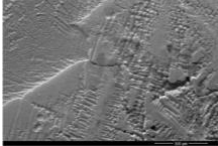
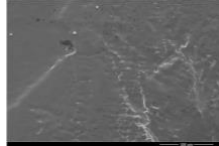
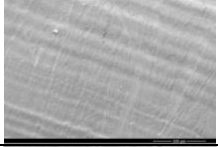
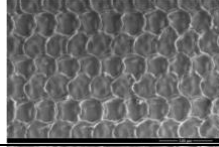

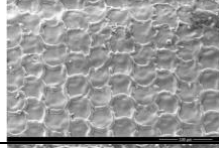
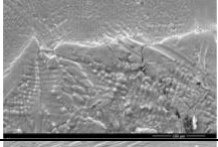
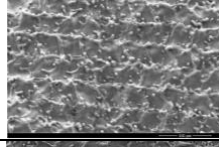
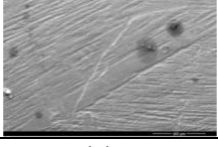
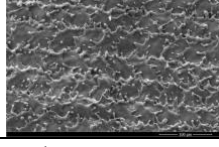


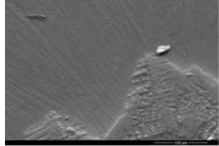
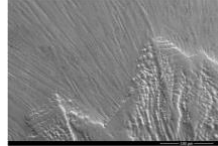
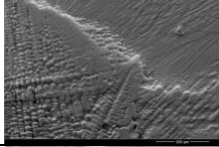
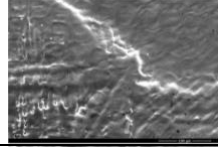
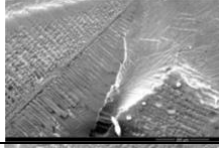
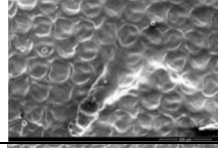
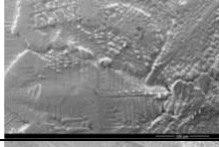
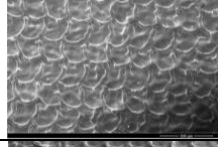
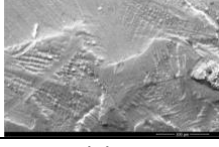
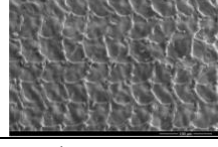
Figure 2.
Images of the welds before and after the laser cleaning process with a laser repetition rate of 200 kHz at different power settings resulting in various fluences.

Results and Discussion:

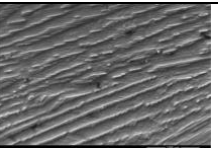
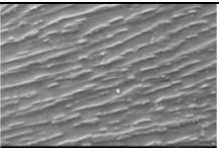
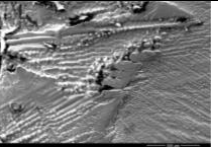
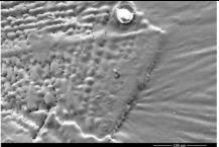
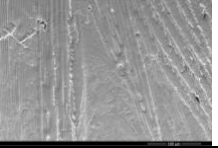
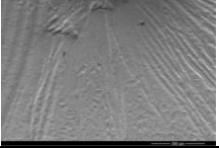
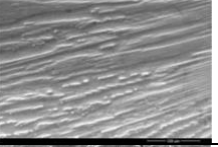
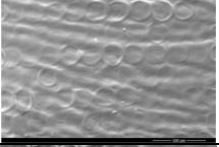
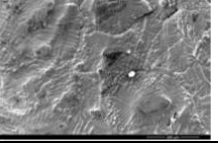
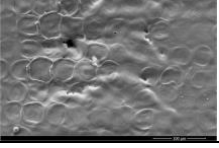
Figure 2. shows images of welded samples before and after laser treatment. Surface cleaning by laser was successful at all investigated laser powers and repetition rates. As an example, the laser repetition rate of 200 kHz can clearly be seen to remove the surface oxides and contaminants from the welded sample surface, even at the lowest tested laser fluence (0.88 J/cm^2).

$F(J/cm^2)$	Before	After
3.52		
7.04		
10.56		
14.08		
17.60		

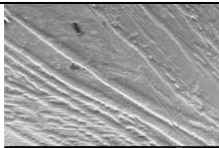
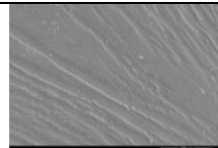
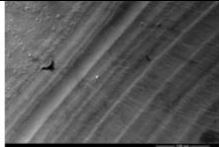
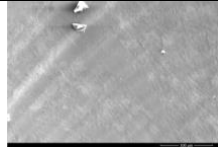
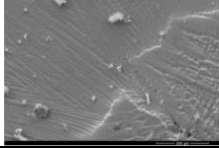
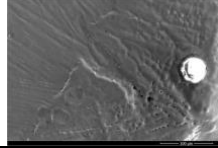
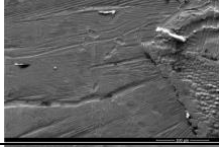
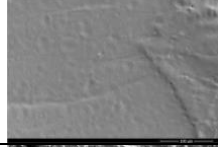
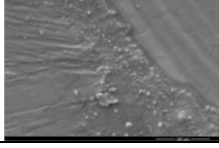
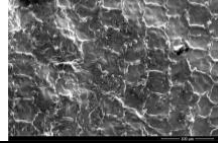
(a) Repetition rate of 50 kHz

$F(J/cm^2)$	Before	After
1.76		
3.52		
5.28		
7.04		
8.80		

(b) Repetition rate of 100 kHz

$F(J/cm^2)$	Before	After
1.16		
2.32		
3.48		
4.64		
5.80		

(c) Repetition rate of 150 kHz

$F(J/cm^2)$	Before	After
0.88		
1.76		
2.64		
3.52		
4.40		

(d) Repetition rate of 200 kHz

Figure 3.

SEM images of the welds before and after the laser cleaning process with varying laser repetition rates.

The laser cleaned surfaces were further examined using a SEM to investigate the surface characteristics after cleaning. For high laser fluence, starting at around 4.4 J/cm^2 , the laser treatment not only cleans the surface of any deposits, but it also can be observed to create surface structures, as can be clearly seen in SEM images as shown in **Figure 3**. Laser fluences below 3.5 J/cm^2 can be used to clean welded surfaces without the appearance of surface texturing. However, when the laser fluences become more than 3.5 J/cm^2 , regular surface roughness becomes apparent. As the fluence increases, and the energy per pulse increases proportionally, the appearance of the surface structure changes, to a more irregular pattern. This irregular surface structure can most clearly be seen in **Figure 3. (a)** at 17.60 J/cm^2 . The explanation for the 3.5 J/cm^2 fluence threshold, and for the change in appearance of the surface structures at higher fluences, is most likely related to the heat capacity and heat conductance of 304 stainless steel. These results suggest that fluences below the 3.5 J/cm^2 threshold do not transfer enough energy to the steel to exceed the heat capacity locally. Since the heat conductance of steel is high, that energy is most likely able to dissipate sufficiently before the next pulse. However, at higher fluences, the energy transfer is higher than the local heat capacity and eventually also exceeds the ability of the steel to conduct the heat away from the vicinity of the laser pulse. This build-up of heat can possibly explain the existence of the surface structures, as well as the change to a more irregular appearance of the surface structures at the highest fluences. If the metal reaches high enough temperatures, it will melt and run. Phase change or temper change effects of the steel may also contribute to the type of structures that form at different fluences.

The laser cleaning at low fluences will be suitable for applications that rely on a smooth surface finish.¹¹ However, when the laser surface structuring begins to dominate the laser cleaning at high laser fluences, the surface structuring results can be useful for applications related to adhesive purposes.¹² Different fluences will result in different surface structures that may be appropriate as a method of surface preparation for different types of coatings.

Conclusion:

Laser cleaning of post weld samples (304 stainless steel) was demonstrated using a pulse fiber laser operating at the wavelength of 1064 nm. The laser fluences are varied by changing the laser powers and laser repetition rates. The laser cleaning can be achieved at the fluences below 3.5 J/cm^2 . Above this fluence, laser structuring will be introduced onto the cleaned surface, causing different types and patterns of surface structures.

Acknowledgements:

This research was supported by Lasers and Optics Research Center, Science and Technology Research Institute, King Mongkut's University of Technology North Bangkok and the Pondpol Group of Companies.

References:

1. Razab M, Noor A, Jafar M, et al. Journal of radiation research and applied sciences. 2018; 11.4: 393-402.
2. Zhou K, Sang S, Wang C, et al. Journal of Physics: Conference Series. IOP Publishing. 2022; 012075.
3. Wei P, Chen Z, Wang D, et al. Materials Letters. 2021; 291: 129549.
4. Kim J, Kim P, Lee J, et al. Applied Sciences. 2021; 11.24: 11832.
5. Zhub L, Sun B, Li Z, et al. Welding in the World. 2020; 64: 1715-1723.
6. Deng J, Zhao G, Lei J, et al. Materials. 2022; 15.16: 5469.
7. Shia T, Wanga C, Mia G, et al. Journal of Manufacturing Processes. 2019; 42: 60-66.
8. Shamsujjoha M, Agnew S, Melia M, et al. Surface and Coatings Technology. 2015; 281: 193-205.
9. Yoo H, Park H, Kim J, et al. Optics & Laser Technology. 2023; 163: 109434.
10. Li X, Wang D, Gao J, et al. Materials. 2020; 13.23: 5363.
11. Hirmaz M. International Journal of Scientific & Engineering Research. 2019; 10.7: 1065-1073.
12. Li X, Huang T, Chong A, et al. Opto-electronic engineering. 2017; 44.3: 340-344.

A TONER-PRINT REMOVAL FROM PAPER USING LONG PULSED LASERS

Kanokwan Homdee,^{1,*} Phil Marinier,^{2,3} Amarin Ratanavis^{1,2}

¹Department of Industrial Physics and Medical Instrumentation, Faculty of Applied Science,

²Lasers and Optics Research Center, Science and Technology Research Institute,

³International College, King Mongkut's University of Technology North Bangkok, Thailand

*e-mail: Chong.Kanokwan@gmail.com

Abstract:

In this study, the use of long pulsed laser radiation at 1064 nm and 1320 nm with pulse widths of 5 to 40 ms was investigated to remove black printer toner from the surface of paper. The laser wavelength of 1064 nm was seen to be more efficient for the removal process than the wavelength of 1320 nm due to its higher absorption. The shortest pulse width of 5 ms was most effective across all investigated fluencies. Approximately 70% reduction of black color was achieved; however, a yellow-brown discoloration is observable on the paper, especially at higher fluences, due to the photo-thermal effect.

Introduction:

As the world attempts to move away from using plastic, paper products are become more popular. Paper is able to naturally decompose and so has less environmental impact than plastic, which is not considered to be biodegradable. However, as the use of wood products has increased steadily through the recent decades, there has been a corresponding increase in environmental impact from deforestation.^{1,2} Sustainable use of wood requires proper forest management so that the trees have enough time to grow to maturity. Paper production from wood also requires a lot of energy, creating further environmental impact.^{3,4} In fact, the pulp and paper industry is ranked as the fourth largest industrial energy user globally, accounting for approximately 6% of global industrial energy use and 2% of direct industrial carbon emissions.⁵ The industry has also been found to emit other pollutants and greenhouse gases, such as Total Volatile Organic Compounds (TVOC), formaldehyde (HCHO), hydrogen sulfide (H₂S), and hydrocarbon compounds (C_xH_y).⁶ There are additional significant life cycle emissions and pollutants associated with the use of paper, especially from the transportation process and the landfill or incineration process.⁷

A partial solution to the environmental impact associated with using paper would be recycling of paper products, however, this would only slightly reduce impact since the production step, whether from recycled material or from wood pulp, is the most energy intensive part of the entire process.^{8,9} The most efficient way to reduce this impact would therefore be the reuse of paper, however, once both sides of a piece of paper have been used, there is currently no way to continue using the paper without recycling. A proposed solution is unprinting, or the removal of printer toner from paper so that it can be reused.

Numerous research studies for unprinting technologies have been reported.¹⁰ Current research focuses on diluting the toner, obscuring existing toner,¹⁰ and the removal of printer toner by solvents, abrasion, ablation, or combinations thereof.^{11,12} Many of these methods do result in reusable paper but also have many limitations, including leftover traces of the original printing, thinning of the paper or other types of deterioration of the paper quality, and large amounts of chemical waste. A laser removal process for printer toner would avoid any chemical waste or chemical or mechanical deterioration of paper quality. This type of process will therefore be investigated in this paper.

High power lasers operating in UV, Visible, and Infrared wavelengths are attractive for toner removal applications. Laser removal of printer toner using Nd:YAG laser pulses has been demonstrated using laser fluencies between 0.3 and 0.9 J/cm².¹³ Laser emission at the wavelength of 532 nm with 4 ns pulse duration was reported as a good candidate for toner removal.¹⁴ In addition, ultrashort pulse lasers was attempted to be used as a tool to remove toner.¹⁵ This work will therefore study the effect of infrared long pulse laser in the magnitude of milliseconds for toner removal. The laser wavelengths used in this study are 1064 nm and 1320 nm. A scanning electron microscope is used for evaluating the removal process. Colorimetric parameters such as absolute changes of color, yellowing, and lightness of sample after laser irradiation are also analyzed.

Methodology:

The toner samples used in the investigation were based on single characters. A series of character-sized black rectangles was printed with an HP LaserJet CF226A-X-XC printer using black toner on white, un-coated, 80 g/m² paper. A Nd:YAG laser system (Laser model: COSJET SR Long-Pulsed 1320 nm & 1064 nm Nd:YAG Laser) with the emission wavelengths at 1064 nm and 1320 nm was used in the experiment. A single laser pulse was used with durations of 5, 10, 20, 30 and 40 milliseconds and a laser spot size of 2 mm. The images of the samples treated by laser beam were taken by using an optical microscope and a scanning electron microscope. The treated samples were also analyzed using a colorimeter, 3nh NH300.

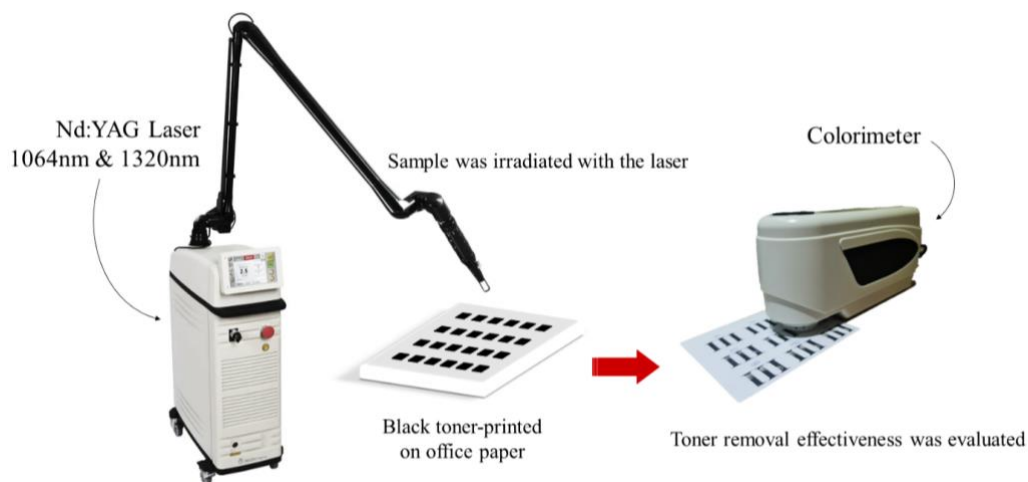


Figure 1.
Experimental Setup

Results and Discussion:

Figure 2. and **Figure 3.** show images of the toner after laser irradiation taken by a camera (Samsung Galaxy Note 20 Ultra). It is evident that the long pulse lasers at wavelengths of both 1064 nm and 1320 nm can effectively remove the toner from the paper. Research indicates that the energy absorption capacity of a 1064 nm laser is higher compared to a 1320 nm laser when used on black soiling on paper.^{16,17} This is consistent with the results of this study, where the laser wavelength of 1064 nm (**Figure 2**) shows better removal results of black toner than the 1320 nm laser treatment (**Figure 3**), especially at higher fluences. Both figures also clearly show a yellow-brown discoloration effect at higher pulse widths. This surface discoloration is similar to results seen by Strilč, M. et al.¹⁷ who found that this

discoloration was caused by thermolytic reactions and can be mitigated by allowing the substrate to cool to minimize heat transfer to the paper. During toner removal, longer pulse widths at the same fluence would allow more heat to be transferred to the substrate resulting in discoloration, therefore these results are consistent. Visually, there seems to be little difference in toner removal between fluences when using a 5 ms pulse, although the effect of fluence will be investigated further below.

The 5 ms pulse width showed the best results across both wavelengths, in terms of removal of toner and minimization of discoloration. This pulse width was therefore used for the next experiments.

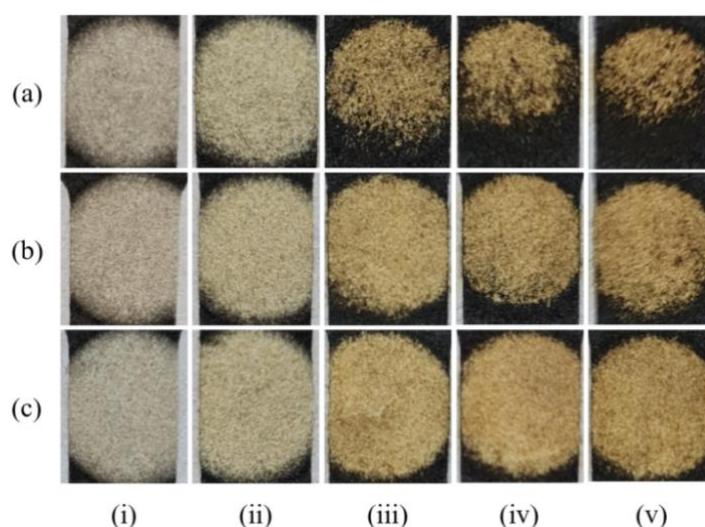


Figure 2.

Images of samples treated by different pulse durations and fluences at 1064 nm. The samples were irradiated at pulse durations of (i) 5 ms, (ii) 10 ms, (iii) 20 ms, (iv) 30 ms, and (v) 40 ms, and at fluences of (a) 120 J/cm², (b) 150 J/cm² and (c) 180 J/cm².

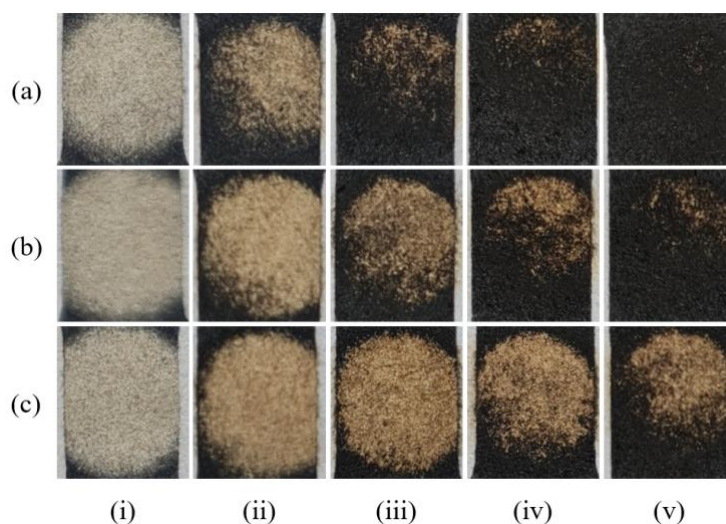


Figure 3.

Images of samples treated by different pulse durations and fluences at 1320 nm. The samples were irradiated at pulse durations of (i) 5 ms, (ii) 10 ms, (iii) 20 ms, (iv) 30 ms, and (v) 40 ms, and at fluences of (a) 120 J/cm², (b) 150 J/cm² and (c) 180 J/cm².

The effect of fluence was investigated by irradiating toner samples at fluences of 90 J/cm², 150 J/cm², and 300 J/cm² using a single 5 ms pulse. The samples were examined with an optical microscope and the results are shown in **Figure 4**. It can be seen that the lowest fluence of 90 J/cm² was the least effective at removing toner. However, there is little visual difference between the results at fluences of 150 J/cm² and 300 J/cm², especially at a wavelength of 1064 nm, even though the highest fluence is double that of the middle fluence. The higher removal of toner when using 1064 nm also suggests that this wavelength may be more efficient.

The optical microscope results indicate that the toner has penetrated some distance into the rough surface of the paper, which suggests a possible explanation for why removal of toner using surface cleaning methods has difficulty in removing all visible marks. The toner closest to the surface is removed while the toner further down into the structure of the paper is shielded by paper threads. The remaining toner also appears to be located at the ends of paper threads, or around single strands, suggesting that toner in these areas may be bonded more strongly to the paper, increasing the difficulty of removal without damage to the paper substrate.

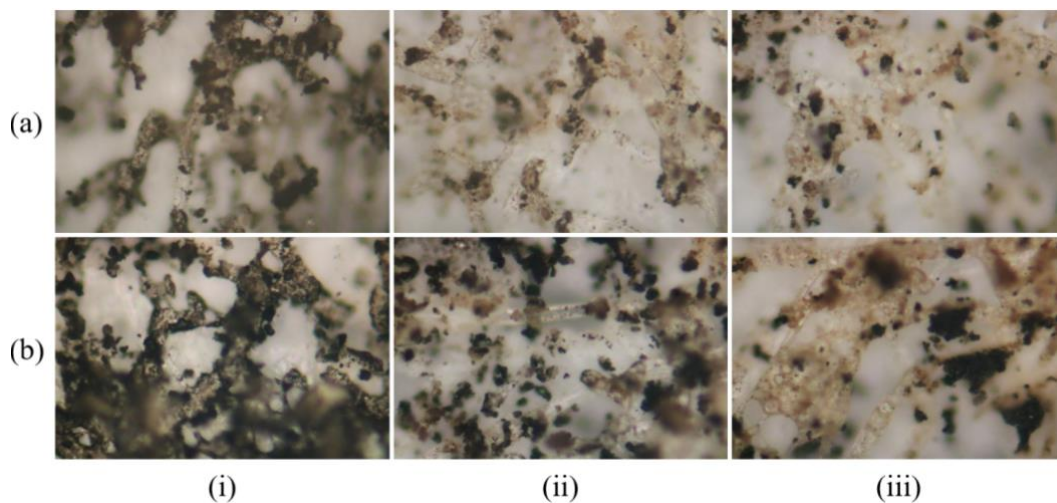


Figure 4.

Optical microscope images of samples irradiated by laser at wavelengths (a) 1064 nm and (b) 1320 nm. The experiments are carried out at (i) 90 J/cm² (ii) 150 J/cm² and (iii) 300 J/cm².

Figure 5(a) and **5(b)** shows scanning electron microscope (SEM) images of blank paper and black toner printed on paper respectively. **Figure 5(c)** and **5(d)** shows the SEM images of the paper samples irradiated with 1064 nm and 1320 nm lasers at a fluence of 150 J/cm² with a 5 ms pulse. At this fluence, the effectiveness of the 1064 nm laser over the 1320 nm is clearly observable. However, some remaining toner in both samples is also observable.

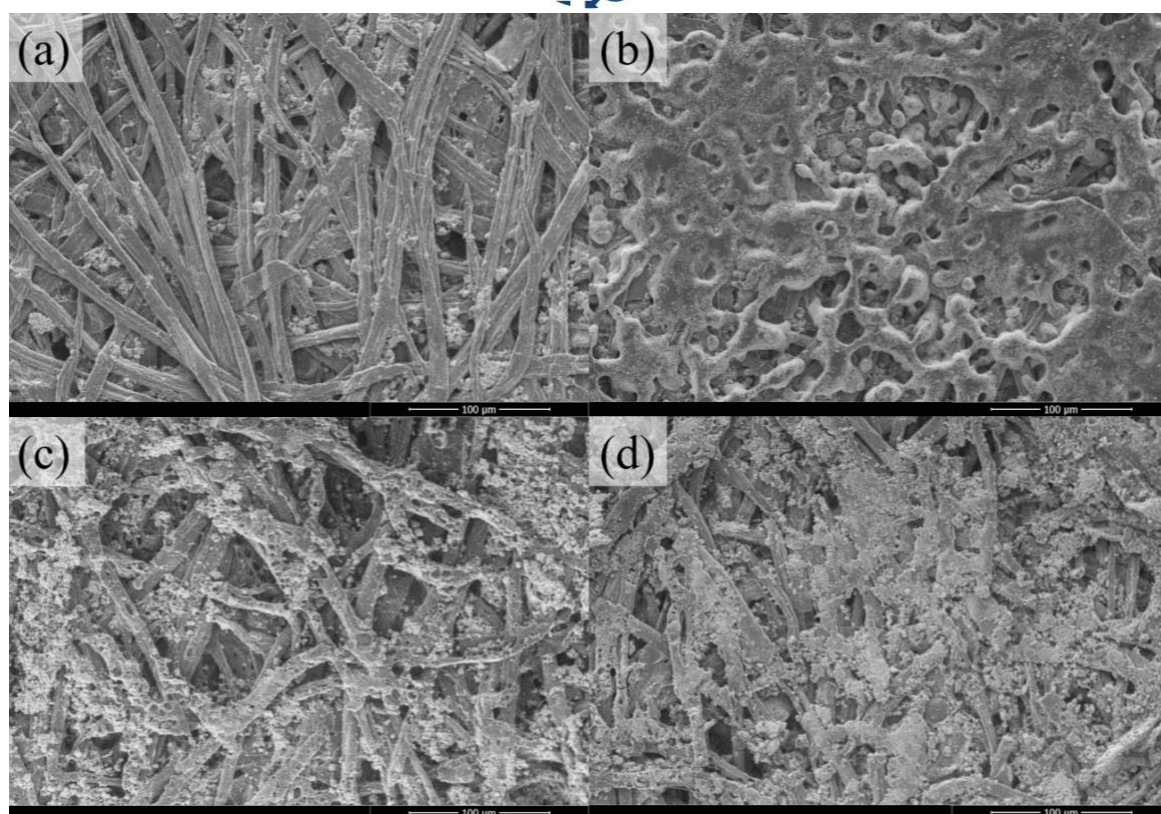


Figure 5.

SEM images of (a) blank paper, (b) toner printed on paper, and toner laser irradiated at a fluence of 150 J/cm² and a 5 ms pulse with (c) 1064 nm and (d) 1320 nm laser light.

The effect of fluence was further investigated by comparing scanning electron microscope images of samples irradiated with a pulse width of 5 ms at fluences of 120 J/cm² to 210 J/cm². As can be seen in **Figure 6(a)**, **6(b)**, **7(a)** and **7(b)**, fluences of 120 J/cm² remove less toner than fluences of 150 J/cm² or higher. However, simply increasing the fluence does not always result in additional removal of toner. For a wavelength of 1064 nm, fluences of higher than 150 J/cm² do not appear to remove additional toner at all, although the samples at higher fluences do appear to have higher instances of surface pitting, as seen in **Figure 6(c)** and **6(d)**, suggesting damage to the substrate. For a wavelength of 1320 nm, there are still many areas of contiguous toner deposited on the paper at a fluence of 150 J/cm², but at 180 J/cm², more toner appears to have been removed and there are no longer any areas of contiguous toner deposit, as seen in **Figure 7(c)**. The higher fluence of 210 J/cm² in **Figure 7(d)** does not seem to remove additional toner. These results confirm that a wavelength of 1320 nm is less efficient at removing toner and so requires a higher fluence to achieve similar levels of toner removal. These results also demonstrate that there is an upper limit of fluence where toner removal no longer occurs and pitting or other damage to the paper substrate increases. This upper limit is higher for a wavelength of 1320 nm since that wavelength is less readily absorbed by the black toner.

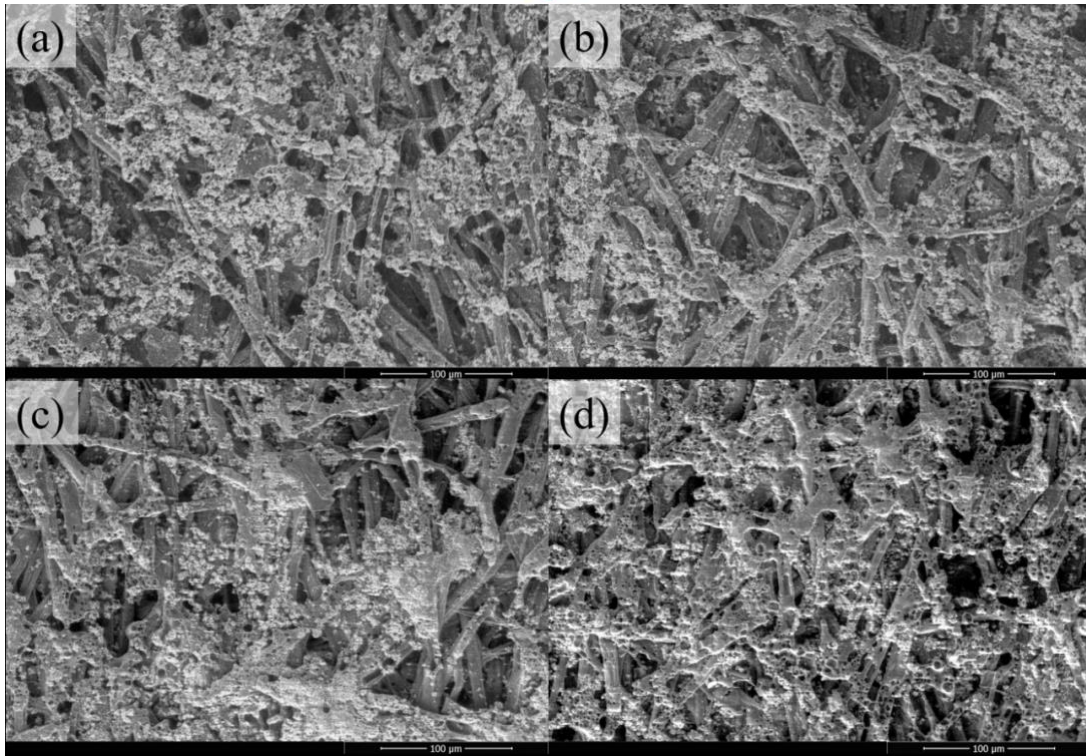


Figure 6.

SEM images of the laser irradiated at wavelength 1064 nm and a pulse width of 5 ms with fluences of (a) 120 J/cm², (b) 150 J/cm², (c) 180 J/cm² and (d) 210 J/cm².

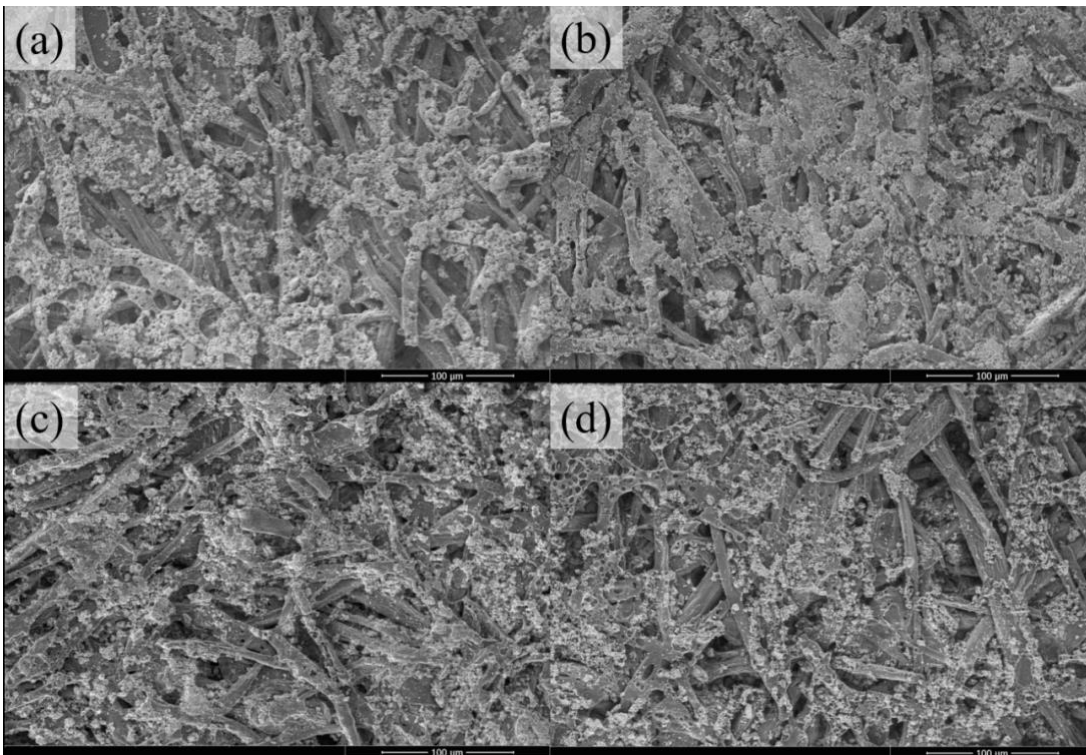


Figure 7.

SEM images of the laser irradiated at wavelength 1320 nm and a pulse width of 5 ms with fluences of (a) 120 J/cm², (b) 150 J/cm², (c) 180 J/cm² and (d) 210 J/cm².

In addition, colorimetric measurements using the LAB color space were performed on toner-printed paper after toner removal with the 1064 nm and 1320 nm lasers and 5 ms pulse width at fluences ranging between 60 and 300 J/cm². The colorimetric parameters in **Figure 8.** and **Figure 9.** are the L*, a*, and b* values of the LAB colors model. The parameter L* refers to the lightness of the color (with values of L* = 0 for black and L* = 100 for white). The parameter a* determines green and magenta tones (negative values indicate green while positive values indicate magenta). The parameter b* presents the yellow and cyan colors in a sample (negative values indicate cyan while positive indicates yellow).

It can be seen from both figures that there is an increasing yellow + magenta color component as fluence increases. This would result in the yellow-brown discoloration which can be seen visually in **Figures 2.** and **Figures 3.** The only result with little to no discoloration was at a fluence of 60 J/cm² and wavelength of 1320 nm. However, this sample also had minimal toner removal, with less than 35% black color removal (**Figure 9.**). As toner removal increases, the yellow-brown discoloration also increases for both wavelengths. The optimal fluence for removal of black color while also minimizing the yellow + magenta color component is 150 J/cm² for a wavelength of 1064 nm and 180 J/cm² for a wavelength of 1320 nm. Beyond these values, black color removal plateaus while discoloration continues to gradually increase. The plateaus at 150 J/cm² and 180 J/cm² are confirmed by the SEM images in **Figures 6.** and **Figures 7.**

The yellow-brown discoloration effect after laser removal has been discussed elsewhere.^{17,18} The photo-thermal process occurs when the IR pulse laser transfers energy to the substrate which introduces discoloration and accelerated aging of the cellulose of the paper.^{13,17,19,20} The increased pitting seen on paper fibers at higher fluences in **Figures 6.** and **Figures 7.** also supports the conclusion that higher fluences are damaging the substrate, further supporting the conclusion that substrate damage is producing the observed discoloration.

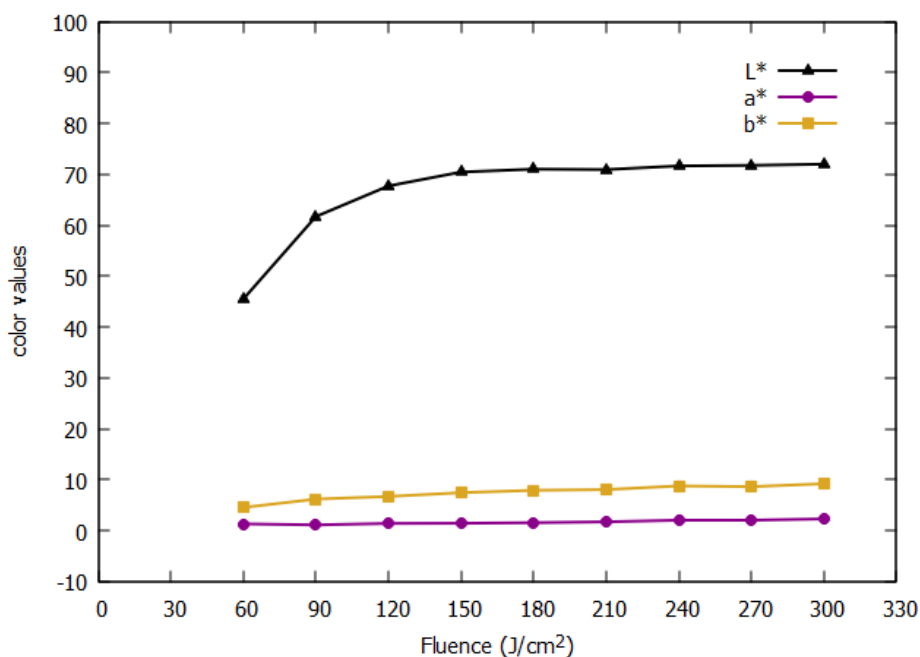


Figure 8.

LAB color graph of samples irradiated with the 1064 nm laser at fluence ranging of 60-300 J/cm².

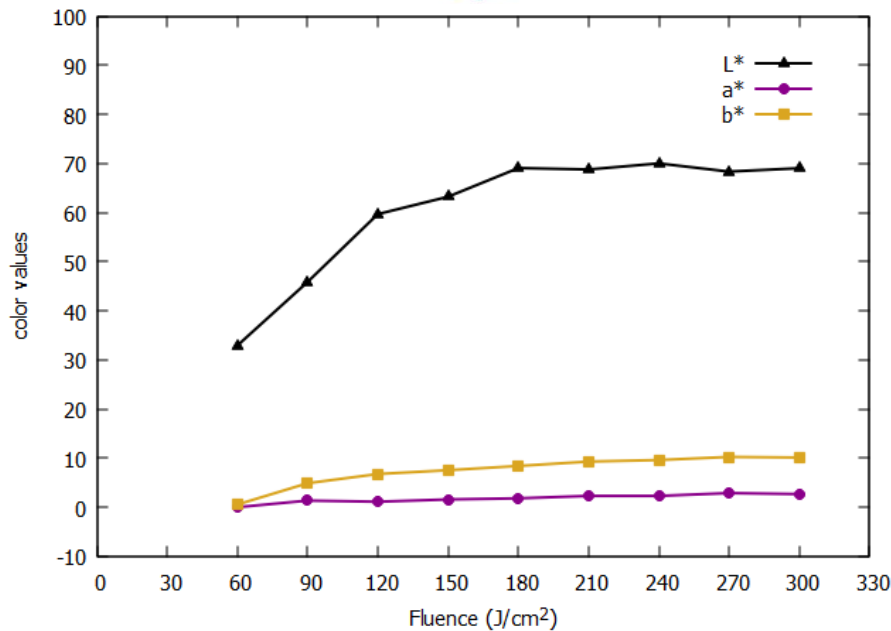


Figure 9.

LAB color graph of samples irradiated with the 1320 nm laser at fluence ranging of 60-300 J/cm².

Conclusion:

Laser toner removal was studied by using laser wavelengths of 1064 nm and 1320 nm. The laser removal process is possible, where the wavelength of 1064 nm using a 5 ms pulse width shows the best removal results. A fluence of 150J/cm² produces the best results at that wavelength, with higher fluences all showing very similar removal levels of approximately 70% removal of black color. A yellowing effect of the paper appears to be inevitable at conditions that can effectively remove the toner due to the photo-thermal process and heat transfer to the substrate.

Acknowledgements:

This work was totally supported by Lasers and Optics Research Center (LANDOS), Science and Technology Research Institute, King Mongkut's University of Technology North Bangkok.

References:

1. Carle, J. & Holmgren, P. Forest Prod. J. 2008;58(12):6–18.
2. Forestry Economics and Policy Division. (2009). The State of the World's Forests 2009 (62-96). Italy: FAO.
3. Allwood, J. M., Ashby, M. F., Gutowski, T. G., & Worrell, E. Resources, Conservation and Recycling. 2011;55:362-381.
4. Subak, S. & Craighill, A. Mitigation and Adaptation Strategies for Global Change. 1999;4:113–135.
5. Furszyfer Del Rio, D.D., Sovacool, B.K., Griffiths, S., Bazilian, M., Kim, J., Foley, A.M., & Rooney, D. Renewable and Sustainable Energy Reviews. 2022;167:112706.
6. Xin, T., Shen, W., Chen, X., & Corriou, J. P. Journal of Cleaner Production. 2018;198:1066-1075.



7. Counsell, T. A. M. & Allwood, J. M. Resources, Conservation and Recycling. 2007;49:340–352.
8. Hekkert, M. P., Reek, J., Worrell, E., & Turkenburg, W. C. Resources, Conservation and Recycling. 2002;36:241–266.
9. Martin, N., Anglani, N., Einstein, D., Khrushch, M., Worrell, E., & Price, L. K. (2000). Opportunities to improve energy efficiency and reduce greenhouse gas emissions in the U.S. pulp and paper industry. No. LBNL-46141. Berkley, USA: Ernest Orlando Lawrence Berkeley National Laboratory.
10. Counsell, T. A. M. & Allwood, J. M. Journal of Materials Processing Technology. 2006;173:111–123.
11. Counsell, T. A. M. & Allwood, J. M. Wear. 2009;266:782–794.
12. Counsell, T. A. M. & Allwood, J. M. Proc. R. Soc. A. 2009;465:3839–3858.
13. Kaminska, A., Sawczak, M., Cieplinski, M., Sliwska, G., & Kosmowski, B. Optica Applicata. 2004;34:121–132.
14. Leal-Ayala, D. R., Allwood, J. M., & Counsell, T. A. M. Appl Phys A. 2011;105:801–818.
15. Leal-Ayala, D. R., Allwood, J. M., Schmidt, M., & Alexeev, I. Proc. R. Soc. A. 2012;468:2272–2293.
16. Pagès, H., Piombini, H., Enguehard, F. & Acher, O. Optical Society of America. 2005;13:7.2351-2357
17. Strlič, M. et al. Appl. Phys. A. 2005;81:943–951.
18. Carter, H. A. Journal of Chemical Education. 1996;73(11):1068.
19. Ihori, H., Inagawa, Y., Ito, N., Fujii, M., & Ninomiya, M. IEEJ T. Fund. Mat. 2012;129(4):205–210.
20. Kolar, J., Strlič, M., & Marincek, M. Appl. Phys. A-Mater. 2002;75:673–676.



APPLICATION OF LOW COST AND LOW PRECISION LASER-SCRIBED CAPACITOR SENSORS

Jidapa Lumpapiwat^{1,*}, Wuttichai Putchana^{1,3}, Phil Marinier^{2,3}, Amarin Ratanavis^{1,3}

¹Department of Industrial Physics and Medical Instrumentation, Faculty of Applied Science,

²International College, ³Lasers and Optics Research Center, Science and Technology Research Institute, King Mongkut's University of Technology North Bangkok, Thailand

*e-mail: jidako22@gmail.com

Abstract:

A low precision and low-cost application of laser scribed reduced Graphene Oxide (rGO) sensors is presented in this paper. Various capacitor patterns are scribed onto Graphene Oxide (GO) touch sensors using a homemade CNC device equipped with a low power diode laser operating at 405 nm. A keypad was constructed and tested to demonstrate this concept. It was shown that precision in the scribing process and in the angles and spacing of the capacitor patterns is not required to produce a reliable keypad, demonstrating that this low-cost approach is feasible.

Introduction:

This research is a continuation of studies about the diverse applications for using Graphene Oxide (GO). The optical absorption properties of GO have been applied as an optical component,¹ saturable absorber medium,² and in Q-switching lasers.³ Furthermore, reduced Graphene Oxide (rGO) has led to applications in sensing devices due to its unique moderate electrical conduction.^{4,5} To produce rGO, laser-induced reduction has been proposed as a simple and chemical-free process that can be performed at room temperature.⁶ The various previous applications of rGO fabricated by laser-induced reduction are reported,^{7,8} especially, the use of rGOs as capacitors that can be further used in sensing devices⁹ and medical applications.¹⁰ However, most of these applications rely on high precision laser scribing, using precision CNC and expensive, high power lasers.

In this work, rGO is produced by a laser scribing method. A low power diode laser in the order of 60 milliwatts is used. This laser is attached to a homemade CNC to serve as a simple and economic setup for laser scribing. This approach is extremely economical, but sacrifices some precision. To demonstrate the feasibility of this concept, a simple keypad is used as an example. A keypad has been used to test properties of higher power precision laser-scribed rGO in other research¹¹. The laser-scribed rGO is used to create capacitors with differing capacitance values that can be assigned to each key on the keypad. Each key will be inscribed with a different capacitor pattern. This will be used to test whether precision in the spacing and angle of the capacitor patterns is necessary for a low-cost sensor setup. This approach can be suggested as a method to achieve functional low-cost sensing results.

Methodology:

Figure 1. shows the circuit diagram for the GO keypad. The design of the keypad is illustrated in **Figure 2.(a)**. Overhead projector slides were used for the construction of the keypad template. The numbers and symbols for the keypad were printed on a single sheet. A hole was made in this sheet at the touch location for each key. Copper tape was used to make the circuit wiring, which was attached to the back of this first plastic slide, as shown in **Figure 2.(b)**. A second plastic sheet was attached onto the back of the first sheet to protect the wiring and to serve as a substrate for the GO to form each key. The assembled template is shown in **Figure 2.(c)**.

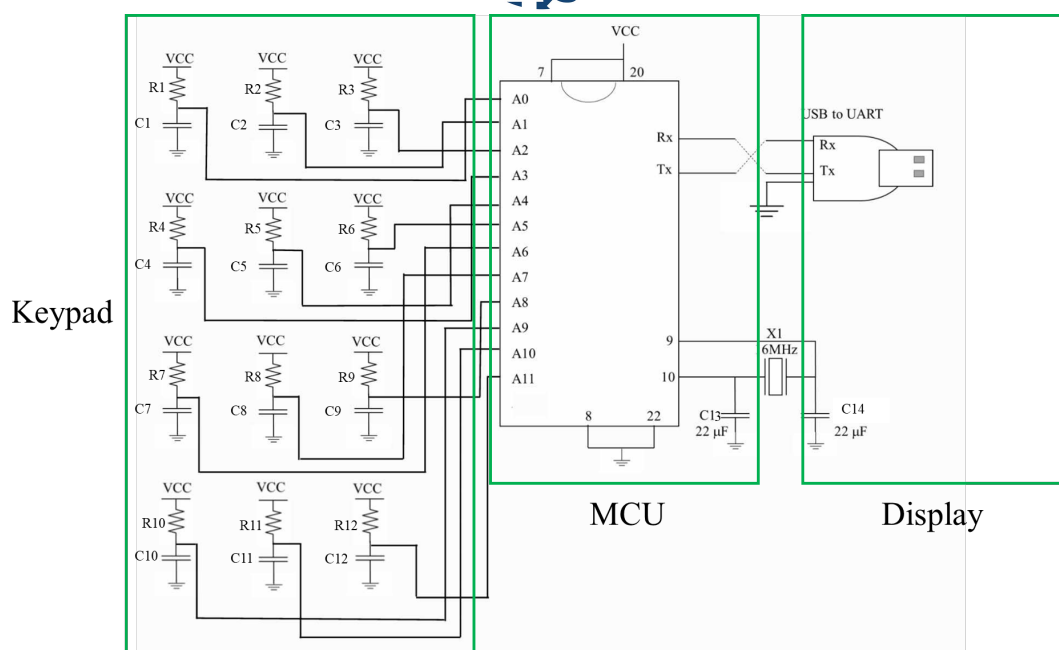


Figure 1.
The circuit diagram for the rGO keypad.

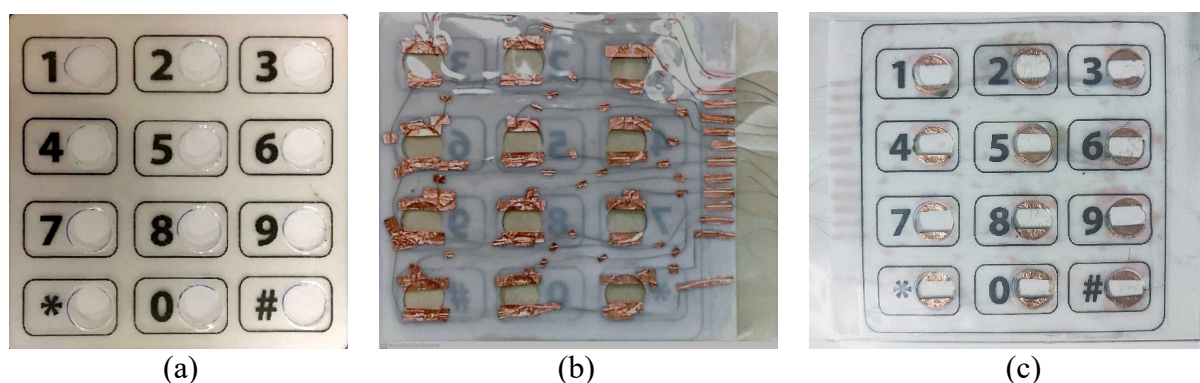


Figure 2.

The construction of the keypad: (a) the keypad layout printed on a plastic projector slide, (b) the copper tape circuit wiring on the back of the slide and (c) the assembled keypad template.

GO films were prepared by dropping 5 w% GO into the prepared holes in the assembled template, as seen in **Figure 3**. The GO solution was purchased from a GO producing company (Goographene, Merrifield, VA, USA). GO films with thicknesses between 1 mm and 2 mm were formed and then were allowed to dry in room temperature. The GO covers the ends of the copper tape wiring, completing the circuit for each key, as seen in **Figure 4**. Finally, the GO is scribed using the laser scribing system seen in **Figure 5**. A CNC system was constructed to move the laser beam in two dimensions. A low-cost diode laser operating at 405 nm was purchased and attached to the CNC device. The CNC is controlled by a computer program, LaserGRBL. The measured laser power output was $57.34 \text{ mW} \pm 1.44 \text{ mW}$.

Each key is inscribed with a unique pattern to provide different capacitances when assigning values to each key, as seen in **Figure 6**. (a). The spacing and angle of the patterns was varied across each of the 12 keys. These patterns were imported to the LaserGRBL

program (**Figure 6. (b)**). Since reduced graphene oxide is conductive, the laser-scribed rGO lines will function as electrodes. When the capacitor is touched, the overall capacitance between the laser-scribed electrodes will increase because of the high dielectric constant of the human body¹². These unique patterns will produce a wide degree of difference in the capacitance values of each key.

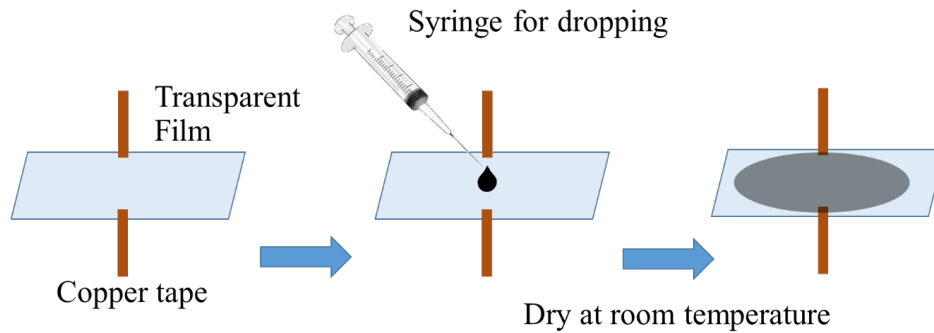


Figure 3.

The steps of producing the GO film on the transparent substrate.



Figure 4.

The GO film on the wired keypad before scribing.

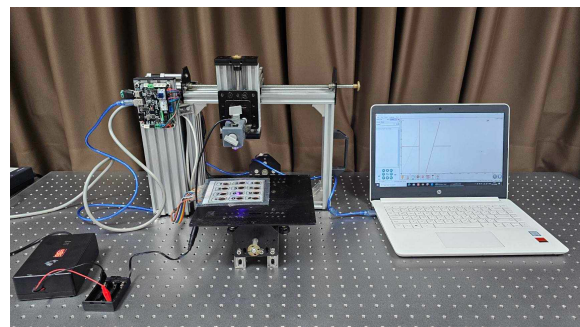
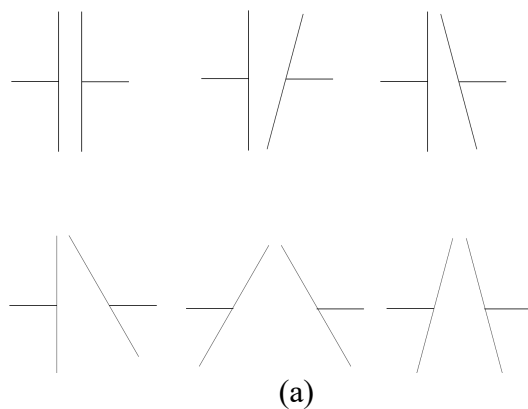
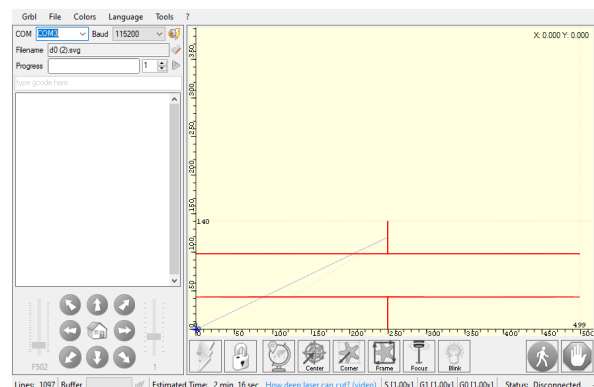


Figure 5.

Laser scribing system



(a)



(b)

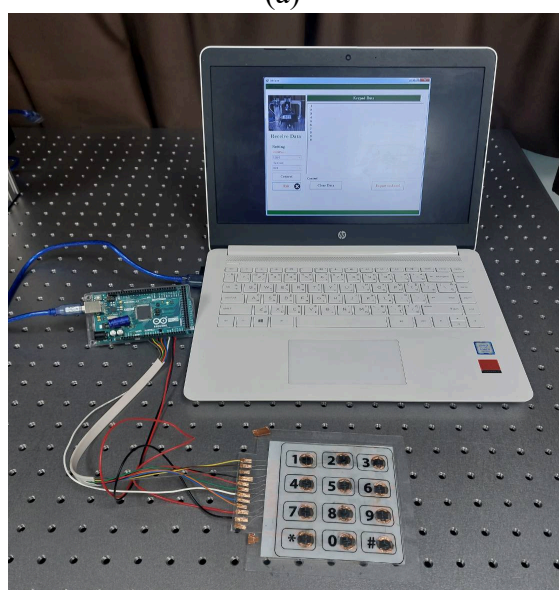
Figure 6.

Capacitor patterns (a) design and (b) exported to the CNC program.

Figure 7.(a) shows the final keypad setup. The variety of laser-scribed patterns provides different capacitance values for each key. The keys are connected to an Arduino mega2560 which can measure the capacitance of each key, as seen in **Figure 7.(b)**.

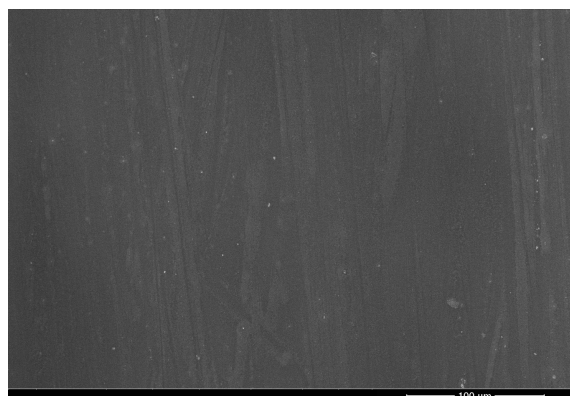


(a)

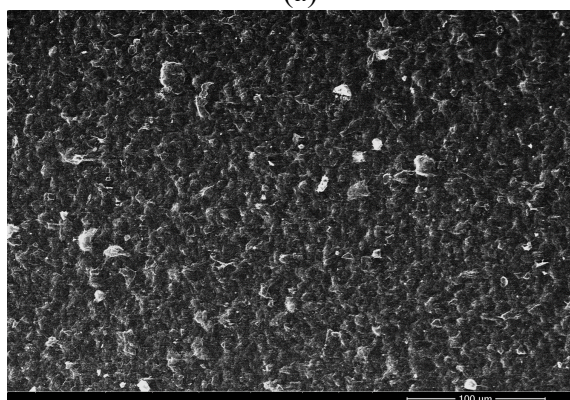


(b)

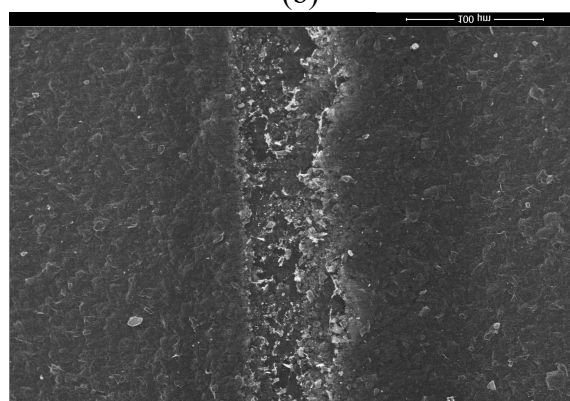
Figure 7.
(a) Final keypad setup and (b) final experimental setup.



(a)



(b)



(c)

Figure 8.
SEM images (a) transparent plastic film (b) GO on the transparent film and (c) portion of rGO obtained by the laser scribing process.

Results and Discussion:

Figure 8. shows examples of Scanning Electron Microscope (SEM) images of the plastic substrate and the GO film both before and after the laser reduction process.

The line of the rGO from the laser scribing can be clearly seen in **Figure 8. (c)** as well as darker zones on either side of the rGO line. These darker lines are most likely the result of heat transfer from the laser scribing process. It can also be seen that the rGO line is not consistent in width. This is a result of the fluctuation of the power output of the diode laser, as well as micro vibrations from the CNC machine. This means that the capacitance of each laser-scribed key will always include some inherent randomness because of the lack of precision and consistency in the components of the low-cost setup.

The capacitances of the fabricated capacitors were measured using a multi-meter. The capacitance values are between 3.5 μF and 8.5 μF and are assigned to the keys as shown in **Figure 9**. Unexpected, it can be seen that many of the capacitance values are similar to each other. For example, '1' and '6' both show nearly identical capacitances of 8.5 μF . This similar capacitance is not caused by being inscribed with the same capacitor pattern. While '1' and '6' do have the same scribed pattern, '9' and '*' are also scribed with a similar pattern (as seen in **Figure 7. (a)**) but have significantly lower capacitances. In fact, some keys with different patterns show very similar capacitances, such as '4' and '5'. This result can be explained by the inherent randomness in the low precision manufacturing of the laser-scribed keys. This suggests that the pattern used in the laser scribing process does not play a crucial role in determining the final capacitance of each key since the imprecision and randomness of the low cost setup creates far larger capacitance differences.

The capacitance when touched also appears to be random, although some keys still have very similar capacitances when touched, irrespective of the pattern used in scribing, such as '3' and '#' (**Figure 9.**). This requires each individual key to be tested and assigned one at a time. This low-cost method does require addition time and care when assigning values to each sensor. However, the time and cost savings associated with using low precision methodology makes this method appropriate for low volume applications.

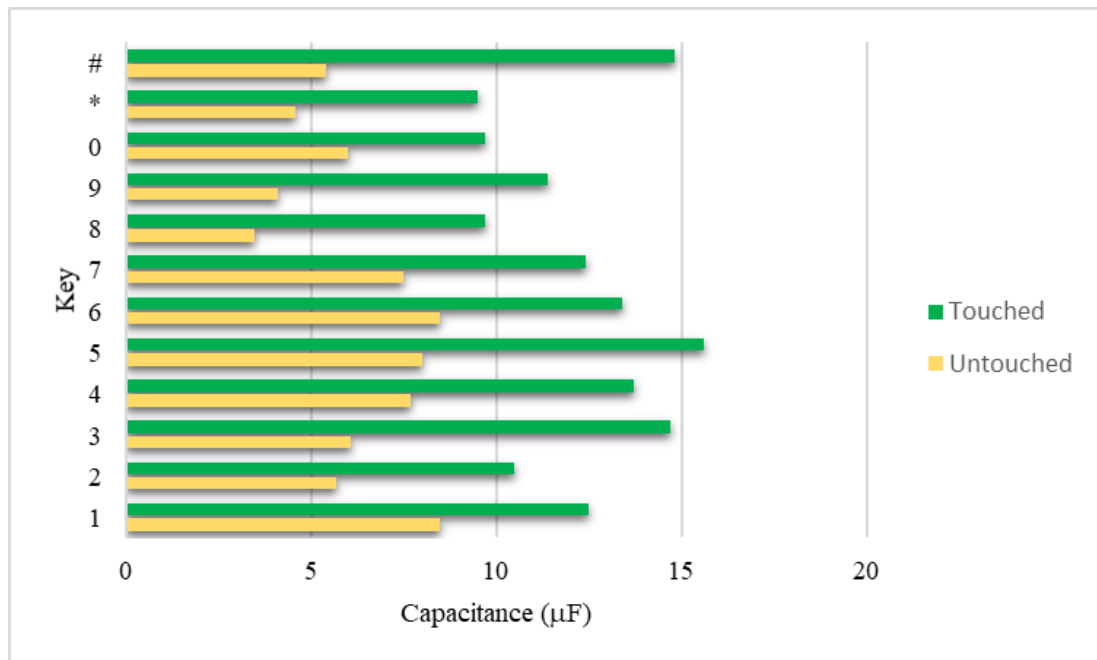


Figure 9.
Touched and untouched capacitance of each rGO scribed key.

The accuracy of the keypad was tested by using the group of numbers “1234567890”. All the keys were successfully detected and correctly assigned to the corresponding numbers, as seen in **Figure 10**.

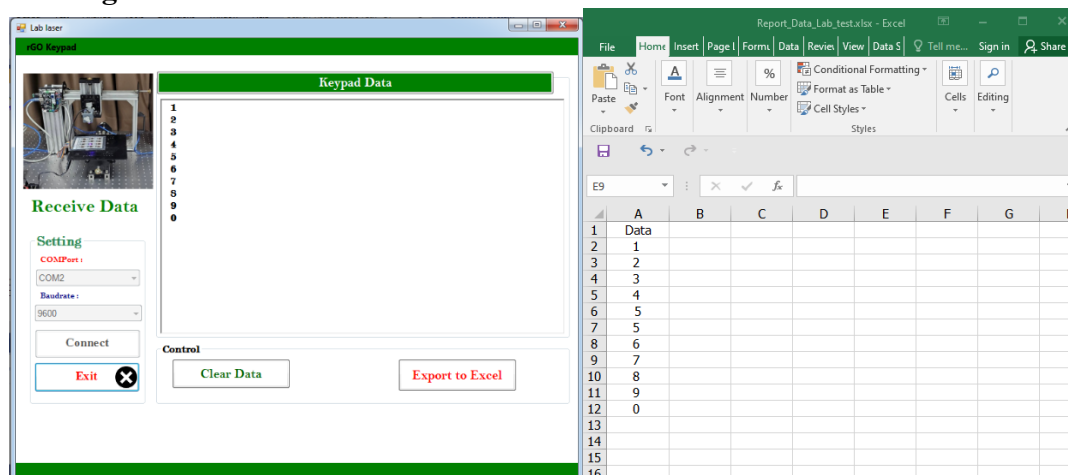


Figure 10.

The final test output of the rGO keypad.

Conclusion:

A simple laser-scribed rGO system using a low-power diode laser operating at 405 nm was demonstrated. The capacitance values of the laser-scribed rGO capacitors are between 3.5 μF and 8.5 μF . The laser power fluctuation and the vibration of the homemade CNC provided a degree of randomness, resulting in different capacitances before and after being touched. The accurate use of these capacitors in a keypad demonstrates the usefulness of these rGO capacitors as low-cost sensors.

Acknowledgements:

This research was supported by Lasers and Optics Research Center, Science and Technology Research Institute, King Mongkut's University of Technology North Bangkok.

References:

1. Wu J, Jia L, Zhang Y, et al. *Advanced Materials*. 2021;33:1-29.
2. Ng E. K., Lau K. Y., Lee H. K, et al. *Optical Materials*. 2020;100:109619.
3. Zaca-Morán P., Gomez C. L., Morán O. Z, et al. *Heliyon*. 2023;9:1-8.
4. Thejas R., Naveen C. S., Khan M. I., et al. *Biomass Conversion and Biorefinery*. 2022;1-11.
5. Zeng Y., Li T., Yao Y., et al. *Advanced Functional Materials*. 2019;29:1-7.
6. Rowley A., Stehle Y., Kilby L., et al. *Journal of Carbon Research*, 2023;9:1-8.
7. Scroccarello A., Álvarez-Diduk R., Della Pelle F., et al. *ACS sensors*. 2023;8:598-609.
8. Ouda E., Yousf N., Morsy M., et al. *Journal of Materials Science: Materials in Electronics*. 2022;33:18241-18251.
9. Park R., Kim H., Lone S., et al. *Sensors*. 2018;18:1-15.
10. Zhao L., Rosati G., Piper A., et al. *ACS Applied Materials & Interfaces*. 2023;15:9024-9033.
11. Kumar P. S., Goel S. *Diamond and Related Materials*. 2021;120:1-10.
12. Qing X., Chen Z. N., See T. S. P., et al. *IEEE*. 2010;10:1-4.

ASSESSING THE INFLUENCE OF PHYSICAL DISTANCING AND FACE MASK USAGE ON RESPIRATORY VIRUS TRANSMISSION: A MATHEMATICAL MODELING STUDY

Thanchanok Lincharoen,^{1,*} Noppamas Yolai,¹ Chayanin Sararat,¹ Sudarat Chartsuthi,² Anuwat Wiratsudakul,³ Charin Modchang^{1,4,5,*}

¹Biophysics Group, Department of Physics, Faculty of Science, Mahidol University, Bangkok 10400, Thailand

²Department of Physics, Research Center for Academic Excellence in Applied Physics, Faculty of Science, Naresuan University, Phitsanulok 65000, Thailand

³Department of Clinical Sciences and Public Health, and the Monitoring and Surveillance Center for Zoonotic Diseases in Wildlife and Exotic Animals, Faculty of Veterinary Science, Mahidol University, Nakhon Pathom 73170, Thailand.

⁴Centre of Excellence in Mathematics, MHEI, Bangkok 10400, Thailand

⁵Thailand Center of Excellence in Physics, Ministry of Higher Education, Science, Research and Innovation, 328 Si Ayutthaya Road, Bangkok 10400, Thailand

*e-mail: thanchanok.lin@student.mahidol.edu, charin.mod@mahidol.edu

Abstract:

Acute respiratory tract infections pose significant global health challenges, which are the primary source of morbidity and mortality and have an impact on healthcare systems, as exemplified by the recent COVID-19 pandemic. This crisis has highlighted the urgent need to comprehend the factors that influence airborne transmission of respiratory viruses. Preventative measures, including face masks and physical distancing, have been crucial to pandemic management. In this study, we applied a mathematical modeling approach and Monte Carlo simulations to investigate the specific influence of such measures on the transmission of respiratory viruses. Simulations were conducted in indoor environments, considering face mask compliance and physical distancing. We found that wearing a face mask and keeping a greater distance between individuals can reduce the probability of infection with the respiratory viruses. Particularly, the risk of infection is more effectively reduced when infected people wear face masks compared to only applying on susceptible individuals. Furthermore, the risk of infection notably decreases when all individuals wear face masks and keep a greater distance from each other in an indoor space. Our modeling results suggest that promoting mask usage and physical distancing in indoor environments is crucial in mitigating the spread of respiratory viruses.

Introduction:

Respiratory viruses are viruses that primarily infect the respiratory tract, which includes the nose, throat, lungs, and bronchial tubes. There are many types of respiratory viruses, for example, influenza viruses, respiratory syncytial viruses (RSV), and adenoviruses. Notably, in December 2019, the emergence of severe acute respiratory syndrome coronavirus 2 (SARS-CoV-2) led to the global COVID-19 pandemic¹. During this devastating outbreak, over 700 million confirmed cases and more than 6 million fatalities were recorded². People who become infected with SARS-CoV-2 have had a wide range of symptoms ranging from mild symptoms to severe symptoms. Symptoms may appear 2-14 days after exposure to the virus.

Respiratory viruses are typically transmitted through contact with respiratory secretions, often via coughing or sneezing of infected individuals. They can also be spread through contact with contaminated surfaces or objects. In general, respiratory viruses are transmitted between individuals when the virus is released from an infected person's respiratory tract and transferred through the environment³. Respiratory viruses can be transmitted via respiratory secretions via multiple independent and concurrent routes, both directly through physical contact and indirectly through contact with contaminated surfaces or objects. Additionally, the viruses can be transmitted through the air from one respiratory tract to another via large respiratory droplets (droplet transmission) or fine respiratory aerosols (airborne transmission)³.

Efforts to reduce the transmission of respiratory viruses include various measures, such as physical distancing, the use of face masks, and maintaining proper hand hygiene. Face masks, when worn correctly, have been shown to significantly decrease the risk of acquiring respiratory infections, according to Cheng et al. (2021)⁴. Physical distancing is another effective strategy for limiting transmission⁵. Nonetheless, the precise impact of these interventions, particularly within indoor environments, remains a subject of ongoing investigation.

This study aimed to explore the influence of physical distancing and face mask usage on the transmission of respiratory viruses in indoor settings. To achieve this, we employed a mathematical modeling approach in tandem with Monte Carlo simulations. We evaluated the effectiveness of maintaining distance from others and wearing face masks in mitigating the spread of respiratory viruses, shedding light on their potential contributions to reducing transmission rates.

Methodology:

Study setting and design.

The default setting used for investigating the effect of physical distancing and face mask-wearing is the square room with a size of $8 \times 8 \times 3 \text{ m}^3$. This room accommodates 25 occupants, comprising 24 susceptible individuals and one infected person. It was assumed that the distances between each individual were equal and symmetric (Figure 1).

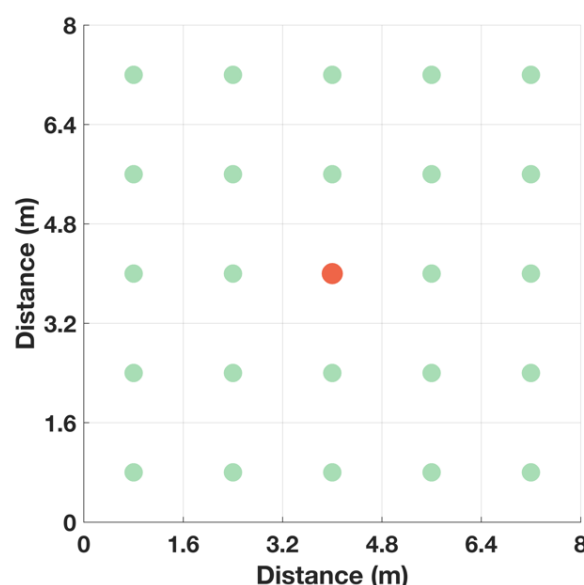


Figure 1. Top view of the study setting. The room measures $8 \times 8 \text{ m}^2$, with the infected individual located at the room's center.



To determine the effect of physical distancing, we adjusted the distance between individuals while keeping the number of individuals in the room fixed. Consequently, the room size was hypothetically increased. Our study was conducted in two distinct room sizes: 64 (8x8) m², representing a typical classroom size as per Ministry of Education guidelines⁶, and 144 (12x12) m², resembling a restaurant area⁷. In both scenarios, there were 25 individuals present. We maintained the assumption of equal and symmetric spacing between individuals within each setting, resulting in two different interpersonal distances: 1.6 meters and 2.4 meters, respectively.

Surgical masks are a commonly employed infection control measure⁸, and as such, our study has chosen to focus specifically on this type of mask to investigate their impact on the transmission of respiratory viruses. Our research explores four distinct face mask strategies within our model: no masks (with no individuals wearing masks), wearer protection (where only susceptible individuals wear masks), source control (with only infected individuals wearing masks), and universal masking (where everyone wears masks). Wearing face masks offers the advantage of reducing the infiltration of virus particles from infected individuals to susceptible ones. This is demonstrated by the penetration rate, which quantifies the potential for virus particles to pass through the mask. When infected individuals wore masks, the quantity of exhaled viruses from their bodies significantly decreased. The data regarding the face mask penetration rate was sourced from Cheng et al.'s 2021 study⁴.

To estimate the probability of infection, we used the model proposed by Cheng *et al.* (2021)⁴, which provides a framework to estimate the number of exhaled and inhaled viruses. A comprehensive description of this model and its components is provided in the subsequent sections, beginning with estimating the number of exhaled and inhaled viruses and then using the inhaled viruses to estimate the probability of infection. Furthermore, Monte Carlo simulations were used to simulate the risk of respiratory virus transmission.

Estimating the exhaled viruses

Exhaled virus referred to viral particles that were released from an infected individual's respiratory system when they exhaled. For an estimate of the probability of infection, we first estimated the number of exhaled viruses. In this work, we used the virus concentration in the particles ($C_{v,fluid}$), representing the viral load in each particle size to calculate the number of viruses in exhaled respiratory particles. We assumed a spherical shape with diameter D_p to represent the size of respiratory particles. Therefore, the number of viruses in exhaled respiratory on particles ($N_{v,ex}$) can be calculated by

$$N_{v,ex} = V_p \cdot C_{v,fluid} = \frac{4\pi}{3} \left(\frac{D_p}{2}\right)^3 \cdot C_{v,fluid} \quad (1)$$

We then calculated the number of emitted viruses per time ($E_{v,emis}(1/h)$) based on the number of emitted respiratory particles per time ($E_{p,emis}(1/h)$)⁹, and the number of viruses in each exhaled respiratory particle size ($N_{v,ex}$) as

$$E_{v,emis}(D_p) = N_{v,ex}(D_p) \cdot E_{p,emis}(D_p). \quad (2)$$

If the face mask usage strategies were source control and universal masking, we multiplied $E_{v,emis}(D_p)$ with a penetration rate of surgical masks ($1 - \eta_{mask}(D_{p,evp})$)⁴.

Exhaled respiratory particles contain water along with other substances from the respiratory tract, including viruses. As these particles evaporate, the water content decreases,

and the size of particles decreases. Regarding this issue, it has been assumed that respiratory particle evaporation causes particles to become smaller by approximately 50% of their initial size^{4,10}. Therefore, the diameter after the evaporation process ($D_{p,evp}$) is $\frac{1}{2}D_p$.

Estimating the inhaled viruses

The respiratory viruses that infected people release into the environment can be inhaled by others. To estimate the number of inhaled viruses, we first estimated the number of viruses per volume containing each susceptible individual as

$$n_{v,indoor}(D_{p,evp}) = \frac{E_{v,evp}(D_{p,evp})}{V_{room}\lambda(D_{p,evp})}. \quad (3)$$

To determine how environmental factors impact the concentration of respiratory viruses in the air, we focused on three crucial factors. These factors included the ventilation rate, particle deposition rate, and inactivation rate¹¹. The ventilation rate refers to the rate at which fresh air is brought into the space, which can dilute the concentration of viruses in the air. The particle deposition rate refers to the rate at which particles, including viruses, settle out of the air and onto surfaces. In addition, we also considered the inactivation rate, which refers to the rate at which viruses are destroyed or become inactive over time. This may occur due to a variety of environmental factors, such as temperature, humidity, and exposure to ultraviolet light¹². We generated these factors as the total loss rate ($\lambda(D_{p,evp})$)^{7,13}.

Accounting for the number of viruses present in a certain volume of air ($n_{v,indoor}(D_{p,evp})$), as well as the volume of air that a potential host breathes in 30-minute period ($V_{breath,30}$) adapted from Landers *et al.* (2003)¹⁴, we determined the number of viruses that were inhaled in 30 minutes ($N_{v,30}(D_{p,evp})$) by multiplying the number of viruses present in a certain volume of air with the volume of air that a potential host breathes in over a 30-minute period. If the face mask strategies were wearer protection and universal masking, we multiplied $N_{v,30}(D_{p,evp})$ with the penetration rate of surgical masks. To determine the total number of viruses that were inhaled, we performed an integration over the particle size from 0.01 to 100 μm follows,

$$N_{v,30}(D_{p,evp}) = \int \frac{dN_{v,30}(D_{p,evp})}{dD_p} dD_p. \quad (4)$$

After the total number of inhaled viruses was estimated, we then calculated the probability of infection, which would be used to explain the risk of a person becoming infected. The parameters used in this study are summarized in Table 1.

Estimating the probability of infection

When a virus enters the body, the chance of getting infected is called the probability of infection for a single virus (P_{single}). The opposite to this chance is the probability of not getting infected. If someone breathes in multiple viruses (N_v), the chance of not getting infected is the chance of not getting infected by one virus raised to the power of how many viruses they breathed in. Therefore, to estimate the chance of infection, we need to estimate the chance of getting infected by subtracting the chance of not getting infected when breathing in the viruses. i.e., the probability of infection (P_{inf}). We then calculated this parameter with the following formula:

$$P_{inf} = 1 - (1 - P_{single})^{N_v}, \quad (5)$$

From equation (5), we estimated the probability of infection from the total number of inhaled viruses—i.e., the risk that the potential host can be infected with the viruses depends on the number of viruses that they inhaled over time.

**Table 1.** The parameters used in this study.

Parameters	Descriptions	Values	Sources
D_p	Particles diameter	0.01-100 μm	4
$E_{p,emis}(D_p)$,	The number of emitted respiratory particles per time	The particle size distribution based on the experimental data	4,9,15,16
$1 - \eta_{mask}(D_{p,evp})$	The penetration rate	Based on the experimental data and model calculations	4,17,18
$\lambda(D_{p,evp})$	Total loss rate	λ_{ven} = ventilation rate $= 1 \text{ h}^{-1}$ λ_{dep} = deposition rate (function of D_p) λ_{inact} = inactivation rate $= 0.6 \text{ h}^{-1}$	11,13
$V_{breath,30}$	Inhaled volume in 30 minutes	The average breathing rate = 8 L/min	14

Risk of transmission

The Monte Carlo simulations were then used to imitate the transmission of respiratory viruses in the indoor setting. Each person in the system has a different probability of infection, i.e., each person in the room has an individual chance of becoming infected with respiratory viruses. We ran 10,000 simulations with 24 susceptible individuals in the setting and estimated the median number of infected and susceptible people resulting from the simulations. We also investigated two factors impacting airborne transmission: physical distancing and face mask usage.

Results and discussion:

We estimated the probability of infection for each individual in the room to assess the effect of control strategies, i.e., physical distancing and face mask usage, on respiratory virus transmission. In the baseline setting in which the room size is $8 \times 8 \times 3 \text{ m}^3$ with no interventions, we found that the probability of infection of the closest people to the infected person (at the center of the room) was 0.99, and of the most distant people from the infected person was 0.46 (Figure 2 (a)). This highlights the substantial influence of interpersonal distance on an individual's susceptibility to infection. Our findings align with prior research indicating a diminishing probability of infection as distance between individuals increases^{19,20}. Nevertheless, a separation of 1.6 meters between individuals may not be sufficient to prevent transmission in this particular scenario.

To explore the potential benefits of increasing the distance between individuals within the room, we examined the infection probability when the distance was extended from 1.6 to 2.4 meters. Under these conditions, we found that the probability of infection for each individual decreased from the range of 0.46-0.99 to 0.24-0.89 (Figure 2 (b)). Thus, implementing physical distancing measures can significantly mitigate the risk of disease transmission in this scenario.

To further assess the risk of an outbreak and the total number of infected individuals in this setting, we employed Monte Carlo simulations. In the initial scenario, there were 25 people, including one infected person positioned at the center of the room. Figure 3 illustrates a box plot representing the number of infected individuals derived from the simulations. Notably, after increasing the distance between individuals from 1.6 to 2.4 meters, the total number of infected individuals decreased from 18 to 12. This observation implies that maintaining a greater distance between infected individuals and those susceptible to infection could prove to be an effective strategy in enhancing control over the virus's spread. This aligns with the findings of Chu et al. (2020)²¹, who also suggested that maintaining a spacing of at least 1 meter between individuals can limit infection, and a distance of 2 meters may be even more effective, supporting our conclusion regarding the importance of increased interpersonal distance in preventing successful transmission.

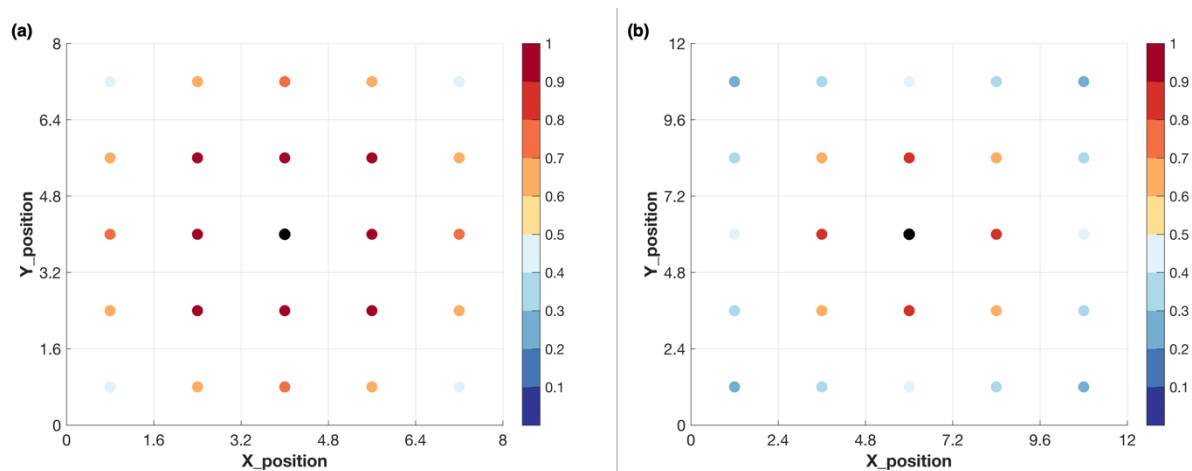


Figure 2 The probability of infection of an individual in different room sizes.

(a) The room size is $8 \times 8 \text{ m}^2$, and (b) $12 \times 12 \text{ m}^2$. There are 24 susceptible and one infected individual in the rooms. Dots represent the locations of individuals in the room. The color bar represents the probability of infection of individuals located at different positions.

Furthermore, we conducted simulations to assess the impact of four different face mask strategies: no masks (everyone without masks), wearer protection (only susceptible individuals wearing masks), source control (only the infected individual wearing a mask), and universal masking (everyone wearing masks). Our results indicated that in the small room setting, the number of infected individuals decreased from 18 to 8 when all susceptible individuals wore masks (as depicted in Figure 3). These findings align with a study by Dixit *et al.* (2023)²², which demonstrated that a higher percentage of individuals wearing face masks can significantly reduce the number of infected individuals in indoor environments.

Nevertheless, we found that the source control strategy, in which only the infected person wore a mask, was more effective than wearer protection. Figure 3 illustrates that, in this case, the total number of infected individuals decreased from 18 to 6. This highlights the effectiveness of having infected individuals wear face masks since masks filter potential virus particles emitted from the body, thereby reducing the number of exhaled viruses.

Finally, when both physical distancing and face mask strategies were combined, the number of infected individuals decreased to just 1 person when everyone wore masks (Figure 3). Therefore, face mask usage emerged as one of the most effective interventions for preventing virus transmission. Comparing the number of infected individuals with universal masking and a 2.4-meter interpersonal distance to the number without any intervention, we

observed a reduction of approximately 18 times in the number of infected individuals. This emphasizes the substantial impact of these combined measures in curbing transmission.

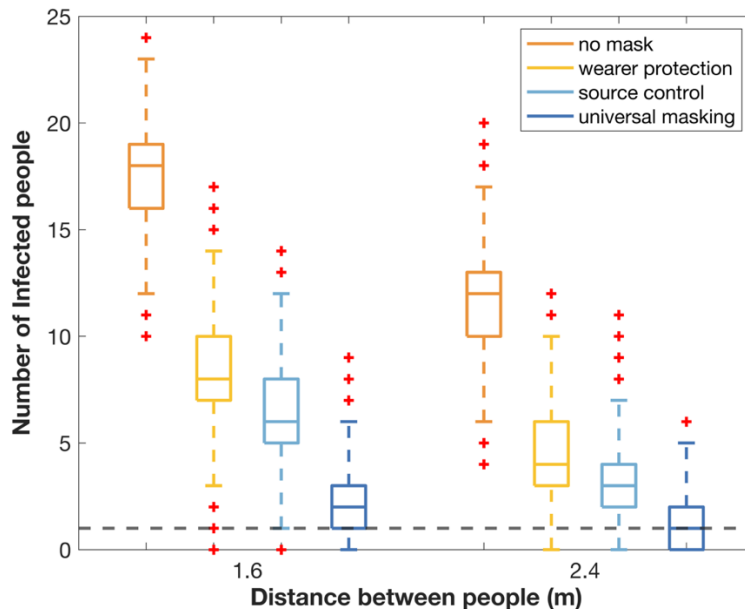


Figure 3. The total number of infected individuals with different distances between people. Each box represents a different face mask-wearing strategy. The number of infected people in the graph indicate the median of 10,000 simulations. The bottom and top of each box are the 25th and 75th percentiles of the simulations. The line in the middle of each box represents the median number of infected people.

Conclusion:

In this study, we investigated the effects of physical distancing and face mask-wearing on the likelihood of infection among people in an indoor setting. We found that increasing the spaces between individuals in the settings and wearing face masks can reduce the likelihood of people in the environment becoming infected. When comparing the number of infections in the most effective intervention scenario, characterized by universal mask-wearing and a 2.4-meter interpersonal distance, to the scenario with no interventions, we observed a substantial reduction in the number of infections, approximately 18-fold fewer cases. These findings underscore the significant role that maintaining interpersonal distance and wearing face masks within enclosed spaces can play in curbing the potential outbreak of respiratory diseases.

Acknowledgements:

We would like to express gratitude to the Department of Physics, Faculty of Science, Mahidol University, and the Development and Promotion of Science and Technology Talents Project (DPST) for their support.

References:

1. Muralidar S, Ambi SV, Sekaran S, Krishnan UM. The emergence of COVID-19 as a global pandemic: Understanding the epidemiology, immune response and potential therapeutic targets of SARS-CoV-2. *Biochimie* 2020; **179**: 85-100.
2. (WHO) WHO. WHO Coronavirus (COVID-19) Dashboard. World Health Organization (WHO); 2023.
3. Leung NHL. Transmissibility and transmission of respiratory viruses. *Nat Rev Microbiol* 2021; **19**(8): 528-45.
4. Cheng Y, Ma N, Witt C, et al. Face masks effectively limit the probability of SARS-CoV-2 transmission. *Science* 2021.
5. Azuma K, Yanagi U, Kagi N, Kim H, Ogata M, Hayashi M. Environmental factors involved in SARS-CoV-2 transmission: effect and role of indoor environmental quality in the strategy for COVID-19 infection control. *Environ Health Prev Med* 2020; **25**(1): 66.
6. Ministry of Education. The Ministry of Education Regulations regarding the establishment of standards for private schools of general education, comprising pre-primary education, primary education, and secondary education. 2007. <https://dl.parliament.go.th/handle/20.500.13072/2371492006>.
7. Li Y, Qian H, Hang J, et al. Probable airborne transmission of SARS-CoV-2 in a poorly ventilated restaurant. *Build Environ* 2021; **196**: 107788.
8. Feng S, Shen C, Xia N, Song W, Fan M, Cowling BJ. Rational use of face masks in the COVID-19 pandemic. *Lancet Respir Med* 2020; **8**(5): 434-6.
9. Holmgren. H, Ljungström. E, Almstrand. A-C, Bake. B, Olin. A-C. Size distribution of exhaled particles in the range from 0.01 to 2.0µm. *Journal of Aerosol Science* 2010; **41**(5): 439-46.
10. Nicas M, Nazaroff WW, Hubbard A. Toward understanding the risk of secondary airborne infection: emission of respirable pathogens. *J Occup Environ Hyg* 2005; **2**(3): 143-54.
11. Liu Y, Ning Z, Chen Y, et al. Aerodynamic analysis of SARS-CoV-2 in two Wuhan hospitals. *Nature* 2020; **582**(7813): 557-60.
12. Bozic A, Kanduc M. Relative humidity in droplet and airborne transmission of disease. *J Biol Phys* 2021; **47**(1): 1-29.
13. Lelieveld J, Helleis F, Borrmann S, et al. Model Calculations of Aerosol Transmission and Infection Risk of COVID-19 in Indoor Environments. *Int J Environ Res Public Health* 2020; **17**(21).
14. Landers. M, Barker. G, Wallentine. S, McWhorter. JW, Peel. C. A comparison of tidal volume, breathing frequency, and minute ventilation between two sitting postures in healthy adults. *Physiotherapy Theory and Practice* 2003; **19**(2): 109-19.
15. Duguid JP. The size and the duration of air-carriage of respiratory droplets and droplet-nuclei. *J Hyg (Lond)* 1946; **44**(6): 471-9.
16. Chao CYH, Wan MP, Morawska L, et al. Characterization of expiration air jets and droplet size distributions immediately at the mouth opening. *J Aerosol Sci* 2009; **40**(2): 122-33.
17. Grinshpun SA, Haruta H, Eninger RM, Reponen T, McKay RT, Lee SA. Performance of an N95 filtering facepiece particulate respirator and a surgical mask during human breathing: two pathways for particle penetration. *J Occup Environ Hyg* 2009; **6**(10): 593-603.
18. Weber A, Willeke K, Marchioni R, et al. Aerosol penetration and leakage characteristics of masks used in the health care industry. *Am J Infect Control* 1993; **21**(4): 167-73.



19. Najmi A, Nazari S, Safarighouzhdi F, MacIntyre CR, Miller EJ, T HR. Facemask and social distancing, pillars of opening up economies. *PLoS One* 2021; **16**(4): e0249677.
20. Ho CK. Modeling airborne pathogen transport and transmission risks of SARS-CoV-2. *Appl Math Model* 2021; **95**: 297-319.
21. Chu DK, Akl EA, Duda S, et al. Physical distancing, face masks, and eye protection to prevent person-to-person transmission of SARS-CoV-2 and COVID-19: a systematic review and meta-analysis. *Lancet* 2020; **395**(10242): 1973-87.
22. Dixit AK, Espinoza B, Qiu Z, Vullikanti A, Marathe MV. Airborne disease transmission during indoor gatherings over multiple time scales: Modeling framework and policy implications. *Proc Natl Acad Sci U S A* 2023; **120**(16): e2216948120.



DESIGN OF DIVERGENT BEAM-BASED SURFACE PLASMON RESONANCE SENSOR FOR MONITORING BACTERIAL BIOFILM FORMATIONS

Joewono Widjaja,^{1,*} Jordan Hakim Hossea²

¹School of Physics, Suranaree University of Technology, Nakhon Ratchasima 30000, Thailand

²Electronics and Telecommunication Engineering, Dar es Salaam Institute of Technology, Dar es Salaam, Tanzania

*e-mail: widjaja@g.sut.ac.th

Abstract:

We propose a divergent beam-based surface plasmon resonance sensor (SPR) for monitoring *Bacillus subtilis* biofilm formations. The designed sensor configuration employs a thin gold chip, an equilateral SF11 prism, and divergent p-polarized light with a wavelength of 632.8 nm. According to geometrical optics analysis, a laser beam line expander and an array image sensor need to generate a divergent beam and detect SPR reflectance signals. The simulation results confirm the designed sensor can linearly map the angles of the light rays incident on a gold chip onto the detecting element of the array sensor. Owing to the linear sensing performance, the proposed configuration has advantages over conventional angular scanning in that it is free from the mechanical system, low-cost, and compact.

Introduction:

In health science, biofilms have a great role in certain infectious diseases and in a variety of device-related infections. A better understanding of biofilms should result in new and effective control strategies for improving public health care. Biofilms are a collective of one or more types of microorganisms that can grow on many different surfaces. Microorganisms that form biofilms include bacteria, fungi, and protists.^{1,2} Conventional methods for microbiological diagnosis rely on the growth properties of bacteria. Analyses can be performed after an incubation period of at least 18 hours, and identification of pathogenic organisms takes at least 36 hours.³ This process becomes problematic when rapid identification of pathogenic agents is urgently needed.

On the other hand, surface plasmon resonance (SPR) sensors have been widely applied to diverse fields of chemical, biological, and health sciences such as medical diagnostics,⁴ food quality and safety,⁵ and environmental monitoring.⁶ Surface plasmons are collective oscillations of free electron density confined to a metallic surface. A resonance of surface plasmons can be done by coupling a light photon to this electron oscillation, provided both plasmons and photons have the same momentum and wavevector.⁷ However, it is a fact that, for a given frequency, the momentum of a surface plasmon is higher than that of a photon in free space. This momentum mismatch can be solved by coupling photons through a medium such as a prism into surface plasmons. According to the Kretschmann configuration,⁸ under total internal reflection, the momentum of an evanescent wave from a p-polarized light can be adjusted to match plasmon momentum by varying the incident angle or the wavelength of the light. When the matching conditions are satisfied, the photon energy is totally converted into a surface plasmon wave, causing a drop in reflected light intensity. Therefore, Kretschmann configuration-based SPR sensors are characterized by a dip in the intensity of the reflected light at a specific angle of incidence, known as the resonance angle. Since the plasmon wave is confined within the metallic surface, it is very sensitive to external dielectric media in contact with the surface. The dependency of the matching conditions on

dielectrics in the vicinity of the metallic surface is useful for the detection of biomolecular interaction in samples using SPR sensors without any markers.

In SPR-based biosensors, microorganisms interact with specific ligands grafted on a thin metal chip, causing a refractive index to change in the vicinity of the metal surface and thus generating a plasmonic resonance signal.⁷ Consequently, to study biofilms using the Kretschmann-based SPR biosensors, the angle of incidence of the readout beam must be varied accordingly.^{9,10} Although the angular beam scanning mechanism can be mechanically implemented by rotating either the laser source or the prism via a motorized stage, SPR systems become complex, costly, and bulky.^{11,12}

The problem of bulky and complex mechanical scanning of SPR sensors can be solved by using a fan-shaped readout beam. This is because the fan-shaped beam consists of a bundle of light rays confined by the beam shape that travel simultaneously in different angular directions. Recently, we have proposed and validated experimentally the illumination and the detection conditions of the divergent beam based SPR system.¹³ Besides being simple and low-cost, the proposed system can detect a large range of refractive index variations with high accuracy. In this project, our proposed divergent beam-based SPR system is designed to monitor bacterial film formation. A gram-positive *Bacillus subtilis* will be used as a model organism.¹⁴ The growth could be extracted from the critical angle position of the SPR curve, while the film formation is monitored by detecting the shift of the resonance angle.

Methodology:

Figure 1 shows a schematic diagram of the proposed Kretschmann prism configuration and divergent beam illumination for sensing bacterial biofilm samples with the refractive index range from n_{s1} to n_{s2} . To be able to measure this refractive index variation, the divergent beam must provide an infinite bundle of fan-shaped light rays that impinge simultaneously on the thin metal chip at incident angles between the corresponding resonance angles α_{i2} and β_{i2} . The angle of the incident light ray can be calculated from the resonance angle of the refractive index of the sample n_s ⁷

$$\beta_{spr} = \sin^{-1} \left(\frac{1}{n_p} \sqrt{\frac{n_m^2 n_s^2}{n_m^2 + n_s^2}} \right), \quad (1)$$

where n_p and n_m are the refractive indices of the prism and the metal layer, respectively.

On the basis of geometrical optics analysis, sensor parameters such as illumination, and detection angles, and beam widths can be determined as follows:¹³

The rays DE and DF of the divergent illumination beam on the prism side AC must be incident at the angles

$$\alpha_{i1} = \arcsin[n_p \cos(\phi/2 + \alpha_{i2})] \quad (2)$$

and

$$\beta_{i1} = \arcsin[n_p \cos(\phi/2 + \beta_{i2})], \quad (3)$$

respectively. As a result, the divergent angle of the illumination beam can be expressed as

$$\theta = \alpha_{i1} - \beta_{i1}. \quad (4)$$

To provide this illumination condition, the principal axis of the beam is oriented at an illumination angle ξ

$$\xi = (\phi + \theta)/2 + \arcsin[n_p \cos(\phi/2 + \beta_{i2})] \quad (5)$$

with respect to the x axis. The angles of the divergent beam GH incident on the side AB of the prism can be linearly mapped onto an image array sensor MN , provided the sensor is placed with at an angle of γ

$$\gamma = (\alpha_{i1} + \beta_{i1})/2. \quad (6)$$

The dip intensity position detected at a particular pixel of the sensor gives the wanted resonance information.

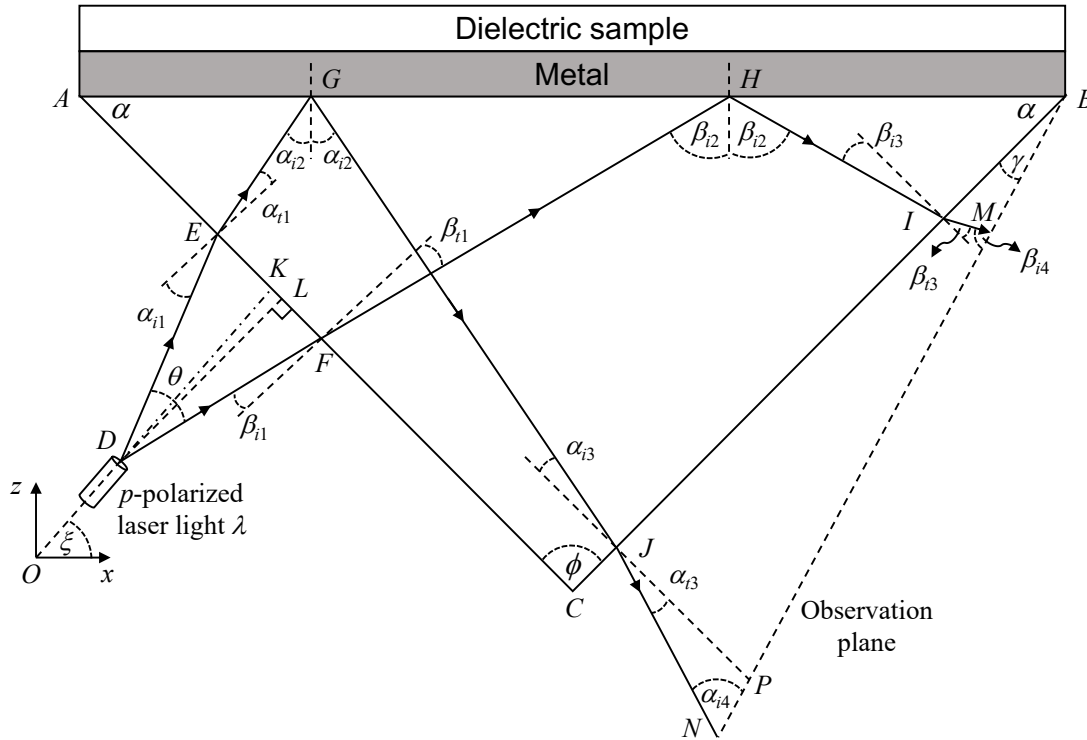


Figure 1.

Schematic diagram of an SPR sensor using divergent beam illumination.

When the normal distance between the prism side AC to the focal point of the divergent beam is set at DL , the width of the incident beam EF can be expressed as

$$EF = \frac{DL \sin \theta}{\cos \alpha_{i1} \cos \beta_{i1}}. \quad (7)$$

Due to the prism's refraction, the beam further widens inside the prism such that the refracted beam strikes the interface between the prism – metal chip with the incident angle varies between α_{i2} and β_{i2} . The refracted beam has the width of GH , which can be mathematically derived from triangles $\triangle AGE$ and $\triangle AHF$

$$GH = AE \left[\frac{\sin(\phi/2 + \beta_{i2})}{\cos \beta_{i2}} - \frac{\sin(\phi/2 + \alpha_{i2})}{\cos \alpha_{i2}} \right] + EF \frac{\sin(\phi/2 + \beta_{i2})}{\cos \beta_{i2}}, \quad (8)$$

with AE is the incident position of the beam EF measured from the vertex A . This beam width GH determines the minimum dimension of the metal chip for sample sensing. After emerging from the side BC of the prism, the SPR reflectance pattern MN

$$MN = \frac{IJ \cos \beta_{i1} + BI(\cos \alpha_{i1} - \cos \beta_{i1})}{\cos \gamma} \quad (9)$$

is detected by using the array image sensor inclined at the angle γ . Equation (9) can be viewed as a mapping of the resonance angle on the detecting element of the array sensor placed on the observation plane. When the mapping of the angle to the position has a linear relationship, the resonance dip information can be detected.

Results and Discussion:

In response to extreme conditions, bacterial spores are inactive and dormant structures of bacteria. When environmental conditions favor bacterial growth and reproduction, spores germinate into vegetative cells. Due to different cell structures, *Bacillus subtilis* exhibits different optical properties: A spectral reflectance and transmittance study over a wavelength interval from 0.2 to 2.5 μm showed that *Bacillus subtilis* spores have a refractive index of about 1.52.¹⁵ However, in vegetative form, the refractive index reduces to about 1.39.¹⁶ To monitor the formation of *Bacillus subtilis* biofilm, the proposed sensor is designed to measure these refractive index variations.

Angles of divergence, illumination, and detection

In this research, a p -polarized He-Ne laser operating at the wavelength $\lambda = 632.8 \text{ nm}$ is used as the illuminating light. The prism coupling is done by placing a thin gold layer with the refractive index $n_m = 0.1726 + j3.4218^{17}$ on top of an equilateral SF11 prism ($n_p = 1.7786$). According to Eq. (1), the resonance angles corresponding to the vegetative and the spore forms are 58.41° and 72.58° , respectively. To ensure that this resonance angle variation is detectable, the range of angles of light incidence on the gold chip GH is designed to be slightly broader, that is, from 58.40° to 72.59° . On the basis of the required angles of incidence, α_{i1} and β_{i1} are first calculated by using Eqs. (2) and (3). The results are then used to obtain the angles of divergence, illumination, and detection. Table 1 presents all the required angles for the proposed SPR implementation.

Table 1.						
Calculated angles of divergence, illumination, and detection.						
Angles ($^\circ$)						
α_{i2}	β_{i2}	α_{i1}	β_{i1}	θ	ξ	γ
58.40	72.59	2.829	21.44	24.27	19.32	18.61

According to the calculated angle θ , either a laser diode or a cylindrical lens cannot generate the required divergent beam because their beam angles are small. A laser beam line expander is suitable for the implementation of the proposed sensor.¹⁸ It produces a broad divergent angle with uniform fields, instead of a Gaussian profile.

Sizes of the gold chip and image sensor

The required size of the gold chip can be calculated by using Eq. (8), which gives the beam size GH . When the illumination distances DL and AE are set to 0.600 and 0.750 cm, respectively, the beam size GH becomes 1.935 cm. This requirement can be satisfied by using 20 mm \times 20 mm Au-evaporated glass plates (BA1000, Nano SPR). Figure 2 shows the beam position on the observation plane as a function of the angle of incidence β_{i2} in the gold chip. This plot using Eq. (9) provides the longest beam size MN on the observation plane, which is 1.490 cm. Equation (9) can also be used to confirm that the angle of the light ray incident on the gold chip is linearly mapped along the detecting element of the array sensor placed on the observation plane. To detect this reflectance beam, an array image sensor with a minimum format of the 4:3 ratio, such as 17.3 mm \times 13 mm, can be used for detecting the SPR reflectance. Sensitivity of the proposed SPR sensor is determined by the beam size MN and the total resolution of the array sensor. When the sensor has a resolution of $m \times n$ pixels, the sensitivity of the proposed sensor can be determined from $(n_{s2} - n_{s1})/m$ (RIU/pixel).

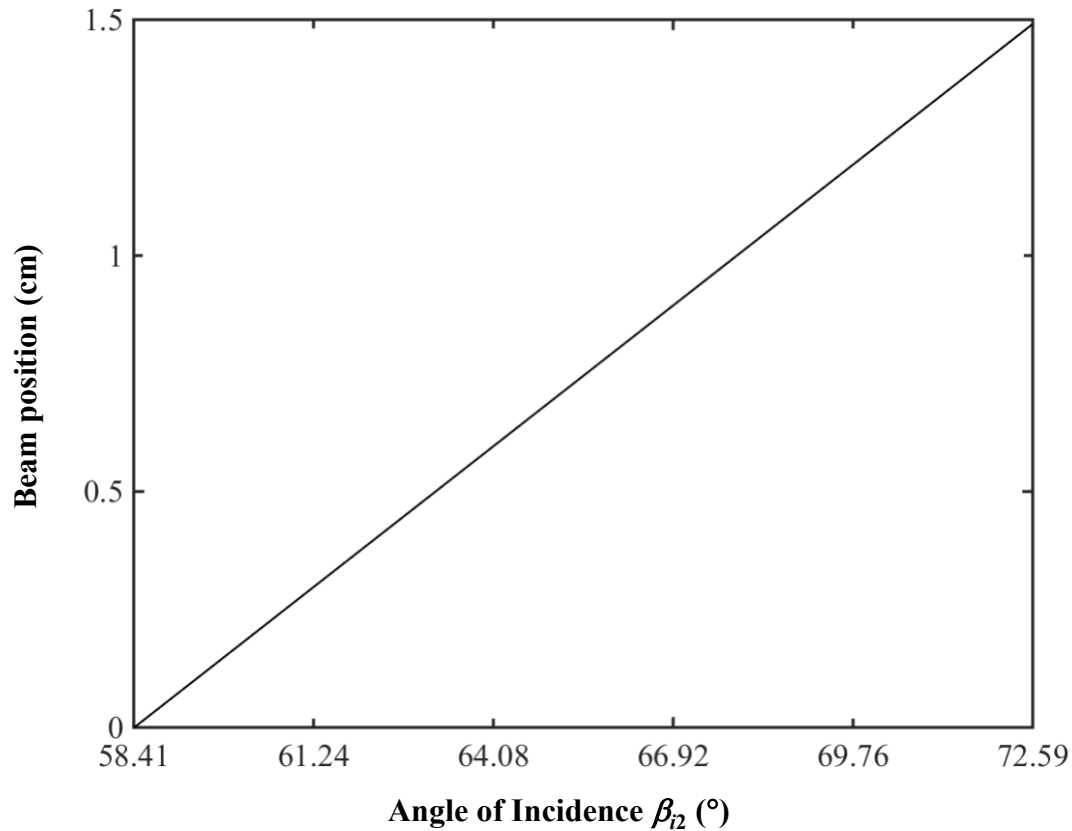


Figure 2.

Beam position on the observation plane as a function of the angles β_{12} of the light rays incident on a gold chip

Conclusion:

We have proposed a divergent beam-based SPR sensor for monitoring the formation of *Bacillus subtilis* biofilms. The designed Kretschmann configuration employs a thin gold chip, an equilateral SF11 prism, and a divergent *p*-polarized laser light with an operating wavelength of 632.8 nm. The beam illumination and detection conditions and the required gold chip size are theoretically studied using geometrical optics analysis. The divergent beam illumination can be generated by using the laser beam line expander, while the SPR reflectance signal needs to be detected by using the array sensor with the 4:3 format. The simulation results confirm the designed configuration can linearly map the angles of the light rays incident on the gold chip onto the spatial position along the array sensor plane. The proposed configuration has advantages over conventional angular scanning in that it is free from the mechanical system, low-cost, and compact.

Acknowledgements:

This material was supported by (i) Suranaree University of Technology (SUT), (ii) Thailand Science Research and Innovation (TSRI), and (iii) National Science, Research and Innovation Fund (NSRF) (NRIIS number 179344).

References:

1. Gondil VS, Subhadra B. BMC Microbiol. 2023;23:203.
2. Donlan RM. Emerg Infect Dis. 2002;8:881–890.
3. Velusamy V, Arshak K, Korostynska O, Oliwa K, Adley C. Biotechnol Adv. 2010;28:232–254.
4. Masson JF. ACS Sens. 2017;2:16–30.
5. Yakes BJ, Buijs J, Elliott CT, Campbell K. Talanta. 2016;156-157:55–63.
6. Saylan Y, Akgönüllü S, Çimen D, Derazshamshir A, Bereli N, Yılmaz F, Denizli A. Sens Actuators B Chem. 2017;241:446–454.
7. Hoa XD, Kirk AG, Tabrizian M. Biosens Bioelectron. 2007;23:151–160.
8. Kretschmann E. Z Phys. 1971;241:313–324.
9. Fillion-Côté S, Melaine F, Kirk AG, Tabrizian M. Analyst. 2017;142:2386–2394.
10. Abadian PN, Tandogan N, Jamieson JJ, Goluch ED. Biomicrofluidics. 2014;8:021804.
11. Lan G, Li S, Ma Y. Opt Commun. 2015;352:49–54.
12. Yesudasu V, Pradhan HS, Pandya RJ. Heliyon. 2021;7:e06321.
13. Widjaja J, Hossea JH. Lasers Eng. 2021;48:17–32.
14. Vlamakis H, Chai Y, Beauregard P, Losick R, Kolter R. Nat Rev Microbiol. 2013;11:157–168.
15. Tuminello PS, Arakawa ET, Khare BN, Wrobel JM, Querry MR, Milham ME. Appl Opt. 1997;36:2818–2824.
16. Katz A, Alimova A, Xu M, Gottlieb P, Rudolph E, Steiner JC, Alfano RR. Opt Lett. 2005;30:589–591.
17. Yamamoto M. Rev Polarogr. 2002;48:209–237.
18. Powell I. Appl Opt. 1987;26:3705–3709.



EVALUATION OF ELIASHBERG GAP EQUATIONS FROM ANALYTIC SUMMATIONS AND BIG DATA FROM INDEPENDENT DFT WORKS

Pakin Tasee^{*}, Komkrit Rientong, Nattawut Natkunlaphat, Udomsilp Pinsook

¹ Department of Physics, Faculty of Science, Chulalongkorn University, Bangkok, 10330, Thailand

*e-mail: pakin613@hotmail.com

Abstract:

In this research paper, we present a comprehensive investigation into the critical temperature (T_c) of superconductors, utilizing a big data compiled from previous studies, including Density Functional Theory (DFT) and experimental data. Our study aims to develop a strong model capable of explaining critical temperatures across a wide range of materials. We introduce the trend line of $\frac{\mathcal{L}}{\lambda}$ as a function of a parameter that relates to critical temperature, where \mathcal{L} is a specific parameter for this study and λ is the average coupling strength. The trend line generated from our model and choose a specific cutoff integer for summation, to effectively encompass the entire sample values. While our model and the Allen-Dynes model exhibit a strong correlation when predicting critical temperatures approaching zero, a significant discrepancy arises for compounds with higher critical temperatures. We attribute this divergence to the limitation of the Allen-Dynes model for weak electron-phonon interactions. Consequently, our study proposes an alternative model, offering potential utility in materials with elevated critical temperatures in future research.

Introduction:

Superconductors, an extraordinary class of materials, have garnered widespread attention due to their exceptional properties. At their core lies the intricate interplay of electrons and lattice vibrations, known as electron-phonon interactions, which are fundamental to understanding this phenomenon. Below a certain temperature known as the critical temperature (T_c), superconductors exhibit an extraordinary attribute: they offer zero electrical resistance and expel magnetic fields, rendering them indispensable for numerous technological applications, including high-speed magnetic levitation (maglev) trains and highly sensitive medical equipment [1].

The Bardeen-Cooper-Schrieffer (BCS) theory, pivotal in superconductivity research, introduced a groundbreaking concept. It predicted the formation of electron pairs, called Cooper pairs, through electron-phonon interactions, enabling superconductivity at extremely low temperatures [1,2]. However, as research progressed, it became evident that BCS theory had limitations, primarily applying to materials with weak electron-phonon interactions and low critical temperatures. This limitation stemmed from BCS theory's reliance on the deduction of the Hamiltonian, restricting its applicability at low temperatures.

To tackle the challenges posed by strong electron-phonon interactions, Eliashberg developed an approach that expanded our comprehension of superconductivity to encompass robust electron-phonon coupling. This pioneering work provided a more accurate framework for predicting critical temperatures in materials with intense interactions. Furthermore, under high-pressure conditions, Carbotte's contributions were pivotal [3]. His calculations, building upon Eliashberg's theory, employed the Eliashberg equation and incorporated the renormalization factor of Matsubara, offering a comprehensive method for calculating critical temperatures in superconductors, especially in novel compounds subjected to extreme conditions [3,4].

Eliashberg's equation shows in equation 1 and 2 [3].

$$\Delta_n Z_n = \pi T \sum_{m=1}^{m_c} (\lambda_{mn} - \mu^*) \frac{\Delta_m}{\sqrt{\omega_m^2 + \Delta_m^2}} \quad (1)$$

$$Z_n = 1 + \frac{\pi T}{\omega_n} \sum_{m=1}^{m_c} \lambda_{mn} \frac{\omega_m}{\sqrt{\omega_m^2 + \Delta^2}} \quad (2)$$

Where Δ represents the energy gap, Z is the renormalization function, T is temperature, m_c denotes cut off integer and ω_m stands for the Matsubara frequency ($\omega_m = \pi T(2m + 1)$).

As scientific inquiry progresses, the need for models offering enhanced accuracy and comprehensiveness, tailored to the unique properties of modern compounds, continues to grow. With an increasing demand for greater accuracy and more comprehensive models designed for modern compounds, there is a necessary push for models capable of better capturing the complexities of superconductivity in new materials. In this work, we gather extensive data from previous studies, including density functional theory (DFT) and experimental data. We derive a mathematical model from this substantial dataset and subsequently compare it to theoretical predictions.

Methodology:

We start with Eliashberg's equation [3],

$$\Delta_n Z_n = \pi T \sum_{m=1}^{m_c} (\lambda_{mn} - \mu^*) \frac{\Delta_m}{\sqrt{\omega_m^2 + \Delta_m^2}}, \quad (1)$$

$$Z_n = 1 + \frac{\pi T}{\omega_n} \sum_{m=1}^{m_c} \lambda_{mn} \frac{\omega_m}{\sqrt{\omega_m^2 + \Delta_m^2}}. \quad (2)$$

At high values of T_c , Δ approaches zero and substituting $n = 1$. We can rewrite equation (1) and (2) to equation (3),

$$1 + \lambda = \sum_{m=1}^{m_c} \frac{\lambda_{m1} - \mu^*}{|m - \frac{1}{2}|} \quad (3)$$

where λ denotes the average coupling strength, μ^* represents the effective Coulomb parameter. To distinguish the equation for independent data and the numerical model, we introduce the parameter \mathcal{L} and modify equation (3) as follows

$$1 + \lambda + \mu^* \sum_{m=1}^{m_c} \frac{1}{|m - \frac{1}{2}|} = \sum_{m=1}^{m_c} \frac{\lambda_{m1}}{|m - \frac{1}{2}|}. \quad (4)$$

Consider the equation (4)

$$\mathcal{L} = \sum_{m=1}^{m_c} \frac{\lambda_{m1}}{|m - \frac{1}{2}|}.$$

After substituting λ_{m1} and performing calculations, we can express equation (4) as equation (5),

$$\frac{\mathcal{L}}{\lambda} = a^2 \sum_{m=1}^{m_c} \frac{1}{|m - \frac{1}{2}|((m-1)^2 + a^2)}; \quad a = \frac{\omega_{ln}}{2\pi T_c} \quad (5)$$

ω_{ln} is average logarithm frequency. We express $\frac{\mathcal{L}}{\lambda}$ instead of \mathcal{L} to avoid the numerical calculation of λ . We set equation (5) to a numerical model by generating the trend line between $\frac{\mathcal{L}}{\lambda}$ and a^2 . This involves substituting the values of a^2 ranging from 10^{-4} to 10^6 and calculating $\frac{\mathcal{L}}{\lambda}$.

Consider the equation (4)

$$\mathcal{L} = 1 + \lambda + \mu^* \sum_{m=1}^{m_c} \frac{1}{|m - \frac{1}{2}|}.$$

According to $\sum_{m=1}^{m_c} \frac{1}{|m - \frac{1}{2}|}$ approaching $\ln(4e^{\gamma} m_c)$, we can calculate $\frac{\mathcal{L}}{\lambda}$ and a^2 from independent DFT and experimental data,

$$\frac{\mathcal{L}}{\lambda} = \frac{1 + \lambda + \mu^* \ln(4e^{\gamma} m_c)}{\lambda}, \quad (6)$$

and

$$a^2 = \frac{\omega_{ln}^2}{(2\pi T_c)^2}, \quad (7)$$

where γ is Euler's constant ($\gamma \approx 0.57721566$). Next, we generate a trendline of $\frac{\mathcal{L}}{\lambda}$ as a function of a^2 from equation (5) and compare it to equations (6) and (7) by substituting from big data from 25 research papers using a semi-logarithmic scale [5-29].

We also calculate $\frac{\mathcal{L}}{\lambda}$ and a^2 using Allen-Dynes model (AD), starting with equation 8 [2,5],

$$T_c = \frac{\omega_{ln}}{1.20} \exp \left[-\frac{1.04(1+\lambda)}{\lambda - \mu^*(1+0.62\lambda)} \right], \quad (8)$$

and the final equation is

$$\frac{\mathcal{L}}{\lambda} = \frac{(\lambda - \mu^*(1+0.62\lambda))}{1.04\lambda} \ln \left(\frac{\omega_{ln}}{1.20T_c} \right) + \frac{\mu^* \ln(4e^\gamma m_c)}{\lambda}, \quad (9)$$

and

$$a^2 = \frac{\omega_{ln}^2}{(2\pi T_c)^2}. \quad (7)$$

We also compare the results obtained from Allen-Dynes model to the trend line. Finally, for other materials, we can calculate T_c by converting $\frac{\mathcal{L}}{\lambda}$ and a^2 values from the graph.

Results and Discussion:

The generation of the trend line in equation (5) is visually represented in Figure 1. This figure illustrates the relationship between the $\frac{\mathcal{L}}{\lambda}$ value and a^2 , with each line on the graph corresponding to a different cutoff integer value m_c . As m_c approaches infinity, $\frac{\mathcal{L}}{\lambda}$ continuously increases as a^2 increases. However, within the range of m_c values between 10 and 130, $\frac{\mathcal{L}}{\lambda}$ stabilizes at a later stage as m_c increases.

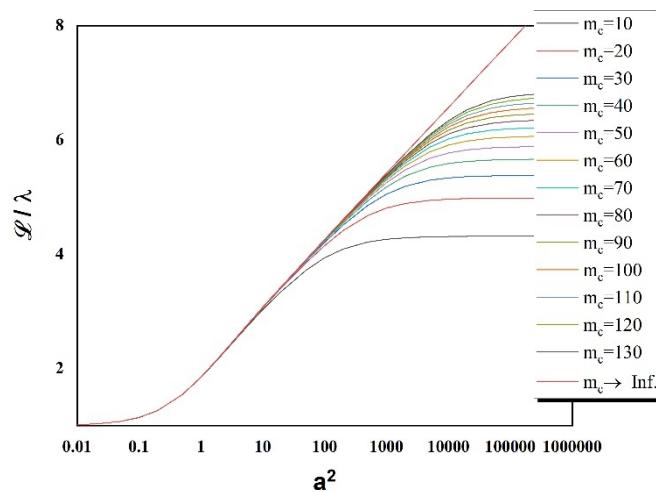


Figure 1. The relationship between $\frac{\mathcal{L}}{\lambda}$ and a^2 generated from equation (5) for each m_c value.



From equation (4), to ensure a correlation between results on both sides of the equation, we set $m_c = 95$ for the best correlation. After we gather necessary parameters from DFT and experiment from 25 research papers, the calculation of $\frac{\mathcal{L}}{\lambda}$ from our model and Allen-Dynes model compare with the trend line shows in figure 2. Details for some of the samples are presented in table 1 [6,7,8].

Table.1 shows some examples of necessary parameters for calculation.

Material	$\omega_{\text{In}}(\text{K})$	λ	μ^*	$T_c(\text{K})$	\mathcal{L}	a^2	ref.
KH ₆	1165	0.9	0.1	70	2.8353	7.0161	6
ScH ₉	1156	1.94	0.1	163	1.8514	1.274	6
TiH ₂	127	0.84	0.1	6.7	2.9664	9.1012	6
VH ₈	876	1.13	0.1	71.4	2.4617	3.8129	6
CrH ₃	568	0.95	0.1	37.1	2.7387	5.9373	6
KH ₁₀	1301	1.34	0.1	148	2.2326	1.9574	6
TiH ₁₄	1063	0.81	0.1	54	3.0392	9.8157	6
SrH ₁₀	767	3.08	0.1	259	1.5363	0.2221	6
YH ₁₀	1282	2.6	0.1	323	1.6353	0.399	6
ZrH	295	0.71	0.1	10	3.3264	22.0437	6
ZrH ₆	914	1.7	0.1	153	1.9716	0.904	6
ZrH ₁₀	1068	1.77	0.1	198	1.9332	0.737	6
NbH ₄	938	0.82	0.1	38	3.0143	15.434	6
TcH ₂	736	0.52	0.1	11	4.1764	113.3993	6
ZrH ₁₆	852	1.19	0.1	88	2.388	2.3744	6
SrH ₆	1316	1.65	0.1	189	2.0011	1.2281	6
YBaH ₈	535.13	1.04	0.1	49.6	2.5882	2.9485	7
YBaH ₈	535.13	1.04	0.13	43.5	2.7762	3.8334	7
YBaH ₈	901.22	1.24	0.1	89.4	2.332	2.5741	7
YBaH ₈	901.22	1.24	0.13	80.3	2.4897	3.1906	7
H ₃ S(Im $\bar{3}$ m)	1603	1.25	0.1	174	2.3214	2.1499	8
H ₃ S(R3m)	1615	0.95	0.1	140	2.7387	3.3708	8
CS ₃ H ₁₂	1370	0.85	0.1	80	2.9432	7.4285	8
CS ₃ H ₁₃	1704	1.01	0.1	142	2.6354	3.6476	8

In the region where a^2 is within the intermediate range on the graph and approaches values around 10^6 , both models exhibit a strong correlation. However, as a^2 lower to the order of 10^{-2} , a notable divergence emerges. In this region, the Allen-Dynes model yields lower values compared to the trend line graph. This discrepancy can be attributed to the fact that Allen-Dynes model is derived from considerations of weak electron-phonon interactions at low

temperatures, rendering it suitable for predicting critical temperatures that tend towards zero. Examining equation (7), we note that a^2 is inversely proportional to the critical temperature, indicating that lower values of a^2 correspond to higher critical temperatures. Consequently, when a^2 approaches the low value of 0.01, it leads to significantly higher critical temperatures that fall outside the scope of applicability for the Allen-Dynes model.

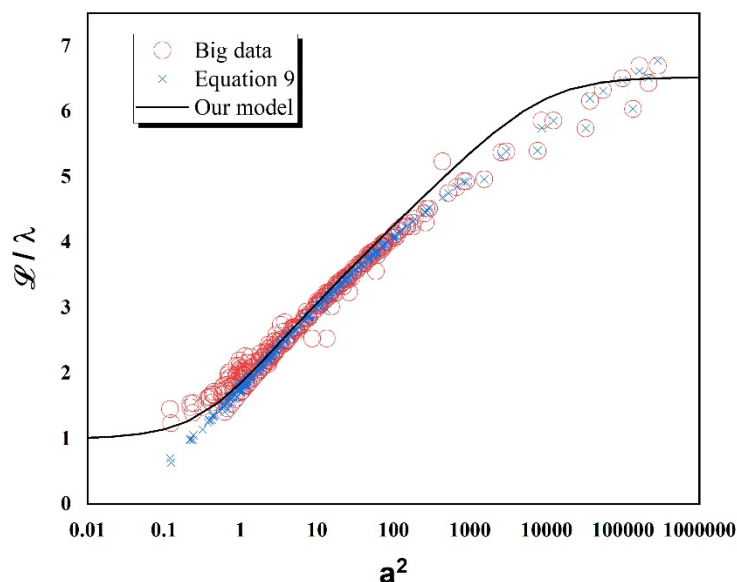


Figure 2. The relationship between $\frac{T_c}{T_d}$ and a^2 generated from big data (red circle) and equation 9 (blue cross) compare to our model while $m_c = 95$.

However, the discrepancies observed in our model may arise from its derivation, which is intricately connected to the optical model only.

Conclusion:

In this study, we have compiled extensive data from previous research, including data from Density Functional Theory (DFT) and experimental sources, to develop a comprehensive model capable of explaining critical temperatures across a wide range. The choice of $m_c = 95$ as the trend line allows us to effectively encompass the entire of sample values. While our model and the Allen-Dynes model exhibit strong correlation when predicting critical temperatures approaching zero, a notable discrepancy emerges for compounds with higher critical temperatures. This divergence can be attributed to the Allen-Dynes model's limitation for weak electron-phonon interactions. In conclusion, this study introduces an alternative model that may prove valuable in handling materials with elevated critical temperatures in future research.



Acknowledgements:

This work was supported by Chulalongkorn University for the research grants and those involved in making this work possible.

References:

- [1] Praiyan.P, Duangnil.A, Imchitr.V, Seeyangnok.J, Pinsook.U. Model of Superconducting Specreal Function. Thai Journal of Physics. (2022).
- [2] Pinsook, U. (2020). "In search for near-room-temperature superconducting critical temperature of metal superhydrides under high pressure: A review." Journal of Metals, Materials and Minerals 30: 31-41.
- [3] Gor'kov, L. P. and V. Z. Kresin (2018). "Colloquium: High pressure and road to room temperature superconductivity." Reviews of Modern Physics 90(1).
- [4] Misra, P. K. (2012). Chapter 14 - Superconductivity. Physics of Condensed Matter. P. K. Misra. Boston, Academic Press: 451-486.
- [5] Allen, P. B. and R. C. Dynes (1975). "Transition temperature of strong-coupled superconductors reanalyzed." Physical Review B **12**(3): 905-922.
- [6] Semenok, D. V., et al. (2020). "On Distribution of Superconductivity in Metal Hydrides." Current Opinion in Solid State and Materials Science **24**(2).
- [7] Liu, H., et al. (2021). "Theoretical study on the Y-Ba-H hydrides at high pressure." Physics Letters A **390**.
- [8] Wang, X., et al. (2022). "Dilute carbon in H₃S under pressure." npj Computational Materials 8(1): 87.
- [9] Ghaffar, A., et al. (2022) High- T_c superconductivity of clathrate Y₃EuH₂₄. arXiv:2205.05906 DOI: 10.48550/arXiv.2205.05906
- [10] Hilleke, K. P., et al. (2023). "Structure, stability, and superconductivity of N-doped lutetium hydrides at kbar pressures." Physical Review B 108(1): 014511.
- [11] Yang, A., et al. (2023). Crystal Structures and High-Temperature Superconductivity in Molybdenum-Hydrogen Binary System Under High Pressure.
- [12] Du, M., et al. (2021). "Pressure-induced superconducting CS(2)H(10) with an H(3)S framework." Phys Chem Chem Phys **23**(39): 22779-22784.
- [13] Yuan, Z., et al. (2022). "Computational design of a new layered superconductor LaOTf(2)." Phys Chem Chem Phys **24**(12): 7331-7337.
- [14] Li, Y. P., et al. (2022). "Phonon-mediated superconductivity in two-dimensional hydrogenated phosphorus carbide: HPC(3)." Phys Chem Chem Phys **24**(16) : 9256- 9262.

- [15] Kumar, J. and H. Singh (2021). "Electron-phonon mediated superconductivity in 1T – MoS₂ and effect of pressure on its transition temperature." Journal of Physics and Chemistry of Solids **156**.
- [16] Shah, A. K., et al. (2021). "First-principles study of pressure dependence superconductivity in technetium and tantalum." Solid State Communications **340**.
- [17] Li, B., et al. (2023). "Theoretical Predictions on Superconducting Phase above Room Temperature in Lutetium-Beryllium Hydrides at High Pressures." Chinese Physics Letters **40**(9): 097402.
- [18] Yang, A., et al. (2023). "First-principles investigation of the origin of superconductivity in TlBi₂." Physical Review B **108**(7): 075203.
- [19] Okazaki, H., et al. (2015). "Signature of high T_c above 25 K in high quality superconducting diamond." Appl Phys Lett **106**(5): 052601..
- [20] Durajski, A. P. and R. Szczesniak (2021). "New superconducting superhydride LaC(2)H(8) at relatively low stabilization pressure." Phys Chem Chem Phys **23**(44): 25070-25074.
- [21] Shi, L.-T., et al. (2021). "Prediction of pressure-induced superconductivity in the novel ternary system ScCaH_{2n} (n = 1–6)." Journal of Materials Chemistry C **9**(23): 7284-7291.
- [22] Li, H., et al. (2022). "Predicted structures and superconductivity of LiYH(n) (n = 5-10) under high pressure." Phys Chem Chem Phys **24**(14): 8432-8438.
- [23] Du, J., et al. (2023). "Pressure-induced stability and superconductivity in LuH(12) polyhydrides." Phys Chem Chem Phys **25**(19): 13320-13324.
- [24] Wei, Y. K., et al. (2020). "Formation and superconducting properties of predicted ternary hydride ScYH₆ under pressures." International Journal of Quantum Chemistry **121**(4).
- [25] Karaca, E., et al. (2021). "Electron–phonon interaction and superconductivity in hexagonal ternary carbides Nb₂AC (A: Al, S, Ge, As and Sn)." Electronic Structure **3**(4): 045001.
- [26] Tsuppayakorn-aek, P., et al. (2020). "Superconductivity of superhydride CeH₁₀ under high pressure." Materials Research Express **7**(8).
- [27] Sadovskii, M. V. (2021). "Limits of Eliashberg theory and bounds for superconducting transition temperature." Physics-Uspekhi **65**(07): 724-739.
- [28] Ding, H.-B., et al. (2023). "Superconductivity at 117 K in H-doped diamond." Materials Today Physics **35**.



- [29] Shutov, G. M., et al. (2023). "Ternary superconducting hydrides in the La–Mg–H system." *Materials Today Physics*: 101300.



INVENTION OF BONE DENSITY MEASURING INSTRUMENT USING STRESS WAVES FOR ASSISTING IN OSTEOPOROSIS DIAGNOSIS

Phattarachai Satsatranurak*, Tanawat Tanwattana, Ou-aukwan Charoenkul, Jatuporn Puntree
Mahidol Wittayanusorn School, Salaya Sub-district, Phutthamonthon District,
Nakhon Pathom Province, Thailand, 73170

*e-mail: phattarac.sat_g31@mwit.ac.th

Abstract:

Osteoporosis is a medical condition in which the internal structure of bone deteriorates, becomes more fragile, and increases the chance of breaking. Mostly found in elderly people around 60 years and above. Moreover, it is more common in women than in men due to dramatic reduction of bone mass after menopause. Patients are generally unaware of osteoporosis because of no indicated symptoms until the accident leads to bone fracture. Currently, the most accurate diagnosis of osteoporosis is the DEXA scanner. However, this method needs to be operated by a specialist, costly and time consuming. Therefore an alternative method of diagnosing the bone mass density for pre-indications of osteoporosis is focused in this work. The method was tested by sending stress waves into the bone. Abnormality of bone densities will be suggested by the change of physical properties of the wave.

Introduction:

Osteoporosis is a significant disease that causes bone density and mass to decrease. The bones deteriorate, become more fragile, deformed, and easily break. The bone capability in weight bearing is considerably reduced. It is mainly due to the imbalance of function of the two types of bone cells, caused by insufficient amount of calcium for the bone formation process. Osteoporosis is currently surging public health attention in many countries as they are proceeding to ageing society. According to research, there is one in every five males and one in every three females aged over 50 are suffering from losing bone mass. It is even worse that osteoporosis is a silent threat due to lack of any physical indications unless the bone fractures in an accident. Therefore, early detection is critically vital for everyone. The best way to prevent the risk of osteoporosis is the bone mass or bone density examination.

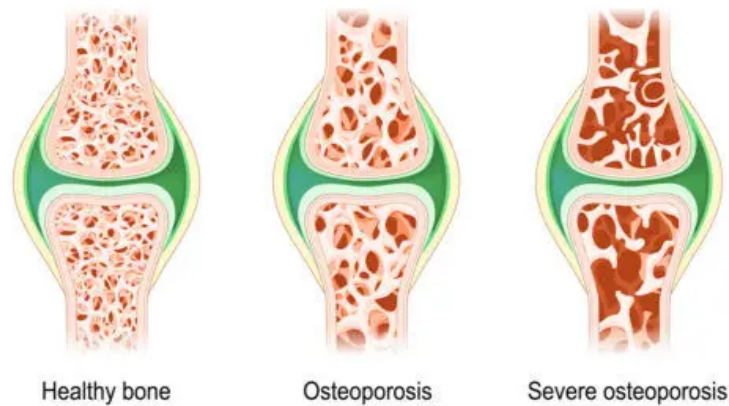


Figure 1. Comparison of the density of healthy bone, osteoporosis, and severe osteoporosis stages.

The current technology for osteoporosis detection is the Dual Energy X-ray Absorptiometry Scanner or DEXA. It accurately takes an x-ray image of bone tissue. However, it might be inconvenient for patients due to the needs of specialists to operate and it requires patients to travel to hospital. Therefore, an alternative method of bone mass detection with cheaper operating cost, convenient for patients and increases accessibility is required.

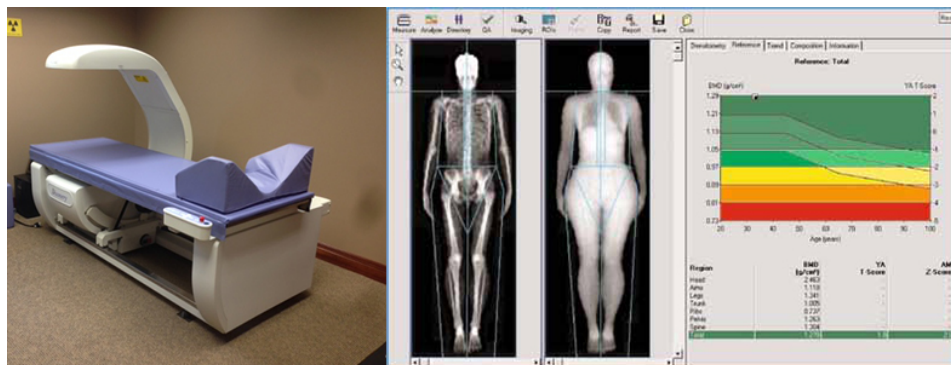


Figure 2. (Left) DEXA Scanner for detecting osteoporosis.
(Middle) Example of an osteoporosis test result from DEXA Scanner.
(Right) Analysing results by determining the T-Score and bone density values.

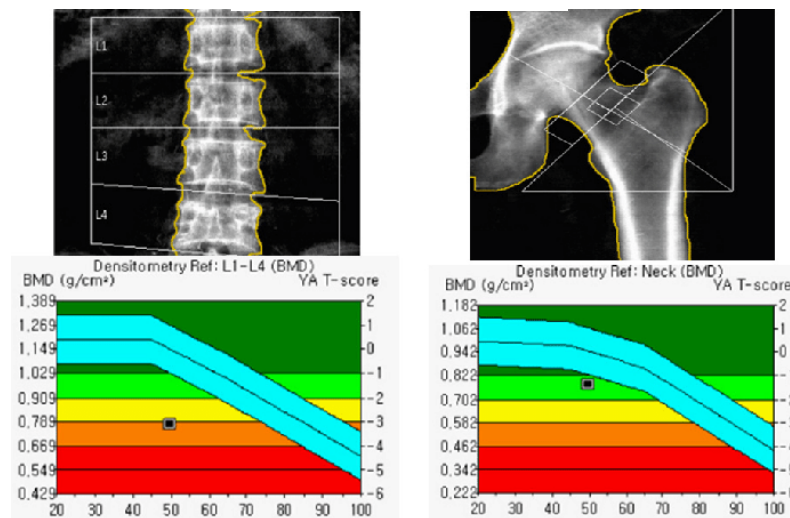


Figure 3. Comparison of T-Score and density of intervertebral discs and joints between pelvis and leg bones.

We are interested in finding an alternative method of bone density analysis that is cheaper and easily accessible for all communities. Stress wave is a mechanical wave that propagates through the medium. It was found that when a stress wave passes through the medium, many physical properties are changed. Such changes indicate the internal property of the medium accordingly. Similarly, when a stress wave passes through the bone, it might possibly suggest the bone properties which, in turn, can be linked with the prevalence of osteoporosis.

The changing of wave frequency is expected in indicating the abnormality of bone. The wave can be simply generated by a speaker. The prototype was set up to create a simple stress wave with constant frequency. Accelerometer and arduino board were brought into data acquisition. The output wave was analysed with Fourier transformation in order to extract the frequency components. Then, the frequency difference between input and output waves leads to the calculation of density.

Related terms

1) Stress wave: The propagation of vibrations in a solid material, consisting of longitudinal waves, transverse waves, and surface waves. The speeds of these three types of waves are not equal but are related by the Poisson ratio. This project focuses mainly on longitudinal waves and surface waves.

2) Modulus of Elasticity (MOE): It is a measure of the stiffness of a material. The MOE can be calculated using the formula $MOE = \text{stress/strain} = F/Ax/l = Fl/Ax$, where F is the force applied perpendicular to the cross-sectional area A of the material, l is the original length of the material, and x is the change in length.

3) Fast Fourier Transform (FFT): It is a mathematical algorithm used to convert a time-domain signal into a frequency-domain representation. In the analysis of vibrations, this technique is used to analyse the relationships between different frequencies. The data obtained from the analysis is used to detect and identify potential problems such as bearing failures, unbalance, misalignment, etc.



Methodology:

1. Equipment lists

1.1 Software

- | | |
|---------------------|----------|
| (1) Arduino | 1 device |
| (2) Microsoft Excel | 1 device |

1.2 Equipment

- | | |
|------------------------|-----------|
| (1) Accelerometer | 2 devices |
| (2) Arduino Nano | 1 device |
| (3) Laptop/Computer | 1 device |
| (4) Bones | 4 pieces |
| (5) Hammer | 1 piece |
| (6) Function generator | 1 device |
| (7) Speaker | 1 piece |
| (8) Breadboard | 1 piece |

2. Experimental method

- (1) Attach the speaker and accelerometer to a stick with 10 and 30 centimetres separation.
- (2) Connect the speaker to a Function generator.
- (3) Turn on the Function generator and use Arduino Nano to acquire raw data from the accelerometer.
- (4) Use MS Excel to analyse the data from the accelerometer.



Figure 4. Experimental methods flow chart.



Results and Discussion:

1. Results

1.1 Results of the 1st experiment in wood

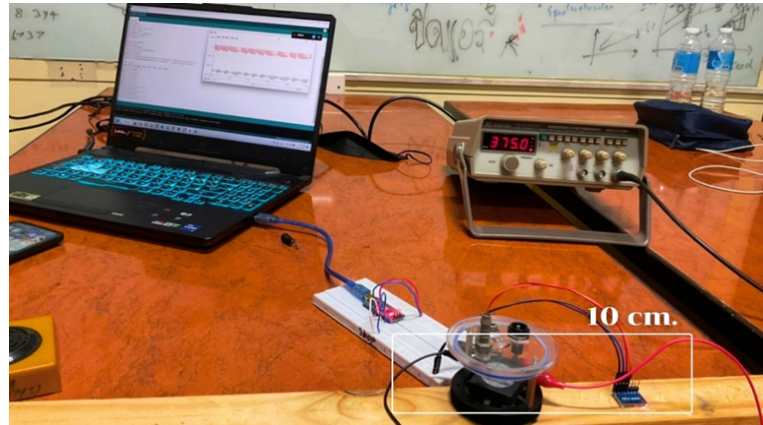


Figure 5. The installation of equipment with a 10 centimetres distance between speaker and accelerometer.

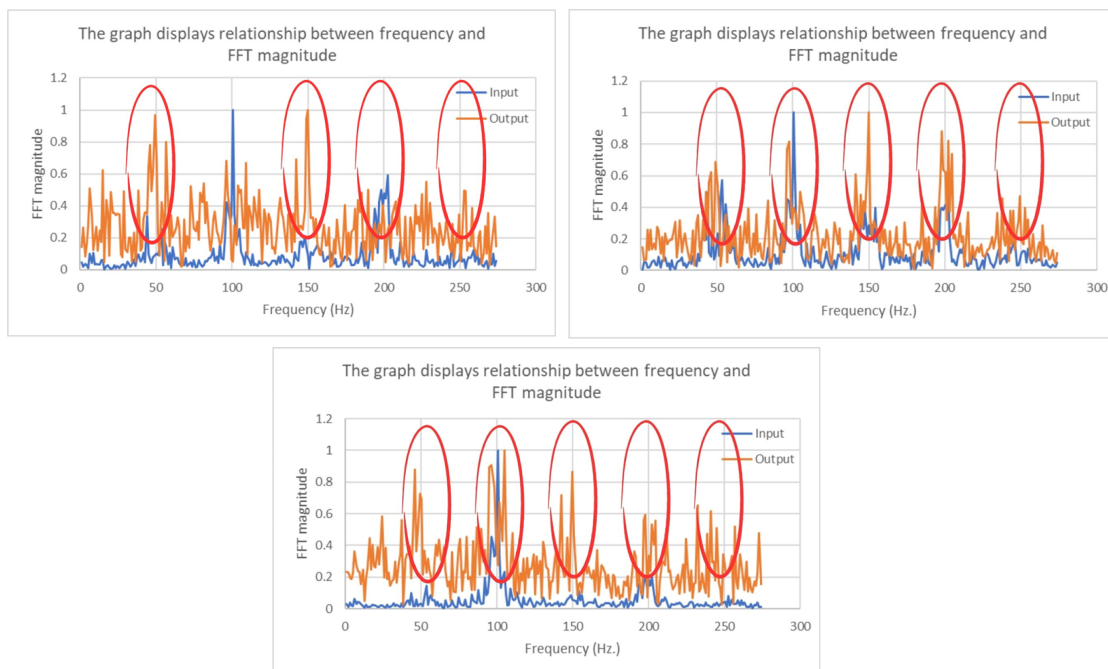


Figure 6. The relationship between a Fast Fourier Transform (FFT) magnitude and frequency of accelerations along the a) x axis, b) y axis and c) z axis with 257 Hz input.



1.2 Results of the 2nd experiment in wood

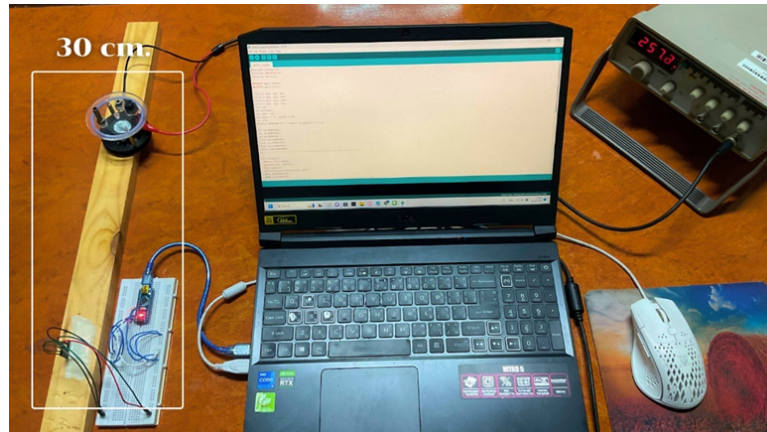


Figure 7. The installation of equipment with a 30 centimetres distance between speaker and accelerometer.

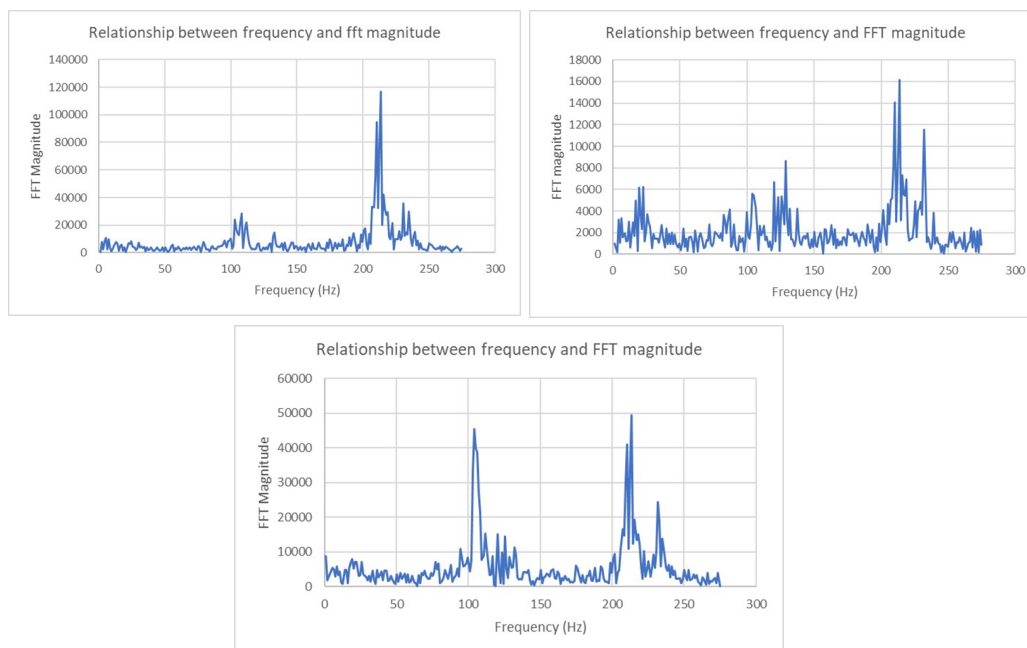


Figure 8. The relationship between a Fast Fourier Transform (FFT) magnitude and frequency of accelerations along the a) x axis, b) y axis and c) z axis with 107 Hz input.

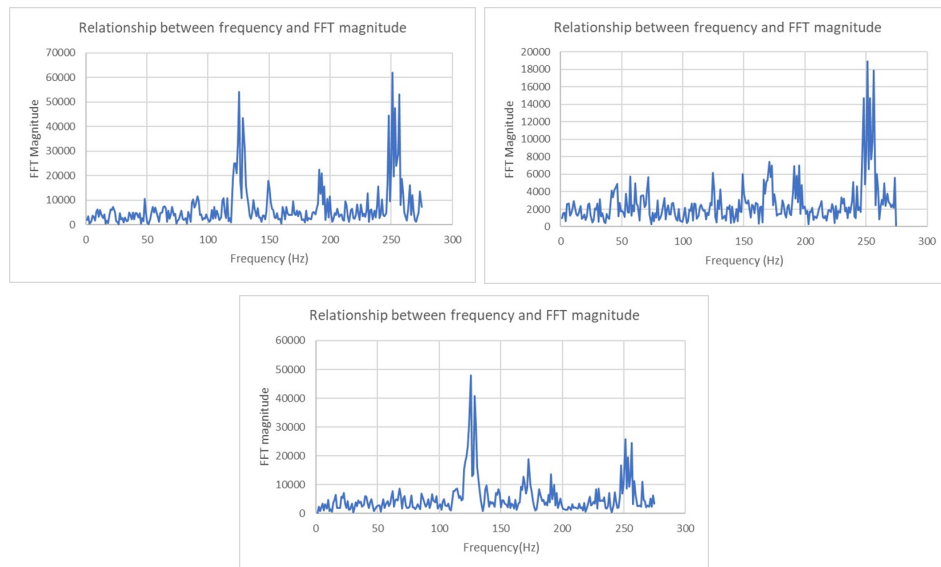


Figure 9. The relationship between a Fast Fourier Transform (FFT) magnitude and frequency of accelerations along the a) x axis, b) y axis and c) z axis with 127 Hz input.

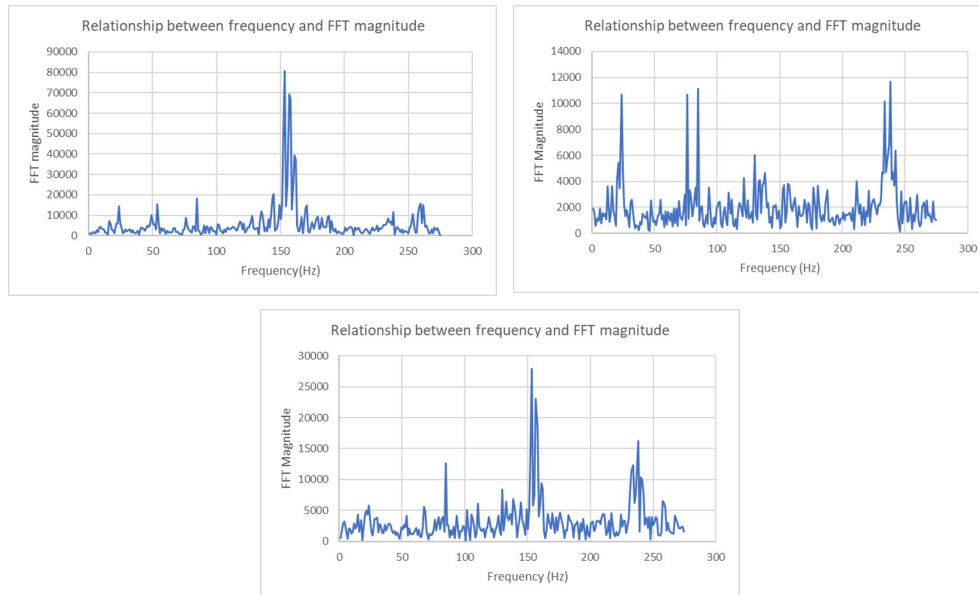


Figure 10. The relationship between a Fast Fourier Transform (FFT) magnitude and frequency of accelerations along the a) x axis, b) y axis and c) z axis with 157 Hz input.

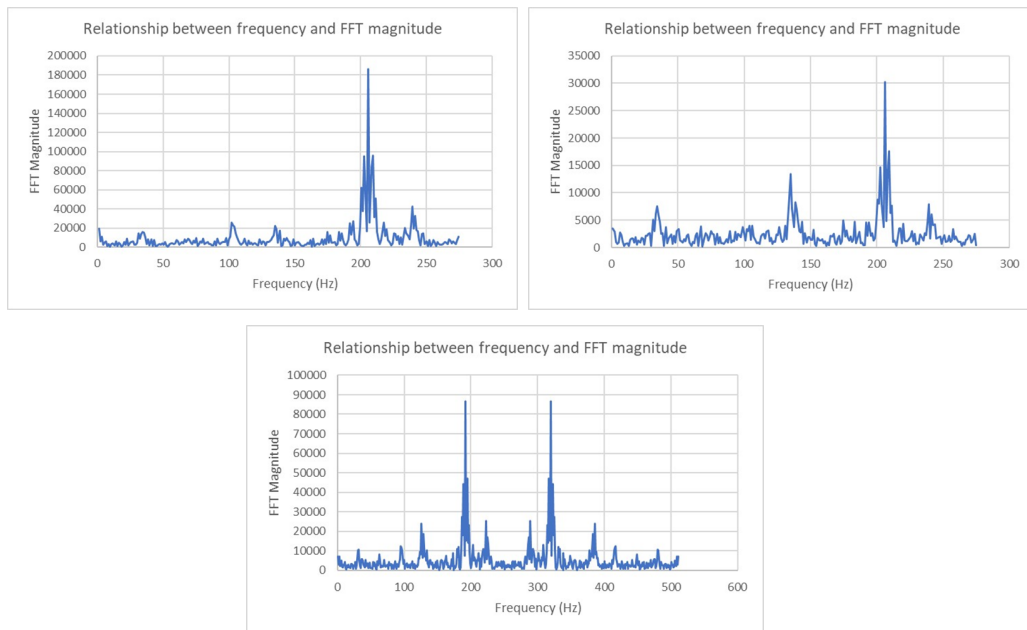


Figure 11. The relationship between a Fast Fourier Transform (FFT) magnitude and frequency of accelerations along the a) x axis, b) y axis and c) z axis with 207 Hz input.

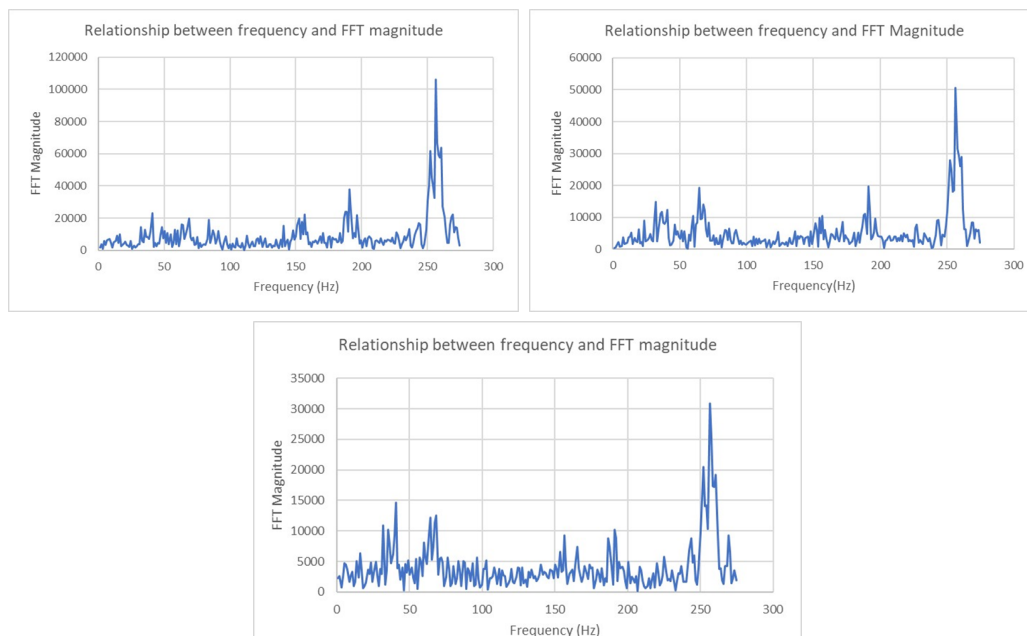


Figure 12. The relationship between a Fast Fourier Transform (FFT) magnitude and frequency of accelerations along the a) x axis, b) y axis and c) z axis with 257 Hz input.



Discussion

Results of the 1st experiment in wood

The preliminary test was carried out by letting 100 Hz input waves propagate through a stick of wood. The result shows that the Fourier transform of acceleration frequency changes approximately 50 Hz. However, it was speculated that this number coincidentally equals the inherent electrical frequency from an outlet. Therefore, we would better change the input frequency not only to mitigate the chance of misinterpreting the involvement of outlet electrical property but also its higher harmonics as the multiplications of 50 Hz.

Results of the 2nd experiment in wood

Then, 5 input frequencies: 107, 127, 157, 207, and 257 Hz were set. After letting these stress waves propagate through a wood specimen one-by-one, the accelerometer passed on the data into Fast Fourier analysis. It was found that all five input frequencies have still been detected by the accelerometer placing 30 centimetres away from the wave source. But at the frequencies 107 and 127 Hz, their second harmonic can obviously be seen. This phenomenon is due to the limitation of the accelerometer data sampling rate. The arduino command line: `mpu1.getMotion6 (&ax2, &ay2, &az2, &gx2, &gy2, &gz2)`, specifically deploys with the accelerometer acquires each measurement value from the sensor in every 1 millisecond. This command inevitably bottlenecks the capability of the arduino board to receive the signal at maximum frequency of 278 Hz. The frequency is estimated from the distance used in the experiment with wood. Dividing the speed by frequency, it was exhibited that a proper length of wooden stick should be at least 11 metres.

Results analysis

According to both experiments, it was found that some graphs along the y-axis exhibit different characters compared to those along the x and z axes. Because the experiment was set up by aligning the y-axis of the accelerometer with the waves propagation direction. This might cause the distinction from the other two axes which lie transversely. The results of the first experiment also show a discrepancy in output-input frequency. While the second experiment showed no change. It was hypothesised that the change of frequency in experiment 1 was caused by electrical waves property from the outlet. Therefore, the results of experiment 2 will be used to summarise the results.

Conclusion:

Due to limitation of data acquisition rate from accelerometer which requires command line: `mpu1.getMotion6 (&ax2, &ay2, &az2, &gx2, &gy2, &gz2)`, which takes 1 millisecond delay process. It would require a wood specimen with at least 11 metres for experiment. Such length is considerably longer than the actual practice that aims to be incorporated in human limbs. It can be concluded that the use of an accelerometer is inappropriate to be used in analysing the propagation of stress waves under the project objective's circumstances.



Further development:

Piezoelectric is capable of acquiring the data at 100 - 15000 Hz which is far faster than an accelerometer. The '*digitalread()*' command which is incorporated with a hardware is at least 250 times faster than *mpul.getMotion6*. Therefore the length of the specimen can be reduced to approximately 16 centimetres. This value is comparatively much more appropriate for practical usage.

References:

1. Center JR, Bliuc D, Nguyen TV, Eisman JA. Risk of subsequent fracture after low-trauma fracture in men and women. *JAMA*. 2007;297:387–94.
2. Peel NF, Johnson A, Barrington NA, Smith TW, Eastell R. Impact of anomalous vertebral segmentation on measurements of bone mineral density. *J Bone Miner Res*. 1993;8:719–23.
3. Wood K, Dhital S, Chen H, Sippel R. What is the utility of distal forearm DXA in primary hyperparathyroidism? *Oncologist*. 2012;17:322–5.



Modification of the Pump Field for Enhanced Spontaneous Parametric Down Conversion in Quantum Key Distribution

Jeerasak Phooarphit, Thanapat Phetvongsakul, Ruchipas Bavontaweepanya, Atirach Ritboon and Ekkarat Pongophas*

Division of Physics, Faculty of Science and Technology, Thammasat University, Pathum Thani 12120, Thailand*Corresponding author.

*E-mail address: e_pong@tu.ac.th

ABSTRACT. A promising quantum mechanics-based method for secure communication is quantum key distribution (QKD). The spontaneous parametric down conversion (SPDC) process, which creates entangled photon pairs that may be used to create a secure key between two parties, is one of the essential parts of a QKD system. In this paper, we investigate the effect of geometrical change in wave vector of the pump field in the SPDC setup to enhance the quantity of the generated entangled photon pairs. We specifically consider the usage of two lenses positioned in front of and behind the Beta Barium Borate (BBO) crystal. The experimental results show that this modification leads to a significant improvement in the signal to-noise ratio of the detected photon pairs, and thus enhances the security of the QKD system.

Introduction

In QKD, particularly in E91 protocol [1-5], the entangled photon pairs are distributed so that Alice and Bob each end up with one photon from each pair. The protocol security is based on the nonlocal correlation between the polarization properties of each pair. Any attempt at eavesdropping will destroy these correlations in a way that Alice and Bob can detect. Thus, the entangled photon source is necessary for constructing the E91 station. The commonly found light source for entangled pairs is an SPDC process in a nonlinear crystal, such as BBO. In addition to QKD, the process of SPDC is a crucial technique as a quantum light sources employed in diverse experiments within the field of quantum optical science. Its applications range from investigating the fundamental behaviors of quantum mechanics [6], managing quantum data [6], creating single-photon detectors [7,8], to defining the characteristics of light-material interactions [6]

In our QKD experiment, we utilize SPDC to generate entangled states, highlighting the significant role of SPDC in such applications. However, the experiment encountered challenges with the SPDC signal receiver, especially in free-space signal transmission, due to signal degradation over distance. Conversely, when utilizing fiber optic signal transmission, the issue arose from signal reduction caused by coupling, posing a challenge in experimental implementation. Therefore, we conducted a study to examine the effect of pump beam intensity on coincidence counting rates in our experiment.

The properties of SPDC photons with respect to various parameters affecting their generation inside the crystal have also been explored. Effects resulting specifically from the spectral properties of the pump beam, on the spatial coherence of the down-converted beams

have been investigated in [10-11]. In addition, the role of the spatial properties of the pump, particularly that of focused pumping [12, 13], have been demonstrated to be of crucial importance for applications that require coupling of signal-idler modes into a pair of single-mode fibers [14, 15]. This is essential requirement for setting up our own cryptography station in Thailand.

In this experiment, our focus is on increasing the rate of entangled photon pair generation from the SPDC process. Theoretical calculations were performed to illustrate that the rate of entangled photon pair generation is indeed dependent on the intensity of the pump beam. Subsequently, experiments were conducted to measure the increase in the entangled photon pair generation rate by incrementing the pump beam intensity. This was achieved by utilizing lens focusing to create a beam waist, which is the region where the light beam has the minimum radius, leading to the highest intensity in this area.

Method

Due to the necessity of using a BBO crystal (thickness 0.5 mm) that requires high-intensity light at a wavelength of 405 nm as the pump beam, which falls in a region that is difficult to see, a He-Ne laser at 632.8 nm was employed to aid in the alignment of the entire setup. Initially, the He-Ne laser was directed through a beam splitter (BS) 1 to split the beam into two. The transmitted beam through BS 1 was then directed to BS 2 to further split it into three beams. The reflected beam from BS 2 was set to pass through two diaphragms spaced 60 cm apart. These diaphragms served as reference points, ensuring that the laser beam is parallel to the floor and facilitating the setup of other components.

Subsequently, the BBO crystal and a 3-degree measuring screen were positioned 21 cm apart, as shown in Figure 1. The beams reflected from BS 1 were then directed through the 3-degree measuring screen and passed through the BBO crystal. The light transmitted through BS 2 was also directed through the 3-degree measuring screen and passed through the BBO crystal. This setup was designed for the alignment of the SPDC emitted from the BBO crystal.

A lens with a focal length of 10 cm was placed behind the BBO crystal at a distance of 10 cm. The role of the lens is to collimate the light generated from the SPDC process into parallel beams. A prism-shaped mirror was then used to reflect the light passing through the lens towards the free-space fiber coupler for optimal coupling with the fiber coupler to the multimode fiber which connect to avalanche photo-diode detectors (APDs). Instead of the detector, the light is then directed backward through the fiber using an optical fault locator. A lens with a focal length of 10 cm is placed in front of the BBO and tuned until the light from the optical fault locator pass through the 3-degree measuring screen. Now the lens is at a distance of 10 cm.

Once the setup is complete, the laser source is switched from the He-Ne laser to a 405 nm laser with an intensity of 45 mW. The alignment of the 405 nm laser is adjusted to pass through both reference diaphragms. The optical fault locator was replaced with the APDs, and the lens position in front of the BBO was adjusted from +10 cm to -10 cm in 1 cm increments. Coincidence signals are then measured at each point, where the coincidence signal represents pairs of photon signals generated from the BBO or SPDC and detected by



the APD, with one serving as the sender and the other as the responder. The data were acquired and processed using the quTAG data acquisition device.

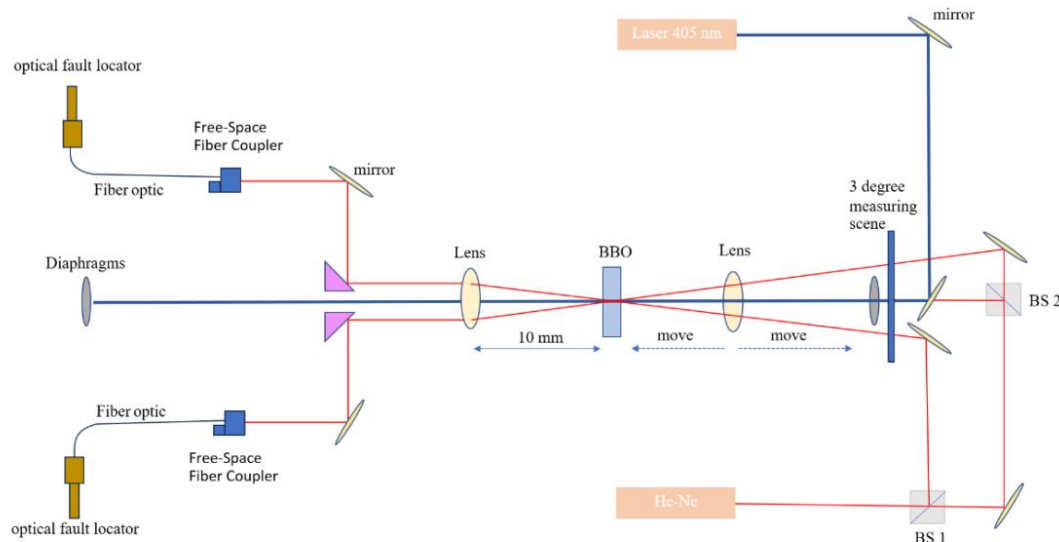


Figure 1 shows a diagram of the setup alignment of all equipment by He-Ne before using a 450 nm laser to measure the coincidence.

Experiment and results



Figure 2 illustrates the measurement of the signal distribution of entangled photon pairs in histograms with a coincidence window of 5 ns. The measurement was conducted by two APDs. Photon signals from the APDs were fed into the start and stop inputs of the time-to-digital converter in the quTAG Data Acquisition system. The quTAG system converted the signals into digital format, recorded the time intervals between the start and stop pulses in nanoseconds, and transmitted the data to the result display window. The time to collect all data is 1 second.

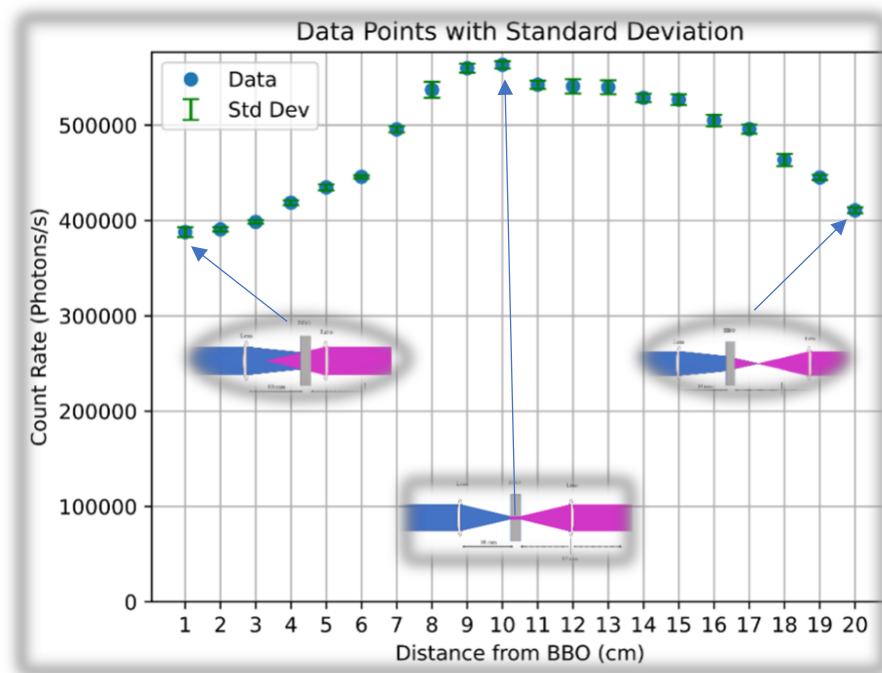


Figure 3 depicts the measurement data of the count rate concerning the distance between the lens and the BBO, ranging from 0 to +20 cm, with the lens positioned 10 cm away from the BBO. The count rate reaches its maximum value of 563,290 photon pairs/s at the focal point, where the pump beam intensity is highest. As the lens is moved away from the focal point, the count rate gradually decreases.

Conclusion

Our experimental results show that the pump beam focused on the BBO crystal greatly increases the SPDC output yield, and as we move the lens in and out of the focusing distance, the coincidence photon signal decreases. Therefore, the range that gets the highest coincidence signal is at the focusing distance where the cross section area of the pump beam is the smallest, therefore its intensity is highest. The results of this experiment show the importance of the geometrical change in wave vector of the pump field in increasing the number of SPDCs for easy measurement in the experiment.



References

- [1] D. Bouwmeester, J. W. Pan, K. Mattle, M. Eibl, H. Weinfurter, and A. Zeilinger, "Experimental quantum teleportation," *Nature* 390, 575-579 (1997).
- [2] T. B. Pittman, B. C. Jacobs, and J. D. Franson, "Single photons on pseudodemand from stored parametric down-conversion," *Phys. Rev. A* 66, 042303 (2002).
- [3] P. Walther, K. J. Resch, T. Rudolph, E. Schenck, H. Weinfurter, V. Vedral, M. Aspelmeyer, and A. Zeilinger, "Experimental one-way quantum computing," *Nature* 434, 169-176 (2005).
- [4] W. Tittel and G. Weihs, "Photonic entanglement for fundamental tests and quantum communication," *Quant. Inf. Comput.* 1, 3-56 (2001).
- [5] W. T. M. Irvine, A. L. Linares, M. J. A. de Dood, and D. Bouwmeester, "Optimal quantum cloning on a beam splitter," *Phys. Rev. Lett.* 92, 047902 (2004).
- [6] Z. Y. Ou and L. Mandel, "Violation of Bells-Inequality and Classical Probability in a 2-Photon Correlation Experiment," *Phys. Rev. Lett.* 61, 50-53 (1988).
- [7] Y. H. Shih and C. O. Alley, "New Type of Einstein-Podolsky-Rosen-Bohm Experiment Using Pairs of Light Quanta Produced by Optical Parametric Down Conversion," *Phys. Rev. Lett.* 61, 2921-2924 (1988).
- [8] P. G. Kwiat, K. Mattle, H. Weinfurter, A. Zeilinger, A. V. Sergienko, and Y. H. Shih, "New High-Intensity Source of Polarization-Entangled Photon Pairs," *Phys. Rev. Lett.* 75, 4337-4341 (1995).
- [9] Özgün Süzer , Does pump beam intensity affect the efficiency of spontaneous parametric down conversion?, *optics express* 20166.
- [10] A. Joobeur, B. E. A. Saleh, and M. C. Teich, "Spatiotemporal Coherence Properties of Entangled LightBeams Generated by Parametric Down-Conversion," *Phys. Rev. A* 50, 3349-3361 (1994)
- [11] W. P. Grice and I. A. Walmsley, "Spectral information and distinguishability in type-II down-conversion with a broadband pump," *Phys. Rev. A* 56, 1627-1634 (1997).
- [12] T. B. Pittman, D. V. Strekalov, D. N. Klyshko, M. H. Rubin, A. V. Sergienko, and Y. H. Shih, "Twophoton geometric optics," *Phys. Rev. A* 53, 2804-2815 (1996).
- [13] C. H. Monken, P. H. S. Ribeiro, and S. Padua, "Optimizing the photon pair collection efficiency: A step toward a loophole-free Bell's inequalities experiment," *Phys. Rev. A* 57,R2267-R2269 (1998).

- [14] C. Kurtsiefer, M. Oberparleiter, and H. Weinfurter, "High-efficiency entangled photon pair collection in type-II parametric fluorescence," *Phys. Rev. A* 64, 023802 (2001).
- [15] F. A. Bovino, P. Varisco, A. M. Colla, G. Castagnoli, G. Di Giuseppe, and A. V. Sergienko, "Effective fiber-coupling of entangled photons for quantum communication," *Opt. Commun.* 227, 343-348 (2003).

OPTIMIZATION OF LINK-LEVEL QUANTUM NETWORK USING GENETIC ALGORITHM

Poramat Chianvichai,^{1,*} Poramet Pathumsoot,² Sujin Suwanna^{1,*}

¹ Optical and Quantum Physics Laboratory, Department of Physics, Faculty of Science, Mahidol University, Bangkok 10400, Thailand

² Keio University Shonan Fujisawa Campus, 5322 Endo, Fujisawa Kanagawa 252-0882, Japan

*e-mails: poramat.cha@student.mahidol.edu, sujin.suw@mahidol.ac.th

Abstract:

Quantum computers in principle possess great potential to solve complex problems using specialized algorithms, but the current leading-edge quantum computers lack the required number of qubits and noise tolerance to fully enable these algorithms. To overcome the former limitation, quantum networks are being developed, connecting quantum devices to allow quantum communication and distributed quantum computing. However, challenges like noise-induced decoherence still hinder practical quantum network implementation. This study aims to enhance a quantum network setup through a genetic algorithm. The objective is to identify conditions for constructing a quantum network in specific configurations, such as an arrangement of ground stations for quantum key distribution. The research simulates a quantum network using the *qwanta* quantum network simulator. Through its application in simulating two distinct experiments, including those based on real-world geographic networks, we use Pareto frontier analysis to visualize capability to address inquiries like identifying the minimum configurations that meet specific network performance criteria. We obtain a set of parameters that yield fidelity surpassing the target value of 0.7. More specifically, the first experiment investigates an equidistant node configuration on a line, while the second uses actual geographic locations within Thailand with Songkhla and Chiang Mai as end nodes and Bangkok as the repeater node situated between them. In the first experiment, each Pareto optimal within the final population achieved the fidelity of 0.828 or greater. In the second experiment, there are only two Pareto optimal points that reach the target fidelity, yielding the highest fidelity at 0.706. While this meets the requisite threshold, there is room for improvement by expanding the search space in the genetic algorithm to account for a wider parameter range.

Introduction

Over the last few decades, quantum computing has advanced significantly, showcasing its proficiency in addressing challenges in classical computing. Unlike classical bits, quantum bits (qubits) possess the capacity to become entangled, giving rise to more complex, faster, and efficient algorithms. Extensive prior research demonstrates the potential for leveraging quantum computing capabilities [1-5]. When quantum computers execute quantum algorithms, they tap into an expanded computational space owing to the quantum properties inherent in their basic computational elements. However, the field faces challenges related to qubit quantity, quantum decoherence, and noise interference.

To address the issue of insufficient qubits, H.J. Kimble proposed the concept of connecting multiple quantum nodes to increase computational power [6], called quantum internet. A quantum internet or quantum network is a communication system that uses the principles of quantum mechanics to disseminate information. These networks exploit quantum

mechanics properties like superposition and entanglement for tasks beyond classical systems, which enable the creation of communication links, known as Bell pairs or EPR pairs, between two parties as illustrated in **Figure 1**. This advancement could transform cryptography, simulation, and optimization by offering remarkable computational power and secure communication. However, the quality of the qubits used and the implementation of the network resources are also crucial. The vision of a quantum internet is to provide fundamentally new internet technology by enabling quantum communication [7].

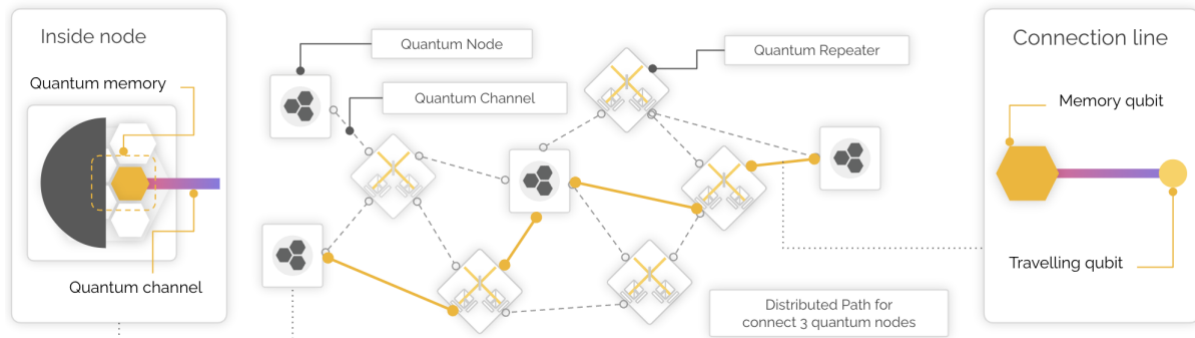


Figure 1.

Demonstrated quantum internet distribution resource between three nodes.

Quantum systems are used as a resource for computation and implementation of quantum network operations such as generating Bell pairs, purification processes, and entanglement swapping. However, noise in the environment can affect these processes. In quantum computing, the time it takes for its state to change, or waiting time of a qubit, is influenced by factors like temperature, noise, and interactions with other qubits. This waiting time is important as it affects the accuracy and reliability of computations. During quantum network operations, errors can occur due to imperfect unitary gates, especially those from multiple qubits, and measurement processes. Most of the noise in quantum networks is categorized from the repeater model. In this research, we simulate a photonic-based quantum repeater, which recently has received great research interest [8-9]. The main obstacle in implementing this type of repeater include the effects of photon loss in free space, and it also faces noise from physical qubit coherence time, gate errors, measurement errors, and depolarizing errors.

There are several strategies to reduce the impact of noise in a quantum network. One such strategy is deploying quantum error correction (QEC) [10], which borrows the concepts of classical error correction for bit-flip errors and extend for phase errors. QEC encodes multiple physical qubits into one tolerant logical qubit, enabling the system to detect and correct errors that occur. Another approach to improve the quality of a quantum network is through optimization. Research has shown that using Bayesian optimization [11] can be effective. This research [12] optimizes photon emitter pulse rate to reduce the waiting time in physical qubit for case non-equal distance between nodes. A study by Francisco Ferreira da Silva et al at QuTech proposed a quantum network optimization algorithm based on a genetic algorithm and simulated a quantum repeater chain [13].

For this research, we propose to employ a genetic algorithm [14-16] to find optimal parameters in a quantum network that lead to the lowest simulation cost, but still satisfy the desired fidelity threshold and certain predetermined network performance benchmarks.

Methodology:

In this section, we describe the methodology for optimization of the quantum internet system, which is simulated by the software `qwanta` [17].

Design cost function for optimization

Cost analysis was performed to assess the performance of the algorithm within the context of a quantum network system. `qwanta` has the capability to simulate linear quantum networks and calculate fidelity using the method of direct fidelity estimation [20]. We try to optimize the four parameters; namely, the photon loss, the gate error, the measurement error, and the coherence time. Initially, we normalize all parameter values to fall within the range of 0 to 1. Subsequently, we establish a cost structure using equation (1) to represent the cost associated with an individual parameter.

$$C_i = \frac{1}{\log_{x_b}(x_{new}^i)} \quad (1)$$

In this context, x_b represents the baseline parameter and x_{new} signifies the parameter after optimization. Consequently, when the optimized parameter's value surpasses that of the baseline, the cost is set to 1, as depicted in **Figure 2**. When considering the collective cost of all ($k = 4$) parameters, the equation for the cost is formulated as equation (2).

$$\sum_{i=1}^4 C_i = \sum_{i=1}^4 \frac{1}{\log_{x_b}(x_{new}^i)} \quad (2)$$

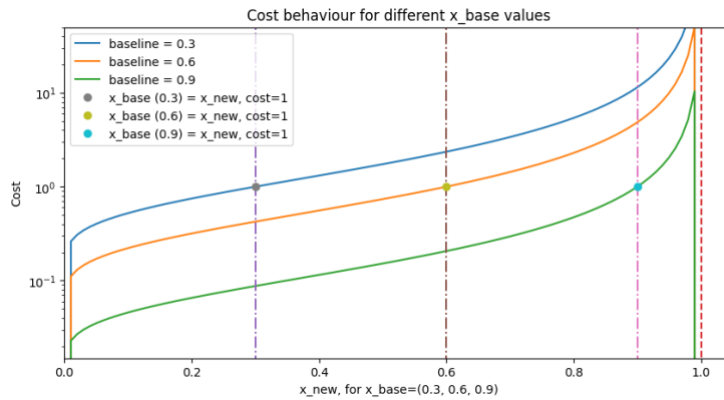


Figure 2.

Cost behavior when baseline value (x_b) = 0.3, 0.6, and 0.9.

However, equation (2) is constructed related to parameters only. To make simulation results more practical, we include the fidelity in the cost function. Finally, the cost function is defined in equation (3)

$$T_C = w\theta(F_{target} - F) + \sum_{i=1}^4 \frac{1}{\log_{x_b}(x_{new}^i)} \quad (3)$$

when T_C is the total cost value constructed from the fidelity term and parameters, Here θ is a Heaviside function, and F_{target} and F are, respectively, the target fidelity and fidelity from the simulation. The weight w is a hyperparameter of the optimization method, meaning that it is

not determined by some algorithm but must instead be chosen. Therefore, our problem finally becomes multi-objective optimization. There are inherent trade-offs among these objectives. For instance, enhancing the durability of memory in a sequence of nodes has a beneficial impact on the overall quality of entanglement over the entire system, but it simultaneously increases the expenses associated with parameters.

Genetic algorithm

Genetic algorithms (GAs) are nature-inspired optimization methods that mimic the processes of natural selection and genetics by maintaining a population of potential solutions, evaluating their fitness, and iteratively selecting, recombining, and mutating chromosomes. See Ref. [18] for comprehensive content. In this research, we employ the algorithm by randomly creating a population of parameter values. Each individual set contains four genes, namely the stated parameters (photon loss rate, coherence time, gate error, and measurement error). Then, all individual will feed into *qwanta* to calculate the fidelity for each set. The results and input parameters will adapt via genetic process by the following procedure:

1. Begin by generating the initial population consisting of 100 individuals.
2. Calculate the cost for each individual using equation (3).
3. Employ the roulette wheel selection method to select parents from the population for the subsequent application of the crossover operation.
4. Introduce the possibility of mutation in each gene of an individual, determined by a mutation probability.
5. Update the population with these newly created individuals and repeat the entire process for 120 iterations.

Fresh individuals are created by applying random crossover and mutation operations. This updated population is subsequently employed in the next iteration of the algorithm, where the simulation is performed with these new individuals.

GA validation

To assess the effectiveness of GAs and understand the impact of the algorithm's hyperparameters, various benchmarking functions have been established [18]. These functions are specifically crafted to assess the performance of different GA implementations when dealing with cost functions characterized by specific properties. To validate GA, we have chosen the Rastrigin objective function defined in equation (4) as the validating cost function. Rastrigin function and results of validation are shown in **Figure 3**.

$$f(x) = A + \sum_{k=1}^n (x^2 - A \cos(2\pi x)) \quad (4)$$

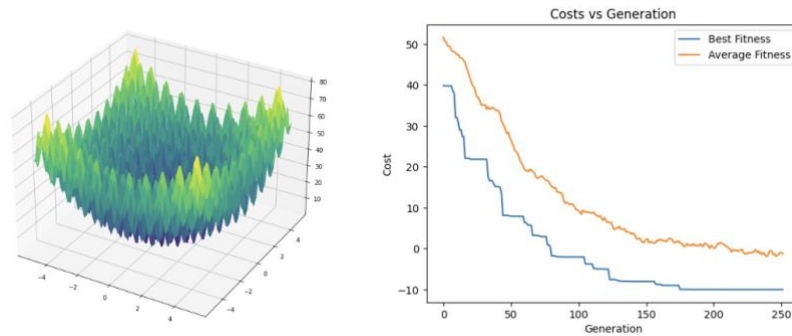


Figure 3.

Rastrigin function (left) and result from validate our GAs algorithm (right)
Main process of quantum network genetic algorithm (*QNET-GA*)

QNET-GA is software developed in this research. This software was developed by consider as a plugin of qwanta simulator. The brief mechanism of the software in terms of flowchart is provided in **Figure 4**. When n denotes the number of iterations (this research uses $n = 120$). At first, we initialize the baseline value and first population randomly.

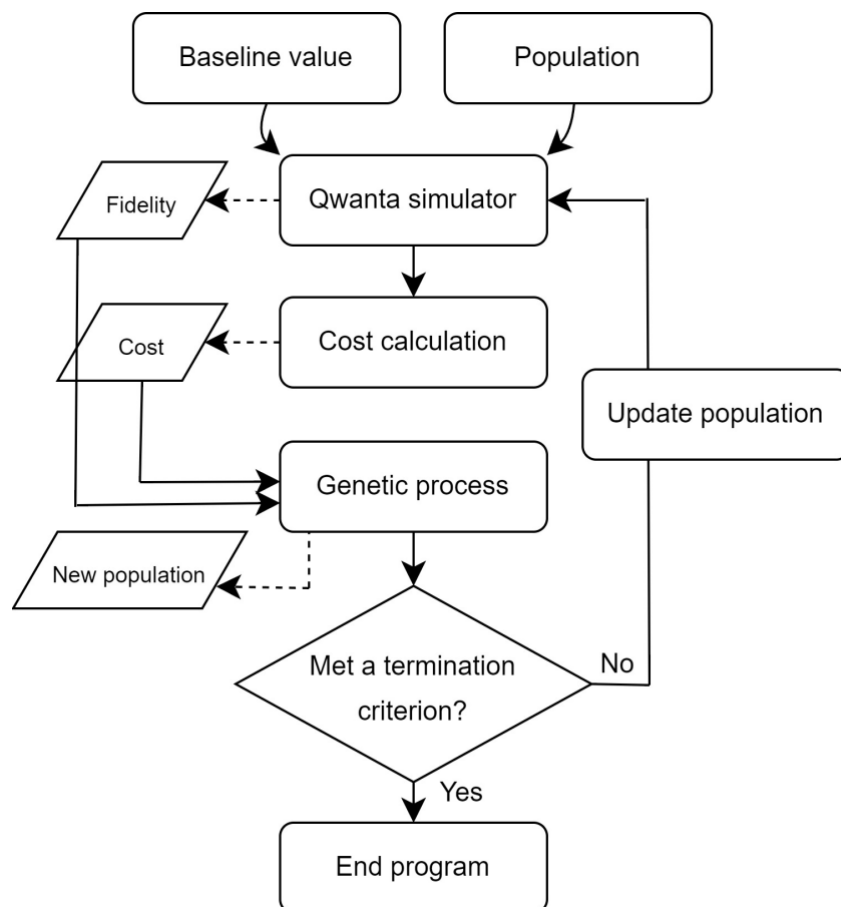


Figure 4.

Flowchart explains the mechanism of *QNET-GA*. First initialize the baseline value and first population. Every iteration, population will update via genetic process

Results and Discussion:

The quantum network optimization using GA is performed in two scenarios; namely (i) equally distanced nodes on a line, and (ii) real locations of three nodes in Thailand, as depicted in **Figure 5**.

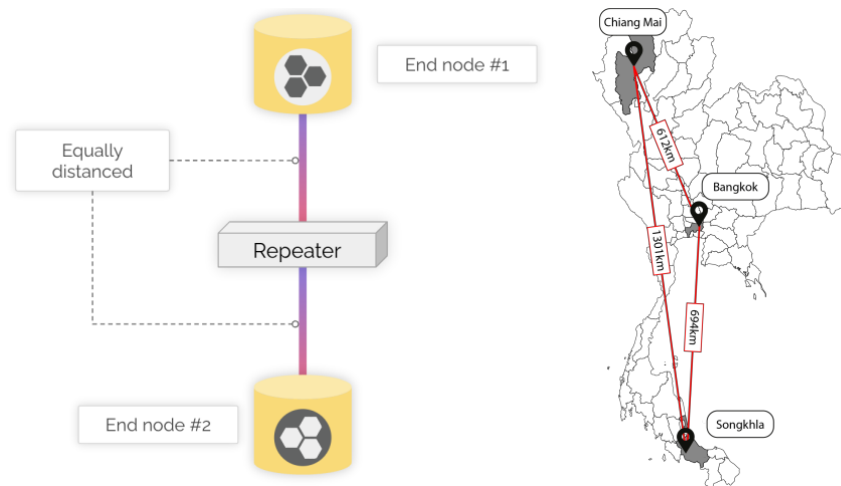


Figure 5.

In a scenario with equally spaced nodes and repeaters (left), place a repeater in Bangkok, with end nodes located in Chiang Mai and Songkhla, Thailand (right).

Equally distanced nodes on a line

We have conducted a simulation of a quantum internet system employing a single quantum repeater in the middle and equally distanced nodes. In **Figure 6** (left), we depict the temporal evolution of fidelity, while simultaneously experimenting with the weight tuning parameter. The tracking cost exhibits a decreasing trend over successive generations as shown in **Figure 6** (right). Nonetheless, sporadic peaks are observed within certain generations. We hypothesize that such peaks may be attributed to certain individuals within the population encountering a situation during the genetic process where their overall genetic makeup resides at the boundary of the search space. Furthermore, upon closer examination, oscillatory behavior within the data becomes apparent. These observations can be attributed to two primary factors: the inherent unpredictability of a genetic algorithm and our utilization of step functions for cost assessment. The second observation can be attributed to a combination of the previously mentioned step functions used in the cost evaluation and the inherent non-deterministic nature of our simulations, we also similarly occurred in previous report [13].

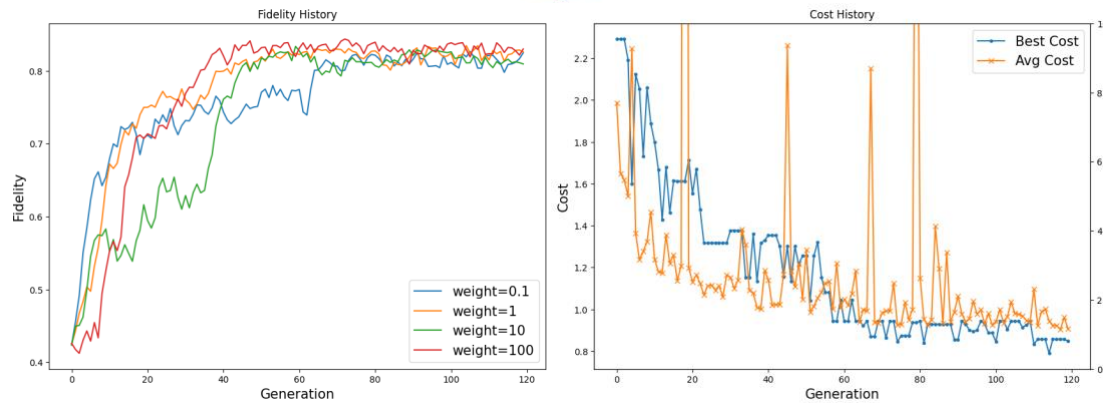


Figure 6.

Evolution of fidelity in 120 generations with different weights of the cost function (left), due to evolution of the cost (right). Peaks occur in some generations, possibly due to population's genes are encounter with extreme condition from genetic process

Real locations of three nodes in Thailand

We shall present a visual representation of the quantum network under investigation. The placement of nodes in this depiction is intended to approximate their respective geographical positions within Thailand. Specifically, a repeater node has been established in Bangkok, while two end nodes are situated in Songkhla and Chiang Mai. The outcomes of our analysis are presented in both **Figure 7**.

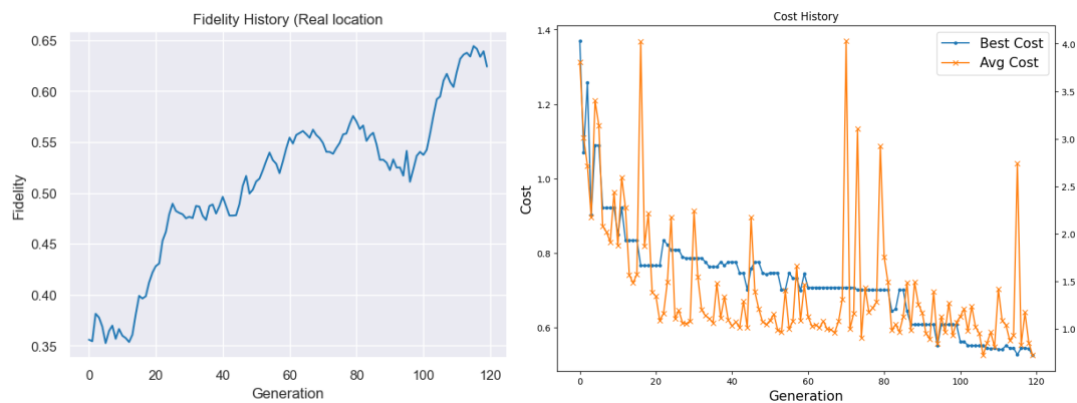


Figure 7.

Evolutional of real location simulation (CM-BKK-SK) (left) and evolutional of cost (right)

Pareto frontier analysis

Pareto frontier or Pareto front is a concept of multi-objective optimization. It represents a set of solution in a given problem space where no solution can be improved in one objective without reducing another. In other words, it delineates the trade-off between conflicting objectives, providing the best compromise solutions. For more concepts, readers can follow Ref. [19]. In this work, we try to optimize both fidelity and loss parameters that conflict. The results show the data of fidelity and its cost of all individuals in the last generation. By concept of Pareto front, we exhibit the result's graph as illustrated in **Figure 8**, as it is reasonable to

represent the x axis as $1 - F$ (the fidelity discrepancy). The Pareto front will minimize two objective functions (cost and $1 - F$).

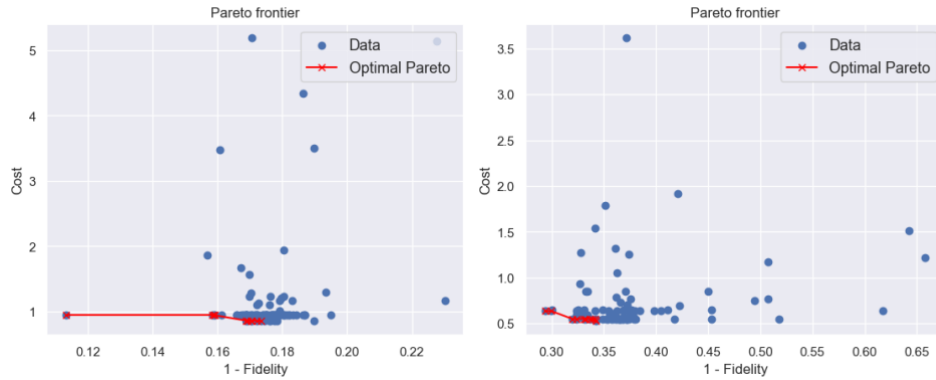


Figure 8.

Final generation of genetic algorithm individuals. The cross red notion is shown as the Pareto optimal point. Equally node distant (left). Real geographic location (right)

The parameters and fidelity of each Pareto optimal point of equally distant node and real geographic location will be shown in tables 1 and 2, respectively.

Table 1.

Pareto optimal of final improved parameters from equally distanced node in a line

Pareto optimal	Fidelity	Coherence time (s)	Measurement error rate (%)	Gate error rate (%)	Photon loss rate (db/km)
Best parameters #1	0.8868	0.0944	1.8761	0.0100	0.0083
Best parameters #2	0.8417	0.0944	2.9884	0.0100	0.0099
Best parameters #3	0.8408	0.0947	2.9885	0.0096	0.0099
Best parameters #4	0.8312	0.0965	2.9885	0.9622	0.0100
Best parameters #5	0.8307	0.0944	2.9885	0.9622	0.0099

Table 2.

Pareto optimal of final improvement parameters from real geographic location

Pareto optimal	Fidelity	Coherence time (s)	Measurement error rate (%)	Gate error rate (%)	Photon loss rate (db/km)
Best parameters #1	0.7065	0.0984	3.0000	1.6072	0.0056
Best parameters #2	0.7002	0.0984	3.0000	1.6072	0.0056
Best parameters #3	0.6805	0.0997	2.9430	1.6072	0.0085
Best parameters #4	0.6583	0.0997	2.9430	1.6071	0.0093
Best parameters #5	0.6573	0.0997	2.9430	0.0100	0.0099

Conclusion:

In this study, we present a new methodology to optimize a quantum network, which is based on a genetic algorithm, aimed at identifying optimal parameters for simulating quantum network systems. The proposed approach involves the development of a bespoke genetic algorithm. The parameters we have chosen to configure the quantum network system encompass critical factors such as qubit coherence time, measurement error, gate error, and photon loss in free space. This research comprises two distinct experiments. The first

experiment involves simulating an equidistant node configuration, while the second leverages actual geographic locations within Thailand with Songkhla and Chiang Mai as end nodes and Bangkok as the repeater node situated between them.

In the first experiment, equally node distant, each Pareto optimal within the final population achieved a fidelity level surpassing the predetermined fidelity target of 0.7. The highest fidelity is 0.8868. Our analysis reveals that, as expected, the cost (both average and best cost) decreases over generations. Most of Pareto's optimal points in the first experiment have met the initial criteria. In the second experiment, real geographic location, which involves simulations based on real geographical locations, there are only 2 Pareto optimal points that reach the target fidelity. While this meets the requisite threshold, we believe there is room for improvement by expanding the search space in genetic algorithms to encourage exploration of a wider parameter range. This research has enabled us to implement the methodology within a more complex model, streamlining the optimization process within a smaller, more manageable search space.

In both cases, nonetheless, certain generations exhibited noticeable peaks. Which we hypothesize that these peaks may be attributed to individuals within the population encountering scenarios during the genetic process where their genetic makeup approaches the boundary of the search space. We also notice oscillations in the data. These fluctuations can be attributed to two main reasons. First, the unpredictable nature of a genetic algorithm plays a role. Second, the use of step functions for cost assessment, along with the inherent randomness in our simulations, contributes to these observations.

This work holds promise as a valuable resource for future initiatives, offering assistance to researchers and engineers in identifying hardware and circuit enhancements necessary for the implementation of a quantum network in diverse locations. Consequently, the proposed methodology stands as a critical asset in a development of a blueprint for the quantum internet.

Acknowledgements:

This work receives funding from the Development and Promotion of Science and Technology Talents Project (DPST) and Mahidol University (Fundamental Fund: fiscal year 2024 by National Science Research and Innovation Fund (NSRF)).

References:

1. C. Cao, J. Hu, W. Zhang, X. Xu, D. Chen, F. Yu, J. Li, H.-S. Hu, D. Lv, and M.-H. Yung, "Progress toward larger molecular simulation on a quantum computer: Simulating a system with up to 28 qubits accelerated by point-group symmetry," *Phys. Rev. A*, vol. 105, p. 062452, Jun 2022.
2. M. B. Hastings, D. Wecker, B. Bauer, and M. Troyer, "Improving quantum algorithms for quantum chemistry," *Quantum Info. Comput.*, vol. 15, p. 1–21, jan 2015.
3. P. W. Shor, "Polynomial-time algorithms for prime factorization and discrete logarithms on a quantum computer," *SIAM Review*, vol. 41, no. 2, pp. 303–332, 1999
4. P. W. Shor and J. Preskill, "Simple proof of security of the bb84 quantum key distribution protocol," *Physical review letters*, vol. 85, no. 2, p. 441, 2000.
5. M. Fujiwara, K. ichiro Yoshino, Y. Nambu, T. Yamashita, S. Miki, H. Terai, Z. Wang, M. Toyoshima, A. Tomita, and M. Sasaki, "Modified e91 protocol demonstration with hybrid entanglement photon source," *Opt. Express*, vol. 22, pp. 13616–13624, Jun 2014
6. H. J. Kimble, "The quantum internet," *Nature*, vol. 453, pp. 1023–1030, Jun 2008.
7. S. Wehner, D. Elkouss, and R. Hanson, "Quantum internet: A vision for the road ahead," *Science*, vol. 362, no. 6412, p. eaam9288, 2018.

8. K. Azuma, K. Tamaki, and H.-K. Lo, “All-photon quantum repeaters,” *Nature Communications*, vol. 6, p. 6787, Apr 2015.
9. D. Buterakos, E. Barnes, and S. E. Economou, “Deterministic generation of all-photon quantum repeaters from solid-state emitters,” *Phys. Rev. X*, vol. 7, p. 041023, Oct 2017.
10. S. J. Devitt, W. J. Munro, and K. Nemoto, “Quantum error correction for beginners,” *Reports on Progress in Physics*, vol. 76, p. 076001, jun 2013.
11. P. Pathumsoot, “Development of simulator for second generation network of quantum repeaters.” Master’s thesis, Department of Physics, Faculty of Science, Mahidol University, 2021.
12. P. Pathumsoot, N. Benchasattabuse, R. Satoh, M. Hajdušek, R. Van Meter, and S. Suwanna, “Optimizing link-level entanglement generation in quantum networks with unequal link lengths,” in *2021 25th International Computer Science and Engineering Conference (ICSEC)*, pp. 179–184, 2021
13. F. F. da Silva, A. Torres-Knoop, T. Coopmans, D. Maier, and S. Wehner, “Optimizing entanglement generation and distribution using genetic algorithms,” *Quantum Science and Technology*, vol. 6, p. 035007, jun 2021
14. G. Acampora, A. Chiatto, and A. Vitiello, “Genetic algorithms as classical optimizer for the quantum approximate optimization algorithm,” *Applied Soft Computing*, vol. 142, p. 110296, 2023.
15. Y. Ye, Q. Huang, Y. Rong, X. Yu, W. Liang, Y. Chen, and S. Xiong, “Field detection of small pests through stochastic gradient descent with genetic algorithm,” *Computers and Electronics in Agriculture*, vol. 206, p. 107694, 2023.
16. P. W. Khan, C. Y. Yeun, and Y. C. Byun, “Fault detection of wind turbines using scada data and genetic algorithm-based ensemble learning,” *Engineering Failure Analysis*, vol. 148, p. 107209, 2023
17. P. Pathumsoot, “qwanta: Quantum network simulation based-on discrete-event simulator using error-propagation model.” <https://github.com/PorametPat/qwanta>
18. J. G. Digalakis and K. G. Margaritis, “On bench-marking functions for genetic algorithms,” *International journal of computer mathematics*, vol. 77, no. 4, pp. 481–506, 2001.
19. Ioannis Giagkiozis, Peter J. Fleming; Pareto Front Estimation for Decision Making. *Evol Comput* 2014; 22 (4): 651–678. doi: https://doi.org/10.1162/EVCO_a_00128.
20. S. T. Flammia and Y.-K. Liu, “Direct fidelity estimation from few pauli measurements,” *Phys.Rev. Lett.*, vol. 106, p. 230501, Jun 201.



SCIENTIFIC LITERACY LEARNING ACTIVITIES IN THE MODULUS OF ELASTICITY FOR SCIENCE HIGH SCHOOL STUDENTS USING AN EXPERIMENTAL SETUP TO MEASURE TENSILE STRESS AND STRAIN OF SOLID WIRES WITH A DIAL GAUGE

Thanyanan Somnam,* Kitisak Boonkham

Department of Physics, Mahidol Wittayanusorn School, Nakhon Pathom, Thailand

*e-mail: thanyanan.phu@mwit.ac.th

Abstract:

For high school students, studying the properties of matter is an important prerequisite for other topics in physics. Nowadays, teachers can easily use a multitude of teaching media such as video clips and animations to virtually demonstrate changes in the motion of constituents in liquids and gases when subjected to external forces. Nonetheless, illustrating the change in dimensions of solids caused by external forces remains challenging. The present study focuses on developing teaching methods for high school students in the context of modulus of elasticity, specifically Young's modulus, which measures a solid's resistance to changes in length due to external forces. The research involves scientific literacy learning activities using a self-designed experimental setup to measure tensile stress and strain in solid wires, with a particular focus on the elasticity of materials. The experiment is supported by a worksheet consisting of scientific literacy activities aligned with the Programme for International Student Assessment (PISA) framework, categorized into 3 dimensions: explaining phenomena scientifically, evaluating and designing scientific enquiry, and interpreting data and evidence scientifically. The assessment was conducted with 114 grade 11 students at Mahidol Wittayanusorn school, a specialized science high school in Thailand. The results of the assessments indicated varying levels of student performance. While students excelled in designing research protocols, conducting experiments, and analyzing data, they showed need for improvement in effectively communicating their findings. The study also evaluated students' skills in experimentation, teamwork, and academic communication, as well as their attitudes during the activities. The majority of students displayed excellent skills and positive attitudes, but some students lacked enthusiasm due to the novelty of the topic. In conclusion, the teaching methodology proved effective in enhancing students' understanding of Young's modulus and scientific skills. However, there is a need to strengthen students' communication skills and improve methods to engage them effectively in scientific activities. The study offers insights into enhancing scientific literacy and can be used as a model for improving teaching in various physics topics.

Introduction:

Studying the properties of matter is an important prerequisite for high school students before progressing to other topics in physics. In today's world, teachers can readily utilize a wide range of instructional media, such as video clips and animations, to virtually illustrate the changes in the motion of constituents in liquids and gases when subjected to external forces. However, depicting the alteration in the dimensions of solids due to external forces remains a challenging task. This pertains to the modulus of elasticity of solid materials, which is a property of a solid that determines its resistance to changes in length, shape, or volume. There are 3 types of elastic moduli depending on how the external force is applied to a solid: Young's modulus, shear modulus, and bulk modulus. At the high school level, teaching and demonstrating Young's modulus for solid materials in one dimension is more straightforward



compared to the other two, primarily due to its simplicity. Young's modulus is defined as the ratio of tensile stress to tensile strain. It can be interpreted as the solid's resistance to a change in length caused by an external force applied to the cross-sectional area of the material. Hence, the objective of this work is to enhance teaching management for the modulus of elasticity of solids, specifically focusing on Young's modulus. This is achieved by designing a competency-based learning activity that utilizes an experimental setup we have developed to measure the tensile stress and strain of solid wires using a dial gauge with a high resolution of 0.01 mm.¹

In order to evaluate and assess students' learning outcomes in this topic, we have developed scientific literacy learning activities that can be assessed according to the Programme for International Student Assessment (PISA) framework established by the Organization for Economic Co-operation and Development (OECD).² The assessment of scientific literacy can be categorized into 3 dimensions: A (explaining phenomena scientifically), B (evaluating and designing scientific enquiry), and C (interpreting data and evidence scientifically). In addition, scientific literacy is classified into 6 levels, depending on the context and the complexity of the situations encountered by students as illustrated in Figure 1.

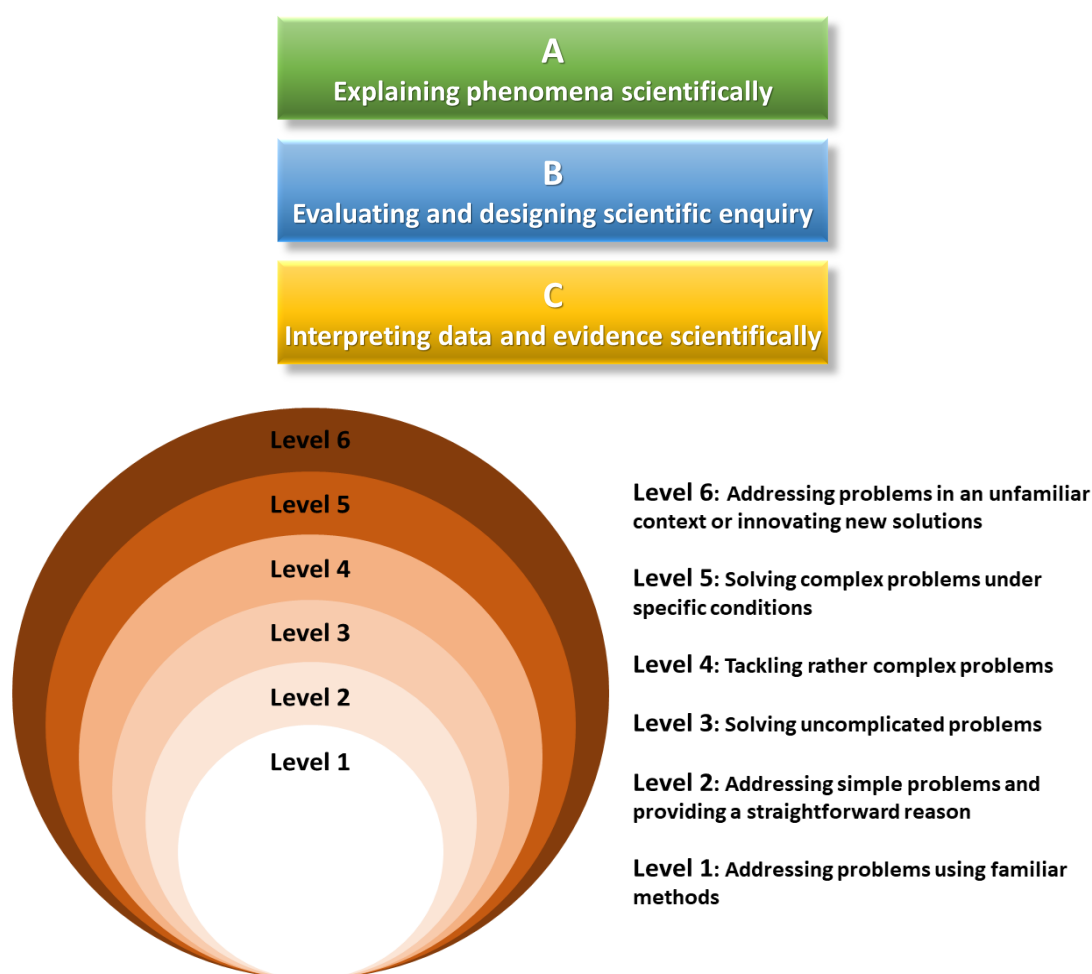


Figure 1.

The 3 dimensions (A, B, and C) of the assessment of scientific literacy and the 6 levels of students' scientific literacy



The assessment of students' scientific literacy was carried out within a 100-minute teaching management session across 5 classes consisting of 114 students in grade 11 in the academic year 2023 at Mahidol Wittayanusorn school, a specialized science high school in Thailand. This institution is dedicated to offering advanced education tailored to the needs of gifted and talented students in the fields of science and mathematics. Furthermore, we observed the students' abilities in conducting experiments, collaborating with their peers, and effectively communicating their academic viewpoints. Additionally, we assessed the students' skills and attitudes throughout the activities by utilizing evaluation checklist items.

Methodology:

Assessment of students' scientific literacy in alignment with PISA

The assessment of students' scientific literacy was conducted in accordance with the PISA framework, employing a worksheet consisting of 3 sections. The first section introduces Young's modulus for one-dimensional solids. The second section provides instructions for using the apparatus to determine Young's modulus for solid wires. The third section presents scientific literacy learning activities related to the determination of Young's modulus for solid wires. This final section includes 5 learning processes, starting with the design of the research protocol and concluding with the study's findings.

The first section: Introduction to Young's modulus for one-dimensional solids

One-dimensional solid materials can exhibit elastic properties. This means that when an external force is applied to the cross-sectional area of a solid, it may either lengthen or shorten. However, upon the removal of the external force, the solid returns to its original length. To investigate this property, Young's modulus is introduced and defined as the ratio of tensile stress (the force applied to the object) to tensile strain (the object's response to the force). It can be understood as the solid's resistance to a change in length resulting from an external force applied to its cross-sectional area. In this study, we specifically focused on the elastic behavior of a solid within its elastic limit, where the relationship between tensile stress and tensile strain is linear. Young's modulus is, therefore, the constant of proportionality between these two physical quantities and can be expressed as follows.³

$$Y = (F/A)/(\Delta L/L)$$

where F is the external force acting as a tensile force applied to a solid wire, A is the cross-sectional area of the solid wire, ΔL is the elongation of the solid wire when the tensile force is presented, and L is the initial length of the solid wire. Here, the term F/A represents tensile stress, and the term $\Delta L/L$ is tensile strain.

The second section: Instructions for using the apparatus to determine Young's modulus of solid wires

Our apparatus for determining Young's modulus of solid wires was designed and crafted at Mahidol Wittayanusorn school workshop. In this study, we considered gravitational force as the external force applied to the cross-sectional area of a solid wire.¹ All the components of the apparatus are depicted in Figure 2(a). Figure 2(b) displays the manual xyz translation stage, which allows for the precise positioning of the dial gauge at the center of the slot weight base before measuring the elongation of the solid wire. Masses of 50 g and 100 g with an uncertainty of ± 1 g, as seen in Figure 2(c), were employed to generate various

tensile stresses. To facilitate self-study of students, we prepared a video clip illustrating the use of the high-resolution (0.01 mm) dial gauge before the class session. This apparatus greatly enhances students' comprehension of the longitudinal expansion of solid wire caused by the external force applied to its cross-sectional area.

In this section, the teacher demonstrated how to use the apparatus and encouraged students to replicate the experimental procedure. To enhance understanding, several questions were posed to guide students in observing the dial gauge after the masses were successively placed on the slot weight rod. The teacher also facilitated a discussion among students regarding the independent and dependent variables in this experiment.

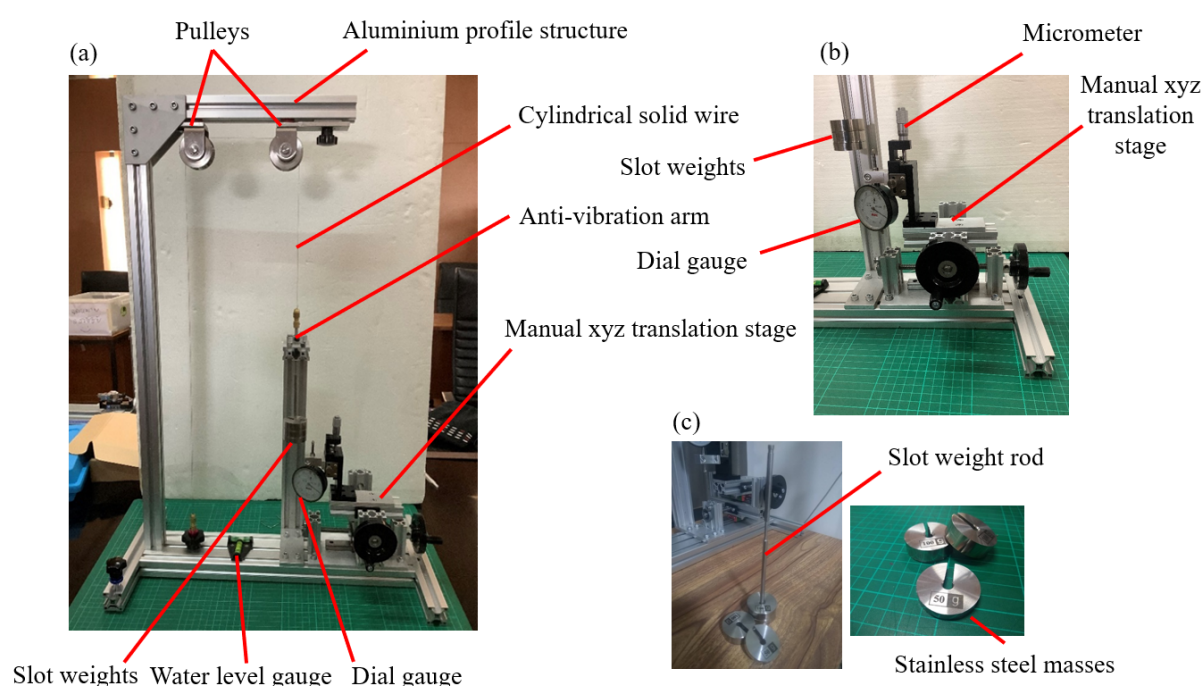


Figure 2.

(a) Developed apparatus to measure Young's modulus of solid wires using gravitational force as an external force. (b) Dial gauge and manual xyz translation stage. (c) Slot weights.

Adapted from our previous work.¹

The third section: Scientific literacy learning activities for determination of Young's modulus of solid wires

Students were organized into groups consisting of 3-4 individuals. The activities encompass 5 learning processes that enable us to assess students' scientific literacy. Here are the details of each process.

1) Setting the apparatus for experimentation

Students were required to provide a comprehensive explanation of the steps to prepare the apparatus for accurately determining Young's moduli of two wires: copper wire and iron wire. The Young's modulus values of the copper wire and iron wire used in the experiment are respectively $1.1 \times 10^{11} \text{ N/m}^2$ and $1.9 \times 10^{11} \text{ N/m}^2$.

- Measure the initial length of the wire used in the study multiple times using a meter stick and record the measurements.



- Measure the wire's diameter both before and after the experiment using a micrometer and record the measurements. Calculate the average value of the wire's radius.
- Thread the wire through two pulleys, securing one end to the experimental setup's base.
- Attach a set of weights to the opposite end of the wire.
- Set the dial gauge to zero. To accomplish this, adjust the probe of the dial gauge with the micrometer mounted on the sliding base in the z-axis so that both the short hand on the small dial and the long hand on the large dial of the dial gauge point to zero.

2) Designing the research protocol

Students were tasked with specifying the dependent and independent variables relevant to the experiment and drafting a comprehensive and accurate research protocol. The following steps are essential for conducting the experiment:

- Define the mass on the rod or the weight of stainless steel masses as the independent variable and the elongation of the wire as the dependent variable.
- Modify the gravitational force applied to the wire by adding at least 5 different masses to the rod using stainless steel weights.
- For each mass value, measure the elongation of the wire 3 times using the dial gauge and calculate the average elongation.

3) Collecting experimental data

Students conducted the experiment independently under the guidance of the teacher. They were required to create a dedicated table for recording experimental data, adhering to the following guidelines:

- The table should include a minimum of 2 columns. The first column should be designated for the independent variables (the masses or weights) with the appropriate units, and the second column should be for the corresponding dependent variables (the elongation of the wire) also with the correct units.
- Students were required to display the 3 measured values recorded for each elongation, including the appropriate units, before calculating the average elongation.

4) Analyzing the experimental data and discussing the findings

Students analyzed the data collected during the experiment and engaged in a discussion of the results. They were encouraged to:

- Create a graph using Microsoft Excel by positioning the independent variables on the x-axis and the dependent variables on the y-axis. Title the graph and label the axes with the relevant units.
- Identify any patterns or trends in the experimental data. It is important to note that the experiment was designed to be conducted within the elastic limit of the solid wire, so the correct trend is a linear regression.
- Interpret the relationship between the elongation of the wire (the dependent variable) and the mass or weight applied (the independent variable). To achieve this, students should, for example, consider the previously mentioned Young's modulus expression and rearrange it to obtain the following relationship: $\Delta L = (gL/YA)m$, where g represents the acceleration due to gravity. Consequently, the slope of the linear graph, gL/YA , can be used to extract the Young's modulus value.
- Compare the Young's modulus values obtained for the copper wire and the iron wire with their reported values. Calculate the corresponding percentage errors to assess the



accuracy of the experimental results. Discuss about some sources of errors that could occur in the experiment.

5) Concluding the study

In the final process, students were tasked with summarizing the findings of the study. They were encouraged to reflect on the following aspects:

- When the wire experiences stress, which is the result of an external force acting perpendicular to the wire's cross-sectional area, it causes the wire to change in length by stretching. This change in length induces strain in the wire.
- The stress and strain experienced by the wire are directly proportional to each other (exhibiting linearity). The constant of proportionality in this relationship is known as the Young's modulus of the wire.
- A wire with a high Young's modulus value exhibits high elasticity because it can effectively withstand stress from a significant external force while experiencing only a minimal change in length relative to its original length. In this experiment, it was observed that the iron wire exhibited greater elasticity compared to the copper wire. This observation is consistent with the concept of Young's modulus.

For the assessment of students' scientific literacy in alignment with PISA within this study, we have chosen 3 dimensions, each rated at level 3, with a maximum total score of 10.0 for each dimension:

A3 level 3: Capable of making reasonable predictions and providing explanations regarding the relationships between changes in events by applying scientific knowledge. This evaluation of scientific literacy was based on the explanations related to the Young's modulus of solid wires, specifically focusing on the final learning process.

B3 level 3: Capable of suggesting a survey method to investigate events that involve a restricted scope of study, effectively constraining certain event parameters, while also outlining a well-defined and systematic survey process. This assessment of scientific literacy was conducted based on the design of the research protocol and the collection of experimental data, which encompass the first three learning processes.

C2 level 3: Capable of analyzing and interpreting data to unveil patterns that emerge from situations with limited conditions, and giving conclusions based on advanced scientific knowledge. This evaluation of scientific literacy was derived from the analysis of experimental data, the discussion of the findings, and the conclusion of the study, which are associated with the last two processes.

Assessment of students' skills

The assessment of students' skills took place in the classroom while they were conducting the experiment. The teacher observed each student's behavior and skills, assigning a score of 0, 1, or 2 for each evaluation checklist outlined in Table 1.

**Table 1.**

An example of behavioral observation form in skill training activities. This form is designed to evaluate students' skills during the learning activities. Each evaluation item can receive scores of 0, 1, or 2.

Evaluation checklist	0^a	1^b	2^c
1. Correct and safe use of tools and equipment in experiments			
2. Skills in observation and data recording			
3. Proficiency in analyzing, discussing findings, and summarizing results			
4. Skills in collaborating with others			
5. Effective and clear academic communication and presentation of ideas			

^aThe score 0 represents students do not exhibit behavior and lack the skills for proper performance.

^bThe score 1 represents students exhibit behavior and/or possess skills for performance, but they are not clear or entirely accurate.

^cThe score 2 represents students exhibit behavior and/or possess skills for proper performance.

The total score from all the evaluation checklists represents each student's skills. The evaluation criteria are as follows: 9-10 points indicate excellent, 7-8 points indicate good, 5-6 points indicate satisfactory, and 0-4 points indicate the need for improvement.

Assessment of students' attitudes

The evaluation of students' attitudes was conducted in the classroom as they were engaged in the experiment. The teacher observed each student's behavior and allocated a score of either 0 or 2 for each item on the evaluation checklist provided in Table 2.

Table 2.

An example of behavioral observation form for attitude assessment. This form is designed to assess and document student's attitudes during the learning activities. Each evaluation item can receive scores of 0 or 2.

Evaluation checklist	0^a	2^b
1. Enthusiasm for the pursuit of knowledge		
2. Collaboration in all the activities		
3. Responsibility for submitting the assignment on time		
4. Positive attitude toward science learning		
5. Recognizing the value of applying knowledge in everyday life		

^aThe score 0 represents students do not exhibit behavior.

^bThe score 2 represents students exhibit behavior.

The total score from all the evaluation checklists represents each student's attitudes. The evaluation criteria are as follows: 10 points indicate excellent, 8 points indicate good, 6 points indicate satisfactory, and 0-4 points indicate the need for improvement.

Results and Discussion:

Following the completion of the class, students were assigned to compose a group report on the experiment. Table 3. displays the results of the assessment of students' scientific literacy, aligned with PISA, across 3 areas: A3 level 3, B3 level 3, and C2 level 3. The table

includes the average scores for each scientific literacy area and the percentage of students achieving a minimum passing score of at least 6 out of 10.

Table 3.

Results from the assessment of students' scientific literacy in alignment with PISA. Average scores for each scientific literacy area and the percentage of students scoring at least 6 out of 10 are reported.

Scientific literacy area aligned with PISA	Average score	% correct (N = 114) ^a
A3 level 3	5.66/10.0	48.25%
B3 level 3	8.07/10.0	100%
C2 level 3	7.06/10.0	78.07%

^aThe percentage of students having the score of at least 6 out of 10, which is the minimum passing criteria. The total number of students is 114.

The results indicate that students performed exceptionally well in the assessment of their scientific literacy B3 level 3, achieving an impressive average score of 8.07 out of 10.0. Furthermore, it is noteworthy that every student (100%) met the minimum passing criteria. This suggests that all students possess the capability to design an appropriate experimental protocol, identify independent (mass or weight applied) and dependent (elongation of the wire) variables, and accurately collect data from the experiment.

In the assessment of scientific literacy C2 level 3, students also demonstrated strong abilities in analyzing experimental data using graphing methods, interpreting the relationship between mass and elongation, extracting the Young's modulus value of the wire, and effectively concluding the study. These findings are substantiated by the high average score of 7.06 out of 10.0, and a majority of students (78.07%) successfully met the minimum passing criteria. This highlights that the apparatus developed to measure Young's modulus of solid wires and the structured learning processes overseen by the teacher have significantly enhanced students' competence in conducting experiments using the scientific method. However, it is essential to acknowledge that a minority of students (21.93%) still require improvement in their experimental skills. Identifying their specific challenges and providing targeted support can further enhance the overall effectiveness of the educational approach.

In contrast to the previous assessments, the evaluation of scientific literacy A3 level 3 has yielded concerning results, with an average score of 5.66 out of 10.0. Furthermore, less than half of the students (48.25%) met the minimum passing criteria. This suggests that while most students are proficient in conducting the experiment effectively, there is a notable need for improvement in their communication skills, both in speaking and writing. To address this issue, it is crucial to focus on enhancing students' abilities to effectively convey their findings from the experiment. Students should be encouraged to provide concise and comprehensive summaries of their results, emphasizing the key results and insights gained from the experiment. Developing strong communication skills in scientific contexts is integral to the overall success of students in scientific education and research. This may involve additional training or exercises to strengthen their ability to articulate their findings clearly and effectively.



Throughout the experiment session, students' skills and attitudes were assessed. The results are presented in Table 4 with the percentage of students attaining each level of performance.

Table 4.

Results from the assessment of students' skills and attitudes. The percentage of students achieving each level of performance is reported.

Assessment	Excellence	Good	Satisfactory
Assessment of students' skills	65.79%	28.07%	6.14%
Assessment of students' attitudes	90.35%	9.65%	

In the assessment of students' skills, the majority of students (65.79%) performed at an excellent level. However, a small portion achieved a good level of performance (28.07%), and a very few were at a satisfactory level (6.14%). Those in the good and satisfactory levels made minor mistakes during the analysis of experimental data using graphing methods and provided unclear discussions regarding their findings. Specifically, students at the satisfactory level encountered challenges in effectively communicating their academic opinions and presenting their ideas clearly. To enhance the skills of these students and help them improve their performance, it may be beneficial to provide additional support and guidance in areas such as data analysis, graph interpretation, and effective communication of scientific findings. This support can aid in bridging the gap and elevating the performance of students who have the potential to excel further.

In the assessment of students' attitudes, a substantial majority of students (90.35%) exhibited excellent level of performance. However, a small group (9.65%) appeared to lack enthusiasm for the pursuit of knowledge. The students in this latter group may not have fully engaged with the topic, possibly due to its novelty, resulting in difficulties in following the instructions and explanations provided by the teacher at the beginning of the session. As a consequence, these students received scores lower than 6 out of 10. To address this issue, it is important to consider strategies for increasing student engagement and motivation, particularly for topics that are new or challenging. Providing additional support, clarifications, or alternative approaches to instruction may help improve the enthusiasm and engagement of these students. Encouraging active participation and a positive learning environment can also contribute to boosting their attitudes and overall performance.

Conclusion:

In conclusion, this study involved the design and implementation of scientific literacy learning activities focusing on the modulus of elasticity for 114 grade 11 students at Mahidol Wittayanusorn school during the academic year 2023. These activities utilized an experimental setup to measure the tensile stress and strain of solid wires with a dial gauge. The design and assessment of the activities were aligned with the PISA framework, and 3 domains of scientific literacy were evaluated: A3 level 3, B3 level 3, and C2 level 3. Additionally, students' skills and attitudes were assessed throughout the activities. The findings from this study indicate that the assessments of students' scientific literacy at the B3 level 3 and C2 level 3 were satisfactory, suggesting that the majority of students performed well in these areas. However, the evaluation of scientific literacy at the A3 level 3 raised concerns, as less than half of the students met the minimum passing criteria. This highlights the need for improvement in students' communication skills, particularly in the context of



articulating their findings clearly and effectively. The assessment of students' skills also revealed that a minority of students faced challenges in effectively communicating their academic opinions and presenting their ideas clearly. In the evaluation of students' attitudes, a small group of students lacked enthusiasm for pursuing knowledge, likely due to the novelty of the topic. This resulted in difficulties in following instructions and explanations provided by the teacher at the beginning of the session. In this work, the teaching methodology proved effective in enhancing students' understanding of the concept of the modulus of elasticity of solids and in improving their scientific skills through scientific literacy learning activities using the developed apparatus. However, it also underscored the importance of strengthening students' communication skills and finding ways to engage them effectively in activities. This study can serve as a pilot teaching model for other physics topics aimed at developing students' scientific literacy and identifying areas within a class that require improvement and reinforcement.

Acknowledgements:

We are thankful for the financial support and the access to facilities provided at the workshop of Mahidol Wittayanusorn school.

References:

1. Boonkham K, Phuphachong T. The 46th International Congress on Science, Technology and Technology-based Innovation (STT46) proceeding. 2020:639–646.
2. OECD. PISA 2018 Assessment and Analytical Framework. 2019:1–304.
3. Serway R A, Jewett J W. Physics for Scientists and Engineers with Modern Physics (9th edition). 2012:373–377.



Simple protocol to create a single photon source by using BBO from Spontaneous Parametric Down-Conversion process in BBO

Thanapat Phetvongsakul, Atirach Ritboon, Ruchipas Bavontaweepanya, Ekkarat Pongophas*

Division of Physics, Faculty of Science and Technology, Thammasat University, Rangsit Center, No. 99, Village No. 18, Phahonyothin Road, Khlong Nueng Subdistrict, Khlong Luang District, Pathum Thani 12120

*e-mail: e_pong@tu.ac.th

Abstract:

A single-photon source generated by spontaneous parametric down-conversion (SPDC) process is very important in quantum optics laboratories. A simple method for setting up SPDC in a Beta Barium Borate (BBO) crystal is proposed. Two He-Ne lasers as guide lasers are passed through four diaphragms positioned at the vertices of an isosceles triangle and at the middle of its base. The angle between the middle line and two equal sides are $\pm 3^\circ$. The BBO crystal is placed at the vertex point of the triangle. This configuration allows precise and easy positioning the other optical devices, especially, the detectors. The heralded single-photon signals with a high signal-to-noise ratio we achieved by this method. Even with a low-cost 405 nm diode laser module, the coincidental count rate reaches 3036 counts/s, with a noise level as low as 18 counts/s.

Introduction:

A single-photon source is an important component in the field of quantum optics, quantum communications, quantum information, quantum cryptography, quantum communication networks[1-5], and quantum processing[6-10]. SPDC is the process that enables the particle-like property of light consequently, it is a simple generation of single photon by absorbing one photon and remitting to two photon lower frequencies[11]. This heralded single photon can be tested by the Hanbury-Brown and Twiss experiment, i.e. a beam to be tested is sent in to a beam splitter to examine the coincidence of two signals from the photon pair detected by two detectors in the reflecting path and the transmitted paths[12]. This proceeding proposes a simple, but effective protocol to set up a single photon source, which is versatile by using four iris diaphragm to construct isosceles triangle. He-Ne lasers guide lasers alignment by four diaphragms positioned at the vertices of an isosceles triangle, that make guide lasers serving as down-conversion with non-collinear making angle of 3° with respect to the pump beam outside the crystal precisely. This configuration make the alignment of optical devices simple and precise. It is a free space setup with BBO crystal as a single photon generator with a cost-effective 500mW continuous laser(priced at 1500 baht) as a pump beam. The set up allows us to avoids the commonly used, but expensive technique, i.e. using the two aluminium rails have the same pivot at the position of the BBO crystal to align optical devices, which need to be specially created. The examples of the experimental set up employing such expensive technique include K Boonkham and P Limsuwan[13], Benjamin VEST and Lionel Jacubowicz[14], Gustavo Armendáriz and Víctor Velázquez[15]. Although some techniques of SPDC do not require two aluminium rails as demonstrated by Muhammad Hamza Waseem, Faizan-e-Ilahi and Muhammad Sabieh Anwar[16], diaphragms used only to calibrate the optical elements to have the same height on the table, doesn't use to alignment position the other optical devices.



Methodology:

Theoretical

BBO crystal for SPDC

SPDC in BBO crystal is a non-collinear phase-matching process, When a pump photon is absorbed by the BBO crystal from NEWLIGHT(PABBO5050-405(I)-HA3), the two daughter photons with half energy of the pump photon are reemitted and makes an angle relative to the pump photon. This process obeys the principles of energy conservation and momentum conservation through this equation(1),

$$\omega_p = \omega_s + \omega_i \text{ and } \vec{k}_p = \vec{k}_s + \vec{k}_i. \quad (1)$$

When ω_p is frequency of pump photon, ω_s is frequency of signal photon and ω_i is frequency of idler photon, \vec{k}_p is wave vector of pump photon, \vec{k}_s wave vector of signal photon and \vec{k}_i wave vector of idler photon.

The angle of down-conversion relative to the pump photon obeys

$$n_p(\omega_p) = n_d(\omega_p/2)\cos\theta_d, \quad (2)$$

when n_p is refractive index of pump photon, n_d is refractive index of down-conversion photon and θ_d is angle of down-conversion photon with respect to pump photon.

For SPDC in BBO type I crystal which e-ray converse to o-ray, the Refractive index from Sellmeier for BBO crystal is

$$n_o^2(\lambda) = 2.7359 + \frac{0.01878}{\lambda^2 - 0.01822} - 0.01354\lambda^2, \quad (3)$$

$$n_e^2(\lambda) = 2.7359 + \frac{0.01878}{\lambda^2 - 0.01822} - 0.01354\lambda^2, \quad (4)$$

when λ given in μm , n_o is ordinary index of refraction in crystal and n_e is extraordinary index of refraction in crystal. The relation of the extraordinary index of refraction with the angle θ from the optical axis is given by

$$n^2(\theta) = \frac{n_e^2(\lambda)n_o^2(\lambda)}{n_e^2(\lambda)\cos^2\theta + n_o^2(\lambda)\sin^2\theta}, \quad (5)$$

where the pump beam enters the crystal with a certain angle θ with respect to the optical axis and the frequency dependence of n_e and n_o is omitted for brevity. The extraordinary index is varied with the incident angles.

To find the angle θ_d when the pump beam of a frequency λ enters the crystal and produces the down-converted photons at frequency of 2λ and optic axis make angle of θ ,

$$n(\theta) = n_p(\lambda_p) = n_d(2\lambda_p)\cos\theta_d, \quad n_d(2\lambda_p) = n_o(2\lambda_p). \quad (6)$$

Then we have

$$(n_o(2\lambda_p)\cos\theta_d)^2 = \frac{n_e^2(\lambda_p)n_o^2(\lambda_p)}{n_e^2(\lambda_p)\cos^2\theta + n_o^2(\lambda_p)\sin^2\theta}, \quad (7)$$

$$\theta_d = \cos^{-1} \left[\frac{1}{n_o(2\lambda_p)} \sqrt{\frac{n_e^2(\lambda_p)n_o^2(\lambda_p)}{n_e^2(\lambda_p)\cos^2\theta + n_o^2(\lambda_p)\sin^2\theta}} \right]. \quad (8)$$

In this setup, the pump beam with a wavelength $0.405 \mu\text{m}$ enters the BBO crystal. This pump beam is the extraordinary ray comparing to the optic axis which making angle of 29.97° to the normal line. This produces the down-converted photons at wavelength of $0.810 \mu\text{m}$ which are the ordinary rays. By substituting these variables into the latest equation, the down-conversion angle θ_d can be find and its value is 3° comparing to the normal line. Consequently, single photon detectors and other optical devices must be located at this angle. Thus, this angle is crucial to the setup and must be focused on precisely.

Three-Detector Measurement of $g_{3D}^{(2)}(0)$

From Figure 4, method of three-detector measurement of $g_{3D}^{(2)}(0)$ [12] is the two daughter photon's beam coming from the BBO are separated, one beam is detected at detector G, while the other goes to the beam splitter and is detected at detectors T and R, because detector T and R have detection conditions at the detector. G therefore expects that the probability will be according to this equation

$$g_{3D}^{(2)}(0) = \frac{P_{GTR}}{P_{GT}P_{GR}}. \quad (9)$$

When P_{GTR} is the probability of coincidence of signals between detector T R and G, P_{GT} is the probability of coincidence of signals between detector T and R, P_{GR} is the probability of coincidence of signals between detector R and G

$$P_{GTR} = \frac{N_{GTR}}{N_G}, \quad P_{GT} = \frac{N_{GT}}{N_G} \text{ and } P_{GR} = \frac{N_{GR}}{N_G}. \quad (10)$$

When $N_{GT}(N_{GR})$ is the number of detections that detector T(R) and detector G have simultaneously and N_{GTR} is number of detections that three detector T(R) and detector G have detections photon signals in same time then

$$g_{3D}^{(2)} = \frac{N_{GTR}N_G}{N_{GT}N_{GR}} \quad (11)$$

Experimental setup

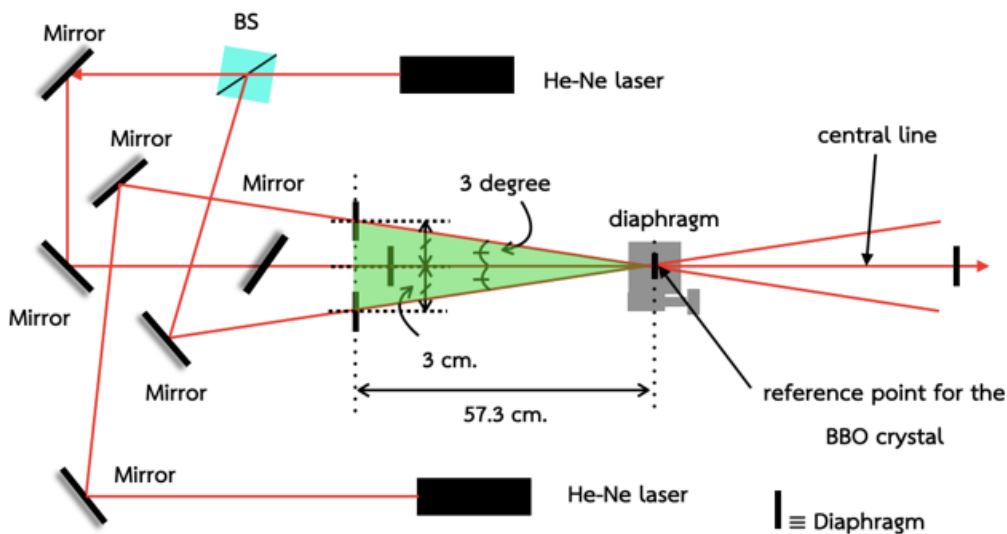


Figure 1. Schematic of the experimental setup to form an isosceles triangle angled at $\pm 3^\circ$ for the pump beam and the signal and idler beams.

In the first step, two He-Ne lasers are used as guide beams and splitted into three beams. The first He-Ne beam is aligned through two diaphragms to create a central line. Other two diaphragms are placed at 3 centimeters beside of the central line on both sides and 57.3 centimeter away from the reference point for the BBO(NEWLIGHT NCBB05300-405(I)-HA3) crystal on the same central line. Its position is the vertex of a triangle. Those diaphragms are used to create an isosceles triangle angled at $\pm 3^\circ$ relative to the crystal. Then two He-Ne laser are aligned these diaphragms, represent the pump beam at the center line, the signal and idler beams angled at $\pm 3^\circ$ from the center line respectively as shown in Figure 1.

In the second step, the prism mirror, mirrors and lenses are placed in signal and idler part to the single photons from BBO. These single photons consequently pass through bandpass filters before reaching avalanche photodiode (APD) detectors placed in each path as shown in Figure 2.

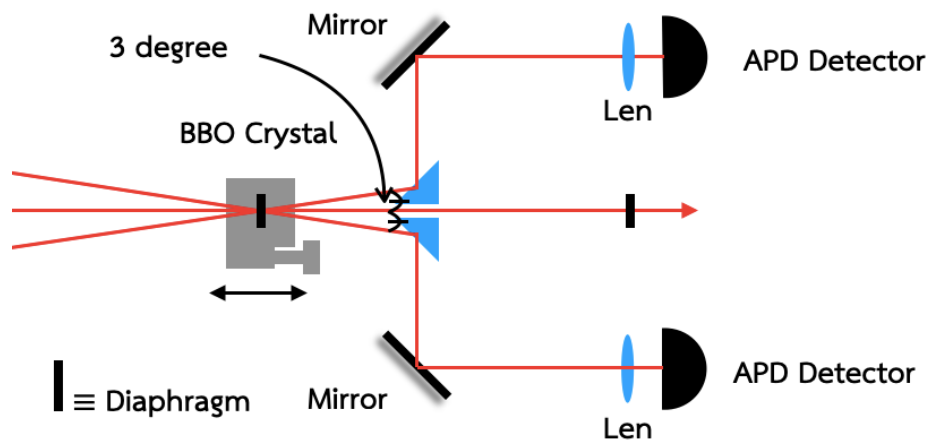


Figure 2. schematic of the setup for aligning the single photon detector

In the last step, a 5mm X 5mm X 3.0mm Type-I BBO crystal is replaced the reference diaphragm and is pumped by a 500 mW, 405 nm laser diode which spatial filter by passing through a lens and a pinhole. Another lens is used to collimate the laser beam and reduce unwanted feedback light reflected into the laser cavity. Finally, the 405 nm laser beam is aligned such that its beam pass through two reference diaphragms on the center line as shown in Figure 3.

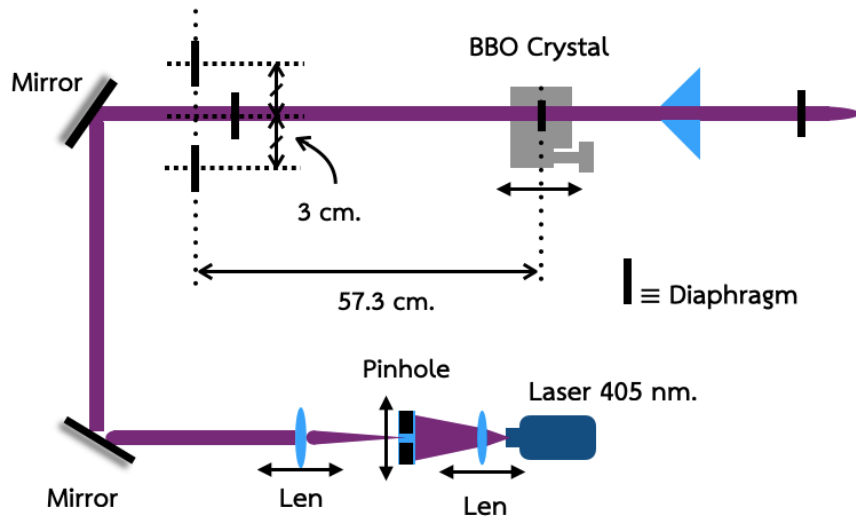


Figure 3. schematic of the experiment setup for 405 nm pump beam

Coincidence signals between signal and idler photons are measured using two APDs and time tagging module (quTAG MC). The signal from the last step, one APD serves as the trigger to start the clock, while the other APD signal is used to stop the clock. These start-stop signals at various time difference are stacked and used to plot the histogram of coincidence signal at different time.

To prove the existing of single-photon signal, the photon antibunching measurements is conducted. A 50:50 beamsplitter is added in front of the stop-clock APD. A another APD are added to receive the reflecting beam of the beamsplitter, serving as another stop-clock signal (HBT setup) as show in Figure 4. The coincidence histogram between the start and stop signals at the reflected output beamsplitter and the start and stop signals at the transmission output beamsplitter are measured. For measure the quantum correlation $g^{(2)}(\tau)$ at different delay time. delay time can change by the time of the stop signal at the reflected output beamsplitter is offset from -10 ns to +10 ns with 200 ps step before calculate coincidence

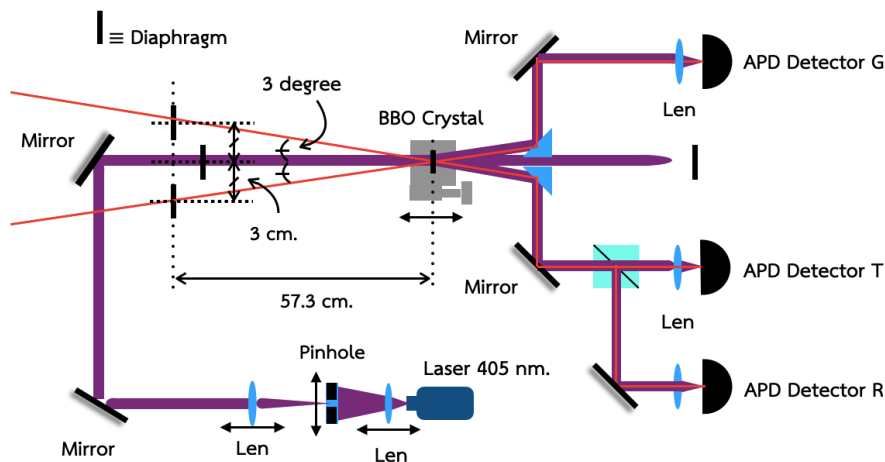


Figure 4 schematic of the HBT setup for photon antibunching measurements and coincidence measurements

Results and Discussion:

To verify that this setup can produce single photon pairs, $g^{(2)}(\tau)$ correlation between signals which is measured by coincidence signals must show peaks located at the time delay corresponding to the path difference of the light beams. The two peaks are at time delay of 14.4 nanoseconds and 23.2 nanoseconds as shown in Figure 5. This corresponds to the correlation between photon signal reaching the detector in the signal-photon beam to start the clock and photon signals reaching one of the two detectors, located at both output port of BS, in the idler photon beam to stop the clock at both output port of BS. The first peak is coincidence between start and stop at the transmission port of BS and the second peak is coincidence between start and stop at the reflection port of BS in which the detector is place in the longer path. The number of pair photons that can produce is represented by the number of coincidence counts of both peaks, sum number of coincidence counts of both peaks at any time delay, the coincidental count rate is 3036 counts/s, with a averaged noise level at 18 counts/s.

The $g^{(2)}(0)$ correlation peak indicate that there is a pair of single photon at small time interval on the signal and idler beam. At zero time delay ($\tau = 0$), the three detector $g^{(2)}(0)$ value is near zero, coincidence window increase make the width of well is and also increase height of the bottom well. With coincidence window at 0.5 ns, 1 ns, 3 ns and 6 ns as a result, the well width are 2.2 ns, 2 ns, 5.8 ns and 11.88 ns and height of the bottom well are 0.020, 0.028, 0.114 and 0.240 respectively as show in Figure 6.

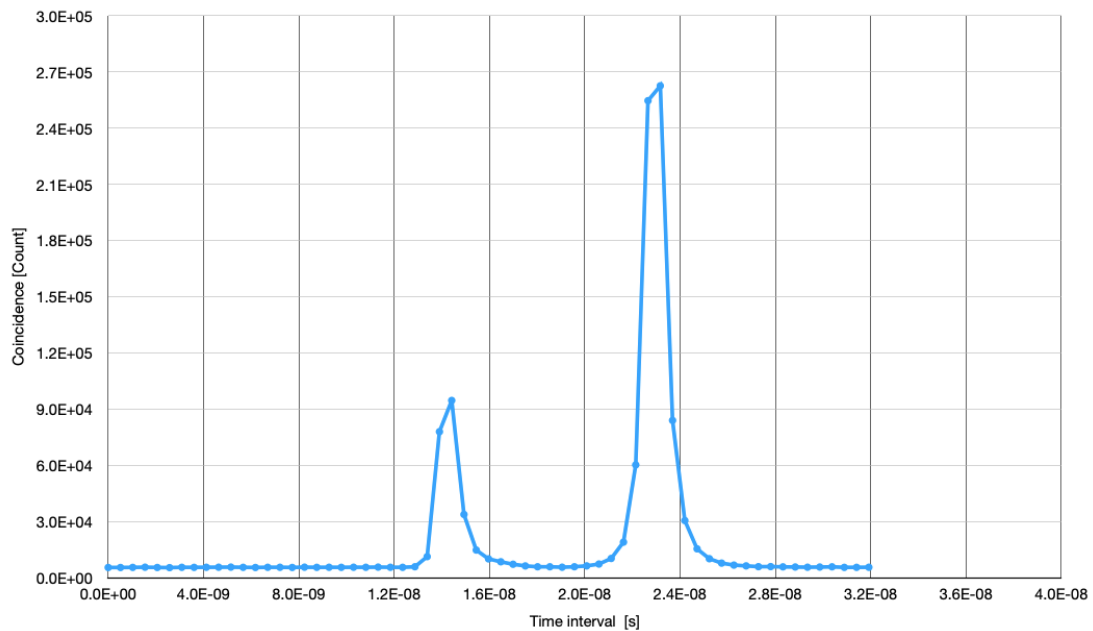


Figure 5. The coincidence signal at each time delay. The blue is a coincidence of 3 detector on HBT setup collection data for 300 s, peaks at a time delay of 14.4 ns and 23.2 ns

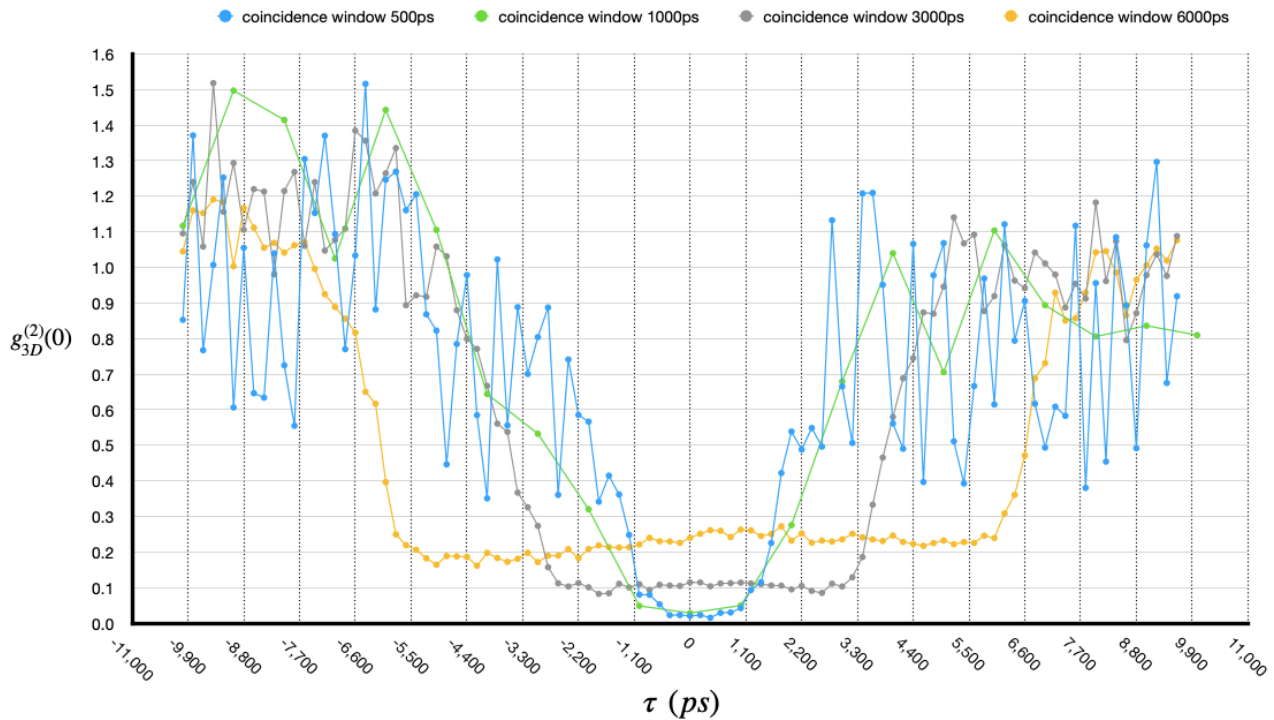


Figure 6. The graph demonstrates the value of $g^{(2)}(\tau)$ as a function of time delay. The blue, green, grey and orange data are the $g^{(2)}(0)$ with a coincidence window of 500 ps, 1000 ps, 3000 ps and 6000 ps respectively.

Conclusion:

In summary, we propose an SPDC setup technique that uses only four diaphragms as reference point and two He Ne lasers as guiding lasers for the signal and idler beam from SPDC process, marking an angles of $\pm 3^\circ$ to the BBO crystal, the position of the optical devices can be tuned precisely and easily and the heralded single-photon signal can be measured with a high signal-to-noise ratio, even with a cost-effective 405 nm diode laser module (1500 THB).

The number of coincidence signals at each time delay shows two peaks at a time delay of 14.4 ns and 23.2 ns. These peaks show that single-photon source can produce pair photons at rate is 3036 count/second with a noise level of 18 count/second. The quantum correlation $g^{(2)}(0)$ at different delay time was measured at four different coincident windows. The minimum value is 0.020 at the coincident window 0.5 ns. We found that the $g^{(2)}(0)$ increases increase with the increase coincidence window. The near zero value of the correlation verifies the particle property of our single photon source

Acknowledgements:

Scholarship for talent student to study graduate program in Faculty of Science and Technology Thammasat University, Contract No.TB 38/2565

This research has received funding support from the NSRF via the Program Management Unit for Human Resources & Institutional Development, Research and Innovation [grant number B37F660011]



References:

1. D. Bouwmeester, J. W. Pan, K. Mattle, M. Eibl, H. Weinfurter, and A. Zeilinger. *Nature*. 1997;137:215–221.
2. T. B. Pittman, B. C. Jacobs, and J. D. Franson. *Phys. Rev. A*. 2002;66:042303.
3. P. Walther, K. J. Resch, T. Rudolph, E. Schenck, H. Weinfurter, V. Vedral, M. Aspelmeyer, and A. Zeilinger. *Nature*. 2005;434:169-176.
4. W. Tittel and G. Weihs. *Quant. Inf. Comput.* 2001;1:3-56.
5. W. T. M. Irvine, A. L. Linares, M. J. A. de Dood, and D. Bouwmeester. *Phys. Rev. Lett.* 2004;92:047902.
6. A. A. Malygin, A. N. Penin, and A. V. Sergienko. *JETP Lett.* 1981;33:477-48.
7. J. G. Rarity, K. D. Ridley, and P. R. Tapster. *Appl. Opt.* 1987;26:4616-4619.
8. A. N. Penin and A. V. Sergienko. *Appl. Opt.* 1991;30:3582-3588.
9. P. G. Kwiat, A. M. Steinberg, R. Y. Chiao, P. H. Eberhard, and M. D. Petroff. *Phys. Rev. A*. 1993;48:R867-R870.
10. P. G. Kwiat, A. M. Steinberg, R. Y. Chiao, P. H. Eberhard, and M. D. Petroff. *Appl. Opt.* 1994;33:1844-1853.
11. Suman Karan, Shaurya Aarav, Homanga Bharadhwaj, Lavanya Taneja, Arinjoy De, Girish Kulkarni, Nilakantha Meher, and Anand K Jha. *Researchgate*. 2018.
12. M. Beck. *Journal of the Optical Society of America B*. 2007;24:2972-2978.
13. K Boonkham and P Limsuwan. *Journal of Physics: Conference Series*. 2019;1380:012043.
14. Benjamin VEST and Lionel Jacubowicz. *Photoniques Number*. 2022;112:22-25.
15. Gustavo Armendáriz and Víctor Velázquez. *Photonics*. 2023;10:775.
16. Muhammad Hamza Waseem, Faizan-e-Ilahi and Muhammad Sabieh Anwar. *Iopscience*. 2020.

THE EFFECT OF POURING TEMPERATURE AND STIRRING SPEED ONTO MECHANICAL BEHAVIOUR OF ALUMINIUM-MAGNESIUM (Al- Mg) ALLOY

N. N. A.Basir¹, N.B.Norazman¹, M.M. Mahat¹, S.M. Yahaya²,

R. Rosmamuhamadani^{1,*}

¹Material Science and Technology Programme, Faculty of Applied Sciences, Universiti Teknologi MARA, 40450 Shah Alam, Selangor, Malaysia

²Applied Chemistry Programme, Faculty of Applied Sciences, Universiti Teknologi MARA, 40450 Shah Alam, Selangor, Malaysia

ABSTRACT

Many researchers have worked on various metal matrix composite (MMC) production procedures, which has reduced their cost to a nominal level when compared to other types of casting processes. Many of the process factors of stir casting route, accurate selection of base matrix, the weight percentage of reinforcements, and reinforcement particle grain size can affect the properties and characteristics of such MMCs materials. The distribution of reinforcements, on the other hand, is determined by the parameters of the stir casting process. The study of the effects of stir casting parameters on particle distribution and the best selection of these remains a challenge for ever-expanding businesses and research. In this research, meticulous efforts were made to investigate the effect of stirring parameters in the stir casting process. Furthermore, best stir casting parameter values were provided, which may be useful to researchers working on Al-MMC development. This paper aiming to offer a comprehensive analysis of Al-MMCs behaviour affected by pouring temperature and speed which produced using the most cost-effective liquid state stir casting process.

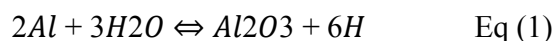
Keywords: *Casting, stir casting, Al-MMCs, stirring parameters, metal matrix composite (MMC)*

INTRODUCTION

Aluminium matrix composites (Al-MMCs), copper matrix composites (Cu-MMCs), and magnesium matrix composites (Mg-MMCs) are some examples of MMCs that are high in demand these days in various applications such as the aerospace, automobile, and electronics industries, amongst many others, due to their appropriate properties and low-price availability (Singh et al., 2016).

Aluminium matrix composites are composites in which the base material (matrix) is aluminium or aluminium alloy, and the reinforcements are usually non-metals. Reinforcements can be added in many forms, such as particles, whiskers, and fibre, and can be added in volume percentage or weight percentage (wt %). More than one reinforcement is added to the aluminium matrix in a hybrid aluminium matrix. And for its high stiffness, strength-to-weight ratio, superior wear resistance, controlled coefficient of thermal expansion, higher fatigue resistance and better stability at really high temperatures, and high electrical and thermal conductivity compared to conventional metals and alloys, particles reinforced aluminium matrix composites are used in automobile, aerospace, and structural applications (Singh. et al., 2016). The selection of processing techniques has a significant impact on the composite's properties.

Stir casting is suitable processing technique to fabricate aluminium matrix composites since it is a mass-production friendly technique and cost-effective. Aluminium is melted in the initial step of stir casting. Aluminium that melts react with the moisture and environment during melting to generate a layer of aluminium oxide (Al_2O_3), as shown in Eq (1). This layer protects the melt's surface from the additional atmospheric reactions.



Stir casting is one of the methods of casting that includes continuously stirring the melt, exposing the melt surface to the atmosphere, and causing continuous oxidation of the aluminium melt. The wettability of the aluminium decreases because of continual oxidation, leaving the reinforcing particles unmixed. Al_2O_3 is a chemical compound that cannot be decreased under normal conditions with maintaining melt wettability. To totally halt the oxidation, an inert atmosphere must be provided, which is fraught with difficulties. As a result, adding wetting agents to the melt, such as borax, magnesium and TiK_2F_6 , is a common solution to this problem and is commonly applied in the fabrication of Al-MMCs (Pai. et al.,1995). Apart from the oxidation issue, another crucial issue in the stir casting method, which is regulated by stirring parameters, is ensuring homogenous particle dispersion in the melt. As a result, stirring parameter selection is crucial in the stir casting process. Stirring time, stirring speed, impeller blade angle, impeller position, and impeller size are all significant factors that can affect the distribution of reinforcements in the matrix.

Porosity formation is one of the most significant issues with cast metal matrix composites (MMCs). Porosities can occur at the interface between the reinforcing particles and the matrix alloy in stir cast MMCs. In a cast MMC, the volume fraction of porosity and also its distribution and size, have a key influence in influencing the material's mechanical properties. Failures generated from particle fracture in the reinforcement-matrix interface due to voids coalescence, pores within the matrix material, and reduced ductility are some of the problems that arise in metal matrix composites due to the presence of porosity. The corrosion resistance of the casting and pores within the matrix material might also be harmed by this type of composite flaws. As a result, porosity levels must constantly be kept to a minimum, (Ahmad et al., 2005).

Objective of this research is to offer a better understanding on the effect of pouring temperature and stirring speed and optimization of pouring temperature and stirring speed for the fabrication of Al-MMCs through stir casting method. Al-Mg alloy was selected as an alloy in this investigation. Other than that, this paper also aiming to analyse the mechanical behaviour of Al-MMCs composite alloys through stir casting process.

METHODOLOGY

Sample preparation

Aluminium-magnesium (Al-Mg) was melted in high temperature furnace by casting technique. Al-Mg alloy was identified for its properties through their mechanical characterizations.

Al-Mg alloys were prepared according to categories, and their parameters. For the first batch, Al-Mg had gone through the process of melting in the furnace at 650, 700 and 750 °C. After the alloy melted, homogenization process had been conducted for about 15 minutes with different stirring speed. The speed that chosen were 100, 200, 400 and 500 rpm. All elements mixed gradually in the furnace and finally the mixture was poured on the stainless steel mould and cooled it in room temperature. [9].

Mechanical Characterization

Hardness testing

The hardness of a substance can be determined using a number of different approaches. The Vickers hardness test with ASTM E384 standard is the test that will be used in this research. Through the scale of penetration of an indenter loaded on a material test-piece, the Vickers scale characterizes the indentation hardness of materials. The diamond indenter is shaped like a right pyramid, with a square base and a 136° angle between opposite vertices. For 15 seconds, a diamond indenter was pressed into the surface of the prepared material with a mass of 200 grams. Five indentations were produced for each sample composition; each indentation was at least 2mm apart, and the average value was taken. The diagonal lengths were measured using a microscope with a changeable slit integrated into the eye piece and a diamond indenter that made a square impression. If the indentation and lengths received from a resolution counter geared to the movement, the width of the slit was modified such that its edges meet with the corner. If the indentation and lengths were received from a resolution counter geared to the movement of the slit, the width of the slit was changed so that its edges meet with the corner. By referring to an ocular chart corresponding to the applied force of 200g, the reading was transformed into Vickers hardness number (Hv), avoiding repetitive calculations.



Figure 1. Vickers hardness tester

Impact Strength Test

An impact test measures a material's toughness, which is defined as its ability to absorb energy during plastic deformation. When compared to the strength achieved under a slowly applied load, impact strength is often lower. As a result, the impact test assesses the energy required to fracture a conventional notch bar when an input load is applied. Impact strength testing by Izod is a common method of assessing impact resistance. On a notched sample, the Izod impact test was performed. Casting was used to create a standard square impact test specimen with dimensions of 75mm x 10mm x 10mm, a notch depth of 2mm, and a notch angle of 45° . The machine could produce impact energies ranging from 0 to 164J. The hammer weighed 22 kg. Figure 4.1 shows schematic diagram of Izod testing setup.

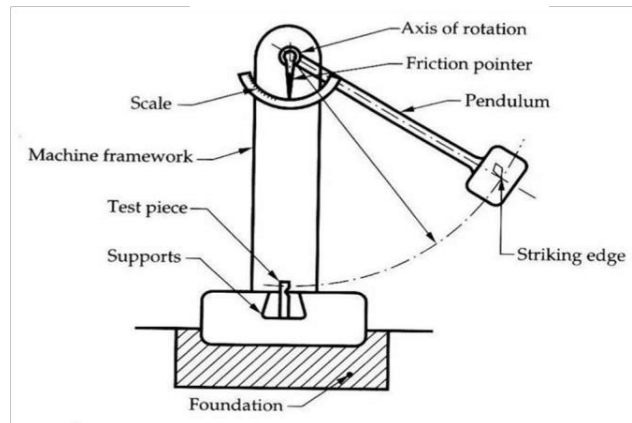


Figure 2. Schematic of Izod Testing Setup

RESULTS AND DISCUSSION

Hardness and Impact Properties

Figure 3(a) and (b) below shows the properties of hardness and Impact strength for Al-Mg alloy against casting stirring speed and the difference in casting temperature. From graph (a), it shows that the optimum hardness value is reached when the stirring speed is 400 rpm. The three same trends are shown by the use of different casting temperatures of 650, 700 and 750 C. However, the highest temperature of 750 C produces the highest hardness value of 85 Hv compared to the use of temperatures of 650 and 700, which are 75 da respectively 73 Hv.

Likewise with the trend for impact strength, the optimum value is also obtained when using stirring speed at 400 rpm. However, the highest value was recorded at the casting temperature of 750 which recorded the highest hardness value of 68 Hv, compared to the casting temperature of 650 and 700 where the respective values were 46 and 53 Hv.

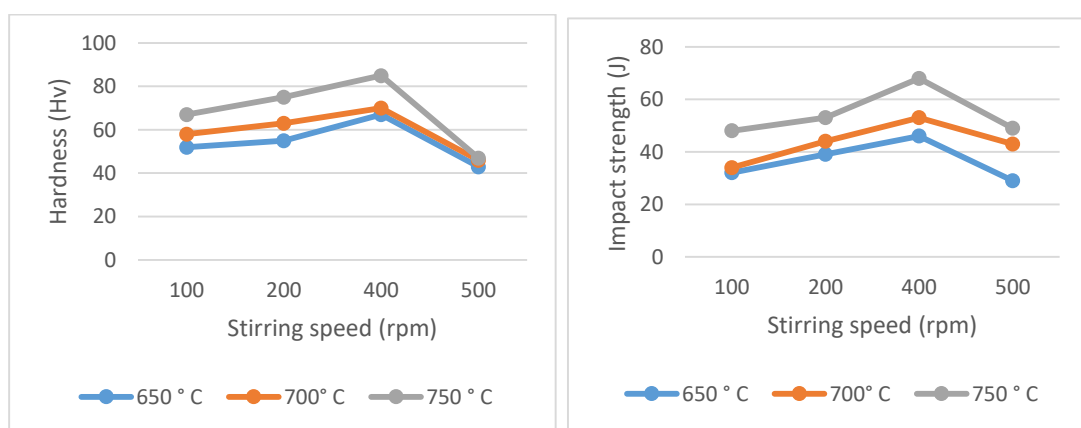


Fig. 3(a) Hardness (Hv), (b) Impact strength (J) of Al-Mg alloy versus casting stirring speed (rpm) with different pouring temperature

Figure 4(a) and (b) below shows the properties of hardness and Impact strength of Al-Mg alloy against casting temperature with difference in stirring speed. From graph (a), it shows that the optimum hardness value is reached when the casting temperature is 750 °C. The three same trends are shown by the use of different stirring speeds of 100, 200, 400 and 500 rpm. However, the highest stirring speed of 400 rpm produces the highest hardness value of 85 Hv compared to the use of temperatures of 650 and 700, which are 75 and 73 Hv respectively.

Likewise with the trend for impact strength, the optimum value is also obtained when using stirring speed at 400 rpm. However, the highest value was recorded at the casting temperature of 750 which recorded the highest hardness value of 85 Hv, compared to stirring speed of 100, 200 and 500 rpm respectively at the casting temperature of 650 and 700 where the respective values were 67, 75 and 47 Hv.

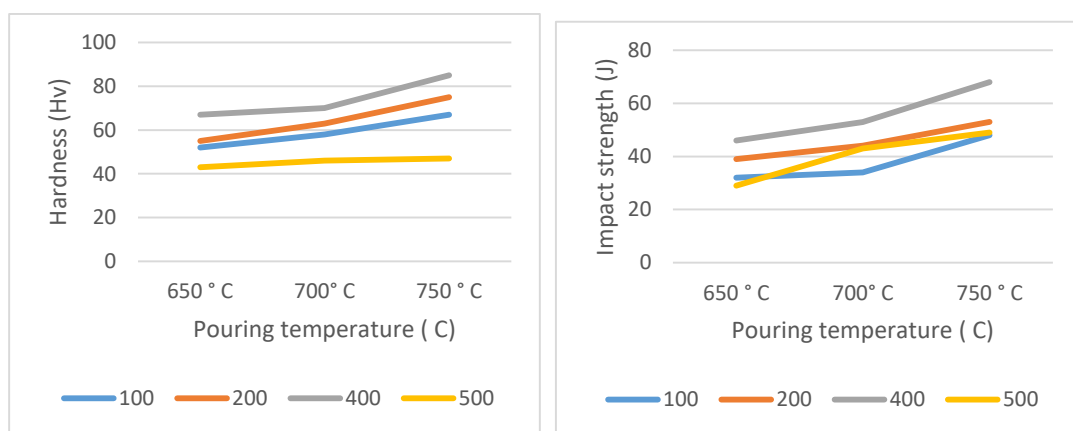


Fig. 4 (a) Hardness (Hv), (b) Impact strength (J) of Al-Mg alloy versus pouring temperature with different stirring speed (rpm)

According to Serajul et al., (2014), indicates that variables (stirring speed and pouring temperature) have a considerable effect on output variables like hardness and impact strength. They carried out that pouring temperatures ranging from 700°C to 750°C provide the best hardness and impact strength for all stirring speeds when the pouring speed is held constant at 2.5 cm/s. The study by Manoj et al., (2009) which suggests that increasing the composition of SiC increases hardness and impact strength, as well as the study's suggestion that homogenous dispersion of SiC particles in the Al matrix exhibits an upward trend in mechanical properties, gives some support to the conclusion. They stated that increasing stirring speed increases the impact strength and hardness of the material up to a certain point, after which these properties drastically decrease. They also reported that stirring speed of 400 rpm gave the ideal value of hardness and impact strength for MMCs.

ACKNOWLEDGMENTS

The author would like to thank the faculty of Applied Sciences, UiTM Shah Alam for the facilities and guidance.

REFERENCES

- Ahmad S. N., Hashim J., Ghazali M. I. (2005). The Effect of Porosity on Mechanical Properties of Cast Discontinuous Reinforcement Metal-Matrix Composite. *Journal of Composite Materials*, 451-466.
- Gagandeep Singh, A. K. (2019). A Review Paper on Stir Casting of Reinforced Aluminium Metal Matrix Composite (MMC). *International Journal of Current Engineering and Technology*.
- Manoj Singla, D. D. (2009). Development of Aluminium Based Silicon Carbide Particulate Metal Matrix Composite. *Journal of Minerals & Materials Characterization & Engineering*, 455-467.
- Pai B. C., Ramani Geetha, Pillai R.M., Satyanarayana K.G. (1995). Role of Magnesium in cast aluminium alloy matrix composites . *Journal of Materials Science*, 1903-1911.
- Prabu S. Balasivanandha, K. L. (2006). Influence of stirring speed and stirring time on distribution of particles. *Journal of Materials Processing Technology*, 268-273.
- Serajul Haque, A. H. (2014). Effect on Pouring Temperature and Stirring Speed on Mechanical, Microstructure and Machining Properties of Al6061-Cu Reinforced SiCp Metal Matrix Composites. *International Journal of Research in Engineering and Technology*, 104-109.
- Sharma S., S. J. (2021). Investigation on mechanical, tribological and microstructural properties of Al-Mg-Si-T6/SiC/muscovite-hybrid metal-matrix composites for high strength applications. *Journal of Materials Research and Technology*, 1564-1581.
- Sigworth K., K. A. (2007). Grain Refinement of Aluminum Casting Alloys. *International Journal of Metalcasting*, 31-40.
- Singh J, Chauhan A. (2016). Characterization of hybrid aluminium matrix composites for advanced applications. *Journal of Materials Research*, 159-169.



SESSION B-BIOLOGICAL SCIENCES

Antibiofilm Effects of Biosurfactants from *Lactobacillus fermentum* on *Escherichia coli* Biofilm and Remineralization of Hydroxyapatite

Bhuvit Charoenpanich,¹ Taechasit Srinutisap,¹ Thanasan Nilsu^{1,*}

¹Kamnoetvidya Science Academy, Thailand

*e-mail: thanasan.n@kvis.ac.th

Abstract:

Remineralizing agents have been widely used for preventive and non-invasive care of non-cavitated carious lesions to restore minerals to demineralized enamel. Nanohydroxyapatite (nHAp) and sodium fluoride (NaF) are among the most effective and commercially available caries-preventing remineralizing agents. Biosurfactants produced by oral bacteria *Lactobacillus* have been shown to inhibit biofilm formation. However, there is limited evidence of *Lactobacillus* biosurfactants' effects on remineralization process. Thus, this research aimed to investigate the emulsifying and antibiofilm activities of the *L. fermentum* biosurfactant (LFB) against *Escherichia coli* biofilm and the effects of LFB in combination with nHAp and NaF on remineralization of initial caries. The emulsifying and biofilm-inhibiting properties of LFB were investigated by oil-spreading and antibiofilm assays, respectively. The remineralization treatments were examined on *E. coli* biofilm-coated and acid-demineralized hydroxyapatite (HA) discs as artificial initial caries. Analysis of microbial growth on the surface of HA discs was performed using the WST-8 assay and SEM-EDX. The results showed that LFB efficiently acted as emulsifiers and significantly reduced biofilm formed by *E. coli* in the co-incubation experiments. Treatments of nHAp and NaF with added LFB were shown to reduce microbial viability in short-term biofilm-precoating experiments. In addition, LFB were demonstrated to form emulsion-based nanoparticles containing nHAp and NaF as revealed by TEM-EDS. Remineralization treatments with preformed nanoparticles increased calcium-phosphorus ratios on the surface of HA discs in biofilm-precoating and co-incubation experiments. These results would suggest further studies on using LFB as antibiofilm agents along with nHAp and NaF for prevention and treatment of initial caries.

Introduction:

Caries lesion is formed when tooth surface or enamel is demineralized or loses its mineral contents, mostly calcium and phosphate, by various causes including biofilm formation, the major one. However, there is the reverse process of demineralization, termed remineralization, which enhances the deposition of minerals, primarily in the form of calcium phosphate or hydroxyapatite crystals, slowing the problem of caries lesion. Consequently, remineralizing agents, such as sodium fluoride (NaF) and nanohydroxyapatite (nHAp), are currently the potential substances to treat dental caries, particularly for an active initial stage or non-cavitated caries lesion.¹

Biosurfactants or biological surfactants are a diverse group of surface-active biomolecules synthesized by various microorganisms, such as bacteria, yeast, and fungi, which can reduce the surface tension between two phases and aid in emulsifying two immiscible substances, unveiling potential properties of antibiofilm and antiadhesion. Additionally, biosurfactants have recently gained attention in various industries because, unlike many synthetic surfactants, they are usually biodegradable, less toxic, ubiquitous, and compatible with ecosystem.^{2,3,4} In this research, we focused on the effectiveness of bacterial biosurfactants on remineralization by virtue of their anti-adhesive properties, which inhibit biofilm formation. However, there is a lack of clear scientific evidence and clinical studies to back up the usefulness and effectiveness of using biosurfactants with other remineralizing agents. Thus, the aim of this study was to investigate the efficacy of NaF and nHAp with biosurfactants extracted from *Lactobacillus fermentum* (LFB), on remineralization of the hydroxyapatite (HA) surface as well as the optimization and functional characterization of isolated LFB. The biosurfactants from such organisms were selected because *Lactobacillus fermentum* is a common oral microbiota in humans, and LFB was reported to be one of the most efficacious agents in inhibiting the growth of microorganisms.³

Methodology:

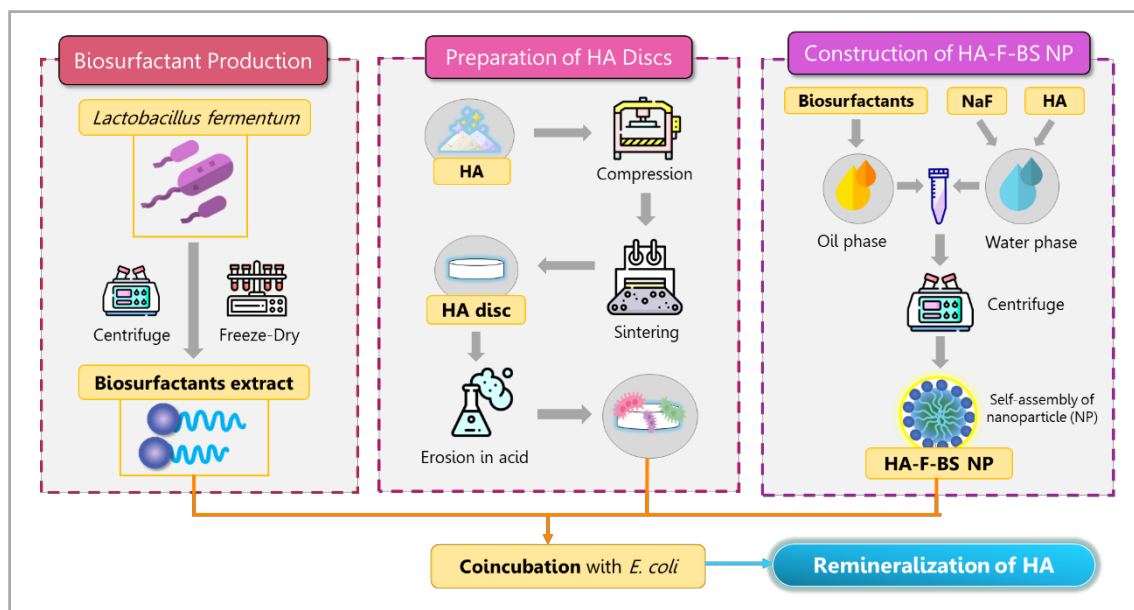


Diagram 1. Schematic diagram of the research methodology

1. Materials and Instrumentation

For culture media, nutrient broth (NB), nutrient agar (NA), and Luria-Bertani broth, Miller (LB) were purchased from HiMedia, India. *Lactobacilli* De Man-Rogosa-Sharpe MRS was purchased from Criterion, Hardy Diagnostics, USA. The other chemicals as follows were commercially obtained: rhamnolipid (AGAE Technologies, USA) sodium fluoride (NaF) (EMSURE, Merck, Germany), hydroxyapatite (HA 60 nm, MySkinRecipes, Thailand), 10% w/v nHAp (aqueous colloidal dispersion form, Alfa Aesar, USA).

The instrumentation is listed as followed: microvolume UV-vis spectrophotometer (Nanodrop One^c, Thermo Scientific, USA), spectrophotometer-microplate reader (Varioskan LUX, Thermo Scientific, USA), lyophilizer (Alpha 2-4 LDplus, Martin Christ, Germany), hydraulic press (Specac, UK), sinter furnace (P330 Nabertherm, Germany, and vortex mixer (Vortex-Genie 2, Scientific Industries, USA).

2. Bacterial Strains and Culture Condition

The *Lactobacillus fermentum* TISTR055 (ATCC 14931) strain was acquired from Thailand Institute of Scientific and Technological Research (TISTR). For *Escherichia coli* OP50 strain was retrieved from the Department of Anatomy, Faculty of Science, Mahidol University. The bacterial strains were stored at -56°C, in a medium supplemented with glycerol (30% v/v). For *L. fermentum*, the frozen stock was inoculated in MRS broth and incubated at 37°C overnight prior to use. For *E. coli*, the frozen stock was inoculated in LB and incubated at 37°C overnight prior to use.

3. Biosurfactants Production

L. fermentum was cultured on MRS agar by the streak plate method and incubated at 37°C overnight. A single colony of *L. fermentum* was inoculated into 100 ml of MRS broth and incubated overnight. The OD₆₀₀ of the broth culture was measured by using a UV-vis spectrophotometer and adjusted to be 0.7 before use.

4. Biosurfactants Isolation

The broth culture of *L. fermentum* was centrifuged (10,000×g, 5 min, 10°C) by a superspeed centrifuge (Sorvall LYNX 4000, Thermo Scientific, USA). The supernatant was collected by pipetting. Subsequently, the supernatant was filtered through a syringe filter CA-CN 25 mm 0.45 micron. The solution was dialyzed against DI water through cellophane at 3°C for 2 h. The dialyzed solution which contains *L. fermentum* biosurfactants (LFB) was separated into 26 tubes, frozen with liquid nitrogen transiently and freeze-dried under the pressure of 1.0 mbar at -87°C for 4 days.⁵

5. Oil Spreading Assay

The oil spreading test measures the diameter of clear zones formed when a droplet of biosurfactants is placed on an oil–water surface allowing the determination of the clearing efficiency of the given biosurfactants. The assay was conducted by adding 20 µl of crude oil to the surface of 50 ml of DI water in a petri dish until it was covered with a thin oil film. Thereafter, the 6 treatments were prepared as: LFB at 25, 50, and 100 mg/ml dissolved in PBS, rhamnolipid at 20 mg/ml as the positive control as well as PBS and MRS broth as the negative controls. 10 µl of each treatment was gently placed onto the thin oil layer by pipetting.⁶ The area of transparent zones was then calculated by ImageJ program (v1.8.0_172, NIH, USA).

6. Antibiofilm Assay

The antibiofilm assay was divided into 3 sub-assays conducted on 96-well microtiter plates—pre-coating, eradication, and co-incubation assays. For the pre-coating assay, the wells were coated with biosurfactants before being treated with *E. coli*, as opposed to the eradication assay, in which *E. coli* were coated before biosurfactants. For the co-incubation assay, the wells were coated with biosurfactants and *E. coli* simultaneously. These antibiofilm assays on microtiter plates can estimate the effective concentrations of biosurfactants in decreasing bacterial adhesion.⁷

For a procedure, *E. coli* was streaked onto nutrient agar (NA) and incubated for 20 h at 37°C for optical density at 600 nm (OD₆₀₀) to be 0.1. Then, the tenfold diluted bacteria suspension was prepared for three different assays. Next, the concentration of LFB was prepared at 100, 10, and 1 mg/ml prior to the antibiofilm assay. The interior wells were added with the treatment following each sub-assay. Following this, the microplate was placed in the incubator at 37°C for 20 h.

Subsequently, the adhered bacterial biomass in each well was stained with 100 µl of 0.1% (w/v) crystal violet solution. After 20 min, each was destained with 100 µl of 70% (v/v) ethanol for 20 min at room temperature with gentle shaking at 150 rpm. Then, the absorbance at 595 nm (A₅₉₅) was determined by a spectrophotometer-microplate reader to determine the antiadhesive efficiency.^{7,8} Eventually, the percentage of biofilm growth for each treatment was determined as follows⁹:

$$\% \text{biofilm growth} = [\text{Sample}_{A595} - \text{SC}_{A595}] / [\text{GC}_{A595} - \text{SC}_{A595}] * 100$$

Where SC_{A595} is the A₅₉₅ value of the sterility control (rhamnolipid treatment) and GC_{A595} is the A₅₉₅ value of the growth control (0 mg/ml LFB treatment).

Because of the anti-adhesion capabilities of biosurfactants, the adhesion test should reveal the decline in the microbial adhesion from 100% indicating the increase in biofilm inhibition in relation to the growth control for a specific treatment.¹⁰

7. Preparation and Demineralization of HA Discs

Firstly, 60 g of hydroxyapatite (HA) powder was added into 600 ml of DI water and autoclaved to improve the crystallinity before being filtered through 150-mm filter paper, pore size of 11 µm, using filtration system. Then, dried HA powder was mashed elaborately using the pestle and crucible and 0.350 g of HA powder was pressed uniaxially in the tablet press metallic mould at 2.0 ton to form a disc with a diameter of 12.00 mm. HA discs were then sintered at 1100°C for 3 h in a sinter furnace.

Before demineralization, HA discs were autoclaved at 121°C for 15 min and then eroded in 1 ml of 0.5 M acetate buffer (pH 4.0) in a 24-well plate for 2 h for demineralization. The surface of the demineralized HA discs was observed under a scanning electron microscope (SEM) (JSM-7610F, JEOL, Japan)¹¹

8. Self-Assembly of Hydroxyapatite, Fluoride, and Biosurfactants Nanoparticle (HA-F-BS NP)

The nano-emulsion is formed when mixing the oil phase, containing NaF and HA in chloroform, and water phase, containing biosurfactants. Biosurfactants play an essential role not only in stabilizing the emulsion forming and oil/water interfaces, but also directing the self-assembly structure of nanoparticles.¹²

To prepare the water phase, LFB was dissolved in DI water to achieve 450 µl of 111 mg/ml. The concentration of biosurfactants was ensured to be higher than the critical micelle concentration (CMC), which was previously determined at 1.0 mg/ml for *L. fermentum* RC-14 and 2.5 mg/ml for *L. fermentum* B54, to successfully induce the formation of nanoparticle-micelle.^{13,14} For the oil phase, 150 µl of 73,600 ppm of NaF and 33.3% (w/v) of HA in chloroform was prepared. The concentrations of NaF and HA were intentionally selected to be equal to those of experimental wells in remineralization experiments.¹²

After that, both phases were filled in a microcentrifuge tube before being centrifuged at 10,000 rpm for 15 min. Then, the assembled nanoparticle or HA-F-BS NP was collected. The HA-F-BS NP was applied to a TEM grid prior to the investigation under transmission electron microscope (TEM) (Atomic Resolution Analytic Microscope, JEM-ARM200F, Accel Arm, USA) equipped with energy dispersive spectroscopy (EDS).

9. Remineralization of Short-term Biofilm-coated HA Discs

Firstly, the *E. coli* culture was prepared at the OD₆₀₀ value of 0.13. For biofilm precoating, HA discs were precoated by immersing them in the 1.0 ml *E. coli* broth for 4 h in shaking condition at 120 rpm and 37°C and gently rinsed with PBS (pH 7.0)¹⁵, following incubation. The treatment of HA discs (n = 24) was divided into 6 treatments, comprising negative control group (CT) containing PBS, and experimental groups (remineralizing solution) as follows (1) nHAp, (2) nHAp + NaF, (3) nHAp + NaF + 100 mg/ml LFB (non-sterilized), (4) nHAp + NaF + 100 mg/ml LFB (autoclaved), and (5) nHAp + NaF + 10 mg/ml LFB (filtered sterile).¹⁶

The non-sterile, autoclaved, and filtered LFB were used as we hypothesized that the denaturation of the peptide in biosurfactants might occur, affecting their function. Then, each HA disc was immersed in each treatment and kept for 3 days at 37°C in an incubator shaker at 150 rpm.^{15,17}

10. Remineralization of Long-term Pre-coated HA Discs

The precoating step was performed as for short-term biofilm-coated HA discs except that the incubation time with *E. coli* was increased to 24 h. Subsequently, treatments of HA discs (n = 16) were divided into 4 treatments, comprised of negative control group (CT) containing merely PBS, and experimental groups (remineralizing solution) as follows: (1) HA + NaF, (2) HA + NaF + 100 mg/ml LFB (autoclaved), (3) HA-F-BS NP solution. Then, each HA disc was immersed in each treatment and kept for 3 days at 37°C in an incubator shaker at 150 rpm.^{15,17}

11. Remineralization of Co-incubated HA Discs

This experiment was conducted as for the biofilm-coated HA discs except that HA discs were not precoated with *E. coli*, but instead, were added with *E. coli* broth and remineralizing solution instantaneously. The treatments were prepared as: negative control (CT) and experimental group as follows: (1) HA + NaF, (2) HA + NaF + 100 mg/ml LFB (autoclaved), (3) HA-F-BS NP solution and (4) sterile LB. All treatments except group (1) were added with 100 µl *E. coli* broth. Remark that the final fluoride ion concentration was 1000 ppm which has been proved efficacious to enhance mineral deposition.¹⁴ Then, each HA disc was immersed in each treatment and kept for 3 days at 37°C in an incubator shaker at 150 rpm.^{15,17}

12. Measurement of Metabolic Activity by WST-8 Assay (Microbial Viability Assay)

Cell Counting Kit-8 (CCK-8, Sigma-Aldrich, Japan) was used to examine the metabolic activity of *E. coli* after treatment. This kit allows colorimetric assays using the tetrazolium salt WST-8, which produces the water-soluble, yellow-colored formazan dye upon the reduction by an electron carrier, 1-methoxy PMS. The HA discs on which *E. coli* was adhered were soaked in a mixture consisting of 114 μ l PBS and 6 μ l of CCK-8 solution for 2 h at RT. Thereafter, the absorbance at 450 nm (A_{450}) was measured to evaluate microbial activity.¹¹

13. Surface Examination by Field Emission Scanning Electron Microscope (FESEM)

FESEM (JSM-7610F, JEOL, Japan) was performed before and after remineralization to qualitatively observe the ultra-morphology of HA discs, calcium phosphate deposits, smoothness and roughness, and porous area of the HA disc surface to understand the progress of remineralization.¹⁸

Before FESEM observation, the HA discs were washed for 5 min in PBS three times, and were then soaked in 1 ml of 2.5% glutaraldehyde for 18 h at 4°C for fixation. To dehydrate, the HA discs were successively immersed in ethanol at concentrations of 25%, 50%, 70%, 90%, and 99% for 15 min. Subsequently, the HA discs surface was sputtered with platinum an auto fine coater (JEC-3000FC, JEOL, Japan), after which the Pt-coated HA disc surface was observed under an FESEM.¹¹

14. Evaluation of Mineral Content by Energy Dispersive X-ray Spectroscopy (EDX)

Following FESEM, EDX (X-MaxN, Oxford Instruments, Japan) was then performed to measure the amount of calcium and phosphate content (%weight), Ca:PO₄ ratio, and fluoride (%weight) on the HA disc surface of all treatments.¹⁹

15. Statistical Analysis

All experiments were at least done in triplicates. The analysis was primarily done at a p-value less than 0.05 ($p < 0.05$) to be considered statistically significant at the confidence level of 95%. Single ANOVA (SPSS version 18.0.0, IBM, USA) and Fisher's least significant difference (LSD) test were employed to determine and analyze the difference of the means between control and sample. Group identified by the same superscripts are significantly differently at $p < 0.05$, unless stated otherwise.

Results and Discussion:

1. Oil Spreading Test

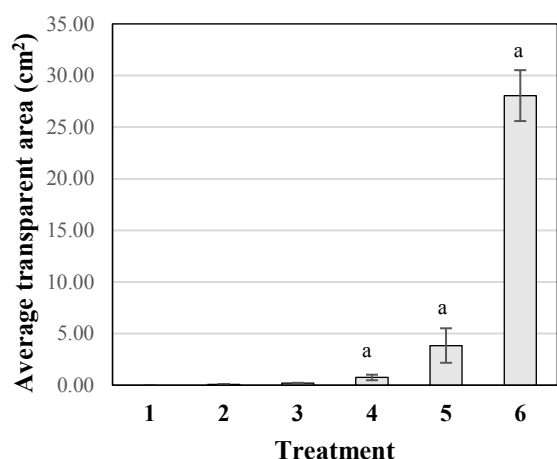


Figure 1. Oil spreading assays: 1) PBS 2) MRS broth 3) LFB at 25 mg/ml 4) LFB at 50 mg/ml 5) LFB at 100 mg/ml 6) Rhamnolipid. ($p < 0.001$)

The experiment involved dropping biosurfactants on an oily layer floating on the water surface to test emulsifying properties, which enable them to make water and oil mixed. When *L. fermentum* extract was added, transparent areas were observed with different sizes and the area calculations were performed using the ImageJ program shown in figure 1. Increasing the *L. fermentum* extract concentration resulted in larger transparent areas, 3.843 ± 1.670 cm² at 100 mg/ml of LFB.

Conversely, when dropping PBS, which served as a vehicle control, no transparent area was observed. However, when a dropping 20 mg/ml of rhamnolipid, an omnipotent biosurfactant, a large transparent area was 28.053 ± 2.466 cm². This experiment led to the conclusion that *L. fermentum* extract exhibited emulsifying properties of biosurfactants.

2. Biofilm Inhibition Assay

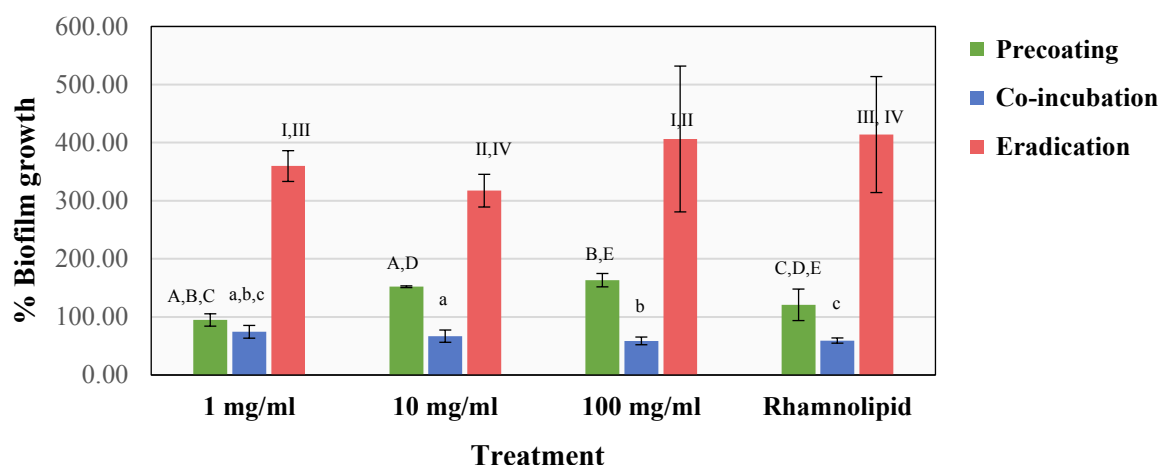


Figure 2. Biofilm inhibition assay results for pre-coating, co-incubation, and eradication assays respectively ($p < 0.001$ for all 3 sub-assays).

HA discs were experimentally treated with different biosurfactants to find the optimum conditions for inhibiting the formation of biofilm. Based on the experimental results, it can be concluded that the LFB had the property to inhibit biofilm formation while the biofilm was being formed. Co-incubation was more effective than inhibition of biofilm eradication after biofilm formation and before biofilm formation (pre-coating). The result is shown in Figure 2.

The properties of biosurfactants, which could reduce the surface tension in the area between the air and the liquid surface, were found to interfere with the adhesion of bacteria to the surface. These properties would make it difficult for biofilm to build up. On the contrary, post-treatment and pre-treatment might have some limitations that prevent the effective inhibition of biofilm formation. For instance, in post-treatment, the bacteria have agglomerated, and biofilm have been formed, which are highly resistant to most antimicrobial agents and disinfectants. These resistance and reduced susceptibility to antimicrobial substances was proposed to be caused by a variety of factors, for example, decreased intimate contact to antimicrobial substances, the bacterial persistence due to de novo mutation, phenotypic variation, or some genetic material which are transferred from those resistant counterparts, or production of antimicrobial degradative or neutralizing enzymes.^{20,21} As a result, bacteria became much more difficult to destroy and would proliferate in the post-treatment phase. Therefore, it could be concluded that the optimal condition for LFB to inhibit biofilms was the co-incubation condition.

3. Microbial Viability by WST-8 Assay

The %microbial viability of *E. coli* on HA discs after the remineralization process was investigated through the calculation of A_{450} where the control (CT) group was defined as 100% microbial viability. The result can be divided into 3 experiments: short-term biofilm pre-coating, long-term biofilm pre-coating, and co-incubation. It was obtained that $p < 0.001$ in all three sub-assays.

3.1 Short-term precoated HA discs

The results showed that the %microbial viability of *E. coli* decreased when treated with remineralizing agents with and without LFB. Among all the treatments compared to the CT group, Treatment 3, which used nHAp, NaF, and non-sterilized LFB, revealed the highest %microbial viability at 68.11%. Treatment 5 (nHAp, NaF, and LFB) revealed the lowest %microbial viability at 3.29%. Therefore, the antibacterial effect of LFB at 10 mg/ml was most efficacious, which was in accordance

with the previous research,^{22,23} as the LFB aggregated at the liquid-air interface altering the hydrophobicity of a substrate surface. These biosurfactants not only hampered the bacteria from clinging to surfaces, but they also caused adherent cells to separate.

3.2 Long-term precoated HA discs

The %microbial viability in Treatment 1 (HA + NaF) was observed to be lower than the control and the other treatment. However, in Treatments 2 and 3, which contained LFB showed %microbial viability higher than 100%. The hypothetical explanation for this was that the longer incubating time could allow the growth *E. coli* in presence of some organic substances found in the *Lactobacillus* extract such as galactose, lactose, malate, and fructose,²⁰ while PBS solution in the CT group contained no nutrient.

3.3 Co-incubated HA discs

All the three treatments had a microbial viability exceeding 100%. The increase of bacterial growth could be due to the presence of nutrient-rich LB. The %microbial viability, however, was greatly minimized in Treatment 3, which contained HA-F-BS NP, compared to addition of HA, NaF, and LFB alone.

4. TEM-EDS Nanoparticle Analysis

Table 1. Mineral content of HA-F-BS NP measured by EDS.

Element	Energy (keV)	Atom (%)	Mass (%)	Mass SD
C	0.277	59.16	39.73	0.12
O	0.525	19.10	17.08	0.09
F	0.677	3.51	3.72	0.04
P	2.013	2.75	4.76	0.04
Ca	3.690	15.49	34.71	0.24
Total	-	100.00	100.00	-

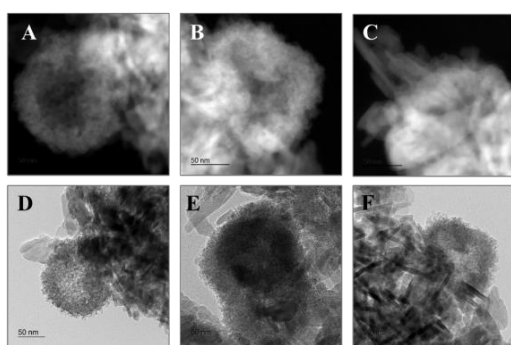


Figure 3. Emulsion self-assembly of HA-F-BS NP shown in dark-field TEM micrographs (A-C) and bright-field TEM micrographs (D-E). 50 nm scale setup is shown.

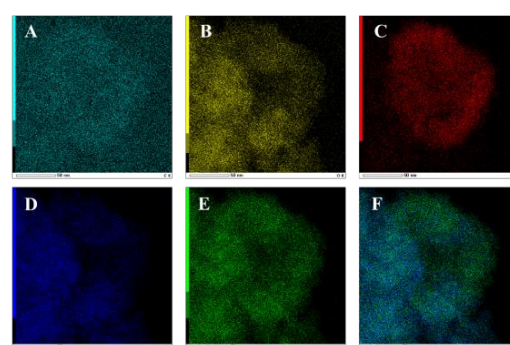


Figure 4. EDS layered images of various elements: (A) carbon (B) oxygen (C) fluoride (D) phosphorus (E) calcium and (F) overlaid image of phosphorus and calcium, alluded to the dark-field TEM micrograph Figure 1 (A). 50 nm scale setup is shown.

TEM is a nano-sized characterization method to observe the particle size, shape, and morphology. The micrographs from 6 selected areas are depicted in Figure 3. The resultant HA-F-BS NP were found to be spherical shape of which porous and hollow structure is observable. The hollow nanoparticles were attributed to the biosurfactants that could encourage the inflow of water or solution

through the nanoparticle membrane and prevent shrinkage of the nanoparticle membrane generated at the oil/water contact corresponding to the previous findings.⁹ Its hollow structure revealed multiple benefits compared to the solid one, for instance, the superior catalytic action inside the hollow chamber, which accounted for their better catalytic characteristics, as well as improving the nano sensing and drug delivery properties.^{24,25,26}

Employing the micrograph A from Figure 3 as the representative and the layered image of each mineral was illustrated in Figure 4 along with quantitative analysis of HA-F-BS NP mineral composition displayed in Table 1. The results illustrated the successful self-assembly of HA-F-BS NP as confirmed by the presence of Ca (34.71%), P (4.76%), and O (17.08%) from HA, F (3.72%) from NaF, and C (39.73%) and O (17.08%) from hydrocarbon composition in LFB. Therefore, it was hypothesized that the addition of biosurfactants in the water phase played a critical role to stabilize the aggregation of the HA-F-BS NP in the oil phase, assuring that the self-assembly of HA-F-BS NP was feasibly applicable.

5. SEM-EDX Analysis of HA Discs

5.1 HA discs after entering the remineralizing process

a) SEM analysis

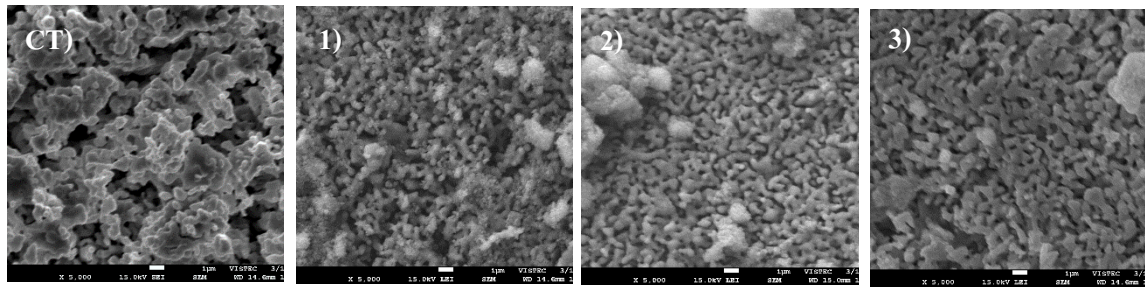


Figure 5. Scanning electron micrographs of long-term pre-coated HA discs (10,000x): CT) PBS 1) HA + NaF, 2) HA + NaF + 10 mg/ml LFB (autoclaved), and 3) HA-F-BS NP.

SEM observation was performed on HA discs after undergoing the remineralization process. The micrographs revealed that the HA discs exhibited larger pores in the absence of both remineralizing agents and LFB as shown in Figures 5. In contrast, when the treatments included remineralizing agents or LFB, the pore size decreased resulted in a smoother surface suggesting the deposition of minerals on HA discs. However, when observed under SEM, short-term pre-coated HA disc and co-incubated HA disc failed to show any significant surface remineralization.

b) EDX analysis

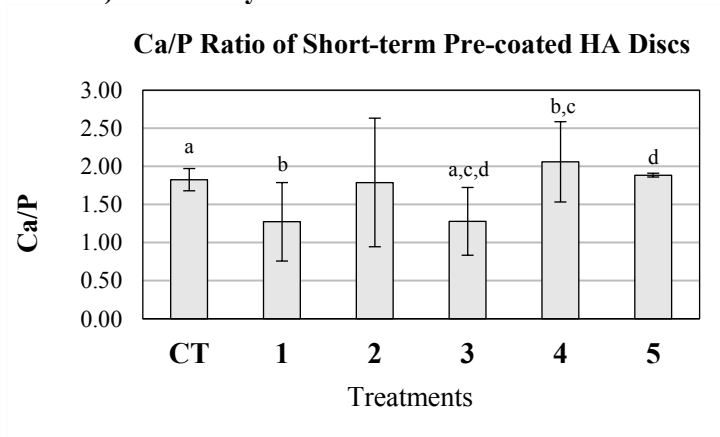


Figure 6. Calcium to phosphorus weight ratio of short-term pre-coated HA discs: CT) PBS, 1) nHAp, 2) nHAp + NaF, 3) nHAp + NaF + 100 mg/ml LFB (non-sterilized), 4) nHAp + NaF + 100 mg/ml LFB (autoclaved), and 5) nHAp + NaF + 10 mg/ml LFB (filtered). The error bar means the standard deviation. ($p < 0.10$)

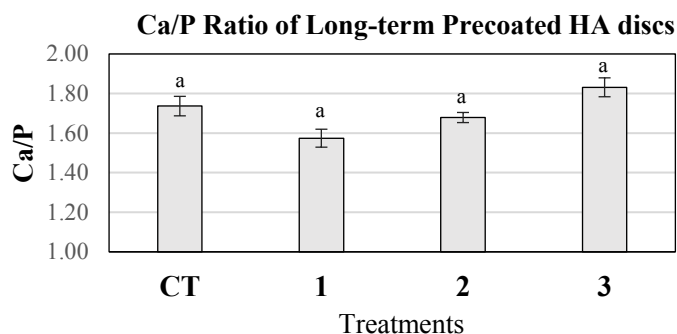


Figure 7. Calcium to phosphorus weight ratio of long-term pre-coated HA discs: CT) PBS, 1) HA + NaF, 2) HA + NaF + 10 mg LFB (sterile), and 3) HA-F-BS NP. The error bar means the standard deviation. ($p < 0.05$)

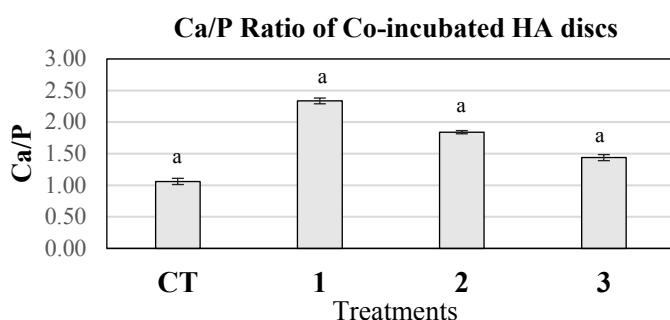


Figure 8. Calcium to phosphorus weight ratio of co-incubated HA discs: CT) PBS, 1) HA + NaF, 2) HA + NaF + 10 mg/ml LFB (autoclaved), and 3) HA-F-BS NP. The error bar means the standard deviation. ($p < 0.001$)

Next, we made further observations from Figures 7 and 8 in experiment set 2) HA + NaF + LFB, and experimental set 3) HA-F-BS NP. The biosurfactants appeared as rather spherical milky white particles, ranging from small to large. This contrasted with the surface of the HA disc quite clearly. It is assumed that these particles may be a combination of HA, NaF, and biosurfactants, with the biosurfactants acting as a stabilizer for this combination.

Additionally, the observed surface smoothness from SEM is related to the EDX illumination effect. The next step was the EDX results to determine the Ca/P ratio, which had a direct positive correlation with the process rate of remineralization. The remineralization of short-term pre-coated HA discs, long-term pre-coated HA discs, and co-incubated HA discs is shown in Figure 6, 7, and 8, respectively, confirming that when the remineralizing agents, LFB, and HA-F-BS NP were inserted, higher calcium and phosphate content was achieved. From the experiments on HA discs in all three conditions, it was found that the long-term pre-coating of HA discs showed the most effective effect of biosurfactants, especially in the form of nanoparticles, in speeding up the remineralization process compared to the control.

Conclusion:

The oil spreading test of the biosurfactant demonstrated that LFB possesses emulsifier properties, enabling it to bind water to oil and inhibit biofilm formation. Co-incubation experiments, involving the presence of a few live bacteria when the concentration of surfactants increased. Simultaneously, proved to be the optimal conditions for biofilm inhibition. Moreover, antibacterial adhesion efficacy of LFB was confirmed through a WST-8 assay. SEM-EDX endoscopic analysis showed that the biosurfactant from *L. fermentum* accelerated remineralization and aided in restoring the enamel layer's structure. Additionally, TEM-EDS assays revealed that the combination of HA and NaF with the biosurfactant resulted in HA-F-BS NP nanoparticles with enhanced stability and structure, proving more effective in resisting bacterial adhesion than conventional mixing methods.

Acknowledgement:

This work was funded and supported by Kamnoetvidaya Science Academy (KVIS) and supported by Vidyasirimedhi Institute of Science and Technology (VISTEC) for the access of laboratory, facilities, equipment, and chemicals.

Reference:

1. Amaechi B T. Springer International Publishing. 2015
2. Satpute S K, Kulkarni G R, Banpurkar A G, Banat I M, Mone N S, Patil R H. *Cameotra SS*. 2016;56(11):1140-1158
3. Zakaria Gomma E. *MBJ*. 2013;59(6):425-436
4. De Giani A, Zampolli J, Di Gennaro P. *Front. Microbiol.* 2021;12
5. Ghasemi A, Moosavi-Nasab M, Setoodeh P, Mesbahi G, & Yousefi G. *Scientific Reports*. 2019;9(1).
6. Madhu A N, Prapulla S G. *Appl. Biochem. Biotechnol.* 2014;172(4):1777-1789
7. Sholouhfar M, Kermanshahi R K, Feizabadi M M, Teimourian S, Safari F. *Infect Genet Evol.* 2022;100:105264
8. Fracchia L, Allegrone G. *Biomed. Sci. Eng. Technol.* 2010:827-837
9. Haney E F, Trimble M J, Hancock R E. *Nat. Protoc.* 2021;16(5):2615–2632
10. Walencka E, Różalska S, Sadowska B, Różalska B. *FM*. 2008
11. Kamitakahara M, Takahashi S, Yokoi T, Inoue C, Ioku K. *Mater. Sci. Eng.* 2016; 61:169-173
12. Park J, Hickey D R, Jun S, Kang S, Hu X, Chen X, Park S. *Adv. Funct. Mater.* 2016;26(43):7791-7798
13. Wei W, Bai F, Fan H. *iScience*. 2019;11:272-293
14. Velraeds M M, Van Der Mei H C, Reid G, Busscher H J. *Urol. J.* 1997;49(5):790-794
15. Wang D, Haapasalo M, Gao Y, Ma J, Shen Y. *Bioact. Mater.* 2018;3(4):418-425
16. Epasinghe D J, Yiu C K Y, Burrow M F. *Aust. Dent. J.* 2015;60(4):463-470
17. Hiraishi N, Sono R, Islam M S, Otsuki M, Tagami J, Takatsuka T. *J. Dent.* 2011;39(5):391-396
18. Junka A, Szymczyk P, Ziolkowski G, Karuga-Kuzniewska E, Smutnicka D, Bil-Lula I, Bartoszewicz M, Mahabady S, Sedghizadeh P P. *PLoS One*. 2017;12(1)
19. El Hagry B, El-Baz G, Abo El Soud, A. *Dent Update*. 2021;2(2):135-143
20. Donlan R M. *Emerg. Infect. Dis.* 2002;8(9):881-890
21. Simões M, Bennett R N, Rosa E. *Nat. Prod. Rep.* 2009
22. Rodrigues L, Banat I M, Teixeira J, Oliveira R. *J. Antimicrob. Chemother.* 2006;57(4):609-618
23. Sánchez S J, Barragán P J, Serna L. *Rev. Colomb. Estad.* 2019;21(2):63-76
24. Brigger I, Dubernet C, Couvreur P. *Adv. Drug Deliv. Rev.* 2002;54(5):631-651
25. Jin R, Wu G, Li Z, Mirkin C A, Schatz G C. *J. Am. Chem. Soc.* 2003;125(6):1643-1654
26. Mahmoud M A, O'Neil D, El-Sayed M A. *J Adhes Dent.* 2013;26(1):44-58



DEVELOPING PREDICTION MODEL FOR THE PREOPERATIVE DIAGNOSIS OF OVARIAN CANCER USING TUMOR MARKER, COMPLETE BLOOD COUNT AND LIVER FUNCTION TESTS

Sorawit Tongyib, Teerapol Saleewong *

Department of Mathematics, Faculty of Science, King Mongkut's University of Technology Thonburi, Bangkok 10140, Thailand

*e-mail: teerapol.sal@kmutt.ac.th

Abstract:

The preoperative diagnosis index without adnexal mass data of ovarian cancer (OC) was developed based on risk factors using secondary data. Binary and multiple logistic regression and the receiver operating characteristic curve were used to analyze the data and explore potential factors or predictors. This research analyzes data from 202 patients, with 116 cases being ovarian cancer. The risk factors consisted of factors in the tumor markers, complete blood count (CBC), and liver function tests groups (LFT). Menopausal status, human epididymis protein 4 (HE4), carbohydrate antigen 19-9 (CA19-9), lymphocytes (LYM), and alkaline phosphatase (ALP) were used as predictors for our index. The area under the receiver operating characteristic curve (AUROC) was 0.916 (95% CI, 0.877 - 0.954). The performance in the validation with a cut-off point of 0.52 revealed sensitivity, specificity, positive predictive value (PPV), negative predictive value (NPV), accuracy, positive likelihood ratio (LR+), negative likelihood ratio (LR-), and odds ratio (OR) of 0.810, 0.919, 0.931, 0.782, 0.856, 9.956, 0.207, and 48.221, respectively. Furthermore, our study demonstrates menopausal status, HE4, CA19-9, and ALP were the risk factor, while LYM was a protective factor.

Keywords: ovarian cancer, tumor marker, complete blood count, liver function tests, preoperative diagnosis index, preoperative diagnosis index without ultrasound

Introduction:

Gynecological cancer is the most common in women worldwide. There are five main types: cervical, ovarian, uterine, vaginal, and vulvar cancer. These cancers often do not show symptoms in the early stages. However, the diagnostic process is complicated due to the cancer found in the pelvis, which requires internal examinations. As a result, early detection and accurate diagnosis are essential for improving the chances of successful treatment and better patient outcomes.

Ovarian cancer is the second most common gynecological cancer and often develops without showing noticeable symptoms in its early stages, leading to it being the number one cause of death among gynecological cancers. The age-standardized incidence rates of ovarian cancer per 100,000 women in countries with high/very high Human Development Index (HDI) in 2020 were 7.1 and 5.8 in countries with low/medium HDI, respectively¹. The important diagnostic method of ovarian cancer is the pelvic examination to detect pelvic masses. If the mass is detected, the transvaginal ultrasound will be used to identify the size, shape, and characteristics of ovarian masses. Ovarian cancer staging is determined using the International Federation of Gynecology and Obstetrics (FIGO) system, which assesses the extent and severity of the cancer within the body. Early detection and timely treatment



improve the outcome or prognosis for patients. Therefore, patients should discuss with gynecologic oncologists, to determine the most suitable treatment plan. Generally, surgery is the initial treatment approach for ovarian cancer. For early-stage ovarian cancer, surgery may involve the removal ovaries, fallopian tubes, and the uterus (hysterectomy) and include staging to determine the extent of the disease, while cytoreductive surgery is usually considered for patients at the advanced stage of ovarian cancer².

The preoperative diagnosis is crucial for ovarian cancer because it enables early detection and appropriate treatment planning, resulting in improved patient outcomes and higher survival rates. For example, if a patient is predicted to be at high risk of malignant ovarian tumors, the patient should be referred to specialist gynecologic oncologists to enhance survival outcomes³ and undergo cytoreductive surgery, while patients in the early stages should be prepared for complete surgical staging. Several indices have been created to aid in preoperative diagnosis, such as the Risk of Malignancy Index⁴ (RMI) and the Risk of Ovarian Malignancy Algorithm⁵ (ROMA). The American College of Obstetricians and Gynecologists (ACOG) recommends RMI as a referral tool to gynecologic oncologists². These indices utilize demographic data, blood tests, morphological patterns, and biomarkers for prognostic purposes in the preoperative diagnosis. RMI and ROMA require morphological patterns data for analysis, which requires gynecologists or ultrasound specialists to interpret results. However, the availability of expert examiners is limited, preventing many hospitals from utilizing these indices for patient analysis. To solve the problem and be an alternative way to diagnose before surgery. Our preoperative diagnostic index was developed which does not use information about the pelvis or morphological patterns for prognosis.

Methodology:

This research aimed to develop a preoperative diagnostic index through a retrospective analysis of clinical data published by Mi et al⁶. The dataset consists of various clinical data, but our focus is on three distinct groups of risk factors associated with ovarian cancer: tumor markers, complete blood count (CBC), and liver function tests (LFT). The factors that were correlated with ovarian cancer from each risk factor group will be utilized as predictors for analysis to construct a preoperative diagnosis index using multiple logistic regression (or binary logistic regression) with SPSS (IBM Corp. Released 2019. IBM SPSS Statistics for Windows, Version 26.0. Armonk, NY: IBM Corp). Significant predictors were identified based on the results of multiple logistic regression, and their predictive significance was assessed using diagnostic odds ratios and p-values. In general, non-significant predictors should be eliminated from the analysis. Subsequently, a new regression analysis was performed to obtain the coefficients of the logistic response function fitting the remaining predictors. Note that non-significant predictors can be retained in the analysis. The calibration of logistic regression models was assessed using the Hosmer-Lemeshow goodness of fit statistics. The ability to discriminate or predict was evaluated by calculating the area under the receiver operating characteristic curve (AUROC), it was a graphical plot between sensitivity against 1-specificity at various possible cut-off points. The optimal cut-off point was determined by considering the point on the receiver operating characteristic curve that was closest to the perfect cut-off point (0,1)⁷. In addition, a 2×2 table provided information on true positive, false positive, true negative and false negative, allowing for the calculation of sensitivity, specificity, positive predictive value, negative predictive value, positive likelihood ratio, negative likelihood ratio, and odds ratio.

Results:

A total of 202 patients' data⁶ were used to analysis and develop our preoperative diagnostic indices. The dataset contains information on the health status, blood test results, biomarkers, and other clinical data of each patient. It included 202 women, dividing into 86 with benign ovarian tumor and 116 with ovarian cancer. Several studies⁸⁻¹⁴ have suggested variables associated with ovarian cancer or that can be used as predictors of ovarian cancer. These variables include human epididymis protein 4, carbohydrate antigen 19-9, basophil cell ratio, lymphocyte count, albumin, alkaline phosphatase, and indirect bilirubin. Due to the data were categorized into three main ovarian cancer risk factor groups: tumor markers, complete blood count, and liver function tests. In the tumor markers group, the focus factors consisted of human epididymis protein 4 (HE4) and carbohydrate antigen 19-9 (CA19-9), while the complete blood count group focused on basophil cell ratio (BASO) and lymphocyte count (LYM). In the liver function tests group, the focus factors included albumin (ALB), alkaline phosphatase (ALP), and indirect bilirubin (IBIL). Moreover, menopause status was also included in our index because postmenopausal patients are known to have a higher risk of developing epithelial cancer.

The characteristics of patient data between the benign ovarian tumor and ovarian cancer groups are presented in Table 1. Patients in the ovarian cancer group had significantly higher serum levels of HE4 (324.33 vs. 46.18 pmol/l, $p < 0.001$) and CA19-9 (74.57 vs. 25.28 U/l, $p < 0.001$), lower basophil cell ratios (0.48% vs. 0.67%, $p < 0.001$), lower lymphocyte counts (1.43 vs. 1.84 $10^9/l$, $p < 0.001$), lower levels of albumin (39.14 vs. 41.78 g/l, $p < 0.001$), higher levels of alkaline phosphatase (82.73 vs. 66.63 U/ml, $p < 0.001$), lower levels of indirect bilirubin (5.12 vs. 5.90 $\mu\text{mol/l}$, $p = 0.023$), and a higher proportion of postmenopausal patients (85.5% vs. 14.5%, $p < 0.001$). To prevent multicollinearity, it is necessary to assess the correlation between predictors and independent variables by Pearson correlation coefficient before performing a logistic regression analysis. The correlations are shown in Table 2. All predictors were correlated with the patient's disease status at a significance level of less than 0.05. Moreover, individual variables were not highly correlated, so there was no multicollinearity problem.

Table 1. Clinical characteristics of benign ovarian tumor vs ovarian cancer.

Clinical Characteristics	Benign Tumor (n=86)		Ovarian cancer (n=116)		P value
	mean	SD	mean	SD	
Serum HE4 (pmol/l) ^a	46.18	11.16	324.33	538.77	<0.001
Serum CA19-9 (U/l) ^a	25.82	38.13	74.57	179.17	0.005
BASO (%) ^a	0.67	0.39	0.48	0.32	<0.001
Lymphocyte ($10^9/l$) ^a	1.84	0.49	1.43	0.55	<0.001
Albumin (g/l) ^a	41.78	3.98	39.14	5.39	<0.001
Alkaline phosphatase (U/ml) ^a	66.63	19.83	82.73	26.14	<0.001
Indirect bilirubin ($\mu\text{mol/l}$) ^a	5.90	2.52	5.12	2.31	0.023
Postmenopausal (%) ^b	14.5		85.5		<0.001

^a Student's *t*-test

^b χ^2 test

Table 2. Correlation of factors

		Correlations								
		Status_c	Menopause	HE4	CA19-9	BASO%	LYM#	ALB	ALP	IBIL
Status_c	Pearson Correlation	1	.441**	.320**	.173*	-.262**	-.361**	-.245**	.320**	-.160*
	Sig. (2-tailed)		.000	.000	.014	.000	.000	.000	.000	.023
	N	202	202	202	202	202	202	202	202	202
Menopause	Pearson Correlation	.441**	1	.307**	-.009	-.236**	-.265**	-.088	.368**	-.027
	Sig. (2-tailed)	.000		.000	.900	.001	.000	.211	.000	.706
	N	202	202	202	202	202	202	202	202	202
HE4	Pearson Correlation	.320**	.307**	1	-.041	-.105	-.259**	-.423**	.119	-.197**
	Sig. (2-tailed)	.000	.000		.560	.136	.000	.000	.091	.005
	N	202	202	202	202	202	202	202	202	202
CA19-9	Pearson Correlation	.173*	-.009	-.041	1	-.046	-.128	-.146*	.134	-.053
	Sig. (2-tailed)	.014	.900	.560		.515	.070	.038	.057	.453
	N	202	202	202	202	202	202	202	202	202
BASO%	Pearson Correlation	-.262**	-.236**	-.105	-.046	1	.164*	.010	-.127	.019
	Sig. (2-tailed)	.000	.001	.136	.515		.020	.885	.071	.785
	N	202	202	202	202	202	202	202	202	202
LYM#	Pearson Correlation	-.361**	-.265**	-.259**	-.128	.164*	1	.247**	-.140*	.175*
	Sig. (2-tailed)	.000	.000	.000	.070	.020		.000	.047	.013
	N	202	202	202	202	202	202	202	202	202
ALB	Pearson Correlation	-.245**	-.088	-.423**	-.146*	.010	.247**	1	-.038	.348**
	Sig. (2-tailed)	.000	.211	.000	.038	.885	.000		.587	.000
	N	202	202	202	202	202	202	202	202	202
ALP	Pearson Correlation	.320**	.368**	.119	.134	-.127	-.140*	-.038	1	.068
	Sig. (2-tailed)	.000	.000	.091	.057	.071	.047	.587		.338
	N	202	202	202	202	202	202	202	202	202
IBIL	Pearson Correlation	-.160*	-.027	-.197**	-.053	.019	.175*	.348**	.068	1
	Sig. (2-tailed)	.023	.706	.005	.453	.785	.013	.000	.338	
	N	202	202	202	202	202	202	202	202	202

** . Correlation is significant at the 0.01 level (2-tailed).

* . Correlation is significant at the 0.05 level (2-tailed).

Model development: Our preoperative diagnosis index

The preoperative diagnosis index was created by using binary logistic regression analysis. Human epididymis protein 4, carbohydrate antigen 19-9, basophil cell ratio, lymphocyte count, albumin, alkaline phosphatase, and indirect bilirubin were utilized as predictors in the creation of a preoperative diagnosis index. The information for each parameter is shown in Table 3, and the logistic response function is as follows

$$P(OC) = \frac{e^{\beta_0 + \beta_1 HE4 + \beta_2 (CA19-9) + \beta_3 BASO\% + \beta_4 LYM\# + \beta_5 ALB + \beta_6 ALP + \beta_7 IBIL + \beta_8 Menopausal}}{1 + e^{\beta_0 + \beta_1 HE4 + \beta_2 (CA19-9) + \beta_3 BASO\% + \beta_4 LYM\# + \beta_5 ALB + \beta_6 ALP + \beta_7 IBIL + \beta_8 Menopausal}}, \quad (1)$$

where β_0 is the regression constant, $\beta_{1 \leq i \leq 8}$ is the regression coefficient of each independent variable, and $0 \leq P(OC) \leq 1$; represents the probability of a patient with ovarian cancer.

Table 3. Parameters and their details for creation of preoperative diagnosis index.

Parameter	Details
Menopausal status	menopausal { postmenopausal ; premenopausal ;
HE4	Level of human epididymis protein 4
CA19-9	Level of carbohydrate antigen 19-9
BASO%	Basophil cell ratio
LYM#	Amount of lymphocyte
ALB	Amount of albumin
ALP	Amount of alkaline phosphatase
IBIL	Amount of indirect bilirubin

After conducting binary logistic regression, the results of parameters predicting ovarian cancer for diagnosis index are presented in Table 4. Significant predictors included levels of serum HE4 and CA19-9 and the amount of LYM.

Table 4. Result of logistic regression analysis for preoperative diagnosis index.

Parameter	Coefficient	OR	95% CI	p-value ^c
Menopausal status	0.480	1.616	0.512–5.101	0.413
HE4	0.050	1.051	1.023–1.080	<0.001
CA19-9	0.011	1.011	1.002–1.020	0.017
BASO%	0.029	1.030	0.329–3.224	0.960
LYM#	-1.289	0.276	0.107–0.713	0.008
ALB	-0.022	0.978	0.879–1.088	0.680
ALP	0.014	1.014	0.996–1.032	0.135
IBIL	-0.053	0.949	0.785–1.146	0.587
Constant	-1.248	0.287	-	0.639

Abbreviations: OR = odds ratio; CI = confident interval

^c Significant at p <0.05.

The final model of the preoperative diagnostic index was developed by eliminating non-significant parameters from the binary logistic regression. Consequently, HE4, CA19-9, LYM#, ALP, and menopausal status were included in the final model, which underwent reanalyzed logistic regression analysis. The results of logistic regression analysis in final model are presented in Table 5, the final model is described as follows:

$$P(OC) = \frac{e^{-2.517+0.052HE4+0.01(CA19-9)-1.273LYM\#+0.013ALP+0.353Menopausal}}{1+e^{-2.517+0.052HE4+0.01(CA19-9)-1.273LYM\#+0.013ALP+0.353Menopausal}}, \quad (2)$$

**Table 5.** Result of logistic regression analysis for final preoperative diagnosis index.

Parameter	Coefficient	OR	95% CI	p-value ^c
Menopausal status	0.353	1.424	0.471-4.302	0.531
HE4	0.052	1.053	1.026-1.082	<0.001
CA19-9	0.010	1.010	1.002-1.019	0.019
LYM#	-1.273	0.280	0.110-0.714	0.008
ALP	0.013	1.013	0.995-1.032	0.144
Constant	-2.517	0.081	-	0.048

^c Significant at p < 0.05.

For discriminative ability of the index was evaluated with the AUROC of the logistic regression models in Figure 1, the area under the receiver operating characteristic curve was 0.916 (95% CI, 0.877–0.954), and the p-value of the Hosmer-Lemeshow goodness-of-fit test was 0.988. Consider the receiver operating characteristic curve (ROC), the point on curve that minimizing the Euclidean distance between the ROC curve and the (0,1) point was 0.52, so the optimal cut-off point was 0.52. With the optimal cutoff point, a 2 × 2 table is shown in Table 6, providing sensitivity, specificity, positive predictive value, negative predictive value, accuracy, positive likelihood ratio (LR+), negative likelihood ratio (LR-), and odds ratio (OR) as follows:

- Sensitivity = $\frac{94}{116} = 0.810$
- Specificity = $\frac{79}{86} = 0.919$
- PPV = $\frac{94}{101} = 0.931$
- NPV = $\frac{79}{101} = 0.782$
- Accuracy = $\frac{173}{202} = 0.856$
- LR+ = $\frac{94}{116} \bigg/ \frac{7}{86} = 9.956$
- LR- = $\frac{22}{116} \bigg/ \frac{79}{86} = 0.207$
- OR = $\frac{94}{7} \bigg/ \frac{22}{79} = 48.221$

Table 6. Result of a 2 × 2 table for preoperative diagnosis index.

		Observed		Overall Percentage
		Status 1	Status 0	
Predicted	Status 1	94	7	
	Status 0	22	79	
Percentage Correct		81.0	91.9	85.6

Note: The optimal cutoff point is 0.52

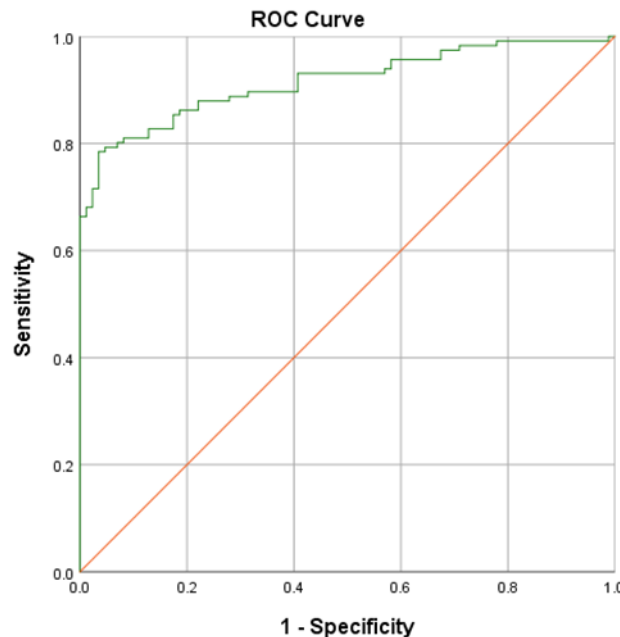


Figure 1.

The receiver operating characteristic curve of final index.

Discussion and Conclusion:

In this study, the binary logistic regression models were developed for the preoperative diagnosis index without adnexal mass of ovarian cancer based on the data of tumor markers, CBC, and LFT. The index showed HE4, CA19-9 levels, and LYM were significant predictive parameters for the prediction of ovarian cancer, while menopausal status and ALP remain in the index due to their relevance to ovarian cancer. Based on the observations from Table 5, the likelihood of ovarian cancer in patients decreased as the amount of LYM increased. Therefore, treatments that result in increased lymphocytes are beneficial for patients. On the other hand, increased levels of HE4, CA19-9, and ALB are associated with an increased likelihood of developing the disease, suggesting that these factors can be considered as risk factors for ovarian cancer. To calculate the chance that a patient has ovarian cancer, you can substitute HE4, CA19-9, LYM, ALP, and menopausal status into Equation 2. If the calculated probability (P) is greater than 0.52, it indicates that the patient has ovarian cancer.

Overall, our study developed the preoperative diagnosis indexes of ovarian cancer using tumor markers, complete blood count, and liver function tests. The preoperative indexes were developed specifically for women without pelvic or adnexal mass data and they could aid general physicians or gynecologists in the evaluation of patients presenting with ovarian tumors, and help with management planning and patient prioritization for surgery, potentially reducing surgical risks

Acknowledgements:

The authors sincerely thank for Science Achievement Scholarship of Thailand and the Department of Mathematics, Faculty of Science, King Mongkut's University of Technology Thonburi for supporting us.



Supplementary Materials: The following supporting information can be downloaded at: <https://www.kaggle.com/datasets/saurabhshahane/predict-ovarian-cancer>.

References:

1. Sung H, Ferlay J, Siegel RL, Laversanne M, Soerjomataram I, Jemal A. Global cancer statistics 2020: GLOBOCAN estimates of incidence and mortality worldwide for 36 cancers in 185 countries. *CA Cancer J Clin* 2021. 2021: 209–249.
2. Chirdchim W, Wanichsetakul P, Phinyo P. Development and Validation of a Predictive Score for Preoperative Diagnosis of Early Stage Epithelial Ovarian Cancer. *Asian Pac J Cancer Prev APJCP* 20. 2019: 1207–1213.
3. Vernooij F, Heintz P, Witteveen E, Van Der Graaf Y. The outcomes of ovarian cancer treatment are better when provided by gynecologic oncologists and in specialized hospitals: A systematic review. *Gynecol. Oncol.* 2007: 801–812.
4. Jacobs I, Oram D, Fairbanks J, et al. A risk of malignancy index incorporating CA 125, ultrasound and menopausal status for the accurate preoperative diagnosis of ovarian cancer. *Br J Obstet Gynaecol.* 1990: 922–929.
5. Moore RG, McMeekin DS, Brown AK, DiSilvestro P, Miller MC, Allard WJ, Gajewski W, Kurman R, Bast RC, Skates SJ. A novel multiple marker bioassay utilizing HE4 and CA125 for the prediction of ovarian cancer in patients with a pelvic mass. *Gynecol Oncol* .2009: 40–46.
6. Data for: USING MACHINE LEARNING TO PREDICT OVARIAN CANCER. Available online: <https://data.mendeley.com/datasets/th7fztbrv9/11> (23 October 2020).
7. Pepe MS. *The Statistical Evaluation of Medical Tests for Classification and Prediction*; Publisher: Oxford University Press, Oxford. 2003.
8. Tomasz Kluz, et al. Human Epididymis Protein 4 (HE4) Reference Limits in Polish Population of Healthy Women, Pregnant Women, and Women with Benign Ovarian Tumors. *Hindawi Disease Markers*. 2019.
9. Lertkhachonsuk A, Buranawongtrakoon S, et al. Serum CA19-9, CA-125 and CEA as tumor markers for mucinous ovarian tumors. *J. Obstet. Gynaecol.* 2020; Vol. 46: 2287–2291.
10. Bax HJ, Chauhan J, et al. Basophils from cancer patients respond to immune stimuli and predict clinical outcome. *Cells*. 2020; 9: 1631.
11. Wang XJ, Yuan ZF, Qiu HF, et al. The relationship between preoperative blood lymphocyte-to-monocyte ratio and the prog-nostic of epithelial ovarian cancer. *Prog Obstet Gynecol.* 2016; 25:654–657
12. Ge LN, Wang F. Prognostic significance of preoperative serum albumin in epithelial ovarian cancer patients: a systematic review and dose-response meta-analysis of observational studies. *Cancer Management and Research*. 2018; 10: 815–825.
13. Orsaria M, Londero AP, Marzinotto S, Loreto CD, Marchesoni D, Mariuzzi L. Placental Type Alkaline Phosphatase Tissue Expression in Ovarian Serous Carcinoma. *Cancer Biomark.* 2016; 17: 479–486
14. Xi XX, Wang HL, et al. Prognostic value of preoperative serum bilirubin levels in ovarian cancer. *Am J Transl Res.* 2020; 12(5) :2267-2280



Efficacy of royal jelly for inhibition of free radical and herpes simplex virus type 1 infection

Kanok-orn Mayer¹ and Yingmanee Tragoolpua^{1,2,*}

¹Department of Biology, Faculty of Science, Chiang Mai University, Chiang Mai 50200, Thailand

²Research Center in Bioresource for Agriculture, Industry, and Medicine, Department of Biology, Faculty of Science, Chiang Mai University, Chiang Mai 50200, Thailand

*e-mail: yingmanee.t@cmu.ac.th or yboony150@gmail

Abstract:

Herpes simplex virus (HSV) is the causative agent of human herpes. HSV can be divided into 2 types; HSV-1 and HSV-2. HSV-1 can cause herpetic gingivostomatitis which is mostly asymptomatic infection. However, the symptoms may appear as blisters or cold sores around the mouth. HSV-1 is typically spread through closely contact with surfaces near the mouth, sores, or saliva. Although, the drug such as acyclovir limits multiplication and spread of HSV but it cannot completely eliminate the virus from patient. In this study, inhibitory efficacy of royal jelly on herpes simplex virus type 1 (HSV-1) and free radicals was investigated. The result showed that royal jelly demonstrated the phenolic and flavonoid contents with the values of 1.40 mg gallic acid/g extract and 0.74 mg quercetin/g extract. The phenolic and flavonoid compound may play the significant role by affecting the ability of antioxidant and anti-HSV-1 activity. Royal jelly had the highest antioxidant activity of 0.316 mg gallic acid/g extract. In addition, royal jelly at the concentrations of 15,000 and 7,500 µg/ml showed the highest inhibitory efficacy against HSV-1 during and after viral attachment by 92.58% and 100.00%, respectively. Moreover, the concentrations of royal jelly at 976.6 and 1953.1 µg/ml promoted cell viability higher than positive control. Therefore, royal jelly demonstrated high ability of anti-HSV-1 and antioxidant activity and should be further studied to produce a new alternative antiviral agent from bee product.

Introduction:

Herpes simplex virus (HSV) is a member of *Herpesviridae* family. At present, there is an estimated 500 million people who were infected with HSV type 1 (HSV-1) or HSV type 2 (HSV-2). Moreover, HSV-1 usually causes an oral infection and also can increase the number of patients with genital herpes infection.¹ HSV can cause long-term health problems that the patient can develop lifelong symptoms because of the latency of HSV. The infection of HSV occurs at a mucocutaneous surface and the virus is transported to the peripheral sensory ganglia. Latent stage of HSV infection can activate by local and systemic stimuli and causes recurrent infection at mucocutaneous surface of the patient.² Acyclovir (ACV) and its derivative are antiviral medications that are currently approved for the treatment of HSV infections. Although ACV may cause toxic side effects and drug resistant strain of HSV may be developed after long-term treatment³. The mutation of HSV usually occurs in HSV-thymidine kinase or DNA polymerase genes and these mutants are crucial opportunistic infectious pathogens in immunocompromised individuals.^{4,5} Due to the mutation against ACV, other agents against viral infection are urgent required. Therefore, the antiviral agent from natural sources such as bee product may be used as an alternative treatment for HSV infection.

Royal jelly is the special food for the queen honey bee larva that produced from worker honey bees.⁶ Fresh royal jelly mainly contained water constitutes of 60-70% (w/w)

and pH is usually ranging between 3.6 and 4.2. Royal jelly is composed of lipids, protein, vitamins, carbohydrates, polyphenols, and mineral salt. There are various bioactive compounds and mineral in royal jelly that give several biological and pharmacological properties such as antioxidant, neurotrophic, anticancer, anti-inflammatory, antidiabetic, antilipidemic, and antimicrobial agent.^{7,8} Moreover, royal jelly also has ability to protects cells from anti-cancer agent-induced toxicities while treating anti-cancer agents with a variety of malignancies in the animal.⁹

Therefore, the aims of this study are to investigate antioxidant and anti-HSV-1 activity of royal jelly. The activity of this research will be applied for royal jelly product development that can be considered as an alternative treatment of herpetic symptoms.

Methodology:

Materials

The dried powder of royal jelly was obtained from Bee Products Industry Co., Ltd., Chiang Mai, Thailand. The samples were kept at room temperature and protected from light. Other analytical grade chemicals were used in this study.

Determination of antioxidant activity, phenolic and flavonoid content of royal jelly

DPPH (2,2-diphenyl-1-picrylhydrazyl) Assay

The antioxidant activity of royal jelly was analyzed by DPPH (2,2-diphenyl-1-picrylhydrazyl) method. In this method, DPPH was used as a source of free radical and methanolic solution of DPPH, 150 µl was mixed with 50 µl of sample in the 96 well plate. Then, the mixture was kept in the dark at room temperature for 15-20 minutes and an absorbance at 517 nm was determined using methanol as control. The result of antioxidant activity was calculated as percentage of antioxidant activity by comparison of DPPH radicals that decrease from the control using the formula as follows.

$$\% \text{ Antioxidant activity} = [(A \text{ control} - A \text{ sample}) / A \text{ control}] \times 100$$

Moreover, IC₅₀ was calculated from the inhibition activity of DPPH radical by 50%. The antioxidant activity was reported in milligrams of gallic acid equivalents per gram of extract (mg GAE/g extract).¹⁰

Analysis of total phenolic compound

The total phenolic compound of royal jelly was determined by the Folin-Ciocalteu method. The methanolic solution of sample, 25 µl was mixed with 12.5 µl of 50% (w/v) Folin-Ciocalteu reagent, 25 µl of 95% ethanol, and 125 µl of distilled water. After 5 minutes incubation, 5% (w/v) Na₂CO₃ 25 µl was added and kept in dark at room temperature for 1 hour. The absorbance was determined at 725 nm. The result was compared with gallic acid as a standard control. The total phenolic compound content was reported in milligrams of gallic acid equivalents per gram of extract (mg GAE/g extract).¹¹

Analysis of total flavonoid compound

The total flavonoid compound of royal jelly was determined by the aluminum chloride colorimetric method. The methanolic solution of sample, 20 µl was mixed with 10% (w/v) aluminum chloride solution, 4 µl, 1M potassium acetate, 4 µl and 112 µl of distilled water. Then, the mixture was incubated in dark at room temperature for 30 minutes and an absorbance was determined at 415 nm using methanol as a control. The result was compared

with quercetin and total flavonoid content was reported as milligrams quercetin equivalents per gram of extract (mg QE/g extract).¹²

Determination of cytotoxicity activity of royal jelly¹³

The cytotoxicity of royal jelly was determined by MTT (3-(4,5-dimethylthiazol-2-yl)-2,5-diphenyl tetrazolium bromide) colorimetric assay. Human epidermal keratinocyte line (HaCaT) at 1.25×10^4 cells/well was added into 96-well plate and further incubated at 37 °C in 5% CO₂ incubator for 24 hours. Then, the medium was replaced with fresh medium containing various concentration of sample and incubated at 37 °C in 5% CO₂ incubator for 72 hours. After incubation, MTT solution was added to each well, and incubated for 4 hours. Next, dimethyl sulfoxide was added to dissolve the formazan product in cell, and measured with microplate reader at 540 and 630 nm. The viability of the cells was calculated comparing to cell control and expressed as percentage of cell viability (%Viability) and 50% cytotoxic dose (CD₅₀).

Investigation of anti-HSV activity of royal jelly¹³

Inhibition of HSV-1 by royal jelly when treatment before viral attachment

The antiviral activity was investigated by plaque reduction assay. Firstly, HaCaT cells at 2×10^5 cells/well was cultured in 24 well plates and incubated at 37 °C in 5% CO₂ incubator for 24 hours. Then, 200 µl of various non-toxic concentrations of royal jelly were added into each well and incubated at room temperature for 1 hour on rocking platform. After incubation, HSV (300-400 PFU/ml), 100 µl was added and incubated at room temperature for 1 hour on rocking platform. After that, 200 µl of the overlay medium was added and incubated at 37 °C in 5% CO₂ incubator for 48-72 hours to allow plaque formation. The infected cells were stained with 0.1% crystal violet in 1% ethanol. The viral plaques were counted and the plaque inhibition was calculated comparing to control infected cells without any treatment. The result was reported as the concentration of extract that reduces the number of viral plaques by 50% (50% Inhibitory Concentration, IC₅₀) and percentage inhibition of plaque reduction.

Inhibition of HSV-1 by royal jelly when treatment during viral attachment

The antiviral activity was investigated by plaque reduction assay. Firstly, HaCaT cells at 2×10^5 cells/well was cultured in 24 well plates and incubated at 37 °C in 5% CO₂ incubator for 24 hours. Then, HSV (300-400 PFU/ml) 100 µl was added into each well, followed by 200 µl of various non-toxic concentration of royal jelly and incubated at room temperature for 1 hour on rocking platform. Next, the inoculum was replaced with 400 µl of medium containing 2% FBS. After that, 200 µl of the overlay medium was added and incubated at 37 °C in 5% CO₂ incubator for 48-72 hours to allow plaque formation. For plaque determination, cells were stained with 0.1% crystal violet in 1% ethanol before counting the numbers of plaque was counted, and calculated the inhibition of plaque reduction in the comparison of mock infected cells without treatment by the royal jelly. The result was reported as the concentration of extract that reduces the number of viral plaques by 50% (50% Inhibitory Concentration, IC₅₀) and percentage inhibition of plaque reduction.

Inhibition of HSV-1 by royal jelly when treatment after viral attachment

The antiviral activity was investigated by with plaque reduction assay. Firstly, HaCaT cells at 2×10^5 cells/well were cultured in 24 well plates and incubated at 37 °C in 5% CO₂ incubator for 24 hours. Next, HSV (300-400 PFU/ml) 100 µl was added to the cells and

incubated at room temperature for 1 hour on rocking platform. After infection, 200 μ l of various nontoxic concentrations of royal jelly were added into each well, followed by 200 μ l of the overlay medium, and incubated at 37 °C in 5% CO₂ incubator for 48-72 hours to allow plaque formation. For plaque determination, cells were stained with 0.1% crystal violet in 1% ethanol and the numbers of plaque was counted, and calculated the inhibition rate of plaque reduction in the comparison of mock infected cells without treatment by the royal jelly. The result was reported as the concentration of extract that reduces the number of viral plaques by 50% (50% Inhibitory Concentration, IC₅₀) and percentage inhibition of plaque reduction.

Results and Discussion:

Determination of antioxidant activity, phenolic and flavonoid content of royal jelly

Royal jelly powder was dissolved with DI water and the antioxidant activity of royal jelly was tested in 96-well well plate. The result in Table 1 showed that royal jelly had the antioxidant activity by 0.316 ± 0.002 mg gallic acid/g extract. Royal jelly showed the amount of phenolic and flavonoid contents with the values of 1.40 ± 0.24 mg gallic acid/g extract and 0.74 ± 0.01 mg quercetin/g extract. These important biochemicals compounds such as the total phenolics and total flavonoid contents affected to antioxidant activity. Moreover, royal jelly contains hydroxy dicarboxylic fatty and their derivatives such as 10-hydroxy-2-decenoic acid (10-HDA) that have been shown to have antioxidant activity.¹⁴ In addition, caffeic acid phenethyl ester in royal jelly was shown as the phenolic compound promoted the antioxidant capacity.¹² This was consistent with the previous report that phenolic compounds had ability to prevent reactive oxygen species including superoxide anion and hydroxyl radical.¹⁵ In addition, royal jelly contained the flavonoids compounds including flavanones, flavones, flavonols, and isoflavonoids.¹⁶ These antioxidant properties of phenolic and flavonoid compounds are important for pharmacological properties of royal jelly.

Table 1 Antioxidant activity, phenolic and flavonoid content of royal jelly

Experiments	Contents
Antioxidant activity * (mg gallic acid/g extract)	0.32 ± 0.00
Total phenolic compound* (mg gallic acid/g extract)	1.40 ± 0.24
Total flavonoid compound * (mg quercetin/g extract)	0.74 ± 0.01

*Data expressed as mean \pm standard deviation for 3 replications

Determination of cytotoxicity activity of royal jelly

The cytotoxicity activity of royal jelly on HaCaT cells using MTT assay was shown with CD₅₀ value of $6,477.93 \pm 318.28$ μ g/ml. The percentage of cell viability in Figure 1 showed that different concentrations of royal jelly at 976.6, 1953.1, 3906.3 and 7812.5 μ g/ml showed the percentage of cell viability at 108.22%, 101.53%, 88.14% and 36.86% respectively. The result showed that the higher concentration of royal jelly affected to the cell viability by reduction of cell viability. The acidic pH of royal jelly at the range of pH 3.6-4.2 can decrease the ability of cell growth and viability. Thus, the lower concentration of royal jelly might be suitable to cell grow and proliferation.¹⁷ The concentrations of royal jelly at 976.6 and 1953.1 μ g/ml promote cell viability higher than positive control (DMEM). This



was consistent with previous report showed that royal jelly affected three cell types which were human gingival fibroblasts (HGF), human periodontal ligament fibroblasts (HPDL) and human hip bone cells (HIP). Thus, royal jelly stimulated alkaline phosphatase activity and cell proliferation that promoted the percentage of cell growth.¹⁸ According to the data from previous study, several important intracellular signaling factors, 57-kDa protein in royal jelly could stimulate DNA synthesis in adult rat hepatocytes culture cells. Moreover, the 57-kDa protein promoted the cell survival regulator such as protein kinase B and prevented cell apoptosis.¹⁹

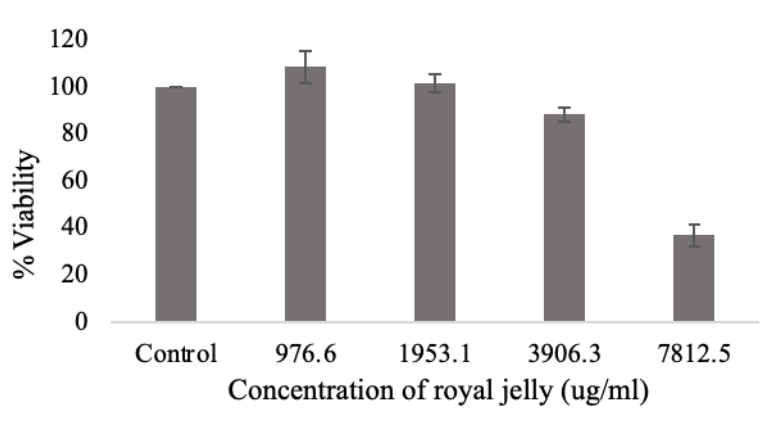


Figure 1 The cell viability percentage of royal jelly on HaCaT cells.

Anti-HSV activity of royal jelly

The result showed that royal jelly at the concentration of 7,500 $\mu\text{g/ml}$ had the highest anti-HSV-1 with the percentage inhibition of 100% when treatment after viral attachment with IC_{50} value of $3,270.53 \pm 237.48$ $\mu\text{g/ml}$ (Figure 4). Moreover, royal jelly at the concentration of 15,000 $\mu\text{g/ml}$ also showed the high ability to inhibit HSV-1 during viral attachment with the percentage inhibition of 92.58% with IC_{50} value of $6,909.52 \pm 667.85$ $\mu\text{g/ml}$ (Figure 3). On the other hand, the inhibitory effect of royal jelly on HSV-1 when treatment before viral attachment showed the lowest percentage inhibition of 38.62% when using royal jelly at the concentration of 15,000 $\mu\text{g/ml}$ (Figure 2). When comparing to the efficacy of acyclovir (ACV) on HSV-1 at the concentration of 1 $\mu\text{g/ml}$, ACV inhibited HSV-1 by 100%. Moreover, 10-hydroxy-2-decenoic acid 10-HDA, the fatty acid in royal jelly demonstrated the antiviral activity by preventing viral infection. Royal jelly had the ability to decrease the viral load when treatment during viral attachment at a concentration of 100 $\mu\text{g/ml}$.²⁰ Moreover, the flavonoids compounds had strong inhibitory activities on viral entry, replication and translation of proteins.²¹ This research supported the result that royal jelly had higher percentage of inhibition when treatment during and after viral attachment. According to earlier research, the flavonoid compounds such as flavanones, flavones and flavonols were showed as the component in royal jelly and showed inhibitory activity against HSV-1.²²

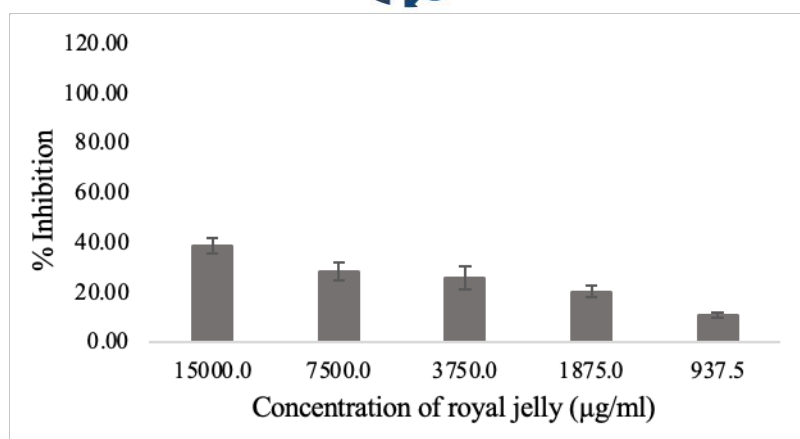


Figure 2 Inhibitory effect of royal jelly on HSV-1 when treatment before viral attachment

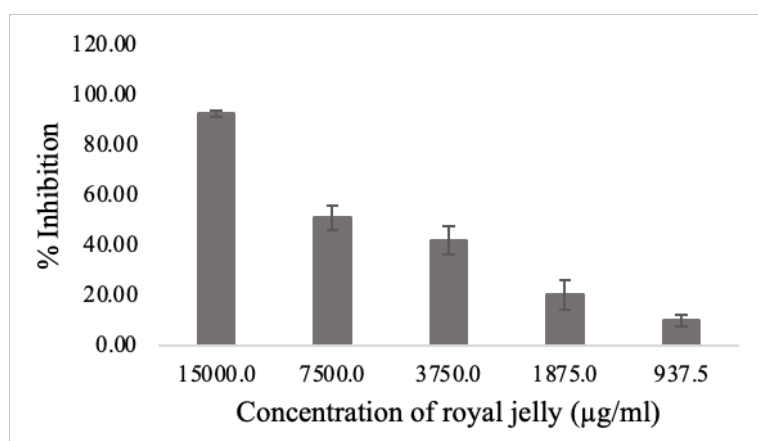


Figure 3 Inhibitory effect of royal jelly on HSV-1 when treatment during viral attachment

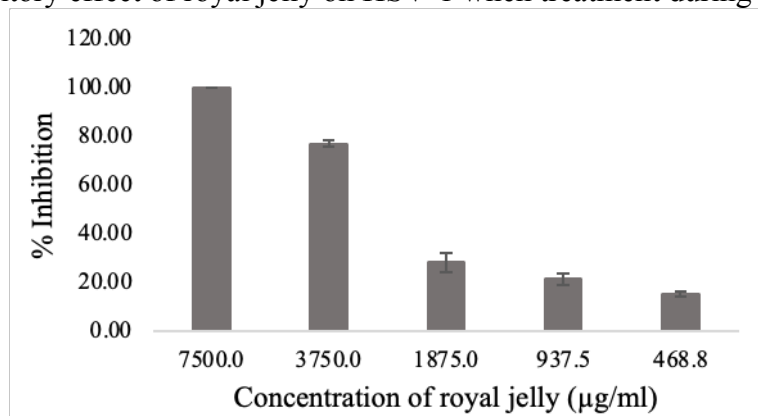


Figure 4 Inhibitory effect of royal jelly on HSV-1 when treatment after viral attachment

Conclusion:

In this study, royal jelly demonstrated antioxidant activity by 0.316 ± 0.002 mg gallic acid/g extract. Phenolic and flavonoid contents of 1.40 ± 0.24 mg gallic acid/g extract and 0.74 ± 0.01 mg quercetin/g extract were found in royal jelly, which may play the important role of antioxidant and anti-HSV-1 activity. Furthermore, higher percentage of HSV-1 inhibition was shown when treatment the virus with royal jelly during and after viral attachment with IC_{50} values of $6,909.52 \pm 667.85$ and $3,270.53 \pm 237.48$ µg/ml respectively. The royal jelly at the concentration of 7,500 µg/ml had the highest anti-HSV-1 with the

percentage inhibition of 100% when treatment after viral attachment. In addition, royal jelly at the concentration of 15,000 µg/ml also showed the high ability to inhibit HSV-1 during viral attachment with the percentage inhibition of 92.58%. Therefore, this research could potentially be applied for product development of royal jelly that can be considered as an alternative treatment of herpetic symptoms.

Acknowledgements:

This project is funded by National Research Council of Thailand (NRCT), N41A650170 and Bee Products Industry Company Limited. The authors also would like to thank Department of Biology, Faculty of Science and the Graduate School, Chiang Mai University, Thailand for the support.

References:

1. Looker KJ, Johnston C, Welton NJ, James C, Vickerman, P., Turner K M E, Boily MC, and Gottlieb SL. The global and regional burden of genital ulcer disease due to herpes simplex virus: a natural history modelling study. *BMJ Glob. Health.* 2020;5:1-15.
2. James C, Harfouche M, Welton NJ, Turner KM, Abu-Raddad LJ, Gottlieb SL, and Looker KJ. Herpes simplex virus: global infection prevalence and incidence estimates 2016. *Bull. World Health Organ.* 2020;98:315–329.
3. Bacon TH, Levin MJ, Leary JJ, Sarisky RT, and Sutton D. Herpes simplex virus resistance to acyclovir and penciclovir after two decades of antiviral therapy. *Clin. Microbiol. Rev.* 2003;16:114–128.
4. Crumacker CS, Schnipper LE, Marlowe SI, Kowalsky PN, Hershey BJ, and Levin MJ. Resistance to antiviral drugs of herpes simplex virus isolated from a patient treated with acyclovir. *N Engl J Med.* 1982;306:343-346.
5. Elion GB. Acyclovir: discovery, mechanism of action, and selectivity. *J Med Virol.* 1993;1:2-6.
6. Balkanska R, Zhelyazkova I, and Ignatova M. Physico-chemical quality characteristics of royal jelly from three regions of Bulgaria. *J. Agric. Sci. Technol.* 2012;4:302-305.
7. Pavel CI, Mărghitaş LA, and Bobiş O. Biological activities of royal jelly review. *J. Anim. Sci. Biotechnol.* 2011;44:108–118
8. Ramadan MF, and Al-Ghamdi A. Bioactive compounds and health-promoting properties of royal jelly: a review. *J. Funct. Foods.* 2012;4:39-52
9. Miyata Y, and Sakai H. Anti-Cancer and Protective Effects of Royal Jelly for Therapy-Induced Toxicities in Malignancies. *Int J Mol Sci.* 2018;19:3270.
10. Singh RP, Chaidamdara M, and Jayaprakasha GK. Studies on the antioxidant activity of pomegranate (*Punica granatum*) peel and seed extracts using in vitro models. *J. Agric. Food Chem.* 2002;50:81-86.
11. Chang CH, Lin HY, Chang CY, and Liu YC. Comparisons on the antioxidant properties of fresh, freeze-dried and hot-air-dried tomatoes. *J. Food Eng.* 2005;77:478-485.
12. Altun SK, and Aydemir ME. Determination of antioxidant capacities with the phenolic and flavonoid contents of royal jelly mixtures. *Bee Studies.* 2022;14:9-15.
13. Yucharoen R, Chansakaow S, and Tragoolpua Y. Inhibitory effect of aromatic herbs, lavender, sage and chamomile against herpes simplex virus infection. *Afr. J. Biotechnol.* 2011;10:15394-15401.
14. Kocot J, Kielczykowska M, Luchowska-Kocot D, Kurzepa J, and Musik I. Antioxidant Potential of Propolis, Bee Pollen, and Royal Jelly: Possible Medical Application. *Oxid Med Cell Longev.* 2018;2018:7074209.



15. Kruk J, Aboul-Enein BH, Duchnik E, and Marchlewicz M. Antioxidative properties of phenolic compounds and their effect on oxidative stress induced by severe physical exercise. *J Physiol Sci.* 2022;72:19.
16. Kunugi H, and Ali AM. Royal jelly and its components promote healthy aging and longevity: From animal models to humans. *Int. J. Mol. Sci.* 2019;20:4662.
17. Sabatini A G, Marcazzan G, Caboni M F, Bogdanov S, and Almeida-Muradian L B. Quality and standardisation of royal jelly. *J Appl Anim Sci.* 2009;1:16.
18. Dhanesuan N, Srisuparbh D, Tiranathanagul S, and Rungsriyanont S. The In Vitro Effect of Royal Jelly, *Apis mellifera*, on Proliferation of Human Gingival, Periodontal Ligament Fibroblasts and Human Bone Cells. *Thai Pharmaceut. Health. Sci. J.* 2011;6:182-187
19. Kamakura M. Signal transduction mechanism leading to enhanced proliferation of primary cultured adult rat hepatocytes treated with royal jelly 57-kDa protein. *J Biochem.* 2002;132:911–919.
20. Hashemipour MA, Tavakolineghad Z, Arabzadeh SA, Iranmanesh Z, and Nassab SA. Antiviral Activities of Honey, Royal Jelly, and Acyclovir Against HSV-1. *Wound J.* 2014;26:47–54.
21. Badshah SL, Faisal S, Muhammad A, Poulson BG, Emwas AH, and Jaremko M. Antiviral activities of flavonoids. *Biomed. Pharmacother.* 2021;14:111596.
22. Lyu SY, Rhim JY, and Park WB. Antiherpetic activities of flavonoids against herpes simplex virus type 1 (HSV-1) and type 2 (HSV-2) in vitro. *Arch Pharm Res.* 2005;28:1293-1301.



IN VITRO ANTI-CANCER EFFECTS OF PHARMACOLOGICAL ASCORBATE AGAINST GLIOBLASTOMA

Sara Shoaib, Visarut Buranasudja*

Department of Pharmacology and Physiology, Faculty of Pharmaceutical Sciences, Chulalongkorn University, Bangkok 10330, Thailand.

*Email: visarut.b@pharm.chula.ac.th

Abstract:

Glioblastoma is one of the most prevalent and aggressive cancers of the central nervous system (CNS). This malignancy is often accompanied by late diagnosis and poor survival. Current treatment protocols including resection, radiotherapy, and temozolomide are not satisfactory to improve the clinical outcomes. Thus, novel treatments are required to promote the effectiveness of standard of care against glioblastoma. The high doses of intravenous ascorbate, called pharmacological ascorbate, have been in the spotlight since the early 21st century due to its selective pro-oxidant activity to cancer cells. Pharmacological ascorbate (P-AscH⁻) executes this action *via* the formation of hydrogen peroxide (H₂O₂) leading to the formation of oxidative stress which then can further be enhanced by redox-metal mediated Fenton reaction upon accumulation of H₂O₂ in the cancer cells, causing the formation of free radical, hydroxyl ion (HO[•]). This reaction takes place on macromolecules leading to site-specific oxidative damage, such as DNA damage, caused by HO[•]. In our current study, we demonstrated that the pharmacological concentration of ascorbate causes a reduction in cell viability; the availability of intracellular labile iron increases cytotoxicity towards P-AscH⁻; and H₂O₂ is a primary factor toward its cytotoxic effects against H4 and U87-MG glioblastoma cell lines. We also showed that there is significant increase in the cytotoxic activity of temozolomide therapy when combined with P-AscH⁻, especially when higher dose of ascorbate was utilized. However, we were unable to depict the extent of synergetic effect owing to high resistance against temozolomide in U87-MG cells. Our preclinical data suggests that there could be a significant improvement in treatment outcomes in clinical practice with the utilization of P-AscH⁻ as an adjuvant in therapies against glioblastoma.

Introduction:

Glioblastoma has a neuroectodermal origin derived from supporting glial cells with aggressive clinical manifestations. Glioblastoma is more predominant in males as compared to females with an extremely poor median survival rate i.e., ranging in months. Despite all the advances in glioblastoma therapies, the life span and quality of life of patients have not been much improved over the decades. Resection, radiation, and temozolomide are currently approved standard treatments.¹ Novel treatment approaches are required against glioblastoma. Pharmacological ascorbate as an adjuvant could be an attractive option to improve the current regimen. Presently, high doses of ascorbate have shown enhanced sensitivity towards radiation as well as chemotherapy in various cancers. The effectiveness of pharmacological ascorbate (P-AscH⁻) against metastatic pancreatic cancer, metastatic ovarian cancer, and metastatic non-small cell lung cancer has already been demonstrated in several studies.²⁻⁴ Studies have shown that pharmacological ascorbate may also be utilized in combating glioblastoma multiforme.



Present data on pharmacological ascorbate suggests that it not only act as chemosensitizer in different type of cancers including glioblastoma but also play an important role in radio-sensitization as well as in enhancing cancer immunotherapy, making cancer more susceptible towards already approved treatment approaches.⁵⁻⁶ To further validate the clinical potential against glioblastoma, we have performed extended research on two glioblastoma cell lines, H4 and U87-MG.

Ascorbate acts as an antioxidant involved in scavenging free radicals in the biological system and as an enzyme cofactor involved in maintaining epigenetics regulation, synthesis of collagen, and cellular responses to hypoxia. However, upon increased plasma concentrations, so-called as P-AscH⁻, it functions as a pro-oxidant leading to oxidative stress. Interestingly, this property is selective towards cancer cells. Pharmacological ascorbate acts as a pro-oxidant *via* an H₂O₂-mediated mechanism initiated by redox-active metals existing in extracellular fluid. This pro-oxidant activity is selective to cancer cells due to the relatively low enzymatic activity of catalase in cancer cells. In contrast, in normal cells, the removal capacity against H₂O₂ by catalase is significantly greater; making normal cells less susceptible to oxidative damage caused by P-AscH⁻.⁷ H₂O₂ induces the imbalance of reactive oxygen species (ROS) in the cancer cell triggering oxidative stress. Further upon accumulation of H₂O₂ in the cancer cells, redox-active metals mediated Fenton reaction is initiated which causes the production of highly oxidizing hydroxyl radical (HO[•]). This is a site-specific reaction that occurs on macromolecules such as proteins, lipids, and most importantly, DNA.⁸ Production of HO[•] at these sites, causes oxidative damage such as DNA damage and thus, death of cancer cells.⁹ To attain this phenomenon, the intravenous route is utilized to achieve concentration i.e., 200 folds higher than that of oral administration. Owing to tightly controlled absorption *via* intestinal transporters, this concentration cannot be achieved through oral administration.¹⁰

In our research, we aimed to investigate a variety of consequences of P-AscH⁻ treatment on glioblastoma cell lines such as reduction in viability, clonogenicity, and bioenergetic levels of ATP. Concentrations of P-AscH⁻ treatment used in our cell culture experiments (0.25-20 mM) correlates with clinically achievable plasma levels i.e., up to 32 mM, through intravenous route.¹¹⁻¹² In this study, we confirmed the involvement of H₂O₂ in the P-AscH⁻ mechanism of pro-oxidant action with the use of H₂O₂ detoxifying enzyme, catalase. Further, to verify the contribution of intracellular labile iron in the oxidation of P-AscH⁻, we used iron chelators i.e., deferoxamine (DFO) and diethylenetriamine pentaacetate (DTPA). We also demonstrated that adjuvant use of P-AscH⁻ in temozolomide treatment can enhance cytotoxicity in glioblastoma cells to a considerable degree. Our investigation firmly proposes that P-AscH⁻ has cytotoxic efficacy as a novel treatment approach against glioblastoma.

Methodology:

Material

L-ascorbic acid (cat. No. A92902), catalase from bovine liver (cat. No. C9322), crystal violet, dimethyl sulfoxide (DMSO), methylthiazolyldiphenyl-tetrazolium bromide (MTT; cat. No. M5655), and paraformaldehyde were purchased from MilliporeSigma (Burlington, MA, USA). Cell culture media and supplements were obtained from Thermo Fisher Scientific (Waltham, MA, USA). Deferoxamine (DFO), diethylenetriamine pentaacetate (DTPA), and



temozolomide (TMZ) were obtained from the Tokyo Chemical Industry (TCI). CellTiter Glo luminescent cell viability assay (cat. No. G7571) was purchased from Promega (Madison, WI, USA).

Cell culture

Human glioblastoma (GBM) cell lines U87-MG and H4 were obtained from the American Type Culture Collection (ATCC; Manassas, VA, USA). Cells were cultured in DMEM, supplemented with penicillin (100 unit/mL) and streptomycin (100 µg/mL), along with 10% FBS. Both cell lines were maintained at 37°C with a humidified atmosphere containing 95% air and 5% CO₂. Both cell lines were used at passage less than 40.

MTT assay

P-AscH⁻ treatments

Cells were seeded at 8×10^3 cells/well in a 96-well plate. After 24 hours of incubation, cells were treated with P-AscH⁻ concentrations ranging from 0 to 20 mM for U87-MG and 0 to 4 mM for H4 for 1 hour in DMEM with 1% FBS. Treatments were used in mM as it will provide sufficient H₂O₂ fluxes for anti-cancer activity. After removing the treatment, cells were incubated for 20 h with DMEM having 10% FBS. Then, the cells were further incubated with 0.4 mg/ml MTT solution prepared in serum-free DMEM for 2 h. After removal of the MTT solution, intracellular formazan crystals were solubilized with DMSO, and their optical density (OD) was quantified spectrophotometrically at 570 nm by a CLARIOStar microplate reader (BMG Labtech, Ortenberg, Germany). The percentage of cell viability was calculated using: % viability = [OD (treatment)/ OD (control)] × 100, where OD (control) is the optical density of untreated cells, and OD (treatment) is the optical density of cells treated with pharmacological ascorbate, respectively.

Temozolomide treatments

Cells were seeded at 8×10^3 cells/well in a 96-well plate. After 24 hours of incubation, cells were pretreated with P-AscH⁻ at concentrations ranging from 0 to 5 mM for U87-MG for 1 hour in DMEM with 1% FBS. Cells were washed and treated with 0.5 mM TMZ dissolved in DMSO for 18 h in DMEM with 10% FBS while keeping the concentration of DMSO at 0.5% v/v exposed to cells. After washing, cells were incubated with 0.4 mg/mL MTT solution for 2 h. DMSO was used to solubilize formazan crystals and absorbance was measured and analyzed as described previously.

Clonogenic assay

P-AscH⁻ treatments

Cells were seeded at 1×10^5 cells/well density for the 6-well plate. After 24 h incubation, cells were treated with varied concentrations from 0 to 8 mM for U87-MG and 0 to 2 mM for H4 of P-AscH⁻ for 1 h in DMEM with 1% FBS. Later, cells were trypsinized and counted by a hemocytometer after suitable dilutions were made. Cells were seeded again at a lower density i.e., 1200 cells/well in DMEM with 10% FBS. After 8-10 days of incubation, cells were fixed and stained using 4% paraformaldehyde and crystal violet solution, respectively. 50 or more cells together were considered as a colony.



Co-treatments of P-AscH⁻ with catalase

Extracellular catalase stock was prepared in water, sterilized with a 0.22 μm filter, and stored at 4 °C. 200 units/mL of catalase were used alone as well as in combination with 2mM of P-AscH⁻. As a positive control, 1 mM hydrogen peroxide (H₂O₂) was used. The rest of the protocol was performed as described previously.

Treatments with deferoxamine (DFO) and diethylenetriaminepentaacetic acid (DTPA)

U87-MG cells were pretreated with chelating agents to prove the interference of labile iron present intracellularly. For ferric chelation, DFO (0.2mM) was used whereas for ferrous chelation, DTPA (1mM) was used altogether for 3 h in DMEM with 10% FBS before 1 h treatment with 2 mM of P-AscH⁻ in DMEM with 1% FBS. Later, the same protocol was performed as described earlier.

Temozolomide treatments

U87-MG cells were pretreated with P-AscH⁻ at concentrations ranging from 0 to 0.5 mM for 1 hour in DMEM with 1% FBS. Cells were washed and treated with 0.5 mM TMZ dissolved in DMSO for 18 h in DMEM with 10% FBS while keeping the concentration of DMSO at 0.5% v/v exposed to cells. The rest of the protocol was performed as described earlier.

ATP bioluminescence assay

P-AscH⁻ treatments

Briefly, cells were seeded at 1×10^5 cells/well density for the 6-well plate. After 24 h incubation, U87-MG cells were treated with varied concentrations from 0 to 8 mM P-AscH⁻ for 1 h in DMEM with 1% FBS. Later, cells were trypsinized and counted by a hemocytometer after making suitable dilutions. 4,000 cells were suspended in 100 μL of ice-cold PBS and added into wells of a 96-well white microplate with an opaque bottom. Then, 100 μL of CellTiter-Glo solution was added to each well to induce cell lysis and initiate the luminescence reaction. Following a 10-minute incubation, the luminescent signals were detected with a CLARIOStar microplate reader. The amounts of ATP were analyzed using a standard curve and then further converted to intracellular ATP per cell with the cell number.

Co-treatment of P-AscH⁻ with catalase

A similar process as described above was employed. Cells were co-treated with 200 units/mL of catalase, and as a positive control, 1 mM H₂O₂ was utilized.

Statistical Analysis

GraphPad Prism was used to perform statistical analysis with significance set at $p < 0.05$. One-way analysis of variance (ANOVA) with Tukey's post hoc was used to examine statistical differences between means for multiple comparisons. All means were computed from two independent experiments. The data were expressed as mean \pm standard error of the mean (SEM).

Result and discussion:

P-AscH⁻ kills glioblastoma in a dose-dependent fashion

Our MTT data demonstrates a significant gradual decrease in cell viability upon increasing the concentration from 0 to 20 mM in the U87-MG cell line and from 0 to 4 mM for the H4 cell



line. In our study, we observed the drop in cell viability and clonogenicity in the H4 cell line requires a significantly lesser concentration of P-AscH⁻ in contrast to the required for the U87-MG cell line. Thus, the H4 cell line appears to be more sensitive towards pharmacological ascorbate as compared to the U87-MG cell line. In addition, data for the effect on clonogenicity of U87-MG cells and H4 cells also depicts similar results. These findings are consistent with previous studies, demonstrating increase in oxidative stress with increase in concentration of P-AscH⁻; thereby affecting the GBM in a dose-dependent fashion.

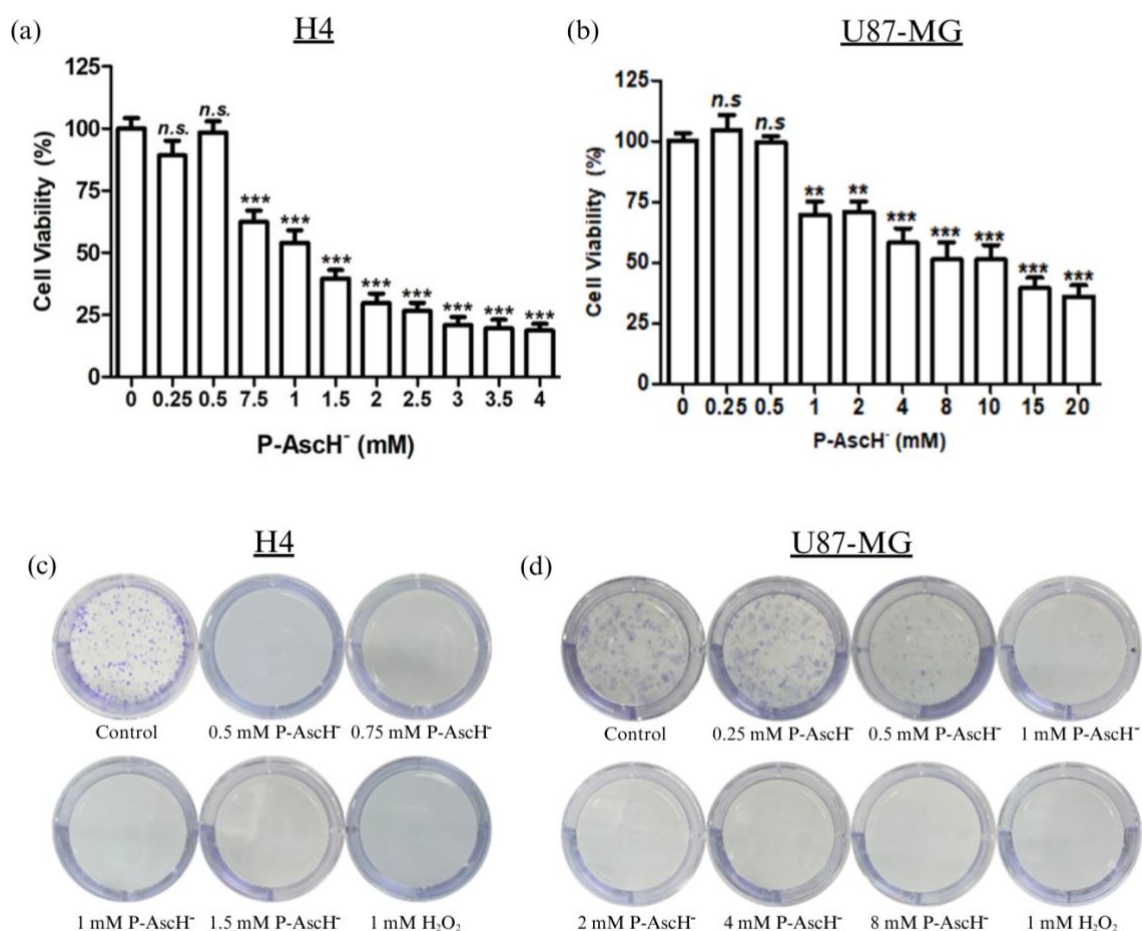


Figure 1: P-AscH⁻ reduces cell viability and clonogenicity of glioblastoma.

(a) and (b) show MTT results after treatment with pharmacological ascorbate performed on H4 and U87-MG cell lines, respectively. We observed a significant trend in the reduction of cell viability with the increase in concentration of P-AscH⁻. (c) and (d) demonstrate the results of clonogenic assay performed on H4 and U87-MG cell lines, respectively. With a gradual increase in P-AscH⁻ the clonogenicity of cells declines. All results are calculated from 2 independent biological replicates with 3 (clonogenic assay) and 8 (MTT assay) technical replicate per experiment; mean \pm SEM (*, $p < 0.05$; **, $p < 0.01$; ***, $p < 0.001$).



H₂O₂ is the primary contributor responsible for pharmacological ascorbate's anticancer activity

Enzymes such as catalase, glutathione peroxidase, and other peroxidases are involved in the detoxification of H₂O₂. Catalase is the primary enzyme responsible for the removal of high fluxes of H₂O₂ that are produced by P-AscH⁻.¹³ The capacity of catalase to remove H₂O₂ is reduced in cancer cells, allowing the accumulation of H₂O₂ in cells and cause oxidative stress resulting in DNA damage and cell death.¹⁴ To confirm this activity in glioblastoma, we investigated the clonogenicity of H4 and U87-MG cancer cell lines *via* co-treatment with catalase and P-AscH⁻. As a positive control, H₂O₂ was used. Data showed a similar trend between P-AscH⁻ treatment and positive control i.e., restoration of clonogenicity upon using the combination with catalase as compared to P-AscH⁻ or H₂O₂ alone. Hence, our results demonstrated that H₂O₂ is the major contributor towards P-AscH⁻ pro-oxidant activity. Furthermore, when H₂O₂ activity is hindered via catalase, it results in restoration of reduction in clonogenicity caused by P-AscH⁻ concluding that P-AscH⁻ functions as a prodrug that delivers high fluxes of H₂O₂ to cancer cells.

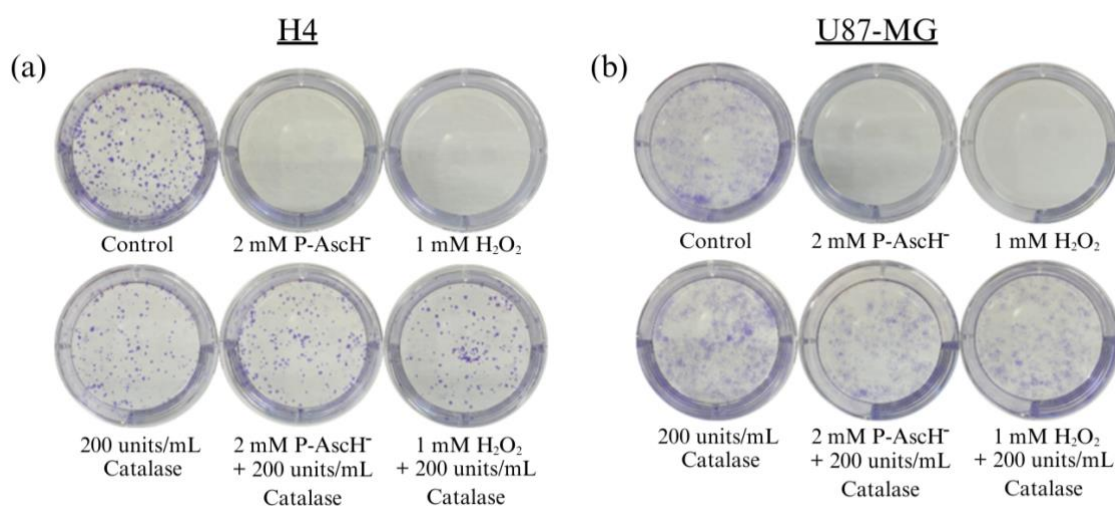


Figure 2: Generation of H₂O₂ by P-AscH⁻ is the main factor responsible for cytotoxicity.

(a) and (b) show the results of clonogenic assays performed on H4 and U87-MG cell lines.

Both cells were treated with varied concentrations of P-AscH⁻ resulting in diminishing clonogenicity. However, when these cells were treated in combination with catalase, restoration of clonogenicity occurred, confirming that H₂O₂ is the primary factor towards cytotoxicity of P-AscH⁻. As a positive control, H₂O₂ was used. Results are analyzed from 2 independent biological replicates with 3 technical replicates per experiment.

P-AscH⁻ disrupts cellular bioenergetics balance of glioblastoma

Due to an increase in the consumption of energy in the cell resulting from damage caused by oxidative stress, cells become depleted in ATP and other bioenergetics levels.⁸ In our investigation, we measured intracellular ATP levels per cell after treatment with P-AscH⁻ for 1 h. We observed a significant drop in ATP levels with the increase in P-AscH⁻ concentrations. To analyze the reversal of this phenomenon, we co-treated cells with catalase. Our experiments



demonstrated the protective role of extracellular catalase, this strongly suggests the involvement of H_2O_2 in the disruption of bioenergetic levels. This fall in bioenergetics level is due to the increase in demand because of activation of DNA repair mechanisms.⁸ Consistent with other studies, our data also suggests that there is decrease in bioenergetics upon treating with pharmacological ascorbate.¹⁴

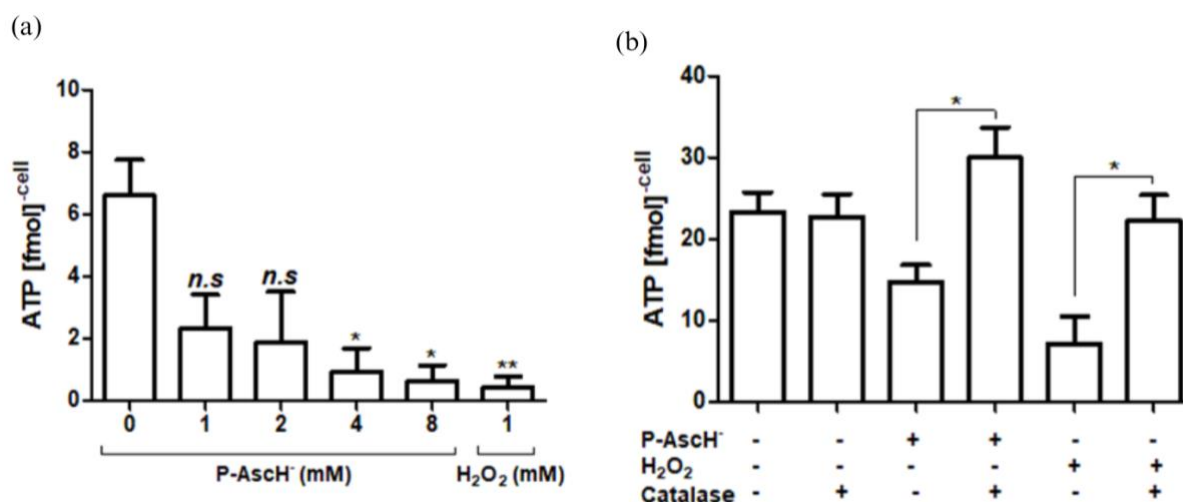


Figure 4: Oxidative damage caused by P-AscH⁻ leads to a reduction in ATP bioenergetic levels.

(a) Bioenergetic levels of ATP in U87-MG cells are reduced to a significant degree after treatment with P-AscH⁻ for 1 h. (b) Catalase has a shielding role against P-AscH⁻ as it can detoxify H_2O_2 extracellularly, protecting cells from the cytotoxic effects of H_2O_2 generated by P-AscH⁻. Thus, restoring the ATP levels as shown in the graph. Results are analyzed from 2 independent experiments, mean \pm SEM (*, $p < 0.05$; **, $p < 0.01$; ***, $p < 0.001$).

Intracellular labile iron partially contributes to P-AscH⁻ anti-cancer activities

Availability of labile iron either intracellular or extracellular plays a crucial role when we consider toxicity caused by ascorbate. Extracellular labile iron is essential to produce ROS i.e., H_2O_2 by the oxidation of ascorbate, whereas intracellular labile iron is crucial in the formation of hydroxyl free radical which is responsible for site-specific damage at macromolecules such as DNA, protein, and lipids.¹⁶ In our study, we used DFO and DTPA to chelate intracellular labile iron. After 3 h of chelation, we proceed to P-AscH⁻ treatment for 1 h to evaluate the clonogenicity of U87-MG. The clonogenicity of control and DFO/DTPA alone was comparable. However, in the case of chelation proceeded with P-AscH⁻ presented with colonies in contrast to P-AscH⁻ alone, where no colony was observed. Interestingly, the number of colonies in case of DFO/DTPA proceeded with P-AscH⁻ were much less than that of DFO/DTPA alone. Owing to the fact, the extracellular environment is the same as that of P-AscH⁻ alone, leading to usual extracellular production of H_2O_2 . That's why there is still significant toxicity caused in case of DFO/DTPA proceeded with P-AscH⁻. However, at the time of P-AscH⁻ treatment, chelated iron was only present intracellularly, thus leading to inhibition of the Fenton reaction resulting in survival of a few colonies. Hence, this experiment



suggests the importance of intracellular labile iron in the Fenton reaction involved in the enhancement of cytotoxicity caused by P-AscH⁻ towards the U87-MG cells. According to several studies, there is increased labile iron pools in the cancer cells as compared to normal cell, this increased availability of labile iron contributes toward enhanced cytotoxicity of P-AscH⁻.¹

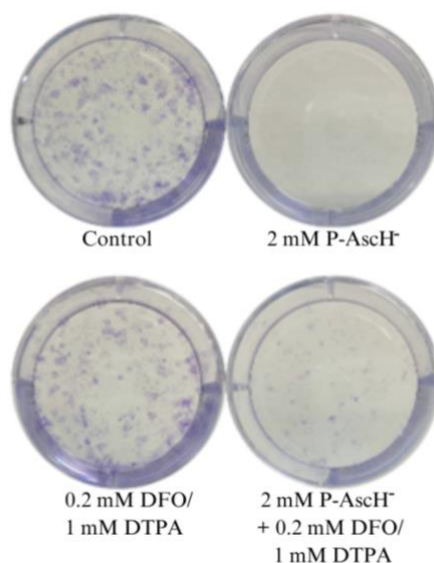


Figure 5: H₂O₂ can lead to the formation of HO[•] via Fenton reaction which causes site-specific oxidative damage.

Intracellular labile iron enhances the cytotoxicity of P-AscH⁻ of U87-MG glioblastoma cell line, thereby inhibiting the redox-active metals mediated by the Fenton reaction. Results were derived from 2 independent biological replicates with 3 technical replicates per experiment.

P-AscH⁻ as an adjuvant with temozolomide increases anti-cancer activity

Temozolomide (TMZ) is currently an approved therapy against glioblastoma.¹⁵ To analyze temozolomide effectiveness when given along with adjuvant pharmacological ascorbate, we pretreated U87-MG cells with P-AscH⁻ for 1 h and then immediately with temozolomide for 18 h. Our data demonstrates that with the increase in the concentration of P-AscH⁻ while keeping the temozolomide at the same concentration, cytotoxicity of combination treatment is increased suggesting that P-AscH⁻ could be the responsible factor for this enhanced toxicity. Similarly, the clonogenicity of U87-MG cells was further diminished due to the combined toxicity of both agents. Our investigation concludes that P-AscH⁻ as an adjuvant with TMZ, produces greater therapeutic outcomes than TMZ alone.

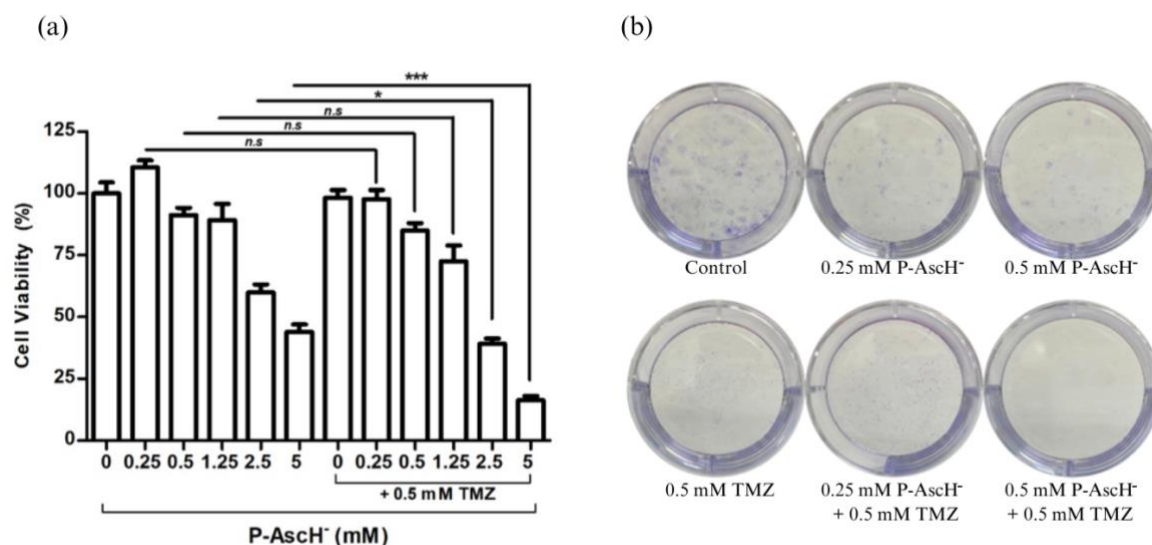


Figure 3: Adjuvant use of P-AscH⁻ in temozolomide therapy induces greater anticancer activity in glioblastoma than temozolomide alone.

(a) and (b) present results from the MTT assay and clonogenic assay performed on the U87-MG cell line. Cells were pretreated with P-AscH⁻ for 1 h and treated with TMZ for 18 h. Our data depicts an increase in anti-cancer activity with the adjuvant use of P-AscH⁻ as compared to TMZ alone. All results are analyzed from 2 independent biological replicates with 3 (clonogenic assay) and 8 (MTT assay) technical replicates per experiment; mean \pm SEM (*, $p < 0.05$; **, $p < 0.01$; ***, $p < 0.001$).

Conclusion:

In summary, our investigation indicates that P-AscH⁻ has anti-cancer activity against glioblastoma. Our *in vitro* data suggests that P-AscH⁻ decreases cell viability and significantly reduces clonogenicity and depletes intracellular bioenergetics levels. Our study demonstrates that H₂O₂ is a responsible contributor towards pro-oxidant activity of P-AscH⁻. Thus, pharmacological ascorbate acts as a prodrug to provide H₂O₂ fluxes to the cells by redox-active metals mediated reactions. With the use of chelators (DFO/DTPA) before P-AscH⁻ treatment, restoration of clonogenicity as compared to P-AscH⁻ alone was observed, demonstrating the involvement of intracellular labile iron in cytotoxicity of P-AscH⁻. Moreover, P-AscH⁻ as adjuvant with temozolomide significantly enhanced anti-cancer activity in glioblastoma cell lines. Our findings present an insightful understanding of P-AscH⁻ as a potential adjuvant in glioblastoma therapy and its possible outcomes. To leverage its significance in clinical practice, extensive *in vivo* studies are required to confirm P-AscH⁻ efficacy against glioblastoma proceeding to clinical trials to analyze adverse effects associated with the use of P-AscH⁻ as adjuvant in temozolomide therapy in GBM patients.



References:

1. Renner O, Burkard M, Michels H, Vollbracht C, Sinnberg T, Venturelli S. *Int. J. Oncol.* 2021;58(6):1-17.
2. Polireddy K, Dong R, Reed G, Yu J, Chen P, Williamson S, et al. *Sci. Rep.* 2017;7(1).
3. Ma Y, Chapman J, Levine M, Polireddy K, Drisko J, Chen Q. *Sci. Transl. Med.* 2014;6(222):222ra18.
4. Furqan M, Abu-Hejleh T, Stephens LM, Hartwig SM, Mott SL, Pulliam CF, et al. *Redox biol.* 2022;53:102318.
5. Herst PM, Broadley KW, Harper JL, McConnell MJ. *Free Radic. Biol. Med.* 2012 Apr 15;52(8):1486-93.
6. Zaher A, Stephens LM, Miller AM, Hartwig SM, Stolwijk JM, Petronek MS, Zacharias ZR, Wadas TJ, Monga V, Cullen JJ, Furqan M. *Front. Immunol.* 2022 Aug 22;13:989000.
7. Erudaitius DT, Buettner GR, Rodgers VG. *Free Radic. Biol. Med.* 2020;156:20-5.
8. Buranasudja V, Doskey CM, Gibson AR, Wagner BA, Du J, Gordon DJ, et al. *Mol. Cancer Res.* 2019;17(10):2102-14.
9. Erudaitius D, Huang A, Kazmi S, Buettner GR, Rodgers VG. *PloS One.* 2017 Jan 20;12(1): e0170442.
10. Schoenfeld JD, Alexander MS, Waldron TJ, Sibenaller ZA, Spitz DR, Buettner GR, et al., editors. *Semi. Radiat. Oncol.* ; 2019: Elsevier.
11. Hoffer LJ, Levine M, Assouline S, Melnychuk D, Padayatty SJ, Rosadiuk K, Rousseau C, Robitaille L, Miller Jr WH. *Ann. Oncol.* 2008 Nov 1;19(11):1969-74.
12. Chen P, Reed G, Jiang J, Wang Y, Sunega J, Dong R, Ma Y, Esparham A, Ferrell R, Levine M, Drisko J. *Clin. Pharmacokinet.* 2022 Sep;61(9):1237-49.
13. Nandi A, Yan LJ, Jana CK, Das N. *Oxid. Med. Cell. Longev.* 2019;2019:9613090.
14. Doskey CM, Buranasudja V, Wagner BA, Wilkes JG, Du J, Cullen JJ, et al. *Redox biol.* 2016;10:274-84.
15. Singh N, Miner A, Hennis L, Mittal S. *Cancer Drug Resist.* 2021;4(1):17.
16. Du J, Wagner BA, Buettner GR, Cullen JJ. *Free Radic. Biol. Med.* 2015;84:289-95.

STUDY THE COMBINATION EFFECTS OF URSOLIC ACID ENCAPSULATION IN PLGA/CS NANOPARTICLES IN BREAST CANCER CELLS

Pattaree Payomhom,¹ Kanlaya Katewongsa^{1,*}

¹Department of Biochemistry, Faculty of Science, Mahidol University, Bangkok, Thailand

*e-mail: Kanlaya.pra@mahidol.edu

Abstract:

Triple-negative breast cancer (TNBC) is a subtype of breast cancer with extremely aggressive, invasive and poor prognosis making it become one of the most difficult cancers to treat. Paclitaxel (PTX) usually used as a front-line in breast cancer treatment however, the development of chemoresistance and side effects from PTX are a huge drawback. Using the combination treatment could overcome these drawbacks. Ursolic acid (UA) which is a non-toxic phytochemical found in various types of plants could be an interesting choice. UA has been reported to show anti-cancer activity in several types of cancer and found to enhance the cytotoxicity of anti-cancer drugs even in drug-resistant breast cancer cells. However, UA has low bioavailability due to its poor water solubility properties which limit its clinical effect. To overcome this limitation, the UA encapsulated chitosan-coated poly (lactic-co-glycolic acid) ((UA)-PLGA/CS) nanoparticles were designed. The obtained nanoparticles had a spherical shape as demonstrated by Scanning Electron Microscopy (SEM) with a size around 260 nm and zeta potential at + 10 mV. The loading efficiency (LE) of 1.5 percent and encapsulation efficiency (EE) of 25 percent. (UA)-PLGA/CS improves the anti-breast cancer activity of UA by significantly decreasing cells viability of MDA-MB-231 cells which is the TNBC. The combination effect between (UA)-PLGA/CS and PTX has been investigated. This work demonstrated the function (UA)-PLGA/CS as a successful carrier for UA with the potential to enhance the anti-cancer efficacy in TBNC cell line. These findings are essential for further developing a better breast cancer treatment that can improve the life quality of cancer patients worldwide.

Introduction:

Triple-negative breast cancer (TNBC) is an aggressive subtype, accounting for 10–15% of all breast cancers and presenting a poor long-term prognosis ^[1]. As it is deficient in progesterone, estrogen, and human epidermal growth factor receptor-2 (HER-2) receptors, it is unresponsive to hormonal or anti-HER2 therapies, making it challenging to treat. In addition, the status of these receptors is considered as the standard prognostic and predictive factors, lack of these receptors leading to late diagnosis possibly allow the metastasis of cancer cells ^[2]. Late detection with advanced stage of TNBC and limited of treatment make it become one of the most challenging cancers to be treated. The most common treatment used for TBNC is chemotherapy.

Paclitaxel (PTX), widely us as a chemotherapeutic agent, is effective against various cancer types ^[3, 4]. In breast cancer cells, PTX is usually utilized as the first-line therapeutic treatment, the mechanisms of PTX are related to the inhibition of cancer cells growth ^[3], causes cell cycle arrest, and ultimately causes cancer cells to undergo apoptosis by encouraging the polymerization of tubulin and stabilizing the ensuing microtubules ^[5] triggers several signaling pathways resulting in programmed cell death ^[6, 7]. However, the drug resistance and the side effects have limited the medical effect of PTX in breast cancer treatment. Up to 90% of cancer deaths are caused by drug resistance ^[8]. Chemotherapeutic medication effectiveness is hampered by multidrug resistance (MDR), which frequently

results in relapse ^[9]. Patients frequently become resistant to treatment, which forces them to alter their therapeutic approach and may contribute to the phenomenon of resistance. After receiving the chemotherapy patients usually suffer from side effects such as hair loss, fatigue, loss of appetite, nausea, and immune problems which affect the quality of life. To necessitate combination treatment to address these challenges.

One of the interesting choices is ursolic acid (UA) is the non-toxic phytochemicals triterpene compound commonly found in several types of plants and fruit, such as thyme, apple peel, and cranberries; recently, UA has been widely studied due to its potential biochemical effects such as anti-cancer activity. Therefore, many studies have reported the anti-breast cancer activity of UA, in many types of cancer including live cancer, gastric cancer, colorectal cancer, and breast cancer. UA was reported to enhance the effect of PTX in the chemoresistance of cancer cells ^[10, 11]. Although UA has shown a lot of benefits for cancer treatment, UA has a huge drawback due to low water solubility that leads to poor bioavailability. This drawback could limit the biological potential of UA. Using an efficient drug delivery system can increase the transportation of the compounds into cells, increase the bioavailability of the drug, and protect the compound from chemical- and bio-degradation. Using nanoparticles (NPs) as a nanocarrier could show great promise in overcoming this problem.

Chitosan-coated poly(lactic-co-glycolic acid) (PLGA/CS) is one of the most widely used nanoparticles for drug delivery which shows highly biocompatible and sustained release properties. The positive charge of the chitosan provides the benefit of mucoadhesive effect ^[12], and increases cellular internalization ^[13] which could result in improved bioavailability of the compounds. Therefore, this UA encapsulated PLGA/CS nanoparticles ((UA)-PLGA/CS) has a huge potential to improve the bioavailability of UA and improve the anti-cancer of UA in breast cancer cells which could lead to enhanced activity of PTX.

Methodology:

Chemical Material

Poly (lactic-co-glycolic acid) (PLGA) (M.W. 45,000-55,000 Da) was purchased from PolySciTech (Akina Inc.). Poly (vinyl alcohol) (PVA) (M.W. 9,000-10,000 Da), Trehalose and Chitosan low molecular weight were purchased from Sigma-Aldrich. Dichloromethane (DCM) and Glacial acetic acid were purchased from Thermo Fisher Scientific, UK. Ursolic acid (UA) was purchased from Tokyo Chemical Industry Co., LTD. Paclitaxel (PTX) was purchased from Med Chem Express, USA. Eagle's minimum essential Medium (EMEM), Dulbecco's modified Eagle medium (DMEM), Fetal bovine serum (FBS) and penicillin/streptomycin solution (P/S) were purchased from Gibco, UK. All aqueous solutions were prepared using Milli-Q water (MQ-water).

Cell lines and culture conditions

TBNC cell line (MDA-MB-231) was purchased from the American Type Culture Collection (ATCC, Manassas, VA, USA). MDA-MB-231 cells were cultured in DMEM medium, supplemented with 10% (v/v) heat-inactivated FBS and 1% P/S and cultured at 37 °C with 5% CO₂ incubator.

Optimization of the synthesis (UA)-PLGA/CS

To optimize the synthesis of (UA)-PLGA/CS, two distinct methods were employed, as previously described ^[14, 15]. Chitosan was dissolved in either water or acetic acid.

The preparation of (UA)-PLGA/CS by using chitosan dissolved in water was reported by Mekseriwattana et al., 2021^[14] chitosan dissolved in water phase. In brief, PLGA and UA powder dissolved in DCM at the final concentration of 50 mg/mL and 5 mg/mL respectively as an oil phase, dropwise into the water phase containing chitosan in 5% PVA while vortex mixing. The mixture was emulsified using a probe sonicator by using 38% power for 30 sec then vortex mixing, repeats for 3 cycles then evaporate the organic solvent by adding the mixture into 0.3% PVA solution and stirred for 3 h at room temperature. The nanoparticles were separated by centrifugation at 18,514 xg for 30 min and washed with water 3 times. Lastly, the trehalose at the concentration of 1 mg/mL as a cryoprotectant was added before lyophilized.

In the second protocol reported by Nag et al., 2021^[15], chitosan dissolved in acetic acid, PLGA (50 mg/mL), and 5 mg/mL of UA were dissolved in 2 mL dichloromethane (DCM) as an oil phase dropwise into the water phase that contained only 0.3% PVA then using probe sonicator for 2 min on ice. The solution was stirred for 5 h to evaporate the solvent and centrifuged at 18,514 xg for 1 h to obtain the pellet of PLGA nanoparticles. The pellet was suspended in the chitosan solution (1% Chitosan (w/v) in 2% glacial acetic acid (w/w)) and stirred overnight at room temperature to yield the CS/PLGA NPs. The solution was centrifuged at 18,514 xg for 30 h and washed 3 times with distilled water. Lastly, the trehalose at the concentration of 1 mg/mL as a cryoprotectant was added before lyophilized.

The resulting nanoparticles were characterized for size, polydispersity index (PDI), zeta potential, yield percentage, encapsulation efficiency (%EE), and loading efficiency (%LE). The nanoparticles were observed under a scanning electron microscope (SEM) to determine morphology and size.

Characterization of (UA)-PLGA/CS

Size

The hydrodynamic size, PDI, and zeta potential of the nanoparticles were measured by dynamic light scattering technique using Zetasizer Nano ZS90 (Malvern Instruments, Malvern, UK). The nanoparticles solutions were injected into disposable cell for size measurement. The zeta potential was measured by using a carbon-coated electrode.

Encapsulation efficiency

The total amount of UA loaded in CS/PLGA was measured using high performance liquid chromatography (HPLC, Waters 2487, Waters Corporation) using UV detector at 210 nm. The UA was separated by using C-18 column (ZORBAX, 4.6x150 nm, 5 µm) at 35°C isocratic mode with mobile phase of Acetonitrile: Methanol = 80: 20 v/v. The UA standard solutions were prepared by dissolving UA in methanol and diluted into different concentrations to generate a standard curve. The (UA)-PLGA/CS was dissolved in methanol and used a probe sonicator for 10 sec to break the particle, then centrifuge to collect the supernatant that used for the amount of UA encapsulated analysis. The amount UA was reported as µg per mg and calculated as encapsulation efficiency (% EE) and loading efficiency (% LE) following these equations:

$$\% \text{ Encapsulation efficiency (\%EE)} = \frac{\text{Amount of Ursolic in the nanoparticles}}{\text{Initials amount of Ursolic acid}} \times 100$$

$$\% \text{ Loading efficiency (\%LE)} = \frac{\text{Amount of Ursolic in the nanoparticles}}{\text{Weight of the nanoparticles}} \times 100$$

Scanning electron microscope

The morphology and size of the lyophilized nanoparticles were observed using field emission scanning electron microscopy (FESEM, JSM-7001F, JEOL, Japan). The thin films of the sample were prepared on a carbon-coated copper grid and coated with gold for conductivity.

Evaluate the anti-cancer activity

To evaluate the cell viability of TNBC cells, the MTT assay was used. MDA-MB-231 cells were seeded into 96 well plates with 8,000 cells/well. UA, PTX, and (UA)-PLGA/CS were prepared by dissolving in serum-free media and vortex for 10 min. The prepared solutions were treated in the cells for 48 h. The positive control was cells treated with serum free medium and 1% of triton-X was used as a negative control. The 0.5 mg/mL MTT solution was added into the cells and incubated for 3 h. Later, the MTT solution was removed and 200 μ L of DMSO was added into every well to dissolve the formazan crystal. Measure the absorbance of the solution at 540 nm. Cell viability percentages were calculated by using the following equation:

$$\% \text{ cell viability} = (\text{average absorbance of the treated cells} / \text{average absorbance of positive control}) \times 100$$

Western blot

MDA-MB-231 cells with 5×10^5 cells/well were seeded into 6 wells plate and treated with UA and (UA)-PLGA/CS for 48 h then extracted the protein by using RIPA buffer. Micro BCA assay (Thermo Fisher Scientific, UK) was used to determine protein concentration. For western blot analysis, protein 50 μ g and 1X protein loading dye were added into the acrylamide gel and separated by SDS-PAGE, then transferred onto PVDF membrane via semi-dry transfer. The membrane was blocked by 5% non-fat dry milk at room temperature for 1 h. The membrane was incubated with an anti-BAX antibody at 4 °C overnight. Then, incubate the membrane with an anti-rabbit secondary antibody conjugated with horseradish peroxidase. A gel documentation system (G:BOX Chemi XX6, The syngene, UK) was used to detect the band on the membrane by using a chemiluminescent HRP substrate (ECL, Biorad, USA) as a substrate.

Statistical analysis

All experiments were replicated for three independent experiments ($n = 3$) except for the western blot experiment which was done two times independently. Data were expressed as mean \pm standard error of the mean (SEM). GraphPad Prism Version 9.5.1 (528) was used for statistical analysis. The data were compared by Two-way ANOVA. Statistical significance was denoted as follows: **** $p \text{ value} \leq 0.0001$, *** $p \leq 0.001$, ** $p \leq 0.01$, * $p \leq 0.05$; ns, not significant ($p > 0.05$).

Results and Discussion:

Characterization of (UA)-PLGA/CS

(UA)-PLGA/CS were prepared by using 2 different methods including chitosan dissolved in water and chitosan dissolved in glacial acetic acid. These 2 methods provide similar percent yields but different in size, PDI, and zeta potential as shown in Table 1. Chitosan dissolved in water methods provide NPs with 252 nm, PDI lower than 0.2 indicating the monodispersed of the NPs and zeta potential with +10.5 mV which can confirm the

successful chitosan coated on PLGA NPs. While chitosan dissolved in acetic acid provides bigger NPs with 746 nm, PDI around 0.3 and high positive value of zeta potential around + 51 mV. The nanoparticles yield from the 2 methods have amount around 85 % and provide a similar %EE and %LE with around 24 % - 28 % and 1.3 % -1.7 % respectively.

The (UA)-PLGA/CS obtained from dissolved chitosan in acetic have bigger size and too high PDI indicating the polydispersity of NPs. The bigger size of nanoparticles trends to have lower cellular uptake ^[16]. Therefore, the (UA)-PLGA/CS NPs using chitosan in water were used in the later parts of the experiment. Further characterization of (UA)-PLGA/CS with 250 nm size was done, and the morphology of NPs was observed by using a scanning electron microscope (SEM). (UA)-PLGA/CS have a spherical shape and smooth surface with a size obtained from SEM image around 137 nm as shown in **Figure 1**.

Table 1. Characterization of (UA)-PLGA/CS prepared by using 2 different methods

Methods	Size (nm)	PDI	Zeta potential (mV)	Yield (%)	EE (%)	LE (%)
Chitosan in water	252 ± 1.4	0.16	10.5 ± 2.9	88.9 ± 4.8	24 ± 7.4	1.3 ± 0.3
Chitosan in acetic acid	746 ± 10.2	0.3	51.5 ± 5.8	83.0 ± 4.3	28.1 ± 1.1	1.7 ± 0.02

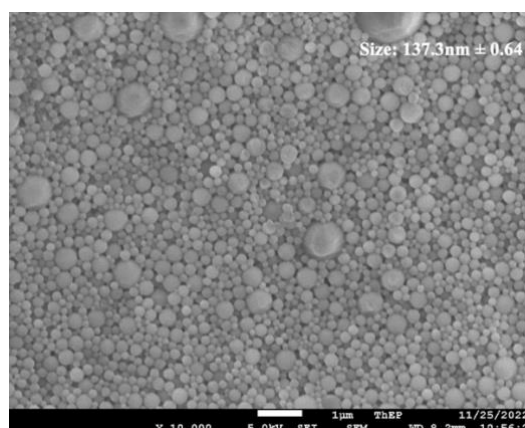


Figure 1. Morphology and size of (UA)-PLGA/CS observed under SEM

To evaluate the anti-cancer activity of UA and (UA)-PLGA/CS

UA has been reported to inhibit cell proliferation in TNBC cells by affecting several signaling pathway ^[17, 18]. The (UA)-PLGA/CS NPs were prepared to improve the anti-cancer activity of UA in TNBC. Therefore, the anti-cancer efficacy of UA and (UA)-PLGA/CS NPs was investigated by performing MTT assay to present the cells viability of TBNC after being treated with UA and (UA)-PLGA/CS NPs. As shown in **Figure 2** both UA and (UA)-PLGA/CS were decreasing cell viability of MDA-MB-231 cells in dose dose-dependent manner.

When comparing the efficacy, (UA)-PLGA/CS exhibited a significantly decreasing cells viability at the same concentration. The IC₅₀ of (UA)-PLGA/CS NPs and UA were 37.73 μM and 85.38 μM respectively, indicating a better anti-breast cancer efficacy of (UA)-PLGA/CS. These results can confirm that the anti-cancer efficacy of UA can be enhanced by PLGA/CS NPs. Similar to the studies of Punfa, Wanisa, et al., 2012 found that PLGA

nanoparticles enhance the activity of curcumin in drug resistance cancer by enhancing the cellular uptake ^[19].

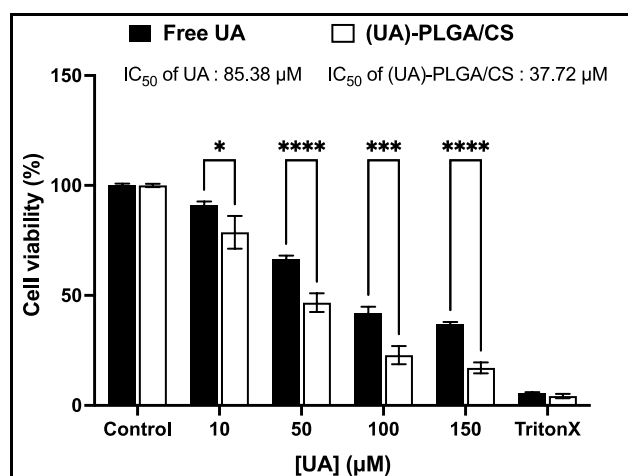


Figure 2. Cells viability of MDA-MB-231 cells treated with UA and (UA)-PLGA/CS for 48 h. **** p value ≤ 0.0001 , *** p ≤ 0.001 , * p ≤ 0.05

Effect of UA and (UA)-PLGA/CS NPs on the BAX expression

To investigate the mechanism underlying anti-cancer activity in TNBC of UA and (UA)-PLGA/CS NPs, the expression of BAX was investigated by western blot analysis. BAX is a member of the Bcl-2 gene family and play a role as pro- apoptotic protein regulates a wide range of cellular processes. As shown in **Figure 3A** cells treated with serum-free as a control show a low expression of BAX but showed higher expression in cells treated with (UA)-PLGA/CS.

Even though, the expression level of BAX in **Figure 3B** shows no significant difference but it was increased when treated with Free UA and highly increased when treated with (UA)-PLGA/CS compared to the control group. These results indicate that (UA)-PLGA/CS induces apoptosis and enhances the anti-cancer efficacy of UA potentially affecting the signaling pathway related to cell apoptosis.

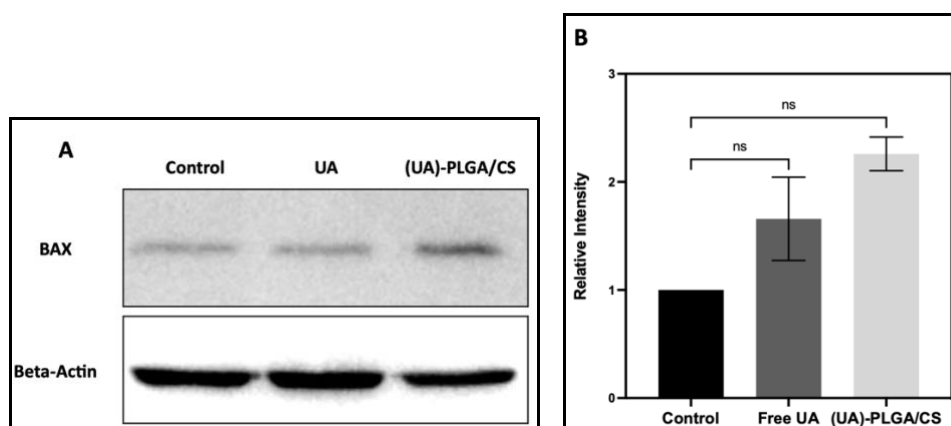


Figure 3. BAX expression of MDA-MB-231 cells treated with serum-free media, UA and (UA)-PLGA/CS respectively **A)** represent the Western blot results **B)** Quantitative results. ns, not significant (p > 0.05)

Effect of (UA)-PLGA/CS on a combination effect with Paclitaxel (PTX)

The studies of Meng *et al.*, 2021 found that UA has the ability to accelerate the function of PTX by inducing cells death in the esophageal cancer Cells [11]. Together with the study of Xu *et al.*, 2017 reported that UA has a synergistic effect with PTX in gastric carcinoma regulated by Cyclooxygenase-2 [20]. There were several studies of synergistic effects between UA and PTX in many types of cancer but not in breast cancer. For breast cancer there was research by Xiang *et al.*, 2019 found that UA can decrease the PTX resistance of breast cancer cells by targeting MiRNA-149-5p/MyD88 [10]. Therefore, this experiment aims to investigate the combination effect of (UA)-PLGA/CS with PTX in breast cancer cells. The combination effect was investigated by using the cells viability experiment as described Jiang, S. *et al.*, 2015 in brief, the single treatment was investigated, then, the concentration of the first drug was fixed, vary the concentration of another drug for the combined treatment, lastly evaluated the effect between two drugs [21]. The MTT assay was done by treating the cells with (UA)-PLGA/CS and PTX. The concentrations of (UA)-PLGA/CS were fixed at IC₂₅ and varied the concentration of PTX at IC₂₅, IC₅₀ and IC₇₅ which are 1 nM, 8 nM, and 20 nM respectively (**Figure 4A**, **Figure 4B**, and **Figure 4C** respectively). As shown in **Figure 4**, all 3 conditions of co-treat between (UA)-PLGA/CS and PTX did not show a significant difference from the PTX treated alone.

This result indicated that (UA)-PLGA/CS did not enhance the anti-cancer activity of PTX and there was no combination effect between (UA)-PLGA/CS and PTX in MDA-MB-231 cells. These could be the results from the (UA)-PLGA/CS NPs required time to release UA that does not affect the function of PTX-treated TNBC cells.

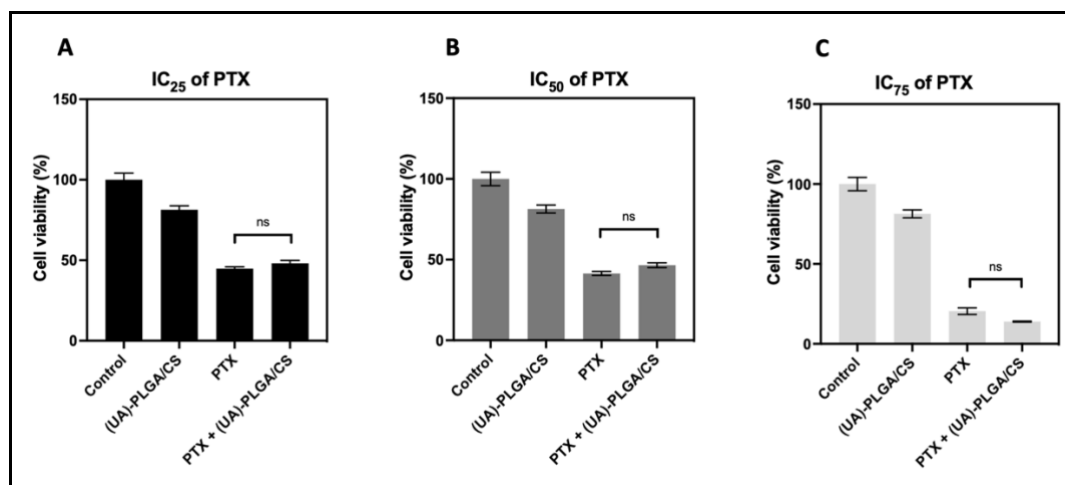


Figure 4. Cell viability results of MDA-MB-231 cells treated with (UA)-PLGA/CS and PTX individually and co-treated between (UA)-PLGA/CS with **A)** IC₂₅, **B)** IC₅₀ and **C)** IC₇₅ of PTX. ns, not significant ($p > 0.05$)

Conclusion:

In conclusion, (UA)-PLGA/CS were developed to enhance the anti-cancer properties of UA in TNBC and studies the effect of (UA)-PLGA/CS when used with PTX. Our study indicates that UA which is the phytochemical demonstrated the anti-cancer activity in TNBC cells, but insoluble properties limit its clinical effect. (UA)-PLGA/CS were prepared to overcome the limitation of UA. (UA)-PLGA/CS exhibits the improvement of anti-cancer properties of UA in TNBC by having lower IC₅₀ value and increased BAX protein expression compared to UA. (UA)-PLGA/CS was found to inhibit the cancer cell proliferation and induced cells death in MDA-MB-231 cells. Therefore, it had the potential to be used as an

anti-breast cancer treatment in TNBC patients. However, the co-treatment between (UA)-PLGA/CS and PTX showed no effect, and cells viability of TBNC were decreased from the effect of PTX only.

Even though the combination effects between (UA)-PLGA/CS and PTX was not observed, the development of (UA)-PLGA/CS has the potential to be used as anti-cancer agent is an advancement in the field of drug delivery and cancer research. Additionally, it might be beneficial to the development of fresh treatment modalities that enhance the quality of life for breast cancer patients worldwide.

Acknowledgements:

This research project is supported by Mahidol University (Basic Research Fund: fiscal year 2022) (BRF1-040/2565) and partly support was provided by the center for scientific instrumentation and platform services grant (CIF), Faculty of Science, Mahidol University. The authors wish to thank Ms.Siraprapa Siritutsoontorn and Ms.Chayanee Laowittawat for their advise during the western blot experiment.

References:

- 1.Sharma, P., Oncologist. 2016; **21**(9): p. 1050-62.
- 2.Al-Mahmood, S., et al.,Drug Deliv Transl Res. 2018; **8**(5): p. 1483-1507.
- 3.Abu Samaan, T.M., et al.,Biomolecules. 2019; **9**(12).
- 4.Ramalingam, S. and C.P. Belani,Expert Opin Pharmacother. 2004; **5**(8): p. 1771-80.
- 5.Stage, T.B., T.K. Bergmann, and D.L. Kroetz,Clin Pharmacokinet. 2018; **57**(1): p. 7-19.
- 6.Wang, T.H., H.S. Wang, and Y.K. Soong,Cancer. 2000; **88**(11): p. 2619-28.
- 7.Zhao, S., et al.,Apoptosis. 2022; **27**(9-10): p. 647-667.
- 8.Łukasiewicz, S., et al.,Cancers (Basel). 2021; **13**(17).
- 9.Kinnel, B., et al.,Cancers (Basel). 2023; **15**(4).
- 10.Xiang, F., et al.,Front Oncol. 2019; **9**: p. 501.
- 11.Meng, R.Y., et al.,Int J Mol Sci. 2021; **22**(21).
- 12.Lima, I.A., et al.,Artif. Cells Nanomed. Biotechnol.2018; **46**(sup2): p. 993-1002.
- 13.Takeuchi, I., M. Ariyama, and K. Makino,J. Oleo Sci. 2019; **68**(4): p. 361-368.
- 14.Mekseriwattana, W., et al.,Photochem. Photobiol., 2021;
- 15.Nag, S. and K. Das Saha,ACS Omega. 2021; **6**(43): p. 28752-28769.
- 16.Nicolete, R., D.F. dos Santos, and L.H. Faccioli,Int Immunopharmacol. 2011; **11**(10): p. 1557-63.
- 17.Zhang, Y., et al.,Front Pharmacol. 2021; **12**: p. 685773.
- 18.Liao, W.-L., et al.,International Journal of Molecular Sciences. 2023; **24**(1): p. 366.
- 19.Punfa, W., et al.,Acta Pharmacologica Sinica. 2012; **33**(6): p. 823-831.
- 20.Xu, X., et al.,Oncotarget. 2017; **8**(54): p. 92770-92777.
- 21.Jiang, S., et al.,Chem Res Toxicol. 2015; **28**(12): p. 2250-2.

Synthesis, characterization, and *in vitro* study of riboflavin-functionalized superparamagnetic iron oxide nanoparticles in breast cancer cells

Sopon Nuchpun, Kanlaya Katewongsa^{1,2*}

¹ Department of Biochemistry, Faculty of Science, Mahidol University, Bangkok, Thailand

² School of Materials Science and Innovation, Faculty of Science, Mahidol University, Bangkok, Thailand

*E-mail: kanlaya.pra@mahidol.edu

Abstract

Superparamagnetic iron oxide nanoparticles (SPIONs) have been widely studied for medical applications such as contrast agents, and magnetic hyperthermia (MH) for cancer therapy. In this work, SPIONs were synthesized using the co-precipitation method of iron (II) and iron (III) chloride in basic condition and coated with riboflavin-citrate ligand (CARf) or citric acid. Rf-SPIONs and C-SPIONs were evaluated for colloidal stability in water and DMEM supplemented with different concentrations of fetal bovine serum (FBS). NPs exhibited different behaviors in water and at lower concentrations of FBS, whereas approximately 200 nm of both NPs were found when dispersed in 10% FBS in DMEM media, which indicated the highest stabilities of Rf-SPIONs and C-SPIONs in biological media for cell culture. The cellular uptake study revealed a significantly higher uptake of the Rf-SPIONs into breast cancer cells (2.9 times SSC signal) compared to normal breast cells (2.3 times SSC signal). This result indicated that the Rf-SPIONs are suitable for breast cancer delivery. In addition, the cellular uptake mechanism of this Rf-SPIONs was investigated. Riboflavin carrier protein (RCP) has been hypothesized to facilitate the cellular uptake of these particles. Surprisingly, the study of the effect of RCP on cellular SPIONs uptake suggested that RCP does not play a role in Rf-SPIONs uptake mechanism. These results could help to understand and be a guideline for the Rf-SPIONs internalization mechanism in other possible pathways for further development and utilization of Rf-SPIONs in breast cancer treatments.

Keywords: Magnetic nanoparticles; Riboflavin; Riboflavin carrier protein

Introduction:

Recently, superparamagnetic iron oxide nanoparticles (SPIONs) have gained wide interest in biomedical applications due to their responsivity to external magnetic fields and biocompatibility¹. For more stability and high specificity of SPIONs, surface modification is essential for SPIONs. Poly(ethylene glycol) (PEG), poly(vinyl alcohol) (PVA), chitosan, and citric acid were widely used for surface modification as they prevent agglomeration and could also provide a functional group for further surface modification of SPIONs, leading to different surface properties, cellular responses, and increase the uptake of SPIONs in specific cells²⁻⁴. Additionally, the stability of NPs in the biological environment is required to be evaluated before utilization. Some proteins in biological media could interact with the SPIONs, resulting in changing their stabilities, behaviors, and cellular recognition of nanoparticles⁵.

On the other hand, to achieve the targeting ability of SPIONs to cancer cells, our previous study reported riboflavin (Rf) can enhance the delivery efficiency of PLGA nanoparticles into breast cancer cells and high SPIONs uptake in MCF-7 cells^{6,7}. According to the experimental results, the internalization of Rf-SPIONs was proposed through the binding with riboflavin carrier proteins (RCP), which has been reported to be overexpressed

in tumor tissues of breast cancer and prostate cancer. However, there is still no direct evidence to clarify the mechanisms of RCP acting as a target for Rf-base nanoparticle uptake in breast cancer cells.

Hence, this study aims to evaluate the stability of Rf-SPIONs when dispersed in different aqueous solutions and perform that Rf could enhance the cellular SPIONs uptake in breast cancer cells, including investigating the role of RCP on cellular uptake mechanism.

Methodology:

Materials

Ferrous chloride tetrahydrate ($\text{FeCl}_2 \cdot 4\text{H}_2\text{O}$, $\geq 99\%$), ferric chloride hexahydrate ($\text{FeCl}_3 \cdot 6\text{H}_2\text{O}$, 97%), and riboflavin were obtained from Sigma-Aldrich[®]. Ammonia solution (NH_4OH , 25%) and tri-sodium citrate dihydrate (99%) were obtained from Merck. Hydrochloric acid was obtained from Riedel-de Haen. Citric acid was purchased from Vidhyasom Co. Ltd. 3-(4,5-dimethylthiazol-2-yl)-2,5-diphenyl-2*H*-tetrazolium bromide (MTT, 98%) was obtained from Pan-Reac AppliChem. Dimethyl sulfoxide (DMSO) was obtained from Fisher Scientific. All chemicals were used as purchased without further purification. All aqueous solutions were prepared using Milli-Q water (MQ-water) obtained from a Plus water purification system (Millipore, Milford, MA, USA). Dulbecco's Modified Eagle's Medium (DMEM), fetal bovine serum (FBS), and Penicillin/Streptomycin were obtained from Gibco[®].

Synthesis and characterization of riboflavin-citrate ester (CARf)

Riboflavin-citrate ester (CARf) was prepared using the protocol from Wid Mekseriwattana *et al*⁷. Rf (1.0 eq.) was mixed with citric acid (1.2 eq.) and dissolved in liquid phenol (30 mL). Then, the reaction was stirred and heated up to reflux condition at 140 °C for 6 hours. After completion, the obtained reaction was cooled down to room temperature and poured into diethyl ether (250 mL), followed by vacuum filtration. The precipitate was washed with EtOAc to remove excess citric acid. Finally, the crude product was incubated for 24 hours and was dried under reduced pressure to provide an orange solid; ¹H NMR (400 MHz, DMSO-*d*₆): δ = 2.39 (s, 3H), 2.47 (s, 3H), 2.49 (s, 4H), 2.74 – 2.83 (m, 2H), 3.63 (s, 3H), 4.22 – 5.35 (m, 3H), 6.74 (dd, *J* = 6.6 Hz, 3H), 7.14 (t, *J* = 6.52 Hz, 2H), 7.89 (d, *J* = 11.2 Hz, 1H), 9.35 (s, 1H), 11.34 (s, 1H).

The CARf ligand was characterized by nuclear magnetic resonance (NMR), high-resolution mass spectroscopy (HRMS) (Bruker Daltonics Data Analysis 3.3), and analyzed by high-performance liquid chromatography (HPLC) (HPLC 2695-UV 2487&PDA 2996) on a reversed-phase C₁₈ column (150 × 4.6 mm) using methanol: water (40:60) as a mobile phase and a fluorescence detector (Intelligent FP-2020) (excitation wavelength, 450 nm; emission wavelength, 510 nm).

Synthesis of SPIONs

Preparation of bare superparamagnetic iron oxide nanoparticles (B-SPIONs)

B-SPIONs were prepared by the co-precipitation method which was modified from Petcharoen and Sirivat⁸. A mixture of iron (II) chloride tetrahydrate (1.0 eq.) and iron (III) chloride hexahydrate (2.5 eq.) was dried in a vacuum for 15 minutes. The obtained mixture was dried under an N₂ atmosphere and dissolved in DI water (100 mL), heated up to 80 °C for 30 minutes. Then, 5 mL of 25% ammonium hydroxide solution was dropwise into the reaction, stirring at 80 °C for 30 minutes. After completion, the resulting reaction was cooled down to room temperature and purified by magnetic separation to collect the SPIONs. 15 mL

of DI water was added to the precipitate and vortexed back to the black solution. Then, SPIONs were collected by magnetic separation. Finally, the precipitate was dispersed in DI water to the desired product as a black solution (100 mL).

Preparation of citrated-coated superparamagnetic iron oxide nanoparticles (C-SPIONs)

C-SPIONs were prepared by using a soft chemical approach that was reported by Nigam *et al*⁹. A mixture of iron (II) chloride tetrahydrate (1.0 eq.) and iron (III) chloride hexahydrate (2.5 eq.) was dried in a vacuum for 15 minutes. Then, the obtained mixture was dried under an N₂ atmosphere and dissolved in DI water (40 mL), heated up to 70 °C for 30 minutes. Then, 10 mL of 25% ammonium hydroxide solution was dropwise into the reaction, stirring for 30 minutes. Next, tri-sodium citrate dihydrate (0.75 g per mL) (1.2 eq.) in DI water (2 mL) was added to the reaction, the reaction was heated up to 90 °C and further stirred for 1 h. After completion, the resulting reaction was cooled down to room temperature and purified by magnetic to collect the desired product as a black solution (100 mL).

Preparation of riboflavin-coated superparamagnetic iron oxide nanoparticles (Rf-SPIONs)

A stirred solution of 50 mg riboflavin-citrate ester (CARf) in DI water (40 mL) was added with B-SPION (10 mL). Then, the mixture was dried and stirred under an N₂ atmosphere at 90 °C for 90 minutes. After completion, the resulting reaction was worked up and cooled down to room temperature. The crude solution was isolated by centrifugation (12000 rpm, 30 minutes), and the precipitated Rf-SPIONs were dispersed in 15 mL of DI water, and centrifuged again. To remove excess CARf ligands, this process was carried out at least three times. The final pellet Rf-SPIONs were collected and dispersed in 10 mL of DI water, kept as a black solution.

Characterization of the SPIONs

SPIONs were diluted in DI water to a concentration of approximately 0.1 mg SPIONs per mL, and characterized in terms of hydrodynamic diameter (D_H) and zeta potential values using a Zetasizer Ultra (Malvern Panalytical, UK). All data were measured and analyzed in individual triplicates, reporting as mean \pm SD values from the three batches.

Effect of FBS supplementation in cell culture media on the colloidal stability of SPIONs

SPIONs were diluted into (10 μ g per mL) in DI water, serum-free Dulbecco's Modified Eagle's Medium (DMEM), and DMEM supplemented with 1%, 5%, and 10% fetal bovine serum. The diluted SPIONs were characterized in terms of hydrodynamic diameter (D_H) by Zetasizer Ultra (Malvern Panalytical, UK). All data were measured and analyzed in individual triplicates, reporting as mean \pm SD values.

Cell line and Cell culture condition

The breast cancer cell line (MDA-MB-231, MCF-7), and human breast epithelial cell line (MCF-10A) were purchased from American Type Culture Collection (ATCC®). Cells were cultured in 75 cm² cell culture flasks (Nest®) in each recommended medium supplemented with 10% fetal bovine serum and 1% Penicillin/Streptomycin at 37 °C under 5% CO₂ in a humidified incubator to allow the cells to reach 70-80% confluence. Cell subculture was done using 0.25% trypsin-EDTA and the media were changed every two

days. All cell culture supplies were purchased from Gibco, UK. Each cell line was treated with its recommended medium, according to **Table 1**.

Table 1. Media and supplements

Cell line	Medium
MDA-MB-231	Dulbecco's Modified Eagle's Medium (DMEM) (Gibco®), 10% fetal bovine serum (FBS), and 1% penicillin-streptomycin
MCF-7	Minimum Essential Medium (MEM) (Gibco®), 10% fetal bovine serum (FBS), and 1% penicillin-streptomycin
MCF-10A	Dulbecco's Modified Eagle's Medium with Nutrient Mixture F-12 (DMEM F-12) (1:1) (Gibco®), 5% horse serum, 20 ng per mL hEGF, 10 µg per mL human insulin, 0.5 µg per mL hydrocortisone, and 1% penicillin-streptomycin

Cellular SPIONs Uptake by Flow Cytometry Analysis

To determine the intracellular SPIONs amount, the cells were seeded onto a 6-well plate (2×10^5 cells per mL, 2 mL) and incubated in a humidified incubator to allow the cells to reach 70 – 80% confluence at 37 °C in the presence of 5% CO₂ for 24 h. The media were discarded and replaced with fresh DMEM containing 100 µgSPIONs per mL of either Rf-SPION or C-SPIONs. Control cells were incubated without SPIONs addition. After an incubation period of 4 h, the cells were washed twice with DMEM rinsed twice with PBS, and trypsinized before fresh DMEM was added. Subsequently, the cells were transferred to a microtube and centrifuged at 5,000 rpm for 5 minutes at 4 °C, followed by washing with ice-cold PBS and further centrifuged for 5 minutes. The pellet cells were fixed with 3.6% formaldehyde on ice for 20 minutes and centrifuged for 5 minutes, followed by washing with ice-cold PBS. The cell suspension was used for the subsequent analysis by flow cytometry using Attune Nxt flow cytometer (ThermoFisher Scientific, MA, USA) where a fixed number of 20,000 gated events were collected and analyzed.

Investigation of the role of RCP on cellular internalization mechanisms of Rf-SPIONs in breast cancer cells

MDA-MB-231 cells were seeded onto a 6-well plate (2×10^5 cells per mL, 2 mL) and incubated in a humidified incubator to allow the cells to reach 70 – 80% confluence at 37 °C in the presence of 5% CO₂ for 24 h. After incubation for 24 h, the media were discarded and rinsed twice with PBS, and the cells were incubated with 0 – 100 µgSPIONs per mL of RCP in Opti-MEM™ for 30 minutes at 37 °C in the presence of 5% CO₂, and then added with DMEM containing 100 µg per mL of Rf-SPION and incubated for 4h. Control cells were incubated without SPIONs addition. After an incubation period of 4 h, the media were prepared for flow cytometry analysis.

Statistical analysis

All studies were replicated for the three independent experiments (n = 3). All data are presented as mean ± SEM from the triplicate analyses. GraphPad Prism 8.0.1 was used for statistical analysis. Data comparison was assessed by either one-way or two-way analysis of variance (ANOVA). The difference was considered statistically significant with a probability (p-value) below 0.001, 0.01, 0.1, and no significant (ns), respectively.

Results and Discussion:

Synthesis of riboflavin-citrate ester (CARf)

The conjugation of riboflavin (Rf) and citric acid was designed to provide potentiality on binding the surface of SPIONs, as the functional groups of Rf are not suitable to interact with SPIONs. In addition, citric acid has been used as a stabilizer for magnetic nanoparticles. The carboxylic acid terminal group assists in more dispersion of NPs in water and gives a functional group for further modification^{3, 7, 10}. The CARf ligand was synthesized under reflux conditions through the esterification reaction as shown in **Figure 1A**. The crude product of CARf was obtained as orange solids and utilized as a coating material for coating the surface of the SPIONs without further purification, as both molecules had similar high polarities, leading to purifying difficulty. However, the crude product of CARf was investigated by HPLC and mass spectroscopy (**Figures 1B and C**). HPLC chromatogram showed a minor peak of CARf at a retention time of 1.9 minutes and a peak of Rf at a retention time of 5.3 minutes. In addition, mass spectrometry showed a peak with the m/z value of CARf of 573.1451, matching the calculated value $[M]^+$: 550.1547; calculated value $[M+Na]^+$: 573.1445.

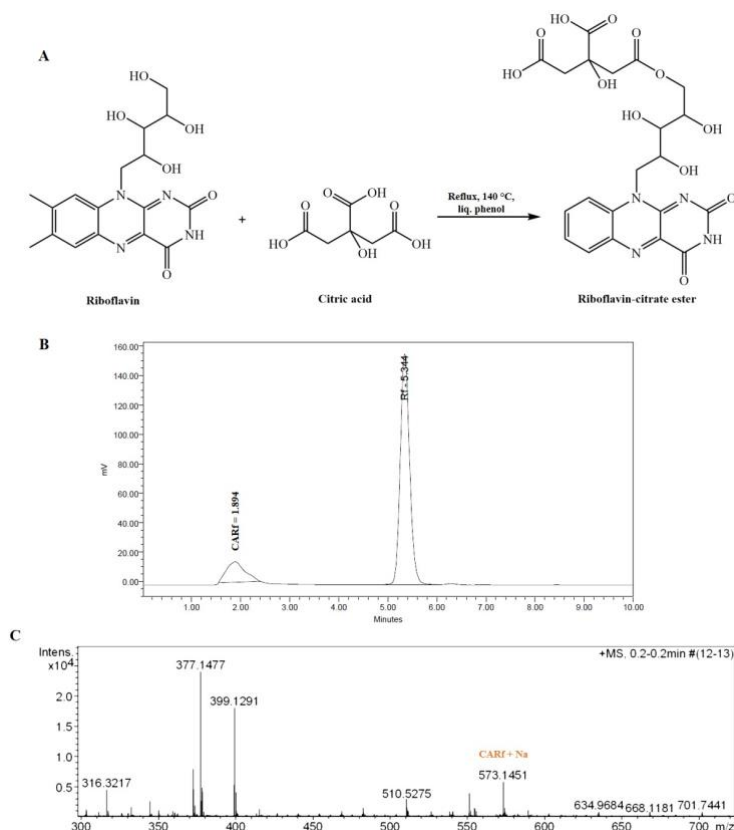


Figure 1. (A) Synthetic scheme of riboflavin-citrate ester. (B) HPLC chromatography shows the peak of CARf ligand and Rf at different retention times. (C) Mass spectrum of the CARf ligand with a peak with the $m/z = 573.1451$.

Synthesis and characterizations of the Rf-SPIONs, C-SPIONs, B-SPIONs

The magnetic nanoparticles were first synthesized as B-SPIONs using the co-precipitation method of iron (II) and iron (III) in basic (25% NH_4OH) conditions before

surface modification with CARf. To compare the role of Rf on the surface of SPIONs, C-SPIONs were also synthesized as control particles (**Figure 2**).

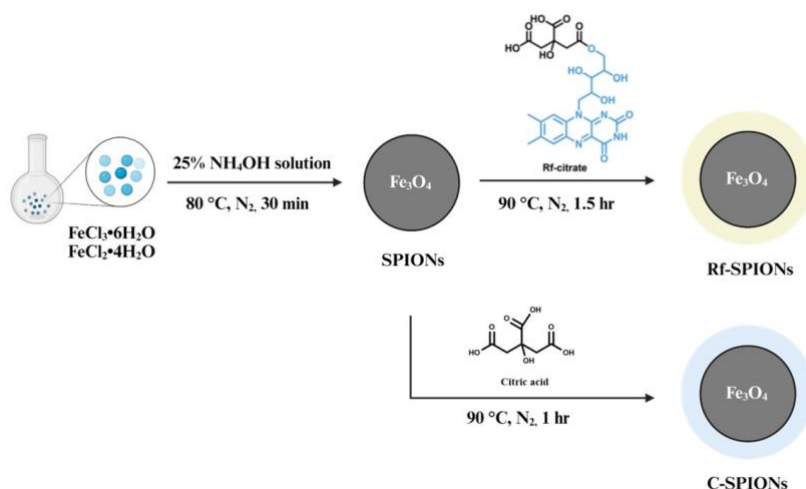


Figure 2. Synthetic scheme of Rf-SPIONs and C-SPIONs.

The hydrodynamic sizes and zeta potential values of obtained SPIONs were characterized by dynamic light scattering (DLS). Table 2 shows a D_H of B-SPIONs, Rf-SPIONs, and C-SPIONs approximately 160, 130, and 100 nm with narrow distribution ($PdI \leq 0.2$). Moreover, the zeta potential values of Rf-SPIONs and C-SPIONs were -32 and -35 mV. These results indicated that CARf ligands and citric acid were modified on the surface of SPIONs, leading to an improvement in the stability of SPIONs compared to their sizes without ligands.

Table 2. Sizes and magnetic properties of SPIONs measured at 10 K

Particle	D_H (nm)	Polydispersity index (PdI)	Zeta potential (mV)
B-SPIONs	161	0.3	36 ± 3
Rf-SPIONs	132	0.2	-32 ± 1
C-SPIONs	108	0.2	-35 ± 1

D_H : hydrodynamic diameter

Ms: saturation magnetization

Study the effect of FBS on the colloidal stability of SPIONs

Our group has previously reported that the fetal bovine serum (FBS) could affect the colloidal stability of magnetic nanoparticles, resulting in different cellular responses⁵. To study the effect of FBS on the colloidal stability and behaviors of SPIONs in DMEM cell culture media before use in cellular studies of SPIONs. The Rf-SPIONs and C-SPIONs were dispersed in different concentrations of FBS at 1%, 5%, and 10%. For 10% which is a commonly used supplement in DMEM media for cell culture. The hydrodynamic diameter (D_H) of both SPIONs was measured by using the DLS technique (**Figure 3**). The results showed that Rf-SPIONs had a small aggregation in DI water with a size around 300 nm, and tend to strongly aggregate when dispersed in free-serum, 1%, and 5% of FBS. These

increased sizes of particles might be due to the partial absorption of serum proteins on the surface of particles, leading to enhanced instability of Rf-SPIONs. While, C-SPIONs showed good dispersion in DI water, and tended to reduce their size when dispersed in increasing FBS, exhibiting that the FBS can prevent the aggregation of the C-SPIONs. This suggested that FBS can affect the colloidal stability and behavior of Rf-SPIONs and C-SPIONs differently. Interestingly, in 10% FBS, the size of both particles was found to be stable around 200 nm, showing the highest stability compared to lower concentrations of FBS and DI water. There might have been enough serum that covered the surface and enhanced the stability of Rf-SPIONs and C-SPIONs. Therefore, this result showed that both Rf-SPIONs and C-SPIONs expressed high stability when dispersed in 10% FBS in DMEM media, and can use this concentration to study the uptake of nanoparticles in the cell line.

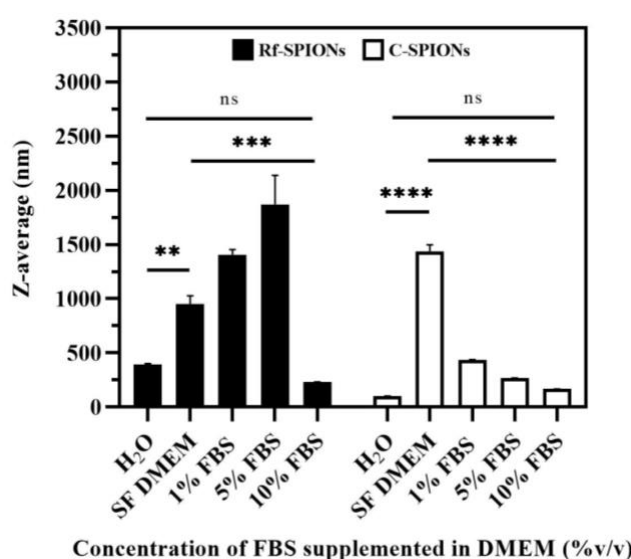


Figure 3. Hydrodynamic diameter of the Rf-SPIONs and C-SPIONs, dispersed in DMEM medium supplemented with different concentrations of FBS.

Cellular uptake study of the Rf-SPIONs and C-SPIONs

It has been previously reported that the Rf can enhance the cellular uptake of the SPIONs as in MCF-7 breast cancer cells⁷. However, the uptake of the Rf-SPIONs in higher aggressive breast cancer cells and more difficult treatment (MDA-MB-231) have not been reported. To investigate the uptake of the Rf-SPIONs and C-SPIONs in MDA-MB231 cells, the cells were incubated with the Rf-SPIONs and C-SPIONs before analyzing the cellular SPIONs uptake using flow cytometry (**Figure 4**). The results showed significant uptake of Rf-SPIONs in breast cancer (MDA-MB231) higher than normal breast (MCF-10A) cells. While C-SPIONs did not show different uptake in both cells. These results suggest that the Rf-SPIONs can be delivered to breast cancer cells better than normal cells which have the potential to be used as a drug delivery system or imaging applications for breast cancer treatments.

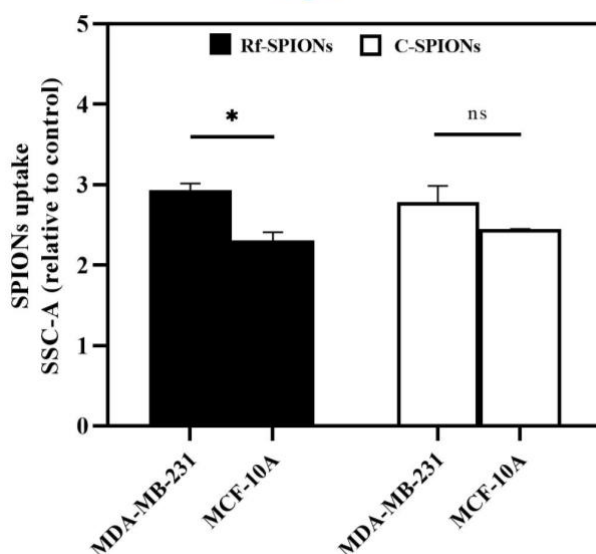


Figure 4. Cellular SPIONs uptake in MDA-MB-231 and MCF-10A cells after incubation with Rf-SPIONs and C-SPIONs (100 $\mu\text{g/mL}$) by relative side scattering signals (SSC), quantified by the SSC of the control cells.

Study the effect of different concentrations of RCP on cellular SPIONs uptake mechanisms

Riboflavin carrier protein (RCP) has been recognized as a potential biomarker for breast cancer patients¹¹⁻¹⁴. Several studies reported that the RCP plays an important role in facilitating the cellular uptake of Rf-base nanoparticles in breast cancer cells^{6, 7, 12}. Our previous study also showed the binding between Rf-SPIONs and RCP using the Isothermal Titration Calorimetry (ITC) technique. Note that this system was studied in the presence of SPIONs and RCP only, which suggested that the uptake of the Rf-SPIONs occurs through the binding with RCP⁷. Therefore, to study the effect of on cellular uptake of Rf-SPIONs. The cells were incubated with different concentrations of RCP at 0, 50, and 100 $\mu\text{g/mL}$ before being treated with Rf-SPIONs and analyzed by flow cytometry.

The result showed a significant decrease in the Rf-SPIONs uptake in MDA-MB-231 cells with increasing the RCP concentration (**Figure 5**). In this experiment, Rf-SPIONs were incubated with RCP in DMEM media, which have various types of biomolecules and serum proteins. Therefore, these proteins also can bind to the surface of SPIONs, leading to less interaction of RCP with Rf-SPIONs, and decreasing the uptake even though the RCP concentration was increased. On the other hand, it has been recently shown by proteomic analysis that upon the addition of RCP in the presence of serum proteins, the RCP binds to the Rf-SPIONs less than the C-SPIONs. The less interaction of RCP to the Rf-SPIONs was further described by molecular dynamic simulation that the Rf binding site partially interacts with SPIONs surface, leading to the restriction of binding site exposure, and less binding of RCP to the Rf-SPIONs. Therefore, the results of this study together with the previous reports by our group suggested that RCP does not play a role in the Rf-SPIONs uptake.

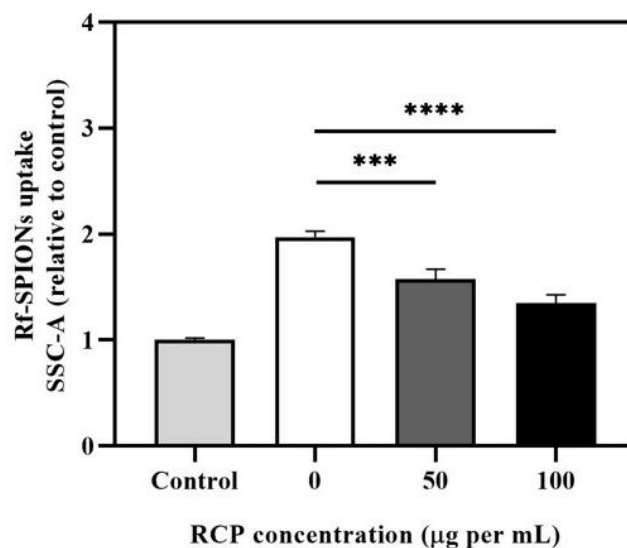


Figure 5. Relative side scattering signals of MDA-MB-231 cells after being treated with the Rf-SPIONs at 37°C for 4h under different RCP concentrations.

Conclusion:

Rf-SPIONs and C-SPIONs were successfully synthesized by a co-precipitation method. Characterization of the SPIONs showed that the Rf-SPIONs appeared as clusters of multicore SPIONs with a core size of approximately 10 nm. The negative zeta values of both Rf-SPIONs and C-SPIONs demonstrated that CARf and citric acid were suitable stabilizers for modification on the surface of the SPIONs. Colloidal stability experiments showed that the Rf-SPIONs and C-SPIONs had the highest stability when dispersed in DMEM cell culture media, supplemented with 10% of FBS, which is a normal concentration for cell culture media. The cellular uptake study showed that Rf can increase the uptake of SPIONs in breast cancer more than normal cells. RCP does not play a role in the cellular uptake of Rf-SPIONs. However, other mechanisms have been proposed and are currently being studied to understand the exact uptake mechanism for further development and utilization of Rf-SPIONs in breast cancer treatments.

Acknowledgments:

This project is funded by the National Research Council of Thailand (NRCT) with Mahidol University: N42A650357 and Mahidol University (MU's Strategic Research Fund): 2023. Partial support was also provided by the CIF and CNI grant, Faculty of Science, Mahidol University. S.N. was supported by the Development and Promotion of Science and Technology Project (DPST). The authors would like to express our gratitude to Prof. Dr. Chutima Kuhakarn for the support of the facilities for the synthesis of the Rf-citrate ligand, Assoc. Prof. Dr. Patompon Wongtrakoongate for the support of DLS measurements.

References:

1. Talluri, S.; Malla, R. R. *Curr Drug Metab* **2019**, *20* (12), 942-945.
2. Zheng, J.; Ren, W.; Chen, T.; Jin, Y.; Li, A.; Yan, K.; Wu, Y.; Wu, A. *Curr Med Chem* **2018**, *25* (25), 3001-3016.
3. Li, L.; Mak, K. Y.; Leung, C. W.; Chan, K. Y.; Chan, W. K.; Zhong, W.; Pong, P. W. *T. Microelectronic Engineering* **2013**, *110*, 329-334.



4. Liu, L.; Hitchens, T. K.; Ye, Q.; Wu, Y.; Barbe, B.; Prior, D. E.; Li, W. F.; Yeh, F. C.; Foley, L. M.; Bain, D. J.; Ho, C. *Biochim Biophys Acta* **2013**, *1830* (6), 3447-53.
5. Mekseriwattana, W.; Srisuk, S.; Kriangsaksri, R.; Niamsiri, N.; Prapainop, K. *AAPS PharmSciTech* **2019**, *20* (2), 55.
6. Mekseriwattana, W.; Phungsom, A.; Sawasdee, K.; Wongwienkham, P.; Kuhakarn, C.; Chaiyen, P.; Katewongsa, K. P. *Photochemistry and Photobiology* **2021**.
7. Mekseriwattana, W.; Guardia, P.; Herrero, B.; Fuente, J.; Kuhakarn, C.; Roig, A.; Katewongsa, K. *Nanoscale Advances* **2022**.
8. Petcharoen, K.; Sirivat, A. *Materials Science and Engineering: B* **2012**, *177* (5), 421-427.
9. Nigam, S.; Barick, K. C.; Bahadur, D. *Journal of Magnetism and Magnetic Materials* **2011**, *323* (2), 237-243.
10. Cheraghipour, E.; Javadpour, S.; Mehdizadeh, A. R. *Journal of Biomedical Science and Engineering* **2012**, *05* (12), 715-719.
11. Adiga, P. R.; Visweswariah, S. S.; Karande, A.; Kuzhandhaivelu, N. *Journal of Biosciences* **1988**, *13* (1), 87-104.
12. Tsvetkova, Y.; Beztsinna, N.; Jayapaul, J.; Weiler, M.; Arns, S.; Shi, Y.; Lammers, T.; Kiessling, F. *Contrast Media Mol Imaging* **2016**, *11* (1), 47-54.
13. Rao, P. N.; Crippin, J.; Levine, E.; Hunt, J.; Baliga, S.; Balart, L.; Anthony, L.; Mulekar, M.; Raj, M. H. *Hepatol Res* **2006**, *35* (2), 83-7.
14. Rao, P. N.; Levine, E.; Myers, M. O.; Prakash, V.; Watson, J.; Stoller, A.; Kopicko, J. J.; Kissinger, P.; Raj, S. G.; Raj, M. H. *Cancer Epidemiol Biomarkers Prev* **1999**, *8* (11), 985-90.

THE EXPRESSION OF WUHAN AND XBB.1.5 N-TERMINAL DOMAIN (NTD) AND RECEPTOR BINDING DOMAIN (RBD) PROTEINS IN *Escherichia Coli* (*E. Coli*)

Ploy Nantapisit,^{1*} Supranee Phanthanawiboon¹

Department of Microbiology, Faculty of Medicine, Khon Kaen University, Khon Kaen, Thailand

*e-mail: nantapisitploy@kkumail.com

Abstract:

SARS-CoV-2, a causative agent of COVID-19, instigated a global pandemic of 2020. The virus exhibits rapid mutations, notably in the NTD and RBD within the S protein, leading to increased transmission rates and diminished vaccine efficacy. The emergence of the Omicron variant, designated as a Variant of Concern (VOC), and the XBB.1.5 subvariant, designated as a Variant of Interest (VOI), raises significant concerns. Understanding the antibody binding and neutralizing ability specific to NTD and RBD protein is important to understand the vaccine efficacy. To develop antibody characterization methods, effective protein production is needed. This study aims to optimize the expression of SARS-CoV-2 Wuhan and XBB.1.5 NTD and RBD proteins using *E. coli* BL21(DE3). The DNA sequences of the proteins were verified through NCBI Virus. Various optimization conditions were used for Wuhan NTD protein expression including IPTG concentrations (0.1, 0.5, 1.0, 3.0 mM), induction temperatures (25°C, 37°C), and durations (2, 3, 4, 6 hours). The optimized condition for Wuhan NTD expression was identified as 3.0 mM IPTG at 37°C for 6 hours, and the XBB.1.5 NTD protein was successfully expressed under these conditions. Wuhan and XBB.1.5 RBD protein expression were induced using 0.1 mM IPTG at 37°C for 2 hours. Western blot result revealed that most of the expressed proteins were presented in an insoluble form which unrelated from total hydrophobic cluster area of each protein. This study underscores the successful expression of NTD and RBD proteins, crucial for advancing methods to characterize antibodies.

Introduction:

SARS-CoV-2 or severe acute respiratory syndrome type 2 causes Coronavirus Disease of 2019 (COVID-19) which is a big outbreak pandemic in 2020 and its effects humans in terms of lifestyle, finances, and especially healthcare. SARS-CoV-2 is a positive single-stranded RNA virus that compose of Spike protein (S), Envelope protein (E), Membrane protein (M) and Nucleocapsid (NCP or N). The S protein is a crucial component of the virus responsible for facilitating viral replication, leading to infection in the host especially by viral entry. There are 2 subunit which is S1 and S2 subunit. S1 subunit compose of 2 proteins: N-terminal domain (NTD) and Receptor binding domain (RBD). NTD plays role in proteolytic activation¹. RBD is responsible for binding to the Angiotensin-converting enzyme 2 (ACE2) host receptor enabling viral endosomal entry. The S2 subunit consists of the Stem Helix region (SH) and Fusion Peptide region (FP), which are involved in proteolytic activation, enabling the virus to release its viral genome into the host.^{2,3}

Since the outbreak began in 2019, SARS-CoV-2 has spread widely, leading to the emergence of Variant of Concerns (VOCs) including Alpha, Beta, Gamma, Delta, and Omicron. Presently, the dominant variant is Omicron.⁴ The virus has undergone rapid and substantial mutations, fostering consistent and widespread transmission. Notably, within the Omicron variant, there are 3 notable subvariants; BA.2, BA.4, and BA.5.⁵

Currently there are many vaccines platform for COVID-19 prevention. To evaluate the vaccine efficacy, the study of the binding characteristics and neutralizing activity of antibodies from vaccinated individuals are crucial. RBD protein is commonly used due to the role in receptor binding. However, the study from Wang et al., epidemic of XBB.1(2022 – 2023) with BA.2 as its parental strain, they found a reduction in mRNA vaccine efficacy when tested against XBB.1. Moreover, key mutation sites were identified in NTD and RBD, leading to a decreased binding affinity towards NTD and RBD monoclonal antibodies.⁶ Therefore, the NTD is an intriguing protein to investigate vaccine efficacy.^{8,9}

This study aims to optimized conditions for expressing NTD and RBD proteins of Wuhan and XBB.1.5, current variant of interest (VOI)⁷, in prokaryotic system. The result of this study will provide the condition to produce adequate protein quantities for subsequent development of technique for vaccine efficacy investigation.

Methodology:

Gene alignment and synthesis

To synthesize SARS-CoV-2 NTD and RBD protein, Wuhan whole genome reference strain DNA sequences (NC_045512.2) were retrieved from NCBI virus database and aligned (Crustal omega; multiple alignment tools) with NTD and RBD protein (YP_009724390.1) converted to DNA sequence to retrieved Wuhan NTD and RBD reference DNA sequence. XBB.1.5 whole genome sequences of represent 1 to 3 countries of each region that reported XBB.1.5 in NCBI Virus collected from December 2022 to June 2023 including USA: New York (OR226362.1), Switzerland (OY101484.1), United Kingdom (OY101140.1), Germany (OR145099.1), Russia (OR177915.1), France (OQ888915.1), Denmark (OQ288266.1), Finland (OQ509907.1), Slovakia (OX464551.1), Japan (BS007352.1), Thailand (OR145091.1), Viet Nam (OR048042.1), Pakistan (OR018339.1), Bahrain (OQ871435.1), Kuwait (OQ843959.1), India (OQ587573.1), Kenya (OR177993.1), Djibouti (OQ989785.1) and South Africa (OQ826160.1). Sequences containing unidentified base in the site of the proteins were excluded. After that XBB.1.5 NTD and RBD retrieved sequence were translated by ExPASy Translated tools for protein sequence and the protein was confirmed by NCBI Blast tools. All DNA sequences were synthesized by U2Bio (Korea) with by 5' *Bam*HI (FastDigest™, Thermo, U.S.) 3' end 6-His and *Not*I (FastDigest™, Thermo, U.S.) and cloned into pET28a (+) as an expression vector with codon optimization.¹⁰

Protein expression and optimization

To express SARS-CoV-2 RBD and NTD, Wuhan and XBB.1.5 RBD and NTD in pET28a (+) plasmids were transformed into *Escherichia Coli* (*E. Coli*) BL21(DE3) using Heat-shock methods. The transformed *E. coli* BL21(DE3) was subsequently plated onto LB agar supplemented with 100 ug/mL Kanamycin and incubated overnight at 37°C. Single colonies were then selected and cultured in 5 mL LB broth, incubated for 16–18 hours at 37°C, 250 rpm. A 1% overnight culture was utilized as a starter culture in LB broth with 100 ug/mL Kanamycin and cultivated until the OD600 reached around 0.5–0.8 (10⁸ cell/mL). Samples were collected to as 'non-induced cells', the RBD expression was induced using 0.1 mM Isopropyl β-D-1-thiogalactopyranoside (IPTG) for 2 hours at 37°C, following Tantiwiwat et al. method.¹³ While NTD expression was optimized by induced with varying IPTG concentrations (0.1, 0.5, 1.0, 3.0 mM) at temperatures of 25°C and 37°C for 2–6 hours, 250 rpm. The induced and non-induced cells were further evaluated for protein expression quality using Sodium Dodecyl Sulfate-Polyacrylamide Gel Electrophoresis (SDS-PAGE).¹⁰

Detection of protein expression property

To detect SARS-CoV-2 proteins property that expressed in a *E. coli*, the induced cells were resuspended in phosphate-buffered saline (PBS) without detergent, followed by cell lysis via sonication after three cycles of freeze-thawing, the lysed mixture were centrifuged at 10,000 rpm, 4 °C 30 minutes, supernatant were collected as 'Soluble form protein'. After obtaining the pellet, it was washed twice using Tris-EDTA buffer (pH 8.0), and then centrifuged at 10,000 rpm, 4°C for 30 minutes. After discarding the supernatant, the pellet was resuspended in denatured buffer (2% SDS in PBS) to unfold the proteins, followed by centrifugation at 10,000 rpm, 4°C for 30 minutes. The resulting supernatant was stored as the 'Insoluble form protein'.¹⁴ Soluble and Insoluble form of the proteins were further detected by directed western blotting analysis. Total hydrophobic cluster area of each protein was investigated by ProteinTools.¹⁵

Protein Evaluation by SDS and Western blotting

For SDS-PAGE analysis, each protein sample, including non-induced cell, induced cell, soluble protein, and insoluble protein, were loaded onto the gel. The stacking gel (5% poly acrylamide gel with SDS) ran at 80 volts for 30 minutes, following which the separating gel (12.5% polyacrylamide gel with SDS) ran at 120 volts until the marker band stands at the end of the gel. The induced and non-induced proteins were visualized using SDS-PAGE after stained with staining buffer (Coomassie Brilliant Blue-R 250, 40% methanol) and subsequently destained by using destain buffer (50% methanol, 10% acetic acid). The SDS-polyacrylamide gel containing soluble and insoluble proteins was immersed in Towbin transfer buffer and transferred onto a nitrocellulose membrane at 15 volts for 1 hour. Subsequently, the membrane, already featuring SARS-CoV-2 RBD and NTD, was rinsed with deionized water (DI water) and then soaked in blocking buffer (5% skim milk in PBS) at 4 °C overnight. Following this, the membrane underwent three washes with PBST (0.05% Tween 20 in PBS) and was incubated with HRP anti-His Tag Antibody (Biolegend®, USA) at room temperature for 1 hour, and then washed membrane 6 times with PBST followed by HRP substrate (PierceTMECL Western Blotting Substrate). The result will be observed under Chemiluminescence.^{10,14}

Results and Discussion:

Alignment and synthesis of SARS-CoV-2 Wuhan and XBB.1.5 NTD and RBD

SARS-CoV-2 Wuhan NTD and RBD from NC_045512.2 is 876 base pair (bp) 292 amino acid residues and Wuhan RBD is 669 bp 223 amino acid residues. These 2 sequences were used as a reference for aligned with XBB.1.5 NTD and RBD sequences retrieved from data base. The result showed that XBB.1.5 genome sequence from Kenya and Pakistan presented N base (Low quality to identify base)¹⁶ at the site of NTD and RBD sequence caused alignment hindrance, therefor they were excluded from the alignment. After alignment XBB.1.5 from Thailand were used because it showed the most represent sequence among selected countries. XBB.1.5 NTD is 864 bp 288 amino acid residues and RBD is 669 bp 223 amino acid residues. After confirmed by NCBI protein blast, the XBB.1.5 NTD and RBD sequence from Thai strain were 100% identify with WLS56688 XBB.1.5 surface glycoprotein protein of Thai strain (Figure 1). The sequences with extra 30 bases (ATG - NTD/RBD -*SalI*- 6His – TGA) were sent for gene synthesis, therefore the length of target genes was extended to 906 bp for Wuhan NTD, 894 bp for XBB.1.5 NTD and 699 bp for Wuhan and XBB.1.5 RBD. The DNA mapping from sequence after synthesized showed in Figure 2.

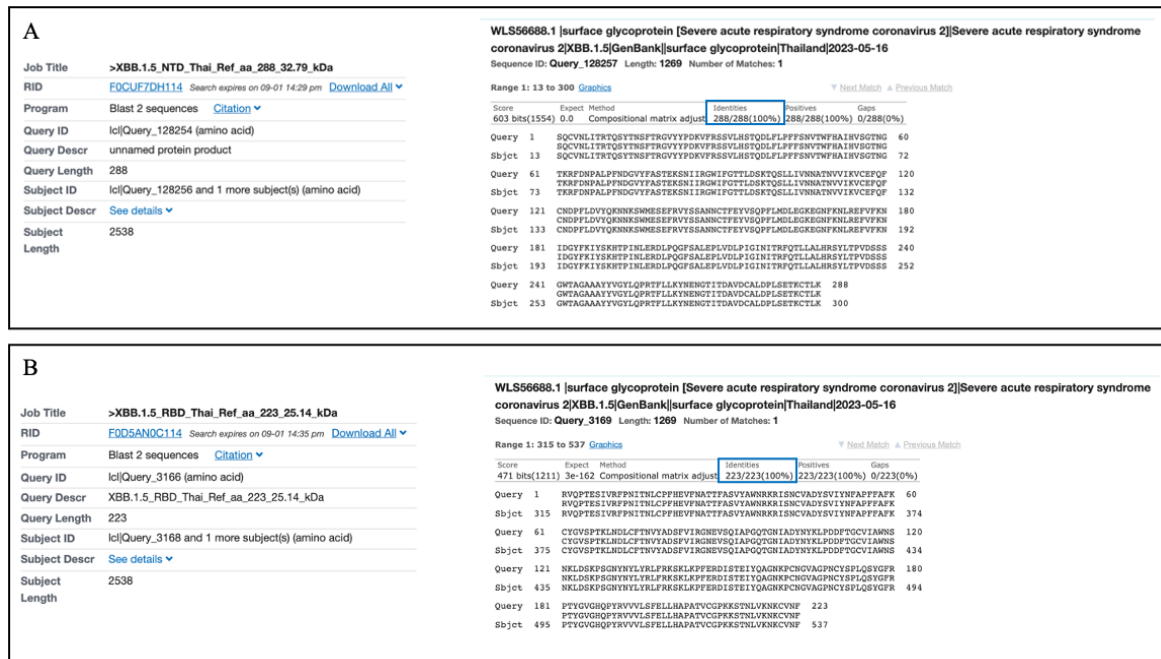


Figure 1. The confirmation of XBB.1.5 NTD and RBD

Left panels display the specific sequence information, while the right panels illustrate the alignment of these sequences with the subject sequences.

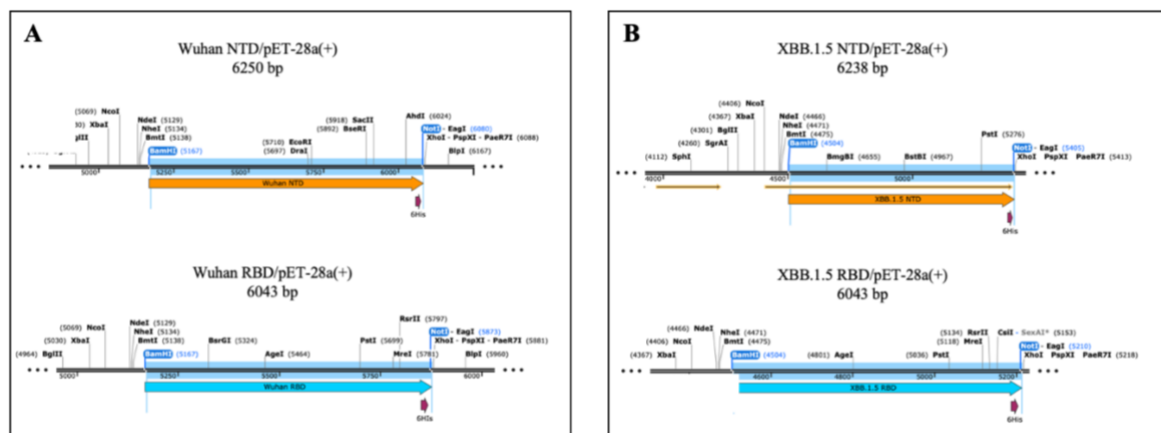


Figure 2. DNA mapping of Wuhan and XBB.1.5 NTD and RBD in pET28a (+)

Panel (A) displays the DNA mapping of Wuhan NTD (top in orange) and RBD (bottom in blue), while Panel (B) exhibits the DNA mapping of XBB.1.5 NTD (top in orange) and RBD (bottom in blue). The 6-His tag site is indicated in purple at the 3' end of the sequences. This figure created by SnapGene® software (from Dotmatics; available at snapgene.com).

SARS-CoV-2 Wuhan and XBB.1.5 NTD and RBD Successfully expressed in *E. coli* BL21 (DE3)

SARS-CoV-2 Wuhan NTD were expressed in varying IPTG concentration, inducing time and temperature. The result showed that *E. coli* that induce expression in 37 °C can produce the protein better than 25°C. At the same temperature and times of expression, *E. coli* that induced by 1.0 mM IPTG gave the most expressed protein than 0.1 mM and 0.5mM

IPTG, respectively. When increased inducing time resulted in higher expression of the protein because of increasing of replication cycle. Interestingly Wuhan NTD optimization revealed distinctive protein expression dynamics, early induction (2 hours) favored higher expression at 0.1 mM IPTG, While the longer induction time; more than 2 hours, where 0.5 mM IPTG induced superior expression (Figure 3A). Wuhan RBD were expressed in 37 °C, 0.1 mM IPTG with 2 hours inducing times can produce a mass of protein (Figure 3B) as well as XBB.1.5 RBD (Figure 3C right). XBB.1.5 NTD were expressed following the optimal condition of Wuhan NTD in 37 °C, 3.0 mM IPTG with 6 hours inducing time (Figure 3C left).

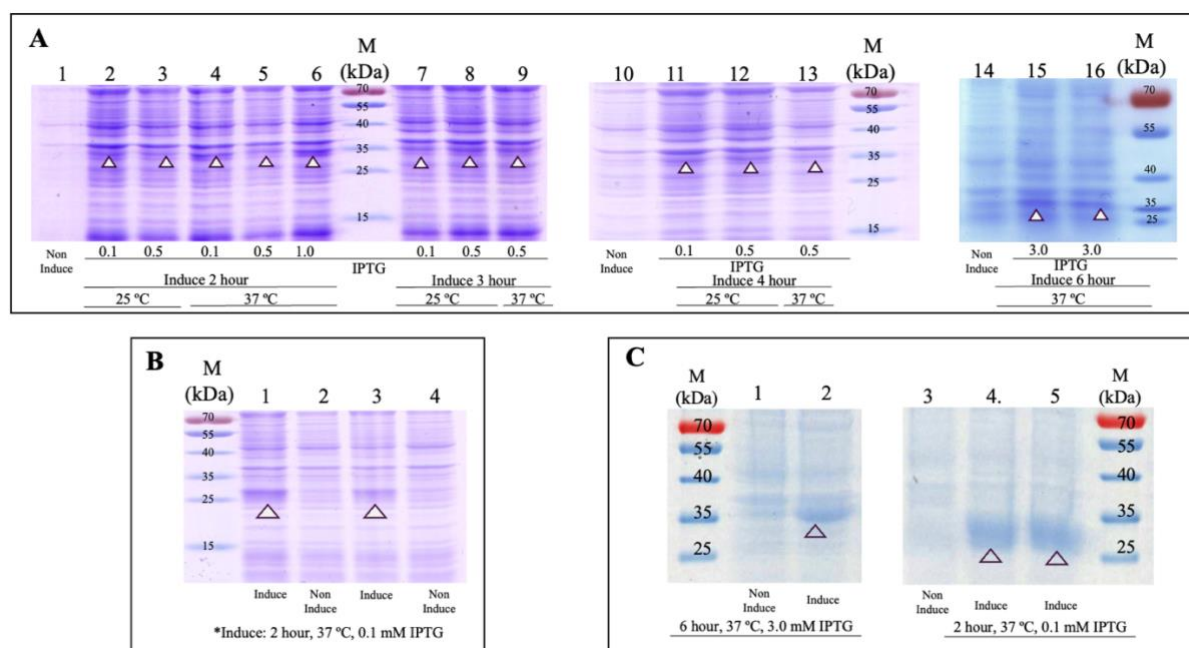


Figure 3. SDS-PAGE Analysis of Protein Expression Optimization

The SDS-PAGE gel displays the results of Wuhan NTD optimization (A), Wuhan RBD expression (B), and XBB.1.5 NTD and RBD expression (C). In Panel A, lanes 1, 10, and 14 represent non-induced conditions, while lanes 2-6, 7-9, 11-13, 15, and 16 represent induced under various conditions. Panel B represent lanes 2 and 4 as non-induced and lanes 1 and 3 as induced expression. For XBB.1.5 NTD (C, left) and RBD (C, right), lanes 1 and 3 represent to non-induced conditions, while lanes 2, 4, and 5 represent induced conditions. The NTD (37 kDa) and RBD (26 kDa) bands are indicated with arrows for clarity.

SARS-CoV-2 Wuhan and XBB.1.5 NTD and RBD Property

After collected each protein in both soluble and insoluble form, the result showed that all proteins presented mainly in insoluble form as shown in Figure 4. To understand the solubilization property, total hydrophobic area (THCA) of each protein were identified. The result showed that NTD protein presented higher THCA than RBD protein. Wuhan NTD and RBD presented THCA as 4,270.60 A² and 2196.58 A², respectively. XBB.1.5 NTD and RBD had THCA as 4,606.58 A² and 2,480.91 A², respectively (Figure 5). XBB.1.5 NTD and RBD showed higher THCA comparing to Wuhan suggesting that XBB.1.5 had more potential to insoluble than Wuhan. However, Western blotting result from Figure 4 did not show difference result between Wuhan and XBB.1.5 proteins. In addition, the core hydrophobic

cluster positions of each protein were identified, the result showed that Wuhan and XBB.1.5 NTD core hydrophobic cluster located in the surface area with same residue number and one difference hydrophobic contact. Moreover, the expression of nonnative bacterial protein with induce overexpression condition can cause insoluble form protein.¹⁷ To identify the protein solubility property, there are many factors including THCA, core hydrophobic cluster position and heterogenous expression should be considered.

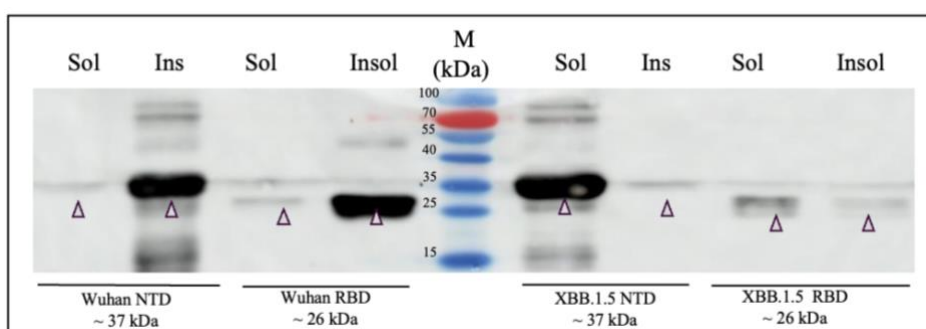


Figure 4. The Detection of Proteins Property.

SARS-CoV-2 Wuhan and XBB.1.5 NTD and RBD protein property. Western blotting results were assessed using anti-histidine HRP. Lanes designated as 'Ins' indicate the insoluble form, while 'Sol' signifies the soluble form of the proteins. The NTD (37 kDa) and RBD (26 kDa) bands are indicated with arrows for clarity.

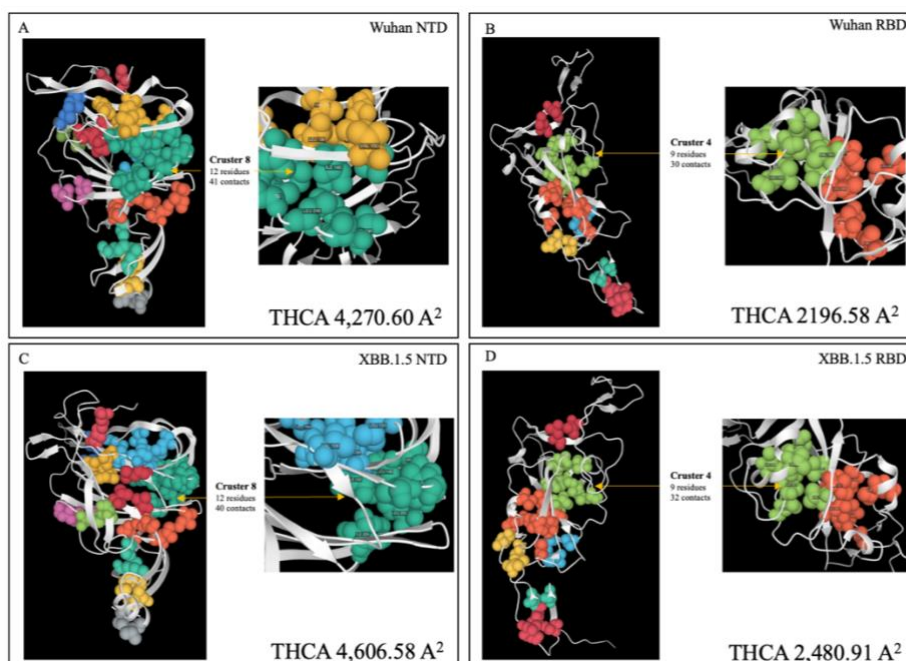


Figure 5. Protein Total hydrophobic Cluster Area.

This figure displays the protein structures of SARS-CoV-2 Wuhan NTD (A), RBD (B), XBB.1.5 NTD (C), and RBD (D). White ribbons represent the protein structure, while colored ball-and-stick models represent each hydrophobic cluster area. The right-hand side of each panel highlights the largest cluster (green), with detailed descriptions provided within the figure.

Conclusion:

SARS-CoV-2 Wuhan and XBB.1.5 NTD and RBD have been successfully expressed in *E. coli* BL21 (DE3). Optimal condition for NTD protein expression is 3.0 mM IPTG, 6 hours induction time in 37 °C. However, despite successful expression, most of the proteins were insoluble which may be due to protein structure with THCA, core hydrophobic cluster on their surface and the high expression level of heterogenous expression in *E. coli*. Although there is potential to express soluble form proteins at lower expression levels, the challenge lies in utilizing the insoluble proteins obtained in sufficient quantities for further use. Addressing this challenge requires exploring optimal denaturant conditions and refolding protocols to facilitate the purification and refolding of these proteins.

Acknowledgements:

We express our profound gratitude to the Department of Medical Microbiology for their unwavering guidance and support, as well as for generously providing the essential resources and facilities crucial to the success of this study. Special thanks are due to the Junior Science Talent Project (JSTP) for their invaluable financial support, which greatly contributed to the realization of our research goals. Finally, we extend our heartfelt appreciation to all the participants whose cooperation and commitment were integral to the successful completion of this study.

References:

1. Qing E, Li P, Cooper L, Schulz S, Jäck HM, Rong L, et al. Cell Reports. 2022 3;39(5):110786.
2. Huang Y, Yang C, Xu X feng, Xu W, Liu S wen. Acta Pharmacol Sin. 2020 ;41(9):1141–9.
3. Chen Y, Zhao X, Zhou H, Zhu H, Jiang S, Wang P. Nat Rev Immunol. 2022 27;1–11.
4. Elbe S, Buckland-Merrett G. Global Challenges. 2017;1(1):33–46.
5. Guo Y, Han J, Zhang Y, He J, Yu W, Zhang X, et al. Frontiers in Immunology. 2022;13.
6. Wang Q, Iketani S, Li Z, Liu L, Guo Y, Huang Y, et al. Cell. 2023 19;186(2):279–286.
7. Chen Y, Zhao X, Zhou H, Zhu H, Jiang S, Wang P. Nat Rev Immunol. 2023 ;23(3):189–99.
8. Rodriguez JH. Sci Rep. 2021 15;11(1):1–12.
9. Hadfield J, Megill C, Bell SM, Huddleston J, Potter B, Callender C, et al. Bioinformatics. 2018 1;34(23):4121–3.
10. Gao X, Peng S, Mei S, Liang K, Khan MSI, Vong EG, et al. Prep Biochem Biotechnol. 2022;52(3):318–24.
13. Tantiwivat T, Thaiprayoon A, Siriatcharanon AK, Tachaapaikoon C, Plongthongkum N, Waraho-Zhmayev D. Mol Biotechnol. 2023 ;65(4):598–611.
14. Long L, Wei J, Lim SA, Raynor JL, Shi H, Connelly JP, et al. Nature. 2021 ;600(7888):308–13.
15. Ferruz N, Schmidt S, Höcker B. Nucleic Acids Research. 2021 2;49(W1):W559–66.
16. Crossley BM, Bai J, Glaser A, Maes R, Porter E, Killian ML, et al. J Vet Diagn Invest. 2020 ;32(6):767–75.
17. Palmer I, Wingfield PT. Curr Protoc Protein Sci. 2004 ;Unit-6.3.

THE FIRST RECORD OF MULTI-MALE MATING BEHAVIOR OF ORNATE FLYING SNAKE, *Chrysopelea ornata* AT PHA-GNAN AND SAMUI ISLANDS, THAILAND

Dawn R. Cook-Price,¹ Pongthep Suwanwaree,^{1,*} Vikas Kumar,² Tom Parkin,³ Philip Brook,⁴

¹ Institute of Science, Suranaree University of Technology, Nakhon Ratchasima, Thailand 30000

² Ecophis Wildlife Llp, J P Nagar Bangalore, South Bangalore Karnataka, India 560078

³ Durham Wildlife Trust, Houghton-le-Spring, Tyne and Wear, England DH4 6PU

⁴ Samui Snake and Wildlife Rescue, Samui, Surat Thani, Thailand 84320

*e-mail: pongthep@sut.ac.th

Abstract:

Courtship behaviors in snakes have long been a fascination for scientists, from male-to-male combat in the iconic king cobra to multi-male courtship observed in Burmese python. This work is the first to document multi-male mating behavior of *Chrysopelea ornata* on the islands of Pha-ngan and Samui in Surat Thani Province of Southern peninsular Thailand. Between 2021 and 2023, we saw two multi-male (4 and 5) mating occasions from 18 rescue calls and 15 opportunistic sightings in Pha-ngan island. Additionally, we had 11 multiple males (up to 16) mating observation records spanning the course of 10 years between 2013 through 2023 in Samui island. Interestingly, we did not see this snake species at all during our field survey for the past 3 years. All mating observations came from rescue calls and all other single snake sightings came from opportunistic encounters between the two islands. In summary, 13 observations of multiple males pursuing and entangled with one female of *C. ornata* have been recorded adding to the collective material for a better understanding of multi-male mating in snakes.

Introduction:

The intricate dance of courtship in snakes, spanning the dramatic male combat in the king cobra to the multi-male engagements of the Burmese python, has captivated scientists for years¹. Notable behaviors such as male combat have garnered attention due to their frequent observation in species like the infamous king cobra (*Ophiophagus hannah*) and the radiated rat snake (*Coelognathus radiatus*); however, other strategies remain understudied². Among these lesser-explored strategies are multi-male courtship behaviors, akin to communal mating, and the intriguing phenomenon of "scramble polygyny." Though the paradise flying snake (*Chrysopelea paradisi*) has been noted to engage in multi-male courtship², assumptions about similar behavior in its relative, *Chrysopelea ornata* – the ornate flying snake, have not been critically assessed³.

Multi-male courtship behavior is the act of multiple males actively pursuing a single female². This can occasionally result in a mating ball and has been documented in such species as red-sided garter snake (*Thamnophis sirtalis parietalis*)³, whereas Burmese python (*Python molurus bivittatus*) engages in copulation with multiple males often culminating in multiple genetic lines in one clutch⁴. The overarching goal is the same as all other mating strategies, which is genetic continuation². Often when males exceed females in size, there is competition for the female resulting in male combat as observed in the courtship behavior of Australian python (*Morelia spilota*)^{5,6}. Alternatively when males are smaller than the female, the males converge together with one female resulting in a mating ball, all vying for a chance to mate.

With grass snake (*Natrix natrix*), a species with similar mating behavior, it has been shown that the size of the male may make a significant difference in the snake's chance for copulation⁷, though no significant data have been shown for *C. ornata* due to the arboreal nature of the snake and its elusive behavior in the wild.

Chrysopelea ornata boasts a vast distribution, spanning India to Hong Kong, with a strong presence throughout Thailand.⁸ While its aerial abilities have been researched, wild mating behaviors remain ambiguous. The species is listed as least concern on the International Union for Conservation of Nature (IUCN) Red List of threatened species⁸, and seems to thrive in both forested and human-dominated landscape. As an arboreal snake, it is adept at climbing and spends most of its time high in trees. It is also a diurnal snake actively hunting a variety of prey items such as frogs and lizards during the day.

The multi-male reproductive strategy might bolster genetic diversity in confined habitats, providing males a competitive edge in gene propagation while allowing females some selectivity.^{1,9} The current data for such strategy is limited to a few wild observations and multiple controlled simulations underscoring the evolutionary benefits of this strategy for various species. With the goal of gaining a better understanding of the benefits this approach has for the different species that utilize this reproductive strategy, the objective of this study was to report the reproductive strategy of *Chrysopelea ornate* during our herpetofauna surveys in Pha-ngan and Samui islands, Surat Thani province, southern peninsular Thailand. We documented the multi-male courtship behavior of *C. ornata* for the first time. This work seeks to bridge the knowledge gap enriching our understanding of the diverse mating strategies employed by the Colubrid family, which, despite its vastness, remains enigmatic in many respects.¹⁰

Methodology:

From November 2021 to September 2023, snake data on Samui and Pha-ngan islands were collected through opportunistic sightings, foot surveys, and rescue calls, with a focus on Pha-ngan island. Teams of up to seven individuals conducted approximately two surveys per week, resulting in a total of 78 visual surveys and 1,343 hours of observation. These surveys primarily occurred at night in national park forest, human-disturbed forest (fragmented landscapes), and human settlement. We employed 32 transects of varying lengths, adapted to the terrain, to document the herpetofauna of both islands. Transect locations were selected based on terrain, water proximity, and habitat types, which included single-line footpaths, dirt roads, paved roads, and streambeds. Torches facilitated the spotting of sleeping diurnal snakes and active or resting nocturnal snakes. Upon sighting, we captured a photograph and recorded geographic coordinates.

In addition to the foot surveys, rescue services were offered to both residents and visitors to mitigate snake-human conflicts. We promoted our services through social media, stickers, and pamphlets, encouraging people to call us instead of harming the snakes. If a resident—local or visitor—was uncomfortable with the presence of a snake or intended to harm it, we conducted a rescue. Conversely, if a resident—local or foreign—was comfortable with a non-threatening snake, it was allowed to move on independently, and coordinates were recorded. Rescued snakes were taken to our field lab for morphometric data collection and released near the capture point within 24 hours; however, immediate release occurred if no data were needed.

Geographic coordinates were also recorded for all snakes encountered, whether seen opportunistically, during surveys, or through rescues. While the primary goal of the surveys was to document island herpetofauna, morphometric data collection was aimed to discern

similarities or differences between island and mainland snake populations. Notably, during our research, we documented opportunistic sightings of the ornate flying snake, including photographs and locations. All data from Pha-ngan island originated from opportunistic sightings or rescue calls, whereas data from Samui island were exclusively from rescue calls.

Results:

Geographical Distribution of Mating Observations:

The ornate flying snake is distributed throughout each island and across all habitats. During concurrent research, the snake was encountered opportunistically and through rescue calls. Opportunistic encounters were often on roads or dirt tracks between forest patches; however, the majority were observed in or around human settlement. On Samui island, 11 instances of mating behavior were observed in response to snake rescue calls (Fig. 1A). While Pha-ngan island had a total of 18 rescue calls, and 15 opportunistic encounters with two instances of mating behavior (Fig. 1B). Mating behavior was predominately observed in manmade structures, despite proximity to forested areas.

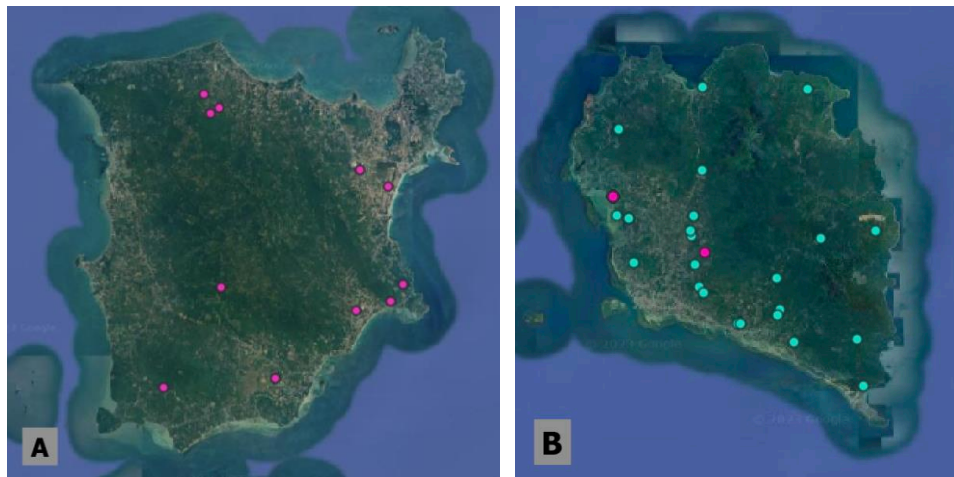


Figure 1.

Distribution of *Chrysopelea ornata* mating behavior observations (pink), and rescues and opportunistic sightings (blue) on Samui island (A) and Pha-ngan island (B).

Observation Summary:

From 13 mating occasions, two observations were made on Pha-ngan island and 11 on Samui island (Table 1). Of the 13 instances reported, 11 showcased multiple males with a single female. The remaining two incidents, both situated in human settlements, had pairs: one male and one female, intertwined; however, not engaged in copulation.

The multi-male mating accounts are described as follows:

1. On 19, January 2013, a group of snakes in roof tiles were observed in Talagnam area of Samui. Due to the elevation and setting of the home, the snakes were not reachable, and the homeowner allowed them to continue and move off on their own.

2. On March 22, 2015, in the Lamai district of Samui, the team was dispatched to a carwash. There, a staggering sixteen males and one female were safely extracted from the bamboo roof.

Table 1.

Numbers of snakes observed at each rescue or observation.

Date	# of Male	Location	Area
19.01.2013	*Observed ball	Roof tiles	Talagnam, Samui
22.03.2015	16	Bamboo roof	Lamai, Samui
05.07.2015	5	Roof tiles	Lamai, Samui
26.05.2015	1	Roof tiles	Chewang, Samui
07.03.2015	1	Roof tiles	Bangkao, Samui
08.02.2016	4	Inside a gate	Chewang, Samui
09.02.2016	*Observed ball	Roof tiles	Chewang, Samui
12.06.2016	5	Bathroom	Mai Nam, Samui
xx.03.2019	9	Recessed ceiling lighting fixture	Lamai, Samui
05.03.2020	3	Roof tiles	Chewang, Samui
13.01.2021	5	Bamboo balcony railing	Baan Nai Suan, Pha-ngan
08.02.2022	4	Roof tiles	Sritanu, Pha-ngan
03.07.2023	4	Roof tiles	Chewang, Samui

3. The 26th of May 2015 yielded five male and a female for the roof tiles of a residence in the Chewang area on Samui.

4. Similarly, on July 5, 2015, in another populated area (Lamai), five males and one female were found clustered. They were subsequently relocated as per the homeowner's request.

5. February 8, 2016, in the Bankao area of Samui, the team removed four males and one female from within a property gate.

6. On 9 February 2016, in a wood yard's roof area in Chewang, the team approached a mating ball. But as they neared, the snakes scattered and could not be caught for relocation.

7. June 12, 2016, yielded yet another incident, where 5 males and one female were recovered from a bathroom in Mai Nam.

8. The first such observation on Pha-ngan (Baan Nai Suan) was reported by a homeowner on 13, January 2021, wherein a female intertwined with four males was observed moving in unison along a bamboo balcony railing. Unfortunately, by the time the authors arrived, the snakes had dispersed. The image provided by the homeowner was carefully analyzed, and the female was determined based on her size relative to the males.

9. The subsequent observation on Pha-ngan was on 8 February 2022. A resident of Pha-ngan (Sritanu area) reported a cluster of *C. ornata* on his property. He observed the cluster originally on his fence moving towards his house. Our team was called because the homeowners were frightened and wanted the snakes removed. Upon our arrival the snakes had moved into the roof tiles (Fig. 2.). During the removal of the snakes from the rooftiles, an additional male was on a nearby property gate approximately eight meters from the house. This event resulted in the collection of six snakes, with a similar configuration as previously observed: one large female and multiple with a similar configuration as previously observed: one large female and multiple males intertwined in a ball-like shape between rooftiles.

10. In another incident occurring in March 2019 within the Lamai district, homeowners expressed deep concern upon spotting multiple snakes in the lighting fixture of a suspended ceiling, especially since there was a baby in the adjacent room. A total of nine males and one female were discovered, intertwined in a distinct ball formation (Fig. 3A).

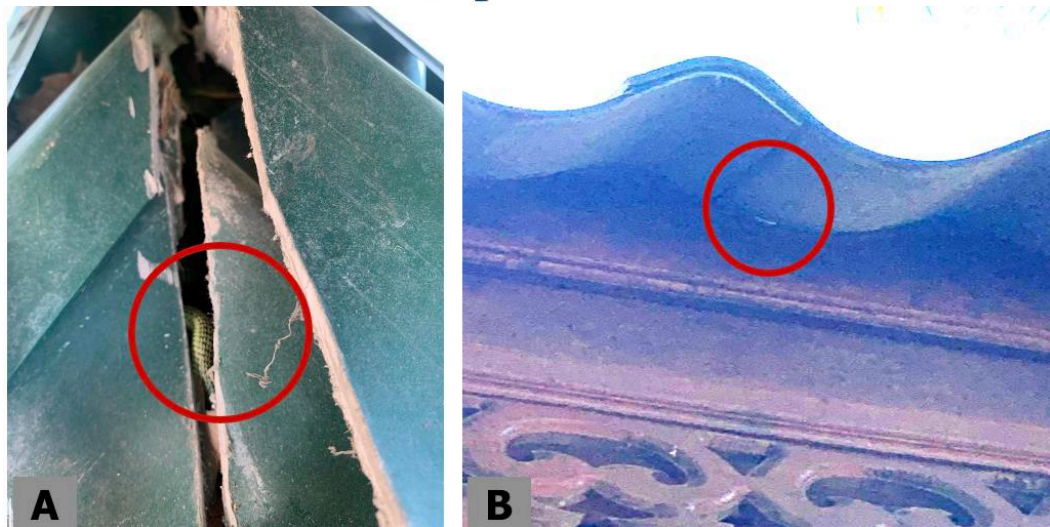


Figure 2.

Partial visual of *Chysopelea ornata* in the roof structure before dispersing (A). Small face appeared as the snakes dispersed from the initial tangle observed (B).

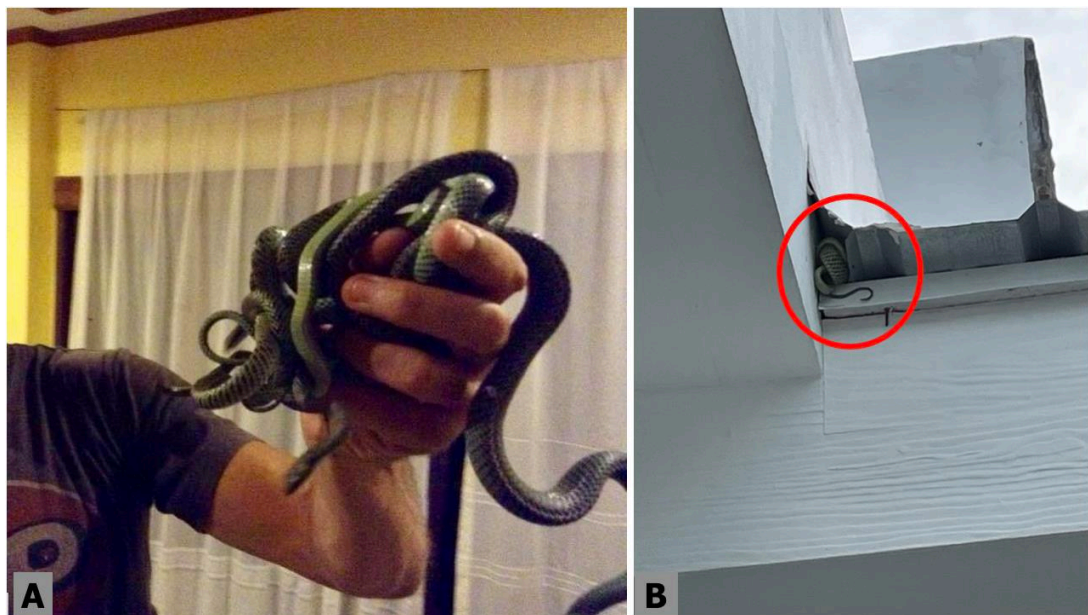


Figure 3.

A cluster of *Chysopelea ornata* removed from a recessed light fixture mounted on the ceiling of a home on Ko Samui (A). *C. ornata* observed in roofing tiles (B).

11. Recently, on July 3, 2023, in the Chewang district of Samui, a similar cluster of four males and one female was spotted. However, due to the challenging elevation and the homeowner's comfort, they weren't retrieved but were left to move away independently (Fig. 3B).

Across our instances, the mating clusters displayed common characteristics, with the snakes either moving as an elongated tangle or forming what could be recognized as a mating ball, typically associated with multi-male courtship behavior. When moving in an elongated manner, males were observed entangled and wrapped around both the female and other males.

Curiously, no instances of actual copulation were observed, even when males were visibly entangled with females.

Discussion:

Chrysopelea ornata has been sighted in all habitats throughout Pha-ngan and Samui islands. Often, this snake can be observed sleeping in the forest canopy at night throughout other areas of Thailand; however, such sightings have never been reported on these islands. All observations have been opportunistic or in response to notifications from homeowners, and as natural habitat dwindles, the snake is forced to navigate human-created habitats, with limited knowledge on how this influences mating behavior. This is especially important in insular areas such as Pha-ngan and Samui islands where available habitat is finite. Once natural areas are razed and replaced with manmade structures, the snake is forced to adapt to the habitat available or perish.

The mating behavior of this snake in the wild seems to be scarcely documented, with our observations possibly marking the first of their kind for this species. Notably, our observations occurred exclusively in manmade structures within human habitats, despite proximity to forested areas. This may be attributed to the arboreal nature of this snake as this behavior has only been previously observed in *C. paradisi*, a relative arboreal snake of the same genus². Other snake species known to use this mating strategy are ground dwelling or aquatic snakes (*Laticauda colubrina*)⁹. The mating behavior of *C. ornata* contrasts markedly with other species such as, *Vipera berus*, *Nerodia sipedon*, *Morelia spilota*, *Eunectes murinus*, *Eunectes notaeus*, *Laticauda colubrina*, *Elaphe obsoleta*, *Crotalus viridis viridis*, *Boa constrictor*, *Thamnophis sirtalis sirtalis*, *Thamnophis butleri*, and *Thamnophis sirtalis parietalis*, known for similar mating strategies⁹. For instance, multiple males form the *T. s. parietalis* have been documented converging outside a female's burrow³, a behavior that occurs on the ground.

In addition, *Chrysopelea ornata* inhabits tropical and semi-tropical habitats while the *Thamnophis* species inhabit North and Central America, where a broader range of temperatures influence brumation due to seasonal changes. Although *T. s. parietalis* and *C. ornata* are both active diurnal, polyandrous mating strategies have also been observed in nocturnal species such as *Python molurus bivittatus*⁴ and *Eunectes murinus*⁹ as well. The so-called mating ball or breeding ball is not the only observed multi-male breeding strategy utilized by snakes. On the tropical island of Madagascar, a multi-male *Dromicodryas bernieri* and *D. quadrilineatus* pursuing and entwining a single female were observed, although no mating ball was seen in these primarily ground-dwelling diurnal species¹⁰.

Documented occurrences suggest that the mating season for *C. ornata* varies geographically. For example, it extends as late as June in Bangkok, Thailand¹¹, while breeding in Surat Thani province occurs from January to April¹². Additionally, in Assam, the northern region of India, a gravid female was collected at the end of April and placed in quarantine at the Assam State Zoo¹³. While in quarantine, she laid a clutch of eggs on the 4th of May, indicating that breeding likely occurred in the previous months. This timing differs from our observations on the islands which, ranged from January through July. Such variations in observed occurrences may indicate geographical influences on mating behaviors, potentially shaped by diverse habitats, weather conditions, or prey availability.

Proactive night surveys did not yield *C. ornata* sightings despite the numerous hours spent in the forest. The arboreal nature of this snake limits visibility during walking surveys due to canopy obstruction, human error, and terrain. This limitation is in stark contrasts with the numerous sightings reported by homeowners. Although our efforts in the forest were

extensive, the use of rescue calls and third-party observations provided more valuable data. We acknowledge that these methods has limitations, potentially skewing the observed mating behaviors toward human-dominated landscapes; however, they were the most effective way to gather data for this study.

The overarching narrative of our observations speaks to the evolution of mating strategies in response to environmental pressures, ensuring reproductive success. The widespread distribution and prevalence of this species warrants further investigation into the advantages conferred by their mating behaviors. For instance, in cases of male combat, the fittest male generally secures the mating opportunity, heightening its attractiveness and ensuring the propagation of its genes. Polyandrous mating may enhance the males' chance of copulation when females are underrepresented in the population. Polygamous strategies of any kind amplify copulation chances¹⁴, though it remains uncertain whether multiple males copulate with a single female in *C. ornata*. It has been demonstrated that many snakes, employing this method of reproduction, show varied paternity within a single clutch⁹. Genetic testing, still unexplored for *C. ornata*, could provide insights into this query.

Conclusion:

While *Chrysopelea paradisi*'s mating behavior has been somewhat chronicled, *C. ornata*'s remains unexplored, leaving significant knowledge gaps, especially concerning wild individuals². While various facets of their biology like clutch size, gestational length, ovary dimensions, and gliding aptitude have been studied, comprehensive understanding of their courtship strategies is still elusive¹¹. Our study documents 13 separate events of multiple males intertwining with a lone female in a formation akin to a mating ball. This observation provides foundational evidence for *C. ornata* courtship behavior, fueling hopes for subsequent research. To truly comprehend the evolutionary intricacies of their reproductive behaviors, additional studies should span across their diverse habitats, and integrate genetic analyses. Our observations coupled with anecdotal evidence from the neighboring islands indicate a pattern of this snake's mating behavior, particularly within Thailand landscape. This underscores the need for more expansive research to delve deeper into their reproductive season and associated behaviors.

Acknowledgements:

This work was supported by (i) Suranaree University of Technology (SUT), (ii) Thailand Science Research and Innovation (TSRI), and (iii) National Science, Research and Innovation Fund (NSRF) (NRIIS number 160357). This work would not be possible without the permission of Department of National Parks and the support of Ko Pha-ngan - Than Sadet National Park staff.

References:

1. Shine R. Proc Biol Sci. 2002;1519:995-1004.
2. Kaiser H, Lim J, Worth HJ. Threat Taxa. 2016;8:8488-8494.
3. Joy JE, Crews DJ. J Comp Psychol. 1985;2:145.
4. Skelton J, Bartoszek I, Beaver CE, Hart KM, Hunter ME. J Herp. 2021;55:355-360.
5. Slip DJ, Shine R. Herpetol. 1988;44:396-404.
6. Shine R, Fitzgerald M. Oecologia. 1995;103:490-498.
7. Luiselli LJ. Zool. 1996;4:731-740.



8. Nguyen TQ, Thy N, Chan-Ard T, Srinivasulu C, Srinivasulu B, Mohapatra P, Shankar G, Agarwal I, Kulkarni NU, Suraj M. IUCN 2021
9. Rivas JA, Burghardt GM. J. Comp Psychol. 2005;119:447.
10. Fukuyama R, Itoigawa A, Mori A. Herpetozoa. 2022;35:225-229.
11. Uetz P, Herpetol Rev. 2000;31:13.
12. Likhityungyuen T, Pimsorn RU, Prompa T, Pongsuchart M, Tumkiratiwong P, Malaysiana S. Sains Malays. 2022;51:1293-1303.
13. Bhattacharjee R, Kumar A, Purkayastha J. Reptiles Amphib. 2023;30:18445-18445.
14. Uller T, Olsson M. Mol Ecol. 2008;17:2566-2580.

THE INVESTIGATION OF ‘PHATUMTHANI 1’ RICE RHIZOSPHERE-FUNGAL COMPOSITION UNDER COMMERCIAL ORGANIC FERTILIZER AND CHEMICAL FERTILIZER TREATMENTS

Gregorius Nico Adi Setiawan¹, Thammaporn Kojonna², Supachitra Chadchawan², Thanin chantarachot², Nuttapon Pombubpa^{1*}

¹Department of Microbiology, Faculty of Science, Chulalongkorn University, Bangkok, Thailand

²Department of Botany, Faculty of Science, Chulalongkorn University, Bangkok, Thailand

*E-mail: Nuttapon.Po@chula.ac.th

Abstract:

Rice is a major staple food source for almost half of the world's population and is mostly produced by Asian countries. Then, the current farming method has shifted from conventional farming using chemical fertilizer to an organic farming system due to consumer demand. Rhizosphere soil microbiome has been known for supporting plant growth, yield, and survivability towards plant pathogens. Also, its composition is highly affected by the soil type, fertilizer treatment, and plant species. Therefore, this research focused on observing the fungal composition and their trophic traits on the ‘Pathumthani1’ rice cultivar at the tillering growth stage under the treatment of commonly used commercial organic (OF) and chemical fertilizer (CF). The tillering stage is one of the crucial stages in rice growth because yield production is affected by the amount of tiller produced, while plant healthiness in this stage also impacts how much yield is made in the ripening stage. The result showed that CF treatment reduced the amount of saprotroph and symbiotroph fungi in this stage but had a lower amount of pathotroph fungi than OF treatment. It indicates that OF treatment provides a more complex substrate for saprotroph fungi and produces beneficial nutrients for other fungi, which might be the reason for higher symbiotroph fungi than CF treatment. Some endophytic fungi like *Talaromyces purpureogenus*, *T. verruculosus*, and *Serendipita indica* were also found to be more abundant in OF treatment. This research is also the first study on the fungal community in the ‘Pathumthani1’ rice cultivar under organic and chemical fertilizers.

Introduction:

Rice is one of the primary staple food sources consumed by almost half of the world's population and is mainly produced by Asian countries. Rice production is expected and needs to be multiple times higher than the current production yield rate to fulfill the continuous growth of the global human population. Thailand is a major contributor to global rice production, particularly known for two major fragrant rice varieties, Thai Jasmine Rice (Khao Dawk Mali 105) and Pathumthani1 rice. Besides that, Pathumthani1 rice can be produced throughout the year due to its insensitivity to light during its reproduction phase, and it is quickly grown in irrigated areas.¹

The tillering stage was chosen because it is the crucial stage for rice production due to the high nutrient and nitrogen demand for the development of panicles, which directly affects the yield result.² Because more panicles can be produced, more spikelets or grains can be obtained from each panicle. Besides that, the seedling and tillering stages are the stages that are very prone to pathogens and diseases. This happens because rice has a meager resistance



to pathogens at the seedling stage, and the tillering stage, as a recovery stage after the disruption of fibrous root during transplantation, may also exhibit more pathogenic fungi.²

Conventional farming that uses chemical fertilizers and pesticides is less favorable nowadays, and farmers have started to move to organic farming methods. The organic farming system provides better soil organic matter than conventional farming, providing more diverse rhizosphere microbial communities and improving yield.³ However, recent research showed that increased soil organic carbon makes the soil and the plants more prone to fungal pathogens.⁴ Furthermore, organic approaches for protecting plants from diseases and pests have many approaches depending on the underlying problems, are difficult to follow, and, commonly based on trial and error, give farmers less certainty of successful treatment.⁵ Some farmers have difficulties finding the original cause of the disease and choosing a suitable treatment. They are concerned about the other remaining pathogens in the phytosphere.

The research on developing automatic diagnostic tools in India detected 15 rice plant diseases caused by the fungal attack, 5 diseases caused by bacterial invasion, and 4 diseases caused by viral attack.⁶ The research from Kenya also found the major foliar diseases were caused by fungi on the leaves or neck of the plant.⁷ According to previous research, rice plant diseases were caused mainly by fungal infection, resulting in significant damage in their ripening stages, which usually reduces rice yield. Besides that, the fungal richness is also affected by the fertilizer types. The chemical fertilizer with high nitrogen content is more likely to increase the fungal richness than the organic fertilizer.⁸ Therefore, this research focused on observing the differences in fungal microbiomes in the rice plant rhizosphere during its tillering growth stage and under the treatment of primarily used commercial organic fertilizer and chemical fertilizer. The objectives of this research are (i) to observe the different rhizosphere fungal communities in rice under organic and chemical fertilizer treatments and (ii) to investigate the trophic mode of the rhizosphere fungal community in both treatments.

Methodology:

Experimental design

The Pathumthani1 rice (Pathumthani Rice Research Center, Bureau of Rice Research and Development, Thailand) plants were grown in black plastic pots (30 cm diameter and 20 cm height) with 8 kg of brown clay soil (16% sand, 26% silt, 58% clay) and a randomized complete block design with four replications. The experiment was done in a greenhouse with controlled temperature and humidity at the Department of Botany, Faculty of Science, Chulalongkorn University. Organic fertilizer (OF) treatment was applied by adding commercial organic fertilizer (Royal Project Organic Fertilizer, composition: leftover material from mushroom cultivation (70%), wood chips (20%), cow dung (10%)) 32.5 g per pot, which was mixed with the soils 7 days before rice seedling transplantation.

Then, the chemical fertilizer (CF) treatment was done following the procedure from Kananont *et al*, (2016) by adding the Rabbit brand chemical fertilizer 16-20-0 (registration number 698/218 (Department of Agriculture), composition: nitrogen (16%), phosphate (P_2O_5) (20%), potassium oxide (K_2O) (0%), calcium oxide (CaO) (2%), sulfur (S) (14%)) at 20 days after transplant (DAT).¹ The addition of nitrogen and phosphorus at this time because those nutrients help plants improve the foliar growth and photosynthesis rate, which was marked by the early seedling stage.^{9,10} Next, the rhizosphere soil samples were collected at the tillering stage after both treatments reached 100% of the total tillering.

Sample extraction



The rhizosphere soil was extracted by removing the upper plant part and cutting the roots and soil formation with a pre-sterilized shovel until it reached the bottom of the pot. Then, the roots near the stem's center were cut, and the extra soil not directly attached to the roots was removed. Next, the chosen roots were placed into the falcon tubes with buffer solutions (130 mM NaCl, 3 mM NaH₂PO₄, 7 mM Na₂HPO₄ with the end pH 7.0) and kept inside the ice box during transportation to the lab. The falcon tubes with the root samples were shaken horizontally by a shaker for 20 minutes at 180 rpm. Then, the samples were centrifuged for 20 minutes at 1500 G, and the supernatant and root samples were removed from the tubes. The obtained soil samples were kept at -80°C after quick freezing with liquid nitrogen.

DNA extraction and DNA sequencing

Metagenomic DNA extraction was done at the OMICS Science and Bioinformatics Center Laboratory, Chulalongkorn University, following the manufactured standard protocols of DNeasy® PowerSoil® Pro Kit (Qiagen). The extraction process was performed using the QIAcube Connect machine (Qiagen). Then, a Denovix DS-11 Nanodrop was used to measure the final concentration of the obtained DNA samples. The final volume adjustment from 50 µL to 30 µL during the elution step was made for some samples with a low DNA concentration on the first extraction to meet the minimum requirement from the sequencing company (DNA concentration > 1 ng/µL). Furthermore, DNA samples were sent to the Biomarker Technologies Company Limited (Hong Kong) to be sequenced on the ITS region with the P250 protocols by Illumina NovaSeq 6000.

Bioinformatics and Statistical Data Analysis

The obtained raw sequence data were processed on quality control and analysis, resulting in amplicon sequence variances (ASVs) by using AMPtk: the Amplicon Toolkit for NGS data (UFITS) (v1.2.4).¹¹ The resulting ASVs were compared against the UNITE taxonomy database (v8.0) with 97% similarity to determine the fungal composition on various taxonomic levels.¹² The taxonomic composition, alpha diversity, and beta diversity were analyzed using phyloseq packages in R (v4.3.2)¹³ and R studio version 2023.09.1-494.^{14,15} Fertilizer treatments were compared using T-test with the 't.test' function in R. Then, beta diversity was analyzed using PERMANOVA with the 'adonis2' function in the 'vegan' package in R (Bray–Curtis distance for fungi, with permutation = 999).¹⁶ The FunGuild (v1.1.py) (<https://github.com/UMNFuN/FUNGuild>) was used to predict the trophic modes of ASVs that have been found.¹⁷

Results and Discussion:

Rhizosphere Fungal Taxonomic Composition Analysis

The taxonomic analysis on the phylum level at the tillering stage showed that the most dominant phyla were *Ascomycota*, *Basidiomycota*, *Chytridiomycota*, and *Mortierellomycota*, which commonly inhabit agricultural soil such as rice crop fields (Figure 1A).^{2,18,19} Some members of *Ascomycota* are known for their ability to degrade cellulose and hemicellulose as their carbon source.²⁰ The mutualism between plants and fungi relies on the fixed carbon provided by the plant, and fungi will facilitate plant nutrient uptakes, such as inorganic phosphate and nitrogen.¹⁹ The *Mortierellomycota* group appeared in the CF treatment but did not appear or might appear as a less than 1% group in the organic treatment (Figure 1A). This phylum is associated with the nitrate nitrogen abundance in the soil, which might be why *Mortierellomycota* is abundant in chemical treatment.² Therefore, *Mortierellomycota* and its related genera can potentially become bio-markers for the chemical farming system due to the high composition of available nitrogen in chemical fertilizers.



A deeper analysis was done at the genus level to investigate which genera were abundant from those dominant phyla. The result showed that *Aspergillus*, *Curvularia*, *Talaromyces*, *Penicillium*, *Scolecobasidium* (belong to *Ascomycota*), *Rhizophlyctis* (belongs to *Chytridiomycota*), *Inocybe* (belongs to *Basidiomycota*), and *Mortierella* (belongs to *Mortierellomycota*), were the abundant genera at the tillering stage (Figure 1B). In this research, the *Aspergillus*, *Penicillium*, and *Mortierella* genera were more abundant in the CF treatment than the OF. These genera can solubilize phosphate and facilitate the soluble phosphate from chemical fertilizer to be absorbed by the plant.²¹ On the other hand, *Scolecobasidium*, which can oxidize inorganic sulfur in soil, was more abundant in the OF treatment than in the CF treatment (Figure 1B).²¹ Then, *Talaromyces* was found to be slightly higher in OF treatment, which could be related to its function to solubilize phosphate. Furthermore, *Talaromyces* can mineralize an organic phosphate from non-phosphorous sources, supporting plant growth in low phosphate conditions.²² *Talaromyces* are also found to be endophytic-rhizospheric fungi that can travel from rhizosphere soil into root cells and move to other plant parts.²³ The available sulfur in soil will interact with phosphate ions to create a stronger bond than sulfate. This sulfur-phosphate bond will improve phosphate uptake by the plant and increase yield production.²⁴ Both phosphate and sulfur are essential in photosynthetic organisms and needed in high amounts, provided by the abundance of *Talaromyces* and *Scolecobasidium* in OF treatment that is low on available phosphate for the plant.

Besides that, the *Curvularia* genus is also known to be plant-pathogenic fungi that mainly cause a blight spot disease in the leaf^{25,26}, stem²⁷, and seed.²⁸ *C. intermedia* and *C. lunata* were present in less than 1% abundance of detected species (the data is not shown). In previous research, *C. intermedia* has been shown to have the ability to generate curvularin and dehydrocurvularin as phytotoxic compounds for seed germination and leaves, which caused the leaves to be brownish, dry, and brittle.²⁹ However, combining *Bacillus thuringiensis* and *C. intermedia* provides symbiotic mutualisms with *Hymenaea courbaril* (neotropical fruit tree) to water restriction as an adaptation to dry soils.³⁰ According to the taxonomic composition on genus level (Figure 1B), the plant in OF treatment has a higher possibility of developing the spot disease on the foliar because of the abundant *Curvularia* in the tiller developmental stage. However, its phytopathogenic profile is opportunistic between each species of *Curvularia* and the associated plants, and *C. lunata* was found to be helpful in phosphate solubilization.^{21,31}

The obtained list of abundant genera (Figure 1B) was further analyzed for the species belonging to these genera. The result has shown that *Penicillium nalgiovense*, *P. oxalicum*, *Rhizophlyctis rosea*, *Talaromyces purpureogenus*, and *T. verruculosus* were more abundant than other species in mentioned genera at the tillering stage (Figure 2). The *P. nalgiovense* was more abundantly present in the CF treatment than in the OF treatment, and the *P. oxalicum* was slightly higher in the CF treatment. The *Penicillium* genus is often known for its ability to produce various bioactive compounds that act as antimicrobial, antifungal, and insecticidal.^{32–34} In agricultural practice, *P. nalgiovense* can produce an antifungal protein that is 100% identical to *P. chrysogenum* antifungal protein (PAF), which induces the formation of intracellular reactive oxygen species (ROS) and activates the programmed cell death (PCD) to the sensitive fungal genera such as *Mortierella*, *Rhizopus*, *Aspergillus*, *Botrytis*, *Fusarium*, *Trichoderma*, and *Microsporium*.³² Chemical fertilizers provide free-form nutrients like nitrogen that can be used directly for the fungi to support their growth, and the excess available nutrients can induce the expression of PAF.³⁵

Then, *Rhizophlyctis rosea*, a zoosporic fungi that belongs to *Chytridiomycota*, is commonly found in cropping rather than natural soils. This indicates that this genus can constantly adapt to the environmental stressors, wide-range temperatures, and the dynamics of cultivated plants.³⁶ The fungi in this phylum are also grouped as aquatic fungi commonly found in well-irrigated rice fields.³⁷ Besides that, *R. rosea* is known for its cellulolytic and hemicellulolytic abilities, which are important to degrade plant debris high on cellulose and hemicellulose and provide extra soil nutrients.^{36,38}

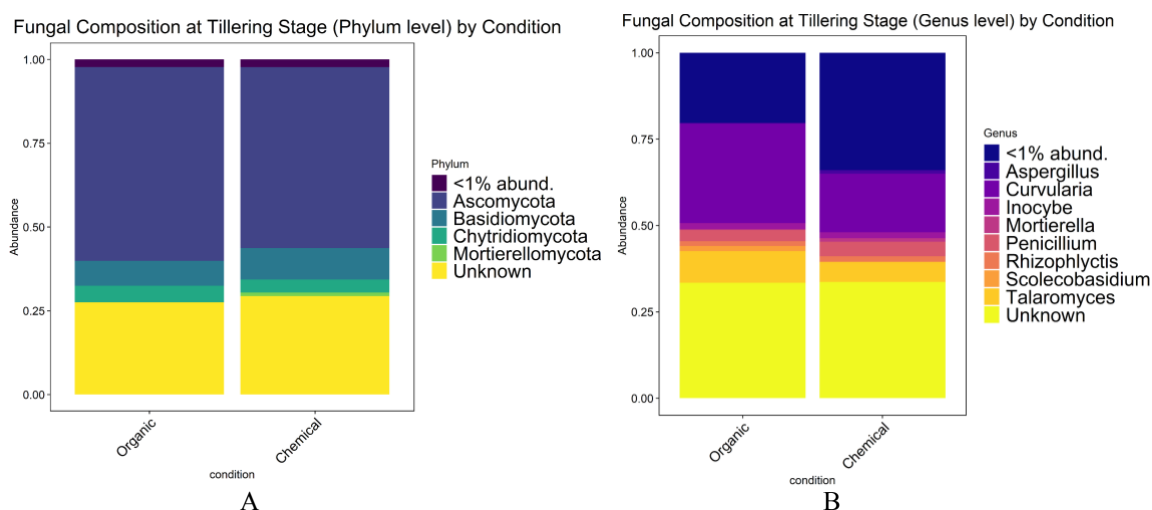


Figure 1. Taxonomic bar plots are based on treatment conditions in the phylum level (A) and the genus level (B).

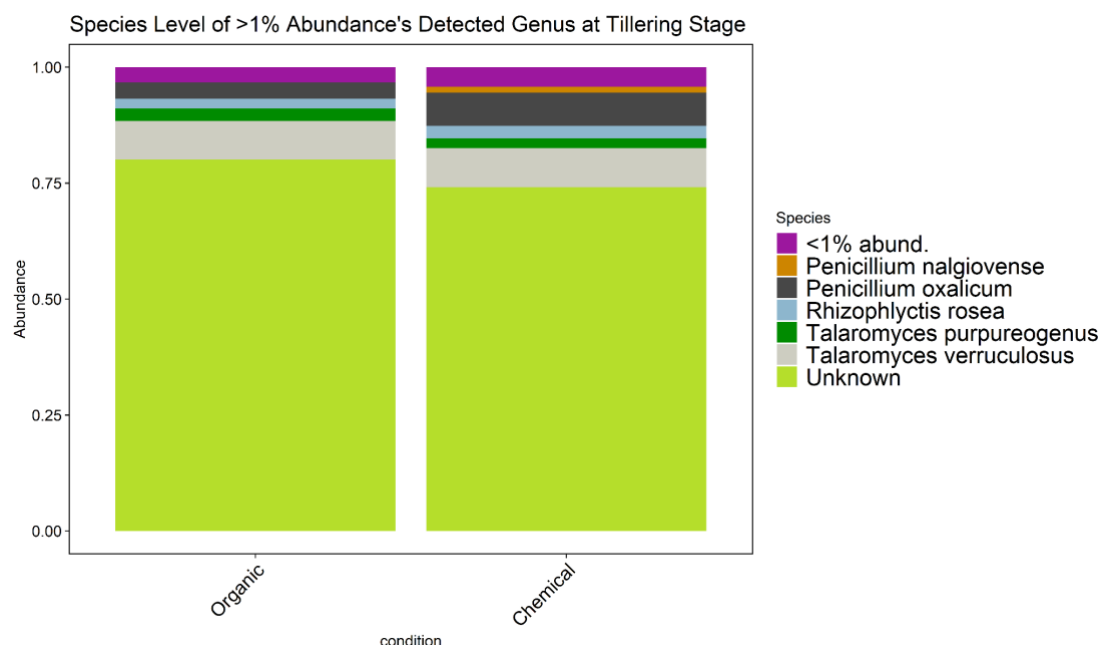


Figure 2. The species level of more than 1% abundance's genus at the tillering stage

Rhizosphere Fungal Diversity and Richness Analysis

According to the different patterns shown in the taxonomic composition, further analysis was performed using alpha- and beta-diversity analysis to investigate whether both fertilizer treatments significantly affect the rhizosphere fungal community. Beta-diversity results showed a significant difference (PERMANOVA, $p = 0.049$) (Figure 3A) in the fungal

compositions between OF and CF treatments. Furthermore, the alpha-diversity results showed no significant difference in the abundance of those prevalent genera between both treatments (Figure 1B). In contrast, other non-dominant fungal genera showed a significantly different result on the alpha diversity. Those fungal genera with significant differences in applied fertilizer treatments included *Geomyces*, *Iodophanus*, *Kodamaea*, *Olpidium*, *Paraphoma*, and *Serendipita*. One of the genera that showed significant differences was *Serendipita* (Figure 3B). Species richness is significantly less in CF than in OR treatments (T-test, $p = 0.01$), and according to the detected ASVs, *Serendipita indica* was found to be the species that belongs to this genus. Other than that, the *Geomyces* genus is only found in OF treatment (data not shown), which is matched to its trophic mode as saprophytic fungi degrading organic matter in organic fertilizer.³⁹

The *S. indica* species has been known as an endophytic-fungi that lives within the plant cell, especially the roots area, and provides a beneficial symbiotic relationship with the plant. *S. indica* plays a crucial role in improving nutrient uptake, maintaining ionic homeostasis, ROS scavenging, and modulating Fe homeostasis to prevent heavy metals like arsenic from reaching the plant shoot and grains.^{40–42} Besides that, *S. indica* also helps to protect the plant from diseases like rice blast disease by producing fungal chitinase that inhibits the conidial germination of pathogenic fungal.⁴³ This species can also improve rice growth and crop yield by the synergistic mechanisms with other bacteria species, like nitrogen-fixing bacteria *Azotobacter vinelandii*⁴⁴ and actinobacterium *Zhihengliuella* sp. ISTPL4.⁴⁵ The OF treatment was found to be able to increase the abundance of *S. indica* compared to CF treatment, which can be caused by the better nutrient availability in the suitable form for the fungi rather than the easy-uptake form for the plants like in the chemical fertilizer.

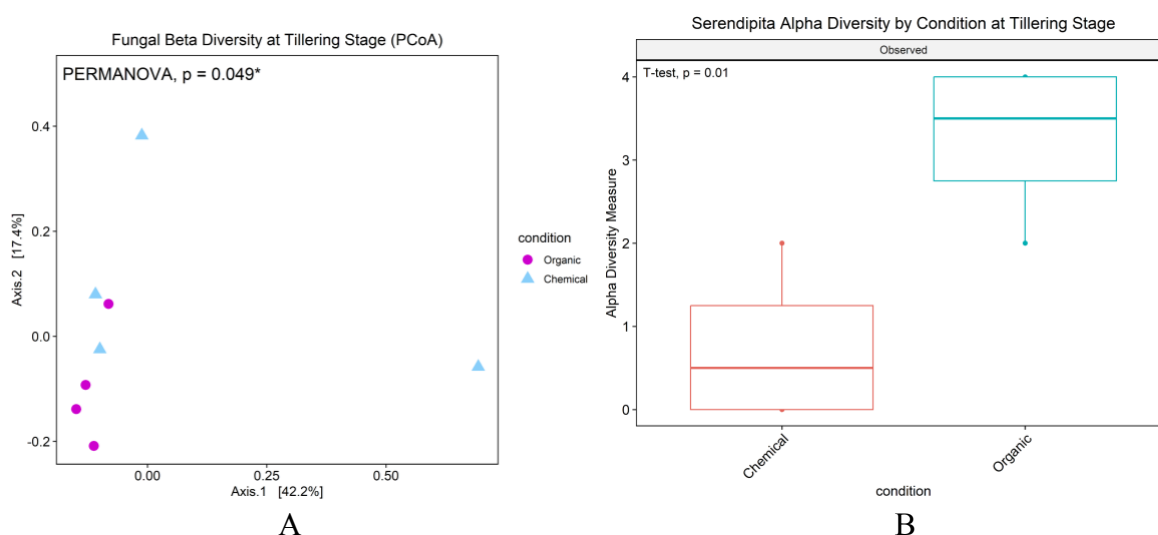


Figure 3. The result of fungal beta-diversity at the tillering stage (A) and alpha-diversity on the *Serendipita* genus at the tillering stage (B).

Rhizosphere Fungal Trophic Mode Analysis

The detected ASVs were then subjected to the FUNGuild analysis to explore their trophic mode as part of the rhizosphere fungal community. The result showed that OF treatment has a greater abundance of pathotroph or potentially pathogenic fungi than CF treatment. However, OF treatment exhibits more saprotroph and symbiotroph fungi than CF (Figure 4). This result matches the previous research, which found that a higher composition



of soil organic matter (SOM) using organic fertilizer possessed more pathogenic fungi than lower SOM using chemical fertilizer.³ Our results at the tillering stage showed the highest abundance of fungi that were related to plant pathogen, which is similar to previous research and will then change at heading and ripening stages as the saprotroph and symbiotroph increase in abundance and significantly reduce in pathotroph.²

The fungal phylum (Figure 1A) showed some fungal phyla that belong to the category of saprotroph due to their ability to degrade organic matter into simpler substrates for other microbes, such as *Ascomycota*, *Chytridiomycota* and *Mortierellomycota*. The existing genera, including *Mortierella*, *Penicillium*, and *Rhizophlyctis*, are examples of fungi under saprotroph trophic mode.^{2,46} This explains the abundance of saprotroph fungal in OF treatment, which consists of hard cellulose, hemicellulose, and lignin material in organic fertilizer. Example of a symbiotroph fungal is *Serendipita indica*, *Talaromyces purpureogenus*, and *T. verruculosus*, which lives as an endomycorrhizal inside the plant root cells.^{23,41,47} Another example is fungi from the genus *Inocybe*, such as *Inocybe curvipes* that was found in the ASVs and play a key role as an ectomycorrhizal that lives in the rhizosphere area to help provide essential nutrients to the plant.⁴⁸

Each ASVs, categorized into pathotroph, saprotroph, and symbiotroph, was also checked for the probability of having mixed traits between each trophic mode. The results are another category that combines each trait, such as pathotroph-saprotroph, pathotroph-saprotroph-symbiotroph, pathotroph-symbiotroph, and saprotroph-symbiotroph (Figure 4). According to this result, the organic farming system needs to be improved to minimize the number of pathotrophs in the tillering stage. This can enhance the possibility of plants growing faster and improve yield production. The abundance of pathotrophs, saprotrophs, and symbiotrophs was not much different, which indicates the high possibility of a turning point between each abundance on the next plant growth stage. However, some adjustments can be made initially, such as sorting the seeds free from diseases and applying bio-stimulator treatment to the rice seeds. Using plant bio-stimulator compounds in plant seeds can protect the seeds from various pathogenic fungi, induce early germination, and improve plant growth.⁴⁹ Therefore, the pathotroph fungi can be reduced from the seedling stage and maintained low at the tillering stage by inducing saprotroph and symbiotroph fungi to grow.

Although the pathotroph was abundant in OF treatment at the early stages, organic fertilizer usage is still better than chemical fertilizer because it improves the presence of symbiotrophs, fostering plant survivability against those fungal pathogens⁵⁰. Other than that, the higher amount of saprotrophs provides essential nutrients for other beneficial fungi to grow and support the plant's health and productivity. From this result, the available fungal traits in OF treatment have a higher possibility of developing more microbial groups in rhizosphere soil consisting of fungal and bacteria, which can provide a complex network structure⁸.

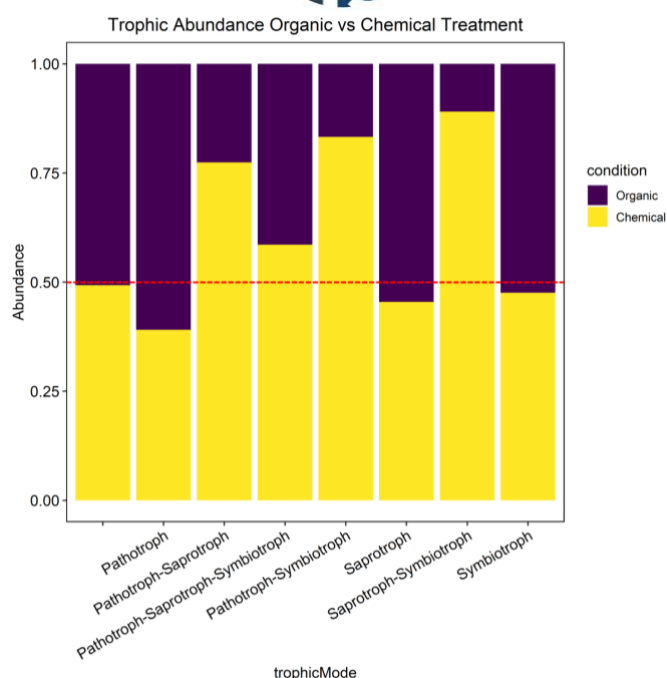


Figure 4. Fungal trophic mode abundance in organic and chemical treatment at the tillering stage.

Conclusion:

Chemical fertilizer provides absorbable macronutrients like phosphate, nitrogen, potassium, sulfur, and calcium for plants in suitable amounts. On the contrary, organic fertilizer tends to contain lesser amounts of absorbable macronutrients for the plant. Therefore, the function of the rhizosphere microbiome is vital to support the solubilization of nutrients in organic fertilizer and improve nutrient uptake in both treatments (OF and CF). Some dominant genera in CF treatment, like *Aspergillus*, *Penicillium*, and *Mortierella*, facilitate nitrogen and soluble phosphate uptake by rice plants. In the OF treatment, *Talaromyces* helps rice plants survive under low phosphate content by solubilizing available phosphate and mineralizing organic phosphate from other microbes. Then, *Scolecobasidium* facilitates oxidizing inorganic sulfur derived from some components in organic fertilizer, like cow dung and leftover material for mushroom cultivation. The availability of sulfur will induce the phosphate uptake by the plant in the form of phosphate-sulfur bonds, which are not easily lost from the soil into the irrigation system like their original form as phosphate and sulfate. Some non-dominant genera like *Serendipita* and *Geomyces* were higher in OF treatment. This is good because *S. indica* protects against phytopathogenic fungi, like *Curvularia*, which was also abundant in OF treatment. Then, *Geomyces* act as saprotrophs by converting the complex substrate from organic fertilizer and supplying nutrients to support the growth of other fungi.

The OF treatment is proven to exhibit more abundance of saprotroph and symbiotroph fungal communities, which can support further rice plant growth development through strong mutualism between rice plant and symbiotroph fungi. The rhizosphere microbial community is known to be affected by the types of soil, fertilizer, and plant species. To the best of our knowledge, this research is the first to observe the fungal rhizosphere community from the 'Pathumthani1' rice cultivar. This research fills the knowledge gap of the rhizosphere fungal community under chemical and organic fertilizers in the 'Pathumthani1' rice cultivar at the tillering stage. However, further observation of bacterial and fungal communities on all

Pathumthanil growth stages is needed to understand the impact of these fertilizer treatments on the rhizosphere microbial community and their function in the ecological network.

Acknowledgements:

This research was financially supported by the Sci-Super VIII fund from the Faculty of Science, Chulalongkorn University.

References:

1. Kananont N, Pichyangkura R, Kositsup B, Wiriyaakitnatekul W, Chadchawan S. *Int J Agric Biol.* 2016; 18: 09–15.
2. Dong H, Sun H, Chen C, Zhang M, Ma D. *Rice.* 2023; 16: 34.
3. Daquiado AR, Kuppusamy S, Kim SY, Kim JH, Yoon Y-E, Kim PJ, Oh S-H, Kwak Y-S, Lee YB. *Applied Soil Ecology.* 2016; 108: 84–91.
4. Du S, Trivedi P, Wei Z, Feng J, Hu H-W, Bi L, Huang Q, Liu Y-R. *mSystems.* 2022; 7.
5. van Bruggen AHC, Gamliel A, Finckh MR. *Pest Manag Sci.* 2016, 72, 30–44.
6. Yakkundimath R, Saunshi G, Anami B, Palaiah S. *Journal of The Institution of Engineers (India): Series B.* 2022; 103: 1047–1059.
7. Nganga EM, Kyallo M, Orwa P, Rotich F, Gichuhi E, Kimani JM, Mwongera D, Waweru B, Sikuku P, Musyimi DM, Mutiga SK, Ziyomo C, Murori R, Wasilwa L, Correll JC, Talbot NJ. *Plants.* 2022; 11.
8. Wang J, Song Y, Ma T, Raza W, Li J, Howland JG, Huang Q, Shen Q. *Applied Soil Ecology.* 2017; 112: 42–50.
9. Irfan M, Aziz T, Maqsood MA, Bilal HM, Siddique KHM, Xu M. *Sci Rep.* 2020; 10: 4278.
10. Jahan A, Islam A, Sarkar MdIU, Iqbal M, Ahmed MdN, Islam MdR. *Geology, Ecology, and Landscapes.* 2022; 6: 24–31.
11. Palmer JM, Jusino MA, Banik MT, Lindner DL. *PeerJ.* 2018; 6: e4925.
12. Nilsson RH, Larsson KH, Taylor AFS, Bengtsson-Palme J, Jeppesen TS, Schigel D, Kennedy P, Picard K, Glöckner FO, Tedersoo L, Saar I, Kõljalg U, Abarenkov K. *Nucleic Acids Res.* 2019; 47: D259–D264.
13. R Core Team. 2018.
14. RStudio Team. 2020.
15. McMurdie PJ, Holmes S. *PLoS One.* 2013; 8.
16. Oksanen J, Simpson GL, Blanchet FG, Kindt R, Legendre P, Minchin PR, O'Hara RB, Solymos P, Stevens MHH, Szoecs E, Wagner H, Barbour M, Bedward M, Bolker B, Borcard D, Carvalho G, Chirico M, Caceres M De, Durand S, Evangelista HBA, John RF, Friendly M, Furneaux B, Hannigan G, Hill MO, Lahti L, McGlinn D, Ouellette M-H, Cunha ER, Smith T, Stier A, Braak CJF Ter, Weedon J. 2022.
17. Nguyen NH, Song Z, Bates ST, Branco S, Tedersoo L, Menke J, Schilling JS, Kennedy PG. *Fungal Ecol.* 2016; 20: 241–248.
18. Otero-Jiménez V, Carreño-Carreño J del P, Barreto-Hernandez E, van Elsas JD, Uribe-Vélez D. *Applied Soil Ecology.* 2021; 167: 104036.
19. Zhang F, Xu N, Zhang Z, Zhang Q, Yang Y, Yu Z, Sun L, Lu T, Qian H. *Environmental Science and Pollution Research.* 2022; 30: 35972–35984.
20. Guo T, Zhang Q, Ai C, Liang G, He P, Lei Q, Zhou W. *Soil Science Society of America Journal.* 2020; 84: 99–114.
21. Seenivasagan R, Babalola OO. *Biology (Basel).* 2021, 10.
22. Sun X, Liu F, Jiang W, Zhang P, Zhao Z, Liu X, Shi Y, Sun Q. *Sustainability (Switzerland).* 2023; 15.
23. Kaur R, Saxena S. *Folia Microbiol (Praha).* 2023; 68: 781–799.
24. Assefa S, Haile W, Tena W. *Heliyon.* 2021; 7.
25. Deb L, Devi RT, Majumder D, Dutta P, Thakuria D, Rajesh T, Ningthoujam K. *Pharma Innov.* 2021; 10: 298–303.
26. Wang S, Lu Z, Lang B, Wang X, Li Y. *ACS Omega.* 2022, 7, 47462–47470.
27. Msikita W, Baimey H, James BD. *Plant Dis.* 2007; 91: 1430–1435.
28. Limtong S, Into P, Attarat P. *Microorganisms.* 2020; 8.
29. Meepagala KM, Johnson RD, Duke SO. *J Agric Chem Environ.* 2016; 05: 12–22.
30. Vitorino LC, de Souza Rocha AF, Bessa LA, Lourenço LL, da Costa AC, Silva FG. *Plant Stress.* 2022; 5.

31. Kodsueb R, Monkhung S, Karunarathna A, Mai Sci CJ, Cheewangkoon R. Phytopathogenic Fungi Identification in Thailand: Current Trends and Future Perspectives, 2021, vol. 48.
32. Galgóczy L, Kovács L, Vágvolgyi C. *Current Research, Technology and Education Topics in Applied Microbiology and Microbial Biotechnology*. 2010: 550–559.
33. Cai R, Wu Y, Chen S, Cui H, Liu Z, Li C, She Z. *J Nat Prod*. 2018; 81: 1376–1383.
34. Anitha S, Sam S, Das M. *J Agrobiotech*. 2017; 8: 33–42.
35. Huber A, Lerchster H, Marx F. *Microorganisms*. 2019; 7: 654.
36. Orrù L, Canfora L, Trinchera A, Migliore M, Pennelli B, Marcucci A, Farina R, Pinzari F. *Front Microbiol*. 2021; 12.
37. Pang Z, Zhao Y, Xu P, Yu D. *Microorganisms*. 2020; 8: 1–18.
38. Liu L, Huang WC, Liu Y, Li M. *Int Biodeterior Biodegradation*, 2021, 163.
39. Zheng X, Song K, Li S, Zhang H, Bai N, Zhang J, Zhang H, Cai S, Lv W, Cao L. *Sci Rep*. 2021; 11.
40. Jangir P, Shekhawat PK, Bishnoi A, Ram H, Soni P. *Physiol Mol Plant Pathol*, 2021, 116.
41. Tyagi J, Chaudhary P, Mishra A, Khatwani M, Dey S, Varma A. *Int J Environ Res*, 2022, 16.
42. Shukla J, Narayan S, Mishra A, Shirke PA, Kumar M. *Rhizosphere*. 2023; 26.
43. Li X, Wajjiha B, Zhang P, Dang Y, Prasad R, Wei Y, Zhang SH. *J Basic Microbiol*. 2023; 63: 734–745.
44. Dabral S, Saxena SC, Choudhary DK, Bandyopadhyay P, Sahoo RK, Tuteja N, Nath M. *Symbiosis*. 2020; 81: 139–148.
45. Sharma N, Dabral S, Tyagi J, Yadav G, Aggarwal H, Joshi NC, Varma A, Koul M, Choudhary DK, Mishra A. *Front Plant Sci*. 2023; 14.
46. Masson AS, Vermeire ML, Leng V, Simonin M, Tivet F, Nguyen Thi H, Brunel C, Suong M, Kuok F, Moulin L, Bellafiore S. *Agric Ecosyst Environ*. 2022; 331.
47. Surendirakumar K, Pandey RR, Muthukumar T. *Vegetos*. 2023.
48. Bonito G, Benucci GMN, Hameed K, Weighill D, Jones P, Chen KH, Jacobson D, Schadt C, Vilgalys R. *Front Microbiol*. 2019; 10: 1–21.
49. Ngasotter S, Xavier KAM, Meitei MM, Waikhom D, Madhulika, Pathak J, Singh SK. *Carbohydrate Polymer Technologies and Applications*. 2023; 6: 100349.
50. Thailand, Seephueak P, Preecha C, Seephueak W. *International Journal of Agricultural Technology*. 2019; 15: 485–500.



SESSION C-CHEMISTRY (ORGANIC & MEDICINAL CHEMISTRY)

DESIGN AND SYHTHESIS OF NOVEL BENZIMIDAZOLE-TRIAZOLE DERIVATIVES FOR EVALUATION OF ANTIOXIDANT ACTIVITY

Pichamon Masnguluem,¹ Uthaiwan Sirion^{1,2,*}

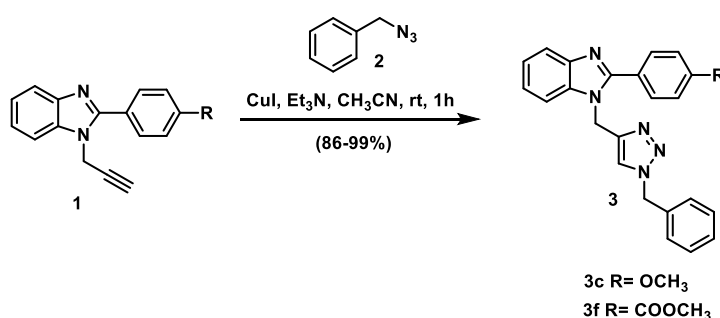
¹Department of Chemistry and Center of Excellence for Innovation in Chemistry, Faculty of Science, Burapha University, Sangesook, Chonburi 20131, Thailand

²The Research Unit in Synthetic Compounds and Synthetic Analogues from Natural Product for Drug Discovery (RSND), Burapha University, Chonburi 20131, Thailand

*e-mail: uthaiwan@go.buu.ac.th

Abstract:

A series of novel benzimidazole-based triazole compounds were designed and synthesized employing click reaction. The reactions were performed by using benzimidazole-based alkynes (**1**) and aromatic azide (**2**) as substrates in the presence of 10 mol% copper iodide and 10 mol% triethylamine in acetonitrile at room temperature for 1 h. Eleven corresponding products (**3**) were successfully obtained in high to excellent yields (86-99%). All derivatives were screened for *in vitro* antioxidant activity by using DPPH radical scavenging assay. Compounds **3c** and **3f** exhibited the best results with moderate %inhibition in 30.29 and 35.89, respectively, compared with standard L-ascorbic acid (88.13%inhibition).



Introduction:

Heterocyclic compounds have a central place in medicinal chemistry, being used as therapeutic agents to treat most diseases.^{1,2} Among them, benzimidazole stands out, as a purine-analog pharmacophore, with a very diverse therapeutic activity. The very broad spectrum of biological activities such as antimicrobial,³ antiviral,⁴ antihistamine,⁵ antiparasitic,⁶ anti-inflammatory,⁷ antihypertensive,⁸ diabetes mellitus,⁹ anticonvulsant,¹⁰ antitumor,¹¹ proton pump inhibitors,¹² anti-alzheimer,¹⁴ analgesic properties¹⁵ and anticoagulant properties.¹⁶

1,2,3-Triazole is a heterocyclic moiety derived from copper-catalyzed click reaction of alkyne and azide substrates. Diversity of 1,2,3-triazoles showed promising biological activities such as antiviral,¹⁷ anti-inflammatory,¹⁸ antitumor,¹⁹ antioxidant,²⁰ antitubercular,²⁰ antihypertensive,²¹ antimicrobial,²² and antiepileptic.²¹ In addition, 1,2,3-triazole derivatives are efficient in the treatment of Alzheimer's disease.²³

Therefore, benzimidazoles containing a triazole ring, so called "benzimidazole-triazoles", displayed promising biological activity. Herein, we present a simple method for the synthesis of novel benzimidazole-triazoles using the copper catalyzed click reaction of benzimidazole-ligated alkyne and benzyl azide. In addition, antioxidant activity of novel analogs was evaluated.

Methodology:

General methods: All chemicals were purchased from commercial sources and used without further purification. ^1H -NMR spectra were recorded at Burapha University using a BRUKER AVANCE (400 MHz). Analytical thin-layer chromatography (TLC) was conducted on pre-coated TLC plates; silica gel 60 F₂₅₄ (E. Merck, Darmstadt, Germany). Open-column chromatography was carried out using silica gel 60 PF₂₅₄ (E. Merck, Darmstadt, Germany). Melting points were measured using a Melting point apparatus (Griffin) and are uncorrected.

*Synthesis of Compound 1:*²⁴ (Scheme 2). To a solution of [DodecIm][HSO₄] (5 mol%) in 95%EtOH (5.0 mL) was added aromatic aldehyde (1 mmol) and *o*-phenylenediamine (1.2 mmol) at room temperature, respectively. The reaction mixture was stirred at room temperature for 12 h and then ethanol was removed by rotary evaporator. The crude residue was diluted with water (5.0 mL) and extracted with ethyl acetate (3 x 20 mL). The combined organic layer was concentrated using rotary evaporator. Then crude residue was dissolved in acetonitrile (5.0 mL), followed by adding KOH (2 mmol) and propargyl bromide (2 mmol) at room temperature, respectively. The reaction mixture was stirred at room temperature for 3 h. After the reaction completed, the reaction mixture was neutralized with sat. NH₄Cl and extracted with ethyl acetate (3 x 20 mL). The combined organic layer was dried over sodium sulfate anhydrous and concentrated using rotary evaporator. The crude product was purified by column chromatography (30-70% ethyl acetate/n-hexane) to give compounds **1a-1f**.

General procedure for the synthesis of Compound 3: Compound **1** was dissolved in acetonitrile, followed by adding triethylamine 10 mol%, benzyl azide (**2**) (1.5 mmol) and copper iodide 10 mol%, respectively. The reaction was stirred at room temperature for 1 h. After the completed conversion, the reaction mixture was neutralized with sat. NH₄Cl and extracted with ethyl acetate (3 x 20 mL). The combined organic layer was dried over sodium sulfate anhydrous and concentrated under rotary evaporator. The crude product was purified by silica gel column chromatography (30-70% ethyl acetate/n-hexane) to give the desired products benzimidazole-triazoles **3a-3f** in 78-99 %yield.

Compound 3a: ^1H NMR (400 MHz, CDCl₃): δ 7.86 (d, 1H, J = 7.2 Hz, Ar-H), 7.79-7.75 (m, 2H, Ar-H), 7.52-7.47 (m, 3H, ArH), 7.42 (d, 1H, J = 7.8 Hz, ArH), 7.36-7.26 (m, 5H, Ar-H), 7.21-7.16 (m, 3H, Ar-H), 5.54 (s, 2H, CH₂), 5.46 (s, 2H, CH₂); ^{13}C -NMR (100 MHz, CDCl₃): δ 153.56, 144.18, 142.98, 135.53, 134.22, 130.02, 129.72, 129.35, 129.11, 128.83, 127.83, 123.13, 122.80, 121.75, 119.98, 110.21, 77.20, 54.25, 40.98; HRMS (ESI-TOF) m/z calcd for C₂₃H₂₀N₅ [M+H]⁺ 366.1713, found 366.1713.

Compound 3b: ^1H NMR (400 MHz, CDCl₃): δ 8.34 (d, 2H, J = 8.8 Hz, Ar-H), 8.07 (d, 2H, J = 8.8 Hz, Ar-H), 7.86-7.83 (m, 1H, Ar-H), 7.41-7.32 (m, 6H, Ar-H), 7.28 (s, 1H, Ar-H), 7.23-7.18 (m, 2H, Ar-H), 5.52 (s, 2H, CH₂), 5.48 (s, 2H, CH₂); ^{13}C -NMR (100 MHz, CDCl₃): δ 151.05, 148.53, 143.42, 143.03, 135.96, 135.79, 134.09, 130.49 (2C), 129.21 (2C), 129.01, 127.94 (2C), 124.04, 123.99 (2C), 123.39, 121.82, 120.52, 110.19, 54.39, 40.95; HRMS (ESI-TOF) m/z calcd for C₂₃H₁₉N₆O₂ [M+H]⁺ 411.1564, found 411.1563.

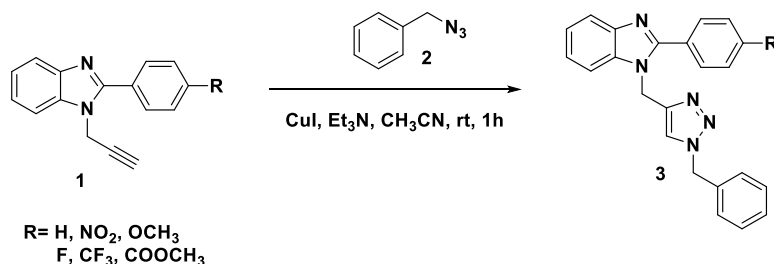
Compound 3c: ^1H NMR (400 MHz, CDCl₃): δ 7.77 (d, 1H, J = 7.6 Hz, Ar-H), 7.67 (d, 2H, J = 8.8 Hz, Ar-H), 7.34-7.20 (m, 6H, Ar-H), 7.18 (s, 1H, Ar-H), 7.16-7.12 (m, 2H, Ar-H), 6.96 (d, 2H, J = 8.8 Hz, Ar-H), 5.46 (s, 2H, CH₂), 5.40 (s, 2H, CH₂), 3.82 (s, 3H, OCH₃); ^{13}C -NMR (100 MHz, CDCl₃): δ 160.74, 153.41, 143.96, 142.81, 135.42, 134.17, 130.63 (2C), 128.87 (2C), 128.55, 127.63 (2C), 122.64, 122.45, 121.80, 121.78, 119.48, 114.08 (2C), 109.92, 55.16, 53.95, 40.72; HRMS (ESI-TOF) m/z calcd for C₂₄H₂₂N₅O [M+H]⁺ 396.1819, found 396.1819.

Compound 3d: ^1H NMR (400 MHz, CDCl₃): δ 7.76-7.71 (m, 3H, Ar-H), 7.32-7.07 (m, 8H, Ar-H), 6.95 (t, 2H, J = 8.8 Hz, Ar-H), 5.41 (s, 2H, CH₂), 5.34 (s, 2H, CH₂); ^{13}C -NMR (100 MHz, CDCl₃): δ 164.75, 162.59 (d, J = 247.0 Hz, C-F), 162.26, 152.43, 143.67, 142.70, 135.34, 131.29 (d, J = 9.0 Hz, C-F), 129.97 (d, J = 3.0 Hz, C-F), 129.62 (d, J = 8.0

Hz, C-F), 125.75 (d, $J = 4.0$ Hz, C-F), 123.00, 122.68, 121.68, 119.71, 115.94 (d, $J = 7.0$ Hz, C-F), 115.72 (d, $J = 7.0$ Hz, C-F), 109.96, 53.21, 40.54; HRMS (ESI-TOF) m/z calcd for $C_{23}H_{19}FN_5$ $[M+H]^+$ 384.1619, found 384.1619.

Compound 3e: 1H NMR (400 MHz, $CDCl_3$): δ 7.97 (d, 2H, $J = 8.4$ Hz, Ar-H), 7.87-7.83 (m, 1H, Ar-H), 7.76 (d, 2H, $J = 8.4$ Hz, Ar-H), 7.43-7.28 (m, 7H, Ar-H), 7.22-7.17 (m, 2H, Ar-H), 5.51 (s, 2H, CH_2), 5.48 (s, 2H, CH_2); ^{13}C -NMR (100 MHz, $CDCl_3$): d 151.95, 143.65, 142.94, 135.61, 134.13, 133.29, 131.79 (q, $J = 33.0$ Hz, C-F), 129.85 (2C), 129.14, 128.90, 127.87 (2C), 125.76 (q, $J = 4.0$ Hz, 2xC-F), 123.77, 123.32, 123.11, 121.78, 120.24, 54.29, 40; HRMS (ESI-TOF) m/z calcd for $C_{24}H_{19}F_3N_5$ $[M+H]^+$ 434.1587, found 434.1584.

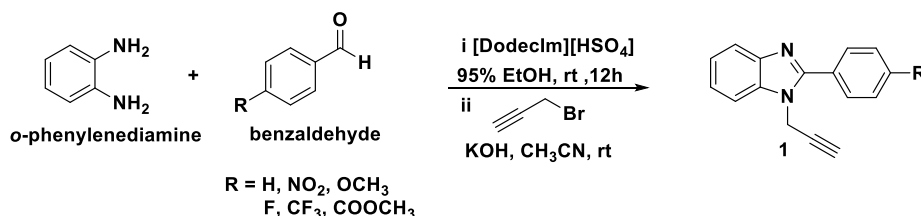
Compound 3f: 1H NMR (400 MHz, $CDCl_3$): δ 8.17 (d, 2H, $J = 8.4$ Hz, Ar-H), 7.86 (d, 2H, $J = 8.8$ Hz, Ar-H), 7.87-7.81 (m, 1H, Ar-H), 7.42-7.27 (m, 6H, Ar-H), 7.20-7.15 (m, 3H, Ar-H), 5.55 (s, 2H, CH_2), 5.49 (s, 2H, CH_2), 3.96 (s, 3H, $COOCH_3$). ^{13}C -NMR (100 MHz, $CDCl_3$): d 166.39, 152.34, 143.83, 142.96, 135.67, 134.16, 133.97, 131.37, 130.02 (2C), 129.42 (2C), 129.16 (2C), 128.90, 127.87 (2C), 123.61, 123.11, 121.72, 120.23, 110.28, 54.31, 52.35, 41.03; HRMS (ESI-TOF) m/z calcd for $C_{25}H_{22}N_5O_2$ $[M+H]^+$ 424.1768, found 424.1768.



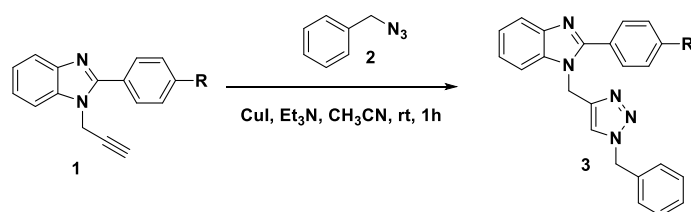
Scheme 1 Synthesis of benzimidazole-triazole compounds (**3**).

Results and Discussion:

To synthesize the novel benzimidazole-based triazole compounds through copper catalyzed click reaction, benzimidazole-linked alkynes (**1**) were employed as substrates. The preparation of substrate compounds **1** was carried out using our previous method (Scheme 2).²⁴ The condensation of *o*-phenylenediamine and aromatic aldehydes afforded 2-substituted benzimidazoles, then followed by *N*-alkylation *via* one-pot process with propargyl bromide under basic condition to produce benzimidazole-linked alkynes (**1**).



Scheme 2 Preparation of benzimidazole-linked alkynes (**1**) as substrates.

Table 1. Synthesis of benzimidazole-triazole compounds^a

Entry	Compound (1)	Product (3)	%Yield ^b
1			90%
2			94%
3			99%
4			86%
5			89%
6			78%

^a All reactions were conducted with **1** (1.0 mmol), azide (**2**, 1.5 mmol), CuI (10 mol%), Et₃N (10 mol%), CH₃CN (5 mL) for 1 h. ^b Isolated yield.

The synthesis of benzimidazole-based triazole analog was investigated through simple copper catalyzed click reaction. The reaction of benzimidazole-linked alkynes (**1**) reacted with benzyl azide (**2**) catalyzed by 10 mol% of copper iodine in the presence of 10 mol% of triethylamine base in acetonitrile at room temperature for 1 h to obtain the corresponding products (**3**) in high to excellent yields, as summarized the synthetic results in Table 1. Several substrates benzimidazole-linked alkynes (**1**) with different substituents (R) on benzene ring were studied, including electron donating group (**1c**, *p*-OCH₃) and electron withdrawing groups (**1b**, *p*-NO₂; **1d**, *p*-F; **1e**, *p*-CF₃ and **1f**, *p*-COOCH₃). The products (**3**) were formed in similar high yields in 90, 94, 99, 86, 89 and 78% yields for compound **3a**, **3b**, **3c**, **3d**, **3e** and **3f** respectively. This indicating that substrates **1** could be suitable for the preparation these new analog products.

Table 2. Antioxidant activity.

Entry	Benzimidazole-Triazole	%Inhibition (5mM) ^a
1	3a	10.22±0.01
2	3b	14.62±0.09
3	3c	30.29±0.06
4	3d	25.65±0.04
5	3e	12.04±0.03
6	3f	35.89±0.02
7	L-ascorbic acid	88.13 ± 0.02

^a DPPH assays.

The synthesized benzimidazole-triazole compounds (**3a-3f**) were screened for *in vitro* antioxidant activity by using DPPH radical scavenging assay as shown in Table 2. It was found that %inhibition of all derivatives was lower than the standard L-ascorbic acid. The derivative of benzimidazole-triazole **3a** without substituents showed the lower antioxidant activity with 10% inhibition. Notably, the antioxidant activity was enhanced when electron-withdrawing groups **3b**, **3d**, **3e** and **3f** and electron-donating group **3c** were present on the structure. This implied that the substituents on benzene-side benzimidazole ring at *para*-position play the important role of antioxidant activity. Among them, compounds **3c** (entry 3) and **3f** (entry 6) exhibited the best results with moderate % inhibition in 30.29 and 35.89, respectively. This indicating that methoxy group (**3c**) and methyl ester moiety (**3f**) on *para*-position of benzene-side benzimidazole moiety played an important role for antioxidant activity, whereas electron withdrawing groups on benzene ring (*p*-NO₂, *p*-F, *p*-CF₃) showed no antioxidant activity.

Conclusion:

In summary, we demonstrated the synthesis of novel benzimidazole-triazole compounds, incorporating between benzimidazoles and 1,2,3-triazoles using click reaction, in high to excellent yields. Antioxidant activity of all derivative products was evaluated. Compounds **3c** and **3f** showed promising antioxidant activity.

Acknowledgements:

This work was financially supported by a Research Grant from Burapha University through the National Research Council of Thailand, the Office of National Higher Education Science Research and Innovation Policy Council (NXPO) (Grant no. BO5F630030), the Center of

Excellence for Innovation in Chemistry (PERCH-CIC) and the Research Unit in Synthetic Compounds and Synthetic Analogues from Natural Products for Drug Discovery (RSND), Burapha University.

References:

1. Kabir E, Uzzaman M. *Results Chem.* 2022;4:100606.
2. Nishanth Rao R, Jena S, Mukherjee M, Maiti B, Chanda K. *Environ Chem Lett.* 2021;19: 3315–3358.
3. Bansal Y, Kaur M, Bansal G, *Mini Rev. Med. Chem.* 2019; 19: 624–646.
4. Chen M, Su S, Zhou Q, Tang X, Liu T, Peng F, He M, Luo H, Xue W J. *Saudi Chem. Soc.* 2021; 25:101194.
5. Brishty S R, Hossain M J, Khandaker M U, Faruque M.R.I, Osman H, Rahman S.M.A. *Front. Pharmacol.* 2021;12:762807.
6. Song B, Park E.Y, Kim K.J, Ki S.H, *Cancers* 2022;14:4601.
7. Kamat V, Yallur B.C, Poojary B, Patil V.B, Nayak S.P, Krishna P.M, Joshi S.D. *J. Chin. Chem. Soc.* 2021;68:1055–1066.
8. Tajane P.S, Sawant R.L, *Int. J. Health Sci.* 2022;6(Suppl. S1):7169–7179.
9. Aboul-Enein H.Y, El Rashedy A.A, *Med. Chem.* 2015;5:318–325.
10. Vasil'ev P.M, Kalitin K.Y, Spasov A.A, Grechko O.Y, Poroikov V.V, Filimonov D.A, Anisimova V.A, *Pharm. Chem. J.* 2017;50:775–780.
11. Song B, Park E.Y, Kim K.J, Ki S.H, *Cancers* 2022;14:4601.
12. Chen W.L, Li D.D, Chen X, Wang Y.Z, Xu J.J, Jiang Z.Y, You Q.D, Guo X.K, *Eur. J. Med. Chem.* 2020;188:112027.
13. Marinescu M, *Antibiotics* 2021;10:1002.
14. Dinparast L, Zengin G, Bahadori M.B, *Biointerface Res. Appl. Chem.* 2021;11:10739–10745.
15. Cheretaev I.V, Korenyuk I.I, Nozdrachev A.D, *Neurosci. Behav. Physiol.* 2018;48:848–853.
16. Hen T.L, Wu P, Chng C.L, Yang W.B, Jayakumar T, Geraldine P, Chou C.M, Chang C.Y, Lu W.J, Sheu J.R, *J. Biomed. Sci.* 2016;23:26.
17. Seliem I.A, Panda S.S, Girgis A.S, Moatasim Y, Kandeil A, Mostafa A, Ali M.A, Nossier E.S, Rasslan F, Srouf A.M. *Bioorg. Chem.* 2021;114:105117.
18. Demchenko S, Lesyk R, Yadlovskiy O, Holota S, Yarmoluk S, Tsyhankov S, Demchenko A. *Sci. Pharm.* 2023;91:26.
19. Bozorov K, Zhao J, Aisa H.A, *Bioorg. Med. Chem.* 2019;27:3511–3531.
20. Gupta O, Pradhan G.T, Chawla G. *J. Mol. Struct.* 2023;1274 Pt 2:134487.
21. Fallah Z, Tajbakhsh M, Alikhani M, Larijani B, Faramarzi M.A, Hamedifar H, Mohammadi-Khanaposhtani M, Mahdavi M. *J. Mol. Struct.* 2022;1255:132469.
22. Chu X.M, Wang C, Wang W.L, Liang L.L, Liu W, Gong K.K, Sun K.L, *Eur. J. Med. Chem.* 2019;166:206–223.
23. Xu M, Peng Y, Zhu L, Wang S, Ji J, Rakesh K.P, *Eur. J. Med. Chem.* 2019;180:656–672.
24. Senapak W, Saeeng R, Jaratjaroonphong J, Promarak V, Sirion U. *Tetrahedron.* 2019;75: 3543–3552.



STRUCTURAL MODIFICATION OF CHRYSIN AND THEIR α -GLUCOSIDASE INHIBITORY ACTIVITY

Toyin Ayandokun, Thi-Kim-Dung Le, Warinthorn Chavasiri*

Center of Excellence in Natural Products Chemistry, Department of Chemistry, Faculty of Science, Chulalongkorn University, Bangkok 10330, Thailand

*e-mail: warinthorn.c@chula.ac.th

Abstract:

Chrysin, a flavone found in many plants, is regarded as an important component of the human diet. It can be found in propolis, honey, and several fruits and vegetables. Chrysin has become a compound of interest due to its crucial medicinal and health benefits. Ten derivatives of chrysin acetohydrazide (**4a-j**) were synthesized through a three-step reaction and evaluated for their α -glucosidase inhibitory activity. Compounds **4a-j** were obtained as a mixture of geometrical isomers (*E/Z* isomers) upon treatment of hydrazide **3** with different aromatic aldehydes. The results showed that all derivatives are active with IC_{50} values ranging from 0.97 to 9.75 μ M with reference to that of acarbose, the standard drug, with the IC_{50} value of 836 μ M. Compound **4i**, a 2,3,4-trihydroxy substituted compound, was the most active compound with the IC_{50} value of 0.97 μ M. The kinetic study was conducted to further investigate the interaction mechanism of **4i**, and the results showed that it was a mixed type of inhibitor. This means that the inhibitor can either bind to the enzyme or enzyme-substrate complex.

Introduction:

Diabetes is a chronic metabolic disease characterized by constant hyperglycemia, a condition for high blood glucose levels in the body.¹ Glucose is the body's primary energy source, which can be obtained from food. Insulin is a hormone in the body that helps to regulate blood sugar. In the case of diabetes, the body does not generate enough insulin or does not use insulin correctly. α -Glucosidase is an enzyme present in the epithelial lining of the small intestine that catalyzes the conversion of 1,4-glycosidic bonds in polysaccharides to readily absorbable sugar units. As a result, the inhibition of glycosidases is a key strategy for lowering blood sugar levels.² Currently, there are several antidiabetic drugs which include acarbose, miglitol, and voglibose but these are associated with many side effects. Hence, there is a need to develop more potent and less toxic α -glucosidase inhibitors.³

Flavonoids are a class of compounds with low molecular weight which include flavanols, flavanols, flavanones, isoflavones, flavones, and dihydroflavonols.⁴ Chrysin is a flavone that occurs naturally in a variety of plants, including the blue passionflower, honey, and propolis. Chrysin has been reported to possess various biological properties including antioxidant, antidiabetic, and anticancer.⁵ Recently, in drug discovery acyl hydrazone moiety has been recognized as an important structure and is easily synthesized through condensation of hydrazides and aldehydes or ketones under acid or base catalysis.⁶ Acyl hydrazone pharmacophore possesses the ability to take part in several interactions with the proposed targets through hydrogen bond acceptor and donor of amino acid residues of the enzyme binding site. This unique moiety exhibited a wide range of pharmacological potencies which include anti-inflammatory⁷, anticancer⁸, and α -glucosidase inhibitors.⁹ Additionally, Schiff bases are among the important moieties that possess various biological activities such as α - and β -glucosidase inhibitory activities.

Based on the hypothesis that acyl hydrazone pharmacophore and Schiff bases play a key role in α -glucosidase inhibition, chrysin acetohydrazide derivatives were synthesized and evaluated for α -glucosidase inhibitory activity.

Methodology:

The general procedure for the synthesis of chrysin acetohydrazide derivatives

Synthesis of methyl 2-((5-hydroxy-4-oxo-2-phenyl-4H-chromen-7-yl)oxy)acetate (2)

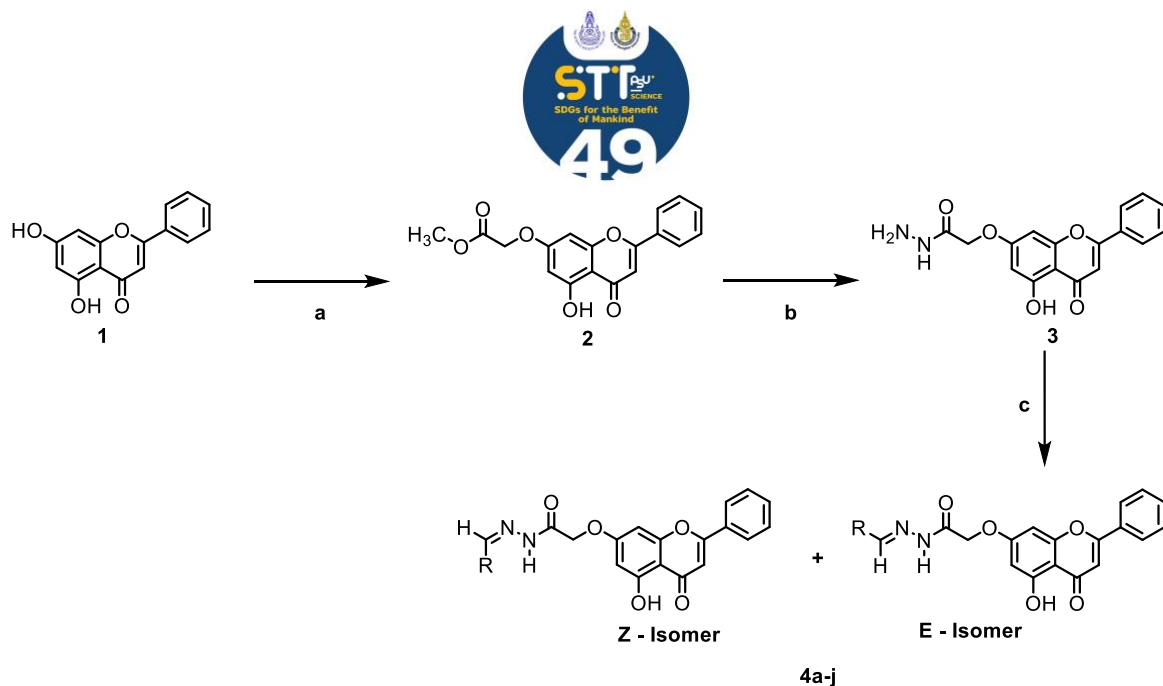
The synthetic route of chrysin acetohydrazide derivatives **4a-j** is shown in **Scheme 1** with their structures displayed in **Table 1**. A mixture of chrysin **1** (500 mg, 1.97 mmol) and K_2CO_3 (817 mg, 5.91 mmol) was dissolved in 15 mL of anhydrous DMF and allowed to cool down to 0 °C in ice bath. After this was the dropwise addition of methyl 2-bromoacetate (0.19 mL, 1.97 mmol) and the reaction was stirred for 3 h at this temperature.¹⁰ The reaction was monitored by TLC. Upon completion, the mixture was poured slowly into ice. Precipitate was formed during this process, filtered, washed with water, and allowed to dry on air to give the title compound as a pure yellow powder. Yield: 83%. 1H NMR (500 MHz, $CDCl_3$) δ_H 12.80 (s, 1H), 7.86 (dd, J = 8.4, 1.6 Hz, 2H), 7.57 – 7.49 (m, 3H), 6.66 (s, 1H), 6.50 (d, J = 2.3 Hz, 1H), 6.35 (d, J = 2.3 Hz, 1H), 4.71 (s, 2H), and 3.83 (s, 3H). ^{13}C NMR (125 MHz, $CDCl_3$) δ_C 182.6, 168.4, 164.3, 163.5, 162.4, 157.7, 132.0, 131.2, 129.2, 126.4, 106.3, 106.0, 98.5, 93.5, 65.2, and 52.6.

Synthesis of 2-((5-hydroxy-4-oxo-2-phenyl-4H-chromen-7-yl)oxy)acetohydrazide (3)

Compound **2** (400 mg, 1.23 mmol) was dissolved in 15 mL of EtOH in a round bottom flask. The mixture was refluxed at 80 °C and hydrazine hydrate (0.11 mL, 3.69 mmol) was added and stirred further for 10 h.¹¹ The reaction was monitored by TLC. The reaction was cooled down to room temperature, and a precipitate was formed which was later filtered to give **3** in 79% yield. 1H NMR (500 MHz, $DMSO-d_6$) δ_H 12.79 (s, 1H), 9.44 (s, 1H), 8.07 (d, J = 7.6 Hz, 2H), 7.64 – 7.56 (m, 3H), 7.03 (s, 1H), 6.80 (d, J = 2.7 Hz, 1H), 6.44 (d, J = 2.7 Hz, 1H), 4.64 (s, 2H), and 4.38 (s, 2H). ^{13}C NMR (125 MHz, $DMSO-d_6$) δ_C 182.7, 166.5, 164.23, 164.3, 161.6, 157.7, 132.8, 131.0, 129.8, 127.0, 105.9, 105.8, 99.4, 94.1, 67.0, 40.5, 40.4, 40.3, 40.2, 40.2, 40.1, 39.9, 39.9, 39.7, 39.6, and 39.4.

General procedure for the synthesis of *N'*-arylidene-2-((5-hydroxy-4-oxo-2-phenyl-4H-chromen-7-yl)oxy)acetohydrazide (**4a-j**)

Compounds **4a-j** were synthesized by reacting **3** (0.77 mmol) with different substituted benzaldehydes (0.77 mmol) in a Schiff base condensation reaction. The reaction was stirred at 80 °C for 8 h in the presence of a catalytic amount of AcOH (4-8 drops) in EtOH. Compounds **4a-j** were obtained in 58-87% by filtration after precipitation. All structures were elucidated using 1H and ^{13}C NMR and shown in **Table 1**.



Scheme 1. Reagents and conditions: (a) methyl 2-bromoacetate, K_2CO_3 , DMF, 0 °C, 3 h: (b) hydrazine hydrate, EtOH, 80 °C, 10 h: (c) different substituted aldehydes, EtOH, glacial AcOH (cat.), 80 °C, 8 h.¹¹

The synthesis of chrysin acetohydrazide derivatives

The chrysin acetohydrazide derivatives **4a-j** gave appropriate analytical and spectroscopic data according to their structures.¹⁰ ^1H and ^{13}C NMR spectra showed that compounds **4a-j** were obtained as a mixture of geometrical isomers (E/Z isomers). The E:Z ratio for each compound was determined from ^1H NMR spectra utilizing the integration of the neat methylene group peaks that appeared as two separated singlets for the two isomers between δ 4.8 and 5.3 ppm. The ^1H NMR spectra for compound **4b**, as an example, showed two characteristic overlapped singlets for the two isomers at δ 12.8 ppm representing the chelated phenolic C5–OH of the 4H-chromen-4-one ring. The CONH protons of the two isomers resonate as two overlapped singlets at δ 11.7 ppm. The N=CH protons of the two isomers appeared as two singlets at δ 8.3 and 8.0 ppm, which can be utilized to confirm the formation of E/Z isomers and their corresponding ratios. Proton atoms present on the phenyl rings (rings B and D) of the two isomers resonated as multiplet signals in the range δ 7.2–8.0 ppm, whereas the three proton atoms that belong to the 4H-chromen-4-one ring (rings A and C) are resonated as three multiplet signals at δ 7.0, δ 6.8, and 6.4 ppm. The methylene protons (CH_2O) for the two isomers appeared as two singlets at δ 5.3 and 4.8 ppm. The ^{13}C NMR spectrum and HRMS data further confirmed the formation of the desired compound.¹⁰

Compound **4a**: (*E,Z*)-*N'*-benzylidene-2-((5-hydroxy-4-oxo-2-phenyl-4H-chromen-7-yl)oxy)acetohydrazide as a white powder in 86% yield; ^1H NMR (500 MHz, $\text{DMSO}-d_6$) (*E:Z*= 1:0.4) δ_{H} 12.84 – 12.76 (m, 1.4H), 11.71 – 11.63 (m, 1.4H), 8.33 (s, 0.4H), 8.09 – 8.02 (m, 4H), 7.76 – 7.69 (m, 2H), 7.63 – 7.51 (m, 5H), 7.48 – 7.41 (m, 3H), 7.04 – 7.01 (m, 1.4H), 6.86 – 6.81 (m, 1.4H), 6.50 – 6.38 (m, 1.4H), 5.32 (s, 2H), 4.84, and (s, 0.94H). ^{13}C NMR (125 MHz, $\text{DMSO}-d_6$) δ_{C} 182.6, 168.8, 164.9, 164.2, 164.1, 164.1, 164.0, 161.7, 161.6, 157.8, 148.6, 144.6, 134.5, 134.4, 132.7, 131.1, 130.6, 129.7, 129.6, 129.3, 127.7, 127.5, 126.9, 105.9, 105.8, 105.6, 99.2, 94.1, 93.9, 67.1, and 65.8.

Compound **4b**: (*E,Z*)-*N'*-(2-fluorobenzylidene)-2-((5-hydroxy-4-oxo-2-phenyl-4H-chromen-7-yl)oxy)acetohydrazide as an off-white powder in 65% yield; ^1H NMR (500 MHz, $\text{DMSO}-d_6$) (*E:Z*= 1:0.4) δ_{H} 12.83 – 12.79 (m, 1.4H), 11.72 – 11.65 (m, 1.4H), 8.31 (s, 0.4),

8.10 – 8.01 (m, 4H), 7.84 – 7.74 (m, 3H), 7.62 – 7.53 (m, 5H), 7.33 – 7.25 (m, 3H), 7.05 – 7.03 (m, 1.4H), 6.86 – 6.83 (m, 1.4H), 6.49 – 6.39 (m, 1.4H), 5.32 (s, 2H), 4.83, and (s, 0.74H). ^{13}C NMR (125 MHz, DMSO- d_6) δ_{C} 182.6, 168.8, 167.2, 164.9, 164.6, 164.3, 164.0, 162.6, 161.6, 157.8, 147.5, 143.5, 132.7, 131.1, 129.9, 129.9, 129.8, 129.7, 129.7, 127.0, 116.6, 116.5, 116.4, 116.3, 105.9, 105.8, 105.6, 99.2, 94.1, 94.0, 67.1, and 65.8.

Compound **4c**: (*E,Z*)-*N'*-(4-fluorobenzylidene)-2-((5-hydroxy-4-oxo-2-phenyl-4H-chromen-7-yl)oxy)acetohydrazide as an off-white powder in 58% yield; ^1H NMR (500 MHz, DMSO- d_6) (*E:Z*= 1:0.4) δ_{H} 12.83 – 12.79 (m, 1.4H), 11.72 – 11.65 (m, 1.4H), 8.31 (s, 0.4H), 8.10 – 8.01 (m, 4H), 7.84 – 7.74 (m, 3H), 7.62 – 7.53 (m, 5H), 7.33 – 7.25 (m, 3H), 7.05 – 7.03 (m, 1.5H), 6.86 – 6.83 (m, 1.5H), 6.49 – 6.39 (m, 1.5H), 5.32 (s, 2H), 4.83, and (s, 0.82H). ^{13}C NMR (125 MHz, DMSO- d_6) δ_{C} 182.6, 168.8, 167.2, 164.9, 164.6, 164.3, 164.0, 162.6, 161.6, 157.7, 147.5, 143.5, 132.7, 132.7, 131.1, 129.9, 129.8, 129.8, 129.7, 129.7, 127.0, 116.6, 116.5, 116.4, 116.3, 105.9, 105.8, 105.6, 99.3, 99.2, 94.1, 94.0, 67.1, and 65.8.

Compound **4d**: (*E,Z*)-2-((5-hydroxy-4-oxo-2-phenyl-4H-chromen-7-yl)oxy)-*N'*-(2-nitrobenzylidene)acetohydrazide as an off-white powder in 84% yield; ^1H NMR (500 MHz, DMSO- d_6) (*E:Z*= 1:0.4) δ_{H} 12.82 (m, 1.4H), 11.98 (m, 1.4H), 8.73 (s, 0.4H), 8.40 (s, 1H), 8.19 – 8.14 (s, 1H), 8.12 – 8.03 (m, 4H), 7.80 (m, 2H), 7.70 – 7.53 (m, 4H), 7.04 (m, 1.4H), 6.86 (m, 1.4H), 6.46 (m, 1.4H), 5.32 (s, 2H), 4.87, and (s, 0.78H). ^{13}C NMR (125 MHz, DMSO- d_6) δ_{C} 182.6, 169.1, 164.9, 164.5, 164.2, 164.0, 161.7, 161.6, 157.8, 148.7, 148.5, 144.0, 140.1, 134.4, 134.1, 132.7, 131.4, 131.2, 131.1, 129.7, 129.1, 128.7, 127.0, 125.3, 125.1, 105.9, 105.9, 105.6, 99.3, 99.2, 94.2, 94.0, 67.1, and 65.9.

Compound **4e**: (*E,Z*)-2-((5-hydroxy-4-oxo-2-phenyl-4H-chromen-7-yl)oxy)-*N'*-(4-nitrobenzylidene)acetohydrazide as a yellow powder in 65% yield; ^1H NMR (500 MHz, DMSO- d_6) (*E:Z*= 1:0.4) δ_{H} 12.85 – 12.81 (m, 1.4H), 12.00 – 11.94 (m, 1.4H), 8.43 (0.4H), 8.31 – 8.27 (m, 3H), 8.13 – 7.96 (m, 7H), 7.64 – 7.55 (m, 5H), 7.07 (d, J = 7.2 Hz, 1.4H), 6.88 (s, 1.4H), 6.51 – 6.43 (m, 1.4H), 5.39 (s, 2H), 4.89, and (s, 0.74H). ^{13}C NMR (125 MHz, DMSO- d_6) δ_{C} 182.6, 168.8, 164.9, 164.9, 164.0, 161.6, 157.8, 148.3, 147.5, 143.4, 142.2, 140.8, 132.8, 132.7, 131.1, 129.8, 129., 129.7, 128.7, 128.5, 127.0, 124.6, 124.5, 116.5, 116.3, 105.8, 105.6, 99.3, 94.0, 67.1, and 65.9.

Compound **4f**: (*E,Z*)-2-((5-Hydroxy-4-oxo-2-phenyl-4H-chromen-7-yl)oxy)-*N'*-(2-hydroxybenzylidene)acetohydrazide as a pale yellow powder in 65% yield; ^1H NMR (500 MHz, DMSO- d_6) (*E:Z*= 1:1) δ_{H} 12.85 – 12.79 (m, 2H), 11.86 (s, 1H), 11.64 (s, 1H), 11.00 (s, 1H), 10.08 (s, 1H), 8.57 (s, 1H), 8.34 (s, 1H), 8.10 – 8.07 (m, 5H), 7.78 – 7.53 (m, 10H), 7.31 – 7.23 (m, 2H), 7.06 – 6.82 (m, 10H), 6.51 – 6.40 (m, 2H), 5.30 (s, 2H), and 4.87 (s, 2H). ^{13}C NMR (125 MHz, DMSO- d_6) δ_{C} 182.7, 182.6, 168.5, 164.9, 164.2, 164.1, 164.0, 163.9, 161.7, 161.6, 157.9, 157.8, 156., 148.7, 142., 132.7, 132.7, 132.1, 131.8, 131.0, 129.7, 129.6, 127.0, 120.5, 119.9, 119.1, 116.9, 116.6, 105.9, 105.9, 105.8, 105.6, 99.3, 99.3, 94.1, 93.9, 67.0, and 65.8.

Compound **4g**: (*E,Z*)-2-((5-hydroxy-4-oxo-2-phenyl-4H-chromen-7-yl)oxy)-*N'*-(4-hydroxybenzylidene)acetohydrazide as a white powder in 70% yield; ^1H NMR (500 MHz, DMSO- d_6) (*E:Z*= 1:0.5) δ_{H} 12.83 – 12.79 (m, 1.5H), 11.52 – 11.42 (m, 1.5H), 9.99 – 9.91 (m, 1.5H), 8.23 – 8.06 (m, 4H), 7.93 (s, 1H), 7.62 – 7.52 (m, 8H), 7.05 – 7.03 (m, 1.5H), 6.85 – 6.81 (m, 5H), 6.48 – 6.39 (m, 1.5H), 5.28 (s, 2H), and 4.80 (s, 1H). ^{13}C NMR (125 MHz, DMSO- d_6) δ_{C} 182.7, 182.6, 168.4, 164., 164.3, 164.1, 163.9, 163.6, 161.6, 161.5, 160.1, 159.8, 157.7, 157.7, 148.9, 144., 132.7, 132.6, 131.0, 129.7, 129.6, 129.5, 129.3, 127.0, 125.4, 116.2, 116.2, 105.9, 105.8, 105.7, 105.5, 99.2, 99.2, 94.1, 93.9, 67.1, and 65.8.

Compound 4h: (*E,Z*)-*N'*-(2,4-dihydroxybenzylidene)-2-((5-hydroxy-4-oxo-2-phenyl-4H-chromen-7-yl)oxy)acetohydrazide as an off white powder in 84% yield; ^1H NMR (500 MHz, $\text{DMSO-}d_6$) (*E:Z*= 1:0.7) δ_{H} 12.84 – 12.78 (m, 1.71H), 11.67 (s, 0.77H), 11.44 (s, 0.65H), 11.17 (s, 0.87H), 10.00 (s, 1.54H), 9.86 (s, 0.53H), 8.42 (s, 0.91H), 8.20 (s, 0.71H), 8.08 (d, J = 7.6 Hz, 4H), 7.63 – 7.53 (m, 6.85H), 7.31 (d, J = 8.8 Hz, 0.93H), 7.03 (d, J = 7.2 Hz, 1.86H), 6.86 (s, 0.97H), 6.81 (s, 0.77H), 6.48 (s, 0.96H), 6.39 (s, 0.73H), 6.36 – 6.29 (m, 3.65H), 5.25 (s, 1.37H), and 4.83 (s, 2H). ^{13}C NMR (125 MHz, $\text{DMSO-}d_6$) δ_{C} 182.6, 182.5, 168.0, 164.9, 164.1, 164.1, 164.0, 163.4, 161.6, 161.5, 161.4, 161.0, 159.8, 158.6, 157.7, 149.7, 143.0, 132.7, 132.6, 131.6, 131.0, 129.6, 129.6, 128.7, 127.0, 112.0, 110.9, 108.3, 108.3, 105.9, 105.8, 105.8, 105.5, 103.1, 102.8, 99.3, 99.2, 94.1, 93.9, 67.0, and 65.8.

Compound 4i: (*E,Z*)-2-((5-Hydroxy-4-oxo-2-phenyl-4H-chromen-7-yl)oxy)-*N'*-(2,3,4- trihydroxybenzylidene)acetohydrazide as a light purple powder in 75% yield; ^1H NMR (500 MHz, $\text{DMSO-}d_6$) (*E:Z*= 1:0.6) δ_{H} 12.84 – 12.79 (m, 1.6H), 11.72 (s, 1H), 11.48 (s, 0.76H), 11.19 (s, 1.04H), 9.61 – 9.52 (m, 1.80H), 9.39 (s, 0.60H), 8.57 – 8.51 (m, 1.90H), 8.38 (s, 1.12H), 8.19 – 8.07 (m, 3.79H), 7.62 – 7.54 (m, 5.07H), 7.06 – 7.00 (m, 2.43H), 6.88 – 6.78 (m, 2.52H), 6.50 – 6.37 (m, 3.10H), 5.26 (s, 1.26H), and 4.85 (s, 2H). ^{13}C NMR (125 MHz, $\text{DMSO-}d_6$) δ_{C} 182.6, 182.6, 167.9, 164.9, 164.2, 164.0, 163.4, 161.6, 161.5, 157.7, 150.8, 149.4, 148.9, 147.9, 147.1, 144.5, 133.2, 133.2, 132.7, 132.6, 131.0, 129.7, 127.0, 121.6, 118.7, 112.6, 111.2, 108.3, 108.2, 105.9, 105.9, 105.8, 105.6, 99.3, 99.2, 94.1, 93.9, 67.0, and 65.8.

Compound 4j: (*E,Z*)-2-((5-Hydroxy-4-oxo-2-phenyl-4H-chromen-7-yl)oxy)-*N'*-(2,4,6- trihydroxybenzylidene)acetohydrazide as a brown powder in 87% yield; ^1H NMR (500 MHz, $\text{DMSO-}d_6$) (*E:Z*= 1:0.2) δ_{H} 12.84 – 12.79 (m, 1.2H), 11.66 (s, 0.84H), 11.48 (s, 0.24H), 10.99 (s, 1.98H), 10.32 (s, 0.47H), 9.88 – 9.85 (m, 1.25H), 8.70 (s, 1.03H), 8.40 (s, 0.24H), 8.12 – 8.08 (m, 2.34H), 7.65 – 7.54 (m, 3.88H), 7.08 – 7.04 (m, 1.13H), 6.91 – 6.84 (m, 1.21H), 6.52 – 6.41 (m, 1.25H), 5.86 – 5.81 (m, 2.52H), 5.20 (s, 0.46H), and 4.82 (s, 2H). ^{13}C NMR (125 MHz, $\text{DMSO-}d_6$) δ_{C} 182.6, 167.1, 164.8, 164.1, 164.0, 163.1, 162.2, 162.0, 161.6, 161.5, 160.2, 159.80, 157.73, 147.79, 144.80, 132.73, 131.05, 129.69, 126.99, 105.94, 105.89, 105.63, 99.38, 99.2, 94.9, 94.8, 94.1, 67.0, and 65.7.

α -Glucosidase inhibition assay

The synthesized chrysin acetohydrazide derivatives were assayed for *in vitro* α -glucosidase inhibition. The α -glucosidase inhibition assay was carried out by using the procedure described by Ramadhan and coworkers with slight modifications.¹² Briefly, α -glucosidase (0.4 U/mL) was prepared using 0.1 M, buffer (pH 6.9), and substrate (3 mM *p*-nitrophenyl- α -D-glucopyranoside) was dissolved in 0.1 M phosphate buffer (pH 6.9). The stock sample was prepared by dissolving 4 mM of the compound in DMSO, and then 1 mM of the loading sample was prepared from this solution. 10 μL of the loading sample was pipetted into the 96 well plate followed by the addition of 40 μL of α -glucosidase and then incubated at 37 $^{\circ}\text{C}$ for 10 min. Subsequently, 50 μL substrate solution was added to the reaction mixture and incubated further at 37 $^{\circ}\text{C}$ for 20 min and the reaction was terminated by adding 100 μL of 1 M Na_2CO_3 solution. The absorbance was read at 405 nm (ALLSHENG AMR-100 microplate reader) in order to analyze the enzymatic activity. The percentage inhibition was calculated as follows: % Inhibition = $[(A_0 - A_1)/A_0] \times 100$, where: A_0 is the absorbance without the sample; A_1 is the absorbance with the sample. The IC_{50} value was deduced from the plot of % inhibition vs concentration of the tested sample. Acarbose was used as a positive control and the experiment was performed in triplicate.

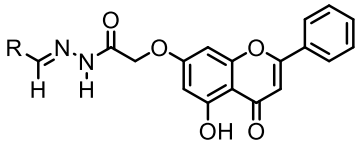
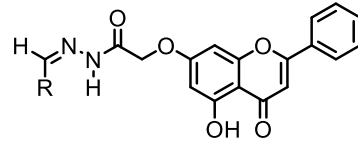
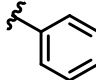
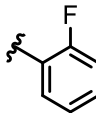
Results and Discussion:

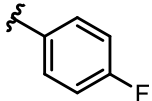
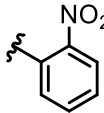
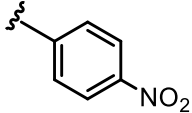
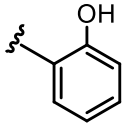
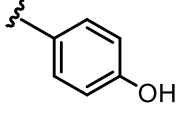
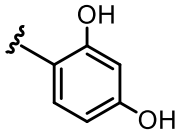
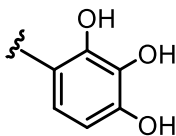
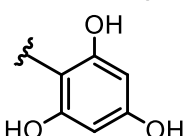
Two new (**4b** and **4d**) and eight known chrysin acetohydrazide derivatives (**4a**, **4c**, **4e**, **4f**, **4g**, **4h**, **4i**, and **4j**)^{10,13} were successfully synthesized, characterized, and evaluated for α -glucosidase inhibitory activity. As shown in **Table 1**, considering the effect of substituents on the aromatic aldehydes against α -glucosidase, except for the fluoro substituents **4b** and **4c**, the derivatives **4d** and **4e** bearing electron-withdrawing groups increased the inhibitory activity as compared to the unsubstituted ring **4a**. Compound **4e** with a nitro substituent at the *p*-position exhibited the IC_{50} value of 9.75 μ M while **4d** with the nitro group at the *o*-position enhanced the activity with the IC_{50} value of 4.66 μ M. This shows that the nitro substituent interacted with the enzyme more effectively at the *o*-position, resulting in increasing the inhibitory activity.

Reviewing the effect of the hydroxyl substituent present on aromatic aldehydes against α -glucosidase revealed that this functional group displayed a significant effect. As observed from the result, **4f** with the hydroxyl derivatives at the *o*-position showed excellent inhibition with the IC_{50} value of 5.50 μ M, but the presence of the hydroxyl group at the *p*-position in **4g** reduced drastically. This might be because the hydroxyl group at the *o*-position had better interaction with the amino acid residue than that at the *p*-position. The enhancement of the inhibitory activity by the hydroxyl substituents could further be seen in **4h**, on the introduction of additional hydroxyl substituent to the *p*-position, the combined effect improved the activity better with the IC_{50} value of 1.99 μ M.

Interestingly, the derivative bearing 2,3,4-trihydroxyl substituent **4i** was the most active with the IC_{50} value of 0.97 μ M which was around eight hundred and sixty-one fold more active than the standard acarbose with the IC_{50} value of 836.10 μ M. In addition, **4j** with 2,4,6-trihydroxyl substituent emerged as the second most active compound with the IC_{50} value of 1.84 μ M. This result revealed that the introduction of hydrophilic substituents with H-bond donating properties like hydroxyl groups on the benzylidene moiety displayed the most interaction with active residues which led to extra interactions and an increase of the α -glucosidase inhibitory activity.

Table 1 α -Glucosidase inhibitory activity of chrysin acetohydrazide derivatives **4a-j**

<div style="display: flex; justify-content: space-around; align-items: center;"> <div style="text-align: center;">  <p>E - Isomer</p> </div> <div>+</div> <div style="text-align: center;">  <p>Z - Isomer</p> </div> </div>				
Compounds	R	E/Z ratio	% Inhibition at 10 μ M	IC_{50} (μ M) ^a
4a		1:0.4	49.53	- ^b
4b		1:0.4	50.87	- ^b

4c		1:0.4	51.10	- ^b
4d		1:0.4	90.90	4.66 ± 0.30
4e		1:0.4	76.81	9.75 ± 1.29
4f		1:1	92.60	5.50 ± 0.30
4g		1:0.5	38.06	- ^b
4h		1:0.7	82.90	1.99 ± 0.19
4i		1:0.6	99.49	0.97 ± 0.05
4j		1:0.2	97.78	1.84 ± 0.26
Chrysin	NA	-	-	67.81 ± 1.69
Acarbose	NA	-	-	836.10 ± 47.19

^aIC₅₀ value was evaluated as mean ± SD from the three independent experiments.

^bIC₅₀ value was not tested if the inhibition rate was less than 70% at 10 μM.

α-Glucosidase inhibition kinetics

To further explore the interaction mechanism of chrysin acetohydrazides, the type of inhibition mode by the most active compound **4i** against *α*-glucosidase was evaluated by Lineweaver-Burk plot analysis. The X-axis showed 1/(PNPG) and 1/V values were plotted on the Y-axis. The activity was examined at different concentrations of *p*-nitrophenyl-*α*-D-glucopyranoside at 0.750, 0.375, 0.187, 0.093, and 0.046 mM in the presence or absence of the active compound.

As depicted in Figure 1, *K_m* increased while *V_{max}* values decreased. This study indicated that **4i** should be a mixed type of inhibitor for *α*-glucosidase. The *K_i* value of 1.82 μM and *K_i'* value of 2.75 μM were directly calculated from the secondary replot of the Lineweaver-Burk plots against the different concentrations of **4i** at 0.00, 0.97, and 1.94 μM.

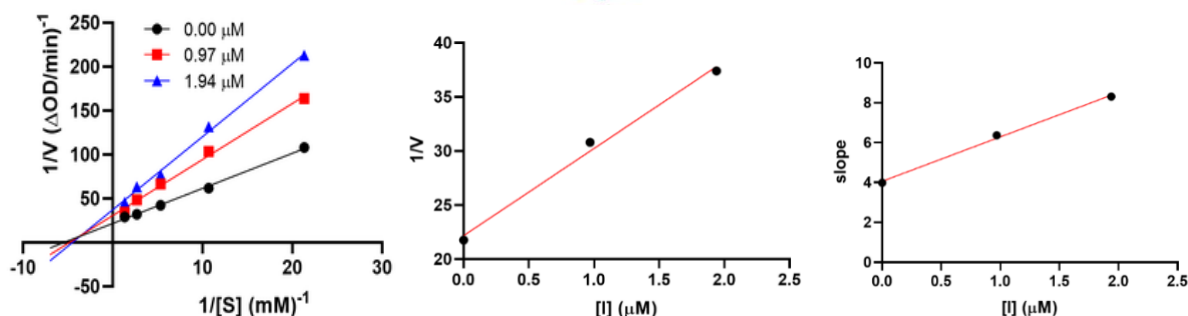


Figure 1. Kinetic study of **4i**. The Lineweaver-Burk plot for α -glucosidase inhibition and plots of slope against different concentrations of **4i** for K_i and K_i' determination.

Conclusion:

Ten chrysin acetohydrazide derivatives were successfully synthesized. The structures were characterized and evaluated for α -glucosidase inhibitory activity. Most of the synthesized compounds are active with the IC_{50} values ranging from 0.97 to 9.75 μ M. The structure-activity relationship established the importance of the OH group on the ring and its significance at the *o*-position. Most of the derivatives displayed better inhibition than chrysin and the positive control, acarbose. Compound **4i** with 2,3,4-trisubstituted of the OH group emerged as the best compound in the series with the IC_{50} value of 0.97 μ M.

Acknowledgements:

Appreciation goes to the Chulalongkorn University's Graduate Scholarship Program for ASEAN or Non-ASEAN Countries (for T.A.).

References:

- Vijayaraghavan K, Iyyam PS, Subramanian SP. Eur J Pharmacol. 2012;680:122–129.
- Kerru N, Singh-Pillay A, Awolade P, Singh P. Eur J Med Chem. 2018;152:436–488.
- Dhameja M, Gupta P. Eur J Med Chem. 2019;176:343–377.
- Beecher GR. J Nutr. 2003;133:3248–3254.
- Fonseca SF, Lima DB, Alves D, Jacob RG, Perin G, Lenardao EJ, Savegnago L. New J Chem. 2015;39:3043–3050.
- Maia RDC, Tesch R, Fraga CAM. Expert Opin Thera Pat. 2014;24:1161–1170.
- Cerqueira JV, Meira CS, de Souza SE, de Aragão França LS, Vasconcelos JF, Nonaka CKV, Melo TL, Filho JM, Moreira DR, Soares MB. Int Immunopharmacol. 2019;75:105735.
- Zhang H, Min S, Zhang L, Li L. J Mol Liq. 2022;348:118034.
- Imran S, Taha M, Ismail NH, Kasif SM, Rahim F, Jamil W, Hariono M, Yusuf M, Wahab H. Eur J Med Chem. 2015;105:156–170.
- Al-Oudat BA, Alqudah MA, Audat SA, Al-Balas QA, El-Elmat T, Hassan MA, Frhat IN, Azaizeh MM. Drug Des Devel Ther. 2019;13:423–433.
- Lin HY, Sun WX, Zheng CS, Han HW, Wang X, Zhang YH. RSC Adv. 2017;7:48404–48419.
- Ramadhan R, Phuwapraisirisan P. Bioorg Med Chem Lett. 2015;25:4529–4533.
- Al-Oudat BA; Ramapuram H; Malla S; Audat, SA; Hussein N; Len JM; Kumari S; Bedi MF; Ashby CR; Tiwari AK. Mol. 2020;13:25.



SYNTHESIS OF RHINACANTHIN RELATED DERIVATIVES AS α -GLUCOSIDASE INHIBITORS

Felicitas Ene, Thi-Kim-Dung Le, Warinthorn Chavasiri*

Center of Excellence in Natural Products Chemistry, Department of Chemistry,
Faculty of Science, Chulalongkorn University, Bangkok 10330, Thailand

*e-mail: warinthorn.c@chula.ac.th

Abstract:

Rhinacanthins are natural products isolated from *Rhinacantus nasutus*. They have been reported to exhibit good biological activities such as anticancer, antibacterial, and antidiabetic. The rhinacanthin structures provide the same core structure, 2-hydroxy-3-(3-hydroxy-2,2-dimethylpropyl)-1,4-naphthoquinone (**1**), after hydrolysis. In order to study the effect of the increased chain length and hydrophobicity on α -glucosidase inhibitory activity, different aliphatic acids were used to synthesize naphthoquinone aliphatic esters leading to two new and eight known naphthoquinone esters **2-11** which were characterized by means of spectroscopy, and evaluated for their α -glucosidase inhibitory activity. Amongst the synthesized compounds, esters with longer chain (C = 8, 9, 12 and 14) that is compounds **5-8** showed better α -glucosidase inhibitory activity with IC_{50} 36.48 ± 2.74 μ g/mL, 5.83 ± 0.59 , 2.60 ± 0.64 and 5.30 ± 0.50 respectively, than that of the starting material and acarbose (IC_{50} = 836.00 ± 47.19) which was used as a positive control. The trend shows that the activity of the compounds increased with the number of carbons from C2 to C12 (**2-8**) and a drop-in activity at C14 (**8**). Amongst the derivatives evaluated, compound **7** showed the best inhibitory activity with IC_{50} 2.6 ± 0.64 μ M.

Introduction:

Diabetes mellitus is a chronic disorder, characterized by elevated blood glucose level leading to increased morbidity and mortality rate.¹ In 2000, 171 million diabetes cases were reported and the incidence of diabetes has been predicted to increase further to 366 by 2023 if nothing is done.² The α -glucosidase is responsible for the hydrolysis of disaccharides into glucose in the small intestine, it cleaves the glycosidic bonds in complex sugars like the disaccharides to form glucose which is absorbed by the body, the increase absorption of glucose results to hyperglycemia which is a risk factor of diabetes. Inhibiting the α -glucosidases is one of the therapeutic methods of treating diabetes as it slows down the digestion of complex sugar and consequently reduces risk of hyperglycemia. There are few α -glucosidase inhibitor drugs clinically available for the treatment of type 2 diabetes including acarbose, voglibose and miglitol. Unfortunately, they have recorded side effects including gastrointestinal effects. Moreover, they are expensive and have long term cardiac health risk.³

Rhinacanthins are naphthoquinones found in *Rhinacantus nasutus* Kurz (family Acanthaceae). They have been reported for their good biological activities including anticancer, antibacterial, and antidiabetics activities.⁴ All rhinacanthins from *R. nasutus* have a similar core structure, for example, 2-hydroxy-3-(3-hydroxy-2,2-dimethylpropyl)-1,4-naphthoquinone, with different ester substituent. Rhinacanthins D, M, N, and Q have aromatic esters while rhinacanthin C contains an aliphatic ester. Rhinacanthin C is the major compound and has been reported to reduce hyperglycemia, hyperlipidemia and pancreatic destruction in diabetes rates.⁴ A report on the α -glucosidase inhibitory effect of rhinacanthins

C, D and N showed that rhinacanthins D and N with aromatic esters had poor α -glucosidase inhibitory activity while rhinacanthin C with long carbon chain was very active with IC_{50} 22.6 ± 0.6 $\mu\text{g/mL}$.⁵ This implies that aromatic substituents on the R group of the rhinacanthins reduce the activity. In addition, from the molecular docking of rhinacanthin C and α -glucosidase, H-bonding and hydrophobic interactions were observed which favored the potency of rhinacanthin C. In other words, this shows the importance of hydrophobic interactions. The first synthesis of naphthoquinone aliphatic ester from 2-hydroxy-3-(3-hydroxy-2,2-dimethylpropyl)-1,4-naphthoquinone was reported for anticancer activities. Increase in chain length from C3 to C7 improved the activity.⁶ Unfortunately, naphthoquinone aliphatic esters have not been reported for α -glucosidase activity.

Owing to the evidence that hydrophobic interactions enhance α -glucosidase activity, a series of naphthoquinone aliphatic ester derivatives were synthesized and screened for their α -glucosidase inhibitory activity.

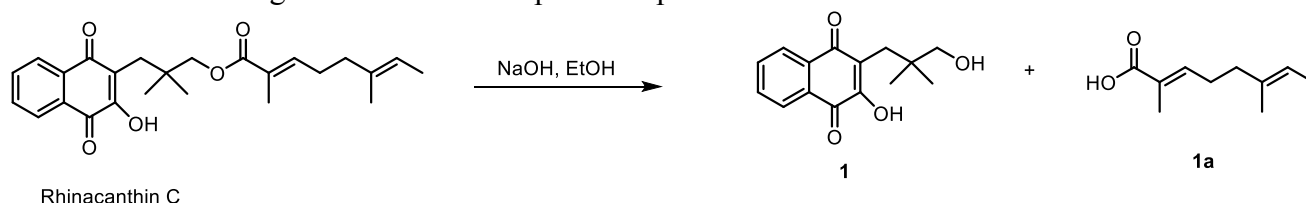
Methodology:

Procedure for hydrolysis of rhinacanthin C

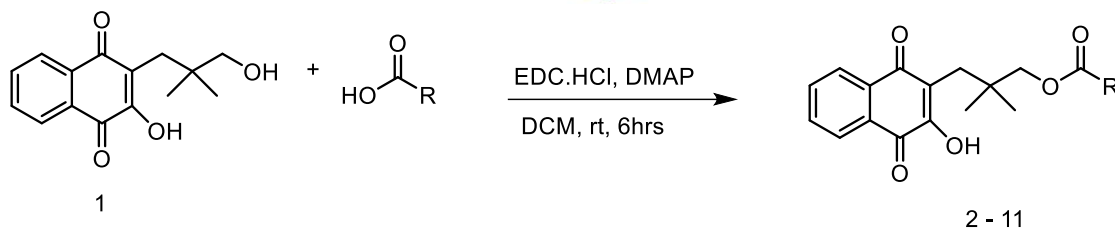
2-Hydroxy-3-(3-hydroxy-2,2-dimethylpropyl)-1,4-naphthoquinone (**1**) was obtained from the hydrolysis of rhinacanthin C as shown in Scheme 1. To a stirred solution of rhinacanthin C (1 g, 0.25 mmol) in EtOH (15 mL), NaOH (2M, 20 mL) was added and refluxed for 3 h.⁷ TLC was used to monitor the progress of the reaction. After completion, the solvents were removed under vacuum and the residue was dissolved in water (20 mL), followed by addition of 5N HCl to adjust the pH to 2. The precipitates were filtered and purified by column chromatography using hexanes:EtOAc (4:1) to afford **1**. The structures were characterized by using ^1H and ^{13}C NMR spectroscopic data.

The general procedure for the synthesis of naphthoquinone aliphatic ester derivatives

The synthetic route of naphthoquinone aliphatic ester derivatives **2** – **11** (Table 1) is shown in Scheme 2. To a stirred solution of **1** (104 mg, 0.4 mmol) in DCM (10 mL), carboxylic acid (0.4 mmol), EDC.HCl (92.85 mg, 0.45 mmol) and DMAP (61.08 mg, 0.45 mmol) were added and allowed to stir for 6 h at room temperature. The reaction was monitored using TLC. The reaction mixture was diluted with DCM (20 mL) and washed with 5% HCl solution (3x10 mL). Subsequently, the organic layer was washed with aqueous NaHCO_3 solution (3x10 mL) and brine, then dried over anhydrous Na_2SO_4 , filtered and concentrated.⁸ The resulting crude mixture was purified by column chromatography using hexanes:EtOAc (9:1). The structures were elucidated using ^1H and ^{13}C NMR spectroscopic data.



Scheme 1. Hydrolysis of rhinacanthin C



Scheme 2. The general procedure of the synthesis of naphthoquinone aliphatic ester derivatives

The synthesis of related naphthoquinone derivatives

2-Hydroxy-3-(3-hydroxy-2,2-dimethylpropyl)-1,4-naphthoquinone (**1**) was obtained as a yellow amorphous powder in 50% yield.

^1H NMR (500 MHz, CDCl_3) δ_{H} (ppm) 8.11 (dd, $J = 7.7, 1.3$ Hz, 1H), 8.08 (dd, $J = 7.6$ Hz, 1H), 7.76 (td, $J = 7.6, 1.4$ Hz, 1H), 7.68 (td, $J = 7.7, 1.4$ Hz, 1H), 7.45 (br s, 1H, OH), 3.83 (s, 2H), 2.67 (s, 2H), and 0.98 (s, 6H). ^{13}C NMR (125 MHz, CDCl_3) δ_{C} (ppm) 185.0, 181.4, 154.4, 135.1, 133.0, 133.1, 129.5, 127.1, 126.3, 121.8, 72.9, 37.2, 32.1, and 25.2

3-(3-Hydroxy-1,4-dioxo-1,4-dihydronaphthalen-2-yl)-2,2-dimethylpropyl acetate (**2**) was obtained as a yellow powder 80% yield after column chromatography, eluting with hexanes:EtOAc (4:1). ^1H NMR (500 MHz, CDCl_3) δ_{H} (ppm) 8.11 (dd, $J = 7.7, 1.3$ Hz, 1H), 8.08 (dd, $J = 7.6$ Hz, 1H), 7.76 (td, $J = 7.6, 1.4$ Hz, 1H), 7.68 (td, $J = 7.7, 1.4$ Hz, 1H), 3.83 (s, 2H), 2.67 (s, 2H), 2.01 (s, 3H), and 0.98 (s, 6H). ^{13}C NMR (125 MHz, CDCl_3) δ_{C} (ppm) 185.0, 181.4, 171.5, 154.4, 135.1, 133.0, 133.1, 129.5, 127.1, 126.3, 121.8, 72.9, 37.2, 32.1, 25.2, and 21.0

3-(3-Hydroxy-1,4-dioxo-1,4-dihydronaphthalen-2-yl)-2,2-dimethylpropyl butanoate (**3**) was obtained as a yellow powder in 84% yield after column chromatography, eluting with hexanes:EtOAc (4:1). ^1H NMR (500 MHz, CDCl_3) δ_{H} (ppm) 8.11 (d, $J = 7.6$ Hz, 1H), 8.08 (d, $J = 7.6$ Hz, 1H), 7.76 (t, $J = 7.1$ Hz, 1H), 7.69 (t, $J = 7.4$ Hz, 1H), 7.49 (s, 1H), 3.84 (s, 2H), 2.67 (s, 2H), 2.24 (t, $J = 7.6$ Hz, 2H), 1.67 – 1.54 (m, 2H), 0.97 (s, 6H), and 0.91 (t, $J = 7.4$ Hz, 3H). ^{13}C NMR (125 MHz, CDCl_3) δ_{C} (ppm) 185.0, 181.4, 173.9, 154.4, 135.1, 133.1, 129.1, 127.2, 126.3, 121.9, 72.7, 36.9, 36.4, 32.0, 25.2, 24.7, 18.6, and 13.9.

3-(3-Hydroxy-1,4-dioxo-1,4-dihydronaphthalen-2-yl)-2,2-dimethylpropyl hexanoate (**4**) was obtained as a yellow powder in 74% yield after column chromatography, eluting with hexanes:EtOAc (4:1). ^1H NMR (500 MHz, CDCl_3) δ_{H} (ppm) 8.11 (d, $J = 7.6$ Hz, 1H), 8.08 (d, $J = 7.6$ Hz, 1H), 7.75 (t, $J = 7.6$ Hz, 1H), 7.69 (t, $J = 7.4$ Hz, 1H), 7.50 (s, 1H), 3.84 (s, 2H), 2.67 (s, 2H), 2.25 (t, $J = 7.6$ Hz, 2H), 1.62 – 1.55 (m, 2H), 1.32 – 1.19 (m, 4H), 0.97 (s, 6H), and 0.86 (t, $J = 7.1$ Hz, 3H). ^{13}C NMR (125 MHz, CDCl_3) δ_{C} (ppm) 185.0, 181.1, 174.1, 154.1, 135.1, 133.1, 129.1, 127.1, 126.1, 121.9, 72.7, 36.7, 34.5, 32.1, 31.4, 25.2, 24.1, 22.4, and 14.1.

3-(3-Hydroxy-1,4-dioxo-1,4-dihydronaphthalen-2-yl)-2,2-dimethylpropyl octanoate (**5**) was obtained as a yellow powder in 86% yield after column chromatography, eluting with hexanes:EtOAc (4:1).

^1H NMR (500 MHz, CDCl_3) δ_{H} (ppm) 8.11 (d, $J = 7.6$ Hz, 1H), 8.08 (d, $J = 7.6$ Hz, 1H), 7.75 (t, $J = 6.7$ Hz, 1H), 7.68 (t, $J = 7.4$ Hz, 1H), 7.50 (s, 1H), 3.84 (s, 2H), 2.67 (s, 2H), 2.25 (t, $J = 7.6$ Hz, 2H), 1.62 – 1.51 (m, 2H), 1.24 (d, $J = 4.2$ Hz, 8H), and 0.97 (s, 6H), 0.90 – 0.78 (m, 3H). ^{13}C NMR (125 MHz, CDCl_3) δ_{C} (ppm) 185.0, 181.4, 174.1, 154.4, 135.1, 133.1, 133.0, 129.5, 127.1, 126.2, 121.9, 72.7, 36.9, 34.5, 32.1, 31.8, 29.8, 29.3, 29.0, 25.2, 25.1, 22.7, and 14.3.

3-(3-Hydroxy-1,4-dioxo-1,4-dihydronaphthalen-2-yl)-2,2-dimethylpropyl nonanoate (**6**) was obtained as a yellow powder in 80% yield after column chromatography, eluting with hexanes:EtOAc (9:1).

^1H NMR (500 MHz, CDCl_3) δ_{H} (ppm) 8.10 (d, $J = 7.7$ Hz, 1H), 8.07 (d, $J = 7.7$ Hz, 1H), 7.75 (t, $J = 7.6$ Hz, 1H), 7.68 (t, $J = 7.6$ Hz, 1H), 7.53 (s, 1H), 3.84 (s, 2H), 2.66 (s, 2H), 2.24 (t, $J = 7.6$ Hz, 2H), 1.60 – 1.52 (m, 2H), 1.32 – 1.18 (m, 10H), 0.97 (s, 6H), and 0.85 (t, $J = 7.0$ Hz, 3H). ^{13}C NMR (125 MHz, CDCl_3) δ_{C} (ppm) 185.0, 180.9, 174.1, 154.4, 135.1, 133.1, 129.5, 127.1, 126.2, 121.9, 72.7, 36.9, 34.5, 32.1, 31.9, 29.3, 29.3, 29.3, 25.2, 25.1, 22.8, and 14.2.

3-(3-Hydroxy-1,4-dioxo-1,4-dihydronaphthalen-2-yl)-2,2-dimethylpropyl dodecanoate (**7**) was obtained as a yellow powder in 87% yield after column chromatography, eluting with hexanes:EtOAc (9:1).

^1H NMR (500 MHz, CDCl_3) δ_{H} (ppm) 8.11 (d, $J = 7.7$ Hz, 1H), 8.08 (d, $J = 7.4$ Hz, 1H), 7.76 (t, $J = 7.6$ Hz, 1H), 7.69 (t, $J = 7.4$ Hz, 1H), 7.47 (s, 1H), 3.84 (s, 2H), 2.67 (s, 2H), 2.25 (t, $J = 7.6$ Hz, 2H), 1.69 (s, 2H), 1.58 (t, $J = 7.3$ Hz, 2H), 1.32 – 1.16 (br s, 16H), 0.98 (s, 6H), and 0.86 (t, $J = 6.9$ Hz, 3H). ^{13}C NMR (125 MHz, CDCl_3) δ_{C} (ppm) 185.0, 181.4, 174.1, 154.3, 135.1, 133.1, 129.5, 127.2, 126.3, 121.9, 77.4, 77.7, 76.9, 72.7, 36.9, 34.6, 32.1, 32.0, 29.7, 29.6, 29.5, 29.4, 29.3, 25.2, 25.1, 22.8, and 14.3.

3-(3-Hydroxy-1,4-dioxo-1,4-dihydronaphthalen-2-yl)-2,2-dimethylpropyl tetradecanoate (**8**) was obtained as a yellow powder in 80% yield after column chromatography, eluting with hexanes:EtOAc (9:1).

^1H NMR (500 MHz, CDCl_3) δ_{H} (ppm) 8.12 (d, $J = 7.7$ Hz, 1H), 8.09 (d, $J = 7.7$ Hz, 1H), 7.76 (t, $J = 7.6$ Hz, 1H), 7.69 (t, $J = 7.6$ Hz, 1H), 7.44 (s, 1H), 3.84 (s, 2H), 2.67 (s, 2H), 2.25 (t, $J = 7.6$ Hz, 2H), 1.65 (s, 2H), 1.60 – 1.55 (m, 2H), 1.24 (s, 20H), 0.98 (s, 6H), and 0.87 (t, 3H). ^{13}C NMR (125 MHz, CDCl_3) δ_{C} (ppm) 185.0, 181.4, 174.1, 154.3, 135.1, 133.1, 129.5, 127.2, 126.3, 121.9, 72.7, 36.9, 34.6, 32.1, 32.1, 29.9, 29.8, 29.8, 29.6, 29.5, 29.4, 29.3, 25.2, 25.1, 22.8, and 14.3.

3-(3-Hydroxy-1,4-dioxo-1,4-dihydronaphthalen-2-yl)-2,2-dimethylpropyl benzoate (**9**) was obtained as a yellow powder in 80% yield after column chromatography, eluting with hexanes:EtOAc (9:1).

^1H NMR (500 MHz, CDCl_3) δ_{H} (ppm) 8.05 (d, $J = 7.7$ Hz, 2H), 7.99 (d, $J = 6.9$ Hz, 2H), 7.72 – 7.63 (m, 2H), 7.51 – 7.47 (m, 1H), 7.45 (s, 1H), 7.35 (t, $J = 7.9$ Hz, 2H), 4.10 (s, 2H), 2.78 (s, 2H), and 1.10 (s, 6H). ^{13}C NMR (125 MHz, CDCl_3) δ_{C} (ppm) 185.1, 181.3, 166.7, 154.4, 135.1, 133.1, 133.0, 132.9, 130.5, 129.6, 129.4, 128.4, 127.2, 126.2, 121.8, 73.3, 37.2, 32.4, and 25.4.

3-(3-Hydroxy-1,4-dioxo-1,4-dihydronaphthalen-2-yl)-2,2-dimethylpropyl 2-phenylacetate (**10**) was obtained as a yellow powder in 80% yield after column chromatography, eluting with hexanes:EtOAc (9:1).

^1H NMR (500 MHz, CDCl_3) δ_{H} (ppm) 8.11 (d, $J = 7.7$ Hz, 1H), 8.08 (d, $J = 7.7$ Hz, 1H), 7.75 (t, $J = 7.6$ Hz, 1H), 7.68 (t, $J = 7.6$ Hz, 1H), 7.28 (t, $J = 7.9$ Hz, 2H), 7.25 (t, $J = 7.9$ Hz, 2H), 7.22 (s, 1H), 3.86 (s, 2H), 3.60 (s, 2H), 2.63 (s, 2H), and 0.93 (s, 6H). ^{13}C NMR (125 MHz, CDCl_3) δ_{C} (ppm) 184.9, 181.3, 171.8, 154.4, 135.1, 134.2, 133.1, 129.4, 128.6, 127.1, 126.2, 121.7, 73.1, 41.6, 36.9, 31.9, and 25.0. HRMS (ESI) calcd for $\text{C}_{23}\text{H}_{22}\text{O}_5$ $[\text{M} + \text{H}]^+$: 378.1467, found 379.1467.

3-(3-Hydroxy-1,4-dioxo-1,4-dihydronaphthalen-2-yl)-2,2-dimethylpropyl 3-phenylpropanoate (**11**) was obtained as a yellow powder in 80% yield after column chromatography, eluting with hexanes:EtOAc (9:1).

^1H NMR (500 MHz, CDCl_3) δ_{H} (ppm) 7.99 (d, $J = 7.7$ Hz, 1H), 7.96 (d, $J = 6.3$ Hz, 1H), 7.63 (t, $J = 7.6$ Hz, 1H), 7.56 (m, 1H), 7.17 – 7.13 (m, 2H), 7.09 (m, 1H), 7.04 (dd, $J = 8.2$, 1.3 Hz, 2H), 3.71 (s, 2H), 2.81 (t, $J = 7.9$ Hz, 2H), 2.53 (s, 2H), 2.50 – 2.46 (m, 2H), and 0.83 (s, 6H). ^{13}C NMR (125 MHz, CDCl_3) δ_{C} (ppm) 185.0, 181.3, 173.1, 154.4, 140.7, 135.1, 133.1, 133.0, 129.5, 128.6, 128.4, 127.1, 126.3, 126.3, 121.7, 77.4, 77.2, 76.9, 72.8, 36.9, 35.9, 31.9, 31.1, 31.0, and 25.1. HRMS (ESI) calcd for $\text{C}_{24}\text{H}_{24}\text{O}_5$ $[\text{M} + \text{H}]^+$: 392.1624, found 393.1697.

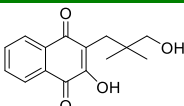
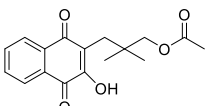
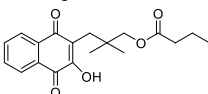
α -Glucosidase inhibition assay

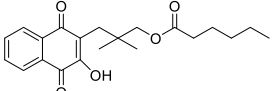
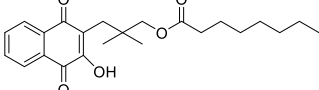
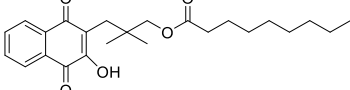
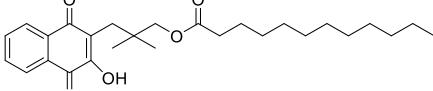
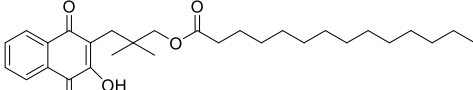
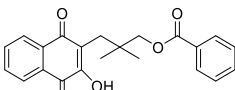
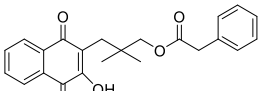
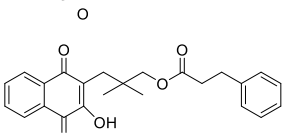
This activity was performed by the method described by Ramadhan and coworkers with little modification.⁹ The α -glucosidase (0.4 U/mL) was prepared using 0.1 M, buffer (pH 6.9) and the substrate (3 mM *p*-nitrophenyl- α -D-glucopyranoside) was dissolved in 0.1M phosphate buffer (pH 6.9). 4 mM of the stock sample were prepared using DMSO, then 1 mM of the loading sample was prepared from the stock sample. 10 μL of the loading sample was pipetted into the 96 well plate followed by the addition of 40 μL of the α -glucosidase enzyme and incubated at 37 $^\circ\text{C}$ for 10min. subsequently, 50 μL substrate solution was added to the reaction mixture and incubated further at 37 $^\circ\text{C}$ for 20 min and the reaction was terminated by adding 100 μL of 1M Na_2CO_3 solution. Enzymatic activity was quantified by measuring the absorbance at 405 nm (ALLSHENG AMR-100 microplate reader). The percentage inhibition was calculated as follows: % Inhibition = $[(A_0 - A_1)/A_0] \times 100$, where: A_0 is the absorbance without the sample; A_1 is the absorbance with the sample. The IC_{50} value was deduced from the plot of % inhibition versus concentration of the test sample. Acarbose was used as a positive control and the experiment was performed in triplicate.

Results and Discussion:

Two new (**10** and **11**) and eight known naphthoquinone esters (**2-9**)^{10,11} were synthesized and screened for α -glucosidase inhibitory activity. Compounds **5-8** showed good activity towards α -glucosidase than the positive control with the IC_{50} values of 36.48 ± 2.74 (**5**), 5.83 ± 0.59 (**6**), 2.6 ± 0.64 (**7**) and 5.3 ± 0.50 (**8**) μM , respectively. This result showed that the increment of chain length significantly increased the activity. The activity increased progressively from C2 (**2**) to C12 (**7**) and the activity dropped at C14 (**8**). Compounds containing benzoate showed better inhibitory activity when the carbon chain length was increased from 1 to 3 % inhibition was increased from 1.00 to 42.09%. Comparing **3** and **11** with similar chain length, it was observed that **11** with benzoate showed better inhibitory activity towards α -glucosidase. Compound **7** exhibited the best activity in this series.

Table 1 α -Glucosidase inhibitory activity of naphthoquinone aliphatic esters

Compound	Structure	% Inhibition at 50 μM	IC_{50} (μM) ^a
1		55.41	– ^b
2		9.84	– ^b
3		13.09	– ^b

4		17.01	- ^b
5		79.48	36.48 ± 2.74
6		98.14	5.83 ± 0.59
7		100.00	2.60 ± 0.64
8		84.14	5.30 ± 0.50
9		-	- ^b
10		1.00	- ^b
11		42.09	- ^b
Acarbose			836.00 ± 47.19

^a IC₅₀ value was expressed as mean ± SD from three independent experiments.

^b IC₅₀ value was not tested if the inhibition rate was less than 70% at 50 μM.

Kinetic study of **7** and α-glucosidase

The enzyme kinetics study of **7** was performed to understand the inhibition mode of the compound against α-glucosidase. The kinetic study was carried out using different concentrations of the substrate *p*-nitrophenyl-α-D-glucosidase (PNPG) at 0.38, 0.19, 0.01, and 0.05 mM in the presence and absence of the inhibitors with varying concentrations. The result was analyzed with Lineweaver-Burk plots. It was found that *K_m* increased whereas *V_{max}* was unchanged, indicating that **7** inhibition mode was competitive with α-glucosidase. The *K_i* value of 14.64 μM was calculated using secondary replot of the Lineweaver-Burk plot against the varying concentrations of the inhibitors at 0.00, 2.60 and 5.20 μM.

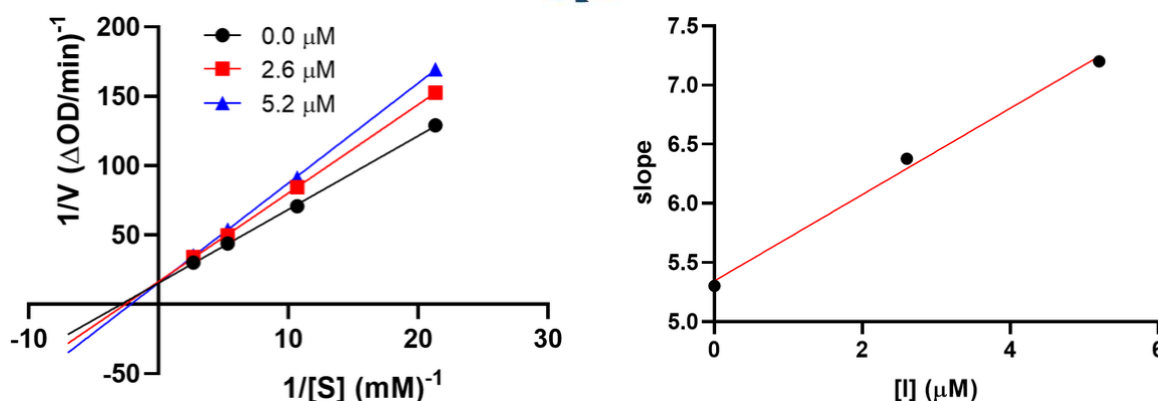


Figure 1. Kinetic study of **7**. The Lineweaver-Burk plot for α -glucosidase inhibition and plots of slope against different concentration of **7** for K_i determination.

Conclusion:

Ten naphthoquinone aliphatic esters derivatives were successfully synthesized, characterized, and evaluated for α -glucosidase inhibitory activity. Four derivatives (**5**, **6**, **7** and **8**) displayed potential inhibition with the IC_{50} values ranging from 36.48 ± 2.74 to $2.6 \pm 0.64 \mu M$ better than the starting material and the positive control, acarbose. The SARs indicates that increase in the carbon chain length of the aliphatic carbons increased the inhibition of the α -glucosidase.

Acknowledgements:

Felicitas Ene is grateful to the Chulalongkorn University's ASEAN or Non-ASEAN Scholarship.

References:

1. Khan I, Rehman W, Rahim F, Hussain R, Khan S, Fazil S, Rasheed L, Taha M, Shah SA, Abdellatif MH. J Pharm. 2023;16-17.
2. Si MM, Lou JS, Zhou CX, Shen JN, Wu HH, Yang B, He QJ, Wu HS. J Ethnopharmacol. 2010;128:154-159.
3. Fisman EZ, Michael M, Tenenbaum A. Adv Cardiol. 2008;154-170.
4. Adam SH, Giribabu N, Rao PV, Sayem AS, Arya A, Panichayupakaranant P. Eur J Pharmacol. 2016;771:173-90.
5. Shah MA, Khalil R, Ul-Haq Z, Panichayupakaranant P. J Funct Foods. 2017;36:325-331.
6. Kongkathip B, Akkarasamiyo S, Hasitapan K, Sittikul P, Kongkathip N. Eur J Med Chem. 2013;60:271-284.
7. Pallavi HM, Al-Ostoot HF, Vivek HK, Khanum SA. J Mol Struct. 2002;1247:131-404.
8. Li GL, Cai CY, He J, Rao LI. Bioorg Med Chem. 2016;24;7:1431-1438.
9. Ramadhan R, Phuwapraisirisan P. Bioorg Med Chem Lett. 2015;25:4529-4533.
10. Kongkathip N, Pradidphol N, Hasitapan K, Grigg R, Kao WC, Hunte C, Fisher N, Warman AJ, Biagini GA, Kongsaree P. J Med Chem. 2010;53;3:1211-1221.
11. Kongkathip N, Luangkamin S, Kongkathip B, Sangma C, Grigg R, Kongsaree P, Prabpai S, Pradidphol N, Piyaviriyagul S, Siripong P. J Med Chem. 2004;47;18:4427-4438.



SESSION D-MATHEMATICS / STATISTICS / COMPUTER SCIENCE / DATA SCIENCE / AI



A NOTE ON FUZZY SEMIBIPOLAR SOFT IDEALS IN ORDERED GROUPOIDS

Rukchart Prasertpong,^{1*} Nares Sawatraksa¹

¹Division of Mathematics and Statistics, Faculty of Science and Technology, Nakhon Sawan Rajabhat University, Nakhon Sawan 60000, Thailand

*e-mail: rukchart.p@nsru.ac.th

Abstract:

Based on the concept of fuzzy semibipolar soft set theory, in this paper, we propose the operations on fuzzy semibipolar soft sets. At this point, the union and intersection of two fuzzy semibipolar soft sets are introduced and provide an example to illustrate the newly established ideas. We then verify the properties of idempotent, identity, commutative, associative, absorption, and distributive. In ordered groupoids, we investigate fuzzy semibipolar soft left (resp., right) ideals via the union and intersection. To support such an examination, we also present the product of two fuzzy semibipolar soft sets.

Introduction:

The concept of fuzzy set theory, generated by Zadeh [1], is an important mathematical tool for the development of algebraic research areas. It is an effective function used for the description or support of the study of algebraic structures. In the first step of the development, in 1971, the concept of fuzzy groups was proposed by Rosenfeld [2]. Therefore, the study based on the fuzzy set theory of other structures such as groupoids, semigroups, rings, and so on has attracted many researchers. At this point, Kuroki [3] proposed the notion of fuzzy ideals and fuzzy bi-ideals in semigroups. In further focus, we know that Molodtsov's soft set theory [4] is one of an extended notion of fuzzy set theory. The algebraic structure is also connected with such an extension. The concept of soft groups is an initial idea generated by soft set theory. This concept was proposed by Aktas and Cagman [5] in 2007 and their properties extend the notion of a group to include the algebraic structures of soft sets. Acar et al. [6] introduced the concept of soft rings in 2010. In the same year, Ali et al. [7] presented the notion of soft semigroups. As examined, observed that the ideal theory is an important section of these developed notions.

Recently, the concept of fuzzy semibipolar soft sets given by Prasertpong [8] is proposed as an extended notion of fuzzy sets and soft sets. Then, in this paper, the combination of ideal theory and such an extended notion is considered. The concept of fuzzy semibipolar soft left (resp., right) ideals, generated in [8], is verified via the union and intersection operation of two fuzzy semibipolar soft sets. The remainder of this paper is organized as follows. In the preliminary section, we shall review some of the earlier definitions and results for the background. In the result section, the contributions of the section are as follows.

1. We introduce the union and intersection operation of two fuzzy semibipolar soft sets and consider the corresponding example.
2. We investigate the properties of idempotent, identity, commutative, associative, absorption, and distributive based on the union and intersection concepts.
3. We establish the product of two fuzzy semibipolar soft sets in ordered semigroups.
4. We investigate fuzzy semibipolar soft left (resp., right) ideals via the union and intersection. At this point, it is proved by using the product of two fuzzy semibipolar soft sets.

In the end, conclusions are summarized in the last section.

Preliminaries:

In this section, we first recall some properties and definitions which will be used in subsequent sections. Throughout this work, A, B , and U denote non-empty sets.

Definition 1. [1] f is said to be a fuzzy subset of U if it is a function from U to the closed unit interval $[0,1]$. Throughout this paper, $\mathcal{F}(U)$ denotes a collection of all fuzzy subsets of U . For all $u \in U$, 1_U is denoted as a fuzzy subset of U defined by $1_U(u) = 1$, and 0_U is denoted as a fuzzy subset of U defined by $0_U(u) = 0$. For $f, g \in \mathcal{F}(U)$, let $f \tilde{\vee} g, f \tilde{\wedge} g$, and $f \tilde{+} g$ be fuzzy subsets of U defined by

$$(f \tilde{\vee} g)(u) := \max\{f(u), g(u)\},$$

$$(f \tilde{\wedge} g)(u) := \min\{f(u), g(u)\},$$

and

$$(f \tilde{+} g)(u) := f(u) + g(u)$$

for all $u \in U$. For $f, g \in \mathcal{F}(U)$, we write $f \tilde{\leq} g$ instead of $f(u) \leq g(u)$ for all $u \in U$. In this way, the statement $f \tilde{\geq} g$ means $g \tilde{\leq} f$.

Remark 1. [1] According to Definition 1, it is obvious that 1_U is the greatest element of $\mathcal{F}(U)$, and 0_U is the least element of $\mathcal{F}(U)$.

Proposition 1. [9] Let $\{f_i : i \in I\}$ be a non-empty family of all fuzzy subsets of U . Define

$$\left(\bigcup_{i \in I} f_i\right)(u) := \sup\{f_i(u) : i \in I\}$$

and

$$\left(\bigcap_{i \in I} f_i\right)(u) := \inf\{f_i(u) : i \in I\}$$

for all $u \in U$. Then $\bigcup_{i \in I} f_i, \bigcap_{i \in I} f_i \in \mathcal{F}(U)$. Furthermore,

$$\bigcup_{i \in I} f_i = \sup\{f_i : i \in I\}$$

and

$$\bigcap_{i \in I} f_i = \inf\{f_i : i \in I\}.$$

Definition 2. [8] A triple $(\mathbb{F}, \neg\mathbb{F}, A)$ is said to be a fuzzy semibipolar soft set over U with respect to A if $\mathbb{F} : A \rightarrow \mathcal{F}(U)$ and $\neg\mathbb{F} : A \rightarrow \mathcal{F}(U)$ are disjoint functions such that $\mathbb{F}(a) \tilde{+} \neg\mathbb{F}(a) = 1_U$ for all $a \in A$. Throughout this work, $\mathcal{C}(U \sim A)$ is denoted as the collection of all fuzzy semibipolar soft sets over U with respect to A .

Definition 3. [8] Let $\mathfrak{F} := (\mathbb{F}, \neg\mathbb{F}, A) \in \mathcal{C}(U \sim A)$ and $\mathfrak{G} := (\mathbb{G}, \neg\mathbb{G}, B) \in \mathcal{C}(U \sim B)$. We say that \mathfrak{F} is a fuzzy semibipolar soft subset of \mathfrak{G} , denoted by $\mathfrak{F} \subseteq \mathfrak{G}$, if it satisfies two conditions below.

1. $A \subseteq B$.
2. $\mathbb{F}(a) \tilde{\leq} \mathbb{G}(a)$ and $\neg\mathbb{F}(a) \tilde{\geq} \neg\mathbb{G}(a)$ for all $a \in A$.

The statement $\mathfrak{F} = \mathfrak{G}$ means $\mathfrak{F} \subseteq \mathfrak{G}$ and $\mathfrak{G} \subseteq \mathfrak{F}$.



Definition 4. [8] If $\mathfrak{F} := (\mathbb{F}, \neg\mathbb{F}, A) \in \mathcal{C}(U \sim A)$ is defined by $\mathbb{F}(a) = 1_U$ and $\neg\mathbb{F}(a) = 0_U$ for all $a \in A$, then \mathfrak{F} is said to be a relative whole fuzzy semibipolar soft set over U with respect to A . Throughout this paper, we denote $\mathfrak{W}_A := (\mathbb{W}_A, \neg\mathbb{W}_A, A)$ instead of a relative whole fuzzy semibipolar soft set over U with respect to A .

Definition 5. [8] If $\mathfrak{F} := (\mathbb{F}, \neg\mathbb{F}, A) \in \mathcal{C}(U \sim A)$ is defined by $\mathbb{F}(a) = 0_U$ and $\neg\mathbb{F}(a) = 1_U$ for all $a \in A$, then \mathfrak{F} is said to be a relative null fuzzy semibipolar soft set over U with respect to A . Throughout this paper, we denote $\mathfrak{N}_A := (\mathbb{N}_A, \neg\mathbb{N}_A, A)$ instead of a relative null fuzzy semibipolar soft set over U with respect to A .

Definition 6. [10] A groupoid is a non-empty set A together with a binary operation $*$ on A , denoted by $(A, *)$. If $(A, *)$ is a groupoid, then we write ab instead of $a * b$ for all $a, b \in A$.

Definition 7. [10] Let \leq_A be a binary relation on A . An ordered groupoid, denoted by $(A, *, \leq_A)$, is a groupoid $(A, *)$ whose elements of A are partially ordered by \leq_A satisfying with the property that for all $a, b, x \in A, a \leq_A b$ implies $xa \leq_A xb$ and $ax \leq_A bx$.

Definition 8. [8] Let $(A, *, \leq_A)$ be an ordered groupoid. $\mathfrak{F} := (\mathbb{F}, \neg\mathbb{F}, A) \in \mathcal{C}(U \sim A)$ is called a fuzzy semibipolar soft left ideal if it satisfies two conditions below.

1. $\mathbb{F}(ab) \tilde{\geq} \mathbb{F}(b)$ and $\neg\mathbb{F}(ab) \tilde{\leq} \neg\mathbb{F}(b)$ for all $a, b \in A$.
2. For all $a, b \in A, a \leq_A b$ implies $\mathbb{F}(a) \tilde{\geq} \mathbb{F}(b)$ and $\neg\mathbb{F}(a) \tilde{\leq} \mathbb{F}(b)$.

Definition 9. [8] Let $(A, *, \leq_A)$ be an ordered groupoid. $\mathfrak{F} := (\mathbb{F}, \neg\mathbb{F}, A) \in \mathcal{C}(U \sim A)$ is called a fuzzy semibipolar soft right ideal if it satisfies two conditions below.

1. $\mathbb{F}(ab) \tilde{\geq} \mathbb{F}(a)$ and $\neg\mathbb{F}(ab) \tilde{\leq} \neg\mathbb{F}(a)$ for all $a, b \in A$.
2. For all $a, b \in A, a \leq_A b$ implies $\mathbb{F}(a) \tilde{\geq} \mathbb{F}(b)$ and $\neg\mathbb{F}(a) \tilde{\leq} \mathbb{F}(b)$.

Results:

In this section, we find the fuzzy semibipolar soft left (resp., right) ideals via operations.

Definition 10. Let $\mathfrak{F} := (\mathbb{F}, \neg\mathbb{F}, A), \mathfrak{G} := (\mathbb{G}, \neg\mathbb{G}, A) \in \mathcal{C}(U \sim A)$.

1. We say that $\mathfrak{F} \tilde{\cup} \mathfrak{G} := ((\mathbb{F} \tilde{\cup} \mathbb{G}), \neg(\mathbb{F} \tilde{\cup} \mathbb{G}), A)$ is a fuzzy semibipolar soft union over U with respect to A if $\mathfrak{F} \tilde{\cup} \mathfrak{G} \in \mathcal{C}(U \sim A)$ is defined by

$$(\mathbb{F} \tilde{\cup} \mathbb{G})(a) = \mathbb{F}(a) \tilde{\vee} \mathbb{G}(a)$$

and

$$\neg(\mathbb{F} \tilde{\cup} \mathbb{G})(a) = \neg\mathbb{F}(a) \tilde{\wedge} \neg\mathbb{G}(a)$$

for all $a \in A$.

2. We say that $\mathfrak{F} \tilde{\cap} \mathfrak{G} := ((\mathbb{F} \tilde{\cap} \mathbb{G}), \neg(\mathbb{F} \tilde{\cap} \mathbb{G}), A)$ is a fuzzy semibipolar soft intersection over U with respect to A if $\mathfrak{F} \tilde{\cap} \mathfrak{G} \in \mathcal{C}(U \sim A)$ is defined by

$$(\mathbb{F} \tilde{\cap} \mathbb{G})(a) = \mathbb{F}(a) \tilde{\wedge} \mathbb{G}(a)$$

and

$$\neg(\mathbb{F} \tilde{\cap} \mathbb{G})(a) = \neg\mathbb{F}(a) \tilde{\vee} \neg\mathbb{G}(a)$$

for all $a \in A$.

Example 1. Suppose that $\mathfrak{F} := (\mathbb{F}, \neg\mathbb{F}, A), \mathfrak{G} := (\mathbb{G}, \neg\mathbb{G}, A) \in \mathcal{C}(U \sim A)$ are defined by

$$\mathbb{F}(a) = 1_U = \neg\mathbb{G}(a)$$

and

$$\neg\mathbb{F}(a) = 0_U = \mathbb{G}(a)$$

for all $a \in A$. Then, it is easy to see that

$$(\mathbb{F} \tilde{\cup} \mathbb{G})(a) = \mathbb{F}(a) \tilde{\vee} \mathbb{G}(a) = 1_U$$

and

$$\neg(\mathbb{F} \tilde{\cup} \mathbb{G})(a) = \neg\mathbb{F}(a) \tilde{\wedge} \neg\mathbb{G}(a) = 0_U$$

for all $a \in A$. Observe that

$$(\mathbb{F} \tilde{\cup} \mathbb{G})(a) \tilde{\dot{+}} \neg(\mathbb{F} \tilde{\cup} \mathbb{G})(a) = 1_U \tilde{\dot{+}} 0_U = 1_U$$

for all $a \in A$. Thus

$$\mathfrak{F} \tilde{\cup} \mathfrak{G} := ((\mathbb{F} \tilde{\cup} \mathbb{G}), \neg(\mathbb{F} \tilde{\cup} \mathbb{G}), A) \in \mathcal{C}(U \sim A).$$

Moreover, we obtain that $\mathfrak{F} \tilde{\cup} \mathfrak{G} = \mathfrak{W}_A$. Consider,

$$(\mathbb{F} \tilde{\cap} \mathbb{G})(a) = \mathbb{F}(a) \tilde{\wedge} \mathbb{G}(a) = 0_U$$

and

$$\neg(\mathbb{F} \tilde{\cap} \mathbb{G})(a) = \neg\mathbb{F}(a) \tilde{\vee} \neg\mathbb{G}(a) = 1_U$$

for all $a \in A$. We see that

$$(\mathbb{F} \tilde{\cap} \mathbb{G})(a) \tilde{\dot{+}} \neg(\mathbb{F} \tilde{\cap} \mathbb{G})(a) = 0_U \tilde{\dot{+}} 1_U = 1_U$$

for all $a \in A$. Whence

$$\mathfrak{F} \tilde{\cap} \mathfrak{G} := ((\mathbb{F} \tilde{\cap} \mathbb{G}), \neg(\mathbb{F} \tilde{\cap} \mathbb{G}), A) \in \mathcal{C}(U \sim A).$$

Obviously, $\mathfrak{F} \tilde{\cap} \mathfrak{G} = \mathfrak{N}_A$.

Theorem 1. Let $\mathfrak{F} := (\mathbb{F}, \neg\mathbb{F}, A), \mathfrak{G} := (\mathbb{G}, \neg\mathbb{G}, A), \mathfrak{H} := (\mathbb{H}, \neg\mathbb{H}, A) \in \mathcal{C}(U \sim A)$. Then, the following properties hold.

1. *Idempotent laws:*

$$\begin{aligned} \mathfrak{F} \tilde{\cup} \mathfrak{F} &= \mathfrak{F}, \\ \mathfrak{F} \tilde{\cap} \mathfrak{F} &= \mathfrak{F}. \end{aligned}$$

2. *Identity laws:*

$$\begin{aligned} \mathfrak{F} \tilde{\cup} \mathfrak{W}_A &= \mathfrak{W}_A, \mathfrak{F} \tilde{\cap} \mathfrak{W}_A = \mathfrak{F}, \\ \mathfrak{F} \tilde{\cup} \mathfrak{N}_A &= \mathfrak{F}, \mathfrak{F} \tilde{\cap} \mathfrak{N}_A = \mathfrak{N}_A. \end{aligned}$$

3. *Commutative laws:*

$$\begin{aligned} \mathfrak{F} \tilde{\cup} \mathfrak{G} &= \mathfrak{G} \tilde{\cup} \mathfrak{F}, \\ \mathfrak{F} \tilde{\cap} \mathfrak{G} &= \mathfrak{G} \tilde{\cap} \mathfrak{F}. \end{aligned}$$



4. *Associative laws:*

$$\mathfrak{F} \circ (\mathfrak{G} \circ \mathfrak{H}) = (\mathfrak{F} \circ \mathfrak{G}) \circ \mathfrak{H},$$

$$\mathfrak{F} \sim (\mathfrak{G} \sim \mathfrak{H}) = (\mathfrak{F} \sim \mathfrak{G}) \sim \mathfrak{H}.$$

5. *Absorption laws:*

$$\mathfrak{F} \circ (\mathfrak{F} \sim \mathfrak{G}) = \mathfrak{F},$$

$$\mathfrak{F} \sim (\mathfrak{F} \circ \mathfrak{G}) = \mathfrak{F}.$$

6. *Distributive laws:*

$$\mathfrak{F} \circ (\mathfrak{G} \sim \mathfrak{H}) = (\mathfrak{F} \circ \mathfrak{G}) \sim (\mathfrak{F} \circ \mathfrak{H}),$$

$$\mathfrak{F} \sim (\mathfrak{G} \circ \mathfrak{H}) = (\mathfrak{F} \sim \mathfrak{G}) \circ (\mathfrak{F} \sim \mathfrak{H}).$$

Proof. We consider the following proofs.

1. We have $\mathfrak{F} \circ \mathfrak{F} = \mathfrak{F}$. Indeed, since

$$(\mathbb{F}(a) \vee \mathbb{F}(a))(u) = \max \{ \mathbb{F}(a)(u), \mathbb{F}(a)(u) \}$$

and

$$\max \{ \mathbb{F}(a)(u), \mathbb{F}(a)(u) \} = \mathbb{F}(a)(u)$$

for all $a \in A, u \in U$, we have

$$\mathbb{F}(a) \vee \mathbb{F}(a) = \mathbb{F}(a)$$

for all $a \in A$. Thus

$$(\mathbb{F} \circ \mathbb{F})(a) = \mathbb{F}(a) \vee \mathbb{F}(a) = \mathbb{F}(a)$$

for all $a \in A$. Since

$$(\neg \mathbb{F}(a) \wedge \neg \mathbb{F}(a))(u) = \min \{ \neg \mathbb{F}(a)(u), \neg \mathbb{F}(a)(u) \}$$

and

$$\min \{ \neg \mathbb{F}(a)(u), \neg \mathbb{F}(a)(u) \} = \neg \mathbb{F}(a)(u)$$

for all $a \in A, u \in U$, we have

$$\neg \mathbb{F}(a) \wedge \neg \mathbb{F}(a) = \neg \mathbb{F}(a)$$

for all $a \in A$. Hence

$$\neg (\mathbb{F} \sim \mathbb{F})(a) = \neg \mathbb{F}(a) \wedge \neg \mathbb{F}(a) = \neg \mathbb{F}(a)$$

for all $a \in A$. Therefore $\mathfrak{F} \circ \mathfrak{F} = \mathfrak{F}$. Similarly, we can prove that $\mathfrak{F} \sim \mathfrak{F} = \mathfrak{F}$.

2. We have $\mathfrak{F} \circ \mathfrak{W}_A = \mathfrak{W}_A$. Indeed, since

$$(\mathbb{F}(a) \vee \mathbb{W}_A(a))(u) = \max \{ \mathbb{F}(a)(u), \mathbb{W}_A(a)(u) \}$$

and

$$\begin{aligned} \max \{ \mathbb{F}(a)(u), \mathbb{W}_A(a)(u) \} &= \max \{ \mathbb{F}(a)(u), 1_U(u) \} \\ &= \max \{ \mathbb{F}(a)(u), 1 \} \\ &= 1 \\ &= 1_U(u) \\ &= \mathbb{W}_A(a)(u) \end{aligned}$$

for all $a \in A, u \in U$, we see that

$$\mathbb{F}(a) \tilde{\vee} \mathbb{W}_A(a) = \mathbb{W}_A(a)$$

for all $a \in A$. Thus

$$(\mathbb{F} \tilde{\cup} \mathbb{W}_A)(a) = \mathbb{F}(a) \tilde{\vee} \mathbb{W}_A(a) = \mathbb{W}_A(a)$$

for all $a \in A$. Since

$$(\neg \mathbb{F}(a) \tilde{\wedge} \neg \mathbb{W}_A(a))(u) = \min \{ \neg \mathbb{F}(a)(u), \neg \mathbb{W}_A(a)(u) \}$$

and

$$\begin{aligned} \min \{ \neg \mathbb{F}(a)(u), \neg \mathbb{W}_A(a)(u) \} &= \min \{ \neg \mathbb{F}(a)(u), 0_U(u) \} \\ &= \min \{ \neg \mathbb{F}(a)(u), 0 \} \\ &= 0 \\ &= 0_U(u) \\ &= \neg \mathbb{W}_A(a)(u) \end{aligned}$$

for all $a \in A, u \in U$, we have

$$\neg \mathbb{F}(a) \tilde{\wedge} \neg \mathbb{W}_A(a) = \neg \mathbb{W}_A(a)$$

for all $a \in A$. Hence

$$\neg(\mathbb{F} \tilde{\cap} \mathbb{W}_A)(a) = \neg \mathbb{F}(a) \tilde{\wedge} \neg \mathbb{W}_A(a) = \neg \mathbb{W}_A(a)$$

for all $a \in A$. Therefore $\mathfrak{F} \tilde{\cup} \mathfrak{W}_A = \mathfrak{W}_A$. In the same way, we can show that the remainder arguments are true.

3. We have $\mathfrak{F} \tilde{\cup} \mathfrak{G} = \mathfrak{G} \tilde{\cup} \mathfrak{F}$. Indeed, since

$$\begin{aligned} (\mathbb{F}(a) \tilde{\vee} \mathbb{G}(a))(u) &= \max \{ \mathbb{F}(a)(u), \mathbb{G}(a)(u) \} \\ &= \max \{ \mathbb{G}(a)(u), \mathbb{F}(a)(u) \} \\ &= (\mathbb{G}(a) \tilde{\vee} \mathbb{F}(a))(u) \end{aligned}$$

for all $a \in A, u \in U$, we have

$$\mathbb{F}(a) \tilde{\vee} \mathbb{G}(a) = \mathbb{G}(a) \tilde{\vee} \mathbb{F}(a)$$

for all $a \in A$. Thus

$$\begin{aligned} (\mathbb{F} \tilde{\cup} \mathbb{G})(a) &= \mathbb{F}(a) \tilde{\vee} \mathbb{G}(a) \\ &= \mathbb{G}(a) \tilde{\vee} \mathbb{F}(a) \\ &= (\mathbb{G} \tilde{\cup} \mathbb{F})(a) \end{aligned}$$

for all $a \in A$. Since

$$\begin{aligned} (\neg \mathbb{F}(a) \tilde{\wedge} \neg \mathbb{G}(a))(u) &= \min \{ \neg \mathbb{F}(a)(u), \neg \mathbb{G}(a)(u) \} \\ &= \min \{ \neg \mathbb{G}(a)(u), \neg \mathbb{F}(a)(u) \} \\ &= (\neg \mathbb{G}(a) \tilde{\wedge} \neg \mathbb{F}(a))(u) \end{aligned}$$

for all $a \in A, u \in U$, we have

$$\neg \mathbb{F}(a) \tilde{\wedge} \neg \mathbb{G}(a) = \neg \mathbb{G}(a) \tilde{\wedge} \neg \mathbb{F}(a)$$

for all $a \in A$. Hence



$$\begin{aligned}
 \neg(\mathbb{F} \tilde{\cap} \mathbb{G})(a) &= \neg\mathbb{F}(a) \tilde{\wedge} \neg\mathbb{G}(a) \\
 &= \neg\mathbb{G}(a) \tilde{\wedge} \neg\mathbb{F}(a) \\
 &= \neg(\mathbb{G} \tilde{\cap} \mathbb{F})(a)
 \end{aligned}$$

for all $a \in A$. Therefore $\mathfrak{F} \tilde{\cup} \mathfrak{G} = \mathfrak{G} \tilde{\cup} \mathfrak{F}$. Similarly, we can prove that $\mathfrak{F} \tilde{\cap} \mathfrak{G} = \mathfrak{G} \tilde{\cap} \mathfrak{F}$.

4. We have $\mathfrak{F} \tilde{\cup} (\mathfrak{G} \tilde{\cup} \mathfrak{H}) = (\mathfrak{F} \tilde{\cup} \mathfrak{G}) \tilde{\cup} \mathfrak{H}$. In fact,

$$\begin{aligned}
 (\mathbb{F} \tilde{\cup} (\mathbb{G} \tilde{\cup} \mathbb{H}))(a) &= \mathbb{F}(a) \tilde{\vee} (\mathbb{G} \tilde{\cup} \mathbb{H})(a) \\
 &= \mathbb{F}(a) \tilde{\vee} (\mathbb{G}(a) \tilde{\vee} \mathbb{H}(a)) \\
 &= (\mathbb{F}(a) \tilde{\vee} \mathbb{G}(a)) \tilde{\vee} \mathbb{H}(a) \\
 &= (\mathbb{F} \tilde{\cup} \mathbb{G})(a) \tilde{\vee} \mathbb{H}(a) \\
 &= ((\mathbb{F} \tilde{\cup} \mathbb{G}) \tilde{\cup} \mathbb{H})(a)
 \end{aligned}$$

and

$$\begin{aligned}
 \neg(\mathbb{F} \tilde{\cap} (\mathbb{G} \tilde{\cap} \mathbb{H}))(a) &= \neg\mathbb{F}(a) \tilde{\wedge} \neg(\mathbb{G} \tilde{\cap} \mathbb{H})(a) \\
 &= \neg\mathbb{F}(a) \tilde{\wedge} (\neg\mathbb{G}(a) \tilde{\wedge} \neg\mathbb{H}(a)) \\
 &= (\neg\mathbb{F}(a) \tilde{\wedge} \neg\mathbb{G}(a)) \tilde{\wedge} \neg\mathbb{H}(a) \\
 &= \neg(\mathbb{F} \tilde{\cap} \mathbb{G})(a) \tilde{\wedge} \neg\mathbb{H}(a) \\
 &= \neg((\mathbb{F} \tilde{\cap} \mathbb{G}) \tilde{\cap} \mathbb{H})(a)
 \end{aligned}$$

for all $a \in A$. Similarly, we can prove that $\mathfrak{F} \tilde{\cap} (\mathfrak{G} \tilde{\cap} \mathfrak{H}) = (\mathfrak{F} \tilde{\cap} \mathfrak{G}) \tilde{\cap} \mathfrak{H}$.

5. Obviously, $\mathfrak{F} \subseteq \mathfrak{F} \tilde{\cup} (\mathfrak{F} \tilde{\cap} \mathfrak{G})$. Conversely, observe that $\mathfrak{F} \tilde{\cap} \mathfrak{G} \subseteq \mathfrak{F}$. By 1, we have

$$\mathfrak{F} \tilde{\cup} (\mathfrak{F} \tilde{\cap} \mathfrak{G}) \subseteq \mathfrak{F} \tilde{\cup} \mathfrak{F} = \mathfrak{F}.$$

It follows that $\mathfrak{F} \tilde{\cup} (\mathfrak{F} \tilde{\cap} \mathfrak{G}) = \mathfrak{F}$. By 1, once again, we can show that $\mathfrak{F} \tilde{\cap} (\mathfrak{F} \tilde{\cup} \mathfrak{G}) = \mathfrak{F}$.

6. We have $\mathfrak{F} \tilde{\cap} (\mathfrak{G} \tilde{\cup} \mathfrak{H}) = (\mathfrak{F} \tilde{\cap} \mathfrak{G}) \tilde{\cap} (\mathfrak{F} \tilde{\cap} \mathfrak{H})$. In fact,

$$\begin{aligned}
 (\mathbb{F} \tilde{\cap} (\mathbb{G} \tilde{\cup} \mathbb{H}))(a) &= \mathbb{F}(a) \tilde{\wedge} (\mathbb{G} \tilde{\cup} \mathbb{H})(a) \\
 &= \mathbb{F}(a) \tilde{\wedge} (\mathbb{G}(a) \tilde{\vee} \mathbb{H}(a)) \\
 &= (\mathbb{F}(a) \tilde{\wedge} \mathbb{G}(a)) \tilde{\wedge} (\mathbb{F}(a) \tilde{\wedge} \mathbb{H}(a)) \\
 &= (\mathbb{F} \tilde{\cap} \mathbb{G})(a) \tilde{\wedge} (\mathbb{F} \tilde{\cap} \mathbb{H})(a) \\
 &= ((\mathbb{F} \tilde{\cap} \mathbb{G}) \tilde{\cap} (\mathbb{F} \tilde{\cap} \mathbb{H}))(a)
 \end{aligned}$$

and

$$\begin{aligned}
 \neg(\mathbb{F} \tilde{\cap} (\mathbb{G} \tilde{\cup} \mathbb{H}))(a) &= \neg\mathbb{F}(a) \tilde{\vee} \neg(\mathbb{G} \tilde{\cup} \mathbb{H})(a) \\
 &= \neg\mathbb{F}(a) \tilde{\vee} (\neg\mathbb{G}(a) \tilde{\wedge} \neg\mathbb{H}(a)) \\
 &= (\neg\mathbb{F}(a) \tilde{\vee} \neg\mathbb{G}(a)) \tilde{\wedge} (\neg\mathbb{F}(a) \tilde{\vee} \neg\mathbb{H}(a)) \\
 &= \neg(\mathbb{F} \tilde{\cap} \mathbb{G})(a) \tilde{\wedge} \neg(\mathbb{F} \tilde{\cap} \mathbb{H})(a) \\
 &= \neg((\mathbb{F} \tilde{\cap} \mathbb{G}) \tilde{\cup} (\mathbb{F} \tilde{\cap} \mathbb{H}))(a)
 \end{aligned}$$

for all $a \in A$. In the same way, we can verify that $\mathfrak{F} \tilde{\cup} (\mathfrak{G} \tilde{\cap} \mathfrak{H}) = (\mathfrak{F} \tilde{\cup} \mathfrak{G}) \tilde{\cap} (\mathfrak{F} \tilde{\cup} \mathfrak{H})$.

In the following, $A := (A, *, \leq_A)$ is denoted as an ordered groupoid.

Theorem 2. If $\mathfrak{F} := (\mathbb{F}, \neg\mathbb{F}, A), \mathfrak{G} := (\mathbb{G}, \neg\mathbb{G}, A) \in \mathcal{C}(U \sim A)$ are fuzzy semibipolar soft left (resp., right) ideals, then $\mathfrak{F} \tilde{\cap} \mathfrak{G} \in \mathcal{C}(U \sim A)$ is a fuzzy semibipolar soft left (resp., right) ideal.

Proof. Suppose $\mathfrak{F}, \mathfrak{G} \in \mathcal{C}(U \sim A)$ are fuzzy semibipolar soft left ideals, and let $a, b \in A$. Then

$$\begin{aligned}
 (\mathbb{F} \tilde{\cap} \mathbb{G})(ab) &= \mathbb{F}(ab) \tilde{\wedge} \mathbb{G}(ab) \\
 &\tilde{\geq} \mathbb{F}(b) \tilde{\wedge} \mathbb{G}(b) \\
 &= (\mathbb{F} \tilde{\cap} \mathbb{G})(b)
 \end{aligned}$$

and

$$\begin{aligned}
 \neg(\mathbb{F} \tilde{\cap} \mathbb{G})(ab) &= \neg\mathbb{F}(ab) \tilde{\vee} \neg\mathbb{G}(ab) \\
 &\tilde{\leq} \neg\mathbb{F}(b) \tilde{\vee} \neg\mathbb{G}(b) \\
 &= \neg(\mathbb{F} \tilde{\cap} \mathbb{G})(b).
 \end{aligned}$$

Suppose $a \leq_A b$. Then $\mathbb{F}(a) \tilde{\geq} \mathbb{F}(b), \neg\mathbb{F}(a) \tilde{\leq} \neg\mathbb{F}(b), \mathbb{G}(a) \tilde{\geq} \mathbb{G}(b)$, and $\neg\mathbb{G}(a) \tilde{\leq} \neg\mathbb{G}(b)$.

Thus

$$\begin{aligned}
 (\mathbb{F} \tilde{\cap} \mathbb{G})(a) &= \mathbb{F}(a) \tilde{\wedge} \mathbb{G}(a) \\
 &\tilde{\geq} \mathbb{F}(b) \tilde{\wedge} \mathbb{G}(b) \\
 &= (\mathbb{F} \tilde{\cap} \mathbb{G})(b)
 \end{aligned}$$

and

$$\begin{aligned}
 \neg(\mathbb{F} \tilde{\cap} \mathbb{G})(a) &= \neg\mathbb{F}(a) \tilde{\vee} \neg\mathbb{G}(a) \\
 &\tilde{\leq} \neg\mathbb{F}(b) \tilde{\vee} \neg\mathbb{G}(b) \\
 &= \neg(\mathbb{F} \tilde{\cap} \mathbb{G})(b).
 \end{aligned}$$

Hence $\mathfrak{F} \tilde{\cap} \mathfrak{G} \in \mathcal{C}(U \sim A)$ is a fuzzy semibipolar soft left ideal.

Definition 11. Let $\mathfrak{F} := (\mathbb{F}, \neg\mathbb{F}, A), \mathfrak{G} := (\mathbb{G}, \neg\mathbb{G}, A) \in \mathcal{C}(U \sim A)$ be given. We say that a triple $\mathfrak{F} \tilde{\circ} \mathfrak{G} := ((\mathbb{F} \tilde{\circ} \mathbb{G}), \neg(\mathbb{F} \tilde{\circ} \mathbb{G}), A)$ is a fuzzy semibipolar soft product over U with respect to A if $\mathfrak{F} \tilde{\circ} \mathfrak{G} \in \mathcal{C}(U \sim A)$ is defined by



$$(\mathbb{F} \circ \mathbb{G})(a) = \begin{cases} \bigcup_{(x,y) \in R_a} (\mathbb{F}(x) \tilde{\wedge} \mathbb{G}(y)) & \text{if } R_a \neq \emptyset, \\ 0_U & \text{if } R_a = \emptyset, \end{cases}$$

and

$$\neg(\mathbb{F} \circ \mathbb{G})(a) = \begin{cases} \bigcap_{(x,y) \in R_a} (\neg \mathbb{F}(x) \tilde{\vee} \neg \mathbb{G}(y)) & \text{if } R_a \neq \emptyset, \\ 1_U & \text{if } R_a = \emptyset, \end{cases}$$

for all $a \in A$. At this point, $R_a := \{(x, y) \in A \times A \mid a \leq_A xy\}$.

Lemma 1. Let $\mathfrak{F} := (\mathbb{F}, \neg \mathbb{F}, A) \in \mathcal{C}(U \sim A)$. Then, the following statements hold.

1. $(\mathbb{W}_A \circ \mathbb{F})(ab) \tilde{\geq} \mathbb{F}(b)$ and $\neg(\mathbb{W}_A \circ \mathbb{F})(ab) \tilde{\leq} \neg \mathbb{F}(b)$ for all $a, b \in A$.
2. $(\mathbb{F} \circ \mathbb{W}_A)(ab) \tilde{\geq} \mathbb{F}(a)$ and $\neg(\mathbb{F} \circ \mathbb{W}_A)(ab) \tilde{\leq} \neg \mathbb{F}(a)$ for all $a, b \in A$.
3. $(\mathbb{W}_A \circ \mathbb{F})(ab) \tilde{\geq} (\mathbb{W}_A \circ \mathbb{F})(b)$ and $\neg(\mathbb{W}_A \circ \mathbb{F})(ab) \tilde{\leq} \neg(\mathbb{W}_A \circ \mathbb{F})(b)$ for all $a, b \in A$.
4. $(\mathbb{F} \circ \mathbb{W}_A)(ab) \tilde{\geq} (\mathbb{F} \circ \mathbb{W}_A)(a)$ and $\neg(\mathbb{F} \circ \mathbb{W}_A)(ab) \tilde{\leq} \neg(\mathbb{F} \circ \mathbb{W}_A)(a)$ for all $a, b \in A$.
5. For all $a, b \in A, a \leq_A b$ implies

$$(\mathbb{W}_A \circ \mathbb{F})(a) \tilde{\geq} (\mathbb{W}_A \circ \mathbb{F})(b) \text{ and } \neg(\mathbb{W}_A \circ \mathbb{F})(a) \tilde{\leq} \neg(\mathbb{W}_A \circ \mathbb{F})(b).$$

6. For all $a, b \in A, a \leq_A b$ implies

$$(\mathbb{F} \circ \mathbb{W}_A)(a) \tilde{\geq} (\mathbb{F} \circ \mathbb{W}_A)(b) \text{ and } \neg(\mathbb{F} \circ \mathbb{W}_A)(a) \tilde{\leq} \neg(\mathbb{F} \circ \mathbb{W}_A)(b).$$

7. For all $a, b \in A$,

$$(\mathbb{F} \circ (\mathbb{W}_A \circ \mathbb{F}))(ab) \tilde{\geq} (\mathbb{F} \circ (\mathbb{W}_A \circ \mathbb{F}))(b)$$

and

$$\neg(\mathbb{F} \circ (\mathbb{W}_A \circ \mathbb{F}))(ab) \tilde{\leq} \neg(\mathbb{F} \circ (\mathbb{W}_A \circ \mathbb{F}))(b).$$

8. For all $a, b \in A$,

$$(\mathbb{F} \circ (\mathbb{F} \circ \mathbb{W}_A))(ab) \tilde{\geq} (\mathbb{F} \circ (\mathbb{F} \circ \mathbb{W}_A))(a)$$

and

$$\neg(\mathbb{F} \circ (\mathbb{F} \circ \mathbb{W}_A))(ab) \tilde{\leq} \neg(\mathbb{F} \circ (\mathbb{F} \circ \mathbb{W}_A))(a).$$

Proof. It is not hard to prove that the statements 1-4 are true. We consider the following proofs of the statements 5-8.

5. Let $a, b \in A$. Suppose that $a \leq_A b$. Then, we consider the following two cases.

Case 1. Suppose $R_b = \emptyset$. Then

$$(\mathbb{W}_A \circ \mathbb{F})(b) = 0_U \tilde{\leq} (\mathbb{W}_A \circ \mathbb{F})(a) \text{ and } \neg(\mathbb{W}_A \circ \mathbb{F})(b) = 1_U \tilde{\geq} \neg(\mathbb{W}_A \circ \mathbb{F})(a).$$

Case 2. Suppose $R_b \neq \emptyset$. Then

$$(\mathbb{W}_A \circ \mathbb{F})(b) = \bigcup_{(x,y) \in R_b} (\mathbb{W}_A(x) \tilde{\wedge} \mathbb{F}(y)) = \bigcup_{(x,y) \in R_b} (\mathbb{F}(y))$$

and

$$\neg(\mathbb{W}_A \circ \mathbb{F})(b) = \bigcap_{(x,y) \in R_b} (\neg \mathbb{W}_A(x) \tilde{\vee} \neg \mathbb{F}(y)) = \bigcap_{(x,y) \in R_b} (\neg \mathbb{F}(y)).$$

Suppose that $(x, y) \in R_b$. Then $a \leq_A b \leq_A xy$. Thus $(x, y) \in R_a$. Hence

$$\begin{aligned}(\mathbb{W}_A \circ \mathbb{F})(a) &= \bigcup_{(w,z) \in R_a} (\mathbb{W}_A(w) \tilde{\wedge} \mathbb{F}(z)) \\ &\tilde{\geq} \mathbb{W}_A(x) \tilde{\wedge} \mathbb{F}(y) \\ &= \mathbb{F}(y)\end{aligned}$$

and

$$\begin{aligned}\neg(\mathbb{W}_A \circ \mathbb{F})(a) &= \bigcap_{(w,z) \in R_a} (\neg \mathbb{W}_A(w) \tilde{\vee} \neg \mathbb{F}(z)) \\ &\tilde{\leq} \neg \mathbb{W}_A(x) \tilde{\vee} \neg \mathbb{F}(y) \\ &= \neg \mathbb{F}(y).\end{aligned}$$

Hence $(\mathbb{W}_A \circ \mathbb{F})(a) \tilde{\geq} \mathbb{F}(y)$ and $\neg(\mathbb{W}_A \circ \mathbb{F})(a) \tilde{\leq} \neg \mathbb{F}(y)$ for all $(x, y) \in R_b$. Whence

$$(\mathbb{W}_A \circ \mathbb{F})(a) \tilde{\geq} \bigcup_{(x,y) \in R_b} (\mathbb{F}(y)) = (\mathbb{W}_A \circ \mathbb{F})(b)$$

and

$$\neg(\mathbb{W}_A \circ \mathbb{F})(a) \tilde{\leq} \bigcap_{(x,y) \in R_b} (\neg \mathbb{F}(y)) = \neg(\mathbb{W}_A \circ \mathbb{F})(b).$$

The proof is complete.

6. The proof is similar to that of 5.

7. Let $a, b \in A$ be given. Then, it is easy to see that $\mathfrak{W}_A \circ \mathfrak{F} \tilde{\subseteq} \mathfrak{F} \circ (\mathfrak{W}_A \circ \mathfrak{F})$. Hence

$$(\mathbb{F} \circ (\mathbb{W}_A \circ \mathbb{F}))(ab) \tilde{\geq} (\mathbb{W}_A \circ \mathbb{F})(ab) \text{ and } \neg(\mathbb{F} \circ (\mathbb{W}_A \circ \mathbb{F}))(ab) \tilde{\leq} \neg(\mathbb{W}_A \circ \mathbb{F})(ab).$$

By 1 and 3, we have

$$\begin{aligned}(\mathbb{F} \circ (\mathbb{W}_A \circ \mathbb{F}))(ab) &\tilde{\geq} (\mathbb{W}_A \circ \mathbb{F})(ab) \\ &\tilde{\geq} \mathbb{F}(b) \tilde{\vee} (\mathbb{W}_A \circ \mathbb{F})(b) \\ &= (\mathbb{F} \circ (\mathbb{W}_A \circ \mathbb{F}))(b)\end{aligned}$$

and

$$\begin{aligned}\neg(\mathbb{F} \circ (\mathbb{W}_A \circ \mathbb{F}))(ab) &\tilde{\leq} \neg(\mathbb{W}_A \circ \mathbb{F})(ab) \\ &\tilde{\leq} \neg \mathbb{F}(b) \tilde{\wedge} \neg(\mathbb{W}_A \circ \mathbb{F})(b) \\ &= \neg(\mathbb{F} \circ (\mathbb{W}_A \circ \mathbb{F}))(b).\end{aligned}$$

8. The proof is similar to that of 7, which is easily obtained by 2 and 4.

Thus, we omit here.

Theorem 3. Let $\mathfrak{F} := (\mathbb{F}, \neg \mathbb{F}, A) \in \mathcal{C}(U \sim A)$ be defined as follows: for all $a, b \in A$,

$$a \leq_A b \text{ implies } \mathbb{F}(a) \tilde{\geq} \mathbb{F}(b) \text{ and } \neg \mathbb{F}(a) \tilde{\leq} \neg \mathbb{F}(b).$$

Then, the following statements hold.

1. $\mathfrak{F} \circ (\mathfrak{W}_A \circ \mathfrak{F}) \in \mathcal{C}(U \sim A)$ is a fuzzy semibipolar soft left ideal.
2. $\mathfrak{F} \circ (\mathfrak{F} \circ \mathfrak{W}_A) \in \mathcal{C}(U \sim A)$ is a fuzzy semibipolar soft right ideal.

Proof. We consider the following proofs.

1. Let $a, b \in A$ be given. Then, by Lemma 1 (7), we get that

$$(\mathbb{F} \circ (\mathbb{W}_A \circ \mathbb{F}))(ab) \tilde{\geq} (\mathbb{F} \circ (\mathbb{W}_A \circ \mathbb{F}))(b)$$

and



$$\neg(\mathbb{F} \cup (\mathbb{W}_A \circ \mathbb{F}))(ab) \lesssim \neg(\mathbb{F} \cup (\mathbb{W}_A \circ \mathbb{F}))(b).$$

Suppose $a \leq_A b$. Then $\mathbb{F}(a) \gtrsim \mathbb{F}(b)$ and $\neg \mathbb{F}(a) \lesssim \neg \mathbb{F}(b)$ due to the property of \mathfrak{F} .

Moreover, we get that

$$(\mathbb{W}_A \circ \mathbb{F})(a) \gtrsim (\mathbb{W}_A \circ \mathbb{F})(b) \text{ and } \neg(\mathbb{W}_A \circ \mathbb{F})(a) \lesssim \neg(\mathbb{W}_A \circ \mathbb{F})(b)$$

due to Lemma 1 (5). Thus

$$\begin{aligned} (\mathbb{F} \cup (\mathbb{W}_A \circ \mathbb{F}))(a) &= \mathbb{F}(a) \vee (\mathbb{W}_A \circ \mathbb{F})(a) \\ &\gtrsim \mathbb{F}(b) \vee (\mathbb{W}_A \circ \mathbb{F})(b) \\ &= (\mathbb{F} \cup (\mathbb{W}_A \circ \mathbb{F}))(b) \end{aligned}$$

and

$$\begin{aligned} \neg(\mathbb{F} \cup (\mathbb{W}_A \circ \mathbb{F}))(a) &= \neg \mathbb{F}(a) \wedge \neg(\mathbb{W}_A \circ \mathbb{F})(a) \\ &\lesssim \neg \mathbb{F}(b) \wedge \neg(\mathbb{W}_A \circ \mathbb{F})(b) \\ &= \neg(\mathbb{F} \cup (\mathbb{W}_A \circ \mathbb{F}))(b). \end{aligned}$$

Therefore $\mathfrak{F} \cup (\mathbb{W}_A \circ \mathfrak{F})$ is a fuzzy semibipolar soft left ideal.

2. The proof is similar to that of 1, which is easily obtained by Lemma 1 (6 and 8). Thus, we omit here.

Conclusion:

From the constructions of union and intersection concepts in this paper, we got that the intersection of two fuzzy semibipolar soft left (resp., right) ideals is a fuzzy semibipolar soft left (resp., right) ideal. Moreover, the union of two fuzzy semibipolar soft sets is a fuzzy semibipolar soft left (resp., right) ideal via the generated fuzzy semibipolar soft product. Based on this research, the given basic operations can be supported to solve the problem of uncertainty or vagueness of data classification. In structural development, some results of this work are fundamental for the semigroup concept which other systems can be used also.

Acknowledgements:

We would like to thank the expert reviewers for their helpful suggestions. We would like to thank supporter organizations: Division of Mathematics and Statistics, Faculty of Science and Technology, Nakhon Sawan Rajabhat University, Thailand.

References:

1. Zadeh LA. Inf. Control. 1965;8:338–353.
2. Rosenfeld A. J. Math. Anal. and Appl. 1971;35:512–517.
3. Kuroki N. Fuzzy Sets Syst. 1981;5:203–215.
4. Molodtsov D. Comput. Math. Appl. 1999;37:19–31.
5. Aktaş H, Çağman N. Inform. Sci. 2007;177:2726–2735.
6. Acar U, Koyuncu F, Tanay B. Comput. Math. Appl. 2010;59: 3458–3463.
7. Shabir M, Ali MI, Shum KP. J. Southeast Asian Stud. 2010;34:595–610.
8. Prasertpong R. IJMCS. 2022;17:1113–1132.
9. Kehayopulu N, Tsingelis M, Soochow J. Math. 2007;33:383–397.
10. Howie JM. Oxford University Press. 1995.

APPLICATION OF LINE CHATBOTS TO SUPPORT IT MAINTENANCE TASKS

Orraya Suwanno,¹ Patitta Suksomboon,^{1*} Wansobree Waemamu² Amarita Ritthipakdee³

¹Faculty of management science, Prince of Songkla university, Thailand

²Faculty of engineering, Prince of Songkla university, Thailand

³Department of science and technology, Phranakhon Rajabhat University, Thailand

*e-mail: patitta.s@psu.ac.th,

Abstract:

LINE Chatbot's application supports the maintenance of IT equipment to study the accuracy, intentional dialogue and user satisfaction using LINE Platform. Dialogflow and LINE Messaging API in development Designed for chatbots with FAQ behavior from the system test, it has an accuracy of 85.5% and the overall satisfaction is at the highest level, with an average of 4.31. That is easily interesting, has the highest average of 4.65, and the technical support group found that the ability to reduce the use of memory resources on Smartphones and the ability to remember how to use them easily have the highest average of 4.64 and found that being a friend can be done without errors and can chat naturally. Has the lowest standard deviation of 0.005. From the results, it can be said that the developed chatbot is a good, efficient system. Interesting to use. Regarded as the LINE Platform Dialogflow is a technology that has a future and has a high chance of being popular. Can develop a variety of systems according to the needs of developers in the future.

Introduction:

Working in the field of information technology equipment maintenance may be commonly referred to as IT support, technical support, technical service engineer or technician, and is currently one of the most popular job positions. The importance of work having roles and responsibilities in maintaining equipment such as computers, printers, UPS and network equipment. Technical skills are developed through instruction, education, or on-the-job [1]. Throughout the past, there have been attempts to find methods or create tools to support operations and reduce errors in service through various methods, such as creating manual documents that include paper documents, digital files, web applications or others. Including searching for information on the internet to update additional new information as current work practices and information from experts or product owners.

Chatbots are systems that are gaining attention and have been developed and widely used to support various works that will help support facilitate and reduce operating costs. Chatbots generate responses by combining pre-existing knowledge acquired from a vast amount of training data with information and patterns present in the task that they are asked to complete [2]. It can be developed or applied to help recommend operational guidelines for maintaining information technology equipment in the form of automatic conversational interactions and can reply to conversations immediately or in real-time. Chatbots are different from manuals that are documentation. Manual in digital web application format including searching for information on the internet, which has steps to search before getting the information you want or asking for advice from various experts via chat that may not be possible immediately. The introduction of Artificial Intelligence (AI) technology has enabled chatbot systems to respond automatically and in real-time to people who want to consult or request information to solve problems. Artificial Intelligence is a rapidly growing field that is transforming many aspects of our lives [3]. With the development of artificial intelligence technology, chatbots are considered to possess unprecedented commercial potential [4]. By typing a message into the

chatbot system which is convenient and quick to use. From past research studies, satisfactory results have been obtained in terms of artificial intelligence technology that is easy to use and can be applied in a variety of hardware, software, applications, and various frameworks.

From the above, we have seen the idea of using chatbots as a conversational support tool to communicate with each other at present and in the near future. LINE application that has LINE chatbot features will help to increase the ability of LINE application to automatically respond to conversations by using Dialog Flow, which is an artificial intelligence technology that has been designed on the LINE application platform. A chatbot system based on a DialogFlow and Line application for graduate school electronic services achieved 83.43 percent user feedback and 88 percent user confidence. [5]

This study aims to use the LINE application to apply the LINE chatbot model, which is the development of a Has AI no Call chatbot. Chatbot is an AI-based approach using Dialog Flow, which is an artificial intelligence technology or a powerful tool for developing conversational robot systems. Based on research on the effectiveness of tools for developing automated conversational robot systems by Konstantin Savenkov, co-founder and CEO of Inten.to.

Methodology:

The researcher's design and guidelines for developing the LINE chatbot system to support IT equipment maintenance operations, there are 3 processes as in Figure 1; 1.) Research study and data collecting 2.) Design and development and 3.) Evaluation

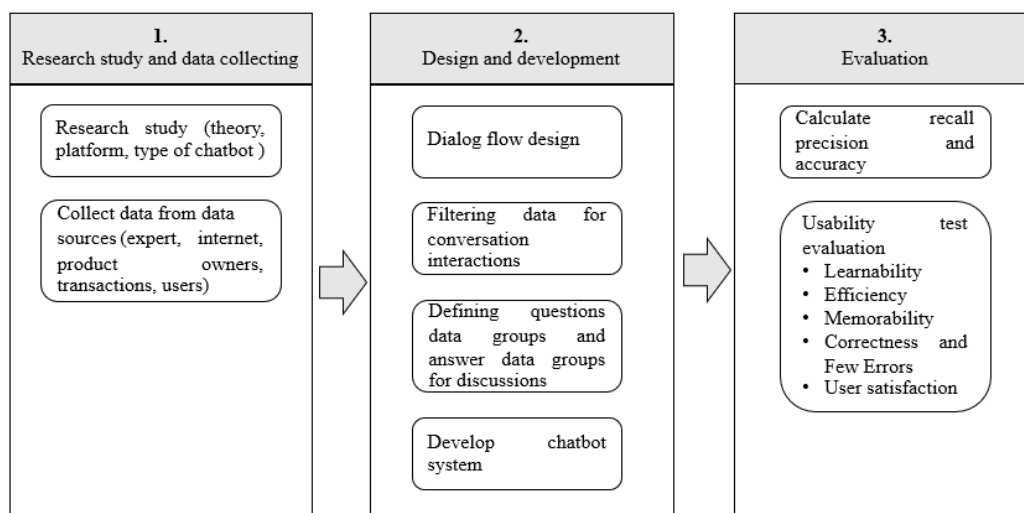


Figure 1.

An overview of the research process for developing the LINE chatbot system.

1. Research study and data collecting is a process for searching for various information related to the development of the LINE chatbot system. This process can be described as follows.

1.1 Research study (theory, platform and type of chatbot). As in Figure 2, study the data that will be used in developing the chatbot system and applying various principles or theories. Related to research studies, the researcher considers that the LINE and Dialog Flow applications are good and appropriate platforms for developing and can develop a Has AI no Call flow chatbot system very well.

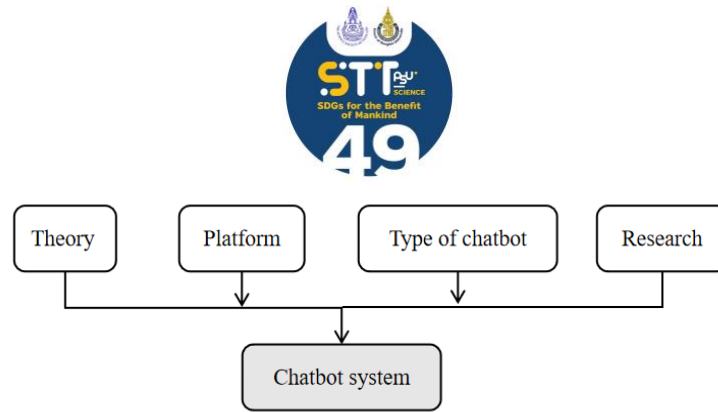


Figure 2.

The process for studying data to develop the LINE chatbot system.

1.2 Collect data from data sources (experts, internet, product owners, transactions and users). Has AI no Call chatbots work according to facts collection or prediction. Upcoming groups of questions and answers must be stored in the Dialog Flow in advance. As in Figure 3, there are various data sources such as experts, the internet, product owners, transactions and users. In this process, the question and answer groups will be given by knowledgeable and experienced people who are experts in IT equipment maintenance. Information on the internet that is used to solve problems from product owners directly through the service. Information from successful problem-solving from the system, which is a recording or reporting system. Users use the chatbot system to collect new questions or problems that don't yet exist in the chatbot system.

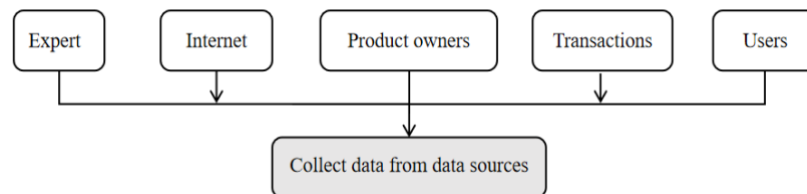


Figure 3.

The process for collecting conversation data in the LINE chatbot system.

2. Design and development of the LINE chatbot system.

2.1 DialogFlow design. The development of LINE's chatbot system will include the Line application or LINE platform, LINE Messaging API, DialogFlow or DialogFlow Platform. The LINE Messaging API is responsible for connecting and sending user information to Dialog Flows. So that the DialogFlow can search or query data based on requests from users. The system task available in DialogFlow is to collect or predict upcoming groups of questions and answers that will be stored in DialogFlow. After DialogFlow can query information as requested by users, DialogFlow is responsible for sending that information through the LINE Messaging API to the LINE platform for users to use that information further.

2.2 Filtering data for conversation interactions. Filtering data to respond to conversations, DialogFlow works on LINE's chatbot system to validate conversations using natural language processing (NLP), machine learning (ML) and other principles. Applied Linguistics to compare Sentences or texts (TF-IDF).

2.3 Defining questions data groups and answer data groups for discussions. Developing the LINE chatbot system using the method of defining question data groups and answer data groups to use in conversational interactions by creating intent based on failure functions or problem characteristics of IT equipment. These data were obtained from the



work of the sample used in this study and continue to create an increasing number of intents based on data received from users of the Dialog Flow system, recording user conversation information in history. This allows developers to use that data to train chatbots to interact with the topic via the training menu.

2.4 Develop a chatbot system. After preparing the question and answer information, the next process is to develop the chatbot system which relies on two main development platforms: LINE Platform and Flow Platform Dialogs. This means that you will need to prepare or have a working LINE application, and an E-mail of Gmail for login to access the Flow dialog box.

3. Evaluation. After developing the LINE chatbot system to support IT equipment maintenance operations., the researchers evaluated the accuracy of LINE's chatbot system in responding to desired conversations and assessed user satisfaction.

3.1 Calculate recall precision and accuracy. A study to evaluate the processing accuracy of the required conversation interactions of the developed IT system supporting the maintenance operations of the LINE chatbot device. This will be evaluated on the effectiveness of machine learning. The classification model is used to describe the performance of the binary classifier model, the confusion matrix is used as a tool to describe and calculate the system performance evaluation results. In this study, recall, precision and accuracy values will be calculated.

3.2 Usability test evaluation. The Questionnaire designed to assess satisfaction with using the system, is divided into 5 areas: learnability, efficiency, memorability, correctness and few errors and user satisfaction.

Results and Discussion:

From a study of the development of LINE's chatbot system for use in conversational interactions to support IT equipment maintenance operations, this system was named "BOT SITMT" (Bot Support IT Maintenance Tasks). The bot can interact with users in a good and satisfying. The ability to recommend or distribute bots to interested users can be done by adding bots as friends in the LINE application. The system will be able to provide advice and techniques for solving hardware problems, basic software and internet usage problems.

For the results of evaluating the efficiency and accuracy of the system according to the binary classifier model from testing conversation interactions separated by intent (intent classification) of 10 intentions which were divided into 2 parts with 100 conversations each, totaling 200 conversations.

The test will be conducted by having a conversation with the LINE chatbot system using messages or conversation sentences that contain both the same sentences and conversation sentences. Those are different or similar to the sentences specified in the question or question group. The same number of values is defined in the intents of the system flow dialog to test the correctness of the system's processing which the same conversation is used for every character. The interaction flow is 100% accurate. From evaluating the performance of the system, it was found that the recall value was at the level of 84% - 87% and the precision value was at the level of 84.46% - 86.59% when calculating these results to find the accuracy value, it was 85.5%, which is considered to be average system processing accuracy. It is considered that the development of LINE's chatbot system was a satisfactory success. This test score can be seen as detailed in Figure 4, most score between 8 and 9.

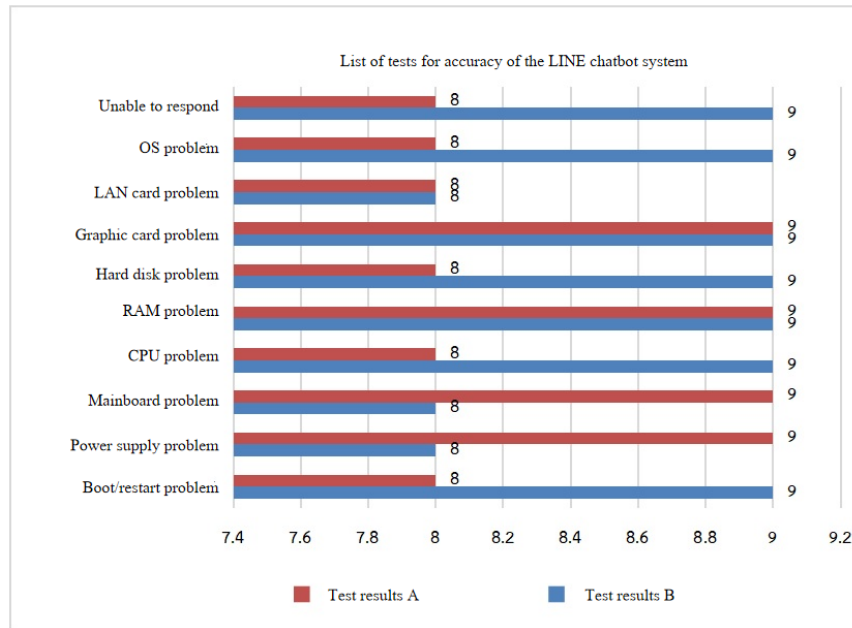


Figure 4.

The results of testing the accuracy of LINE's chatbot system.

When the results obtained from testing the functionality of the LINE chatbot system are all calculated, summed up and arranged in a format according to the confusion matrix guidelines for use in further calculations. It will be shown as shown in Figure 5.

	A	B	
A	TP 87	FN 16	Precision
B	FP 13	TN 84	
	Recall		

Figure 5.

The results of testing the accuracy of LINE's chatbot system.

From Figure 5, the system performance test results can be used to calculate the accuracy as shown in Table 1.

**Table 1.**

The recall, precision and accuracy calculation of LINE's chatbot system.

Recall A = $87 / (87+13) = 87 / 100$ = 0.87 or 87%	Recall B = $84 / (84+16) = 84 / 100$ = 0.84 or 84%
Precision A = $87 / (87+16) = 87 / 103$ = 0.84466 or 84.46%	Precision B = $84 / (84+13) = 84 / 97$ = 0.86597 or 86.59%
Accuracy = $(87+84) / (100+100) = 171 / 200$ = 0.855 or 85.5%	

From Table 1, it can be explained that Recall A outperforms Recall B at 87%, a difference of 3%. Recall B has an efficiency of 84%. In terms of accurate calculations, it was found that Precision B received better calculation results than Precision A at 86.59%, with Precision A receiving calculation results at 84.46%. If we compare the best results of the two values (Recall A and Precision B), the difference is 0.40%. And if we compare the results of other values with smaller results the difference was found to be 0.47%. It can be seen that the difference between the two results is 0.07%, and if the difference between the two is calculated to find the average, the result is 0.435%. This value may indicate stability, the correctness or stability of the system's operation. From the results of this study, it was found that in 200 tests, the system worked or processed correctly according to the set requirements 171 times. There were 29 errors, and when the results were calculated to find the average, the result was 0.855 or 85.5%. It can still be considered that the LINE chatbot system developed is highly efficient and satisfactory.

Results of user satisfaction assessment when using LINE chatbots to help or support IT equipment maintenance work. A research study using a questionnaire to assess the satisfaction of the target group. The average score of this research study was divided into 4 areas as follows:

1. Overall satisfaction results of both target groups.
2. Satisfaction results of the target group of general users.
3. Satisfaction results of the target group of technical support.
4. Results of comparing the mean scores and standard deviations (SD) between the target groups of general users and technical supporters.

For the overall satisfaction results of both target groups, evaluation of service user satisfaction using questionnaires, the target group of this research is 62 people, divided into 2 subgroups: 1.) General user group (Users) 37 people and 2.) Technical Support group (Technical Support) 25 people. Population criteria for considering an average of 4.21 - 5.00 means the highest level of satisfaction. An average of 3.41 - 4.20 is considered to be a high level of satisfaction. An average of 2.61 - 3.40 is considered to be at a moderate level of satisfaction. An average of 1.81 - 2.60 means that there is satisfaction. Satisfied at a low level and an average of 1.00 - 1.80 means the lowest level of satisfaction.

From the research study, it was found that the results were satisfactory. The total number received by both target groups according to the consideration criteria that have already been determined. The average is at the highest level of satisfaction. In terms of benefits of use received the highest average score of 4.61, followed by the ability to easily



remember how to use. An average score of 4.60 it is about using voice commands effectively and being able to respond correctly. The lowest average was 4.35, followed by being able to work without errors.

Satisfaction results of the target group of general users, when classifying the scores of the target group of 37 general users from the average scores according to the specified criteria, it was found that they were at the highest level of satisfaction. With the matter of being able to easily distribute it to other interested users, the highest average is 4.65. The issue of ease of use and utility had an average score of 4.62 that could be answered correctly. The lowest average was 4.30, followed by the understanding of the help system.

Satisfaction results of the target group of technical support. When categorizing the scores of the target group of 25 technical supporters from the average scores according to the criteria set for consideration, they were at the highest level of satisfaction. Both in helping reduce the use of memory resources on the smartphone and being able to remember how to use it easily with the highest average is 4.64. The second is the ability of the help system to understand both in terms of utility and necessity for actual use in the future had an average score of 4.60 while the test subjects were able to use voice commands effectively. The lowest average was 4.16. When considered according to the criteria that have been set, is considered to be a high satisfaction rating. The second is that it is easy to use. The average is 4.36.

Results of comparing the mean scores and standard deviations between the target groups of general users and technical supporters. In addition, when comparing the average scores of the two target groups. It was found that the standard deviation was very low, less than 0.10, in 6 data or subjects. Standard deviation can refer to the reliability of data that can indicate the accuracy of data obtained from the same questionnaire or the direction of data from two target groups. The lowest standard deviation is the most reliable value and the maximum standard deviation likely to be the most reliable. It was found that information or adding friends can be done without errors and conversations can be made naturally. The standard deviation is at the lowest level of 0.00 or approximately 0.005. The second is the ability to properly interact with users and be able to work immediately, the standard deviation was 0.01. Third was the ability to easily converse and request necessary information. The ability to work without errors and be useful in use with a standard deviation of 0.02. Fourth is ease of learning, ability to use systems using resources efficiently, future practical needs and attractiveness of use, it had a standard deviation of 0.04. Fifth place is the ability to quickly interact with users, you can easily remember how to use it and when you haven't used it for a while you still remember how to use it, had a standard deviation of 0.05 and finally ranked 6th is the ability to help reduce the use of memory resources on smartphones, the standard deviation is 0.07.

While the matter of being able to use voice commands effectively, the standard deviation is at the highest level of 0.23. Support system which can be explained understandably, the standard deviation is 0.19. This may indicate that the data may be less reliable as a result of the data or results obtained from the same questionnaire for both target groups in a way that is different or has a high standard deviation but is still at a very low level.

Conclusion:

From studying and developing the LINE chatbot application to support IT equipment maintenance work which is a chatbot system that was developed to help, advice, or suggestions on how to analyze and find the cause of problems that occur with IT equipment and repairs or fix additional problems to help reduce operational errors. The results of the study can be summarized into 4 areas as follows:

1. This study and development of LINE chatbots was successful. The system can be used according to the set goals at a satisfactory level.

2. The accuracy evaluation result of 85.5% is at a satisfactory level, exceeding expectations. It is considered a good sign or shows the efficiency of the system and technology used in development that can be further developed to be even more efficient than before and can be applied in the future.

3. Developing a chatbot on the LINE application or LINE platform. From a satisfaction study from a sample group, very satisfactory results were obtained. The results had an average score level that was in the most satisfactory range. Overall, the average score was 4.31.

4. The working or conversational response of LINE's chatbot system from the study results from the sample group is still consistent with past research mentioned above. The system can converse naturally, correctly and appropriately, etc. according to the research mentioned above.

Discussion of results

The work of the developed chatbot is satisfactory to a certain extent, able to interact with users quickly and on time. It takes time when the system still does not respond to the user's needs or intentions, which may be due to low levels of training and information on the system and techniques or processes that developers use in development that may not be good or appropriate. However from the overall evaluation study, it can be considered that the system can work satisfactorily.

LINE Platform and Dialog Flow are interesting tools or technologies. It is often used in developing chatbot systems to help with call center operations. In addition, the chatbot system will be another channel to help serve customers by providing advice, solving problems, or other services related to government agencies, private organizations, business organizations or others. For examples as follows: The BOTSIT can provide technical consulting services in resolving problems with computer equipment or other IT equipment. The same as providing services through call centers of various IT companies that currently provide technical consulting services. In addition, chatbot systems can help with e-commerce to present and sell various products or services currently available online, such as hotel booking system, air ticket booking systems, financial transaction systems, educational systems, or e-learning. This is because chatbot systems interact with users in a way that affects their emotions better as compared to conventional systems or applications. Chatbot systems developed on various social media platforms will be easier to access and reach target groups compared to other platforms. This is the reason why it has received much attention and has led developers to develop chatbot systems to provide customer service which in the future has the possibility of replacing websites and mobile applications.



References:

1. Cacciolatti L, Lee S. H, Molinero C. M. Clashing institutional interests in skills between government and industry: An analysis of demand for technical and soft skills of graduates in the UK. *Technological Forecasting & Social Change* 2017;119:139-153.
2. Chem J. Educ. Investigating the Use of an Artificial Intelligence Chatbot with General Chemistry Exam Questions. 2023;100:2821–2824.
3. Mondal B, Recent Trends and Advances in Artificial Intelligence and Internet of Things. 2020; 172:389-425.
4. King, M.R. The Future of AI in Medicine: A Perspective from a Chatbot. *Ann Biomed Eng.* 2023;51:291–295.
5. Crolic C, Thomaz F, Hadi R, Stephen AT. J. Blame the Bot: Anthropomorphism and Anger in Customer–Chatbot Interactions. *Journal of Marketing.* 2022;86:132–148.
6. Rukhiran M, Netinant P. *IJEC.* 2002;12:5330-5338.



MATHEMATICAL MODEL FOR HEAT TRANSFER IN CORRUGATED BOX WITH BC FLUTE.

Narongrid Rorsena, Warisa Yomsatieankul*

Department of Mathematics, Faculty of Science, King Mongkut's University of Technology Thonburi, Thailand.

*e-mail: warisa.yom@kmutt.ac.th

Abstract:

The global transportation industry, particularly for food and perishables, requires precise temperature control to maintain freshness and safety. Foam boxes are essential for temperature control, but they decompose quickly, causing global warming concerns. Corrugated boxes are suitable for short-distance transport but not ideal for long-distance. One of the advantages is their ability to decompose, making them a more environmentally friendly option. This study investigates the performance of a corrugated box using BC flute insulation. To achieve this, we monitored temperature changes over 8 hours in the controlled ambient by attaching sensors at 6 different points within the box, considering ice as the product. A 2D heat equation is used to describe heat transfer inside the box. After that, we analyzed and compared the results obtained from the experiments and simulation. The result shows that the simulation results are in the same direction as the experiment.

Introduction:

The global transportation industry has expanded significantly. It involves the transportation of items like food and perishables, which require precise temperature control to maintain freshness and safety. Temperature instability can cause deterioration in package contents, making temperature control crucial for reducing food damage and ensuring food safety. Transport boxes, the primary food safety precaution, are essential for transportation. Foam boxes are widely used in transportation for temperature control and shock reduction. However, Styrofoam boxes take around 1,000 years to decompose, causing significant global warming concerns. In contrast, corrugated boxes decompose in 2–5 months, highlighting the environmental trade-off between efficient transport and sustainability. However, they have limitations and are suitable for short-distance transport but may not be ideal for long-distance transport because long-distance transportation makes it difficult to control a stable temperature. In 2017, Paquette, J.C. et al. used two stacked boxes with a multiple-layer box and a corrugated box as insulation to simulate the internal temperature of the box and added aluminum foil on the internal surface of the corrugated box. The heat transfer model was achieved using COMSOL Multiphysics and validated with experiments. The results showed that the addition of aluminum foil to the internal surface of the box can reduce heat radiation by up to 10% for the first 30 hours of storage. Placing the gel packs should be farthest from the exterior of the box, and in this work, it was found that placing the gel pack in the center of the box can double the preservation time. A sensitivity analysis was conducted, and it showed that the thermal conductivity of the walls of the box and the emissivity of the internal surface of the box and of the gel packs are the most critical input parameters affecting the performance. Laguerre et al. (2019) studied the temperature changes of fish in two insulated foam boxes. They developed two models to predict fish temperature changes until the ice is completely melted: an analytical 1-D model and a 3-D model. The results showed that the 1-D model predictions are in good agreement for the first experiment, but in real conditions, the 1-D model underestimates the temperature evolution, while the 3-D model gives better predictions, but the model is complex to use. They also compared the advantages and

disadvantages of the 1-D model and the 3-D model to their performance. The 1-D model simplifies the prediction of key practical parameters, such as the highest temperature and the time it takes for ice to melt, with the uncertainty of certain parameters. The inclusion of empirical corrections or safety factors could enhance the accuracy of this approach. Gray-Stuart et al. (2019) measured the thermal conductivity of six different paper types of boxes that were used to form a liner, medium, and internal liner of single-wall corrugated board and used board types B flute and C flute. Thermal conductivity has been used to validate the finite element model with and without radiation. The results showed the paper has highly anisotropic thermal conductivity in the machine and cross machine directions, which is almost larger than in the thickness direction. The finite element model shows that the majority of heat transfer in corrugated fiberboard is through the fluted medium. The use of corrugated boxes with BC flute is on the rise in the transportation industry, therefore the objective of this work was to investigate the performance of a corrugated box that utilizes BC flute as insulation in order to monitor temperature changes inside the box. A 2D heat transfer model was employed to describe the heat transfer occurring inside the box, considering the presence of an ice as the product within the box.

Methodology:

As part of the methodology in this work, we are monitoring the temperature change and collecting the data. After that, the 2D heat transfer model was applied to describe the temperature change. The details are as follows:



Figure 1. A double-wall corrugated box with BC flute.

Experimentation

For the experiment, a double-wall corrugated box with BC flute (**Figure 1**) was used as insulation, and the dimensions of the box were measured. The external dimension of $20 \times 30 \times 20$ cm. In the experiment, we placed ice, which weighs 1700 grams, inside a corrugated box using BC flute as insulation material. Moreover, we controlled environmental factors like sensor placement for accuracy. The thickness of the corrugation from the outside wall to the inside wall of the box is 0.6 cm. Throughout the entire physical simulation experiment, we maintained the temperature room at a controlled level of $24.5 \pm 1.5^\circ\text{C}$ to minimize the impact of ambient temperature and replicate delivery conditions similar to those in Thailand. As our work primarily focused on short-distance transport, the experiments were conducted to monitor temperature changes for a duration of 8 hours. Data is collected every 10 seconds. In this work, we use 6 sensors at different positions to measure the temperature changes. The placement of the sensors was as follows: The first three sensors were positioned at the same height, closed to an ice 2 cm, and 7 cm from the bottom of the box, and they were spaced 5 cm apart from each other. The remaining two sensors were positioned at different heights, with one placed 11 cm from the bottom of the box and 4 cm above the bottom sensor, and the other one positioned 15 cm from the bottom of the box. Additionally, there was a sensor placed outside the box to measure the ambient temperature. The temperature measurement positions are shown in **Figure 2**.

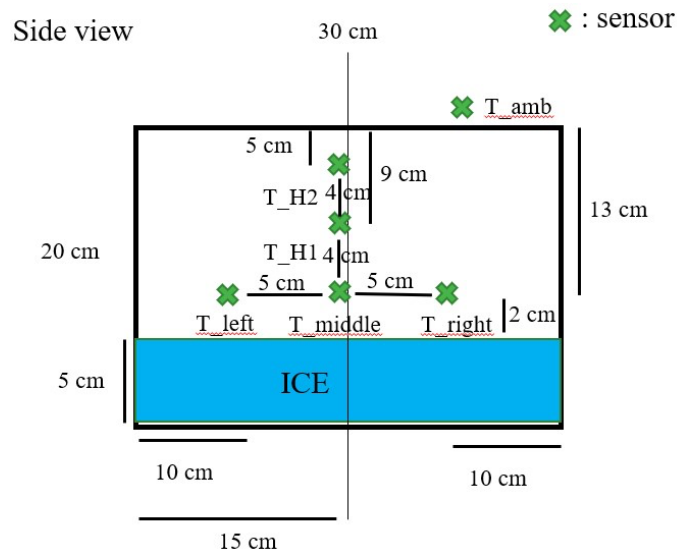


Figure 2. The position of sensors in the box.

Mathematical Model

In this work, we are interested in the temperature inside the box that uses a corrugated box with BC flute as insulation. We simulate the temperature changes inside a box that contains the ice. After that, the heat transfer equation was used to describe the change in temperature, taking into account only heat conduction to study the temperature changes. The following assumptions were made within this model:

- The thermal properties are independent of the temperature.
- Natural convection inside the box is negligible.
- The box is made of a homogeneous material with constant thermal conductivity.
- The box is filled with a homogeneous material that does not interact chemically with the box or the surroundings.

The direction of heat transfer is assumed to occur in a direction in which heat flows from outside the box into the box, as the temperature inside the box is lower than the outside temperature. The box wall thickness is 6 mm.

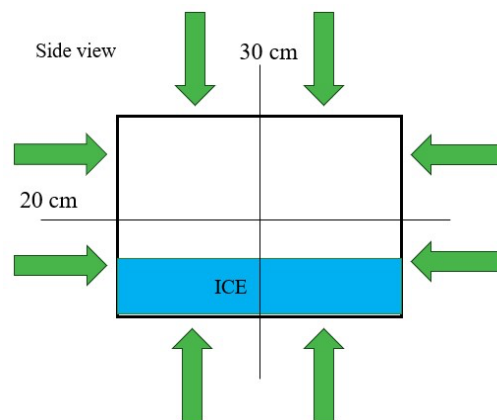


Figure 3. The direction of heat flow.

The temperature inside the box was described by an energy balance as follows:

$$k \left(\frac{\partial^2 T}{\partial x^2} + \frac{\partial^2 T}{\partial z^2} \right) = \rho C_p \frac{\partial T}{\partial t}$$

where k is thermal conductivity ($W / m \cdot K$), T is temperature (K), ρ is density (kg / m^3), C_p is heat capacity ($J / kg \cdot K$), t is time (s). Regarding the boundary conditions, we applied the first boundary condition to the bottom surface of the box and three of its sides. For the bottom surface, the boundary condition was set as $T = 0$, while the three sides of the box were defined by $T = T_{bc}$ where T_{bc} is the temperature outside of the box. As for the initial condition, we used the average value of the five sensors inside the box. The heat transfer model was solved by the finite element method in MATLAB R2022a. The thermal properties used for simulation are shown in Table 1.

Table 1. The thermal properties used for model simulation.

Material	Mass Density (kg / m^3)	Specific heat Capacity ($J / kg \cdot K$)	Thermal Conductivity ($W / m \cdot K$)	Reference
Air	1.28	1000	0.026	[1]

Results and Discussion:

In this section, we will present the results and compare the experimental data with the simulation results. The experiment spanned 8 hours, utilizing an initial condition equivalent to the average temperature measured by the 5 sensors within the box, which was 16.82 degrees Celsius. For the three-sided boundary condition (i.e., the two sides on top of the box), we used the average temperature of the environment, which was 24.59 degrees Celsius. The temperature field at the final time, as obtained from the simulation program, is depicted in **Figure 4 (a)**. The temperature variations at each position are illustrated in **Figure 4 (b) to (f)**. In these figures, the solid line represents the temperature changes obtained from the experiment, while the dashed line represents the results from the mathematical model. Specifically, the temperature changes at the left(T_{left}), middle(T_{middle}), and right(T_{right}) positions are shown in **Figure 4 (b) to (d)**, respectively. It can be seen that the experimental temperature changes at these positions exhibit a clustered temperature distribution, fluctuating up and down. The average temperature remains around 15 ± 1 degree Celsius. In contrast, the mathematical model produces relatively linear temperature profiles with minimal temperature fluctuations, maintaining an average temperature of approximately 16 degrees Celsius. The temperature changes at a position 11 cm above the bottom of the box(T_{H1}) are shown in **Figure 4 (e)**. In this figure, it can be observed that the temperature changes obtained from the experiment are higher compared to those recorded by the sensors positioned below. The average temperature at this position is approximately 18 ± 1 degrees Celsius. Finally, the temperature changes at a position 15 cm above the bottom of the box(T_{H2}) are shown in **Figure 4 (f)**. The result shows that the temperature distribution at this particular position is higher than that measured at the other two positions. The average temperature at this position is approximately 19 ± 1 degrees Celsius. Against that, the results from the mathematical model at positions T_{H1} and T_{H2} reveal a nearly linear pattern with a minor change occurring around 28,000 seconds. This change is so slight that it appears almost negligible. The temperature change results obtained from the mathematical model, which show a linear trend at all five points inside the box, could be considered reasonable due to our assumption that the temperature started at the same temperature initially. However, in reality, the temperature changes at each point are different. Additionally, in the boundary

condition, we assumed a constant, whereas in reality, the outside temperature undergoes continuous fluctuations, rising and falling, even though we attempt to control it. However, the temperature results obtained from the mathematical model have the same direction as the experimental results, and the box has insulating properties. This insulation allows it to maintain temperatures below 20 degrees Celsius for up to 8 hours in an environment with controlled temperature conditions.

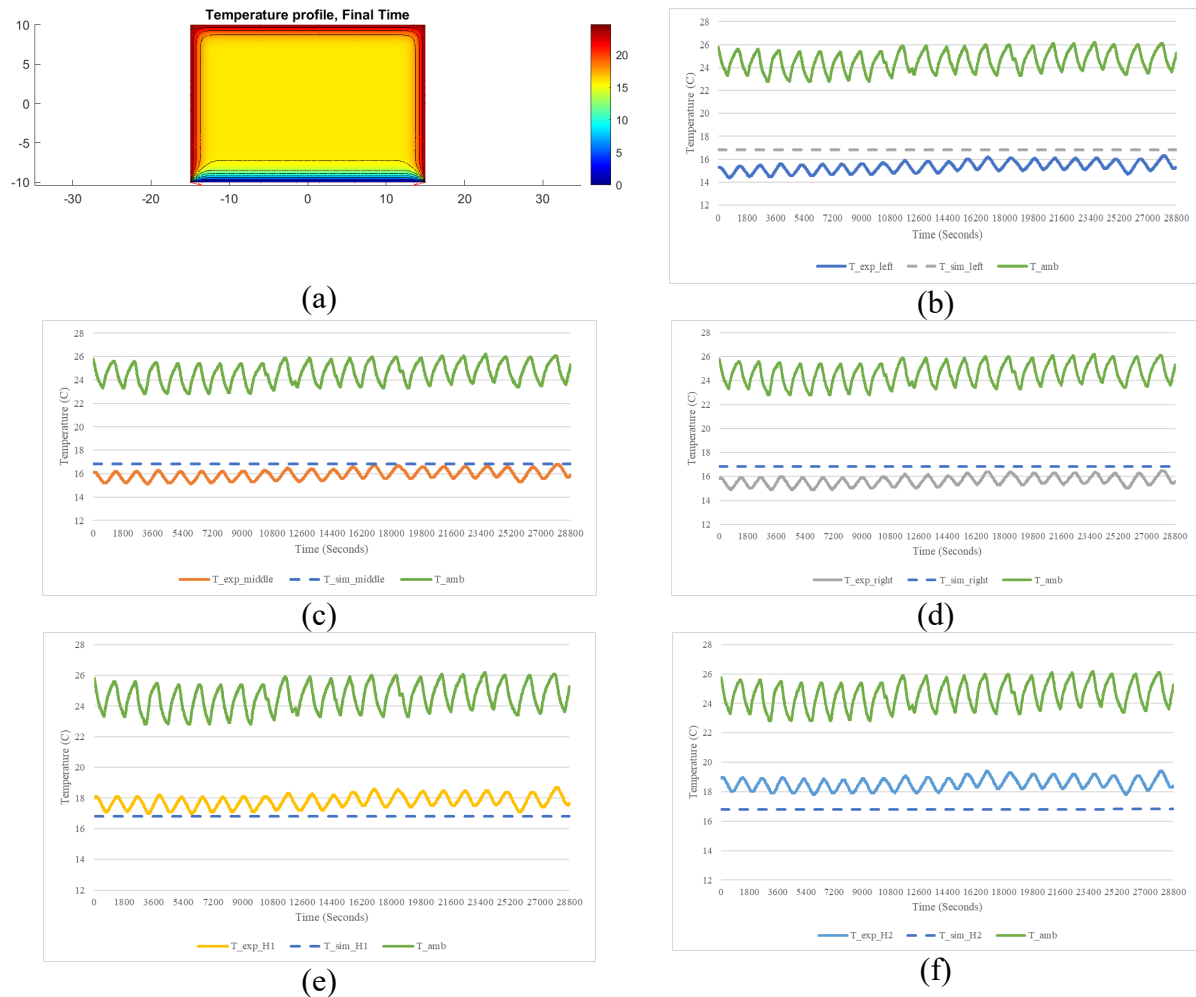


Figure 4.

Comparison of temperature changes at each position from experiment and simulation

Conclusion:

In this study, we investigated the temperature changes inside a box insulated with corrugated BC flute material, with ice as the product placed inside the box. To monitor temperature variations, we placed sensors at five points within the box and an additional sensor outside the box to measure the environmental temperature. The five sensors inside the box were placed in different positions. Three of them were placed at the same vertical position from the bottom of the box but at different horizontal distances from each other. In contrast, the remaining two sensors were placed in different vertical positions. The sensors monitored temperature changes over an 8-hour duration while the environmental temperature was controlled. After that, the 2D heat transfer was applied to explain the temperature changes occurring inside the box by using boundary conditions as constants and using the finite

element method through MATLAB to solve the heat transfer equations. The experimental results indicated that temperature changes at the same vertical position at varying horizontal distances showed similar temperature distributions. On the other hand, temperature changes at different vertical positions displayed significantly different temperature profiles. In contrast, the results obtained from the mathematical model consistently showed linear temperature profiles, according to the assumptions and constant boundary conditions used in the model. However, the results were in the same direction as the experimental results, and it was observed that the corrugated box effectively maintained temperatures below 20 degrees Celsius. It's important to note that this work represents an initial experiment and simulation. In future studies, adjustments to the boundary conditions may be necessary to better reflect real-world scenarios and provide a more accurate explanation of temperature changes.

Acknowledgements:

The authors would like to thank the Science Achievement Scholarship of Thailand (SAST) and Department of Mathematics, Faculty of Science, King Mongkut's University of Technology Thonburi for the financial support.

References:

1. East A, Smale N, 2008. *Vaccine* 2008; 26:1322–1334.
2. Paquette, J.C., Mercier, S.; Marcos, B., Morasse, S. *Food Bioprod. Process.* 2017;105; 77–85.
3. Gray-Stuart E.M., Bronlund JE, Navaranjan N, Redding GP. *Cellulose* 2019; 26:5695–5705.
4. Kucharek M., Yang L, Wang K. *Packaging Technology and Science*. 2020;33(2):65-73.
5. Laguerre O, Chaomuang N, Derens E, Flick D. *Int J Refrig* 2019;100:196-207.
6. Chaitanoo, N., P. Ongkunaruk, and D. Leingpibul. In *IOP Conference Series: Materials Science and Engineering*. 2020;773(1): 012018.
7. Wang K., Yang L., Kucharek M. *Packaging Technology and Science* 2020;33(6):227–236.

THE DEVELOPMENT OF PROGRAM FOR DETERMINING THE OPTIMAL ROUTE FOR TAKING THE PHOTHONG BUS IN PHUKET

Prarinwaris Pangprasertgul*, Pacharakamon Wattanasiri, Monsikarn Jansrang, Sittichoke Som-am

Mahidol Wittayanusorn School, Thailand

*e-mail: parinwari.pan_g31@mwit.ac.th

Abstract:

This project was developed to address the inconvenience of traveling on the Phothong bus in Phuket, which is caused by a lack of easily accessible information regarding stops, routes, fares, and schedules. Our project aimed to address this gap by creating a program that identifies the optimal bus route and calculates the fare, making it a useful tool for Phothong users. This project takes the shortest path available as the optimal bus route. The data for Phothong maps, stops, and fare rates were collected from the PKCD website, a city development company in Phuket, and then visualized as a line graph using draw.io for the subsequent processes. The weighted Phothong map in Phuket has over 125 stops categorized into main and sub-stops. A sub-stop was defined as a bus stop where the bus routes passing by it are identical to those of the connected stops, while the remaining stops were categorized as main stops. To find the optimal route, we adapted Dijkstra's algorithm as the core route-finding method. The program will calculate the shortest path in the main graph, which consists of only main stops, instead of the shortest path in sub-stops. This reduces the time spent on the same subgraph. The program calculated the shortest route between the starting node and connected main stops, the ending node and connected main stops, as well as both previously mentioned main stops separately. This approach allowed the algorithm to determine the optimal route while minimizing overall runtime, and the PriorityQueue library was implemented in the program to find the shortest route in the graph according to Dijkstra's algorithm. Additionally, the PyQt5 module was used to create a user-friendly interface for the program, allowing users to input their starting point and destination and the program would subsequently provide the shortest route, along with fare details and recommended lines to take. The developed application was capable of recommending the shortest Phothong route to the destination, along with details such as the price and specific Phothong bus lines. The runtimes of the application run using the modified algorithm were approximately 25633 times less than the runtime using Dijkstra's algorithm, proving the program's increase in efficiency. As a part of our future development, we planned for this algorithm to consider additional factors such as waiting time and the number of transfers.

Introduction:

Public transportation is a mode of transport that is currently in development in many countries around the world. Decreasing the use of personal vehicles and switching to public transport can help solve road congestion problems in major cities, and also lessen the use of fuel which eventually decreases air pollution. The presence of multiple public transportation options leads to fewer cars on the roads, resulting in a reduction in car crashes and other road accidents. Thailand currently offers various transportation options, including buses, boats, and trains. However, many of these options are predominantly available in the Bangkok Metropolitan area. In other provinces, "Songthaew" or minibus is the main public transportation mode. Most people still have a negative viewpoint towards commuting by local public transit. For instance, surveys conducted in Amnatcharoen [1] revealed that the current public transportation modes available are inconvenient compared to personal cars,

which offer more flexibility and convenience. There are several applications that assist public transportation users, such as ViaBus, which detects the real-time location of buses in over 20 provinces in Thailand, which solves the problem of waiting for a long time or getting lost. Furthermore, the application features English language support, catering towards foreign tourists. Overall, these types of applications that guide and provide information for users have the potential to increase public transportation usage.

Phuket is a worldwide famous tourist destination of Thailand. The province was in the top 10 'World's Best Place to Visit' rankings from the poll by U.S. News & World Reports' website in 2020-2021. Phuket attracts a substantial number of visitors annually. Surprisingly, the province lacks a comprehensive bus or rail network, relying primarily on the local Songthaew bus, known as Phothong. There are many Phothong lines which service routes to popular tourist attractions at a relatively low cost. However, there is a lack of easily accessible data on routes, schedules, and fares, which poses a significant inconvenience, especially for new visitors. Developing an application which contains information about the Phothong system and can calculate the best routes and fares will help increase the popularity of using the Phothong bus.

To create the route-finding application, we utilize Dijkstra's algorithm to find the shortest path between two points in a weighted graph by creating a tree graph, which contains the shortest path from the starting point to all points in the graph. By transforming the Phothong map into a weighted graph, we can use the algorithm to apply in finding the shortest route in taking the Phothong bus in Phuket from the starting point to the destination.

According to available data, there are over 125 Phothong stops in Phuket. Running Dijkstra's algorithm on a graph with that size can be inefficient. Therefore, we proposed a new approach to calculating the shortest route in a graph. The program will only run Dijkstra's algorithm on the main graph, which contains points of intersection or line termination. The insignificant points, which are part of a continuous line in the graph, will be connected to the nearest main point.

While there has been development of query systems which utilizes Dijkstra's algorithm to find the shortest route in a weighted graph [3], it is done on a smaller scale compared to Phuket's Phothong bus system. Dijkstra's algorithm calculated on a simple graph is also only able to provide the shortest route, but not the Phothong lines to take. In order to offer more convenience, our developed application also returns the Phothong lines to take in the route.

In this project, the developed application will find the most efficient route by considering only distance. More complicated factors, such as schedules and traffic data, are left for future work.

Methodology:

Data Collection and Processing

Data of routes, lines, and fares of the Phothong network in Phuket was collected from the website of Phuket City Development Co., Ltd. The website contains information in the form of map images. The information was reorganized into a manageable manner in the form of Excel sheets. The distance between each Phothong stop was obtained through Google Maps routing feature. The data of Phothong stops and distances between stops were visualized as a weighted graph in draw.io for subsequent processes.

Over 125 Phothong stops in Phuket were numbered and classified into 'main stops' and 'sub stops.' Stops with the same Phothong bus lines as the stops connected to them are

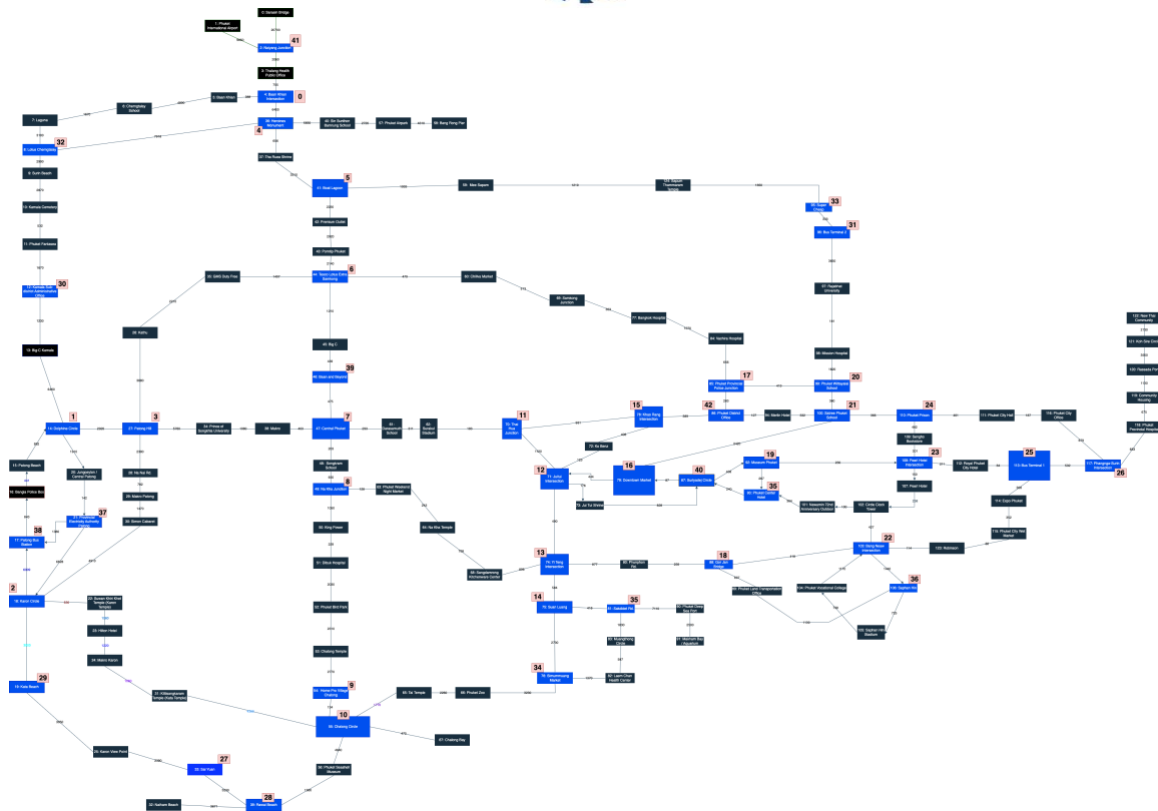


Figure 2. The graph showing all distances between stops created in draw.io. Main stops are indicated as blue.

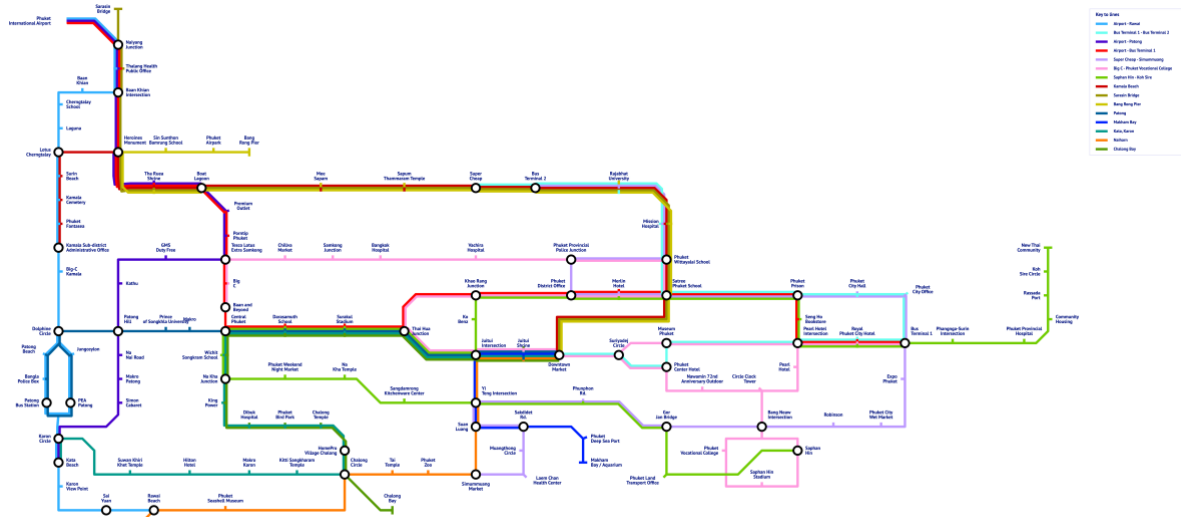


Figure 3. A re-drawn graph showing all Phothong lines in Phuket. Main stops are indicated as circles.

Route-Finding Algorithm

The program was coded with Python language on Visual Studio Code, and Dijkstra's algorithm was implemented into the program using PriorityQueue to assist in minimizing runtime. In the program, users can input their starting point and destination, then the program

subsequently returns the shortest Phothong route to take, Phothong lines to take, and total fare. The route-finding algorithm can be described as follows:

1. In the graph containing all Phothong stops, the source and the destination are connected to their nearest main stops. The distance from the source to its nearest stop and the distance from the destination to its nearest stop are obtained.
2. Dijkstra's algorithm is run on the main graph. Its starting point to run the algorithm is based on the point with fewer connecting points to reach the main stop.
3. The distance values are all combined and shown as the total distance from start to finish.
4. The algorithm returns a list containing stops that the route passes through.

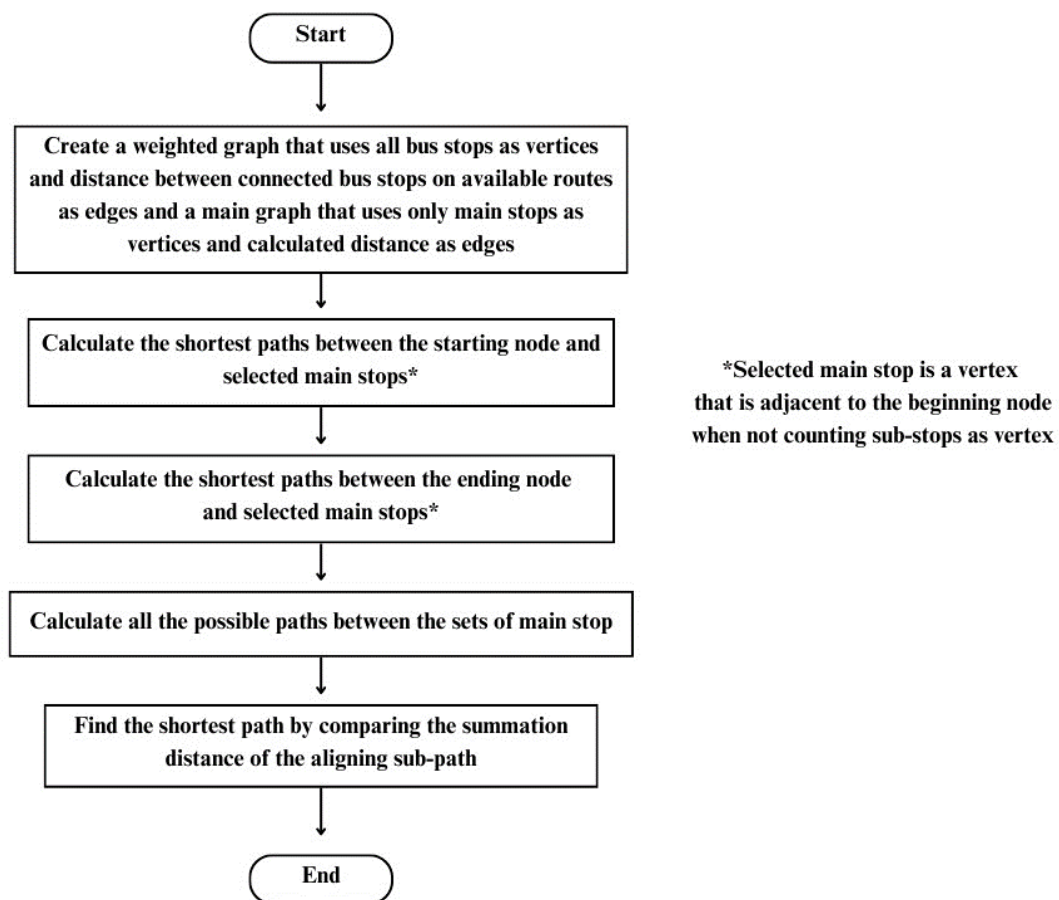


Figure 4. The flowchart of route-finding algorithm

Phothong Lines Assigning Algorithm

A dictionary containing all stops and lines that pass through each stop was created. Phothong lines are represented as letters in the code (e.g., 'A', 'B', and so on). After the shortest route is calculated, the program eventually runs through processes to assign the Phothong lines needed to take. The process is as follows:

1. The program creates a list of lines that pass through the stop for each stop in the route.
2. In the first list, remove any lines that do not appear in the list next to it.

3. In the second list, remove any lines that do not appear in the list before or after it. Then iterate the same procedure over all lists.
4. In the first list, only keep the Phothong lines with the cheapest fare and remove other items.
5. In the second list, only keep the Phothong line that appears in the first list. This process is repeated on all items except in an empty list.
6. In the case of an empty list, which indicates the need for line transfer, the items in the two lists beside it are added and the list is tagged as point of transfer.
7. The final list contains multiple lists inside it which contain the Phothong lines to take.
8. After the Phothong lines are obtained, the fares of each line are added together and returned as the total fare.

After calculating and assigning all the necessary information, the program returns the full distance, the Phothong lines to take, the total fare, and where to transfer if needed.

Program Evaluation

To evaluate our program, we compare the runtime of Dijkstra's algorithm with our adjusted Dijkstra's algorithm. The process is as follows:

1. Create a graph of the Phothong stops in Phuket.
2. Choose random stops as starting stops and ending stops and run the program, then compare the results with the program that uses normal Dijkstra's algorithm.
3. Collect runtimes in both programs.

Implementing an Interface Evaluation

To display the result, we created an interface with Python language on Visual Studio Code. PyQt5 module is selected to assist in creating a graphical user interface because its property enables Python to be used as an application development language on all supported platforms including Windows, macOS, Linux, iOS, and Android. The process is as follows:

1. Planning layouts and events considering user experience.
2. Create a main application class by inheriting both the interface class and the main PyQt widget class that suits your application needs.
3. Compile information from the previous calculation
4. Style, display, and adjust all elements based on Comprehensible and visibility

Results and Discussion:

Our algorithm classifies stops into main stops and sub-stops and works as follows. Firstly, the program identifies the path from the starting node to the main node avoiding other main nodes. Secondly, the program repeats the process with the ending node. As a result, only 34 main stops are needed to run Dijkstra's algorithm. The following is an example case of how the algorithm worked when calculating the route from Tha Ruea Shrine to Samkong Junction.

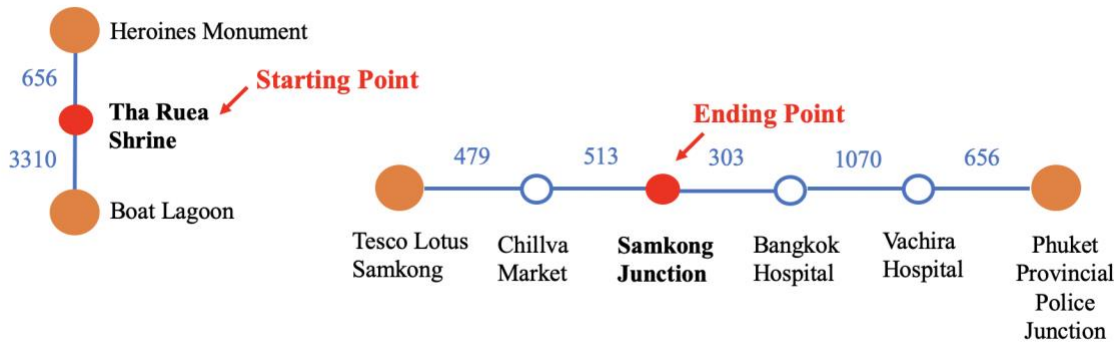


Figure 5. The graphs of Phothong maps from Tha Ruea Shrine and Samkong Junction main stops in Phuket

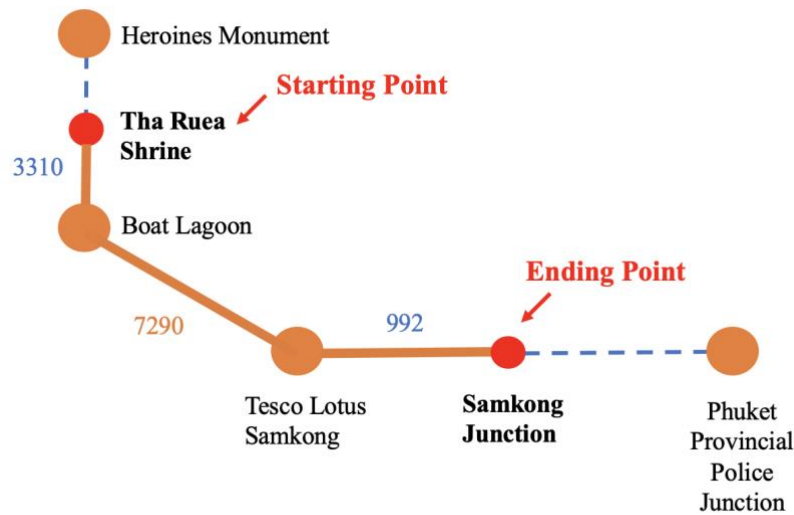


Figure 6. The graphs of Phothong maps using Dijkstra's algorithm which runs on an optimal route.

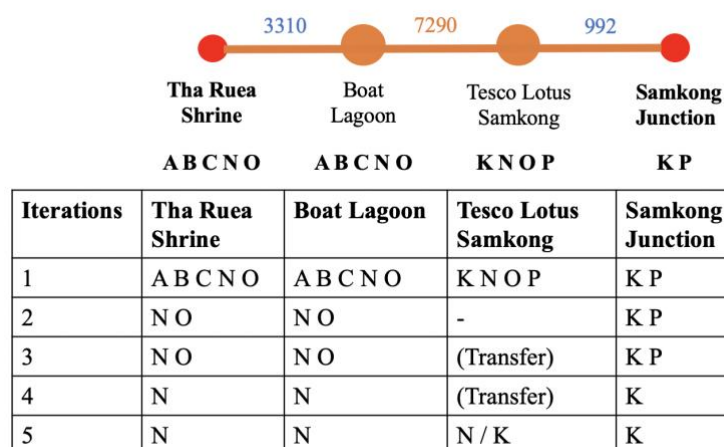


Figure 7. The diagram showing an example of assigning Phothong lines to the obtained route.

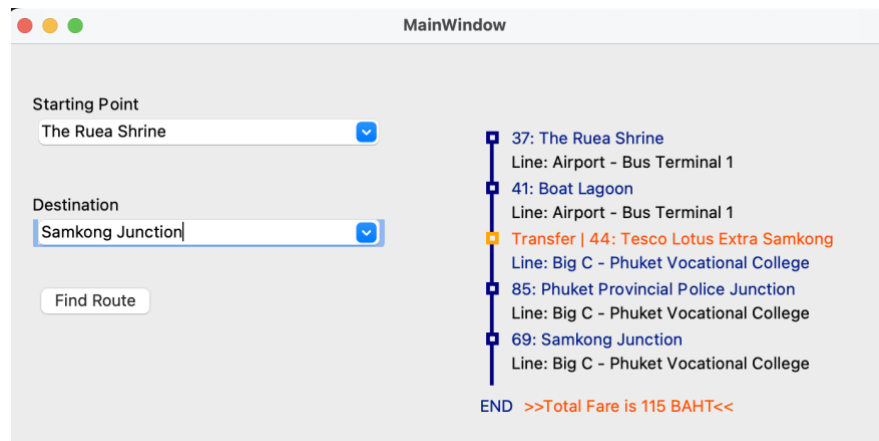


Figure 8. The examples of graphical user interface

In the end, the shortest route is traveling from Phuket Airpark through Heroines Monument and Baan Khian Intersection to Cherngtalay School which is 19,967 meters. Therefore, this program can successfully find the optimal path in every case and can use this information to calculate fare details and recommended lines to take.

Table 1. Runtimes comparisons on random routes

Optimal route			Runtime (seconds)	
Starting point	Ending point	Number of the Stops	Program's algorithm	Dijkstra's algorithm
Phuket Zoo	Baan Khian	13	0.000163	4.124861
Provincial Hospital	Songkhla University	11	0.000165	3.711982
Phuket Airport	Chalong Circle	11	0.000183	2.035965
Vocational College	Kata Temple	8	0.000250	8.837714
Patong Hill	Tai Temple	8	0.000162	2.299687
Rajabhat University	Rassada Port	6	0.000204	12.736772
Suan Luang	Central Phuket	5	0.000178	4.044885
Kata Beach	Chillva Market	5	0.000182	3.130895
Naiharn Beach	Dibuk Hospital	5	0.000196	2.177035
Gor Jan Bridge	Phuket Wet Market	3	0.000189	4.886444

Our algorithm was developed in Visual Studio Code Version 1.82.2. It was implemented on an AMD Ryzen 5 4500U with Radeon Graphics 2.38 GHz processor and 8.00 GB RAM, running on the Microsoft Windows Feature Experience Pack 1000.22662.1000.0

Comparing the runtime of the adjusted Dijkstra's algorithm to the original Dijkstra's algorithm, it is obvious that classifying stops into main stops and sub-stops makes the program's efficiency in calculating routes on the Phothong bus map. The approximate runtime in the program run using the adjusted algorithm decreased by 25633 times compared to Dijkstra's algorithm.

Conclusion:

This program successfully finds the optimal path considering the distance that the Photong bus needs to provide to travel from the starting node to the ending node. Our algorithm's classification of stops into main stops and sub-stops improves the program's performance, with the runtime decreased by 25633 times compared to the program run using unadjusted Dijkstra's algorithm. The application provides optimal travel routes, guides the user through all the stops with remarks for changing bus lines, and calculates the price for users. The application has the potential to be more useful when it includes additional factors such as waiting time and the number of transfers.

Acknowledgements:

We would like to express our gratitude to our advisors, Dr. Monsikarn Jansrang and Dr. Sittichoke Som-am, for supporting the project by giving us exceptional guidance. Special thanks are extended to the developers of the public transportation application ViaBus, whose innovative solution served as a reference and inspiration for our project.

References:

1. Anatapak V. SUTIR. 2011.
2. Tuaycharoen N, Sakcharoen A, Cha-aim W. Procedia Comput Sci. 2016;86:441-444.
3. Chen R. Adv Econ Bus Manag Res. 2022;654:321-325.
4. Tirastittam P, Waiyawuththanapoom P. World Acad Eng Technol. 2014;8:54-59.
5. Anon S, Kunya W. ICETA. 2018;61-70.
6. Al-Qerem A, Al-Shraha B, Ninio R. Int J Comput Sci. 2015;4:888-894



THE PROBABILITY DISTRIBUTION OF FLIGHT DEPARTURE DELAYS AT CHIANG MAI INTERNATIONAL AIRPORT

Kamonpan Junlat,^{1,*} Phisanu Chiawkhun,¹ Pimwarat Srikummoon¹

¹Department of Statistics, Faculty of Science, Chiang Mai University, Mueang Chiang Mai, Chiang Mai 50200, Thailand

*e-mail: kamonpan_jun@cmu.ac.th

Abstract:

The objective of this research is to study the probability distribution of flights departure delays domestic from Chiang Mai International Airport to airports located in the central region of Thailand. The total flight data were collected from 2017 to 2019 to estimate the parameters of 20 distributions using the Maximum Likelihood Estimation method and the goodness of fit test with the Anderson-Darling test. This research used the Akaike Information Criterion and the Bayesian Information Criterion as criterion to select the appropriate distribution, and considering the statistical accuracy criterion was Mean Absolute Error, Mean Absolute Percentage Error, and Root Mean Square Error. The results were as follows; flight delays of 6 hours or more were 0.04% of all flights. Most flight delays were between 1 - 45 minutes, with 67.68% in the central region experiencing delays. The maximum delay time occurred in the year 2017, with an average delay time was 14.30 minutes and a median was 11 minutes. Finally, we found that the Log Pearson Type 3 distribution was the most appropriate for describing the delay time of domestic flights departing from Chiang Mai International Airport to airports located in the central region of Thailand.

Introduction:

Flight delays can occur and have economic consequences for passengers, airlines, airports, and the global economy.¹ Causes of flight delays include many factors such as inadequate airport capacity to handle a high volume of aircraft, inappropriate flight scheduling, turbulent weather conditions, late passenger boarding, or delayed loading of baggage, etc., These events are unforeseen circumstances, and when any of these events occur, they can affect subsequent flights and have an impact on the overall operational plans of the airport.²

The analysis of the probability distribution is used to measure, predict, and estimate the likelihood of achieving certain outcomes. Additionally, it is also used to determine confidence intervals around estimated values.³ When we fit a probability distribution to flight delay times, the benefits of this distribution are as follows: airports can plan suitable flight schedules, airlines can budget their expenses, and passengers can prepare for potential events, helping them allocate their time and reduce waiting time losses during flight delays. However, numerous research studies have examined flight delays. For example, in 2002, researchers in the USA analyzed the characteristics of aircraft arrival and departure delays. They suggested Normal distribution for the created flight arrival delay and Poisson distribution that fits the flight departure delay.⁴ In 2014, the flight departure delays of Garuda airline from Indonesia were analyzed, and the most suitable model was found Log Normal distribution for the distribution of departure delay duration and Mixture of Normal distributions with four components was good model for departure delay time distribution.⁵ In 2018, the flight delays of airlines in China were analyzed by following the separate causes of flight delay. They found Weibull distribution suitable for flight delays caused by inclement weather.⁶ This distribution corresponds to what was discovered in the flight delays of 11 countries in Southeast Asia.⁷ In 2020, researchers from Thailand analyzed flight departure delays for one airline at Don Mueang International Airport. They found that the most suitable distributions for flight delays were Log Pearson Type 3 distribution and Burr distribution.⁸

We are interested in studying the distribution of departure flights from Chiang Mai International Airport because Chiang Mai is the main province in the northern region and serves as a hub for tourism and aviation. This study involves an examination of destination airports in the central region, considering them separately for each year. Additionally, our research aims to estimate the parameters associated with the appropriate distribution of delay times for flights departure.

Methodology:

We collected secondary data on the departure time of domestic flights from Chiang Mai International Airport to various destination province, including Phitsanulok, Sukhothai, Phetchabun, and Bangkok (Don Mueang and Suvarnabhumi), for the years 2017 to 2019. The data was obtained from the website <http://webmac.dyndns.info:9023/> and calculated the delay time of flights only departure in the originating province⁸ defined as

$$\text{Delay} = \text{Actual Departure Time (ADT)} - \text{Scheduled Departure Time (SDT)} \quad (1)$$

The ADT is the departure time following the local time when the airplane began its ascent into the sky. The SDT is the departure time following the announcement on boarding pass, indicating when the airplane starts moving away from the boarding gate.

The delay time is x , where x is greater than 0 minutes. The next step is to check for outlier values in the data using the Interquartile range (IQR) and a box plot. After removing the outliers from the data, we can proceed to estimate parameters based on a probability distribution selected from the literature review. We found that most of the data show a unimodal distribution, and upon plotting a histogram, it becomes evident that the data follows a right-skewed curve. As a result, we have considered a total of 20 right-skewed curve probability distributions, as follows.

- 1). Exponential distribution⁹: $f(x) = \frac{1}{\beta} \exp\left(-\frac{x}{\beta}\right)$ where β is scale parameter ($\beta > 0$).
- 2). Gamma distribution¹⁰: $f(x) = \frac{1}{\Gamma(\alpha)\beta^\alpha} x^{\alpha-1} \exp\left(-\frac{x}{\beta}\right)$ where $\Gamma(\alpha)$ is gamma function, α is shape parameter ($\alpha > 0$), and β is scale parameter ($\beta > 0$).
- 3). Three – parameter Gamma distribution¹¹: $f(x) = \frac{1}{\Gamma(\alpha)\beta^\alpha} (x-\gamma)^{\alpha-1} \exp\left(-\frac{x-\gamma}{\beta}\right)$ where α is shape parameter ($\alpha > 0$), β is scale parameter ($\beta > 0$), and γ is threshold parameter ($-\infty < \gamma < \infty$)¹².
- 4). Generalized Gamma distribution¹³: $f(x) = \left[\left(\frac{\delta}{\theta^\kappa} \right) x^{\kappa-1} \exp\left(-\left(\frac{x}{\theta}\right)^\delta\right) \right] / \Gamma\left(\frac{\kappa}{\delta}\right)$ where θ is scale parameter ($\theta > 0$)¹⁴, κ is shape parameter ($\kappa > 0$)¹⁴, and δ is shape parameter ($\delta > 0$)¹⁴.
- 5). Log Normal distribution⁹: $f(x) = \frac{1}{x\sigma\sqrt{2\pi}} \exp\left(-\frac{(\log x - \mu)^2}{2\sigma^2}\right)$ where σ is shape parameter ($\sigma > 0$), and $\mu = \log m$, which m is the median (scale parameter) ($\mu > 0$).
- 6). Weibull distribution¹⁵: $f(x) = \frac{\alpha}{\beta} \left(\frac{x}{\beta}\right)^{\alpha-1} \exp\left[-\left(\frac{x}{\beta}\right)^\alpha\right]$ where α is shape parameter ($\alpha > 0$), and β is scale parameter ($\beta > 0$).

- 7). Exponentiated Weibull distribution¹⁶: $f(x) = \left(\frac{\alpha\theta}{\sigma}\right) \left[1 - \exp\left(-\left(\frac{x}{\sigma}\right)^\alpha\right)\right]^{\theta-1} \exp\left(-\left(\frac{x}{\sigma}\right)^\alpha\right) \left(\frac{x}{\sigma}\right)^{\alpha-1}$ where α , θ are shape parameter ($\alpha > 0$) and ($\theta > 0$), and σ is scale parameter ($\sigma > 0$).
- 8). Generalized Weibull distribution¹⁷: $f(x) = \frac{1}{\gamma\sigma} \left[1 - \lambda(x/\sigma)^{1/\gamma}\right]^{(1/\lambda)-1} (x/\sigma)^{(1/\gamma)-1}$ where γ , λ are shape parameter ($\gamma > 0$) and ($\lambda \in \mathbb{R}$), and σ is scale parameter ($\sigma > 0$).
- 9). Burr Type III distribution¹⁸: $F(x) = \left(1 + \frac{1}{\gamma_1} \left(\frac{x}{\beta}\right)^{\gamma_2}\right)^{-\gamma_1\gamma_2}$ where γ_1 , γ_2 are shape parameters ($\gamma_1 > 0$) and ($\gamma_2 > 0$), β is scale parameter ($\beta > 0$).
- 10). Burr type XII distribution¹⁹: $f(x) = \frac{ck}{\alpha} \left(\frac{x}{\alpha}\right)^{c-1} \left(1 + \left(\frac{x}{\alpha}\right)^c\right)^{-(k+1)}$ where c is inner shape parameter ($c > 0$), k is outer shape parameter ($k > 0$), and α is scale parameter ($\alpha > 0$).
- 11). Inverse Burr distribution²⁰: $f(x) = \alpha\beta \left(\frac{x}{\theta}\right)^{\alpha\beta} \left/x \left[1 + \left(\frac{x}{\theta}\right)^\beta\right]^{\alpha+1}\right.$ where α is shape1 parameter ($\alpha > 0$), β is shape2 parameter ($\beta > 0$), and θ is scale parameter ($\theta > 0$).
- 12). Log Pearson type 3 distribution²¹: $f(x) = \frac{1}{|\beta|x\Gamma(\alpha)} \left(\frac{\ln x - \tau}{\beta}\right)^{\alpha-1} \exp\left(-\frac{\ln x - \tau}{\beta}\right)$ where α is shape parameter ($\alpha > 0$), β is scale parameter ($\beta > 0$), and τ is location parameter by $\exp[\tau]$ is lower bound.
- 13). Log Logistic distribution²²: $f(x) = \left(\frac{\beta}{\alpha}\right) \left[\left(\frac{x}{\alpha}\right)^{\beta-1} / \left[1 + \left(\frac{x}{\alpha}\right)^\beta\right]^2\right]$ where α is scale parameter ($\alpha > 0$), and β is shape parameter ($\beta > 0$).
- 14). Generalized Extreme Value distribution²³: $f(x) = \alpha^{-1} \exp[-(1-\kappa)y - \exp(-y)]$
By $y = -\kappa^{-1} \log\left(1 - \frac{\kappa(x-\xi)}{\alpha}\right)$ when $\kappa \neq 0$ where ξ is location parameter ($\xi > 0$), α is scale parameter ($\alpha > 0$), and κ is shape parameter ($\kappa < 0$) when $\xi + \frac{\alpha}{\kappa} \leq x < \infty$.
- 15). Inverse Gaussian distribution⁹: $f(x) = \left(\frac{\lambda}{2\pi x^3}\right)^{1/2} \exp\left(\frac{-\lambda(x-\mu)^2}{2\mu^2 x}\right)$ where μ is location parameter ($\mu > 0$), and λ is scale parameter ($\lambda > 0$).
- 16). Generalized Inverse Gaussian distribution²⁴: $f(x) = \frac{\left(\frac{\chi}{\psi}\right)^{\lambda/2}}{2K_\lambda(\sqrt{\psi\chi})} x^{\lambda-1} \exp\left(-\frac{1}{2}\left(\psi x + \frac{\chi}{x}\right)\right)$ where χ is shape parameter ($\chi \geq 0$), ψ is shape parameter ($\psi > 0$), λ is shape parameter ($\lambda > 0$), and K_λ denotes the modified Bessel function of the third kind with index λ .
- 17). Beta Prime distribution²⁵: $f(x) = \left[\left(1 + \left(\frac{x}{\sigma}\right)\right)^{-\alpha-\beta} \left(\frac{x}{\sigma}\right)^{-1+\alpha}\right] / [\sigma B(\alpha, \beta)]$ where α , β are shape parameter ($\alpha > 0$) and ($\beta > 0$), σ is scale parameter ($\sigma > 0$), and $B(\alpha, \beta)$ is beta function.

18). Generalized Beta (first kind) distribution²⁶: $f(x) = \frac{\tau}{\theta^\alpha B(\alpha, \beta)} x^{\tau\alpha-1} \left(1 - \left(\frac{x}{\theta}\right)^\tau\right)^{\beta-1}$ where τ , α , and β are shape parameter ($\tau > 0$), ($\alpha > 0$), and ($\beta > 0$), and θ is scale parameter ($\theta > 0$).

19). Generalized Beta (second kind) distribution²⁷: $f(x) = \frac{r_3}{\beta B(r_1, r_2)} \left(\frac{x}{\beta}\right)^{r_3-1} \left(1 + \left(\frac{x}{\beta}\right)^{r_3}\right)^{-(r_1+r_2)}$ where r_1 , r_2 , and r_3 are shape parameter ($r_1 > 0$), ($r_2 > 0$), and ($r_3 > 0$), and β is scale parameter ($\beta > 0$).

20). Generalized Pareto distribution²⁸: $f(x) = \frac{1}{\sigma} \left(1 + \xi \frac{x - \mu}{\sigma}\right)^{-\left(\frac{1}{\xi} + 1\right)}$ when $\xi \neq 0$ where ξ is shape parameter ($\xi \in \mathbb{R}$), μ is location parameter ($\mu \in \mathbb{R}$), and σ is scale parameter ($\sigma > 0$).

As mentioned above, the Probability Density Function (PDF) is where we employ the Maximum Likelihood Estimation (MLE) method to estimate parameters.

We use R programming (version 4.2.3) to analyze the data. R codes for the statistical analyses done are available at https://github.com/KamonpanJun/flightdelay_distribution.git Evaluating the goodness of fit of a PDF involves the following steps:

1. Akaike Information Criterion (*AIC*) The best model is determined by statistics with the lowest *AIC*.^{29,30}

$$AIC(\hat{\theta}) = (-2) \log(\hat{L}) + 2k \quad (3)$$

where k is the number of parameters in the reliability model, and \hat{L} the maximized value of the likelihood function for the estimated model.

2. Bayesian information Criterion (*BIC*) stronger than *AIC* when penalizing additional parameters.³⁰ In several competing models, the one with the lowest *BIC* is preferred.

$$BIC(\hat{\theta}) = (-2) \log(\hat{L}) + k \log(n) \quad (4)$$

where k is the number of parameters in the reliability model, n the number of observations in the given data set, and \hat{L} the maximized value of the likelihood function for the estimated model.

3. Anderson – Darling Test (AD^2)³¹ When the Anderson-Darling test statistic is at a minimum, it indicates that the observed data is very close to the expected values under the hypothesized distribution.

$$AD^2 = -n - \frac{1}{n} \sum_{i=1}^n (2i-1) \left[\ln F^*(X_i) + \ln(1 - F^*(X_{n+1-i})) \right] \quad (5)$$

where $F^*(X_i)$ is an expected cumulative distribution function, X_i is the observed delay of the flight, and n is the sample size.

4. Accuracy measurement methods this research considers three common metrics: Mean Absolute Error (*MAE*), Mean Absolute Percentage Error (*MAPE*), and Root Mean Square Error (*RMSE*) to explain the model's fit to the dataset. To indicate that a model fits the dataset well, it should have low values for *MAE*, *MAPE*, and *RMSE*.^{32,33}

$$MAE = \frac{\sum_{i=1}^n |y_i - x_i|}{n}, \quad MAPE = \frac{100}{n} \sum_{i=1}^n \left| \frac{(x_i - y_i)}{x_i} \right|, \text{ and } RMSE = \sqrt{\frac{\sum_{i=1}^n (y_i - x_i)^2}{n}} \quad (6)$$

where y_i is the predicted delay time of domestic flights departure (minutes) created by Probability Density Function (PDF), and n is the sample size.

5. In the evaluation process, arrange the ranks of the criteria and test statistics used to assess the appropriateness of the distribution by ranking the models from the lowest to the highest value. Finally, we choose the rank sum, considering the lowest rank sum, to determine which probability distribution best fits the data for the delay time of domestic flight departures.

Results and Discussion:

The scope of this study focuses on destination airports in the central region. Between the years 2017 and 2019, we found 49,520 flights experienced delays of 1 minute or more. These findings are illustrated in Figure 1, which features a pie chart and a histogram depicting the frequency of flight delays for domestic flights departure. The histogram reveals a right-skewed distribution of flight delays from 2017 to 2019, with most delays not exceeding 1 hour.

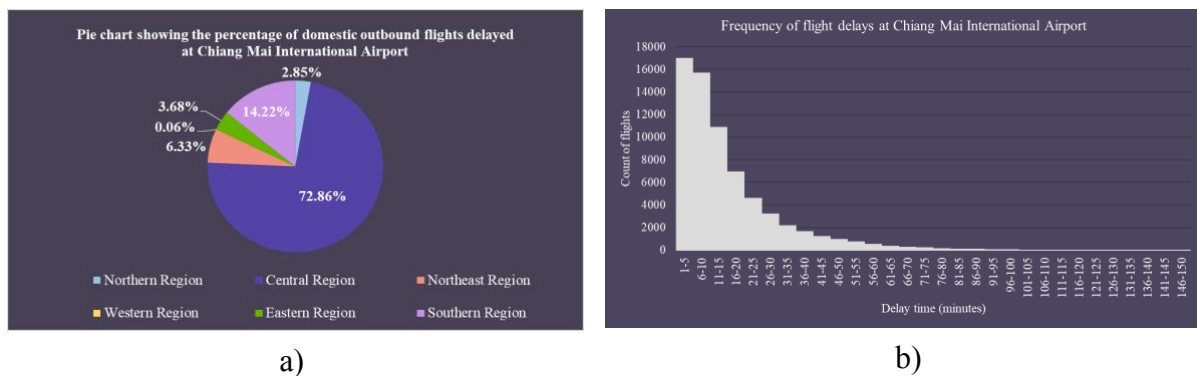


Figure 1.

a) Percentage of delay times categorized by region and b) Histogram shows the distribution of frequency of flight departure delays at Chiang Mai International Airport (year 2017 – 2019).

The data related to the central region with delay times ranging from 1 to 45 minutes total 46,001 flights. When we proceeded to create a dataset of domestic flight departure delays ranging from 1 to 45 minutes for journeys to the central region, the next step was to plot a histogram the data distribution and observe its characteristics. We found that the flight delay data for each year show a right-skewed distribution, like the distribution of all departure delay times in Figure 1 (b).

As part of descriptive statistics, we calculated the average delay of flights (\bar{x}), standard deviation (S.D.), median, interquartile range (IQR), coefficient of skewness, and coefficient of kurtosis, as shown in Table 1 below. We found that in 2017, average delays were 14.30 minutes higher than other years, while 2018 had a 12-minute higher median. The standard deviations were close, indicating consistent patterns. A positive skewness suggests a right-skewed distribution, and kurtosis more than 0 implies non-normal distribution.

Table 1.

Descriptive statistics of delay times for domestic flights departure whose destinations are airports located in the central region.

Year	n (flight)	Min (minutes)	Max (minutes)	\bar{x} (minutes)	S.D.	Median (minutes)	IQR	Skewness	Kurtosis
2017	14,801	1	45	14.30	10.60	11.00	14.00	0.96	3.17
2018	15,837	1	45	14.10	10.20	12.00	14.00	0.96	3.27
2019	15,363	1	45	13.98	10.30	11.00	14.00	0.98	3.27
Total	46,001								

Table 2.

Estimating Distribution Parameters and Assessing Suitability for Modeling Flight Delay Times of Domestic Flights departure to Central Region Airports (2017-2019)

Distribution	Parameter Estimation and Consideration of Suitability Criteria	Year		
		2017	2018	2019
1. Exponential	Parameter estimation	$\beta = 14.323$	$\beta = 14.139$	$\beta = 13.977$
	AIC (Ranking)	108,401.3 (19)	115,577.7 (19)	111,766.1 (19)
	BIC (Ranking)	108,408.9 (19)	115,585.3 (19)	111,773.7 (19)
	AD^2 (Ranking)	341.084 (18)	438.769 (19)	366.329 (19)
	MAE (Ranking)	14.291 (17)	14.107 (19)	13.945 (19)
	MAPE (Ranking)	99.240 (4)	99.256 (2)	99.204 (3)
	RMSE (Ranking)	17.822 (20)	17.427 (19.50)	17.372 (19)
	Rank Sum	97.00	97.50	97.00
2. Gamma	Parameter estimation	$\beta = 8.636, \alpha = 1.659$	$\beta = 8.131, \alpha = 1.739$	$\beta = 8.380, \alpha = 1.668$
	AIC (Ranking)	106,436.6 (9)	113,106.7 (11)	109,684.3 (10)
	BIC (Ranking)	106,451.8 (9)	113,122 (11)	109,699.5 (10)
	AD^2 (Ranking)	29.550 (3)	27.587 (7)	28.658 (4)
	MAE (Ranking)	14.290 (10)	14.105 (10)	13.943 (7.50)
	MAPE (Ranking)	99.407 (9.50)	99.425 (8)	99.382 (8.50)
	RMSE (Ranking)	17.820 (12)	17.424 (11.50)	17.370 (14.50)
	Rank Sum	52.50	58.50	54.50
3. Three parameter Gamma	Parameter estimation	$\alpha = 2.076, \beta = 7.531, \gamma = -1.311$	$\alpha = 1.413, \beta = 9.518, \gamma = 0.691$	$\alpha = 1.275, \beta = 10.336, \gamma = 0.801$
	AIC (Ranking)	106,930.2 (13)	112,944 (4)	109,431.1 (3)
	BIC (Ranking)	106,953 (13)	112,967 (4)	109,454 (3)
	AD^2 (Ranking)	38.315 (10)	46.197 (13)	60.249 (13)
	MAE (Ranking)	14.278 (3)	14.109 (20)	13.947 (20)
	MAPE (Ranking)	99.212 (2)	99.465 (18)	99.403 (17)
	RMSE (Ranking)	17.812 (3)	17.427 (19.50)	17.373 (20)
	Rank Sum	44.00	78.50	76.00
4. Generalized Gamma	Parameter estimation	$\theta = 13.220, \kappa = 1.456, \delta = 1.229$	$\theta = 13.757, \kappa = 1.476, \delta = 1.298$	$\theta = 13.076, \kappa = 1.455, \delta = 1.242$
	AIC (Ranking)	106,407.1 (6)	113,050.2 (6)	109,648.2 (7)
	BIC (Ranking)	106,429.9 (6)	113,073.2 (7)	109,671.1 (8)
	AD^2 (Ranking)	30.288 (4)	25.583 (3)	28.346 (3)
	MAE (Ranking)	14.290 (10)	14.105 (10)	13.944 (14.50)
	MAPE (Ranking)	99.411 (12)	99.430 (11.50)	99.386 (12)
	RMSE (Ranking)	17.820 (12)	17.424 (11.50)	17.370 (7)
	Rank Sum	50.00	49.00	51.50
5. Log Normal	Parameter estimation	$\sigma = 0.899, \mu = 2.331$	$\sigma = 0.877, \mu = 2.335$	$\sigma = 0.897, \mu = 2.309$
	AIC (Ranking)	107,857.6 (17)	114,748.8 (17)	111,213.8 (17)
	BIC (Ranking)	107,872.8 (17)	114,764.2 (17)	111,229.1 (17)
	AD^2 (Ranking)	132.813 (17)	154.209 (17)	146.050 (17)
	MAE (Ranking)	14.107 (2)	13.920 (2)	13.757 (2)
	MAPE (Ranking)	96.141 (1)	96.270 (1)	95.993 (1)
	RMSE (Ranking)	17.729 (2)	17.328 (2)	17.276 (2)
	Rank Sum	56.00	56.00	56.00
6. Weibull	Parameter estimation	$\alpha = 1.363, \beta = 15.667$	$\alpha = 1.404, \beta = 15.539$	$\alpha = 1.368, \beta = 15.297$
	AIC (Ranking)	106,414.8 (8)	113,054.4 (8)	109,655.2 (9)
	BIC (Ranking)	106,430 (7)	113,069.8 (6)	109,670.4 (7)
	AD^2 (Ranking)	32.125 (7)	26.449 (4)	29.798 (7)
	MAE (Ranking)	14.291 (17)	14.105 (10)	13.944 (14.50)
	MAPE (Ranking)	99.412 (13.50)	99.430 (11.50)	99.386 (12)
	RMSE (Ranking)	17.820 (12)	17.424 (11.50)	17.369 (7)
	Rank Sum	64.50	51.00	56.50
7. Exponentiated Weibull	Parameter estimation	$\alpha = 1.283, \theta = 1.111, \sigma = 14.600$	$\alpha = 1.326, \theta = 1.111, \sigma = 14.495$	$\alpha = 1.292, \theta = 1.104, \sigma = 14.315$
	AIC (Ranking)	106,411.7 (7)	113,054 (7)	109,652.2 (8)
	BIC (Ranking)	106,434.5 (8)	113,077.1 (8)	109,675.1 (9)

Distribution	Parameter Estimation and Consideration of Suitability Criteria	Year		
		2017	2018	2019
8. Generalized Weibull	AD^2 (Ranking)	30.717 (6)	26.801 (6)	28.669 (5)
	MAE (Ranking)	14.290 (10)	14.105 (10)	13.944 (14.50)
	MAPE (Ranking)	99.412 (13.50)	99.431 (13.50)	99.386 (12)
	RMSE (Ranking)	17.820 (12)	17.424 (11.50)	17.369 (7)
	Rank Sum	56.50	56.00	55.50
	Parameter estimation	$\gamma = 0.797, \lambda = 0.150$ $\sigma = 17.119$	$\gamma = 0.760, \lambda = 0.118$ $\sigma = 16.608$	$\gamma = 0.784, \lambda = 0.126$ $\sigma = 16.455$
	AIC (Ranking)	106,355.3 (4)	113,011.8 (5)	109,609.4 (5)
	BIC (Ranking)	106,378.1 (4)	113,034.8 (5)	109,632.3 (5)
	AD^2 (Ranking)	39.950 (11)	31.206 (8)	35.592 (9)
	MAE (Ranking)	14.291 (17)	14.106 (17)	13.944 (14.50)
	MAPE (Ranking)	99.409 (11)	99.427 (10)	99.382 (8.50)
	RMSE (Ranking)	17.820 (12)	17.424 (11.50)	17.370 (14.50)
	Rank Sum	59.00	56.50	56.50
	Parameter estimation	$\beta = 22.053, \gamma_1 = 1.178,$ $\gamma_2 = 0.302$	$\beta = 22.038, \gamma_1 = 1.203$ $\gamma_2 = 0.286$	$\beta = 21.546,$ $\gamma_1 = 1.182, \gamma_2 = 0.299$
	AIC (Ranking)	107,135 (14.50)	113,734.6 (14.50)	110,353 (14.50)
9. Burr Type III	BIC (Ranking)	107,157.8 (14.50)	113,757.6 (14.50)	110,375.9 (14.50)
	AD^2 (Ranking)	52.228 (12)	46.030 (12)	48.931 (11)
	MAE (Ranking)	14.298 (20)	14.106 (17)	13.944 (14.50)
	MAPE (Ranking)	99.825 (19)	99.441 (16)	99.399 (16)
	RMSE (Ranking)	17.816 (4)	17.424 (11.50)	17.369 (7)
	Rank Sum	84.00	85.50	77.50
	Parameter estimation	$c = 1.406, k = 16.611$ $\alpha = 112.140$	$c = 1.439, k = 20.6$ $\alpha = 124.125$	$c = 1.402, k = 19.820$ $\alpha = 125.466$
	AIC (Ranking)	106,469.3 (10)	113,096.9 (10)	109,698.6 (11)
	BIC (Ranking)	106,492.1 (10)	113,119.9 (10)	109,721.5 (11)
	AD^2 (Ranking)	32.192 (8)	26.463 (5)	29.218 (6)
	MAE (Ranking)	14.290 (10)	14.105 (10)	13.944 (14.50)
	MAPE (Ranking)	99.414 (16)	99.431 (13.50)	99.387 (14)
	RMSE (Ranking)	17.820 (12)	17.424 (11.50)	17.369 (7)
	Rank Sum	66.00	60.00	63.50
	Parameter estimation	$\alpha = 0.355, \beta = 3.313$ $\theta = 21.009$	$\alpha = 0.344, \beta = 3.498$ $\theta = 20.904$	$\alpha = 0.354, \beta = 3.343$ $\theta = 20.477$
10. Burr type XII	AIC (Ranking)	107,135 (14.50)	113,734.6 (14.50)	110,353 (14.50)
	BIC (Ranking)	107,157.8 (14.50)	113,757.6 (14.50)	110,375.9 (14.50)
	AD^2 (Ranking)	52.242 (13)	45.957 (11)	48.840 (10)
	MAE (Ranking)	14.290 (10)	14.104 (4)	13.943 (7.50)
	MAPE (Ranking)	99.407 (9.50)	99.420 (6)	99.380 (7)
	RMSE (Ranking)	17.819 (5)	17.423 (4)	17.369 (7)
	Rank Sum	66.50	54.00	60.50
	Parameter estimation	$\alpha = 0.355, \beta = 3.313$ $\theta = 21.009$	$\alpha = 0.344, \beta = 3.498$ $\theta = 20.904$	$\alpha = 0.354, \beta = 3.343$ $\theta = 20.477$
	AIC (Ranking)	107,135 (14.50)	113,734.6 (14.50)	110,353 (14.50)
	BIC (Ranking)	107,157.8 (14.50)	113,757.6 (14.50)	110,375.9 (14.50)
	AD^2 (Ranking)	52.242 (13)	45.957 (11)	48.840 (10)
	MAE (Ranking)	14.290 (10)	14.104 (4)	13.943 (7.50)
	MAPE (Ranking)	99.407 (9.50)	99.420 (6)	99.380 (7)
	RMSE (Ranking)	17.819 (5)	17.423 (4)	17.369 (7)
	Rank Sum	66.50	54.00	60.50
11. Inverse Burr	Parameter estimation	$\alpha = 0.355, \beta = 3.313$ $\theta = 21.009$	$\alpha = 0.344, \beta = 3.498$ $\theta = 20.904$	$\alpha = 0.354, \beta = 3.343$ $\theta = 20.477$
	AIC (Ranking)	107,135 (14.50)	113,734.6 (14.50)	110,353 (14.50)
	BIC (Ranking)	107,157.8 (14.50)	113,757.6 (14.50)	110,375.9 (14.50)
	AD^2 (Ranking)	52.242 (13)	45.957 (11)	48.840 (10)
	MAE (Ranking)	14.290 (10)	14.104 (4)	13.943 (7.50)
	MAPE (Ranking)	99.407 (9.50)	99.420 (6)	99.380 (7)
	RMSE (Ranking)	17.819 (5)	17.423 (4)	17.369 (7)
	Rank Sum	66.50	54.00	60.50
	Parameter estimation	$\alpha = 0.355, \beta = 3.313$ $\theta = 21.009$	$\alpha = 0.344, \beta = 3.498$ $\theta = 20.904$	$\alpha = 0.354, \beta = 3.343$ $\theta = 20.477$
	AIC (Ranking)	107,135 (14.50)	113,734.6 (14.50)	110,353 (14.50)
	BIC (Ranking)	107,157.8 (14.50)	113,757.6 (14.50)	110,375.9 (14.50)
	AD^2 (Ranking)	52.242 (13)	45.957 (11)	48.840 (10)
	MAE (Ranking)	14.290 (10)	14.104 (4)	13.943 (7.50)
	MAPE (Ranking)	99.407 (9.50)	99.420 (6)	99.380 (7)
	RMSE (Ranking)	17.819 (5)	17.423 (4)	17.369 (7)
12. Log Pearson type 3	Rank Sum	66.50	54.00	60.50
	Parameter estimation	$\alpha = 3.723, \beta = -0.210$ $\tau = 1.793$	$\alpha = 3.928, \beta = -0.198$ $\tau = 1.790$	$\alpha = 3.881, \beta = -0.204$ $\tau = 1.795$
	AIC (Ranking)	12,401.95 (1)	12,402.81 (1)	12,794.21 (1)
	BIC (Ranking)	12,424.76 (1)	12,425.82 (1)	12,817.13 (1)
	AD^2 (Ranking)	28.951 (1)	22.836 (1)	26.349 (2)
	MAE (Ranking)	0.255 (1)	0.231 (1)	0.242 (1)
	MAPE (Ranking)	Inf (20)	Inf (20)	Inf (20)
	RMSE (Ranking)	0.412 (1)	0.398 (1)	0.406 (1)
	Rank Sum	25.00	25.00	26.00
	Parameter estimation	$\alpha = 3.723, \beta = -0.210$ $\tau = 1.793$	$\alpha = 3.928, \beta = -0.198$ $\tau = 1.790$	$\alpha = 3.881, \beta = -0.204$ $\tau = 1.795$
	AIC (Ranking)	12,401.95 (1)	12,402.81 (1)	12,794.21 (1)
	BIC (Ranking)	12,424.76 (1)	12,425.82 (1)	12,817.13 (1)
	AD^2 (Ranking)	28.951 (1)	22.836 (1)	26.349 (2)
	MAE (Ranking)	0.255 (1)	0.231 (1)	0.242 (1)
	MAPE (Ranking)	Inf (20)	Inf (20)	Inf (20)
	RMSE (Ranking)	0.412 (1)	0.398 (1)	0.406 (1)
13. Log Logistic	Rank Sum	25.00	25.00	26.00
	Parameter estimation	$\alpha = 10.955, \beta = 1.954$	$\alpha = 11.025, \beta = 2.012$	$\alpha = 10.734, \beta = 1.963$
	AIC (Ranking)	108,068.3 (18)	114,880.4 (18)	111,385.1 (18)
	BIC (Ranking)	108,083.5 (18)	114,895.7 (18)	111,400.4 (18)
	AD^2 (Ranking)	102.150 (16)	114.562 (16)	108.465 (16)
	MAE (Ranking)	14.290 (10)	14.105 (10)	13.943 (7.50)
	MAPE (Ranking)	99.430 (17)	99.450 (17)	99.409 (18)
	RMSE (Ranking)	17.820 (12)	17.424 (11.50)	17.370 (14.50)
	Rank Sum	91.00	90.50	92.00
	Parameter estimation	$\alpha = 10.955, \beta = 1.954$	$\alpha = 11.025, \beta = 2.012$	$\alpha = 10.734, \beta = 1.963$
	AIC (Ranking)	108,068.3 (18)	114,880.4 (18)	111,385.1 (18)
	BIC (Ranking)	108,083.5 (18)	114,895.7 (18)	111,400.4 (18)
	AD^2 (Ranking)	102.150 (16)	114.562 (16)	108.465 (16)
	MAE (Ranking)	14.290 (10)	14.105 (10)	13.943 (7.50)
	MAPE (Ranking)	99.430 (17)	99.450 (17)	99.409 (18)
	RMSE (Ranking)	17.820 (12)	17.424 (11.50)	17.370 (14.50)
	Rank Sum	91.00	90.50	92.00

Distribution	Parameter Estimation and Consideration of Suitability Criteria	Year		
		2017	2018	2019
14.Generalized Extreme Value	Parameter estimation	$\zeta = 8.691, \alpha = 6.924$ $\kappa = -0.221$	$\zeta = 8.849, \alpha = 6.877$ $\kappa = -0.181$	$\zeta = 8.541, \alpha = 6.779$ $\kappa = -0.209$
	AIC (Ranking)	107,761.6 (16)	114,402.5 (16)	111,023.7 (16)
	BIC (Ranking)	107,784.4 (16)	114,425.5 (16)	111,046.6 (16)
	AD^2 (Ranking)	70.726 (14)	66.761 (15)	68.232 (14)
	MAE (Ranking)	14.290 (10)	14.105 (10)	13.943 (7.50)
	MAPE (Ranking)	99.464 (18)	99.480 (19)	99.443 (19)
	RMSE (Ranking)	17.820 (12)	17.423 (4)	17.369 (7)
	Rank Sum	86.00	80.00	79.50
15.Inverse Gaussian	Parameter estimation	$\mu = 14.328, \lambda = 11.636$	$\mu = 14.142, \lambda = 12.221$	$\mu = 13.971, \lambda = 11.384$
	AIC (Ranking)	109,187.2 (20)	116,231.2 (20)	112,635.6 (20)
	BIC (Ranking)	109,202.4 (20)	116,246.6 (20)	112,650.8 (20)
	AD^2 (Ranking)	381.747 (19)	424.288 (18)	417.928 (19)
	MAE (Ranking)	14.288 (4.50)	14.103 (3)	13.941 (3.50)
	MAPE (Ranking)	99.328 (5)	99.351 (4)	99.304 (4)
	RMSE (Ranking)	17.821 (19)	17.426 (18)	17.371 (18)
	Rank Sum	87.50	83.00	84.50
16.Generalized Inverse Gaussian	Parameter estimation	$\chi = 0.849, \Psi = 0.213$ $\lambda = 1.460$	$\chi = 0.644, \Psi = 0.232$ $\lambda = 1.589$	$\chi = 0.755, \Psi = 0.221$ $\lambda = 1.486$
	AIC (Ranking)	106,370.2 (5)	113,066.4 (9)	109,624.5 (6)
	BIC (Ranking)	106,393 (5)	113,089.4 (9)	109,647.4 (6)
	AD^2 (Ranking)	42,078 (20)	45,271 (20)	42,327 (20)
	MAE (Ranking)	14.290 (10)	14.105 (10)	13.943 (7.50)
	MAPE (Ranking)	99.393 (6)	99.415 (5)	99.368 (5)
	RMSE (Ranking)	17.820 (12)	17.424 (11.50)	17.370 (14.50)
	Rank Sum	58.00	64.50	59.00
17. Beta Prime	Parameter estimation	$\alpha = 1.792, \beta = 16.920$ $\sigma = 127.862$	$\alpha = 1.929, \beta = 14.096$ $\sigma = 96.858$	$\alpha = 2.043, \beta = 6.886$ $\sigma = 40.987$
	AIC (Ranking)	106,586.3 (12)	113,329.6 (12)	110,157.7 (13)
	BIC (Ranking)	106,609.1 (12)	113,352.6 (12)	110,180.6 (13)
	AD^2 (Ranking)	35.658 (9)	39.402 (9)	56.475 (12)
	MAE (Ranking)	14.290 (10)	14.105 (10)	13.943 (7.50)
	MAPE (Ranking)	99.405 (7)	99.426 (9)	99.376 (6)
	RMSE (Ranking)	17.820 (12)	17.424 (11.50)	17.370 (14.50)
	Rank Sum	62.00	63.50	66.00
18.Generalized Beta (first kind)	Parameter estimation	$\tau = 0.663, \alpha = 2.338$ $\beta = 4.875, \theta = 71.350$	$\tau = 0.442, \alpha = 3.825$ $\beta = 4.031, \theta = 61.613$	$\tau = 0.899, \alpha = 1.761$ $\beta = 10.506, \theta = 117.555$
	AIC (Ranking)	106,180.9 (3)	112,805.4 (3)	109,540.7 (4)
	BIC (Ranking)	106,211.3 (3)	112,836.1 (3)	109,571.2 (4)
	AD^2 (Ranking)	29.196 (2)	24.155 (2)	26.346 (1)
	MAE (Ranking)	14.291 (17)	14.106 (17)	13.944 (14.50)
	MAPE (Ranking)	99.405 (8)	99.421 (7)	99.383 (10)
	RMSE (Ranking)	17.820 (12)	17.424 (11.50)	17.369 (7)
	Rank Sum	45.00	43.50	40.50
19.Generalized Beta (second kind)	Parameter estimation	$\beta = 64.594, r_1 = 0.894,$ $r_2 = 8.175, r_3 = 1.529$	$\beta = 23.363, r_1 = 0.477,$ $r_2 = 1.593, r_3 = 2.694$	$\beta = 37.021, r_1 = 0.70,$ $r_2 = 3.937, r_3 = 1.886$
	AIC (Ranking)	106,533.3 (11)	113,534.2 (13)	109,876 (12)
	BIC (Ranking)	106,563.7 (11)	113,564.9 (13)	109,906.6 (12)
	AD^2 (Ranking)	30.318 (5)	40.407 (10)	35.389 (8)
	MAE (Ranking)	14.291 (17)	14.105 (10)	13.944 (14.50)
	MAPE (Ranking)	99.413 (15)	99.437 (15)	99.392 (15)
	RMSE (Ranking)	17.820 (12)	17.423 (4)	17.369 (7)
	Rank Sum	71.00	65.00	68.50
20.Generalized pareto	Parameter estimation	$\zeta = -0.249, \mu = 0.872$ $\sigma = 15.695$	$\zeta = -0.342, \mu = 0.979$ $\sigma = 17.696$	$\zeta = -0.239, \mu = 0.918$ $\sigma = 15.106$
	AIC (Ranking)	105,520.7 (2)	111,912.8 (2)	108,670.3 (2)
	BIC (Ranking)	105,543.6 (2)	111,935.8 (2)	108,693.2 (2)
	AD^2 (Ranking)	85.484 (15)	63.252 (14)	101.351 (15)
	MAE (Ranking)	14.288 (4.50)	14.105 (10)	13.941 (3.50)

Distribution	Parameter Estimation and Consideration of Suitability Criteria	Year		
		2017	2018	2019
	MAPE (Ranking)	99.217 (3)	99.293 (3)	99.168 (2)
	RMSE (Ranking)	17.820 (12)	17.424 (11.50)	17.370 (14.50)
	Rank Sum	38.50	42.50	39.00

From Table 2, it is evident that the rank sum of the Log Pearson Type 3 distribution consistently ranks lower than that of other distributions, with sums of 25, 25, and 26 for the years 2017, 2018, and 2019, respectively. A rank of 1 is assigned to criteria with the minimum value within a range of 1 to 20. These criteria encompass AIC, BIC, the Anderson-Darling test, and statistical accuracy measures such as MAE, MAPE, and RMSE.

The Log Pearson Type 3 distribution with the lowest AIC values 12,401.95, 12,402.81, and 12,794.21 for the years 2017, 2018, and 2019, respectively also exhibits the lowest BIC values 12,424.76, 12,425.82, and 12,817.13 for the same years. In terms of the Anderson-Darling test, it achieves the lowest values of 28.951, 22.836, and 26.349 for the respective years. Additionally, the distribution demonstrates superior accuracy as indicated by the lowest MAE values 0.255, 0.231, and 0.242 for the years 2017, 2018, and 2019 and the lowest RMSE values 0.412, 0.398, and 0.406 for the same years.

However, it's important to note that the MAPE of the Log Pearson Type 3 distribution results in infinite values due to taking the log base 10 of raw data during the processing, leading to some values being zero. Consequently, this contributes to a low rank sum for the Log Pearson Type 3 distribution. The method for determining the appropriate distribution for delay times of domestic outbound flights should consider the ranking of criteria or test statistics to assess the distribution's suitability.

Among the six mentioned criteria, the distribution with the fewest results for each criterion or test statistic is deemed to have the lowest ranking. In conclusion, based on the lowest rank sum, we assert that the Log Pearson Type 3 distribution is the most appropriate probability distribution for describing the dataset of delay times for flights departing from Chiang Mai International Airport to airports in the central region for the years 2017, 2018, and 2019.

Comparing the results of our analysis in Table 2 with findings from other studies in the literature review, it's worth noting that our dataset pertains to flight delay times, representing continuous data. This choice is different from the analysis of flight characteristics for inbound and outbound airplanes in the USA.⁴ Furthermore, in a study on modeling the probability distribution of outbound flight delays in Indonesia.⁵ It was suggested that a distribution with four parameters provides the best fit for modeling flight delay. In our research, we considered both the Generalized Beta (first kind) distribution and the Generalized Beta (second kind) distribution, both of which include four parameters. Notably, the Generalized Beta (first kind) distribution ranked lower in our analysis, whereas the Generalized Beta (second kind) distribution received a higher ranking.

In addition, this study findings align with the results of analysis of the delay distribution of flights departure within Thailand.⁸ In their research, analyzing data related to flight delays from one airline at Bangkok, they similarly found that the Log Pearson Type 3 distribution and the Burr distribution provided the best fit for their data, which is consistent with our own findings. Thus, the Log Pearson Type 3 distribution appears to be the most appropriate model for our data as well.

For future research, we propose narrowing down the suitable probability distribution for delay times, with the goal of minimizing the time needed to identify extensive statistical distributions. Once the appropriate probability distribution for the delay times of domestic

outbound flights is identified, we can use this distribution to construct a model for in-depth studies. These studies will focus on reducing delays, analyzing economic losses, budgeting costs, and planning airline, airport, and passenger operations.

Conclusion:

The study investigated the probability distribution of delays time of domestic flights departure from Chiang Mai international airport to airports located in the central region during the years 2017 to 2019. Our findings revealed that the most popular domestic flights departure was those heading to airports in the central region, accounting for 72.86% of the total experiences of flight delays.

As a result, our research collected a dataset of flight delay times (1 to 45 minutes), evaluated 20 distribution models, and found that the Log Pearson Type 3 distribution, estimated using Maximum Likelihood Estimation, provided the best fit. Various fit criteria supported this choice, making it the most appropriate for modeling delay times in domestic flights departure from Chiang Mai International Airport to central region airports from 2017 to 2019.

However, when considering flight delays, it's crucial to consider potential contributing factors such as adverse weather conditions, delayed inbound flights, passenger density at the airport, and other relevant variables. Future researchers exploring this topic should consider significant global events that could impact flight delays. Additionally, they may need to divide the data into smaller subgroups for more effective data management.

Acknowledgements: Thank you to the Department of Statistics, Faculty of Science, Chiang Mai University, and Chiang Mai International Airport for their support in completing this research.

References:

1. Chen X, Chen L, Xie W, Mueller ND, Davis SJ. Flight delays due to air pollution in China. *Journal of Environmental Economics and Management*. 2023;119:102810.
2. Ding Y. Predicting flight delay based on multiple linear regression. *IOP Conference Series: Earth and Environmental Science*. 2017;81:012198.
3. Glantz M, Kissell R. Chapter 2 - A Primer on Risk Mathematics. *Multi-Asset Risk Modeling*. 2014;21-61.
4. Mueller E, Chatterji G. Analysis of Aircraft Arrival and Departure Delay Characteristics. *AIAA's Aircraft Technology, Integration, and Operations (ATIO) 2002 Technical Forum*. 2002;1-14.
5. Novianingsih K, Hadiani R. Modeling flight departure delay distributions. *2014 International Conference on Computer, Control, Informatics and Its Applications (IC3INA)*. 2014;30-34.
6. Wu W, Wu C-L, Feng T, Zhang H, Qiu S. Comparative Analysis on Propagation Effects of Flight Delays: A Case Study of China Airlines. *Journal of Advanced Transportation*. 2018;2018:5236798.
7. Guleria Y, Cai Q, Alam S, Li L. A Multi-Agent Approach for Reactionary Delay Prediction of Flights. *IEEE Access*. 2019;7:181565-181579.
8. เทววงษ์ น, วิริยะปรีดาน, ปทุมพรพิชัย ช, บุญมาก. การวิเคราะห์การแจกแจงความล่าช้าของเที่ยวบินขาออก. *Thai Science and Technology Journal*. 2020;957-968.
9. Forbes C, Evans M, Hastings N, Peacock B. *Statistical Distributions*. Wiley; 2011.
10. THOM HCS. A NOTE ON THE GAMMA DISTRIBUTION. *Monthly Weather Review*. 1958;86:117-122.
11. Basak I, Balakrishnan N. Estimation for the three-parameter gamma distribution based on progressively censored data. *Statistical Methodology*. 2012;9:305-319.
12. Nagatsuka H, Balakrishnan N. Parameter and quantile estimation for the three-parameter gamma distribution based on statistics invariant to unknown location. *Journal of Statistical Planning and Inference*. 2012;142:2087-2102.
13. Stacy EW. A Generalization of the Gamma Distribution. *The Annals of Mathematical Statistics*. 1962;33:1187-1192.
14. Suksaengrakcharoen S, Bodhisuwan W. A new family of generalized gamma distribution and its application. *J Math Stat*. 2014;10:211-220.
15. Jia X. Reliability analysis for Weibull distribution with homogeneous heavily censored data based on Bayesian and least-squares methods. *Applied Mathematical Modelling*. 2020;83:169-188.
16. Mudholkar GS, Srivastava DK. Exponentiated Weibull family for analyzing bathtub failure-rate data. *IEEE Transactions on Reliability*. 1993;42:299-302.
17. Wilding GE, Mudholkar GS, Kollia GD. Two sets of isotones for comparing tests of exponentiality. *Journal of Statistical Planning and Inference*. 2007;137:3815-3825.

18. Papalexiou SM. Unified theory for stochastic modelling of hydroclimatic processes: Preserving marginal distributions, correlation structures, and intermittency. *Advances in Water Resources*. 2018;115:234-252.
19. Xin H, Zhu J, Tsai T-R. Parameter estimation for the three-parameter Burr-XII distribution under accelerated life testing with type I censoring using particle swarm optimization algorithm. *Int J Innov Comput Inf Control*. 2018;14:1959-1968.
20. Klugman SA, Panjer HH, Willmot GE. *Loss models: from data to decisions* Fourth Edition. 2012;715:464.
21. Griffiths VW, Stedinger JR. Log-Pearson Type 3 Distribution and Its Application in Flood Frequency Analysis. I: Distribution Characteristics. *Journal of Hydrologic Engineering*. 2007;12:482-491.
22. Lima SR, Cordeiro GM. The extended log-logistic distribution: properties and application. *Anais da Academia Brasileira de Ciências*. 2017;89:03-17.
23. Hosking JRM, Wallis JR. *Regional Frequency Analysis: An Approach Based on L-Moments*. Cambridge University Press; 1997.
24. Zhang X, Reiter JP. A Generator for Generalized Inverse Gaussian Distributions. *arXiv preprint arXiv:2211.13049*. 2022;1-21.
25. Moghaddam MD, Mills J, Serota R. Generalized beta prime distribution: Stochastic model of economic exchange and properties of inequality indices. *arXiv preprint arXiv:1906.04822*. 2019;1-19.
26. Ahmed A, Mir K, Reshi J. On size biased generalized beta distribution of first kind. *Journal of Mathematics*. 2013;5:41-48.
27. Chen L, Singh VP. Generalized Beta Distribution of the Second Kind for Flood Frequency Analysis. *Entropy*. 2017;19:1-17.
28. Xiong H, Ma L, Ning M, Zhao X, Weng J. The tolerable waiting time: A generalized Pareto distribution model with empirical investigation. *Computers & Industrial Engineering*. 2019;137:106019.
29. Danwihan S, Maha P, Neamvonk J. Probability Distribution of Solar Radiation Intensity in Eastern Part of Thailand. *วารสารวิทยาศาสตร์ บุรพา*. 2022;27:702-716.
30. Krishna H, Kumar K. Reliability estimation in generalized inverted exponential distribution with progressively type II censored sample. *Journal of Statistical Computation and Simulation*. 2013;83:1007-1019.
31. Sharma MA, Singh JB. Use of probability distribution in rainfall analysis. *New York Science Journal*. 2010;3:40-49.
32. Kousar S, Khan AR, Ul Hassan M, Noreen Z, Bhatti SH. Some best-fit probability distributions for at-site flood frequency analysis of the Ume River. *Journal of Flood Risk Management*. 2020;13:e12640.
33. Wadi M, Elmasry W. Statistical analysis of wind energy potential using different estimation methods for Weibull parameters: a case study. *Electrical Engineering*. 2021;103:2573-2594.

THE STUDY OF AWARENESS OF CHILD CAR RESTRAINT COMPLIANCE AND THE PREDICTION OF PARENTS' INTENTION TO USE IN THAILAND

Sawanya Suwannawong,¹ Pannathadh Chomchark,² Anchalee Supithak^{1,*}

¹Faculty of Engineering, Thai-Nichi Institute of Technology, Bangkok, Thailand.

²Faculty of Business Administration, Thai-Nichi Institute of Technology, Bangkok, Thailand.

*e-mail: anchalee_s@tni.ac.th

Abstract:

This research aimed to investigate the awareness of parents in compliance with child car restraint regulations in Thailand. This work considered various factors, i.e., the Theory of Planned Behavior, Government Influence, Price Fairness, and Safety Awareness. The Theory of Planned Behavior consists of Attitude, Subjective Norm, and Perceived Behavioral Control. A survey questionnaire was completed by randomly selected parents in Thailand and only qualified subjects were included in the study. The data was collected from 409 participants and results showed that certain variables have a significant impact on parents' intention to use car seats. An analysis of variance was conducted to test the null hypothesis that all variables are not have a significant effect. Hence, A multiple linear regression model was performed to explain the intention to use car seats based on Attitude, Perceived Behavioral Control, Price Fairness, and Safety Awareness scores. The model met all necessary assumptions and was successful in explaining the intention to use score with the correlation coefficient (R-square) of 0.873.

Keywords : Theory Planned Behavior (TPB), Multiple Regression Analysis, Child Car Restraint

Introduction:

The car accident causes injured and public health problem. In Thailand, people lack awareness of using safety belt and child care restraints (CCR) for the passengers. Until now, not every family with kids uses child car seats. In a moving vehicle, parents usually put kids on their lap or in the back seat. Recently, Thailand finally has a law that children under six must be placed in a car seat or a special seat for safety while sitting in a moving vehicle. The violations could mean a fine of up to 2,000 baht [1]. Recent research [2] in Thailand aims to study the parent's knowledge in child car seat, however, the effect and results should be more followed up and evaluated since the compulsory use of CCR started on September 5, 2022. In Singapore, the study of Parental knowledge and beliefs on the use of child car restraints has been study using a qualitative method for example focus group discussion [3]. The model of information, motivation, and behavior skill was applied to evaluate the CCR usage behavior in China [4]. The study results revealed that parents' cognitive, motivation and behavioral skills of CCR using have a significant impact on increasing parents' use of CCR. Many researchers have studied parents' social and economic factors as well as their attitudes toward the use of CCR [3-4]. In addition, the study involving parent groups, both CCR user and non-user groups, was studied and compared [5]. In Malaysia, most parents were aware about the using of CCR, but only half had a car seat for their current newborn [6].

This research aimed to study the awareness and obstacles of CCR compliance to use infant restraint in Bangkok, Thailand. The interesting model composes of Theory Planned Behaviors, Government Influence, Price Fairness, and Safety Awareness. The research method is to develop a survey questionnaires and to analyze relationship of variables in the intention to use. There are three objectives of this research. The first objective is to survey for the awareness of child car restraint compliance of parents or pregnancy women in Bangkok. The second objective is to evaluate the suitable model used to predict the parents' intention in

using or buying car seat. The third objective is to propose the successive methods to enhance using child car restraints.

A number of prior studies have shown that the theory of planned behavior (TPB) is effective in predicting intentions and behavior. This basic theory can explain the principles of consumer choice. The study is based on clarity about the context of social and individual processes that aid consumer decision-making. Two fundamental theories are relevant to this research. First, consumer decision-making patterns and buying behavior; and second, the Theory of Planned Behavior (TPB). The selection of theories concern consumer decision-making and purchasing behavior, because choosing a car seat is a consumer decision. The theory is consistent with the decisions of other similar consumers. Selection of the Theory Planned Behavior (TPB) is because it is generally trusted for understanding the decision-making process on the consumer side [7]. The consumer decision-making model and planned behavior theory is a cognitive model which deals with external situations and consumer stimuli which are internal processes, and prior learning (cognition). TPB is implemented to predict the parents' intention to use child car restraints in Thailand. The government can influence environmental knowledge and behaviour through policies, regulations, monetary incentives and public campaigns [8]. The governmental influence as an individual's perception of the environmental rules and regulations enacted by the government to promote pro-environmental behaviors. The rules and regulations put forth by the government have a tremendous impact on businesses, yet the impact on consumers is less know. For the price fairness, Equity Theory states that fairness is related to the distribution of outcomes and perceived fairness elicits as a result of the comparison between consumers' expectations and the outcome that they receive [9]. Equity theory also stressed that comparison between products elicits price fairness evaluations [10]. Based on this view, it can be considered that when the price of the private label product is higher, it should provide additional benefit to the consumer for the price of this product to be evaluated as fair. Price fairness is "a consumer's assessment and associated emotions of whether the difference (or lack of difference) between a seller's price and the price of a comparative other party is reasonable, acceptable, or justifiable" [10]. The Safety Awareness is one variable that affect parent decision of using car seat for their children. Road injuries are the leading cause of preventable deaths and injuries to children by using the right car seat in the right way. Correctly used child safety seats can reduce the risk of death by as much as 71 percent. Lastly, the intention to use or the intentional use refers to the intention behaviour of parents using the car seat for the safety of the child. TPB has been postulated as one of the key concepts for understanding consumer behavior.

Methodology:

According to Figure 1, The survey research questionnaire was conducted according to the Theory Plan Behavior (TPB) [7], Government Influence, Price Fairness and Safety Awareness to evaluate the parents' intention of buying car seat for their children. The TPB composes of Attitude, Subjective Norms, and Perceived Behavioral Control, was applied to develop the survey questionnaire. Therefore, the survey questionnaire composes of 7 parts : 1) General Information, 2) Attitude, 3) Subjective Norms, 4) Perceived Behavior Control, 5) Government Influence, 6) Safety Awareness and 7) Price Fairness. The first part is about general information of the respondents. The 2), 3) and 4) part is theory plan behavior. The 5) part is the government influence issues to evaluate the perception of government policy about the CCR law enforcement, car seat's price and consumer tax benefit, and the car seat supply by the government. The 6) part is about safety concern. The 7) part is about the car seat's price perception of parents. The last part is to evaluate parents' intention to use. The questionnaire used a 5-point Likert scale.

The survey questionnaire is developed according to Table 1. The null hypothesis is all six independent variables are not significant affect the intention to use car seat of parent. The alternative hypothesis is at least one independent variable significantly affecting the intention to use. To analyze the relationship between the factors in the problem model, the multiple regression analysis is applied. The data was processed using the Statistical Package for Social Sciences version 23 (IBM Corp, Armonk, NY, USA) [11].

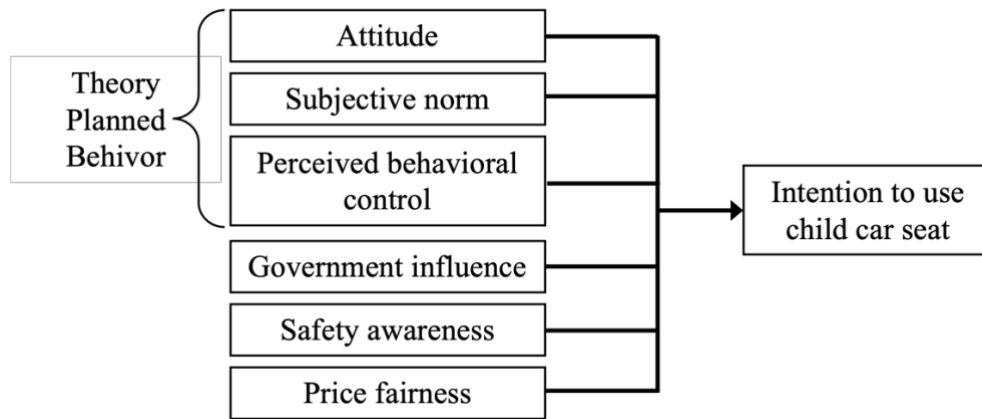


Figure 1
The Research Framework

Table 1
Research Questionnaire

<p>Part 1 Theory Plan Behavior (TPB)</p> <p>Attitude (A):</p> <ol style="list-style-type: none"> 1. I think car seat is necessary for safety of children. 2. I think car seat is a valuable product 3. I am interested in searching car seat information 4. Using car seat for child is normal and must strictly compliance 5. I am agreeing with the concept of car seat design for child's safety <p>Subjective Norms (SN):</p> <ol style="list-style-type: none"> 6. Important person to you also recommend me to use car seat for your children 7. Important person to you also realize the usefulness of using car seat 8. Important person to you also realize that car seat is safety equipment for children 9. Important person to you also realized that car seat can relieve injuries for children. 10. The parents who I know mostly use car seat for their children <p>Perceived Behavioral Control (PBC):</p> <ol style="list-style-type: none"> 11. I dedicate my time to search for more information of car seat for vehicle 12. I have enough budget to buy car seat for my children 13. I am ready if I must buy car seat for my children to install to my vehicle 14. I believe that car seat can protect my children 15. I will choose the vehicle that support car seat installation easily.
<p>Part 2 Government Influence (GI):</p> <ol style="list-style-type: none"> 16. The benefit of tax discount for import car seat will encourage my decision of buying 17. The compliance of Thai's law of car seat will stimulate car seat purchasing 18. The government explicitly complies the child car restraints 19. Car seat pricing policy supported by the government and the related organization 20. Strategy and plan for car seat manufacturing supported by the government, thus the car seat price decrease and parent can effort.

<p>Part 3 Safety Awareness (SA):</p> <p>21. I think car accident results in serious injury and death will explicitly relieve if parent use car seat with their child.</p> <p>22. I realized that car seat is importance for travelling with children</p> <p>23. I think car seat is importance even though it is expensive.</p> <p>24. My children always ride with car seat</p> <p>25. I insist my children to use car seat even though they refuse</p>
<p>Part 4 Price Fairness (PF):</p> <p>26. I think the car seat price is appropriate especially comparing to safety concerning.</p> <p>27. I agree and trust with the material and design of car seat in the market</p> <p>28. The car seat price is reasonable for me to buy</p> <p>29. The car seat price is affordable for other parents</p> <p>30. The car seat models and price are variety and valid for buying justification of parents.</p>
<p>Part 5 Intention to Use (IU):</p> <p>31. I plan to buy car seat once I have a child.</p> <p>32. I plan and ready to buy car seat for my child.</p> <p>33. Car seat is the important appliance which I certainly supply for my child</p> <p>34. Even though car seat' price is high but I will certainly purchase for my child.</p> <p>35. Car seat is the best solution for my child when travelling.</p>

Results and Discussion:

The research was conducted by using the filtering questions for only parents whose children' age is under seven years old. The useable collected data are from 409 subjects which are classified as 93 males and 316 females. The proportion is 77.3 percentage of female and 22.7 percentage of male. The descriptive statistics of subjects is described in Table 2. The most respondents' age are 25 to 44 years old (87.5%). The respondents' education mostly are bachelor's and master's degree (82.9%). Most respondents have salary between 15,000 to 65,000 baths and live in Bangkok, the capital of Thailand (77.3%). Most respondents about 75.2 percentage of parents have one kid and about 21 percentage of parents has two kids. The multiple regression analysis is applied according to the six independent variables which are as following:

- X₁ is Attitude Variable of TBP
- X₂ is Subjective Norm Variable of TBP
- X₃ is Perceived Behavioral Control of TPB
- X₄ is Government Influence Variable
- X₅ is Safety Awareness Variable
- X₆ is Price Fairness Variable
- Y is the intention to use, dependent variable

The research null hypothesis is all six independent variables do not affect the intention of use (Y) and the alternative hypothesis is at least one independent variable affect the intention of use (Y). The multiple linear regression analysis is applied. According to the analysis of variance for the regression model in Table 3, the fitting model well represents the data since the p-value is less than 0.05. The correlation coefficient value of 0.873 mentioned in Table 4 also present high degree of correlation in data with the fitting model.

$$Y = -0.426 + 0.195X_1 + 0.264X_3 + 0.565X_5 + 0.110X_6$$

For the analysis of variance according to Table 5, the independent variables those significantly affects the intention of use are Attitude (X₁), Perceived Behavioral Control (X₃), Safety Awareness (X₅), and Price Fairness (X₆) since the significant values are less than 0.05.

Table 2
Data Descriptive of Respondents

Characteristics		Frequency	Percentage
Sex	Male	93	22.7
	Female	316	77.3
Age	25 to 30	173	42.3
	35 to 44	185	45.2
	45 to 54	47	11.5
	55 to 64	3	0.7
	65 and over	1	0.2
Education	Under bachelor's degree	58	14.2
	Bachelor's degree	226	55.3
	Mater's Degree	113	27.6
	Doctor's Degree	12	2.9
Salary	Less than 15,000 Baht.	52	12.7
	15,000 to 40,000	185	45.2
	40,001 to 65,000	91	22.2
	65,001 to 90,000	33	8.1
	90,001 to 125,000	18	4.4
	Over 125,000	30	7.3
Occupancy	Private Company Employee	191	46.7
	Public Employee	35	8.6
	Government officer	46	11.2
	Freelance	53	13.0
	Business Owner	51	12.5
	Housewife/husband	33	8.1
Residency/ Address	Bangkok	316	77.3
	Central of Thailand	41	10.0
	Eastern of Thailand	13	3.2
	Western and South of Thailand	8	2.0
	North of Thailand	14	3.4
	East-North of Thailand	17	4.2
Car Seat Accepted Price	Lower than 1000 Baht	13	3.2
	1,001 to 2,000	59	14.4
	2,001 to 3,000	95	23.2
	3,001 to 4,000	56	13.7
	4,001 to 5,000	65	15.9
	More than 5,001	121	29.6
Number of your Children	1	308	75.3
	2	86	21.0
	3	8	2.0
	4	5	1.2
	5 and Over	2	0.5
Type of Vehicle for installing Car Seat	Standard Car with 5 seats	243	59.4
	B-SUV with 5 seats for Less	37	9.0
	SUV with 5 to 7 seats	81	19.8
	Truck	26	6.4
	Van	22	5.4

Table 3
Analysis of Variance of Multiple Linear Regression Model

Model	Sum of Squares	df	Mean Square	F	significance
Regression	166.592	6	27.765	214.835	0.000 ^b
Residual	51.955	402	0.129		
Total	218.547	408			

^aDependent Variable: Intention to use (Y)

^bPredictors: (Constant), PF26_30, Attitude1_5, GI16_20, SN 6_10, PBC 11_15, SA 21_25

Table 4
The regression model summary

Model	R	R-square	Adjusted R-Square	Std. Error of the Estimate
1	0.873 ^a	0.762	0.759	0.35950

Table 5
Analysis of variance of the Multiple Linear Regression Model

Model	Mean Score (base on 5-point scale)	Unstandardized Coefficients		Standardized Coefficients	t	Significance
		Beta	Std. Error	Beta		
Constant		0.426	0.159		-2.684	0.008
X ₁ : Attitude	4.59	0.195	0.047	0.154	4.123	0.000
X ₂ : Subjective Norm	4.29	0.047	0.032	0.047	-1.481	0.139
X ₃ : Perceived Behavioral Control	4.31	0.264	0.040	0.254	6.625	0.000
X ₄ : Government Influence	4.11	0.026	0.029	0.025	0.896	0.371
X ₅ : Safety Awareness	4.49	0.565	0.043	0.504	13.111	0.000
X ₆ : Price Fairness	3.96	0.110	0.029	0.116	3.773	0.000

The results based on Theory Planned Behavior (TPB) show that respondents have highest score for the attitude (4.59) of using car seat and greater than perceived behavioral control (4.31) and subjective norm (4.29). Most parents aware of their children's safety since the score is 4.49. Finally, the majority of the parents intend to use car seat since the score is 4.48.

Conclusion:

Most of the parents of the respondents living in Bangkok have high attitude of intention to use car seat and high awareness of safety. The intention to use highly related to

parents' attitude, perceived behavioral control, safety awareness, and price fairness. The government influence and subjective norm are not affecting the parents' intention to use car seat. Since, most parents have only one child, and some of them have two children, the cost of car seat may affect the parents' decision. Therefore, the possible policy is providing the system of second hand or used car seat from the only child parents. In addition, the government should put more effort to announce the child car restraint law and to provide variety sources of purchasing car seat.

Acknowledgements:

This research is granted by Mitsui Sumitomo Insurance Welfare Foundation Research Grant, Thailand 2022.

References:

1. The Land Traffic Act B.E. 2565. Government Gazette 2022;139(28):5-22.
2. Termworasin P, Lumbiganon D., Prueksapraopong C. Vajira Med J. 2020;65(2):95-106.
3. Tan RMR, Dong C, Shen GQ *et al.* Singapore Med J. 2020;61(2):102-107.
4. Sun Y., Liu T., Chen J. *et al.* BMC Pediatr. 2023;23:2.
5. Champahom T., Jomnonkwao S., Thotongkam W., Jongkol P., Rodpon P. and Ratanavaraha V., Sustainability. 2023;15(4):2896.
6. Ang J.Y., Lai J.M., Hss A.S. *et al.* Traffic Injury Prevention. 2020;21:278-282.
7. Ajzen I., Fishbein M., Lohmann S. and Albarracín D. The Influence of Attitudes on Behavior. 2005.
8. Newman T.P. and Fernandes R. Environmental Education Research. 2016;22:153-175.
9. Ashworth L. and McShane L. Journal of Retailing. 2012;88(1):145-155.
10. Xia L., Monroe K.B. and Cox J.L. Journal of Marketing. 2004;68(4):1-15.
11. IBM Corp. Released 2015. IBM SPSS Statistics for Windows, Version 23.0. Armonk, NY: IBM Corp.

Using Augmented Reality Technology in Learning Statues depicting a Thai Massage (Nuad Boran) in Wat Pho

Sathit Prasomphan^{1*}, Setawit Namwongsa¹, Naruchon Ngamkasem¹

Department of Computer and Information Science,
King Mongkut's University of Technology North Bangkok, Bangkok, 10800 THAILAND
*e-mail: sathit.p@sci.kmutnb.ac.th

Abstract:

Wat Pho, aspiring for UNESCO World Heritage Site recognition, has garnered international acclaim for its inscription, offering rich insights into Thai culture and the era of Phra Phutthayotfa Chulalok Maharaj. Recognized as Thailand's earliest public education center, UNESCO acknowledges its marble illustrations and inscriptions. Wat Pho, renowned for its Thai medicine school and as the birthplace of traditional Thai massage, provides a unique experience with a historical hermit statue displaying exercise postures. To preserve this history and offer a modern experience, we developed a mobile application integrating Google Maps for navigation, 3D and AR for hermit statue display, and Firebase for data management. In a machine learning experiment, we successfully employed convolutional neural networks to detect the hermit statue, achieving an 87.92 percent accuracy in classifying its exercise posture.

Introduction:

Wat Pho is actively seeking recognition as a UNESCO World Heritage Site, with the inscription of Wat Pho gaining international acclaim. This recognition is attributed to the rich historical information it provides about Thai culture, especially the Phra Phutthayotfa Chulalok Maharaj era. The temple features a notable hermit statue displaying historical exercise postures and massage techniques, offering visitors a unique perspective on Thai culture and a deeper understanding of history. As the earliest center for public education in Thailand, UNESCO acknowledges Wat Pho for its marble illustrations and inscriptions, serving as a valuable resource for public instruction. Beyond its educational role, the temple is a hub for Thai medicine education and is renowned as the birthplace of traditional Thai massage, which continues to be actively taught and practiced. Recognizing the significance of this historical site, a mobile application has been developed to facilitate a contemporary exploration of Wat Pho. The application leverages Google Maps for direct navigation within the temple premises, supplemented by subtitles to provide historical context for each location. Additionally, the app incorporates 3D technology and Augmented Reality (AR) via smartphones to present the hermit statue in a 360-degree view. To enhance the visitor experience, the application also provides recommendations for popular restaurants near the temple, with efficient data management facilitated by Firebase.

In summary, the mobile application serves as a bridge between the modern and historical aspects of Wat Pho, contributing to an enriched visitor experience and supporting the tourism sector. In this project, the statue of a hermit that shows the exercise posture was detected using machine learning-based object detection. The experimental results indicate that adopting a convolutional neural network for training to detect a hermit that shows the exercise posture can be successfully used to detect. The proposed algorithms can be utilized

to classify the type of a hermit that shows the exercise posture with an accuracy rate of 87.92 percent.

Related Theory:

A. Wat Pho

Wat Pho, officially named Wat Phra Chetuphon Wimon Mangkhalaram Rajwaramahawihan, holds the prestigious status of a first-grade royal monastery, making it a paramount establishment during the reign of King Rama I from the Chakri Dynasty. Its significance lies in the king's commendable restoration efforts for Wat Phodharam, an ancient monastery dating back to the Ayudhya period. This monastery was subsequently re-established as a royal sanctuary located in close proximity to the Grand Palace.

Underneath the pedestal of the principal Buddha image, known as Phra Buddha Deva Pāmākorn in the main chapel, some ashes of King Rama I are preserved. Occupying a vast area of 20 acres, Wat Pho is situated to the south of the Grand Palace, bordered by Thai Wang Road to the north, Sanam Chai Road to the east, Se hakan Road to the south, and Maharat Road to the west. Enclosed by a towering white wall along Chetuphon Road, the monastery is divided into two primary quarters: the sacred section (Buddhavas) and the residential area (Sangghavas), each serving distinct purposes [1][2].

B. Machine Learning

Machine Learning (ML) [3] is the use of mathematics and computer science to teach computers to learn and make judgments without having to follow strict rules. Machine learning can read and interpret the information offered by humans so that they can make the judgments that human desire. There are numerous versions, including the following tasks.

a. Predict new types of data that machine learning has never seen before, what is the value, and what category does it belong to.

b. Group data by using information in the same group that has similar qualities.

c. Separate particular types of data from the rest of the data, such as speech from voice and environment.

d. Learning from the original interests to introduce new pieces of information that humans are predicted to be interested. The advantages of machine learning are numerous. Anyone or any organization that wants to employ machine learning in their job.

Machine learning can be divided into two categories: the first category is supervised learning which provide a class label in the dataset. For instance, regression that can find numerical responses, such as nutritional information for child, what the expected height of this child is. Classification that come up with a categorical answer, such as a prophecy for the Thoracic X-ray image. Whether or not the patient has lung cancer (the answer is yes/no, hence the name is binary). Alternatively, supply information about a child's relatives in order to anticipate the child. This one is in the good development/normal development/slow development category (the answer will have many groups which called multiclass classifications). The second category is unsupervised learning which the fact that no one knows the correct answer is. For example, clustering which build communication strategies with diverse categories of customers, group information, such as donor information, into three groups. Other non-clustering difficulties, such as detecting part data, are addressed in section. Other example of unsupervised learning are anomaly detection, recommendation system that provides material that users are likely to be interested in.

C. Nomad sculpt

Nomad Sculpt [7] is a 3D sculpting application designed for use on mobile devices, such as tablets and smartphones. It provides a portable and intuitive platform for artists and designers to create digital sculptures using touch-based controls. Key features of Nomad Sculpt may include: **Sculpting Tools:** Nomad Sculpt typically offers a variety of sculpting tools, allowing users to shape, mold, and refine their digital creations. **User Interface:** The interface is optimized for touch-based input, making it easy for users to navigate and interact with the sculpting tools. **Multiresolution Sculpting:** Users can work with multiple mesh resolutions, allowing for flexibility in adjusting the level of detail during the creative process. **Voxel Remeshing:** This feature allows for quick and uniform remeshing of the mesh, which can be useful for refining shapes during the initial stages of sculpting. **Dynamic Topology:** Dynamic topology enables the refinement of the mesh locally under the brush, automatically adjusting the level of detail as needed. **Painting Tools:** Nomad Sculpt often includes painting tools for adding color, roughness, and other material properties to the sculptures. **Layers:** Sculpting and painting operations can be recorded separately in layers, providing a non-destructive workflow and easy iteration. **File Compatibility:** The application may support file formats such as glTF, OBJ, and STL, allowing users to save and open their sculpted creations.

F. Related work.

In [4] delivers a thorough examination of augmented reality (AR) technology, capturing its state at that time and projecting insights into applications, challenges, and future paths. Azuma defines AR as a system merging real world and computer-generated elements in a real-time interactive environment. Characteristics include real-time interaction, 3D registration of virtual and real-world coordinates, and a display seamlessly blending virtual and real imagery. The paper delves into essential AR system components, covering hardware (sensors, displays) and software (tracking algorithms, rendering). Technologies such as head-mounted displays, spatial tracking, and registration techniques are explored. Azuma identifies diverse AR applications: medical visualization, maintenance, gaming, education, and collaborative workspaces. Each application undergoes scrutiny for its specific challenges and contributions to AR technology development. Addressing challenges like tracking inaccuracies, display technologies, and the need for improved user interfaces. Azuma's survey establishes a foundational understanding of AR, presenting a categorization framework and insights into applications. Despite its 1997 publication, the concepts and challenges discussed retain relevance, offering enduring value to AR researchers and practitioners.

In [5], the paper anticipates widespread integration of Augmented Reality (AR) technologies, poised to revolutionize our perception of the environment through enhanced visual, auditory, and sensory experiences. Intended applications span diverse fields like education, maintenance, design, and reconnaissance. The document provides an overview of AR, encompassing a concise definition, historical development, enabling technologies, and their features. It surveys the current state of the field, highlighting recent applications and acknowledging human factor limitations in AR system use, emphasizing the challenges developers must address.

In [6], Over the past decade, the utilization of augmented reality (AR) applications to aid individuals with special needs, including intellectual disabilities, autism spectrum disorder (ASD), and physical disabilities, has significantly increased. This growth, particularly in supporting individuals with autism, has spurred extensive research into the technology's efficacy in addressing autism-related challenges. This study conducts a

systematic review using the PRISMA methodology to assess the effectiveness of AR in rehabilitating and training individuals with ASD. After a thorough search of relevant databases, 25 articles meeting inclusion criteria were selected for analysis. The studies covered diverse areas such as social interaction, emotion recognition, cooperation, learning, cognitive skills, and living skills. The results demonstrate that AR interventions were most effective in enhancing social skills, followed by improvements in learning, behavioral, and living skills. The systematic review identifies limitations in current research designs, control groups, sample sizes, and assessment methods, offering insights for future research. Overall, the findings suggest that augmented reality holds promise as a practical tool for supporting individuals with ASD in daily activities and fostering their social interactions.

Methodology:

In this section, we describe procedures and methods of developing application as follows.

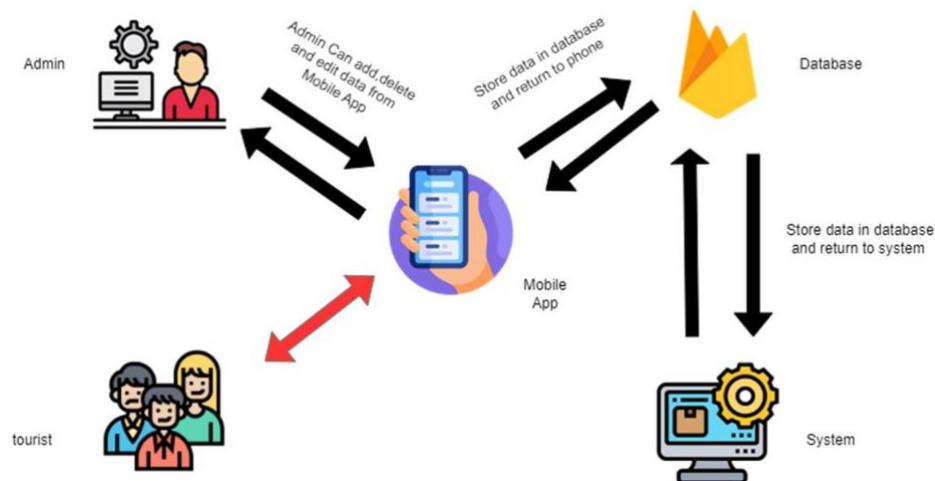


Figure 3.
System Architecture overview.

Figure 3 provides an overview of the system architecture. The system architecture details are as follows: Admin Functions: The administrator has the capability to add, delete, and edit data directly from the mobile application. Tourist Usage: Tourists can utilize the mobile application while exploring Wat Pho, gaining access to detailed historical information about the site. Database Operations: Admin actions, such as adding, deleting, or editing interesting places, are recorded in the database. The data related to these actions are transmitted to the server, facilitating information exchange within the system. The usecase diagram of system are shown in Figure 4.

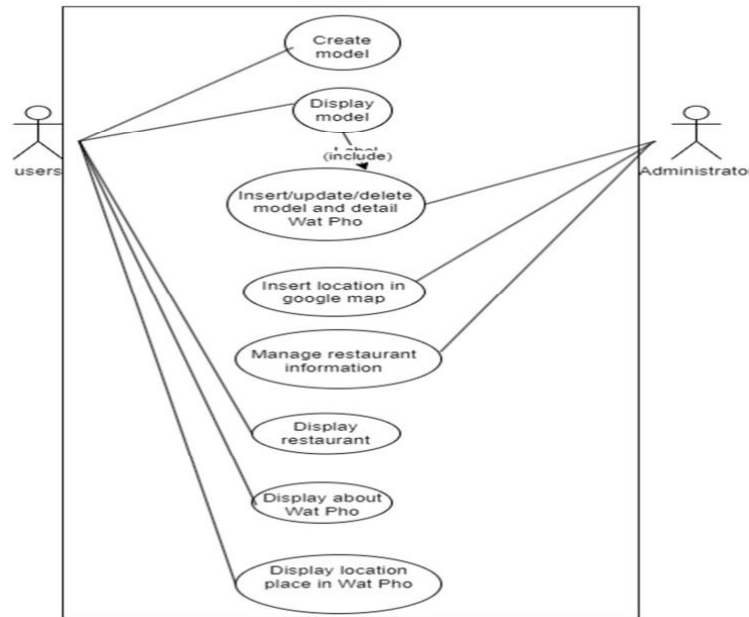


Figure 4.

Use case diagram.

In this research, we use the dataset to train the YOLOv4 network on the class hermit that shows the exercise posture in Wat Pho. You Only Look Once is referred to as YOLO. One-Stage Detectors and Two-Stage Detectors are the two primary families of this object detection model, which is employed in deep learning use cases. The category of One-Stage Detectors includes YOLO. A sliding window strategy combined with classification entails looking at the image and classifying it for each window. In terms of accuracy (average precision) and speed (FPS), the two metrics often use to evaluate an object identification algorithm, YOLOv4 has improved over YOLOv3. The YOLOv4 model's greatest strength is its ability to train models on a single GPU.

The hermit statue detection process involves two models. In the first model (model 1), an uploaded user image undergoes processing to identify bounding boxes containing predicted persons, each associated with a probability score. Instead of returning these outputs to the user, the system forwards them to the second model (model 2). Model 2 is responsible for determining the specific type of exercise posture exhibited by the hermit statue. Users have the flexibility to input images of varying sizes and resolutions, as the program automatically adjusts the image size to 416x416 pixels, following the YOLO format. The algorithm seamlessly integrates object detection to identify the hermit statue and subsequently determines its exercise posture type. Finally, all outputs, including the 3D model of the hermit statue displaying the identified exercise posture, are presented to the user for display.

Results and Discussion:

This section focuses on presenting the outcomes of the mobile application, highlighting its functionality within the predefined scope of the project. Specifically, it delves into the Home Page of the application, which serves as the main menu. The application's home page is visually represented in Figure 5.



Figure 5.
Home Page.

The application's "Display Place Details" page displays information about various locations within the temple along with their respective historical details. Users are provided with the option to select their preferred language from Thai, Chinese, or English, offering a multilingual feature, as illustrated in Figure 6.



17:13 ๕ ๑ ๓ ...

๑๙

← พระมหาเจดีย์ดิลกธรรมกรนิทาน



ประวัติ

พระมหาเจดีย์ประจำรัชกาลที่ 2 เมื่อทรงปฏิสังขรณ์วัดพระเชตุพนวิมลมังคลาราม ใน พ.ศ. 2375 นั้น พระบาทสมเด็จพระนั่งเกล้าเจ้าอยู่หัว รัชกาลที่ 3 โปรดเกล้าฯ ให้สถาปนาสมเด็จพระสังฆราชเจ้า กรมหลวงวชิรญาณวงศ์ (รัชกาลที่ 2) องค์แรกตั้งเป็นต้นสายพระเนตรสืบเชื้อสายมา พจนานุกรมศัพท์พระยศเจ้าอยู่หัว รัชกาลที่ 4 ได้พระราชทานนามแก่พระเจดีย์ว่า "พระมหาเจดีย์ดิลกธรรมกรนิทาน"

17:28 ๕ ๑ ๓ ...

๑๙

← ประวัติวัดโพธิ์



เกร็ดประวัติวัดโพธิ์

กรุงเทพมหานคร เมืองหลวงของราชอาณาจักรไทยที่มีความหมายเป็นนครแห่งสามเทพ มีทั้งโอบอุ้มคุ้มครองโดยอินทร์ชั้นใน อันเป็นที่ตั้งในแรกสร้างพระนคร นับเป็นพื้นที่ที่สังคมหลากหลายวัฒนธรรมและภูมิปัญญาไทยไว้ให้ประชาชนได้สืบสานได้เรียนรู้ได้รับรู้ถึงเกิดความรู้และนำความรู้ที่ได้สืบทอดมาป้อนมาปฏิบัติตาม ประกอบอาชีพที่สืบทอดมาจากรุ่นสู่รุ่นมาจนถึงทุกวันนี้ วัดโพธิ์ หรือนามทางราชการว่า วัดพระเชตุพนวิมลมังคลารามราชวรมหาวิหาร เป็นพระอารามหลวงชั้นเอก และเป็นวัดประจำรัชกาลที่ ๑ แห่งราชวงศ์จักรี เนื่องจากพระบาทสมเด็จพระพุทธยอดฟ้าจุฬาโลกมหาราชทรงพระกรุณาโปรดเกล้าฯ ให้สถาปนาวัดโพธารามวัดเก่าที่มีอยู่มาแต่ครั้งกรุงศรีอยุธยาเป็นวัดหลวงสำหรับพระบรมมหาราชวัง และในฐานะวัดประจำรัชกาลเป็นพระอารามหลวง พระประธานในพระอุโบสถเป็นพระพุทธรูปปางนาคปรกของพระองค์ท่านไว้ด้วย

พระอารามหลวงแห่งนี้ มีเนื้อที่ ๕๑ ไร่ ๒ งาน ๕๔ ตารางวาอยู่ด้านใต้ใต้ของพระบรมมหาราชวัง ทิศเหนือจดถนนเจริญกรุง ทิศตะวันออกจดถนนสนามไชย ทิศใต้จดถนนนครไชยการ ทิศตะวันตกจดถนนมหาไชย มีถนนเชตุพนชนานสายกำแพงสูงสี่วาแบ่งเขตพุทธาวาสและสงฆ์วาสชัดเจนมีเสกฐานปรากฏในศิลาจารึกไว้ว่า หลังจากพระบาทสมเด็จพระพุทธยอดฟ้าจุฬาโลกมหาราช ทรงสถาปนาพระบรมมหาราชวังแล้วทรงพระราชดำริว่า มีวัดเก่าแก่บางพระบรมมหาราชวัง ๒ วัด ด้านเหนือ คือวัดสลัก (วัดมหาธาตุ) ด้านใต้ คือ วัดโพธาราม จึงทรงพระกรุณาโปรดเกล้าฯ ให้ขุนนางเจ้าพระกรม ข้างซ้ายอยู่ฝ่ายหน้าการบูรณปฏิสังขรณ์ เริ่มเมื่อพ.ศ. ๒๓๓๘ เสร็จวัดโพธาราม มีสภาพทรุด

17:28 ๕ ๑ ๓ ...

๑๙

← ประวัติวัดโพธิ์



จารึกเรื่องทรงสร้างวัดพระเชตุพน

ครั้งรัชกาลที่ ๑

(อยู่ในพระวิหารทิศพระโลกนาถมุขหลัง)

๑ คุยมืดพระพุทธรูปทรงสร้างแล้วสองต้นสามร้อยสามสิบแปดพระชนา ณ วันจันทร์เดือนสิบแปดแรมปีระกาภิเศกสิริเอกศก สมเด็จพระบรมมหาราชเจ้าพระยาจักรีเจ้ากรมการโยธาธิบดี บรมนาถบรมมพิตรพระพุทธรูปเจ้าอยู่หัวผู้ผ่านพิภพโศการยาริบัติกิจราช ภูมิจักรพรรดิพระราชมหาราชมหาดิลกพระนครราชธานี มุขมิ่งอุดมพระราชมหาสถาน เสด็จทอดพระเนตรเห็นวัดโพธารามเก่าชำรุดปรักหักพังเป็นอันมากทรงพระราชดำริจะปฏิสังขรณ์สร้างไว้กับบูรณการมาขึ้นกว่าครั้งที่เป็นสมุดด่อนด้วยคลองสระบ่อรองอยู่ ณ พระพุทธมณฑลในเกาะสองฝั่งแม่น้ำเจ้าพระยาแล้ว รุ่งขึ้นเป็นวันสองปีกับอุปสมถ์ไม่จึงให้ขุดมูลดินถมขึ้นพระอารามให้ ส่องระเฝ้าซึ่งสิบเก้าตำลึงจึงให้ปราบที่มูลดินถมขึ้นแล้ว ครั้นวันพฤหัสบดีเดือนสิบสองแรมปีระกาภิเศกสิริเอกศก ให้จัดการปฏิสังขรณ์และสร้างพระอุโบสถมีกำแพงแก้วรอบสระบ่อรองอยู่รอบพื้นที่ในกำแพงแก้ว แล้วทรงพระเมตตาขึ้นในชั้นแรกก่ออิฐทำขึ้นแล้ว

Figure 6.
Display Place Details.

Admin can add, edit, and delete place details from this page as shown in Figure 7.

© The 49th International Congress on Science, Technology and Technology-based Innovation (STT 49)

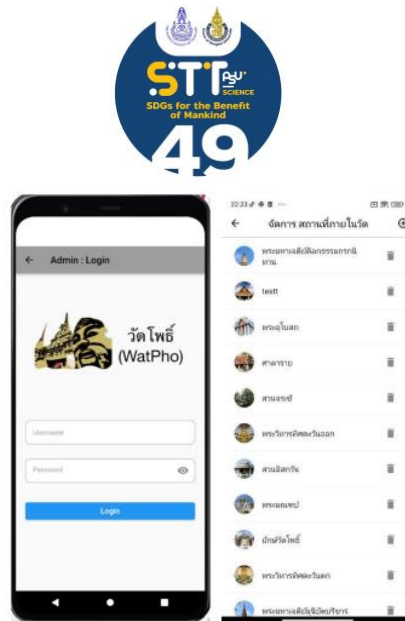


Figure 7.
Admin page.

The application employs Augmented Reality (AR) technology to present a 360-degree view of the Hermit, accessible via smartphones. Users have the option to choose their preferred Hermit, as depicted in Figure 8 and Figure 9. This feature allows for an interactive and immersive experience with the Hermit using AR technology.

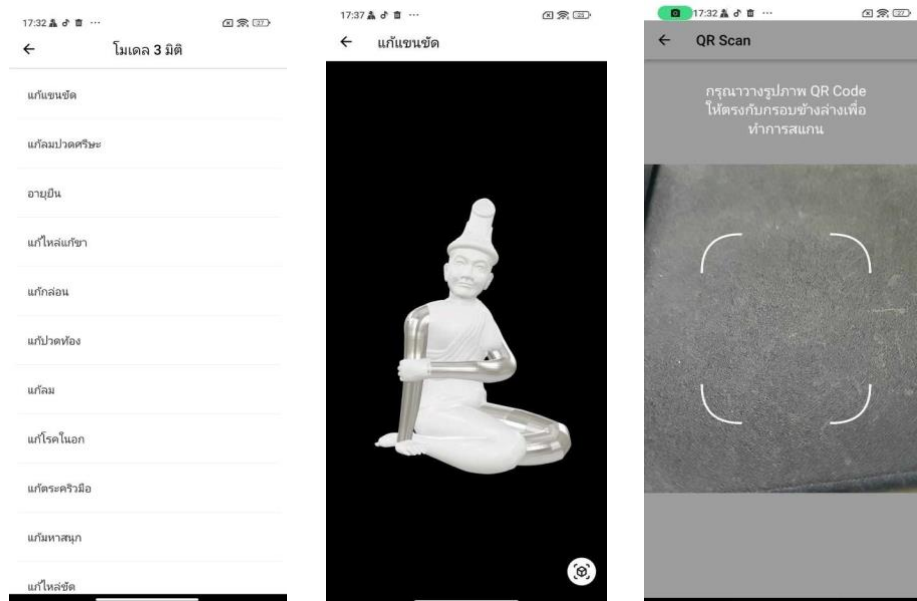


Figure 8.
3D Twisted Hermit.

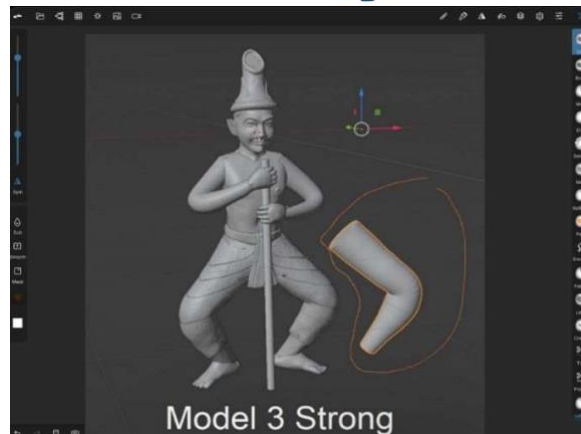


Figure 9.
3D Twisted Hermit.

Performance Indexed

The confusion matrix is a potent technique for assessing the performance of classification results. It provides a detailed representation of predicted and actual classes, aiding in the visualization of classification errors. The matrix is structured such that each row corresponds to the predicted class, and each column represents the original class. The evaluation metrics derived from the confusion matrix include precision, recall, F1 score, and accuracy, calculated using the following equations::

$$\text{Precision} = \frac{TP}{TP+FP} \quad (1)$$

where TP is the true positive value and FP is the false positive value. Precision is the value that measures the number of correct predicting answers by dividing by the total number of images in the dataset.

$$\text{Recall} = \frac{TP}{TP+FN} \quad (2)$$

where TP is the true positive value and FN is the false negative value. Recall is the value that measures the number of correct predicting answers for each class and is divided by the total number of that class which is the ground truth.

$$\text{F1-Score} = 2 \frac{\text{Precision} \times \text{Recall}}{\text{Precision} + \text{Recall}} \quad (3)$$

where Precision is the precision value calculated from (1) and Recall is the recall value calculated from (2).

$$\text{Accuracy} = \frac{TP+TN}{N} \quad (4)$$

where TP is the true positive value, TN is the true negative value, and N is total number of images.

The classification results obtained by applying the proposed algorithms to detect the hermit that shows the exercise posture inside image were used to demonstrate the experimental findings. Consequently, the classification accuracy ensures the efficiency of our image classification algorithms. **Table. 1** illustrates the categorization accuracy. The experimental results indicate that adopting a convolutional neural network for training to detect a hermit statue in image can be successfully. The proposed algorithms can be utilized to classify the type of activity of the hermit that shows the exercise posture with an accuracy rate of 87.92 percent.

Table 1: Comparison of average precision of classification between traditional deep learning and proposed classification technique

Classification technique	Precision
AlexNet	87.18%
YOLO	85.67%
CNN	86.85%
proposed classification	87.92%

Conclusion:

In conclusion, this section provides a comprehensive overview of the operational outcomes of the Wat Pho application, emphasizing its key functionalities. The major achievements include users gaining access to historical information, exploring a 3D model of the temple, utilizing navigation features, obtaining information about surrounding shops, and accessing travel details to the temple. Despite these successes, certain challenges were encountered, such as the large installer size, camera connectivity issues on specific devices, inaccurate model display on some devices, and occasional slow operation. To address these challenges and further enhance the application, the following suggestions are proposed: optimize the installer size, improve camera connectivity, enhance model rendering, optimize application performance, and ensure full functionality within the entire Wat Pho area. Future development should focus on increasing application speed and incorporating additional user functionalities.

References:

1. Prasomphan S and Pinngoen N, "Feature Extraction for Image Matching in Wat Phra Chetuphon Wimonmangklararam Balcony Painting with SIFT Algorithms," 2021 IEEE 4th International Conference on Computer and Communication Engineering Technology (CCET), Beijing, China, 2021:79-84.
2. Bantukwattanatham S., Thai Traditional Painting, 2001; 610(3).
3. Hao Su, Fan Wang, Li Yi, Leonidas Guibas, "3D-Assisted Image Feature Synthesis for Novel Views of an Object", CoRR, 2014;11.
4. Azuma R. T. A Survey of Augmented Reality. Presence: Teleoperators and Virtual Environments. 1997; 6(4): 355–385.
5. Van Krevelen, Rick and Poelman, Ronald. A Survey of Augmented Reality Technologies, Applications and Limitations. International Journal of Virtual Reality. 2010; 9:1.
6. Doulah, A. and Rasheduzzaman, Mirza and Arnob, Faed and Sarker, Farhana and Roy, Nipa and Ullah, Md and Mamun, Khondaker. Application of Augmented Reality Interventions for Children with Autism Spectrum Disorder (ASD): A Systematic Review. Computers 2023;12: 215.
7. Xah Lee. "List of 3D Modeling Software". xahlee.org. Archived from the original on 3 February 2018.
8. Deng L and Yu D, "Deep learning: methods and applications foundations and trends," Signal Processing, 2014;7(3-4): 197–387.



UTILIZING CLOUD COMPUTING FOR EFFICIENT MANAGEMENT OF BLOCKCHAIN-BASED JUDGING COMPETITIONS IN TAEKWONDO POOMSAE

Kittimasak Naijit¹

¹Department of Computer Science, School of Science,
King Mongkut's Institute of Technology Ladkrabang, Bangkok, Thailand

*e-mail: kittimasak.na@kmitl.ac.th

Abstract:

The described system presents an all-encompassing framework for the management of taekwondo poomsae competitions. It seamlessly integrates blockchain technology, wireless networks, mobile computing, and cloud computing, providing abundant computational resources to network operators, mobile consumers, and cloud computing providers. Comprising four primary components, namely the competition-verified network system, the judging and scoring competition mobile application, the display competition mobile application, and the competition information mobile application, these applications are compatible with both Android and iOS platforms. The system ensures highly accurate and reliable competition results, adhering to the layout regulations stipulated by World Taekwondo (WT). To safeguard participants' private data, the mobile application encrypts device information and stores a unique identifier (hash) of the encrypted data on a blockchain. Digital credentials can be stored in a dedicated system or within the mobile application for convenient sharing and printing. Referees gain the ability to verify the origin, recipient, and authenticity of competition results. The scoring system establishes standardized patterns for the issuance and validation of credentials across different blockchains. Employing a blockchain-based routing scheduling model, the system allows routing nodes to dynamically request and obtain routing information. A proof-of-authority consensus algorithm, tailored for private networks, guarantees data integrity, prevents signature delays, and fortifies against malicious node attacks. With a remarkably low processing time of 0.297 seconds, significantly faster than other algorithms, the proposed algorithm capitalizes on the strengths of both DL and LIF algorithms.

Introduction:

Taekwondo Poomsae represents the traditional facet of Korean martial art in Taekwondo, characterized by a structured sequence of offensive and defensive maneuvers executed against an imaginary opponent. It constitutes a predetermined set of movements that progressively increase in complexity as one advances in learning. In preparation for the upcoming advertising exam, individuals typically learn a specific poomsae for each belt level. The practice of each poomsae involves mentally envisioning imaginary adversaries attacking from various directions. The regulations outlined here pertain to internationally recognized poomsae and adhere to the norms and competition rules established by World Taekwondo (WT). The rules for poomsae competitions are designed to handle matters related to competitions at all levels, as promoted and organized by the WT, its Continental Unions, and National Associations. The overarching goal is to ensure fair and smooth management of poomsae competitions while implementing uniform regulations. The research also mentions the categorization of poomsae taekwondo competitions into two types:

1. Poomsae: This category encompasses poomsae patterns that have been officially defined and scoring follows the guidelines provided by WT.



2. Free Style Poomsae: Contestants in this category create their own poomsae patterns within the principles of Taekwondo's combat techniques, accompanied by music. Free Style Poomsae patterns are designed by individual Taekwondo practitioners.

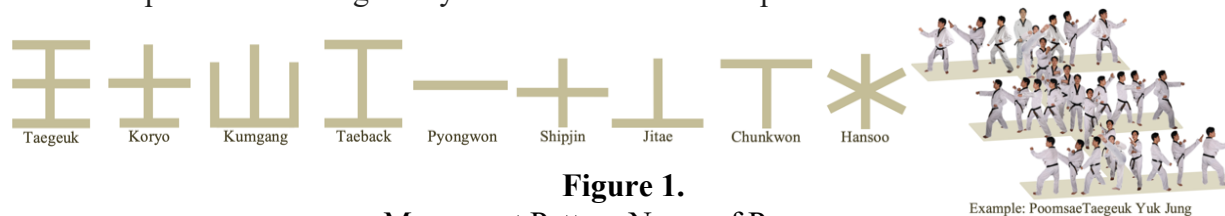


Figure 1.
Movement Pattern Name of Poomsae

Methodology:

The methodology aims to describe the system for managing taekwondo poomsae competitions, which utilizes blockchain technology, wireless networks, mobile computing, and cloud computing. The system is designed to provide abundant computational resources to network operators, mobile consumers, and cloud computing providers. This methodology outlines the four main components of the system and how they work together to ensure highly accurate and reliable competition results while safeguarding participants' private data. The methodology of the system described in the Abstract is as follows:

1. The competition area layout is designed to follow the regulations set by WT.
2. A mobile application is developed for judges and scorers to use during competitions. The mobile application encrypts device information and stores a unique identifier (hash) of the encrypted data on a blockchain to protect participants' private data. Digital credentials can be stored in a dedicated system or within the mobile application for easy sharing and printing. Referees can verify the origin, recipient, and authenticity of competition results.
3. A blockchain-based scoring system is established to standardize patterns for granting and validating credentials across different blockchains.
4. A blockchain-based routing scheduling model is employed to allow routing nodes to dynamically request and obtain routing information.
5. A proof of authority consensus algorithm, is used to ensure data integrity, prevent signature delays, protect against malicious node attacks.

Results and Discussion:

The results show that the system is highly scalable and can handle a large number of users and transactions. The system is also able to achieve a high level of accuracy and reliability in competition results. The proposed system offers several advantages over traditional taekwondo poomsae competition management systems. First, the system uses blockchain technology to ensure the security and integrity of competition data. Second, the system uses mobile computing technologies to provide a convenient and user-friendly experience for judges and scorers. Third, the system uses cloud computing technologies to provide abundant computational resources and scalability. The system has the potential to revolutionize the way taekwondo poomsae competitions are managed. The system can help to improve the accuracy and reliability of competition results, reduce the workload on judges and scorers, and make the competition experience more enjoyable for everyone involved. The system is able to provide real-time feedback to participants, as evidenced by the use of scoreboards and electronic displays. The results and discussion section should provide a detailed analysis of the system's performance, including its strengths, weaknesses, and limitations.

1. System

The system integrates blockchain technology with mobile cloud computing and utilizes various programming languages. The system is built on a background architecture driven by blockchain, ensuring the accuracy and reliability of competition results. The competition area layout adheres to the requirements of WT and is divided into four main parts:

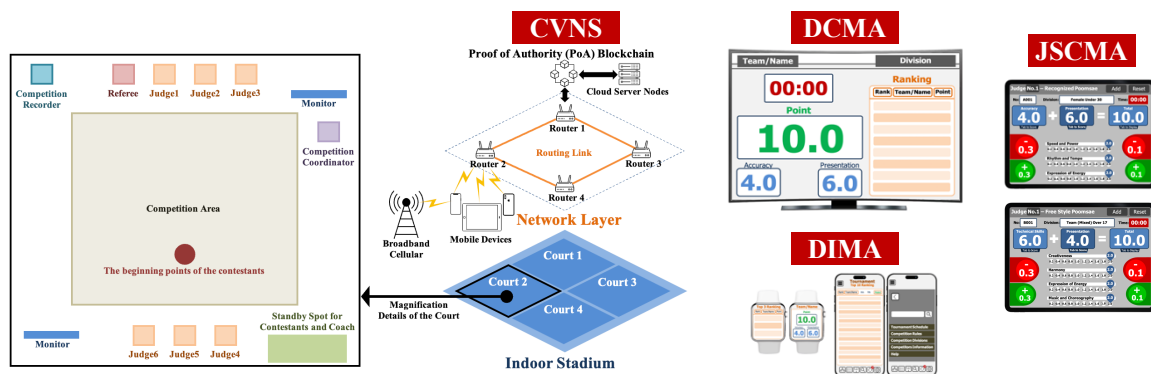


Figure 2.
Judging Competitions System

1.1 Competition Verifies Network System (CVNS): This component establishes a wireless communication network architecture to support mobile device usage. Transaction information is supervised using a proof of authority blockchain platform, providing a distributed routing environment.

1.2 Judging and Scoring Competition Mobile Application (JSCMA): The mobile application empowers judges to allocate points to athletes based on predefined scoring criteria, resulting in more equitable judgments. The app incorporates embedded features that enhance the efficiency of the judging process, thereby streamlining competition management.

1.3 Display Competition Mobile Application (DCMA): This element is dedicated to presenting live competition results to the audience. Judges input their scores into the JSCMA system following each poomsae performance. The DCMA monitors automatically display the comprehensive scores, omitting the highest and lowest scores assigned by the judges. Subsequently, the final score and individual scores are showcased on the monitors for audience viewing.

1.4 Competition Information Mobile Application (CIMA): This element enables regular users to track and access tournament information, offering the choice to receive immediate notifications regarding competition outcomes. Emphasizing app wrapping, it prioritizes functionality, efficiency, and user satisfaction, permitting adaptable IT management for application implementation and policy adjustments. CIMA presents a comprehensive set of competition data, facilitating the monitoring of competition progress in each court for spectators, officials, athletes, coaches, and judges.

2. Operations

The system's operations encompass network management, competition scoring, data security, and user accessibility to ensure the accurate and secure management of taekwondo poomsae competitions, all while adhering to the rules and standards set by WT.

2.1 Verified Blockchain-Secured

The increasing prevalence of blockchain technology as a distributed ledger for information sharing. It compares the operation of blockchain to the propagation of ge-netic

information in living organisms, where new blocks are added to the blockchain as transactions occur and the system becomes more complex.

A blockchain-based identification scheme for judges, where each judge is uniquely identified by their public key. Judges authenticate themselves by using their secret private key, often associated with a biometric identifier like a fingerprint. Their personally identifiable information is recorded and linked to their public key using a mobile application installed on their device. The application encrypts private data, uploads a hash to the blockchain, and stores digital credentials either externally or within the app. This enables judges to easily share and validate their credentials. The scoring system aims to establish standardized patterns, allowing for the issuance and verification of credentials across any blockchain. It emphasizes the importance of individuals having ownership and the ability to demonstrate their significant digital records in a secure and reliable manner.

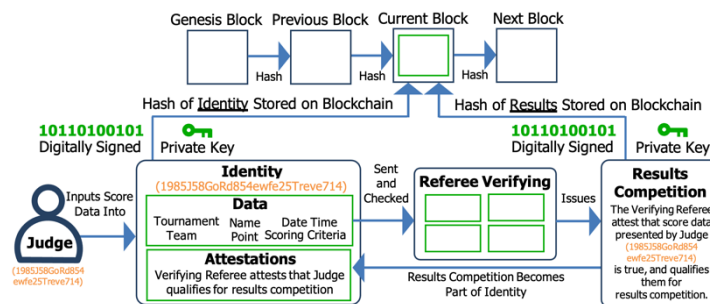


Figure 3.

Structure of Verified Blockchain-Secured Identity

2.2 Node Routing Network

The routing network consists of routing nodes and terminals, with routing nodes maintaining individual networks to connect multiple terminals. Their main function is to receive and forward packets within the network. In our blockchain-based platform, the transaction information is collectively supervised by all network nodes, creating a distributed routing environment for obtaining global routing information. With our proposed blockchain-based routing scheduling model, routing nodes have the capability to actively request and acquire routing information from the blockchain network.

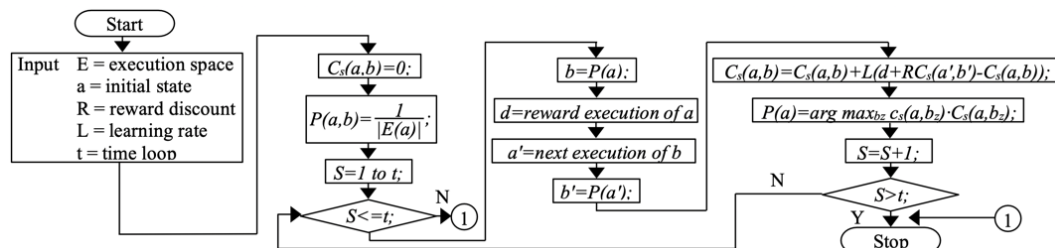


Figure 4.

Algorithm of Strengthening Learning and Routing on Blockchain

This model also establishes a trusted routing environment that complements traditional routing algorithms. The blockchain network operates on a consensus system known as Proof of Authority, which requires validation from more than half of the authenticated nodes in order to upload transactions and update routing information. As a result, the data stored on the blockchain cannot be manipulated by individuals. The nodes in the network record various blockchain transactions, including token-release agreement transactions, transfer



tokens transactions, and transactions related to the operational features of routing nodes in contracts. These transactions contribute to the comprehensive record of the blockchain's activities in the routing domain.

The proposed research introduces a supplement schedule leveraging the dynamic, global, and reliable information provided by the blockchain platform. In the context of the study, C_s denotes the table containing packets sent to the routing node ds . Valuable insights are extracted from the blockchain network learning model, including the timestamp of token transactions denoted by S array. The current position of the packets to be transmitted is represented by state a , indicating their location at routing node a . The action P , derived from the current state a , entails forwarding the packets to the subsequent routing node db . The execution space $E(a)$ encompasses the entire range of activities performed by the routing nodes. The metric $C_s(a, b_z)$ quantifies the differential queue length between routing nodes d_a and d_{az} . This metric plays a crucial role in determining the likelihood of d_a transmitting packets to d_{az} . A higher value of this metric increases the probability of transmission. Consequently, if a routing node manipulates the queue length to appear reduced, it can enhance the likelihood of receiving packets from other routing nodes.

$$C_s(a,b) = C_s(a,b) + L(d + RC_s(a',b') - C_s(a,b));$$

When the value of L is set to one, it indicates that the learning algorithm disregards the original C_s . The parameter L , with $0 \leq L \leq 1$, represents the learning rate of the C variable. The reward discount R signifies the significance of the next state in relation to the current C_s . A higher value of R implies a stronger influence of the next state on the present C_s . The reward value d plays a significant role in motivating routing nodes to optimize their routing decisions. It is calculated based on various factors, including the transmitted timestamp and the address array. In our reinforcement learning framework, denoted as d , the reward value is associated with the number of tokens offered, discouraging malicious nodes from engaging in non-forwarding behavior as outlined in the threat model.

$$P(a) = \arg \max_{b_z} c_s(a,b_z) \cdot C_s(a,b_z);$$

The learning model aims to generate a routing node policy, P , by analyzing relevant routing data from the blockchain. This policy determines the next hop for packets based on $c_s(a,b_z) \cdot C_s(a,b_z)$ values. The probability distribution of b_z is selected based on the state and action space, ensuring accurate routing. Higher values of $c_s(a,b_z) \cdot C_s(a,b_z)$ indicate a higher likelihood of executing the policy $P(a)=b_z$.

2.3 Judge and Referee of Hybrid Signature

The advantages of both the Large Integer Factorization (LIF) and Discrete Logarithm (DL) algorithms. By combining these two algorithms, the hybrid signature algorithm achieves a robust. The objective is to achieve data integrity, minimize signature latency, protect against malicious node attacks. The algorithm consists of three main components: parameter selection, signing, and verification.

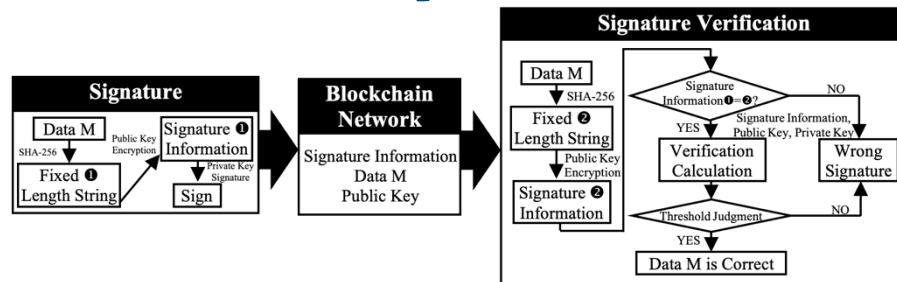


Figure 5.

Process of Hybrid Signature

The LIF algorithm is known for its lightweight blockchain public key system, relying on the difficulty of factoring large integers, while the DL algorithm is the foundation of the Digital Signature Standard, based on the complexity of the discrete logarithm. By combining these algorithms in a hybrid approach, the proposed signature algorithm enhances both security and efficiency in data signing and verification processes. The goal is to meet safety requirements while minimizing signature latency. This approach provides robust data authentication in various applications by leveraging the complementary strengths of the LIF and DL algorithms.

2.3.1 Parameter Settings

The proposed hybrid signature algorithm involves the reception of raw data and key pairs by the node and smart terminal respectively. Additional parameters, consistent with the DL algorithm, are incorporated alongside the primary parameter settings. The utilization of public parameters (H, q, p, g) in the data signature process by the node enhances the security and reliability of the signature.

2.3.2 Signature

The hybrid signature algorithm involves the node performing calculations to generate the signature (s, σ, r) using the public y_2 and private x_1 keys obtained from the smart contract. These calculations include determining a random value r , computing the signature $\sigma'(m)$, calculating the signature coefficient s' . Once generated, a signature is shared with other nodes in the blockchain network.

$$r' = (y_2^k \bmod p) + m \bmod q$$

r' incorporates the parameter m . By adding m to the result of $y_2^k \bmod p$, we introduce an additional factor that can influence the value of r' . The modulo operation $\bmod q$ ensures that the resulting value r' remains within the range specified by q . The parameter m can represent a random value, a nonce, any other factor that adds complexity and enhances the security properties of the resulting value r' .

$$\sigma'(m) = H(\text{concat}(y_2, r\text{hash}m), m)$$

$\sigma'(m)$ represents the updated value of the signature σ that incorporates the concatenation of y_2 and $r\text{hash}m$ as the input to the *hash* function H . The hash function H calculates a fixed-size *hash* value based on the concatenated input. By using the concatenation of y_2 and $r\text{hash}m$ as the input, we ensure that the resulting hash value incorporates both the value of y_2 and the hash of m in a secure manner.

$$s' = k^{-1} (m + x_1 \cdot (r' - \sigma(m))) \bmod q$$



s' represents the updated value of s . We have rearranged the terms to have x_1 outside the parentheses and simplified the expression $x_1 \cdot r' - x_1 \cdot \sigma(m)$ to $x_1 \cdot (r' - \sigma(m))$.

2.3.3 Signature Verification

The proposed algorithm includes a signature verification process conducted by the service provider. This process involves using the private key x_2 and the public key y_1 to verify the signatures (s, σ, r) . By validating the parameters $\sigma'(m)$ and the signed data, the algorithm prevents unauthorized manipulation of sensitive physiological information, thus preserving the integrity and trustworthiness of diagnoses.

1) Signature Parameter Verification: In order to validate the signature parameter $\sigma'(m)$, the service provider presents the data m for verification. If the signature parameter and the provided data are found to be the same, it confirms the correctness of the signature parameter. The subsequent stage entails the validation of the signature configuration. However, if they do not match, the algorithm must be halted.

2) Signature Data Verification: The validation process involves using the private key x_2 and public key y_1 to verify the signature. The determination of the first parameter for verification, incorporate a scaling factor k , denoted as α' , β' , and d' , can be described as follows:

$$\begin{aligned}\alpha' &= s - 1 \cdot m \cdot (k \bmod q) \\ \beta' &= s - 1 \cdot r \cdot (k \bmod q) \\ d' &= y_2 - \sigma(m) \cdot (k \bmod p)\end{aligned}$$

Following, the verification coefficient v' can be computed utilizing the acquired parameters. Additionally, the validity string (M', N') and the threshold ε' are evaluated by the smart contract. The verification coefficient v' , along with the verification sequences M' and N' , and the threshold ε' , can be expressed as follows:

$$\begin{aligned}v' &= (g^a \cdot y_1^\beta \bmod p)^{x_2} \bmod q \\ M' &= H(\text{hash}(m) \parallel r') \\ N' &= H(\text{hash}(m) \parallel v')\end{aligned}$$

We have concatenated the values of $\text{hash}(m)$ and r using the “//” operator to represent their combination in a single input for function H of the hash. The value of N' by applying the hash function H to the concatenated value of $\text{hash}(m)$ and v' .

The hybrid signature algorithm employed in this research incorporates a computationally efficient and collision-resistant hash function. By utilizing such a hash function, the algorithm enhances the system's security by increasing the difficulty of malicious attacks. During the initial verification process, the uniqueness of hybrid data signature plays a crucial role in ensuring the legitimacy of the data source. This mechanism allows only authorized access to the signed data, providing an additional layer of security and trust in the system.

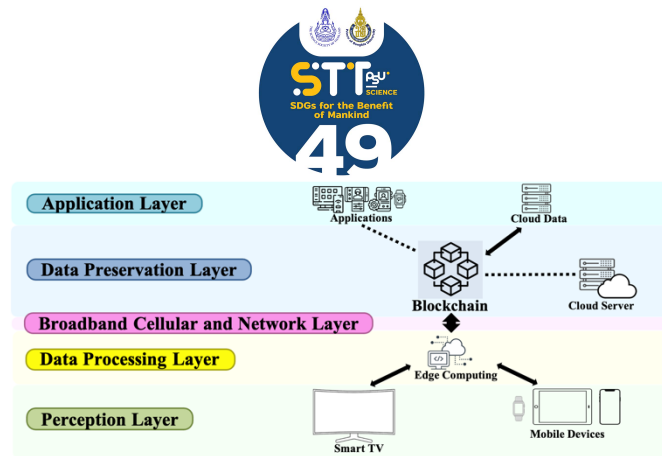


Figure 6.
Architecture of Competitive Real-Time Judging Platform

2.4 Competitive Real-Time Judging Platform

This study presents an innovative real-time judging platform that integrates Wi-Fi, cellular broadband, and blockchain technology. It overcomes the constraints of passive methods by enabling immediate data collection via mobile devices on the broadband cellular network. The platform encompasses various functions including data preprocessing, pattern mining, identification, forecasting, and visualization to analyze the collected data and securely transmit results to the cloud and applications through blockchain encryption. The adoption of blockchain technology guarantees the integrity of data while safeguarding against tampering and manipulation.

3. Results

In order to assess the efficiency and effectiveness of the proposed approach, the researchers implemented a prototype and conducted performance and efficiency evaluations. The performance evaluation involved comparing the system with a traditional Proof of Work blockchain-based system, focusing on metrics such as delay, throughput, and resource consumption. The efficiency evaluation, on the other hand, compared the proposed approach with trust-based algorithms and other blockchain-based algorithms, considering computational overhead, network utilization, and consensus mechanism.

3.1 Efficiency

The detailed analysis and comparison of the efficiency between blockchain-based systems utilizing the Proof of Authority (PoA) consensus mechanism and the traditional Proof of Work (PoW) approach. The researchers conducted a series of experiments to gather data and evaluate the performance of each system.

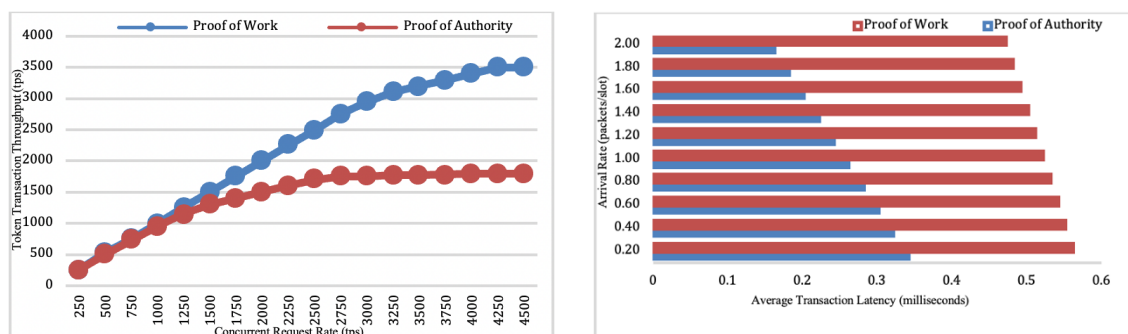


Figure 7.
Average Transaction Latency of Blockchain-based System

The evaluation of transaction token throughput of blockchain systems, specifically the PoA scheme and the traditional PoW scheme. The evaluation involved subjecting the systems to a range of token transaction requests, from 0 to 4000 transactions per second (tps), to measure their performance under different levels of concurrent requests. The results showed that the PoA blockchain scheme achieved a stable and efficient throughput of 3500 tps, outperforming the PoW scheme, which had a lower throughput of approximately 1800 tps. These findings demonstrate the superior transaction processing capacity of the PoA scheme, making it suitable for high-demand environments.

3.2 Effectiveness

The effectiveness of a system was evaluated through comparative experiments focusing on blockchain token transaction throughput. Additionally, tests were conducted involving the introduction of 50% malicious routing nodes into the routing environment to assess the system's performance in the presence of such nodes.

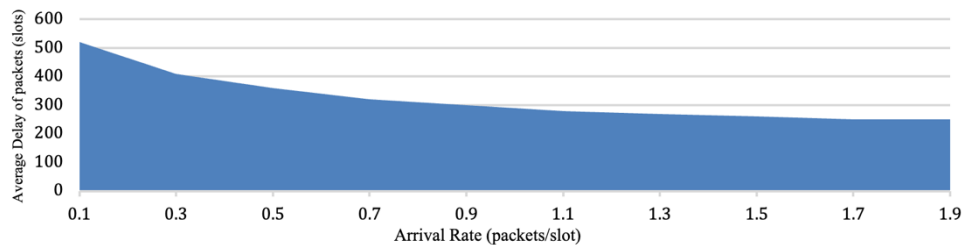


Figure 8.

Average Packet Delay in the Presence of Malicious Nodes

The implemented algorithm demonstrated robust performance, even when faced with a large number of malicious nodes attempting to disrupt the routing scheduling process. These malicious nodes engaged in activities such as manipulating algorithm parameters and providing false information to interfere with regular scheduling operations. The intentional inclusion of malicious nodes aimed to create interference and test the system's resilience. The experiments provided insights into the system's reliability and security, highlighting its ability to withstand disruptive actions and maintain performance.

3.3 Runtime of the Hybrid Data Signature

The signature generation time achieved by the proposed algorithm is recorded as 0.199 seconds. Similarly, the verification process demonstrates an impressive time of 0.078 seconds. When considering the overall processing time, which combines both signature generation and verification, the proposed hybrid data signature algorithm achieves a remarkably low time of 0.297 seconds. Comparatively, these results indicate that the proposed hybrid data signature algorithm outperforms both the LIF (Large Integer Factorization) and DL (Discrete Logarithm) algorithms in terms of runtime efficiency. This achievement can be attributed to the unique advantage of the proposed algorithm, which combines the strengths of DL and LIF algorithms. By leveraging the benefits of both approaches, the proposed algorithm achieves the shortest processing time, demonstrating its effectiveness in handling data signature tasks.

**Table 1.** Time of Signature Algorithms

Methods	Signature Time (s)	Verification Time (s)	Processing Time (s)
LIF (Large Integer Factorization)	0.2987902	0.4187321	0.7126573
DL (Discrete Logarithm)	0.2286547	0.2525453	0.4965931
Hybrid	0.1992167	0.0783648	0.2971679

Table 1 presents a comprehensive comparison of the runtime between the proposed hybrid data signature algorithm and the traditional LIF (Large Integer Factorization) and DL (Discrete Logarithm) algorithms. To ensure accurate results, multiple experiments were conducted, and the findings were combined. The table reveals the respective times for signature generation, verification, and overall processing using the proposed hybrid data signature algorithm.

Conclusion:

This study delves into the utilization of blockchain technology within mobile edge computing environments to uphold privacy in secure data communication and the safeguarding of patient information. The research explores diverse blockchain types and elucidates the associated consensus algorithms. Proposing a hybrid data signature algorithm for securing sensitive physiological data, the study underscores the merits of blockchain technology in mobile applications across diverse devices. It facilitates peer-to-peer and distributed information services while ensuring the integrity and privacy protection of data. In the context of taekwondo poomsae competitions, the conventional setup involves judges and a referee positioned linearly alongside a score-keeping table to evaluate participants' performances. However, accurately assessing a poomsae performance necessitates consideration of factors beyond technical proficiency. This research introduces a system that integrates multiple applications, leveraging interconnected devices and blockchain technology. The system adeptly organizes tournaments, consolidates real-time information, and elevates operational efficiency through seamless data management and analysis.

Within the realm of secure data transmission, the pivotal role of key pairs among judge nodes, coaches, and athletes cannot be overstated. These key pairs constitute a dual key structure crucial for executing hybrid signatures on data records, effectively thwarting node attacks during the transmission of data. The integration of blockchain technology further ensures distributed transmission, thereby bolstering data integrity. Despite the challenges faced by blockchain technology, its potential for future advancements and widespread adoption is highly promising. As the technology matures and undergoes refinement, it is poised to unlock myriad possibilities across various fields and applications. The rapid growth and development of blockchains position them to become a ubiquitous phenomenon, reminiscent of the transformative impact the Internet had decades ago. In Proof of Authority blockchain networks, authorized accounts, referred to as validators, play a central role in validating transactions and creating blocks. These validators leverage software to automate the transaction placement process within blocks, eliminating the necessity for continuous monitoring of mobile devices. Addressing tournament complaints is imperative for ensuring a fair and accurate resolution of issues that may arise during the game. The introduced system offers an efficient process for problem resolution not only in taekwondo poomsae but also in other emerging contexts.

Acknowledgements:

All computational resources were supported by Department of Computer Science, School of Science, King Mongkut's Institute of Technology Ladkrabang, Bangkok, Thailand.

References:

1. Adil. O. Y. Mohamed. International Journal of Interactive Mobile Technologies 2023; 17(04); 37-46.
2. Deqing MaJinsong Hu. International Journal of Production Economics 2022; (254); 108633.
3. Firdous Kausar, Fahad M. Senan, Kaamran Raahemifar. (2022). Alexandria Engineering Journal 2022; 61(6); 4295-4306
4. Huifang Yu, Zhirui Lv. Journal of King Saud University - Computer and Information Sciences 2023; 35 (7); 101602; 1-9.
5. Ian J. Scott, Miguel de Castro Neto. Computers & Industrial Engineering 2023; (182); 109347; 1-17.
6. Jiajia Jiang, Yushu Zhang, Youwen Zhu, Xuewen Dong b, Liangmin Wang, Yong Xiang. Journal of King Saud University - Computer and Information Sciences 2023; 7988-7999.
7. Manuel Adelin Manolache, Sergiu Manolache, Nicolae Tapus. Procedia Computer Science 2022; (199); 580-588.
8. María Isabel Ortiz-Lizcano, Enrique Arias-Antunez, Ángel Hernández Bravo. Computer Methods and Programs in Biomedicine 2023. (231); 107379; 1-9.
9. Marin Jovanovic, Nikola Kostić, Tomaz Sedej. Technological Forecasting and Social Change 2022; (184); 121981; 1-15.
10. Mohanad A. Mohammed, Hala B. Abdul Wahab. International Journal of Interactive Mobile Technologies 2022; 16 (20); 162-176.
11. Samar Raza Talpur, Alhamzah F. Abbas, Nohman Khan, Sobia Irum, Javed Ali. International Journal of Interactive Mobile Technologies 2023; 17 (08); 23-38.
12. Yan Zhen, Hanyong Liu. Digital Communications and Networks 2020; 6 (2); 229-237.
13. Yassine Azizi, Mostafa Azizi, Mohamed Elboukhari. International Journal of Interactive Mobile Technologies 2022; 16 (15); 4-15.



SESSION E-ENERGY / ENVIRONMENTAL & EARTH SCIENCE / MATERIALS SCIENCE / CHEMICAL TECHNOLOGY

APPLICATION OF THE XRF CORE SCANNER TO ASSESS THE ENVIRONMENTAL CHANGES IN SOUTHERN THAILAND

Kanokpon Surijamorn,^{1,*} Ludvig Löwemark,² Kweku Afrifa Yamoah,³ Akkaneeewut Jirapinyakul⁴

¹Earth Science Program, Department of Geology, Faculty of Science, Chulalongkorn University, Bangkok 10330, Thailand

²Department of Geosciences National Taiwan University, No.1, Sec. 4, Roosevelt Rd., Da-an Dist., Taipei City 10617, Taiwan (R.O.C.)

³BioArc, Department of Archaeology, University of York, York YO10 5DD, UK

⁴Department of Geology, Faculty of Science, Chulalongkorn University, Bangkok 10330, Thailand

*e-mail: 6472001623@student.chula.ac.th

Abstract:

Environmental reconstruction can contribute information to understand climate changes in the future better. This research aimed to reconstruct the paleoenvironment from lake sediment using the XRF-core scanning technique. The sediment cores were taken from Nong Thale Pron (NTP), Thung Yai district, Nakhon Si Thammarat Province, southern Thailand. According to the lithostratigraphic correlation to the previous study, this sedimentary sequence was possibly deposited during 23.3 to 8.39 cal ka BP. The principal component analysis was applied to find the relationship between each element before applying element ratios to reconstruct the paleoenvironmental. The elemental ratios of K/Ti, Si/Al, Mn/Fe, and Ca concentration were used to assess the chemical weathering, runoff intensity, lake level, and groundwater supply to the lake. These results demonstrated the wet conditions at 23.3-21.2, 17-16, 15-14, and 11 cal ka BP. The dry conditions can be determined at 21, 19, 16, 12, and 10 cal ka BP.

Introduction:

Thailand is located in the Indochina Peninsula (Figure 1). The Asian monsoons have been considered the primary driver of its climate.¹ The southwest monsoon brings warm and moist air masses from the Indian Ocean, increasing precipitation from May to October. In contrast, the northeast monsoon from Central Asia transports cold and dry air masses, making precipitation decline from November to February.¹ Since climate patterns play a crucial role in environmental shifts, understanding the past environment can help insight into future climate changes. The reconstruction of the past climate generally relies on geological archives, e.g., speleothem, marine, and lake sediments. The lake sediments are one of the most popular archives because of their simple chronology and deposited together with various proxies, e.g., pollen, diatom, grain size, geochemical compositions.

Although paleolimnological studies in Thailand have increased during the last ten years, most of them were constrained to the Holocene. The record obtained from Nong Thale Pron (NTP) by Smittenberg et al. (2021)² is one of a few studies that can provide insight into the late Pleistocene. Consequently, in this study, we collected the new core from NTP (17°11'N, 99°23'E) located in Thung Yai district, Nakhon Si Thammarat province, Southern Thailand (Fig.1). NTP was formed by a sinkhole in karst topography. It covers approximately 0.04 km² and <4 m water depth.³ The southern part of the lake was developed into a reservoir in 2017, while the northern part is undisturbed.

In this study, the paleoenvironment in NTP was reconstructed relying on XRF-core scanning, which is fast and has a high resolution of relative variations in the geochemical compositions of the sediment core surface. This technique is prevalent because it can be applied with untreated sediment and does not destroy the sediment core.⁴

Methodology:

The thirteen sediment cores were retrieved using the Russian corers (10 cm diameter, 1 m length) on a modified rubber boat from the deepest part of NTP in November 2022. Three continued sediment sequences of 3-8 m, 3.5-8.5 m, and 7.88-10.8 m were collected approximately 30 m from each other. The sediment cores were carefully placed in PVC pipe and wrapped in plastic film before being transported for further analysis. At the Department of Geology at Chulalongkorn University, the sediments were described based on Wohlfarth (2014).⁵ After that, they were correlated to construct the adjusted depth and the lithostratigraphic column. These cores were subsequently transported to the Department of Geosciences at the National Taiwan University for XRF-core scanner.

The samples were analyzed with ITRAX XRF core scanner using Mo X-ray tube. The sediment cores were prepared by removing, cleaning, and smoothing the sediment surface in a parallel direction with a plastic spatula. The prepared cores were then wrapped in PTFE plastic film before being placed in the scanner for an optical image. After that, XRF parameters were set following the laboratory protocol, i.e., 5 s exposure times, 30 kV potential difference, 50 mA electric current, and 0.2 mm step size. The XRF measurement was validated by the correlation coefficient between replicate measurements of samples. Eventually, the principal component analysis was applied to insight into the relationship of each element.

The chronology of this sediment core was constructed by lithostratigraphic correlation with NTP-CP1² relied on the boundary between clayey gyttja and algae gyttja.

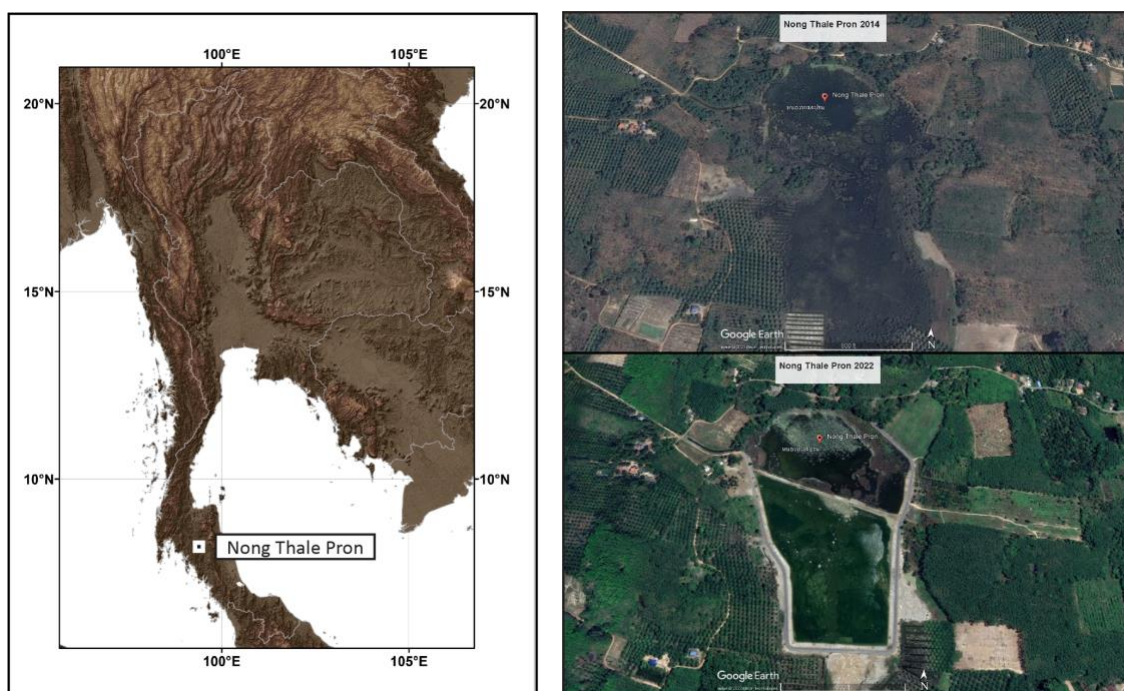


Figure 1.
Location of this study (left) and lake in 2014 and 2022 (right)

Results and Discussion:

A. Lithostratigraphy and chronology

The sedimentary sequence contains five distinct sedimentary units (Figure 2). Unit A consists of clayey gyttja (10.8-7.83m) with a calcareous layer at the top. It was overlaid by gyttja clay and gyttja of unit B (7.83-5.72m), algae gyttja of unit C (5.72-4.12m), gyttja clay and gyttja of unit D (4.12-3.88m), and algae gyttja of unit E (3.88-3.335m), respectively, from bottom to top.

According to the previous study, the sediment rate was a slight change of 0.05 cm/yr.² The age of the sediment sequence, therefore, extended from 8.39-23.31 cal ka BP.

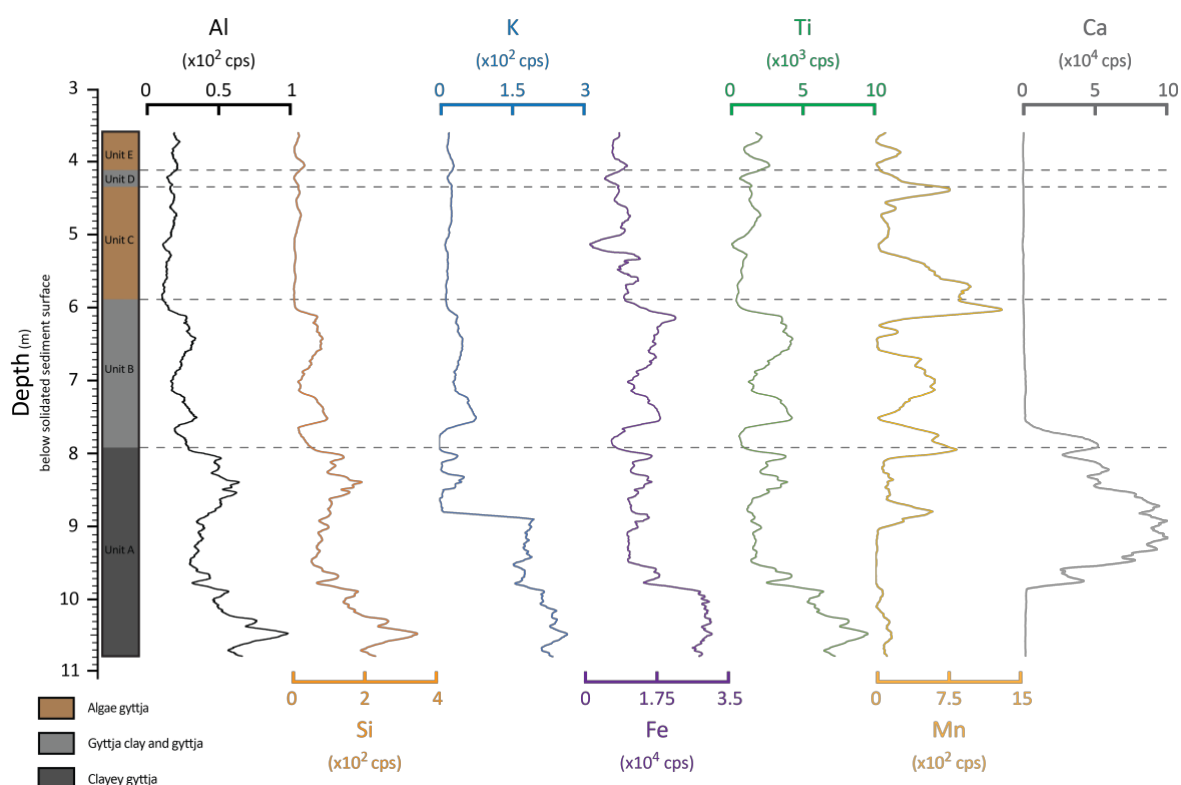


Figure 2.

Lithostratigraphy and Al, Si, K, Fe, Ti, Mn, and Ca counts of NTP-CP6 sediment sequence

B. XRF analysis

Since Al, Si, K, Fe, Ti, Mn, and Ca had low uncertainty and were continuously detectable through the sedimentary sequence, they were then selected for further analysis. The variations of Al, Si, K, Fe, and Ti concentrations demonstrated a similar pattern of gradual decrease in unit A, fluctuation in unit B, and relatively insignificant changes in units C to E. Ca concentration abruptly increased in the upper part of unit A and was relatively stable in the other units. In contrast, Mn concentration was slightly changed in unit A before fluctuations in units B to E.

The first two components of the PCA scores explained approximately 73.6% of the cumulative variance. Consequently, components 1 and 2 were selected to identify the drivers of geochemical compositions in the sediment sequence. Component 1 consists of Al, Si, K, Fe, and Ti, opposing Mn. And Ca is only a member of component 2.

The elemental ratios are frequently applied to paleoenvironmental reconstruction.⁴ Since K is a mobile element relatively water soluble and Ti is an immobile element, the chemical weathering can be assessed by K/Ti.⁶ Si/Al can be referred to as sedimentary grain size, reflecting the intensity of inflow to the lake.⁷ Fe/Mn is a proxy for redox conditions in which a higher Fe/Mn ratio indicates the anoxic condition that is related to the lake water level. Since NTP is a sinkhole, the Ca concentration is possibly derived from the groundwater.

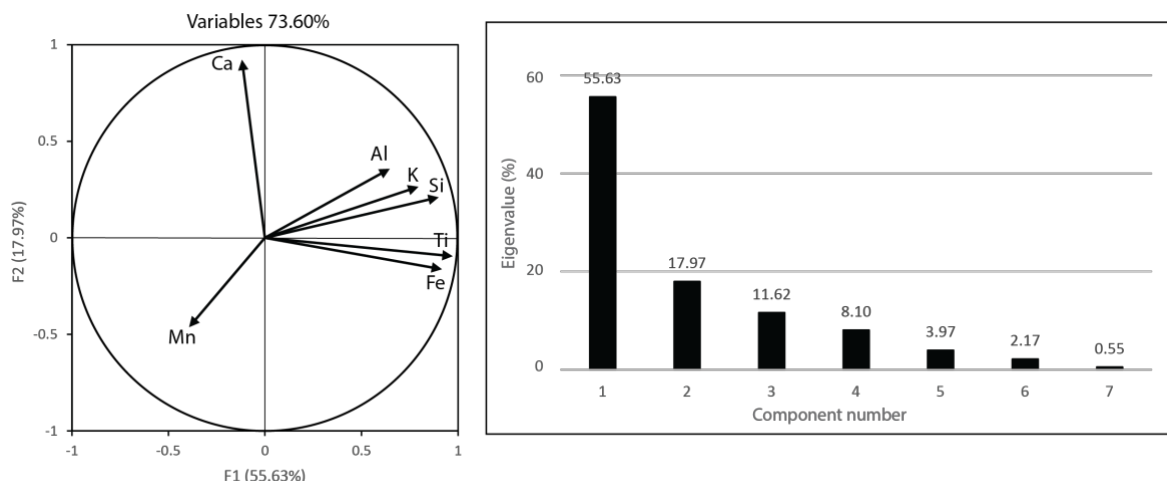


Figure 3.

Plot of the element variables defined by the first two eigenvectors of PCA (left) and Eigenvalues of each component (right)

C. Paleoenvironmental reconstruction at NTP from 8.39-23.31 cal ka BP

High Si/Al and Fe/Mn values indicate high inflow intensity and lake level between 23.3 to 21.2 cal ka BP. At the same interval, K/Ti and Ca values are relatively stable, suggesting stable chemical weathering in the surrounding area and groundwater supplied to the lake. The sudden increase in Ca concentration and K/Ti were synchronous with the decrease in Fe/Mn and Si/Al ratios at 21.2-18.5 cal ka BP. These results point to the dry interval of low lake level and runoff to the lake. The occasionally high and low lake levels and runoff can be assessed by the Si/Al and Fe/Mn fluctuation at 18.5-12 cal ka BP. Interestingly, the K/Ti ratio suddenly increased, which was contemporary with the steady Ca concentration and declines in the Si/Al and Fe/Mn ratios at 12 cal ka BP. These results possibly demonstrated the decrease in runoff and lake level while the inflow transported the weathering material to the lake. At 11.6-8.3 cal ka BP, the K/Ti ratio and Ca concentration were insignificant changes. However, the fluctuation of runoff and lake levels can be described by the changes in Si/Al and Mn/Fe during this time interval.

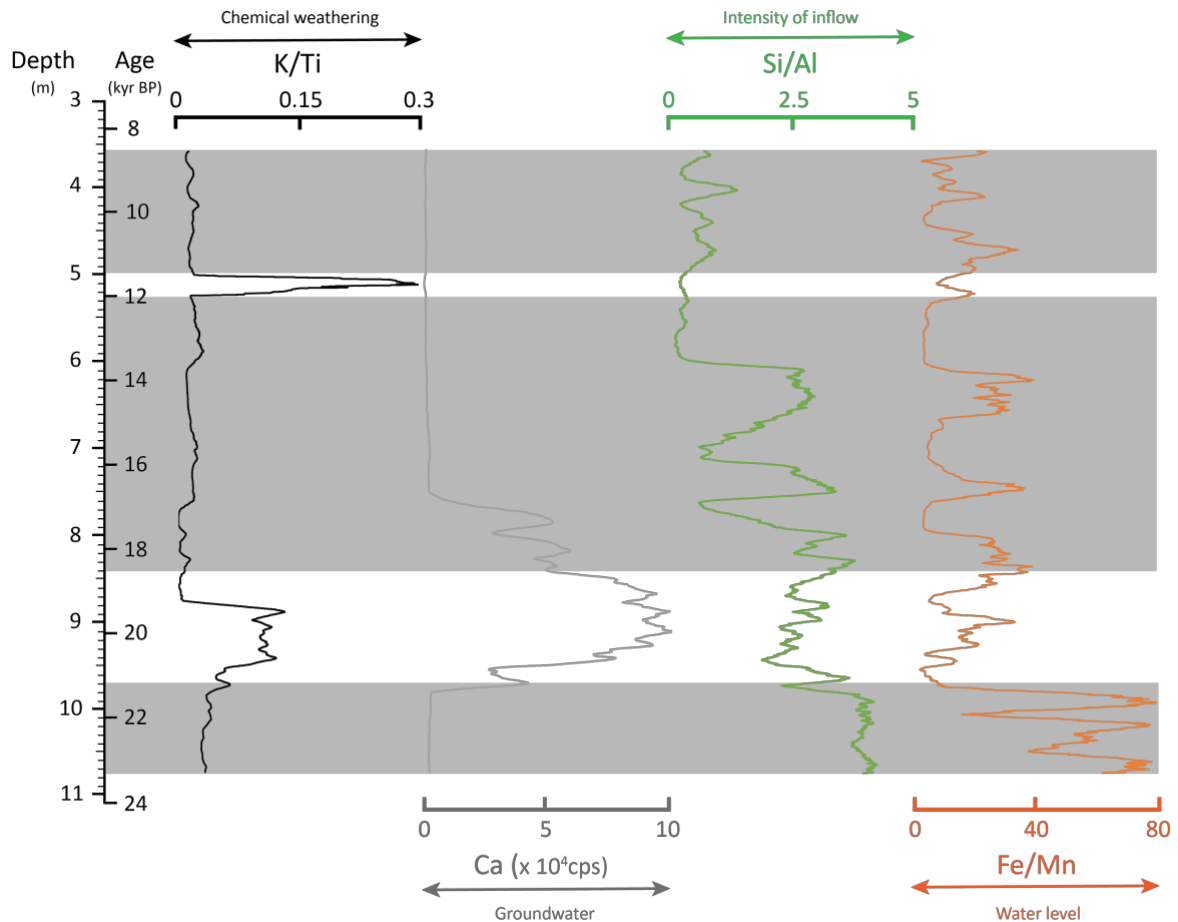


Figure 4.
Chronology and proxies: K/Ti, Ca, Si/Al, and Fe/Mn

Conclusion:

Since the southwest monsoon plays a crucial role in rainfall in this area, these results indicate the strengthening of the monsoon at 23.3-21.2, 17-16, 15-14, and 11 cal ka BP. In contrast, the weakening of the southwest monsoon and/or prevailing of the northeast monsoon can be reconstructed at 21, 19, 16, 12, and 10 cal ka BP.

Recommendation:

Understanding the paleoenvironment using proxies from lake sediment can be achieved quickly and continuously with XRF core scanner, which shows trends in environmental changes that are linked to climate change. However, an additional analysis is required to support the accuracy, and need to be aware of the process and relationship of each element.

Acknowledgements:

This research was supported by the Paleoenvironmental Sediment Laboratory Department of Geosciences, National Taiwan University, and Sci-Super VII, Faculty of Science, Chulalongkorn University.

References:

1. Chabangborn A, Punwong P, Phountong K, Nudnara W, Yoojam N, Sainakum A, Won-In K, Sompongchaiyakul P. *Quat. Int.* 2020;536:103-113.
2. Smittenberg RH, Yamoah KA, Schenk F, Chabangborn A, Chawchai S, Välranta M, Wohlfarth B. *EarthArXiv*. 2021.
3. Yamoah KA, Callac N, Chi Fru E, Wohlfarth B, Wiech A, Chabangborn A, Smittenberg RH. *BG*. 2016;13:3971-3980.
4. Löwemark L, Bloemsma M, Croudace I, Daly JS, Edwards RJ, Francus P, Gallowa JM, Gregory BRB, Steven Huang JJ, Jones AF, Kylander M, Luo Y, Maclachlan S, Ohlendorf C, Patterson RT, Pearce C, Profe J, Reinhardt EG, Stranne C, Tjallingii R, Turner JN. *Quat. Int.* 2019;514:16-29.
5. Wohlfarth B. *Egec*. 2014;3:504.
6. Arnaud F, Révillon S, Debret M, Revel M, Chapron E, Jacob J, Giguët-Covex C, Poulenard J, Magny M. *Quat. Sci. Rev.* 2012;51:81-92.
7. Gebregiorgis D, Giosan L, Hathorne EC, Anand P, Nilsson-Kerr K, Plass A, Lückge A, Clemens SC, Frank M. *Geochem Geophys.* 2020;21.
8. Corella J, Brauer A, Mangili C, Rull V, Vegas-Vilarrúbia T, Morellón M, Valero-Garcés B. *Quat. Res.* 2012;78:323-332.

CAFFEINE REMOVAL FROM WASTEWATER USING COPPER/CARBON/SILICA NANOCOMPOSITE AS ADSORBENT

Sasiprapa Radchatawin,¹ Phetlada Kunthadee,¹ Ratchadaporn Puntharod,¹ Satit Yousatit,² Chawalit Ngamcharussrivichai,² Sakdinun Nuntang,^{1,*}

¹Applied Chemistry Program, Faculty of Science, Maejo University, Chiang Mai 50290, Thailand

²Department of Chemical Technology, Faculty of Science, Chulalongkorn University, Pathumwan, Bangkok 10330, Thailand

*e-mail: Sakdinun.nt@gmail.com

Abstract:

The elimination of caffeine (CAF) in water resources is significant because of its wide distribution and possible toxicity. The present work developed copper supported on mesoporous carbon/silica nanocomposite (Cu/MCS) as novel adsorbent for removal caffeine in aqueous. The Cu/MCS materials were prepared via carbonization using the synthesized mixture of copper acetate and natural rubber (NR) dispersed in hexagonal mesoporous silica (HMS) as a precursor. The Cu/MCS exhibited a high dispersion of copper incorporated into the mesoporous carbon/silica framework as confirmed by Powder X-ray diffraction (XRD) and X-ray Fluorescence (XRF). The Cu/MCS composites possessed a high specific surface area (523–748 m² g⁻¹) and large pore volume (0.80–0.86 cm³ g⁻¹). Fourier Transform Infrared Spectroscopy (FT-IR) revealed the carbonaceous moieties and CuO in Cu/MCS materials. The Cu/MCS(0.01) adsorbent with high amount of copper loading exhibited an effective for CAF removal when compared with other adsorbents. Moreover, the maximum adsorption capacity of this adsorbent for CAF was 55.8 mg/g.

Introduction:

Caffeine is one of the most consumed psychotropic substances in the world and can be used as ingredient in a wide variety of foods, drinks and medicines [1,2] It is a purine alkaloid. Due to its low metabolization rates allied with high consumption worldwide, CAF is frequently found in environmental matrices, making it an important anthropogenic pollutant. According to the Environmental Protection Agency (EPA), CAF has been considered a potential tracer for sanitary wastewater, serving as an indicator to evaluate the efficiency of treatment systems of sewages and waters [3,4] In front of the environmental and public health problems that CAF can cause, researchers are focusing the attention to the development of new strategies to remove these compound and other contaminants from environmental matrices. According to literature data, caffeine can be removed from aqueous with the use of advanced technologies such as ozonation [5], advanced oxidation processes [6], membrane filtration [7] and adsorption [8]

The adsorption method is a potential application for the removal of CAF since it exhibits many advantages such as low initial cost, simple and flexible design, easy operation, the possibility of effluent reuse, and insensitivity to toxic pollutants. In addition, intermediate by-products are not generated during this process [1]. Over the past years, several adsorbents have been employed for antibiotics adsorption such as activated carbon, zeolite, metal-

organic frameworks (MOFs), and mesoporous silica [1,3]. Recently, there have been reports about the synthesis of carbon xerogels modified with amine groups and copper for efficient adsorption of caffeine. Moreover, they exhibited high sorption capacities in the range 91–118 mg/g [8].

Mesoporous carbon/silica nanocomposites (MCS) have garnered significant attention in diverse fields such as catalysis, adsorption, energy storage, and drug delivery [9]. The appeal lies in the combination of inorganic silica and organic carbon, which contributes to their unique mesostructure. Silica provides high mesoporosity, specific surface area, and excellent thermal and mechanical stability. Its surface can be easily modified by direct co-condensation or post-synthesis grafting to introduce various chemically active functionalities, broadening their range of applications. The preparation of MCS materials typically involves two steps. Initially, an organic substance (e.g., glucose, furfuryl alcohol, phenol, or formaldehyde) is introduced as a carbon source into mesostructured silica. Subsequently, the organic substance undergoes carbonization or hydrothermal treatment to convert it into carbon within the silica framework. This process allows for the creation of versatile materials with applications in various fields [10]. Previous study, Yousatit *et al.* reported the preparation of mesoporous carbon/silica nanocomposites using natural rubber (NR) as a renewable and cheap carbon source and applied them as the potential adsorbent for diclofenac adsorption [11].

The aim of this study was the synthesis and characterization of copper supported on natural rubber-derived carbon/silica nanocomposite (Cu/MCS) in various Cu loadings, and their application as adsorbents of caffeine from aqueous. The textural and structural properties of Cu/MCS with respect to adsorption were examined by advanced analyses. The adsorption performance of Cu/MCS for removal of CAF was evaluated by studying the effects of types of Cu/MCS adsorbents.

Methodology:

Preparation of MCS

The preparation of MCS nanocomposite was conducted, as previously reported by Satit *et al.* [11]. A NR/HMS nanocomposite was a precursor to synthesis of MCS material. The NR/HMS nanocomposite was prepared via an *in-situ* sol-gel method. Typically, 0.5 g of the NR sheet was swollen in TEOS at room temperature for 16 h. The swollen NR sheet was measured for the content of TEOS absorption and then stirred for 24 h in THF to obtain colloidal solution. Subsequently, DDA was mixed with a colloidal solution, followed by the dropwise addition of TEOS with stirring. After 30 min, deionized water was slowly added into the mixture while stirring at 40 °C for 1 h. The obtained gel was aged at 40 °C for 3 days and then, it was precipitated with ethanol. The solid product was recovered by filtration and drying at 100 °C overnight. In addition, 3.0 g of as-synthesized NR/HMS was acid treated with a 150 mL of 1 M H₂SO₄/ethanol solution for 4 h, followed by washing with ethanol and drying at 100 °C for 2 h.

MCS nanocomposite was achieved by the carbonization of NR/HMS material, performed in a tubular furnace under an argon flow at 350 °C, 450 °C or 700 °C each step was held for 1 h with a heating rate of 2 °C min⁻¹. The resulting black powder was washed with deionized water and then filtered and dried at 100 °C for 2 h to obtain the MCS material.

Preparation of Cu/MCS

The Cu/MCS composite materials with different amount of Cu loading were prepared by adapting from previous report of Satit *et al.* [11]. and Ptazkowska-Koniarz *et al.*[8]. First, the NR colloidal solutions were prepared the same procedure of synthesis of MCS for 3 batches. And then, DDA was mixed with each batch of rubber solution, followed by the dropwise addition of TEOS with stirring. After 30 min, copper acetate solutions with different concentrations of 0.003, 0.005 and 0.010 M were slowly added into the mixture while stirring at 40 °C for 1 h. The resulting blue gels were aged at 40 °C for 3 days and then, they were precipitated with ethanol. Finally, the recovery of the solid product and the template removal procedure were the same as those described in the synthesis of MCS. The template-free nanocomposites were named Cu/NR/HMS materials.

The Cu/MCS nanocomposites were prepared by the carbonization of Cu/NR/HMS materials. The carbonization condition and procedure were the same as the preparation of MCS material in the synthesis of MCS. The resultant Cu/MCS samples are Cu/MCS (*n*), where *n* represents the concentration of copper acetate solution.

Adsorption procedure

The performance of MCS and Cu/MCS materials in CAF adsorption was evaluated through static adsorption at room temperature. Typically, 10 mL of CAF solution was mixed with 0.01 g of a dried adsorbent in a 50 mL Erlenmeyer flask. The flask was sealed tightly and shaken on an incubation orbital shaker at 120 rpm for 12 h to ensure adsorption equilibrium. Subsequently, the solution was filtered to remove the adsorbent and subjected to HPLC analysis. Equation (1) was used to calculate the adsorption capacity (q_e).

Adsorption capacity:

$$q_e = \frac{(C_0 - C_e)V_i}{W} \quad (1)$$

where q_e is adsorption capacity at adsorption equilibrium (mg/g_{dried adsorbent}); C_0 and C_e are the initial and equilibrium concentrations, respectively, of CAF in the solution (mg/L); V_i is the volume of the initial solution (mL); and W is the weight of the dried adsorbent (g).

Results and Discussion:

Characterization of the synthesized adsorbents

The XRD patterns of the MCS and Cu/MCS with different Cu loading amounts are shown in Figure 1. All composite materials exhibited the reflection peak at 2θ in the range of 15–30°, which corresponded to amorphous silica[12]. The characteristic peaks of Cu and/or CuO were not observed for Cu/MCS (0.003), indicating the small crystallites of Cu and/or CuO well dispersed on the MCS surface.

An increase in the amount of Cu loaded on the MCS surface to 0.005 and 0.010 M enhanced the characteristic peaks of CuO at $2\theta = 38^\circ$ and 64.5° related to (111) and (022) reflection plane of CuO phase, respectively [13]. In addition, the characteristic peak of Cu was observed at $2\theta = 44^\circ$ related to (111) reflection of Cu [13]. These results indicated partly enlarged Cu and/or CuO particles in MCS structure [14].

Figure 2 show TEM images of MCS and Cu/MCS materials. All samples showed the conventional uniform wormhole-like mesopores, corresponding to previous report of Satit *et al.*[11]. In addition, the Cu/MCS materials were observed with a high dispersion of Cu and/or CuO crystallites on the MCS surface but formed agglomerates at an increased Cu loading level.

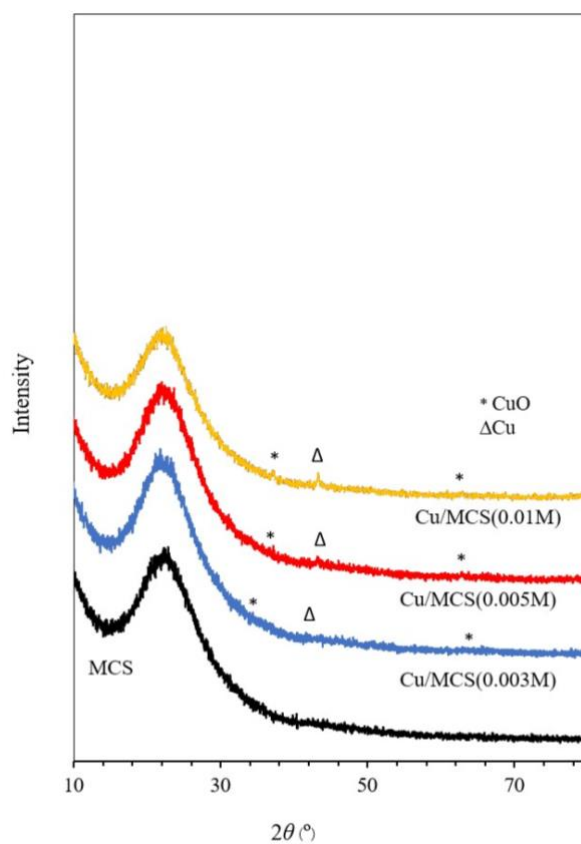


Figure 1.

XRD patterns of MCS and Cu/MCS nanocomposites with different Cu loading amounts

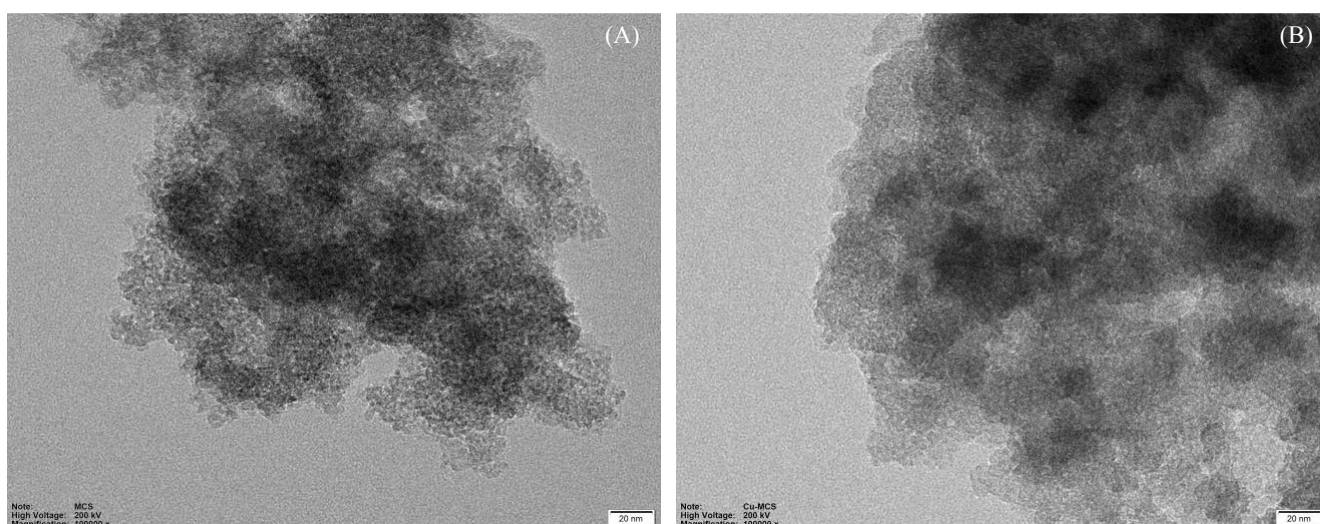


Figure 2.

TEM images of representative (A) MCS and (B) Cu/MCS nanocomposites at magnification of 100,000 \times .

FTIR analysis was used to evaluate the presence of aromatic carbon and/or CuO in the silica structure of the MCS and Cu/MCS composites. As shown in Figure 3, the MCS and Cu/MCS composites were observed between 1000 and 1300 cm^{-1} , which represented the Si–O–Si stretching of the silica framework and exhibited a broad band at 3450 cm^{-1} related to free silanol groups (Si–OH) [15]. In addition, they observed the bands which corresponded to characteristics of the aromatic carbon at 1,580–1615 cm^{-1} , which corresponded to C=C–C stretching [11]. These results suggested that the NR phase was converted to aromatic carbon residue after the carbonization process.

The presence of CuO in the MCS structure (Figure 3) was deduced from the bands observed between 400 and 500 cm^{-1} , which corresponded to the CuO [13]. The Cu/MCS materials were found the intense peak at around 480 cm^{-1} , compared to the initial MCS material. This result implied that CuO was incorporated into silica framework.

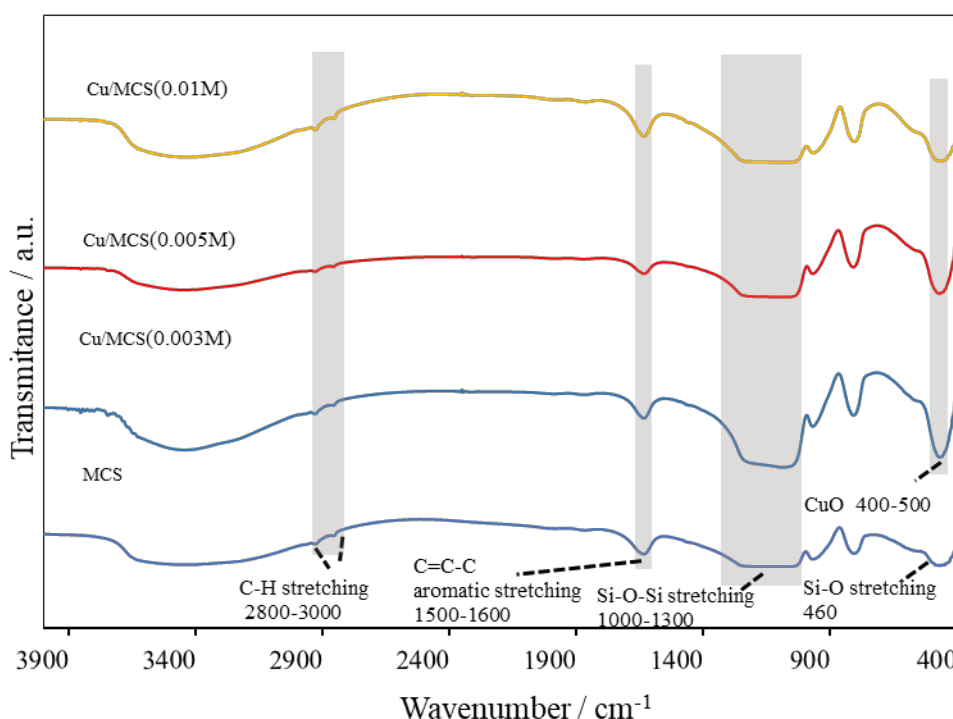


Figure 3.

FTIR spectra of MCS and Cu/MCS nanocomposites.

The Cu content and textural parameters of MCS and Cu/MCS composites are summarized in Table 1. An increasing concentration of copper acetate loading in synthesis mixture resulted in an enhancement of Cu content in Cu/MCS materials. However, the incorporation of Cu content onto MCS decreased S_{BET} , V_t , and D_p , which confirmed the presence of Cu species dispersed on the surface of mesostructured MCS. In addition, with increasing the amount of Cu loading (0.003–0.01M), the Cu/MCS series exhibited an enhancement of textural properties. These results should be due to the amount of copper increasing the conversion of natural rubber into mesoporous carbon species after carbonization process.

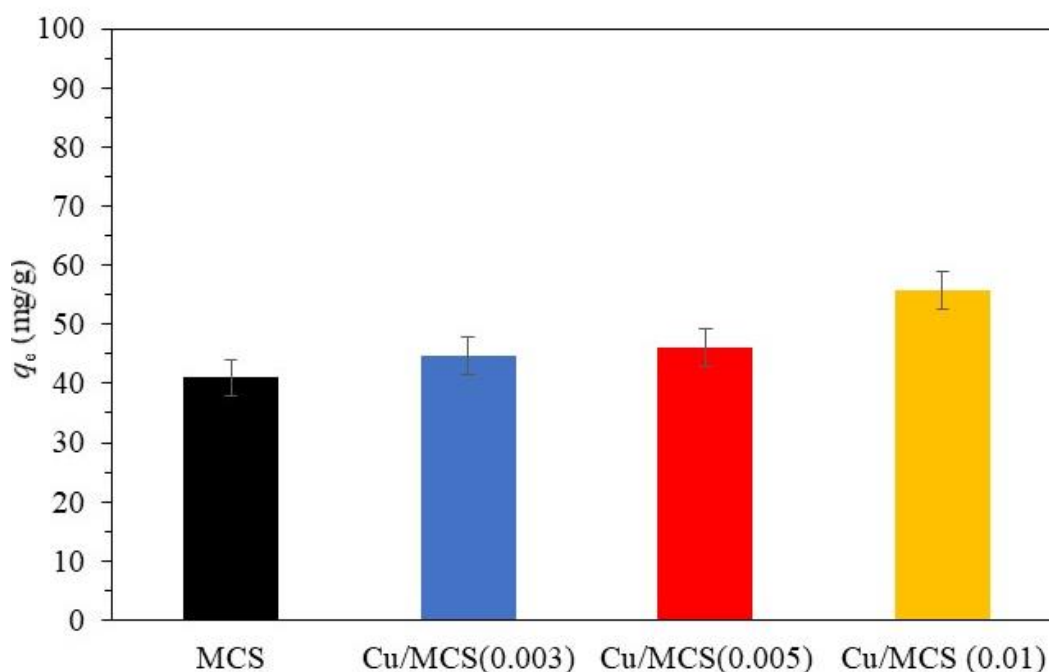
**Table 1.**

Cu content and textural properties of MCS and Cu/MCS materials.

Sample	Cu Content ^a (wt.%)	S_{BET}^b ($\text{m}^2 \text{g}^{-1}$)	D_p^c (nm)	V_t^d ($\text{cm}^3 \text{g}^{-1}$)
MCS	<i>n.d.</i>	834.42	2.70	0.97
Cu/MCS(0.003)	4.2	523.66	3.07	0.80
Cu/MCS(0.005)	10.3	570.07	3.16	0.84
Cu/MCS(0.01)	18.6	747.70	3.30	0.85

^a Determined by XRF.^b BET surface area^c Pore diameter, calculated by the BJH method^d Total pore volume, determined by the volume adsorbed at $P/P_0 = 0.99$ **Adsorption of CAF on MCS and Cu/MCS composites**

Figure 4 shows the CAF adsorption capacity of MCS and Cu/MCS composites in the simulated solutions. Although the Cu/MCS adsorbents had a lower S_{BET} , V_t , and D_p than the MCS material, the amounts of CAF adsorbed on these composites were higher than those on the MCS material. These results were consistent with the study of Ptazkowska-Koniarz *et al.* [8] reported that the caffeine molecule comprises a heterocyclic-N group which shows strong affinity to copper (II) ions present on the carbon xerogel adsorbent modified its surface with copper. The Cu/MCS(0.01) adsorbent with high amount of Cu loading exhibited the highest CAF adsorption capacity to 55.8 mg/g.

**Figure 4.**

Adsorption capacity of CAF on MCS and Cu/MCS composites (adsorbent dose: 0.01 g, aqueous solution: 10 mL, agitation speed: 120 rpm, time: 12 h, temperature: room temperature).

Conclusion:

The Cu/MCS composites with diverse mesoporosity and amount of Cu loading were successfully prepared via carbonization using the synthesized mixture of copper acetate and natural rubber dispersed in hexagonal mesoporous silica as a precursor. They were applied as a potential hybrid/composite adsorbent for CAF removal from aqueous. It was found to be a suitable adsorbent for adsorption of CAF from water compared to pristine MCS materials. Characterization analysis revealed that Cu/MCS composites possessed an amorphous silica structure with aromatic carbon residue and CuO incorporated into their surface. Moreover, they possessed a high surface area and pore volume, making them an efficient adsorbent. According to the adsorption results, the Cu/MCS(0.01) adsorbent with high amount of Cu loading exhibited effectiveness for CAF removal. The maximum adsorption capacity of this Cu/MCS(0.01) for CAF was 55.8 mg/g.

Acknowledgements:

The authors are grateful for the financial support from Maejo University's Disciple Scholarship. The financial support from the National Research Council of Thailand (NRCT), annual government statement B.E. 2567, (Project code 4708045) is acknowledged. The financial support from the Thailand Research Fund (TRF) under the International Research Network: Functional Porous Materials for Catalysis and Adsorption (Grant no. IRN61W0003) is acknowledged.

References:

1. Li, S., He, B., Wang, J., Liu, J., & Hu, X. *Chemosphere*. 2020;243:125343
2. Bachmann, S. A. L., Calvete, T., & F  ris, L. A. *Sci Total Environ*. 2021;767:144229
3. Santos-Silva, T. G., Montagner, C. C., & Martinez, C. B. R. *Environ Toxicol Pharmacol*. 2018;58:237-242
4. Ondarza, P. M., Haddad, S. P., Avigliano, E., Miglioranza, K. S. B., & Brooks, B. W. *Sci Total Environ*. 2019;649:1029-1037
5. Ternes, T. A., St  ber, J., Herrmann, N., McDowell, D., Ried, A., Kampmann, M., & Teiser, B. *Water Res*. 2003;37:1976-1982
6. Afonso-Olivares, C., Fern  ndez-Rodr  guez, C., Ojeda-Gonz  lez, R. J., Sosa-Ferrera, Z., Santana-Rodr  guez, J. J., & Rodr  guez, J. M. D. *J. Photochem. Photobiol*. 2016;329:130-138
7. Mahlangu, T. O., Msagati, T. A. M., Hoek, E. M. V., Verliefe, A. R. D., & Mamba, B. B. *Phys Chem Earth*. 2014;76-78:28-34
8. Ptaszowska-Koniarz, M., Goscianska, J., & Pietrzak, R. J. *Chem. Eng*. 2018;345:13-21
9. Hu, Q., Kou, R., Pang, J., Ward, T., Cai, M., Yang, Z., Tang, J. *Chem comm*. 2007;601-603
10. Castillo, R. R., & Vallet-Reg  , M. J. *Mol. Sci*. 2019;20:
11. Yousatit, S., Pitayachinchot, H., Wijitrat, A., Chaowamalee, S., Nuntang, S., Soontaranon, S., Ngamcharussrivichai, C. *Sci. Rep*. 2020;10:12977
12. Khumho, R., Yousatit, S., & Ngamcharussrivichai, C. *Catal*. 2021;11:887
13. Tounsi, N., Barhoumi, A., Chaffar Akkari, F., Kanzari, M., Guermazi, H., & Guermazi, S. *Vacuum*. 2015;121:9-17
14. Yin, Z., Fan, W., Ding, Y., Li, J., Guan, L., & Zheng, Q. *ACS Sustain. Chem. Eng*. 2015;3:507-517
15. Jermjun, K., Khumho, R., Thongoiam, M., Yousatit, S., Yokoi, T., Ngamcharussrivichai, C., & Nuntang, S. *Mol*. 2023;28:6019

ENHANCING OCEAN LITERACY THROUGH WHALE WATCHING: A CASE STUDY OF THE GULF OF THAILAND

Sittinon Sanor,¹ Somrudee Meprasert Jitpraphai,^{1,2,*} Saowanee Wijitkosum³

¹ Department of Marine Science, Faculty of Science, Chulalongkorn University, Bangkok, Thailand

² Center of Excellence in Microbial Technology for Marine Pollution Treatment (MiTMaPT), Department of Microbiology, Faculty of Science, Chulalongkorn University, Bangkok, Thailand

³ Environmental Research Institute Chulalongkorn University, Bangkok, Thailand

*e-mail: somrudee.j@chula.ac.th

Abstract:

Whale watching holds significant potential for advancing science education. This study aims to evaluate the knowledge levels of whale watchers regarding Bryde's whales and marine environments in the upper Gulf of Thailand. Using an on-site questionnaire, the study compared participants' understanding before and after the whale watching activity across six distinct categories, including "Bryde's whale behaviors," "Whale risks," "Land-sea interactions," "Whale Watching Entrepreneur Network," "Cultural values," and "Keystone species." A total of 112 voluntary participants contributed to the survey. The findings revealed a notable improvement in participants' comprehension across all six categories following their engagement in the activity ($p < 0.001$). Particularly significant was the substantial increase in understanding related to the "Network of whale watching entrepreneur," "Bryde's whale behavior," and "Cultural value" categories, respectively. The results suggest that by enhancing educational content during whale watching activities with an integration of scientific insights, marine environmental awareness, and cultural significance, whale watching experience in the Gulf of Thailand provides a distinctive opportunity to enhance ocean literacy.

Introduction:

The marine ecosystems of Thailand are home to 28 cetacean species, with the Gulf of Thailand hosting twenty marine mammal species as of 2023^{1,2}, constituting 71% of the country's marine mammal diversity. Bryde's whale, a top consumer in the food chain, plays a crucial role in ecological balance. The Department of Marine and Coastal Resources reports around 90 Bryde's whales in Thailand, with their population likely increasing. However, human activities in the Gulf, including coastal urbanization, transportation, and fishing, pose potential threats to whale populations. In 2019, Bryde's whales gained protected status under Thailand's Wild Animal Conservation and Protection Act, with the International Union for the Conservation of Nature (IUCN) classification of 'least concern'.

The Bryde's whale, a medium-sized baleen whale, is characterized by three parallel ridges around the rostrum—a feature unique among whales. Notably, the Bryde's whale in the Gulf of Thailand exhibits a novel feeding behavior known as tread-water feeding³, a behavior first observed in this species globally. This distinctive feeding strategy is adapted to the shallow, turbid waters of the Gulf of Thailand, where limited dissolved oxygen near the surface attracts small fish. The ability of Bryde's whales to adjust their feeding behaviors to changing environmental conditions is exemplified by tread-water feeding³. Furthermore, this unique behavior serves as a captivating attraction for tourists visiting Thailand to observe whales.



Whale watching serves as a profitable wildlife tourism activity, contributing substantially to the economies of coastal regions⁴. In 2008, the industry attracted an estimated 13 million enthusiasts across 119 countries, generating significant economic impact and providing revenue streams for coastal cities⁵. With over 13,000 employees worldwide and an annual income exceeding two billion US dollars, whale watching has become a major global tourism sector⁶. The upper Gulf of Thailand, particularly off the provinces of Samut Sakhon, Samut Songkhram, and Phetchaburi, witnessed the emergence of whale watching tourism in 2010. This industry, especially focused on Bryde's whale watching, plays a significant role in the region, with an estimated economic value of 9.7 million baht in 2016⁷.

The whale watching industry not only contributes to the economic well-being of many countries but also serves as a global tool for cetacean conservation awareness^{8,9,10}. Nature-based tourism, such as whale watching, has the potential to foster conservation-minded attitudes and active contributions to species and ecosystem well-being¹¹. Integrating educational experiences into such trips has been suggested to enhance environmental awareness and positive attitudes, promoting environmentally sustainable behavior¹². This approach aligns with the principle of ocean literacy.

Ocean literacy is essential for comprehending our connection to the ocean and engaging in informed discussions about its future¹³. Defined by Cava et al., ocean literacy encompasses an understanding of the ocean's influence on us and our impact on the ocean. The ocean literacy campaign has outlined seven principles and 45 concepts to promote this understanding. Moreover, the Intergovernmental Oceanographic Commission (IOC) of UNESCO has proposed the declaration of 2021–2030 as the Decade of International Ocean Science for Sustainable Development¹⁴. This initiative aligns with the Sustainable Development Goals (SDGs), particularly the 14th SDG focused on the ocean. Despite this, research indicates a limited understanding of ocean-related concepts among the general population, impacting their ability to make informed judgments about the ocean's overall health^{15,16,17}.

Recent studies worldwide reveal a widespread lack of public knowledge regarding marine-related matters¹⁶, coupled with misconceptions¹⁸ and a general lack of awareness about marine environmental issues and their solutions⁹. This deficit in understanding poses a risk of worsening negative effects on the oceanic environment due to increased ignorance¹⁹. Promoting positive attitudes and sustainable behaviors towards the ocean requires comprehensive education on ocean processes and the impacts of human actions¹⁶. Therefore, whale-watching serves as a potential educational platform to convey knowledge about cetacean ecology to the wider community²¹.

This study is the first exploration of whale watching activity in Thailand, focusing on the marine mammal and environmental knowledge acquired by participants as part of an informal education strategy to promote ocean literacy. While previous research has examined the knowledge of whale watchers and whale-watching tourism globally^{20,21,22,23}, limited attention has been given to these aspects in Thailand. The study specifically targets whale watchers in the upper Gulf of Thailand, aiming to assess their knowledge and foster awareness of the marine environment and ocean literacy. The findings would contribute valuable insights to the development of sustainable Bryde's whale watching tourism initiatives, recommending a model program tailored to the unique context of Thailand.

Methodology:

1. Project approval from the Human Research Ethics Committee

The research project obtained certification and approval from the Human Research Ethics Committee (Project ID: 650214). The Multi-Institutional Group, Set 2: Social Sciences,

Humanities, and Fine Arts at Chulalongkorn University assessed research ethics in accordance with the principles outlined in the Declaration of Helsinki, the Belmont Report, CIOMS guidelines, and the International Conference on Harmonization – Good Clinical Practice (ICH-GCP). As per the project regulations, all participating whale watchers were unpaid volunteers, and their involvement was entirely voluntary. Prior to completing the questionnaires, whale watchers were informed about the research's nature and sought for their consent. To safeguard their privacy, personal information was kept anonymous, with each whale watcher assigned a unique code to maintain confidentiality.

2. Questionnaire design

The questionnaire comprised two sections. In the initial section, each participant was tasked with evaluating their understanding before and after engaging in whale watching across six predefined categories. These categories for knowledge assessment were formulated in alignment with the ocean literacy principles established by UNESCO and supplemented by additional secondary data.^{26,27,28,29}

Category 1: "Bryde's Whale Behaviors". Whale watching is primarily designed to offer observers insights into Bryde's whale behaviors. These behaviors encompass activities such as blowing, feeding, mating, sleeping, and parental care. Notably, the residential Bryde's whales in the upper Gulf of Thailand have developed a distinctive feeding behavior known as tread-water feeding, which is influenced by the shallow waters in the region.³

Category 2: "Whale Risks". The upper Gulf of Thailand experiences a significant concentration of human activities, posing elevated risks to Bryde's whale dwellers. Anthropogenic threats include entanglement in fishing gear, collisions with vessels, and disturbance from loud underwater acoustics generated by ships and other activities. Additionally, coastal habitat degradation, water pollution, and marine debris further contribute to the risks faced by whales in this region.

Category 3: "Land and Sea Interaction". This category explores the interaction between human activities on land and the marine environment inhabited by Bryde's whales. The discussion aims to illustrate the connection between human lifestyles on land and the dynamics of marine ecosystems.

Category 4: "Whale Watching Entrepreneur Network". This category explores into the collaborative efforts of diverse operators forming teams with local fishermen to locate whales for the purpose of whale watching. Additionally, they actively exchange valuable information and resources related to whale watching.

Category 5: "Cultural Value". This knowledge category highlights the core belief in mother nature within the local culture. The coastal residents of the upper Gulf of Thailand, particularly local fishermen, hold the Bryde's whale in reverence, considering it sacred and associating it with abundance. The presence of Bryde's whales is believed to bring good luck and contribute to successful fishing endeavors according to their cultural beliefs.

Category 6: "Keystone Species". Bryde's whales play a crucial role as the apex consumers in the Gulf of Thailand's food chain. Their presence signifies fertile waters, reflecting a healthy marine environment. Conversely, a decline in the health of the whale population serves as an indicator of the degradation of coastal and marine ecosystems.

The knowledge assessment utilized a Likert scale, ranging from 0 to 10, where 0 denoted "very low," and 10 indicated "very high." The Likert scale is a well-established method widely employed across various disciplines, particularly in social science research, business, education, and psychology, to gauge the opinions or attitudes of respondents.

The second section involved collecting participants' information on gender, age, and educational background.



3. Data collection

Due to the adverse effects of the COVID-19 pandemic on the tourism sector during the study, the researcher utilized the number of tourists in Thailand reported by the Ministry of Tourism and Sports in the year 2017 and 2021, before the pandemic and shortly after the relaxation of COVID-19 regulations. The sample size for whale-watching participants was determined using the total number of tourists in Thailand 2021 that decreased 74.8% nationwide from the year 2017 and employing the Toro Yamane formula (1973). Although the formula recommended a minimum of 96 datasets to represent the tourist population, the research successfully collected 112 datasets from whale watchers aged 18 and older.

Numerous field observations were carried out in the upper Gulf of Thailand. The researcher collaborated closely with eight participating whale-watching operators in Phetchaburi, Samut Songkhram, and Samut Sakhon provinces. Data collection spanned approximately one year, from October 2022 to September 2023. Whale watching operations occurred consistently throughout the year, as Bryde's whales inhabit the Gulf of Thailand year-round. The activity gains popularity from September to December due to the northeast monsoon wind. Wildlife photographers are attracted to Thailand during bird migrations, offering insights into the interactions between Bryde's whales and other species. The minimal rainfall during this period also make travel safer than in the wet season.

Whale watchers were sampled based on their willingness to complete questionnaires and participation in tours organized by four entrepreneurs. Semi-structured interviews were conducted on whale watching trips. On the boat, questionnaires were distributed, and participants were invited to join if interested. Semi-structured interviews enriched data on whale watchers' experience and knowledge across all six categories during the activity.

4. Data analysis

All survey data were analyzed using Excel and 'SPSS version 28.0.0.0'. Descriptive statistics were used to understand sample demographics. Demographic data included age, gender, and educational background. Kolmogorov-Smirnov test was used to the normality test. The mean score of whale watcher awareness was evaluated by Likert Rating Scale showed in Table 1. In order to compare the pre- and post-whale watching datasets, the paired samples Wilcoxon test (also known as the Wilcoxon signed-rank test) was used^{30,31}. It is non-parametric alternative to the pared t-test used to compare paired data, which was used because the data were not normally distributed. The null hypothesis (H_0) is no difference between pre- and post-awareness and the alternative hypothesis (H_1) is difference. Mann-Whitney U-test was used to compare independent data³², which was knowledge for gender, age, and educational background.

The 10-point Likert scale was used in this research, and ordinal scales were utilized to convert the whale-watcher's awareness into a scale that would make statistical analysis easier. Table 1 provides a clearer representation of the 10-point scale. To obtain a weighted mean, the scale was divided into equal mean intervals.

Table 1.
The Comparison Definition 10-point Likert Scale

Intensity of Knowledge Likert Scale	Definition
0-2.00	Very low
2.01-4.00	Low
4.01-6.00	Moderate
6.01-8.00	High
8.01-10.00	Very high

Results and Discussion:

1. Whale Watchers' Demographic Profile

A total of 112 participants engaged in the questionnaire, with 69% identifying as 'Female,' 30% as 'Male,' and 1% as 'other.' The sex ratio was 0.44 male/female ($n = 34/77$). The predominant age groups among whale watchers were Generation X and Generation Y, constituting 35% and 33%, respectively. Baby Boomers comprised 19%, while Generation Z accounted for 13%. The majority of whale watchers (47%) held a bachelor's degree. Other educational levels included master's degrees and higher (43%), secondary education (6%), associate's degree (3%), and primary education (1%).

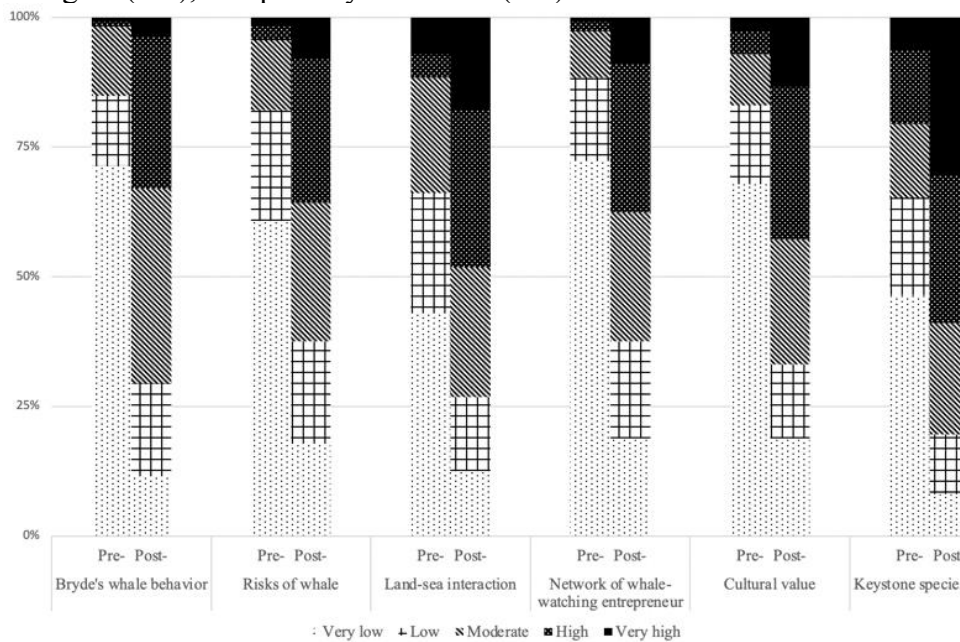


Figure 1. Stacked bar plot illustrating knowledge percentages on a Likert scale before and after whale watching activity.

Table 2. Comprehensive knowledge levels across six categories before and after whale watching activity. Significant differences between the two were identified using the Wilcoxon Signed-Rank test and are indicated by (*).

Categories	Pre-WW activity			Post-WW activity			Z	P
	Mean	Median	Mode	Mean	Median	Mode		
Whale Watching Entrepreneur Network	1.66±2.24	0	0	5.58±2.76	6	8	-8.141*	<0.001
Bryde's whale behavior	1.92±2.23	2	0	5.72±2.21	6	6	-8.335*	<0.001
Cultural value	2.22±2.62	2	0	5.81±2.89	6	8	-7.963*	<0.001
Keystone species	3.66±3.16	4	0	7.09±2.59	8	8	-8.251*	<0.001
Whale Risks	2.46±2.40	2	0	5.55±2.61	6	8	-8.423*	<0.001
Land-sea interaction	3.60±2.86	4	0	6.33±2.71	6	8	-7.638*	<0.001

Table 3.
Gender-related knowledge among whale watchers before and after their whale-watching activity.

Categories	Pre-WW activity			Post-WW activity		
	Mean	Median	Mode	Mean	Median	Mode
Male (n = 34)						
Whale Watching Entrepreneur Network	1.91±2.31	1	0	5.44±2.98	6	6
Bryde's whale behavior	2.06±2.51	2	0	5.35±2.16	6	6
Cultural value	1.97±2.72	1	0	5.18±3.01	6	2
Keystone species	4.00±3.18	4	0	7.15±2.43	7	6
Whale Risks	2.71±2.48	2	0	5.32±2.59	6	4
Land-sea interaction	3.71±2.84	4	6	5.76±2.90	6	8
Female (n = 77)						
Whale Watching Entrepreneur Network	1.55±2.22	0	0	5.69±2.66	6	8
Bryde's whale behavior	1.86±2.12	2	0	5.88±2.24	6	8
Cultural value	2.34±2.60	2	0	6.14±2.79	6	8
Keystone species	3.53±3.17	3	0	7.13±2.62	8	8
Whale Risks	2.35±2.38	2	0	5.68±2.64	6	8
Land-sea interaction	3.57±2.89	4	0	6.58±2.62	8	8

Table 4.
Age-related knowledge among whale watchers before and after their whale-watching activity.

Categories	Pre-WW activity			Post-WW activity		
	Mean	Median	Mode	Mean	Median	Mode
Generation X (n = 39)						
Whale Watching Entrepreneur Network	1.74±2.07	1	0	5.10±2.58	5	6
Bryde's whale behavior	1.95±2.21	0	0	5.38±2.18	6	6
Cultural value	2.31±2.58	2	0	5.41±2.63	5	8
Keystone species	3.69±2.80	4	2	6.79±2.45	8	8
Whale Risks	2.77±2.23	2	0	5.69±2.51	6	6
Land-sea interaction	3.77±2.69	4	2	6.54±2.51	8	8
Generation Y (n = 37)						
Whale Watching Entrepreneur Network	1.46±2.16	0	0	6.05±3.00	6	8
Bryde's whale behavior	1.70±2.17	0	0	6.14±2.18	6	6
Cultural value	2.08±2.67	1	0	6.46±2.71	8	8
Keystone species	4.05±3.73	4	0	7.76±2.80	8	10
Whale Risks	2.35±2.61	2	0	5.92±2.67	6	8
Land-sea interaction	3.68±2.89	4	4	6.46±2.81	6	8

Table 5.

Educational background-related knowledge among whale watchers before and after their whale-watching activity.

Categories	Pre-WW activity			Post-WW activity		
	Mean	Median	Mode	Mean	Median	Mode
Bachelor's degree (n = 53)						
Whale Watching Entrepreneur Network	1.83±2.24	0	0	5.81±2.61	6	8
Bryde's whale behavior	1.98±2.11	2	0	5.58±2.21	6	6
Cultural value	2.17±2.45	2	0	5.49±2.82	6	8
Keystone species	3.96±3.21	4	0	7.23±2.55	8	10
Whale Risks	2.26±2.11	2	0	5.30±2.33	6	6
Land-sea interaction	3.66±2.58	4	4	6.17±2.55	6	8
Master's degree and higher (n = 48)						
Whale Watching Entrepreneur Network	1.23±1.92	0	0	5.27±2.88	6	6
Bryde's whale behavior	1.75±2.39	0	0	5.77±2.30	6	8
Cultural value	2.04±2.71	2	0	6.00±2.72	6	8
Keystone species	3.33±3.14	3	0	7.02±2.51	8	8
Whale Risks	2.52±2.63	2	0	5.81±2.51	6	6
Land-sea interaction	3.23±3.05	3	0	6.21±2.93	6	8

2. Knowledge levels of whale watchers

In the complete dataset of 112, initial knowledge gaps were evident regarding Bryde's whale presence in the Gulf of Thailand. However, substantial improvements emerged after participants participated in whale-watching activities. This heightened understanding spanned all six categories, with notable growth observed in areas like "Whale Watching Entrepreneur Network," "Bryde's whale behavior," and "Cultural value." (figure 1,2 and table 2).

2.1 Whale Watching Entrepreneur Network

Figure 1 illustrates that before engaging in whale-watching activities, 72% of participants lacked clarity about the "Whale Watching Entrepreneur Network," a percentage that decreased to 19% post-activity. The most substantial knowledge gap between pre- and post-whale watching activities was observed in this aspect ($D = 3.92$). Pre-activity, a "very low" knowledge level about whale watchers was reported, with the lowest score across all categories (1.66 ± 2.24) (see Table 2). However, following the whale-watching session, participants' knowledge level increased to "Moderate" (5.58 ± 2.76). A Wilcoxon Signed-Rank test revealed a statistically significant change in knowledge among whale watchers regarding the "Whale Watching Entrepreneur Network" after participating in the activity ($Z = -8.141$, $P < 0.001$).

2.2 Bryde's whale behavior

Before engaging in whale-watching activities, participants possessed minimal knowledge about Bryde's behavior or biology. Concerning Bryde's whale behavior, the majority had a "very low" knowledge level in the pre-activity phase (1.92 ± 2.23 , Median = 2, Mode = 0). However, post-activity (see Figure 2A), their knowledge level significantly increased to a "moderate" level (5.72 ± 2.21). The Wilcoxon Signed-Rank test revealed

significant differences in participants' understanding of Bryde's whale presence before and after the activity ($Z = -8.335$, $P < 0.001$).

2.3 Cultural value

Before embarking on whale-watching activities, 68% of participants were unaware of the cultural importance of whales (see Figure 1). Pre-activity, the understanding of "cultural value" was characterized as "low" (2.22 ± 2.62). However, following whale-watching activities, major whale watchers' knowledge levels elevated to "moderate" (5.81 ± 2.89 , Median = 6, Mode = 8) (see Table 2), with the percentage at the "very low" level dropping from 68% to 19% (see Figure 1). Comparing knowledge levels before and after the whale-watching session revealed a statistically significant difference ($Z = -7.963$, $P < 0.001$). These findings underscore that whale watching can convey culturally significant knowledge, illustrating how coastal traditions harmonize with the marine environment.

2.4 Keystone species

When comparing all six categories, the understanding of Bryde's whale as a "keystone species" stood out as the most robust both before and after the activity. Pre-activity knowledge scores were assessed as "low" (3.66 ± 3.16), with nearly half (46%) of whale watchers having "very low" scores. However, after participating in whale watching, the percentage of whale watchers at this level decreased to 8%. Post-activity (7.09 ± 2.59), the knowledge level elevated to a "high" level, with half of the whale watchers recognizing Bryde's whales as a "keystone species" (Median = 8, Mode = 8)—the highest level among all six categories (see Figure 2C, 2D). A statistically significant difference was noted between pre and post-whale watching activities, as indicated by a Wilcoxon Signed-Rank test ($Z = -8.251$, $P < 0.001$). These results highlight that whale watchers gain more knowledge about the roles played by Bryde's whales in the marine environment and ecosystem following their whale-watching experience. Even before engaging in any activity, they were already aware of the fundamental importance of Bryde's whales as keystone species in marine ecosystems.

2.5 Whale Risks

Following the activity, the percentage of whale watchers with a "very low" understanding of the "Whale Risks" decreased from 61% to 18% (see Figure 1). The average knowledge scores for pre- and post-whale watchers were 2.46 ± 2.40 and 5.55 ± 2.61 , respectively. The knowledge level about the "Whale Risks" increased from "low" to "moderate," with the "high" knowledge level rising from 3% to 28% post-activity. The change in knowledge levels before and after whale watching was statistically significant ($Z = -8.423$, $P < 0.001$). These findings highlight that participating in activities enabled whale watchers to acquire knowledge about the risk factors affecting Bryde's whale.

2.6 Land-sea interaction

The smallest mean change between pre- and post-activity times was observed in "land-sea interaction" ($D = 2.73$). Following whale-watching activities, whale watchers reported a "high" level of "land-sea interaction" knowledge (6.33 ± 2.71), marking a two-level increase from "low" (3.60 ± 2.86) and ranking as the second-highest level among all six categories (see Table 2). A statistically significant difference was evident between pre and post-whale watching activities, as indicated by a Wilcoxon Signed-Rank test ($Z = -7.638$, $P < 0.001$). This implies that before participating in the activity, whale watchers were already aware of land-sea interactions and received additional information during the activity.

After engaging in whale-watching activities, whale watchers' overall understanding significantly improved. However, the Mann-Whitney U test was employed to explore the correlation between gender, age, and educational background and the enhanced understanding of whale watchers. The analysis revealed no significant difference in knowledge across all six

categories ($p > 0.05$), as indicated in tables 3, 4, and 5. This suggests that Bryde's whale watchers, regardless of gender, age, or educational level, could obtain knowledge following whale-watching activities. Consequently, a universal format can be used to effectively communicate information about Bryde's whales and marine and coastal resources.

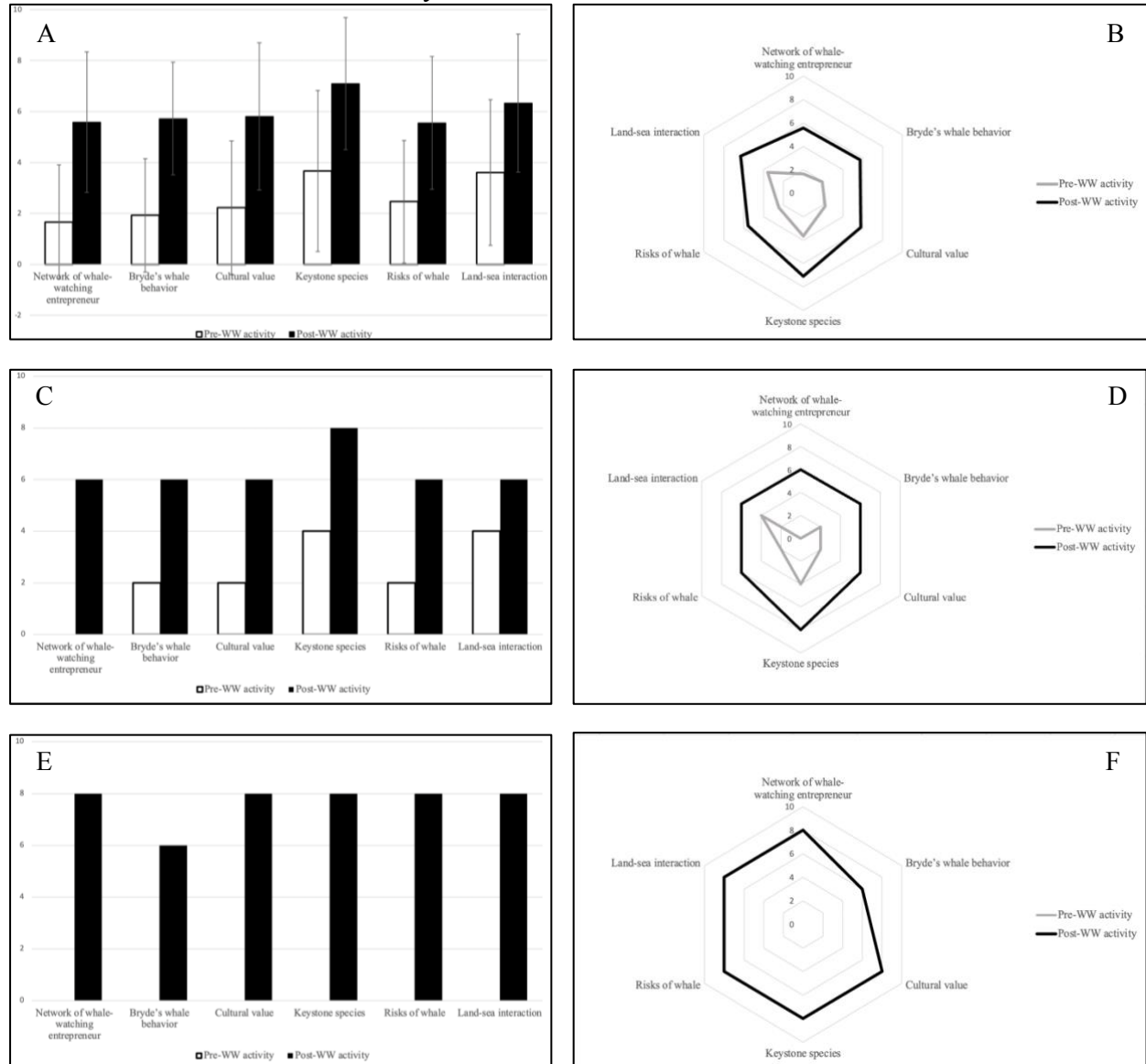


Figure 2.

The Likert-scale knowledge levels of whale watchers during whale-watching activity. In

Figures 2A, 2C, 2E, bars depict the mean, median, and mode of knowledge levels, respectively. White bars represent before whale-watching activity, while black bars represent after whale-watching activity. In Figures 2B, 2D, 2F, radar charts illustrate the mean, median, and mode of knowledge levels, respectively. Gray lines represent before, and black lines represent after whale-watching activity.

3. Whale watching and its influence on informal education and knowledge levels

The knowledge of watchers across all six categories significantly increased after participating in whale watching activities in the Gulf of Thailand. Both during Bryde's whale watching tours and operator lectures, participants gained knowledge about whale behavior. This finding aligns with a study on humpback whales (*Megaptera novaeangliae*) and long-beaked common dolphins (*Delphinus capensis*) in Peru, where 18.8% of whale watchers discovered during the tour that whales were mammals and cetaceans, indicating a notable increase in their knowledge compared to the pre-trip survey²¹. In New Zealand, 29% of whale watchers who did not participate in 'swim with dolphin' trips 'strongly agreed' that the tour was instructive, with 17.6% 'strongly agreeing' that they had gained a lot of knowledge about dolphins³⁴.

Participation in whale watching activities can increase awareness among watchers regarding marine and coastal risk factors affecting Bryde's whale populations in the Gulf of Thailand. Insights from semi-structured interviews revealed that watchers gained knowledge about various threats to whales, including the presence of ships, marine pollution, fishing gear, marine debris, overfishing, and the importance of maintaining a safe distance from the whales. Concerns were expressed about non-compliant whale watching vessels posing risks to Bryde's whales. Proximity to the whales did not significantly influence watcher satisfaction³⁴. Those with stronger pro-environmental sentiments acknowledged the harmful effects of boats on whales³⁵. Considering the legal protection of Bryde's whales, operators should exercise responsibility to minimize harm from whale watching tourism. A study on whale watching in Mexico also suggested that conservation attitudes and perceived congestion influence tourists' likelihood of returning for future whale watching excursions³⁶.

The finding highlights whale watching as an effective platform for enhancing ocean literacy through informal education, aligning with the 21st Century skills for lifelong learning. The activity inspired public interest in cetaceans, marine conservation, and environmental issues. Similar findings in a study on whale watching in Panama emphasized the role of education in promoting whale conservation and the need for enforcing laws and monitoring programs³⁷. Whale watchers expressed willingness to adapt their lifestyles to continue participating in whale watching³⁸. The study suggests that encouraging behavioral intentions and invoking emotions and responsibility among whale watchers is more effective than solely providing knowledge on whale biology and ecology^{39,40}.

Conclusion:

Findings of the research provide valuable insights across academic disciplines, especially science education. Firsthand experience on a boat observing large marine mammals significantly enhances individuals' understanding of the marine environment. This is particular importance for cultivating 21st-century skills as part of lifelong learning opportunities. This study is the first multi-disciplinary effort to assess the knowledge of whale watchers regarding whale watching activities in the upper Gulf of Thailand. The study confirms that engaging in whale watching proves to be an effective method for conveying ocean literacy in informal contexts. Lastly, whale watching experience possess the potential to disseminate information, raise public awareness about the marine ecosystem and contribute to the fulfillment of Sustainable Development Goals (SDGs), specifically the SDG 12th (Responsible Production and Consumption) and SDG 14th (Life Below Water) during the Ocean Decade (2021-2030).

Acknowledgements:

This project is funded by the Center of Excellence in Microbial Technology for Marine Pollution Treatment (MiTMaPT) and the Development and Promotion of Science and Technology Talents Project (DPST). The researchers express their thanks to the Department of Marine Science, Faculty of Science, Chulalongkorn University, the Department of Marine and Coastal Resources, Thaiwhales, all whale watching entrepreneurs and all participants.

References:

1. Hines E, Ponnampalam L, Jamal Hisne F, Tara S, Jackson-Ricketts J, Kuit S, Acebes J. CMS Tech. 2015;32:105–109.
2. Chantra R, Nganvongpanit K, Yaowasooth P, Thongsukdee S, Kitiwatthanawong K, Thongcharoenchaikit C, Piboon P. Basel. 2023;15(4):532.
3. Iwata T, Akamatsu T, Thongsukdee S, Cherdsukjai P, Adulyanukosol K, Sato K. Curr. Biol. 2017;27(21): R1154-R1155.
4. Chung-Lin C. Ocean Coast. Manag. 2010;53:487–492.
5. New L F, Hall A J, Harcourt R, Kaufman G, Parsons E C M, Pearson H C, ... & Schick R S. Ocean Coast. Manag. 2015;115:10-16.
6. Cunningham P A, Huijbens E H, Wearing S L. J. Sustain. Tour. 2012;20:143–161.
7. Yaowasud P, Thongsukdee S, Srisaowaluck A, Passada S, Prempee T, Chantra R. DMCR (Poster). 2560.
8. Anderson M S, & Miller M L. Tour. Mar. Environ. 2006;2:111–118.
9. Corkeron P J. Conserv. Biol. 2004;18:847–849.
10. Orams M B. Aust. J. Environ. Educ. 1994;10:21–34.
11. Forestell P H, & Kaufman G D. Proc. Coast. Mar. Tour. 1991;2:399-407.
12. Orams M B. Tour. Manag. 1995;16(1):3-8.
13. Fauville G, Strang C, Cannady M A, & Chen Y F. Environ. Educ. Res. 2019;25(2):238-263.
14. Ryabinin V, Barbière J, Haugan P, Kullenberg G, Smith N, McLean C, Rigaud J. Front. Mar. Sci. 2019;6:470.
15. Eddy T D. Mar. Policy. 2014;46:61-67.
16. Guest H, Lotze H K, Wallace D. Mar. Policy. 2015;58:98-107.
17. Plankis B, Marrero M. Int. Electron. J. Environ. Educ. 2010;1(1):21-46.
18. Ballantyne R. Geo. J. 2004;60:159-163.
19. María C U, Borja Á. Mar. Pollut. Bull. 2016;104(1-2):1-2.
20. Bertulli C G, Leeney R H, Barreau T, Matassa D S. J. Mar. Biol. Assoc. U. K. 2016;96(4):969-977.
21. García-Cegarra A M, Pacheco A S. Aquat. Conserv.: Mar. Freshw. Ecosyst. 2017;27(5):1011-1020.
22. Cárdenas, S., Gabela-Flores M V, Amrein A, Surrey K, Gerber L R, & Guzmán H M. Front. Mar. Sci. 2021;8:627348.
23. Tkaczynski A, Xie J, Rundle-Thiele S R. J. Vacat. Mark. 2023;29(3):428-444
24. Likert R. Arch. Psychol. 1932;140:1–55.
25. Sangthong M. Thail. Stat. 2020;18(1):55-64.
26. Cherdsukjai P, Thongsukdee S, Passada S, & Prempre T. Proc. DSCE. 2015;3:1-5.
27. Harino H, Ohji M, Wattayakorn G, Adulyanukosol K, Arai T, Miyazaki N. Arch. Environ. Contam. Toxicol. 2007;53(1):119-125.
28. Adulyanukosol K, Thongsukdee S, Pasada S, Prempre T, Wannarungsri T. DMCR. 2011;195.



29. Orams M B. *Aus. Geo.*1996;27(1):39-51.
30. Wilcoxon, F. *Biom. Bull.* 1945;1:80–83.
31. Mokos M, Realdon G, Zubak Čižmek, I. *Sustain.* 2020;12:24.
32. Mann H B, Whitney D R. *Ann. Math. Stat.* 1947;18:50-60.
33. Lück M. *Ocean Coast. Manag.* 2003;46:943–956.
34. Orams M B. *Tour. manag.* 2000;21(6):561-569.
35. Schuler A R, Pearson H C. *Tour. Mar. Environ.* 2019;14(4):231-248.
36. Ávila-Foucat V S, Vargas A S, Jordan A F, & Flores O R. *Ocean Coast. Manag.* 2013;78:12-17.
37. Cárdenas S, Gabela-Flores M V, Amrein A, Surrey K, Gerber L R, & Guzmán H M. *Front. Mar. Sci.* 2021;8:627348.
38. Cornejo-Ortega J L, Chávez-Dagostino R M, Ivanova-Boncheva A. *Int. J. Sustain. Dev. Plan.* 2014;9(4):553-567.
39. Draheim M, Bonnelly I, Bloom T, Rose N, Parsons E C M. *Tour. Mar. Environ.* 2010;6:175-183.
40. Kessler M, Harcourt R, Bradford W. *Tour. Mar. Environ.* 2014;10:21-30.



PETROGRAPHY AND GEOCHEMISTRY CHARACTERISTICS OF LIMESTONE, BAN DAN CHANG SUB-DISTRICT, NA KLANG DISTRICT, NONG BUA LAMPHU PROVINCE

Piyakorn Preedeesanith,* Wimon Sukplum, Vimoltip Singtuen

Department of Geotechnology, Faculty of Technology, Khon Kean University, Khon Kean, Thailand

*e-mail: prpiyakorn@kkumail.com

Abstract:

Nong Bua Lamphu is located in the northeastern part of Thailand. The area contains sedimentary rocks, igneous rocks, and metamorphic rocks. This study focused on carboniferous limestone scattered covers the northwest part of the study area and aims to classify rock names and environmental deposits. The petrographical investigations on these rocks were carried out using a polarizing microscope and geochemical analysis was measured by handle ED-XRF. The limestones show micrite and sparite textures with fossils 5-80, which consist of crinoid, bryozoan, and fusulinid. The mineral compositions of these limestones mainly consist of calcite and a minor of dolomite, additionally, some samples are composed of a small amount of quartz and opaque minerals. According to Folk's 1959 and 1962 theories, the rocks were classified into 4 types consisting of fossiliferous biomicrite, sorted biosparite, poorly sorted biosparite, and spares biomicrite. In addition, the rocks were also divided into 4 categories, including mudstone, packstone, grainstone, and floatstone following Dunham's 1962 theory. The geochemical composition of samples can be classified by major oxides as calcite carbonate. In addition, based on Mg/Ca can be divided sample into 2 groups namely magnesium limestone and pure limestone. Moreover, the stratigraphic correlation suggests the studied rocks were deposited in the inner ramp to mid ramp at shallow marine.

Introduction:

Rocks classified as carbonate include a main of calcite in excess of 50% and dolomite.¹ The limestones in Thailand are generally referred to as all stratified rocks containing significant calcium carbonate and magnesium carbonate.² The Permo-Carboniferous limestone is exposed over large areas, in west-central Thailand and along the west side of the Khorat Plateau.² In northeast Thailand, Carboniferous rocks are widely exposed in Loei (Wang Saphung) and Nong Bua Lamphu Provinces, an area of 20-40 km. long. The rocks lay uniformly beneath the Permian rocks³ and uniformly overlay the Silurian-Devonian rocks in the western part of the northern region, near the upper western region.⁴ Nong Bua Lamphu Province is mainly composed of Carboniferous limestone, which is distributed in Na Klang District and the northern part of Sri Bun Reaung District.⁵ Additionally, the Department of Mineral Resources (2009)⁵ describes that Nong Bua Lamphu is a concern area for sinkhole disasters, making agriculture hard and dangerous for people in this area. The Ban Dan Chang Sub-district, the most problem of sinkholes, is located in the Na Klang District Nong Bua Lamphu Province area. This area is constituted by the Carboniferous Wang Saphung Formation⁶ which consists mainly of sandstone shale with some thin limestone beds and conglomerate. Furthermore, the environmental deposits are shallow marine origin with some fossils.⁷ The Carboniferous fossils important discovery in Thailand including algae (*Bersella* and others) are the very abundant and dominant framework in the middle Carboniferous at Loei area. Radiolarians have been extracted from cherts and siliceous shale. Foraminifera are

a group of microfossils as single-chambered foraminifera which are widespread in Carboniferous-Permian. Corals are mainly found in dendroid tubulata, solitary, fasciculate, and massive rugosa forms deposited during the lower to upper Carboniferous in the Loei region.⁸

Study area

The study area is composed of rock units from the ages of Carboniferous, Triassic, and Quaternary as shown in **Figure 1**. The Carboniferous Wang Saphung Formation consists of conglomeratic sandstone, greywacke, sandstone, shale, and limestone lens. Triassic strata consist of sedimentary rocks of the Nam Pong Formation and the Khorat group. In addition, this area is covered by Triassic to Permian of igneous rocks consisting of andesite, rhyolite, tuff, agglomerate, and granodiorite. Quaternary sediment consists of alluvial deposits such as sand, silt, clay, and fine-grained.⁷

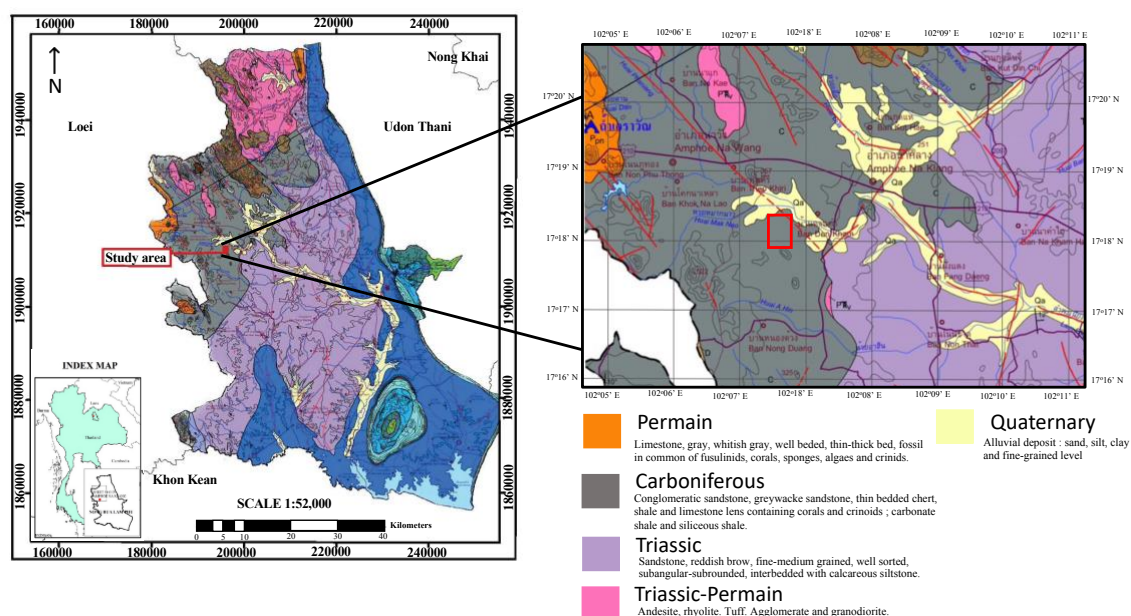


Figure 1.

Geologic map of the studied area in Nong Bua LampPhu Province. The red point/square shows the study area.⁶

Methodology:

The boreholes of limestone were drilled by coring for 8 boreholes in the study area. The depth of each borehole is approximately 20 meters from the surface, approximately. In addition, real-time kinematics (RTK) was used to measure elevation and location at the boreholes. Then, the samples from the borehole were visualized by hand lens to classify the lithology and specific characteristics for dividing the rock group. After that, the 14 samples were selected for petrographic analysis. The description of representative samples is presented in **Table 1**. The 14 thin sections were prepared and analyzed for classifying rock names and mineral compositions. The petrographic analysis and photomicrograph analysis by ZEN core Imaging Software, linking ZEISS imaging and microscope solution at the

Department of Geotechnology, Khon Kean University. Furthermore, the result was used to interpret the environment and make correlation logging.

The geochemistry of the samples was studied by Olympus Vanta handheld XRF analyzers to analyze their major oxides at the Department of Geotechnology Khon Kean University. This method can measure the percentage of concentration levels (ppm levels up to practically 100% by weight), but it is unable to detect elements with atomic numbers below 12.

Table 1.

The location of boreholes and samples No.

Borehole	Location	Sample No.	Depth (m.)
DH1	N1911860E194958	DH1-1	10-11
DH1	N1911860E194958	DH1-2	12-13
DH2	N1911786E195214	DH2-1	13-14
DH3	N1911938E195214	DH3-1	11-12
DH3	N1911938E195214	DH3-2	14-15
DH4	N1911371E195290	DH4-1	11-12
DH4	N1911371E195290	DH4-2	12-13
DH4	N1911371E195290	DH4-3	17-18
DH5	N1911813E195565	DH5-1	6-7
DH5	N1911813E195565	DH5-2	9-10
DH6	N1912271E195043	DH6-1	9-10
DH6	N1912271E195043	DH6-2	14-15
DH7	N1912185E195006	DH7-1	13-14
DH8	N1912185E195006	DH8-1	10-11

Petrography

The theory of Folk (1959, 1962)⁹⁻¹⁰ and Dunham (1962)¹¹ were applied for petrographic analysis and classification names of rocks. Fossiliferous biomicrite, sorted biomicrite, poorly sorted biosparite, and spares biomicrite are the names of rocks following the theory of Folk. Moreover, mudstone, packstone, floatstone, and grainstone are the names of rocks following the theory of Dunham.

The fossiliferous biomicrites (DH1-1, DH4-2, DH4-3, and DH5-2) are composed of allochems 5% mainly of triserial foraminifera and bryozoan partially replaced by sparry calcite, and embedded in micrite groundmass. The texture of fossiliferous biomicrite is considered to it transported by low energy current. In addition, the samples found quartz 0.1-0.2 millimeters and distributed in DH5-2 and vein in DH4-2. The sorted biosparite (DH5-1 and DH1-2) is composed of allochems 30-40% mainly of triserial foraminifera, peloid, oolite, crinoid, brachiopod, and cortoids that present with sparite textures and granular calcite. The sorted biosparite was considered to it transported by a high-energy current. The poorly sorted biosparite (DH6-1, DH6-2, and DH7-1) composed of allochems 70-80% mainly of milioline and uniserial foraminifera, peloid, brachiopod, and bryozoan with sparite texture. The sorted biosparite is considered to it transported by high energy wave current. The sample of spare

biomicrite (DH2-1, DH3-1, DH4-1, and DH8-1) composed of allochems 25-50% mainly of triserial foraminifera, fusulinid, brachiopod, bryozoan and gastropod with micrite texture. The sorted biosparite is considered deposited by low energy current. DH3-2 is defined as recrystalline limestone, which presents calcite granular and opaque minerals. Moreover, the mudstone (DH1-1, DH4-2, DH4-3, and DH5-2) is composed of allochems 5% size 0.5-2 millimeter and matrix support frameworks mainly with foraminifera and bryozoan. The packstone (DH3-1 and DH2-1) is composed of allochems 30-50% size 0.5-1 millimeter and framework support mainly with triserial foraminifera and small bryozoan. The grainstone (DH4-1, DH5-1, DH6-2, and DH7-1) is composed of allochems 30-80% mainly of triserial foraminifera, peloid, brachiopod, cortoid, gastropod, bryozoan and crinoid. The floatstone (DH4-1, DH8-1, and DH1-2) is composed of allochems 25-40% size 2-5 millimeter and grain support frameworks mainly with triserial foraminifera, peloid, oolith, crinoid, brachiopod, and cortoids. The petrographic result of the samples is described in **Table 2**

Table 2.

The result of the petrographic analysis of 14 samples from drilllogs.

Borehole	Percent of fossil	Matrix / Grain supports	Texture	Folk's (1959, 1962)	Dunham's (1962)
DH1-1	40	Grain support	Sparite	Sorted biosparite	Floatstone
DH1-2	5	matrix support	Micrite	Fossiliferous biomicrite	Mudstone
DH2-1	50	Grain support	Micrite	Spares biomicrite	Packstone
DH3-1	30	Grain support	Micrite	Spares biomicrite	Packstone
DH3-2	-	-	Dismicrite	Recrystalline limestone	
DH4-1	40	Matrix support	Micrite	Spares biomicrite	Floatstone
DH4-2	5	Matrix support	Micrite	Fossiliferous biomicrite	Mudstone
DH4-3	5	Matrix support	Micrite	Fossiliferous biomicrite	Mudstone
DH5-1	30	Grain support	Sparite	Sorted biosparite	Grainstone
DH5-2	5	Matrix support	Micrite	Fossiliferous biomicrite	Mudstone
DH6-1	80	Grain support	sparite	Poorly sorted biosparite	Grainstone
DH6-2	70	Grain support	Sparite	Poorly sorted biosparite	Grainstone
DH7-1	80	Grain support	Sparite	Poorly sorted biosparite	Grainstone
DH8-1	25	Matrix support	Micrite	Spares biomicrite	Floatstone

Geochemistry

The bulk chemistry, SiO₂, Al₂O₃, Fe₂O₃, MnO, MgO, CaO, Na₂O₃, K₂O, and P₂O₅, was ascertained by using X-ray fluorescence (XRF). The major oxides of samples are presented in **Table 3**. According to several researchers, they typically classify carbonate rocks as containing more than 50% carbonate minerals.¹² The mostly limestone sample was filled with more than 50% calcite, except DH3-1 (46.9%) and DH3-2 (47.2%). Furthermore, the sample had a CaO of more than 50% refers to calcite (CaCO₃). The DH3-1

and DH3-2 contain some MgO refers to dolomite ($\text{MgCa}(\text{CO}_3)_2$) or magnesite (MgCO_3). The DH2-1, DH3-1, DH3-2, and DH5-2 contain some SiO_2 and Al_2O_3 refer to clay minerals. According to Todd (1996),¹³ the entirety of samples were indicated to be pure limestone, whereas DH3-1 and DH3-2 were indicated to be magnesian limestone.

Table 3.

The result of the sample's major oxides by x-ray fluorescence.

Name	SiO_2	TiO_2	Al_2O_3	FeO	MnO	MgO	CaO	K_2O	P_2O_5	SUM	LE
DH1-1	0.13	0	0	0.03	0.018	0	58.47	0	0	58.66	41.34
DH1-2	0.49	0	0	0.04	0.03	0	57.67	0	0	58.24	41.76
DH2-1	8.68	0.1	0.37	0.06	0	0	53	0.04	0	62.26	37.74
DH3-1	6.77	0.12	2.93	1.01	0.045	2.33	46.93	0.29	0	60.44	39.56
DH3-2	8.41	0.11	2.6	0.96	0.025	2.54	47.24	0.24	0	62.14	37.87
DH4-1	0	0	0	0.03	0.023	0	56.82	0	0	56.88	43.13
DH4-2	0.23	0.12	0	0.03	0.015	0	58.8	0	0	59.19	40.81
DH4-3	0	0.14	0	0.09	0.05	0	56.53	0	0	56.81	43.19
DH5-1	0.19	0	0	0.4	0.056	0	57.93	0	0	58.58	41.42
DH5-2	4.06	0.18	0.45	0.24	0.032	0	55.06	0.06	0	60.09	39.91
DH6-1	0.3	0	0	0.03	0.019	0	58.69	0	0	59.04	40.96
DH6-2	0.17	0.09	0	0.04	0.019	0	57.12	0	0	57.46	42.54
DH7-1	0.67	0	0	0.1	0	0	57.44	0	0	58.21	41.79
DH8-1	0	0	0	0.03	0.011	0	59.3	0	0	59.34	40.66

Conclusion:

The limestones in Ban Dan Chang Sub-district, Na Klang District, Nong Bua Lamphu Province were classified as pure limestone by chemical classification. The chemistry from X-ray fluorescent (XRF) shows $\text{CaO} > 50\%$, $\text{SiO}_2 < 1\%$, and without MgO except the DH3-1 and DH3-2, which is interclastics grainstone, found CaO 46.92–47.23%, SiO_2 8.42–6.78%, and MgO 2.54–2.33%. It occurs from the storm wave environment according to granular microclasts evidence.¹⁴ Moreover, each of the samples is slightly different in chemistry components. The result of all samples is presented as pure calcite or calcite limestone. The mineral composition from petrology and chemistry from X-ray fluorescence (XRF) were also compatible. However, the sample was different for textures, weathering, and percentages of fossils. Therefore, the samples can be divided into 4 types including fossiliferous biomicrite, sorted biosparite, poorly sorted biosparite, and spare biomicrite following Folk's theory.⁹⁻¹⁰ As well as the samples can be divided the limestones into 4 types including mudstone, grainstone, floatstone, and packstone following Dumham's theory.¹¹ The Wang Saphung Formation was deposited during the upper Mississippian to Pennsylvanian (300-330 Ma).¹³ The stratigraphic sequence consists of conglomeratic sandstone, greywacke sandstone, chert, shale, and limestone lens containing the corals and overlay by Permian rocks.¹⁵ The result of the correlation shows the percentage of fossils is 5-80. The correlations are present in **Figure 3 to Figure 5**. The range of fossil 30-80% is the mid-ramp to the inner ramp zone in which the zone of greatest organic carbonate sediment is deposited.¹⁶ Furthermore, the range of fossil 5-25% is the change in production profile from the shoreline to the basin (open

marine).¹⁶ In addition, there are outcrops of shale interbedded with limestone nearby, supporting that the studied sedimentary rocks were deposited at the mid-ramp to the outer ramp. Hence, limestones in the study area are carbonate deposited in the inner ramp to the mid ramp, which are transition to open marine during Permian Period¹⁷, on shallow marine present in **Figure 6**.

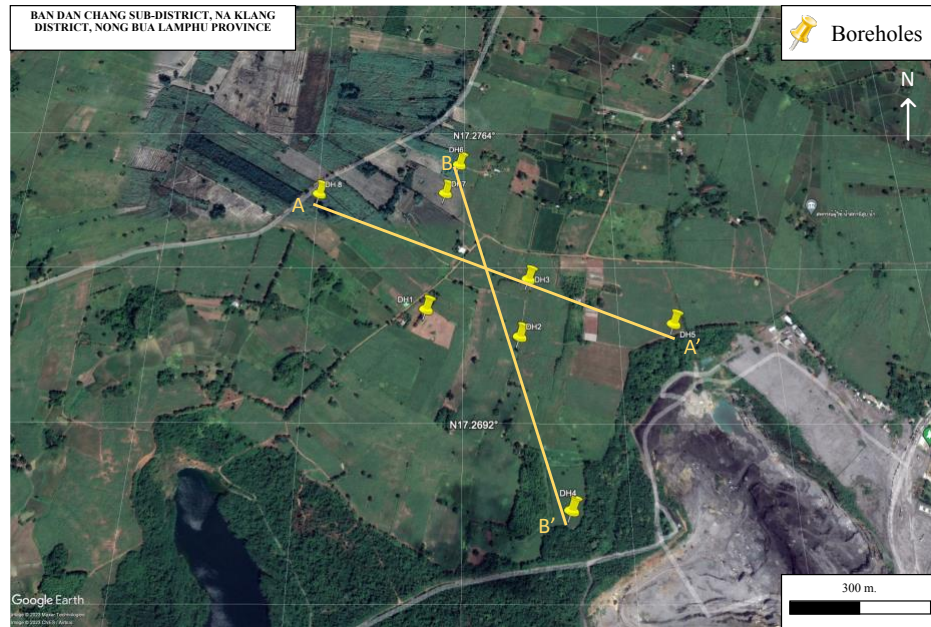


Figure 3

The cross-section line of A-A' and B-B' (modified from Google Earth Pro, 2023)

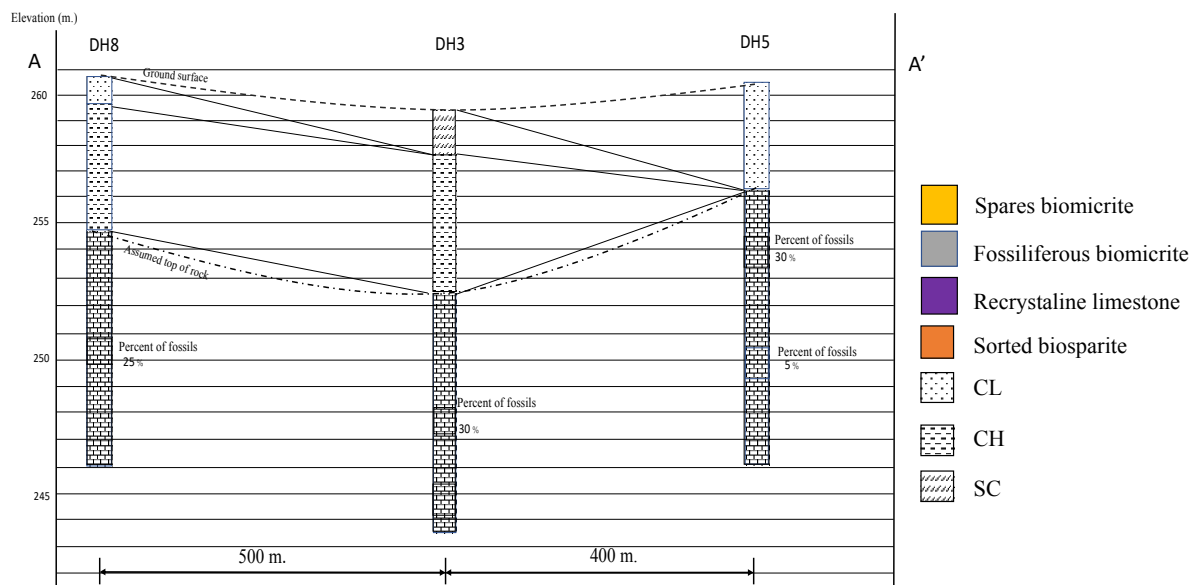


Figure 4

The cross-section of line A-A' .

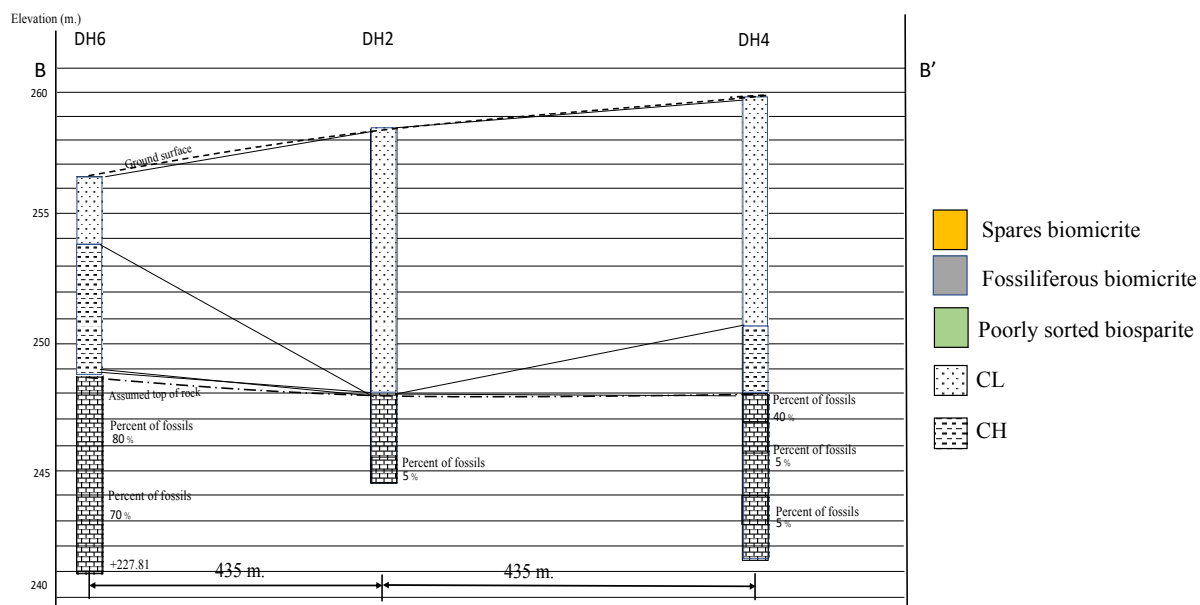


Figure 5
The cross-section of line B-B'.

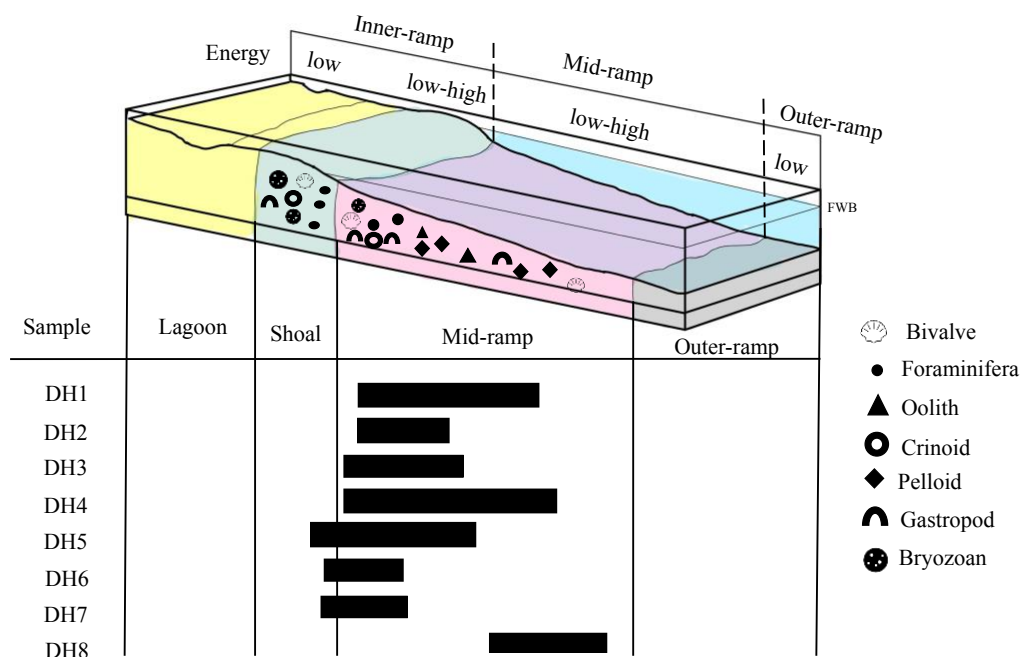


Figure 6
The carbonate ramp defined from DH1 to DH8 facies associate.



References:

1. Richard C. Selley, L. Robin M. Cocks, Ian R. Plimer. Eng Geol. 2005;-: 543-554.
2. DMR. Sci. investig. rep. 1983: 1
3. Fontaine, H., Suteethorn, V., & Vachard, D. J. Southeast Asian Earth Sci.1995; 12(1-2): 1
4. Bunopas, S. Proc. Int. 1983; 1: 29-76.
5. DMR. Sci. investig. rep.2009
6. DMR. 2009
7. Ueno, K., & Charoentitirat, T. Geosci. J. 2011;85-99
8. Fontaine, H., Salyapongse, S., & Suteethorn, V. NHBSS.2005;53(1): 44-56
9. Folk, R. L. AAPG bulletin. 1959; 43(1): 1-38.
10. Folk, R. L. AAPG bulletin .1962: 62-84.
11. Dunham, Robert J. AAPG.1962:108-121.
12. Bissell, H. J., & Chilingar, G. V. Sediment. Geol. 1967;9:87-168
13. Todd, T.W. J. Sediment. Petrol. 1966;36(2):317-34
14. El Tabakh, M., & Utha-Aroon, C. Sediment. Geol. 1998; 121(1-2): 97-119.
15. Ruansorn, T. Research and Development J. 2019; 6.
16. Burchette, T. P., & Wright, V. P. Sediment. Geol.1992; 79(1-4): 3-57.
17. Kavinate, S., Udchachon, M., & Fontaine, H. Elsevier sci.2019; 105(3): 191-199.

STENGTH REDUCTION FACTOR OF BLOCK ON MATRIX AND WEATHERED SANDSTONE SLOPES

Chonticha Suwan,* Wimon Sukplum, Ladda Wannakao

Department of Geotechnology, Faculty of Technology, Khon Kaen University, Khon Kaen, Thailand

*e-mail: chontis@kkumail.com

Abstract:

Spillway slope of Phra Archan Jue Reservoir Project (Lam Kra Juan), Chaiyaphum Province consist of block in matrix and weathered sandstone which is more complicated than a general soil slope or rock slope. Therefore, it is necessary to analyze the slope stability by 2D Finite Element Method to obtain a Critical Strength Reduction Factor (Critical SRF) indicating the stability of the slope in the study area, which is comparable to the Factor of Safety (FS) obtained from assessing slope stability by other methods. In this study, the characteristics of slope in the study area are divided into two characteristics that are the area of weathered sandstone slope with block in matrix slope on the top, and the area of all blocks in matrix slope. Different engineering properties of rock and soil obtained from field and laboratory tests are used to assess slope stability in this study area. The rock block in block in matrix slope were set at 0, 20, 30, 40 and 50%. In this study find out the parameter that has the greatest effect on the Critical SRF is the internal friction angle of block in matrix. The internal friction angle of block in matrix that raise the highest Critical SRF is 30%. The result of slope stability in the study area are unstable, Critical SRF are between 0.25 to 0.88. The slip surface occurs at the slope face of block in matrix slope. Therefore, a preliminary slope stability enhancement is propose by deciding drainage pipes and spraying concrete (shotcrete) on the slope face on the block in matrix slope to prevent the failure of block in matrix slope in the study area.

Introduction:

Block in matrix is a matrix of rock blocks and matrix. It can be found in various locations such as mine waste dumps, reservoir, mountain road or highly weathered strata with remaining boulders. Block in matrix was defined by Medley¹ as a mixture of rocks composed of geotechnically significant blocks within a bonded matrix of finer mixture, definition of geotechnically significant blocks is a sufficient mechanical contrast between blocks and weaker matrix, and that size distributions and volumetric block proportion influence the rock mass properties as all scales of engineering interest.²⁻⁵ The size of blocks that can be classified as block in matrix must between 5% to 75% of slope height.^{1,5-7} The engineering characteristics and mechanical behavior of the block in matrix are more complicated than matrix-only or rock-only materials. Slopes that are composed of block in matrix was defined as “BIMslope/Block in matrix slope” by Khorasani, Amini, Hossaini & Medley.⁸ The block content that can be classified as block in matrix slope must between 25 to 75%, the mechanical behavior of less than 25% of block content is approximate to only-soil slope and the mechanical behavior of more than 75% of block content is approximate to only-rock slope.^{2,6,9,10} Slope stability of able to analyzed in several ways but the geomechanics of the block in matrix slope is complex. Currently, there are no theories or solutions for analyzing the stability of block in matrix slopes and there are very limited number of publications related to block in matrix slope is available. For this reason, the analysis met and relevant



influencing parameters for the block in matrix slope stability were studied. The most previous investigations on block in matrix slope stability used finite element method as a tool while some investigations use limit equilibrium or discrete element method. It was found that previous researches focus on a total of seven parameters, these are: 1) block content (or the volumetric block proportion),^{3,5,6,8,11-17} 2) the orientation of blocks,⁶ 3) block angularity,^{5,13} 4) block aspect ratio (ratio between the width and length),¹³ 5) unit weight ratio between matrix and rock blocks,¹⁶ 6) slope height¹⁶ and 7) slope inclination.^{17,18} From reviewing the previous works, it can be concluded that there are many unanswered questions and there is still much work to be done in this area.

The aim of this study is to estimate the block in matrix and weathered sandstone slope stability at spillway slope of Phra Archan Jue Reservoir Project (Lam Kra Juan), Chaiyaphum Province by using 2D finite element method with different block content and engineering properties of sandstone and matrix in study area.

Study area

Chaiyaphum province is located in the northeastern of Thailand and the Khorat plateau. The Khorat plateau was separated by Phu Phan range into two basin, Phun Phan basin on the north and Khorat basin on the south, which is consist of nine formations, arranged from older to younger (Triassic to Tertiary age) as follows: Huai Hin Lat, Nam Phong, Phu Kradung, Phra Wihan, Sao Khua, Phu Phan, Khok Kruat, Maha Sarakham and Phu Thok (**Figure 1**). The geological conditions at spillway slope of Phra Archan Jue Reservoir Project (Lam Kra Juan) is Phu Phan formation, medium to very coarse grained, light grey and reddish brown sandstone (**Figure 2**).

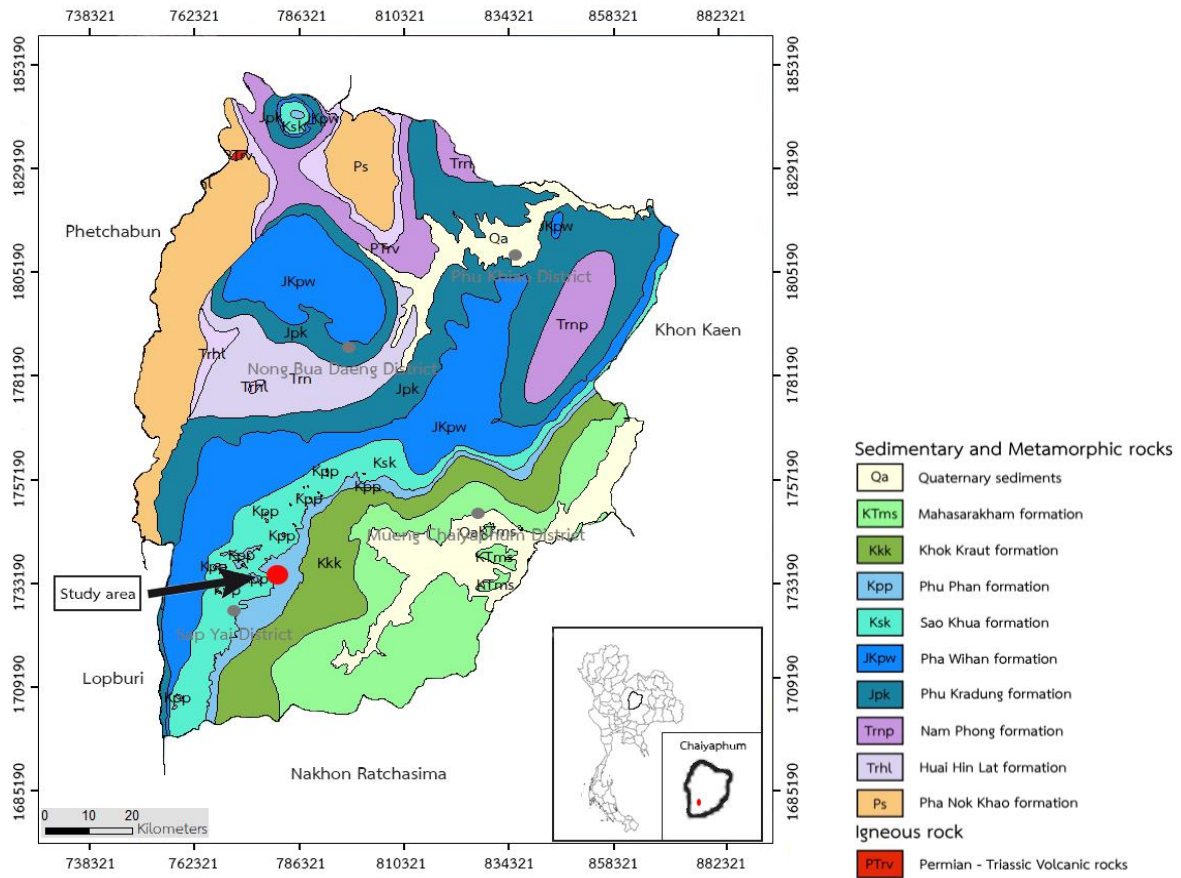


Figure 1.
Geological map of Chaipaphum province (DMR, 2010)



Figure 2.
Study area, Phra Archan Jue Reservoir Project (left), Spillway slopes (right)

Methodology:

Field study and Assessment of the slope stability parameters

In order to identify rock units and slope group regions that are suitable for assessing slope stability, the field study collected the data in the study area that are required to perform so, including rock type, rock shape, rock size, rock orientation and geological structure. The rebound hammer was also used to categorize the strength and degree of weathering of the in-situ

rocks. Rock core and block in matrix samples were consequently obtained for testing in the laboratory. According to the degree of weathering, three groups of rock samples are divided. The A₁ is lightly weathered, the A₂ is moderately weathered and the A₃ is highly weathered. Three core samples from each group were used for testing in the laboratory (**Figure 3.**) The rock samples were prepared and subsequently processed to measure the uniaxial compression test, elastic modulus, unit weight and Poisson's ratio. Meanwhile, the block in matrix sample was sampling from three different regions. In order to determine the unit weight and grain size of the soil and to classify the soil group, it is necessary to know the general values of the elastic modulus and Poisson's ratio of that soil group. After that, the parameters that were influencing the stability of the block in matrix were assessed. The first parameter is the block content, which is the quality of blocks in the slope used to assess the stability. There are five different level: 0, 20, 30, 40 and 50%. The second parameter is shear strengths, which are cohesion and friction angles with different unit weight of the block in matrix. A large-scale direct shear test with dimensions of 20 x 20 x 6 centimeters (width, length and height) was applied to determine shear strength parameters. The last parameter is the weathering degree of rocks, which is determined by the strength of the rock specimen. All of the laboratory tests for the engineering properties of rock and block in matrix are performed according to the American Society for Testing and Materials (ASTM) standards.²⁰⁻²⁴

Specifications of the slopes

The slopes were modelled to assess the stability by the AutoCAD software based on the slope designed by the Royal Irrigation Department and the geological characteristics in the study area. The slope has four benches, 5 meters in height, and slope gradient is 1:1. The slope divided into two groups with different block content, group one is the weathered sandstone slope with the slope face of two bench on the top is block in matrix and group two is the weathered sandstone slope with the all slope face is block in matrix (**Figure 4.**) The position of the blocks in the slope is random with dodge overlapping boundary of blocks and the blocks has square shape due to the influence of joint and rock blasting.



Figure 3.

Rock samples, The A₁ is lightly weathered (left), the A₂ is moderately weathered (center), the A₃ is highly weathered (right).

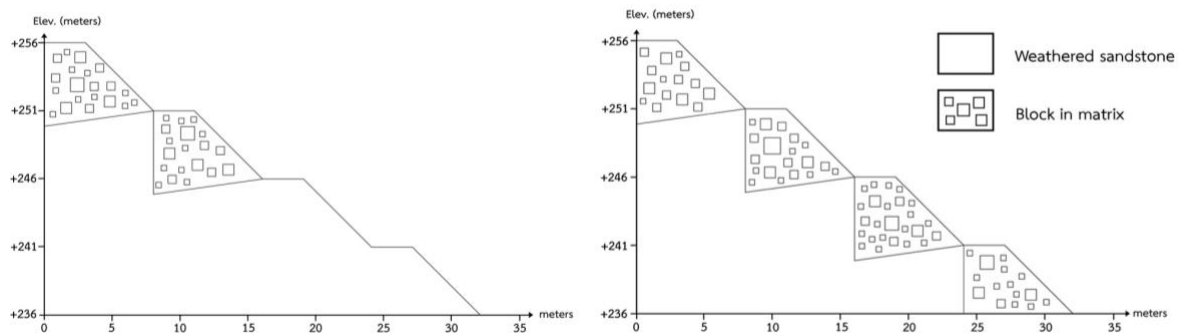


Figure 4.

The block in matrix and weathered sandstone slope models, group one model (left) and group two model (right)

Finite element Modelling

Finite element slope stability analysis was conducted using the RS2 software from Rocscience.²⁵ The models were discretized using the uniform six nodes triangular elements. The mesh size of the elements was smaller than the smallest block in the slope model. The boundary condition was fixed along the left, right and bottom boundaries, while the top surface of the slope was set free. In addition, the model was simulated under the natural gravity force. The engineering properties of weathered sandstone and block in matrix were acquired from the laboratory tests. The matrix was assumed to follow the Mohr-Coulomb failure criteria without shearing within the blocks and the rocks was assumed to follow the Hoek-Brown failure criteria. The Shear Strength Reduction was used to compute the Critical SRF, which is comparable to the Factor of Safety. The result of slope stability analysis shown the maximum shear strain that indicate the area where the failure may occur for each scenario. A total of 90 models was simulated according to the combination of the block content and engineering properties of block in matrix and weathered sandstone.

Results and Discussion:

Field observation

The representative rock in the study area is Phu Phan Formation, which is medium to very coarse grained, light grey and reddish-brown sandstone. In some areas found gravel in sandstone. The bedding of sandstone has dips around eight degrees into the slope face and one joint set, which is perpendicular to bedding. The measurement of one hundred rock samples in the area revealed that the block size are 0.25 to 2.20 meters. The sandstone in the study area has three levels of the uniaxial compressive strength as a result of the degree of weathering (**Table 1.**). The block in matrix is the combination between the weathered sandstone blocks and the matrix is sand that came form the weathering of sandstone in the study area.

Laboratory results

The rock testing was performed with three different degrees of weathering, resulting in three different levels of shear strength of the rocks (**Table 1.**). The matrix is a poorly graded sand (SP) group, which obtained from grain size analysis. The block in matrix have three levels of the unit weight which are derived from field testing, the shear strength of block in matrix was tested on the samples with varying the unit weight and block content. The shear strength of block in matrix is directly proportional to block content, so it was found that the shear

strength tends to increase as block content increases. All parameters of the laboratory testing are tabulated in **Table 2**.

Table 1. Engineering properties of weathered sandstone

Parameters	Sample		
	A ₁	A ₂	A ₃
Average unit weight (kN/m ³)	22.2	22.8	23.0
Average uniaxial compressive strength (MPa)	21.7	41.0	50.7
Average elastic modulus (GPa)	13.81	12.99	16.64
Average poisson's ratio (-)	0.49	0.25	0.24
m _b (-)	5.82	8.32	9.95
s (-)	0.04	0.11	0.19

Table 2. Engineering properties of block in matrix

Sample	Parameters					
	Unit weight (kN/m ³)	Block content (%)	Elastic modulus (MPa)	Poisson's ratio (-)	Cohesion (MPa)	Friction angle (degrees)
SP ₁	12	0	40	0.3	0	22.29
		20				23.75
		30				30.54
		40				31.80
		50				32.62
SP ₂	13	0	40	0.3	0	23.27
		20				25.64
		30				30.96
		40				33.02
		50				34.99
SP ₃	14	0	40	0.3	0	31.38
		20				32.21
		30				37.60
		40				38.31
		50				41.67

Finite element analysis

The input engineering parameters of block in matrix and weathered sandstone are shown in Table 2. and Table 3. The slope stability results show the Critical SRF of model one and model two are 0.45 to 0.88 and 0.25 to 0.76, respectively (**Figure 5.**). Model one has a higher Critical SRF than model two due to the characteristics of the slopes; model one has only two benches of block in matrix at slope face but model two has four benches of block in matrix at slope face (**Figure 6.**) and the Critical SRF directly proportional to the block content and friction angle of block in matrix (**Figure 7.**). The Critical SRF of all models are lower than 1.0, indicates that the slope is unstable, the failure area is at the slope face. The slope face is block in matrix, which is composed of weathered sandstone blocks, poorly graded sand (cohesionless soil) and there is no compacted the block in matrix at spillway slope.

The stabilization was performed by inserting 2-inch diameter horizontal drainage with a distance of 4 meters between the pipes and spraying concrete (shotcrete) 5 centimeters thick. The properties of concrete are tabulated in **Table 3**. After the stabilization, the Critical SRF of all models is increases to 1.35 to 1.86, which is indicated that the slopes have stability (Critical SRF>1.0). Considering the increase of the Critical SRF before the stabilization, it is found the most affected parameter to Critical SRF is friction angle of block in matrix. Friction angle of block in matrix is directly proportional to the Critical SRF and the cause of the increases friction angle is the increased block content of block in matrix. The optimum block content that gives the highest Critical SRF is block content at 30%. If the block content is up to 40%, the Critical SRF will decrease due to the position of blocks in the slope, when the failure occurs then movement of blocks and matrix will increase. From the results of slope stability analysis showing the failure area occurred, an abnormality was found in the 0% of block content models. The failure area did not occur at the slope face, this abnormality occurs due to the 0% of block content slopes comprising only poorly graded sand. It can be classified as only-soil slope. The grain size of poorly graded sand is smaller than the element that used to evaluate the stability of slope, which is not suitable for this models. A₁, SP₁

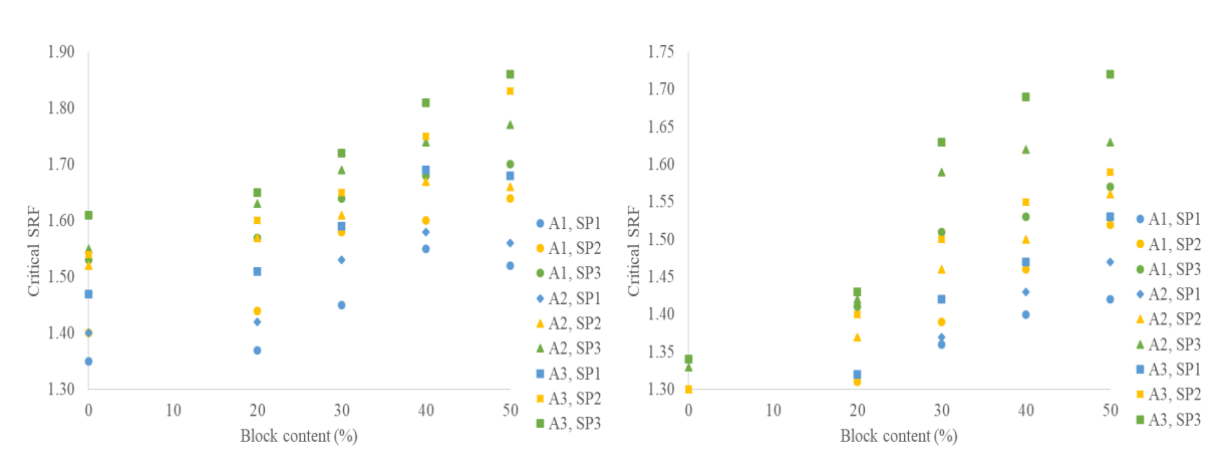


Figure 5.

Critical SRF relative to block content and the engineering properties of block in matrix and weathered sandstone, group one model (left) and group two model (right)

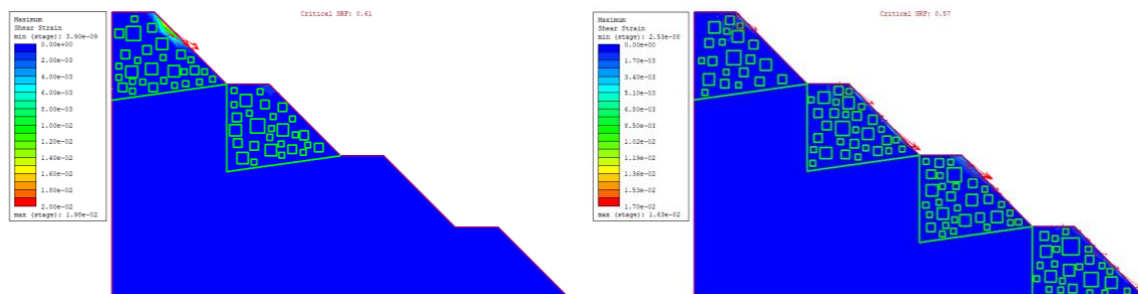


Figure 6.

The example models of block in matrix and weathered sandstone slope, group one model (left) and group two model (right)

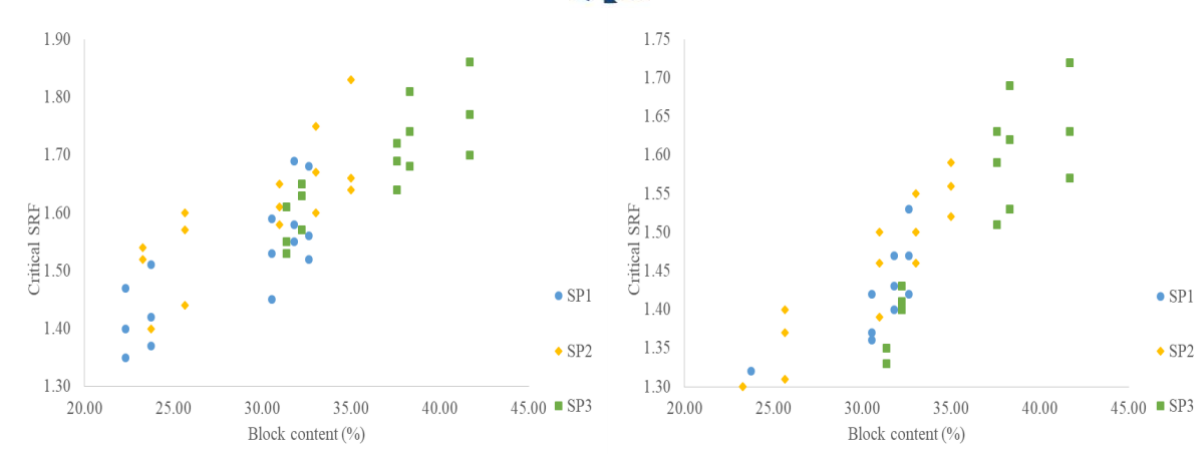


Figure 7.
Critical SRF relative to friction angle of block in matrix, group one model (left) and group two model (right)

Table 3. The engineering properties of concrete

Properties	Value
Unit weight (kN/m ³)	25.0
Elastic modulus (GPa)	30.0
Poisson's ratio (-)	0.15
Uniaxial compressive strength (MPa)	35.0
Shear strength (MPa)	3.0

Rocscience, 2021

Conclusion:

The results of block in matrix and weathered sandstone slope stability analysis show that the Critical SRF of model one is greater than that of model two due to the characteristic of slopes. The Critical SRF of all models are between 0.25 to 0.88, which indicates that the slope are unstable. The area of the failure may occur on the slope face of block in matrix due to the matrix with poorly graded sand exhibiting no cohesion and has no compact. It is proposed to stabilize by adding the 5 centimeters thick shotcrete and 2-inch diameter horizontal drain with a distance between drainage of 4 meters. Critical SRF of all models after the stabilization are between 1.35 and 1.86, which indicates that the slope is stable. The parameter that most affects to the Critical SRF is friction angle of block in matrix, which is directly proportional to the Critical SRF and the thing that affects the friction angle is block content of block in matrix. The optimum block content that gives the highest Critical SRF is block content at 30%, if block content was up to 40%, the Critical SRF is decreases. The abnormal results were found in the 0% of block in matrix slopes, the failure area did not occur at the slope face due to the size of elements is greater than the grain size of poorly graded sand. That is not suitable for the only-soil slopes.

References:

1. Medley EW. Ph.D. Dissertation University of California at Berkeley. 1994.
2. Medley EW, Lindquist ES. Rock Mechanics Proceeding of the 35th U.S. Symposium. 1995:907-914.
3. Medley EW, Sanz Rehermann PF. Eurock 2004 & 53rd Geomechanics Colloquium. 2004:425-300.
4. Marinos P, Medley EW. Bull Eng Geol Environ. 2001; 60:85-92.
5. Kalender A, Sonmez H, Medley EW, Tunusluoglu C, Kasapoglu KE. Eng Geol. 2014;183:65-79.
6. Lindquist ES, Goodman RE. Proceeding of the 1st North America Rock Mechanics Symposium. 1994:843-850.
7. Medley EW. Proceeding of 5th North American Rock Mechanics Symposium. 2002:509-606.
8. Khorasani E, Amini M, Hossani MF, Medley EW. Geomech Eng. 2019;17(3):279-285.
9. Sonmez H, Gokceoglu C, Tuncay E, Medley EW, Nefeslioglu HA. Felsbau Rock Soil Eng J Eng Geol Geomech Tunn. 2004;22(5):27-34.
10. Medley EW. Felsbau Rock Soil Eng J Eng Geol Geomech Tunn. 2004;22(5):35-60.
11. Sonmez H, Gokceoglu C, Medley EW, Tuncay E, Nefeslioglu HA. Int J Rock Mech Min Sci. 2006;43:554-561.
12. Ji T, Shen Z, Wang S, Xue Q, Zhang Q. Adv Mater Sci Eng. 2019:1-13.
13. Lu Y, Tan Y, Li X. Eng Geol. 2018;244:116-124.
14. Guerra C, Pinzon J, Padra L, Ramos A. Proceeding of Geo-Chicago Sustainable Geoenvironmental System. 2016:658-667.
15. Hu J, Huang X, Liu S, Wang W, Zhou A. Math Probl Eng. 2018:1-15.
16. Montoya-Araque EA, Suarez-Burgoa OL, Medley EW. Bull Eng Geol Environ. 2020;79(1):5329-5340.
17. Napoli ML, Barbero M, Ravera E, Scavia C. Int J Rock Mech Min Sci. 2018;101:41-49.
18. Yang Y, Sun G, Zheng H. Eng Anal Bound Elem. 2019;109:153-160.
19. DMR (Department of Minerals Resources). Geological map of Chaiyaphum province. 2010.
20. ASTM International. ASTM D2487 Standard Practice for Classification of Soils for Engineering Purposes (Unified Soil Classification System). Pennsylvania: ASTM International; 2020.
21. ASTM International. ASTM D3080-04 Standard Test Method for Direct Shear Test of Soils Under Consolidated Drained Conditions. Pennsylvania: ASTM International; 2004.
22. ASTM International. ASTM D421-85 (2007) Standard Practice for Dry Preparation of Soil Samples for Particle-Size Analysis and Determination of Soil Constants. Pennsylvania: ASTM International; 2007.
23. ASTM International. ASTM D5873-14 Standard Test Method for Determination of Rock Hardness by Rebound Hammer Method. Pennsylvania: ASTM International; 2014.
24. ASTM International. ASTM D7012-14 Standard Test Method for Compressive Strength and Elastic Moduli of Intact Rock Core Specimens under Varying States of Stress and Temperatures. Pennsylvania: ASTM International; 2014.
25. Rocscience. RS2 [Computer software]. Version 11.012. Ontario: Toronto; 2021.



SURVEY OF INFORMATION ON THE MANAGEMENT OF AGRICULTURAL WASTE FROM OIL PALM GARDENT AND THE USE OF PALM OIL BRANCH AS AN ALTERNATIVE FUEL FOR CLAY BRICK BURNING

Wikanda Thongnueakhaeng^{1*} and Thawatchai Tepnual²

¹Biological and Environmental Sciences, Faculty of Science and Digital Innovation, Thaksin University, Thailand

²Physics, Faculty of Science and Digital Innovation, Thaksin University, Thailand

*e-mail: vikandat@hotmail.com

Abstract:

This research aims to explore the management of agricultural waste from oil palm plantations and to study the use of oil palm branches as an alternative fuel in the production of clay bricks. It was found that the most problematic agricultural waste from palm plantations is the oil palm branch, which occurs at approximately 931.01 pieces/rai/year. None of the farmers surveyed reported having guidelines for managing this waste. This research involved collaboration with a clay brick factory to conduct an experiment using oil palm branches as fuel for burning clay bricks. The researchers replaced the originally used rubber wood fuel with oil palm branches in proportions of 0%, 10%, 20%, and 30%. The results indicated that replacing rubber wood with oil palm branches at a rate of 30% led to a reduction in rubber wood consumption from 40,000 to 28,000 kg/stove. (60,000 bricks/stove). Burning time was reduced from 96 to 84 hours, and the quality of bricks obtained after burning increased from 54,500 to 59,500 bricks. Oil palm branches are smaller and more uniform in size than rubber wood. This characteristic makes it easy to feed fuel into the brick stove and control the strength of the flame.

Introduction:

The southern region of Thailand holds the distinction of being the largest area for oil palm cultivation, a vital economic crop for the country. The ambitious oil palm and palm oil strategic plan for 2015-2026 outlines a goal to expand plantation areas by 3.0 million rai, aligning with efforts to boost production and meet market demand. Emphasizing sustainability, farmers are actively encouraged to adhere to the internationally recognized RSPO (Roundtable on Sustainable Palm Oil) standards, ensuring that palm oil production processes remain environmentally friendly. Reflecting the industry's global impact, Thailand's palm oil exports to Europe soared to a value of 2.4 million euros in 2017 (Department of International Economic Affairs, 2019). The RSPO standard has garnered significant interest within the Thai oil palm industry, particularly attracting large companies that have become active members (RSPO. MEMBERS, 2019). Membership in the RSPO group has proven beneficial for farmers, leading to increased quantity and improved quality of palm oil production. Additionally, these farmers enjoy the advantage of selling their palm oil at a premium compared to their non-member counterparts. Joining the RSPO also equips farmers with effective waste management practices for palm plantations, aligning with compliance requirements and endorsed by network factories. Practices such as spreading leaves to cover the entire plantation or using palm bunches to cover the base of oil palm trees contribute to maintaining or restoring soil fertility¹.

In light of the existing challenge where numerous palm oil plantations are situated far from RSPO member mills, a lack of incentives and opportunities hampers the promotion of effective agricultural waste management. To address this issue, a research initiative was undertaken to gather data on the management and utilization of agricultural waste materials

from palm plantations in regions distant from factories. Collaborating with a clay brick factory, the study aimed to explore the feasibility of using oil palm branches as a substitute fuel for rubber wood in the clay brick burning process. This research not only holds promise in incentivizing farmers to adopt better waste management practices but also contributes to a sustainable approach aligning with the principles of the Bio Economy – Circular Economy – Green Economy (BCG Model), thereby fostering benefits for both farmers and the overall environment.

Methodology:

1. Survey of information on waste management of agricultural materials from palm oil plantations

1.1 Population and sample

The population in this study was oil palm farmers in Krasae Sin District, Songkhla Province, Thailand 359 households. The sample group was calculated the sample size using the formula of Yamane (1973)², which can be calculated according to the formula to have a sample size equal to 189 households, allowing an error of 5 percent ($e = 0.05$)¹ where the study used a sample group to collect data on a total of 190 households.

$$n = N/(1+N(e)^2)$$

n = Sample size

N = Population size

e = Accuracy/confidence level 0.05

To get the number of samples mentioned above. The researcher used simple random sampling from the population of the sample. Structured Questionnaire were used in this research which consists of closed-ended questions which has specified answers to choose and open-ended questions that allows respondents to be free to give answers or express their opinions and semi-open-ended and closed-ended questions. The researcher tried using a structured interview before collecting actual data. The steps are in order as detailed below.

- Study concepts, knowledge and related documents as well as preliminary surveys (Reconnaissance survey/preliminary survey) to determine the structure and questions in a structured interview that can collect data according to the research objectives.
- Take the structured interview form to 3 experts to evaluate and then use it to calculate the Index of Item Objective Congruence (IOC), which has the following formula:

$$IOC = \sum R/N$$

IOC = Conformity index value

$\sum R$ = Sum of expert opinion scores

N = Number of experts

The scoring criteria is to give 1 point if you are sure that the content of the question meets the research objectives. Give 0 points if you are not sure that the question can be measured according to the research objectives. Give -1 point if it is certain that the question cannot be measured according to the research objectives. Any question with a consistency index of 0.5-1.0 indicates that the question is consistent with the research objectives³.

- Modify questions in the structured interview format. It was then piloted with 15 oil palm farmers to evaluate the effectiveness of the interview before using it to collect actual field data.



1.2 Data analysis

In this research, data analysis was conducted through descriptive analysis, employing a pre-existing statistical program for data processing. The statistical measures utilized encompassed percentage, mean, standard deviation, maximum, and minimum. The researcher extracted the outcomes from the analysis and presented them in a summarized form, accompanied by detailed descriptions to enhance comprehension. The results, particularly those derived from answering questions based on farmers' perspectives, were compiled and incorporated into educational materials for dissemination during lectures, facilitating a more accessible understanding of the research findings.

2. An experiment on using palm oil branch as fuel for burning clay bricks in an establishment

2.1 Determine the energy properties of oil palm branch

The heat value analyzed by Bomb Calorimeter according to ASTM D3286 standard. Put the sample to be analyzed for heat value into the Bomb. Surrounding the sample in Bomb is water that controls the temperature. The machine will work by igniting the sample to burn the sample completely and produce heat. The machine will measure the change in water temperature and calculate the heat energy value. From the heat that will radiate to the water surrounding the Bomb.

2.2 Experimental research in clay brick production factory

In the experimental research conducted at a clay brick production factory equipped with a stove boasting a capacity of 60,000 bricks per firing cycle (Brick size is 8.5x19x6 cm), the study focused on incorporating oil palm branches in different ratios with rubber wood during the brick production process. Data collection aimed to compare this novel approach with the traditional method of burning bricks using solely rubber wood. Key parameters assessed included burning time, brick quality, and fuel cost. By systematically analyzing these factors, the research aimed to provide insights into the feasibility and potential benefits of utilizing oil palm branches as a supplementary fuel source in clay brick production, offering a comparative perspective with the established practice of using rubber wood alone.

Results and Discussion:

1. Results of a survey of information on waste management of agricultural materials from palm oil plantations

Data collection for this study was conducted among a sample of farmers in Krasae Sin District, Songkhla Province, Thailand, representing regions situated at a distance from palm oil factories. The findings revealed that 76.52% of the farmer respondents were male, with an average age of 56.55 years. A significant portion of the participants, accounting for 57.22%, had no more than primary school education. Remarkably, all the farmers surveyed were engaged in oil palm plantation work concurrently with other occupations. It was observed that 84.25% of the farmers derived their primary income from oil palm plantations, emphasizing the economic significance of this sector in the livelihoods of the surveyed population.

Farmers in the study area cultivate oil palm on an average of 26.50 rai per person. The data reveals that oil palm in this region has an average lifespan of 7.24 years, indicating that the palm plantations have been established relatively recently. This contrasts with findings from Sikao District, Trang Province, Thailand, where farmers reported an average oil palm plantation experience of 20.53 years⁴ and Surat Thani Province, where farmers had an average of 18.94 years of experience in oil palm plantation¹.

In terms of production and sales, the study observed that in 2022, farmers achieved an average yield of 2,358.55 kilograms per rai per year. The harvesting period for oil palm production occurred approximately every 17.25 days on average. This aligns with similar findings from Nakhon Si Thammarat Province, Thailand, where oil palm was harvested every 16.90 days⁵. Additionally, oil palm bunches were harvested every 19.34 days on average in Surat Thani province, Thailand¹. Regarding planting practices, 85.50 percent of farmers in the study area reported planting oil palm trees at a spacing of 9X9X9 meters. These details provide a comprehensive overview of the agricultural practices and production dynamics in the oil palm sector within the study region.

Agricultural waste generated from oil palm plantations includes oil palm branches, which need to be cut down during the harvesting of oil palm bunches. This waste category also encompasses imperfect oil palm bunches, such as those that are small or have imperfect fruit, as well as raw oil palm bunches that have been discarded from the oil palm product purchase yard. Despite the presence of agricultural waste like oil palm bunches, farmers do not perceive it as a significant management problem due to the relatively low quantity, averaging less than 1.00 percent of all harvested oil palm bunches. Currently, the management practice involves placing this waste in the garden to decompose naturally. For oil palm branches, farmers typically cut about two branches per tree per harvesting cycle. Given that farmers plant 22 oil palm trees per rai, this results in approximately 44 branches per rai as agricultural waste in a single harvesting cycle. In this area, where the harvesting cycle occurs approximately every 17.25 days on average, the oil palm branches generated during harvesting amount to about 931.01 branches per rai per year. Considering that each oil palm branch weighs approximately 5 kilograms⁶, the agricultural waste from oil palm branches can be estimated at up to 4,655.07 kilograms per rai per year.

The study revealed that 100 percent of farmers did not implement effective management practices for oil palm branches. Instead, they left the branches in the garden, either by stacking them on top of each other or depositing them into water channels. Interestingly, it was observed that the decomposition of oil palm branches took more than one year. Furthermore, none of the farmers utilized oil palm leaves by creating leaf paths across the plantations, citing concerns about additional labor costs. This finding aligns with the results of a study by Kunsangkaew et al. (2020)¹, which reported that an increase in oil palm plantation area by one rai decreased the likelihood of farmers complying with RSPO standards. These standards include spreading oil palm leaves over the entire plantation area to aid in soil conservation and weed control, a process requiring additional time and labor to cut off hard and thorny parts of the branches before spreading. Farmers expressed the need for guidelines on managing and utilizing oil palm branches and expressed hope that these branches could be monetized similarly to other agricultural waste.

2. Results of an experiment in using oil palm branch as alternative fuel for burning clay bricks in an establishment

The oil palm branch can be divided into two distinct parts: the base of the branch, characterized by its hardness and sharp thorns, and the leaf part, as illustrated in Figure 1.

2.1 The energy properties of oil palm branch

Table 1 show the energy properties of oil palm branch (base of branch and leaf part) after being cut from the tree. The oil palm branches were stored in a well-ventilated shaded area inside the brick factory, left to dry for various periods of time, and subsequently analyzed to determine their heat value. The results were showed in Table 1.



Figure 1.

Oil palm branches: the base of the branch (left) and the leaf part (right)

Table 1.

Heat value of palm oil branch

Oil palm branch after being cut from the tree (Day)	Heat value of base of branch (MJ/kg)	Heat value of the leaf part (MJ/kg)
0	12.35±0.12	11.05±0.08
5	13.15±0.10	11.24±0.10
10	14.32±0.15	12.85±0.10
15	14.45±0.08	13.12±0.12
20	14.84±0.12	13.15±0.10
25	15.22±0.10	13.46±0.12
30	15.56±0.08	13.95±0.10

The findings indicate that the base of the branch exhibited a higher heat value content compared to the leaf part. Specifically, the base of the branch, after being cut from the trees for 0, 5, 10, 15, 20, 25, and 30 days, showed heat contents of 12.35±0.12, 13.15±0.10, 14.32±0.15, 14.45±0.08, 14.84±0.12, 15.22±0.10, and 15.56±0.08 MJ/kg, respectively. These results align with the findings of Nattawut *et al.* (2017)⁷, who reported that oil palm branches (base of branch and leaf part) yielded a heat value of 14.78 MJ/kg.

2.2 Clay brick burning using base of oil palm branch as co-fuel in an establishment



Figure 2.

Clay brick: before burning (left) and after burning (right)

The research experiments were carried out at the Wirat Brick Factory in Choeng Sae Subdistrict, Krasae Sin District, Songkhla Province, Thailand. The factory is equipped with a stove boasting a capacity of 60,000 bricks per firing cycle. Initial data collection focused on brick burning using the original fuel, rubber wood, encompassing burning time, fuel cost, labor, and brick quality. Burning 60,000 raw bricks required 40,000 kilograms (40,000 baht)

of rubber wood, resulting in 54,500 quality red bricks, 2,000 raw bricks, 2,000 black (burnt) bricks, and 1,500 broken bricks. The process took 96 hours, equivalent to 4 days and 4 nights. This preliminary data serves as a basis for comparison with subsequent experiments involving the burning of bricks using a combination of rubber wood fuel and oil palm branches in different proportions. Figure 3 illustrates the preparation of oil palm branches (base of branch) for clay brick burning.

As indicated in Table 1, oil palm branches, which require sufficient drying time, were utilized for their high heat value. Dried oil palm branches, left to dry for more than 15 days, were employed in the burning process. The combination of oil palm branches and rubber wood for burning clay bricks is depicted in Figure 4. The study explored using oil palm branches (base of branch) instead of rubber wood at rates of 10%, 20%, and 30% of the amount used by the factory's original fuel. The detailed results of this study are presented in Table 2.



Figure 3.

Preparation of oil palm branches for clay brick burning



Figure 4.

Using oil palm branches along and rubber wood for burning clay bricks

The experimental results highlight that replacing rubber wood with oil palm branches at a rate of 30% can lead to significant benefits. Specifically, this substitution reduces the amount of rubber wood transported from outside the area from 40,000 kilograms to 28,000 kilograms per burning cycle. This translates to a reduction of 12,000 kilograms of rubber fuelwood per cycle, resulting in cost savings given a price of 1.0 Baht per kilogram.

Table 2.
Results of burning clay bricks by rubber wood along with oil palm branch

Data	Rubber wood 100%	Oil palm branch 10%	Oil palm branch 20%	Oil palm branch 30%
Fuel and time for burning				
Rubber wood (Kg)	40,000	36,000	32,000	28,000
Base of oil palm branch (Kg)	0	4,000	8,000	12,000
Time for clay brick burning (hour)	96	84	84	84
Quantity and quality of clay bricks				
Raw clay bricks (before burning) (Brick)	60,000	60,000	60,000	60,000
Quality clay bricks (Brick)	54,500	57,500	57,450	59,500
Water absorption value of quality bricks (%) ^a	10	9.4	9.5	9.3
Broken bricks (Brick)	1,500	1,500	1,500	500
Black (burnt) bricks (Brick)	2,000	1,000	1,050	-
Raw bricks (Brick)	2,000	-	-	-

^a Hollow bricks or bricks with holes for building walls require to have an average water absorption value of 5 bricks not exceeding 10% (TIS 153-2540 standard)

Furthermore, the findings indicate a notable reduction in burning time, from 96 hours to 84 hours, while still producing 59,500 high-quality clay bricks (red bricks) and maintaining consistent quality. The positive outcomes include only 500 broken bricks, with no raw bricks or burnt black bricks. This research demonstrates that the base of oil palm branches is a suitable alternative fuel for clay brick burning due to its smaller and more uniform size compared to rubber firewood. This characteristic facilitates easier feeding of fuel into the brick kiln and better control over the flame's strength during brick burning. The results align with the principles influencing heating value, indicating that smaller, uniformly shaped pieces of wood burn more efficiently than larger pieces due to the increased surface area exposed to air during burning⁸.

Conclusion:

Oil palm branches, a prevalent agricultural waste in Thailand, often necessitate the hiring of workers for cutting and collection. The base of the oil palm branch, despite being challenging to decompose naturally due to its hardness, holds a high heat value. This characteristic makes it a promising alternative fuel source, particularly for establishments situated in areas with extensive palm oil cultivation. In the context of clay brick factories, which traditionally use rubber wood as fuel, this study demonstrates that the base of oil palm branches is a suitable and advantageous alternative.

Burning clay bricks with oil palm branches as fuel leads to an improvement in the quality of clay bricks, accompanied by reductions in broken bricks, raw bricks, and burnt black bricks. Additionally, the utilization of oil palm branches as fuel results in decreased burning time, contributing to cost savings in labor and expediting the production cycle. This research underscores the potential of oil palm branches as a sustainable and efficient

alternative fuel for clay brick factories, aligning with the broader goal of optimizing resource utilization in the agricultural sector.

Acknowledgements:

The success of this research project was made possible through the generous research funding provided by National Research Council of Thailand (NRCT) for the fiscal year 2022. The author extends gratitude to Thaksin University, Wirat Brick Factory, Krasae Sin District Organic Fertilizer Producers and Users Cooperative Limited, and Khao Nai Oil Palm Large-Scale Enterprise for their valuable support in terms of location, utilities, and various other forms of assistance throughout the course of this research. Their collaborative efforts have greatly contributed to the accomplishment and insights gained from this study.

References:

1. Kunsangkaew C, Thongrak S, Kiatpathomchai S. Factors Affecting the Implementation of RSPO Standard Practices of the Smallholders in Surat Thani Province. *KKU Research Journal of Humanities and Social Sciences (Graduate Studies)*. 2020; 8(3): 97-112.
2. Yamane T. *Statistics: An Introductory Analysis* (3rd Ed). 1973; New York: Harper and Row Publ.
3. Pasunon P. Validity of Questionnaire for Social Science Research. *Journal of Social Science Srinakharinwirot University*. 2015; 18(1): 375-396.
4. Jumnon S, Sriboonruang P, Choocharoen C. Factors Affecting the Success of Community Enterprise Management according to The Standard of Roundtable on Sustainable Palm Oil (RSPO), Sikao District, Trang Province. *King Mongkut's Agr. J.* 2020; 38(3): 408 – 416.
5. Boonyanuphong P, Chuaysakul N. Factors Determining Farmer's Decision on Area Expansion of Oil Palm Plantation in Pak Phanang Basin Area, Nakhon Si Thammarat province. *Journal of Administration and Management*. 2019; 9(2): 88-99.
6. Seephueak P, Wongpisal P, Preecha C, Seephueak W. Effect of Fungi on Physical and Nutrient of Compost from Oil Palm Frond (*Elaeis guineensis* Jacq.). *RMUTSV Research Journal*. 2020; 12(3): 552-565.
7. Dutsadee N, Buacharoen S, Sasujit K, Homduang N. Production of fuel gas from the biomass gasification process from oil palm and tar reduction using low heat plasma techniques. Complete research report. 2017.
8. Wood energy development work. Collection of research abstracts from 1982-2007. Forest Product Development Group, Forest Research and Development Office, Royal Forest Department. 2007.



SESSION F-FOOD SCIENCE AND TECHNOLOGY/AGRICULTURAL SCIENCE

Development of a Healthy Spread with Riceberry Rice and Black Garlic

Peeraporn Pakakaew¹, Yuthana Phimolsiripol², Siraphat Taesuwan^{1,3}, Sarawut Kumphune⁴, Suwanna Decharatanangkoon², Kanyarat Suthapakti² and Niramun Utama-ang^{2,3,5*}

¹ Division of Food Science and Technology, Faculty of Agro-Industry, Chiang Mai University, Chiang Mai 50100, Thailand

² Division of Product Development Technology, Faculty of Agro-Industry, Chiang Mai University, Chiang Mai 50100, Thailand

³ Cluster of Innovative Food and Agro-Industry, Chiang Mai University, Chiang Mai 50100, Thailand

⁴ Biomedical Engineering Institute, Faculty of Engineering, Chiang Mai University, Chiang Mai 50200, Thailand

⁵ Cluster of High Value Product of Thai Rice and Plants for Health, Chiang Mai University, Chiang Mai 50100, Thailand

*e-mail: niramun.u@cmu.ac.th

Abstract:

This study employed a D-optimal mixture design to create nine formulations of a healthy spread using three key ingredients: butter (A; 40%-55%), riceberry rice (B; 5%-15%), and black garlic (C; 5%-15%). The formulations were analysed for their physical properties, chemical properties, and sensory evaluation to identify the optimal combination. The results revealed that the best formulation consisted of 49.08% butter, 11.45% black garlic, and 6.47% riceberry rice. This optimal formulation exhibited promising nutritional content, providing 6.07 mg of S-allyl cysteine, 29.65 mg of 5-hydroxymethylfurfural, and 1.40 mg of cyanidin per 100 g of dry sample. The overall liking score for the product was 6.42, indicating a moderate level of consumer preference. Notably, of the 200 consumers, 86% accepted the product and approximately 52% expressed that they would purchase the product. These findings highlight the successful development of a healthy riceberry rice and black garlic spread and demonstrate its potential as a functional ingredient.

Introduction:

In recent years, the pursuit of healthier food options has gained momentum as consumers prioritise nutrition and well-being. This shift in preferences has fuelled innovation in the food industry, with researchers exploring novel ingredient combinations for functional foods¹. Among the various food products, spreads play a prominent role in daily meals, offering versatility and flavour enhancement. Consequently, there is an opportunity to develop a healthy spread product that satisfies taste preferences and contributes to a balanced and nutritious diet with enhanced potential health benefits.

Butter, a widely consumed dairy product, is known for its creamy texture and distinct flavour². However, its high saturated fat content has prompted concerns about its impact on cardiovascular health³. To address this concern, researchers have explored strategies to optimise butter formulations or to identify suitable alternatives that reduce saturated fat while preserving sensory appeal.

Riceberry rice, a newer Thai rice variety, has garnered attention due to its potential health benefits⁴. This hybrid grain, a cross between Thai Jasmine rice and Hom Nin rice, has a dark purple colour and boasts a high antioxidant content⁵. The presence of anthocyanins, phenolic compounds, and other bioactive substances in riceberry rice has been linked to anti-

inflammatory and antioxidant effects, suggesting potential protection against chronic conditions such as cardiovascular diseases and certain cancers⁶⁻⁸.

Another ingredient with notable health-promoting properties is black garlic. Derived from the fermentation of fresh garlic, black garlic undergoes an ageing process that alters its flavour, texture, and nutritional composition^{9,10}. This transformation leads to the development of unique compounds, including organosulphur compounds and antioxidants, which are absent in fresh garlic^{10,11}. Black garlic has shown promise in terms of antioxidant, anti-inflammatory, and antimicrobial effects, as well as potential benefits for immune function and cardiovascular health¹².

This study aims to develop a healthy spread product that preserves the appealing sensory characteristics of butter while incorporating the health benefits of riceberry rice and black garlic. Different proportions of butter, riceberry rice, and black garlic were studied using a D-optimal mixture design to achieve an optimal spread formulation with favourable physical, chemical, and sensory attributes while enhancing the nutritional value and providing consumers with an enjoyable sensory experience.

Methodology:

Plant materials

Garlic (*Allium sativum* L.) was purchased from local markets in Srisaket province (Jae Mam Phant), Thailand. Fresh garlic was peeled and sized; only clean whole cloves were selected to produce black garlic at 60 °C and 80% relative humidity for 1 week¹⁰. Riceberry rice grains were purchased from a local shop (Mussy Rice) located in Mueang Pan District, Lampang Province, Thailand. The rice grains were mashed and sieved through a 100 mesh screen, and the powder was rapidly stored in an aluminium foil bag. Butter was purchased from a super market (Makro).

Chemicals and reagents

2,2-Diphenyl-1-picrylhydrazyl (DPPH), 2,2'-azino-bis(3-ethylbenzothiazoline-6-sulphonic acid) diammonium salt (ABTS), S-allyl-L-cysteine (SAC), and 5-(hydroxymethyl)furfural (5HMF) were purchased from Sigma-Aldrich (St. Louis, MO, USA). Ethanol was purchased from RCI Labscan Ltd. (Bangkok, Thailand). All other chemicals and reagents used in the experiments were analytical grade.

The formulation development of rice berry and black garlic spread

A D-optimal mixture design was employed in this study to investigate the effects of three independent components: butter (A) 40%-55%, riceberry rice (B) 5%-15%, and black garlic (C) 5%-15%, for 26 responses using Design-Expert software (Version 6.0.2, Stat-Ease, Minneapolis, MN, USA). Other components in the formulation such as water, parsley, xanthan gum, and locust bean gum were constant at 30%, 2.85%, 0.075%, and 0.075% (w/w), respectively. Nine formulations were prepared and evaluated (Table 1).

The riceberry rice and black garlic spread was produced by dissolving xanthan gum and locust bean gum in water, gradually mixing it with melted butter and riceberry rice flour, followed by black garlic and parsley, and then heated to 60 °C. The spread was packed into cleaned glass bottles and then sterilized at 121°C for 15 minutes. All nine formulations were subjected to analysis of physical properties (colour [L*, a*, b*, and ΔE] and texture attributes [firmness, work of penetration, and adhesiveness]), chemical properties (pH; water activity; antioxidant activity based on the ABTS and DPPH radical scavenging assays; and SAC, 5HMF, and cyanidin contents), and sensory evaluation by 50 consumers (appearance, colour, spreadability, overall aroma, salt taste, butter flavour, garlic flavour, riceberry flavour, sweet taste, viscosity, aftertaste and overall liking using a 9-point hedonic scale). Statistical analysis

was performed to select the optimal formulation. For validation, the optimal formulation was produced; its physical properties, chemical properties, and bioactive compounds were again analysed. In addition, 200 consumers indicated their acceptance and willingness to purchase the formulation.

Table 1 The parameters studied in preparing rice berry and black garlic spread

Treatment	Butter (40-55%)	Riceberry rice (5-15%)	Black garlic (5-15%)
1	47.33	9.83	9.83
2	47.00	15.00	5.00
3	51.00	5.00	11.00
4	40.00	15.00	12.00
5	47.33	9.83	9.83
6	47.00	5.00	15.00
7	40.00	12.00	15.00
8	47.00	15.00	5.00
9	55.00	5.00	7.00

Physical properties

The colour values (L^* , a^* , b^* , and ΔE) of the garlic samples were measured using a MiniScan EZ 4500L spectrophotometer (Hunter Associates Laboratory, Inc., Reston, Virginia, USA) calibrated with black and white porcelain reference plates following the method of Phimolsiripol et al.¹³. Textural attributes (firmness, work of penetration, and adhesiveness) were analysed with the TA.XT. Plus texture analyser (Stable Micro Systems, Godalming, United Kingdom). The method was slightly modified from Lis and Ziajka¹⁴ and involved a penetration test with a 6 mm cylinder probe (P/6, Stable Micro Systems). Test parameters included a penetration depth of 12 mm, an applied load of 0.049 N, and a probe speed of 2.0 mm/s.

Chemical properties

Determination of the SAC, 5HMF, and cyanidin content with high-performance liquid chromatography (HPLC)

The extracts were filtered through 0.45 μm syringe filter before being injected into a high-performance liquid chromatograph with a UV detector (Agilent Technologies, Santa Clara, CA, USA) to analyse the SAC, SAC, and 5HMF content. The HPLC column was a Inertsil ODS-3 (C18 column, 5 μm , 4.6 \times 250 mm, GL Sciences Inc., Tokyo, Japan). An isocratic HPLC method was used for the analysis. For the SAC and 5HMF analysis, the mobile phase was 50 mM phosphate buffer (pH 2.8)/methanol (85:15, v/v)¹⁰; for the cyanidin analysis, the mobile phase was water, methanol, and formic acid (75:18:7 v/v)¹⁵. All reagents were HPLC grade. The mobile phase flow rate was 1 ml min⁻¹, with a sample injection volume of 10 μl and a column temperature of 25 °C. The detection wavelength was 205 nm for SAC detection¹⁶, 285 nm for 5HMF¹⁷, and 510 nm for cyanidin¹⁵.

Antioxidant activities

DPPH radical scavenging activity

The DPPH radical scavenging activity was determined based on the method by Lu et al.¹⁸ with minor modifications. Specifically, 300 μl of garlic extract was mixed with 3000 μl of 0.208 mM DPPH solution. The mixture was incubated in the dark at room temperature for 30 minutes, followed by measurement of its absorbance at 515 nm. Trolox at concentrations

of 0-500 $\mu\text{mol/L}$ was used as the calibrating standard. The antioxidant capacity of the sample is expressed as mg Trolox equivalent antioxidant capacity (TEAC) per 100 g dry weight.

ABTS radical cation scavenging activity

The ABTS radical cation scavenging activity analysis was modified from the method developed by Surin et al.¹⁹. Briefly, the ABTS•+ solution was prepared by mixing 7 mM ABTS solution in distilled water with 2.45 mM potassium persulphate and incubating the mixture in the dark at room temperature for 12-16 hours. Next, the ABTS•+ solution was adjusted with 0.1 M sodium phosphate buffer (pH 7.4) to an initial absorbance of 0.75 ± 0.005 at 734 nm. The reaction was initiated by adding 2900 μl of the ABTS•+ solution to 100 μl of garlic extract. Then, the mixture was incubated in the dark at room temperature for 10 minutes, followed by measurement of its absorbance at 734 nm. Trolox was used as the calibrating standard. The antioxidant capacity of the sample is expressed as mg TEAC per 100 g dry weight.

Statistical analysis

All experiments were conducted in triplicate. Basic statistical parameters such as means and standard errors of the mean were determined using SPSS Statistics 17.0 for Windows (SPSS Inc., Chicago, IL, USA). Differences among the garlic cultivars were determined using one-way ANOVA with Duncan's multiple range post hoc analysis at the 95% confidence level.

Results and Discussion:

Physical properties of the nine riceberry rice and black garlic spread formulations

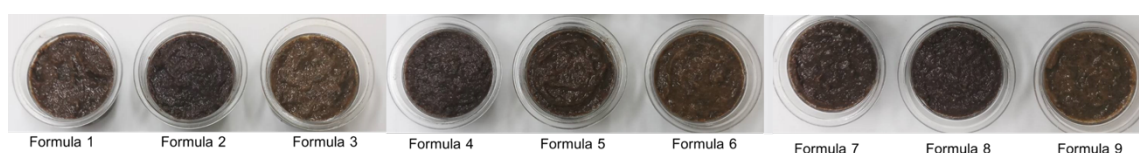


Figure 1 The appearance of the nine riceberry rice and black garlic spread formulations

Figure 1 shows the appearance and colour of the nine riceberry rice and black garlic spreads. The values for L^* , a^* , b^* , and ΔE of the samples ranged from 23.93 to 31.40, from 4.20 to 5.81, from 9.03 to 17.47, and from 26.18 to 36.30, respectively (Table 2). These values are consistent with the dark purple colour of the samples because riceberry rice, a variety obtained from crossbreeding Hom-Nil rice and Khao-Dok-Mali 105 rice²⁰, contains a high anthocyanin content²¹. The texture profile analysis revealed that firmness, work of penetration, and adhesiveness ranged from 10.05 to 20.58 g, from 8.48 to 44.79 g.sec, and from -7.39 to -38.48 g.sec, respectively (Table 2). Formulation 4 with the lowest butter content (40%) and the high riceberry rice content (15%) had the highest firmness, work of penetration, and adhesiveness. Meanwhile, formulation 9 with the highest butter content (55%) and the lowest riceberry rice content (5%) had the lowest firmness, work of penetration, and adhesiveness. These data suggest that the balance between butter and riceberry rice levels significantly impacts the texture characteristics of the final product. Specifically, riceberry rice absorbs water during cooking for gelatinisation. In a more concentrated gel, water molecules appear to have less mobility, as they are closely packed and more extensively hydrogen bonded to relatively large and immobile starch molecules²². This reduced mobility of water molecules affects firmness and adhesiveness, leading to a significant increase in these parameters ($p < 0.05$). As a result, the sample is perceived as less wet or oily and has a lower spread, meaning it is more self-supporting²³.

Table 2 The physical properties of the nine riceberry rice and black garlic spread formulations

Physical properties	Formulations								
	1	2	3	4	5	6	7	8	9
Colour									
L*	26.16 ^b ±0.68	23.93 ^b ±2.67	28.91 ^a ±0.65	24.44 ^b ±2.32	26.16 ^b ±1.90	31.40 ^a ±2.38	25.83 ^b ±2.49	24.41 ^b ±2.01	30.85 ^a ±1.59
a*	5.81 ^a ±0.19	5.55 ^{ab} ±0.30	5.17 ^{bc} ±0.10	5.55 ^{ab} ±0.31	5.37 ^{ab} ±0.38	4.82 ^c ±0.47	5.67 ^a ±0.49	5.59 ^{ab} ±0.22	4.20 ^d ±0.13
b*	13.31 ^c ±0.17	9.03 ^c ±0.63	16.96 ^a ±0.46	9.28 ^c ±0.42	13.47 ^c ±0.45	17.47 ^a ±0.92	12.41 ^d ±0.76	9.24 ^c ±0.68	16.00 ^b ±0.44
ΔE	29.93 ^b ±0.62	26.18 ^c ±2.59	33.92 ^a ±0.74	26.74 ^c ±2.18	29.93 ^b ±1.70	36.30 ^a ±1.53	29.24 ^b ±2.39	26.70 ^c ±2.01	35.02 ^a ±1.20
Texture Profile Analysis									
Firmness (g)	13.08 ^d ±0.86	17.96 ^b ±0.68	11.57 ^c ±0.86	20.58 ^a ±1.22	12.83 ^d ±1.20	10.59 ^e ±0.71	13.40 ^d ±0.53	15.18 ^c ±0.44	10.05 ^f ±0.51
Work of Penetration (g.sec)	19.07 ^d ±2.34	30.36 ^b ±1.73	13.68 ^c ±2.04	44.79 ^a ±1.93	16.94 ^d ±1.21	13.41 ^c ±0.94	23.42 ^c ±2.54	22.35 ^c ±2.77	8.48 ^f ±1.51
Adhesiveness (g.sec)	-21.13 ^c ±1.82	-24.68 ^b ±2.54	-13.20 ^c ±1.90	-38.48 ^a ±1.77	-17.50 ^d ±1.74	-12.90 ^c ±0.86	-20.69 ^c ±2.30	-20.76 ^c ±2.42	-7.39 ^f ±1.65

Different superscripts (^{a-f}) within the same row indicate significant differences ($p \leq 0.05$).

Table 3 The chemical properties of the nine riceberry rice and black garlic spread formulations

Chemical properties	Formulations								
	1	2	3	4	5	6	7	8	9
pH	5.23 ^d ±0.01	5.42 ^a ±0.01	5.15 ^c ±0.01	5.30 ^c ±0.01	5.20 ^c ±0.01	4.99 ^b ±0.01	5.09 ^e ±0.02	5.33 ^b ±0.03	5.23 ^d ±0.01
Water activity	0.981 ^{ab} ±0.001	0.982 ^{ab} ±0.007	0.986 ^a ±0.003	0.982 ^{ab} ±0.005	0.986 ^a ±0.002	0.983 ^{ab} ±0.002	0.979 ^b ±0.002	0.984 ^{ab} ±0.002	0.985 ^{ab} ±0.001
Moisture content (%)	42.44 ^c ±0.47	39.95 ^d ±1.44	44.83 ^{ab} ±0.47	43.53 ^{bc} ±0.64	45.87 ^a ±0.89	45.98 ^a ±0.43	43.13 ^c ±1.13	46.26 ^a ±0.60	41.02 ^d ±0.18
Bioactive compounds (mg/100g sample)									
SAC	4.91 ^c ±0.12	3.94 ^f ±0.12	6.57 ^a ±0.16	5.58 ^d ±0.14	3.58 ^e ±0.09	6.33 ^b ±0.02	6.06 ^c ±0.01	3.34 ^h ±0.02	5.01 ^c ±0.11
SHMF	27.52 ^b ±0.64	14.19 ^e ±0.32	28.01 ^{ab} ±0.12	18.52 ^a ±0.35	27.54 ^b ±0.11	26.54 ^c ±0.17	28.76 ^a ±0.52	15.65 ^f ±0.73	25.18 ^d ±0.98
Cyanidin	1.413 ^d ±0.004	1.511 ^c ±0.010	1.380 ^f ±0.002	1.584 ^a ±0.008	1.406 ^{de} ±0.003	1.396 ^e ±0.000	1.341 ^e ±0.005	1.562 ^b ±0.014	1.284 ^h ±0.001
Antioxidant activity (mg Trolox/100g sample)									
ABTS	847.59 ^a ±55.51	724.03 ^b ±5.10	740.53 ^b ±10.06	864.38 ^a ±7.34	856.14 ^a ±14.93	842.79 ^a ±17.72	860.36 ^a ±21.76	747.73 ^b ±10.07	649.06 ^c ±74.74
DPPH	148.20 ^b ±0.94	155.21 ^b ±7.00	123.23 ^c ±0.51	188.50 ^a ±2.99	149.77 ^b ±7.95	149.63 ^b ±3.26	176.56 ^a ±8.40	155.80 ^b ±4.11	103.82 ^d ±9.41

Different superscripts (^{a-h}) within the same row indicate significant differences ($p \leq 0.05$).

Table 4 The sensory evaluation of the nine riceberry rice and black garlic spread formulations

Attribute	Formulations								
	1	2	3	4	5	6	7	8	9
Appearance	6.34 ^a ±1.55	4.82 ^d ±1.83	4.92 ^{cd} ±1.79	5.64 ^{abc} ±1.80	4.70 ^d ±1.81	4.80 ^d ±1.69	5.86 ^{ab} ±1.74	5.18 ^{bcd} ±1.61	4.52 ^d ±1.91
Colour	5.76 ^a ±1.66	5.80 ^a ±1.69	4.82 ^b ±1.81	5.44 ^{ab} ±1.63	5.68 ^a ±1.67	5.16 ^{ab} ±1.66	5.64 ^a ±1.66	5.30 ^{ab} ±1.47	5.04 ^{ab} ±1.74
Spreadability	6.68 ^{ab} ±1.17	5.70 ^c ±1.84	6.66 ^{ab} ±1.45	5.68 ^c ±1.67	6.64 ^{ab} ±1.38	6.50 ^{ab} ±1.56	6.74 ^a ±1.52	6.04 ^{bc} ±1.31	6.42 ^{ab} ±1.64
Overall aroma	6.06 ^{ab} ±1.52	5.44 ^{bc} ±1.43	6.10 ^a ±1.59	5.94 ^{abc} ±1.15	6.08 ^{ab} ±1.40	6.06 ^{ab} ±1.17	5.66 ^{abc} ±1.86	5.36 ^c ±1.54	6.20 ^a ±1.21
Saltness	5.90 ^a ±1.34	4.96 ^b ±1.41	5.84 ^a ±1.52	5.30 ^{ab} ±1.47	5.48 ^{ab} ±1.67	5.88 ^a ±1.48	5.24 ^{ab} ±1.86	5.28 ^{ab} ±1.37	5.56 ^{ab} ±1.73
Butter flavour	5.60 ^{ab} ±1.62	5.14 ^{bc} ±1.43	5.92 ^a ±1.41	5.18 ^{bc} ±1.45	5.74 ^{ab} ±1.52	6.04 ^a ±1.29	5.24 ^{bc} ±1.71	4.82 ^c ±1.52	5.94 ^a ±1.49
Garlic flavour	5.72 ^{bc} ±1.65	5.06 ^d ±1.71	6.30 ^{ab} ±1.58	5.28 ^{cd} ±1.31	5.82 ^{abc} ±1.62	6.42 ^a ±1.37	5.84 ^{abc} ±1.58	5.22 ^{cd} ±1.49	6.12 ^{ab} ±1.41
Riceberry flavour	5.74 ^{ab} ±1.24	6.02 ^a ±1.39	5.52 ^{ab} ±1.01	5.90 ^a ±1.07	5.80 ^{ab} ±1.36	5.28 ^b ±1.01	5.86 ^a ±1.23	6.04 ^a ±1.43	5.60 ^{ab} ±1.37
Sweetness	5.36 ^{abc} ±1.57	4.66 ^d ±1.33	5.80 ^a ±1.64	5.02 ^{bcd} ±1.39	5.24 ^{abcd} ±1.46	5.60 ^{ab} ±1.43	5.02 ^{bcd} ±1.57	4.80 ^{cd} ±1.34	5.86 ^a ±1.65
Viscosity	6.22 ^a ±1.34	5.24 ^b ±1.38	6.04 ^a ±1.37	5.38 ^b ±1.38	6.10 ^a ±1.18	6.04 ^a ±1.41	6.06 ^a ±1.25	5.34 ^b ±1.45	6.00 ^a ±1.29
Aftertaste	5.76 ^{abc} ±1.45	5.22 ^c ±1.46	6.06 ^a ±1.30	5.32 ^{bc} ±1.42	5.76 ^{bc} ±1.27	5.80 ^{abc} ±1.51	5.88 ^{ab} ±1.55	5.36 ^{bc} ±1.56	6.14 ^a ±1.23
Overall liking	6.02 ^{ab} ±1.32	5.20 ^c ±1.37	6.22 ^a ±1.17	5.30 ^c ±1.31	5.58 ^{bc} ±1.49	6.00 ^{ab} ±1.41	6.00 ^{ab} ±1.59	5.30 ^c ±1.37	5.62 ^{bc} ±0.83

Different superscripts (^{a-d}) within the same row indicate significant differences ($p \leq 0.05$).

Chemical properties of the nine riceberry rice and black garlic spread formulations

The pH and water activity of the samples ranged from 4.99 to 5.42 and from 0.979 to 0.986, respectively (Table 3). The formulations with 15% black garlic exhibited the lowest pH, which is attributed to the acidity present in black garlic resulting from the Maillard reaction products¹⁰. Formulation 3 had the highest SAC concentration at 6.57 mg/100 g of sample, followed by formulation 6 (6.33 mg/100 g) and formulation 7 (6.06 mg/100 g). Formulation 7 had the highest 5HMF content at approximately 28.76 mg/100 g, which was not significantly different ($p > 0.05$) from formulation 3 (28.01 mg/100 g). Furthermore, formulation 4 had the highest cyanidin content at approximately 1.584 mg/100 g, followed closely by the formulation 8 (1.562 mg/100 g). Both SAC and 5HMF are found in black garlic¹⁰, while cyanidin is found in riceberry rice²¹; these compounds contribute to antioxidant activity. Formulations 1, 4, 5, 6, and 7 demonstrated the highest antioxidant activity among the tested formulations, with values ranging from 842 to 864 mg Trolox/100 g of sample according to the ABTS radical scavenging assay. Formulations 4 and 7 also exhibited the highest antioxidant activity based on the DPPH radical scavenging assay, registering values of 188 and 176 mg Trolox/100 g, respectively (Table 3).

Sensory evaluation of the nine riceberry rice and black garlic spread formulations

Table 4 presents the sensory evaluation results for the nine riceberry rice and black garlic spread formulations. Formulation 3 received the highest overall liking score of 6.22, showing no significant difference from formulations 1, 6, and 7, which scored 6.02, 6.00, and 6.00, respectively, in overall liking. Moreover, these four formulations exhibited no significant differences ($p \leq 0.05$) in spreadability, overall aroma, salt taste, viscosity, and aftertaste. Formulation 3 also scored the highest in butter flavour, garlic flavour, and sweet taste, with scores of 5.92, 6.30, and 5.80, respectively. Although the riceberry flavour score of formulation 3 (5.52) was lower than that of the formulation 1 (5.74) and formulation 7 (5.86), the differences were not significant ($p \leq 0.05$). However, the appearance and colour scores of formulation 3 were lower than those of formulations 1 and 7, which exhibited the highest scores in these attributes.

Regression analysis and optimisation of the riceberry rice and black garlic spread

The mixture regression models, as adjusted and presented in Table 5, were significant ($p \leq 0.05$) for a range of variables, including L^* , ΔE , firmness, work of penetration, adhesiveness, pH, antioxidant activity based on the ABTS radical scavenging assay, antioxidant activity based on the DPPH radical scavenging assay, the SAC content, the 5HMF content, the cyanidin content, overall aroma, butter flavour, garlic flavour, riceberry rice flavour, sweetness, viscosity, aftertaste, and overall liking of the formulation. As indicated in Table 5, the variable responses exhibited a strong fit to the models, with high determination coefficients ($R^2 > 0.7000$).

In the contour plot illustrating physical property responses (Figure 2), a clear correlation emerged, indicating that firmness, work of penetration, and adhesiveness were directly proportional to the percentage of riceberry rice but inversely proportional to the percentage of butter. As discussed previously, the significant increase in firmness and adhesiveness observed in riceberry rice can be attributed to its impact on the reduced mobility of water molecules during gelatinisation. This finding aligns with the study by Fradinho et al.²², who reported that a higher rice flour concentration leads to an increased gel structure due to the formation of more gel linkages during cooking. In support of this view, Muego et al.²⁴, reported a negative correlation between the maximum force during penetration and wetness/spread, and a positive correlation with hardness. In the context of riceberry spread samples, this implies that higher force values were recorded for samples rated low for

wetness and spreadability but high for hardness. The firmness, work of penetration, and adhesiveness of butter depend on various factors such as the composition, storage temperature, storage time, and manufacturing conditions²⁵. Generally, butter exhibits a stable structure but poor spreadability at refrigeration temperatures. In contrast, it shows poor structural stability and may experience issues such as oiling off and moisture migration at room temperature²⁵, resulting in a decrease in these properties as the butter content increases.

Table 5 Regression analysis of riceberry rice and black garlic spread

Variable	Regression equations	P- Value	R ²
L*	$1.22*A + 12.79*B + 11.78*C - 0.31*A*B - 0.27*A*C - 1.29*B*C + 0.03*A*B*C$	0.0055	0.9982
ΔE	$1.11*A + 9.44*B + 9.40*C - 0.23*A*B - 0.21*A*C - 0.98*B*C + 0.02*A*B*C$	0.0035	0.9988
Firmness	$0.09*A + 0.81*B + 0.17*C$	0.0105	0.7808
Work of Penetration	$-0.17*A + 2.15*B + 0.74*C$	0.0126	0.7675
Adhesiveness	$0.12*A - 1.781*B - 0.71*C$	0.0105	0.7808
pH	$0.08*A + 0.09*B + 0.06*C$	0.0010	0.8993
ABTS	$16.99*A + 269.61*B + 199.53*C - 6.09*A*B - 4.37*A*C - 35.05*B*C + 0.81*A*B*C$	0.0192	0.9936
DPPH	$2.89*A + 63.36*B + 39.98*C - 1.32*A*B - 0.83*A*C - 5.84*B*C + 0.12*A*B*C$	0.0008	0.9997
SAC	$4.11E-003*A + 0.72*B - 0.48*C - 0.01*A*B + 0.02*A*C$	< 0.0001	0.9970
5HMF	$-0.19*A + 0.20*B - 7.88*C + 0.20*A*C + 0.17*B*C$	0.0006	0.9860
Cyanidin	$0.02*A + 0.04*B + 0.02*C$	0.0041	0.8393
Overall aroma	$0.18*A + 1.95*B + 0.95*C - 0.05*A*B - 0.02*A*C - 0.19*B*C + 4.33E-003*A*B*C$	0.0132	0.9956
Butter flavour	$0.09*A + 3.66E-003*B + 0.10*C$	0.0007	0.9096
Garlic flavour	$0.09*A - 7.72E-005*B + 0.13*C$	< 0.0001	0.9820
Riceberry rice flavour	$0.04*A - 0.91*B - 0.57*C + 0.02*A*B + 0.02*A*C + 0.10*B*C - 2.01E-003*A*B*C$	0.0122	0.9959
Sweetness	$0.09*A - 1.02E-003*B + 0.09*C$	0.0005	0.9208
Viscosity	$0.07*A - 0.89*B + 0.07*C + 0.02*A*B + 0.02*B*C$	0.0004	0.9878
Aftertaste	$0.09*A + 0.03*B + 0.10*C$	0.0099	0.7850
Overall liking	$0.09*A + 0.04*B + 0.13*C$	0.0240	0.7114

Note: A = Butter, B = Riceberry rice and C = Black garlic.

Figure 3 highlights a clear inverse correlation between pH and the percentage of black garlic. This is due to the production of organic acids, such as acetic acid, during the thermal or ageing processes of black garlic production in browning reactions²⁶. The presence of these acids is closely tied to the sour taste of black garlic. Furthermore, 5HMF is produced in browning reactions. This compound is derived from 1,2-enolisation, dehydration, and cyclisation reactions of hexose sugars, and the degradation of Amadori products during the Maillard reaction under acidic conditions²⁷. Furthermore, the heat treatment in black garlic production increases SAC due to γ -glutamyl-S-allylcysteine catabolism^{10,28}. Therefore, the formulations with a high black garlic content had a low pH and elevated levels of SAC and 5HMF. Additionally, they exhibited high antioxidant activity, which is attributed to SAC and 5HMF and other Maillard reaction products and various compounds containing or not containing sulphur in black garlic. Moreover, the cyanidin content showed direct proportionality to the percentage of riceberry rice. As a result, samples with high levels of black garlic and riceberry rice, namely formulations 4 and 7, exhibited the highest antioxidant activity.

Regarding the effects of processing components on sensory properties (Figure 4), both butter and black garlic contributed positively to their respective flavours. In contrast, riceberry rice had a negative effect on the butter and black garlic flavours. Conversely, riceberry rice enhanced its own flavour positively, while butter and black garlic had a negative influence on the riceberry rice flavour. This results may be attributed to the presence of dimethyl trisulphide and acetic acid in butter, which impart mature cheese-like and vinegar-like flavours²⁹, a characteristic also found in black garlic³⁰. The common volatile compounds in butter and black garlic could potentially support their flavours. On the other hand, the main volatile compounds of riceberry rice, including vanillin (vanilla note), guaiacol (smoky note), 4-vinylguaiacol (clove, spicy, smoky note), and p-hydroxyphenylbutan-2-one (sweet, candy, fruity, berry note)³¹, differ from those in butter and black garlic. Therefore, it is reasonable to anticipate that samples with a high level of

riceberry rice may present a superior riceberry aroma, resulting in higher scores for the riceberry flavour. Conversely, samples with a low level of riceberry rice or a high level of butter or black garlic may receive lower scores for the riceberry flavour. The decrease in the level of riceberry rice also resulted in higher acceptance ratings for sweetness, viscosity, aftertaste, and overall liking of riceberry and black garlic spread.

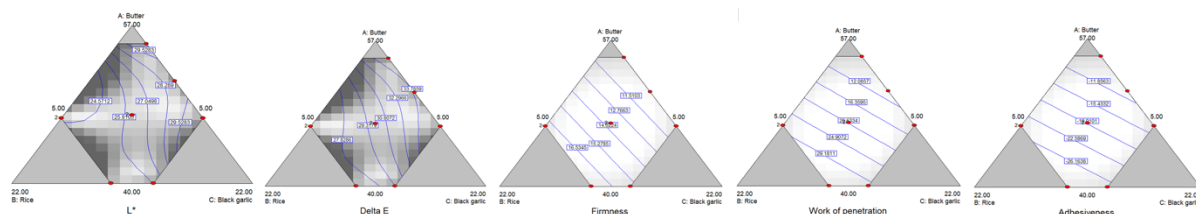


Figure 2 Contour plot of the effects of processing components on physical properties: L^* , ΔE , firmness, work of penetration, and adhesiveness

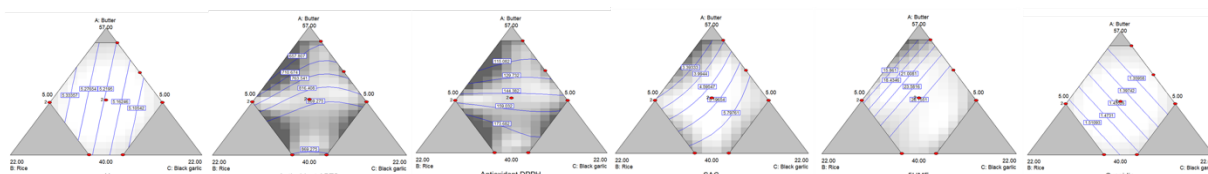


Figure 3 Contour plot of the effects of processing components on chemical properties: pH, antioxidant activity based on the ABTS radical scavenging assay, antioxidant activity based on the DPPH radical scavenging assay, the SAC content, the 5HMF content, and the cyanidin content

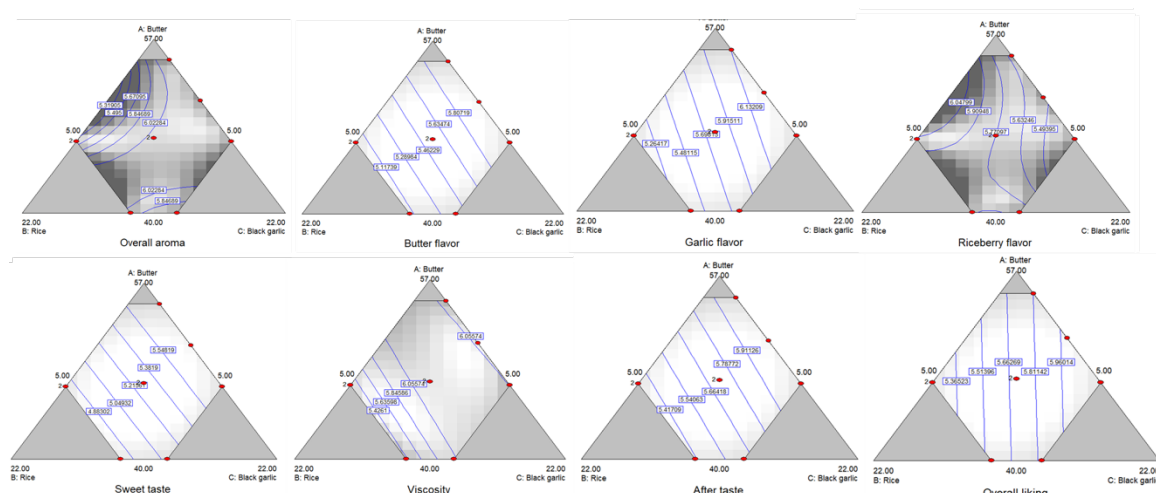


Figure 4 Contour plot of the effects of processing components on sensory properties: overall aroma, butter flavour, garlic flavour, riceberry flavour, sweet taste, viscosity, aftertaste, and overall liking

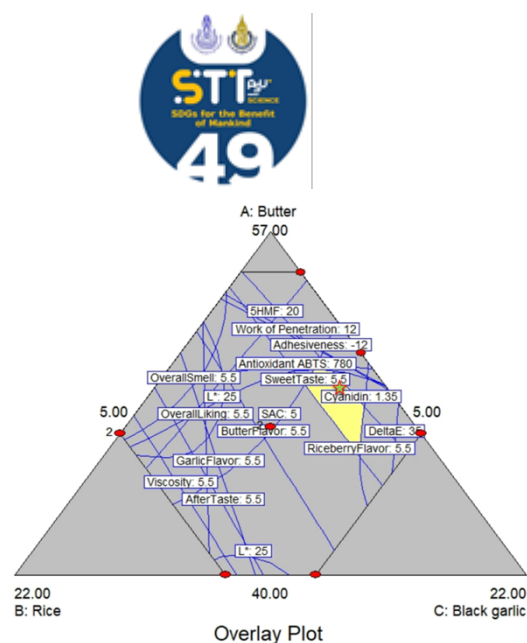


Figure 5 Overlay plot of riceberry rice and black garlic spread

To achieve the optimal formulation with high bioactive compound content, antioxidant activity, and consumer satisfaction, it is recommended to use the following proportions: 49.08% butter, 6.47% riceberry rice, and 11.45% black garlic. This optimal point is represented by a star symbol on the overlay plot in Figure 5, while the yellow-shaded zone represents all suitable solutions provided by the software. Regarding prediction accuracy, the percentage errors between the predicted and observed values were generally less than 10%, except for L* and antioxidant activity measured by DPPH radical scavenging (Table 6). This optimal formulation received an 86% acceptance rate among consumers, and 52% indicated they would purchase the produce (Table 6).

Although the final product received a very high overall acceptance rate, the willingness to purchase was relatively low. The scores for the various sensory attributes did not exceed 7 points; a highly acceptable sensory quality should have a mean liking score of ≥ 7 on a 9-point scale³². Therefore, there is a need to refine the final product in the future to enhance consumer satisfaction.

Table 6 The predicted and the observed values of the final product

Attribute	Predicted value	Observed value	Percentage error
L*	28.28	24.83	13.89
ΔE	32.94	31.68	3.97
pH	5.13	5.06	1.32
Firmness	11.36	11.69	2.81
Work of Penetration	14.13	14.09	0.30
Adhesiveness	-13.81	-13.24	4.28
Antioxidant ABTS	809.83	846.52	4.33
Antioxidant DPPH	136.31	153.55	11.23
SAC	5.57	6.07	8.24
SHMF	27.51	29.65	7.21
Cyanidin	1.35	1.40	3.65
Overall aroma	6.13	6.32	3.01
Butter flavour	5.87	6.48	9.41
Garlic flavour	6.16	6.49	5.08
Riceberry flavour	5.56	5.75	3.30
Sweet taste	5.61	5.95	5.71
Viscosity	6.17	6.82	9.53
Aftertaste	5.95	6.46	7.89
Overall liking	5.94	6.42	7.48
Consumer acceptance	accepted		86%
	not accepted		14%
Purchase decision	will buy		52%
	will not buy		48%

Conclusion:

This study successfully developed a reduced-fat healthy spread using riceberry rice, black garlic, and butter. While the formulation received over 80% consumer acceptance, only 52% indicated they would be willing to purchase the product. Future improvements should focus on enhancing the flavour and taste to increase consumer liking and to increase the willingness to purchase. These findings highlight the demand for healthier food options and emphasise the need for ongoing innovation to meet consumer preferences. The study contributes to the development of a healthier food market that caters to health-conscious consumers seeking nutritious and flavourful spreads. It also promotes the development of agricultural products.

Acknowledgements:

Authors would like to thank the Faculty of Agro-Industry, Chiang Mai University for operation and providing the facilities of the scientific laboratory and equipment. This work was supported by the Royal Golden Jubilee (RGJ) Ph.D. Program. (Grant No. PHD/0053/2560).

References:

1. Siró, I., Kápolna, E., Kápolna, B. & Lugasi, A. *Appetite*. 2008;51:456-467.
2. Fearon, A. M. *Dairy Ingredients Food Process*. 2011;199-223.
3. Judd, J. T. *et al. Am. J. Clin. Nutr.* 1998;68:768-777.
4. Rungrat, T. & Poothab, C. *Agr. Nat. Resour.* 2019;53:292-297.
5. Mbanjo, E. G. N. *et al. Front. Genet.* 2020;11:229.
6. Suttiarporn, P. *et al. Nutrients*. 2015;7:1672-1687.
7. Anuyahong, T., Chusak, C., Thilavech, T. & Adisakwattana, S. *Nutrients*. 2020;12:2930.
8. Leardkamolkarn, V. *et al. Food Chem.* 2011;125:978-985.
9. Najman, K., Sadowska, A. & Hallmann, E. *Appl. Sci.* 2020;10:8638.
10. Pakakaew, P. *et al. Sci. Rep.* 2022;12:11493.
11. González-Ramírez, P. *et al. Food Biosci.* 2022;48:101827.
12. Ahmed, T. & Wang, C.-K. *Molecules*. 2021;26:5028.
13. Phimolsiripol, Y. *et al. Foods*. 2021;10:1241.
14. Lis, A., Staniewski, B. & Ziajka, J. *International Journal of Food Properties*. 2021;24:1744-1757.
15. Salee, N. *et al. Food Sci. Technol.* 2023;43:e123022.
16. Ichikawa, M. *et al. J. Agric. Food Chem.* 2006;54:1535-1540.
17. Kalábová, L. & Večerek, V. *J. Food Nutr. Res.* 2006;45:34-38.
18. Lu, X. *et al. Food Chem.* 2011;129:637-644.
19. Surin, S. *et al. Int. J. Food Sci. Technol.* 2018;53:994-1004.
20. Pensri, J., Supot, D. & Wananya, T. *GMSARN Int. J.* 2021;15:21-26.



21. Ngamdee, P., Jamkrajang, S. & Yankin, S. RMUTP sci J. 2020;14:45-56.
22. Fradinho, P., Sousa, I. & Raymundo, A. Int. J. Food Sci. Technol. 2019;54:1109-1120.
23. Tanti, R., Barbut, S. & Marangoni, A. G. Food Hydrocolloids. 2016;61:399-408.
24. Muego, K., Resurreccion, A. & Hung, Y. C. J. Texture Stud. 1990;21:61-74.
25. Wright, A., Scanlon, M., Hartel, R. & Marangoni, A. J. Food Sci. 2001;66:1056-1071.
26. Liang, T. *et al.* J. Agric. Food Chem. 2015;63:683-691.
27. Chen, Y. *et al.* Ind. Crops Prod. 2019;135:146-152.
28. Bae, S. E. *et al.* LWT-Food Sci. Technol. 2014;55:397-402.
29. Cheng, Z. *et al.* Int. J. Dairy Technol. 2022;75:761-790.
30. Kilic-Buyukkurt, O. *et al.* Heliyon. 2023;9:e19056.
31. Kullananant, N., Chaiseri, S. & Lorjaroenphon, Y. J. Food Sci. 2020;85:1764-1771.
32. Samakradhamrongthai, R. S., Jannu, T. & Renaldi, G. Heliyon. 2021;7:e07776.



The antihyperglycemic effects of microencapsulated Kluai Tani (*Musa balbisiana*) fruit extract in the instant drink powder

A. Tohteb¹, P. Boonyanupong¹, T. Kaewmanee¹, T. Utaipan^{2*}

¹ Department of Food Science and Nutrition, Faculty of Science and Technology, Prince of Songkla University, Pattani Campus, Pattani 94000, Thailand.

² Department of Science, Faculty of Science and Technology, Prince of Songkla University, Pattani Campus, Pattani 94000, Thailand.

*E-mail: tanyarath.u@psu.ac.th

Abstract:

Musa balbisiana fruit, commonly known as "Kluai Tani", is a wild banana endemic to Eastern South Asia that is enriched with phytochemical and nutraceutical content with anti-hyperglycemic properties. The present study aimed to evaluate the *in vitro* anti-hyperglycemic potential of microencapsules from *M. balbisiana* extract (MBM) and the developed instant drink powder containing MBM (D-MBM). Herein, total phenolic content was investigated based on the Folin-Ciocalteu method. The activities of α -glucosidase and dipeptidyl peptidase-4 (DPP-4) were evaluated by enzymatic inhibitory assays. The predicted glycemic index (pGI) of carbohydrates relative to glucose was calculated using the incremental area under the curve method. The result showed that MBM had a total phenolic content of 23.11 ± 1.28 mg GAE/g dried powder. MBM effectively inhibited α -glucosidase and DPP-4 activities with an IC_{50} value of 1.84 ± 0.005 μ g/ml and $41.20 \pm 2.22\%$, respectively. The D-MBM containing 10% w/w of MBM showed a pGI value of 75.25 ± 0.05 after 120 minutes of digestion, while a commercial product had a pGI value of 99.96 ± 0.04 . As a result, our study suggests that *M. balbisiana* microencapsulate has a low glycemic index and also has the ability to prevent hyperglycemia by inhibiting intestinal enzymes related to blood glucose control. In the future, microencapsulated *M. balbisiana* extract may be used as a functional ingredient in meal replacement products to resolve hyperglycemia.

Introduction:

Hyperglycemia is a condition characterized by abnormally elevated blood sugar levels. It is greater than 100 mg/dL when fasting and greater than 140 mg/dL after 2 hours of postprandial¹. In a healthy individual, this condition is associated with an elevated chance of developing diabetes. In diabetes, hyperglycemia occurs when there is insufficient insulin action to keep blood glucose levels within the normal range. This can cause a wide range of symptoms and long-term complications². Therefore, blood glucose control is one of the most significant treatments for diabetes. The primary component of expenditure for the treatment of diabetes is pharmaceutical medications. According to a study in 2014, it was shown that the unit cost of diabetes mellitus in patients receiving care at a general hospital in Thailand exceeded 2 million baht³. The mean overall expenditure per patient during the initial year exceeded 22,000 baht⁴. The data indicated that the expenses associated with diabetes are increasing annually.

In recent years, there has been a growing use of medicinal plants due to their potential for cost savings and the prevention of side effects from drug-induced hypoglycemia². Green bananas (*Musa* spp.), particularly *Musa balbisiana* (known as "Kluai Tani" in Thai), are an important plant native in many Asian countries, including Thailand. It has been demonstrated that various parts of this plant, including the fruit, inflorescence, and leaf, possess biological activities due to their phytochemical contents and secondary metabolites such as polyphenols,

flavonoids, tannins, monoterpenoids, sesquiterpenoids, quinones, and saponins⁵. According to research reports, extracts derived from various components of *M. balbisiana* exhibit anti-diabetic benefits *in vitro* and *in vivo*. In an *in vitro* model, *M. balbisiana* seed extracts have been demonstrated to inhibit α -amylase and α -glucosidase enzymes with IC₅₀ values of 36.67 and 100.61 μ g/ml, respectively⁶. In an *in vivo* model, inflorescence extracts of *M. balbisiana* have the potential to reduce fasting blood glucose and glycated hemoglobin levels by restoring serum insulin in Wistar rats⁷. Fruit and peel extracts of *M. balbisiana* have the potential to lower serum glucose, urea, uric acid, creatinine, triglyceride and total cholesterol⁸. These extracts have been documented to inhibit specific enzymes, resulting in the delayed absorption of glucose. This process aids in preventing elevated blood glucose levels, thereby contributing to the regulation of blood glucose and subsequently reducing postprandial hyperglycemia⁹.

As a result, this study aimed to evaluate the *in vitro* anti-hyperglycemic potential of microencapsules from *M. balbisiana* extract (MBM) by enzyme inhibition of α -glucosidase and dipeptidyl peptidase-4 (DPP-4). Furthermore, a newly instant drink powder that contained MBM (D-MBM) was formulated to determine its glycemic index in order to develop a prototype of meal replacement product exerting anti-hyperglycemia properties.

Methodology:

Materials

Green bananas (*Musa balbisiana*) in the 1st-2nd stage of maturity (100-110 days after the blossoms appeared) were harvested from Nakhon Si Thammarat in 2021. The whole fruit (peel, pulp, and seed) of bananas were washed, sliced, and dried at 55 ± 1 °C until the moisture content was less than 10%. The dried slices were ground and glided through a 1.0 mm. steel mesh. The banana powder was stored in an aluminum foil bag at cold temperature until extraction. All isolate protein powders were purchased from Unify chemical co. Ltd. and Food ingredient technology co. Ltd. Non-dairy creamer powder was purchased from King rice oil group co. Ltd. and Dietary fiber was purchased from Krung thep chemi co. Ltd.

Preparation of microencapsulate from *M. balbisiana* extract (MBM)

The banana powder was dissolved in distillation water and extracted by Ultrasonic assistant (Model. BXMZDX51-T, 20 kHz, 100 W) at a power of 150-200 watts for 60 minutes. After extraction, the solution was microencapsulated through the spray-drying technique (spray dryer, mobile Minor/GEA Niro S/N, China). The feed flow of the solution to be dried was 5 ml/min, and the inlet and outlet air temperatures were 140 °C and 80 °C, respectively. After spray drying, powders were recovered and stored in an aluminum foil bag at a cold temperature until evaluation.

Preparation of instant drink powders containing MBM (D-MBM)

Three formulations were prepared for the development of instant drink powder (D-MBM), as shown in Table 1. The composition of each formula consisted of the same fundamental ingredients with varying amounts of MBM. The D-MBM formula 1 (F1), formula 2 (F2), and formula 3 (F3) included 2%, 5%, and 10% weight/weight (w/w) of MBM, respectively. The components were thoroughly combined and kept in an aluminum foil bag. The D-MBM samples were stored in a refrigerator until they were investigated.

Table 1. Formulas of instant drink powders containing MBM (D-MBM)

Ingredients	Formula			
	Control	F1	F2	F3
Protein (Soy protein isolate, Pea protein and Sodium caseinate, ratio 2:2:1) (%)	42.9	42.9	42.9	42.9
Fat (rice bran oil non-dairy rice bran oil) (%)	30	30	30	30
Carbohydrate (unripe banana flour) (%)	15.6	15.6	15.6	15.6
Dietary fiber (%)	6.5	6.5	6.5	6.5
Cocoa powder (%)	5	5	5	5
MBM (%)	-	2	5	10

Total phenolic content

The total phenolic content (TPC) was measured using Folin-Ciocalteu's colorimetric assay¹⁰. MBM was dissolved in distillation water and mixed by vortex mixer. The solution was centrifuged at 5000 rpm for 15 minutes. After that, 250 µl of supernatant was mixed with 1250 µl of 10% Folin-Ciocalteu reagent. 1000 µl of 7.5% Na₂CO₃ was added to the mixture and incubated at room temperature for 60 minutes. The absorbance of the solution was determined at 765 nm. The same method was employed to determine the TPC for D-MBM. The total phenolic content (TPC) was calculated using a standard gallic acid equivalent (GAE) curve.

α-Glucosidase inhibitory assay

The effect of the MBM on α-glucosidase inhibitory activity was determined following an enzyme inhibition assay with minor modification¹¹. 20 µg of MBM was dissolved in 0.5 ml 100% DMSO and sonicated for 1-2 minutes. 50 µl of 50 mM phosphate buffer (pH 6.9), 50 µl of α-glucosidase (0.57 unit/ml) and MBM solution was added in 96-well plate and incubated at 37°C for 10 minutes. After that, 50 µl of 5 mM p-nitro phenyl glucopyranoside (p-NPG) was added to the mixture and incubated at 37°C for 20 minutes. The absorbance of the solution was determined at 405 nm. Acarbose was used as a positive control (concentration range 200 µg/ml to 3200 µg/ml). The α-glucosidase inhibitory activity was calculated and expressed as the percentage of α-glucosidase inhibition.

$$\% \alpha - \text{Glucosidase Inhibition} = \left\{ 1 - \frac{Abs_{sample} - Abs_{sample blank}}{Abs_{control} - Abs_{control blank}} \right\} \times 100$$

Dipeptidyl peptidase-4 (DPP-4) inhibitory assay

The effect of the MBM on DPP-4 inhibition activity was determined following an enzyme inhibition assay with minor modification¹². 20 µg of MBM was dissolved in 0.5 ml 100% DMSO and sonicated for 1-2 minutes then the solution was adjusted with 50 mM Tris-maleate buffer (pH 8.0) to obtain final concentration of 200 µg/ml. 20 µl of DPP-4 (0.05 unit/ml) and 40 µl of sample solution were added in 96-well plate and incubated at 37°C for 10 minutes. After that, 100 µl of 0.2 mM GP-p-NA substrate was added in mixture and incubated at 37°C for 30 minutes. The reaction was stopped with 30 µl of 25% CH₃COOH. Diprotin A was used as a positive control. The absorbance of the solution was determined at 405 nm. The DPP-4 inhibitory activity was calculated and expressed as the percentage of DPP-4 inhibition.



$$\%DPP - 4 \text{ Inhibition} = \left\{ 1 - \frac{Abs_{sample} - Abs_{sample \text{ blank}}}{Abs_{control} - Abs_{control \text{ blank}}} \right\} \times 100$$

In vitro starch hydrolysis and predicted glycemic index (pGI)

D-MBM, MBM, white bread, and a commercial product were subjected to the examination of starch hydrolysis and pGI as follows:

Total starch determination

Total starch content was modified and determined followed Goñi¹³. 50 mg of DMBM was dispersed in 6 ml of 1 M NaHCO₃ and incubated in a shaking water bath at 37 °C for 30 minutes. After that, 3 ml of 50 mM Sodium maleate buffer and 1.2 ml of PAA/AMG was added and incubated at 60 °C for 120 minutes. Glucose content was determined using D-Glucose Assay Kit (Megazyme, Ireland). The absorbance of the sample was read at 510 nm using a UV-vis spectrophotometer. Total starch was calculated as mg of glucose using a conversion factor.

Starch digestibility determination

Starch digestibility was modified and determined according to the method proposed by Goñi¹³. 100 mg of DMBM was dispersed in 1.2 ml of distillation water and incubated in a shaking water bath at 40 °C for 5 minutes. 0.1 ml 10% α-amylase was added and incubated for 1 minute. Then, 1.5 ml of HCl-KCl buffer (pH 1.5) and 1 ml of 10% Pepsin in HCl-KCl buffer were added into the mixture, and incubated in a shaking water bath at 40 °C for 60 minutes. 32 µl of 1 M NaHCO₃, 5 ml of 10% bile salt, 5 ml of 50 mM Sodium Maleate buffer (pH 6), 1.8 ml of PAA/AMG and 0.4 ml of distillation water were added to the mixture, and incubated in a shaking water bath at 40 °C. A 0.5 ml aliquot sample was taken at every 30, 60, 90, 120, 150, 180 and 240 minutes into 2 ml of absolute ethanol for enzyme inactivation. Glucose content was determined using the D-Glucose Assay Kit (Megazyme, Ireland). The absorbance of the sample was read at 510 nm using a UV-vis spectrophotometer.

Starch content was calculated as mg of glucose using a conversion factor and starch hydrolysis rate was expressed as the percentage of total starch hydrolyzed at different times (30, 60, 90, 120, 150, 180 and 240 minutes). The hydrolysis index (HI) was calculated by dividing the area under curve (AUC) for a sample by the AUC of a reference (commercial white bread) as follows:

$$HI = \frac{AUC_{sample}}{AUC_{reference}} \times 100$$

The pGI was obtained according to the equation as follows:

$$pGI = 39.71 + 0.549HI$$

Statistical analysis

In this study, all the analyses were performed in triplicate and the data obtained was presented as mean ± standard deviation (S.D). The results were analyzed statistically by SPSS 24.0 software (SPSS 16.0 for Windows, SPSS Inc., Chicago, IL, USA) using one-way analysis of variance (ANOVA) and Duncan's multiple range test. The significance of the difference was defined at $p < 0.05$.

Results and Discussion:

Total phenolic content and enzyme inhibitory activities of MBM

Prior to formulating the instant drink powder, MBM was assessed for its total phenolic content (TPC) and enzyme inhibitory properties. As detailed in Table 2, MBM exhibited a total phenolic content of 23.11 ± 1.28 mg GAE/g dried powder. For enzyme inhibitory activities, it was found that MBM exhibited a potent inhibitory activity against α -glucosidase, evidenced by an IC_{50} value of 1.84 ± 0.005 μ g/ml, which was stronger than acarbose ($IC_{50} = 622.27 \pm 6.89$ μ g/ml). Furthermore, MBM could inhibit DPP-4 activity by $41.20 \pm 2.22\%$, but this action was weaker than diprotinA, which could inhibit the DPP-4 activity by $91.79 \pm 1.25\%$.

It was suggested that the inhibitory activity against blood glucose control enzymes was due to the TPC in MBM. TPC from bananas (*Musa sapientum* L.) has been shown in a recent study to inhibit the α -glucosidase enzyme via major polyphenols such as catechin, epicatechin, and gallic acid¹⁴. Apiforol, a phenolic compound derived from *M. balbisiana* seed extracts, inhibited the glucosidase enzyme effectively⁶. Because our MBM was extracted from the whole fruit (peel, pulp, and seed) of *M. balbisiana*, MBM may contain these phenolic compounds that inhibit α -glucosidase. However, there are no recent reports studying the inhibitory effect of DPP-4 from banana extract. Nonetheless, a study on another source of phenolics, specifically phlorizin, a phenol glycoside compound from *C. latifolia* extract, demonstrated a significant level of DPP-4 inhibition ($66.15 \pm 4.09\%$) as well as α -glucosidase inhibition⁹. This may be due to the binding of phenolic compounds to the active site of the enzymes, resulting in competitive inhibition. Some of these phenolic compounds had been shown to exhibit the strongest inhibition capacity towards α -glucosidase and DPP-4 by forming hydrogen bonds and hydrophobic interactions with crucial amino acid residues of α -glucosidase and DPP-4¹⁵. Therefore, it is necessary to conduct a detailed analysis of phenolic profiling in MBM throughout our future research in order to determine the major bioactive compounds targeting these enzymes.

Table 2. Total phenolic content and enzyme inhibitory activities of MBM

Sample	Enzyme inhibition		
	TPC (mgGAE/g dried powder)	α -Glucosidase (IC_{50} , μ g/ml)	Dipeptidyl peptidase-4 (%inhibition)
MBM	23.11 ± 1.28	1.84 ± 0.005	41.20 ± 2.22
Positive control*	-	622.27 ± 6.89	91.79 ± 1.25

*Positive control: acarbose was used as a positive control of α -glucosidase and diprotinA was used for dipeptidyl peptidase-4

Formulation of D-MBM and their total phenolic content.

The objective of D-MBM development is to produce a prototype of an instant drink powder that will serve as a replacement for a complete meal. Herein, three formulations of D-MBM were created using varying concentrations of MBM (Figure 1a) at 2%, 5%, and 10% (%),

w/w) designated as F1, F2, and F3, respectively. The product was formulated by blending protein ingredients, such as soy protein isolate, pea protein isolate, and sodium caseinate. Carbohydrates sourced from unripe banana flour, along with fat from rice bran oil non-dairy creamer, were incorporated, complemented by the addition of dietary fiber and cocoa powder. The D-MBM exhibited the physical appearance of a fine brown powder, as illustrated in Figure 1b. The total phenolic content (TPC) for F1, F2, and F3 were 0.56 ± 0.04 , 0.65 ± 0.01 , and 1.01 ± 0.23 mgGAE/g dried powder, respectively (Table 3). Notably, D-MBM F3 containing 10% MBM exhibited 2-fold increase in TPC ($p < 0.05$) compared to the control (Table 3). Hence, D-MBM F3 exhibited the greatest presence of total phenolic compounds. However, it was suggested that exceeding a 10% addition of MBM in the product might influence the sensory attributes. According to these findings, we hypothesized that our prototype product, D-MBM, would exhibit anti-hyperglycemic properties by inhibiting enzymes and reducing the glycemic index. Therefore, D-MBM F3 was selected to determine the predicted glycemic index.

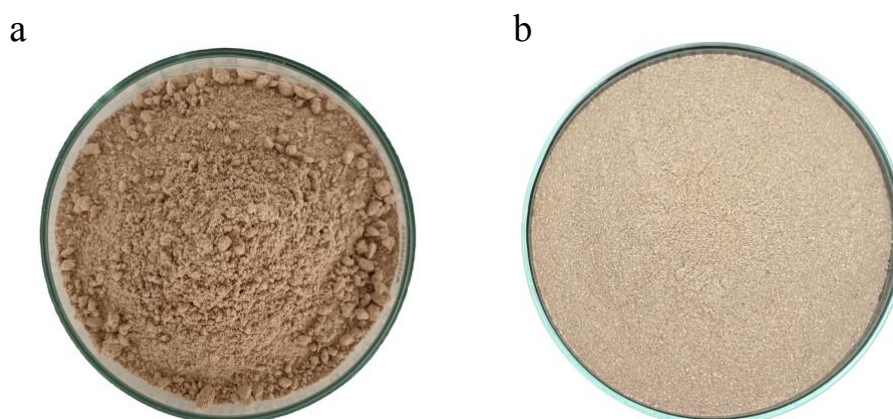


Figure 1. MBM (a) and D-MBM (b)

Table 3. Formulations of D-MBM and their total phenolic content

Sample	TPC (mgGAE/g dried powder)			
	Control	F1	F2	F3
D-MBM	0.48 ± 0.03^b	0.56 ± 0.04^b	0.65 ± 0.01^b	1.01 ± 0.23^a

a-b: the mean values within the same row with different superscripts were significantly different ($p < 0.05$)

Predicted glycemic index (pGI)

The glycemic response of meals in the intestine digestive system can be evaluated using a simple experimental method known as starch hydrolysis in an *in vitro* model¹⁶. This method provides predictive data before conducting *in vivo* experimental designs. In this study,

predicted glycemic index (pGI) of MBM and D-MBM F3 were compared to white bread (used as the reference control) and a commercial product (an instant complete nutrient powder). In the initial 30 minutes of digestion, MBM, D-MBM, the commercial product, and white bread displayed a rapid increase in the hydrolysis rate, followed by a steady glucose release until the end of the 180-minute digestion period. At 180-minute, white bread and the commercial product exhibited hydrolysis rates of $98.43 \pm 0.14\%$ and $101.47 \pm 0.31\%$, respectively. Notably, D-MBM had the lowest hydrolysis rate of $63.22 \pm 0.32\%$, followed by MBM, which had a hydrolysis rate of $79.65 \pm 0.00\%$ (Figure 2).

The predicted glycemic index (pGI) is an *in vitro* technique for calculating the rate of carbohydrate hydrolysis in foods. As shown in Figure 3, the white bread and the commercial product exhibited pGI values of 100 and 99.96 ± 0.04 , respectively. The MBM had pGI of 85.38 ± 0.21 , while D-MBM had a considerably lower pGI value of 75.25 ± 0.05 compared to both white bread and the commercial product ($p < 0.05$). This reduction in pGI observed in D-MBM could be attributed to the inclusion of MBM containing phytochemicals, especially phenolic compounds known for their ability to inhibit carbohydrate-digesting enzymes¹⁸.

Additionally, the glycemic index of D-MBM may be influenced by the inclusion of resistant starch obtained from unripe banana flour, which comprises approximately 40.9-58.5% (g/100 g (d.b.))¹⁹. The presence of resistant starch in banana flour has been documented to exhibit resistance to hydrolysis or digestion in the small intestine of the gastrointestinal tract^{16,17}. This resistance in digestion could potentially decelerate the breakdown of carbohydrates into simpler sugars, consequently resulting in a moderated blood glucose response. Therefore, our D-MBM has the potential to be a significant health product for improving metabolic outcomes associated with insulin resistance and blood glucose control in the future.

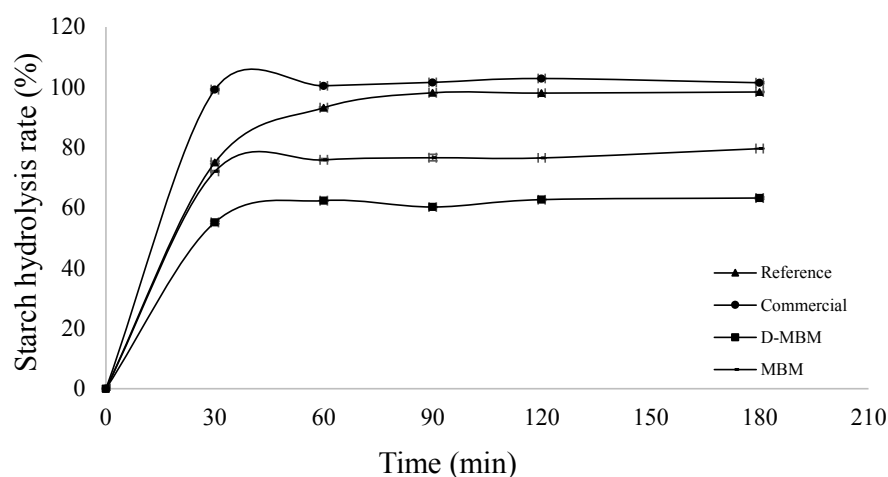


Figure 2. Hydrolysis rate of MBM and D-MBM

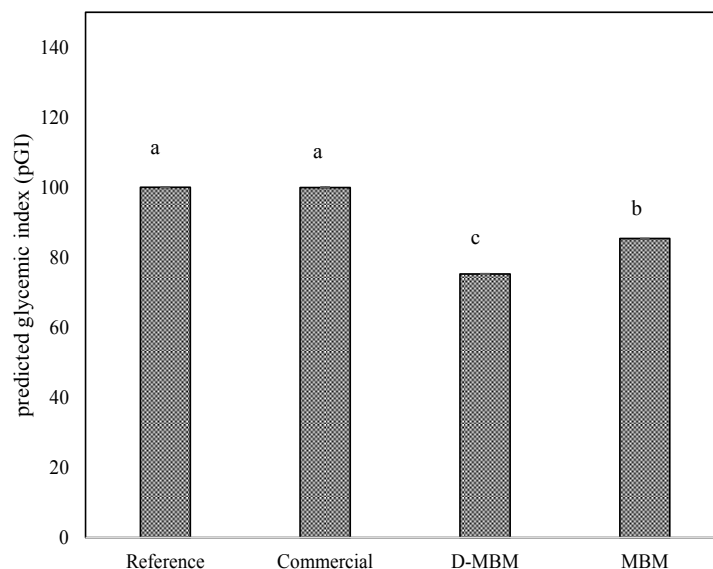


Figure 3. pGI of Commercial, D-MBM and MBM

a-c: the mean value within the same row with difference superscripts were significantly difference ($p < 0.05$)

Conclusion:

M. balbisiana microcapsules (MBM) exert the ability to reduce hyperglycemia through the inhibition of α -glucosidase and DPP-4. Additionally, the instant drink powder from this study has low pGI values attributed to the carbohydrate enzyme inhibition of phenolic compounds in MBM, retarding hydrolysis in the GI system *in vitro* and leading to a low glycemic index. Thus, MBM has the potential for healthy product development for blood glucose control.

Acknowledgements:

This research was financially supported by a National Science, Research and Innovation Fund (NSRF) and Prince of Songkla University [SAT6601300M], The Scholarship Awards for Master and Ph.D. Studies from Faculty of Science and Technology, Prince of Songkla University Pattani Campus [1/2565], and Thesis Research Grant from Graduate School of Prince of Songkla University.

References:

1. Sharma A. J Diabetic Complications Med. 2021; 6:143.
2. Mustafa S B, Akram M, Asif H M, Qayyum I, Hashmi A M, Munir N, Khan F S, Riaz M, Ahmad S. Dose-Response: An International Journal. 2019; 27:1-6.
3. Wongsin U, Wannasri A. ThaiJo. 2018;45:45-49.
4. Phrommintikul A, Dilokthornsakul P, Permsuwan U. Front. Endocrinol. 2022;13:1-9.
5. Swargiary A, Kumar R M, Akram M. Pharmacognosy Reviews. 2021;15:91-95.
6. Gopalan G, Prabha B, Joe A, Reshmitha T. R, Sherin D R, Abraham B, Sabu M, Manojkumar T K, Radhakrishnan K V, Nisha P J. Sci Food Agric. 2019;99:2521–2529.
7. Borah T, Washmin N, Bora N J, Saikia J, Bomzon P S, Ahmed T H, Manna P, Saikia S P, Banik D. British Food Journal. 2021;123:3624–3637.
8. Zakaria R, Abelbaky M S. Abo-Raya A O. Egyptian J Appl Sci. 2020;35:143-57.



9. Zabidia N A, Ishaka N A, Hamidc M, Asharib S E, Latif M A M. J Enzyme Inhib Med Chem. 2021;36:109-121.
10. Seiquer I, Rueda A, Olalla M, Cabrera-Vique C. Food Chem. 2015;188:496-503.
11. Wongnawa M, Tohkayomatee R, Bumrungwong N, Wongawa S. J. Sci. Technol 2014;36:541-546.
12. Al-Masri, I M, Mohammad M.K, Tahaa M O. J. Enzym Inhib. Med. Chem. 2009;24:1061–1066.
13. Goñi I, García D, Saura-Calixto F. Nutrition Research. 1997;17:427-437.
14. Tongkaew P, Tohraman A, Bungaramphai R, Mitrpant C, Aydin E. scientific reports. 2022;12:1-8.
15. Li M, Bao X, Zhang X, Ren H, Cai S, Hu X, Yi J. LWT. 2022;162:1-10.
16. Barine K K D, Yorte G S. Journal of Food Research. 2016;5:73-80.
17. Englyst H N, Kingmans S M, Gummings J H. European Journal of Clinical Nutrition. 1992;46:335-505.
18. Ugur H, Catak J, Ozgur B, Efe E, Gorunmek M, Belli I, Yaman M. Food Sci. Technol. 2022;42:1-7.
19. Tribess T B, Herna'ndez-Uribe J P, Me'ndez-Montealvo M G C, Menezes E W, Bello-Perez L A, Tadini C C. LWT. 2009;42:1022-1025.



SESSION SP5: ENVIRONMENTALLY FRIENDLY RUBBER AND ITS FUTURE

PIEZORESISTIVE BEHAVIOR OF FLEXIBLE STRAIN SENSORS BASED ON NATURAL RUBBER COMPOSITES: EFFECTS OF SENSOR SHAPES AND DIMENSIONS

Rawiporn Promsung,^{1,*} Arthittaya Chuaybamrung,¹ Antonia Georgopoulou,² Yeamporn Nakaramontri,³ Frank Clemens,² Ekwipoo Kalkornsurapranee¹

¹Division of Physical Sciences, Faculty of Science, Prince of Songkla University, Hat-Yai, Thailand

²Laboratory for High Performance Ceramics, Department Advanced Materials and Surfaces, Empa-Swiss Federal Laboratories for Materials Science and Technology, Dübendorf, Switzerland

³Sustainable Polymer & Innovative Composite Materials Research Group, Department of Chemistry, Faculty of Science, King Mongkut's University of Technology Thonburi, Bangkok, Thailand

*e-mail: rawiporn402@gmail.com

Abstract:

This study explores the piezoresistive behavior of flexible strain sensors based on natural rubber composites. Conductive carbon black and carbon nanotubes as hybrid fillers were incorporated into the natural rubber latex matrix using glutaraldehyde as a low-temperature curing agent. The mechanical and electrical properties of the composites were explored in conjunction with tensile testing. It was observed that the composites enhanced a high tensile strength and a superior elongation at break up to 7.06 MPa and 678%, respectively. In addition, the NR composites demonstrated the excellent sensitivity, which indicated by the superior gauge factor under a specific strain. Moreover, the effect of sensor shape and dimensions on piezoresistive behavior was examined while subjecting the sensors to 150 cycles of the motion on a tendon-based actuator. Different shapes and lengths of the sensors influence piezoresistive behavior, as characterized by initial resistance, difference of relative resistance, and electrical signal drift. It is found that the composite sensors, designed with a U-shape and a length of 30 mm, displayed excellent sensitivity and low signal drift, which demonstrated the optimal performance for the present actuator. Thus, the work is found to be beneficial to the future development and design of the piezoresistive sensors.

Introduction:

Recently, flexible strain sensors, known as piezoresistive sensors, have gained widespread use in various applications, including soft robotic sensors, wearable devices, health monitoring, prosthetic devices, and motion detection.¹ These sensors are particularly attractive due to several advantages such as high flexibility and stretchability, a wide strain range, high sensitivity, and good durability.²⁻³ Piezoresistive sensors are able to detect substantial mechanical deformations in materials through changes in electrical resistance.⁴ To attain the desired electrical and piezoresistive properties of sensors, the selection of conductive materials and testing parameter must be considered. Generally, various conductive fillers can be employed in the fabrication of piezoresistive sensors, such as nanowires (NWs), nanoparticles (NPs), carbon-based materials as graphene, graphene oxide, carbon black (CB), and carbon nanotubes (CNTs), along with their hybrid micro/nanocomposites.⁴⁻⁸ The carbon-based materials exhibit outstanding mechanical

properties, as well as high electrical and thermal conductivity.⁹ Moreover, in manufacturing piezoresistive sensors, the flexibility and elasticity of the substrate materials are crucial parameters. Common flexible substrates used in the fabrication of these sensors including, polydimethylsiloxane (PDMS), polyethylene terephthalate (PET), polyethylene (PE), polyurethane (PU), Ecoflex silicone rubber and natural rubber (NR).¹

NR is an important material, which widely used as flexible strain sensors, and have been studied by many researchers.¹⁰⁻¹⁴ Tamil Selvan Natarajan *et al.*¹⁰ developed a conductive natural rubber (NR) composite filled with CNT, CB, and their filler combinations. The composite demonstrated the highest gauge factor (GF) of 20 at approximately 120% strain. Furthermore, the synergistic effect of the CB/CNT conductive filler exhibited a consistently stable signal even after a large number of repeated loading-unloading cycles (around 3600 cycles). Nevertheless, the composite containing CNTs still exhibited an irregular electrical signal during cyclic testing. In 2023, Sripornsawat *et al.*¹¹ developed sensors based on NR composite with hybrid CNT/CCB fillers. These sensors were further enhanced by the incorporation of a modified deep eutectic solvent (mDES) to improve their properties. It was found that the addition of 5 phr mDES, the GF of the NR composite with the hybrid conductive filler network showed a significant increase at high strains (>60%). However, the NR composite without mDES observed a shoulder peak during tensile cyclic testing. Recently, in 2023, Georgopoulou *et al.*¹² developed a sensor using acetylene black (AB)/NR composite through two distinct methods: casting and vat-based 3D printing. In comparison, the cast sensor strips demonstrated greater sensitivity with GF of 9, and the 3D-printed sensor strips with GF of 3 at 0-10% strain. Nevertheless, the shoulder peaks are observed during cyclic tensile testing for the composites form both casting and vat-based 3D printing method, as well as the noise signals are observed during monitoring the bending the finger. According to the previous works, the piezoresistive sensors based on NR have demonstrated a broad working range under large strains, exhibiting fast responsivity even at very low strain levels due to the exceptional flexibility of NR. Additionally, these sensors exhibited high sensitivity along with durable sensing performance.¹ Thus, the development of piezoresistive sensors typically focuses on critical factors such as gauge factors (GF), signal drift, and relaxation, which necessitate thorough investigation.¹ However, there are remained the shoulder peaks and noise signal during dynamic cyclic testing on the wearable device and the actuator. Nevertheless, shoulder peaks and noise signals continue to be present during dynamic cyclic testing on the actuators. This could be attributed to various factors, including the unsuitability of the shape and dimensions of the sensors, particularly influencing sensor resistance.

Therefore, this present work mainly aimed to study the effect of sensor shape and dimensions on the piezoresistive properties of flexible strain sensors based on NR composites. The hybrid CCB/CNT fillers were incorporated in NR latex matrix and using glutaraldehyde (GA) as a low-temperature curing system.¹⁵⁻¹⁶ The NR composites were cut by a laser cutter as a sample geometry needed including, small-rectangle, large-rectangle and U-shaped sensors. Then, the mechano-electrical properties of the composites were explored in conjunction with tensile testing in term of modulus, tensile strength, elongation at break and gauge factor (*GF*). Furthermore, the piezoresistive properties on the motion of actuator of the NR composite sensors were investigated in term of initial resistance, relative resistance differences, and electrical signal drift.

Methodology:

Materials

A commercial high ammonia concentrated NR latex with 60% dry rubber content (DRC) was purchased from Chalong Latex Industry (Songkhla, Thailand). Glutaraldehyde (GA) was procured from Wing Great Industry Co., Ltd, (Bangkok, Thailand). As a primary conductive filler, a conductive carbon black, CCB (Vulcan XC72) with 30 nm particle diameter, procured by Cabot Corporation (Texas, USA) was used. As a second conductive filler, carbon nanotube, CNT (NC7000) was purchased from Nanocyl S.A. (Sambreville, Belgium). The NC7000 is a 90 pure multiwalled CNT material with a diameter of 9.5 nm, a length of $\sim 1.5 \mu\text{m}$. The sodium dodecyl sulfate (SDS) used to disperse CCB and CNT particles in the latex deionized water was manufactured by Banksia Scientific Company (Queensland, Australia).

Preparation of CCB/CNT filled NR composites

Hybrid CCB/CNT filled NR latex with CCB 20 phr and 1.5 phr of CNT. CCB/CNT dispersion was initially prepared by mixing of CCB/CNT and 20 wt% of SDS with deionized water (deionized water for diluting 60 to 45 wt% DRC of NR latex). The mixture dispersion was sonicated using an ultrasonicator probe (Qsonica Sonicators, Qsonica LLC, USA) for 10 min. Finally, a 12.5 wt% of GA aqueous solution was slowly added into NR latex under mechanical stirring at 200 rpm for 30 min using a magnetic stirrer. The conductive NR composites were cast on a glass plate and later dried in a hot air oven at 50°C for 24 h. The crosslinked NR composite films, with a thickness of $1.0 \pm 0.5 \text{ mm}$, were laser cut (Thunder laser machine, Allplast GmbH, Germany) into the sample geometry needed for the different mechanical characterization method.

Characterization

For the mechano-electrical characterization, the samples were cut into rectangular sensor strips with dimensions $30 \times 7 \text{ mm}^2$. The samples were fixed in an universal tensile testing machine (Zwick & Roell Z005, Zwick & Roell GmbH & Co., Germany). The stress-strain behavior of the NR composite was analyzed to investigate the modulus at 10, 100 and 300% strain, tensile strength and elongation at break. The electrical signal was recorded with a Keithley 2450 source meter (Keithley Instruments, Solon, OH, USA) by applying a voltage of 5 Voltage. During the tensile testing, the electrical resistance was recorded with a sampling rate of 10 Hz. Tensile testing was performed with a crosshead speed of 200 mm/min at room temperature until reached the point of fracture.

The relative resistance (R_{rel}) was calculated using the following Equation (1).¹¹

$$R_{rel} = \frac{R - R_0}{R_0} \quad (1)$$

where R is the value of the electrical resistance, and R_0 is the resistance value without applied strain.

The gauge factor (GF), also known as sensitivity, of the NR composites was evaluated from the slope of the relative resistance-strain curves and the GF was calculated with the following Equation (2).¹¹

$$GF = \frac{\Delta R_{rel}}{\Delta \epsilon} \quad (2)$$

Soft tendon-based actuator elements (**Figure 1**) were 3D printed using a thermoplastic polyurethane (TPU) filament with Shore hardness 90A from Spectrum Group (Pecice, Poland) using a filament-based FDM 3D printer Voladora Nx+ (International Technology 3D

Printers S.L., Spain). The actuators were equipped with a stainless-steel tendon wire of 0.5 mm diameter. For the actuation of the tendon-based soft robotic element, a Dynamixel AX-12A servomotor from Robotis (Lake Forest, Illinois, USA) and an Arduino microcontroller were used. The NR composite samples were cut as sample geometry needed and attached to the surface of the soft tendon-based actuator using UHU Sekundenkleber Superflex gel from Bolton Swiss S.A. (Massagno, Switzerland). Conductive past (Bare Conductive Paste, RS Components, UK) was painted on the edge of the sample sensor elements and connected with conductive yarns as shown in **Figure 1**. The electrical sensor signal was recorded with a Keithley 2450 (Keithley Instruments, Solon, OH, USA) source by applying a voltage of 5 Voltage.

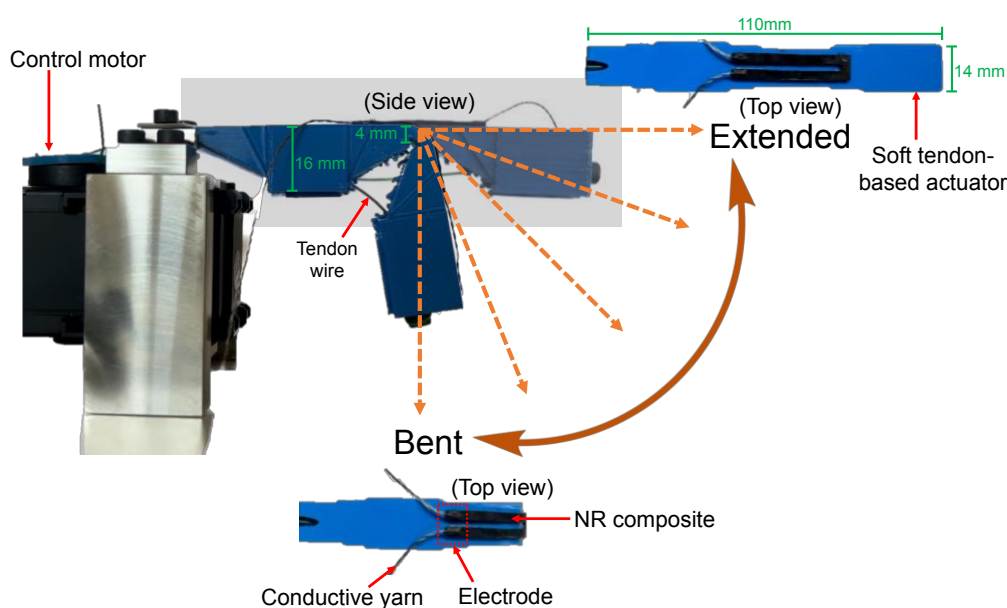


Figure 1.

Setting-up of the tendon-based actuator with incorporated NR composite sensor during the motion of the actuator.

Results and Discussion:

Mechanical properties

Mechanical properties of the NR composite were investigated in term of stress behavior, modulus, tensile strength and elongation at break. Figure 2 displays the stress-strain curve of the NR composite. It was observed that stress strongly increased at the strain below 100%. This phenomenon is ascribed to the stiffness of the composite caused by the entanglement of rubber molecular chain, impeding the expansion of the samples according to the Neo-Hookean theory.¹⁵ Beyond the 100% strain, the stress continued to rise until reaching the fracture point, indicating the self-reinforcement of the NR composite due to strain-induced crystallization. Furthermore, overall mechanical properties of the composite are summarized in Table 1. It was observed that 10, 100 and 300% moduli are 1.61 MPa, 2.95 MPa, 4.17 MPa, respectively. It has to be noticed that the modulus of rubber refers to its elastic modulus, which is a measure of a material's stiffness in response to an applied force.¹⁷ In addition, the NR composite enhanced tensile strength and elongation at break up to 7.06

MPa and 678%, respectively, which indicating the strength and flexibility of the composite under tension.

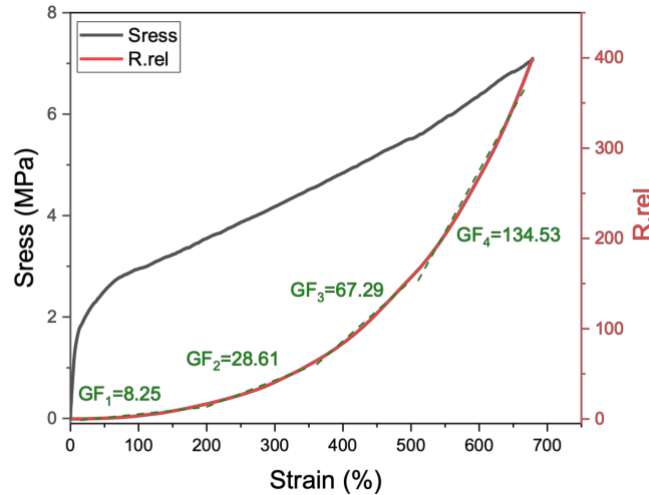


Figure 2.

Stress (black line) and relative resistance, R_{rel} (red line) as a function of strain together with the GF values of the NR composite.

Table 1. Mechanical properties from tensile testing of the NR composite.

Properties	Values
10% modulus (MPa)	1.61 ± 0.14
100% modulus (MPa)	2.95 ± 0.18
300% modulus (MPa)	4.17 ± 0.24
Tensile strength (MPa)	7.06 ± 0.96
Elongation at break (%)	678.37 ± 17.87

Electrical properties

The relative resistance-strain curve between 0% and 678% strain of NR composites as shown in Figure 2 (red line). As expected, the R_{rel} of the NR composites increased upon strain. This is due to a larger distance between the conductive fillers occurred during the stretching leading to a decrease of the electron transport in the NR composite.¹⁸ Moreover, the GF values was calculated from the slope of the plot of R_{rel} changes of the NR composite. It was found that the GF values can be investigated into four linear regions including, 0–200% ($GF=8.25$), 200–350% ($GF=28.61$), 350–500% ($GF=67.27$) and 500–678% ($GF=134.53$). A higher GF corresponds to a more significant change in resistance under a specific strain, which indicating the excellent sensitivity of the composite.¹

Piezoresistive properties

The NR composite was studied the effect of different sensor shape on the piezoresistive properties of the NR composite during the motion of tendon-based actuator. Figure 3 showed the variation in R_{rel} during the motion of the actuator of the NR composite sensors during the 150 cycles. It is clearly seen that the electrical signal can be detected during the motion of the NR composite sensors. For both small and large rectangle shapes observed unwanted signal is called as noise signal, which interferes with the original electrical signal of the composites. In addition, piezoresistive behavior of the NR composites were evaluated by certain factors i.e., difference of relative resistance (ΔR_{rel}) and drift of

electrical signal as illustrated in Figure 4. Table 2 summarizes the piezoresistive properties including, the initial resistance (R_0), the ΔR_{rel} and the drift of signal at higher (top) and lower (bottom) signal of the NR composites. It is observed that R_0 related to the shape of NR composite sensors, as large-rectangle, small-rectangle and U-shaped showed the R_0 of 1.02, 3.59 and 4.76 k Ω , respectively. This is due to the resistance depends on the length and the cross-section area of the sensor, following Ohm's Law. It has to be noticed that the electrical resistance of an object quantifies its resistance to the flow of electric current. A lower resistance indicates the ease with which an electrical current can pass through a given object.¹ Therefore, the larger area (length x width) of large-rectangle sensor facilitated the easy path of electrical current, leading to a lower R_0 than the other two sensors. Conversely, the U-shaped sensor showed the highest R_0 due to its higher distance between the electrodes (total length = 30+7+30 mm) than the small-rectangle sensor with the length of 30 mm at the same width (2.5 mm).

In addition, the sensitivity of the NR composite sensors was examined as the difference of relative resistance (ΔR_{rel}) which can be calculated by the difference of R_{rel} at maximum and minimum in each peak as summarized in Table 2. It was observed that the large-rectangle and U-shaped sensors exhibited higher ΔR_{rel} than that small-rectangle sensor. A higher ΔR_{rel} indicates the better sensitivity caused by a larger change in resistance during the motion of the actuator. This changes well correlated with the area of deformation of the sensors. Furthermore, to study the sensing behavior in long-term performance, the electrical signal drift was calculated as the percentage difference of the resistance value at maximum (or minimum) of R_{rel} peak between 3-150 cycles of the NR composites as summarized in Table 2. It was found that the large-rectangle sensor observed the highest drift of signal in both top and bottom signals following by U-shaped and small-rectangle sensors, respectively. This is well correlated with the area of sensors, a larger area leading to the temporary deformation of the sensors caused by the breaking of filler-filler networks in NR composites after many consequent cycles.¹⁸

According to the piezoresistive properties of the NR composite sensors with different shapes, the U-shaped sensor demonstrated superior sensing performance, which ability to detect without noise signal, with high ΔR_{rel} and low signal drift after 150 cycles. Therefore, the U-shaped sensor was selected to further study the effect of sensor dimension on piezoresistive behavior of the NR composite sensors.

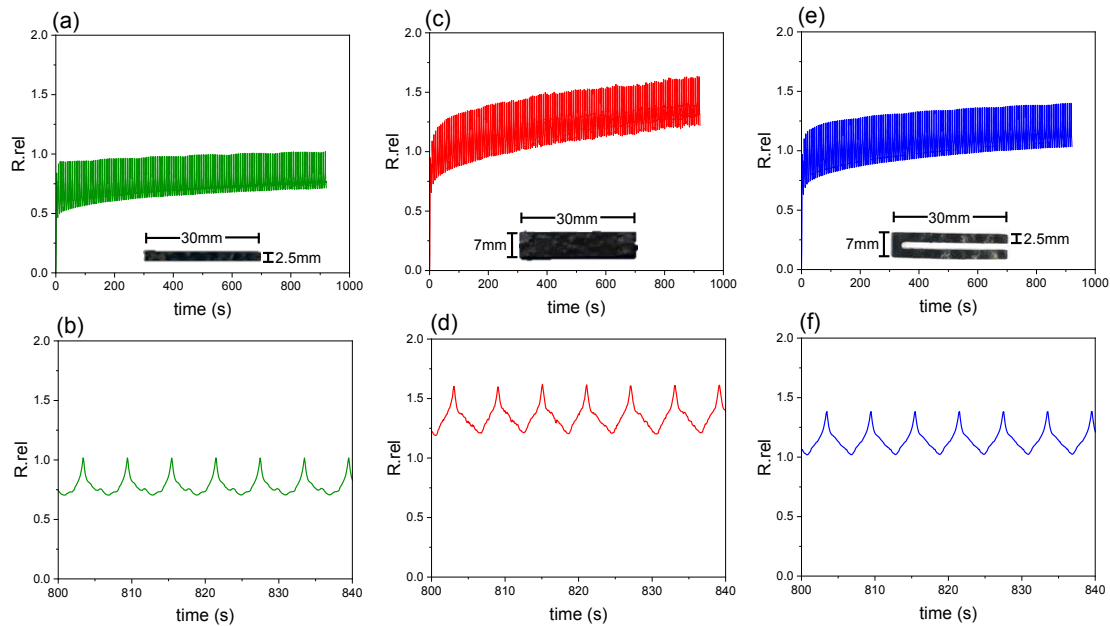


Figure 3.

The variation in R_{rel} during the motion of the actuator of the NR composites with different sensor shapes during the 150 cycles and zoom of the variation, Small-Rectangle (a-b), Large-Rectangle (c-d) and U-shaped (e-f).

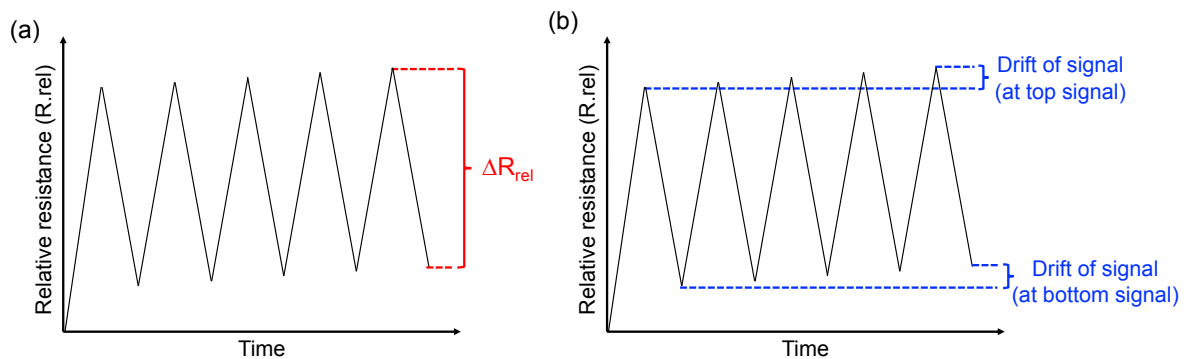


Figure 4.

Definition of difference resistance (ΔR_{rel}) signal (a) and drift behavior (b) in a dynamic cycling test.

Table 2 The initial resistance (R_0), ΔR_{rel} and the drift of signal at higher and lower signal of NR composites.

Composites with different shapes	R_0 (k Ω)	ΔR_{rel}	Drift of signal (%) (3-150 cycles)	
			top signal	bottom signal
Small-Rectangle	3.59	0.33 ± 0.01	8.93	43.15
Large-Rectangle	1.02	0.41 ± 0.02	43.17	69.02
U-shaped	4.76	0.40 ± 0.02	22.64	43.81

The piezoresistive behavior of the NR composite sensors with different length including, 20, 30 and 40 mm were investigated. Figure 5 showed the variation in R_{rel} during the motion of the actuator of the NR composite sensors with different length during the 150

cycles. It was observed that the U-shaped sensor, with the length of 20 mm, could not detect the electrical signal due to glue failure during the motion. This limitation stemmed from its insufficient length on the actuator, as illustrated in Figure 5(b). In addition, the 40 mm of U-shaped sensor showed irregularities in the top signal, as depicted in Figure 5(e). Furthermore, piezoresistive properties of the sensors with different length in term of R_0 , ΔR_{rel} and the drift of signal were summarized in Table 3. It was found that the R_0 of the sensors increased with the length of the sensors, attributed to the larger distance between the electrodes.¹⁸ Additionally, the 30 mm of U-shaped sensor demonstrated a higher ΔR_{rel} which refers the better sensitivity of the sensor than that U-shaped sensor with 40 mm. For the signal drift in both the top and bottom signals shows no significant difference between the 30 mm and 40 mm U-shaped sensors. As results, it can be concluded that the piezoresistive behavior of the NR composite sensors attached on the actuator depends on the shapes and dimensions of the sensors.

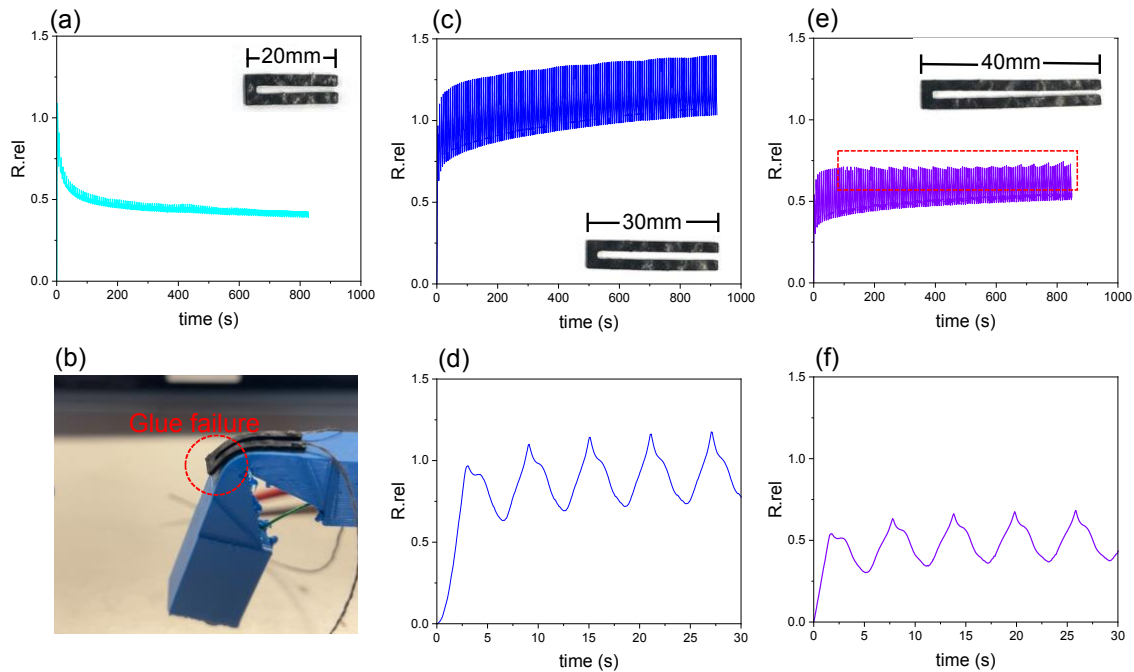


Figure 5.

The variation in R_{rel} during the motion of the actuator of the NR composites with different length of U-shaped sensors during the 150 cycles and zoom of the variation, 20 mm (a-b), 30 mm (c-d) and 40 mm (e-f).

Table 3 The initial resistance, ΔR_{rel} and the drift of signal at higher and lower signal of latex-NR composites.

Composites	R_0 (k Ω)	ΔR_{rel}	Drift of signal (%) (3-150 cycles)	
			top signal	bottom signal
20 mm	1.82	-	-	-
30 mm	4.76	0.40 ± 0.02	22.64	43.81
40 mm	5.84	0.25 ± 0.04	22.98	42.13

Conclusion:

The flexible sensors based on NR composites were successfully prepared and investigated. It is observed that the NR composites demonstrated the excellent sensitivity which indicated by the superior GF under a specific strain. Additionally, the NR composite sensors were affixed to the actuator and successfully detected electrical signal. The piezoresistive behavior of the NR composite sensors are contingent on their shape and dimensions. In conclusion, it can be summarized that the NR composite sensor with a U-shaped design and a length of 30 mm exhibited the most optimal performance for the present actuator.

Acknowledgements:

This research was supported by Prince of Songkla University under the Postdoctoral Fellowship Program. The authors would like to express their gratitude to the Faculty of Science, Prince of Songkla University, Hat Yai Campus. The authors also would like to thank King Mongkut's University of Technology Thonburi and Laboratory for High Performance Ceramics, Department Advanced Materials and Surfaces, Empa-Swiss Federal Laboratories for Materials Science and Technology for the technical supports.

References:

- Georgopoulou A, Clemens F. *ACS Appl. Electron. Mater.* 2020;2:1826–1842.
- Liu H, Li Q, Zhang S, Yin R, Liu X, He Y, Dai K, Shan C, Guo J, Liu C, Shen C, Wang X, Wang N, Wang Z, Wei R, Guo Z. *J. Mater. Chem. C.* 2018;6(45):12121–12141.
- Guo X, Huang Y, Zhao Y, Mao L, Gao L, Pan W, Zhang Y, Liu P. *Smart Mater. Struct.* 2017;26:095017.
- Afsarimanesh N, Nag A, Sarkar S, Sabet GS, Han T, Mukhopadhyay SC. *Sens. Actuator A. Phys.* 2020;315:112355.
- Kang D, Pikhitsa PV, Choi YW, Lee C, Shin SS, Piao L, Park B, Suh KY, Kim T, Choi M. *Nature.* 2014;516:222–226.
- Zhang S, Zhang H, Yao G, Liao F, Gao M, Huang Z, Li K, Lin Y. *J. Alloys Compd.* 2015;652:48–54.
- Yi W, Wang Y, Wang G, Tao XJ. *Polym. Test.* 2012;31(5):677–684.
- Guo F, Cui X, Wang K, Wei JJ. *Nanoscale.* 2016;8(46):19352–19358.
- Lu Y, Biswas MC, Guo Z, Jeon JW, Wujcik EK. *Biosens. Bioelectron.* 2019;123:167–177.
- Natarajan TS, Bhagavatheswaran ES, Stöckelhuber KW, Wiessner S, Potschke P, Heinrich G, Das A. *ACS Appl. Mater. Interfaces.* 2017;9:4860–4872.
- Sripornsawat B, Georgopoulou A, Tulapho S, Thitithammawong A, Johns J, Nakaramontri Y, Clemens F. *EXPRESS Polym. Lett.* 2023;17(1):69–89.
- Georgopoulou A, Srisawadi S, Wiroonpochit P, Clemens F. *Polymers.* 2023;15:2410.
- Kampioti K, Matos CF, Galembeck F, Jaillet C, Derre A, Zarbin AG, Peñicaud A. *ACS Omega.* 2018;3:1367–1373.
- Tjahyono AP, Aw KC, Travas-Sejdi J. *Sens. Actuators B Chem.* 2012;166–167:426–437.
- Promsung R, Nakaramontri Y, Uthaipan N, Kummerlöwe C, Johns J, Vennemann N, Kalkornsurapranee E. *EXPRESS Polym. Lett.* 2021;15(4):308–318.
- Johns J, Nakason C, Thitithammawong A, Klinpituksa P. *Rubber. Chem. Technol.* 2012;85(4):565–575.
- Promsung R, Nakaramontri Y, Kummerlöwe C, Johns J, Vennemann N, Kalkornsurapranee E. *EXPRESS Polym. Lett.* 2022;16(8):871–880.
- Nakaramontri Y, Kummerlöwe C, Vennemann N, Wisunthorn S, Pichaiyut S, Nakason C. *EXPRESS Polym. Lett.* 2018;12(10):867–884.

POSTER PRESENTATION



SESSION PLENARY SPEAKERS



SESSION A-PHYSICS / APPLIED PHYSICS

DEVELOPING AN EXPERIMENTAL INSTRUMENT TO MEASURE THE APPARENT MAGNITUDE OF STARS

Pearapol Thuadchob,² Ketwadee Rongrat,² Jakkree Boonlakhorn,¹ Suwit Khongpakdee¹, *

¹Department of Basic Science and Mathematics, Faculty of Science and Digital Innovation, Thaksin University, Songkhla Campus, Songkhla 90000, Thailand

²Bachelor of Education Program in Physics, Faculty of Education, Thaksin University, Songkhla Campus, Songkhla 90000, Thailand

*e-mail: khsuwit@tsu.ac.th

Abstract:

The goal of this study is to create an experimental setup for determining the apparent magnitude of stars and to investigate the relationship between apparent magnitude, brightness, and distance. A light bulb, a light intensity sensor, an aluminum rail with a scale, and an Arduino Uno R3 board comprise the experimental set. In the experiment, we measured the brightness and apparent magnitude of the light bulb from 10 centimeters away from the sensor. The light bulb was then moved backward in ten-centimeter increments until it reached 80 centimeters. The experiment was repeated four times, and the collected data was used to create graphical representations of the correlations between brightness and distance, apparent magnitude and distance, and apparent magnitude and brightness. The results of the experiment revealed that the star's brightness decreases with distance. The result has an error value of 7.10 percent relative to the theory, but the apparent magnitude value increases. Compared to the theory, the result has a 7.20 percent error rate. And, as predicted by theory, the apparent magnitude increases as brightness decreases.

Introduction:

The study of astronomy is a fundamental principle that science students must fully comprehend. Learning about astronomy focuses on the study of celestial phenomena and the interaction between life on Earth and the stars [1]. Therefore, astronomy education is a priority for a number of nations. In 2008, Thailand also established the Basic Education Curriculum, which mandates that all students study the evolution of the solar system, stars, galaxies, universe, space technology, etc [2]. Nevertheless, the field of astronomy continues to face numerous challenges in the realm of education. Due to the abstract nature of the content. Moreover, the system in question is of considerable magnitude. Studying astronomy necessitates the utilization of considerable imaginative faculties among students. Previous studies have revealed that a considerable number of students possess misconceptions regarding the field of astronomy [3-5]. From teaching astronomy and space at the undergraduate level, it has been determined that students struggle to comprehend the relationship between stellar distance and magnitude, including confusion between the apparent and absolute magnitudes of celestial objects. Students continue to struggle with comprehending the relationship between variables in Logarithmic equations. As a result, students perceive magnitude numbers to be tough and are disinclined to study them. Hipparchus, a Greek astronomer, established the apparent magnitude scale between 190 and 120 B.C. by classifying stars according to their brightness as observed from Earth. He used a 1 to 6 scale to compare the brightness of stars, with 1 being the brightest and 6 being barely visible to the naked eye. In the year 1856, Pogson N. [6] established the system by precisely delineating a star of first magnitude as being 100 times more radiant than an average star of sixth magnitude. In the realm of physics, it is observed that the equivalence between a difference of five 'magnitudes' and a brightness ratio of 100 can be expressed mathematically as $B_2/B_1 = 2.512^{(m_1-m_2)}$ or $m_2 - m_1 = -2.5\log(B_2/B_1)$. As per the

findings of Agrawal [7], students frequently encounter a state of perplexity when attempting to establish a correlation between two distinct equations documented in the literature.

Creating an apparatus that illustrates the relationship between brightness (B), magnitude (m), and distance (r) is one method for facilitating students' understanding of magnitude. So that students can observe relationships with their own eyes rather than relying solely on their imaginations or the words of their teachers. Therefore, practical experiments play a crucial role in enhancing students' comprehension of lesson content. In order to enhance students' observational skills, it is crucial to gather information through a systematic and scientific process. In addition, they can think analytically and solve problems, resulting in the creation of new knowledge [2]. This is consistent with Tobin's [8] explanation that organizing science experiment activities and conducting experiments is a way for students to learn and comprehend more theoretical content, as well as generate new knowledge. As a result, the researcher is interested in designing an experiment to measure the apparent magnitude of stars and comparing the relationship between brightness, magnitude, and distance observed in the experiment to that predicted by theory.

Methodology:

The research method for this study consists of two parts: the method for creating an experimental set and the method for conducting experiments. The specifics are provided below.

Methodology for building experimental set

- 1) Construct an aluminum rail measuring 3 centimeters in width and 1 meter in length, and attach a distance scale strip.
- 2) The 3D printing of two 5x5 centimeter rail support bases.
- 3) Creating a base for the light bulb, with dimensions of 4 centimeters in width and 6 centimeters in height.
- 4) Creating a base for attaching a brightness sensor, width 4 centimeters, height 11.5 centimeters.
- 5) Creating a 12-by-12-by-6-centimeter control box for the Arduino Uno board's microcontroller, LCD, and on/off switch.
- 6) The circuit is enclosed within the container by establishing connections between the wires of the LED bulbs and the Dimmer switch, as well as connecting the jumper wires of the sensors and LCD.

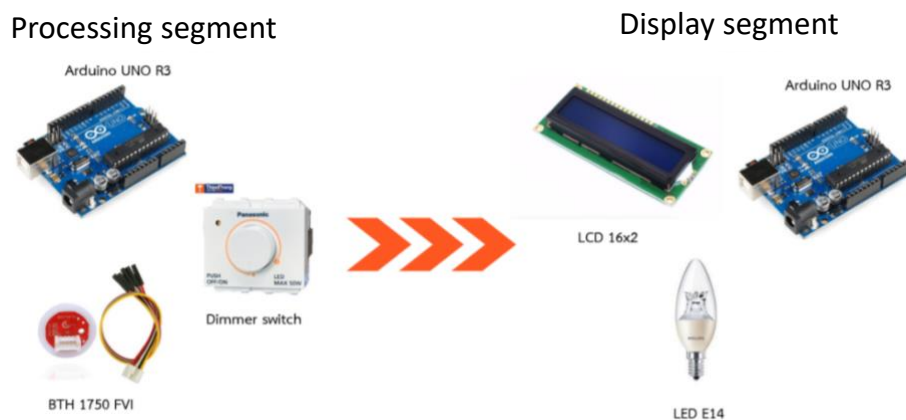


Figure 1.
The equipment used to create the experimental set.

- 7) The components depicted in **Figure 1** are integrated and assembled to create an overall experimental configuration of apparent magnitudes.
- 8) Formulating a series of algorithms to govern the Arduino board to regulate the Sensor's capacity to quantify the luminosity emitted by the light bulb. The LCD screen will exhibit the luminosity value and the magnitude value.

Instruction for student

- 1) Plugging in and turning on the switch to light the bulb.
- 2) Repositioning the lightbulb 10 centimeters from the sensor. On the LCD screen, note the brightness (B) and apparent magnitude (m) values.
- 3) Moving the bulb away in 10-centimeter increments and measuring the brightness. The magnitude value is displayed on the LCD screen up to 80 centimeters away.
- 4) Repeating the experiment four times.
- 5) Plotting the relationship between brightness (B) and distance (r) using the data acquired.
- 6) Utilizing the acquired data, we construct a graphical representation illustrating the correlation between the apparent magnitude (m) and the distance (r) of the light bulb.
- 7) Utilizing the acquired data, a semi-logarithmic graph is constructed to illustrate the correlation between apparent magnitude (m) and distance (r).
- 8) Utilizing the data at hand, an analysis is conducted to graphically represent the correlation between apparent magnitude (m) and brightness (B).
- 9) Utilizing the acquired data, the relationship between apparent magnitude (m) and brightness (B) can be graphically represented on a semi-logarithmic scale.
- 10) Analyzing the data depicted on the graph to ascertain the correlation between apparent magnitude, luminosity, and distance in space.

Results and Discussion:

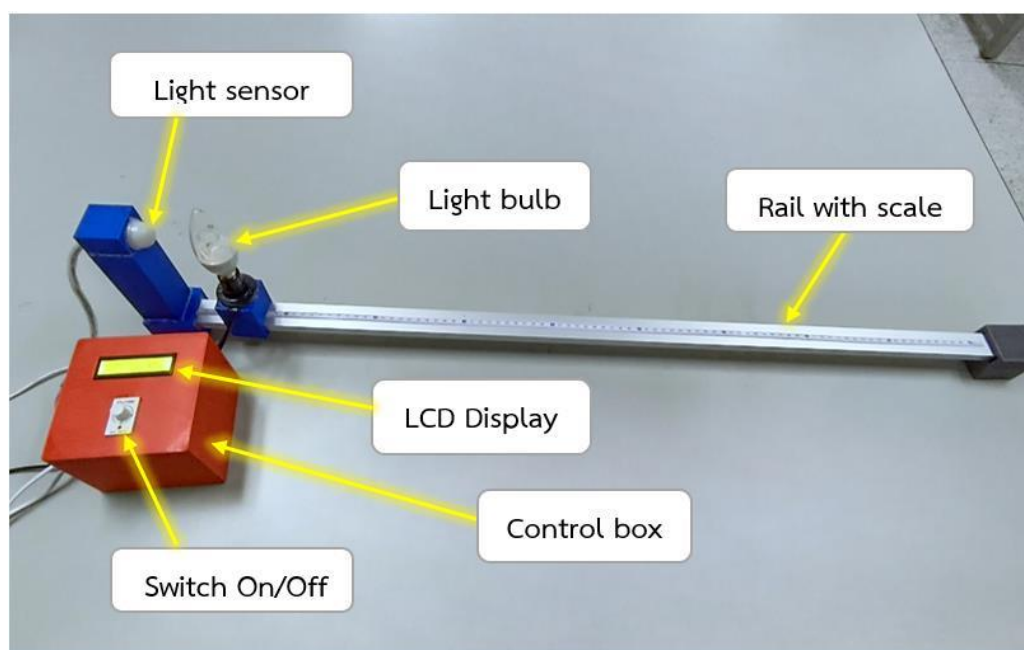


Figure 2.

The experiment set for apparent magnitude measurement.

The experimental setup for measuring apparent magnitude comprises several components, including an Arduino Uno R3 board, a light brightness sensor, a light bulb, an LCD screen, and a rail with a scale. By providing a specific representation of the light bulb to symbolize the luminosity of the star. The aforementioned components are affixed to a scale rail, which possesses the capability to modify the distance of the bulb as required. The BH1750 FVI sensor is utilized to quantify the luminosity emitted by the light bulb. The collected data is subsequently transmitted to the Arduino board for processing, wherein the sensor's recorded brightness is computed to determine the apparent magnitude (m). Finally, the obtained data is relayed to the LCD screen for display. Two values will be shown on the LCD screen: Brightness and apparent magnitude. The device displays readings at regular intervals of 5 seconds.

Results of brightness vs distance

The results of analyzing the relationship between the luminosity and distance of stars in the experimental set are presented in **Table 1**. As shown in **Figure 3**, when the data were used to plot a graph between brightness and distance, it was an exponential curve graph. On a log-log graph, the relationship between brightness and distance was plotted as a straight line, as shown in **Figure 4**.

Table 1 Relationship between the brightness and distance of stars from the experimental set.

Distance (cm)	Brightness (lx)					\bar{B}
	1	2	3	4	5	
10	799	799	799	799	799	799
15	380	380	380	380	380	380
20	223	223	223	223	223	223
25	146	146	146	146	146	146
30	106	106	106	106	106	106
35	80	80	80	80	80	80
40	63	63	63	63	63	63
50	40	40	40	40	40	40
60	29	29	29	29	29	29
70	23	23	23	23	23	23
80	16	16	16	16	16	16

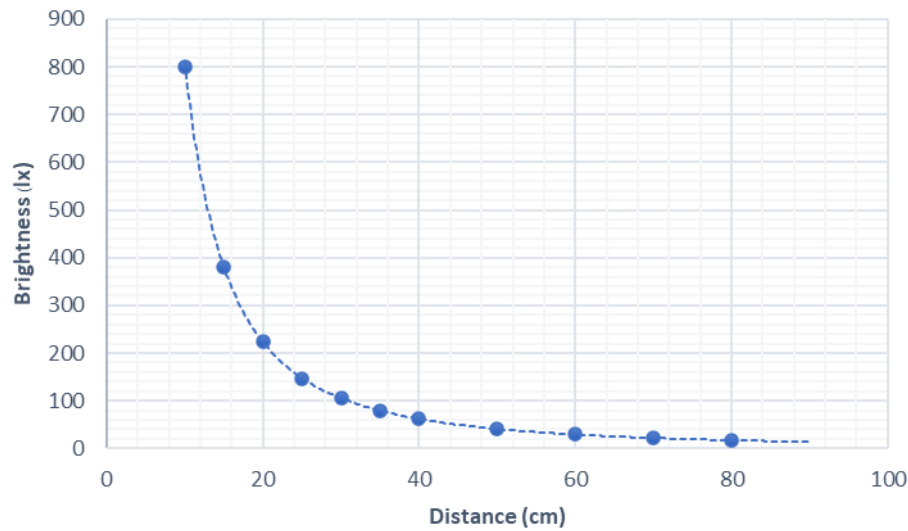


Figure 3.
Relationship between Brightness and distance.

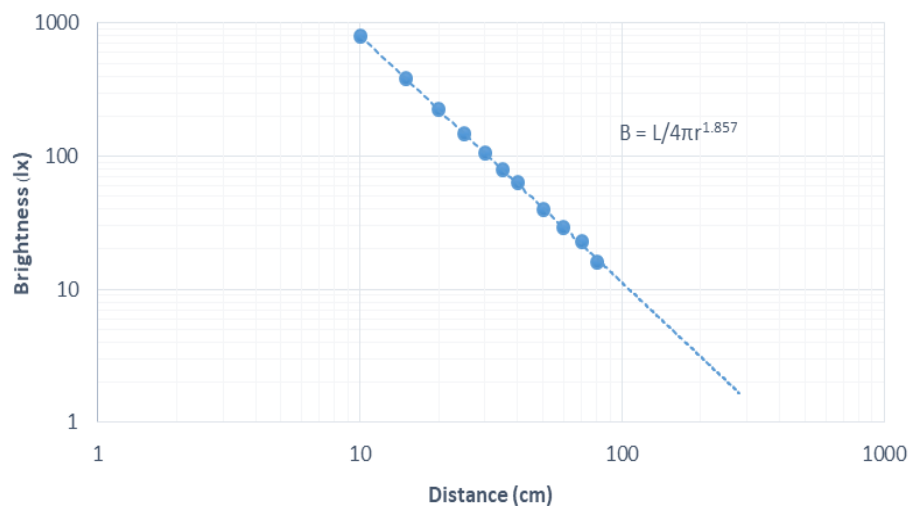


Figure 4.
Relationship between Brightness vs distance on a log-log graph.

As indicated by the graph of the relationship between Brightness and Distance from the experiment set, the star's brightness decreases as the distance increases. The equation of $B = L / 4\pi r^{1.857}$ is consistent with a theoretical correlation of $B = L / 4\pi r^2$. The power numbers of r obtained from this experiment were compared to the theoretical equation to calculate the error. The power numbers of r observed in this study and the theoretical equation are 1.857 and 2, respectively. By calculation, only an error of 7.15 percent could be obtained.

Results of the study apparent magnitude vs distance

The data presented in **Table 2** illustrate the findings obtained from the examination of the correlation between the magnitude and distance of stars within the experimental dataset.

Subsequently, upon utilizing the data to construct a graphical representation depicting the relationship between magnitude and distance, it becomes evident that the resulting plot assumes a curved path, as depicted in **Figure 5**. A linear relationship is observed when plotting a graph of magnitude against distance on a semi-logarithmic scale, as depicted in **Figure 6**.

Table 2 Relationship between apparent magnitude and distance.

Distance (cm)	Apparent magnitude					\bar{m}
	1	2	3	4	5	
10	- 0.75	- 0.75	- 0.75	- 0.75	- 0.75	- 0.75
15	0.06	0.06	0.06	0.06	0.06	0.06
20	0.63	0.63	0.63	0.63	0.63	0.63
25	1.09	1.09	1.09	1.09	1.09	1.09
30	1.44	1.44	1.44	1.44	1.44	1.44
35	1.75	1.75	1.75	1.75	1.75	1.75
40	2.01	2.01	2.01	2.01	2.01	2.01
50	2.50	2.50	2.50	2.50	2.50	2.50
60	2.85	2.85	2.85	2.85	2.85	2.85
70	3.1	3.1	3.1	3.1	3.1	3.1
80	3.49	3.49	3.49	3.49	3.49	3.49

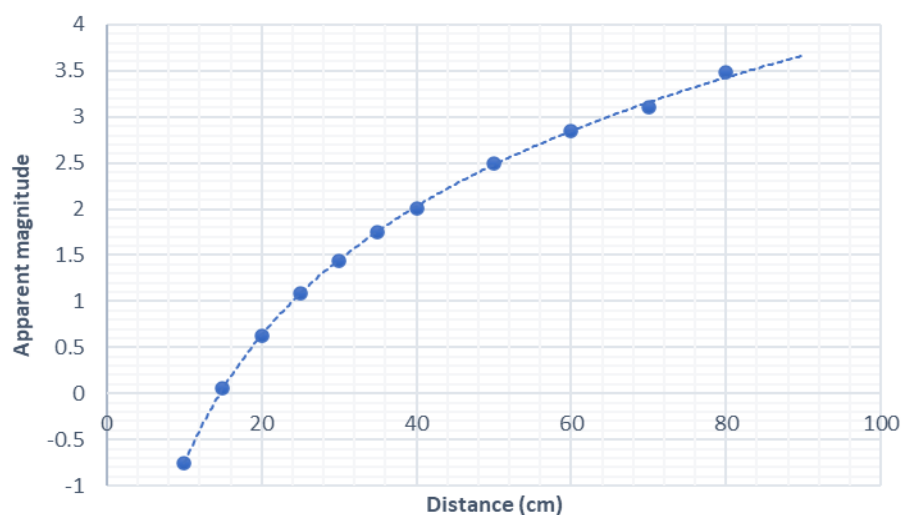


Figure 5.
Relationship between apparent magnitude and distance.

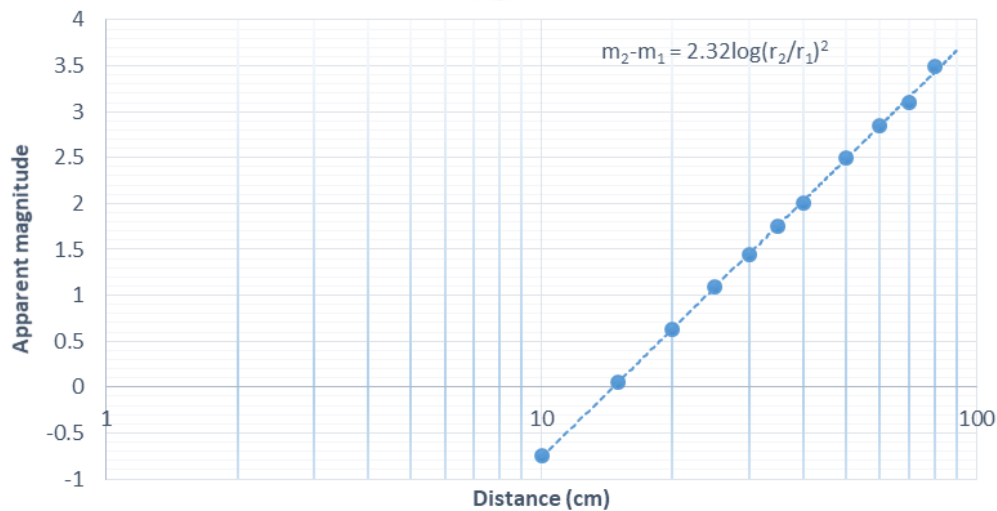


Figure 6.

Relationship on a semi-log graph between apparent magnitude and distance.

According to the graphical representation depicting the correlation between apparent magnitude and distance, it is observed that an increase in distance corresponds to an increase in the magnitude value, as indicated by the equation. The equation $m_2 - m_1 = 2.32 \log(r_2/r_1)^2$ aligns with the principles and concepts of the underlying theoretical framework. The error value is 7.20 percent.

Results of apparent magnitude vs brightness

The data presented in **Table 3** illustrate the findings obtained from the examination of the correlation between the magnitude and brightness of stars within the experimental dataset. Subsequently, upon utilizing the collected data to graph the relationship between magnitude and brightness, the resulting plot exhibits a curved pattern, as depicted in **Figure 7**. A linear relationship is observed when plotting a graph between magnitude and brightness on a semi-logarithmic scale, as depicted in **Figure 8**.

Table 3 Relationship between apparent magnitude and brightness.

Distance (cm)	Brightness (lx)	Apparent magnitude
10	799	- 0.75
15	380	0.06
20	223	0.63
25	146	1.09
30	106	1.44
35	80	1.75
40	63	2.01
50	40	2.50
60	29	2.85
70	23	3.1
80	16	3.49

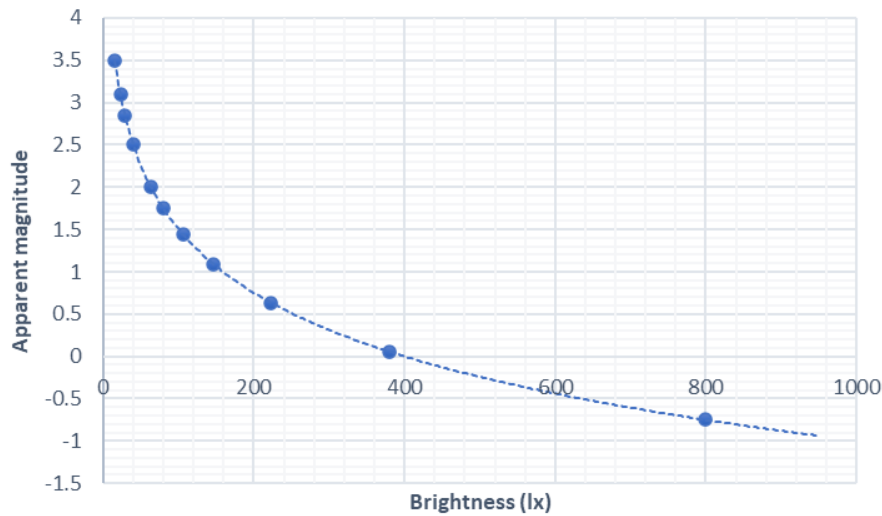


Figure 7.

Relationship between apparent magnitude vs brightness.

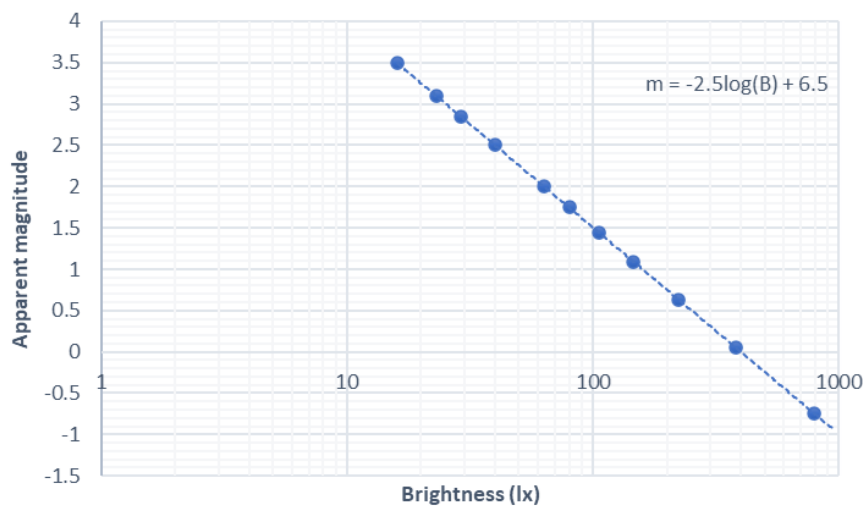


Figure 8.

Relationship between apparent magnitude vs brightness on a semi-log graph.

The graph depicting the correlation between apparent magnitude and brightness reveals that an increase in brightness is associated with a decrease in apparent magnitude, as indicated by the equation. The equation $m_2 - m_1 = 2.5 \log(B_2/B_1)$ is in accordance with established theoretical principles.

A sequence of experiments on stellar apparent magnitude was conducted, resulting in empirical findings regarding the correlation between apparent magnitude values. The determination of the distance value in relation to the brightness value is derived from the theoretical concept proposed by Pogson N. [6]. This approach is employed due to the utilization of a light bulb, which possesses a substantial luminous power despite its relatively diminutive size in comparison to the distance from the light sensor. Furthermore, within the measurement command code, the calibration of light intensity is performed in order to account for any potential interference caused by ambient light present in the environment.

The experimental findings align with the research conducted by Agrawal [7], which posits that incandescent lamps serve as effective generators of electromagnetic energy emissions. Consequently, students can utilize these lamps to explore the concept of apparent magnitude through both theoretical and experimental approaches.

Conclusion:

The star apparent magnitude experiment kit comprises an Arduino Uno R3 board, a light sensor, an LED light bulb, an LCD screen, and an aluminum rail with a scale. The simultaneous display of brightness and apparent magnitude values can be achieved. According to experimental observations, it has been determined that the luminosity of a star diminishes as the distance between the observer and the star increases. The theory exhibited an error value of 7.15 percent. The observed magnitude value should exhibit an augmentation. The error for the magnitude value of 7.20 percent can be determined. As the luminosity diminishes, the corresponding apparent magnitude exhibits an upward trend, in accordance with established theoretical principles.

Acknowledgements:

The research was funded by the Faculty of Science and Digital Innovation, Thaksin University, Thailand.

References:

1. Vipu Rujopakarn. 2005. *Universe: To understand the nature of the universe*. Bangkok: Nanmeebooks publication.
2. Ministry of Education. (2008). *The Basic Education Core Curriculum A.D. 2008*. Bangkok: Kurusapa Printing Lad-phrao.
3. Zeilik et al. (1998). Misconceptions and their change in university-level astronomy courses. *Phys Teach.*, 36(2), 104-107.
4. Trumper, R. (2001). A cross-age study of junior high school students' conceptions of basic astronomy concepts. *Int. J. Sci. Educ.*, 23(11), 1111-1123.
5. Taylor, I.; Barker, M.; & Jones, A. (2003). Promoting mental model building in astronomy Education. *Int. J. Sci. Educ*, 25(10), 1205-1225.
6. Pogson, N. (1856). Magnitudes of Thirty-six of the Minor Planets for the First Day of each Month of the Year 1857. *Mon. Not. R. Astron. Soc.*, 17(1), 12–15.
7. Dulli Chandra Agrawal. 2018. Apparent magnitude scale: incandescent lamps. *Phys Educ*, 53(5), 2.
8. Tobin, K.G. (2003). Research on science laboratory activities; in pursuit of better questions and answers to improve learning. *Sch. Sci. Math.*, 90(1), 403-418.



MODELING GAS DETECTION UTILIZING ONE-DIMENSIONAL PHOTONIC

Saisudawan Suttiyan¹, Thammarat Taengtang^{2*}

Department of Applied Physics, King Mongkut's Institute of Technology Ladkrabang, 10520 THAILAND

*e-mail: Thammarat.ta@kmitl.ac.th

Abstract— Recent years have witnessed an increased focus on advancing the utilization of photonic crystals (PCs) within the realm of detection. The potential of employing these materials as gas sensors is very compact. This study aims to investigate a resonant microsystem predicated on one-dimensional photonic crystals. Such microsystems hold potential for applications like high-quality optical devices tailored for the precise detection, and quantification of airborne gas concentrations. Specifically, we introduce an adapted gas monitoring architecture, a nano-system composed of alternating layers of silicon dioxide (SiO_2) and air, housing a resonant nanocavity of gases at its core. Computational simulations demonstrate that the emergence of a resonance peak within the Photonic Band Gap (PBG) stems from the formation of the nano-cavity within the periodic 1D arrangement. The experimental results of this model found that the resonance peak is a viable reference for real-time detection, and the refractive index of each test gas in this work affects the resonance peak of the shifted slight wavelength. Furthermore, our experiment is a comprehensive theoretical assessment of these photonic systems, probing the impact of the intrinsic and extrinsic parameters of the model on detection performance. The intrinsic and extrinsic parameters such as the thickness layer, refractive index, number of periodic layers, and electromagnetic wave must be appropriate.

Introduction:

Photonic crystals (PCs) are synthetic materials constructed using periodic arrangements of dielectric or metallic building units. The presence of photonic band gaps (PBGs) has introduced an unparalleled ability to manage and control the propagation of electromagnetic (EM) waves [1–3]. The most basic manifestation of a photonic crystal takes the form of a one-dimensional periodic structure, referred to as a Bragg mirror. Comprising alternating layers with high and low refractive indices, its layer thicknesses adhere to the Bragg condition: $n_h d_h = n_l d_l = \lambda/4$, where λ denotes the reference wavelength [4]. Unlike the complexities of two- and three-dimensional counterparts, the appeal of the one-dimensional photonic crystal lies in its practical fabrication across a range of wavelengths. One crucial function of a PBG is to function as an exceedingly effective reflective mirror (exceeding 99%). Thus, a strategy for achieving more adaptable band gap configurations might involve expanding the width of the PBGs. In recent times, multiple research endeavors have centered on the application of photonic crystals in the field of sensors [5–7]. The potential of utilizing photonic crystals as gas sensors holds great promise within research domains, attributed to their compactness. This study will unveil the viability of a one-dimensional (1D) photonic crystal, comprised of alternating layers of silicon (SiO_2) and air, featuring an empty "defect" layer at its core. This structure demonstrates the capacity to operate as an optical sensor for gauging gas concentrations in the atmosphere, particularly when illuminated by incident light in a perpendicular manner.



Methodology:

The transfer matrix method [8] holds significant significance when dealing with an arbitrary number of dielectric layers, allowing for the simulation of various light behaviors such as reflectivity, absorption, and transmission. In the context of this method, let's consider an electromagnetic plane wave λ that is incident perpendicularly upon a vertical arrangement of dielectric materials. These dielectric layers possess distinct thicknesses (d_j), refractive indices (n_j), and angles of incidence (θ_j). The interaction of the incident light results in both reflected and transmitted components, depicted in Figure 1. As this light traverses the layers, its behavior can be accurately described by the transfer matrix, represented by equation (4). Additionally, the phase difference (Z) between interface fields 'a' and 'b' is quantified in equation (5).

$$\begin{bmatrix} B \\ C \end{bmatrix} = \begin{bmatrix} \cos \delta & -i \sin \delta / n_j \\ -i n_j \sin \delta & \cos \delta \end{bmatrix} \begin{bmatrix} 1 \\ n_{j+1} \end{bmatrix} \quad (4)$$

Equation (4) encapsulates the essence of the transfer matrix technique, providing a quantitative framework for evaluating the interactions between light and the dielectric layers. This equation takes into account a range of factors including layer thicknesses and refractive indices, enabling the prediction of light distribution and modification as it traverses the layered structure.

$$\delta = 2\pi n_j d_j \cos \theta_j / \lambda \quad (5)$$

Furthermore, equation (5) introduces the concept of phase difference (δ) between interface fields 'a' and 'b', shedding light on the phase relationships that arise from the interaction of light with diverse dielectric layers. This phase difference contributes to phenomena like interference, influencing the overarching optical behavior observed within the system. Where R is reflectance, T is transmittance, and A is absorptance.

$$R = \left(\frac{n_0 B - C}{n_0 B + C} \right) \left(\frac{n_0 B - C}{n_0 B + C} \right)^* \quad (6)$$

$$T = \frac{4n_0 \operatorname{Re}(n_j)}{(n_0 B + C)(n_0 B + C)^*} \quad (7)$$

$$A = \frac{4n_0 \operatorname{Re}(BC^* - n_j)}{(n_0 B + C)(n_0 B + C)^*} \quad (8)$$

The refractive index of materials:

The fundamental dielectric materials for the optical sensor in this work are the nonlinear refractive indices. They have complex equations. However, scientists have attempted to search and discover some complex equations of dielectric materials. We have to choose some known complex equations of dielectric materials. The housing sensor is silicon dioxide, which the complex equation of Malitson [9] shown in equation (9).



$$n_{SiO_2} - 1 = \frac{0.696166\lambda^3}{\lambda^2 - 0.0684043^2} + \frac{0.4079426\lambda^3}{\lambda^2 - 0.1162414^2} + \frac{0.8974794\lambda^3}{\lambda^2 - 9.896161^2} \quad (9)$$

$$n_{O_2} - 1 = \frac{0.05792105\lambda^3}{238.0185 - \lambda^{-2}} + \frac{0.00167917}{57.362 - \lambda^{-2}} \quad (10)$$

$$n_{CO_2} - 1 = \frac{6.99100 \times 10^{-2}}{166.175 - \lambda^2} + \frac{1.44720 \times 10^{-3}}{79.609 - \lambda^2} + \frac{6.42941 \times 10^{-5}}{56.3064 - \lambda^2} + \dots$$

$$\dots + \frac{5.21306 \times 10^{-5}}{46.0196 - \lambda^2} + \frac{1.48847 \times 10^{-6}}{0.0584738 - \lambda^2} \quad (11)$$

$$n_{NH_3} - 1 = \frac{0.032053}{90.392 - \lambda^{-2}} \quad (12)$$

The oxygen, carbon dioxide, and ammonia are test gases to simulate and create the sensor model. The Refractive Index Info website has determined the constant parameters of the refractive index functions, which are the standard functions.

1D photonic crystal model:

The prototype of a 1D photonic crystal model shows a structure in Fig1. The periodic stack structure of a high (H) and low (L) refractive index is type $H(LH)^J$, J with J keeping the value $J = 7$, and it consists of silicon dioxide (SiO_2) and Air (O_2) layers [14] related to refractive indices, respectively. For this work, the improved photonic structure is $J = 3$, and the changed silicon layer to the silicon dioxide (SiO_2) layer shows the new model in Figure 1. The calculated thickness of silicon dioxide and the air was found with Bragg condition: $n_h d_h = n_l d_l = \lambda/4$, where λ reference wavelength [4]. The considering wavelength will find each thickness layer from the types of desired test gas with this model. The three types of test gas are Air, Carbon dioxide (CO_2), and Ammonia (NH_3). In this paper, the air is the default to calculate the thickness layers. All materials in this work are nonlinear refractive indices due to changed wavelength. The public refractive index database is on the website, and it shows some equations of the refractive index materials. There is a display of equations (1-5) of all materials in this paper. The refractive index database of all used substances has more differences in boundary wavelength. So, we must choose the middle wavelength that appears together in the boundary wavelength of all materials. The central wavelength is about 0.6171 micrometers when the thickness of Silicon and Oxygen are 105.85 and 154.24, respectively.

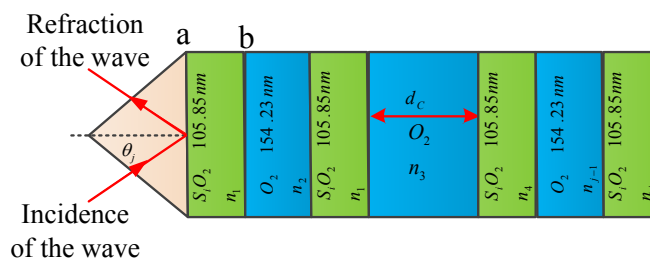


Figure 1.

Three periodic of 1D photonic crystal model to simulate the effect gases



The other defect layer is the thickest in the middle of the new structure, which is the layer of thickness of the cavity shown in Fig1, and has varied the cavity width from $d_c=154.23 \times N$ ($N=1,2,\dots,7$) to show the effect on the spectrum behavior of such a nanostructure. The EMW transmittance shown in Table 1 travels through the photonic crystal for different thicknesses of the defect layer.

Table 1.

The relation between the defect layer width (nm) and the peak wavelengths (nm)

O_2	$5d_c$	$6d_c$	$7d_c$	$8d_c$
peak wavelength	525.6	605.5	684.3	757.8
intensity	0.6862	0.8387	0.9685	0.9946

Table 2.

The relation between the test gases and the peak wavelengths (nm)

	O_2	CO_2	NH_3
peak wavelength	683.9	685.4	684.3
intensity	0.9685	0.9674	0.9684

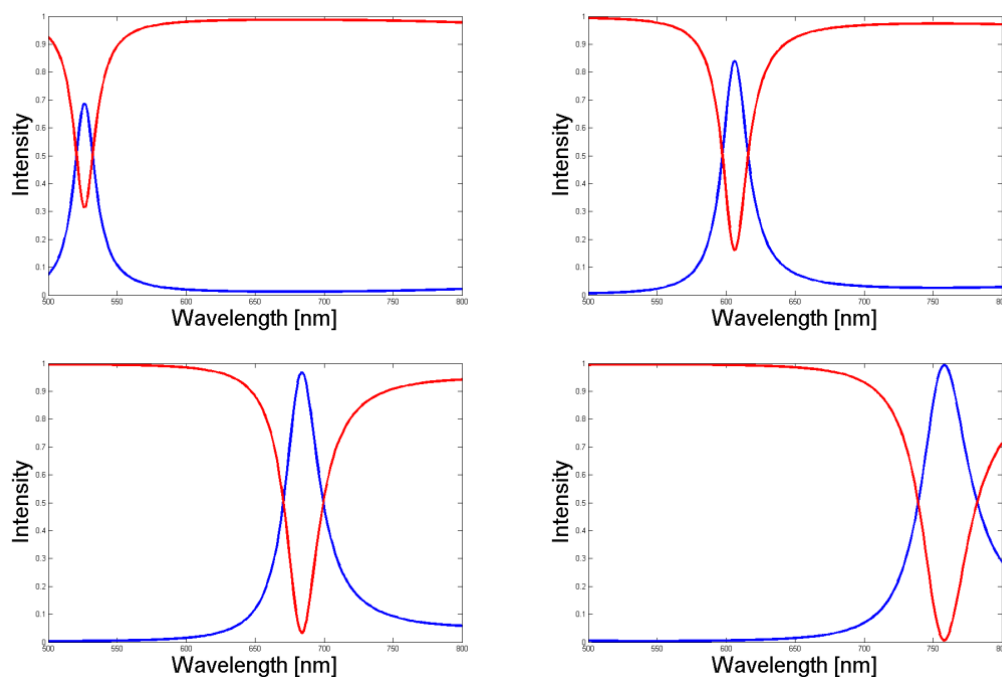


Figure 2.

Example of transmittance (red) and reflectance (blue) of oxygen at $5d_c$ (top left), $6d_c$ (top right), $7d_c$ (down left), and $8d_c$ (down right).

Results and Discussion:

In this study, we divided into two calculations of the results, studying the effect of the defect layer width that implicates wavelength and gas tests, using oxygen as the test gas to search width, in the simulation related to the maximum peak at wavelength of the EM transmission. The first result presents in Table 1 and Fig 2 a connection between the defect layer width and wavelength that shows the more defect layer width, the more the maximum peak wavelength in the range 500-800nm with TE mode and 40.25 degrees of the incident wave. We found that



the intensity directly varies with the defect layer width. In Table 2 of the 7Dc width for each test gas, the second result displays the relationship between the three test gases and the maximum peak for the specific wavelength; there are few differences in transmittance intensity at each maximum peak at wavelength for test gases. In the second relation of Table 2, each test gas that associates the top peak of each wavelength discovers the opportunity to apply the 1-D photonic crystal model for detecting gases due to shifting of a vertex peak at wavelength. When the phase difference 'this designed model with the refractive index of oxygen' has changed due to the refractive index of CO₂ and NH₃, the effect of shifted wavelength on the periodic stack structure. The effectiveness of shifted wavelength depends on J keeping the value. In Table 2, shown difference of intensities and wavelength of oxygen, ammonia, and carbon dioxide.

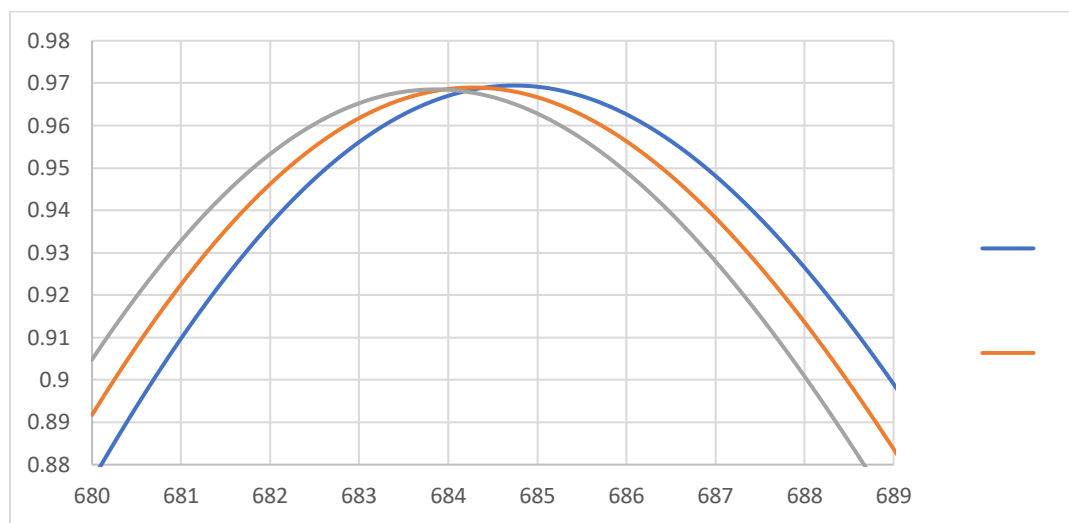


Figure 3.

The shifted wavelength of three test gases.

Conclusion:

This project adapted and simulated the 1-D photonic crystal model to detect gases because of the few little dissimilar refractive index properties of gases. The simulation results are an attentive intensity and peak wavelength of the EM transmittance. The intensity results of this model can separate the very few differences at a peak of wavelength, and each test gas affects the peak of wavelength to move a little for some gases shown in Fig 3. The little difference in these results should arise from a few layers of the model. The problem in this paper may be from too few periodic layers of silicon dioxide and oxygen.

References:

- 1 Packiaraj, D., K. J. Vinoy, and A. T. Kalghatgi. Progress In Electromagnetics Research C, Vol.7, 2009; 111–123.
- 2 Sang, H.-Y., Z.-Y. Li, and B.-Y. Gu. Chinese Physics Letters, Vol. 22, 2005; 2:365.
- 3 Golmohammadi, S., M. K. Moravvej-Farshi, A. Rostami, and A. Zarifkar. Progress In Electromagnetics Research, Vol. 75, 2007; 75:69–84.
- 4 Kittel, C., et al. Introduction to Solid State Physics, Vol. 8, 1976; 32.
- 5 Wang, X., Z. Xu, N. Lu, J. Zhu, and G. Jin. Optics Communications, Vol.281, 2008; 6:1725–1731.



- 6 D'undar, M. A., E. C. Ryckebosch, R. N'otzel, F. Karouta, L. J. van Ijzendoorn, and R. W. van der Heijden. *Optics Express*, Vol. 18, 2010; 5:4049–4056.
- 7 Liu, Y. and H. Salemink. *Optics Express*, Vol. 20, 2012; 18:19912–19920.
- 8 Macleod, H. A. *Thin-film optical filters*. CRC press, 2010.
- 9 Malitson, I.H. *Journal of the Optical Society of America*, 1968; 55:1205-1208.
- 10 J. Zhang, Z. H. Lu, and L. J. Wang. *Appl. Opt* 2008; 47:3143-3151.
- 11 P. Křen. *Appl. Opt.* 2011; 50:6484-6485.
- 12 A. Bideau-Mehu, Y. Guern, R. Abjean and A. Johannin-Gilles. *Opt. Commun*, 1973; 9:432-434.
- 13 C. Cuthbertson and M. Cuthbertson. *Phil. Trans. R. Soc. Lond. A*, 1914; 213:1-26.
- 14 Oumayma Habli1, Yassine Bouazzil, and Mounir Kanzari1. *Progress In Electromagnetics Research C*. 2019; 92:251–263.



THE FABRICATION AND REFRACTIVE INDEX MEASUREMENT OF DIY ACRYLIC CONVEX LENSES

Juthamas Promrachkaew, Prasong Kessaratikoon*

Department of Basic Science and Mathematics, Faculty of Science, Thaksin University, Songkhla Campus, Muang, Songkhla, 90000, Thailand

*e-mail: prasong@tsu.ac.th

Abstract:

A set of DIY bifacial convex lenses made of 10 mm thick transparent acrylic sheet, was designed and produced. The DIY bifacial convex lens set consists of 3 DIY bifacial convex lenses with the same thickness of 2 cm. They have a height of 5, 6 and 6.5 cm and front (R1) and rear (R2) curvature radius of the lens are 4, 5 and 6 cm, respectively. A computer laser machine was used to cut the transparent acrylic sheets to the desired shape of the lens. The set of DIY bifacial convex lenses was taken to perform the experiment with a light source and 2- and 3-slot slit plates at the basic laboratory of the Faculty of Science Laboratory Building, Thaksin University, Songkhla Campus. We can measure the focal length of DIY lens and the refractive index of the transparent acrylic plates for making the set of the convex lenses by using the light refractive principle and the lens maker's equation. It was found that the mean values of the focal length of the set of DIY bifacial convex lens were equal to 5.99 ± 0.18 , 8.09 ± 0.67 and 8.33 ± 0.41 cm, respectively. In addition, the refractive index of the transparent acrylic sheet used to make this set of lenses, calculated by using the lens maker's equation, equal to 1.33 ± 0.01 , 1.31 ± 0.03 and 1.36 ± 0.02 with the error from the actual value of 11, 12 and 9%, respectively. Although, the errors were slightly high, but they were within the acceptable criteria. The set of DIY convex lens should be designed with a smaller thickness that will cause the value of the error to be reduced.

Introduction:

It is well known that organizing the teaching of science subjects, especially physics, in high school requires suitable and high-quality materials and experimental equipment. Teachers can use these materials and equipment to demonstrate experiments or conduct real experiments to make the teaching and learning process effective, accurate, and minimally error-prone. This helps students learn and understand the content of the physics subject, leading to good learning outcomes [1-2]. Currently, Office of the Basic Education Commission (OBEC), the Ministry of Education has been emphasizing student-centered teaching and incorporating STEM (Science, Technology, Engineering, and Mathematics) education principles since 2016. These principles require a considerable amount of materials and equipment that are complete and readily available [3-5]. The Ministry has made efforts to procure materials and equipment produced in Thailand at reasonable prices, but in some cases, it has to import them at higher costs, which may not fully meet the school's needs. Additionally, when there is damage or wear and tear, it is not always possible to replace them immediately, resulting in a shortage of effective and efficient teaching materials and equipment. This affects students' learning outcomes. For teaching physics in high school, research has been conducted on designing and creating simple, low-cost materials and tools for use in teaching. For example, a study by Nakchuay, et al. (2018) [6] introduced a set of experiments on sound resonance using a smartphone and a 1-meter-long PVC pipe with one open end and one closed end. They used this setup to demonstrate sound resonance, and the experiment was carried out with clarity. This low-cost experiment could accurately calculate wave length and sound



velocity, with an error margin of less than 6%. This experiment proved to be highly effective for teaching purposes. Another example is a study by Thepnurat, et al. (2017) [7], who designed and created a DIY lens and convex lens set using locally available materials. This was intended to demonstrate the principles of lens design and manufacture, focusing distance, and light refraction through lenses. These experiments aimed to help students understand the natural phenomena related to lenses, focal lengths, and light refraction. Consequently, this research is particularly interested in creating and developing self-made materials and experimental equipment for physics, especially those related to light refraction through convex lenses, which can be used effectively in teaching and learning. This research provides guidance for designing and creating low-cost, DIY science materials and equipment in the future.

Methodology:

For conducting research, the steps are as follows.

1. Study of the Problem and Research Significance. We studied the problem and significance of the research, particularly research related to the lack of materials and teaching equipment for the high school physics curriculum. This includes topics related to light and vision and other related research. We also examined existing materials and equipment to conduct experiments related to light refraction through convex lenses to obtain accurate data for calculating the focal length (f) and refractive index (n) of self-made acrylic lenses. Additionally, the researcher explored information about businesses or shops that offer modern tools for cutting acrylic sheets, which are essential for creating the DIY lens set.

2. Study of Relevant Theory and Research. We conducted a study of relevant theories and research related to the project, focusing on reviewing knowledge and understanding of theories concerning light refraction through convex lenses, equations, and formulae related to the subject, particularly the lens maker's equation which is $1/f = (n - 1) \cdot [(1/R_1) - (1/R_2)]$ for the thin lens [8]. We also researched previous works related to determining the refractive index and the design and creation of DIY lenses using various methods of interest. Furthermore, we studied and practiced designing lens shapes using A4 paper and consulted with experienced individuals in the field.

3. Design and Creation of the Experiment Set. We designed and created a DIY bifacial convex lenses set made from 10-mm thick transparent acrylic sheets to be used with existing materials and equipment in the basic physics laboratory at Thaksin University, Songkhla Campus, in the Department of Science and Mathematics. The materials and equipment include light sources and slit experiments with 2- and 3-slot slit plates, among others. The process for designing and creating the DIY bifacial convex lens set is divided into two steps:

3.1. Design Step. Draw circular shapes with radii of 4, 5, and 6 centimeters on A4 paper, creating curved shapes that intersect to form bifacial convex lenses. The width of all three lenses should be 2 centimeters, and the height should be approximately 5, 6, and 6.5 centimeters, as illustrated in Figure 1(a), (b) and (c), respectively. Afterwards, transfer the design onto a 10-mm thick clear acrylic sheet to prepare it for cutting into the desired DIY bifacial convex lens, as outlined in the following steps.

3.2 Steps to Create a DIY Bifacial Convex Lens Set, Using 10-mm Clear Acrylic Sheets. Take the 10-cm clear acrylic sheet with the designs for the DIY bifacial convex lens set, as described in step 3.1, and cut it into the desired lens shapes using an acrylic sheet cutting machine, as shown in Figure 2. This will yield a DIY bifacial convex lens set made from 10-mm thick clear acrylic.

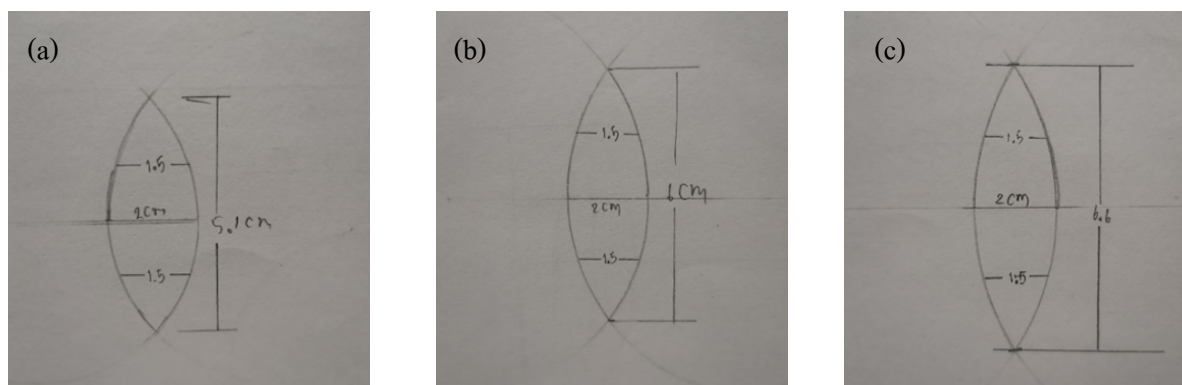


Figure 1.

A DIY bifacial convex lens set which have the width of all three lenses equal to 2 cm, and the height should be approximately 5, 6, and 6.5 cm as shown in (a), (b) and (c) respectively.



Figure 2.

Acrylic sheet laser cutting machine.

This set comprises three lenses of equal thickness, measuring 2 cm each, with heights of 5, 6, and 6.5 cm. These three lenses have the same front (R1) and back (R2) radii of curvature, measuring 4, 5, and 6 cm, respectively, as depicted in Figure 3.

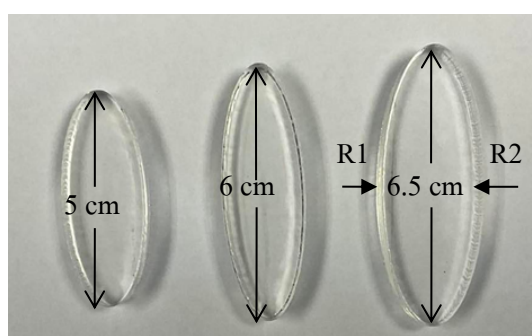


Figure 3.

The DIY bifacial convex lens set is crafted from 10-mm thick clear acrylic sheets, obtained by cutting with a laser cutter. These lenses have equal thickness, approximately 2 cm, and come in heights of 5, 6, and 6.5 cm. The radii of curvature for both the front (R1) and back (R2) of these lenses are the same, measuring 4, 5, and 6 cm, respectively.

4. Experiment and Collect Data. The DIY bifacial convex lens set were taken to perform the special and designed experiments with materials and equipment available in the laboratory. These materials and equipment were light sources, wires, light bulbs, transformers, A4 paper sheets, 2- and 3-slot slit plates, etc., as shown in Figure 4.

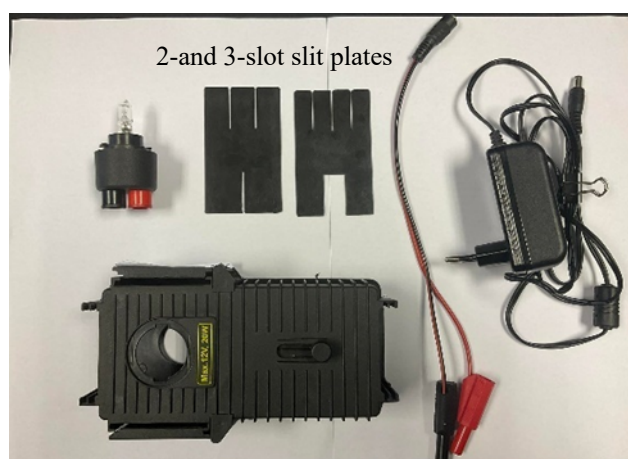


Figure 4. Materials and equipment available in the laboratory.

Use the DIY bifacial convex lens set to conduct experiments with the prepared materials and equipment. Follow the steps below:

4.1 Organize the materials, equipment, and tools for the experiment on the refraction of light using the DIY bifacial convex lens set. Place the lens in front of the light source connected to the power supply to create the desired bright light, as shown in Figure 5.



Figure 5. Experimental setup for light refraction through the DIY bifacial convex lens set.

4.2 Place the 2 slot slit plates near the front of the light source to separate the light into two straight beams. These two beams will pass through the DIY bifacial convex lens set up as described in step 4.1. Observe the phenomenon of light refraction through the lens where they intersect at a particular point, as shown in Figure 6.

4.3 Measure the distance at which the intersecting of the refracted light occurs through the DIY bifacial convex lens and record this data as the focal length of the DIY lens. Take this focal length value to calculate the refractive index of the clear acrylic sheet used for making the lens by using the lens maker's equation.

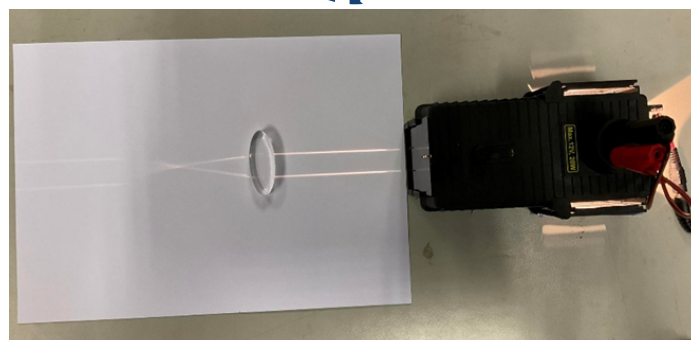


Figure 6. Using the 2-slot slit plates to separate light into two straight beams before passing through the DIY bifacial convex lens.

4.4 Invert the orientation of the DIY bifacial convex lens, moving it from top to bottom and from left to right, then repeat the experiment from step 4.1 to 4.3.

4.5 Repeat the experiment from step 4.1 to 4.4 using all the DIY bifacial convex lens sets created.

4.6 Repeat the experiment from step 4.1 to 4.5, changing the 2-slot slit plates to a 3-slot slit plates, and observe and record the experimental results in the form of a data table.

4.7 Analyze and summarize the experimental results obtained.

Results and Discussion:

The data obtained from the experiment using the DIY bifacial convex lens set made from 10-cm thick clear acrylic sheets in the study of light refraction, as detailed in Section 4, is presented in the form of three tables as follows:

Table 1. Experimental data when using the DIY bifacial convex lens made from 10-cm thick clear acrylic sheets with radii of curvature (R1 and R2) equal to 4 centimeters (DIY 1).

Lens type	Slit type	Side of lens	The experimental results obtained		Mean and standard deviation			
					Focal length (f) in cm.		Refraction index (n)	
			Focal length (f) in cm.	Refraction index (n)	Mean	S.D.	Mean	S.D.
Convex lens DIY1 1 st time	2-channel type	Side 1 (top)	6.25	1.32	6.40	0.21	1.31	0.01
		Side 1 (bottom)	6.40	1.31				
		Side 2 (top)	6.70	1.30				
		Side 2 (bottom)	6.25	1.32				
	3-channel type	Side 1 (top)	6.00	1.33	6.03	0.10	1.33	0.01
		Side 1 (bottom)	6.10	1.33				
		Side 2 (top)	5.90	1.34				
		Side 2 (bottom)	6.10	1.33				
Convex lens DIY1 2 nd time	2-channel type	Side 1 (top)	5.50	1.36	5.86	0.27	1.34	0.01
		Side 1 (bottom)	5.95	1.34				
		Side 2 (top)	6.15	1.33				
		Side 2 (bottom)	5.85	1.34				
	3-channel type	Side 1 (top)	5.80	1.34	5.69	0.14	1.35	0.01
		Side 1 (bottom)	5.65	1.35				
		Side 2 (top)	5.50	1.36				
		Side 2 (bottom)	5.80	1.34				
Convex lens DIY1					5.99	0.18	1.33	0.01

From Table 1, it can be seen that f and n of the DIY bifacial convex lens made of a 10 cm thick clear acrylic sheet with radii of curvature (R_1 and R_2) are equal to 4 cm (DIY 1) has a value equal to 5.99 ± 0.18 cm and 1.33 ± 0.01 , respectively.

Table 2. Experimental data when using the DIY bifacial convex lens made from 10-cm thick clear acrylic sheets with radii of curvature (R_1 and R_2) equal to 5 cm (DIY 2).

Lens type	Slit type	Side of lens	The experimental results obtained		Mean and standard deviation			
					Focal length (f) in cm.		Refraction index (n)	
			Focal length (f) in cm.	Refraction index (n)	Mean	S.D.	Mean	S.D.
Convex lens DIY2 1 st time	2-channel type	Side 1 (top)	8.25	1.30	8.14	0.83	1.31	0.03
		Side 1 (bottom)	7.00	1.36				
		Side 2 (top)	8.30	1.30				
		Side 2 (bottom)	9.00	1.28				
	3-channel type	Side 1 (top)	7.75	1.32	8.43	0.99	1.30	0.03
		Side 1 (bottom)	8.05	1.31				
		Side 2 (top)	8.00	1.31				
		Side 2 (bottom)	9.90	1.25				
Convex lens DIY2 2 nd time	2-channel type	Side 1 (top)	8.05	1.31	7.76	0.33	1.32	0.02
		Side 1 (bottom)	8.00	1.31				
		Side 2 (top)	7.35	1.34				
		Side 2 (bottom)	7.65	1.33				
	3-channel type	Side 1 (top)	8.75	1.29	8.03	0.52	1.32	0.02
		Side 1 (bottom)	7.50	1.33				
		Side 2 (top)	7.90	1.32				
		Side 2 (bottom)	7.95	1.33				
Convex lens DIY2					8.09	0.67	1.31	0.03

From Table 2, it can be seen that f and n of the DIY bifacial convex lens made of a 10 cm thick clear acrylic sheet with radii of curvature (R_1 and R_2) are equal to 5 cm (DIY 2) has a value equal to 8.09 ± 0.67 cm and 1.31 ± 0.03 , respectively.

Table 3. Experimental data when using the DIY bifacial convex lens made from 10-cm thick clear acrylic sheets with radii of curvature (R_1 and R_2) equal to 6 cm (DIY 3).

Lens type	Slit type	Side of lens	The experimental results obtained		Mean and standard deviation			
					Focal length (f) in cm.		Refraction index (n)	
			Focal length (f) in cm.	Refraction index (n)	Mean	S.D.	Mean	S.D.
Convex lens DIY3 1 st time	2-channel type	Side 1 (top)	9.10	1.33	9.01	0.09	1.33	0.01
		Side 1 (bottom)	9.00	1.33				
		Side 2 (top)	8.90	1.34				
		Side 2 (bottom)	9.05	1.33				
	3-channel type	Side 1 (top)	8.10	1.37	8.40	0.58	1.36	0.03
		Side 1 (bottom)	9.05	1.33				



Convex lens DIY3 2 nd time	2-channel type	Side 2 (top)	8.70	1.34	7.66	0.51	1.39	0.03
		Side 2 (bottom)	7.75	1.39				
		Side 1 (top)	8.15	1.37				
		Side 1 (bottom)	7.20	1.42				
		Side 2 (top)	8.05	1.37				
	3-channel type	Side 2 (bottom)	7.25	1.41	8.24	0.48	1.37	0.02
		Side 1 (top)	8.95	1.34				
		Side 1 (bottom)	8.00	1.38				
		Side 2 (top)	8.00	1.38				
		Side 2 (bottom)	8.00	1.38				
Convex lens DIY 3					8.33	0.41	1.36	0.02

From Table 3, it can be seen that f and n of the DIY bifacial convex lens made of a 10 cm thick clear acrylic sheet with radii of curvature (R_1 and R_2) are equal to 6 cm (DIY 3) has a value equal to 8.33 ± 0.41 cm and 1.36 ± 0.02 , respectively.

Conclusion:

We can summarize the findings as follows:

1. We gained experience and knowledge from designing and constructing the DIY bifacial convex lens set using 10-mm-thick transparent acrylic sheets obtained by cutting identical pieces from acrylic sheets with a thickness of approximately 2 cm. The lenses had heights of 5, 6, and 6.5 cm, with front and back radii of curvature (R_1 and R_2) that were the same and measured 4, 5, and 6 cm. These lenses were successfully used in experiments related to light refraction to determine focal length and refractive index.

2. When experimenting and calculating the focal length of the DIY bifacial convex lens set made from 10-mm-thick transparent acrylic sheets with uniform thickness of approximately 2 cm, and lens heights of 5, 6, and 6.5 cm, with identical front and back radii of curvature (R_1 and R_2) measuring 4, 5, and 6 cm, the average values were found to be 5.99 ± 0.18 , 8.09 ± 0.67 , and 8.33 ± 0.41 cm, respectively.

3. When experimenting and calculating the refractive index of light for the DIY bifacial convex lens set made from 10-mm-thick transparent acrylic sheets with uniform thickness of approximately 2 cm, and lens heights of 5, 6, and 6.5 cm, with identical front and back radii of curvature (R_1 and R_2) measuring 4, 5, and 6 cm, using the lens maker's equation, the average values were found to be 1.33 ± 0.01 , 1.31 ± 0.03 , and 1.36 ± 0.02 , respectively.

4. When comparing the refractive index of light for the three lenses in the DIY bifacial convex lens set made from 10-mm-thick transparent acrylic sheets to the standard refractive index of 1.49 for acrylic sheets, a percentage deviation of 9-12% was observed, as shown in the following table.



Table 4. Comparison of the refractive index values of the three DIY bifacial convex lens sets made of 10 mm thick clear acrylic sheets with the standard values of the refractive index values of the clear acrylic sheets.

Convex lens DIY	Experimentally calculated refractive index value (n)	Refractive index of clear acrylic sheet (n)	Error (%)
DIY 1	1.33 ± 0.01	1.49	11
DIY 2	1.31 ± 0.03		12
DIY 3	1.36 ± 0.02		9

It can be observed that the DIY bifacial convex lens set made from 10-mm-thick transparent acrylic sheets, consisting of three lenses designed and constructed, can be effectively used in experiments involving light refraction with the materials and equipment available in the Department of Basic Science and Mathematics laboratory of the Faculty of Science, Thaksin University, Songkhla campus. These lenses were successfully used to conduct experiments and determine the focal length of each lens, yielding values of 5.99 ± 0.18 , 8.09 ± 0.67 , and 8.33 ± 0.41 cm, respectively. Furthermore, the refractive index of the DIY bifacial convex lens set, calculated using the lens maker's equation, resulted in average values of 1.33 ± 0.01 , 1.31 ± 0.03 , and 1.36 ± 0.02 , respectively. In addition, when comparing the refractive index of light for the three lenses in the DIY bifacial convex lens set made from 10-mm-thick transparent acrylic sheets to the standard refractive index of 1.49 for acrylic sheets, a percentage deviation of 9-12% was observed, which falls within an acceptable range. The reason the error value is higher than 10% is because the thickness of the lens created is relatively too thick, causing refraction and making the focal length measured from the experiment not correspond to reality. Furthermore, the uneven edges of the lens also contribute to inaccuracies in the experiment for measuring the focal length of the DIY lens. However, it is recommended that future iterations of the DIY bifacial convex lens set should consider reducing the thickness of the lenses to further minimize the percentage deviation in the refractive index [9].

Acknowledgements:

Due to the Department of Basic Science and Mathematics, Faculty of Science, Thaksin University, Songkhla Campus, granting permission and facilitating access to the basic physics laboratory, including materials and equipment related to the refraction of light through concave lenses, until complete and comprehensive data was obtained, the researchers would like to express their deep gratitude at this juncture.

References:

1. Jongsala S, Seebut S. Parichart J., Thaksin Univ. 2008; 21(1): 8–18. Retrieved from <https://so05.tci-thaijo.org/index.php/parichart/journal/article/view/70036> [in Thai].
2. Koocharoensal N, Wongwattana J, Buawkaew P. J. Educ. Naresuan Univ. 2019; 21(4): 166–182. Retrieved from https://so06.tci-thaijo.org/index.php/edujournal_nu/article/view/92158/152314 [in Thai].
3. Suwanich C. J. Educ. Silpakorn Univ., 2017; 15(1): 18–27. Retrieved from <https://so02.tci-thaijo.org/index.php/suedujournal/article/view/174819/125137> [in Thai].
4. Promboon S, Finley F N, Kaweeijmanee K. In: Fry G. (eds) Education in Thailand. Education in the Asia-Pacific Region: Issues, Concerns and Prospects, 2018; 42: 423–429. Springer, Singapore. https://doi.org/10.1007/978-981-10-7857-6_17



5. Polyon P, Thedsakhulwong A, Wonglao P. J. MCU Peace Stud. 2019; 7: (Supplement Issue), S298–S312. Retrieved from <https://so03.tci-thaijo.org/index.php/journal-peace/article/view/186891/134488> [in Thai].
6. Nakchuay T, Kessaratikoon P, Khongpakdee S. Thaksin Univ. J., 2018; 21(3): 183–190. Retrieved from <https://ph02.tci-thaijo.org/index.php/tsujournal/article/view/151788/110925> [in Thai].
7. Thepnurat M, Saphet P, Tong-on A. J. Phys.: Conf. Ser. 2017; 901: 012120. <https://doi.org/10.1088/1742-6596/901/1/012120>
8. Ling S. J. Lensmaker's Equation, 2023; Retrieved from <http://www.physicsbootcamp.org/lens-maker-equation.html>
9. Lu T, Song J, Wu Q. et al. Sci. Rep. 2021; 11: 19284. <https://doi.org/10.1038/s41598-021-98817-9>



SESSION B-BIOLOGICAL SCIENCES



A COMPARATIVE BIOINFOMATICS STUDY OF PILA PROTEIN FROM *Burkholderia mallei*

Tamonwan Lotangchanintra¹, Kittikhun Wangkanont²

¹Program in Biotechnology, Faculty of Science, Chulalongkorn University, Bangkok, Thailand 10330

²Department of Biochemistry, Faculty of Science, Chulalongkorn University, Bangkok, Thailand 10330

*e-mail: kittikhun.w@chula.ac.th

Abstract:

Burkholderia, a genus of gram-negative bacteria, consists of both potentially beneficial and pathogenic members to plants, animals, and humans. Most members of *Burkholderia* genus cause medical concerns, being associated with diseases in humans and has potential as bioweapons. Infections by these bacteria manifest a spectrum of symptoms, from chronic infections to acute sepsis, which cause a high mortality in patients. The species of the concerned and selected to this study include *Burkholderia mallei*, *Burkholderia pseudomallei*, *Burkholderia cenocepacia*, *Burkholderia gladioli*, *Burkholderia multivorans*, and *Burkholderia vietnamiensis*. Pilin is a protein required for attachment and colonization. Studying the structure and function of pilin in these bacteria has the potential to facilitate the development of new therapeutics. Therefore, we performed comparative study of pilin in these bacteria by predicting protein structures based on primary amino acid sequences. The PilA amino acid sequences were retrieved through BLASTp searches, followed by multiple sequence alignments using Clustal Omega. Additionally, we used AlphaFold to predict the PilA protein structure, visualizing and highlighting the results with UCSF Chimera. Our multiple sequence alignment results revealed high sequence identity percentages between *B. mallei* and other *Burkholderia* spp., especially in the first 40 amino acids. The conserved residues are located within the N-terminal α -helix of the core structure. The predicted PilA structure comprised the N-terminal α -helix, the globular head domain with structural features such as the $\alpha\beta$ -loop and D-region. These findings suggested commonalities with previously solved structures and indicated significant variations within the protein structure. This dataset serves as a valuable resource for guiding future experimental investigations into *B. mallei* PilA protein.

Introduction:

Burkholderia is a genus of the gram-negative bacteria. Many *Burkholderia* are pathogens to plants, animals, and humans. Some of the members have agricultural benefits and even have potential in industrial applications, such as *Burkholderia ambifaria*^[1]. Some of the members can cause opportunistic infections in cystic fibrosis patient, as well as a cause of glanders, melioidosis and have been considered for potential use as a biological weapon^[2, 3]. The infected patients have varies symptoms range from chronic infection to acute sepsis^[4]. The species that are considered possible danger are *Burkholderia mallei*, *Burkholderia pseudomallei* both considerate as a biological weapon^[5] and *Burkholderia cenocepacia*, *Burkholderia gladioli*, *Burkholderia multivorans* and *Burkholderia vietnamiensis*^[6].

The infection pathway involves bacterial adherence and formation of a microcolony to the host cell, which is mediate by type IV pili (T4P). The T4P are a group of pilin protein,



found in gram-negative bacteria, forming into the pilus of bacteria and mediate adhesion, microcolony formation, DNA binding, motility etc.^[7-10]. PilA protein is the major small structural protein of T4P. The structure consists of N-terminal helix, β -sheet and disulfide-bonded^[5, 8, 11].

Studying these bacteria requires at least biological safety level 2 (BSL2) or even higher. For *B. pseudomallei*, a BSL3 biosafety cabinet in a biological safety level 3 (BSL3) facility is necessary, which comes with a lot of management and safety restrictions^[12]. To overcome the biosafety challenges, using bioinformatics to predict the protein structure before conducting the experimental study could minimize the risks and reduce the use of time and resource^[13]. Additionally in structural biology, bioinformatics not only guide the way of studying a protein of interested but also allow us to find the potential of the obtained data in conceptual application in many possible ways. For example, to explore the protein interaction to protein ligand, drug, etc. The predicted structure could be used in many docking software upon the research respective field of interest^[14]. The deep-learning method like AlphaFold could predict the protein structure based on primary amino acid sequence employing the large amount of solved proteins data available in Protein Data Bank (PDB)^[15-17]. In this study, our aim is to use the bioinformatics method to determine the structure of PilA protein from *B. mallei* to choose the proper sequence for further study.

Methodology:

Sequence retrieval and multiple sequence alignment

The *Burkholderia* sp. PilA amino acid sequence were selected using a search conducted with the Basic Local Alignment Search Tool (BLAST)^[18] and were listed according to the pathogenic potential. Subsequently, multiple alignment was performed using Clustal Omega, and the results were visualize by Jalview program^[19].

Determination of PilA protein similarities and differences in B. mallei structure

To locate the similarities and differences within the PilA protein structure of *B. mallei*, the amino acid sequence was processed using AlphaFold^[13]. This resulted in the generation of secondary and the tertiary structure of PilA protein which were virtualized by UCSF Chimera^[20]

Results and Discussion:

The sequence of *B. mallei* PilA amino acid was used as a query in BLASTp search. The percent identity results of *B. pseudomallei*, *B. gladioli*, *B. multivorans*, *B. cenocepacia* and *B. vietnamiensis* to *B. mallei* were 99.47%, 77.47%, 76.24%, 75.94%, 75.41% respectively as outlined with accession number in Table 1.

The results of multiple sequence alignment shown in Figure 1 revealed conserved residues within the initial 40 amino acids at N-terminus, which are predicted to be an N-terminal α -helix that functions as a transmembrane region (Figure 3). The N-terminal α -helix of PilA comprises two parts: the α 1-N at the N-terminus and the α 1-C, which is embedded in the globular domain of the structure.^[8] The predicted Local Distance Difference Test (pLDDT) is a score providing the expected reliability of the region. From the Figure2, the score of predicted structure mostly more than 90 represent in dark blue color code of the predicted structure which expected to be modelled with high accuracy. The presence of a low pLDDT score region at the late N-terminal could be attributed to insufficient sequence coverage in the underlying database. The structure of the PilA protein from *B. mallei*, as predicted by



AlphaFold (Figure 3), similarly comprises of an α 1-N at N-terminal and the globular head domain which divided into α 1-C, 5- β sheet, and the intervening loop regions. The loops have 2 significant structures: the $\alpha\beta$ -loop and D-region. The $\alpha\beta$ -loop connected between-terminal α -helix and β -sheet, predicted to have role in pilin subunit interaction. The D-region included conserve cysteines which form disulfide bond. From the results, overall sequence variations were found located in the globular domain of the structure (Figure 4). Compared to previous study of PilA from *Aggregatibacter actinomycetemcomitans*, both proteins composed of N-terminal α -helix which are a hydrophobic residue and the structurally diverse globular domain. The researchers found that having N-terminal α -helix decreases the solubility of the recombinant protein led to an aggregation^[10]. The truncated α -helix or the globular domain is significant for ability to uptake DNA and cytokines via electropositivity surface and DNA-binding site residues^[10, 21].

Table 1 Description, percent identity and accession number of selected *Burkholderia* sp. PilA protein sequence from BLASTp search

Description	Scientific name	Percent identity (%)	Accession number
type IV pilus assembly protein PilA [<i>Burkholderia mallei</i>]	<i>Burkholderia mallei</i>	100	WP_305953588.1
PilA [<i>Burkholderia pseudomallei</i>]	<i>Burkholderia pseudomallei</i>	99.47	AAT34993.1
pilin [<i>Burkholderia gladioli</i>]	<i>Burkholderia gladioli</i>	77.42	WP_186062829.1
pilin [<i>Burkholderia multivorans</i>]	<i>Burkholderia multivorans</i>	76.24	WP_217097923.1
pilin [<i>Burkholderia cenocepacia</i>]	<i>Burkholderia cenocepacia</i>	75.94	WP_124594621.1
pilin [<i>Burkholderia vietnamiensis</i>]	<i>Burkholderia vietnamiensis</i>	75.41	MBR7963306.1

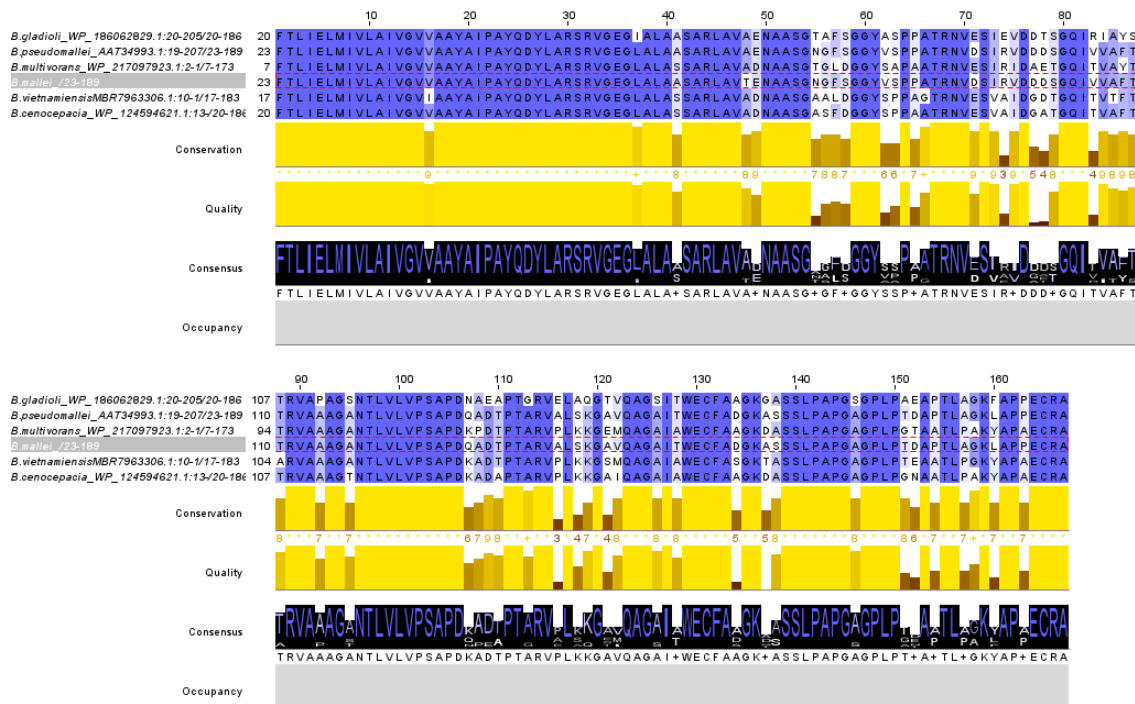


Figure 1 Alignment of PilA amino acid sequence from *B. mallei*, *B. pseudomallei*, *B. cenocepacia*, *B. gladioli*, *B. multivorans* and *B. vietnamiensis* by Clustal Omega (visualized by Jalview program).

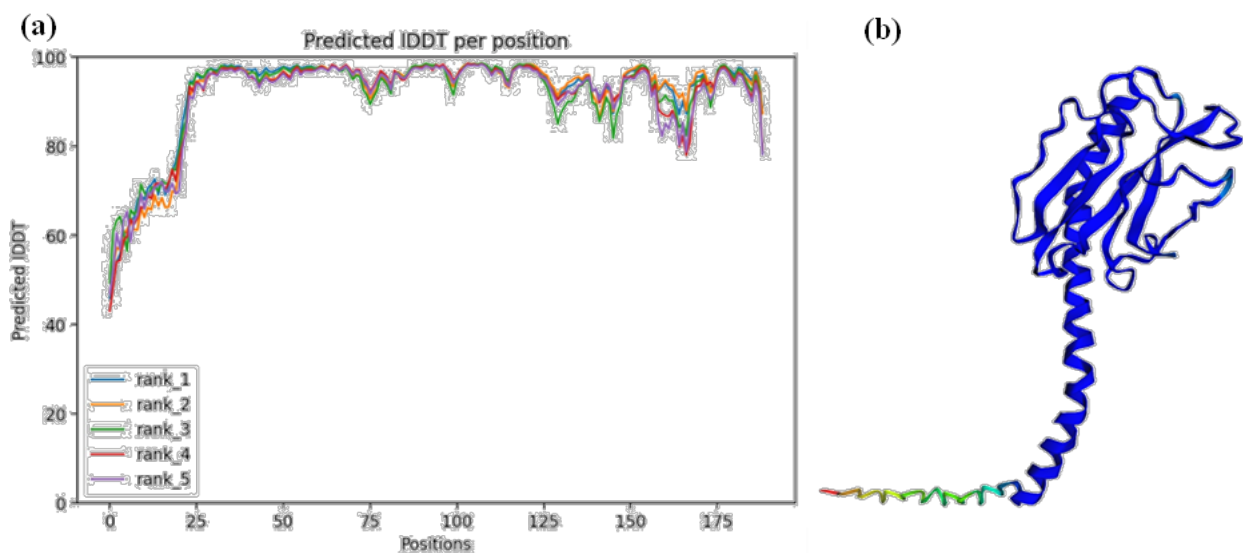
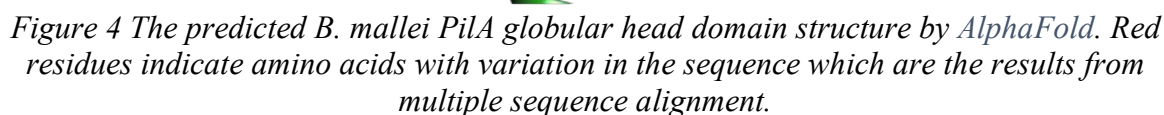


Figure 2 The predicted LDDT of the *B. mallei* PilA structures predicted by AlphaFold. (a) The pLDDT score obtained from first five range structure (b) The rank1 structure, the color correlated with pLDDT. The color code of the structure are dark blue, light blue, green, yellow and red indicated confidential of the structure which are very high(>90), confident(80), ok(70), low(60) and very low(<50).



In this study, we have conducted a comparative analysis of PilA proteins from *Burkholderia* sp. using multiple alignment tools Clustal Omega. Additionally, we described the *B. mallei* PilA protein structure predicted from AlphaFold. The predicted structure comprises an N-terminal α -helix (consisting of $\alpha 1$ -N and $\alpha 1$ -C) and a structurally diverse globular domain. Most of the N-terminal α -helix is highly conserved, which agree with prior findings in structural research on type IV pili (T4P) structures. Furthermore, the integration of multiple sequence alignment with the predicted structure not only revealed components of the



B. mallei PilA protein structure that share similarities with experimentally solved structures, and it also identified significant variations in the protein structure. This dataset can serve as a valuable resource for guiding the design of future experimental investigations into the PilA protein of *B. mallei*.

Acknowledgements:

This work is partially supported by the 90th Anniversary of Chulalongkorn University Scholarship, Chulalongkorn University.

References:

1. Parke, J.L. and D. Gurian-Sherman, *DIVERSITY OF THE BURKHOLDERIA CEPACIA COMPLEX AND IMPLICATIONS FOR RISK ASSESSMENT OF BIOLOGICAL CONTROL STRAINS*. Annual review of phytopathology, 2001. **39**(1): p. 225-258.
2. Bzdyl, N.M., et al., *Pathogenicity and virulence of Burkholderia pseudomallei*. Virulence, 2022. **13**(1): p. 1945-1965.
3. Larsen, J.C. and N.H. Johnson, *Pathogenesis of Burkholderia pseudomallei and Burkholderia mallei*. Military medicine, 2009. **174**(6): p. 647-51.
4. Warapitiya, D.S., et al., *Severe Sepsis with Multiorgan Failure due to Melioidosis: A Lesson to Learn*. Case reports in medicine, 2021. **2021**: p. 5563214.
5. Craig, L. and J. Li, *Type IV pili: paradoxes in form and function*. Current opinion in structural biology, 2008. **18**(2): p. 267-277.
6. Eberl, L. and P. Vandamme, *Members of the genus Burkholderia: good and bad guys*. BMC structural biology, 2016. **5**.
7. Pizarro-Cerda, J. and P. Cossart, *Bacterial adhesion and entry into host cells*. Cell, 2006. **124**(4): p. 715-27.
8. Craig, L., M.E. Pique, and J.A. Tainer, *Type IV pilus structure and bacterial pathogenicity*. Nature reviews microbiology, 2004. **2**(5): p. 363-78.
9. Ronish, L.A., et al., *The structure of PilA from Acinetobacter baumannii AB5075 suggests a mechanism for functional specialization in Acinetobacter type IV pili*. Journal of biological chemistry, 2019. **294**(1): p. 218-230.
10. Vahvelainen, N., et al., *Pilus PilA of the naturally competent HACEK group pathogen Aggregatibacter actinomycetemcomitans stimulates human leukocytes and interacts with both DNA and proinflammatory cytokines*. Microbial pathogenesis, 2022. **173**(Pt A): p. 105843.



11. Nguyen, Y., et al., *Structural characterization of novel Pseudomonas aeruginosa type IV pilins*. Journal of molecular biology, 2010. **395**(3): p. 491-503.
12. Gassiep, I., et al., *Laboratory Safety: Handling Burkholderia pseudomallei Isolates without a Biosafety Cabinet*. The journal of clinical microbiology, 2021. **59**(7): p. e0042421.
13. Varadi, M., et al., *AlphaFold Protein Structure Database: massively expanding the structural coverage of protein-sequence space with high-accuracy models*. Nucleic acids research, 2021. **50**(D1): p. D439-D444.
14. Xia, X., *Bioinformatics and Drug Discovery*. Current topics in medicinal chemistry, 2017. **17**(15): p. 1709-1726.
15. Baek, M., et al., *Accurate prediction of protein structures and interactions using a three-track neural network*. Science, 2021. **373**(6557): p. 871-876.
16. Bryant, P., et al., *Predicting the structure of large protein complexes using AlphaFold and Monte Carlo tree search*. Nature communications, 2022. **13**(1): p. 6028.
17. Jumper, J., et al., *Highly accurate protein structure prediction with AlphaFold*. Nature, 2021. **596**(7873): p. 583-589.
18. Altschul, S.F., et al., *Basic local alignment search tool*. Journal of molecular biology, 1990. **215**(3): p. 403-10.
19. Waterhouse, A.M., et al., *Jalview Version 2—a multiple sequence alignment editor and analysis workbench*. Bioinformatics, 2009. **25**(9): p. 1189-1191.
20. Pettersen, E.F., et al., *UCSF Chimera—a visualization system for exploratory research and analysis*. Journal of computational chemistry, 2004. **25**(13): p. 1605-12.
21. Cehovin, A., et al., *Specific DNA recognition mediated by a type IV pilin*. Proceedings of the national academy of sciences, 2013. **110**(8): p. 3065-70.



Antibacterial Green Synthesized Silver Nanoparticles and Transdermal Patch Applications

Teerapat Onyala¹, Tonghathai Phairatana², Julinthip Puttawong²,
Chitchamai Ovatlarnporn³, Suchera Thananimit^{1,4*}

¹ Program in Molecular Biotechnology and Bioinformatics, Division of Biological Science, Faculty of Science, Prince of Songkla University, Songkhla 90112, Thailand

² Department of Biomedical Sciences and Biomedical Engineering, Faculty of Medicine, Prince of Songkla University, Songkhla, 90110 Thailand

³ Faculty of Pharmaceutical Sciences, Prince of Songkla University, Hat Yai, Songkhla, 90112, Thailand

⁴ Center for Genomics and Bioinformatics Research, Faculty of Science, Prince of Songkla University, Songkhla 90112, Thailand

*E-mail: thananimit@yahoo.com

Abstract:

The synthesis of green synthesized silver nanoparticles (GSNPs) using guava leaf phenolic extract (GLPE) as a reducing agent provides a sustainable and environmentally favorable method for enhanced nanoparticle production. The nano-sized GSNPs particles were effectively synthesized in the present investigation. The GSNPs were then characterized using optical density (OD) and zeta potential (ZP) measurements. At a wavelength of 424 nm, the analysis demonstrated a maximum absorbance peak. ZP analysis of GSNPs revealed the existence of two distinct size distributions. 88.4% of the first distribution had a size of 180.50 nm, while the second distribution had a size of 28.48 nm. The MIC and MBC values of GSNPs against *Bacillus subtilis* (BS), *Staphylococcus aureus* (SA), and *Salmonella Typhimurium* (ST) ranged from 0.98 μ M to 7.85 μ M and from 3.93 μ M to 31.50 μ M, respectively, indicating strong antibacterial capabilities. Subsequently, these GSNPs were incorporated into a transdermal patch (TP) using micro-molding techniques and crosslinking with polymeric matrices. To evaluate its continued relevance, GSNPs-TP performed an assessment on human dermal fibroblast cells, applying GSNPs-TPs/GSNPs at concentrations ranging from 0.5 to 50 μ M. The experimental results suggest that cell survival varied between 93% and 70%, indicating a reduced level of toxicity in comparison to the utilization of GSNPs alone. The GSNPs-TP could have potential for biomedical applications, especially in the research of infection control and pharmaceutical drug delivery.

Introduction:

Silver nanoparticles (AgNPs) have emerged as remarkable nanomaterials with applications in biotechnology and biomedical research. The AgNPs exhibited excellent antimicrobial activity by damaging the bacterial cell membranes, allowing huge amounts of AgNPs to directly penetrate the cell and inhibit DNA replication – transcription that ultimately leads to bacterial death¹. Traditional physical or chemical methods of metal nanoparticle synthesis have obvious limitations and drawbacks; therefore, green chemical processes have appeared as a new manufacturing strategy. Recently, the utilization of biological extracts derived from various plants for the synthesis of metal nanoparticles has attracted a great deal of interest from the nanobiotechnology research community due to its

rapid, highly reproducible, ecological, environmentally friendly, and cost-effective procedure². Green synthesis of nanoparticles is based on the plant extract containing biomolecule/s (phenolics, terpenoids, glycosides, peptides, proteins and tannins) that is responsible for the reduction, capping, and stabilization of nanoparticles. Previous studies showed the potential use of plant phenolic extract for the synthesis of metal nanoparticles³. One of them is the guava leaf phenolic extract (GLPE), which previously exhibited an excellent bioresource for the synthesis of nanoparticles due to its high availability and low cost⁴. Therefore, the GLPE could be a good alternative to synthesize GSNPs and incorporate them into novel nanoparticle-based drugs and formulations in biomedical Transdermal Patches.

Transdermal patch (TP) is an alternative method of drug delivery by distributing pharmaceuticals through the skin to improve drug absorption and prevent tissue or nerve damage. One of the example is small microneedles, used as microarray patches, which can penetrate the stratum corneum and reach the dermal layer⁵. Its efficacy represent an alternative application method for the next step. Consequently, the primary objective of this research is to characterize the physical properties and antibacterial activity of GSNPs. Then, GSNPs-TP was fabricated and cell cytotoxicity was evaluated.

Methodology:

Materials

The guava leaves were purchased locally in Songkhla, Thailand. Silver nitrate (AgNO_3) was purchased from Sigma-Aldrich (USA), and Carboxymethyl cellulose (CMC) was purchased from Sigma-Aldrich (USA). Hyaluronic acid (HA) was purchased from Chemipan Corporation (Bangkok, TH).

Synthesis of GSNPs

300 g of guava leaf powder was extracted with 100 ml of 70% ethanol (v/v) using an electric stirrer at 180 rpm for 24 h. The solution was placed at room temperature to separate the precipitate. The upper solution was filtered by the paper filter to remove the other organic compounds. Precipitate was re-extracted by repeating the extraction–filtration. Extract fractions were pulled and evaporated to remove the ethanol under reduced pressure. The phenolic extracted solution was freeze-dried and kept at 4 °C. Folin-Ciocalteu assay was used to evaluate the amount of phenolic constituents. The quantity of gallic acid in the phenolic extracted solution was calculated using the standard curve; the result was expressed in milligrams of gallic acid equivalent per gram of GLPE dry weight (mg of gallic acid/g of GLPE). GLPE was used as a reducing agent to synthesize the GSNPs. The 25 ml of GLPE solution (5 mg/ml); adjusted pH to 9.0 was added to 475 mL of 1 mM AgNO_3 . The mixture is stirred on a magnetic stirrer at the maximum speed for 10 min and kept at 4 °C.

Characterization of silver nanoparticle

GSNPs was detected using a UV-visible spectrophotometer in term of optical density across the wavelength ranging from 190 to 820 nm at room temperature. Sizes of GSNPs were observed by Zetasizer Nano ZS (Malvern Instruments, Worcestershire, UK). GSNPs were subsequently sonicated for 5 minutes prior to analysis. The hydrodynamic particle diameters were then determined under controlled conditions, with all measurements performed at a constant temperature of 25 °C using fixed-angle light scattering detection.



Antimicrobial activity

Preparation inoculum

Bacillus subtilis (BS), and *Staphylococcus aureus* (SA) and *Salmonella Typhimurium* (ST) were employed. One colony of each species was selected and inoculated into 1 ml of Tryptic soy broth (TSB) in a 1.5 ml microcentrifuge tube. The inoculum was incubated in a shaking incubator at 37 °C until reaching the log phase for BS, SA, and ST at 18 – 24 hours, 6 – 9 hours, and 5 hours respectively. The twenty microliters of inoculum after incubation was added into 2 ml of 0.85% (w/v) NaCl adjusted to 0.5 McFarland (1.5×10^8 CFU/ml). The bacterial cell was adjusted to 10^6 CFU/ml by using Mueller Hinton broth (MHB).

Minimum Inhibitory Concentration (MIC) and Minimum Bactericidal Concentration (MBC)

The MIC was performed using broth microdilution assay in a 96-well plate with various concentrations of 50 μ l GSNPs. Serial dilution was performed in the range of 0.4 – 300 μ M of GSNPs. The bacterial suspension (1×10^6 CFU/mL) was inoculated into each well, and the plates were incubated at 37 °C for 16 – 18 hours. The vancomycin was used as a positive and the bacteria cell as a negative control. Turbidity in each well was measured at 620 nm and used to determine the MIC value. The MBC was determined using the GSNPs that yielded significant MIC values by dropping the culture onto Muller Hinton Agar (MHA) plates. After incubation at 37 °C for 16 – 18 h, the MBC was evaluated. The entire experiment was performed three times with three independent repetitions.

GSNPs-TP fabrication and toxicity test

The utilization of GSNPs in the biomedical transdermal patch was incorporated into the polymeric solution used in the fabrication of TP. Micromolding techniques were applied for the fabrication procedure, double layer. The solution consisted of carboxymethyl cellulose (CMC) that had been cross-linked with hyaluronic acid (HA); GSNPs were then added before being deposited onto TP molds. The TP was baked in a desiccator with silica gel and allowed to dry for 24-48 hours prior to its removal from the silicone mold.

3-(4,5-dimethylthiazol-2-yl)-2,5-diphenyltetrazolium bromide (MTT) assay was performed to evaluate the biocompatibility and biosafety of GSNPs and its TP formulation. Human dermal fibroblasts (HDFs) were seeded at 1×10^4 with DMEM containing 10% FBS in 96-well plates. After 24 hours, they were incubated with GSNPs and GSNPs-TP in solution form at 37 °C in 5% CO₂ for 48 hours. MTT solution (5 mg /ml) was added to each well and incubated at 37 °C for 4 h and then replaced medium with DMSO. The absorbance at 550 nm was measured using a microplate reader. Percentage cell viability was calculated using absorbance of sample/absorbance of control) x 100.

Results and Discussion:

Characterization of GSNPs

In this study, phenolic extract from guava leaf was prepared using an inexpensive and environmentally friendly method to use ecological solvents. The total phenolic content of the extract was 537.14 ± 21.83 mg of gallic acid/gram of GLPE. The powder was light brown and hydrophilic. This is advantageous for the potential productive synthesis of biogenic silver nanoparticles due to the high phenolic content found in the guava leaf.

GSNPs were synthesized successfully, resulting in the production of GSNPs in Figure 1A as compared to phenolic solution prior to GSNP synthesis. The peak was determined to be

424 nm, which corresponds to the findings of a previous study indicating that GSNPs exhibited an absorption peak at approximately 425 nm⁴. In additional studies involving various phenolic plant extract, AgNPs exhibit an absorbance peak around 420 nm^{6,7}. Figure 1B represents the zeta potential of GSNPs, which indicates that GSNPs have two sizes distribution, 180.50 nm at 88.4% and 28.48 nm at 11.6%. Due to the fact that synthesis is dependent on many variables, such as pH, temperature, and the concentration of reducing (phenolic extract), these may have an effect on the sizes of GSNPs. Previous research exhibited silver nanoparticles with a single distribution size, as determined by DLS (zeta potential). Using various phenolic plant extracts, the average particle size was reported to be between 17.2 nm⁴ and 75 nm⁷.

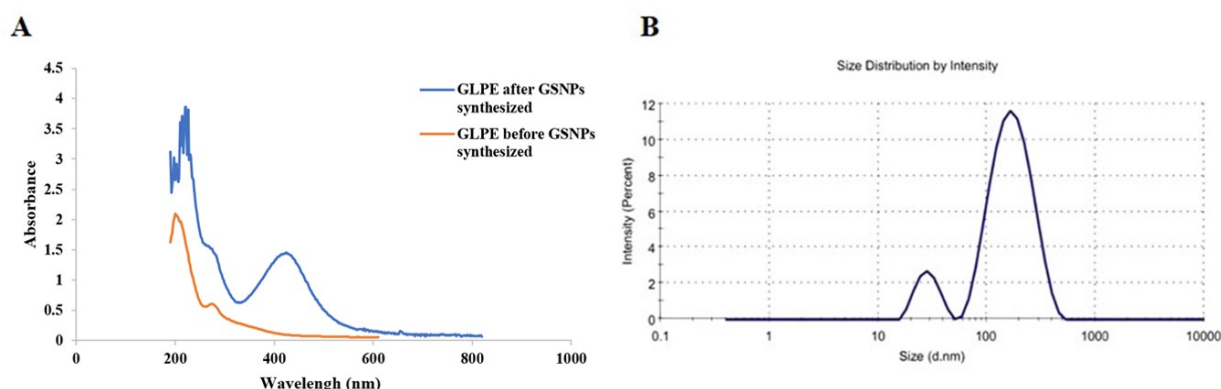


Figure 1 The UV-Vis absorption spectra of GLPE extract before and after GSNPs synthesis (A). Zeta – an average of GSNPs in phenolic solution (B).

Antimicrobial activity of GSNPs

It is well known that AgNPs exhibit antimicrobial properties. The objective of this study is to assess the effectiveness of inhibition on the growth of bacteria, including ST as a representative of gram-negative bacteria and BS and SA as representatives of gram-positive bacteria. As shown in Table 1, GSNPs can inhibit the growth of bacteria in both Gram-positive and Gram-negative. MIC values of BS, SA, and ST were 0.98, 7.85, and 1.96 μM , respectively. Additionally, the MBC value of GSNPs was approximately four times higher than the minimum inhibitory concentration (MIC) indicating effectively killed all types of bacteria.

Table 1 The MIC and MBC values of GSNPs.

Species of Bacteria (gram+,-)	MIC (μM)	MBC (μM)
BS (+)	0.98	> 3.93
SA (+)	7.85	31.50
ST (-)	1.96	7.85

Biocompatibility evaluation of GSNPs-TP

Antibacterial GSNPs were incorporated into polymer solutions to produce GSNPs-TP. The completed size of the patch (dimensions; 3.4 x 6.7 cm shown in Figure 2A) was then dissolved in PBS and treated with cells using the MTT assay to determine its toxicity, which

was measured by loss of structure or cell function, including lethal cytotoxicity. Figure 2B illustrates the percentage of viable cells for GSNPs-TP and GSNPs alone. The concentration of GSNPs and GSNPs-TP (0.5 – 100 μM) was treated in the HDFs cell for 48 hours. The results indicate that GSNPs at concentrations of 75 and 100 μM are extremely toxic to cells, resulting in a 15% cell viability while at the same concentration of GSNPs-TP are still non-toxic, indicating by 60% of the viable cells. The findings indicate that GSNPs-TP exhibits a satisfactory level of safety within the concentration range of 0.5 – 50 μM , as evidenced by a cell viability rate of 70 – 96%. This shows that GSNPs-TP have minimal cytotoxicity, hence making them a promising candidate for future biomedical applications. Furthermore, this concentration range represents the minimum bactericidal concentration (MBC) required for effectively eliminating the bacterial cells responsible for the wound infection. Hence, it would be interesting to conduct further research on the effectiveness of GSNPs-TP.

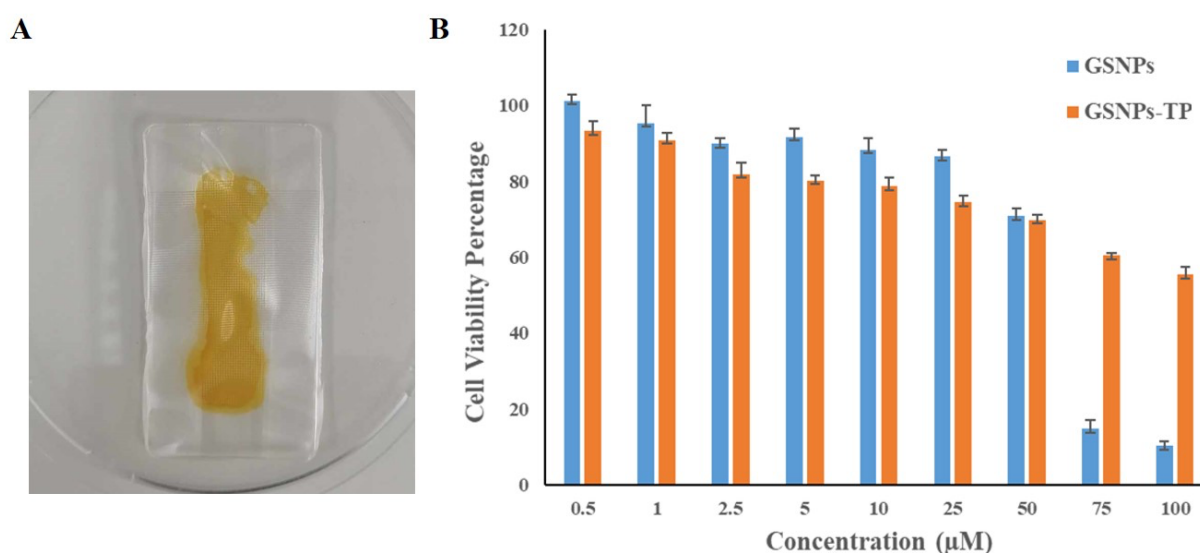


Figure 2 (A) GSNPs-TP and (B) the cell viability of GSNPs-TP and GSNPs via MTT assay on fibroblast cells.

Conclusion:

In this investigation, phenolic extract from the leaf of the guava plant was used to synthesize GSNPs. The benefit of this work is its low-cost and environmentally friendly method. The majority of the particle sizes of GSNPs with antimicrobial properties were 180.50 nm. The GSNPs were further incorporated into the Transdermal Patch (TP) for beneficial application. This revealed non-toxicity to fibroblast cells within a certain concentration of dissolving patches, demonstrating the safety of using GSNPs-TP for drug delivery in the epidermis. Additional research could be conducted to assess the properties and efficacy of GSNPs-TP.

Acknowledgements:

This research was supported by the Sci-Pharm-Med Clustering Program and supported by the Program in Molecular Biotechnology and Bioinformatics, Division of Biological Science (Faculty of Science), Faculty of Pharmaceutical Sciences, and Department of Biomedical Sciences and Biomedical Engineering (Faculty of Medicine) for facilitating all equipment.

References:

1. Bruna T, Maldonado-Bravo F, Jara P, Caro N. *Int. J. Mol. Sci.* 2021;22:7202.
2. Rónavári A, Igaz N, Adamecz DI, Szerencsés B, Molnar C, Kónya Z, Pfeiffer I, Kiricsi M. *Mol.* 2021;26:844.
3. Shumail H, Khalid S, Ahmad I, Khan H, Amin S, Ullah B. *Endocr. Metab. Immune. Disord. Drug Targets.* 2020;21:994–1007.
4. Eze FN, Ovatlarnporn C, Nalinbenjapun S, Sripetthong S. *Arab. J. Chem.* 2022;15:104167.
5. Isopencu GO, Covaliu-Mierlă CI, Deleanu IM. *Plants.* 2023;12:2661.
6. Asif M, Yasmin R, Asif R, Ambreen A, Mustafa M, Umbreen S. *Dose-Response.* 2022;20:1–11.
7. Saad AM, El-Saadony MT, El-Tahan AM, Sayed S, Moustafa MA, Taha AE, Taha TF, Ramadan MM. *Saudi J. Biol. Sci.* 2021;28:5674–5683.



CHARACTERIZATION OF A DIHYDROFOLATE REDUCTASE FROM *Leptospira interrogans*

Charin Chandit,¹ Kittikhun Wangkanont,^{2,*}

¹Department of Biochemistry, Faculty of Science, Chulalongkorn University, Bangkok, Thailand

*e-mail: Kittikhun.w@chula.ac.th

Abstract:

Dihydrofolate reductase (DHFR) is an enzyme that is found in all eukaryotic and prokaryotic cells. It plays a key role in the folate pathway and DNA synthesis. DHFR uses NADH or NADPH as a reductant to catalyze the reduction of dihydrofolate (DHF) to tetrahydrofolate (THF). Tetrahydrofolate is a precursor in purine, thymidylate, and several amino acids synthesis. Inhibiting DHFR results in decreased intracellular tetrahydrofolate levels, suppression of RNA and DNA synthesis, and cell death. Consequently, DHFR has been recognized as a potential target for the development of novel medications to combat bacterial infections. Dihydrofolate reductase from *Leptospira interrogans* (*LiDHFR*) was expressed in *Escherichia coli* and purified with Ni-NTA resin affinity chromatography. Furthermore, the enzymatic activity was measured via spectrophotometry. However, the enzymatic activity was not detected. The sequence alignment with the *E. coli* dihydrofolate reductase (*EcDHFR*) reveals that key catalytic residues are not conserved. The characterization of *LiDHFR* or *LiDHFR*-like enzyme provides the basis for the search for the potential drug targets for the treatment of Leptospirosis. The *LiDHFR* characterized in this work is inactive, thus the search for its substrate and the true *LiDHFR* in *L. interrogans* should be further investigated.

Introduction:

Leptospirosis is a zoonotic disease caused by the bacteria *Leptospira*, which can infect humans and mammals. Leptospirosis is one of the most common zoonotic illnesses in the world, with an estimated 1,000,000 cases and 50,000 deaths per year. In Thailand, *L. interrogans* is the *Leptospira* species that infects people most frequently (Narkkul et al., 2021). Dihydrofolate reductase (DHFR) is a universal housekeeping enzyme in biology that catalyzes the conversion of 5,6,7,8-tetrahydrofolate (THF) from 7,8- dihydrofolate (DHF) via NADPH as a cofactor. Its major function is responsible maintenance the tetrahydrofolate pool in the cell. DHFR plays an important part in the production of thymidines and purines, as well as various other amino acids such as glycine, methionine, serine, and N-formyl-methionyl tRNA (Wróbel, A, 2020). Inhibition of the DHFR target led to a cessation of purine and thymine synthesis, resulting in cell death. Therefore, we aim to clone and characterize *LiDHFR*.

Methodology:

Expression and purification of LiDHFR

The *E. coli* containing an expression plasmid for *LiDHFR* was cultured at 37 °C in Terrific broth until the O.D.600 reached 0.4. IPTG was used to induce the protein expression of cells to 0.1 mM for 6 hours at 30 °C. Centrifugation was used to collect the cells. For protein purification, the pellet was sonicated in 20 mM HEPES, 150 mM NaCl, 25 mM imidazole, pH 7.5). The mixture was centrifuging at 40,000 x g for 15 min at 4 °C. The His-tagged *LiDHFR* in the supernatant was purified using Ni-NTA resin. The column was washed with 25 mM imidazole to 100 mM imidazole wash buffer (20 mM HEPES, 150 mM NaCl, 25-100mM



imidazole, pH 7.5) before being eluted with 250 mM imidazole elution buffer (20 mM HEPES, 150 mM NaCl, 250 mM imidazole, pH 7.5). Each protein fraction was analyzed by SDS-PAGE using the Tris-glycine buffer system at 200 V for 45 minutes. The Gel was stained with Coomassie Blue for 30 minutes and de-stained for 3x15 minutes. The molecular weight of *LiDHFR* calculated from the amino acid sequence is 22.6 kDa. The *LiDHFR* fractions were pooled and dialyzed against 20 mM Tris pH 7.0 overnight. The concentration of *LiDHFR* was measured by spectrophotometry at 280 nm (extinction coefficient 41,940 M⁻¹cm⁻¹).

Enzymatic activity of *LiDHFR*

The enzymatic activity of *LiDHFR* on reduction of NADH or NADPH was performed in MTEN buffer (50 mM MES, 25 mM Tris, 100 mM NaCl, 25 mM Ethanolamine) (R&D Systems) at pH 7.0. The reaction solution contained 1 mM DHF, 0.1 mM NADPH and 1000 nM *LiDHFR*. The positive control is *E. coli* dihydrofolate reductase (*EcDHFR*) assayed with the same condition as *LiDHFR*. To characterize enzymatic activities, we measured absorbance at 340 nm to follow the reduction of NADPH cofactor every second for 3 minutes at room temperature.

Results and Discussion:

The His-tagged *LiDHFR* was purified with affinity chromatography method using Ni-NTA resin. SDS-PAGE suggested that pure *LiDHFR* was obtained with molecular weight 22.6 kDa (Figure 1).

To characterize the enzymatic activity of *LiDHFR*, we measured absorbance at 340 nm to follow the reduction of NADPH for 3 minutes. The results show that the reduction of NADPH was not detected, while the *EcDHFR* as a positive control can be detected (Figure 2). It is possible that *LiDHFR* is not a DHFR enzyme, even though the NCBI suggested that this protein sequence is a dihydrofolate reductase from *L. interrogans*. Moreover, the sequence alignment between *LiDHFR* and *EcDHFR* (*E. coli* dihydrofolate reductase) that have several published in database suggested that crucial catalytic residues are not conserved with similarity 28.9% although the conserved domains are same. The active site cleft of the DHFR structure has two subdomains, the adenosine binding subdomain, and the major subdomain. The smaller adenosine binding subdomain is a cofactor binding site, while the major subdomain consists of three loops on the ligand binding surrounding the active site (Schnell et al., 2004). The active site of *LiDHFR* contains Glu40 and His74, while the active site of *EcDHFR* contains Asp27 and Arg57 in the corresponding positions, which is the conserved regions of DHFR enzyme (Figure 3). The Asp27 at one end of the active site is crucial for protonating the N5 atom of the DHF (Wan, Q, 2021). Even though the Glu40 of *LiDHFR* is an acidic amino acid same as the Asp27 of *EcDHFR*, the Glu40 of *LiDHFR* not be same position as Asp27 of *EcDHFR*. However, His74 in the active site of the *LiDHFR* is different from the Arg57 found in *EcDHFR*. The arrangement and structural configuration of Arg70 in human dihydrofolate reductase (*hDHFR*) stabilize through a complex network of persistent hydrogen bond interactions originating from the side chains of Thr38 and Thr39 within the active site helix of *hDHFR*. Furthermore, this stability is influenced by the backbone carbonyl and amide groups of Lys68 and Asn64 in *hDHFR*. This assessment is drawn from an exhaustive examination of the intermolecular contacts that pertain to the inhibitor's side chain carboxylate and the universally conserved Arg within the active site (Cody & Schwalbe, 2006). Therefore, The His74 of



*Li*DHFR probably cannot stabilize the interaction between the active site and substrate. Moreover, the homology modelling of *Li*DHFR using phyre2 superimposed with *Ec*DHFR suggested that the three-dimensional structure of *Li*DHFR did not fitted particularly well, with the RMSD value of 1.218 Å, and the expected catalytic residues did not align (Figure 4). For these reasons, we reason that *Li*DHFR does not contain the key catalytic residues and thus does not have a DHFR activity.

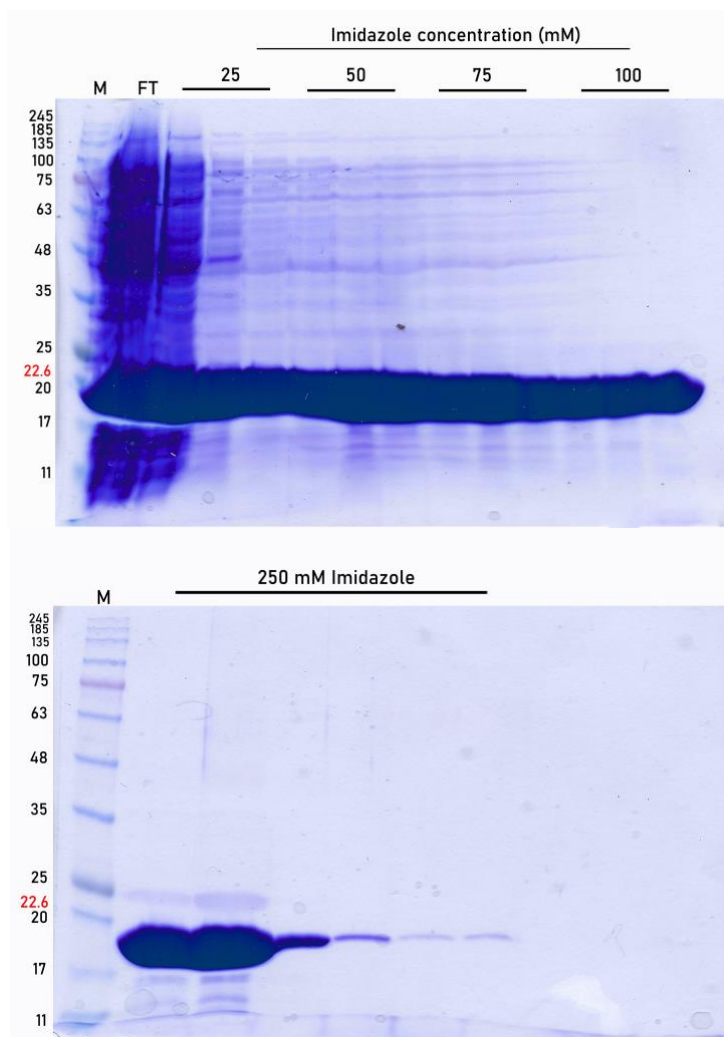


Figure 1.

SDS-PAGE of His-tagged *Li*DHFR purification using Ni-NTA affinity chromatography.

*Li*DHFR was purified using Ni-NTA resin after eluting with 20 mM HEPES pH 7.5, 150 mM NaCl, and imidazole concentrations ranging from 25 mM to 250 mM. For SDS-PAGE no.1 comprising Lane M is tricolor broad protein marker. Lane FT is flowthrough. Lane 3-5 represents the elute proteins at 25 mM imidazole. Lane 6-8 represents the elute proteins at 50 mM imidazole. Lane 9-11 represents the elute proteins at 75 mM imidazole. Lane 12-14 represents the elute proteins at 100 mM imidazole respectively. SDS-PAGE no. 2 comprising Lane M is tricolor broad protein marker. Lane 2-7 represents the elute proteins at 250 mM imidazole.

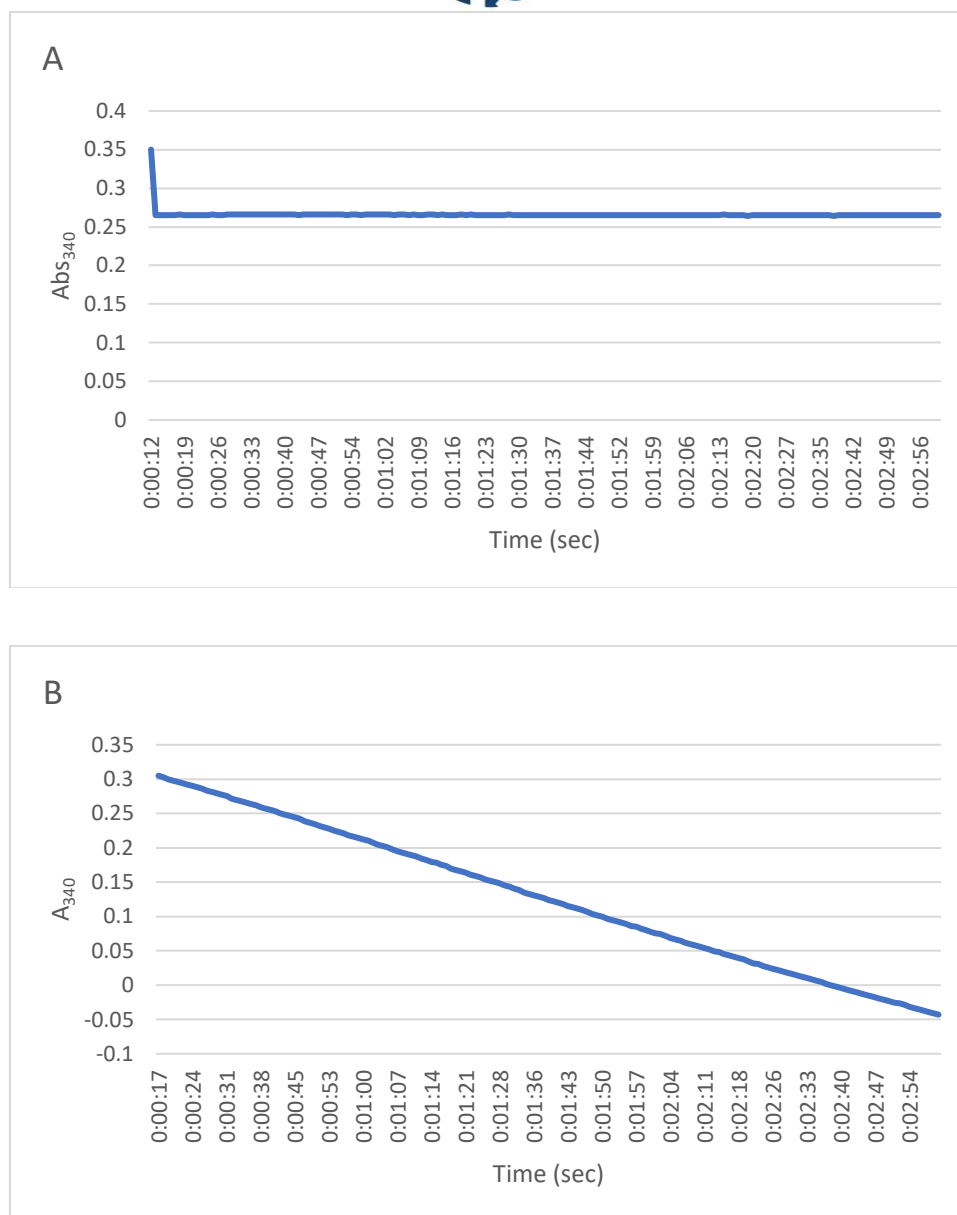


Figure 2.

The enzymatic activity of *Li*DHFR (A) and *Ec*DHFR (B) on reduction of NADPH. The *Li*DHFR and *Ec*DHFR activity were measured absorbance at 340 nm following the reduction of NADPH for 3 minutes.

Figure 3.

The sequence alignment between *Ec*DHFR and *Li*DHFR from EMBL-EBI pairwise sequence alignment tools shows that the active site of *Ec*DHFR contains Asp27 and Arg57, while the active site of *Li*DHFR contains Glu42 and His74.

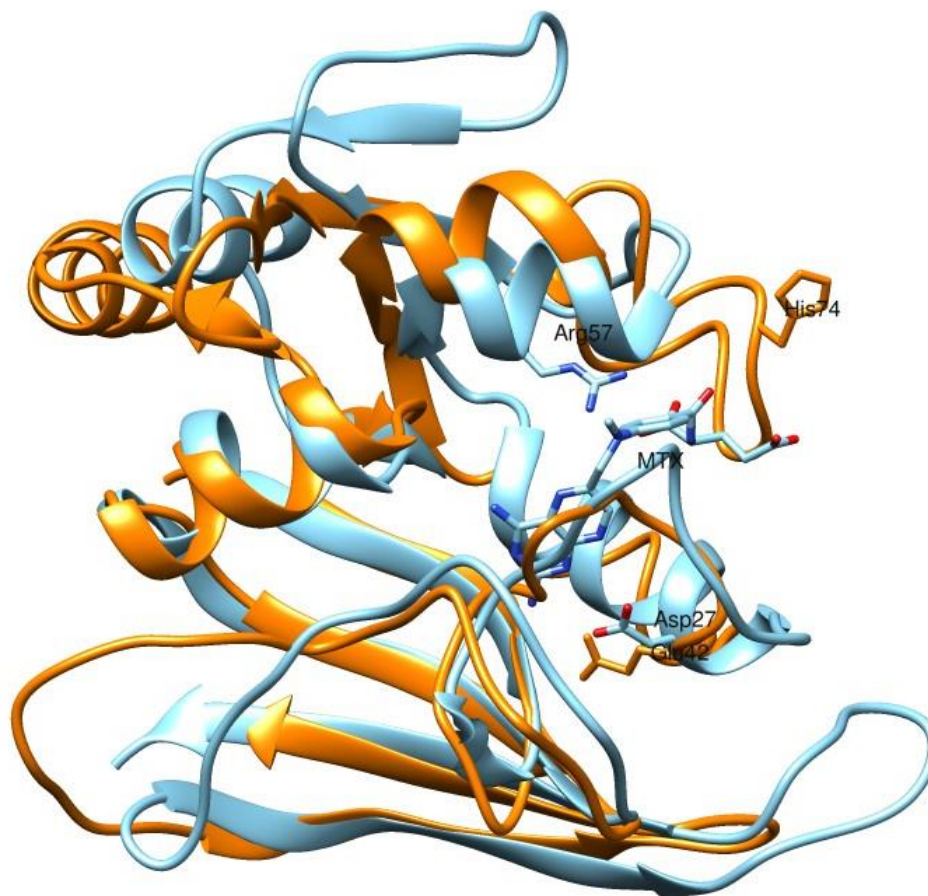


Figure 4.

The protein structural superposition between *EcDHFR* and *LiDHFR* with RMSD = 1.218 Å.

The *EcDHFR* is represents in blue color of ribbon structure (PDB; 1ddr chain B) with the conserved residues, Asp27 and Arg57, in active site and methotrexate (MTX) as an inhibitor, while the *LiDHFR* is represents in orange color of ribbon structure with Glu42 and His74.

Conclusion:

Previously, we expected that this enzyme to be a dihydrofolate reductase from *Leptospira interrogans*. We could express and purify the enzyme by using affinity chromatography. The activity of *LiDHFR* was tested, but no enzymatic activity was identified for the NADPH reduction using spectrophotometry at 340 nm. It is possible that this enzyme is not dihydrofolate reductase, but it is another enzyme in oxidoreductase family. Moreover, the sequence alignment between *EcDHFR* and *LiDHFR* suggests that the active site of *LiDHFR* is different from *EcDHFR*. Moreover, the superposition demonstrated that the *LiDHFR* did not fitted well with *EcDHFR* and the catalytic residues do not align. Therefore, these reasons suggest that this enzyme might not be a dihydrofolate reductase.

Acknowledgements:

This work is partially supported by the 90th Anniversary of Chulalongkorn University Scholarship, Chulalongkorn University.



References:

1. Cody V, Schwalbe CH. Crystallography Reviews. 2006; 12(4):301-333.
2. Narkkul U, Thaipadungpanit J, Srisawat N, Rudge JW, Thongdee M, Pawarana R, Pan-Ngum W. Scientific reports. 2021;11(1):1-13.
3. Schnell JR, Dyson HJ, Wright PE. Annual Review of Biophysics and Biomolecular Structure. 2004; 33:119-140.
4. Wan Q, Bennett BC, Wymore T, Li Z, Wilson MA, Brooks III CL, Langan P, Kovalevsky A, Dealwis CG. ACS catalysis. 2021;11(9):5873-5884.
5. Wróbel A, Arciszewska K, Maliszewski D, Drozdowska D. The Journal of antibiotics. 2020;73(1):5-27.



COMBINED TOXICITY OF IMIDACLOPRID AND GLYPHOSATE ON AQUATIC OLIGOCHAETES (*Tubifex tubifex* Müller, 1774)

Nalena Praphiraksit¹, Panyawut Rattanarom^{2*}

¹ Department of Biology, Faculty of Science, Srinakharinwirot University, Bangkok 10300, Thailand

² Department of Science and Technology, Benjamarachutit School, Nakhon Si Thammarat 80000, Thailand

*e-mail: panyawut@benjama.ac.th

Abstract:

This study aimed to examine the toxic concentrations of imidacloprid, glyphosate and its mixture on *Tubifex tubifex*. The findings demonstrated that after 24 and 48 hours of pesticide exposure, imidacloprid alone caused toxic effects on *T. tubifex* more than glyphosate did. The interactions of these two pesticides at 24 and 48 hours were antagonistic and additive effects, respectively. This research further assessed sublethal concentrations by investigating the alterations in enzyme activity and histopathology. The Completely Randomized Design (CRD) was used in this study. The result disclosed a significant increase ($p < 0.05$) in the catalase activity at 24 and 48 hours in both single and mixed toxicity test. The significant increase ($p < 0.05$) in acetylcholinesterase activity was also observed after the worms exposed to imidacloprid alone at 24 and 48 hours. However, when exposed to glyphosate and the mixture at 24 and 48 hours, *T. tubifex* showed a significant decrease ($p < 0.05$) in acetylcholinesterase activity. H&E staining revealed degeneration in *T. tubifex* tissues caused by oxidative stress. The overexpression of chloragosomes was additionally noticed in treated worms. This present study indicated that alteration in histology, catalase activity, and AChE activity can be used as biological markers to assess the toxicity of imidacloprid, glyphosate and its mixture on *T. tubifex*.

Introduction:

Several types of pesticides are widely utilised in a farming system in order to manage pest species or enhance the productivity of agricultural crops^{1, 2, 3}. Despite there being benefits from using these agrochemicals, the improper application might contribute to contamination in aquatic ecosystems^{4, 5, 6}. One of the most ubiquitously used pesticides and whose residues have been frequently detected in freshwater ecosystems is imidacloprid, a neonicotinoid insecticide^{7, 8}. This insecticide binds irreversibly to the nicotinic acetylcholine receptor site on the postsynaptic nerve cells, resulting in overstimulation of nerve impulses, eventually induces paralysis and death in aquatic animals^{9, 10}. Nowell et al. (2017)⁸ reported that imidacloprid was the most frequently occurring insecticide in streams, and its detection frequency reached to over 80% in Midwestern US streams. In addition, the maximum residue measured so far in the aquatic environment from 11 countries was up to 320 $\mu\text{g L}^{-1}$ which is higher than the regulatory thresholds for aquatic lives¹¹. These reports are of much concern since Gerhardt (2009)¹² published that 90 $\mu\text{g L}^{-1}$ of imidacloprid had the potential to impair locomotion behaviour of *T. tubifex* after being exposed for 24 hours. Moreover, this insecticide can influence acetylcholinesterase (AChE) activity in *Eisenia fetida* and catalase (CAT) activity in *Daphnia magna*^{13, 14}.

Under the field condition where both pests and weeds are presented, the single used insecticide is inadequate to control unwanted species, therefore, herbicides are also applied synchronously¹⁵. According to earlier studies, and similarly to insecticides, herbicides are also commonly found in aquatic systems. For example, herbicides were detected more



frequently and at greater concentrations than insecticides in the same stream⁸. Surveys such as that conducted by Mahler et al. (2016)¹⁶ exhibited that glyphosate, an organophosphorus herbicide, was found in streams with the high detection frequency being at 87%. Furthermore, the presence of glyphosate in the water resource of Indiana, the United States reached a peak of 427 $\mu\text{g L}^{-1}$ as analysed by Scribner et al. (2007)¹⁷. Even though designed specifically to be a weed-killing chemical, glyphosate poses numerous threats to aquatic animals. A case study with *Mytilus galloprovincialis*, for example, demonstrated that 100 $\mu\text{g L}^{-1}$ of glyphosate caused the alterations in AChE activity and CAT activity in those that were treated for 7 days¹⁸. Another research on *Crassostrea giga* tissues depicted that glyphosate can induce histological changes at a low concentration¹⁹. Although extensive studies today have been complete on the single toxicity of imidacloprid and glyphosate on aquatic animals, much uncertainty still exists about their interaction in the water ecosystem. This would obscure the existent impacts of these two pesticides on aquatic animals^{3, 20}. Thus, the combined toxicity assessment needs to be considered as also recommended by the European Commission (2012)⁷ and Cang et al. (2017)²¹.

In this study, *Tubifex tubifex*, commonly known as a tubificid worm, was selected as a biological model owing to its widespread availability in the freshwater ecosystem²². The tubificid worms additionally play key functional roles in the ecological system including organic matter decomposition, restructuring of sedimentary deposits, and being an important source of nutrients for other aquatic species²³. Consequently, provided that the number of tubificid worms undergoes a steep decline because of pesticide toxicity, other aquatic species will be gruelling to avoid consequence. This would lead to an ecological imbalance and diversity of aquatic creatures. According to previous studies which found that the activity of acetylcholinesterase and catalase can be used as biomarkers for toxicity assessment in *T. tubifex*^{24, 25}. Another pivotal parameter, which has been used to assess toxicity in other oligochaete worms, was the alteration in histology^{26, 27, 28}. Until recently, there has yet to be a report on the impact of pesticides on the histology of the tubificid worms. Hence, the main objective of this investigation was to assess the lethal and sub-lethal concentrations of imidacloprid, glyphosate, and its mixture, including the impacts of those pesticides on acetylcholinesterase activity, catalase activity, and histology of *T. tubifex*. To achieve this goal, *T. tubifex* was exposed to several concentrations of imidacloprid, glyphosate, and its mixture. Subsequently, they were examined the alterations in AChE activity, CAT activity, and histology.

Methodology:

Maintenance of test organism

A population of the oligochaete *T. tubifex* was obtained from a commercial hatchery located in Bangkok, Thailand. They were reared in 15 L plastic tanks filled with distilled water which was renewed daily. Aeration was provided in each tank and the animal maintenance system was under the controlled condition with the water temperature ($24.13 \pm 0.22^\circ\text{C}$), pH of water (7.91 ± 0.12), the oxygen dissolved in water ($5.23 \pm 0.31 \text{ mg L}^{-1}$), and 12 h light and dark cycles. The test species were handled in the best practice framework of Institute of Animal for Scientific Purposes Development (IAD), Thailand (License number U1-07745-2561).

Chemicals and reagents

The analytical standard (purity $\geq 98.0\%$) of imidacloprid and glyphosate were used as experimental compounds for toxicity assessment. These two chemicals were purchased from

Sigma-Aldrich, Switzerland. Stock solutions were prepared freshly by dissolving the chemicals in distilled water until it had the required concentration.

Toxicity of single pesticide

To determine the median lethal concentration (LC_{50}) of each pesticide, the toxicity tests were performed in three replicates per concentration, and 30 worms per replicate. Each replication comprised of seven treatment groups and an untreated group.

Toxicity of combined pesticide

For investigating the combined toxicity, imidacloprid and glyphosate were mixed in a ratio of 1:1. The lower LC_{50} value obtained from the above experiment was used as an initial concentration in that ratio. Six dilutions were subsequently prepared to attain the LC_{50} of the mixture by using distilled water as a medium. The experimental design was performed similarly to the single pesticide test. Once the LC_{50} values of each pesticide and combined LC_{50} value were obtained, the interaction of toxicants was examined via the Marking additive index method along with Wang et al. (2018)²⁹. The initial step was to calculate the biological activity (S) using the equation as follows: $S = (A_m/A_i) + (B_m/B_i)$; where A_m and B_m are the toxicity (LC_{50}) of toxicants A and B when present in the mixture, A_i and B_i are the single LC_{50} of toxicants A and B, while S represents the sum of biological activity. The biological activity was then used to calculate an additive index (AI) value. If the biological activity is less than 1, the formula, $AI = (1/S) - 1$, is used. On the contrary, if the biological activity is more than or equal to 1, the following formula, $AI = 1 - S$, is used.

The obtained result can predict the behaviours of mixed pesticides. If the AI value is less than -0.2, the interaction is considered as an antagonistic effect. If the value of AI ranges from -0.2 to 0.25, an additive effect takes place. And if AI value is more than 0.25, the interaction is classified as a synergism²⁹.

Histological examination

The sublethal concentrations were selected to examine the histopathological effects. Moreover, the concentrations at LC_{50} value were also established to confirm the toxicity of these pesticides after treatment for 24 and 48 hours. The worms were examined histologically using the standard method of Humason (1962)³⁰.

Enzymatic measurements

For the total protein content, it was assayed following the method of Bradford. The reference protein was bovine serum albumin (BSA). Determinations of absorbance at 514 nm were monitored three times per sample from each concentration³¹. A colourimetric determination of acetylcholinesterase activity was analysed following the method of Ellman et al. (1961)³² and Erp et al. (2002)³³. The measurement of the catalase activity was studied as described by Aebi (1984)⁵¹.

Statistics

The LC_{50} values were expressed as milligram of chemicals per litre of water with the 95% confidence interval (95% CI). For the enzyme activity, the data were analysed using One-way ANOVA and considered a significance level of 0.05. The Bonferroni *t* post hoc test was selected to confirm the significant differences between treatments.

Results and Discussion:

The lethal effect of single pesticide exposure on T. tubifex

Acute exposure to imidacloprid and glyphosate individually exhibited the lethal toxicological effect in tubificid worms. Each pesticide showed different LC_{50} values to *T. tubifex* at various exposure times as shown in Table 1.

Table 1. The single toxicity of imidacloprid and glyphosate on *T. tubifex* after 24 and 48 hours of exposure.

Pesticides	Exposure time (hours)	LC ₅₀ (95% CI) mg L ⁻¹	Regression equation	R ² linear
Imidacloprid	24	1.545 (0.763-2.722)	Y = -0.17 + 0.76X	0.981
	48	1.982 (0.287-5.622)	Y = 0.02 + 0.55X	0.983
Glyphosate	24	201.438 (187.810-210.938)	Y = -17.1 + 7.54X	0.982
	48	190.300 (182.545-194.966)	Y = -71.69 + 31.53X	0.984

Note: In the regression equation, Y represents the number of mortal worms while X represents the pesticide concentration (mg L⁻¹).

The study such as that was carried out by Hassoon and Salman (2016)³⁴ disclosed that the LC₅₀ value of *D. pulex* exposed to imidacloprid for 24 hours was 1.5 mg L⁻¹. After that, the LC₅₀ value increased slightly to 1.9 mg L⁻¹ after being exposed to imidacloprid for 48 hours. A possible explanation for this result might be due to a low persistent in the aqueous solution of this insecticide with a half-life of 24.2 hours³⁵. On account of this property, it could conceivably be hypothesized that imidacloprid tends to affect acutely on aquatic organisms. The research regarding the toxicity of glyphosate in *Eriocheir sinensis* also concurs with the present result by revealing that the 24-h and 48-h LC₅₀ values were 461.54 and 97.89 mg L⁻¹, respectively³⁶. This result suggested that the glyphosate toxicity increases with the increased exposure time. Furthermore, as compared to other oligochaete worms, *T. tubifex* is prone to be more susceptible to imidacloprid insecticide than others. Chen et al. (2014)³⁷ reported that the LC₅₀ values of *E. fetida* exposed to imidacloprid for 24 and 48 hours were 3.39 and 3.63 mg L⁻¹, respectively. Likewise, Wang et al. (2012)³⁸ discovered that 2.89 mg L⁻¹ of imidacloprid at 48 hours caused the lethal toxicity in *E. fetida*.

The lethal effect of mixed pesticide exposure on T. tubifex

Co-exposure to imidacloprid and glyphosate exhibited the lethal toxicological effect in tubificid worms as presented in Table 2.

Table 2. The combined toxicity of imidacloprid and glyphosate on *T. tubifex* after 24 and 48 hours of exposure.

Mixed pesticide	Exposure time	
	24 hours	48 hours
LC ₅₀ (95% CI) mg L ⁻¹	7.997 (7.428-8.385)	1.790 (1.560-1.973)
Regression equation	Y = -7.39+8.75X	Y = -0.29+3.31X
R ² linear	0.912	0.837
Biological activity	5.216	0.913
Additive index (95% CI)	-4.216 (-10.034 to -1.764)	0.096 (-5.885 to 2.503)
Interaction	Antagonistic effect	Additive effect

Note: In the regression equation, Y represents the number of mortal worms while X represents the pesticide concentration (mg L⁻¹).



Although the coexistence of imidacloprid and glyphosate has commonly been found in the freshwater environment⁸, its interaction mechanism is not yet examined in aquatic organisms. Goñalons and Farina (2018)³⁹ investigated a combined effect of imidacloprid and glyphosate on a honey bee, *Apis mellifera*. This previous study showed unclear interaction effects of these two pesticides. However, the researchers presumed that when exposed to both imidacloprid and glyphosate, bees accumulated less toxic than those exposed to imidacloprid alone. Another finding by Zhu, Y. C. et al. (2017)⁴⁰ further confirmed that imidacloprid-based insecticide combined with glyphosate-based herbicide at the LC₂₀ did not demonstrate additive or synergistic effect in honey bees. Moreover, Wang et al. (2015)¹³ and Cang et al. (2017)⁷ found that the joint toxicity of imidacloprid and organophosphorus pesticides on the earthworm, *E. fertida*, displayed the antagonistic response. The possible explanation for the antagonistic mechanism might be that imidacloprid has a great potential to prompt the function of a monooxygenase system. This system basically plays a pivotal role in xenobiotic metabolism. The enzymes in the monooxygenase system are likely to favour imidacloprid as a substrate more than glyphosate. By doing this, the transformation rate of glyphosate to become a more toxic structure (high-water soluble form) will be deferred. As a result, the toxicity of imidacloprid cooperated with glyphosate would be lessened^{41, 42, 43}. It seems that antagonistic action of the mixed chemicals can decelerate the lethality in organisms, however, this interaction may cause morbidity effects in organisms such as alteration in enzyme activity, paralysis, or losing the ecological functions³. Despite exhibiting the antagonistic effect at 24 hours, the interaction of imidacloprid and glyphosate in *T. tubifex* transitioned to the additive effect after 48 hours of exposure. These obtained results suggested that the combined toxicity of these two pesticides is more severe when the exposure time increases. Presumably, glyphosate might be progressively catalyzed by monooxygenase enzyme in *T. tubifex* and transformed to the more noxious form after being exposed over 24 hours. By that time, imidacloprid and glyphosate would possibly show the complete extent of toxic potency, leading to the occurrence of additive effect.

Alterations in enzyme activity in T. tubifex

As was presented in Figure 1, the activity of catalase was measured in *T. tubifex* to monitor the function of the detoxification system as a response to pesticides exposure. After 24 and 48 hours of exposure, the catalase activity in *T. tubifex* exposed to sublethal concentrations of imidacloprid and glyphosate separately were significantly higher than the untreated groups ($p < 0.05$). As the concentration of pesticides increased, the catalase activity also increased significantly ($p < 0.05$). Similarly, the catalase activities of the mixed pesticide exposure at 24 and 48 hours were significantly increased as compared to the untreated groups and it continued to increase as the mixed pesticide concentrations increased ($p < 0.05$).

We further measured the AChE activity to comprehend the toxicity of these two pesticides on neural function (Figure 2). The results showed that the AChE activity in *T. tubifex* after being exposed to sublethal concentrations of imidacloprid for 24 and 48 hours were significantly greater than the control groups ($p < 0.05$). At 24 hours of exposure, significant escalation ($p < 0.05$) was also observed in the treated groups with increased imidacloprid concentrations. Contrary to both 24 and 48 hours of glyphosate alone and mixed pesticide exposure, it was found that the AChE activities of imidacloprid-treated worms were significantly lower than the control group ($p < 0.05$).

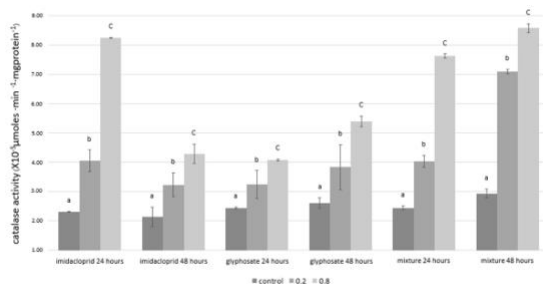


Figure 1. Effects of single and combined toxicity of imidacloprid and glyphosate on the activity of catalase in *T. tubifex*.

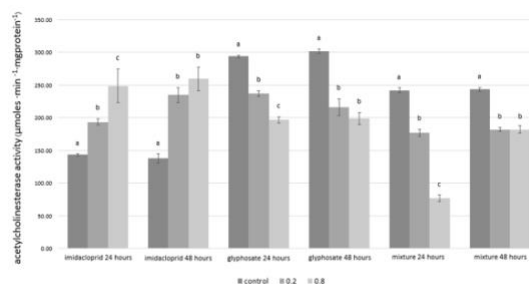


Figure 2. Effects of single and combined toxicity of imidacloprid and glyphosate on the activity of acetylcholinesterase in *T. tubifex*.

Pesticides generate an important source of excessive reactive oxygen species (ROS) which are discharged by drug metabolic reactions⁴⁴. Overproduction of ROS can contribute to the cell damage, causing a process known as oxidative stress^{45, 46}. One of the most vital detoxification enzymes found in peroxisomes of organisms is catalase. This enzyme is responsible for defending against the cellular oxidative stress by converting hydrogen peroxide to water and oxygen molecules²⁵. The results in this study are consistent with previous reports of Samanta et al. (2014)⁴⁷ and Qi et al. (2018)¹⁴ who demonstrated that exposing either glyphosate or imidacloprid in teleostean fish and *D. magna* presented a remarkable augmentation in the catalase activity. However, there was no research focus on the influence of imidacloprid and glyphosate mixture toward the alteration in catalase activity. One related study was done to examine the combined toxic effect of imidacloprid and other two herbicides on the catalase activity of zebrafish (*Danio rerio*). This research showed a significant enhancement in catalase activity as compared to the untreated group⁴⁴. Interestingly, the relation between pesticide interaction and catalase activity is noticed in this study. At 24 hours, *T. tubifex* exposed to the pesticide mixture expressed the activity of catalase less than the summation of catalase activities of individual pesticide. This coincides with the antagonism observed in the toxicity of the combined pesticide test. In addition, the catalase activity of mixed pesticide at 48 hours was approximately equal to the summation of catalase activities of individual pesticide. These results relate to the additive effect observed in the above experiment. Therefore, this study supports the fact that these pesticides can induce free radical production. Then, the catalase is activated to eliminate the oxidizing agents as well as to maintain the normal physiological condition of organisms.

Acetylcholinesterase is involved in the inactivation of a crucial neurotransmitter, acetylcholine, at the synaptic cleft. This enzyme activity is widely used as a significant biological marker for assessing pesticide neurotoxicity¹⁰. For Imidacloprid, this insecticide has the nicotinic-like structure which can compete with acetylcholine to bind irreversibly with nicotinic acetylcholine receptors, causing the overstimulation of nerve impulse transmission^{9, 48}. This might lead to the overaccumulation of acetylcholine at synaptic cleft and subsequently expresses more AChE to maintain neuronal function. We also observed paralysis after *T. tubifex* was exposed to imidacloprid for 24 and 48 hours. A possible explanation for this could be muscle fatigue after over-contraction. Supporting our finding, previous reports published that AChE activity increased significantly after honey bees (*A. mellifera*) and bird cherry-oat aphids (*Rhopalosiphum padi*) exposed to imidacloprid at sublethal concentrations^{40, 48}. Oppositely, exposing to glyphosate alone and the mixture, the worms showed the reduction in the AChE activity. The results in this study coincide with the study of Matozzo et al. (2018)¹⁸ and Sánchez et al. (2017)⁴⁹ who exhibited that glyphosate-based herbicide suppressed the AChE activity in the gills of *M. galloprovincialis* and the

muscle of *J. multidentata*. In addition, Zhu et al. (2017)⁴⁰ reported that the mixture of organophosphate pesticide with the imidacloprid-based insecticide showed a significant decrease in AChE activity of *A. mellifera*.

Histopathological examination

The transverse sectional views were depicted in figure 3 (A, B, C, and D). The untreated worms (A) in both single and combined toxicity tests showed the unimpaired body structure. On the other hand, worms exposed to imidacloprid (B), glyphosate (C) and the mixture (D) revealed pathological tissues. However, both single and mixed toxicity in this study did not show a dose-time-response relationship.

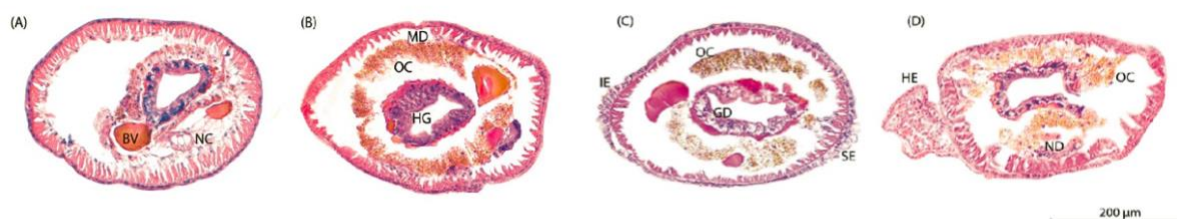


Figure 3. Effects of single and combined toxicity of imidacloprid and glyphosate on the histopathology of *T. tubifex*. BV: normal Blood Vessel, NC: normal ventral Nerve Cord, MD: Muscle Degeneration, OC: Overexpression of Chloragosomes, HG: Hyperplasia of Gut cells, IE: Irregular surface of Epidermis, GD: Gut cell Degeneration, SE: Swelling of Epidermal cells, HE: Hyperplasia of Epidermal cells, and ND: Nerve Degeneration

The observed tissue injuries in this study might be indicative of ROS overproduction. These molecules can attack the structure of biomolecules in cells, resulting in the destruction of cell structure²⁶. The present findings agreed with the study of Wang et al. (2015)²⁸ which showed that imidacloprid caused the degeneration of epidermal cells and midgut cells in *E. fetida*. Stanley & Joy (2014)²⁶ also showed similar histopathological changes in earthworms (*Nsukkadrilus mbae*) exposed to glyphosate herbicide. They found muscle degeneration, detachment of the muscular layer, and irregular surface of the epidermis in the worms. Additionally, the overexpression of chloragosomes in chloragogenous tissues was probably due to the response of the detoxification mechanism in *T. tubifex* after pesticide exposure. Kwak et al. (2014)⁵⁰ elucidated that chloragosomes play a role in neutralizing toxic substances which is similar to a function of the liver in vertebrate animals.

Conclusion:

Investigation on toxicological impacts of imidacloprid, glyphosate, and its mixture in this study revealed the acute sublethal and lethal effects on aquatic oligochaete worms, *T. tubifex*. After 24 and 48 hours of pesticide exposure, imidacloprid caused toxic effects on *T. tubifex* more than glyphosate did. The antagonistic and additive effects were observed in the combined toxicity test at 24 and 48 hours, respectively. Moreover, alterations in catalase and AChE activity were observed after the worms exposed to imidacloprid, glyphosate, and its mixture at sublethal concentrations for 24 and 48 hours. The findings on histopathology also emphasise that these two pesticides including its mixture at sublethal doses are able to cause adverse effects on tubifex worms. This denotes that alteration in histology, catalase activity, and AChE activity can be employed as biological markers to assess the toxicity of imidacloprid, glyphosate and its mixture on *T. tubifex*. Moreover, the LC₅₀ values reported in this study can be used to established aquatic life benchmark for imidacloprid, glyphosate, and its mixture.

References:

1. Cooper, J., & Dobson, H. (2007). The benefits of pesticides to mankind and the environment. *Crop Protection*, 26(9), 1337-1348.
2. Hvězdová, M., Kosubová, P., Košíková, M., Scherr, K. E., Šimek, Z., Brodský, L., ... & Krkošková, L. (2018). Currently and recently used pesticides in Central European arable soils. *Science of the Total Environment*, 613, 361-370.
3. Uwizeyimana, H., Wang, M., Chen, W., & Khan, K. (2017). The eco-toxic effects of pesticide and heavy metal mixtures towards earthworms in soil. *Environmental toxicology and pharmacology*, 55, 20-29.
4. Brown, C. D., & Van Beinum, W. (2009). Pesticide transport via sub-surface drains in Europe. *Environmental Pollution*, 157(12), 3314-3324.
5. Elbert, A., Haas, M., Springer, B., Thielert, W., & Nauen, R. (2008). Applied aspects of neonicotinoid uses in crop protection. *Pest Management Science: formerly Pesticide Science*, 64(11), 1099-1105.
6. Verro, R., Finizio, A., Otto, S., & Vighi, M. (2009). Predicting pesticide environmental risk in intensive agricultural areas. II: Screening level risk assessment of complex mixtures in surface water. *Environmental science & technology*, 43(2), 530-537.
7. Cang, T., Dai, D., Yang, G., Yu, Y., Lv, L., Cai, L. & Wang, Y. (2017). Combined toxicity of imidacloprid and three insecticides to the earthworm, *Eisenia fetida*. *Environmental Science and Pollution Research*, 24(9), 8722-8730
8. Nowell, L. H., Moran, P. W., Schmidt, T. S., Norman, J. E., Nakagaki, N., Shoda, M. E., ... & Hladik, M. L. (2018). Complex mixtures of dissolved pesticides show potential aquatic toxicity in a synoptic study of Midwestern US streams. *Science of the Total Environment*, 613, 1469-1488.
9. Morrissey, C. A., Mineau, P., Devries, J. H., Sanchez-Bayo, F., Liess, M., Cavallaro, M. C., & Liber, K. (2015). Neonicotinoid contamination of global surface waters and associated risk to aquatic invertebrates: review. *Environment international*, 74, 291-303.
10. Topal, A., Alak, G., Ozkaraca, M., Yeltekin, A. C., Comaklı, S., Acil, G., ... & Atamanalp, M. (2017). Neurotoxic responses in brain tissues of rainbow trout exposed to imidacloprid pesticide: assessment of 8-hydroxy-2-deoxyguanosine activity, oxidative stress and acetylcholinesterase activity. *Chemosphere*, 175, 186-191.
11. Sánchez-Bayo, F., Goka, K., & Hayasaka, D. (2016). Contamination of the aquatic environment with neonicotinoids and its implication for ecosystems. *Frontiers in Environmental Science*, 4, 71.
12. Gerhardt, A. (2009). Screening the toxicity of Ni, Cd, Cu, ivermectin, and imidacloprid in a short-term automated behavioral toxicity test with *Tubifex tubifex* (Müller 1774) (Oligochaeta). *Human and Ecological Risk Assessment*, 15(1), 27-40.
13. Wang, Y., Chen, C., Qian, Y., Zhao, X., & Wang, Q. (2015). Ternary toxicological interactions of insecticides, herbicides, and a heavy metal on the earthworm *Eisenia fetida*. *Journal of hazardous materials*, 284, 233-240.
14. Qi, S., Wang, D., Zhu, L., Teng, M., Wang, C., Xue, X., & Wu, L. (2018). Neonicotinoid insecticides imidacloprid, guadipyr, and cycloxaprid induce acute oxidative stress in *Daphnia magna*. *Ecotoxicology and environmental safety*, 148, 352-358.
15. Ma, X.-Y., Wu, H.-W., Jiang, W.-L., Ma, Y.-J., & Ma, Y. (2016). Weed and insect control affected by mixing insecticides with glyphosate in cotton. *Journal of Integrative Agriculture*, 15(2), 373-380.
16. Mahler, B. J., Metre, P. C. V., Burley, T. E., Loftin, K. A., Meyer, M. T., & Nowell, L. H. (2017). Similarities and differences in occurrence and temporal fluctuations in glyphosate and

atrazine in small Midwestern streams during the 2013 growing season. *Science of the Total Environment*, 579, 149–158.

17. Scribner, E. A., Battaglin, W. A., Gilliom, R. J., & Meyer, M. T. (2007). *Concentrations of Glyphosate, Its Degradation Product, Aminomethylphosphonic Acid, and Glufosinate in Ground and Surface Water and Soil Samples Collected in the United States, 2001-06*.
18. Matozzo, V., Fabrello, J., Masiero, L., Ferraccioli, F., Finos, L., Pastore, P., ... & Bogialli, S. (2018). Ecotoxicological risk assessment for the herbicide glyphosate to non-target aquatic species: a case study with the mussel *Mytilus galloprovincialis*. *Environmental Pollution*, 233, 623-632.
19. Mottier, A., Séguin, A., Devos, A., Le Pabic, C., Voiseux, C., Lebel, J. M., ... & Costil, K. (2015). Effects of subchronic exposure to glyphosate in juvenile oysters (*Crassostrea gigas*): From molecular to individual levels. *Marine pollution bulletin*, 95(2), 665-677.
20. Schnug, L., Leinaas, H. P., & Jensen, J. (2014). Synergistic sub-lethal effects of a biocide mixture on the springtail *Folsomia fimetaria*. *Environmental pollution*, 186, 158-164.
21. COM, E. (2012). The combination effects of chemicals-chemical mixtures. *Communication from the Commission to the Council*, 252, 252.
22. Sakset, A., Gallardo, W. G., & Ikejima, K. (2012). Physicochemical conditions and biodiversity in the freshwater fishing area of Pak Phanang River Basin, Thailand. *International Journal of Sustainable Development & World Ecology*, 19(2), 172-188.
23. Paris-Palacios, S., Mosleh, Y. Y., Almohamad, M., Delahaut, L., Conrad, A., Arnoult, F., & Biagianti Risbourg, S. (2010). Toxic effects and bioaccumulation of the herbicide isoproturon in *Tubifex tubifex* (Oligochaeta, Tubificidae): a study of significance of autotomy and its utility as a biomarker. *Aquatic toxicology*, 98(1), 8-14.
24. Kılıç, G. A., & Kılıç, V. (2011). Metallothionein induction, acetylcholine esterase activity and antioxidative response as biomarkers of thallium toxicity in *Tubifex tubifex* (Oligochaeta, Tubificidae). *Abstracts/Toxicology Letters* 205S, 60(S179), S179.
25. Di, S., Liu, R., Cheng, C., Chen, L., Zhang, W., Tian, Z., ... & Diao, J. (2017). Biomarkers in *Tubifex tubifex* for the metalaxyl and metalaxyl-M toxicity assessment in artificial sediment. *Environmental Science and Pollution Research*, 24(4), 3618-3625.
26. Stanley, O. N., & Joy, O. A. (2014). Histopathological effects of glyphosate and its toxicity to the earthworm (*Nsukkadrilus mbae*). *British Biotechnology Journal*: 149-163.
27. Dittbrenner, N., Schmitt, H., Capowiez, Y., & Triebkorn, R. (2011). Sensitivity of *Eisenia fetida* in comparison to *Aporrectodea caliginosa* and *Lumbricus terrestris* after imidacloprid exposure. Body mass change and histopathology. *Journal of soils and sediments*, 11(6), 1000.
28. Wang, K., Pang, S., Mu, X., Qi, S., Li, D., Cui, F., & Wang, C. (2015). Biological response of earthworm, *Eisenia fetida*, to five neonicotinoids. *Chemosphere*, 132, 120-126.
29. Wang, Y., Wu, S., Chen, J., Zhang, C., Xu, Z., Li, G., ... & Wang, Q. (2018). Single and joint toxicity assessment of four currently used pesticides to zebrafish (*Danio rerio*) using traditional and molecular endpoints. *Chemosphere*, 192, 14-23.
30. Humason, G. L. (1962). Animal tissue techniques. *Animal tissue techniques*.
31. Bradford, M. M. (1976). A rapid and sensitive method for the quantitation of microgram quantities of protein utilizing the principle of protein-dye binding. *Analytical biochemistry*, 72(1-2), 248-254.
32. Ellman, G. L., Courtney, K. D., Andres Jr, V., & Featherstone, R. M. (1961). A new and rapid colorimetric determination of acetylcholinesterase activity. *Biochemical pharmacology*, 7(2), 88-95.

33. Erp, S. V., Booth, L., Gooneratne, R., & Ohalloran, K. (2002). Sublethal responses of wolf spiders (Lycosidae) to organophosphorous insecticides. *Environmental Toxicology*, 17(5), 449–456.
34. Hassoon, H. A., & Salman, S. A. (2016). The Acute Effect of Pesticides Carbaryl and Imidacloprid on *Daphnia pulex* species. *Journal of International Environmental Application and science*, 11(1), 18-25.
35. Thuyet, D. Q., Watanabe, H., Yamazaki, K., & Takagi, K. (2011). Photodegradation of imidacloprid and fipronil in rice–paddy water. *Bulletin of environmental contamination and toxicology*, 86(5), 548-553.
36. Hong, Y., Yang, X., Yan, G., Huang, Y., Zuo, F., Shen, Y., . . . Cheng, Y. (2017). Effects of glyphosate on immune responses and haemocyte DNA damage of Chinese mitten crab, *Eriocheir sinensis*. *Fish & shellfish immunology*, 71, 19-27.
37. Chen, C., Wang, Y., Zhao, X., Wang, Q., & Qian, Y. (2014). Comparative and combined acute toxicity of butachlor, imidacloprid and chlorpyrifos on earthworm, *Eisenia fetida*. *Chemosphere*, 100, 111-115.
38. Wang, Y., Cang, T., Zhao, X., Yu, R., Chen, L., Wu, C., & Wang, Q. (2012). Comparative acute toxicity of twenty-four insecticides to earthworm, *Eisenia fetida*. *Ecotoxicology and Environmental Safety*, 79, 122–128.
39. Goñalons, C. M., & Farina, W. M. (2018). Impaired associative learning after chronic exposure to pesticides in young adult honey bees. *Journal of Experimental Biology*, 221(7), jeb176644.
40. Zhu, Y. C., Yao, J., Adamczyk, J., & Luttrell, R. (2017). Synergistic toxicity and physiological impact of imidacloprid alone and binary mixtures with seven representative pesticides on honey bee (*Apis mellifera*). *PloS one*, 12(5).
41. Gaughan, L. C., Engel, J. L., & Casida, J. E. (1980). Pesticide interactions: effects of organophosphorus pesticides on the metabolism, toxicity, and persistence of selected pyrethroid insecticides. *Pesticide biochemistry and physiology*, 14(1), 81-85.
42. Hernández, A. F., Parrón, T., Tsatsakis, A. M., Requena, M., Alarcón, R., & López-Guarnido, O. (2013). Toxic effects of pesticide mixtures at a molecular level: their relevance to human health. *Toxicology*, 307, 136-145.
43. Svendsen, C., Siang, P., Lister, L. J., Rice, A., & Spurgeon, D. J. (2010). Similarity, independence, or interaction for binary mixture effects of nerve toxicants for the nematode *Caenorhabditis elegans*. *Environmental Toxicology and Chemistry*, 29(5), 1182-1191.
44. Shukla, S., Jhamtani, R. C., Dahiya, M. S., & Agarwal, R. (2017). Oxidative injury caused by individual and combined exposure of neonicotinoid, organophosphate and herbicide in zebrafish. *Toxicology reports*, 4, 240-244.
45. Vieira, C. E. D., Pérez, M. R., Acayaba, R. D. A., Raimundo, C. C. M., & dos Reis Martinez, C. B. (2018). DNA damage and oxidative stress induced by imidacloprid exposure in different tissues of the Neotropical fish *Prochilodus lineatus*. *Chemosphere*, 195, 125-134.
46. Li, M.-H., Ruan, L.-Y., Zhou, J.-W., Fu, Y.-H., Jiang, L., Zhao, H., & Wang, J.-S. (2017). Metabolic profiling of goldfish (*Carassius auratus*) after long-term glyphosate-based herbicide exposure. *Aquatic Toxicology*, 188, 159-169.
47. Samanta, P., Pal, S., Mukherjee, A. K., & Ghosh, A. R. (2014). Biochemical effects of glyphosate-based herbicide, Excel Mera 71 on enzyme activities of acetylcholinesterase (AChE), lipid peroxidation (LPO), catalase (CAT), glutathione-S-transferase (GST) and protein content on teleostean fishes. *Ecotoxicology and environmental safety*, 107, 120-125.



48. Azevedo-Pereira, H. M. V. S., Lemos, M. F. L., & Soares, A. M. (2011). Effects of imidacloprid exposure on *Chironomus riparius* (Meigen) larvae: linking acetylcholinesterase activity to behaviour. *Ecotoxicology and environmental safety*, 74(5), 1210-1215.
49. Sánchez, J. A. A., Junior, A. S. V., Corcini, C. D., da Silva, J. C., Primel, E. G., Caldas, S., ... & Martins, C. D. M. G. (2017). Effects of Roundup formulations on biochemical biomarkers and male sperm quality of the livebearing *Jenynsia multidentata*. *Chemosphere*, 177, 200-210.
50. Kwak, J. I., Kim, S. W., & An, Y. J. (2014). A new and sensitive method for measuring in vivo and in vitro cytotoxicity in earthworm coelomocytes by flow cytometry. *Environmental research*, 134, 118-126.
51. Aebi, H. (1984). [13] Catalase in vitro. *Methods in enzymology*, 105, 121-126.



***IN SILICO* DRUG REPURPOSING FOR SATELLITE CELL DIFFERENTIATION TARGETING ACTIVIN TYPE II B RECEPTOR**

Prant Chotiphantawanon,¹ Utid Suriya,¹ Wimon Siri Puegsa,¹ Tavan Janvilisri¹, *

¹Department of Biochemistry, Faculty of Science, Mahidol University, Bangkok 10400, Thailand

*e-mail: tavan.jan@mahidol.ac.th

Abstract:

Myostatin (MSTN) is a crucial negative regulator of myogenic differentiation and a key player in inhibiting muscle growth. Inhibition of MSTN has shown potential for increasing muscle mass, making it an attractive target for medical and agricultural applications. This study aimed to identify potent inhibitors specific to the activin type IIB receptor (ActRIIB), a critical component of the MSTN signaling pathway, through molecular docking. A library of 3,206 compounds sourced from the ZINC 20 database was screened using AutoDock VinaXB software. Remarkably, 36 FDA-approved drugs displayed higher binding affinities for ActRIIB than the reference ligand GW788388. For this purpose, we selected the top four compounds showing the highest magnitude of binding strength to inspect intermolecular interactions within the ActRIIB binding site. It was found that the four candidate compounds could form a stable complex with ActRIIB, mostly via hydrophobic interactions. Some common interacting residues were found in accordance with the binding of a well-known ActRIIB inhibitor (GW788388) including TYR60, TRP78, and PHE101, suggesting a similar pattern of binding mode towards the ActRIIB receptor. From the *in silico* study, the four compounds identified here might be promising candidates for repurposing as a supplement to increase myogenic cell differentiation. However, experimental evaluation of screened compounds should be further conducted to validate the computational prediction and their biological activities.

Introduction:

Myostatin (MSTN) is a member of the transforming growth factor- β (TGF- β) superfamily, recognized as a negative regulator of myogenic differentiation and playing a pivotal role in inhibiting muscle growth. Upon activation of MSTN, satellite cells are induced into a quiescent state, subsequently leading to the upregulation of muscle-specific ubiquitin ligases, resulting in a decrease in muscle mass [1, 2]. In murine models, inhibition of MSTN has been reported to significantly increase muscle mass [3]. The activation of the MSTN signaling pathway initially occurs through the binding of MSTN, along with activin A (ActA), to the activin type IIB receptor (ActRIIB). This interaction leads to the phosphorylation of Smad2, inducing satellite cells to enter the quiescence stage. Phosphorylation of Smad2 also results in the dephosphorylation of FOXO3a, subsequently activating the transcription of E3 ubiquitin ligases, MuFR1, and Atrogin1. These ligases, in turn, lead to muscle degradation and the development of Cachexia. Conversely, when MSTN/ActA signaling is blocked, it reduces phosphorylated Smad2 levels, promoting muscle hypertrophy and the reversal of the cachexia [2]. Many studies tried to regulate the myostatin signaling pathway for medical treatment or agriculture applications. Previous studies have demonstrated the use of antibody-based drugs, MIF1/MIF2 peptide inhibitors, Vitamin D, and natural compounds (e.g., sulforaphane) to modulate the MSTN signaling pathway for the increase of myogenic differentiation [1, 4-7].



Molecular docking, a structure-based computational methodology employed for compound screening, originating after the discovery of crystallographic protein structures. The fundamental concept behind molecular docking is the precise placement of a small molecule, acting as a ligand, into a binding site of macromolecular targets, facilitating the identification of potentially active compounds [8, 9]. These ligands, integral to the molecular docking process, can be readily sourced from various databases, such as ZINC and PubChem [9] and 3D protein structures can be retrieved from the available database, the RCSB Protein Data Bank (PDB) [10].

Therefore, in this study, we employed molecular docking as a computational approach to search for highly effective inhibitors that specifically bind to ActRIIB, a pivotal component in regulating the MSTN signaling pathway. We screened a library comprising 3,206 compounds, which has been sourced from the ZINC 20 database (<http://zinc.docking.org>). Compared to a well-known inhibitor (GW788388), the compounds showing a higher binding affinity were selected as “hits”, which tend to bind to ActRIIB. Finally, this study is considered an initial important step in identifying potential compounds promoting myogenic differentiation and could be useful guidance for further biochemical investigations.

Methodology:

Ligand preparation

A total of 3,206 FDA-approved drugs from the ZINC 20 database were selected for utilized as a ligand library in molecular docking studies for screening potential inhibitor drugs targeting negative regulators of myogenic differentiation [11]. The drugs retrieved from the ZINC 20 database (<http://zinc.docking.org>) are in ‘mol2’ format, which was subsequently converted to ‘pdbqt’ format for the screening step using AutoDockTools software to prepare the format for using in AutoDock VinaXB. GW788388 which is the compound that has been reported the activity to inhibit Activin type IIB receptor (ActRIIB) *in vivo* and *in vitro* was used as a reference ligand for molecular docking [12]. The chemical structure of the GW788388 was drawn and prepared in the ‘mol2’ format using MarvinSketch.

Protein Structure Preparation

The RCSB Protein Data Bank (PDB) is the database that collects protein structures derived from various methods, including X-ray diffraction. The three-dimensional structure of the ActRIIB in complex with its antibody inhibitor Bimagrumab was retrieved from the PDB (PDB ID: 5NGV) [4]. Bimagrumab, the inhibitor, was used to identify the binding site of the ActRIIB focusing on the frequently bound amino acid (GLU52, LYS55, TRP78, ASP80, PHE82, ASN83, and PHE101).

Molecular Docking

AutoDock VinaXB, one of the common freeware molecular docking software programs operating under the Linux operating system, was used in the molecular docking step to screen the compounds from the ligand library and predict the interaction (binding energy) between each compound and protein targets [10, 13]. GW788388, a known inhibitor of ActRIIB, was redocked to the binding site, which had X, Y, and Z coordinates of 11.48, 17.68, and 25.61, respectively, while the box size was set to 20 Å for all dimensions and used as a reference molecule. The binding energy of each compound was then ranked to select their potential to strongly bind to the protein target and act as an inhibitor compared to GW788388 as a reference molecule.

Results and Discussion:

To rapidly screen potential compounds capable of inhibiting ActRIIB, 3,206 FDA-approved drugs were retrieved and subjected to docking-based virtual screening to observe and rank the binding strength termed “binding energy” in comparison to a well-known inhibitor (GW788388). The three-dimensional structure of ActRIIB in complex with Bimagrumab derived from the protein databank (PDB ID: 5NGV) was illustrated in Figure 1a. To identify the crucial amino acids responsible for the antibody binding, the frequency of interactions between Bimagrumab and ActRIIB, including hydrogen bond, hydrophobic, and electrostatic interaction was analyzed and shown in Figure 1b. It can be observed that the most frequently bound amino acids include GLU52, ASP54, LYS55, TRP78, ASP80, PHE82, ASN83, and PHE101. Accordingly, we set the most frequently bound residues as the docking site for virtual screening. Before conducting molecular docking, we validated the docking protocol by redocking the known inhibitor into the identified docking site as shown in Figure 2a and inspecting the pattern of molecular recognition with the amino acids as illustrated in Figure 2b. We found that the residues including LYS74, TRP78, LEU79, and Phe101 interacted with GW788388, which corresponds to the residues having a high frequency of intermolecular interactions with the previous crystalized antibody (TRP78 and PHE101). This indicates that the grid box was set appropriately, and the docking protocol verified the reliability of the docking run.

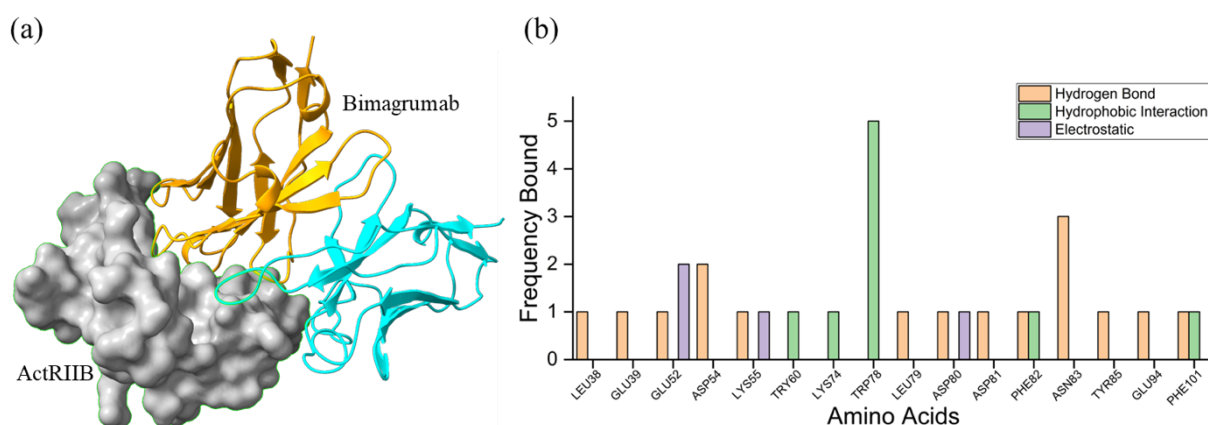


Figure 1. (a) Crystallized structure of ActRIIB together with antibody inhibitor, Bimagrumab
(b) Frequency of interactions between each ActRIIB residue and the antibody inhibitor

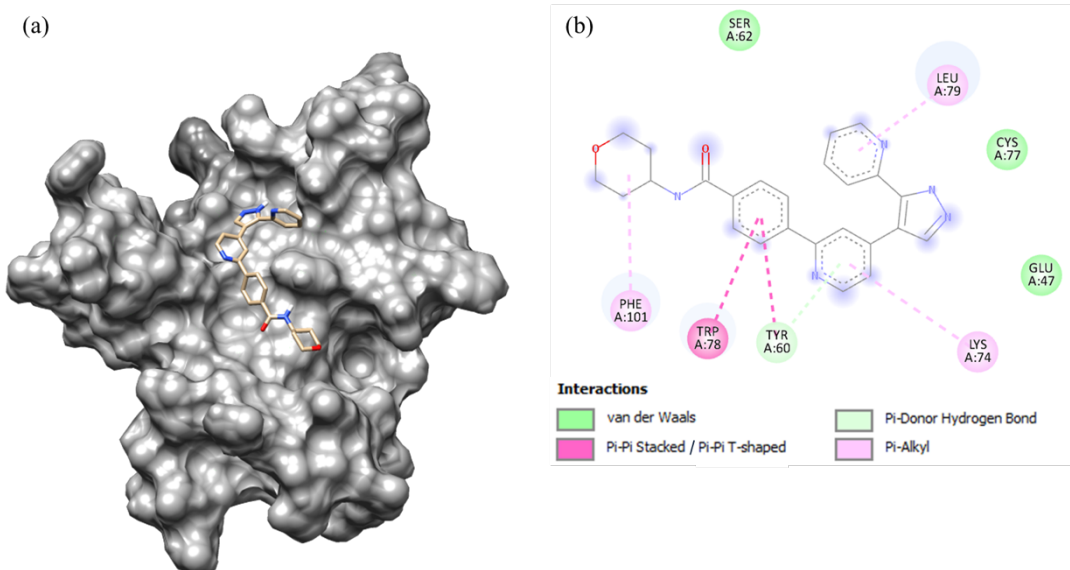


Figure 2. (a) 3D-Structure of Activin type II B receptor with the GW788388, a known inhibitor of ActRIIB [14] visual by ChimeraX 1.6.1 (b) 2D-Interaction between ActRIIB and GW788388 displayed in different colors using Discovery Studio Visualizer

For the first-round screening, a total of 3,206 compounds from an FDA-approved drug library were ranked according to the predicted binding energy. As shown in Figure 3, there were 36 compounds exhibiting a lower binding energy value when compared to GW788388 (-7.6 kcal/mol). To this end, the top 10 compounds in which the binding energy was in the range of -9.5 to -8.1 kcal/mol were selected to analyze intermolecular interactions compared to GW788388 (Figure 4a).

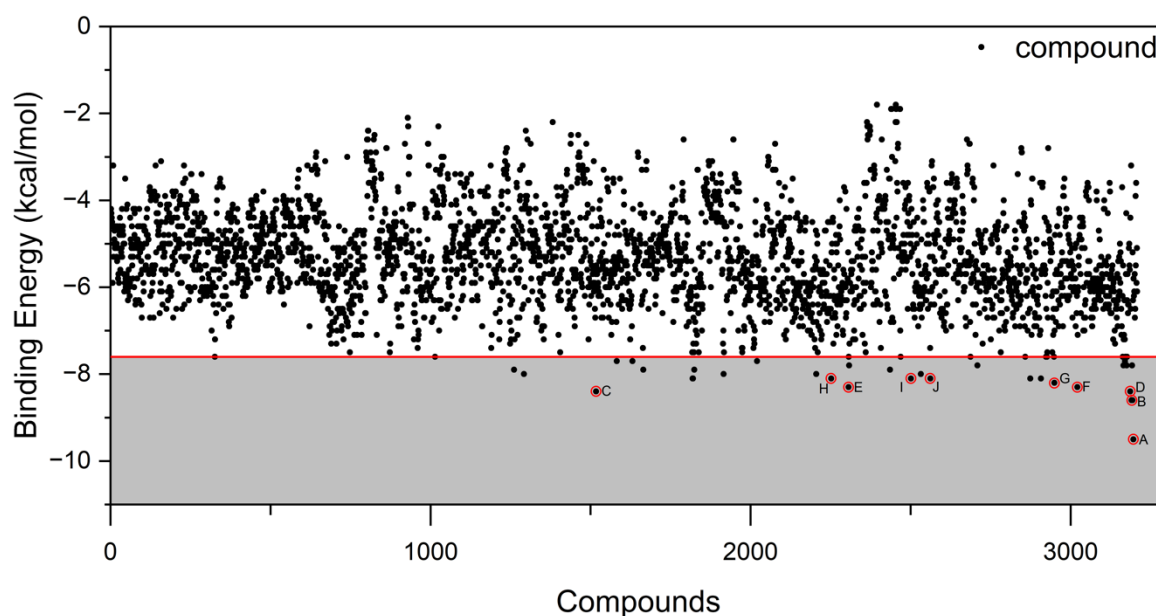


Figure 3. The binding energy of 3,206 compounds from an FDA-approved drug library. The reference line is the binding energy of GW788388 (-7.6 kcal/mol).

Apart from the binding energy, the molecular recognition in terms of non-covalent interactions was inspected. It is well-established that noncovalent interactions play a crucial role in ligand binding. Compounds that demonstrate strong interactions, both qualitatively and quantitatively, are more likely to possess enhanced binding potential, leading to the formation of stable complexes [15, 16]. For this purpose, we selected only the top 4 compounds (compounds A-D) to examine the binding interaction analysis. As illustrated in Figure 4b, there are three types of non-covalent interactions including hydrogen bonds, hydrophobic, and electrostatic interaction that are responsible for the compound binding. There were four interactions with compound A including TYR60, TRP78, PHE101, and CYS103. In the case of compound B, the interactions with CYS77, LEU79, and ASN83 were observed. Moreover, interactions with compound C were observed in the highest numbers including TYR31, TYR60, TRP78, LEU79, ASN83, and CYS103, whilst compound D interacted with five residues TYR60, TRP78, THR93, PHE101, and CYS103.

Subsequently, we listed the interactions of all screened compounds and GW788388 to observe the commonly bound amino acids. As illustrated in Table 1, we found some common amino-acid residues including TYR60, TRP78, LEU78, and PHE101 in the binding of almost all selected candidates and GW788388. Interactions of inhibitors with TYR60, TRP78, and PHE101 are necessarily required since these residues were reported as a centralized hydrophobic triad that ActRIIB used to engage the ActA and GDF11 [17]. Thus, compounds disrupting these interactions may be “effective ActRIIB inhibitors” and these residues are considered “hotspots” for inhibitor binding that could be used to guide further rational design of more potent inhibitors.

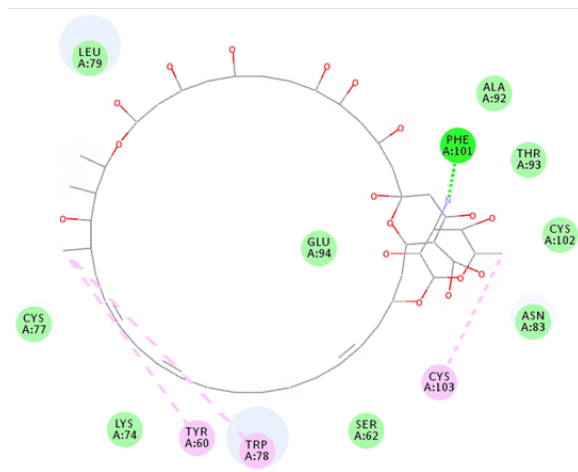
(a)

Compound	BE (kcal/mol)	TYR31	GLU47	LYS55	TYR60	LYS74	CYS77	TRP78	LEU79	ASP81	ASN83	THR93	GLU94	PHE101	CYS102	CYS103
Compound A	-9.5															
Compound B	-8.6															
Compound C	-8.4															
Compound D	-8.4															
Compound E	-8.3															
Compound F	-8.3															
Compound G	-8.2															
Compound H	-8.1															
Compound I	-8.1															
Compound J	-8.1															
GW788388	-7.6															

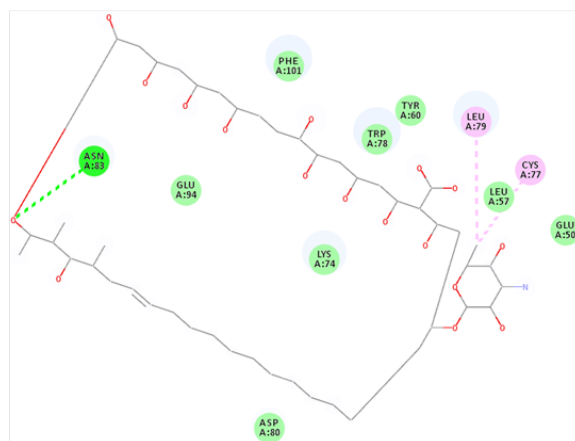
Hydrogen bond
Hydrophobic interaction
Electrostatic interaction

(b)

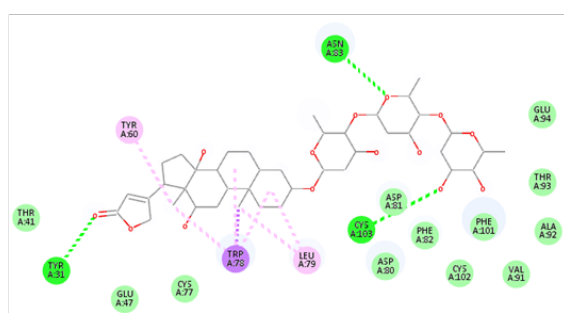
Compound A



Compound B



Compound C



Compound D

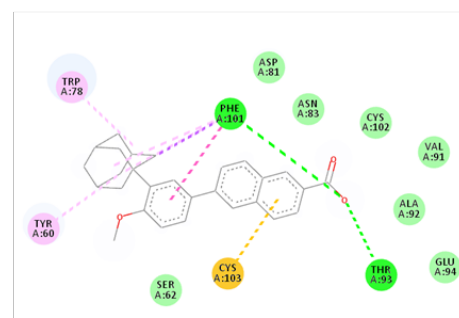


Figure 4. (a) Map of intermolecular interactions of ActRIIB and top 10 screened candidates in comparison to GW788388. Each type of noncovalent interaction was also illustrated in different colors (b) 2D-Interaction for docking analysis of compounds A, B, C, and D displayed in Discovery Studio Visualizer

Conclusion:

This study screened 3,206 compounds from the FDA-approved drugs accessible in the ZINC database and found that the 4 FDA-approved drugs exhibited higher binding affinities than GW788388 and formed a stable complex with ActRIIB. Moreover, most compounds demonstrated interactions with crucial amino acids including TYR60, TRP78, and PHE101 that ActRIIB uses to engage its normal substrates, indicating the potential of being successful ActRIIB inhibitors. These findings could accelerate the discovery of potential compounds disrupting ActRIIB biological function that may provide beneficial outcomes in promoting myogenic cell differentiation. However, experimental validations especially in cell-based assays will be necessary to evaluate the potency of the screened candidates.



Acknowledgements:

This research has received funding support from the NRSF via the Program Management Unit for Human Resources, Institutional Development, Research, and Innovation [grant number B05F650014]

References:

1. Chen, M.-M., et al., *Regulation of myostatin on the growth and development of skeletal muscle*. Frontiers in Cell and Developmental Biology, 2021. **9**: p. 785712.
2. Farhang-Sardroodi, S. and K.P. Wilkie, *Mathematical Model of Muscle Wasting in Cancer Cachexia*. Journal of Clinical Medicine, 2020. **9**(7): p. 2029.
3. Joulia-Ekaza, D. and G. Cabello, *The myostatin gene: physiology and pharmacological relevance*. Current Opinion in Pharmacology, 2007. **7**(3): p. 310-315.
4. Morvan, F., et al., *Blockade of activin type II receptors with a dual anti-ActRIIA/IIB antibody is critical to promote maximal skeletal muscle hypertrophy*. Proceedings of the National Academy of Sciences, 2017. **114**(47): p. 12448-12453.
5. Lee, E.J., et al., *MIF1 and MIF2 Myostatin Peptide Inhibitors as Potent Muscle Mass Regulators*. International Journal of Molecular Sciences, 2022. **23**(8): p. 4222.
6. Fan, H., et al., *Sulforaphane causes a major epigenetic repression of myostatin in porcine satellite cells*. Epigenetics, 2012. **7**(12): p. 1379-1390.
7. Braga, M., et al., *Vitamin D induces myogenic differentiation in skeletal muscle derived stem cells*. Endocrine Connections, 2017. **6**(3): p. 139-150.
8. Amaro, R.E., et al., *Ensemble docking in drug discovery*. Biophysical journal, 2018. **114**(10): p. 2271-2278.
9. Guedes, I.A., C.S. De Magalhães, and L.E. Dardenne, *Receptor–ligand molecular docking*. Biophysical Reviews, 2014. **6**(1): p. 75-87.
10. Ferreira, L., R. Dos Santos, G. Oliva, and A. Andricopulo, *Molecular Docking and Structure-Based Drug Design Strategies*. Molecules, 2015. **20**(7): p. 13384-13421.
11. Irwin, J.J., et al., *ZINC: A Free Tool to Discover Chemistry for Biology*. Journal of Chemical Information and Modeling, 2012. **52**(7): p. 1757-1768.
12. Levolger, S., et al., *Inhibition of activin-like kinase 4/5 attenuates cancer cachexia associated muscle wasting*. Scientific Reports, 2019. **9**(1).
13. Suriya, U., P. Mahalapbutr, and T. Rungrotmongkol, *Integration of In Silico Strategies for Drug Repositioning towards P38α Mitogen-Activated Protein Kinase (MAPK) at the Allosteric Site*. Pharmaceutics, 2022. **14**(7): p. 1461.
14. Hulmi, J.J., T.A. Nissinen, F. Penna, and A. Bonetto, *Targeting the Activin Receptor Signaling to Counteract the Multi-Systemic Complications of Cancer and Its Treatments*. Cells, 2021. **10**(3): p. 516.
15. Sottriffer, C., *Docking of covalent ligands: challenges and approaches*. Molecular Informatics, 2018. **37**(9-10): p. 1800062.
16. Adhav, V.A. and K. Saikrishnan, *The Realm of Unconventional Noncovalent Interactions in Proteins: Their Significance in Structure and Function*. ACS Omega, 2023. **8**(25): p. 22268-22284.
17. Goebel, E.J., et al., *Structures of activin ligand traps using natural sets of type I and type II TGFβ receptors*. iScience, 2022. **25**(1): p. 103590.



IN SILICO SCREENING OF NOVEL GSK3 β INHIBITORS FOR PROMOTING CELL PROLIFERATION

Wimonsiri Puegsa,¹ Utid Suriya,¹ Prant Chotiphantawanon,¹ Tavan Janvilisri¹, *

¹Department of Biochemistry, Faculty of Science, Mahidol University, Bangkok 10400, Thailand

*e-mail: tavan.jan@mahidol.ac.th

Abstract:

Culture meats are produced by *in vitro* animal cell culture with a mixture of nutrients and growth factors. Promoting cell proliferation requires high-cost growth supplements, which pose an issue for practical use. One of the proven strategies is to use small molecules to inhibit the protein signaling cascade of the Wnt pathway. Herein, we focused on the novel discovery of the glycogen synthase kinase 3 beta (GSK3 β) inhibitors by using an *in silico* molecular docking approach. From 3,208 compounds, we found that four compounds (compounds A-D) exhibited higher binding affinity when compared to a well-known GSK3 β inhibitor (CHIR99021). The binding mode analysis revealed that these four compounds carried sufficient interactions with commonly interacting residues including Phe67, Val70, and Cys199. From the line of binding energy and intermolecular interactions, the four compounds identified here might be viable candidates to promote myogenic cell proliferation. However, *in vitro* experiments are further required to evaluate the candidate compounds as a growth-promoting supplement in lab-scale cultured meat production.

Introduction:

The traditional method of meat production requires a significant amount of resources, contributes to negative environmental effects such as greenhouse gas emissions, raises concern about animal welfare, and is associated with several public health issues, including the potential for animal-transmitted pandemics and antibiotic resistance [1]. According to the increasing global population, demand for meat is predicted to rise significantly [2]. One proposed solution to reduce meat consumption is the development and utilization of culture meat, which can be produced from animal cells without animal slaughter [3]. Cultured meat, also known as lab-grown or cell-based meat, is meat produced by culturing animal cells using tissue engineering techniques. Cultured meat reduces greenhouse gas emissions, land usage, concerns about animal welfare, and animal suffering by using a smaller number of animals [4, 5]. Additionally, culture meat can decrease contamination from animal epidemics [6]. Satellite cells, which can be differentiated into muscle fibers, are a key component of cultured meat [7]. To begin, culturing meat has two stages: proliferation and differentiation. The goal of the proliferation phase is to increase the number of doubling of cells before they differentiate into muscle cells. These cells are then placed in a bioreactor and multiplied. They are then placed in a matrix or scaffold where they develop into muscle fibers and tissue [8]. However, enhancing the proliferation rate and maintaining satellite cells are some of the challenges in cultured meat production.

A previous study investigated the effects of GSK3 β inhibition on porcine muscle satellite cells, which showed that inhibiting GSK3 β could be a promising method for promoting porcine muscle satellite cell proliferation and survival *in vitro* [9]. Glycogen synthase kinase (GSK3) is a serine/threonine protein kinase that was initially investigated for its role in glycogen synthase regulation. There are 2 isoforms of GSK3 expressed in mammals which are GSK3 α (51 kDa) and GSK3 β (47 kDa) [10]. GSK3 is currently known to play a critical role in various processes, including protein synthesis initiation, cell proliferation, differentiation, and



apoptosis, and it is required for embryonic development as a component of the Wnt signaling pathway [11]. Accordingly, inhibition of GSK3 β is highlighted as an attractive approach in many applications, owing to its potential to modulate key cellular processes and its involvement in critical signaling pathways [12]. The previous study showed that CHIR99021 (GSK3 inhibitor) inhibits GSK3 and enhances mouse embryonic stem cells (mESC) self-renewal via stabilizing cytoplasmic β -catenin, a key component of the canonical Wnt signaling pathway [13]. The data show that inhibiting GSK3 β is a promising protein target for enhancing proliferation, and thus, some studies have tried to find ligands that can interact with the GSK3 β [14] and inhibit its function which could be highlighted as an attractive approach for many applications.

One approach that can be considered for identifying novel inhibitors for GSK3 β is the use of *in silico* methods. Molecular docking is one of the computational-based techniques that is widely used in the molecular biology field and drug discovery. Molecular docking is used to predict the binding energy of protein-ligand complexes and rank the candidate compounds in an accelerated manner [15]. In this study, we used the model of GSK3 β in complex with CHIR99021 (PDB ID: 5HLN) retrieved from Protein Data Bank (PDB) as a protein target, and 3,208 compounds which are the FDA-approved drug were obtained from the ZINC 20 database as ligand inputs. All ligands were docked against the GSK3 β binding pocket and were carried out using AutoDock VinaXB to rank potential inhibitor(s) according to the predicted binding energy from its scoring function. The objective of this study was to rank potential inhibitors based on their predicted binding energies derived from the scoring function of AutoDock VinaXB. In summary, this study provides a significant impact by identifying novel GSK3 β inhibitors, which can serve as a starting point for future research and applications in various fields.

Methodology:

Ligand preparation

A total of 3,204 reported Food and Administration (FDA)-approved drugs were retrieved from the ZINC database (<http://zinc.docking.org>) for use in performing molecular docking studies to screen and identify potential inhibitors of FDA-approved drugs, specifically GSK3 β . Subsequently, the mol2 file was converted into PDBQT format using AutoDockTools (ADT) [16].

Protein structure preparation

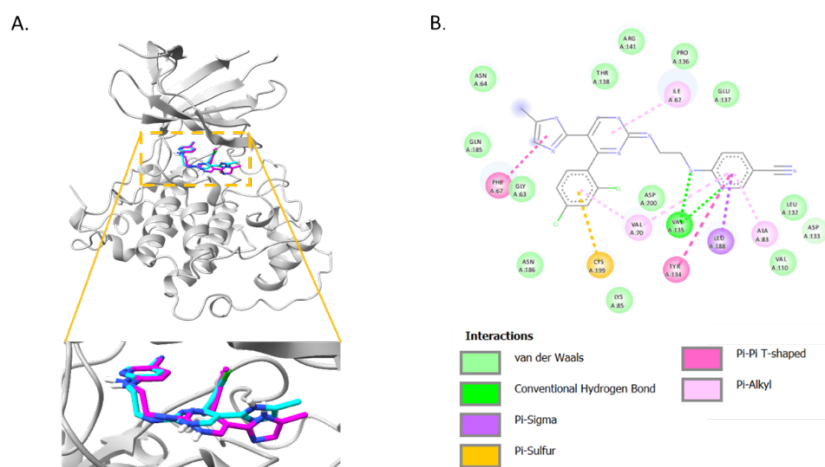
The GSK3 β complex with the known inhibitor (PDB ID: 5HLN) was obtained from the Protein Data Bank (PDB), accessible at <https://www.rcsb.org/>, a database for the 3D structure of biological molecules, including proteins or nucleic acids, retrieved through various methods, including X-ray crystallography. To prepare the free protein, BIOVIA Discovery Studio 2017 was used to eliminate all ligands, ions, and hydrogen molecules. Subsequently, the mol2 file was converted into PDBQT format using AutoDockTools (ADT) [16].

Molecular docking

Molecular docking approaches were used to identify possible binding targets to understand inhibitory actions at the atomic level. The binding affinity concerning the predicted binding energy of candidate inhibitors and a target protein was examined and compared to reference ligands. Firstly, docking was performed with a reference molecule of the target protein to validate the docking protocol [17]. The grid box size was set to 20 Å×20 Å×20 Å

Results and Discussion:

Subsequently, all 3,208 compounds from the FDA-approved drugs database were automatically docked into the binding site of GSK3 β using Autodock VinaXB. For a first-round screening, we utilized the binding energy predicted from the Autodock VinaXB scoring function as a main parameter. It was obvious that the compounds showing low binding energy are likely to effectively inhibit the protein targets in an *in vitro* assay [19]. As illustrated in Figure 2, there were four hundred compounds displaying lower binding energy when compared to CHIR99021. For this purpose, we selected only the top four compounds (table 1) representing as compound A-D for further investigation. The binding energy for compound A, compound B, compound C, and compound D with GSK3 β was -12.9, -12.4, -12.1, and -11.5 kcal/mol, respectively while CHIR99021 was -9.3 kcal/mol.



© The 49th International Congress on Science, Technology and Technology-based Innovation (STT 49)

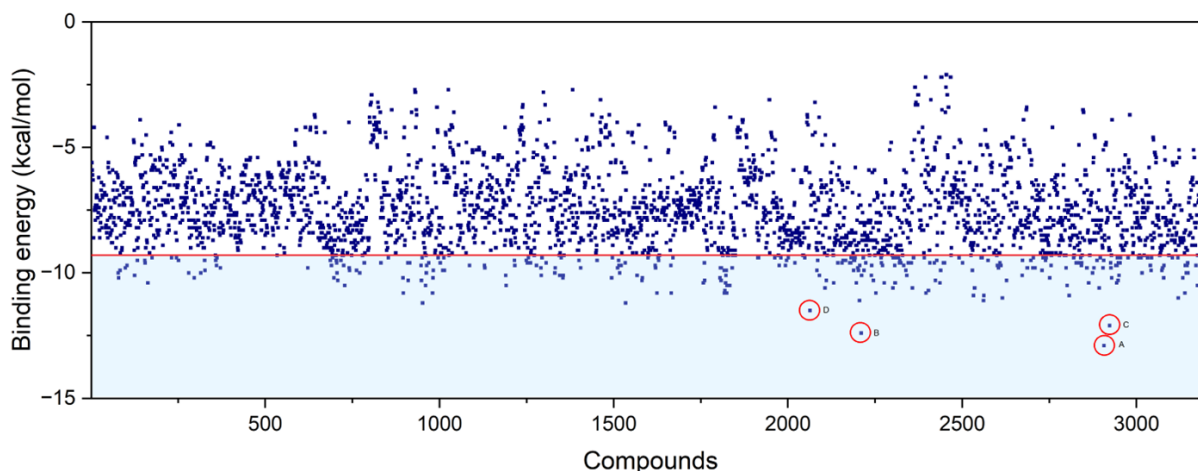


Figure 2. Virtual screening of 3,208 compounds in comparison to known inhibitor, CHIR99021, in the red line.

Apart from binding energy prediction, we then inspected the compounds' binding mode in terms of intermolecular interactions. Note that all interactions were visualized by using BIOVIA Discovery Studio 2017. As observed in Figure 3, all the top compounds could form a stable complex by the ensembles of non-covalent interactions (H-bond, hydrophobic, electrostatic, and halogen bond), and shared some common amino-acid residues to CHIR99021 including Phe67, Val70, and Cys199 (Figure 3A). These findings indicated that the compounds were docked to a similar site occupied by CHIR99021 and tended to be able to inhibit GSK3 β . Specifically, compound A formed a hydrogen bond with Gln185 and five hydrophobic interactions with Phe67, Val70, Lys85, Tyr140, and Cys199 (Figure 3B). Compound B forms a hydrogen bond and a halogen bond with Val135 and shows eight hydrophobic interactions with Ile62, Phe67, Val70, Ala83, Leu132, Leu188, and Cys199 (Figure 3B). Compound C does not form any hydrogen bonds while it shows hydrophobic interactions with Phe67, Val70, Ala83, Lys85, Leu188, and electrostatic interactions with Cys199 (Figure 3B). Compound D does not form any hydrogen bonds while showing eight hydrophobic interactions with Phe67, Val70, Ala83, Lys85, Val110, Leu132, Leu188, and Cys199 (Figure 3B). The interacting residues corresponded to the previous studies of GSK3 β inhibitors including NPD13432 [13], LY-2090314 [20], cpd1 [14], and SB216763 [14]. For instance, it was reported that NPD13432 bound to the binding pocket of GSK3 and could form interactions with Lys85, Asp133, Tyr134, Val135, Pro136, Leu188, Cys199, and Asp200 with a docking affinity of -8.7 kcal/mol. In addition, a candidate compound identified by molecular docking could promote self-renewal in mouse embryonic stem cells (mESCs) evaluated by an *in vitro* assay, highlighting the consistent and productive roles of the computational docking model that accelerated the discovery of novel GSK3 inhibitors [13]. Altogether, the computational model was successful in guiding the selection of compounds as a growth-promoting supplement and the compounds identified here were considered promising candidates for further studies in biochemical experimentation.

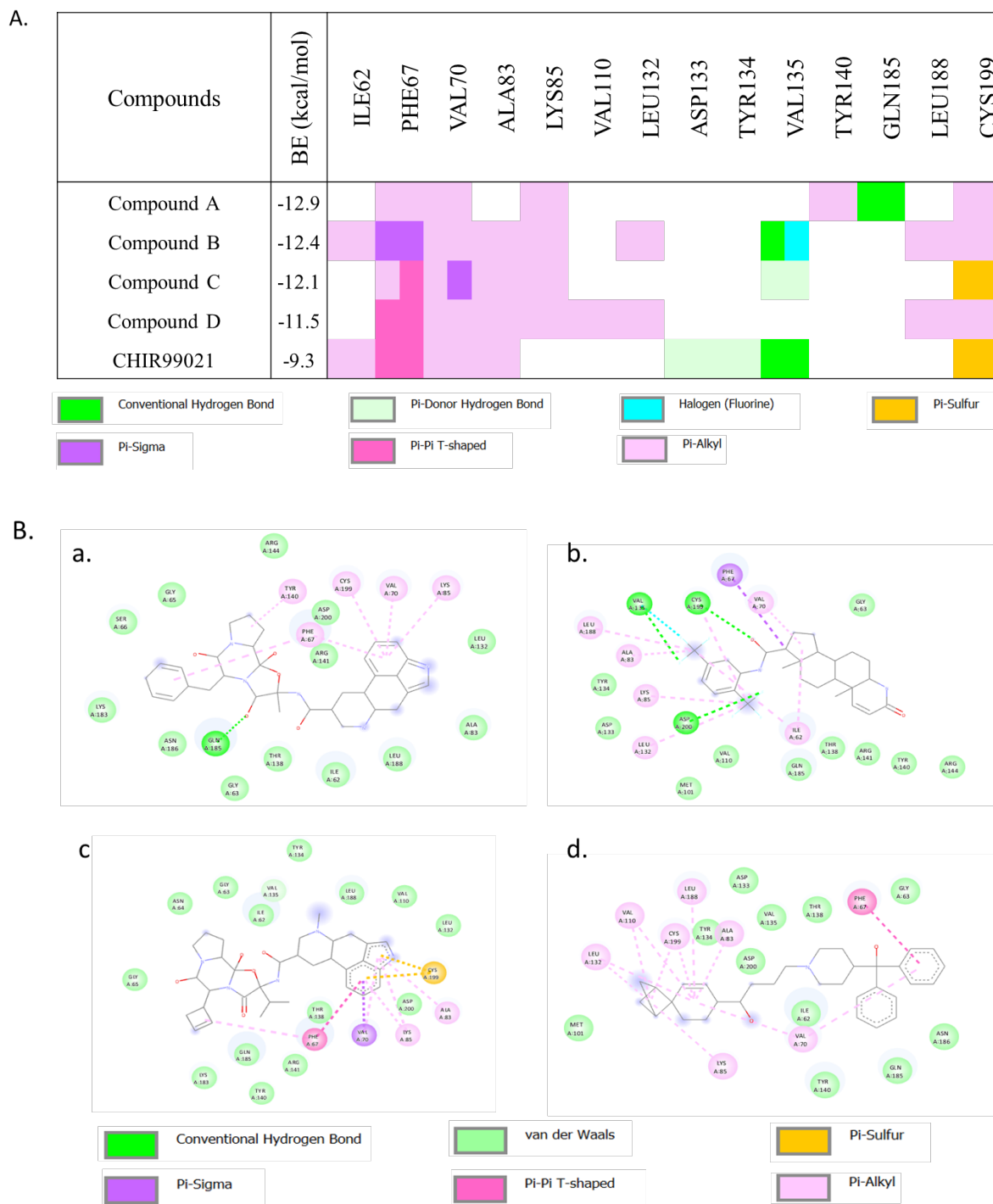


Figure 3. (A) Docking-based virtual screening of four candidate compounds in comparison to the known drug, CHIR99021. (B) 2D representation for docking analysis of (a) compound A, (b) compound B, (c) compound C, (d) compound D.



Conclusion:

This study aimed to investigate novel inhibitors against GSK3 β from a library of 3,208 FDA-approved drugs by molecular docking. Based on the binding energy prediction and molecular recognition analysis, we proposed that compounds A, B, C, and D could be able to effectively bind to the GSK3 β binding site. In particular, hydrophobic interactions (Pi-Sigma, Pi-Pi T-shaped, and Pi-Akyl) were the main forces driving the protein-inhibitor complex formation, and residues including Phe67, Val70, and Cys199 were found to be “hotspot” for all hit compounds’ binding and CHIR99021. Taken together, our finding suggests that the four candidate compounds have the potential to be used in developing a novel and cost-effective medium which can be applied in cultured meat production. However, further investigations, including molecular dynamics simulations and cell-based assays, were necessarily required.

Acknowledgements:

This research has received funding support from the NRSF via the Program Management Unit for Human Resources and Institutional Development, Research, and Innovation [grant number B05F650014].

References:

1. Bryant, C.J., *Culture, meat, and cultured meat*. J Anim Sci, 2020. **98**(8).
2. Geneva, S., *Food and Agriculture Organization of the United nations*. Rome, Italy, 2006.
3. Post, M.J., *Cultured meat from stem cells: Challenges and prospects*. Meat Science, 2012. **92**(3): p. 297-301.
4. Bhat, Z.F., H. Bhat, and S. Kumar, *Chapter 73 - Cultured meat—a humane meat production system*, in *Principles of Tissue Engineering (Fifth Edition)*, R. Lanza, et al., Editors. 2020, Academic Press. p. 1369-1388.
5. Tuomisto, H.L. and M.J. Teixeira de Mattos, *Environmental Impacts of Cultured Meat Production*. Environmental Science & Technology, 2011. **45**(14): p. 6117-6123.
6. Rubio, N.R., N. Xiang, and D.L. Kaplan, *Plant-based and cell-based approaches to meat production*. Nature Communications, 2020. **11**(1): p. 6276.
7. Lei, Q., et al., *Efficient expression of a cytokine combination in Saccharomyces cerevisiae for cultured meat production*. Food Research International, 2023. **170**: p. 113017.
8. Treich, N., *Cultured Meat: Promises and Challenges*. Environ Resour Econ (Dordr), 2021. **79**(1): p. 33-61.
9. Park, J., H. Choi, and K. Shim, *Inhibition of GSK3 β Promotes Proliferation and Suppresses Apoptosis of Porcine Muscle Satellite Cells*. Animals (Basel), 2022. **12**(23).
10. Wu, D. and W. Pan, *GSK3: a multifaceted kinase in Wnt signaling*. Trends Biochem Sci, 2010. **35**(3): p. 161-8.
11. Luo, J., *Glycogen synthase kinase 3beta (GSK3beta) in tumorigenesis and cancer chemotherapy*. Cancer Lett, 2009. **273**(2): p. 194-200.
12. Hottin, C., M. Perron, and J.E. Roger, *GSK3 Is a Central Player in Retinal Degenerative Diseases but a Challenging Therapeutic Target*. Cells, 2022. **11**(18).
13. Kobayashi, H., et al., *A novel GSK3 inhibitor that promotes self-renewal in mouse embryonic stem cells*. Biosci Biotechnol Biochem, 2020. **84**(10): p. 2113-2120.



14. Lee, Y., et al., *Discovery of GSK3 β Inhibitors through In Silico Prediction-and-Experiment Cycling Strategy, and Biological Evaluation*. *Molecules*, 2022. **27**(12).
15. Cruz, J., et al., *Computational design of new protein kinase 2 inhibitors for the treatment of inflammatory diseases using QSAR, pharmacophore-structure-based virtual screening, and molecular dynamics*. *Journal of Molecular Modeling*, 2018. **24**.
16. Suriya, U., P. Mahalapbutr, and T. Rungrotmongkol, *Integration of In Silico Strategies for Drug Repositioning towards P38 α Mitogen-Activated Protein Kinase (MAPK) at the Allosteric Site*. *Pharmaceutics*, 2022. **14**(7).
17. Joshi, T., et al., *In silico screening of natural compounds against COVID-19 by targeting Mpro and ACE2 using molecular docking*. *Eur Rev Med Pharmacol Sci*, 2020. **24**(8): p. 4529-4536.
18. Koebel, M., et al., *AutoDock VinaXB: Implementation of XBSF, new empirical halogen bond scoring function, into AutoDock Vina*. *Journal of Cheminformatics*, 2016. **8**.
19. Suriya, U., et al., *Quinoxalinones as A Novel Inhibitor Scaffold for EGFR (L858R/T790M/C797S) Tyrosine Kinase: Molecular Docking, Biological Evaluations, and Computational Insights*. *Molecules*, 2022. **27**(24).
20. Maciej, J.Z.-G., et al., *Pharmacokinetics, Metabolism, and Excretion of the Glycogen Synthase Kinase-3 Inhibitor LY2090314 in Rats, Dogs, and Humans: A Case Study in Rapid Clearance by Extensive Metabolism with Low Circulating Metabolite Exposure*. *Drug Metabolism and Disposition*, 2013. **41**(4): p. 714.



ISOLATION AND CHARACTERIZATION OF BACTERIOPHAGE AGAINST ANTIBIOTIC RESISTANT *Campylobacter jejuni*

Narongsak Sriwiran¹, Tavan Janvilisri¹, Jamorn Somana¹, Methinee Pipatthana², Taradon Luangtongkum³, Surang Chankhamhaengdech^{4*}

¹ Department of Biochemistry, Faculty of Science, Mahidol University, Thailand

² Department of Microbiology, Faculty of Public Health, Mahidol University, Thailand

³ Department of Veterinary Public Health, Faculty of Veterinary Science, Chulalongkorn University, Thailand

⁴ Department of Biology, Faculty of Science, Mahidol University, Thailand

*e-mail: surang.cha@mahidol.ac.th

Abstract:

Campylobacter jejuni is a gram-negative bacterium commonly found in animal intestines and has emerged as a major global foodborne pathogen, causing severe enteric diseases in humans. The increasing prevalence of antibiotic resistant *C. jejuni* strains raises significant concerns. In response, this study focuses on isolating and comprehensively characterizing lytic bacteriophages that specifically target *C. jejuni*, particularly antibiotic-resistant isolates sourced from Thai Chicken farms. Among the isolated bacteriophages, ΦCJ1 displayed remarkable infectivity against sensitive host strains. Host range determination revealed its narrow specificity, primarily infecting *C. jejuni* isolates M-352 and M370 while demonstrating no activity against *C. coli* or other related bacterial species. Additionally, another notable phage, ΦCJ2, exhibited distinct infectivity patterns against a broader range of *C. jejuni* isolates, thereby expanding and diversifying the repertoire of isolated phages. The stability of phages was determined by pH and thermal stabilities. The results indicated that the phage exhibited significant resilience across a wide temperature spectrum. Nevertheless, it is important to highlight that the percentage of infectivity decreased with rising temperatures. Regarding pH stability, the phages displayed their maximum infectivity at pH 7, while infectivity was entirely lost at pH levels 1–3. Transmission Electron Microscopy (TEM) elucidated the structural characteristics of ΦCJ1, confirming their classification within the *Caudovirales* order, *Siphoviridae* family. These isolated *Campylobacter* bacteriophages hold promise as a strategic intervention to target *Campylobacter* colonization in the poultry gastrointestinal tract. This breakthrough not only addresses the challenges posed by antibiotic resistant strains but also paves the way for the development of effective treatments against *Campylobacter* infection, enhancing overall control measures in the poultry industry.

Keyword: *Campylobacter jejuni*, Antibiotic resistance, Bacteriophage, Alternative treatment.

Introduction:

Campylobacter jejuni, a leading cause of bacterial gastroenteritis worldwide, is often contracted through the consumption of undercooked poultry, unpasteurized milk, and contaminated water, resulting in symptoms such as diarrhea, abdominal cramps, fever, and vomiting (1). The widespread prevalence of this pathogen places a significant burden on public health systems, especially considering its impact on campylobacteriosis, a major public health concern in countries like the United States (2). This concern is underscored by the significant number of cases, hospitalizations, and some instances, fatalities it generates annually (3). Additionally, *Campylobacter* infections can result in long-term health



consequences, with a notable percentage of patients at risk of developing severe complications like Guillain-Barré syndrome, a rare but debilitating neurological disorder (4). Consequently, controlling *C. jejuni* infections is of paramount importance. Economically, the impact of *C. jejuni* extends beyond healthcare costs (5). In the chicken industry of Thailand, a major poultry exporter, the presence of *C. jejuni* can disrupt export opportunities due to strict regulations on food product contamination in importing countries (6). This leads to substantial revenue losses, affecting the entire poultry sector. Product recalls are another consequence of detecting *C. jejuni* in chicken products. Not only are these recalls costly, but they also damage the reputation of poultry producers and processors, impacting consumer trust, sales, and market share. These factors emphasize the importance of comprehensive control measures and food safety practices to address the challenges posed by *C. jejuni* in the chicken industry (6). The transfer of *C. jejuni* from the chicken industry to humans poses a significant challenge to food safety and public health. This bacterium frequently establishes itself in the gastrointestinal tracts of chickens, and infected chickens may not display obvious signs of illness, complicating the detection of affected flocks (7). Contamination of poultry products can occur as the bacteria from the chicken's gastrointestinal tract spreads to the meat's surface. This contamination can result from contact with feces, contaminated equipment, or cross-contamination between birds. Ready-to-eat products like chicken cuts, ground chicken, and processed poultry items are particularly at risk for carrying *C. jejuni* (8).

In the treatment of *C. jejuni* infection, the choice of antibiotics depends on various factors, including the patient's age, overall health, the severity of the infection, and local antibiotic resistance patterns (4). Commonly prescribed antibiotics for *C. jejuni* infection include macrolides and fluoroquinolones. Macrolides, such as erythromycin and azithromycin, are often the first-line antibiotics for campylobacteriosis, known for their effectiveness against *C. jejuni* and lower antibiotic resistance rates. Fluoroquinolones, like ciprofloxacin, can also be effective in treating *C. jejuni* infections but carry an increased risk of antibiotic resistance. According to antibiotic resistance, *C. jejuni* displays resistance to various antibiotics, such as fluoroquinolones, macrolides, and tetracyclines, with mechanisms arising from genetic mutations or the acquisition of resistance genes. Misuse and overuse of antibiotics in human medicine and agriculture contribute to widespread resistance in *Campylobacter* species. Specific antibiotics like ciprofloxacin and erythromycin face increasing resistance in *C. jejuni*. Tetracycline resistance is also a concern, and some strains carry genes conferring resistance. The emergence of multidrug-resistant strains complicates treatment options. Efforts to tackle antibiotic resistance involve surveillance, prudent antibiotic use, and measures to reduce agricultural antibiotic use. Ongoing research explores alternative treatments and the development of new antibiotics to address the challenges posed by antibiotic-resistant *Campylobacter* infections (9).

Bacteriophage therapy, also known as phage therapy, offers a potential alternative for the treatment of bacterial infections (10). It utilizes bacteriophages, which are viruses with a high specificity for infecting and killing bacteria. An advantage of bacteriophage therapy is that bacteriophages can self-replicate, meaning a small quantity can continue to replicate and combat bacteria even after the initial treatment. This research lays the groundwork for the study's emphasis on isolating and characterizing lytic bacteriophages specific to *C. jejuni*, particularly those sourced from Thai chicken farms. With the ultimate goal of advancing our understanding and addressing the challenges posed by *C. jejuni* in the context of food safety and public health, this work holds implications for the development of effective interventions in the poultry industry.

Methodology:

Sample collection and phage enrichment

Retail chicken portions were purchased from at least 10 different supermarkets based on distinct product bar codes and processing unit numbers. The animal-feces contaminated soil samples were collected from Chonburi and Chanthaburi Province. During transportation, the samples were maintained at a temperature of 4°C in an anaerobic jar with a gas pack, creating microaerophilic conditions. The portions were collected from four different producers. Swabs were soaked in Maximum Recovery Diluent (Oxoid code CM733; Basingstoke, United Kingdom) and were used to wipe a 10 cm² area of the chicken skin. These swabs were then utilized to inoculate 200 µl of a 24-hour culture of a mixture of 50 isolates of *C. jejuni*. The mixtures were cultured at 42°C for 24 hours under microaerobic conditions (5% O₂, 5% H₂, 10% CO₂, 80% N₂). After incubation, the supernatant of the mixture was considered to contain phage particles. Bacterial cells were separated from the culture by centrifugation at 5,000 x g for 15 minutes at 4°C. The supernatant was collected, filtered using sterilized using a 0.22 µm pore size syringe-driven filter unit (Millipore), and stored at 4°C (11).

Chicken intestinal samples were divided into five sections. Subsequently, 10 g of each section was suspended in Salt-Magnesium (SM) buffer and 2x NZCYM broth supplemented with 10 mM MgCl₂ and 1M CaCl₂. Next, 200 µl of a 24-hour culture of 50 isolated strains of *C. jejuni* was added to the mixture and incubated for 24 hours under microaerophilic conditions at the optimal temperature of 42°C to facilitate phage enrichment. Following incubation, the supernatant of the mixture was considered to contain phage particles. Bacterial cells were separated from the culture by centrifugation at 5,000 x g for 15 minutes at 4°C. The supernatant was filter sterilized using a 0.22 µm pore size syringe-driven filter unit (Millipore) and stored at 4°C.

High throughput screening of bacteriophage against C. jejuni

The high-throughput screening method was performed in 96-well microtiter plates as described below. Each *C. jejuni* isolate was cultured in NZCYM broth and incubated overnight at 42°C under microaerophilic conditions. A volume of 180 µl of each *C. jejuni* culture was added to the X-axis of the 96-well plate. Conversely, 20 µl of the candidate phage solution obtained from the phage isolation process was added to the Y-axis of the 96-well plate. The mixture of each *C. jejuni* isolate and phage solution was then measured the initial optical density using a microplate reader at OD₆₀₀ and was incubated overnight at 42°C under microaerophilic conditions. After overnight incubation, viable bacterial cell density was measured using a microplate reader at OD₆₀₀. The relationship between the OD₆₀₀ values before and after the phage challenge was compared and plotted on a graph (1).

Detection of lytic phage specific to C. jejuni by plaque forming assay

To detect lytic phages specific to *C. jejuni*, each *C. jejuni* isolate was inoculated into 3 ml of NZCYM broth and incubated at 42°C under microaerophilic conditions for 24 hours. Subsequently, 1.5 ml of each *C. jejuni* isolate was transferred to 3 ml of 0.6% molten TY agar (top layer) and was immediately overlaid onto 1.5% BHI agar (bottom layer). The agar plates with a double layer were allowed to stand for 15 minutes to solidify. To confirm the presence of phages in the phage solution obtained from phage isolation, 10 µl of the enriched supernatant was spotted on a lawn of the *C. jejuni* indicator strain. Following a 12-hour

incubation at 42°C under microaerophilic conditions, the formation of plaques or zones of inhibition where the supernatant was spotted would indicate the presence of lytic phages (12).

Detection of lytic phage specific to C. jejuni by overlay assay

For the detection of lytic phages specific to *C. jejuni*, each of *C. jejuni* isolate was added to 3 ml of NZCYM broth and were cultured for 24 hours at 42°C under microaerophilic conditions. Subsequently, 100 µl of the phage solution was combined with 1.5 ml of each *C. jejuni* culture. This mixture was then added to 3 ml of 0.6% molten TY agar (top layer) and was immediately overlaid onto 1.5% BHI agar (bottom layer). The plate was allowed to stand for 10 minutes to solidify. Subsequently, the double-layer plates were incubated at 42°C under microaerophilic conditions (12).

Phage propagation

The *C. jejuni* host strains were cultured in NZCYM broth and were incubated at 42 °C overnight under microaerophilic conditions to increase the number of bacteriophages. After that, the mixture of 1.5 ml of *C. jejuni* isolates and 100 µl phage solution was transferred to 3 ml of 0.6% molten TY agar (top) containing 10 mM MgCl₂, and 1 mM CaCl₂ and was immediately overlaid on the 1.5% BHI agar (Bottom). The plate was stood for 15 minutes for solidification. Next, the plaques that derive from the overlay assay were added with 2 ml of SM buffer. Then, using a bent sterile pasture spreader, they were loosened, and the phage was harvested by scraping off the top of the double-layer agar, transferring the dense bacteriophage to the beaker, and vortexing thoroughly with a stirrer (13).

Phage purification

The culture that derived from the last step of phage propagation was centrifuged at 5,000 x g, 4 °C for 15 minutes to remove 0.6 % soft TY agar-containing bacteria. The supernatant was collected, and 1 M NaCl and 10 % (v/v) PEG was added. Then, the solution was kept at 4°C for overnight. After that, the solution was centrifuged at 15,000 x g, 4 °C for 15 minutes. The pellet was collected and resuspended by 1 ml of SM buffer. This solution was centrifuged at 15,000 x g, 4 °C for 15 minutes. The supernatant was filtered through a 0.45 µm syringe filter. The purified phage solution was kept at 4°C (14).

Measurement phage titer

C. jejuni isolates were cultured in NZCYM broth and were incubated at 42 °C overnight under microaerophilic conditions. 1.5 ml of *C. jejuni* isolates were transferred to 3 ml 0.6% molten TY (top) containing 10 mM MgCl₂, and 1 mM CaCl₂ and were immediately overlaid on the 1.5% BHI agar (Bottom). The plate was stood for 15 minutes for solidification. Phage was incubated at 42 °C overnight under microaerophilic conditions (15). The plaque was observed and counted by using the following formula

$$\frac{\text{PFU}}{\text{ml}} = \frac{\text{Number of plaques}}{\text{Dilution} \times \text{Phage volume (10}\mu\text{l)}}$$

Host range determination

The spot test analysis was conducted to determine the host range of the obtained phages. 37 Antibiotic resistant *C. jejuni* isolates (Table 1) were tested with the isolated phage, along with other *Campylobacter* species such as 7 strains of *C. coli*. (16).

Phage morphology observation by TEM

The phage samples were stained with 2% uranyl acetate, serving as the negative stain for TEM observation. The 300-mesh formvar-carbon coated grid was induced to the hydrophilic property by high voltage glow discharge. Two methods were employed for discharging the grids. In the first method, the grid was glow discharged with argon gas for 30 seconds using the Q150R rotary-pumped sputter coater. Alternatively, the grids were exposed to UV radiation for 20 minutes, with the grid positioned nearest to the UV lamp. Subsequently, 10 µl of the phage solution sample was added to the carbon side of the grid and allowed to stand for 2 minutes for the phage to be absorbed into the grid. The filter paper was ripped into small pieces and used to remove the remaining phage lysate, with the edge side of the filter absorbing liquid until the grid got damp. The phage absorbed grid was immersed in 10 µl of 2% uranyl acetate deposited on parafilm for 1 minute for staining the phage sample. Subsequently, filter paper was used to remove the 2% uranyl acetate. The grid was left at room temperature for 15 minutes before TEM observation. Phage morphology was examined under TEM (Tecnai T20 G2) with an accelerating voltage of 120 kV. A Gatan CCD camera, along with Digital Micrograph analysis software, was employed to capture the digital image (17).

pH and thermal stability of bacteriophage

To determine the ability of *C. jejuni* phage to survive under various conditions of pH, 100 µl of phage lysate was mixed with 900 µl of SM buffer in a pH range of 2-10 and incubated at 42 °C overnight under microaerophilic conditions. For temperature stability, 50 µl of phage lysate was incubated for 1 hour at different temperatures including 4, 20, 25, 30, 37, 42, 50, and 60 °C. After incubation, the infectivity of phage in each of the mixtures was determined by using plaque forming assays. (16).

Results and Discussion:

The systematic isolation of phages in this study involved an extensive sampling encompassing a variety of environmental sources, specifically animal-feces contaminated soil samples, chicken intestines, and chicken meat procured from both fresh markets and supermarkets. This approach was designed to ensure a diverse pool of potential phages targeting antibiotic resistant *C. jejuni* isolates. The isolation process involved a meticulous screening methodology utilizing the phage enrichment method, with a focus on 37 distinct antibiotic resistant *C. jejuni* isolates. This targeted approach aimed to identify phages with the potential to combat antibiotic resistance, a critical issue in the context of *C. jejuni* infections. Upon comprehensive screening, two samples derived from chicken intestines, sourced from both fresh markets and supermarkets, exhibited positive results in the plaque forming assay against the host isolates of *C. jejuni*. These findings led to the isolation and subsequent purification of two distinct phages designed as ΦCJ1 and ΦCJ2. The activity of ΦCJ1 was particularly noteworthy as it demonstrated effectiveness against two *C. jejuni* isolates, M-352 and M-370 (Fig. 1 and Table. 1). Of significance is the fact that *C. jejuni* M-352 is a multidrug resistant strain, underscoring the potential of ΦCJ1 in addressing antibiotic resistant strains of *C. jejuni*. Conversely, ΦCJ2 demonstrated clear activity against a broader spectrum activity, targeting five *C. jejuni* isolates including A-523, A-527, A-533, B-174, and M-370 (Fig. 2 and Table. 1). This broader range of efficacy suggests that ΦCJ2 may have a more diverse host range or possess mechanisms that allow it to combat a variety of *C. jejuni* strains, making it a promising candidate for therapeutic applications.

Moreover, an additional noteworthy observation was made when equal proportion of isolated phages were used in the plaque assay. Higher numbers of plaque-forming units (PFUs) were observed from Φ CJ2 compared to Φ CJ1. This result indicates that Φ CJ2 exhibits higher infectivity or a more efficient replication cycle, potentially contributing to its increased efficacy. The implications of this finding extend to the practicality of phage-based therapies, suggesting that Φ CJ2 may require lower doses for effective treatment, which could enhance its feasibility in clinical applications.

The broader spectrum of activity displayed by Φ CJ2 against multiple *C. jejuni* isolates, along with its heightened infectivity as reflected in 1×10^5 PFU counts, designates it as a promising candidate for further exploration in the realm of phage therapy. The increased infectivity observed in Φ CJ2 prompts a need for deeper investigations into the potential mechanisms behind this enhancement, offering valuable insights for optimizing its therapeutic application. These findings contribute significantly to the expanding knowledge of phage-based interventions against antibiotic-resistant *C. jejuni* strains, underscoring the importance of considering both specificity and infectivity when selecting phages for therapeutic purposes. Subsequent research endeavors could delve into unraveling the molecular mechanisms governing the activities of both Φ CJ1 and Φ CJ2, paving the way for the development of targeted and effective strategies to counter antibiotic resistance in *C. jejuni*.

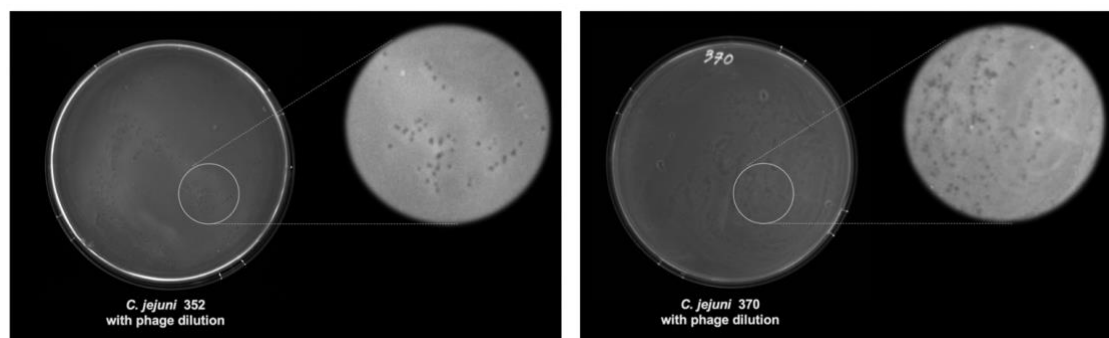


Figure 1. Plaque morphology of the environmentally-isolated *Campylobacter* phage. Φ CJ1 plaque on *C. jejuni* isolate M-352 and M-370.

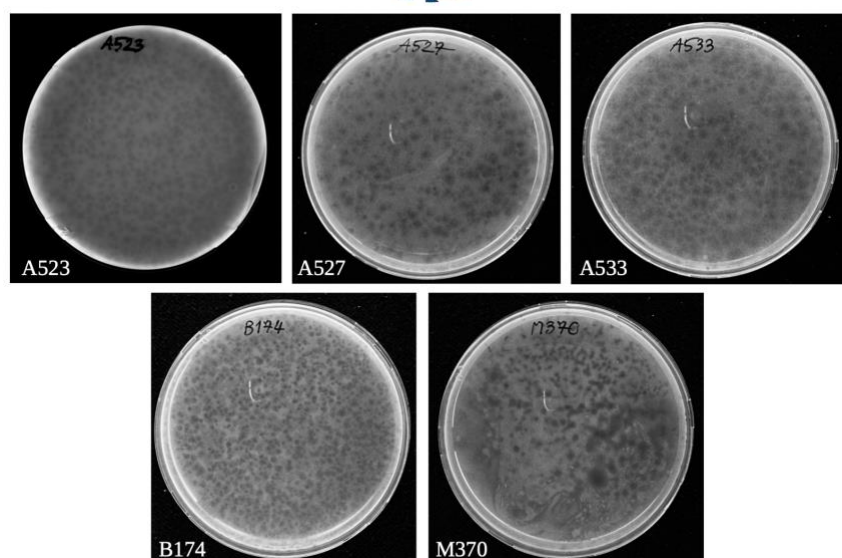


Figure 2. Plaque morphology of the environmentally-isolated *Campylobacter* phage. ΦCJ2 plaque on *C. jejuni* isolates A-523, A-527, A-533, B-174 and M-370 respectively.

Table 1. Host range determination of *Campylobacter* phage. Different bacterial species and strains were used as the host to determine the host spectrum of phage using a spot test.

Bacterial strains	Isolate	Genotypic identification			Resistance pattern	Plaque forming of ΦCJ1	Plaque forming of ΦCJ2
		flaA SVR type	MLST				
			Sequence type (ST)	Clonal complex (CC)			
Campylobacter jejuni	M-26	112	2274	Unassigned	AMP-CIP	-	-
	M-62	2	354	ST-354 complex	AMP	-	-
	M-91	97	5	ST-353 complex	AMP-CIP-TET	-	-
	M-93	97	5	ST-353 complex	AMP-CIP-TET	-	-
	M-97	54	1919	ST-52 complex	AMP-CIP-TET	-	-
	M-152	54	51	ST-443 complex	AMP-CIP-TET	-	-
	M-165	783	5213	ST-353 complex	AMP-CIP-TET	-	-
	M-213	162	161	ST-52 complex	AMP-CIP-TET	-	-
	M-272	208	8835	Unassigned	AMP-CIP-TET	-	-
	M-351	208	N/A	N/A	AMP-CIP-TET	-	-
	M-352	767	872	ST-828 complex	AMP-CIP-TET	+	-
	M-363	67	6736	Unassigned	AMP-CIP-TET	-	-
	M-370	783	5213	ST-353 complex	CIP	+	+
	M-379	36	298	ST-21 complex	AMP-CIP-TET	-	-
	M-392	237	583	ST-45 complex	AMP-CIP	-	-
	M-399	2	45	ST-45 complex	AMP-CIP-TET	-	-
	M-406	524	137	ST-45 complex	AMP-CIP-TET	-	-



	M-417	312	9765	ST-574 complex	AMP-CIP-TET	-	-
	M-430	45	2409	Unassigned	AMP-CIP	-	-
	M-445	68	N/A	N/A	AMP	-	-
	M-451	1568	N/A	N/A	AMP-CIP-TET	-	-
	A-512	54	464	ST-464 complex	CIP	-	-
	A-514	54	464	ST-464 complex	CIP	-	-
	A-515	54	464	ST-464 complex	CIP	-	-
	A-520	54	464	ST-464 complex	CIP	-	-
	A-522	54	464	ST-464 complex	CIP	-	-
	A-523	54	464	ST-464 complex	CIP	-	+
	A-526	54	464	ST-464 complex	CIP	-	-
	A-527	54	464	ST-464 complex	CIP	-	+
	A-528	1639	464	ST-464 complex	CIP	-	-
	A-529	54	464	ST-464 complex	CIP	-	-
	A-530	54	464	ST-464 complex	CIP	-	-
	A-531	54	464	ST-464 complex	CIP	-	-
	A-533	54	464	ST-464 complex	CIP	-	+
	A-536	54	464	ST-464 complex	CIP	-	-
	A-541	54	464	ST-464 complex	CIP	-	-
	B-174	68	464	ST-464 complex	CIP	-	+
<i>Campylobacter coli</i>	M-23	767	3119	ST-828 complex	AMP-CIP-ERY-TET-KAN	-	-
	M-45	1217	3119	ST-828 complex	AMP-CIP-ERY-TET-KAN	-	-
	M-51	767	3119	ST-828 complex	AMP-CIP-ERY-TET-KAN	-	-
	M-198	759	3119	ST-828 complex	CIP-ERY-TET	-	-
	M-413	767	3073	ST-828 complex	AMP-CIP-ERY-TET	-	-
	M-449	30	N/A	N/A	AMP-CIP-TET	-	-
	M-450	30	N/A	N/A	AMP-CIP-TET	-	-

(+) was phage can infect bacterial species strain.

(-) was phage cannot infect bacterial species strain.

Antibiotics: AMP, ampicillin; CIP, ciprofloxacin; TET, tetracycline; ERY, erythromycin; KAN, kanamycin.

Resistance breakpoints, MICs were interpreted using the EUCAST and CLSI criteria: Ampicillin resistance, $>16^b$ $\mu\text{g/mL}$; Ciprofloxacin resistance, $> 0.5^a$ $\mu\text{g/mL}$; Tetracycline resistance, $> 2^a$ $\mu\text{g/mL}$; Erythromycin resistance, $> 4^a$ $\mu\text{g/mL}$; Kanamycin resistance, $> 32^b$ $\mu\text{g/mL}$. ^a Data source EUCAST, ^b Data source CLSI.

In the characterization of bacteriophages, the examination of phage morphology was conducted using negative strain transmission electron microscopy (TEM). Specifically, the ϕCJ1 phage was classified within the order *Caudovirales* in the family *Siphoviridae*, as evident from its distinctive features. The phage exhibited an icosahedral head coupled with a long non-contractile tail and a tail fiber, as illustrated in Fig. 2A and 2B. Notably, the

icosahedral capsid head displayed dimensions ranging from 45-70 nm in diameter, intricately connected to a long, non-flexible, contractile tail spanning 90-100 nm in length.

While the morphological characteristics provide valuable insights into the phage, it was observed that the phage purification technique requires refinement. The TEM images of the isolated phage unveiled the presence of numerous contaminants in the solution, encompassing macromolecules from the isolation process, proteins, broken tails, and capsids. This suggests the need for improved purification methods to enhance the purity of the isolated phage.

To evaluate the thermal resilience of the Φ CJ2 phage, trials were carried out over a temperature spectrum from 4 to 42 °C. Remarkably, heightened infectivity was noted at temperatures of 20 and 42 °C. Conversely, infectivity diminished when the temperature exceeded 50 °C. The results, depicted in Fig. 3A, revealed that the phage demonstrated high tolerance to a broad temperature range. However, it is noteworthy that the percent infectivity experienced a decline as the temperature increased. In Fig. 3B, depicting pH stability, ϕ CJ1 phage demonstrated the highest infectivity at pH 7 and pH 6 and 8 also show 55-70% infectivity, but infectivity was completely lost at pH 1–3. The noted observation leads to additional discussions about how temperature and pH can affect the phage's ability to infect, prompting a need to optimize conditions for using the phage in various scenarios.

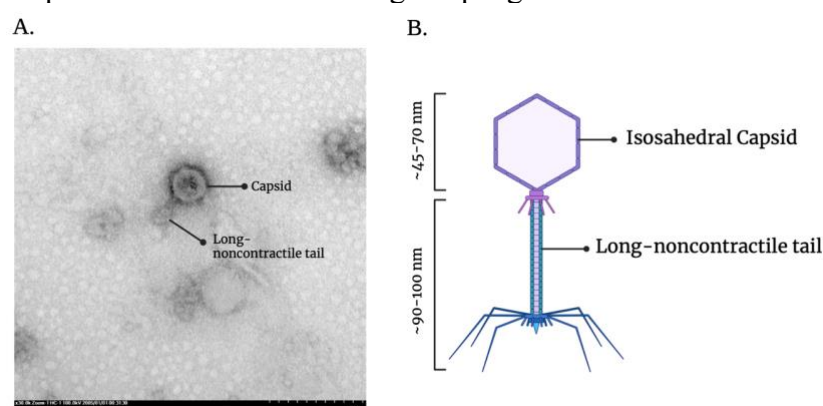


Figure 2. Morphology of *Campylobacter* phage. A, Φ CJ1 phage was determined by negative staining and transmission electron microscopy (TEM). B, Φ CJ1 phage with capsid size and the tail length indicated.

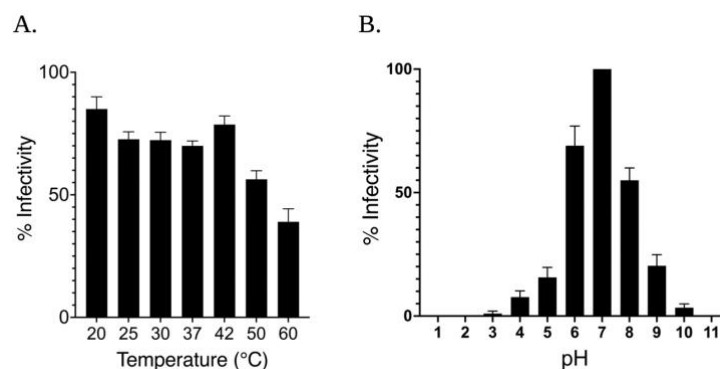


Figure 3. Phage infectivity. A, Phage infectivity in different temperatures. B, Phage infectivity in different pH.

Conclusion:

In conclusion, the successful isolation and purification of phages through the described method have led to the identification of novel members within the *Caudovirales* order, specifically in the *Siphoviridae* family. While exhibiting typical morphological characteristics, the notable narrow host range observed in both Φ CJ1 and Φ CJ2 phages, with no specificity to *C. coli*, underscores their potential as targeted agents against *C. jejuni*. The adaptability of these phages to the chicken gastrointestinal environment, coupled with their robust infectivity across a broad pH range and temperature spectrum, highlights their promising therapeutic and diagnostic applications. This significant advancement in understanding *C. jejuni* phages offers new prospects for innovative treatments and diagnostic tools, contributing substantially to the ongoing efforts in *C. jejuni* infection research and treatment. Further investigations into the specificities of these isolated phages hold great promise for addressing the challenges associated with *C. jejuni*, emphasizing the potential efficacy of phage-based interventions in combating this bacterial pathogen.

Acknowledgements:

This research project is supported by the East Asia Science and Innovation Area Joint Research Program through the National Research Council of Thailand (NRCT; N10A650693). Further support was generously provided by the Development and Promotion of Science and Technology Talents Project, Thai government scholarship (DPST) for Narongsak Sriwiran.

References:

1. Ushanov L, Lasareishvili B, Janashia I, Zautner AE. Application of *Campylobacter jejuni* phages: challenges and perspectives. *Animals*. 2020;10(2):279.
2. Blaser MJ. Epidemiologic and clinical features of *Campylobacter jejuni* infections. *Journal of Infectious Diseases*. 1997;176(Supplement_2):S103-S5.
3. Peterson MC. Clinical aspects of *Campylobacter jejuni* infections in adults. *Western Journal of Medicine*. 1994;161(2):148.
4. Acheson D, Allos BM. *Campylobacter jejuni* infections: update on emerging issues and trends. *Clinical infectious diseases*. 2001;32(8):1201-6.
5. Buzby JC, Allos BM, Roberts T. The economic burden of *Campylobacter*-associated Guillain-Barré syndrome. *Journal of Infectious Diseases*. 1997;176(Supplement_2):S192-S7.
6. Premaratne JMKJK, Satharasinghe DA, Huat JTY, Basri DF, Rukayadi Y, Nakaguchi Y, et al. Impact of human *Campylobacter* infections in Southeast Asia: The contribution of the poultry sector. *Critical reviews in food science and nutrition*. 2017;57(18):3971-86.
7. Young KT, Davis LM, DiRita VJ. *Campylobacter jejuni*: molecular biology and pathogenesis. *Nature Reviews Microbiology*. 2007;5(9):665-79.
8. Müllner P, Collins-Emerson JM, Midwinter AC, Carter P, Spencer SE, van der Logt P, et al. Molecular epidemiology of *Campylobacter jejuni* in a geographically isolated country with a uniquely structured poultry industry. *Applied and Environmental Microbiology*. 2010;76(7):2145-54.
9. Moore JE, Barton MD, Blair IS, Corcoran D, Dooley JS, Fanning S, et al. The epidemiology of antibiotic resistance in *Campylobacter*. *Microbes and infection*. 2006;8(7):1955-66.
10. Sulakvelidze A, Alavidze Z, Morris Jr JG. Bacteriophage therapy. *Antimicrobial agents and chemotherapy*. 2001;45(3):649-59.



11. Jäckel C, Hammerl JA, Hertwig S. *Campylobacter* phage isolation and characterization: what we have learned so far. *Methods and protocols*. 2019;2(1):18.
12. Furuta M, Nasu T, Umeki K, Minh DH, Honjoh K-I, Miyamoto T. Characterization and application of lytic bacteriophages against *Campylobacter jejuni* isolated from poultry in Japan. *Biocontrol science*. 2017;22(4):213-21.
13. Hammers CM, Stanley JR. Antibody phage display: technique and applications. *The Journal of investigative dermatology*. 2014;134(2):e17.
14. Luong T, Salabarria A-C, Edwards RA, Roach DR. Standardized bacteriophage purification for personalized phage therapy. *Nature Protocols*. 2020;15(9):2867-90.
15. Weld RJ, Butts C, Heinemann JA. Models of phage growth and their applicability to phage therapy. *Journal of Theoretical Biology*. 2004;227(1):1-11.
16. Thammatinna K, Egan ME, Htoo HH, Khanna K, Sugie J, Nideffer JF, et al. A novel vibriophage exhibits inhibitory activity against host protein synthesis machinery. *Scientific reports*. 2020;10(1):2347.
17. Aprea G, D'Angelo AR, Prencipe VA, Migliorati G. Bacteriophage morphological characterization by using transmission electron microscopy. *J Life Sci*. 2015;9(1):214-20.
18. Mabelebele, Monnye, *et al*. "Comparison of gastrointestinal tract and pH values of digestive organs of Ross 308 broiler and indigenous Venda chickens fed the same diet." (2014).

Lichen family Physciaceae and Caliciaceae in public parks in Bangkok, Thailand

Sanya Meesim,^{1*} Weerayut Inboonma,¹ Sudjai Phutphat,¹ Supattara Phokaeo², Kawinnat Buaruang² and Kajonsak Vongshewarat²

¹Scientific Instruments Center, School of Science, King Mongkut's Institute of Technology Ladkrabang, Bangkok, 10520

²Lichen Research Unit, Department of Biology, Faculty of Science, Ramkhamhaeng University Bangkok, 10240

*E-mail: sanya.me@kmitl.ac.th

Abstract

The objective of this study is to investigate biodiversity of lichens found in the public park in Bangkok, including foliose and crustose lichens of the family Physciaceae and Caliciaceae. Lichen specimens were collected from 11 public parks in Bangkok Thailand, from January 2022 to February 2022. One hundred and forty-two of corticolous lichens were collected and dried under room temperature for taxonomic study. Six genera and 9 species, were identified 4 genera of foliose including *Dirinaria* (Tuck.) Clem., *Hyperphyscia* (Müll.Arg.), *Physcia* (Schreb.) Michaux and *Pyxine* Fr. The other specimen, 2 genera were crustose lichens, *Amandinea* M. Choisy ex Scheid. & M. Mayrhofer, and *Rinodina* (Ach) Gray, the lichen *Pyxine cocoas*, were found in all public parks. The most lichens were found Thonburirom, Thawiwanarom and Serethai Garden respectively.

Keywords: foliose lichen, crustose lichen, Physciaceae, Caliciaceae.

Introduction

The lichen flora of Thailand is rich due to the high diversity of habitats especially in montane forests and coastal forests. There are more than 1,200 reports of lichens found in Thailand, especially Family Physciaceae and Caliciaceae with 174 species (Kawinnat et al. 2017). Lichens family Physciaceae is characterized by the thick wall and dark color of 1–3 transeptate ascospore within cylindrical bitunicate ascus and family Caliciaceae is characterized by the presence of thin-walled and short-lasting asci (spore-bearing cells) and a mazaedium, which is an accumulation of loose, maturing spores covering the surface of the fruiting body. The lichens may produce lecideine or lecanorine apothecium. The cosmopolitan lichenized ascomycete lichen family are widespread in almost all areas from lowland to mountain summits. It grows very well at the good ventilation, strong light intensity and high humidity of coastal sea lines with attaching on living tree and rock (Gorts-Van Rijn, 1987). There are many uses for lichens indicators of urban pollution in many countries in Europe (Cislaghi and Nimis, 1997. Nimis et al 2002, Loppi and Frati, 2005). Bangkok faces the problems of air pollution caused by traffic and industry. There are many parks located in the city center and the suburb of the city, which has different local weather conditions. From a survey of the diversity of lichens in Bangkok reported 7 lichens species (Boonpragob et al 2003), and at 8 public parks were found 17 species of lichens (Thanomjitt, 2009).

The purpose of this investigation is to survey the diversity of lichens to use as based-line information to assess the air quality of public parks in Bangkok. This research is part of the plant genetics conservation project under the royal initiative of Her Royal Highness Princess Maha Chakri Sirindhorn. Princess Maha Chakri Sirindhorn (RSPG).

Methodology

Lichen samples collected from 11 public parks from PTT Metroforest learning center., Benchakitti Park, Serethai Garden, Chatuchak Park, Thawiwanarom Park, Thonburirom Park, Lumpini Park, Queen Sirikit Park, Saranrom Park, Santiphap Park and Nong Chok Park in Bangkok Thailand (Figure 1), were dried under room temperature for herbarium preservation and taxonomic study. All specimens were identified characterized by morphological and anatomical features under a light microscope Olympus SZ30 and light microscope (OLYMPUS, CH). The chemical characters were by spot test and Thin Layer Chromatography (TLC) (White & Jame 1985). Taxa were determined according to (Elix, 2009, Mongkolsuk, et al., 2012, Marbach., 2000., Sipman 2003).

Results and Discussion

A total of Physciaceae and Caliciaceae, 142 collected samples were identified into 6 genera 9 species (Figure 2), foliose lichen 4 genera; *Dirinaria* (Tuck.) Clem., *Physcia* (Schreb.) Michaux and *Pyxine* Fr. and crustose lichen 2 genera; *Amandinea* M. Choisy ex Scheid. & M.Mayrhofer, and *Rinodina* (Ach).

Table 1 Number of lichens found the public parks in Bangkok Thailand.

Family	Lichens	Public Park											Total
		1	2	3	4	5	6	7	8	9	10	11	
Caliciaceae	<i>Amandinea diorista</i>			5		5	2		2				14
	<i>Amandinea efflorescens</i>		1		3	5		2	2			1	14
	<i>Dirinaria applanata</i>						3						3
	<i>Dirinaria confluens</i>						1						1
	<i>Dirinaria picta</i>	2				1	2					1	6
	<i>Pyxine cocoes</i>	2	2	13	3	10	26	3	8	1	1	12	81
	<i>Rinodina</i> sp. 1			1	1	1			1				4
	<i>Hyperphyscia adglutinata</i>					1							1
Physciaceae	<i>Physcia undulata</i>	1		1		2	8	1	2			3	18
	Total	5	3	20	7	25	42	6	15	1	1	17	142

1. PTT Metroforest learning center., 2. Benchakitti Park, 3. Serethai Garden, 4. Chatuchak Park, 5. Thawiwanarom Park, 6. Thonburirom Park, 7. Lumpini Park, 8. Queen Sirikit Park, 9. Saranrom Park, 10. Santiphap Park, 11. Nong Chok Park.

All specimens were examined for their morphological, anatomical and chemical characters as follow Macroscopic Examination. Thallus foliose lobate, irregular 2–4 cm wide. Lobes discrete or contiguous, closely adnate and appressed to ascending and loosely attached, linear or linear cuneate to spatulate, ± dichotomously to irregularly branched, Upper surface whitish, gray to yellow-gray, plane to convex, or concave towards the periphery, dull or glossy, with or without isidia or dactyl and soredia. Medulla layer compose of hyphae, which are anticlinal or periclinal arrangement. Upper cortex which is formed from anticlinal hyphae, patterning paraplectenchyma and lower cortex is ventral layer, which is formed by pseudoparenchymatous tissue of mycobionts such as *Physcia* (Table 2).

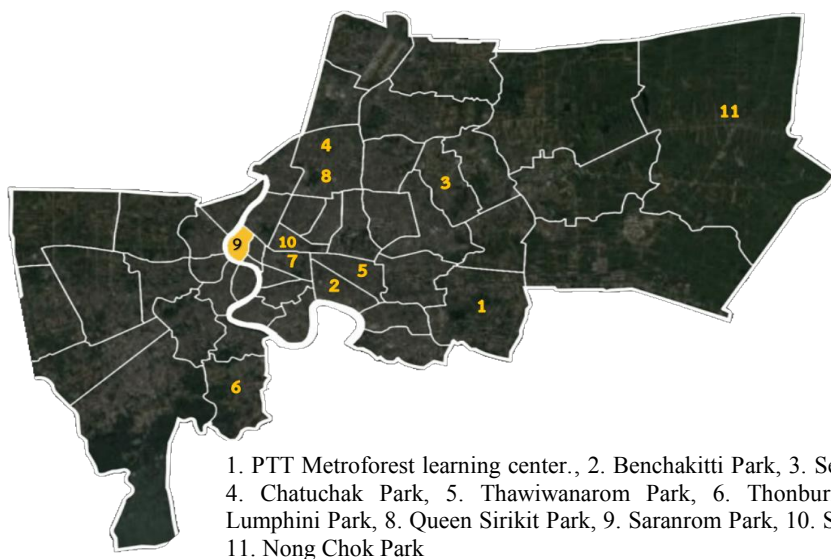


Figure 1 Public parks in Bangkok Thailand (Applied from: <https://www.homezoomer.com>)

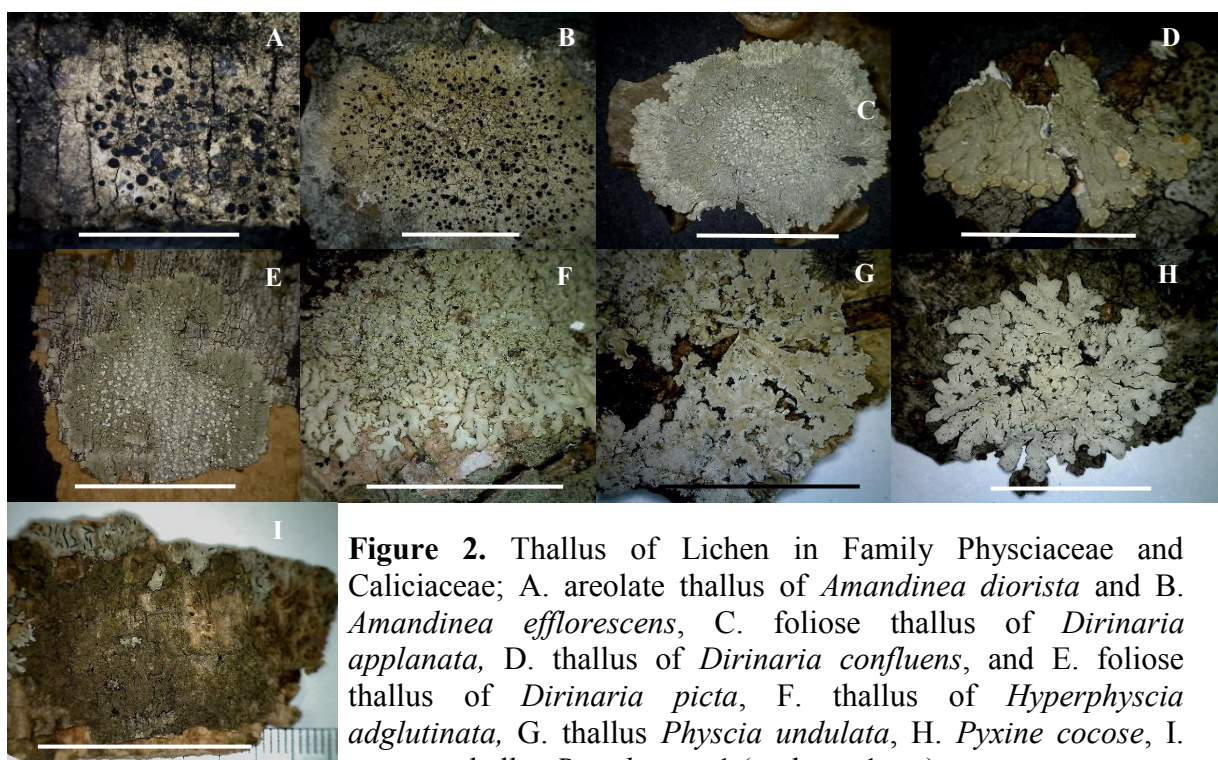


Figure 2. Thallus of Lichen in Family Physciaceae and Caliciaceae; A. areolate thallus of *Amandinea diorista* and B. *Amandinea efflorescens*, C. foliose thallus of *Dirinaria applanata*, D. thallus of *Dirinaria confluens*, and E. foliose thallus of *Dirinaria picta*, F. thallus of *Hyperphyscia adglutinata*, G. thallus *Physcia undulata*, H. *Pyxine cocose*, I. crustose thallus *Rinodina* sp.1 (scale — 1 cm).

Lower surface rhizines occur exclusively in the species of *Pyxine cocoes* with a corticate lower surface Apothecia laminal or terminal, rounded, sessile to stipitate, lecanorine or lecideine, hymenium colorless with or with oil globule, Asci cylindrical to subclavate or

clavate, *Physcia*-type, with 8 ascospores; apex wall layers thickened; apex amyloid, with a distinct axial mass (Hafellner et al. 1979).

Crustose lichens, ecorticate thallus. The thallus may lack a cortex or have only a poorly develop and ill-defined cortex, the algal being superficial or scattered among medullary hyphae or crystalline inclusion such as *Amandinea diorista*. The areolae are enlarged in their upper part and become partially free from the substrate.

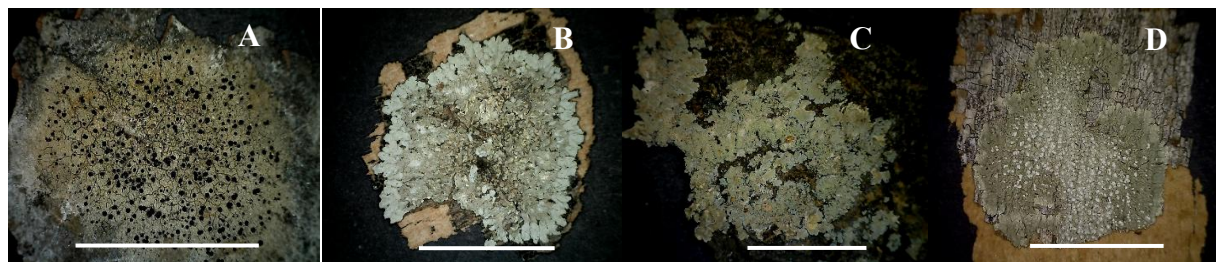


Figure 3. The four common lichens public park in Bangkok Thailand, A. *Amandinea efflorescence*, B. *Pyxine cocoes*, C. *Physcia undulata*, D. *Dirinaria picta* (scale —1 cm).

The study noted that the 9 species of lichens habited in the park. The highest and subsequently lower number of species were recorde from Thawiwanarom (7 sp.), Thonburirom (6 sp.), Queen Sirikit (5 sp.), Serethai Garden (sp.4), Nong Chok (4 sp.), Chatuchak (3 sp.), Lumpini (3 sp.), PTT Metro Forest Learning Center (3 sp.), Benchakitti (2 sp.), Santiphap (sp.1), Saranrom (sp.1), and respectively (Table 1).

Almost all lichen genera distribute over Thonburirom Park such as *Amandinea diorista*, *Dirinaria applanata*, *D. confluens*, *D. picta*, *Pyxine cocoes* and *Physcia undulata*. It's a small garden. It has an area of only 63 rai, it is a garden in an area where traffic is not very heavy, and most of the surrounding area is green space. Thawiwanarom Park is a park with green space. And it's in the suburbs as well. Most of the lichens found in this survey were species including; *Pyxine cocoes*, *Physcia undulata*, *Amandinea efflorescence*, and *Dirinaria picta* (Figure 3). As for the public parks in the center of the city, there are few lichens such Saranrom park, Santiphap park and Lumpini park, because they have to faces the problems of air pollution caused by traffic and industry. There are many parks located in the city center and the suburb of the city, which has different lalcal weather conditions, thus causing different lichens to be found.

Conclusion

One hundred and forty-two of corticolous lichens specimens collect from host trees, were classified into lichen family Physciaceae and Caliciaceae. In consisted 6 genera and 9 species, 4 genera were foliose lichens including, *Dirinaria* (Tuck.) Clem., *Hyperphyscia* (Müll.Arg.), *Physcia* (Schreb.) Michaux and *Pyxine* Fr. The other specimens were crustose lichens 2 genera, *Amandinea* M. Choisy ex Scheid. & M. Mayrhofer, and *Rinodina* (Ach) Gray. The lichen *Pyxine cocoes* were found in all park. The highest and subsequently lower number of species were record form Thonburirom, Thawiwanarom and Serethai Garden respectively. Most of the lichens found in this survey were species including; *Pyxine cocoes*, *Physcia undulata* *Amandinea efflorescence* and *Dirinaria picta* etc.

Table 2 Important characteristics of lichens found the public parks in Bangkok, Thailand.

Structure	Family	Genera-species	Characteristic		
			Thallus	Apothecia / Reproductive structures	Other
Crustose	Caliciaceae	<i>Amandinea diorista</i>	rugose, to areolate	lecideine	ascospore brown, 1-septate, ecorticate thallus
Crustose	Caliciaceae	<i>Amandinea efflorescens</i>	rugose to areolate	lecideine	ascospore brown, 1-septate,
Foliose	Caliciaceae	<i>Dirinaria applanata</i>	Smooth	not found	rhizine absent
Foliose	Caliciaceae	<i>Dirinaria confluens</i>	Smooth	not found	rhizine absent
Foliose	Caliciaceae	<i>Dirinaria picta</i>	Smooth	not found	rhizine absent
Foliose	Physciaceae	<i>Hyperphyscia adglutinata</i>	Smooth	not found	rhizie absent
Foliose	Caliciaceae	<i>Pyxine cocoas</i>	Smooth	not found	rhizines present
Crustose	Caliciaceae	<i>Rinodina</i> sp. 1	rugose to areolate	lecanorine	ascospore brown, 1-septate
Foliose	Physciaceae	<i>Physcia undulata</i>	Smooth- shiny	not found	upper cortex parapletenchyma, lower cortex pseudoparenchy matous

Acknowledgements

This research was part of the Plant Genetic Conservation Project under the Royal Initiation of Her Royal Highness Princess Maha Chakri Sirindhorn (RSPG). We are thankful for funding supported by staff of public parks in Bangkok Thailand. We are also very grateful to thank Ramkhamhaeng University herbarium (RAMK) and colleagues at the excellent organization team of the Lichen Research Unit, Biology Department, Faculty of Science and Ramkhamhaeng University for using instruments and facilities in the laboratory.

References

1. Boonpragob, K. Kotphab, P. and Pornprom, P. Lichens as Bioindicator of Air Quality Gradient from Bangkok to Khao Yai National Park. 29th Congress on Science and Technology of Thailand. 2003.
2. Cislaghi, C and Nimis, P.L., Lichen, air pollution and lung cancer. Nature 1997;387:463-464.
3. Elix J. A., Physciaceae. In McCarthy P. M. (Ed.), Flora of Australia Melbourne, Australia: 2009;494-533.
4. GÖrts-Van Rijn. A.R.A., Flora of The Guianas. Koeltz Scientific Books, The Netherland. 1987.

5. Hafellner J., Mayrhofer H.& Poelt J., Die Gattungen der Flechten familie Physciaceae. Herzogia, 1979;5,39-79.
6. Kawinnat et al., A new checklist of lichenized fungi occurring in Thailand, Mycokey, 2017;23:1-91.
7. Loppi, S. and Frati, L. Lichen diversity and lichen transplants as monitor of air pollution in rural area of central Italy. Environmental Monitoring and Assessment. 2005;114: 361-375.
8. Marbach B., Corticole und lignicole Arten der Flechtengattung *Buellia* sensu lato inden Subtropenund Tropen. Bibliotheca Lichenologica, 2000;74, 46-384.
9. Mongkolsuk P., Meesim S., Poengsungnoen V. and Kalb K., The Lichen Physciaceae in Thailand - I. The genus *Pyxine*. Phytotaxa 59:2012; 32-54.
10. Nimis, P.L. Scheidegger, C. and Wolseley, P. Monitoring with Lichens-Monitoring Lichens. 2002.
11. Sipman H., Artificial key to Marbach's tropical *Buellia* s.l. with short diagnoses: Retrieved February 3, 2003, from [http://www.bgbm.org/sipman/keys/Jav agenera.htm](http://www.bgbm.org/sipman/keys/Jav%20genera.htm). 2003.
12. Thanomjitt R., Boonpeng C., Boonpragob K., Biodiversity of Lichens in Public Park in Bangkok. The 3th Botanical Conference of Thailand (BCT 3th). 2009;99-103.
13. White F. J., and Jame P. W. A., New guide to microchemical techniques for the identification of lichen substances, British Lichen Society Bulletin No.57,1985;1-41.



MORPHOLOGICAL AND MOLECULAR IDENTIFICATION OF PATHOGENIC *Acanthamoeba* spp. IN WATER AND SOIL SOURCES ASSOCIATED WITH HUMAN ACTIVITIES IN 3 PROVINCES OF SOUTHERN THAILAND

Thitiporn Promnil^{1,*}, Nongyao Sawangjaroen¹, Kruawan Hounkong²

¹Division of Biological Science, Faculty of Science, Prince of Songkla University, Hat Yai, Songkhla, Thailand

²Faculty of Medicine, Princess of Naradhiwas University, Muang, Naradhiwas, Thailand

*email: giftgift.tp@gmail.com

Abstract:

Acanthamoeba spp. are free-living amoeba (FLA) found in various environmental sources such as lakes, ponds, drinking water and soil. Some strains of *Acanthamoeba* spp. may cause serious illness such as granulomatous amoebic encephalitis (GAE), painful and sight-threatening infection of the cornea or amoebic keratitis (AK). In this study, 55 water samples and 43 soil samples were collected from areas associated with human activities in Songkhla (27 water, 17 soil), Phatthalung (13 water, 12 soil) and Nakhon Si Thammarat (15 water, 14 soil), Southern Thailand. FLA were obtained by culture the samples in Non-nutrient agar (NNA) plates pre-coated with heat-inactivated *Escherichia coli* and incubated at ambient temperature. The plates were identified for *Acanthamoeba* spp. by their trophozoites and cyst morphology under the microscope. DNA of *Acanthamoeba* spp. were extracted and 18S rDNA gene were amplified and sequences. The PCR products were analyzed and genotyped. Under microscopy, *Acanthamoeba* spp. were found in 41 samples (18/55; 32.73% from water and 23/43; 53.48% from soil). By cyst characteristic, 10, 2, 29 were belong to groups I (3/18; 16.67% water, 7/23; 30.43% soil), II (1/18; 5.55% water, 1/23; 4.35% soil), and III (14/18; 77.78% water, 15/23; 65.22% soil), respectively. DNA from 13 *Acanthamoeba* spp. were successfully amplified and 9 were successfully sequenced. The blast results indicated 1, 3, 1, 3, 1 isolate belong to T4, T5, T9, T17 and T18 genotypes, respectively. *Acanthamoeba* spp. belong to groups II, and III and genotypes T4, T5, and T18 are believed to be associated with human infection. This study indicates the occurrence of pathogenic strain of *Acanthamoeba* spp. in these 3 provinces. The policy of the appropriate surveillance guidelines must be implemented to avoid the consumption or contact with contaminated water in the study area.



Introduction:

Free-Living Amoeba (FLA) are widely distributed in the environment. Among many FLA members, only four genera, *Acanthamoeba* spp., *Naegleria fowleri*, *Balamuthia mandrillaris*, and *Sappinia diplpidea*, are known to cause infections in humans and animals.¹ Among these, *Acanthamoeba* spp. are the most commonly detected. They have been found in soil; fresh, brackish, and sea water; sewage; swimming pools; contact lens equipment; medicinal pools; dental treatment units; dialysis machines; heating, ventilating, and air conditioning systems; mammalian cell cultures; vegetables; human nostrils and throats; and human and animal brain, skin, and lung tissues.²

Some strain of *Acanthamoeba* spp. play a significant role in the development of a number of human diseases, including granulomatous amoebic encephalitis (GAE) and *Acanthamoeba* keratitis (AK). GAE is a brain infection of which the patient's brain tissue is swollen causing the pressure inside the brain increased, seizures, and ultimately passes away. AK is an infection of the human cornea that results in corneal inflammation and, in severe cases, blindness. Risk factors that cause the disease include swimming, using a hot tub, or showering, wearing lenses.³

People may be at a higher risk of getting into contact with natural water and soil, particularly when swimming or playing with water, working outdoors, or participating in children's activities. Nevertheless, in these three provinces, there have been no previous reports of FLA in natural water or soil.

The purpose of this study was to determine the prevalence of pathogenic *Acanthamoeba* spp. in water and soil sources associated with human activities in 3 provinces, Southern Thailand, by the culture and molecular methods.

Methodology:

Samples collection

A total of 55 water samples and 43 soil samples at the area related to human activities were collected from Songkhla, Phatthalung and Nakhon Si Thammarat provinces, Southern Thailand as indicated in Table 1. At least 2 liters of water at a depth of 1 foot were collected at each site, and soil samples (~200 g each) at a depth of 2-5 cm in areas not exposed to direct sunlight were collected.⁴

Table 1: Water and soil samples collected from 3 Provinces

Province	Water	Soil	Total
Songkhla	27	17	44
Phatthalung	13	12	25
Nakhon Si Thammarat	15	14	29
Total	55	43	98

Cultivation of free-living amoeba

Each water sample was filter through a sterile filter paper with a pore size of 1.2 micrometer. The sediment on the filter paper were washed with 30 ml Page's Amoeba Saline (PAS) ($\text{MgSO}_4 \cdot 7\text{H}_2\text{O}$, Na_2HPO_4 , NaCl , $\text{CaCl}_2 \cdot 2\text{H}_2\text{O}$, KH_2PO_4 : Merck, Darmstadt, Germany) and centrifuged at 2600g for 30 minutes. The supernatant was discarded and the remainder of 1 ml of cell suspension was placed onto non-nutrient agar (NNA) pre-coated with heat-inactivated *E. coli* and left for 5 minutes. For a soil sample, 2 g was suspended in 10 ml of PAS, centrifuged at 2600g for 10 min and pellet was cultured in NNA as described for water samples. The culture dishes were wrapped in parafilm and incubated at room temperature in the dark for 10–14 days.⁵

Detection of Free-Living Amoeba

During the first 1 -3 days, the culture dishes were observed every day under the inverted microscope with a 40X magnification for the FLA trophozoites which is irregular in shape with feet (pseudopodia) move slowly spreading throughout the surface of the medium. After 3 days, trophozoites will changes to cyst form.



The FLA were identified as *Acanthamoeba* spp. by appearance of trophozoite movement in a needle-like projection and their cyst morphology were classify into Group I: specimen exhibited a large cyst (diameter $>18\ \mu\text{m}$) with smooth or mildly wrinkled outer cell walls; group II: specimen exhibited two-layer membranes (diameter $<18\ \mu\text{m}$) with moderately undulating ectocyst and endocyst walls exhibiting a polygonal arrangement connected at the pore zone; and group III: specimen exhibited a cyst (diameter $\leq 18\ \mu\text{m}$) with a thin, smooth ectocyst closely opposed to round endocyst.⁶

Molecular detection of Free-Living Amoeba

Harvesting of Free-Living Amoeba trophozoite

Acanthamoeba spp. isolates were subcultured in new NNA and incubated at room temperature. Approximately 3-4 plates of log phase trophozoites were harvested by adding 5 ml of sterile cold Phosphate Buffered Saline (PBS), pH 7.2 to detach the cells from the surface of agar. The suspension was transferred into 4 microcentrifuge tube (volume 1.5 ml) and centrifuged for 5 minutes at 2000g). Supernatant were discarded and the pellet containing the trophozoites were washed at least twice with PAS solution. The resuspended pellets were accumulated in one microcentrifuge tube followed by adjusted to a final volume of 200 μl prior to the DNA extraction.

Extraction of Free-Living Amoeba genomic deoxyribonucleic acid (DNA)

Extraction of *Acanthamoeba* spp. DNA were performed using the manufacturer's protocol of QIAamp DNA Mini extraction kit (Qiagen, Hilden, Germany). Approximately 5×10^6 cells of trophozoite were centrifuged for 5 minutes at 300g. The supernatant was discarded and the sediment were resuspended in 200 μl PBS before extracted for DNA.

Polymerase chain reaction (PCR) amplification

Confirmation of *Acanthamoeba* genus were performed by *Acanthamoeba* specific primer pair JDP1 (5'- GGG CCC AGA TCG TTT ACC GTG AA -3') and JDP2 (5'- CTC ACA AGC TGC TAG GGG AGT CA -3'). PCR were performed in a volume of 20 μl containing: DNA template 4 μl , 1 μl of each primer (10 mM), and 10 μl of 250 units Top Taq Master Mix Kit (Qiagen, Hilden, Germany). The thermal cycling condition were performed as follows: a pre-PCR cycle at 94°C for 5 minutes, followed by 40 cycles at 94°C for 1 minutes, 60°C for 1 minute, 72°C for 1 minute and an extension at 72°C for 5 minutes⁷. As for negative control, the DNA template were replaced with the same volume of distilled water.



Agarose gel electrophoresis of PCR product

Agarose gel (2%) electrophoresis were carried out to observe the DNA that has been amplified after PCR. The PCR products around 400-550 bp were visualized as bands on an ethidium bromide agarose gel.

DNA sequencing analyses

PCR products were sent for sequencing by Ward Medic LTD., Part. Sequences were aligned by the BioEdit alignment program after matching with reference sequences in GenBank.⁸

Results and Discussion:

Microscopic identification of *Acanthamoeba* spp. from water and soil

The prevalence of *Acanthamoeba* spp. recognized in culture by their trophozoite morphology from each province were indicated in Table 2 and the group of *Acanthamoeba* spp. according to cysts morphology were shown in Table 3.

Table2: The prevalence of *Acanthamoeba* spp. from culture method

Province	Water (%)	Soil (%)	Total (%)
Songkhla	13/27 (48.15)	12/17 (70.58)	25/44 (56.82)
Phatthalung	3/13 (23.08)	2/12 (16.66)	5/25 (20.00)
Nakhon Si Thammarat	2/15 (13.33)	9/14 (64.28)	11/29 (37.93)
Total	18/55 (32.73)	23/43 (53.49)	41/98 (41.84)

Table3: The prevalence of *Acanthamoeba* spp. classified by cyst morphology.

<i>Acanthamoeba</i> spp. cyst	Songkhla (n=44)		Phatthalung (n=25)		Nakhon Si Thammarat (n=29)		Total (n=98)	
	Water (n=27)	Soil (n=17)	Water (n=13)	Soil (n=12)	Water (n=15)	Soil (n=14)	Water (n=55)	Soil (n=43)
Group I	1	3	1	0	1	4	3	7
Group II	1	1	0	0	0	0	1	1
Group III	11	8	2	2	1	5	14	15
Total	13	12	3	2	2	9	18	23

From this study, 25/44 (56.82%), 5/25 (20%), 11/29 (37.93%) of *Acanthamoeba* spp. were found in water and soil from Songkhla, Phatthalung and Nakhon Si Thammarat provinces, Southern Thailand, respectively. There were several reported of *Acanthamoeba* spp. found from various part of Thailand, such as 71.4% from water and soil samples in Chiang Mai in 2010⁹, 48.3% from natural water sources from communities near the University of Phayao in 2017¹⁰, 73.33% from soil in Narathiwat Province in 2021.¹¹ Our finding provides the first information of *Acanthamoeba* spp. found in these 3 provinces.

Acanthamoeba spp. in group I are non-pathogenic except *A. astronyxis*, *A. byersi* and *A. comandoni*¹², however, *Acanthamoeba* spp. belong to group II and group III often reported to cause infection of the brain, eg: *A. culbertsoni*, *A. healyi* and *A. lenticulate*.¹³ The most prevalence of *Acanthamoeba* spp. found in this study were belong to groups III (29.59%) follow by group I (10.20%). The preponderance of group III *Acanthamoeba* spp. collected indicates pathogenic potential of amoebae in southern Thailand.

Molecular identification of *Acanthamoeba* spp.

The prevalence of *Acanthamoeba* spp. recognized by their PCR and sequencing analysis from each province are summarized in Table 4. From 41 isolated of *Acanthamoeba* spp. described by their morphology, 13 (31.71%) were confirmed as *Acanthamoeba* spp. by PCR amplification of 18S rDNA (450-bp amplicon), 6 from water and 7 from soil samples. The 9 successfully genotyped found were T4 (1), T5 (3), T9 (1), T17 (3) and T18 (1).

Table 4: Prevalence of *Acanthamoeba* spp. identified by molecular method

Province	Water		Soil	
	PCR	Genotype	PCR	Genotype
Songkhla	5	2 (T4, T5)	2	1 (T17)
Phatthalung	0	0 (-)	0	0 (-)
Nakhon Si Thammarat	1	1 (T17)	5	5 (T5, T5, T9, T17, T18)
Total	4	3	7	6

On the basis of the 18S ribosomal DNA gene sequences, 23 genotypes (T1-T23) of the *Acanthamoeba* spp. were documented.¹⁴ Our studies found T4, T5, T9, T17 and T18 genotypes. Almost all genotypes except T7, T16 and T17 have been proven to be involved in GAE and AK diseases.¹⁵ The most of *Acanthamoeba* spp. from environmental and clinical samples are found to belong to T4 and T5 genotype. Other rare genotypes like T8, T9, and T14 can be present in the environment but are often not thought to be harmful.¹⁶ Genotypes T4, T5, and T18 found in our studies are believed to be associated with human infection.¹⁷

The findings of this study indicate the presence of *Acanthamoeba* spp. originating from natural sources. In these cultural communities, individuals are at risk of infection through physical contact or submersion, potentially leading to the contraction of AK and GAE. Furthermore, individuals face the possibility of infection associated with pathogenic parasites present in the soil and water sources, particularly when they come into contact with damp soil and water.

Precautions such as avoiding contact with contaminated water and soil, which could include freshwater lakes and rivers, not showering, swimming, or using a hot tub while wearing contact lenses, and washing your hands before touching your eyes, must be seriously taken to avoid *Acanthamoeba* spp. infection. However, the relevant health authorities must acknowledge potential risks and offer comprehensive guidelines to safeguard the well-being of individuals.

Conclusion:

This research showcased the presence of harmful *Acanthamoeba* spp. in natural water and soil reservoirs within Songkhla, Phatthalung, and Nakhon Si Thammarat. Residents of these regions are at risk of contracting diseases linked to AK and GAE. It is imperative to observe hygienic measures before coming into contact with or engaging in activities involving water and soil. Consequently, healthcare practitioners bear the responsibility of identifying, educating, and averting human infections.

References:

1. Kofman A, Guarner J. Infections Caused by Free-Living Amoebae. *Journal of Clinical Microbiology*. 2022;60(1).
2. Cope JR, Ali IKM, Georgacopoulos O. Free-living ameba. Neurological complications of infectious diseases. 2021:255-70.
3. Fanselow N, Sirajuddin N, Yin XT, Huang AJW, Stuart PM. Acanthamoeba Keratitis, Pathology, Diagnosis and Treatment. *Pathogens*. 2021;10(3).
4. Hounkong K, Sornying P, Saechan V, Sawangjaroen N. Isolation and identification of *Acanthamoeba* spp. from water and soil in Southern Thailand. *Southeast Asian Journal of Tropical Medicine and Public Health*. 2022;53(1):9-20.
5. Yousuf FA, Siddiqui R, Khan NA. Presence of rotavirus and free-living amoebae in the water supplies of Karachi, Pakistan. *The Revista do Instituto de Medicina Tropical de São Paulo*. 2017;59: e32.
6. Pussard M, Pons R, Mas-Pons R. Morphologies of the cystic wall and taxonomy of the genus *Acanthamoeba* (Protozoa, Amoebeida). *Protistologica (Paris)*. 1977;13:557-610.
7. Schroeder JM, Booton GC, Hay J, Niszl IA, Seal DV, Markus MB, et al. Use of subgenic 18S ribosomal DNA PCR and sequencing for genus and genotype identification of *Acanthamoebae* from humans with keratitis and from sewage sludge. *Journal of Clinical Microbiology*. 2001;39(5):1903-11.
8. El-Badry AA, Aufy SM, El-Wakil ES, Rizk EM, Mahmoud SS, Taha NY. First identification of *Naegleria* species and *Vahlkampfia* *ciguana* in Nile water, Cairo, Egypt: Seasonal morphology and phylogenetic analysis. *Journal of Microbiology, Immunology and Infection*. 2020;53(2):259-65.
9. Chaiwong P, Bunchoo M, Morakote N. Occurrence of thermotolerant *Naegleria* and *Acanthamoeba* in some natural water sources in Chiang Mai. *Chiang Mai Med J*. 2010;48.

10. Suwancharoen C, grichoom W. Survey of Acanthamoeba in Natural Water Sources in Communities around the University of Phayao, Phayao Province, Thailand. Thai Journal of Public Health. 2017;47(3):255-63.
11. Hounkong K, Sukchan P, Sujiwattanarat P, Dangmanee N, Sornying P. Survey of Free-living Amoeba from Soil Sources using Culture Method in Narathiwat Province, Thailand. Princess of Naradhiwas University Journal. 2021;13(1):279-90.
12. Qvarnstrom Y, Nerad TA, Visvesvara GS. Characterization of a new pathogenic Acanthamoeba Species, *A. byersi* n. sp., isolated from a human with fatal amoebic encephalitis. Journal of Eukaryotic Microbiology. 2013;60(6):626-33.
13. Xuan Y, Shen Y, Ge Y, Yan G, Zheng S. Isolation and identification of Acanthamoeba strains from soil and tap water in Yanji, China. Environmental health and preventive medicine. 2017;22:1-6.
14. Putapornpip C, Kuamsab N, Nuprasert W, Rojrung R, Pattanawong U, Tia T, et al. Analysis of Acanthamoeba genotypes from public freshwater sources in Thailand reveals a new genotype, T23 Acanthamoeba bangkokensis sp. nov. Scientific reports. 2021;11(1):11: 17290.
15. Hounkong K, Sornying P, Buatong J, Sawangjaroen N. Genotyping of Acanthamoeba spp. from Soil in Narathiwat Province, Thailand. Princess of Naradhiwas University Journal. 2022;14(1):33-43.
16. Azizan NF, Yusof H. Distribution of Acanthamoeba genotypes isolated from recreational water resources: a review. Science, Engineering and Health Studies. 2021;15, 21010002.
17. Ng S-L, Nordin A, Abd Ghafar N, Suboh Y, Ab Rahim N, Chua K-H. Acanthamoeba-mediated cytopathic effect correlates with MBP and AhLBP mRNA expression. Parasites & vectors. 2017;10(1):1-14.

***N, N, N*-trimethyl chitosan nanoparticle (TMC NP) is an effective vehicle in delivery of SARS-CoV-2 protein into lung cells.**

Jidapar Wathanaphol¹, Panya Sunintaboon², Sukathida Ubol^{1,*}

¹ Department of Microbiology, Faculty of Science, Mahidol University, Bangkok, 10400

² Department of Chemistry, Faculty of Science, Mahidol University, Bangkok, 10400

*e-mail: sukathida.ubo@mahidol.ac.th

Abstract:

With the current COVID-19 outbreak, vaccination is vital for preventing virus infection and controlling transmission. The recent platforms of vaccines, both subunit and nucleic acid vaccines, require delivery systems such as lipid or carbohydrate nanoparticles. The main advantage of nanocarrier is that it can protect immunogens from premature degradation. This study aims to investigate the efficacy of nanocarrier made from *N, N, N*-trimethyl chitosan (TMC) on delivering COVID-19 immunogens into cells, which are originated from the target organ of SARS-CoV2. The TMC NP was chosen due to its biophysical properties. That is TMC NP can adhere well to mucosal tissue and be able to penetrate between the mucosal cells. The RBD proteins of SARS-CoV-2 were encapsidated into TMC particles (RBD-TMC NPs). The cytotoxicity and delivery capability of TMC NP were monitored in lung cells, including Calu-3, MRC-5, and A549. Results revealed that treatment with the RBD-TMC NPs at 25-100 µg/ml had no toxicity. Based on the intracellular immunostaining, 60% of cells treated with RBD-TMC NPs exerted an intracellular RBD positive within 12 hours and peaked at 24 hours of treatment. The early detection and high percentage of RBD-positive cells indicated that TMC NPs effectively delivered immunogens into lung cells. In addition, the delivery efficiency had a dose-dependent pattern. This was evidenced that 100 µg/ml of RBD-TMC NPs delivered immunogen faster and higher than the low dose of RBD-TMC NPs. This data suggested that TMC NPs served as an appropriate delivery system for lung cells.

Introduction:

The continuous Coronavirus disease 19 (COVID-19) pandemic has affected public health systems and disrupted economic growth. The causative agent of COVID-19 has high transmissibility. This leads to a rapid spread worldwide. The preventive strategy to limit and control its spreading is vaccination⁽¹⁾. Currently, COVID-19 vaccines are administered via the intramuscular (IM) route. However, the limitation of intramuscular injection is that it mainly stimulates systemic immunity that prevents only disease development but neither blocks infection nor control transmission. The fact is COVID-19 viruses enter the body through the respiratory tract and initiate infection of the mucosal tissue⁽²⁾. A recent study showed that vaccinated people through IM route remain susceptible to SARS-CoV-2 infection and can transmit the virus to other individuals. In contrast, immunization through the intranasal (IN) route is shown to prevent replication and shedding of COVID-19 viruses. This due to the sufficiency of mucosal immunity induction⁽³⁾. This means that in order to control infection and spreading of COVID-19 viruses, a vaccine that induces strong respiratory mucosal immunity must be applied. However, there are some limitations to immune stimulation via an IN route such as nasal anatomy, an mucociliary clearance activity etc. These may limit the absorption of immunogens by mucosal cells of the nasal cavity. To solve this problem, the nanodelivery-based vaccines have been emerged to facilitate delivery of immunogens into the respiratory tract. This form of vaccine uses its mucoadhesive property to deliver immunogens into the mucosal cell barrier in the respiratory tract. This mucoadhesive delivery system can

prolong the nanoparticle's residence at the mucosal membrane and increase the nanoparticle's absorption⁽⁴⁾. Among these nanodelivery system, the chitosan derivative known as *N, N, N* - trimethylated chitosan (TMC) is suitable to be used in the biomedical field due to its water-soluble property, biodegradable and mucoadhesive compound⁽⁵⁾.

In this study, the TMC nanoparticles were used as a vehicle to deliver immunogens of COVID-19 virus (RBD) into 3 types of lung cells including Calu-3, MRC-5, and A549. The cytotoxicity and the efficiency of delivery were monitored.

Methodology:

Preparation of RBD protein of SARS-CoV-2: The recombinant RBD protein of SARS-CoV-2 was produced by RBD transformed *P. pastoris* in a methanol-inducible condition. The purification of recombinant RBD protein in the culture supernatant was carried out using affinity chromatography on Ni²⁺ conjugated chelating resin (Invitrogen) under native condition. The purified RBD protein was validated by SDS-PAGE using Coomassie Blue staining and immunoblotting assay using rabbit anti-SARS-CoV-2 RBD polyclonal antibody (Sino Biological, China).

Cultivation of Lung cells: The Human lung carcinoma epithelial cells (Calu-3) were cultured in a 1:1 mixture of Dulbecco's Modified Eagle Medium (DMEM), and Ham's F-12 medium supplemented with 10% FBS, 1% MEM Non-Essential Amino Acid solution. Human lung fibroblast cells (MRC-5) were grown in Minimum Essential Medium (MEM) supplemented with 10% FBS, 1% L-glutamine. The Carcinoma human alveolar epithelial cells (A549) were cultured in DMEM supplemented with 10% FBS at 37°C, 5% CO₂.

Preparation of SARS-CoV-2 RBD nanoparticles: The Empty and RBD-TMC NPs were generated using the ionotropic gelation method. Briefly, 0.222 mg/ml sodium tripolyphosphate (TPP) solution and 300 µg of recombinant RBD protein (RBD) in 5 mM HEPES pH 7.4 were mixed to 1 mg/ml TMC solution with 1% tween 80 in HEPES buffer under continuous stirring at room temp. To harvest the RBD-TMC NPs, the suspension was centrifuged at 10,000 x g for 15 minutes. The supernatant containing the free TMC, TPP, and unbound proteins were harvested to quantify the percentage of loading efficacy (%LE). The NPs pellets were resuspended in 5mM HEPES buffer, pH 7.4. The characteristics including size, Polydispersity Index (PDI), and zeta potential were determined using a Zetasizer (NanoZs4700 nano series, Malvern Instruments, UK) at 25°C. The entrapment of RBD protein in NPs was estimated by calculating the % LE using the following formula.

$$\%LE = \frac{\text{Total amount of loaded protein} - \text{the amount of non loaded protein}}{\text{Total amount of loaded protein}} \times 100$$

Cytotoxicity assay: The Calu-3, MRC-5, and A549 were seeded in a 96-well plate and cultured overnight at 37°C in a 5% CO₂ atmosphere. The monolayers were washed with 1XPBS twice. The cultures were treated with the empty or RBD-TMC NPs at the concentration of 25, 50, 100, 200, and 400 µg/ml. Treatment with 10% DMSO or medium were used as a positive and a negative control for the assay, respectively. The percentage of cell viability at 24- and 48-hour post treatments was determined by using CellTiter 96® Aqueous One Solution Cell Proliferation Assay (Promega, USA) according to the manufacturer protocol. The amount of formazan released into culture medium is found to correlate with cell viability. Therefore, this experiment was performed to quantitate the level of formazan in medium of cultures treated with various concentrations of TMC NPs or RBD-TMC NPs using the CellTiter 96® Aqueous One Solution Reagent. 20 µl of the CellTiter 96®

Aqueous One Solution Reagent were added into 100 μ l of culture medium harvested from each treated condition. After incubation at 37°C for 4hr., the absorbance was recorded at 490 nm.

Cellular uptake of RBD-TMC NPs: Calu-3, MRC-5, and A549 were seeded into each well of 24-well plate. Cells were treated with 25 or 100 μ g/ml of empty-TMC NPs, RBD-TMC NPs, soluble RBD proteins, or the culture medium and then incubated for 12, 24, and 36 hours at 37°C, 5% CO₂ atmosphere. After incubation, the treated cultures were washed with 1X PBS, fixed with 4% paraformaldehyde (200 μ l/well) for 15 minutes, and permeabilized with Buffer A (500 μ l/well, 0.25-0.5% triton X, 10% goat serum or 10 mg/mL BSA in PBS buffer) for 10 minutes at room-temperatures. After permeabilization, cells were washed with Buffer B (500 μ l/well, 0.02-0.05% triton X, 10% goat serum, or 10 mg/mL BSA in PBS buffer) and then blocked with Buffer B for at least 1 hour. The intracellular antigens were detected by staining with rabbit anti-RBD antibody (Sini Biological, primary antibody) for 18 hours at 4°C. After incubation, the cultures were washed with 1X PBS 3 times and counter-stained with Alexa Fluor 488-conjugated goat anti-mouse antibody (Invitrogen, secondary antibody). The percentages of Alexa Fluor 488 positive cells were measured under fluorescent microscopy and analyzed using ImageJ.

Statistical Analysis: Statistical analysis was performed using Stat View for Windows. Student's *t* test was used. Differences were considered significant for $p < 0.05$.

Results:

Purification of recombinant RBD protein: To produce RBD protein, RBD transformed yeast were activated with 1% (v/v) methanol in culture medium. The RBD-protein in culture medium were purified using affinity column. The purified RBD protein was validated using SDS-PAGE and immunoblotting as shown in Figure 1. Results revealed that the size of purified RBD protein was approximately ~50 kDa in SDS-PAGE. Moreover, the immunoblotting using rabbit anti-SARS-CoV-2 RBD polyclonal antibody revealed the specific interaction between proteins and antibodies. Unexpectedly, SDS-PAGE and the immunoblotting of RBD proteins revealed the smear signals. This may due to some of RBD proteins was degraded. In contrast, some of the larger size of RBD may indicate the heavy glycosylated RBD.

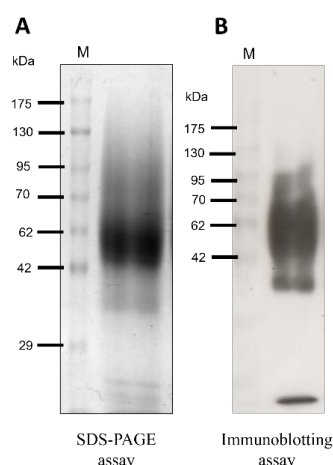


Figure 1: Characterization of recombinant RBD protein. The purified RBD was subjected to SDS-PAGE (A) and immunoblotting (B). the expected molecular weight and specific interaction between RBD and the anti-SARS-CoV-2 RBD polyclonal antibody was determined. M represents the protein molecular weight marker.

Formation of RBD-loaded TMC nanoparticles (RBD-TMC NPs): The RBD-TMC NPs were generated using ionotropic gelation method. The incorporation of protein into NPs was based on the interaction of the positive charge TMC and the negative charge sodium TPP. This method yielded a nanoscale of NPs with a mean diameter of 397 ± 5.101 nm and a size distribution of 0.351 ± 0.019 (Table 1). In addition, the zeta potential of prepared NPs was $+16.4 \pm 0.351$. This suggested that the NPs contained a cationic moiety on the surface. The loading efficiency of RBD protein into TMC NPs was as high as 92.59%, which suggested that RBD protein was efficiently entrapped into TMC NPs (Table 1). The successful entrapment of RBD into NP was also validated by SDS-PAGE and immunoblotting. The results showed that encapsulated protein interacted with the tested antibodies in immunoblotting. These results showed the antigenicity of RBD was unaltered after encapsulation in TMC NPs. This suggested that the ionotropic gelation method can be used for encapsulating the RBD antigen without interfering with RBD antigenicity (Figure 1). The empty-TMC NPs were generated in parallel and characterized as shown in table 1.

Table 1: Characteristics of Nanoparticles

Nanoparticles	Size (nm)	Polydispersity Index (PDI)	Zeta-potential (mV)	Loading efficiency (%)
Empty-TMC NPs	298 ± 2.623	0.341 ± 0.016	$+16.4 \pm 0.153$	-
RBD-TMC NPs	397 ± 5.101	0.351 ± 0.019	$+16.4 \pm 0.351$	92.59%

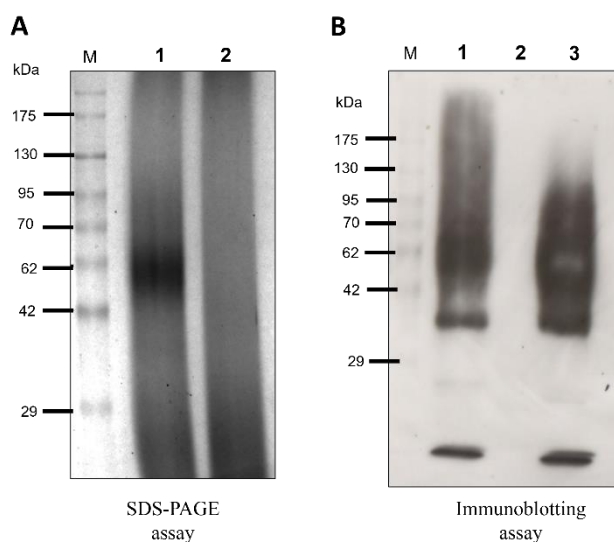


Figure 2: Detection of RBD protein in TMC NPs. The entrapped RBD protein in TMC NPs was detected by SDS-PAGE using Coomassie blue staining (A) and the immunoblotting using anti-SARS-CoV-2 RBD polyclonal antibody (B). For (A); M represented the protein molecular weight marker while 1 and 2 were RBD-TMC NPs and the empty-TMC NPs, respectively. For (B); M was the protein molecular weight marker. Lane 1, 2, and 3 were soluble RBD, empty-TMC NPs and RBD-TMC NPs, respectively.

Cytotoxicity of empty and RBD-TMC NPs on lung cells: The toxicity of the RBD-TMC nanoparticles on three different cell types were assessed. The viability of Calu-3, MRC-5, and A549 cells were quantified after being treated with various concentrations of TMC NPs and RBD-TMC NPs (25, 50, 100, 200, and 400 $\mu\text{g/ml}$) for 24 and 48 hours. While 10% DMSO was used as a positive control. Both TMC-NPs and RBD-TMC NPs treatment at 25, 50, or 100 $\mu\text{g/ml}$ exerted no detectable or had only a slight cytotoxicity effect on Calu-3, MRC-5, and A549. The percentages of viability of Calu-3 were 100% , $97.42\% \pm 4.45$, and $94.35\% \pm 5.46$ at 25, 50, and 100 $\mu\text{g/ml}$ treatment, respectively. Similar results were found for RBD-TMC NPs treated MRC-5. Results revealed that cell viabilities were 100% , $98.45\% \pm 2.67$, and $95.77\% \pm 4.16$ after treated with 25, 50, and 100 $\mu\text{g/ml}$, respectively. For A549 cells, treatment with those three concentrations of RBD-TMC NPs did not cause any cell death. Notably, the treatment with higher concentrations (200 and 400 $\mu\text{g/ml}$) caused a significant reduction of cell viability comparing to the mock-treated control group (Figure 3). These results indicated that TMC NPs as high as 100 $\mu\text{g/ml}$ exerted no harmful for human lung cells. This suggested that TMC NPs delivery system is not toxic for lung cells.

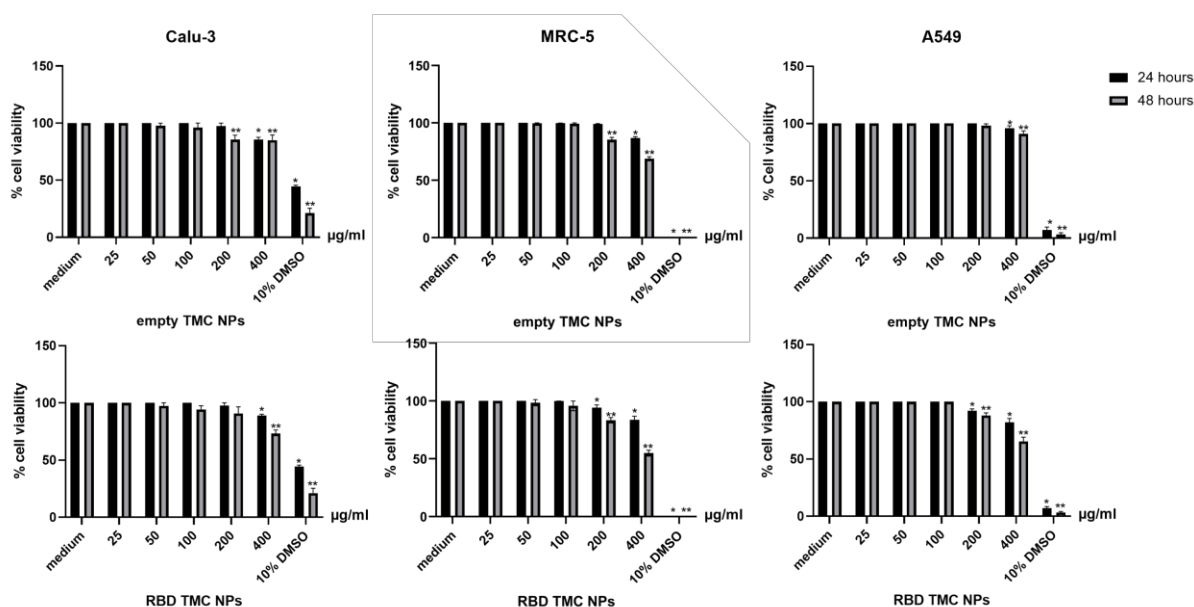
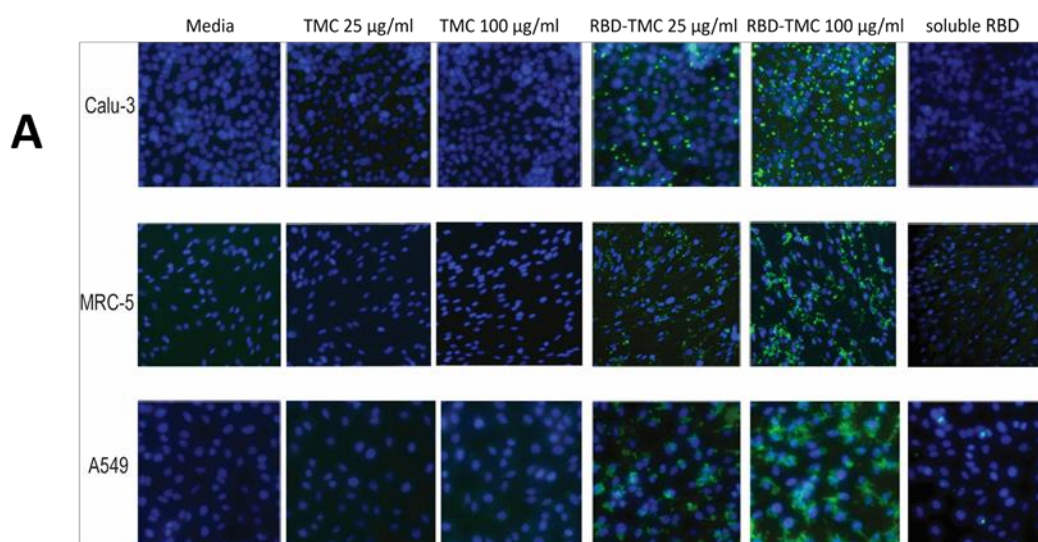


Figure 3: An effect of TMC NPs or RBD-TMC NPs treatment on cell viability: Calu-3, MRC-5, and A549 were treated with various concentrations (25, 50, 100, 200, and 400 $\mu\text{g/ml}$) of TMC NPs or RBD-TMC NPs for 24 and 48 hours. The 10% DMSO treatment was used as a positive control. The cell viability was quantitated by CellTiter 96® Aqueous One Solution Cell Proliferation Assay. Data is presented as mean \pm SD ($n=3$). *, ** indicating the significant difference between medium control and the empty-TMC NPs or RBD-TMC NPs ($p < 0.05$) at 24 and 48 hours, respectively.

The efficiency of TMC NPs on delivery of protein into Calu-3, MRC-5, and A549: To demonstrate the efficiency of TMC NPs on delivery of the immunogens, the internalization of RBD protein into Calu-3, MRC-5, and A549 were investigated. These cell lines were cultured and treated with various concentrations of TMC NPs, RBD-TMC NPs and soluble RBD at 37°C for 12-, 24-, and 36-hours. The treated cells were fixed and intracellular stained with rabbit anti-RBD antibody. The percentage of fluorescent positive cells were quantitated using immunofluorescence assay (Figure 4). The results revealed that cultures treated with the RBD-TMC NPs revealed higher percentages of RBD positive cells than cultures treated with soluble RBD.

As shown in figure 4. The percentage of positive cells in RBD-TMC NPs treated Calu-3 were $77.69 \pm 2.97\%$, $87.61 \pm 3.77\%$, and $71.58 \pm 2.73\%$ %, while the positive cells in soluble RBD treatment were $1.19 \pm 0.16\%$, $0.74 \pm 0.07\%$, and 0% % at 12, 24, and 36 hours, respectively. In RBD-TMC NPs treated MRC-5, the percentage of RBD positive cells were $84.49 \pm 2.72\%$, $89.75 \pm 2.70\%$, and $82.49 \pm 1.40\%$ %, while treatment with soluble RBD yielded the positive cells at $4.17 \pm 4.00\%$, $4.00 \pm 0.17\%$, and $2.27 \pm 0.38\%$ % at 12, 24, and 36 hours, respectively. Lastly, RBD-TMC NPs treated A549 revealed the RBD positive cells at $84.49 \pm 2.72\%$, $89.75 \pm 2.70\%$, and $82.49 \pm 1.40\%$ %, while positive cells of soluble RBD treatment were $4.17 \pm 4.00\%$, $4.00 \pm 0.17\%$, and $2.27 \pm 0.38\%$ % at 12, 24, and 36 hours, respectively. In addition, we found that the efficiency of delivery was dose dependent. This was evidenced by treatment at a higher dose (100 $\mu\text{g/ml}$) had a higher number of positive cell than treatment with the lower dose (25 $\mu\text{g/ml}$). These results demonstrated that TMC NPs effectively deliver RBD into the lung cells.



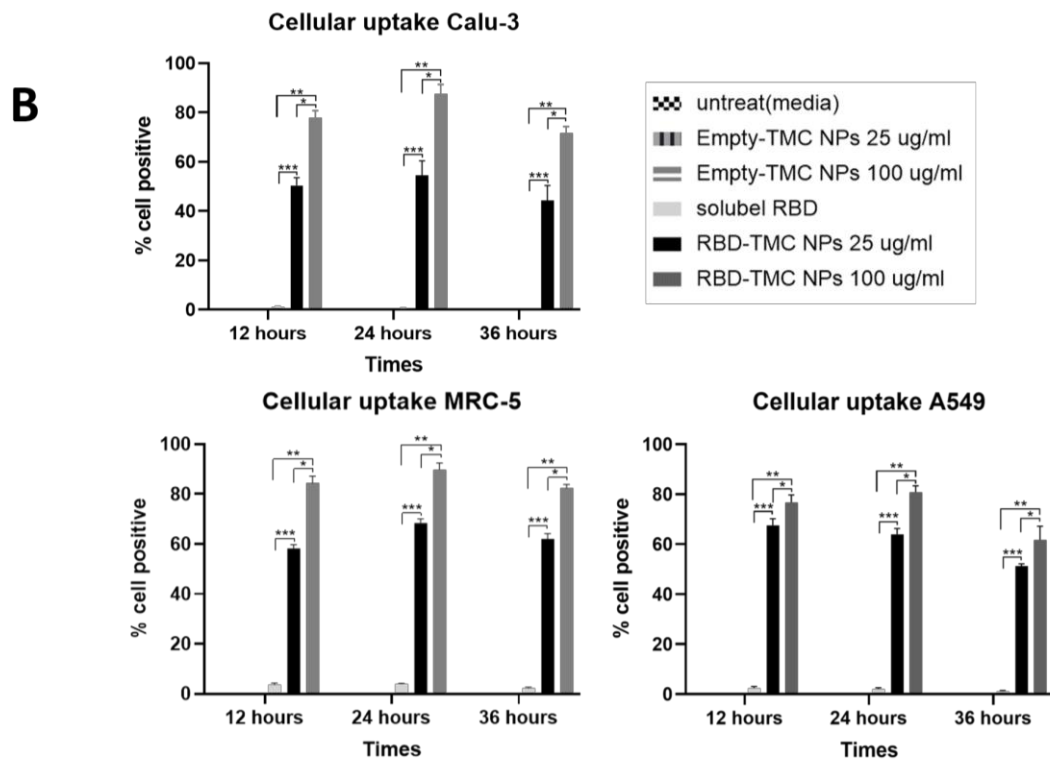


Figure 4: Cellular uptake of RBD-TMC NPs. Calu-3, MRC-5, and A549 were treated with 25 or 100 $\mu\text{g/ml}$ of empty-TMC NPs or RBD-TMC NPs at 37°C for 12-, 24-, and 36-hours. Intracellular RBD-antigens were detected by antibody staining with rabbit anti-RBD antibody and analyzed by IFA. (A) The fluorescent image of cellular uptake, (B) the percentage of RBD-positive cells. Data is presented as mean \pm SD ($n=3$). * Indicating the significant difference between 25 $\mu\text{g/ml}$ RBD-TMC NPs treatment and 100 $\mu\text{g/ml}$ RBD-TMC NPs treatment. ** Indicating the significant difference between 100 $\mu\text{g/ml}$ RBD-TMC NPs and soluble RBD. *** Indicating the significant difference between 25 $\mu\text{g/ml}$ RBD-TMC NPs and soluble RBD ($p < 0.05$).

Discussion:

An intranasal vaccine is a promising option because it closely matches the normal route of infection, self-administration is easy, and it could gain a fair market share in future years. Intranasal immunization elicited high neutralizing antibody responses and mucosal IgA and T cell responses that almost completely vanishes the SARS-CoV2 infection in both the upper and lower respiratory tract ⁽⁶⁾. A nasal spray, unlike injection, is painless and appeals to those who are afraid of needles. Based on these advantages, the intranasal subunit vaccine specific to SARS-CoV-2 has been developed by our team.

The RBD protein of COVID-19 virus was successfully produced and encapsulated into TMC NPs. The vaccine candidate was *in vitro* tested using 3 types of cells which



originated from lung tissue. Results shown here indicated that RBD protein was effectively encapsulated within TMC NPs. This high loading resulted from ionic interaction among negative charge RBD, positive charge TMC and the cross-linking activity of TPP. We found that TMC NPs aid efficient internalization of RBD protein. This was evidenced by the higher percentage of RBD positive cells in all cell types treated with the RBD-TMC NPs but not in soluble RBD treated cells. The route of entry of RBD-TMC NPs was not investigated in the present work. However, we believe that uptake of RBD-TMC NPs may be mediated through interaction between the positively charged surfaces of NPs and the negatively charged cell membrane. Enhancement of antigen uptake through NPs has previously been reported for hepatitis B surface antigen and DENV ^(7, 8). Yue and colleagues have shown that polylactide NPs enhance hepatitis B surface antigens uptake via interaction between NPs and mannose surface receptors on macrophages ⁽⁹⁾.

In conclusion, this study demonstrated that *N, N, N*-trimethyl chitosan (TMC) nanoparticles effectively delivered immunogens into lung cells. The concentration of TMC NPs up to 100 µg exerted no toxicity to Calu-3, MRC-5, and A549. This means that TMC NPs may be a promising delivery system in intranasal COVID-19 vaccine development.



Reference:

1. Hu B, Guo H, Zhou P, Shi Z-L. Characteristics of SARS-CoV-2 and COVID-19. *Nature Reviews Microbiology*. 2021;19(3):141-54.
2. Bridges JP, Vladar EK, Huang H, Mason RJ. Respiratory epithelial cell responses to SARS-CoV-2 in COVID-19. *Thorax*. 2022;77(2):203-9.
3. Tiboni M, Casettari L, Illum L. Nasal vaccination against SARS-CoV-2: Synergistic or alternative to intramuscular vaccines? *International Journal of Pharmaceutics*. 2021;603:120686.
4. Cho C-S, Hwang S-K, Gu M-J, Kim C-G, Kim S-K, Ju D-B, et al. Mucosal Vaccine Delivery Using Mucoadhesive Polymer Particulate Systems. *Tissue Engineering and Regenerative Medicine*. 2021;18(5):693-712.
5. Zhao J, Li J, Jiang Z, Tong R, Duan X, Bai L, et al. Chitosan, N,N,N-trimethyl chitosan (TMC) and 2-hydroxypropyltrimethyl ammonium chloride chitosan (HTCC): The potential immune adjuvants and nano carriers. *Int J Biol Macromol*. 2020;154:339-48.
6. Birkhoff M, Leitz M, Marx D. Advantages of Intranasal Vaccination and Considerations on Device Selection. *Indian J Pharm Sci*. 2009;71(6):729-31.
7. Chen F, Zhang Z-R, Huang Y. Evaluation and modification of N-trimethyl chitosan chloride nanoparticles as protein carriers. *International Journal of Pharmaceutics*. 2007;336(1):166-73.
8. Mangal S, Pawar D, Garg NK, Jain AK, Vyas SP, Rao DSVR, et al. Pharmaceutical and immunological evaluation of mucoadhesive nanoparticles based delivery system(s) administered intranasally. *Vaccine*. 2011;29(31):4953-62.
9. Yue H, Wei W, Fan B, Yue Z, Wang L, Ma G, et al. The orchestration of cellular and humoral responses is facilitated by divergent intracellular antigen trafficking in nanoparticle-based therapeutic vaccine. *Pharmacological Research*. 2012;65(2):189-97.



PARTIAL PURIFICATION AND CHARACTERIZATION OF CANTHAXANTHIN FROM GREEN ALGA *Tetraspora* sp. CU2551

Thanaporn Maswanna,^{1,*} Cherdsak Maneeruttanarungroj^{2,3}

¹Scientific Instruments Center, School of Science, King Mongkut's Institute of Technology Ladkrabang, Bangkok 10520, Thailand

²Department of Biology, School of Science, King Mongkut's Institute of Technology Ladkrabang, Bangkok 10520, Thailand

³Bioenergy Research Unit and Department of Biology, School of Science, King Mongkut's Institute of Technology Ladkrabang, Bangkok 10520, Thailand

*e-mail: thanaporn.ma@kmitl.ac.th

Abstract:

Secondary carotenoids are highly valuable antioxidants that can be produced by certain algae when subjected to nutrient deficiency. To that aim, we characterized the stress-induced carotenoid production of green alga *Tetraspora* sp. CU2551, which was previously identified as a strain capable of exceptional biohydrogen generation. The microalgal sample was saponified after the crude canthaxanthin was extracted using ethanol. The pigment extract was partially purified and fractionated using thin-layer chromatography (TLC). High-performance liquid chromatography with a diode array detector (HPLC-DAD) was used to confirm the fractions before they were identified and confirmed through Liquid Chromatograph-Quadrupole Time of Flight-Mass Spectrometry (LC-QTOF-MS). Our results represent a specific microalgal strain that can produce the main secondary carotenoid of canthaxanthin. It also reveals that the microalgae of *Tetraspora* sp. CU2551 has the potential to be turned into bioactive components for use in the cosmetic, pharmaceutical, nutraceutical, functional food, and animal feed industries.

Introduction:

Primary and secondary carotenoids derived from microalgae are bioactive chemicals with antioxidant properties that may have a variety of uses in human and animal nutrition and pharmaceuticals.¹ They can be used as food additives and colorants, as well as in cosmetics and as active compounds in pharmaceutical products.² Secondary carotenoids, including astaxanthin and canthaxanthin, can be synthesized in algal cell cultures and are proposed to be stronger antioxidants than primary carotenoids.³ Canthaxanthin was more potent free radical scavengers and antioxidants *in vitro* than carotene carotenoids, such as lycopene and β -carotene. Canthaxanthin can also be an efficient scavenger of excited triplet states of endogenous photosensitizers.⁵ The antioxidant effectiveness of canthaxanthin pigments was also reported by IC₅₀ values in around 225 to 284 $\mu\text{g/mL}$.⁶ Furthermore, the peroxyl trapping activity⁷ and the hydroxyl radical scavenging⁸ of canthaxanthin are more potent than β -carotene.

In microalgae, the main carotenoids are astaxanthin and β -carotene.^{9,10} Canthaxanthin, which is rarely found, can be produced by some microalgae when exposed to environmental stress. Many researchers reported that the optimal conditions for carotenogenesis in microalgae included restricted growth and other stress factors, and in particular, nutrient deprivation,¹¹ for example, green alga *H. pluvialis*.¹²

A green alga *Tetraspora* sp. CU2551 is one of the algae discovered that is capable of producing carotenoids. This cell type was previously identified and characterized as a unicellular green

alga with remarkable biohydrogen production when incubated in nutrient-deprived conditions.^{13,14} The main goals of this study were to qualitatively analyze and identify the carotenoid of canthaxanthin produced from the green alga *Tetraspora* sp. CU2551.

Methodology:

Chemicals

The solvents used in TLC and HPLC were of HPLC grade. Methanol, dichloromethane, and acetonitrile were purchased from Merck (Darmstadt, Germany). Analytical grade solvents used in the pigment extraction and partial purification procedure (ethanol, methanol, and diethyl ether), sodium sulfate anhydrous and potassium hydroxide were purchased from Carlo Erba Reagents (Val de Reuil, France).

Algal culture and nutrient deficiency

In the growth phase, the green alga *Tetraspora* sp. CU2551 cells were inoculated in 125 mL Erlenmeyer flasks containing 50 mL standard Tris-Acetate-Phosphate (TAP) medium, pH 7.2, with an initial optical density at 730 nm, OD₇₃₀ = 0.1. The culture flasks were placed in shaking incubators (rotary speed 140 rpm, light intensity 29 mol photons m⁻² s⁻¹, 24 h, 36 °C, previously determined to be optimal for *Tetraspora* sp. CU2551).¹⁵

Following the growth phase, carotenogenesis commenced as the green algae were transferred to the nitrogen-deprived TAP medium (TAP-N). Behind 43 days of pigment production, *Tetraspora* sp. cells turned reddish orange in the nitrogen-deprived TAP medium (TAP-N). The cells incubated in TAP-N (see Table 1 for nutrient composition) were chosen for pigment extraction based on their level of reddish orange appearance.

Table 1.
Nitrogen deprived medium compared to normal TAP composition in 1 L.

Medium	TAP	TAP-N
NH ₄ Cl	0.40 g	0.44 g ^a
CaCl ₂	0.05 g	0.05 g
MgSO ₄	0.10 g	0.10 g
Tris-base	2.42 g	2.42 g
Acetic acid	1 mL	1 mL
KH ₂ PO ₄	0.05 g	0.05 g
K ₂ HPO ₄	0.10 g	0.10 g
EDTA-Na ₂	0.05 g	0.05 g
H ₃ BO ₃	11.40 mg	11.40 mg
ZnSO ₄	22.00 mg	22.00 mg
MnCl ₄	5.52 mg	5.52 mg
FeSO ₄	5.60 mg	5.60 mg
CoCl ₂	0.16 mg	0.16 mg
CuSO ₄	0.16 mg	0.16 mg
(NH ₄)Mo ₇ O ₂₄	1.10 mg	2.08 mg ^b

^areplacement instead by NaCl

^breplacement instead by NaMoO₄

Pigments extraction

The pigment extraction method was adapted from Sivathanu and Palaniswamy.¹⁶ The harvested wet algal cell yield of approximately 6.1 g was used for pigment extraction with absolute ethanol. Vortexing was used to mix the pigments until all of them were removed. The tube was centrifuged to collect the ethanol extract, and the extraction procedure was repeated until the cell pellet was bleached. To prevent further oxidation of trans-carotenoids to cis-carotenoids or isomerization during the subsequent processes, 0.5 g of BHT (2,6-di-tert-butyl-p-cresol) and 0.5 g CaCO₃ were added to the pooled ethanol extracts. To the mixture, an equal volume of diethyl ether was added, followed by distilled water, until two layers formed. Before drying overnight, the ether upper layer was collected and concentrated in a rotary evaporator. To remove fat and oil, the crude extract was saponified with 10% methanolic KOH and left at room temperature overnight in the dark. To solubilize intact pigment molecules, an equal volume of diethyl ether was added to the reaction mixture. The ether fraction crude pigments were then washed twice with distilled water to remove excess alkali, dried over anhydrous Na₂SO₄, and the solvent was removed using a rotary evaporator. The crude pigment yield of about 0.1 g wet weight was stored in the dark under nitrogen at –20 °C until further examinations. A schematic representation of the extraction process is shown in Figure 1.

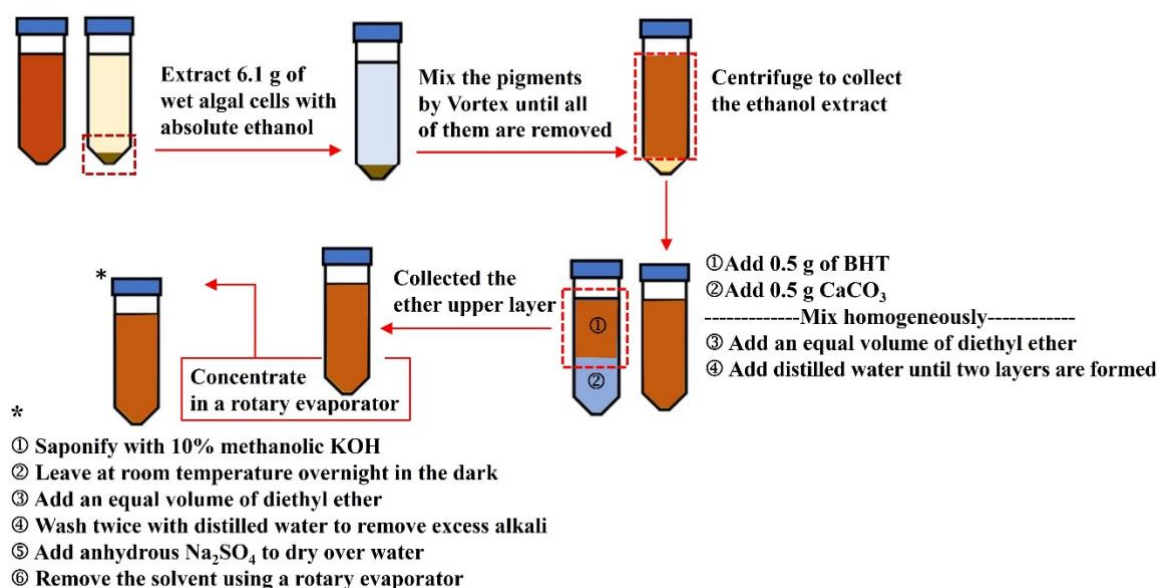


Figure 1.

A schematic representation of the extraction process of canthaxanthin from microalgae.

Thin layer chromatography

The crude pigments were substantially purified for carotenoid separation with a silica gel 60 F₂₅₄ aluminum plate (Merck, Darmstadt, Germany). The dried extract was dissolved in methanol and spotted onto a TLC plate, with diethyl ether providing a mobile phase. After separation, major bands were visible; consequently, the TLC plate was cut into band-shaped sections, and each section was re-extracted for canthaxanthin with diethyl ether, which was subsequently subjected to HPLC and LC-QTOF-MS analysis.



HPLC measurement

The carotenoids were extracted from crude pigments using an HPLC (Chromaster, Hitachi, Japan) equipped with a pump, degasser, autosampler, and injection valve with a 20 μL loop. The equipment was linked in series to a Diode Array Detector (DAD) (Hitachi Chromaster 5430, Japan). Carotenoids were measured at 450 nm. A reverse phase C18 YMC column (5 m, 250 x 4.6 mm id.) with an isocratic solvent system of dichloromethane: acetonitrile: methanol (20:70:10, v/v/v) at a flow rate of 1 mL/min and a column temperature of 25°C was used to separate the samples. The dried fraction samples were dissolved in 1,000 μL of methanol and analyzed using HPLC. Also, the absorption spectrum (λ_{max}) of each fraction was detected by DAD. The carotenoids were identified by a comparison to standards and data from the literature.

LC-QTOF-MS analysis

The carotenoids were identified using Liquid Chromatography-Quadrupole Time-of-Flight-Mass Spectrometry (LC-QTOF-MS) (1290 Infinity II LC-6545 Quadrupole-TOF, Agilent Technologies, USA). Pigment mass spectra were collected using a m/z detector and a Diode Array Detector with a 50-1000 scan range at 450 nm. The positive ion mode (APCI) was used in LC-QTOF-MS to detect pigments with a total ion current (TIC) capillary voltage of 2000 V. The vaporizer temperature was 350°C, and the nebulizer gas flow rate was 5 L/min. Identification of the individual components was performed by comparing mass spectra to databases on Agilent Mass Hunter METLIN Metabolite PCD (Personal Compound Database) and PCDL (Personal Compound Database and Library) version 8.

Results and Discussion:

Pigment extraction and partial purification

After ethanol extraction and saponification, N_2 blowing was used to dry approximately 0.1 g wet weight of crude pigments. The dried powder was resolubilized in methanol before being partially purified on a silica gel 60 plate with a diethyl ether chromatographic solvent system. An interesting band was cut from the TLC plate, resolubilized, and the absorption spectrum was measured, as shown in Figure 2. The fraction was orangish in color, which was found to have the absorption spectrum of 475 nm.

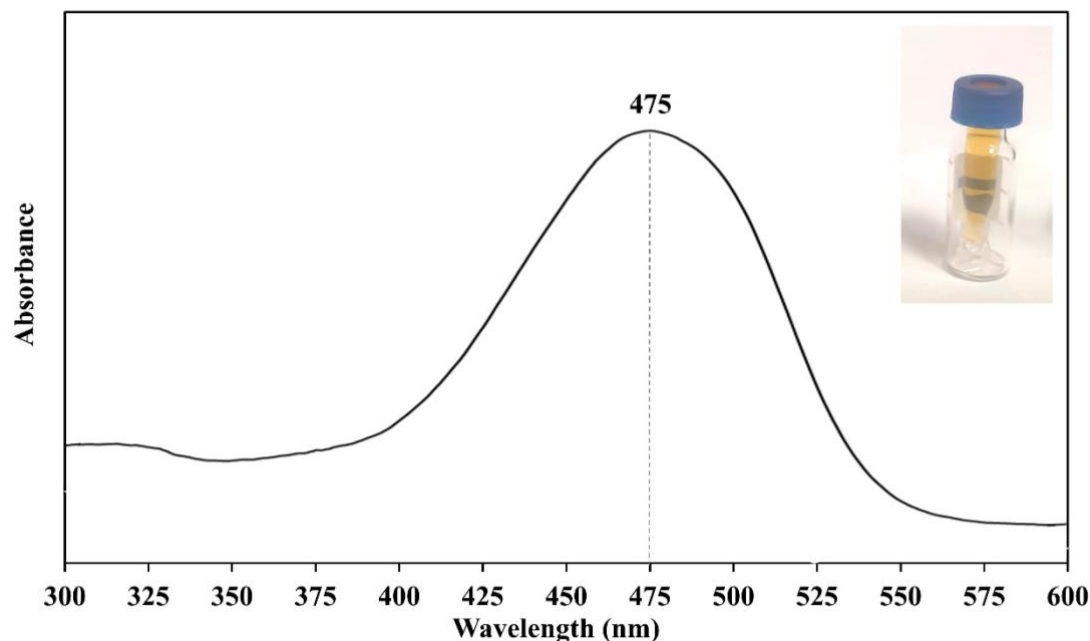


Figure 2.

The UV-VIS absorption spectra of TLC-purified canthaxanthin. Figure inset presents the appearance of samples for spectrum scanning.

Furthermore, the resolubilized fractionated pigment was analyzed using HPLC, identifying visible carotenoids under 450 nm light. The HPLC chromatogram of partially purified carotenoid, separated in 30 minutes by a C18 column and eluted under isocratic conditions, is shown in Figure 3. The absorption spectra of each peak were monitored using a diode array detector, and we determined that the absorption spectrum of peaks with retention times of 12.007 min as shown in Figure 3. Peak A corresponds to canthaxanthin. The purity of the TLC-purified canthaxanthin was 66%. Also presented in Figure 3 is the chemical structure of canthaxanthin. The identification of TLC-purified canthaxanthin has been confirmed further by LC-APCI-QTOF-MS.

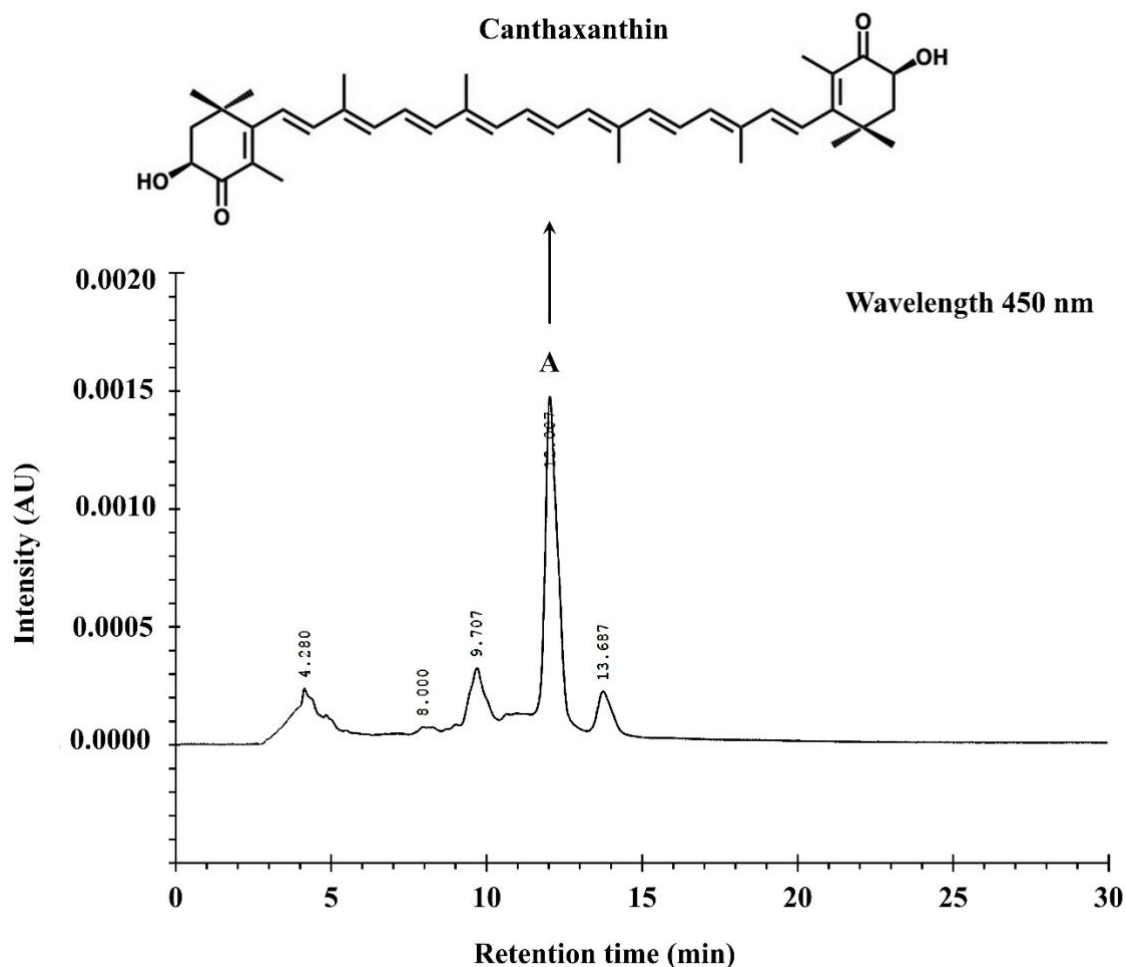


Figure 3.

Chromatogram of TLC-purified canthaxanthin from the alga *Tetraspora* sp. CU2551 by HPLC analysis as well as the chemical structure of canthaxanthin, A = canthaxanthin.

Identification

For chemical identification, the TLC-purified pigment (Peak A) was first identified as canthaxanthin by comparing the UV-Vis absorption spectra to the data reported in the literature. The UV-Vis absorption spectra of this fraction showed λ_{max} at 475 nm, which was identical to the values published in various previous studies^{3,9,11} as shown in Table 2.

The mass spectra of this TLC-purified pigment (Peak A) revealed a parent ion peak at 565 m/z, consistent with $\text{C}_{40}\text{H}_{52}\text{O}_2$ (Table 2). They had the same molecular mass as canthaxanthin.^{11,18} Finally, the carotenoid found in TLC-purified pigment was identified and confirmed to be canthaxanthin.^{9,17}

The significant carotenoid pigments found in *Tetraspora* sp. CU2551 was canthaxanthin, which was similar to those found in other green algae, such as the green alga *H. phycalis*.¹² Although there are numerous microalgae species, few of them that have the ability to synthesize canthaxanthin. Our findings reveal a unique microalgal strain capable of producing the main secondary carotenoid of canthaxanthin.

Canthaxanthin has more potent antioxidant and free radical scavenging activities than other carotenoids¹⁸; it also attracted attention as a protective agent in skin photo-related disorders. Canthaxanthin can be an efficient scavenger of excited triplet states of endogenous photosensitizers¹⁹. Moreover, Canthaxanthin not only had more vital free radical scavengers and antioxidants, as explained above, but also showed to be effective in the treatment of erythropoietic protoporphyria⁴ and was widely used as a natural skin-tanning agent in cosmetics, as well as in animal food products and feed supplements.⁵ Furthermore, canthaxanthin supplementation has been shown in a review to improve biological effects in poultry species²⁰, such as enhanced productive and reproductive performance and decreased embryo mortality in broiler breeders.²¹ The presence of canthaxanthin in *Tetraspora* sp. CU2551, indicating that it has the potential to be developed into bioactive ingredients for the pharmaceutical, nutraceutical, functional food, animal food, feed supplements, and cosmetic industries.

Table 2.

UV–Vis spectrum and mass spectral data obtained from a mass spectrometry analysis of the saponified canthaxanthin identified in *Tetraspora* sp. CU2551.

	Absorption Spectrum		[M+H ⁺]	Fragment ions
	λ_{\max} (nm)	Solvent	(m/z)	(m/z)
This study	475	HPLC system ^a	565	565, 547
	472 ²²	Acetone		
Previous report	474 ²³	HPLC system ^b	565 ^{4,18,19}	547 ^{4,18,19}
	475 ²³	HPLC system ^c		
	475 ²⁴	Petroleum ether		

^a Dichloromethane: Acetonitrile: Methanol (20:70:10, v/v/v)

^b Methanol: Tert-butyl-methyl-ether (tBME): H₂O (81:15:4, v/v/v) and Methanol: tBME: H₂O (6: 90: 4, v/v/v)

^c Methanol: Water (90: 10, v/v)

Conclusion:

Secondary carotenoid production of canthaxanthin was found in *Tetraspora* sp. CU2551. Under nitrogen deficiency, canthaxanthin was the main carotenoid produced. Canthaxanthin is rarely seen in microalgae, which makes *Tetraspora* sp. CU2551 has attracted interest in the field of carotenoid production. Our findings reveal a unique microalgal strain capable of producing the main secondary carotenoid of canthaxanthin. This implies that the *Tetraspora* sp. CU2551 can be used as the source of canthaxanthin, which acts as an animal feed, cosmetics, pharmaceuticals, functional foods, and nutraceutical supplements. The downstream process, such as biological activity, will be investigated in the future.

Acknowledgements:

We acknowledge the support of the Scientific Instruments Center, School of Science, King Mongkut's Institute of Technology Ladkrabang, for the HPLC analysis.

References:

1. Plaza M, Santoyo S, Jaime L, Reina GGB, Herrero M, Senorans FJ, Ibanez E. *Pharm Biomed Anal.* 2010;51:450–455.
2. Higuera-Ciajara I, Felix-Valenzuela L, Goycoolea FM, *Crit. Rev Food Sci. Nutr.* 2006;46:185–196.
3. Jin E, Lee CG, Polle JEW. *Microbiol Biotechnol.* 2006;16:821–831.
4. Rebelo BA, Farrona S, Ventura MR, Abranches R *Plants.* 2020;9(8):1039.
5. Fiedor J, Burda K. *Nutrients.* 2014;6(2):466–488.
6. Bera S, Bharadwaj V, Chaudhuri S, Dutta D. *Biomed Mater Eng.* 2015;129–136.
7. Surai PF. *Worlds Poult Sci J.* 2012;68(3):465–475.
8. Chang CS, Chang CL, Lai GH. *Kaohsiung J. Med Sci.* 2013;29(8):412–421.
9. Chekanov K, Fedorenko T, Kublanovskaya A, Litvinov D, Lobakova E. *FEMS Microbiol Ecol.* 2020;96(1).
10. Liu C, Hu B, Cheng Y, Guo Y, Yao W, Qian H. *Bioresour Technol.* 2021;337: 125398.
11. Deli J, Gonda S, Nagy LZ, Szabó GG, Agócs A, Marton K, Vasas G. *Food Res Int.* 2014;65:215–223.
12. Choubert G, Heinrich O. *Aquaculture.* 1993;112:217–226.
13. Maswana T, Phunpruch S, Lindblad P, Maneeruttanarungroj C. *Biomass Bioenerg.* 2018;111:88–95.
14. Maswana T, Lindblad P, Maneeruttanarungroj C. *J Appl Phycol.* 2020;32(5):2937–2945.
15. Maneeruttanarungroj C, Lindblad P, Incharoensakdi A. *Int J Hydrog Energy.* 2010;35:13193–13199.
16. Sivathanu B, Palaniswamy S. *Biomed Prev Nutr.* 2012;2:276–282.
17. Rodrigues DB, Flores Érico MM, Barin JB, Mercadante AZ, Jacob-Lopes E, Zepka LQ. *Food Res Int.* 2014;65:144–148.
18. Wang N, Manabe Y, Sugawara T, Paul NA, Zhao J. *Food Chem.* 2018;242:247–255.
19. Kao TH, Chen CJ, Chen BH. *Analyst.* 2011;136(15):3194.
20. Melendez-Martinez AJ, Stinco CM, Mapelli-Brahm P. *Nutrients.* 2019;11(5):1093.
21. Nabi F, Arain MA, Rajput N, Alagawany M, Soomro J, Umer M, Soomro F, Wang Z, Ye R, Liu J. *J Anim Physiol Anim Nutr (Berl).* 2020;104(6):1809–1818.
22. Rosa AP, Scher A, Sorbara JO, Boemo LS, Forgiarini J, Londero A. *Poult Sci.* 2012;91(3):660–666.
23. Meléndez-Martínez AJ, Britton G, Vicario IM, Heredia FJ. *Food Chem.* 2007;101:1145–1150.
24. Takaichi S, Mochimaru M, Maoka T, Katoh H. *Plant Cell Physiol.* 2005;46(3):497–504.



PHYLOGENETIC ANALYSIS OF *Plasmodium knowlesi* ISOLATES FROM CLINICAL SAMPLES IN SOUTHERN THAILAND: PERSPECTIVE FROM MITOCHONDRIAL CYTOCHROME B AND MEROZOITE SURFACE PROTEIN-1 GENES

Thunchanok Khammanee¹, Nongyao Sawangjaroen¹, Hansuk Buncherd², Suwannee Jitueakul³, Chatree Ratcha⁴, Supinya Thanapongpichat^{2,*}

¹ Division of Biological Science, Faculty of Science, Prince of Songkla University, Hat Yai, Songkhla 90110, Thailand

² Faculty of Medical Technology, Prince of Songkla University, Hat Yai, Songkhla 90110, Thailand

³ Haematology Unit, Department of Medical Technology and Pathology, Suratthani Hospital, Surat Thani Province, Thailand

⁴ Medical Technology Laboratory, Phanom Hospital, Phanom District, Surat Thani, 84250, Thailand

*Corresponding author : supinya.th@psu.ac.th

Abstract:

In Southern Thailand, the increasing prevalence of *Plasmodium knowlesi*, a simian malaria parasite, among human cases raises concerns due to the potential severity of infections. The presence of this parasite, previously documented to be circulating in Malaysia where it is a region in close geographical proximity to Southern Thailand, heightens the need for investigation. The aim of the study was to explore the evolutionary relationships among prevalent *P. knowlesi* strains in Southern Thailand by conducting a phylogenetic analysis of clinical samples, using the mitochondrial cytochrome b and merozoite surface protein-1 genes as molecular markers. In the phylogenetic analysis, the partial DNA sequences of *msp1* and *cytb* show close lineages with parasites derived from both humans and monkeys that circulated in areas of southern provinces and the eastern province closer to Cambodia and Malaysia. The Thai neighboring borders between these countries are recognized hotspots for malaria, suggesting that these regions may contribute as sources to the circulation of *P. knowlesi* in Southern Thailand.

Introduction:

Plasmodium knowlesi, a simian malaria parasite, has emerged as a human public health problem in various Southeast Asian countries. Non-human primates, including long-tailed macaques (*Macaca fascicularis*), pig-tailed macaques (*Macaca nemestrina*) and banded-leaf monkeys (*Presbytis melalophos*), can transmit the parasite to humans through mosquito in the *Anopheles leucophyrus* species complex bites¹. The parasite multiplies quickly with a 24-hour life cycle and can infect both young and mature erythrocytes, resulting in hyperparasitemia and other complications². Thai patient infected with *P. knowlesi* was first described in 2004 from a man who returning from a trip to Prachuab Khirikhan province, southwestern Thailand near the Myanmar border³. Since then the low incidence of *P. knowlesi* were reported in Thai populations^{4,5} as well as in wild macaques. Recently, The Department of Disease Control, Ministry of Public Health issued a new warning concern about the rise in human *P. knowlesi* infection in Southern part which



gradually increased from 6 cases in 2017 to more than 100 cases in 2022 ⁸. The factors contributing to the spread of malaria include increased encounters between people, vectors, and macaques due to population growth, deforestation, and agricultural land usage ^{9,10}. The overlap of these three practices is crucial for the transmission of malaria. The adaptability of *P. knowlesi* to shift between simian hosts and humans drives an ongoing evolutionary process. This adaptability highlights the intricate interplay between ecology and the dynamics of malaria transmission⁹. However, there is limited data available to use to characterize the origin of *P. knowlesi* in this area.

The *merozoite protein 1 (msp1)*, protein found on the surface of merozoites, playing a crucial role in erythrocyte invasion. It is one of the antigenic immunogenicity that enhance host immunity, leading to its use as a vaccine candidate in clinical trials ¹¹. The gene diversity influenced by host immune selective pressure and intragenic recombination. The mitochondrial *cytochrome b (cytb)*, one component of mitochondrial DNA, exhibits maternal inheritance with a lack of recombination and has been frequently used in investigating the evolutionary histories of species ¹².

In this study, phylogenetic trees were constructed from partial sequences of *msp1* and *cytb* genes of *P. knowlesi* clinical strains isolated from provinces in southern and Trat province in the eastern part of Thailand. Their diversity was compared with *P. knowlesi* isolated previously from Thailand, Laos and Malaysia to elucidate the origin of parasite population.

Methodology:

Ethical approval

The use of these samples was approved by the Research Ethics Committee of the Faculty of Medical Technology, Prince of Songkla University (HRECMT64-003).

Sample collection

A total of 38 blood samples, collected between 2018-2022 from patients with *P. knowlesi* infection that confirmed by nested PCR based on *cytb* ¹³ were used. The sampling areas included: Chumphon (n=16), Surat Thani (n=15), Ranong (n=3) and Phang-nga (n=2) in southern Thailand and Trat (n=2) from eastern part, (**Figure 1**). The genomic DNA were extracted using a QIAamp DNA Mini kit (Qiagen, Germany) according to the guidelines of the manufacturer.

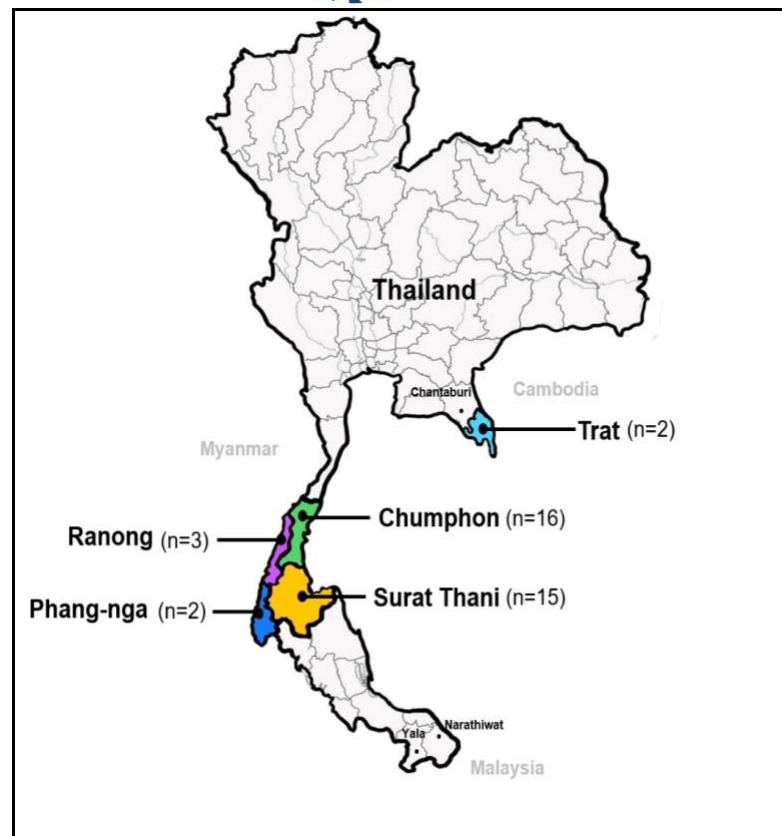


Figure 1. Sampling locations of *P. knowlesi* infection.

PCR amplification of *cytb* and *Pkmsp1* gene

The PCR primers specific to the *cytb* gene which covers 227 bp, included PCBF (5'-ATGCTTTATTATGGATTGGATGTC-3') and PCBR (5'-CAGACCGTAAGGTTATAATTATGT-3'). Briefly, a total master mix volume of 20 µl contained 3 µl of DNA template, 1X PCR buffer, 3 mM MgCl₂, 0.3 µM of each primer, 2.5 mM dNTPs, and 0.4 U of Taq DNA polymerase. The primary PCR program was initial denaturation at 95°C for 5 min, followed by 25 cycles of 94°C for 40 sec, 50°C for 30 sec, 72°C for 30 sec and final extension at 72°C for 4 min and 30 cycles for nested amplification.

The *PkMSP1* gene was amplified by semi-nested PCR using PkMSP1 F3 (5'-TAGCACTGGTGTGCTGGTC-3') and PkMSP1 R2 (5'-TGGGTAGGTCTCCTTCAACG-3') in the primary reaction which covered 520 nucleotides. For the second PCR run, PkMSP1 F2 (5'-GGTGCTGGAATTCACCTGC-3') and PkMSP1 R2 were primed to the targeted nucleotide, producing 480 bp of sequence length. The target sequence PCR reaction was accomplished in 20 µl consisting of parasite DNA, 1X reaction buffer, 3 mM of MgCl₂, 250 µM of dNTPs, 150 nM of each primer and 0.1 µl of DNA polymerase using a condition of initial denaturing at 94°C for 4 min followed by 25 cycles of 94°C for 40 sec, 50°C for 30 sec, 72°C for 30 sec and final extension 72 °C for 5 min. The same thermal program was used in secondary amplification and of 35 cycles in thermal program. The PCR products of each gene fragment were purified and subsequently sequenced at Macrogen sequencing company in South Korea.

DNA analysis and phylogenetic tree construction

The DNA sequencing chromatogram was checked for quality and trimmed by using DNASTAR Lasergene SeqMan software. The DNA sequences were blasted with the NCBI database (<http://blast.ncbi.nlm.nih.gov/Blast.cgi>). The phylogenetic trees were constructed based on partial sequence of *Pkmsp1* and *cytb* and then compared with gene sequences previously published in GenBank databases. The *msp1* reference sequences included 5 sequences from monkeys (JF837339 Monkey Narathiwat Thailand, JF837340 Monkey Narathiwat Thailand and JX046792 Monkey Narathiwat Thailand, JX046795 Monkey Narathiwat Thailand, JX046796 Monkey Narathiwat Thailand) and 10 sequences from humans in Thailand (JF837343 Human Prachuab Khirikhan Thailand, JF837345 Human Prachuab Khirikhan Thailand, JF837346 Human Yala Thailand, JF837347 Human Yala Thailand, JF837348 Human Narathiwat Thailand, JF837350 Human Chantaburi Thailand, JF837351 Human Chantaburi Thailand, JF837352 Human Narathiwat Thailand, JF837353 Human Narathiwat Thailand and JX046791 Human Narathiwat Thailand)^{14,15} and 1 was from a Lao patient (LC327234 Human Laos)¹⁶. All DNA sequences were aligned with the reference sequence from *P. knowlesi* strain H (XM 002258546) and *P. coatneyi* (AB266180), *P. cynomolgi* (AB266196) and *P. fieldi* (AB44406) were used as the out-group of the analysis.

The nucleotide sequence of the mitochondrial *cytb* gene consisted of 5 human (EU880446 Human Sarawak Malaysia, EU880447 Human Sarawak Malaysia, EU880453 Human Sarawak Malaysia, EU880455 Human Sarawak Malaysia and EU880465 Human Sarawak Malaysia) and 3 monkey isolates from Malaysia (EU880495 Monkey Sarawak Malaysia, EU880496 Monkey Sarawak Malaysia and EU880499 Monkey Sarawak Malaysia) and 1 from Laos (LC327233 Human Laos)^{16,17}. The simian malaria species, *P. coatneyi* (AB354575), *P. cynomolgi* (AB444128) and *P. fieldi* (AB444132), were included as an outgroup.

Alignment of nucleotide sequences and phylogenetic analysis were conducted using MEGA11. The alignment with the MUSCLE option was performed and manually edited. The evolutionary history was inferred using the Neighbor-Joining method. The percentage of replicate trees clustered together in the bootstrap test with 1000 replicates. The evolutionary distances were computed using the kimura 2-parameter. All positions containing gaps and missing data were eliminated (complete deletion option). The phylogenetic tree was edited using the Interactive Tree of Life (iTOL) web tool.

Results and Discussion:

Results of phylogenetic analysis of *P. knowlesi*

Through sequencing, 32 *cytb* sequences and 25 *Pkmsp1* sequences showed acceptable quality in the chromatogram. A phylogenetic tree based on the *Pkmsp1* gene revealed that *P. knowlesi* isolated from southern Thailand clustered into two clades (**Figure 2**). In the first group, a total of 14 isolates (3 from Chumphon, 2 from Ranong, 1 from Phang-nga and 8 from Surat Thani) were identical to the *P. knowlesi* clinical isolate from Human Chantaburi and Human Prachuap Khirikhan strains (accession number JF837343, JF837345, JF837350 and JF837351). Of these, the phylogenetic tree data showed that parasites that circulated southern Thailand is closed to *P. knowlesi* strain that adjacent to Cambodia in the east and Myanmar in the west. Another group, 11 *P. knowlesi* sequences were shared a closer phylogenetic relationship with Narathiwat and Laos human isolates and Narathiwat monkey

strains (accession number JF837348, LC327234, JF837339, JX046791, JF837340, JF837352, JX046792, JX046795 and JX046796). These *P. knowlesi* strain were circulated in Narathiwat where borders with Malaysia. The *P. knowlesi cytb*, however, is relatively conserved. No distinct separation of geographical regions was found in the phylogenetic tree of mitochondrial *cytb* between sequences from Thailand, Malaysia and Laos. All isolates were closely related to either *P. knowlesi* derived from humans or monkeys from Sarawak, Malaysia and Laos (**Figure 3**).

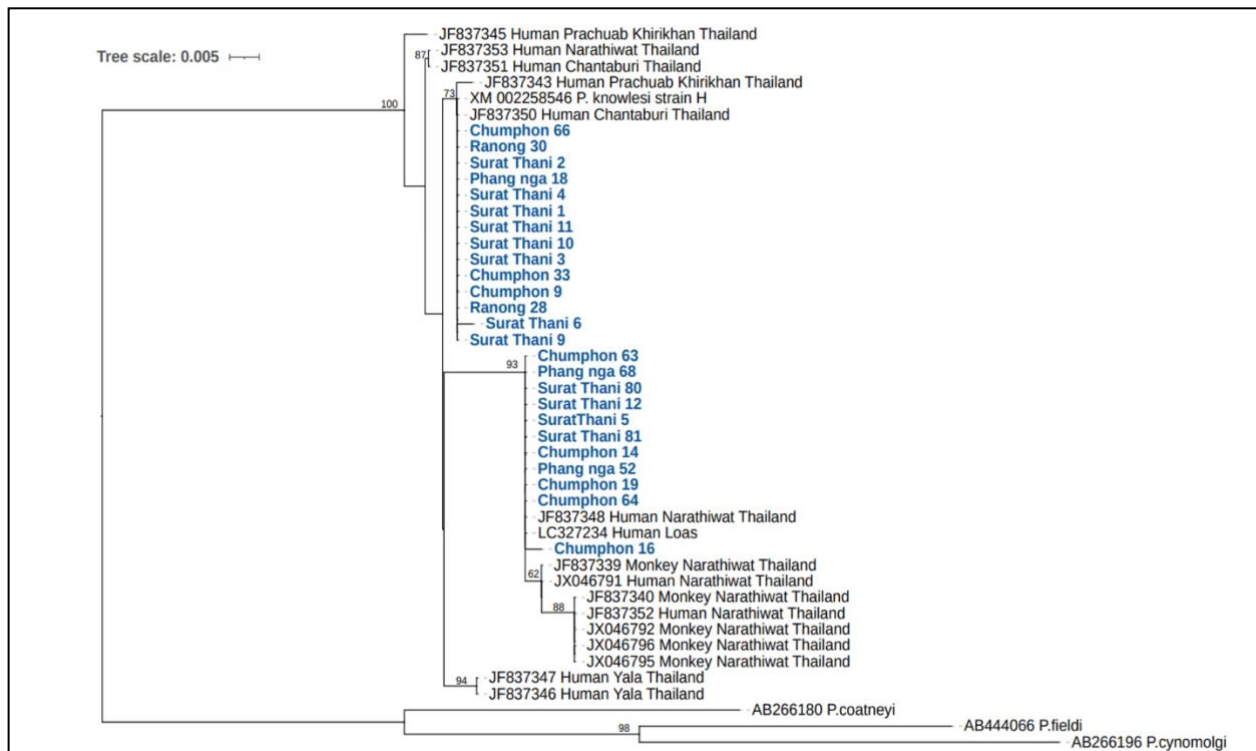


Figure 2. Phylogenetic tree constructed using MEGA11 from the partial nucleotide sequences of the *msp1* gene of *P. knowlesi*. The evolutionary relationship was inferred by using the Neighbor-Joining method with the bootstrap test with 1000 replicates.

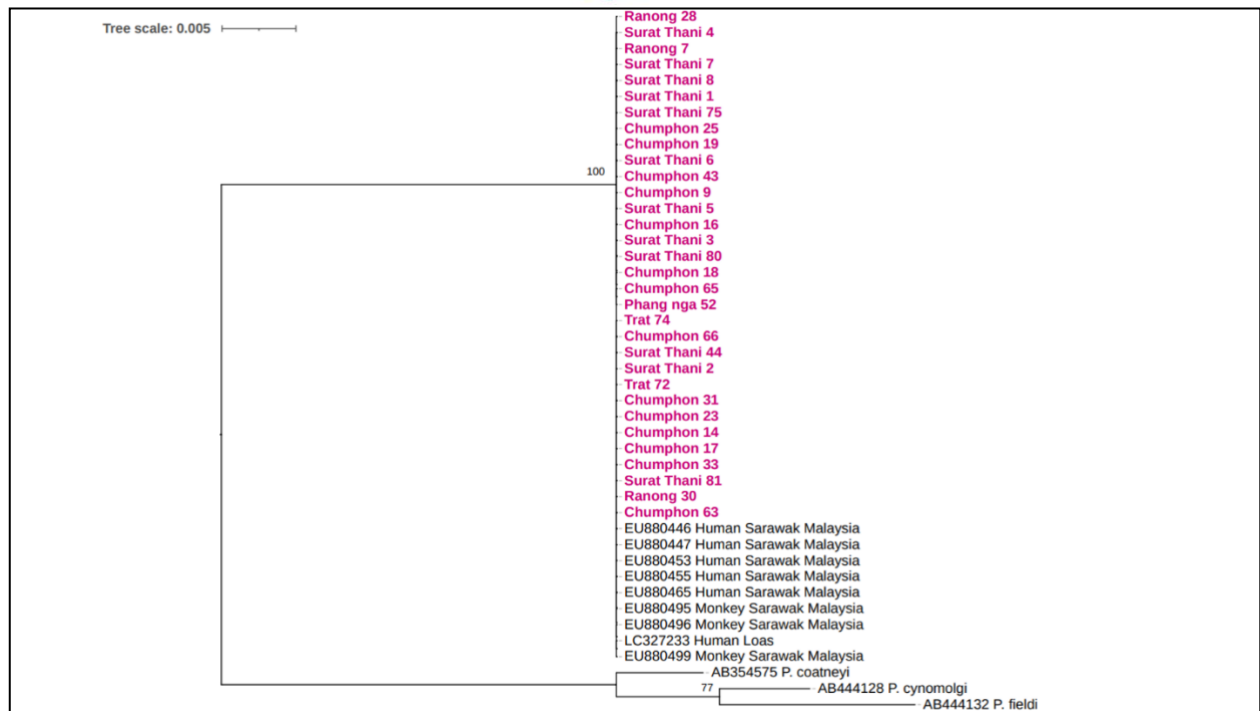


Figure 3. Phylogenetic tree constructed using MEGA11 from the partial nucleotide sequences of the *cytb* gene of *P. knowlesi*. The evolutionary relationship was inferred by using the Neighbor-Joining method with the bootstrap test with 1000 replicates.

Discussion of genetic diversity

Human infection with *P. knowlesi* is linked to activities that expose them to forest-dwelling vectors and monkey hosts^{10,18}. The south of Thailand has the highest burden of *P. knowlesi*, accounting for 80% of reported cases in the malaria situation online in 2022⁸. The genetic diversity of several DNA gene sequences including circumsporozoite, mitochondrial DNA, small subunit ribosomal RNA, and *msp1* shared polymorphism among humans and macaques, particularly those living in the nearby region, indicated phylogenetic evolutionary similarities^{5,14,17,19}. In this study, the phylogenetic relationship was created based on the partial sequences of *msp1* and the *cytb* gene from clinical *P. knowlesi* isolates. Based on identical *msp1* gene sequences, the *P. knowlesi* parasites from the upper provinces in the south were separated into two major clusters. One group was phylogenetically related to parasites from Prachuab Khirikhan which is near Chumphon and Myanmar in the west, and Chantaburi which is in the east. Another group shared similar gene sequences with parasites isolated from patients and monkeys in Narathiwat, the lower part of the south, and also from Laos patient. The naturally infected Laos patient previously reported that *P. knowlesi msp1* were identical to parasites derived from humans and macaques from Narathiwat, Thailand¹⁶. This could suggest that the *P. knowlesi* parasite which is distributed in the upper parts of southern Thailand originated from two independent sources. The *cytb* gene of the *P. knowlesi* isolates used in this investigation shared phylogenetic similarities with the *P. knowlesi* isolates from patients and monkeys in Malaysia and Laos. Malaysia, which shares a border with Narathiwat and exhibits the highest prevalence of *P. knowlesi*, may serve as a potential source of the parasites. Likewise, the parasite from Chantaburi could share a common ancestor with the parasites that isolated Cambodia. The parasites that derived from different

regions in Thailand, including Tak, Prachuab Khirikhan, Yala, Narathiwat, and Chantaburi, were identical to those from Malaysia, based on the *18S rRNA* gene⁴. According to a recent study using *msp1* sequencing and microsatellite genotyping, *P. knowlesi* isolates collected from southern Thailand are genetically related to *P. knowlesi* isolates from Malaysia, and the parasites from eastern parts showed close relationships with the *P. knowlesi* isolates from Cambodia²⁰. The phylogenetic analysis indicates a close relationship between *P. knowlesi* parasites isolated in Southern Thailand and those found near Cambodia and Malaysia. Malaysia and Cambodia share a border with Thailand, spanning approximately 600 and 800 kilometers, respectively. The geographical features, including mountains and forests, heighten the potential for cross-border transmission of malaria. The phylogenetic analysis is a valuable tool for understanding *P. knowlesi* infections in Thailand. Identifying transmission patterns emphasizes the importance of enhanced monitoring and surveillance mechanisms, contributing to the sustainability of the malaria eradication campaign.

Conclusion:

Currently, *P. knowlesi* is more prevalent and widespread in Thailand than previously known. The adaptation of the parasite population to environmental changes over time underlines the importance of understanding its epidemiology. This understanding is instrumental in shaping effective public health strategies for disease control. This study provides evolutionary relationships between *P. knowlesi* strains in southern Thailand closely related to neighboring countries. Further studies should involve comprehensive investigations, including surveys on humans, identification of *Anopheles* mosquitoes, and studying monkeys.

Acknowledgements:

We extend our sincere gratitude to Ms. Arunya Pinyoratanachote at the Office of Disease Prevention and Control 11, Nakhon Si Thammarat, for her generous contribution of DNA samples. This research has received funding from a grant provided by Prince of Songkla University, under contract no. MET6402038S, and the PSU Ph.D. Scholarship, under contract no. PSU_PHD2562-004.

References:

1. Amir A, Cheong FW, de Silva JR, Liew JWK, Lau YL. *Plasmodium knowlesi* malaria: current research perspectives. *Infect Drug Resist.* 2018; 11:1145-1155.
2. Seilmaier M, Hartmann W, Beissner M, Fenzl T, Haller C, Guggemos W, et al. Severe *Plasmodium knowlesi* infection with multi-organ failure imported to Germany from Thailand/Myanmar. *Malar J.* 2014;13(1):1–5.
3. Jongwutiwes S, Putaporntip C, Iwasaki T, Sata T, Kanbara H. Naturally acquired *Plasmodium knowlesi* malaria in human, Thailand. *Emerg Infect Dis.* 2004;10(12):2211-2213.
4. Putaporntip C, Hongsriruang T, Seethamchai S, Kobasa T, Limkittikul K, Cui L, et al. Differential prevalence of *Plasmodium* infections and cryptic *Plasmodium knowlesi* malaria in humans in Thailand. *J Infect Dis.* 2009;199(8):1143–1150.
5. Sermwittayawong N, Singh B, Nishibuchi M, Sawangjaroen N, Vuddhakul V. Human *Plasmodium knowlesi* infection in Ranong province, southwestern border of Thailand. *Malar J.* 2012;11(1):1–6.



6. Putaporntip C, Jongwutiwes S, Thongaree S, Seethamchai S, Grynberg P, Hughes AL. Ecology of malaria parasites infecting Southeast Asian macaques: evidence from cytochrome b sequences. *Mol Ecol*. 2010;19(16):3466–3476.
7. Fungfuang W, Udom C, Tongthainan D, Kadir KA, Singh B. Malaria parasites in macaques in Thailand: stump-tailed macaques (*Macaca arctoides*) are new natural hosts for *Plasmodium knowlesi*, *Plasmodium inui*, *Plasmodium coatneyi* and *Plasmodium fieldi*. *Malar J*. 2020;19(350): doi.org/10.1186/s12936-020-03424-0.
8. ThaiMOPH. Thailand Malaria Elimination Program. Ministry of Public Health. 2022. Available from: https://malaria.ddc.moph.go.th/malariaR10/index_newversion.php
9. Davidson G, Chua TH, Cook A, Speldewinde P, Weinstein P. Defining the ecological and evolutionary drivers of *Plasmodium knowlesi* transmission within a multi-scale framework. *Malar J*. 2019;18(66):doi.org/10.1186/s12936-019-2693-2.
10. Fornace KM, Abidin TR, Alexander N, Brock P, Grigg MJ, Murphy A, et al. Association between landscape factors and spatial patterns of *Plasmodium knowlesi* infections in Sabah, Malaysia. *Emerg Infect Dis*. 2016;22(2):201-208.
11. Takala SL, Plowe C V. Genetic diversity and malaria vaccine design, testing and efficacy: preventing and overcoming ‘vaccine resistant malaria.’ *Parasite Immunol*. 2009;31(9):560–573.
12. Chong ETJ, Neoh JWF, Lau TY, Lim YA-L, Chua KH, Lee P-C. Genetic and haplotype analyses targeting cytochrome b gene of *Plasmodium knowlesi* isolates of Malaysian Borneo and Peninsular Malaysia. *Acta Trop*. 2018; 181: 35–39.
13. Putaporntip C, Buppan P, Jongwutiwes S. Improved performance with saliva and urine as alternative DNA sources for malaria diagnosis by mitochondrial DNA-based PCR assays. *Clin Microbiol Infect*. 2011;17(10):1484–1491.
14. Jongwutiwes S, Buppan P, Kosuvin R, Seethamchai S, Pattanawong U, Sirichaisinthop J, et al. *Plasmodium knowlesi* malaria in humans and macaques, Thailand. *Emerg Infect Dis*. 2011;17(10):1799–1806.
15. Putaporntip C, Thongaree S, Jongwutiwes S. Differential sequence diversity at merozoite surface protein-1 locus of *Plasmodium knowlesi* from humans and macaques in Thailand. *Infect Genet Evol*. 2013;18: 213–219.
16. Iwagami M, Nakatsu M, Khattignavong P, Soundala P, Lorphachan L, Keomalaphet S, et al. First case of human infection with *Plasmodium knowlesi* in Laos. *Public Library of Science San Francisco, CA USA*; 2018. 12(3): e0006244.
17. Lee K-S, Divis PCS, Zakaria SK, Matusop A, Julin RA, Conway DJ, et al. *Plasmodium knowlesi*: reservoir hosts and tracking the emergence in humans and macaques. *PLoS Pathog*. 2011;7(4): e1002015.
18. Shimizu S, Chotirat S, Dokkulab N, Hongchad I, Khowsroy K, Kiattibutr K, et al. Malaria cross-sectional surveys identified asymptomatic infections of *Plasmodium falciparum*, *Plasmodium vivax*, and *Plasmodium knowlesi* in Surat Thani, a southern province of Thailand. *Int J Infect Dis*. 2020; 96:445-451.
19. Singh B, Sung LK, Matusop A, Radhakrishnan A, Shamsul SSG, Cox-Singh J, et al. A large focus of naturally acquired *Plasmodium knowlesi* infections in human beings. *Lancet*. 2004;363(9414):1017–1024.
20. Sugaram R, Boondej P, Srisutham S, Kunasol C, Pagornrat W, Dondorp AM, et al. Genetic population of *Plasmodium knowlesi* during pre-malaria elimination in Thailand. *Malar J*. 2021; 20(1):454. doi: 10.1186/s12936-021-03990-x.

PLASMID AND HOST IDENTIFICATION FOR CLONING AND EXPRESSION OF CD163 SRCR5-6

Sitapun Jethanajun¹, Jamorn Somana¹, Tavan Janvilisri¹, Phurt Hanvoravongchai²,
Surang Chankhamhaengdech^{2*}

¹Department of Biochemistry, Faculty of Science, Mahidol University, Thailand

²Department of Biology, Faculty of Science, Mahidol University, Thailand

*e-mail: surang.cha@mahidol.ac.th

Abstract:

In this study, the expression of the CD163 SRCR5-6 protein, a key player in porcine reproductive and respiratory syndrome (PRRS) infection, was investigated using various molecular biology techniques. The CD163 SRCR5-6 gene was successfully amplified and validated through gel electrophoresis, restriction enzyme digestion, and sequencing. Three varieties of plasmids were selected as the expression vector due to their consistent and efficient protein production characteristics, with the highest level of expression observed when using pGEX-KG plasmid. Different expression levels of CD163 SRCR5-6 were observed across different *E. coli* host strains, with SHuffle® standing out as the optimal host for soluble protein production. The results underscored the significance of host-vector compatibility in achieving the successful expression of recombinant CD163 SRCR5-6 protein and enhancing protein production efficiency. This research represents a substantial advancement in recombinant protein production methodology, offering insights into the intricate interplay between host organisms and protein expression, with promising implications for the development of innovative antiviral interventions and biotechnological applications in diverse fields.

Keywords: Protein expression, PRRSV, CD163, Scavenger receptor cysteine-rich domain

Introduction:

Porcine reproductive and respiratory syndrome (PRRS) poses a significant challenge to the global swine industry, resulting in substantial economic losses. This viral disease is caused by the PRRS virus (PRRSV), and current prevention and treatment strategies have proven to be ineffective (1, 2). Consequently, there is an urgent need to develop novel approaches to combat this pervasive threat. The scavenger receptor cysteine-rich 5 (SRCR5) domain of CD163 is a cell surface receptor protein, which primarily expressed on macrophages in pig lungs and lymphatic organs (3). This SRCR5 domain has emerged as a key player in facilitating PRRSV infection, making it a promising target for the development of innovative antiviral interventions. However, the inclusion of SRCR6 alongside SRCR5 in the study of CD163 is crucial. Previous attempts focused solely on expressing SRCR5 faced challenges, possibly due to its size as a single domain. Therefore, incorporating SRCR6 becomes essential to ensure the successful overexpression of the CD163 SRCR5-6 protein. The overexpression of the CD163 SRCR5-6 protein is pivotal for further investigation, as the purified CD163 SRCR5-6 protein is a preliminary requirement for exploring alternative drug targets capable of disrupting the PRRSV infection process.

Recombinant protein expression in heterologous systems is a fundamental practice in molecular biology and biotechnology. It enables the production of a wide range of proteins for various purposes, including research, industry, and therapeutics. Traditionally, eukaryotic cells have been preferred for expressing eukaryotic proteins due to their ability to perform complex post-translational modifications essential for protein functionality. However, as the



demand for rapid, cost-effective, and high-yield protein production has grown, prokaryotic hosts, particularly *Escherichia coli*, have gained prominence as a robust alternative (4).

E. coli, as a well-characterized prokaryote model, provides a streamlined platform for protein expression owing to its robust genetic background and scalable bioprocessing capabilities (5). This shift toward prokaryotic hosts becomes particularly relevant when the primary objective is efficient and cost-efficient protein production. However, it is essential to recognize that expressing specific proteins, especially those with attributes like membrane associations, complex structures, toxicity concerns, or intricate post-translational modifications, can pose significant challenges. These challenges are magnified when prokaryotic hosts such as *E. coli* are employed, as they may lack the necessary cellular machinery for specific protein modifications. Overcoming these challenges often requires innovative strategies, including the meticulous selection of plasmids and *E. coli* host strains, optimization of growth conditions, co-expression with chaperones or modifying enzymes, and the utilization of advanced molecular biology techniques. This ongoing pursuit of versatile and reliable protein expression systems underscores the importance of host-vector compatibility, particularly in achieving the successful expression of the recombinant CD163 SRCR5-6 protein, thereby enhancing overall protein production.

In the context of this study, our primary objective was to address the expression of CD163 SRCR5-6, a crucial protein recognized for its essential role in PRRSV infection (3). This protein possesses unique challenges due to its transmembrane segment and the presence of three disulfide bonds in each domain (6). Understanding and effectively addressing these complexities is of utmost importance, as CD163 SRCR5-6's role in PRRSV infection has been identified as a potential target for intervention strategies, including the development of antiviral agents. To tackle this complexity, we employed a comprehensive strategy involving the selection of plasmid and host. Our methodology encompassed the amplification and validation of the *CD163 SRCR5-6* gene through techniques such as gel electrophoresis, restriction enzyme digestion, and sequencing. The choice of plasmids and hosts played a crucial role in consistently improving production efficiency.

In conclusion, our research presents a significant advancement in the methodology of recombinant protein production. It sheds light on the intricate relationship between host organisms and protein expression, offering promising insights for further exploration and optimization of protein expression in heterologous systems. These findings hold the potential to shape the future of molecular biology and biotechnology, with exciting prospects on the horizon as we work to find alternative drug targets that can disrupt PRRSV infection by targeting the CD163 SRCR5-6 protein. Moreover, the abundance of CD163 SRCR5-6 protein achieved through our methodology offers practical advantages, which could be exploited as a starting point for the development of targeted antiviral strategies against PRRSV, reducing its impact on swine health and the global food supply. Additionally, overproducing CD163 SRCR5-6 protein enhances our understanding of virus-host interactions, benefiting PRRSV intervention strategies and advancing the broader fields of virology and immunology.

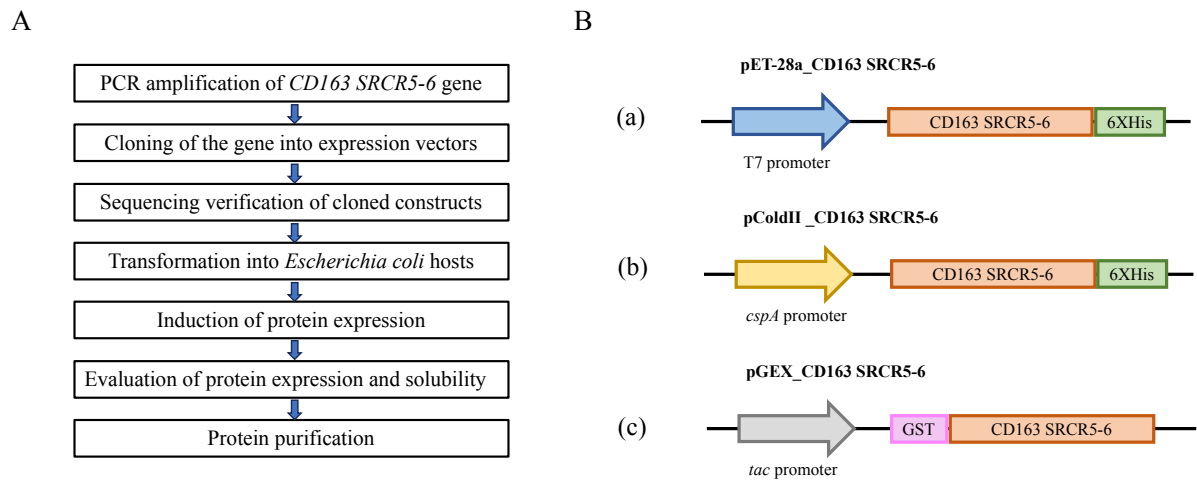


Figure 1: (A) Experimental workflow for cloning and expression of the CD163 SRCR5-6 protein. (B) Schematic representation of the vector suite with different characteristics. 6xHis, His-Tag; GST, Glutathione-S-transferase-Tag.

Methodology:

Cell culture

PAM (Porcine Alveolar Macrophage) cells of the 3D4/21 cell line (ATCC CRL-2843), were cultured in RPMI medium (Hyclone Laboratories, UT) supplemented with 10% fetal bovine serum (FBS) and penicillin/streptomycin. Simultaneously, HEK293T cells were maintained in DMEM medium (Hyclone Laboratories, UT) supplemented with 10% FBS and penicillin/streptomycin. Both cell lines were incubated in a humidified incubator at 37°C with 5% CO₂.

Bacterial strains and plasmids

E. coli strains, including NEB® Stable, BL21 Star™ (DE3), SHuffle®, and Rosetta 2(DE3). These strains were cultured in Luria-Bertani (LB) medium at 37°C with constant agitation. Additionally, the plasmids pET-28a(+), pColdII, and pGEX-KG were provided from co-authors's laboratory stocks.

RNA extraction and cDNA synthesis

RNA extraction from the 3D4/21 cell line was conducted following the manufacturer's protocol of the RiboEx™ (GeneAll Biotechnology, South Korea). Subsequently, the extracted RNA was subjected to DNaseI treatment (Thermo Fischer Scientific, California, United States) to remove carried-over DNA. First-strand cDNA synthesis was accomplished using the SuperScript™ III First-Strand Synthesis System (Thermo Fisher Scientific, CA). This process was initiated with 5 µg of total RNA and produced cDNA used as the template for *CD163 SRCR5-6* gene amplification.

Cloning of *CD163 SRCR5-6* gene

Primers were designed based on the porcine CD163 nucleotide sequence (GenBank accession no. EU016226). Subsequent to PCR amplification, the amplified genes were cloned into vectors, pET-28a(+), pColdII, and pGEX-KG. The resulting ligation mixtures were

introduced into *E. coli* NEB® Stable and transformants were cultured on LB agar supplemented with the appropriate antibiotic. Transformants were then screened for the presence of the target gene within the expression vector through colony PCR, employing forward and reverse primers specific to the inserted gene. *E. coli* clones exhibiting positive PCR results were selected for further cultivation in LB broth supplemented with the corresponding antibiotics. Following growth, the recombinant plasmids were extracted and their validity was confirmed through sequencing (Celemics, South Korea).

Expression and purification of the recombinant pCD163 SRCR5-6

Heterologous expression of the CD163 SRCR5-6 was conducted by ligating the gene into three plasmids including pET-28a(+), pColdII, and pGEX-KG, and transformed each recombinant plasmid into each of the three *E. coli* host strains, including BL21 Star™ (DE3), SHuffle®, and Rosetta 2(DE3). A single colony of the resulting transformant was selected and incubated in 10 mL of LB broth supplemented with the corresponding antibiotics at 37°C for 16 hours with agitation at 180 rpm. Subsequently, 1% of the culture was used to inoculate fresh LB broth containing the corresponding antibiotics. The culture was allowed to grow until the optical density (OD) at 600 nm reached the range of 0.4-0.6. At this point, isopropyl β-D-1-thiogalactopyranoside (IPTG) was added to the culture to a final concentration of 0.5 mM, and the cells were further cultivated at 16°C for 12 hours with agitation at 180 rpm. After induction, the cells were harvested via centrifugation, followed by resuspension in 20 mM HEPES buffer pH 7.4 (20 mM 4-(2-hydroxyethyl)-1-piperazineethanesulphonic acid, 200 mM NaCl, 0.1 mM PMSF). The resuspended cells were then subjected to ultrasonication, utilizing a 40% amplitude setting for 20 cycles (30 seconds on, 15 seconds off). Subsequently, the protein extract solution was obtained by centrifugation at 13,000xg at 4°C for 30 minutes.

The recombinant CD163 SRCR5-6 protein was achieved from *E. coli* SHuffle harboring pGEX_CD163 SRCR5-6 plasmid and was subjected to GSTrap™ HP Column for purification. Following, SDS-PAGE and western blot were used to assess the purity of the SRCR5-6 proteins. Equal amounts of protein samples were loaded onto 12% SDS-PAGE gels for electrophoresis, and subsequently, the separated proteins were transferred onto PVDF membranes. These membranes were then blocked with a solution of 5% w/v skim milk in TBS-T and probed with the specified antibodies. The specific binding of the antibodies to their respective targets was detected by using HRP-conjugated secondary antibodies, and the results were visualized using an ECL substrate. Chemiluminescence signals were captured using a ChemiDoc MP imaging system (Bio-Rad Laboratories, Hercules, CA, United States) and subsequently analyzed with Image Lab software (Version 5.1, Bio-Rad Laboratories).

Results and Discussion:

Plasmid construction

The experimental workflow for cloning and expressing the CD163 SRCR5-6 protein is illustrated in Figure 1A. The *CD163 SRCR5-6* gene was amplified from the cDNA of PRRSV using PCR with gene-specific primers, aiming for an expected product size of 606 bp. Subsequent gel electrophoresis was performed to validate the PCR product, revealing an observed product size in the range of approximately 600 bp (Figure 2A). This confirmation solidified the presence of the *CD163 SRCR5-6* gene. This gene was then successfully integrated into various plasmids, namely, pET-28a(+), pColdII, and pGEX-KG, which are depicted in Figure 1(B). Each plasmid presented distinct characteristics and expression systems for the CD163 SRCR5-6 gene. In pET-28a(+), the CD163 SRCR5-6 gene was

controlled by the *T7* promoter and featured a His-tag at the C-terminus. The pColdII plasmid employed the *csp4* promoter to regulate the CD163 SRCR5-6 gene and also incorporated a His-tag at the C-terminus. On the other hand, the pGEX-KG plasmid utilized the *tac* promoter to drive the expression of the CD163 SRCR5-6 gene and introduced a GST tag at the N-terminus of the gene. These diverse plasmid constructs allowed us to explore a range of expression conditions and strategies in our study.

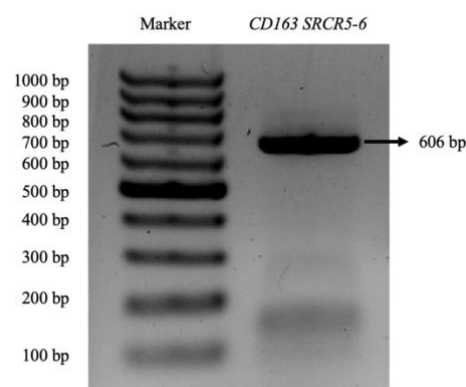
To further ascertain the integrity of the recombinant plasmids, validation was performed through restriction enzyme digestion and subsequent gel electrophoresis. Table 1 provides details on the specific restriction enzymes employed and the expected sizes post-digestion for each plasmid. The gel electrophoresis results confirmed that the observed bands aligned with the expected pattern of digestion (Figure 2B). To conclusively confirm the identity of the colony containing the *CD163 SRCR5-6* gene-inserted plasmid, sequencing was conducted.

This rigorous process of gene amplification, plasmid ligation, and validation represents a critical foundation in the successful construction of plasmids for the subsequent expression of the CD163 SRCR5-6 protein, ensuring the accuracy and integrity of the genetic constructs employed in this study.

Table 1: Plasmid Information and Restriction Enzyme Digestion Site

Plasmid	Restriction Enzyme	Plasmid Size (bp)	Expected Fragment Size (bp)
pET-28a(+)	<i>Xba</i> I, <i>Xma</i> I	5369	3965, 1404
pET-28a(+)_SRCR5-6	<i>Xba</i> I, <i>Xma</i> I	5860	3963, 1332, 511
pColdII	<i>Xho</i> I, <i>Eco</i> RV	4392	3124, 1268
pColdII_SRCR5-6	<i>Xho</i> I, <i>Eco</i> RV	4965	3088, 1877
pGEX-KG	<i>Nhe</i> I, <i>Eco</i> RI	5005	5005
pGEX SRCR5-6	<i>Nhe</i> I, <i>Eco</i> RI	5647	5403, 244

A



B

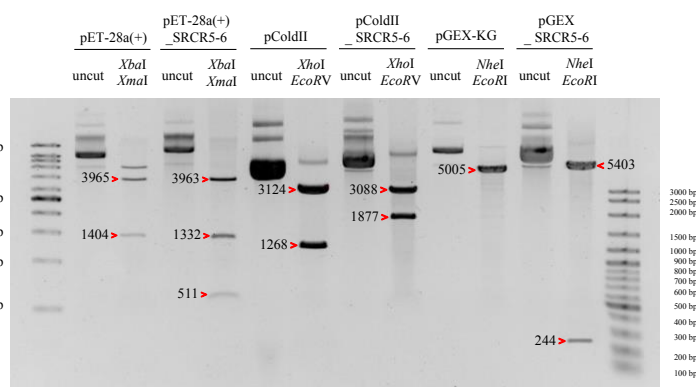


Figure 2 PCR product and restriction digestion analysis of the recombinant plasmids.

(A) Amplification of CD163 SRCR5-6 gene. The successful amplification of the CD163 SRCR5-6 gene from PRRSV cDNA via PCR is visually represented. Gel electrophoresis confirmed the presence of the gene. Notably, the observed product size ranged approximately 600 - 700 bp, aligning with expectations.

(B) The agarose gel electrophoresis confirmed the presence of the desired bands, aligning with the expected outcomes, indicating the successful construction of the plasmids.

The expression of CD163 SRCR5-6 protein

Following, the recombinant plasmid was transformed into different host organisms, including BL21 Star™ (DE3), SHuffle® and Rosetta2(DE3). Interestingly, successful expression of the protein was achieved exclusively when using the pGEX-KG plasmid in all host strains (Figure 3A). Notably, the pGEX-KG plasmid consistently demonstrated superior production efficiency due to glutathione S-transferase (GST) fusion protein in the plasmid. This 26 kDa peptide tag is part of a family of cytosolic proteins present in eukaryotes, can be expressed at high levels in bacteria which aligns with our study's focus on CD163 SRCR5-6; eukaryotic proteins, and it contributes to the plasmid's effectiveness in our research (7). However, it's essential to note that for functional studies or downstream applications involving the CD163 SRCR5-6 protein, the GST fusion protein needs to be cleaved off. This observation suggests that the choice of expression host and vector can significantly impact the successful expression of the CD163 SRCR5-6 protein. The results highlight the importance of careful selection of expression systems in recombinant protein production, as the compatibility between the plasmid and host organism plays a critical role in achieving successful protein expression.

The protein was expressed both in the cell supernatant and as inclusion bodies in all host organisms (Figure 3B). Among the available host organisms, SHuffle® was chosen for its exceptional capability to yield the highest levels of protein expression in the soluble fraction. Likewise, a previous study introduces a robust *E. coli*-based platform for efficient cytoplasmic production of full-length IgG antibodies, termed 'cyclonals.' By utilizing engineered *E. coli* strains which is SHuffle®, stable disulfide bond formation is achieved within the cytoplasm, eliminating the need for refolding or membrane translocation. This innovative approach results in the production of functional cytoplasmic IgGs with clinical relevance (8).

This selection was made with the specific intention of using this host for subsequent steps in the experimental process, including protein purification and Western blot analysis. For the purification of the CD163 SRCR5-6 protein, which has an approximate size of 50 kDa, including the GST tag, a GSTrap affinity column was employed. The purification protocol involved loading the clarified cell lysate onto the GSTrap column, allowing the GST-tagged CD163 SRCR5-6 protein to selectively bind. Non-specific contaminants were efficiently removed through washing steps, and the purified protein was subsequently eluted. The elution fractions containing the CD163 SRCR5-6 protein were collected and analyzed for purity and concentration. To confirm the successful purification, a GST-Tag Antibody was used for western blotting. This approach verified the presence of the GST-tagged CD163 SRCR56 protein and ensured the reliability of the purification process as demonstrated in Figure 3C and 3D.

The significance of this selection extends beyond simple high expression levels. SHuffle® has a unique advantage in correctly folding proteins with multiple disulfide bonds in the cytoplasm, a crucial factor for our study as CD163 SRCR5-6 contains such disulfide bonds in its structure. This compatibility between SHuffle® and the protein's structural requirements underlines the importance of host selection not only for successful protein expression but also for achieving the desired form of expression. The observed dual expression patterns emphasize the intricate relationship between the host organism and the protein's folding capacity.

These results emphasize the critical role of host selection, not only in successful protein expression but also in achieving the desired form of expression, and they pave the way for further investigations into the factors influencing the dual expression patterns observed in this study. Understanding these dynamics holds promise for refining protein production strategies and advancing our comprehension of CD163 SRCR5-6 protein behavior in different cellular contexts.

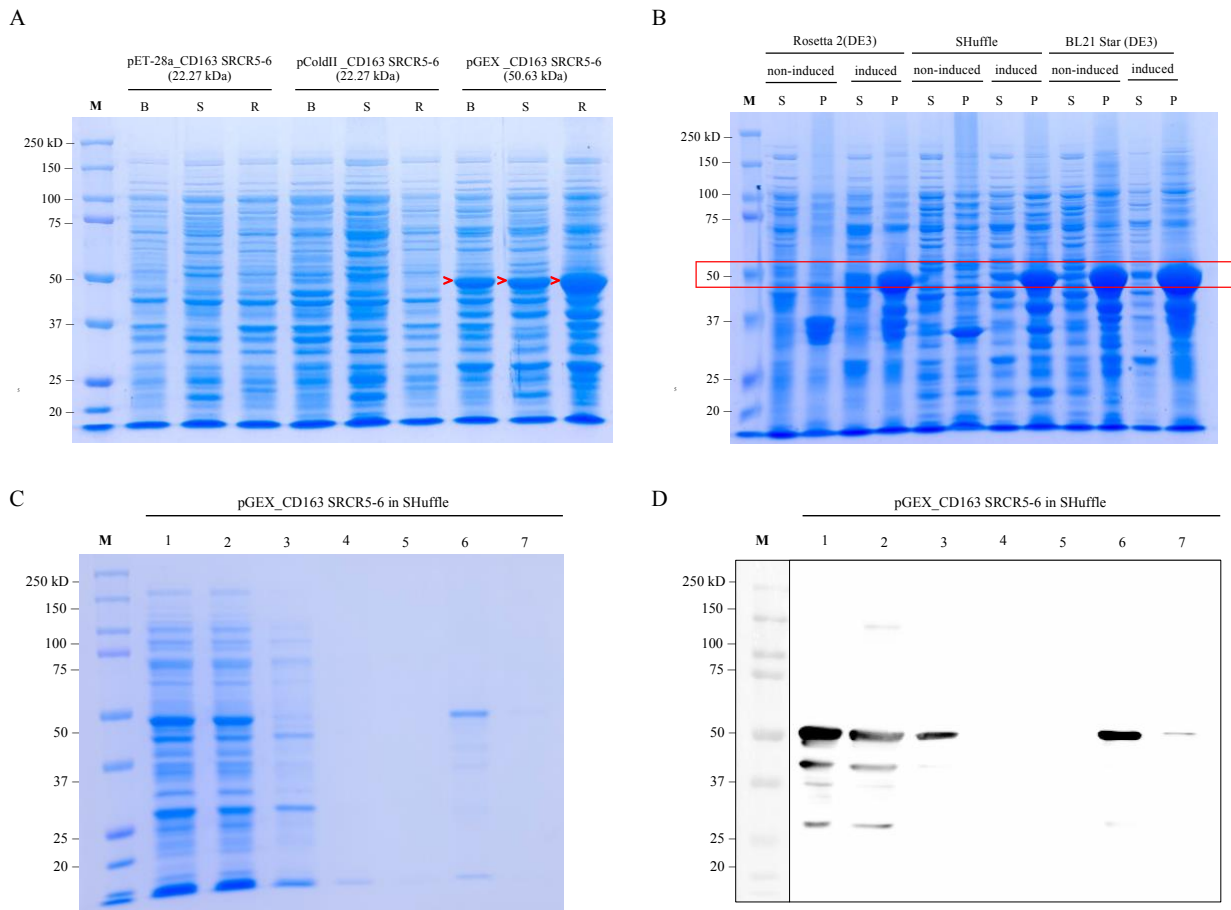


Figure 3 Expression, purification, and Western blotting of CD163 SRCR5-6 protein. (A) Expression analysis of CD163 SRCR5-6 proteins was performed by SDS-PAGE (Coomassie blue-stained) Lanes: M, molecular mass protein marker; B, BL21 StarTM (DE3); S, SHuffle®; R, Rosetta 2(DE3). (B) Expression analysis of insoluble and soluble fractions after induced with IPTG. Lanes: M, molecular mass protein marker; S, supernatant; P, pellet. SDS-PAGE (C) and western blot (D) analysis. Lane M, molecular mass protein marker; 1, Cell lysate; 2, Flow through; 3, 4, and 5, Washes; 6 and 7, Elutions.

Conclusion:

In this study, we addressed the intricate challenge of recombinant protein expression, focusing on the CD163 SRCR5-6 protein, which plays a pivotal role in successful infection with PRRSV. CD163 SRCR5-6 is a protein of particular complexity, characterized by a transmembrane segment and the presence of three disulfide bonds in each domain. To successfully navigate these complexities, we employed a comprehensive strategy involving plasmid and host selection. We began by amplifying and validating the CD163 SRCR5-6

gene through gel electrophoresis, restriction enzyme digestion, and sequencing. A crucial factor in our success was the selection of the pGEX-KG plasmid, which consistently demonstrated superior production efficiency.

Notably, the expression of CD163 SRCR5-6 protein presented a dual pattern in all host organisms, both in the cell supernatant and as inclusion bodies. Our results underscore the critical role of host selection, as it significantly impacted the successful expression of this complex protein. Among the available host organisms, SHuffle® emerged as the preferred host, given its ability to correctly fold proteins with multiple disulfide bonds—an essential characteristic for CD163 SRCR5-6.

The importance of host selection extends beyond mere high expression levels; it encompasses the achievement of the desired form of expression. These findings open avenues for further exploration into the factors influencing dual expression patterns, with potential implications for optimizing protein production strategies and enhancing our understanding of CD163 SRCR5-6 behavior in diverse cellular contexts.

In conclusion, our research represents a significant advancement in the methodology of recombinant protein production, shedding light on the intricate interplay between host organisms and protein expression. Moreover, this study lays the foundation for downstream investigations that can leverage the produced recombinant CD163 SRCR5-6 protein. Elaborating on downstream studies is crucial, such as utilizing these proteins for drug screening purposes or delving into the mechanisms of infection facilitated by PRRSV. Understanding the behavior of CD163 SRCR5-6 in diverse cellular contexts opens avenues for exploring its implications in disease mechanisms and host-pathogen interactions. These downstream studies are integral in maximizing the potential impact of our findings beyond protein expression optimization. Additionally, our work showcases the suitability of SHuffle® for efficiently expressing proteins with complex structural requirements, particularly those with disulfide bonds, offering exciting prospects for future biotechnological applications and scientific research. This study contributes to the ongoing pursuit of versatile and reliable protein expression systems, with the potential to impact various fields, including industrial, therapeutic, and research applications.

Acknowledgements:

This study was supported by the Program Management Unit for Competitiveness (PMUC) Office of National Higher Education Science Research and Innovation Policy Council (grant numbers C10F640021/1).

References:

1. Albina E. Epidemiology of porcine reproductive and respiratory syndrome (PRRS): an overview. *Veterinary microbiology*. 1997;55(1-4):309-16.
2. Neumann EJ, Kliebenstein JB, Johnson CD, Mabry JW, Bush EJ, Seitzinger AH, et al. Assessment of the economic impact of porcine reproductive and respiratory syndrome on swine production in the United States. *Journal of the American Veterinary Medical Association*. 2005;227(3):385-92.
3. Wang X, Wei R, Li Q, Liu H, Huang B, Gao J, et al. PK-15 cells transfected with porcine CD163 by PiggyBac transposon system are susceptible to porcine reproductive and respiratory syndrome virus. *Journal of virological methods*. 2013;193(2):383-90.



4. Sahdev S, Khattar SK, Saini KS. Production of active eukaryotic proteins through bacterial expression systems: a review of the existing biotechnology strategies. *Molecular and cellular biochemistry*. 2008;307:249-64.
5. Rosano GL, Ceccarelli EA. Recombinant protein expression in *Escherichia coli*: advances and challenges. *Frontiers in microbiology*. 2014;5:172.
6. Welch S, Calvert J, Slade S, Shields S. Scavenger receptor CD163 is a cell permissive factor for infection with porcine reproductive and respiratory syndrome viruses. UniProtKB/Swiss-Prot entry Q2VL90. 2005.
7. Smith DB, Johnson KS. Single-step purification of polypeptides expressed in *Escherichia coli* as fusions with glutathione S-transferase. *Gene*. 1988;67(1):31-40.
8. Robinson M-P, Ke N, Lobstein J, Peterson C, Szkodny A, Mansell TJ, et al. Efficient expression of full-length antibodies in the cytoplasm of engineered bacteria. *Nature communications*. 2015;6(1):8072.



Screening of compounds that can alleviate toxicity of α -Syn using the developed yeast-based assay

Chayanook Seetha¹, Anyaporn Sangkaew¹, Parichat Suebsakwong², Apichart Suksamrarn² and Chulee Yompakdee^{1,*}

¹ Department of Microbiology, Faculty of Science, Chulalongkorn University, Bangkok, Thailand

² Department of Chemistry and Center of Excellence for Innovation in Chemistry, Faculty of Science, Ramkhamhaeng University, Bangkok, Thailand

*e-mail: chulee.y@chula.ac.th

Abstract:

Parkinson's disease (PD) is attributed to the accumulation of aggregated α -synuclein (α -Syn). Although the exact molecular mechanisms underlying α -Syn aggregation have not yet been elucidated, oxidative stress is known to contribute to this process. Therefore, compounds that decrease oxidative stress generated by α -Syn aggregation may be a potential drug for PD treatment. The aim of this research was to screen natural compounds that mitigate α -Syn toxicity using our previously developed yeast-based assay. We found that three compounds, AS-CY 223, AS-CY 225, and AS-CY 226, could enhance the relative cell survival of the yeast indicator cells more than the untreated control. The effect of compounds against intracellular reactive oxygen species (ROS) level utilizing H₂DCFDA assay was investigated. In comparison to untreated cells, cells exposed to each compound exhibited reduction on accumulation of intracellular ROS level. The reduction of ROS level of each compound did not correlate with their antioxidant activity detected by DPPH assay. Thus, all candidate compounds could relieve α -Syn toxicity in the α -Syn overexpressed yeast, mediated by the modulation of intracellular ROS level independent of their antioxidant activity. These candidate compounds could potentially be developed to pharmaceuticals or dietary supplements for the prevention and/or treatment of PD.

Introduction:

Parkinson's disease (PD) is one of the most common age-related neurodegenerative disorders, affecting quality of life. The incidence of PD increases steadily with age, with the highest prevalence in the population older than 80 years of age. PD is a progressive neurodegenerative disease characterized by the loss of dopaminergic neurons in the Substantia nigra compacta of the brain, resulting in a decrease in dopamine levels.¹ This leads to a combination of symptoms such as slow imprecise movements (bradykinesia), tremors at rest, rigidity, facial paucity (hypomimia), shuffling gait, difficulty walking, freezing, and postural instability.² Nowadays, there are several medications available designed to help manage various Parkinson's symptoms and maintain quality of life. However, there is not currently a treatment that can slow or halt the disease progression. Therefore, disease-modifying therapy is the most important for the treatment of PD.³⁻⁵

α -Synuclein (α -Syn) is an intrinsically disordered protein that adopts a helical structure upon lipid membrane binding. The normal functions of α -Syn have been believed to be implicated in synaptic plasticity, neurotransmitter release, and synaptic vesicle pool maintenance. Under pathological conditions, α -Syn tends to form aggregates and is found as a major constituent of Lewy bodies, the pathological hallmark of PD.⁶ Despite, the cause of α -Syn aggregation to form Lewy bodies is still unclear, the evidence demonstrated that mitochondrial dysfunction, including oxidative stress are important mechanisms of α -Syn leading to neuronal cell death. Therefore, the reduction of α -Syn aggregation by directly



interacting with α -Syn, stabilizing non-toxic form or by indirect mechanisms, such as through the reduction of oxidative stress and/or the stimulation of α -Syn degradation pathways is the therapeutic approach for PD.⁷

The budding yeast *Saccharomyces cerevisiae* is a unicellular eukaryotic fungus that is widely used as a model organism in scientific studies or to discover new knowledge on important human biological processes. In the last decade, *S. cerevisiae* has proven to be a useful model system to study the fundamental processes of human neurodegenerative disorders such as PD.⁸ In yeast, several pathways involved in α -Syn-associated toxicity are conserved in another eukaryotic model of PD. Overexpression of α -Syn in *S. cerevisiae* causes high amounts of ROS production, which accelerates protein misfolding and aggregation. As a result, these protein aggregates can obstruct the proteasome's function, causing additional harm in the form of cytotoxicity and cell death.⁹⁻¹⁰ Therefore, the compound that can inhibit α -Syn-induced cell death might be a potential lead compound for PD treatment.

Sangkaew et.al.¹¹ developed a novel yeast-based assay in a high-throughput screening system to search for small molecules that can alleviate α -Syn-induced cytotoxicity. Cell viability was measured by determining innate metabolic activity using redox indicators, resazurin. Resazurin (7-hydroxy-3H-phenixazin-3-one-10-oxide) assay is used in redox based fluorometric/colorimetric assay to determine cellular metabolic reduction. The resazurin indicator changes from the oxidized form (blue, non-fluorescence) to the reduced form (red, fluorescence) by the dehydrogenase enzyme in living cells. If the test compound can alleviate the toxicity caused by α -Syn, in the yeast cell over-expressed α -Syn will survive and exhibit increased fluorescent intensity compared to the untreated control. Interestingly, the candidate compounds that can protect the α -Syn overexpressed yeast cells from toxicity would be “positively identified” by their potential to facilitate the growth of the yeast indicator cells suffering from α -Syn toxicity. Therefore, the toxicity of the test compound is simultaneously determined during screening. Our previously developed yeast-based assay system has been shown to be effective for screening compounds against α -Syn with high specificity and sensitivity.¹²

Trichosanthes cucumerina L. is a Thai medicinal plant in the Cucurbitaceae family. It is mainly distributed in the tropical zone of Southeast Asia and Australia, and it is the largest genus of the family with over 100 species, 17 species of which are found in Thailand. There have been reports of the pharmacological effects, including anti-inflammatory, antidiabetic, hypoglycemic, hepatoprotective, gastroprotective, antifertility, and larvicidal properties.¹³ However, the effects of *T. cucumerina* on neuroprotection have not yet been reported. The aims of this study is to screen pure compounds isolated from *T. cucumerina* that can alleviate cytotoxicity induced by α -Syn accumulation using our previously developed yeast-based assay. Then, the effects of candidate compounds on lowering ROS levels and their antioxidant activity were also determined.

The screening results using the developed yeast-based assay showed that three pure natural compounds isolated from *T. cucumerina* significantly increased the relative cell survival of the yeast indicator cells as compared to the untreated control. These compounds were designated as AS-CY 223, AS-CY 224, and AS-CY 225. Here, we found that these compounds could reduce the amount of intracellular ROS accumulation consistent with the growth observation. It is surprising that the reduction in ROS levels did not correlate with their antioxidant activity detected by the DPPH assay. The action mechanism of these three candidate compounds on alleviating α -Syn toxicity needs to be further elucidated.



Methodology:

1. Screening of natural bioactive compounds alleviating human α -Syn toxicity using the developed yeast-based assay

The overexpression of α -Syn in the indicator yeast cells (yeast HT01 [pYES2(α -Syn-GFP)]) cause α -Syn accumulation in the cells, resulting in cytotoxicity and affecting cell growth.¹¹ Resazurin(7-hydroxy-3H-phenixazin-3-one-10-oxide) was used as an indicator dye according to previously described.¹¹ The yeast strain HT01 [pYES2(α -Syn-GFP)] was cultured in synthetic complete medium lacking uracil (SR-Ura; 2% raffinose, 0.67% yeast nitrogen base without amino acids, and 10 \times amino acid mix lacking uracil) for overnight, then adjusted to 2 \times 10⁵ cells/mL in Yeast Nitrogen Base dropout uracil (YNB-Ura + 0.1 M MOPs, pH 6.0). Cells were incubated with or without test compound for 30 minutes at 30 $^{\circ}$ C before adding 20% galactose to induce α -Syn expression. After that, 10 μ L of resazurin was added to each well. The fluorescence intensity was measured at 590 nm excitation and 540 nm emission wavelengths using a microplate reader (Molecular Devices, USA). Relative cell survival values were calculated by equation (1), and the percentage reduction of toxicity (% reduction of toxicity) was calculated by equation (2):

$$\text{Relative Cell Survival} = \text{RFU/min (treated)}/\text{RFU/min (untreated control)}] \dots\dots (1)$$

$$\% \text{ Reduction of toxicity} = [\text{RFU/min (treated)} - \text{RFU/min (untreated control)}] \times 100 \dots\dots (2)$$

where RFU, the fluorescent value at the time of control (not exposed to the tested compound), remains a linear line, and min is the time (in minutes) that the graph of the control unit remains a straight line.

2. Investigation on the involvement of candidate compounds in modulating oxidative stress induced by α -Syn accumulation

To measure the intracellular ROS level caused by α -Syn accumulation, measurement of the ROS level was carried out in 96-well plate using fluorescent indicator 2',7'-dichlorodihydrofluorescein diacetate (H₂DCFDA) (Sigma Aldrich, USA) according to previously described.¹⁴ Either the yeast strain HT01 [pYES2(α -Syn HA)] or HT01 [pYES2] cultured in SG-Ura with or without test compound overnight was harvested and centrifuged at 6,000 g for 10 minutes and the pellet was washed twice in 0.1 M phosphate buffer (pH 7.4). Cells were incubated with 10 μ M H₂DCFDA in the same buffer and protected from light for 30 minutes. The cell pellet was collected, and then resuspended in 100 μ L of 0.1 M phosphate buffer (pH 7.4). The fluorescence intensity was measured at 504 nm excitation and 524 nm emission wavelengths using a microplate reader (Molecular Devices, USA).

3. Determination of antioxidant activity by DPPH assay

The free radical scavenging ability of the extracts was tested by DPPH radical scavenging assay as described.¹⁵ The hydrogen atom donating ability of the test compound was determined by the decolorization of methanol solution of 2,2-diphenyl-1-picrylhydrazyl (DPPH). DPPH produces violet/purple color in methanol solution and fades to shades of yellow color in the presence of antioxidants. A solution of 0.025 mg/ mL DPPH in methanol was prepared, and 90 μ L of this solution was mixed with 10 μ L of the test compound in DMSO at different concentrations. The reaction mixture was left in the dark at room temperature for 30 min. The absorbance of the mixture was measured at 515 nm. Ascorbic acid was used as reference. Percentage of DPPH radical scavenging activity was calculated by the following equation (3):

$$\% \text{ DPPH radical scavenging activity} = ((A^0 - A^1)/A^0) \times 100 \dots\dots (3)$$

where A⁰ is the absorbance of the absence of the test compound, and A¹ is the absorbance of the presence of the test compound. Then % of inhibition was plotted against concentration of compound. The experiment was repeated three times at each concentration.

Results and Discussion:

1. Screening of compounds that can alleviate toxicity of α -Syn using the developed yeast-based assay

In yeast, α -Syn overexpression causes cytotoxicity and inhibits cell growth. Therefore, the test compounds that could reduce α -Syn toxicity should show better growth of yeast indicator cell than the untreated control. In this study, the cell viability of the yeast cells was measured by determining metabolic activity using resazurin as indicator dye. Upon screening of 11 compounds isolated from *T. cucumerina*, three test compounds, namely AS-CY 223, AS-CY 225, and AS-CY 226 showed significant increase in the relative cell survival up to 1.56, 1.34, and 1.49, respectively, in comparison to the untreated control. (**Table 1 and Fig 1**).

Table 1.

Relative cell survival of the yeast indicator cells exposed to the representative of test compound at the concentration of 0.08 μ g/ mL

Compound	Relative cell survival
Untreated (control)	1
AS-CY 216	1.25
AS-CY 221	1.12
AS-CY 222	1.20
AS-CY 223	1.56
AS-CY 224	1.23
AS-CY 225	1.34
AS-CY 226	1.49

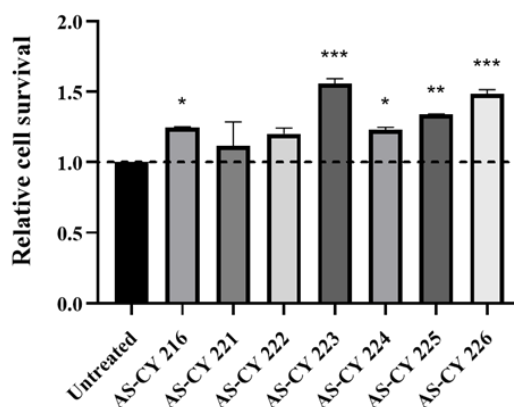


Figure 1

Relative cell survival of the yeast indicator cells exposed to the representative of test compounds at the concentration of 0.08 μ g/mL. Untreated control was the yeast indicator cells exposed to solvent (0.5% DMSO). The data shown in the graph are mean \pm standard deviation from three iterative trials, which *, ** and *** represent statistically significant difference.

2. Measurement of intracellular ROS level

It is known that yeast overexpressing α -Syn causes an excess of ROS and eventually lead to the cell death. In order to determine whether the effect of test compounds promoting cell viability is associated to a lowered intracellular ROS level, the level of intracellular ROS in cells exposed to the test compound was compared to that of the untreated cells. The ROS level of yeast cells expressing α -Syn without the test compounds was set as a control at 100% fluorescence signal. In the presence of either AS-CY 223, AS-CY 225, or AS-CY 226, the intracellular ROS level was found to decrease significantly by 20.9%, 18.6%, and 21.1%, respectively. (**Fig 2**).

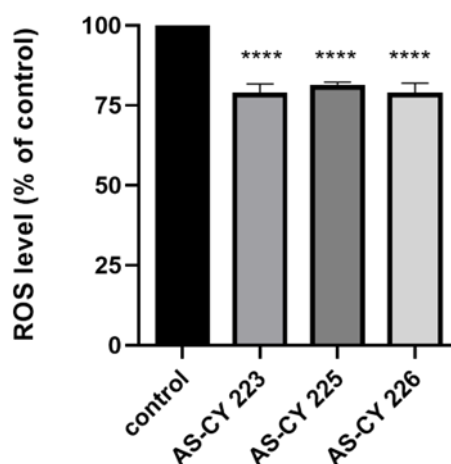


Figure 2

Relative level of intercellular ROS determination of the yeast cells exposed to 0.08 μ g/mL of the tested compound. The control was the yeast cells exposed to only 0.5% DMSO solvent.

The experiment was performed in triplicates, which **** represent statistically significant differences at $p < 0.000$, when compared to the untreated cells.

3. Determination of antioxidant activity by DPPH assay

Previous studies have shown antioxidants can decrease intracellular ROS level. In this study, the antioxidant activity of AS-CY 223, AS-CY 225, and AS-CY 226 was evaluated using the 2,2-diphenyl-1-picrylhydrazyl (DPPH) as an indicator dye, which antioxidant will turn purple. Ascorbic acid (vitamin C), a typical antioxidant vitamin, was used as a positive control. Our results revealed that ascorbic acid has high DPPH scavenging activity. Surprisingly, all of the test compounds did not show the antioxidant activity at the effective concentration (0.08 μ g/mL) (**Fig 3**).

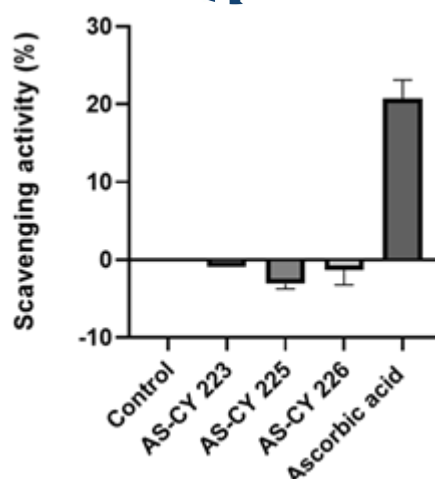


Figure 3

The antioxidant activity of AS-CY 223, AS-CY 225, and AS-CY 226 at a concentration of 0.08 ug/mL. The control contained only DPPH and 100% DMSO. The data shown in the graph is the mean \pm standard deviation from 3 iterative trials.

Conclusion:

The budding yeast *S. cerevisiae* was utilized as a model in the experiment to screen compounds that attenuated α -Syn toxicity and proved their ability to reduce ROS accumulation. Upon the screening of natural compounds isolated from *T. cucumerina* L. We found that three effective compounds, namely AS-CY 223, AS-CY 225, and AS-CY 226, increased the relative cell survival of the yeast cell overexpressing α -Syn. These indicate that these three compounds could decrease the toxicity of α -Syn. At an effective concentration (0.08 ug/mL), these three compounds did not show antioxidant activity but could significantly reduce intracellular ROS levels. The result suggested that the ability of these three compounds to alleviate α -Syn toxicity might be through modulating the level of ROS generated by α -Syn, independent of their antioxidant properties. However, the detailed action mechanism of these compounds needs further investigation.

Acknowledgement:

This work was supported by the 90th Anniversary of Chulalongkorn University Fund.



References:

1. Meade, R.M., Fairlie, D.P. & Mason, J.M. *Mol. Neurodegener.* 2019;14:29.
2. Dauer, W., S. Przedborski. *Neuron*, 2003;39:889-909.
3. Zhang H, Tong R, Bai L, Shi J, Ouyang L. *Bioorg Med Chem.* 2016;24:1419-1430.
4. El-Agnaf, O.M.A, Paleologou K.E, Greer B, Abogrein, A.M, King J.E, Salem S.A, Fullwood N.J, Benson F.E, Hewitt R, Ford K.J, Martin F.L, Harriott P, Cookson M.R, Allsop D. *FASEB J.* 2004;18:1315-1317.
5. Li BD, Bi ZY, Liu JF, Si WJ, Shi QQ, Xue LP, Bai J. *CNS Neurosci Ther.* 2017;23:827-842.
6. Henderson MX, Trojanowski JQ, Lee VM. *Neurosci Lett.* 2019;709:134316.
7. Vidović M, Rikalovic MG. *Cells.* 2022;11:1732.
8. Pereira C, Bessa C, Soares J, Leão M, Saraiva L. *J. biotechnol. biomed.* 2012;2012:941232.
9. Tenreiro S, Franssens V, Winderickx J, Outeiro TF. *Curr Opin Genet Dev.* 2017;44:74-83.
10. Farrugia G, Balzan R. *Front Oncol.* 2012;2:64.
11. Sangkaew A, Kojornna T, Tanahashi R, Takagi H, Yompakdee C. *J Appl Microbiol.* 2022;132:1409-1421.
12. Seetha C. [Unpublished individual study]. Chulalongkorn University.
13. Suebsakwong P, Chulrik W, Chunglok W, Li J, Yao Z, Suksamrarn A. *RSC Adv.* 2020;10:10461-10470.
14. Edwin J.E, Fiji N, Roy D, Mg D, Shihabudeen M.S, Chattopadhyay D, Thirumurugan K. *Anal Methods.* 2015;7:8572-8575.
15. Blois M.S. *Nature.* 1958;181:1199-1200.

SEARCHING FOR PEPTIDES WITH MUSHROOM TYROSINASE INHIBITION ACTIVITY IN THE FERMENTED UNPOLISHED BLACK RICE SAP

Yanika Chantachot,¹ Orrarat Sangkaew,¹ Sittirak Roytrakul,² Chulee Yompakdee^{1,*}

¹ Department of Microbiology, Faculty of Science, Chulalongkorn University, Thailand

² Functional Proteomics Technology, National Center for Genetic Engineering and Biotechnology (BIOTEC), National Science and Technology Development Agency (NSTDA), Thailand

*e-mail: Chulee.Y@chula.ac.th

Abstract:

Tyrosinase, a key rate-limiting enzyme involved in melanogenesis, is important for protecting harmful effects from UV radiation. However excessive melanin production leads to aesthetic problems. Currently, active ingredients used in skin whitening products cause side effects like burns and dryness. Therefore, safer tyrosinase inhibitors are of wide-ranging interest. Peptides are active compounds with many biological activities including anti-tyrosinase activity. Our previous study reported that fermented unpolished black rice sap (FUBRS) could inhibit melanogenesis in B16F10 cells. Hence, we aimed to identify peptides from the FUBRS that can reduce tyrosinase activity. The results revealed that after FUBRS purification by C18 column, a fraction contained anti-mushroom tyrosinase activity could be detected. Then, this fraction was subjected to the OFFGEL-fractionator at pH 3-10 and found two fractions, I-23 and I-24, containing mushroom tyrosinase inhibition activity and antioxidant activity. After further purification using the OFFGEL-fractionator at pH 6-11, fractions II-5 and II-13 with the desired activity were subjected to LC/MS spectrometry. Six synthetic peptides derived from LC-MS data analysis showed the ability to reduce mushroom tyrosinase activity as well as antioxidant activity. These results suggested that those 6 peptides might be novel tyrosinase inhibitor peptides that could be further developed for use in cosmeceuticals.

Introduction:

Melanin is a large pigment molecule that is produced and stored in melanosomes and is responsible for the color of human skin. Melanin is synthesized from the precursor, the amino acid L-tyrosine, with the key enzyme tyrosinase (EC 1.14.18.1) functioning as a catalyst to convert L-tyrosine into 3,4-dihydroxyphenylalanine (DOPA) and catalyze L-DOPA to dopaquinone then resulting in Indole-5,6-quinone which functions as a substrate for the subsequent processes that lead to melanin synthesis (Figure 1) ¹. The Raper-Mason pathway, or the oxidation of tyrosine to L-DOPA, is the first step of the sequence ². The conversion of tyrosinase to L-DOPA is considered the most important and the rate-limiting step in melanin production.

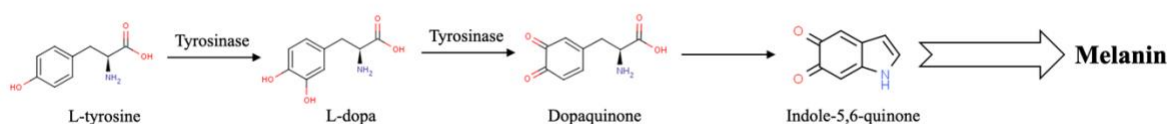


Figure 1.

Simplified melanin biosynthesis pathway with tyrosinase catalyzing two of the early steps from the amino acid L-tyrosine



Typically, eumelanin and pheomelanin are combined, resulting in a wide variety of human skin tones ³. One of the processes in place to protect the skin from UV radiation is skin darkening ⁴. UV light, for example, causes oxidative stress by increasing superoxide anion (O_2^-) and activating the tyrosinase enzyme which results in melanin production ². However, excessive melanin pigment accumulation results in undesirable cosmetic issues such as dark skin, sunburn, and freckles.

Due to the significant role of the tyrosinase enzyme in the melanin production, many skin-whitening products containing active substances can inhibit the activity for this enzyme ⁵. Commercialized skin depigmenting compounds like L-ascorbic acid, kojic acid, ellagic acid, tranexamic acid, and hydroquinone have been proven to result in negative effects when used constantly for a prolonged amount of time ⁶. The side effects include burns, dryness, peeling, and carcinogenicity. As a result, the usage of certain compounds must be limited. Hence, the search for novel compounds with safety and reduction in melanin pigment so as to prevent skin color problems continues to be in high demand.

A peptide, also known as a bioactive peptide, is a protein fragment that consists of amino acids linked in short chains of 2 to 30 amino acids. The biological activity of each peptide is determined by its structure, which includes its composition, amino acid sequence, from length, and terminal type (N- or -C). Peptides have been shown in studies to exhibit a variety of biological functions, including antioxidant activity ⁷, anti-hypertensive activity ⁸, antimicrobial activity ⁹, anti-inflammatory activity, anti-cancer, immunomodulatory activity, and anti-melanogenesis activity ^{10, 11}.

Many studies have revealed biologically active peptides obtained from various sources with varying biological activities. Some research has discovered harmless peptides that can inhibit the activity of the tyrosinase enzyme, resulting in decreasing melanin production. For example, Ochiai, et al. (2016) ¹² created a peptide known as decapeptide TH10 that can block the activity of the enzyme mushroom tyrosinase. In addition, peptides isolated from natural products have also been found to reduce melanin production as shown in the report from Ochiai, et al. (2016) ¹³ that the peptide CT-2 consists of Leu-Gln-Pro-Ser-His-Tyr isolated from rice bran was found to be safe and could reduce melanin production in B16F10 melanoma cells. Moreover, the report by Zhang, et al. (2020) ¹⁴ also found the peptides (Leu-Leu-Lys, Leu-Pro-Lys, and pyroGlu-Lys) from rice bran hydrolysates had ability to reduce melanogenesis by suppressing the microphthalmia-associated transcription factor (MITF) expression. There were various methods to obtain the biological peptides such as chemical synthesis, enzymatic hydrolysis, food processing and fermentation ¹⁵.

Previous study of Sangkaew and Yompakdee (2020) ¹⁶ found that the liquid obtained from the fermentation of unpolished black rice with specific microorganisms (fermented unpolished black rice sap; FUBRS) showed a reduction in melanin production in B16F10 melanoma cells, while samples obtained from the unfermented one showed no effect. FUBRS can stimulate the phosphorylation of p38 and extracellular signal-regulated kinases (ERK) leading to the destruction of important transcription factor MITF and also stimulates the phosphorylation of Akt that downregulates MITF expression, as a result decreasing expression of tyrosinase, tyrosinase-related protein 1 (TYRP1) and tyrosinase-related protein (TYRP2).

Therefore, this study has focused on searching for peptides derived from the FUBRS that have effective anti-tyrosinase activity to develop as depigmenting agents in cosmetic products.



Methodology:

1. Preparation of FUBRS

The preparation of FUBRS was performed as described, according to Sangkaew and Yompakdee (2020) ¹⁶.

2. Purification and identification of peptides from FUBRS

2.1 Sample purification

The FUBRS was applied to a reversed phase C18 HPLC column (3.9 x 150 mm; Waters, USA) and equilibrated with 0.1% formic acid. Next, the sample was eluted with 100% acetonitrile ¹⁷. Sample was collected and kept at -20 °C for further purification steps.

2.2 Peptide fractionation

Sample obtained from C18 HPLC column were extracted and used for peptide fractionation using 3100 OFFGEL fractionator and OFFGEL kit pH 3 – 10 (Agilent Technologies, CA, USA). Next, 0.72 mL of sample was mixed with 2.88 mL of peptide OFFGEL stock solution (1.25X). Later, the prepared protein solution was deposited on 24-well plate of immobilized pH gradient strips, and the proteins were separated by electric potential difference using a voltage of 200 V for 90 min, 2000 V for 90 min, 3,000 V for 90 min and 5,000 V until the voltage reached 64 kV/h ¹⁸.

2.3 Identification of peptides sequence by LC/MS

Each fraction from OFFGEL-fractionator with anti-mushroom tyrosinase and antioxidant activity was injected into liquid chromatography-mass spectrometry (LC/MS) ¹⁹. Amino acid sequences were identified through comparisons of experimentally obtained fragment masses and theoretical peptide masses of proteins in the Rice Annotation Project database ²⁰. All identified peptides that exceeded threshold values of 95% confidence interval levels ($p < 0.05$) would consider significant for this study. Then, selected peptide sequences were synthesized by Pepmic Co., Ltd., China.

3. Determination of mushroom tyrosinase activity

Peptides containing fractions from FUBRS were screened for anti-melanogenic activity by using mushroom tyrosinase. As described by Ochiai, et al. (2016) ¹³ with minor modifications, the reaction mixture was consisted of 50 µl of 2 mM L-tyrosine, 22.5 µl of 50 mM potassium phosphate buffer (pH 6.8), 5 µl of peptide. The mixture was incubated in the dark condition at 30 °C for 10 min. Subsequently, 62.5 µl of mushroom tyrosinase (400 U/ml), Sigma-Aldrich (MO, USA) was added and incubated in the same condition. The reaction was measured at 492 nm and calculated as the relative mushroom tyrosinase inhibition activity (%) as follow:

$$\text{Relative mushroom tyrosinase inhibition activity (\%)} = \left[\frac{\left(\frac{A-B}{A} \right)}{C} \right] \times 100$$

where A and B are the absorbance of the control without sample and with sample at 492 nm, respectively and C is the protein concentration of sample, respectively. Kojic acid at final concentration was 0.03 mg/ml as a positive control.



4. Determination of DPPH radical scavenging activity

The DPPH radical scavenging activity was performed as described by Brand-Williams and Cuvelier (1995)²¹ with modifications. The reaction consisted of 10 µl of peptide mixed with 90 µl of DPPH solution (0.025 mg/ml), Sigma-Aldrich (MO, USA). The mixture was incubated in dark condition at room temperature for 30 min. The absorbance was measured at 515 nm and calculated as the DPPH radical scavenging activity (%) as follow:

$$\text{DPPH radical scavenging activity (\%)} = \left(\frac{A-B}{A} \right) \times 100$$

where A and B are the absorbance of the control without sample and with sample at 515 nm, respectively. Ascorbic acid at final concentration was 0.015 mg/ml as a positive control.

5. Statistical analysis

All experiments were performed with three replications. The data were analyzed for statistically significant using Graphpad Prism by one-way analysis of variance (ANOVA). A *p*-value < 0.05 was accepted as significant.

Results and Discussion:

FUBRS contains high sugar contents so on to remove the sugars or the high polarity substance out of FUBRS for an easier next step of peptide purification. So, FUBRS was subjected to a C18 reversed HPLC column based on the difference in polarity²². Both fractions, bound (less polar) and unbound (high polar) were tested for their mushroom tyrosinase inhibition activity. The results indicated that both fractions could reduce the enzyme activity, in similarity with that of kojic acid as the positive control (Figure 2). In this study, we focused on bound fraction for further purification however the unbound fraction will be investigated in further study.

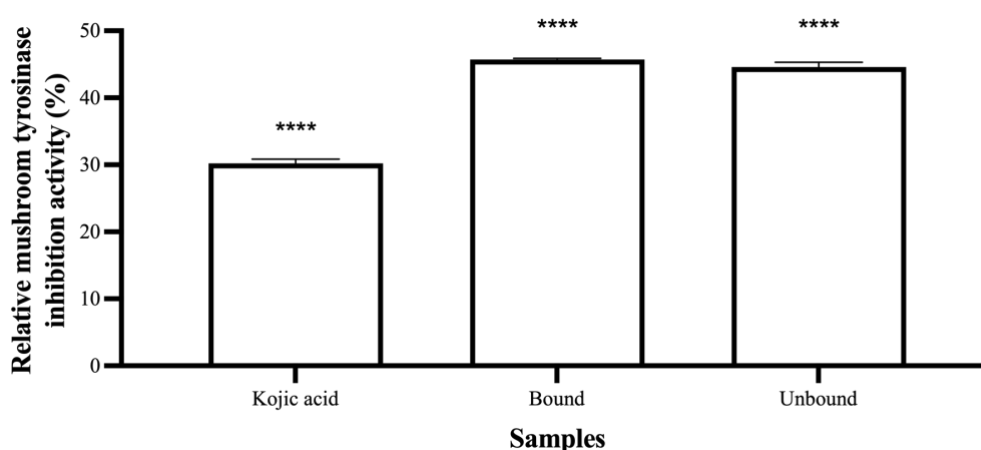


Figure 2.

Relative mushroom tyrosinase inhibition activity of fractions from C18 HPLC column. Kojic acid (0.03 mg/ml) was used as a positive control. All experiments were performed with three replications. Statistically significant differences compared with the untreated were indicated by ***p* < 0.05, *** < 0.01, and **** < 0.001.

Fraction from C18 HPLC column was injected into OFFGEL fractionator that separated peptides based on their isoelectric point (pI) with pH ranging from 3 to 10 and expected isoelectric point (pI) of each fractions were reported in Chenau, et al. (2008) ²³. The device was set up for the separation of 24 fractions and a 24 cm long IPG gel strip with a linear pH gradient. After testing of inhibition activity, fractions I-23 and I-24 showed the inhibition activity (Approximately from 65% - 70%) Since UV radiation causes free radicals, which could induce melanin production, the antioxidant may decrease melanin production ²⁴. Hence, both fractions were examined for antioxidant activity. Fraction I-23 and I-24 showed DPPH radical scavenging activity (Approximately from 35% - 40%). Therefore, these two fractions were further separated by OFFGEL fractionator that was setup using an 18 cm long IPG strip with pH ranging from 6 to 11.

The results showed that all of 17 fractions from the OFFGEL fractionation with a pH 6–11 exhibited mushroom tyrosinase inhibition activity. Notably, fractions II-5 and II-13, showed the highest relative mushroom tyrosinase inhibition activity, with the value of 122.50% and 191.85%, respectively (Table 1). In addition, most of the fractions displayed DPPH radical scavenging activity, except for fractions II-1 and II-13 (Table 1).

Table 1.

Mushroom tyrosinase inhibition activity and DPPH radical scavenging activity of separated 17 fractions. All experiments were performed with three replications and data represented the mean \pm SD. Statistically significant differences compared with the untreated control were indicated by ** p < 0.05, *** < 0.01, and **** < 0.001.

Number of fractions	Relative mushroom tyrosinase inhibition activity (%)	DPPH radical scavenging activity (%)
II-1	9.67 \pm 1.709	2.91 \pm 27.700
II-2	12.97 \pm 0.792	18.75 \pm 21.800
II-3	56.52 \pm 13.320 ***	43.33 \pm 4.714 **
II-4	90.05 \pm 30.220 ****	42.92 \pm 2.946 **
II-5	122.50 \pm 19.870 ****	47.42 \pm 1.369 ***
II-6	105.88 \pm 13.020 ****	46.67 \pm 7.071 ***
II-7	110.30 \pm 1.399 ****	49.58 \pm 0.589 ***
II-8	115.63 \pm 0.737 ****	50.83 \pm 3.536 ***
II-9	107.64 \pm 2.095 ****	47.50 \pm 4.714 ***
II-10	93.42 \pm 2.193 ****	57.08 \pm 0.589 ****
II-11	78.53 \pm 3.110 ****	44.17 \pm 4.714 **
II-12	111.25 \pm 4.605 ****	15.00 \pm 5.893
II-13	191.85 \pm 5.686 ****	0
II-14	110.58 \pm 17.480 ****	8.75 \pm 1.768
II-15	100.20 \pm 9.390 ****	12.92 \pm 6.482
II-16	105.85 \pm 5.133 ****	10.00 \pm 2.357
II-17	94.23 \pm 0.784 ****	13.75 \pm 7.660

After that, fractions II-5 and II-13 that showed the highest mushroom tyrosinase inhibition activity were selected for further purification and determination of the amino acid sequence using LC/MS spectrometry. Nineteen peptides out of 3,484 peptides obtained from fractions II-5 and II-13 were selected for further study, considering their intensity, scores, Q-value, and length of peptide sequences then the selected peptide sequences were synthesized by Pepmic Co., Ltd. (China). Figure 3 indicated that peptide sequence FR-6, FR-12, FR-13, FR-14, and FR-18 showed significant inhibition activity against mushroom tyrosinase. Moreover, they also showed DPPH radical scavenging activity (Figure 4). Among candidate peptides, peptide sequence FR-18 showed the highest anti-mushroom tyrosinase activity (Figure 3 and 4).

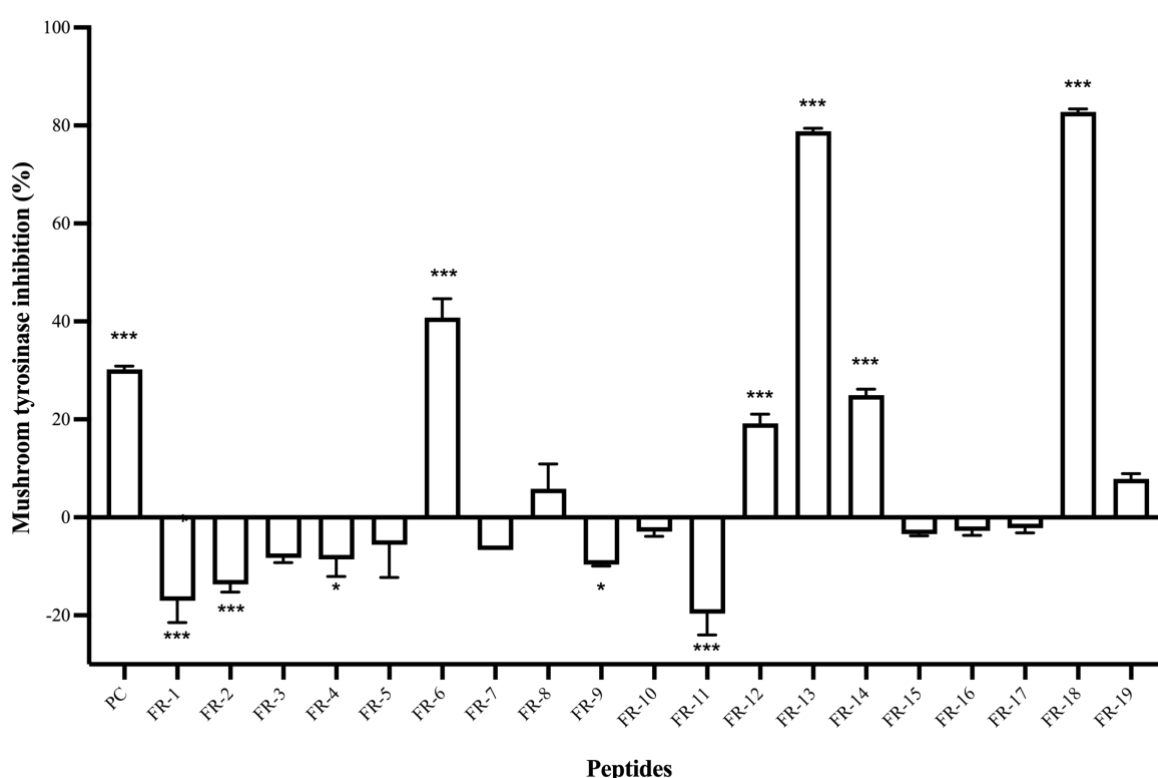


Figure 3.

Mushroom tyrosinase inhibition activity of each peptide. Kojic acid (0.03 mg/ml) was used as a positive control (PC). All experiments were performed with three replications. Statistically significant differences compared with the untreated control were indicated by ** $p < 0.05$, *** $p < 0.01$, and **** $p < 0.001$.

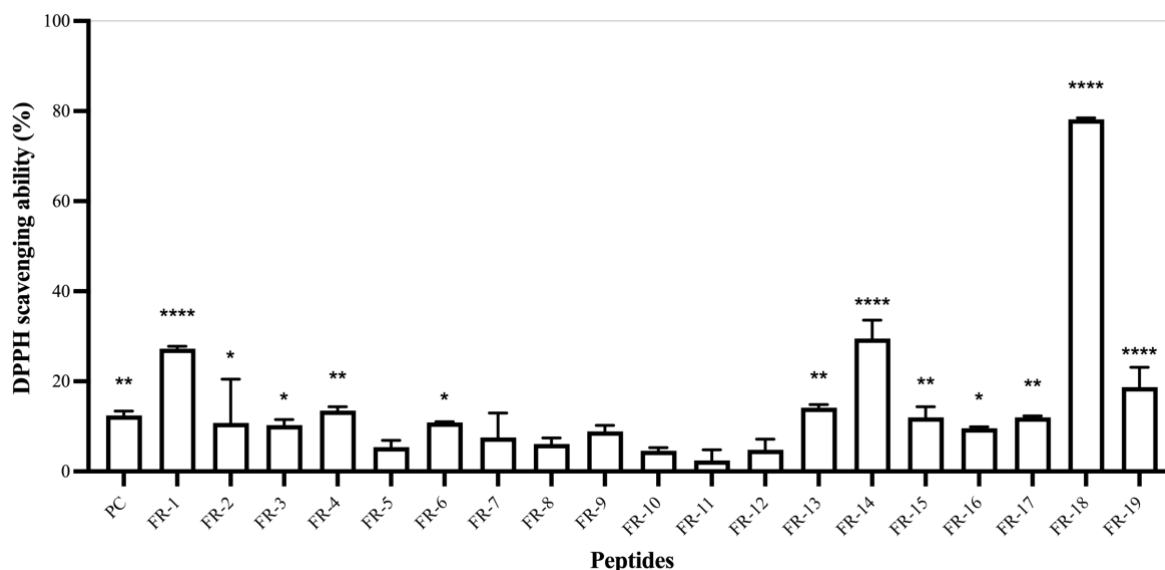


Figure 4.

DPPH radical scavenging activity of each peptide. Ascorbic acid (0.015 mg/ml) was used as a positive control (PC). All experiments were performed with three replications. Statistically significant differences compared with the untreated control were indicated by ** $p < 0.05$, *** < 0.01 , and **** < 0.001 .

Conclusion:

We have obtained new peptide sequences (peptide sequence FR-6, FR-12, FR-13, FR-14, and FR-18) derived from fermented unpolished black rice sap (FUBRS) that could inhibit mushroom tyrosinase activity and had radical scavenging effect, especially the peptide sequence FR-18. According to the findings, peptide sequences with mushroom tyrosinase inhibitory activity could be further developed as novel whitening agents in the cosmetic industry. Furthermore, these candidate peptide sequences will be investigated further for their mechanism on melanogenesis inhibition in mammalian cell lines.

Acknowledgements:

The authors thank the King Bhumibhol Adulyadej's 72nd Birthday Anniversary Scholarship and the 90th Anniversary of Chulalongkorn University Scholarship for financial supports.

References:

1. Wang N, Hebert DN. Pigment Cell Res. 2006;19(1):3-18.
2. Hearing VJ. J. Dermatol. 2011;131:E8-E11.
3. Slominski A, Tobin DJ, Shibahara S, Wortsman J. Physiol Rev. 2004.;84(4):1155-228.
4. Brenner M, Hearing VJ. Photochem. Photobiol.. 2008.;84(3):539-549.
5. Gillbro JM, Olsson MJ. Int. J. Cosmet. Sci. 2011;33(3):210-221.
6. Kwak YJ, Kim KS, Kim KM, Yu HY, Chung ES, Kim SJ, Cha JY, Lee YC, Lee JH. Biosci. Biotech. Biochem. 2011;75(5):841-847.

7. Shen Z, Wang Y, Guo Z, Tan T, Zhang Y, J Enzyme Inhib Med Chem. 2019;34(1):1633-1640.
8. Chen JW, Liu SS, Ye R, Cai GX, Ji B, Wu YN. J. Funct. Foods. 2013;5(4):1684-1692.
9. Kukowska M, Kukowska-Kaszuba M, Dzierzbicka K. Bioorganic Med. Chem. Lett. 2015;25(3):542-546.
10. Corpuz HM, Fuji H, Nakamura S, Katayama S. Brain Res. 2019;1720:1-12.
11. Martinez-Villaluenga C, Peñas E, Frias J. Fermented Foods in Health and Disease Prevention. 2017:23-47.
12. Ochiai, A, Tanaka S, Imai Y, Yoshida H, Kanaoka T, Tanaka T, Taniguchi M. J. Biosci. Bioeng. 2016;121(6):607-613.
13. Ochiai A, Tanaka S, Tanaka T, Taniguchi M. J. Nat. Prod. 2016;79(10):2545-2551.
14. Zhang R, Wei Y, Li M, Cai R, Ma Y, Chen L, Wang J. Food Funct. 2020;11(10):8757-8767.
15. Sánchez A, Vázquez A. Food Qual. Saf. 2017;1(1):29-46.
16. Sangkaew O, Yompakdee C. J. Microbiol. Biotechnol. 2020;30(8):1184-1194.
17. Crabb JW, Johnson C, West K, Buczylo J, Palczewski K, Hou J, McKeehan K, Kan M, McKeehan WL, Huddleston MJ, Carr SA. Techniques in Protein Chemistry IV. 1993;4:171-178.
18. Hörth P, Miller CA, Preckel T, Wenz C. Mol. Cell. Proteomics. 2006;5(10):1968-1974.
19. Ahmed FE. Expert Rev. Proteomics. 2008;5(6):841-64.
20. Tanaka T, Antonio BA, Kikuchi S, Matsumoto T, Nagamura Y, Numa H, Sakai H, Wu J, Itoh T, Sasaki T, Aono R, Fujii Y, Habara T, Harada E, Kanno M, Kawahara Y, Kawashima H, Kubooka H, Matsuya A, Nakaoka H, Saichi N, Sanbonmatsu R, Sato Y, Shinso Y, Suzuki M, Takeda J, Tanino M, Todokoro F, Yamaguchi K, Yamamoto N, Yamasaki C, Imanishi T, Okido T, Tada M, Ikeo K, Tateno Y, Gojobori T, Lin YC, Wei FJ, Hsing YI, Zhao Q, Han B, Kramer MR, McCombie RW, Lonsdale D, O'Donovan CC, Whitfield EJ, Apweiler R, Koyanagi KO, Khurana JP, Raghuvanshi S, Singh NK, Tyagi AK, Haberer G, Fujisawa M, Hosokawa S, Ito Y, Ikawa H, Shibata M, Yamamoto M, Bruskiewich RM, Hoen DR, Bureau TE, Namiki N, Ohyanagi H, Sakai Y, Nobushima S, Sakata K, Barrero RA, Sato Y, Souvorov A, Smith-White B, Tatusova T, An S, An G, Ota S, Fuks G, Fuks G, Messing J, Christie KR, Lieberherr D, Kim H, Zuccolo A, Wing RA, Nobuta K, Green PJ, Lu C, Meyers BC, Chaparro C, Piegu B, Panaud O, Echeverria M. The Rice Annotation Project Database (RAP-DB). 2008;36:1028-1033.
21. Brand-Williams W, Cuvelier ME, Berset C. LWT-Food Sci Technol. 1995;28(1):25-30.
22. Shen CH. Diagnostic Molecular Biology. 2019;187-214.
23. Chenau J, Michelland S, Sidibe J, Seve M. Proteome Sci. 2008;6:9-16.
24. Wang Y, Hao MM, Sun Y, Wang LF, Wang H, Zhang YJ, Li HY, Zhuang PW, Yang Z. Molecules. 2018;23(1):106-118.



SEQUENCING ANALYSIS OF INDEL1922 MARKER IN LOCAL RICE VARIETIES FROM SOUTH THAILAND

Kedsirin Ruttajorn*

Department of Biology, Faculty of Science and Digital Innovation, Thaksin University,
Phatthalung, Thailand

*e-mail: kedsirin@tsu.ac.th

Abstract:

In South Thailand, the *Oryza sativa indica* rice varieties is widely grown. However, the assessment of rice germplasm resources has been traditionally limited to morphological characteristics. To improve rice germplasm, molecular markers has applied as an important tool, offering powerful technical support and information for crop breeding, quality control of varieties, and molecular marker-assisted breeding. This research is focused on the application of insertion/deletion (InDel) markers and analysis of their sequences within the local rice varieties of Southern Thailand, specifically Khao Dawk Mali 105, Lep Nok Pattani, Sang Yod Phatthalung, and Chiang Phatthalung. Sequencing analysis was performed, aligning with five sequences retrieved from GenBank. The results revealed that the InDel marker produced amplicons with a length of 249 bp, mainly corresponding to the *indica* group. In contrast, other InDel lengths ranging from 33 to 36 bp were observed in the sequences associated with the *japonica* group. Furthermore, microsatellite and single nucleotide polymorphism (SNP) genotypes were also identified. The microsatellite presented repeats of AAT, spanning from (AAT)₅, (AAT)₁₆, to (AAT)₁₇, while an A/T transversion was detected in the SNP. The marker revealed high concordance between AAT-microsatellite repeat and two-rice subspecies indicating that the result could be used to determine the *indica* and *japonica* subspecies. Remarkably, there was a strong correlation between the AAT-microsatellite repeat and the two rice subspecies, suggesting that this marker could be used effectively to distinguish between *indica* and *japonica* rice subspecies.

Introduction:

Different rice varieties consist of two major subspecies: *Oryza sativa* spp. *indica* and *O. sativa* spp. *japonica*. These subspecies are highly distinct in morphology characters and geographical distribution. The *japonica* subspecies known as glutinous rice, is a short-grain, erect plant with compact panicles and oval to round grains. These varieties are found mainly in Japan. On the other hand, the *indica* subspecies, are known for their non-glutinous rice, tall, spreading plant types with diversity in the morphological traits. These are extensively cultivated across tropical and sub-tropical regions throughout Asia.^{1,2} Thailand cultivates substantial quantities of *indica* rice. One of the widely recognized high-quality rice varieties is known as jasmine rice, referred to as Khao Dawk Mali 105. In the southern region, there exists a high genetic diversity of local rice varieties, such as Sang Yod Phatthalung and Chiang Phatthalung, characterized by long grains and slender-shaped seeds, while the Lep Nok Pattani variety features short grains and medium-shaped seeds. The size of the grain significantly impacts both the yield and quality of rice.³ As a result, grain size stands as a key target trait in efforts to enhance rice yield within the breeding program. Nonetheless, understanding the relationship between genetic background and characteristic traits remains unclear. Fortunately, molecular markers offer an efficient way of overcoming these limitations. Among them, InDel

markers stand out due to readily genotype based on fragment length polymorphism in insertion/deletion (InDel) DNA fragments. This simplicity and accessibility make InDel markers a valuable tool. To date, InDel markers are widely used in genotyping, genetic diversity analysis and even marker-assisted selection in various studies and breeding programs.

A previous study introduced the InDel marker to demonstrate that the InDel marker is a robust tool for accurately and efficiently identifying rice germplasm, distinguishing between *indica* and *japonica* rice.⁴ Moreover, the InDel1922 marker is associated with the putative WAX2 protein and its relation to drought and salt stress in rice.⁵ This marker was instrumental in determining genetic variation in rice populations. The use of DNA markers in plant breeding has significantly impacted crop development, with PCR-based DNA marker protocols becoming a standard in plant genomic analysis. Advances in various aspects of plant genetics have deepened our understanding of DNA markers, genetic diversity within plant species, and have greatly contributed to the success of plant molecular breeding.⁶

In this research, the InDel marker was used to assess local *indica* rice varieties in Southern Thailand. Sequences from this analysis are compared with those of *indica* and *japonica* rice from GenBank. Consequently, this research is helpful in screening samples for enhancing rice breeding programs.

Methodology:

DNA extraction

Four *indica* rice varieties, *O. sativa* L. spp. *indica*, were derived from the Phatthalung Rice Research Center in South Thailand. These varieties include Khao Dawk Mali 105 (KDML 105), Lep Nok Pattani (LNP), Sang Yod Phatthalung (SYP) and Chiang Phatthalung (CHP). To extract DNA for analysis, a pooling of two-week-old young fresh leaves from five individuals was initially ground into a fine powder using liquid nitrogen resulted in better yields and purity of DNA. Subsequently, DNA extraction followed a modified Doyle and Doyle⁷ methodology, which based on a 2% CTAB extraction buffer consisting of 100 mM Tris-HCl at pH 8.0, 20 mM EDTA, and 1.4 M NaCl. During the lysis step, the lysate was incubated at 65 °C for 30 min, shook and vortexed every 5 min resulted in higher yields than simply inverting. To assess the quantity and quality of the extracted DNA, measurements were conducted using a Nanodrop, specifically the NanoDrop One microvolume UV-Vis spectrophotometer from Thermo Fisher, with readings taken at OD 260/280. The DNA was stored at -20°C for further analysis and use.

InDel marker

The InDel1922 marker was amplified using the PCR technique. Genomic DNA served as the template for amplifying the *WAX2* region, and this process involved the use of a primer set, according to the previous studied (forward primer: 5'-GTGGTGCTCCCACCCTTC-3' and reverse primer: 5'-TTCCTCCGTTTCATATTACAGTCA-3').⁵

PCR reactions were carried out in a total volume of 25 µL using the Biometra TOne Thermal Cycler (Analytik Jena). PCR mixtures contained: 1X ViBuffer A, 1.5 mM of MgCl₂, 0.4 mM of each primer, 0.2 mM of each dNTPs, and 1.25 U of *Taq* DNA polymerase (Vivantis). Additionally, each reaction contained 100 ng of template DNA. The PCR cycling conditions were as follows: an initial denaturation step at 94 °C for 5 minutes, followed by 35 cycles of denaturation at 94 °C for 30 seconds, annealing at 55 °C for 30 seconds, and extension at 72 °C for 30 seconds. The reaction was finalized with an extension step at 72 °C for 5 minutes. After the PCR amplification, all of the resulting products were separated by electrophoresis on 2% agarose gels in 0.5X Tris-acetate-EDTA (TAE) buffer. These gels were

stained with ViSafe Red Gel Stain and subsequently visualized under UV light using the Gel Doc™ EZ System (Bio-Rad).

Sequencing analysis

Following the PCR amplification, the DNA fragments were separated based on size through agarose gel electrophoresis. Once the electrophoresis was completed, the desired DNA bands were excised from the agarose gel, and the DNA fragments were purified using the E.Z.N.A. Gel Extraction Kit from Omega Bio-Tek, USA, following the manufacturer's protocol.

For further analysis, Sanger direct sequencing was conducted by Ward Medic Ltd. in Bangkok, Thailand. To assess DNA polymorphism, the MISA tool⁸ (<http://pgrc.ipk-gatersleben.de/misa/>) was employed. The obtained sequences were aligned and processed to produce interpretable results using QIAGEN CLC Main Workbench 21.0 from QIAGEN in Aarhus, Denmark. Additionally, sequences from available databases of rice varieties were downloaded from GenBank (<https://www.ncbi.nlm.nih.gov/>). These databases included two major subspecies: the *indica* group, which comprised Minghui 63, Zhenshan 97, and Shuhui 498 (with accession numbers CP054677, CP056053, and CP018158, respectively), and the *japonica* group, consisting of Nipponbare, and Changxianggeng 1813 (with accession numbers NW_015379175, and CP101148, respectively).

Results and Discussion:

The amplicons of InDel1922 marker in local rice *indica* varieties from the Southern region of Thailand were found to be 249 bp in size (**Fig. 1**). Subsequently, the nucleotide dataset derived from the amplicon sequencing of the four local rice varieties, along with sequences retrieved from GenBank (five varieties), was used for alignment, and the results are represented in **Fig. 2**. This alignment indicated the utility of the InDel1922 marker in distinguishing between *indica* and *japonica* subspecies within the rice germplasm.

Furthermore, the InDel1922 marker revealed a novel microsatellite that was closely associated with a single nucleotide polymorphism (SNP). The microsatellite consisted of 3-base pair repeats, with sequences of 249 bp and 33 to 36 bp in different lengths. These sequences contained (AAT)_n repeats, where n ranged from 5 to 16 and 17. Notably, three different alleles of the (AAT)_n repeat were identified: the *indica* group contained the (AAT)₅ allele, while the *japonica* group featured the (AAT)₁₆ and (AAT)₁₇ alleles.

This utilization of InDel markers for distinguishing between *indica* and *japonica* groups is consistent with previous research, as reported by Lu et al. (2009)⁴, Prathepha and Srisa-ard (2014)⁹, Whankaew et al. (2020)⁵ and Long et al. (2022)¹⁰. Furthermore, various DNA markers have been explored for classifying major rice subspecies, such as RAPD^{11,12}, SSR¹³ and STS¹⁴. The InDel1922 marker, specifically, demonstrates allele discrimination to the differentiation of major rice subspecies. Moreover, DNA fragment sequence analysis amplified from the InDel1922 marker revealed polymorphic microsatellites and led to SNP identification. The observed polymorphism of InDel1922 between *indica* and *japonica* groups might be associated with adaptations in the rice cultivation region. *Japonica* varieties are adapted to more temperate climates, while *indica* varieties are typically suited for tropical lowland cultivation¹⁵, leading to variations in the number of AAT-microsatellites. InDel polymorphism usually affects gene function. Therefore, the InDel1922 marker related to putative drought and salt stress gene will be useful for genetic research and the development of gene-based InDel marker.

The SNP was positioned immediately after the microsatellite repeat region, with one nucleotide variation observed in nine different varieties. Among these, five had the nucleotide T, while the remaining four had A. By combining the information from the AAT-microsatellite

with the A-T SNP, a total of four haplotypes were identified (**Table 1**). This combination of the microsatellite and linked SNPs can be considered a small haplotype¹⁶, making it a potentially valuable tool in the field of population genetics.

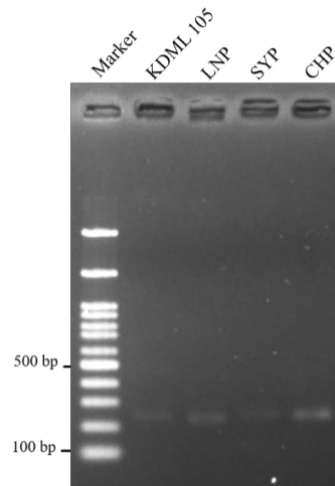


Figure 1.
The amplicons of the InDel1922 marker in local rice varieties.

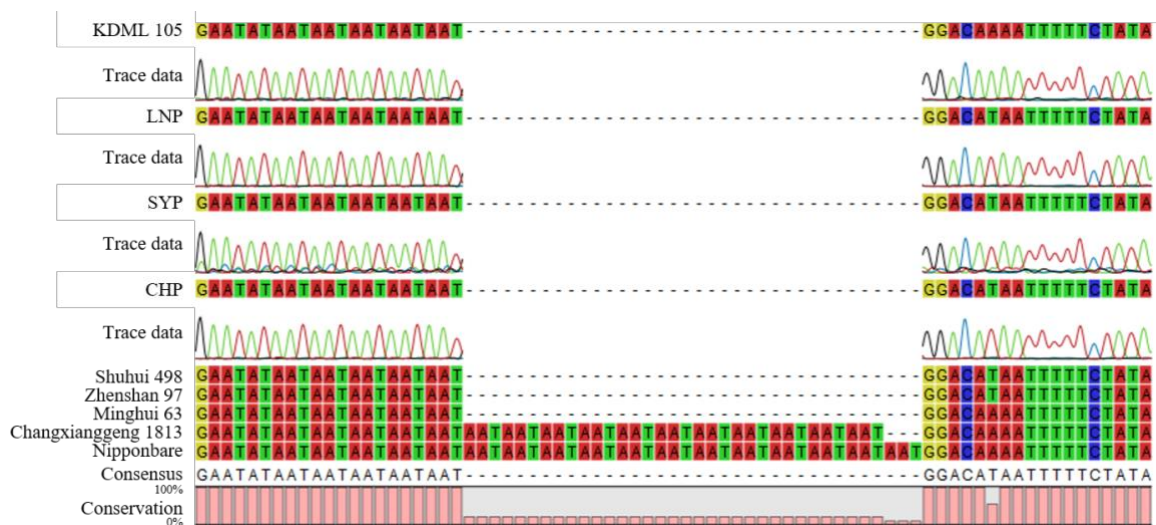


Figure 2.
The sequencing results revealed a novel AAT-microsatellite, featuring repeats ranging from (AAT)₅, (AAT)₁₆ to (AAT)₁₇, along with a SNP involving an A/T variation within the two distinct rice subspecies.

**Table 1.**

The sequence analysis, an ATT-microsatellite repeat and a SNP with A/T alleles were identified.

Subspecies	Varieties	Microsatellite	SNP
<i>Indica</i> rice	KDML 105	(AAT) ₅	A
	LNP	(AAT) ₅	T
	SYP	(AAT) ₅	T
	CHP	(AAT) ₅	T
	Minghui 63 (CP054677)	(AAT) ₅	A
	Zhenshan 97 (CP056053)	(AAT) ₅	T
	Shuhui498 (CP018158)	(AAT) ₅	T
<i>Japonica</i> rice	Nipponbare (NW_015379175)	(AAT) ₁₇	A
	Changxianggeng 1813 (CP101148)	(AAT) ₁₆	A

Conclusion:

The InDel1922 marker associated with drought and salt stress displayed a monomorphic band among *indica* subspecies. However, when the sequences were aligned with those retrieved from the *japonica* subspecies in GenBank, it became evident that there were distinct groupings between the *indica* and *japonica* subspecies. Furthermore, during the sequence analysis, an ATT-microsatellite and a SNP featuring an A/T transversion were observed.

The results of this analysis indicated a strong agreement between the insertion/deletion region and the microsatellite among the subspecies in the rice germplasm. This result suggests that genetic variation has remained notably higher between subspecies variation, supporting the genetic distinctiveness between *indica* and *japonica* rice varieties.

Acknowledgements:

This work has been supported by Department of Biology, Faculty of Science and Digital Innovation, Thaksin University.

References:

1. Khush GS. Plant Mol Biol. 1997;35:25–34.
2. Garriss AJ, Tai TH, Coburn J, Kresovich S, McCouch S. Genetics. 2005;169:1631–1638.
3. Li P, Chen YH, Lu J, et al. Rice. 2022;15–18.
4. Lu BR, Cai X, Jin, X. Prog Nat Sci. 2009;1241–1252.
5. Whankaew S, Kaewmanee S, Ruttajorn K, et al. Physiol Mol Biol Plants. 2020;26(6):1237–1246.
6. Amiteye S. Heliyon. 2021;7:e08093.
7. Doyle JJ, Doyle JL. Focus. 1990;12:13–15.
8. Beier S, Thiel T, Münch T, et al. Bioinform. 2017;33:2583–2585.
9. Prathepha P, Srisa-ard K. Thai J Genet. 2014;7(2):87–96.
10. Long W, Li Y, Yuan Z, et al. PLoS One. 2022;17:e0274418.
11. Yu LX, Nguyen HT. Theor Appl Genet. 1994;87:668–672.
12. Chinn JH, Kim JH, Kwon SW, et al. Korean J Breed. 2003;35:1–7.
13. Pal S, Jain S, Saini N, et al. Indian J Biotechnol. 2004;3:519–526.
14. Chinn JH, Kim JH, Jiang W, et al. J Crop Sci Biotech. 2007;10:175–184.
15. Johns MA, Mao L. Funct. Intergr. Genomics. 2007;7:135–151.
16. Agrafioti I, Stumpf MPH. Nucleic Acids Res. 2007;35:D71–D75.



Short Chain Fatty Acids Derived from Probiotic *Lactobacillus* Strains Inhibit the Accumulation of Lipids in 3T3-L1 Adipocytes

Oranit Sriwichian¹, Nuntiya Pahumunto², Rawee Teanpaisan², Suchera Thananimit^{1,3*}

¹Program in Molecular Biotechnology and Bioinformatics, Division of Biological Science, Faculty of Science, Prince of Songkla University, Songkhla 90112, Thailand

²Department of Oral Diagnostic Sciences, Faculty of Dentistry, Prince of Songkla University, Songkhla 90110, Thailand

³Center for Genomics and Bioinformatics Research, Faculty of Science, Prince of Songkla University, Songkhla 90112, Thailand

*Email: s.thananimit@yahoo.com

Abstract:

Short Chain Fatty Acids (SCFAs) are one of the numerous compounds produced by probiotic bacteria that are involved in metabolic processes. However, their roles in lipid metabolism and the underlying mechanisms are still unknown. In this investigation, the effect of SCFAs metabolites produced in the MRS culture medium of various probiotic bacteria including (*Lactobacillus paracasei* SD1, *Lactobacillus rhamnosus* SD11, *L. paracasei* SD1 and *L. rhamnosus* SD11, and *Lactobacillus rhamnosus* GG) was examined. This study focused on propionic acid (PA) which could inhibit the fat production of adipocytes. The highest PA production was obtained with the combination of *L. paracasei* SD1 and *L. rhamnosus* SD11 during probiotics fermentation at 24 hours and 45 °C. The SCFAs lyophilized powder of these combinations was then applied to adipocyte cells. The MTT assay revealed that SCFAs lyophilized powder was not cytotoxic to 3T3-L1 adipocytes. The intracellular lipid accumulation was reduced by observation using Oil Red O staining. Additionally, the total phenolic content (TPC) and antioxidant activities of cell-free supernatants obtained from all probiotic isolates were investigated. SCFAs lyophilized powder of *L. paracasei* SD1 had the maximum TPC (1103.01 ± 38.95 mg of gallic acid equivalents (GAE) per gram of SCFAs lyophilized powder). However, the greatest antioxidant activity was obtained from *L. paracasei* SD1 and *L. rhamnosus* SD11. These findings suggest that SCFAs obtained from the MRS culture medium of studied probiotic bacteria could be utilized as functional fermented foods.

Introduction:

Short chain fatty acids (SCFAs) are primarily produced by the fermentation of dietary fiber by the microbiota. There are three main volatile acids, which include acetic acid, propionic acid, and butyric acid¹. Recent evidence suggests that SCFAs play a significant role in human health, particularly in the development of metabolic disorders associated with an imbalance in the intestinal microbiota that leads to obesity². The SCFAs could also exert an anti-obesity effect via other different pathways. SCFAs act as signal transduction molecules by binding and activating cell surface G-protein-coupled receptors, e.g., GPR 41 and GPR 43. This activation might affect the intestine and host metabolism resulting in an increase of the satiety hormones; PYY and GLP-1 and through the inhibition of HDACs³. SCFAs can also improve glucose homeostasis in an AMPK-dependent manner involving PPARγ-regulated effects on gluconeogenesis and lipogenesis⁴. SCFAs can stimulate adipocyte differentiation

and decrease lipid plasma levels through the inhibition of lipolysis and stimulation of lipogenesis and cholesterol plasma levels, enhancing its hepatic uptake. Among SCFAs, propionate enhances glucose-stimulated insulin release via GPR-43 and increases β -cell mass⁵.

Therefore, the objective of this research is to examine the effect of short chain fatty acids (SCFAs) on the accumulation of lipids in the 3T3-L1 adipocyte cell model. Additionally, this study aimed to explore the potential of enhancing systemic SCFA levels by means of dietary supplementation. The quantification of propionic acid, derived from certain probiotic strains (*L. paracasei* SD1, *L. rhamnosus* SD11, and LGG; commercially available probiotics), was conducted to represent SCFAs. The *in vitro* study investigated the effect of several doses of lyophilized powder containing SCFAs on 3T3-L1 adipocytes. Furthermore, the total phenolic content (TPC) and antioxidant activity of SCFAs lyophilized powder were evaluated for different probiotic strains. The SCFAs lyophilized powder exhibits potential as a replacement for live probiotic cells in food applications and has shown efficacy in the uncomplicated production of postbiotic products⁶.

Methodology:

Preparation of SCFAs lyophilized powder produced by bacteria probiotics

The probiotic strains include *L. paracasei* SD1, *L. rhamnosus* SD11, a combination of *L. paracasei* SD1 and *L. rhamnosus* SD11, and *L. rhamnosus* GG (ATCC 53103) (LGG). These strains were obtained from the Department of Oral Diagnostic Sciences at the Faculty of Dentistry, Prince of Songkla University. The bacterial strains were incubated for cultivation at a temperature of 45 °C for 24 hours in MRS broth. The cells of each strain were separated by centrifugation at 8500 rpm for 10 minutes at 4 °C, and 100 ml of the supernatant of MRS culture medium was prepared as a powder by freeze-drying method. For SCFAs extraction, the lyophilized powder was then dissolved in 10 ml of ultrapure water and mixed with 4 g of NaCl, 2 ml of H₂SO₄ (50% v/v), and 5 ml of pure diethyl ether. Then SCFAs were extracted by shaking for 30 minutes in a reaction vessel. After centrifugation at 5000 rpm for 10 minutes at 4 °C, the upper diethyl ether fractions were collected and subsequently allowed for air-dried at 25 °C. Next, they were suspended in 200 μ l of PBS and examined for propionic acid concentration using gas chromatography-flame ionization detection (GC-FID) (Agilent 7890A GC system with a flame ionization detector, Agilent Technologies Inc., Santa Clara, CA, USA) and a GC column (Agilent J & W GC column DB-FATWAX UI; 30 m \times 0.25 mm \times 0.25 μ m). The injected sample for analysis was 1 μ l. A calibration curve of propionic with a GC grade purity (Sigma Aldrich, St. Louis, MO, USA) ranging from 0.08 to 50 mM was used for quantification of propionic acid with the Agilent ChemStation plus software.

Cell culture and differentiation

3T3-L1 cells (mouse immortalized fibroblasts) preadipocytes are cultured in DMEM supplemented with 10% FBS, 1% amphotericin b, and 1% Penicillin-Streptomycin (P/S) under humidified conditions (5% CO₂, 37 °C). The 3×10^4 3T3-L1 cells were seeded in a 24-well plate and grown until 100% confluence. For adipocyte differentiation, the cell culture medium is changed to DMEM medium containing 10% FBS and 1% penicillin-streptomycin



(P/S) with differentiation solutions consisting of 0.5 mM IBMX, 1 μ M DEX, and 10 μ g/ml insulin (Day0). Subsequently, the cell culture medium was changed to DMEM containing 10% FBS and 10 μ g/ml insulin (Day 3), and the medium was replaced every 3 days until analysis (Day 9). On day 9, 3T3-L1 cells were fixed and stained with 0.5% Oil Red O solution to evaluate the accumulation of lipids in 3T3-L1 cells.

Cell viability of 3T3-L1 cells

The cytotoxic effect of SCFAs lyophilized powder was evaluated via MTT assay. The 3T3-L1 preadipocytes were seeded on a 96-well plate at a density of 5×10^3 cells/well. Cells were grown in DMEM until confluency of 80%. The 3T3-L1 cells are treated with various concentrations of SCFAs lyophilized powder (5 and 10 μ M of PA) and then incubated for 24 hours. Subsequently, 20 μ l of 5 mg/ml solution of MTT was added to each sample and incubated for 4 hours. The formazan crystals were dissolved in DMSO and the absorbance at 570 nm was measured using a microplate reader. Percentage cell viability was calculated using absorbance of sample/absorbance of control (MTT solution without sample) \times 100.

Lipid accumulation by Oil Red O staining

Adipocyte cells on day 0, 3, and 6 were treated with different concentrations of propionic acid. On day 9, the differentiated 3T3-L1 cells were rinsed twice with PBS, fixed with 1 ml of 10% buffered formalin at room temperature for 1 hour followed by washing with 60% isopropanol. The cellular lipids were stained with 0.5% Oil Red O solution for 1 hour. Then the cells were washed twice with distilled water. The cells were observed under an inverted microscope (LionheartTMFX Automated Microscope, BioTek Instruments Inc., Winooski, VT, USA).

DPPH radical scavenging assay

Free radical scavenging activity of different SCFAs lyophilized powder obtained from probiotics was measured by 1,1-diphenyl-2-picrylhydrazyl (DPPH) radical with the modified method from Brand-Williams et al. Briefly, the stock solution of 24% w/v of DPPH solution was prepared with analytical grade methanol and stored at 4 °C. The SCFAs lyophilized powder was dissolved in DI water in order to prepare 20 mg/mL stock sample solutions and then serial dilution with DI water was performed to prepare the required concentrated solutions (900, 1200, 1500, 1800, 2100, 2400 μ g/mL). A 30 μ l of SCFAs solution from each concentration was taken in a microplate well and 170 μ L of DPPH solution was then added to each well. The mixture was kept in complete darkness for 30 minutes. The absorbance was measured at wavelength 515 nm using and ascorbic acid as a positive control. Each sample was conducted in triplicate. The percentage of scavenging activity was calculated according to $[A_{\text{control}} - (A_{\text{sample}} - A_{\text{blank}})] / A_{\text{control}} \times 100$, where A_{control} = the absorbance of DPPH solution, A_{sample} = the absorbance of the sample and DPPH solution, and A_{blank} = the absorbance of the sample with methanol. The 50% inhibitory concentration; IC₅₀ was obtained from linear regression analysis and used to evaluate the antioxidant capacity of each sample.

Determination of TPC

The TPC of the SCFAs lyophilized powder was spectrophotometrically determined using the Folin–Ciocalteu method. Aliquots of 25 μl of the SCFAs lyophilized powder (10 $\mu\text{g}/\mu\text{l}$) were mixed with 100 μl of 25% (V/V) Folin–Ciocalteu reagent in a 96-well microplate. After 4 minutes, 75 μl of 10% (W/V) Na_2CO_3 was then added and incubated at room temperature for 2 hours. The absorbance of the incubated solution was determined at 750 nm using a microplate reader (Thermo Scientific™ Varioskan™ LUX multimode microplate reader). Total phenolic contents were reported as gallic acid equivalents (mgGAE/g dry mass). Each sample was conducted in triplicate.

Results and Discussion:

Determination of PA concentration in SCFAs lyophilized powder

The PA concentration of the SCFAs lyophilized powder produced from various probiotics strains by cultivation at 24 hours at 45 °C was analyzed using GC-FID. The results demonstrated that the combination of *L. paracasei* SD1 and *L. rhamnosus* SD11 can produce the highest concentration of PA (16.50 \pm 0.16 mM) compared to other probiotics, as shown in Table 1. There are also significant differences between the various probiotic strains. This result supported our previous work that the combination of probiotic strains exhibited strong SCFAs producer compared to the individual strain. Thus, this strain combination was chosen to test in the cell model.

Table 1 PA concentration produced from various probiotic strains

Probiotic	PA concentration (mM)
<i>L. paracasei</i> SD1	14.77 \pm 0.08 ^D
<i>L. rhamnosus</i> SD11	15.05 \pm 0.08 ^B
<i>L. paracasei</i> SD1 and <i>L. rhamnosus</i> SD11	16.50 \pm 0.16 ^A
LGG	14.93 \pm 0.06 ^C

Uppercase letters show significant differences between different probiotic strains (A-D) at the same incubation time for 24 hours at 45 °C ($P < 0.05$). Statistical analysis was performed with the Kruskal–Wallis test, followed by the Mann–Whitney U test.

Effect of SCFAs lyophilized powder on lipid accumulation

MTT assay

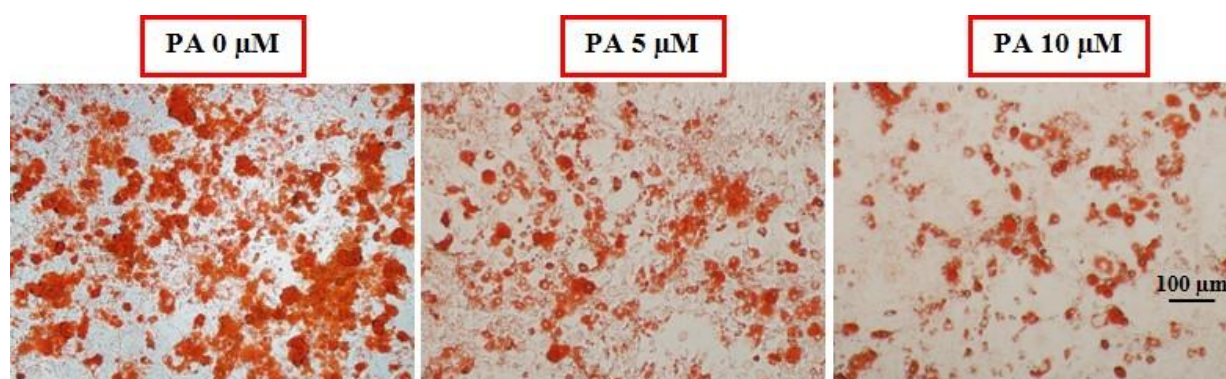
To evaluate the cytotoxicity, the cells were then treated with the SCFAs lyophilized powder derived from the combination of *L. paracasei* SD1 and *L. rhamnosus* SD11. The PA concentrations treated were 5 and 10 μM . The cell viability of PA at 10 μM was slightly decreased comparing to control (0 μM); 95.62 \pm 0.33%. However, MTT results revealed that the lyophilized powder of SCFAs has no cytotoxic effect on preadipocyte 3T3-L1 cells followed by ISO 10993-5 (Table 2). In the subsequent investigation, the SCFAs lyophilized powder at these concentrations was applied.

Table 2 Cell viability by MTT assay

PA concentration (μM)	Cell viability Percentage
0	101.63 ± 1.94
5	97.69 ± 3.04
10	95.62 ± 0.33

Oil Red O staining

To investigate the effects of SCFAs lyophilized powder on lipid accumulation in the adipocyte 3T3-L1 cell, Oil Red O staining was performed. In the differentiation state, the cell morphology progressively altered from an original fiber form (fibroblast cell) to a circular shape. Figure 1 displays a decrease in lipid droplets (red spot) in both PA concentrations of 5 and 10 μM when compared to the control group. These results suggest that SCFAs lyophilized powder dose-dependently inhibited lipid accumulation in 3T3-L1 adipocytes. The formation of lipid accumulation was found to be significantly reduced when cell-free metabolites (CM), particularly SCFAs derived from *Bacillus ginsengihumi*-RO6 (CMRO6) were present at a concentration of 100 $\mu\text{g/ml}$, in comparison to the control group and other concentrations⁷. Moreover, the SCFAs lyophilized powder at 5,000 $\mu\text{g/ml}$ inhibited lipid accumulation in this investigation. Various concentrations of SCFAs produced by distinct isolates may therefore have an inhibition effect at different levels on 3T3-L1 adipocytes. Additional consideration is given to the dose dependence of the total metabolite concentrations investigated in the cell model. Among the metabolites of the postbiotics, the function of SCFAs could protect against diet-induced obesity^{4,8}. In particular propionic acid (PA) has an effect on decreasing cholesterol synthesis by inhibiting the activity of the enzyme acetyl-CoA synthetase, acting as a precursor for hepatic gluconeogenesis thereby decreasing the hepatic synthesis of cholesterol and inhibiting the expression of resistance in human adipose tissue⁹. Nevertheless, additional investigation of alternative metabolites that inhibit lipid accumulation is also required.

**Figure 1** Effects of SCFAs lyophilized powder on lipid accumulation in 3T3-L1 adipocytes.
Determination of antioxidant capacity and TPC of SCFAs lyophilized powder
DPPH assay

The antioxidant activity was studied by using a DPPH assay. Then, the IC_{50} value was calculated to determine the concentration of the sample required to inhibit 50% of the radical. The lower the IC_{50} value, the greater the antioxidant activity of the SCFAs lyophilized powder as a beneficial bioproduct derived from probiotics. In Table 3, the IC_{50} values of the

combination of *L. paracasei* SD1 and *L.rhamnosus* SD11 exhibited the significantly highest antioxidant activity ($1153.59 \pm 66.97 \mu\text{g/ml}$) followed by *L. paracasei* SD1 ($1329.59 \pm 33.89 \mu\text{g/ml}$), LGG ($1408.03 \pm 36.24 \mu\text{g/ml}$), and *L. rhamnosus* SD11 ($1681.59 \pm 48.98 \mu\text{g/ml}$) respectively. According to another study reported that the scavenging activity of lyophilized cell-free supernatant (LCFS) of *Lactobacillus* isolates is in the range of 115.9 ± 0.47 – $117.2 \pm 0.26 \mu\text{g/ml}$ ¹⁰ since the phenolics and flavonoids are the major compounds responsible for the greater antioxidant activities. While the major metabolite of our work was SCFAs.

TPC assay

The results of total phenolic content indicated that the SCFAs lyophilized powder produced from *L. paracasei* SD1 contained the maximum levels of phenolic content ($1103.01 \pm 38.95 \text{ mgGAE/g powder}$) compared to other probiotics, and there were significant differences between different probiotic strains (Table 3). The TCP value of the LCFS of *Lactobacillus* in a previous investigation ranged from $202.7 \pm 1.42 \mu\text{gGAE/g}$ to $283.4 \pm 11.91 \mu\text{gGAE/g}$, which is lower than the phenolic content in our studied probiotics¹⁰.

Table 3 IC₅₀ value and TPC of the SCFAs lyophilized powder

SCFAs lyophilized powder sample	IC ₅₀ ($\mu\text{g/ml}$)	TPC (mgGAE/g powder)
<i>L. paracasei</i> SD1	$1329.59 \pm 33.89^{\text{B}}$	$1103.01 \pm 38.95^{\text{A}}$
<i>L. rhamnosus</i> SD11	$1681.59 \pm 48.98^{\text{D}}$	$946.97 \pm 34.73^{\text{D}}$
<i>L. paracasei</i> SD1 and <i>L. rhamnosus</i> SD11	$1153.59 \pm 66.97^{\text{A}}$	$1020.59 \pm 23.89^{\text{B}}$
LGG	$1408.03 \pm 36.24^{\text{C}}$	$980.24 \pm 25.49^{\text{C}}$

Uppercase letters show significant differences between different probiotic strains (A-D) at the same incubation time for 24 hours at 45 °C ($P < 0.05$). Statistical analysis was performed with the Kruskal–Wallis test, followed by the Mann–Whitney U test.

Conclusion

The present study revealed that SCFAs lyophilized powder from the probiotic bacteria *L. paracasei* SD1 and *L. rhamnosus* SD11 with the highest concentration of propionic acid exhibit the suppression of lipid accumulation in 3T3-L1 cell *in vitro*. Additionally, SCFAs lyophilized powder produced from various probiotics has different phenolic content and antioxidant activities. The next study will focus on elucidating the mechanism underlying the effect of SCFAs and the *in vivo* investigation for preventing or treating obesity.

Acknowledgements

This research was supported by the Scholarship as a research assistant from the faculty of science and the Prince of Songkla University Research Fund (SCI6601196S) from the Fundamental Fund: FF, Prince of Songkla University. The authors also would like to thank the Program in Molecular Biotechnology and Bioinformatics, Division of Biological Science, Faculty of Science and Department of Oral Diagnostic Sciences, Faculty of Dentistry for facilitating all equipment.

References:



1. Markowiak-Kopeć P, Ślizewska K. *Nutrients*. 2020;12:1107.
2. Zhang D, Jian YP, Zhang YN, Li Y, Gu LT, Sun HH, Liu MD, Zhou HL, Wang YS, Xu ZX. *Cell Commun. Signal*. 2023;21:1-20.
3. Wang Z, Liu J, Li F, Luo Y, Ge P, Zhang Y, Wen H, Yang Q, Ma S, Chen H. *Pharmacol. Res.* 2022;182:106321.
4. May KS, den Hartigh LJ. *Nutrients*. 2021;13:3666.
5. Rosli NSA, Abd Gani S, Khayat ME, Zaidan UH, Ismail A, Abdul Rahim MBH. *Mol. Cell. Biochem.* 2023;478:517-30.
6. Thorakkattu P, Khanashyam AC, Shah K, Babu KS, Mundanat AS, Deliephan A, Deokar GS, Santivarangkna C, Nirmal NP. *Foods*. 2022;11:3094.
7. Lee KD, Ilavenil S, Karnan M, Yang CJ, Kim D, Choi KC. *Int. J. Mol. Sci.* 2022;23:4727.
8. Chakraborti CK. *World J Gastrointest Pathophysiol.* 2015;6:110.
9. Al-Lahham SH, Peppelenbosch MP, Roelofsen H, Vonk RJ, Venema K. *Biochim Biophys Acta Mol Cell Biol Lipids.* 2010;1801:1175-1183.
10. Sornsene P, Chatatikun M, Mitsuwan W, Kongpol K, Kooltheat N, Sohbenalee S, Pruksaphanrat S, Mudpan A, Romyasamit C. *PeerJ.* 2021;9:e12586.

STRUCTURE DETERMINATION AND KINETIC PROPERTIES OF ATP SULFURYLASE FROM DURIAN *Durio zibethinus*

Gunn Tangkanont, Kittikhun Wangkanont*

Department of Biochemistry, Faculty of Science, Chulalongkorn University, Bangkok, 10330, Thailand,

*e-mail: kittihun.w@chula.ac.th

Abstract:

ATP sulfurylase (ATPS) is the first enzyme of the sulfur assimilation pathway in plants. The enzyme functions as a nucleotidyl transferase that catalyzes the adenylation of sulfate to yield adenosine 5'-phosphosulfate (APS). APS is then further converted into sulphur-containing amino acids, as well as various secondary metabolites. Durian (*Durio zibethinus*) fruit is rich in volatile sulfur compounds. Thus, we are interested in the characterization of ATPS in durian. ATP sulfurylase from durian was expressed in *Escherichia coli* and purified using Ni-NTA resin affinity chromatography and ion exchange chromatography. The enzyme activity was measured using a coupled assay.

Introduction:

ATP sulfurylase (ATPS) is a key enzyme in the sulfur assimilation pathway in various organisms, including plants, bacteria, and fungi. This enzyme is a nucleotidyl transferase which catalyzes the adenylation of sulfate to adenosine 5'-phosphosulfate (APS). APS is the substrate for further synthesis of cysteine, methionine, and other sulfur-containing compounds. In plants, ATPS is located in the chloroplasts (Prioretti et al. 2014). In several organisms, ATPS is the rate-limiting enzyme of the sulfur assimilation process. Since the durian fruit is rich in sulfur-containing compounds, investigation of ATPS from durian (*Durio zibethinus*) may lead to more understanding of the sulfur assimilatory pathway. This study aims to characterize the kinetic property of durian ATPS.

Methodology:

Enzyme expression and purification

The durian ATPS gene is cloned into pET-24a. This gene sequence is verified and the transformed *Escherichia coli* was then inoculated into the LB medium supplemented with 50 µg/mL kanamycin and incubated at 37 °C overnight as a starter culture. The overnight culture was inoculated into a fresh TB broth (1:50) containing 50 µg/mL kanamycin, and cultured at 37°C. The optical density (OD) at 600 nm was measured every hour until the value reached 0.6. Isopropyl β-d-1-thiogalactopyranoside (IPTG) was added to 0.1 mM and incubated at 16 °C overnight. The cells were lysed and the enzyme was purified by Ni-NTA affinity chromatography and ion exchange chromatography. The purity of the enzyme is analyzed by SDS-PAGE. The protein concentration was determined by UV-visible spectrophotometry.

Enzymatic activity of ATPS

The activity of ATP sulfurylase from durian were assayed using a couple enzyme assay (Phartiyal et al., 2006). The activity was measured in a buffer solution containing 0.05 U APS kinase, 20 U pyruvate kinase, 30 U lactate dehydrogenase, 15 mM MgCl₂, 250 mM

NaCl, 0.2 mM NADH, 20 mM Na₂SO₄, 0-10 mM ATP and 20 mM Tris buffer (pH 8.0). The rate of NADH consumption was monitored by spectrophotometry at 340 nm.

Results and Discussion:

The durian ATPS with a His-tag was purified by a Ni-NTA affinity column, as shown in (Figure 1). The SDS-PAGE result showed large ATPS bands but other minor bands were clearly visible. Thus, the protein was further purified by anion exchange chromatography to be used in further experiments (Figure 2).

To measure the enzymatic activity of ATPS, the enzyme coupled assay was used and the initial rate was measured as the decreasing NADH absorbance at 340 nm (Figure 3). The *K_m* for ATP is 0.3 mM, which is comparable to soybean ATPS (around 0.2 mM) (Phartiyal et al., 2006).

The amino acid sequence of durian ATPS and soybean ATPS were also compared by sequence alignment (Figure 4) Durian ATPS (residue Arg-201, Asn-202, Arg-302 and His-208) shared the same transition state stabilizing amino acids as soybean ATPS (residue Arg-248, Asn-249, His255 and Arg349). This observation explains the similarity in catalytic activity between durian ATPS and soybean ATPS. Rate measurements at various sulfate concentrations to obtain more reliable *K_m* values, as well as investigation of the reverse reaction is currently in progress.

In addition to sequence alignment, the 3D structure of durian ATPS was explored through homology modeling using phyre2 (Figure 5). As expected, phyre2 suggests that soybean ATPS (PDB: 4maf) (Hermann et al., 2014) shares the highest similarity with durian ATPS at 88% identity the RMSD of 0.040 Å. The catalytic residues of durian ATPS could be modeled into the homologous position as in soybean ATPS. Therefore, durian ATPS is expected to have a very similar structure as soybean ATPS. Experimental structure determination of durian ATPS by X-ray crystallography is in progress.

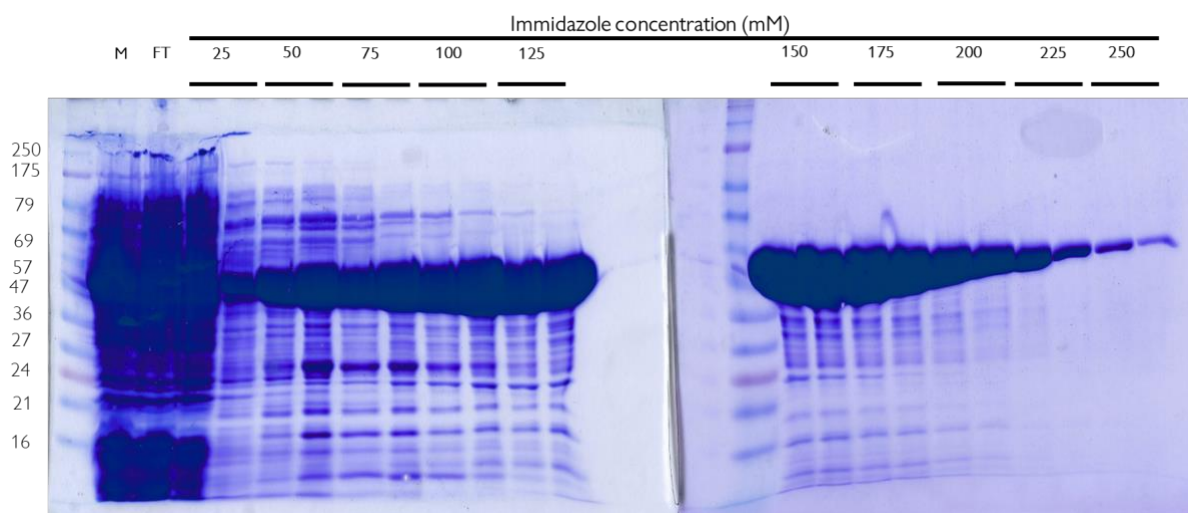


Figure 1.

SDS-PAGE results of Ni-NTA affinity chromatography of durian ATPS. M = marker and FT = flow-through.

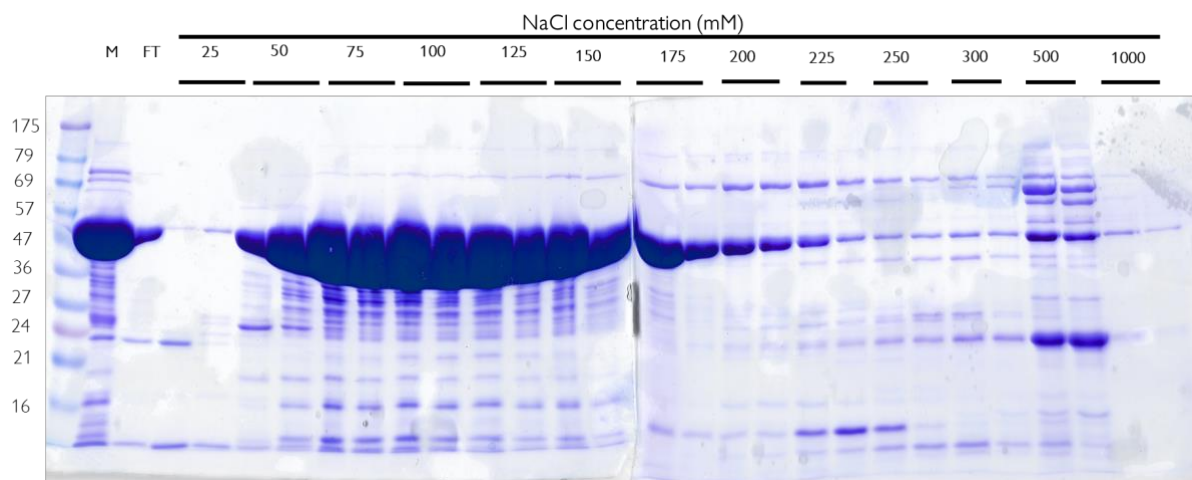


Figure 2.

SDS-PAGE results of anion exchange chromatography of durian ATPS after Ni-NTA affinity chromatography. M = marker and FT = flow-through.

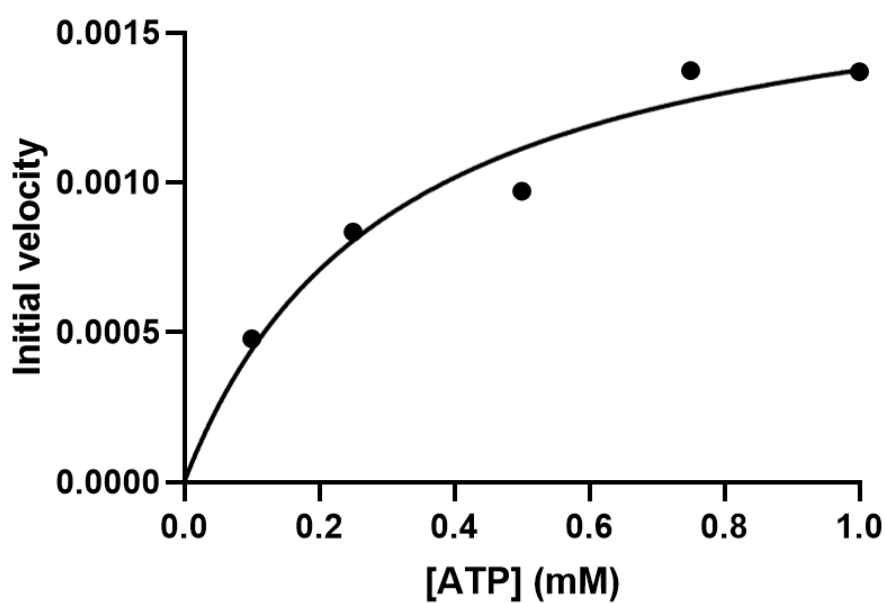


Figure 3.

Enzymatic activity of durian ATPS at 20 mM sulfate concentration

[illegible]

Figure 4.

The sequence alignment between durian ATPS (DZ) and soybean ATPS (GM). Active site residues are noted in red. The sequence alignment shows that all amino acids at the active site are the same.

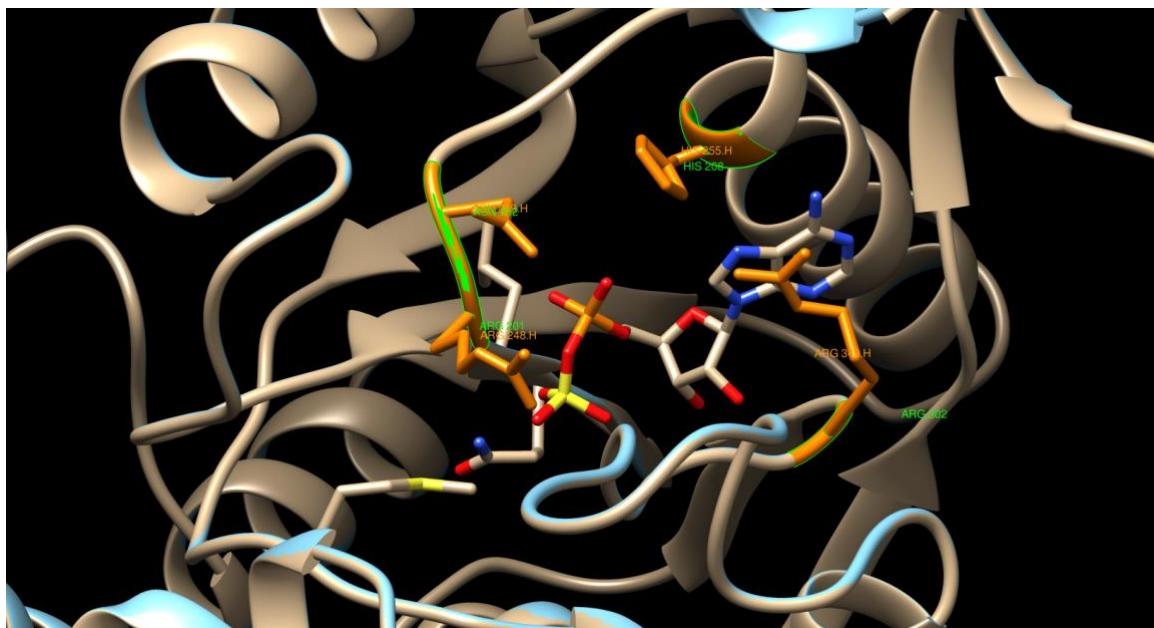


Figure 5.

Active site superposition of soybean ATPS (PDB; 4maf chain H, brown) and homology model of durian ATPS (light blue) with transition state stabilizer amino acids colored in orange.

Conclusion:

Durian ATPS can be express and purified with Ni-NTA affinity chromatography and followed by anion exchange chromatography. The ATPS activity of durian ATPS was confirmed. The active site residues are conserved between durian and soybean ATPS. The three-dimensional structure of these two proteins are also expected to be similar.

References:

1. Prioretti L, Gontero B, Hell R, and Giordano M. Diversity and Regulation of ATP sulfurylase in Photosynthetic Organisms. *Frontiers in Plant Science*. 2014;5:597.
2. Herrmann, J., Ravilious, G., Mckinney, S., Westfall, C., Lee, S., Baraniecka, P., Giovannetti Koprivova A, and Kopriva S. Molecular Mechanisms of Regulation of Sulfate Assimilation: First Steps on a Long Road. *Frontiers in Plant Science*. 2014;5: 589.
3. Herrmann J, Ravilious G, Mckinney S, Westfall C, Lee S, Baraniecka P, Giovannetti M, Kopriva S, krishnan H, and Jez J. Structure and Mechanism of Soybean ATP Sulfurylase and The Committed Step in Plant Sulfur Assimilation. *Journal of Biological Chemistry*. 2014;289:10919-10929.
4. Phartiyal P, Kim W, Cahoon R, Jez J, and Krishnan H. Soybean ATP Sulfurylase, a Homodimeric Enzyme Involved in Sulfur Assimilation, is Abundantly Expressed in Roots and Induced by Cold Treatment. *Archives of Biochemistry and Biophysics*. 2006;450:20-29.



THE ROLE OF LECTIN DOMAIN IN SPIKE PROTEINS OF SARS-COV-2 AND SARS-LIKE COV

Praepan Lapphaisal¹, Sopita Visamol^{1,2}, Sakonwan Kuhaudomlarp^{1,3,*}

¹Department of Biochemistry, Faculty of Science, Mahidol University, Thailand

²Department of Microbiology, Faculty of Science, Mahidol University, Thailand

³Centre for Excellence in Protein and Enzyme Technology, Faculty of Science, Mahidol university, Thailand

*Corresponding e-mail: sakonwan.kuh@mahidol.edu

Abstract:

The spike protein of coronavirus is a multidomain glycoprotein that contains a receptor binding domain (RBD) which plays a pivotal role in binding to the host cell receptor ACE2, and an N-terminus domain (NTD) whose functional attributes in SARS-CoV-2 and other related non-human coronaviruses remain incompletely elucidated. It has been proposed that the sialylated glycans present on the surface of host cells engage in interactions with the NTD spike protein which mediates the virus's attachment to the host cell. To demonstrate the role of the SARS-CoV-2 and bat SARS-like CoVs' NTD domains in glycan binding and viral infection process, we will utilize a variety of biophysical techniques and conduct cell-based assays. This knowledge regarding the role of NTD domain is crucial for further exploring its significance in glycan binding, and for discovering potential inhibitors preventing glycan-spike interaction during viral entry.

Introduction:

The spread of coronavirus disease 2019 (COVID19) has caused millions of deaths among the human population. COVID19 is caused by severe acute respiratory syndrome coronavirus 2 (SARS-CoV-2). SARS-CoV-2 exhibits a higher transmission efficiency compared to other human coronaviruses.¹ The emergence of COVID19 pandemic accelerates the research and knowledge against this situation. Currently, Omicron variant is one of the prominent circulating variants of concern (VOCs), emerged in November 2021.² New sub-lineages continue to emerge and spread around the world.³

SARS-CoV-2 variants have undergone numerous mutations in the S gene encoding for spike protein. Since the primary vaccine strategy relies on the design of mRNA encoding spike protein, the alterations of the spike protein's sequence and structure potentially enhance affinity to the host receptor or enable evasion of antibody recognition.⁴ The N-terminal domain (NTD) of spike protein represents an interesting study target because it exhibits the highest number of sequence variants among different SARS-like CoVs from various host species. Moreover, accumulation of new mutations within this domain are rapidly rising in SARS-CoV-2 strains detected in human population. Previous studies have shown that the NTDs of SARS-like CoVs, such as MERS-CoV, BCoV, and HCoV act as lectins.⁵⁻⁸ Lectins are glycan binding proteins found in many organisms including viruses, which are components of viral surface proteins. 3D structures of spike proteins from these viruses in complex with sialoglycans have been solved by cryo-EM which identify the location of the



sialoglycan binding site in NTD and the amino acid epitopes that participate in the sialoglycan interaction.^{6, 7, 9} The viral-glycan interactions facilitate attachment through binding between viral lectin and host glycan on the surface of cells. Sialoglycans are found prevalently on vertebrate cell surface and have been demonstrated as receptors for several viral lectins.¹⁰ Given the important roles of viral-lectin-to-host-glycan interaction in viral pathogenicity, interference of viral lectin-host-glycan interaction can therefore be explored as an alternative antiviral strategy. In addition to their involvement in human viral infections, NTD of non-human coronavirus displayed varying levels of glycan binding capability on a glycoprotein *in vitro*, but the biological significance and the exact identity of the glycan that engaged the NTD remain unknown.¹¹ The conservation or loss of NTD-glycan interaction in SARS-CoV-2 and bat SARS-like CoVs as well as the role played by this domain in the evolution and inter-/intra-species transmission of the viruses, can serve as a marker for monitoring and predicting the potential emergence of new SARS-like CoVs that may pose a threat to humans or animal livestock.

In this research, analysis of sequence and structure of NTD domains from bat SARS-like CoV and human SARS-CoV-2 were performed to elucidate the conservation or variation of the putative glycan binding site in the NTD domains. To gain understanding in the function of the putative glycan binding site on viral entry, we used pseudotyped virus of SARS-CoV-2 wild type (WT) and its variants as a tool to study the effect of mutations of the glycan binding site on viral entry. Lastly, we used dynamic light scattering (DLS) to investigate an interaction between SARS-CoV-2 pseudotyped virus and sialoglycan-containing glycoprotein. Our study can shed light on the role of glycan-lectin interaction in the viral pathogenesis in human and other organisms.

Methodology:

Computational analysis of NTD domain

The sequence and structure of SARS-CoV-2 and bat CoV spike proteins were compared to find possible sialoglycan-binding site. Data of a sequence and structure of the SARS-CoV-2 and bat SARS-like CoVs spike proteins were available in GenBank and Protein Data Bank (PDB). The protein sequences of these NTD spike proteins were aligned using Clustal Omega to generate multiple sequence alignments. Experimentally-solved protein structure of the SARS-CoV-2 variants and RaTG13 spike were retrieved from PDB. RacCS203 and BANAL-236 NTD structures were predicted and modelled by AlphaFold. The protein structure of SARS-CoV-2 variants and bat SARS-like CoV NTDs were visualized by PyMOL.

Production of SARS-CoV-2 pseudovirus

Spike-pseudoviruses were produced using HIV-based lentiviral system. This system requires co-transfecting cells with a lentiviral backbone encoding, a plasmid expressing Spike and plasmids encoding the other HIV proteins necessary to assemble viral particles. The protocol was adapted from Crawford KHD, et al.¹² All plasmids were obtained from BEI resources (<https://www.beiresources.org/>).



HEK293T cells were seeded to the confluency of 60%-80%. Then, the cells were transfected with plasmids encoding lentiviral backbone, a plasmid expressing spike and plasmids encoding the other HIV proteins necessary to assemble viral particles using jetPRIME (Polyplus-transfection), including 1:2 DNA to jetPRIME reagent in jetPRIME buffer. The transfected cells were incubated at 37°C under humidified atmosphere with 5% CO₂. At 24 hr post-transfection, the transfection media was replaced with a complete media (DMEM-HG with 10% FBS). The next day (48 hr post-transfection), the media was collected and stored at 4 °C overnight, then added a fresh complete media. Lastly, at 72 hr post-transfection, all harvested media from each day were pooled, centrifuged for 5 mins at 3,000 x g, room temp, and stored at -80 °C.

Spike-mediated pseudovirus entry assay

To investigate the infectivity of SARS-CoV-2 pseudoviruses, luciferase assay was performed in mammalian cells. Spike-pseudovirus containing specific sialoglycan-binding site mutation of SARS-CoV-2, was used for analyzing an involvement of sialic acid in viral entry and cell-cell fusion.

HEK293T-ACE2 cell was seeded to 60%-80% confluence in a 96-well plate. 24-hour after seeding, pseudoviruses were used to enter recipient cells, HEK293T-ACE. After incubation of pseudoviruses with recipient cells at 37°C under humidified atmosphere with 5% CO₂ for 48 h, the media was removed followed by the addition of luciferase substrate, Bright-Glo following the manufacturer's instructions (Promega). Luminescence was measured using a Cytation 7 imaging reader (Agilent BioTek). All measurements were carried out on three technical replicates.

Dynamic light scattering (DLS)

Interaction study of pseudovirus, and glycan were performed by dynamic light scattering (DLS). Glycan that will be used in DLS is fetuin, a glycoprotein containing sialylated N-linked and O-linked glycans to detect an interaction with pseudoviruses. DLS measurements were performed with a Malvern Zetasizer Nano ZS instrument. All samples were prepared in filtered PBS including 10X dilution of SARS-CoV-2 pseudotyped viruses and sialoglycan-containing glycoprotein, fetuin (New England Biolabs). The mixture of pseudotyped virus and fetuin was pre-incubated at room temperature for 30 min prior to measurement. The measurements were performed at a controlled temperature of 25 °C with three repetitions. The correlogram and size distributions were obtained from the Zetasizer software.

Results and Discussion:

The sequence and structural analysis of NTDs

To investigate the conservation of sialoside-binding site within the NTDs spike of bat SARS-like CoVs, a multiple sequence alignment was performed on SARS-CoV-2 and bat SARS-like CoV NTDs. The information of SARS-CoV-2 variants and bat SARS-like CoVs under our investigation are summarized in **Table 1**. Our sequence analysis (**Figure 1**) showed

that the Omicron variant displayed a deletion ($\Delta 145$) within its sialoside-binding site, which raises the possibility that this deletion may compromise the interaction between the NTD and sialic acid. The sialoside-binding site of RaTG13 exhibited conservation, while this conservation was not observed in RacCS203 and BANAL-236. In BANAL-236, specific amino acids were changed to F145 and G246, resulting in a significant alteration in their ability to form hydrogen bonds with sialic acid. In the case of RacCS203, although amino acids Q136, T168, and N236 underwent modifications, a functional group capable of potentially forming a hydrogen bond with sialic acid remained.

Table 1. SARS-CoV-2 variants and bat SARS-like CoVs in our study.

Coronaviruses	Zoonotic origin
SARS-CoV-2 WT	Human
SARS-CoV-2 Omicron (BA. 2)	Human
RaTG13	<i>Rhinolophus affinis</i>
RacCS203	<i>Rhinolophus acuminatus</i>
BANAL-236	<i>Rhinolophus marshalli</i>



Figure 1. Sequence alignment of SARS-CoV-2 and SARS-like CoVs NTDs obtained from Clustal Omega. Dark blue, amino acids are conserved; light blue, amino acid changes with similar properties; white, amino acid changes with different properties; red box, putative sialoglycan-interacting residues; black box, other residues in the sialoglycan binding pocket.

The analysis of SARS-CoV-2 and bat SARS-like CoVs NTD-spike proteins involved the use of various computational tools available online, including PDB, AlphaFold, and Clustal Omega. While the 3D structures of SARS-CoV-2 and RaTG13 spike proteins are currently accessible from PDB, the structures of bat RacCS203 and BANAL-236 spike proteins have not been experimentally solved. To address this, the protein structure prediction software, AlphaFold, was employed to predict the structures of RacCS203 and BANAL-236 NTDs. Subsequently, a comparison of the structures of WT and Omicron variants, along with those of bat SARS-like CoV NTDs (RaTG13, RacCS203, and BANAL-236), were generated and presented in **Figure 2A**. The overall structures exhibited similarities and displayed a β -sandwich-like architecture, which is a conserved feature in all beta-coronaviruses. **Figure 2B** specifically highlights key residues within the sialoglycan binding site of SARS-CoV-2 WT

NTD. These residues, Y145, Q183, and S247, form hydrogen bonds with *N*-Acetyl- α -neuraminic acid (Sia), which is a terminal sugar in sialoglycan. Sia was also surrounded by additional residues, including H69, W152, L249, and T259.¹³

From a structural perspective, RaTG13 appears to have a deep groove or pocket that is well-suited for binding to glycan molecules. This suggests that RaTG13 is likely to have a conserved glycan-binding capability due to the substantial space available within the binding site. In contrast, RacCS203 features a moderately sized pocket, indicating a moderate level of space available for accommodating sialic acid or glycan molecules. BANAL-236, moreover presents a relatively flat region to accommodate glycan. This suggests that BANAL-236 may have a reduced capacity for glycan binding, given the limited space within its binding site. It can be implied that the glycan binding capability in BANAL might be different from both RaTG13 and RacCS203, possibly less effective or even altered.

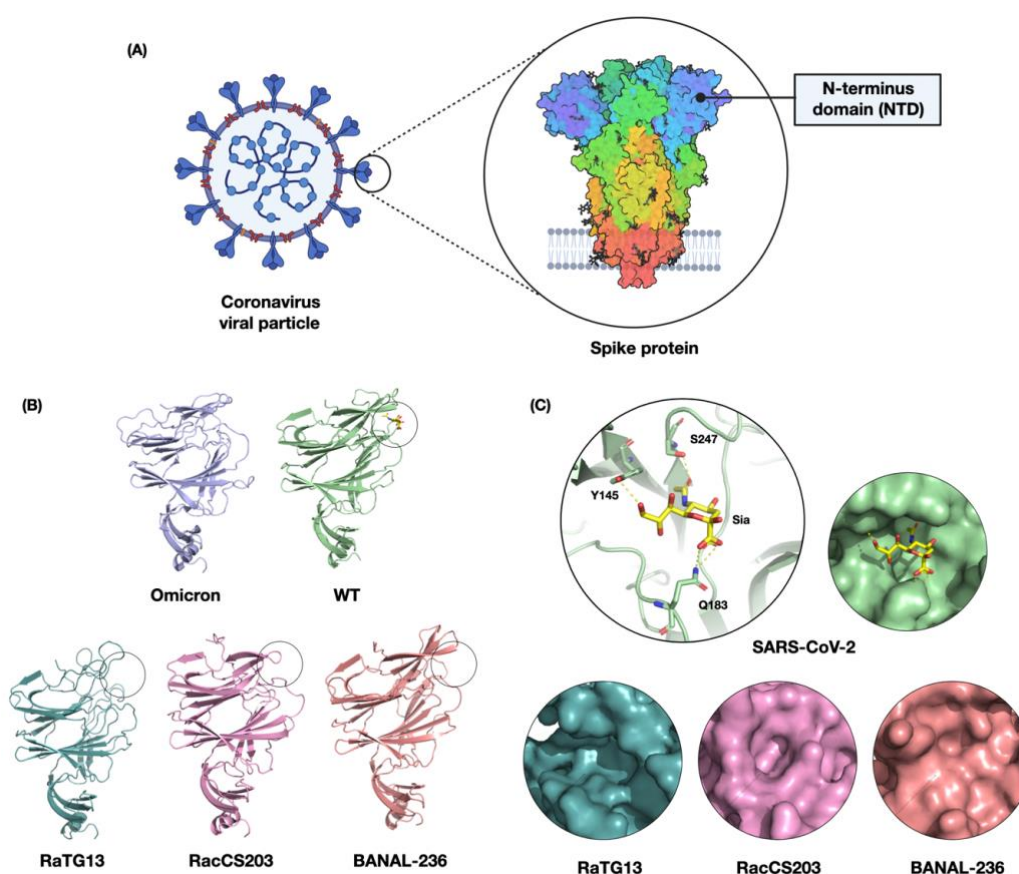


Figure 2. Structural analysis of SARS-CoV-2 and SARS-like CoVs NTDs. (A) Coronavirus and spike protein visualization. (B) The NTD structure of SARS-CoV-2 WT (PDB:7QUR), Omicron (PDB:7T9J), RaTG13 (PDB:7CN4), RacCS203, and BANAL-236 (AlphaFold). (C) The sialoside-binding site of SARS-CoV-2 NTD in complex with *N*-Acetyl- α -neuraminic acid and the putative binding pocket in the structural models of RaTG13, RacCS203 and BANAL-236.

Interaction study of SARS-CoV-2 pseudotype virus and glycoprotein



The pseudovirus-spike of SARS-CoV-2 WT and variants are non-propagative viral particles bearing spike proteins on the particle surface. These pseudoviruses were produced and subjected to analysis to determine their interaction with fetuin glycoprotein, a highly sialylated glycoprotein standard. Dynamic Light Scattering (DLS) was employed for this purpose, as it is a valuable tool for examining the size and aggregation of molecules. In our study, DLS was used to investigate any increases in the size of the glycoprotein and the viral particles which would indicate the interaction between the viral particles and the glycoprotein.

Mixtures of pseudovirus from WT and Omicron, along with fetuin, were pre-incubated at room temperature for 30 minutes before DLS measurement. The correlograms for all measurements displayed good quality, with y-intercepts falling within the range of 0.7 to 1. The size distribution profile of the pseudovirus revealed three distinct populations. For the WT variant, the sizes were approximately 10, 50, and 770 nm, whereas the Omicron variant had a size of 570 nm. Notably, there were also DLS reports of virus-like particles typically falling within the size range of around 50 nm, which exhibited similarities to the pseudovirus.¹⁴ In **Figure 3A**, the average diameter of the pseudovirus cluster from WT shifted from 770 nm to 1200 nm, suggesting a likely interaction between the pseudovirus and the glycoprotein. However, in **Figure 3B**, the average diameter of the pseudovirus cluster associated with Omicron remained consistent at 570 nm. This observation suggests that there is only minor interaction between pseudovirus Omicron and fetuin glycoprotein, aligning with a previous study that demonstrated reduced binding of the Omicron NTD spike to sialoglycan using protein nuclear magnetic resonance (NMR) method.¹³

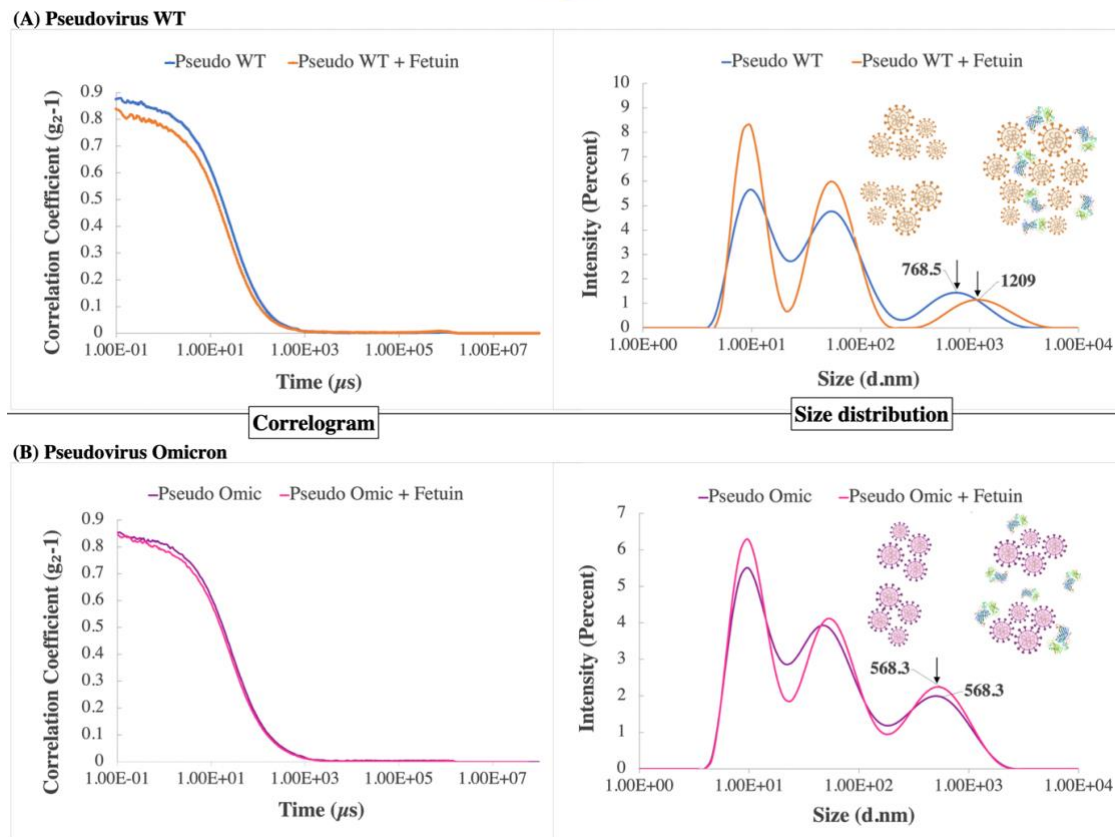


Figure 3. Correlogram and size distribution of pseudovirus and fetuin mixture.

- (A) Pseudovirus WT (blue) sample and a mixture of pseudovirus WT and fetuin (orange).
 (B) Pseudovirus Omicron (purple) sample and a mixture of pseudovirus Omicron and fetuin (magenta).

The infectivity of SARS-CoV-2 pseudoviruses

Specific mutations in the NTD domain may affect the molecular interactions between host sialoglycan and the virus, which may subsequently disturb the viral entry. To investigate the effect of NTD mutations in the putative glycan binding site on the viral entry, we generated pseudoviruses carrying the spike protein of SARS-CoV-2 bearing H69 and Y145 deletions. The infectivity of these pseudoviruses was assessed by infecting HEK293T-ACE2 cells with luciferase-expressing pseudotyped viruses. Surprisingly, pseudotyped virus containing H69 and Y145 deletions exhibited a significant increase in infectivity, as shown in **Figure 4**. Although NTD of Omicron variants, including the Y145 deletion, have demonstrated reduced binding to sialoglycan according to our previous DLS experiment and a report in the study by Buchanan et al. in 2022, it is possible that this reduction in sialoglycan attachment is possibly compensate by other spike-mediated functions. For instance, the increase in the viral entry of caused by H69 deletion observed in our study corresponded with the study on the H69/70 deletion observed in the alpha variant, where the virus enhanced infectivity through increased incorporation of spike proteins into viral particles.¹⁵ Additionally, it has also been proposed that some NTD mutations cause the

allosteric modulation of the NTD domain that influence spike properties related to viral infection process such as virus fusogenicity to host cell.^{16, 17}

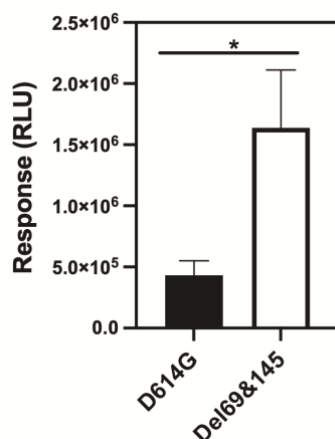


Figure 4. Entry of pseudovirus containing WT(D614G) and delH69&Y145 spike to HEK293T-ACE2 cell as measured by luciferase assay. The data represent triplicates.

Conclusion:

Our research focused on investigating the interactions of the N-terminal domain (NTD) of the SARS-CoV-2 and bat SARS-like CoVs spike glycoprotein with sialoglycan. The goal is to gain insights into how these interactions may influence and contribute to viral infection. The structural analysis of NTDs revealed a common β -sheet arrangement forming a sandwich-like architecture, a feature conserved across all coronaviruses. Although the conservation and possible glycan binding site were explored by sequence and structural analyses, further investigations into the functions of these NTDs, particularly their glycan-binding abilities, will be pursued. Highly sensitive biophysical techniques, such as surface plasmon resonance (SPR), will be employed to validate and confirm the interactions of these NTD domains with different types of sialoglycans in order to determine the specificity of the interaction.

SARS-CoV-2 variants have accumulated numerous mutations within the NTD. Given the mutations identified in the sialoglycan binding site of the Omicron variant, we proceeded to assess the interaction between the pseudovirus and sialoglycan-containing glycoprotein through the application of dynamic light scattering (DLS). The pseudovirus bearing WT spike displayed a significant increase in particle size upon incubation with fetuin, indicating an interaction between the glycoprotein and WT pseudoviruses. However, the interaction was attenuated in the Omicron variant. These results corresponded with the hypothesis that certain SARS-CoV-2 variants, including Omicron, have undergone mutations that lead to the attenuated ability to bind to human glycans to facilitate the release of the virions from the host cells after cell lysis.

The molecular mechanism through which these mutations impact the interaction between the spike protein and auxiliary receptors, such as sialylated glycans, and consequently alter infectivity, are still not fully understood. We created the pseudotyped



bearing mutations in the sialoglycan binding site of SARS-CoV-2 (deletion of H69 and Y145), which, to our surprise, exhibited an enhancement in viral entry. We hypothesized that the enhancement in the entry may be due to the allosteric effect on the NTD that results in an increase in the ability of the viral to fuse with the host membrane. Nevertheless, it is still a matter of investigation to understand how these spike mutations, including other residues within the sialoside binding site, influence the virus's binding to sialic acid and subsequently impact infectivity and virus fusogenicity.

In addition to the preliminary findings indicate to an interaction between SARS-CoV-2 pseudovirus and sialoglycan, it is crucial to investigate the role of the NTD domain in glycan binding, its involvement in viral infections, as well as the effect of sialoglycan-binding site and sialic acid in infectivity and fusogenicity. However, the identification of the glycans engaging the NTD in bat coronaviruses remains unknown. To address this, we will express and purify NTD recombinant proteins from SARS-like CoVs and SARS-CoV-2. These proteins will be used for in-depth investigations into the functions of the NTD in protein-glycan interactions.

Acknowledgements:

We acknowledged the National Council of Thailand (NRCT) (Research grant for Young Talented Researchers No. N41A640121) and Mahidol University for research funding. Praepan Lapphaisal is supported by DPST (Development and Promotion of Science and Technology Talents) scholarship. We thank Assoc. Prof. Arunee Thititanyanont for her valuable advice on the project.

References:

1. Madewell ZJ, Yang Y, Longini IM, Jr., Halloran ME, Dean NE. JAMA Netw. Open. 2020;3(12):e2031756-e.
2. Viana R, Moyo S, Amoako DG, Tegally H, Scheepers C, Althaus CL, et al. Nature. 2022;603(7902):679-86.
3. Chatterjee S, Bhattacharya M, Nag S, Dhama K, Chakraborty C. Viruses. 2023;15(1):167.
4. McLean G, Kamil J, Lee B, Moore P, Schulz TF, Muik A, et al. Mbio. 2022;13(2):e02979-21.
5. Li W, Hulswit RJG, Widjaja I, Raj VS, McBride R, Peng W, et al. Proc Natl Acad Sci USA. 2017;114(40):E8508-e17.
6. Peng G, Xu L, Lin Y-L, Chen L, Pasquarella JR, Holmes KV, et al. J. Biol. Chem. 2012;287(50):41931-8.
7. Tortorici MA, Walls AC, Lang Y, Wang C, Li Z, Koerhuis D, et al. Nat.Struct. Mol. Biol. 2019;26(6):481-9.
8. Sun X-L. Glycobiology. 2021;31(10):1245-53.
9. Yuan Y, Cao D, Zhang Y, Ma J, Qi J, Wang Q, et al. Nat. Commun. 2017;8(1):15092.
10. Wasik BR, Barnard KN, Parrish CR. Trends Microbiol. 2016;24(12):991-1001.
11. Guo H, Li A, Lin HF, Liu MQ, Chen J, Jiang TT, et al. J Virol. 2022;96(15):e0095822.



12. Crawford KHD, Eguia R, Dingens AS, Loes AN, Malone KD, Wolf CR, et al. *Viruses*. 2020;12(5):513.
13. Buchanan CJ, Gaunt B, Harrison PJ, Yang Y, Liu J, Khan A, et al. *Science*. 2022;377(6604):eabm3125.
14. Petersen JD, Lu J, Fitzgerald W, Zhou F, Blank PS, Matthies D, et al. *Viruses*. 2022;14(5).
15. Meng B, Kemp SA, Papa G, Datir R, Ferreira IATM, Marelli S, et al. *Cell Reports*. 2021;35(13).
16. Meng B, Datir R, Choi J, Baker S, Dougan G, Hess C, et al. *Cell Reports*. 2022;40(7):111220.
17. Cantoni D, Murray MJ, Kalemira MD, Dicken SJ, Stejskal L, Brown G, et al. *EMBO reports*. 2022;23(10):e54322.



SESSION C-CHEMISTRY (ANALYTICAL CHEMISTRY)



PREPARATION AND APPLICATION OF INTELLIGENT FILMS INCORPORATED WITH NATURAL ANTHOCYANIN EXTRACT FOR TRACING SEA FOOD SPOILAGE

Trin Khawsang¹, Somrak Panphon², Weeraya Treewanjutha^{3*}

Department of Science, Faculty of Science and Technology, Prince of Songkla University, Pattani, 94000

*e-mail: weeraya.k@psu.ac.th

Abstract:

Intelligent film is film that can detect the freshness of food. It is consisted of two parts: a film forming agents and pH-sensitive dyes. Thus, dyes used for this purpose, should be safe for consumers such as natural dyes. Anthocyanins are found in high content in natural edible fruits and flowers. Its structure changes with different pH conditions, resulting in different color development. Thus, anthocyanin derived from colored rice could be used as a natural dye for pH-sensitive indicator film. Therefore, this project was aimed to extract anthocyanins from colored rice grown in Pattani province, Thailand, namely Jeudanor (JD), for fabrication of an intelligent film. The pH-differential method was used to determine the anthocyanin content of Jeudanor rice, and the pH sensitivity of the obtained anthocyanin was also investigated. According to the results, JD extract with 50% ethanol had the highest anthocyanin content. The color of JD extract changed as the pH increased from 10 to 12. Furthermore, anthocyanins and phycocyanins extracted from three different sources; butterfly pea (BP), mulberry (ML), and wakame (WK), were mixed with JD rice extracted. The color of JD mixed with butterfly pea (BP) extract had clearly changing results in a pH solution ranging from 8 to 10. The intelligent film was then fabricated by combining 6:1 anthocyanin extract from JD and BP with carboxymethyl cellulose (CMC) and sodium alginate (SA). The addition of JD and BP extract in film forming matrices increased the films' thickness, moisture content, and water solubility. The FTIR results revealed that the main function groups of anthocyanin extract were compatible with those found in the film-based materials. The developed intelligent film was sensitive to volatile ammonia and showed a visual color change from light purple to dark-green for the monitoring of shrimp and fish freshness during 48 h of storage at 4 °C.

Keywords: Intelligent film, Spoilage, Anthocyanin, Carboxymethyl cellulose

Introduction:

In general, bacteria that decompose protein from meats cause the spoilage of sea food or other animal products. This process generates volatile basic nitrogen-containing compounds (VBN), including ammonia, which causes acidity changes in the food packaging environment¹. A variety of intelligent indicator films, including pH indicator film², CO₂ indicator film³, are now widely used for food monitoring. The intelligent film plays a major role as a medium between food products and consumers. The film's primary function is to monitor the environmental status of food packages in real time. The indicator film was fabricated of a target compound sensitive component and solid support carriers⁴. For example, pH indicator film was consisted of pH sensitive dyes and its solid support. Since the film is used in food products, the dyes and film used must be safe. Anthocyanin is commonly used as a pH-sensitive dye because it is naturally abundant, safe, soluble in water, has a wide range of color variations in response to pH changes, and is inexpensive⁵. Anthocyanin is found in purple to blue nature fruits, flowers, and cereal grains such as rice, maize, sorghum, and others. Numerous rice species are grown in Thailand's southern border provinces, including Jeudanor rice which grown in Ban-Klang subdistrict, Panare district, Pattani province, Thailand. Jeudanor rice has



a dark purple pericarp which is rich of anthocyanin and can be used for pH indicator film. However, to broaden the color alteration of the pH indicator film made from colored rice extracted, the combination of the other natural dyes should be investigated. The novel intelligent films containing mixed anthocyanin-based dyes and phycocyanin for tracing fish spoilage were reported by Luo et al., 2023⁶. All the intelligent labels demonstrated excellent color variation with volatile ammonia and the degree of fish freshness, except the phycocyanin-containing label alone. Therefore, other well-known and abundant anthocyanin sources, such as butterfly pea, mulberry, and wakame, are interesting candidates for combining with JD rice extracted in the fabrication of pH indicator film to broaden the pH range.

Methodology:

1. *Jeudanor rice extract and pH sensitivity study*

Jeudanor (JD) rice was dried in a hot air oven at 40 °C for 48 h. 300 g of rice was macerated in 400 mL of hexane for 48 h. Then, continue macerate for 72 h in various water-to-ethanol ratios. The extracted solvent was evaporated using a rotary evaporator until it was dry. Then, 0.1 g of rice anthocyanin crude extract was precisely weighed, dissolved in 1 mL of DMSO, and the volume was made up to 10 mL with 70% (v/v) ethanol. The pH sensitivity test was carried out by adding JD rice anthocyanin extract into a pH solution ranging from 1 to 12. The UV-Vis spectra of pH solution were then measured between 380 and 780 nm. The color alteration of the pH solution was observed and recorded.

2. *Determination of anthocyanin in JD rice and other plants extract*

The anthocyanin content of JD rice and other plant extracts was determined using a slightly modified method from Sholikhah et al, 2021⁷. 50 mL of 50% (v/v) ethanol was used to extract 10 g of JD rice, butterfly pea (BP), mulberry (ML), and wakame (WK). The extracted solvent was evaporated until dry at 40°C. The crude extract was then weighed, and the total volume was made up to 10 mL with ethanol. The pH-differential method was used to determine the anthocyanin content. Then, the content was calculated using the following equation. Whereas, the pH sensitivity of anthocyanin extracted and mixed dyes solution in the pH range of 6-10 was evaluated and compared.

$$\text{Anthocyanin content (cyanidin-3-glucoside equivalents, mg/L)} = \frac{A \times MW \times DF \times 10^3}{\epsilon \times l}$$

$$\text{where } A = (A_{520\text{nm}} - A_{700\text{nm}})_{\text{pH}1.0} - (A_{520\text{nm}} - A_{700\text{nm}})_{\text{pH}4.5}$$

$$MW = 449.2 \text{ g/mol for cyanidin-3-glucoside}$$

$$DF = \text{dilution factor}$$

$$l = \text{pathlength in cm}$$

$$\epsilon = 26,900 \text{ M}^{-1}\text{cm}^{-1} \text{ of cyanidin-3-glucoside}$$

$$10^3 = \text{factor for conversion from g to mg}$$

3. *Intelligent film preparation*

Intelligent film was prepared using the slightly modified method from Yang et al., 2022². 0.6% (w/v) of sodium alginate (SA) and 0.32% (w/v) of carboxymethyl cellulose (CMC) were added to 100 mL of distilled water. The film forming solution was then mixed with 0.2% (w/v) of glycerol and 4% (v/v) of anthocyanin extracts. A total of 40 mL of intelligent film solution was transferred in a petri dish. Finally, the intelligent film was dried for 24 h at 50 °C.

4. *Intelligent film characterization and physical properties determination*

The intelligent film's molecular functional groups were examined using a Fourier Transform Infrared Spectrometer (FT-IR). Teclock micrometer was used to measure the thickness of the film. Thermal drying to a constant weight at 105 °C was used to determine the moisture content (MC) of films. The film's water solubility (WS) was determined by precisely



weighing it. Then immersed the film sample in 10 mL of distilled water for 24 h under shaking at 25 °C. The remaining film was collected, dried for 24 h at 105 °C, weighed, and finally the WS was calculated.

5. *Sensitivity of intelligent film to volatile ammonia*

Color alteration of the intelligent films when exposure to ammonia solution was carried out. The films were hung 1 cm above a 100 mL solution level of 10 mM ammonia. The film was photographed every 4 min for 20 min. Color changes were captured with a smartphone camera (Samsung Galaxy A32, SM-A325F/DS, Display resolution *1800×2400 pixels, Number of display colors: 16 million colors, Samsung, Korea). Using the color picker and helper application, the photo data were converted to CIE (L^* , a^* , b^*) color values, where L^* indicates lightness that ranges from 0 (black) to 100 (white); a^* ranges from greenness to redness; and b^* ranges from blueness to yellowness. The total color difference (TCD) or ΔE was calculated using the following equation⁸

$$\text{TCD } (\Delta E) = ((L^* - L_0)^2 + (a^* - a_0)^2 + (b^* - b_0)^2)^{1/2}$$

where, L_0 , a_0 and b_0 were the values at 0 min, and L^* , a^* , and b^* were the values at the sampling time.

The relative color change (%S) was calculated as follows:

$$S(\%) = \frac{(R_i - R_f) + (G_i - G_f) + (B_i - B_f)}{R_i + G_i + B_i}$$

Where, R_i , G_i and B_i were the values recorded at 0 min, and R_f , G_f , and B_f were the values at the sampling time.

6. *Application of intelligent film for monitoring seafood spoilage*

The intelligent films were fixed inside a packaging cover containing 100 g of shrimp and fish fillet purchased from a local market in Muang district, Pattani province, and then stored at 4 °C for 48 h. The color variations were recorded using a smartphone camera (Samsung Galaxy A32, SM-A325F/DS, Display resolution *1800×2400 pixels, Number of display colors: 16 million colors, Samsung, Korea), the total color difference (ΔE) and %S were calculated using an equation from the previous section⁹.

Results and Discussion:

1. *Anthocyanin extraction*

Anthocyanins are water-soluble flavonoid pigments that widely found in fruits, flowers, seeds, and leaves of plants. Anthocyanin extraction is primarily accomplished using solvents such as methanol, ethanol, acidified water, or acidified ethanol. For safety aspects, ethanol and water were used as extraction solvent in this study. According to the results in **Figure 1**, Jeudanor rice extracted with 50% ethanol had the highest anthocyanin content at 12.557 ± 0.542 mg/L due to the moderate polarity of the 50% ethanol used was compatibility to anthocyanin¹⁰.

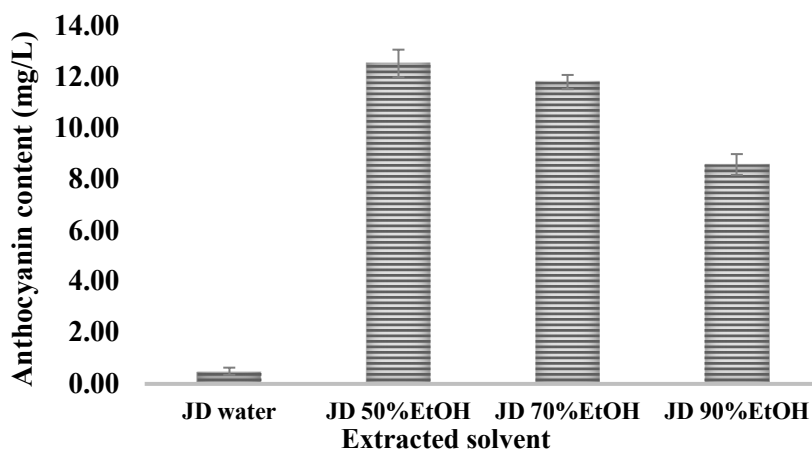


Figure 1. Anthocyanin content from JD rice extracted using different organic solvents.

2. Anthocyanin content in Jeudanor rice and the other plants

Figure 2 depicts the anthocyanin content of Jeudanor rice and other plants, including butterfly pea and mulberry. butterfly pea (BP), Mulberry (ML), and Jeudanor (JD) had anthocyanin contents of 3.60 ± 0.42 , 26.93 ± 0.59 , and 7.47 ± 0.70 mg/L, respectively. To broaden the color change in different pH values, all other natural pigment sources were used as co-pigment with Jeudanor rice extracted. Because of the similarity in anthocyanin content, BP was chosen as a co-pigment in this study. In addition, wakame (*Undaria pinnatifida*) which is an edible brown seaweed was extracted. The main pigment extracted from wakame was blue-green pigments or phycocyanin¹¹. Phycocyanin is a pigment-protein complex that gives blue color due to its absorption of red to orange visible light wavelengths. Therefore, wakame contains no anthocyanin.

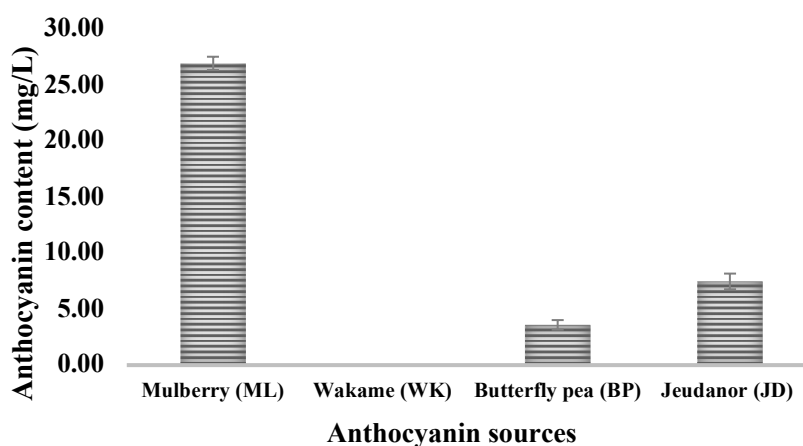


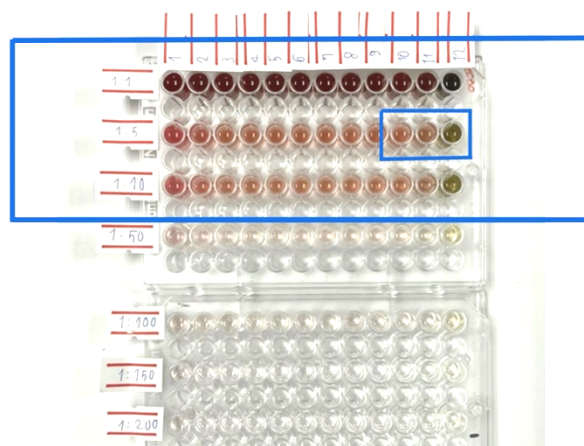
Figure 2. Anthocyanin content in different plants used in this study.

3. Spectra of indicator dyes at different pH

To validate their reliability as colorimetric sensors, the color differences of the indicator dyes at different pH buffers were examined. The color of JD extract was altered at pH levels ranging from 10 to 12. As shown in **Figure 3A**, the color of JD extracted was reddish-brown in pH solution at pH 1-9, brownish at pH 10-11, and dark green at pH 12. These color alterations probably caused by the protonated and deprotonated or -OH groups of the B-ring in anthocyanin structure. Blueness increases as the number of hydroxyl groups increases, while redness increases as methylation in the B-ring increases¹². The color of BP extract was altered at pH levels ranging from 8 to 10. As shown in **Figure 3B**, the color of BP was purple-blue in pH solution at pH 6-8, blue at pH 9, and green at pH 10. Whereas, the color variation of JD

extracted mixed with butterfly pea (BP) extracted at a 6:1 ratio was clearly observed in pH solution at 8-10. The color of the solution was dark blue when the pH was 4.5-7, lighter blue when the pH was 8, pale blue when the pH was 9, and green-blue when the pH was 10. **Figure 4** depicts the different profiles of UV-Vis spectra of the JD mixed BP (6:1) at pH from 6 to 10 solution and their color alteration.

A



B

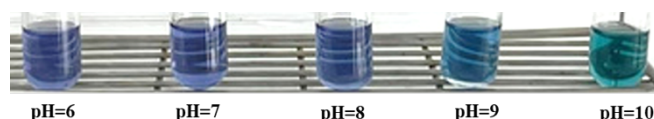


Figure 3. A = Color of JD extracted in pH solution ranging from 1-12, B = Color of BP extracted in pH solution ranging from 6-10.

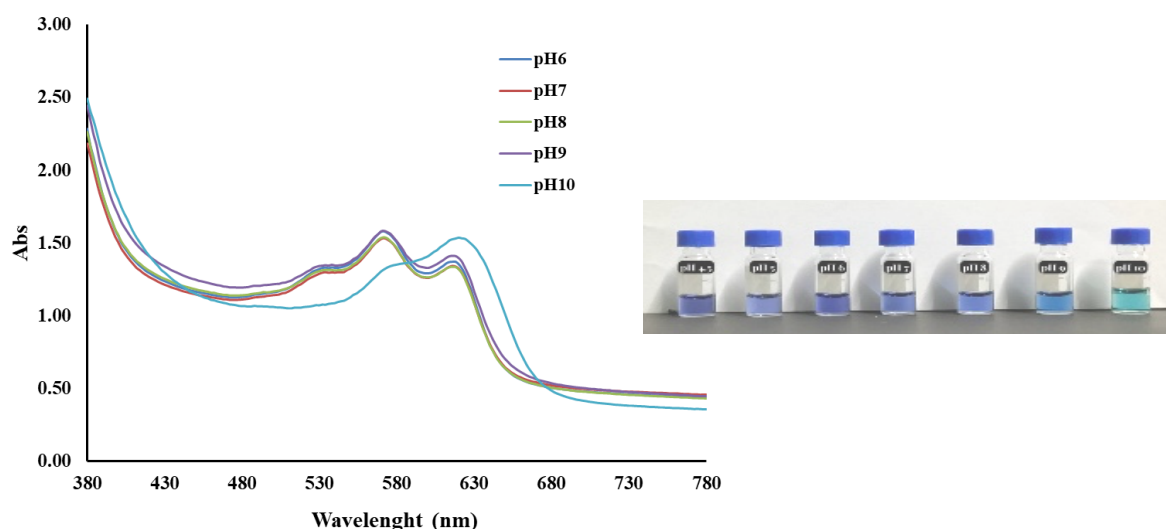


Figure 4. The UV-Vis spectrum and color of JD mixed with BP extracted at a 6:1 ratio at pH levels ranging from 6 to 10.

The maximum absorbance peaks for pH 6-9 were observed between 570 and 630 nm, while the maximum absorbance for pH > 10 was observed between 580 and 650 nm. The addition of BP reduced the range of color change in the dye's mixture due to the increasing of anthocyanin content. The major anthocyanin in BP extracted increases the blueness of the solution by protonating the B-ring. **Figure 5A-C** illustrated the color of a conducted intelligent film containing CMC/SA, CMC/SA and JD extract, and CMC/SA and JD mixed with BP, respectively. The CMC and SA-containing film, shown in **Figure 5A**, is pale yellow in color,

and transparency. **Figure 5B** depicts the CMC and SA incorporated with JD extracted film, which has a light brown color due to the 4% v/v of JD extracted. **Figure 5C** depicts the CMC/SA incorporated with JD mixed BP (6:1 ratio) film with transparency light purple due to anthocyanin color from BP.

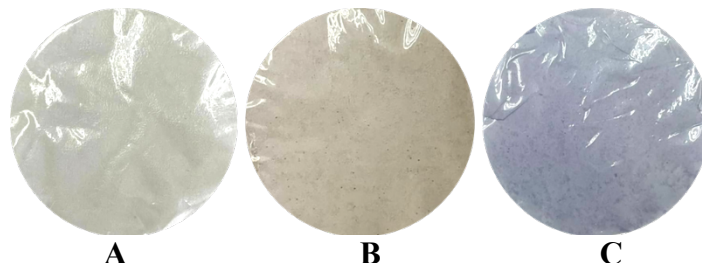


Figure 5. Intelligent film based on CMC/SA incorporated with JD and BP; A = CMC/SA film, B = CMC/SA incorporated with JD extracted film, C = CMC/SA incorporated with JD mixed BP (6:1) extracted film.

The FTIR spectrum of CMC/SA film is similar to the FTIR spectrum of CMC/SA-based incorporated with JD mixed BP intelligent film which shown in **Figure 6**. The O-H and C-H stretching vibrations were represented by the broad peak at 3261 cm^{-1} and the smaller peak at 2929 cm^{-1} , respectively. The C-H bending is represented by the small peak around 1319 cm^{-1} . The C-OH stretching and C-C skeletal stretching have a relatively small peak at 1023 cm^{-1} and a small peak around 950 cm^{-1} , respectively. The C-C stretch (in-ring) aromatics of carbonyls ethers functional group and ethers functional group (C-O stretch) of anthocyanin showed wave number at 1023 cm^{-1} , which indicate the interaction of the aromatic rings of natural dyes with the film matrices. The results agree with previous research that the intensity of the peaks around 1600 cm^{-1} decreased after the mixed dyes were added to the film forming agents⁶. This reduction could be due to the formation of new hydrogen bonds between anthocyanins in mixed dyes and the functional groups of polymers matrices¹³. Thus, the FTIR spectra demonstrated that the mixed JD and BP dyes were successfully incorporated into the CMC/SA film.

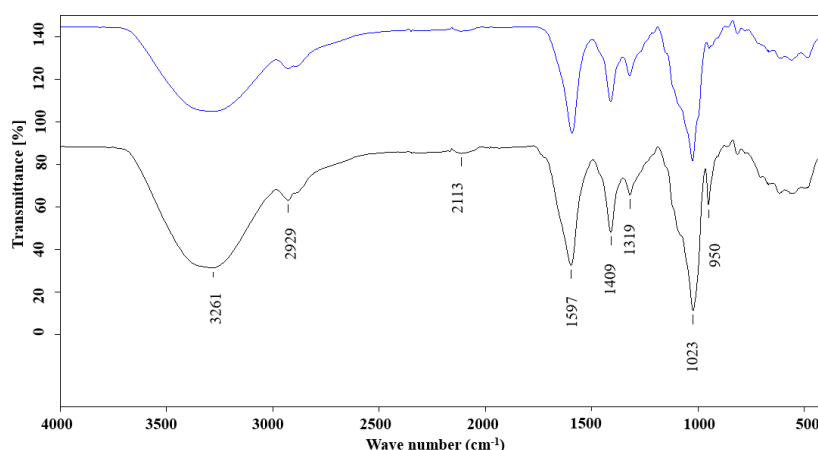


Figure 6. FTIR spectrum of CMC/SA based film based (—line) and FTIR spectrum of CMC/SA incorporated with JD mixed BP intelligent film (—line).

Because of the hydrophilicity of anthocyanins and related compounds, the incorporation of JD mixed BP extracted increased the thickness, moisture content, and water solubility of CMC and SA based intelligent films compared to control films. **Table 1** displays the results of thickness, moisture content, and film solubility in water. The control film had the smallest thickness (0.055 mm), but the greatest moisture content (15.33%) and water solubility (76.77%). However, there was no significant difference in moisture content across all samples.







Table 1. Intelligent film physical properties.

Film	Thickness (mm)	Moisture content (%)	Water solubility (%)
Control	0.055±0.011	15.33±0.007	76.77±1.090
JD	0.062±0.012	12.26±0.008	87.34±1.255
JD+BP	0.071±0.007	16.78±0.008	85.29±1.199

4. Sensitivity of intelligent film to volatile ammonia

To determine the color change of the intelligent films when exposed to volatile gas, the obtained films were introduced to the 10 mM ammonia solution for 20 min and their color change was recorded, as shown in **Table 2**.

Table 2. Intelligent film response to volatile ammonia.

Time (min)	ΔE	S (%)	Film color
0	0.00	0.00	
4	14.05	31.69	
8	17.15	36.31	
12	19.96	41.54	
16	22.85	32.62	
20	23.44	30.15	

Ammonia diffused into the film, generated an alkaline environment, and changing the color of the pH-sensitive intelligent film¹⁴. The ΔE and %S values of intelligent film incorporated with JD mixed BP dyes increased sharply until 16 min, then gradually increased. While, the color of the film was changed from light purple to green. According to the results shown in **Figures 3A and B**, both JD and BP extracts turn green in alkaline solution, and thus the film turns green when ammonia is present in the packaging environment.

5. Application of intelligent film for monitoring seafood spoilage













Meat spoilage and degradation are caused by microorganisms, which produce a variety of organic amines, including volatile nitrogen compounds. The intelligent films containing JD mixed with BP were fixed inside packaging as on-package labels without contacting with the shrimp and fish fillet samples. The color of the film changed from light purple to green and gradually darkened at 12 h, as shown in **Figure 7**, and the ΔE and %S values increased sharply from 0-12 h and gradually decreased after 18 h, as shown in **Table 3**. The films displayed more significant color changes when shrimp and fish fillet samples were stored for 48 hours, whereas the color of the control film showed no color change during storage.



Figure 7. Intelligent film based on CMC/SA incorporated with JD mixed with BP applied for tracing sea food spoilage.

According to the findings of this study, the color difference of films between fresh state and initial spoilage states of shrimp and fish fillet samples can be distinguished by naked eyes.

Table 3. Application of intelligent film to monitor the freshness of seafood.

Time (hours)	ΔE (Fish)	S (%)	Film color (Fish)	ΔE (Shrimp)	S (%)	Film color (Shrimp)
0	0.00	0.00		0.00	0.00	
6	9.44	3.56		9.97	7.25	
12	15.79	1.78		10.65	30.21	
18	12.31	14.95		10.47	21.15	
24	9.24	3.56		6.39	6.04	
48	8.81	5.34		12.86	10.27	

As results showed here, a combination of JD and BP dyes can be used as indicator dyes in intelligent films to monitor the freshness of sea food products.

Conclusion:

Intelligent film was fabricated by combining 6:1 anthocyanin extract from JD and BP with CMC and SA. The FTIR analysis revealed that both anthocyanin extracts used were compatible with the CMC and SA film-based systems. The addition of JD and BP extract increased the thickness, moisture content, and water solubility of intelligent films based. The developed intelligent film was sensitive to volatile ammonia in the packaging and changed color from light purple to green while storing shrimp and fish fillets at 4 °C for 48 h. Thus, anthocyanin from JD rice mixed with anthocyanin from BP in a 6:1 ratio may be a good alternative choice for preparing intelligent films to monitor the freshness of food products.



Acknowledgements:

This project was supported by the Department of Science, Faculty of Science and Technology, Prince of Songkla University, Pattani Campus. The chemistry division's personnel were also acknowledged.

References:

1. Bekhit A E-D A, Holman B W B, Giteru S G, Hopkins D L. Trends Food Sci. Technol. 2021; 109: 280-302.
2. Yang Y, Yu X, Zhu Y, Zeng Y, Fang C, Liu Y, et al. Food Chem. 2022; 393: 133342.
3. Noiwan D, Suppakul P, Rachtanapun P. Polymers. 2022; 14: 3616.
4. Shaoyun H, Yabo X, Yang Z, Qingfeng D, Fuyuan D, Xinghai L, Houbin L. Food Hydrocoll. 2019; 90: 198-205.
5. Khoo H E, Azlan A, Tang S T, Lim S M. Food Nutr. Res. 2017; 61(1): 1361779.
6. Tavakoli S, Mubango E, Tian L, Bohoussou NDri Y, Tan Y, Hong H, et al. Food Chem. 2023; 402: 134203.
7. Umami S, Parjanto Handoyo T, Yunus A. IOP Conf. Series: Earth and Environmental Science. 2021; 709: 012076.
8. Cijian Z, Guohou S, Lele C, Lijuan W. Food Hydrocoll. 2020; 108: 106012.
9. Chen H-Z, Zhang M, Bhandari B, Yang C-H. Food Hydrocoll. 2020; 100: 105438.
10. Oancea S, Stoia M, Coman D. Procedia Eng. 2012; 42: 489-495.
11. Osório C, Machado S, Peixoto J, Bessada S, Pimentel F B C. Alves R, Oliveira M B P P. Separations. 2020; 7(2): 33.
12. Mattioli R, Francioso A, Mosca L, Silva P. Molecules. 2020; 25(17): 3809.
13. Yanlan M, Siying L, Tengteng J, Wenqi W, Sameen D E, Ahmed S, Qin W, Dai J, Yaowen L. Carbohydr. Polym. 2020; 247: 116738.
14. Rut F-M, Susana C M, Fernandes M, Sánchez Á A, Labidi J. Food Hydrocoll. 2022; 123: 107119.



SESSION C-CHEMISTRY (INORGANIC CHEMISTRY)

EFFICIENT MAGNETIC COMPOSITE: AC, NiAl-LDO and Fe₃O₄ for REMOVING MALACHITE GREEN and ERIOCHROME BLACK T DYES in WATER

Kantima Rattana¹, Chamaiporn Janphum¹, Pannawat dumnit¹, Kittiya Srisaiphetr¹, Kanyanut Sukkerd¹, Wanita Bukehya-ah¹, Nisarath Sopee¹, Kritsada Chaichinda¹, Soraida Bosoy², Sonchai Intachai^{2,*}

¹ Department of Basic Science and Mathematics, Faculty of Science, Thaksin University, Songkhla 90000, Thailand

² Innovative Materials Chemistry for Environment Center, Department of Chemistry, Faculty of Science and Digital Innovation, Thaksin University, Phatthalung, 93210, Thailand

*e-mail: sonchai.i@tsu.ac.th

Abstract:

In this work, the composite of activated carbon derived from coconut husk (AC), NiAl-layered double oxide (NiAl-LDO) and magnetite (Fe₃O₄) was carried out by solid-solid reaction as the adsorbent for eliminating both cationic and anionic dyes in water. The as-prepared composite (AC/NiAl-LDO@Fe₃O₄) was verified by XRD, FT-IR, and the magnetic interaction to an external magnet. The strong magnetization between product powder and magnet could confirm the formation of magnetic composite. The as-synthesized composite performed high capacity on removing both malachite green (74%) and eriochrome black T (66%), as a result of AC for removing cationic dye and NiAl-LDO for removing anionic dye. Interestingly, the separation of adsorbent particles was easily conducted by the magnetic operation. This study may provide a valuable method to generate multifunctional adsorbent for purifying both toxic cation and anion in water.

Introduction:

Inorganic solid material has been received much interest based on structural rigidity, easy collection and utilization¹. Besides, multifunctional capacity is intensively engineered, especially decorating active sites with both positively and negatively charged surface². Recently, composite material is mostly developed due to fabricating various characteristics based on the used precursors³. Activated carbon (AC) is a favorite carbon-based material as an excellent adsorbent on capturing dangerous cations due to its large surface area and negatively charge surface^{4,5,6}. Besides, AC can be easily prepared by using biomass as a carbon precursor such as husk and shell of fruits through chemical activation⁴. The added value, adsorption capacity and quantity are also considered to select the carbon source⁵. However, the reuse of AC adsorbent is quite complicated on the step of solid-liquid separation using a centrifugation, therefore, a facile separation is required to support the adsorption process. Mostly reported that magnetite (Fe₃O₄) is a strong magnet, which is extensively mixed with non-magnet to generate the magnetic composite with the synergistic effect of magnetic separation^{1,7}. Recently, toxic species that polluted in water are composed of cationic and anionic forms due to easily dissolved by water. Consequently, the multifunctional capacity of adsorbent is addressed on removing both cation and anion in water, as well as easy separation.

Layered double hydroxide (LDH) has positively-charged surface, and different structure with varying divalent (M²⁺) and trivalent (M³⁺) metal, and interlayer anion (Aⁿ⁻) based on the typical formula of $[M^{2+}_{1-x}M^{3+}_x(OH)_2]^{y+} \cdot A^{n-}_{(y/n)} \cdot mH_2O$ that provides the different characteristics in electrical, optical and/or magnetic properties^{8,9}. Interestingly, the calcination of LDH material can transfer into layered double oxide (LDO) that sometimes



gains larger surface area and higher performance^{10,11}. The adsorbents of NiAl-LDH and its calcined one (NiAl-LDO) has been developed for removing toxic dyes in water, where NiAl-LDO was as the best adsorbent due to larger surface area^{10,11}.

In present study, AC that prepared from coconut husk as carbon precursor was solid-solid mixed with NiAl-LDO and Fe_3O_4 to obtain the magnetic composite as the adsorbent on eliminating both malachite green and eriochrome black T in water. The representative dyes are categorized as one of dangerous chemicals that possibly caused cancer. This study may provide a practical and potential process for purifying dye-wastewater by using the multifunctional adsorbent for eliminating both cationic and anionic dyes with easy magnetic separation.

Materials and method:

Materials

Nickel(II) chloride hexahydrate ($\text{NiCl}_2 \cdot 6\text{H}_2\text{O}$), aluminium(III) chloride hexahydrate ($\text{AlCl}_3 \cdot 6\text{H}_2\text{O}$), and sodium hydroxide (NaOH) were purchased from Carlo Erba Reagenti. Urea ($(\text{NH}_2)_2\text{CO}$) was purchased from Asia Pacific Specialty Chemicals LTD. Phosphoric acid (H_3PO_4) was supplied by Sigma-Aldrich. Ferric chloride hexahydrate ($\text{FeCl}_3 \cdot 6\text{H}_2\text{O}$) was sponsored by KemAus. Ammonium ferrous sulfate ($(\text{NH}_4)_2\text{Fe}(\text{SO}_4)_2 \cdot 6\text{H}_2\text{O}$) was purchased from Ajax Finechem. Malachite green ($\text{C}_{23}\text{H}_{25}\text{ClN}_2$) and eriochrome black T ($\text{C}_{20}\text{H}_{12}\text{N}_3\text{O}_7\text{SNa}$) were obtained from Acros. All chemicals are the reagent grade that were used directly without any further purification.

Preparation of NiAl-LDO

The NiAl-LDH was used as NiAl-LDO precursor, which was conducted by mixing the aqueous solution of $\text{NiCl}_2 \cdot 6\text{H}_2\text{O}$ (0.1 M), $\text{AlCl}_3 \cdot 6\text{H}_2\text{O}$ (0.05 M), and $(\text{NH}_2)_2\text{CO}$ (0.35 M) in aqueous solution under magnetic stirring for 15 min. The resulting solution was transferred in the Teflon-line autoclave, consequently hydrothermally treated at 150 °C for 48 h. The NiAl-LDH solid was obtained by centrifugation, washed several times with deionized (DI) water, and then ethanol, finally dried at 70 °C for 24 h. The appropriated amount of NiAl-LDH was calcined at 400 °C for 2 h to form NiAl-LDO.

2.3 Preparation of AC

Activated carbon (AC) derived from the coconut husk through chemical activation, firstly, the coconut husk was cleaned by water, dried at 110 °C for 24 h, and calcined at 400 °C for 2 h. The biochar was obtained and then activated by the excess amount of H_3PO_4 under magnetic stirring for 24 h. The activated powder was washed by DI water several time until the pH = 7, and dried at 110 °C for 24 h, finally calcined at 1000 °C for 2 h. The resulting activated carbon was small powdered, which was labeled as AC.

Preparation of Fe_3O_4

The aqueous solution of $(\text{NH}_4)_2\text{Fe}(\text{SO}_4)_2 \cdot 6\text{H}_2\text{O}$, $\text{FeCl}_3 \cdot 6\text{H}_2\text{O}$ and NaOH based on the molar ratio of 2:1:5, respectively, were mixed under vigorously magnetic stirring for 15 min. The product (Fe_3O_4) was collected by using the external magnet, and washed with DI water several times until the supernatant pH = 7, then ethanol, and dried at 50 °C for 24 h.

Synthesis of magnetic composite

Three precursors of AC, NiAl-LDO and Fe_3O_4 with the weight ratio of 2:2:1, were carried out by the solid-solid method that mechanically mixed by a pestle in mortar using acetone as a mixer for 30 min. The as-prepared composite was abbreviated as AC/NiAl-LDO@ Fe_3O_4 .

Adsorption process

The capacity of all of as-prepared samples was evaluated by removing malachite green and eriochrome black T in water, where the chemical structure is depicted in Figure 1. The amount of 0.01 g adsorbent was added in an aqueous solution of dye (100 ppm 0.05 L) under magnetic stirring for 60 min in the dark, where the solution pH was in the range of 6.0 – 6.9. At any time, the aqueous dye solution was dropped for 10, 20, 30, 40, 50 and 60 min to measure the absorbance by using UV-VIS spectrophotometry, and the resulting data were taken to calculate the adsorption efficiency and capacity (q_t) following as the equations in Table 1.

Table 1. Equation of the adsorption efficiency and capacity

Parameter	Equation
Adsorption efficiency (%)	$(C_i - C_t)/C_i \times 100$
Adsorption capacity at any time (q_t)	$(C_i - C_t)/m \times V$

Where C_i and C_t (mg/L) are the concentration of the aqueous dye solution at initial time and any time. q_t (mg/g) is adsorption capacity at any time, m (g) is the mass of adsorbent, V (L) is the volume of aqueous dye solution.

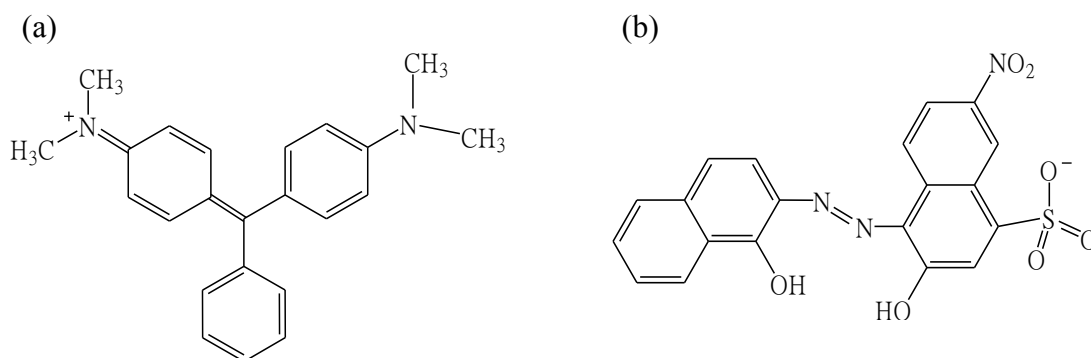


Figure 1. Dye structure of (a) malachite green and (b) eriochrome black T

Characterization:

The structure of samples was verified by powder X-ray diffraction (XRD) using a Bruker D8 ADVANCE diffractometer by a PANalytical Empyrean powder diffractometer. The functional group of samples was investigated by attenuated total reflection-Fourier transform infrared spectroscopy (ATR-FTIR) using a G8044AA-Agilent Technologies. UV-visible absorption spectra of dye solution were performed using a Shimadzu UV-1700 Pharmaspec UV-VIS spectrophotometer.

Result and discussion:

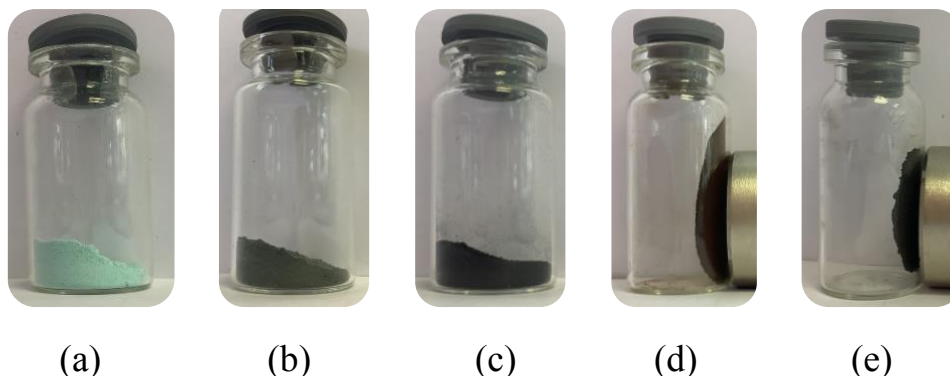


Figure 2. Color of sample powder of (a) NiAl-LDH, (b) NiAl-LDO, (c) AC, (d) Fe₃O₄ and (e) AC/NiAl-LDO@Fe₃O₄

As seen in Figure 2, the powder of NiAl-LDH, NiAl-LDO, AC, Fe₃O₄ and AC/NiAl-LDO@Fe₃O₄ exhibited green, grey, black, black and black, respectively, which was in accordance with the previous reports^{8,12}. Whereas, only Fe₃O₄ of the precursors was responsive to the external magnet, which was indicative of the magnetic particle^{2,7}. After mixing, whole particles of AC/NiAl-LDO@Fe₃O₄ could be lifted by the external magnet, which could confirm the formation of magnetic composite with surrounding of Fe₃O₄.

The XRD patterns are shown in Figure 3, where the diffraction peaks of Fe₃O₄ (Figure 3a) were corresponding to the reflections due to (220), (311), (400), (511) and (440), which could verify the fabrication of magnetite (Fe₃O₄)^{2,7}. For the diffraction peaks of AC (Figure 3b) was in accordance with the reflections of (002) and (110), corresponding to the graphitic-like structure of AC⁴. In Figure 3c, the diffraction peaks of NiAl-LDH were according to the reflections of (003) and (006) owing to the brucite-like structure of LDH^{7,8,9}. Meanwhile the basal spacing (d_{003}) that calculated by the Bragg's equation was about 7.5 Å, which was attributed to the interlayer carbonate (CO₃²⁻), indicating the formation of CO₃²⁻-intercalated NiAl-LDH¹⁰. After calcination, the (003) reflection was disappeared due to the decomposition of the interlayer CO₃²⁻ corresponding to the delamination, and the diffraction characteristics due to mixed metal oxide (NiO and/or NiAl₂O₄) were observed (Figure 3d), as the results of the formation of NiAl-LDO¹¹. For the XRD pattern of composite product (Figure 3e) displayed the diffraction peaks due to Fe₃O₄ and NiAl-LDO, whereas any reflection of AC was disappeared due to very low crystallinity^{5,6}.

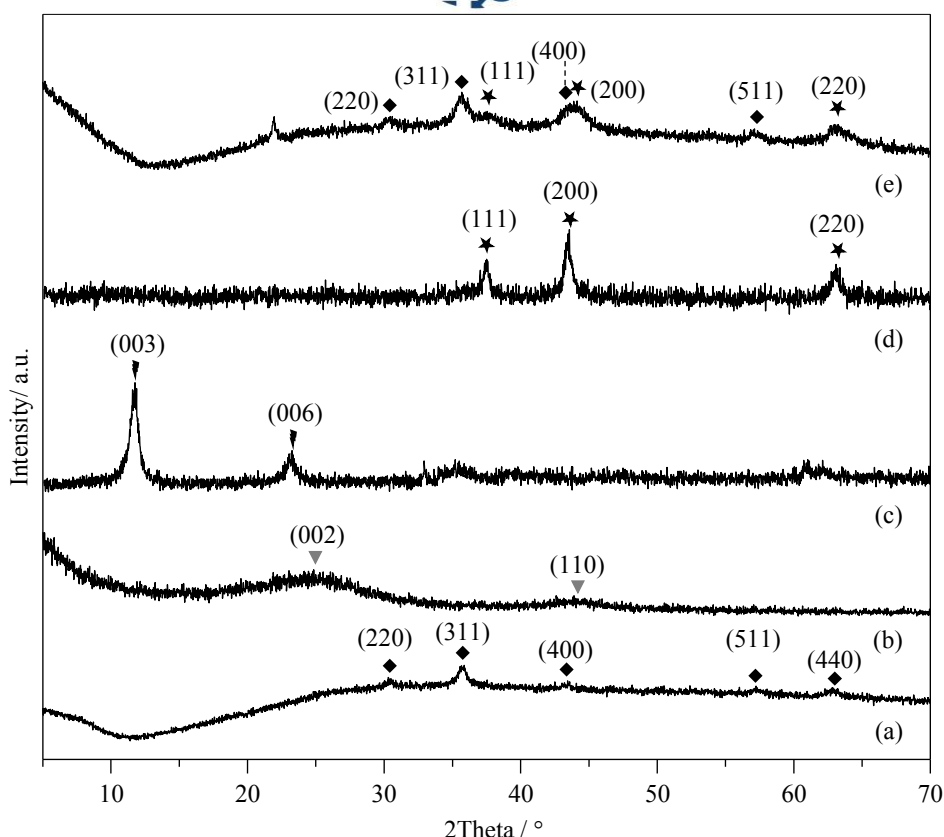


Figure 3. XRD patterns of (a) Fe_3O_4 , (b) AC, (c) NiAl-LDH, (d) NiAl-LDO and (e) AC/NiAl-LDO@ Fe_3O_4

To further verify, the infrared spectra of Fe_3O_4 (Figure 4a), NiAl-LDH (Figure 4c) and NiAl-LDO (Figure 4d) showed the absorbance below 1097 cm^{-1} , according to M–O and/or M–O–M bonds where M is possible either Fe, Ni or Al. In Figure 4b, AC showed the FT-IR bands at 1547 , 1091 and 897 cm^{-1} corresponding to C=C, –COOH and C–O bonds, respectively^{4,5}. The FT-IR spectrum of NiAl-LDH displayed the bands at 3370 and 1598 cm^{-1} due to the interlayer –OH of LDH, and the adsorbed water molecules, respectively, and at 1347 and 809 cm^{-1} due to the FT-IR features of CO_3^{2-} . After calcination, the FT-IR bands due to the interlayer CO_3^{2-} (1347 and 809 cm^{-1}) were disappeared, which could confirm the formation of NiAl-LDO^{10,11,12}. For composite (AC/NiAl-LDO@ Fe_3O_4 in Figure 2e), the FT-IR characteristics were in accordance with AC and Fe_3O_4 . Consequently, the XRD and FT-IR results were indicative of the formation of composite composed of AC, NiAl-LDO and Fe_3O_4 .

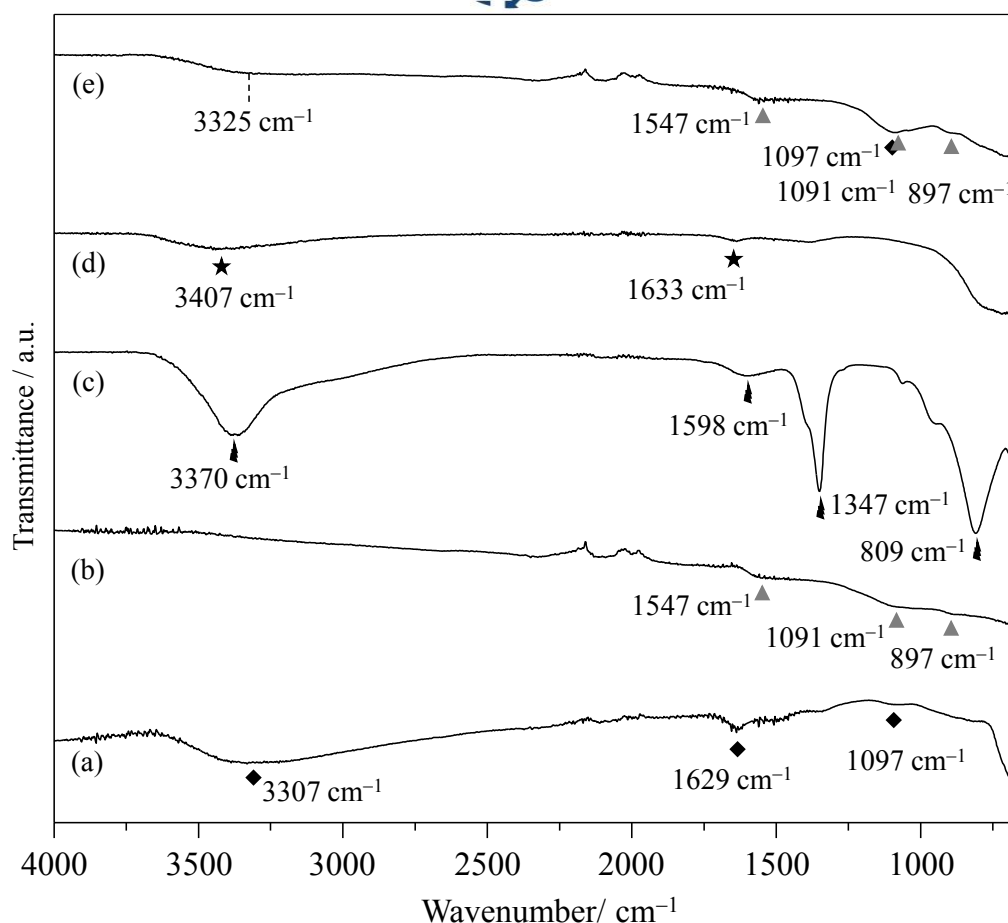


Figure 4. ATR-FTIR spectra of (a) Fe_3O_4 , (b) AC, (c) NiAl-LDH, (d) NiAl-LDO and (e) AC/NiAl-LDO@ Fe_3O_4

All of the as-prepared samples showed the adsorptive capacity, where the data are listed in Table 2. For AC, NiAl-LDH, Fe_3O_4 and AC/NiAl-LDO@ Fe_3O_4 exhibited the removal efficiency of malachite green (Figure 5), and eriochrome black T (Figure 6) (in the parenthesis) of 88 (18), 17 (100), 3 (1) and 74 (66) %, respectively. It was found that AC was the best adsorbent for removing cationic malachite green and NiAl-LDO was the best adsorbent for removing anionic eriochrome black T. As a result, the composite could eliminate both of malachite green eriochrome black T, besides it could be easily collected by magnetic separation. The result was according to the previous reports due to the surface of AC and NiAl-LDO was negative and positive charge that was highly affinitive to capture cation and anion, respectively based on the electrostatic force^{8,9,10,11,12}.

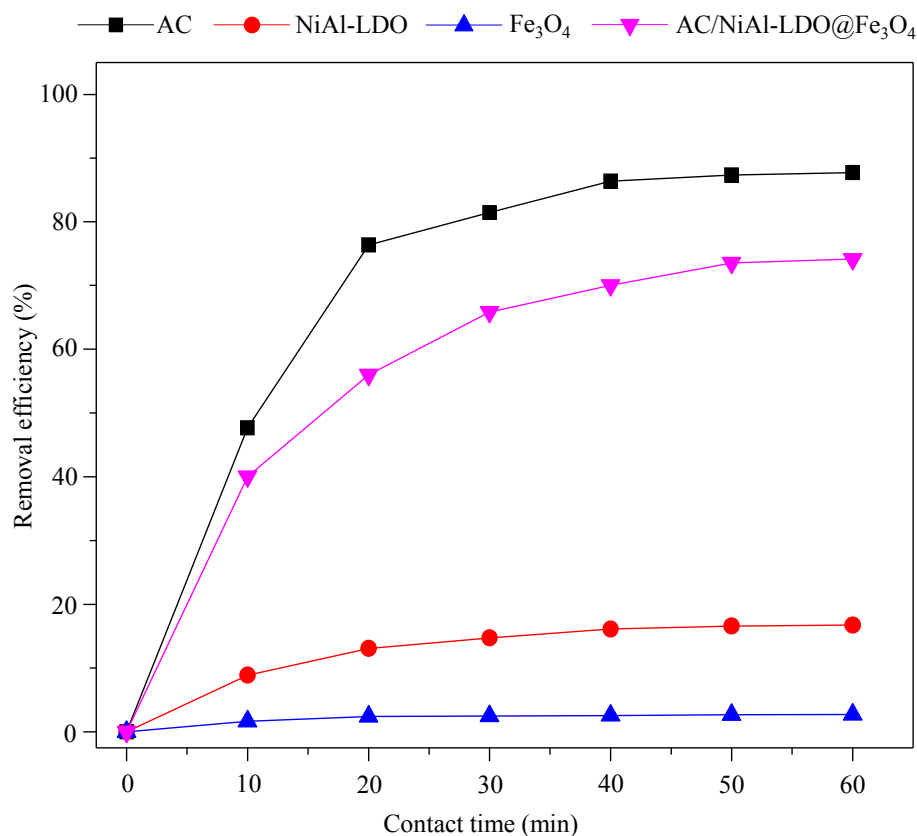


Figure 5. Removal efficiency of malachite green in water using Fe₃O₄, AC, NiAl-LDO and AC/NiAl-LDO@Fe₃O₄

Table 2. Adsorption efficiency and capacity of as-prepared adsorbents

Adsorbent	Adsorption efficiency (%)		Adsorption capacity (mg/g) at 60 min	
	Malachite green	Eriochrome black T	Malachite green	Eriochrome black T
AC	88	18	439	90
NiAl-LDO	17	100	84	498
Fe ₃ O ₄	3	1	14	6
AC/NiAl-LDO@Fe ₃ O ₄	74	66	371	328

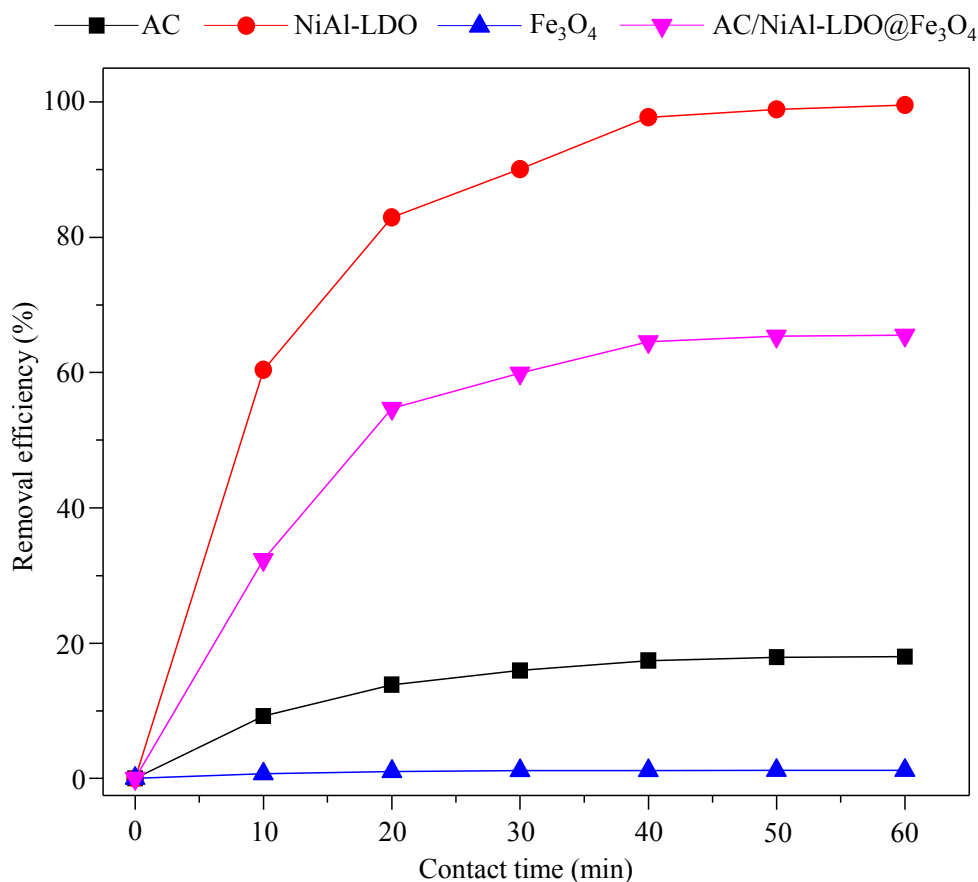


Figure 6. Removal efficiency of eriochrome black T in water using Fe₃O₄, AC, NiAl-LDO and AC/NiAl-LDO@Fe₃O₄

In Table 2, the adsorption capacity at 60 min (q_t) of AC, NiAl-LDH, Fe₃O₄ and AC/NiAl-LDO@Fe₃O₄ for removing malachite green and eriochrome black T (in the parenthesis) of 439 (90), 84 (498), 14 (6) and 371 (328) mg/g, respectively, which was corresponding to the removal efficiency based on the electrostatic interaction between cationic malachite green and negatively-charge surface of AC, as well as anionic eriochrome black T and positively-charge surface of NiAl-LDO. The slight lower adsorption capacity of composite was due to lower number of active sites relative to pure AC (for removing malachite green) and NiAl-LDO (for removing eriochrome black T)^{1,6,7}, however it performed the advantage on the magnetic separation.

Conclusions:

The magnetic composite of coconut husk-derived activated carbon (AC), NiAl-LDO and Fe₃O₄ was successfully prepared by the solid-solid reaction. The results of magnetic interaction to the external magnet, XRD and FT-IR could confirm the formation of magnetic composite that composed of AC, NiAl-LDH and Fe₃O₄. The as-prepared magnetic composite displayed the adsorptive features on eliminating both malachite green ($q_t = 371$ mg/g) and eriochrome black T ($q_t = 328$ mg/g) with the additional synergistic effect of magnetic separation. This study may give the valuable procedure on simple preparation of multifunctional material efficient wastewater purification contaminated with both toxic cation and anion.

Acknowledgments:

This work was funded by Innovative Materials Chemistry for Environment Center, Thaksin University Research Fund, Thailand.

References:

1. Suppasso C, Pongkan N, Intachai S, Ogawa M, Khaorapapong N. *Appl Clay Sci.* 2021;213:106115.
2. Mallakpoura S, Hatami M. *Appl Clay Sci.* 2019;174:127-137.
3. Dai X, Jing C, Li K, Zhang X, Song D, Feng L, Liu X, Ding H, Ran H, Zhu K, Dai N, Rao SYJ, Zhang Y. *Appl Clay Sci.* 2023;233:106815.
4. Mikhalovsky SV, Nikolaev VG. Elsevier Ltd., 2006;pp 529-561.
5. Bouchelkia N, Tahraoui H, Amrane A, Belkacemi H, Bollinger JC, Bouzaza A, Zoukel A, Zhang J, Mouni L. *Process Saf Environ Prot.* 2023;170:513-535.
6. Intachai S, Sumanatrakul P, Pankam P, Suppasso C, Khaorapapong N. *J Inorg Organomet Polym Mater.* 2022;32:1999-2008.
7. Yimin D, Jiaqi Z, Danyang L, Lanli N, Liling Z, Yi Z, Xiaohong Z. *Colloids Surf A Physicochem Eng Asp.* 2018;550:90-98.
8. Intachai S, Na Nakorn M, Kaewnok A, Pankam P, Sumanatrakul P, Khaorapapong N. *Mater Chem Phys.* 2022;288:126388.
9. Intachai S, Sumanatrakul P, Khaorapapong N. *Environ Sci Pollut Res.* 2023;30:63215–63229.
10. Intachai S, Tongchoo P, Sumanatrakul P, Pankam P, Khaorapapong N. *Korean J Chem Eng.* 2022;39: 2675-2684.
11. Intachai S, Pimchan P, Sumanatrakul P. *Naresuan University J: Sci Technol.* 2019;27:66-74.
12. Intachai S, Nakato T, Khaorapapong K. *Appl Clay Sci.* 2021;201:105927.

IRON(III) OXIDE PHOTOCATALYST SUPPORTED ON SILICA DERIVED FROM RICE HUSK FOR DEGRADATION OF METHYLENE BLUE DYE UNDER VISIBLE LIGHT

Kanyarat Prasankan¹, Toiyeebah Yanya¹, Netnapid Ongsuwan², Saowapa Chotisuwan^{3,*}

¹Faculty of Education, Prince of Songkla University, Pattani campus, Thailand

²Department of Food Science and Nutrition, Faculty of Science and Technology, Prince of Songkla University, Pattani campus

³Department of Science, Faculty of Science and Technology, Prince of Songkla University, Pattani campus, Thailand

*e-mail: saowapa.c@psu.ac.th

Abstract:

Pure silica can be synthesized from rice husk biomass. The synthesis of silica from rice husk and its usage as a support material for iron (III) oxide and titanium (IV) oxide were the goals of this research. Fourier transform infrared spectrophotometer (FT-IR) was used to characterize surface functional groups and scanning electron microscope (SEM) was used to characterize the morphology of silica-derived rice husks. An investigation on the efficiency of the methylene blue (MB) degradation process using these catalysts was carried out. Under ultraviolet and visible light, the degradation of MB dye solution with a concentration of 60 ppm, 50 mL at room temperature using catalyst amount at 0.05 g. It was discovered that the greatest percentage of MB degradation under UV light catalyzed by 3.8 wt %. iron (III) oxide on the silica support was 87%, and that the maximum percentage of MB degradation under UV light catalyzed by 40 wt %. titanium (IV) oxide on the silica support was 81%. The percentage of MB that degraded when exposed to visible light irradiation and catalyzed by titanium (IV) oxide on the silica support was 81%, while the percentage of MB that degraded when exposed to iron (III) oxide on silica was 92%. Because of this, the iron (III) oxide catalyst supported on the silica exhibited a better level of catalytic performance when subjected to irradiation by visible light as opposed to UV light. While titanium (IV) oxide supported on silica catalyst can be catalyzed under ultraviolet light in a more efficient manner than it can under visible light.

Introduction:

Rice husk (RH) is one of the most important agricultural biomasses in Thailand; it can be used as a fuel source, a composite in construction materials, in landfills, and as a source of high-value silicon or carbon-based materials.¹ In addition, RH contains a high percentage of silica, approximately 15-20%, so it can be used as a silica source. Simple chemical procedures, including acid or base extraction, the sol-gel method, and calcination, can be used to extract high-purity silica from biomass.² Due to its good porosity, chemical activity, excellent adsorption, and high surface area, it can be used for a variety of applications including adsorbents, rubber, coating, ceramics, catalysts, and support materials.³ Synthesized silica containing active photocatalysts such as titanium (IV) oxide (TiO₂) was prepared to catalyze photocatalytic degradation of synthetic dyes in the presence of light.⁴ In addition, certain metal oxides, including iron-based materials and iron (III) oxide (Fe₂O₃), exhibit photocatalytic activity.⁵ Iron (III) oxide is an excellent catalyst for Fenton-like processes; therefore, it will be used as a cheap photocatalyst and tested for catalytic

performance of dye degradation under UV and visible light.^{6,7} Figure 1 demonstrates the chemical structure of MB, one of the synthetic dyes typically used to test photodegradation efficacy.⁷

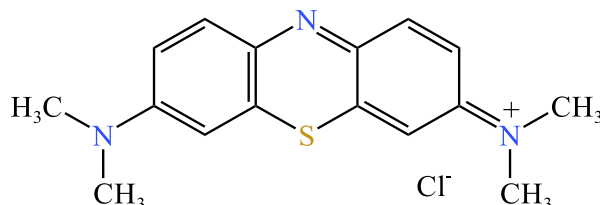


Figure 1. Chemical structure of methylene blue

Methodology:

Materials

Rice husk biomass was collected at Pakarong village, Muang, Pattani, Thailand. The chemicals used in this work such as HCl, NH₃, cetyltrimethylammonium bromide (CTAB), CH₃COOH, C₆H₈O₇, methylene blue, TiO₂, and Fe(NO₃)₃·6H₂O were analytical grade. Light sources were Hg lamp (20W, Phillips) and a LED daylight lamp (20W, Phillips).

Extraction of silica from rice husk

The rice husk was rinsed with deionized water and dried at 100 °C for 3 h. Then, 100 g of rice husk was stirred with 1 N HCl and refluxed at 90 °C for 1 h. After filtration, the solid was dried at 100 °C for 3 h and calcined at 900 °C for 3 h. Prior to use, the silica-derived rice husk powder was stored in a desiccator. The surface functional groups of silica-derived rice husks were characterized by Fourier transform infrared spectrophotometer (FT-IR) (Bruker, Tensor27) and morphology was observed by scanning electron microscope (Thermo Fisher Scientific, Phenom Pro G6).

Catalysts preparation and characterization

In a 500 mL round-bottom flask, 1.7 g of CTAB, 0.2 g of titanium dioxide, 200 mL of methanol, 7.2 mL of ammonia, and 17.2 mL of deionized water were dispersed. The mixture was stirred continuously at ambient temperature for 3 h before 0.5 g SiO₂ was added. It was aged at 3 °C for 3 h before being stored at ambient temperature for 24 h. The white solid was filtered, dried at 60 °C for 3 h, and then calcined at 550 °C for 4 h to give 40 % wt. TiO₂-SiO₂.

Fe₂O₃-SiO₂ catalyst containing 3.8% wt. Fe₂O₃ was produced by continuously stirring 0.05 g acetic acid (CH₃COOH), 0.05 g citric acid (C₆H₈O₇), 0.1 g Fe(NO₃)₃·6H₂O, and 0.5 g SiO₂ in hexane solvent. The mixture was then poured into 500 mL of 10 M NH₃ solution. The solid was subsequently filtered, rinsed with deionized water, and dried at 80 and 180 °C. It was then calcined at 800 °C for 2 h.⁵ FT-IR (Bruker, Tensor27) was used to identify the surface functional groups of photocatalysts.

Degradation efficiency of MB dye solution

The catalytic performance of synthesized catalysts for MB dye degradation was evaluated for 3 replicates using 0.05 g of catalyst dispersed in 50 mL of 60 ppm MB and stirring the mixture in the dark for 1 hour to complete the MB adsorption, then exposed to UV/visible light. The absorbance of MB solution at 664 nm was then measured using a UV-Visible spectrophotometer (Biochrome, Libra S22) at 0, 10, 30, 60, 120, and 180 minutes during the reaction. The MB dye degradation efficiency was calculated by the equation (1).

$$\text{MB dye degradation efficiency (\%)} = \frac{C_0 - C_t}{C_0} \times 100 \quad (1)$$

Where C_0 and C_t are initial MB concentration and MB concentration at t (0, 10, 30, 60, 120, and 180 minutes), respectively.

The used catalysts were separated from the MB solution by filtration, washed with 99.9% ethanol, and dried at 80 °C for 1 h before being retested for catalytic MB dye degradation.

Results and Discussion:

Morphology of silica-derived RH

As shown in Figure 2(a), untreated RH and white powder silica derived from RH biomass were obtained by acid leaching to remove metal impurities and calcination at 900 °C to eliminate carbon and other volatile impurities. The morphology of silica derived RH characterized by SEM is shown in Figure 3, representing non uniformly, amorphous silica particles with low particle size distribution and some large silica particles with diameter larger than 5 μm were also observed. The silica particles synthesized in this work were larger than those synthesized by Lubis et al.⁶



Figure 2. Untreated RH (a) and silica from rice husk after acid treatment and calcined at 900 °C (b).

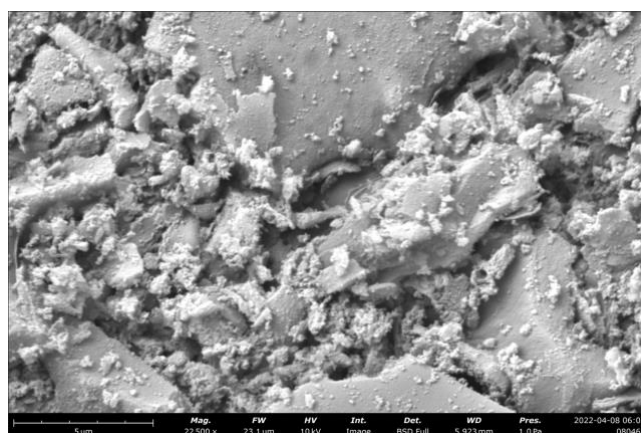


Figure 3. SEM image (at 22,500X) of silica derived from RH after reflux in acid and calcined at 900 °C.

Surface functional groups on silica derived from RH and photocatalyst incorporating silica.

FT-IR was used to characterize the infrared spectra of surface functional groups on silica powder derived from RH, as displayed in Figure 4, which represents pure silica with a

significant transmission band at wavenumber $3,455\text{ cm}^{-1}$ of the surface hydroxyl group: O-H stretching. The peak at $1,637\text{ cm}^{-1}$ belongs to the deformation mode of the surface hydroxyl groups. Siloxane Si-O-Si symmetric stretching is observed with the strongest FT-IR band at wavenumber $1,102\text{ cm}^{-1}$, while Si-O-Si asymmetric stretching is observed at wavenumber 803 cm^{-1} . Peak at 468 cm^{-1} corresponds to Si-O surface deformation vibrations.⁸ Low absorption peak at wavenumber $2,920\text{ cm}^{-1}$ indicates symmetric and asymmetric stretching vibrations of aliphatic C-H bonds in $-\text{CH}_3$ and CH_2 groups in the structures of cellulose, hemicellulose, and lignin, respectively.²

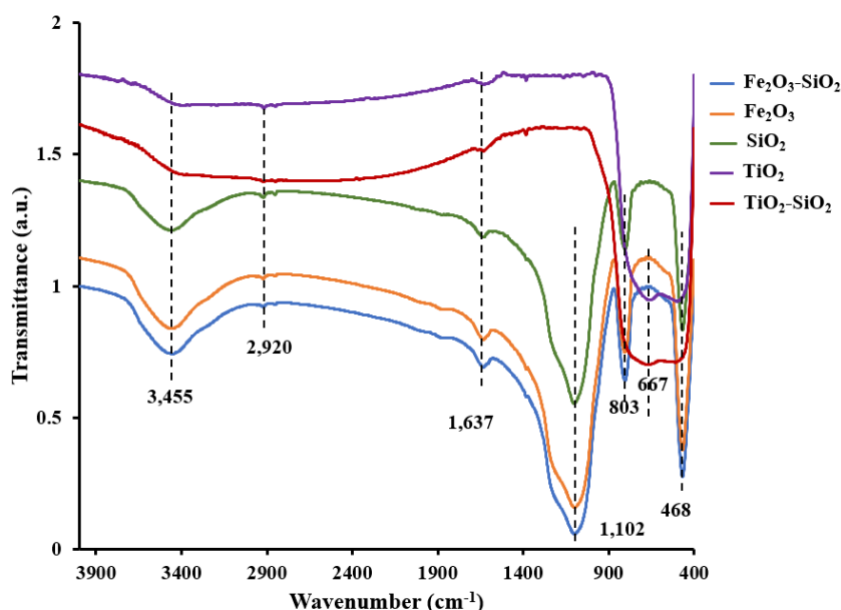


Figure 4. FT-IR spectra of silica from rice husk after reflux in acid and calcined at $900\text{ }^{\circ}\text{C}$ (a), TiO_2 (b), $\text{TiO}_2\text{-SiO}_2$ (c), Fe_2O_3 , (d), and $\text{Fe}_2\text{O}_3\text{-SiO}_2$ (d).

Figure 4 illustrates the overlay FT-IR spectrum of $\text{TiO}_2\text{-SiO}_2$ photocatalyst, which exhibits a broad absorption band between $2,000$ and $3,500\text{ cm}^{-1}$ due to surface hydroxyl groups: O-H stretching for adsorbed water (H-O-H). The Ti-O stretching groups are observed at approximately 667 and 654 cm^{-1} .^{4,9} The surface functional groups on $\text{Fe}_2\text{O}_3\text{-SiO}_2$ also observed as in Figure 4, FT-IR band at $3,453\text{ cm}^{-1}$ indicating surface hydroxyl groups, $1,100\text{ cm}^{-1}$ belongs to Si-O-Si symmetric stretching group, 805 cm^{-1} is from Si-O-Si asymmetric stretching, and 469 cm^{-1} is corresponded to the deformation vibrations for Si-O groups from the silica surface.⁸ However, the small bands at 685 and 604 cm^{-1} that correspond to the stretching vibrations of Fe-O and Si-O-Fe, respectively, were not observed due to small amount of Fe_2O_3 : $3.8\text{ wt } \%$. These peaks will confirm that SiO_2 interacts with Fe_2O_3 .¹⁰

Methylene blue dye degradation catalyzed by photocatalysts incorporating silica.

After adsorption of MB on the catalysts for 1 h in the dark, the photocatalytic performance of synthesized $\text{TiO}_2\text{-SiO}_2$ and $\text{Fe}_2\text{O}_3\text{-SiO}_2$ was determined by measuring the degradation of 60 ppm MB over 180 minutes in the presence of UV and Visible light at room temperature. The percentage of MB degradation under UV irradiation catalyzed by various catalysts is depicted in Figure 5(a). At 180 minutes , the silica derived from RH also resulted in 67% decolorization of MB, which was caused by effective adsorption of MB, as evidenced by the presence of a blue color on the surface of the silica after the addition of 60 ppm MB solution

(figure not shown). Under UV light, bare TiO_2 can degrade 60 ppm MB solution at 71%, while 40 wt % $\text{TiO}_2\text{-SiO}_2$ can achieve up to 81% MB degradation, and 3.8 wt % $\text{Fe}_2\text{O}_3\text{-SiO}_2$ catalyzes the greatest MB degradation at 87%. This trend is also observed with Visible light irradiation, as depicted in Figure 5(b), with maximal MB degradation occurring at 92% when catalyzed by 3.8 wt % $\text{Fe}_2\text{O}_3\text{-SiO}_2$.

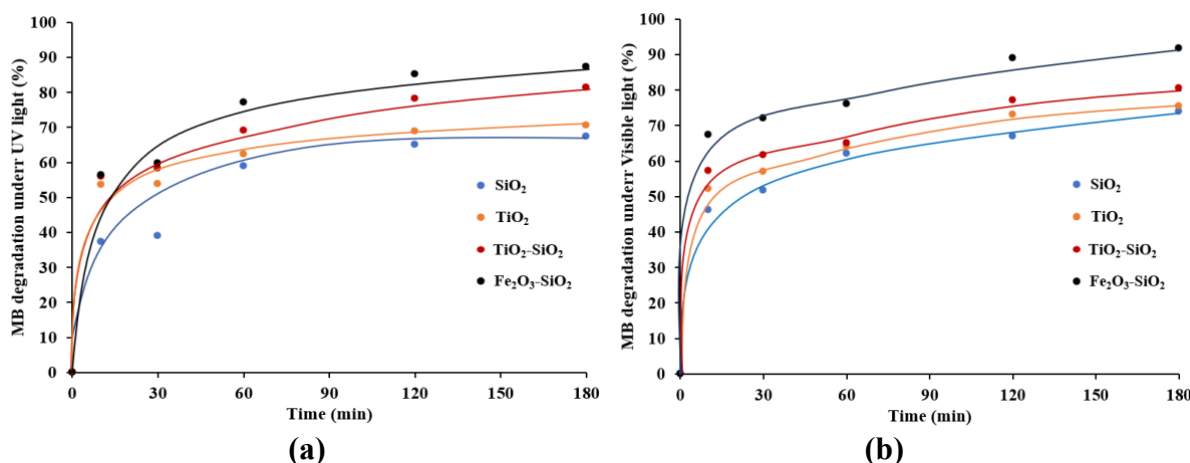
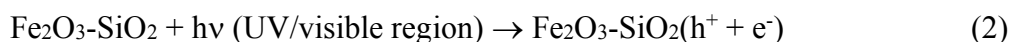


Figure 5. Methylene blue dye degradation catalyzed by catalysts under UV (a) and visible light (b): 60 ppm MB dye solution, 50 mL, catalyst loading 0.050 g at room temperature.

The band gap energy of the Fe_2O_3 semiconductor has been reported to range from 1.9 to 2.2 eV, which is lower than the band gap energy of TiO_2 (3.0–3.2 eV), and the occurrence of rapid recombination of electron and hole is observed for these photocatalysts.^{11, 12} When photons, such as UV or visible light, are absorbed by photocatalysts, electron-hole pairs form, producing active free radical species such as $\cdot\text{OH}$ and $\cdot\text{O}_2^-$, then react with MB molecules forming degradation products such as carbon dioxide, sulfate ion, nitrate ions, and water, as in equation (2)-(6).^{11, 13} Silica can absorb electrons from the photocatalyst's conduction band, thereby decreasing or preventing rapid electron-hole pair recombination and enhancing the oxidation reaction of MB.^{4,6}



After testing the reusability of used photocatalysts that had been washed and dried, it was discovered that the percentage of MB degradation catalyzed by $\text{Fe}_2\text{O}_3\text{-SiO}_2$ decreased from 92% to 71% under the same conditions for visible light irradiation due to deactivation of photocatalyst such as pore blocking, and MB remained adsorbed on the photocatalyst surface.

Conclusion:

The pure, non-uniform micron-sized silica particles can be extracted from rich husk biomass through simple acid treatment, extraction, and calcination at 900 °C. It was combined with TiO₂ and Fe₂O₃ to generate 40 wt % TiO₂-SiO₂ and 3.8 wt % Fe₂O₃-SiO₂, respectively, and used as a photocatalyst for 180 minutes to degrade 60 ppm methylene blue dye under UV/visible light irradiation. Fe₂O₃-SiO₂ demonstrated a maximum MB degradation efficiency (92%) at a catalyst concentration of 0.05 g with 50 mL of 60 ppm methylene blue solution under visible light irradiation.

Acknowledgements:

We express our gratitude to the central instrument center of the Faculty of Science and Technology at Prince of Songkla University, Pattani campus, for providing access to the FT-IR and SEM instruments.

References:

1. Kitsanadecha K, Sinmak C, Onchomchan P, Hantanasirisakul K, Kwamman T, Anantachaisilp S. *J Met Mater Miner*. 2023;33(3):1687, 1-8.
2. Azat S, Sartova Z, Bekseitova K, Askaruly K. *Turkish J Chem*. 2019;43(5):1258-1269.
3. Ajeel SA, Sukkar KA, Zedin NK. *IOP Conf Ser Mater Sci Eng*. 2020; 881(1):1-12.
4. Le MC, Le TH, Bui Thi TH, Nguyen QD, Do Thi TH, Tran Thi MN. *Front Chem*. 2021; 9(September):1-12.
5. Pai RV, Morajkar R, Gumber N, Banerjee AM, Meena SS. *J Nanoparticle Res*. 2021;23(10):1-18.
6. Lubis S, Mustafa I, Ermanda Y, Ramadhani M. *J Phys Conf Ser*. 2021; 1819(1), 1-7.
7. Selpiana H, Aritonang AB, Wibowo MA, Warsidah W, Adhitiawarman A. *JKPK (Jurnal Kim dan Pendidik Kim)*. 2022;7(3):277-286.
8. Niculescu VC, Raboaca MS. *Catalysts*. 2021; 11(7):1-19.
9. Budiarti HA, Puspitasari RN, Hatta AM, Sekartedjo, Risanti DD. *Procedia Eng*. 2017;170:65-71.
10. Vu AT, Xuan TN, Lee CH. *J Water Process Eng*. 2019; 28(January):169-180.
11. Allawi F, AM, Radhi SW. *AIP Conf. Proc*. 4 December 2020;2290 (1) 030020, 1-16.
12. Ola O, Maroto-Valer MM. *J Photochem Photobiol C Photochem Rev*. 2015;24:16-42.
13. Khan I, Saeed K, Zekker I, Zhang B, Hendi AH, Ahmad A, Ahmad S, Zada N, Ahmad H, Shah LA, et al. *Water*. 2022;14(2):242,1-30.



PHOTO-FENTON DEGRADATION OF RHODAMINE B DYE SOLUTION BY $\text{Fe}(\text{IO}_3)_3/\text{FeOOH}$ UNDER VISIBLE LIGHT IRRADIATION

Thanapon Chakarothai,^{1,2*} Sumetha Suwanboon,¹ Pongsaton Amornpitoksuk^{1,2}

¹Division of Physical Science, Prince of Songkla University, Hat-Yai, Songkhla

²Center of Excellence for Innovation in Chemistry, Division of Physical Science, Prince of Songkla University, Hat-Yai, Songkhla

*e-mail: thanapon.rthai@gmail.com

Abstract:

The $\text{Fe}(\text{IO}_3)_3/\text{FeOOH}$ composite Fenton catalyst was synthesized by reacting KIO_3 and FeSO_4 at room temperature. The Fenton activity of this composite was investigated through the degradation of a rhodamine B (RhB) dye solution under visible light irradiation. The catalyst could degrade RhB in the dark via the Fenton reaction, but the degradation increased when visible light was applied. The effects of operational parameters such as H_2O_2 concentration, catalyst loading, and initial dye concentration were studied for the photo-Fenton degradation of RhB. From the experimental results, it was observed that the degradation of RhB increased with increments in H_2O_2 and catalyst concentrations. Conversely, an increase in the initial dye concentration led to a decrease in the degradation of RhB. Additionally, it was found that the degradation of RhB decreased with an increasing number of reuse cycles for the catalyst.

Introduction:

Water pollution poses a significant concern for many countries since clean water is essential for all living organisms. The textile industry, in particular, is notorious for generating substantial volumes of wastewater, which often contains dyestuffs that significantly reduce light penetration due to their high color intensity. Nevertheless, some of these dye molecules are highly toxic and resistant to biodegradation. Consequently, it is imperative to treat this wastewater before releasing it into the environment.

Conventional treatment methods such as adsorption, precipitation, and ion-exchange are readily applicable. However, these methods can merely transform pollutants from one form to another, necessitating further treatment processes. To address these limitations, advanced oxidation processes (AOPs) have been developed. AOPs generate the reactive species to efficiently degrade pollutants, offering a more comprehensive and effective solution. [1-2]. The homogeneous Fenton reaction is a popular choice among AOPs. However, this reaction also yields a significant amount of iron sludge [3]. In order to minimize the by-products of this reaction, there has been a growing focus on heterogeneous Fenton catalysts, which are gaining considerable attention. Iron oxide, in particular, is a widely used heterogeneous Fenton catalyst [4]. However, this catalyst functions most effectively in an acidic environment. FeOOH is a widely used photo-Fenton catalyst, but its activity is relatively low, showing excellent performance primarily in acidic conditions [5-6]. From literature, iodate compounds such as $\text{Bi}(\text{IO}_3)_3$ and AgIO_3 can exhibit photocatalytic properties and enhance the degradation efficiency of some catalysts [7-8]. However, there is no report regarding the photo-Fenton reaction of the $\text{Fe}(\text{IO}_3)_3/\text{FeOOH}$ composite.

In this study, the $\text{Fe}(\text{IO}_3)_3/\text{FeOOH}$ composite was prepared using the co-precipitation method. The capability of the prepared catalyst to degrade pollutants was examined by investigating its performance in the degradation of a rhodamine B dye solution through a photo-Fenton reaction.

Methodology:

The $\text{Fe}(\text{IO}_3)_3/\text{FeOOH}$ composite was synthesized using an ion-exchange method. Specifically, 100 mL of 0.010 mol of KIO_3 was added to 100 mL of a 0.005 mol FeSO_4 solution. This mixture was stirred for 1 hour at 80°C in a water bath. The resulting precipitate was then filtered and dried at 100°C in a hot air oven. X-ray diffractometry (XRD, Empyrean, PANalytical) using $\text{Cu } K_\alpha$ irradiation was employed to identify the structure of the prepared catalyst. Fourier transform infrared (FT-IR) spectrum of sample was recorded using the Nicolet iS5 FTIR spectrometer. The photo-Fenton reaction of the prepared catalyst was investigated by degrading a RhB solution in the presence of H_2O_2 under visible light irradiation. The remained concentrations of RhB at different reaction times were determined by UV-Vis spectrophotometer (UV1800, Shimadzu). Iron leaching due to the photo-Fenton reaction was determined by inductively coupled plasma optical emission spectrometry (ICP-OES, Avio500, PerkinElmer).

Results and Discussion:

Powder X-ray diffraction (XRD) was employed to identify the phase of the prepared catalyst, and the results are depicted in **Figure 1** (black line).

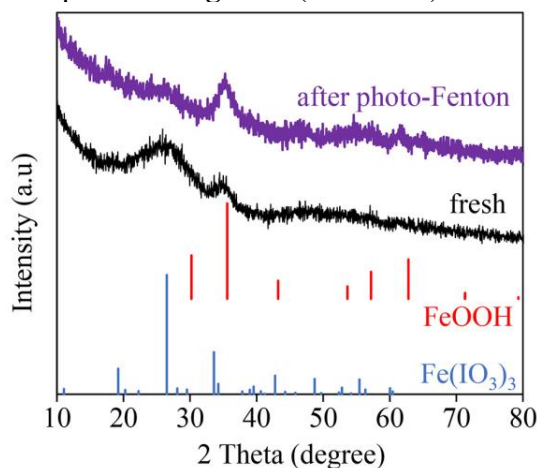


Figure 1. XRD pattern of prepared catalyst before and after photo-Fenton process.

It was evident that the prepared catalyst is a mixture of $\text{Fe}(\text{IO}_3)_3$ and FeOOH , since the XRD pattern was broad, it indicated that the $\text{FeOOH}/\text{Fe}(\text{IO}_3)_3$ was amorphous.

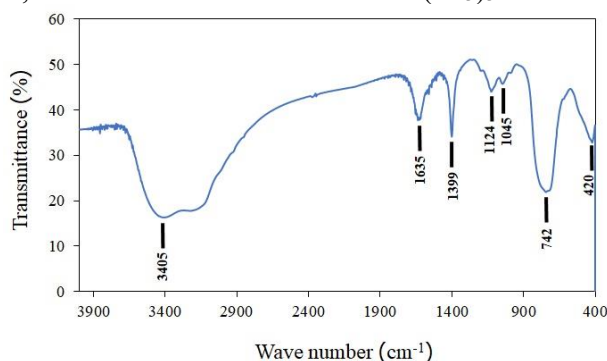


Figure 2. FTIR spectrum of synthesized catalyst.

FTIR spectrum of prepared catalyst was shown in **Figure 2**. The Fe-O stretching was appeared at 420 cm^{-1} and the broad band centered at 742 cm^{-1} was assigned to IO_2 stretching mode in IO_3^- [9]. Two broad peaks at $1630\text{--}1633$ and $3442\text{--}3452 \text{ cm}^{-1}$ were assigned to the bending and stretching modes of the O-H group, respectively, indicating the presence of



adsorbed water on the surface of α -FeOOH [10]. The vibration frequencies at 1045 and 1124 cm^{-1} can be attributed to α -FeOOH [11].

Given that the reduction potential of $\text{Fe}^{3+}/\text{Fe}^{2+}$ (0.77 V) [12] is lower than that of IO_3^-/I_2 (1.10 V) [13], a redox reaction occurs between Fe^{2+} and IO_3^- , as follows:



Produced Fe^{3+} could react with IO_3^- to form $\text{Fe}(\text{IO}_3)_3(\text{s})$:



Some Fe^{2+} could be oxidized to $\text{FeOOH}(\text{s})$:

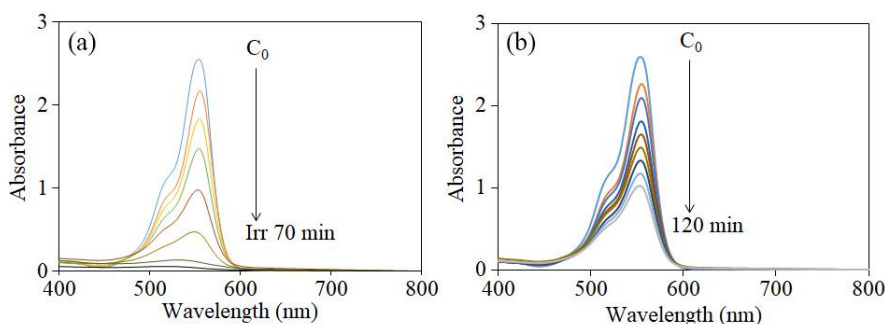


Figure 3. Changes in absorption spectra of RhB at difference reaction times (a) with and (b) without visible light irradiation.

Experimental conditions: $[\text{RhB}] = 1.5 \times 10^{-5} \text{ M}$, $[\text{H}_2\text{O}_2] = 100 \mu\text{L}$, and catalyst loading = 0.05 g.

Photo-Fenton activity was evaluated by monitoring the degradation of RhB under visible light irradiation. The absorption spectrum of the RhB solution revealed a characteristic peak at 554 nm, and its absorbance decreased over time during irradiation (**Figure 3(a)**). To confirm that this reduction in absorbance is not attributable to the Fenton reaction, the experiment was conducted in the absence of light, and the corresponding results are displayed in **Figure 3(b)**. Degradation was quantified using the following equation

$$\text{Degradation (\%)} = [(A_0 - A_t)/A_0] \times 100 \quad (4)$$

where A_0 and A_t are absorbances of RhB at 554 nm for initial solution and after irradiation for time t . **Figure 4** provides a comparative study of RhB degradation both in the presence and absence of visible light irradiation. As depicted in **Figure 4**, RhB degradation occurred in the absence of light, primarily through the Fenton reaction. However, the degradation rate significantly increases when exposed to visible light irradiation. Hence, it could be concluded that the main driving force behind the degradation of RhB in this study was the photo-Fenton reaction.

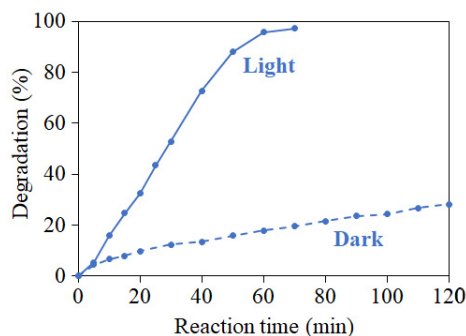
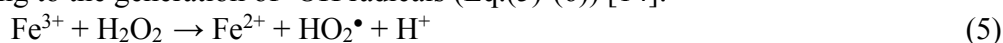


Figure 4. Degradation of RhB in the presence of FeOOH/Fe(IO₃)₃ and H₂O₂ with and without visible light irradiation.

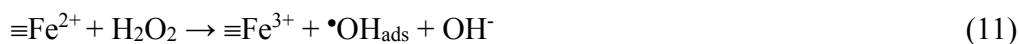
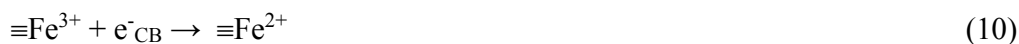
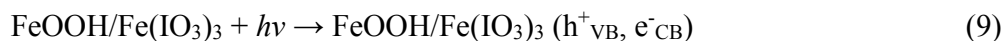
According to the literature, heterogeneous photo-Fenton catalysts typically release iron ions into the solution, and these liberated iron species in the solution can function as homogeneous photo-Fenton catalysts. To investigate the impact of this phenomenon on the degradation of RhB, the solution after the photo-Fenton reaction was introduced to ICP-OES to determine the concentration of leached iron, which was found to be 12.4 ppm. The presence of Fe³⁺ ions in the solution allows them to serve as homogeneous Fenton catalysts, leading to the generation of •OH radicals (Eq.(5)-(6)) [14]:



Upon the addition of FeCl₃ to the RhB solution at a concentration determined by ICP-OES, RhB degradation reached 40% under visible light irradiation. As presented in Figure 3, under dark condition, this composite exhibited Fenton reaction [14]:



In comparison to the dark experiment, the degradation efficiency significantly increased under visible light irradiation. Based on this evidence, it can be concluded that the degradation of RhB using FeOOH/Fe(IO₃)₃ primarily arises from the heterogeneous photo-Fenton reaction (Eq.(9)-(11)) [14]:



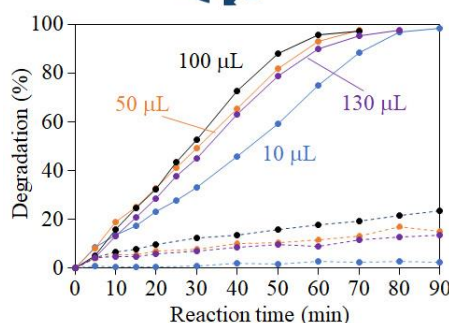


Figure 5. Effect of H_2O_2 volume on photo-Fenton degradation of RhB (dotted lines represent the experiments conducted in the absence of light).
Experimental conditions: $[\text{RhB}] = 1.5 \times 10^{-5} \text{ M}$ and catalyst loading = 0.05 g.

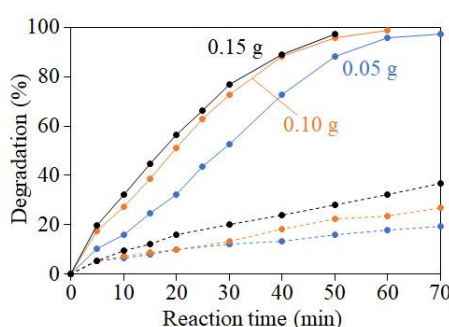


Figure 6. Effect of catalyst loading on photo-Fenton degradation of RhB (dotted lines represent the experiments conducted in the absence of light).
Experimental conditions: $[\text{RhB}] = 1.5 \times 10^{-5} \text{ M}$ and $[\text{H}_2\text{O}_2] = 100 \mu\text{L}$.

The photo-Fenton degradation of RhB using $\text{FeOOH}/\text{Fe}(\text{IO}_3)_3$ can be influenced by various operational parameters, including H_2O_2 volume, catalyst quantity, and initial dye concentration. **Figure 5** illustrates the impact of H_2O_2 on the photo-Fenton degradation of RhB. It was observed that the degradation of RhB increased as the volume of H_2O_2 was raised from 10 μL to 100 μL . Since H_2O_2 serves as a source of $\bullet\text{OH}$ radicals, the increase in H_2O_2 volume led to higher generation of $\bullet\text{OH}$ radicals, consequently enhancing the oxidation rate. However, when the H_2O_2 volume was further increased to 130 μL , the degradation of RhB decreased. This decline can be attributed to the reaction between excess H_2O_2 and $\bullet\text{OH}$ radicals (Eq.(12)) [15]:



Compared to $\bullet\text{OH}$, the $\text{HOO}\bullet$ is much less reactive; therefore, the degradation of RhB was reduced when the volume of H_2O_2 was more than 100 μL .

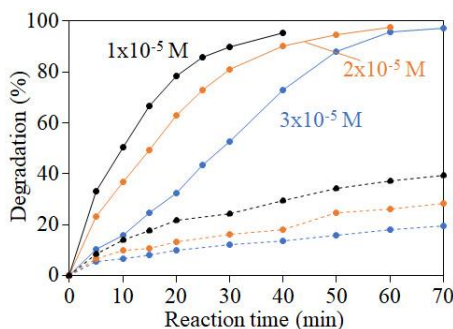


Figure 7. Effect of initial dye concentration on photo-Fenton degradation of RhB (dotted lines represent the experiments conducted in the absence of light).

Experimental conditions: $[H_2O_2] = 100 \mu L$ and catalyst loading = 0.05 g.

The influence of catalyst dosage on the photo-Fenton degradation of RhB is depicted in **Figure 6**. The curves presented in **Figure 6** illustrate that as the catalyst dosage increased from 0.05 to 0.15 g, the degradation of RhB also increased. These results can be explained by the increase in active sites due to the higher catalyst dose, which, in turn, leads to a more robust generation of $\bullet OH$ radicals and an improved degradation rate. In contrast, **Figure 7** demonstrates that an increase in the initial dye concentration resulted in a decrease in the degradation of RhB. This phenomenon is due to the fact that, for a constant catalyst loading, an increment in dye concentration also decreased the $[dye]/[\bullet OH]$ ratio, ultimately reducing the degradation efficiency.

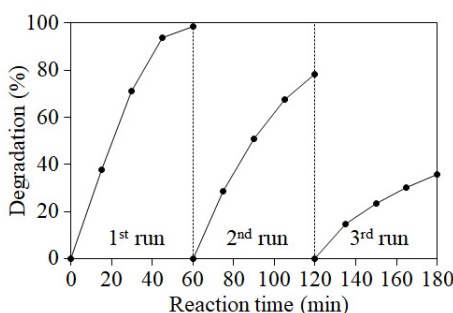


Figure 8. Reusability in RhB degradation in the presence of $FeOOH/Fe(IO_3)_3$.

To assess the stability of the prepared catalyst, $FeOOH/Fe(IO_3)_3$ was examined in terms of its ability to recycle the degradation of RhB solution under visible light irradiation. **Figure 8** illustrates the reusability of $FeOOH/Fe(IO_3)_3$ over three cycles for the degradation of RhB. It is evident that the degradation efficiency decreased with the number of reuses. In **Figure 2** (violet color), the XRD pattern of $FeOOH/Fe(IO_3)_3$ after the photo-Fenton process is displayed. The intensity ratio of the $Fe(IO_3)_3$ and $FeOOH$ peaks in the catalyst after the photo-Fenton process was reduced compared to the fresh catalyst. This reduction could be attributed to the dissolution of $Fe(IO_3)_3$ or its transformation into $FeOOH$. During the photo-Fenton process, the generated $\equiv Fe^{2+}$ (as in Eq(7) or (10)) could react with H_2O_2 and H_2O to produce $FeOOH$ [16]. The decrease in $Fe(IO_3)_3$ content might result in a lower RhB degradation.



Conclusion:

The photo-Fenton catalyst, $\text{FeOOH}/\text{Fe}(\text{IO}_3)_3$, was effectively synthesized using the ion-exchange method. Under neutral conditions, it degraded a rhodamine B solution through the Fenton reaction in the absence of light. However, the degradation efficiency significantly improved when exposed to visible light, owing to the photo-Fenton process. Nevertheless, in the third cycle, the performance of this composite catalyst exhibited a degradation efficiency lower than 80%.

Acknowledgements:

This research was supported by Center of Excellence for Innovation in Chemistry (PERCH-CIC), Ministry of Higher Education, Science, Research and Innovation.

References:

1. Kumari P, Kumar A, Results Surf. Interfaces, 2023; 11:100122.
2. Cuerda-Correa EM, Alexandre-Franco MF, Fernández-González C. Water, 2020; 12:102.
3. Mohammed Bello M, Aziz Abdul Raman A, Asghar A, Process Saf. Environ. Prot., 2019; 126: 119-140.
4. Nidheesh PV, RSC Adv., 2015; 5: 40552-40577.
5. Jiang J, Liang Y, Wang H, Zhao J, Hu J, Wang M, Fibers Polym, 2023; 24: 1641–1648.
6. Ma W, Wu Y, Han C, ChemistrySelect 2019; 4: 10181– 10186.
7. Huang H, He Y, He R, Jiang X, Lin Z, Zhang Y, Wang S, Inorg. Chem. Commun., 2014; 40: 215-219.
8. Zeng C, Ding H, Bao L, Su Y, Wang Z, Ind. Eng. Chem. Res., 2021; 60: 13115–13126.
9. Ristic M, Music S, Ivanda M, J. Mol. Struct., 1999; 480-481: 637-640.
10. Wu S, Lu J, Ding Z, Li N, Fu F, Tang B, RSC. Adv., 2016; 6: 82118-82130.
11. Bashir S, McCabe RW, Boxall C, Leaver MS, Mobbs D, J. Nanopart. Res. 2009; 11: 701–706.
12. Barrocas BT, Osawa R, Oliveira MC, Monteiro OC, Mater., 2023; 16: 2051.
13. Miseki Y, Sayama K, RSC Adv., 2014; 4: 8308-8316.
14. Chen Y, Miller CJ, David Waite T, Environ. Sci. Technol., 2021; 55: 14414–14425.
15. Xu J, Ma Q, Feng W, Zhang X, Lin Q, You C, Wang X, RSC Adv., 2022; 12: 24439–24446.
16. Zhou L, Zhang X, Lei L, J. Environ. Chem. Eng., 2021; 9: 106796.



SESSION C-CHEMISTRY (ORGANIC & MEDICINAL CHEMISTRY)



APORPHINE ALKALOIDS FROM THE LEAVES OF *Alphonsea elliptica*

Natchapong Chuangsom,¹ * Nattarika Chaichana,² Natthawan Sermwittayawong,²

Yaowapa Sukpondma¹

¹Division of Physical Science and Center of Excellence for Innovation in Chemistry, Faculty of Science, Prince of Songkla University, Hat Yai, Songkhla 90112, Thailand

²Division of Biological Science, Prince of Songkla University, Hat Yai, Songkhla 90112, Thailand

*e-mail: 6210220042@psu.ac.th

Abstract:

Three aporphine alkaloids, corydine (**1**), isoboldine (**2**), and corydine-*N*-oxide (**3**), were isolated from the leaves of *Alphonsea elliptica* through phytochemical investigation. Their structures were characterized using a variety of spectroscopic techniques, such as 1D and 2D NMR data (COSY, HMBC, HMQC and NOESY). The antibacterial activity of corydine (**1**) was observed at concentrations greater than 2,048 µg/mL.

Introduction:

Alphonsea is a small genus of the family Annonaceae. The genus *Alphonsea* comprises 23 to 34 species that are found in India, Sri Lanka, Bangladesh, Myanmar, China, Thailand, Laos, Cambodia, Vietnam, Malaysia, Indonesia, Papua New Guinea, and Philippines. In Thailand, 6 to 12 species including *A. glandulosu*, *A. kinggii*, *A. malayana*, *A. pallida*, *A. lucida* and *A. siamensis* were reported.¹

The bark of *A. elliptica* was investigated to provide two oxoaporphines, two dioxoaporphines and an azafluorenone alkaloids.² These compounds showed various biological activities such as antioxidative activity, oxidase inhibitory activity, and cytotoxicity against breast cancer cell lines in a prior paper. In this study, chemical investigation of the leaves of *A. elliptica* resulted in the isolation of three aporphine alkaloids as corydine (**1**), isoboldine (**2**), and corydine-*N*-oxide (**3**). These compounds were tested for antibacterial activity against *Staphylococcus aureus*, *S. epidermidis* and methicillin-resistant *S. epidermidis*.

Methodology:

General experimental procedures

Infrared spectra (IR) were obtained on a FTS165 FT-IR spectrometer or a Perkin Elmer Spectrum GX FT-IR system and recorded on wavenumber (cm⁻¹). ¹H and ¹³C-Nuclear magnetic resonance (¹H and ¹³C NMR) spectra were recorded on a FTNMR Bruker Avance 300 MHz or 500 MHz spectrometers using tetramethylsilane (TMS) as an internal standard. Spectra were recorded as chemical shift parameter (δ) value in ppm down field from TMS (δ 0.00). Ultraviolet spectra (UV) were measured with a UV-160A SHIMADSU spectrophotometer. Principle bands (λ_{max}) were recorded as wavelengths (nm) and log ϵ in MeOH solution. Optical rotations were measured in methanol solution or chloroform solution with sodium D line (590 nm) on a JASCO P-2000 polarimeter.



Plant materials

The leaves of *Alphonsea elliptica* were collected from Nakhon Si Thammarat Province, Thailand. A voucher specimen (C. Leeratiwong 20-1792) was identified by Associate Professor Dr. Jarun Leeratiwong (Division of Biological Science, Prince of Songkla University, Thailand).

Isolation and purification

The leaves of *A. elliptica* (942.0 g) were successively extracted with methanol at room temperature for 7 days. The solvent was evaporated under reduced pressure to give the crude methanol extract (153.0 g) as a dark-green viscous. It was dissolved in dichloromethane to give the dichloromethane soluble (AED) and the insoluble fractions (AEM).

AED was separated by column chromatography over silica gel using 100% dichloromethane and then increased the amount of methanol until 80% methanol in dichloromethane to give five fractions (AED1-AED5). Fraction AED3 was separated by column chromatography over silica gel using 5% methanol in dichloromethane and then increased the amount of methanol until 70% methanol in dichloromethane to give compound **1** (8.2 mg).

AEM was dissolved in acetone to give the acetone soluble (AEA) and insoluble fractions (AEI). Fraction AEA was separated by column chromatography over silica gel. Elution was conducted with 100% dichloromethane and then increased the amount of methanol until 60% methanol in dichloromethane to give compound **1** (414.8 mg). Fraction AEI was further separated by column chromatography over Sephadex LH-20. Elution was conducted with 100% methanol to afford three subfractions (AEI1-AEI3). Subfraction AEI2 was separated by column chromatography over silica gel. Elution was conducted with 5% methanol in dichloromethane and then increased the amount of methanol until 60% methanol in dichloromethane to give compounds **2** (18.0 mg) and **3** (5.0 mg).

Antibacterial assay

The antimicrobial activity of compound **1** against pathogens including *Staphylococcus aureus*, *S. epidermidis* and Methicillin-Resistant *S. epidermidis* was determined through the broth microdilution method in a 96-well polystyrene microtiter plate as described with slight modifications.³ For preparing the working solution, the stock solution of compound **1** (8,192 µg/ml) was two-fold serially diluted in Mueller-Hinton broth (MHB) to the final concentration ranging from 4,096 to 256 µg/ml. The overnight pathogen cultures were adjusted to 0.5 McFarland in fresh MHB and diluted to the final concentration of 10⁵ CFU/ml. Then, 100 µl of pathogen cultures were inoculated in 100 µl of each compound **1** dilution. The plate was incubated at 37 °C for 24 hours with every 1-hour measurement of the kinetic growth curve at optical density (OD) 600 nm. The experiment was performed in duplicate.

Results and Discussion:

The dichloromethane soluble and insoluble fractions, extracted from the leaves of *A. elliptica*, were separated by column chromatography over silica gel and Sephadex LH-20 to obtain three known alkaloids. The known alkaloids included corydine (**1**), isoboldine (**2**) and corydine-*N*-oxide (**3**). Spectroscopic techniques such as 1D and 2D NMR, IR, and HRESI-MS were used to identify the structures of these known alkaloids, and the spectroscopic data were compared with previously reported data.

Compound **1** was obtained as a pale brown amorphous solid. The melting point is 125-128 °C. The IR absorption bands at 3423 (O-H stretching), 1638 and 1466



(C=C stretching) cm^{-1} indicated the presence of hydroxy group and benzene ring. The ^1H and ^{13}C NMR spectra of **1** (Table 1) displayed signals characteristic of an aporphine alkaloid⁴ bearing two aromatic rings [δ_{H} 7.09 (*d*, $J = 9.0$ Hz, H-8), 6.88 (*d*, $J = 9.0$ Hz, H-9) and 6.69 (*s*, H-3); δ_{C} 152.0 (C-10), 149.3 (C-2), 144.0 (C-11), 142.4 (C-1), 131.1 (C-7a), 128.4 (C-1b), 126.7 (C-11a), 124.5 (C-8), 124.2 (C-3a), 119.4 (C-1a), 111.5 (C-3) and 111.0 (C-9)]. In addition, the NMR data indicated the presence of signals for a *N*-methyl group (δ_{H} 2.54, *s*), three methylene groups [δ_{H} 3.13 (*td*, $J = 15.0, 6.0$ Hz, H_a-4), 2.66 (*d*, $J = 15.0$ Hz, H_b-4), 3.02 (*dt*, $J = 13.0, 3.0$ Hz, H_a-5), 2.48 (*m*, $J = 13.0, 3.0$ Hz, H_b-5), 3.05 (*t*, $J = 3.6$ Hz, H_a-7) and 2.40 (*m*, H_b-7)]. The positions of *N*-Me and two methylene protons (H_{ab}-4 and H_{ab}-5) were assigned by HMBC and ^1H - ^1H COSY correlations. HMBC cross peaks of *N*-Me (δ_{H} 2.54) to C-5 and C-6a and those of the methylene H_{ab}-5 to C-3a, C-4 and C-6a, as well as COSY correlation between H_{ab}-4/H_{ab}-5 established a Me-*N*-CH₂CH₂ unit which linked the *N*-Me and the terminal methylene group with C-6a and C-3a, respectively. In addition, the remaining methylene group (H_{ab}-7) showed HMBC correlation with C-7a and C-6a which further attached this methylene group with these carbons. The location of hydroxyl group was assigned at C-1 by HMBC correlations of OH-1 to C-1, C-2 and C-1a whereas those of three methoxy groups at C-2, C-10 and C-11 were established by the same correlations of the methoxy protons of two methoxy groups at δ_{H} 3.91 to C-2 and C-10 and those of a methoxy group at δ_{H} 3.73 to C-11. Furthermore, these assignments were confirmed by NOEDIEF experiment. Irradiation of 1-OH, H-9 and H-3 enhanced signals intensity of 11-OMe, 10-OMe and 2-OMe, respectively. Finally, the specific rotation of compound **1**, $[\alpha]_{\text{D}} +173$ (*c* 0.2, MeOH), was similar to that of corydine, $[\alpha]_{\text{D}} +198$ (*c* 0.2, MeOH).⁵ Thus, compound **1** was elucidated as corydine.⁶

Compound **2** was obtained as a brown amorphous solid. The melting point is 118-121 °C. The UV and IR spectra of compound **2** were similar to those of compound **1**, indicating that they possessed an aporphine skeleton. Their ^1H NMR spectra were similar, except that D ring of compound **2** has two singlet aromatic protons at δ_{H} 6.72 and 7.98 and one methoxy group at δ_{H} 3.87 instead of two *ortho*-coupled aromatic protons of compound **1** (δ_{H} 7.09 and 6.88). These singlet protons were attributed to H-8 and H-11, respectively, according to HMBC correlations of H-8 to C-10 (δ_{C} 145.3) and C-11a (δ_{C} 124.2) and H-11 to C-7a (δ_{C} 129.5) and C-9 (δ_{C} 144.7). The methoxy group resonating at δ_{H} 3.87 was attached to C-10 based on HMBC correlation of these methoxy protons with C-10. Finally, a hydroxy group was located on C-9 because of the chemical shift value of C-9. The absolute configuration of C-6a was suggested to be *S* by comparing the specific rotation of compound **2**, $[\alpha]_{\text{D}} +36.3$ (*c* 0.1, CHCl₃), with the previous reported data for isoboldine⁷ $[\alpha]_{\text{D}} +35$ (*c* 0.1, CHCl₃). Therefore, compound **2** was assigned as isoboldine.⁸

Compound **3** was obtained as a yellow gum. The UV and IR data supported aporphine core. The ^1H and ^{13}C NMR spectra of **3** were very similar to **1** (Table 1) except for the downfield shifts of methylene, methine and methyl carbons at C-5 (δ_{C} 65.0), C-6a (δ_{C} 72.3) and *N*-Me (δ_{C} 58.4), respectively, which suggested that compound **3** was an *N*-oxide derivative of compound **1**. Comparison of the chemical shift values of C-5, C-6a, and *N*-Me of compound **3** with those of corydine (**1**) indicated that the chemical shift values of these carbons in compound **3** were greater than those of compound **1**.⁹ As a result, compound **3** was established as corydine-*N*-oxide.¹⁰

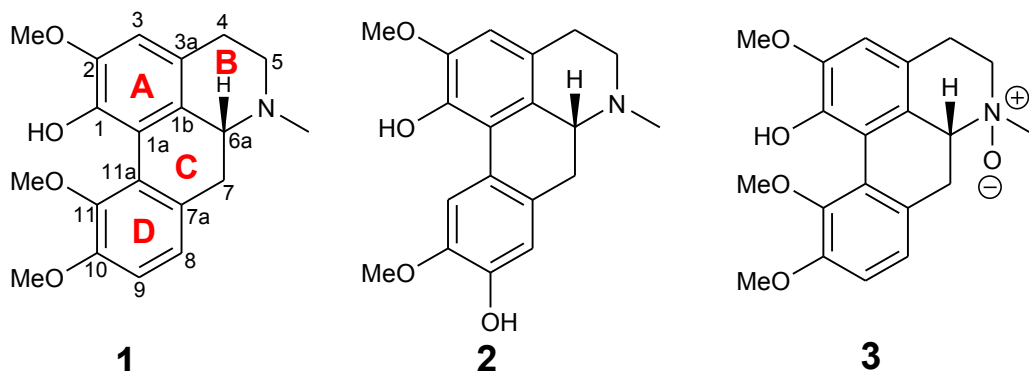


Figure 1. Chemical structures of alkaloids 1-3

Table 1. NMR data of 1 (CDCl₃) and 2 (CDCl₃+CD₃OD) at 300 MHz and 3 (CD₃OD at 500 MHz)

Position	1		2		3	
	δ_c	δ_H	δ_c	δ_H	δ_c	δ_H
1	142.4 (C)	-	140.7 (C)	-	144.0 (C)	-
1a	119.4 (C)	-	119.8 (C)	-	120.8 (C)	-
1b	128.4 (C)	-	127.0 (C)	-	123.8 (C)	-
2	149.3 (C)	-	146.0 (C)	-	151.2 (C)	-
3	111.5 (CH)	6.69 (<i>s</i>)	108.8 (CH)	6.50 (<i>s</i>)	112.5 (CH)	6.89 (<i>s</i>)
3a	124.2 (C)	-	123.9 (C)	-	123.5 (C)	-
4	29.3 (CH ₂)	a: 3.13 (<i>dt</i> , 15.0, 6.0) b: 2.66 (<i>d</i> , 15.0)	28.8 (CH ₂)	a: 3.09 (<i>m</i>) b: 2.60 (<i>m</i>)	25.2 (CH ₂)	a: 3.57 (<i>m</i>) b: 2.79 (<i>m</i>)
5	53.0 (CH ₂)	a: 3.02 (<i>dt</i> , 13.0, 3.0) b: 2.48 (<i>d</i> , 13.0)	53.5 (CH ₂)	a: 3.00 (<i>m</i>) b: 2.49 (<i>m</i>)	65.0 (CH ₂)	a: 3.73 (<i>m</i>) b: 3.60 (<i>m</i>)
6a	63.0 (CH)	2.94 (<i>m</i>)	62.7 (CH)	3.05 (<i>m</i>)	72.3 (CH)	4.35 (<i>dd</i> , 13.5, 3.0)
7	35.8 (CH ₂)	a: 3.05 (<i>t</i> , 3.6) b: 2.40 (<i>m</i>)	34.1 (CH ₂)	a: 2.91 (<i>m</i>) b: 2.51 (<i>m</i>)	31.6 (CH ₂)	a: 3.17 (<i>m</i>) b: 3.00 (<i>m</i>)
7a	131.1 (C)	-	129.5 (C)	-	129.3 (C)	-
8	124.5 (CH)	7.09 (<i>d</i> , 9.0)	114.2 (CH)	6.72 (<i>s</i>)	125.9 (CH)	7.23 (<i>d</i> , 8.0)
9	111.0 (CH)	6.88 (<i>d</i> , 9.0)	144.7 (C)	-	113.3 (CH)	7.05 (<i>d</i> , 8.0)
10	152.0 (C)	-	145.3 (C)	-	153.8 (C)	-
11	144.0 (C)	-	112.0 (CH)	7.98 (<i>s</i>)	145.7 (C)	-
11a	126.7 (C)	-	124.2 (C)	-	126.5 (C)	-
2-OCH ₃	56.2 (CH ₃)	3.91 (<i>s</i>)	56.2 (CH ₃)	3.85 (<i>s</i>)	56.7 (CH ₃)	3.88 (<i>s</i>)
10-OCH ₃	56.2 (CH ₃)	3.91 (<i>s</i>)	56.2 (CH ₃)	3.87 (<i>s</i>)	56.7 (CH ₃)	3.90 (<i>s</i>)
11-OCH ₃	62.1 (CH ₃)	3.73 (<i>s</i>)	-	-	62.2 (CH ₃)	3.67 (<i>s</i>)
1-OH	-	8.70 (<i>s</i>)	-	-	-	-
N-CH ₃	44.2 (CH ₃)	2.54 (<i>s</i>)	43.8 (CH ₃)	2.50 (<i>s</i>)	58.4 (CH ₃)	3.38 (<i>s</i>)

Table 2. ¹H NMR data of compounds (1-3) compared with corydine, isoboldine and corydine-*N*-oxide

Position	Corydine ⁶	1	Isoboldine ⁸	2	Corydine- <i>N</i> -oxide ⁹	3
	δ _H	δ _H	δ _H	δ _H	δ _H	δ _H
1	-	-	-	-	-	-
1a	-	-	-	-	-	-
1b	-	-	-	-	-	-
2	-	-	-	-	-	-
3	6.67 (s)	6.69 (s)	6.60 (s)	6.50 (s)	6.64 (s)	6.89 (s)
3a	-	-	-	-	-	-
4	3.18 (m)	a: 3.13 (<i>dt</i> , 15.0, 6.0)	a: 2.94 (<i>m</i>)	a: 3.09 (<i>m</i>)	a: 3.24 (<i>ddd</i> , 18.0, 12.5, 6.0)	a: 3.57 (<i>m</i>)
	2.67 (m)	b: 2.66 (<i>d</i> , 15.0)	b: 2.57 (<i>m</i>)	b: 2.60 (<i>m</i>)	b: 3.03 (<i>dd</i> , 18.0, 6.0)	b: 2.79 (<i>m</i>)
5	3.06 (m)	a: 3.02 (<i>dt</i> , 13.0, 3.0)	a: 2.94 (<i>m</i>)	a: 3.00 (<i>m</i>)	a: 4.07 (<i>dd</i> , 12.5, 6.0)	a: 3.73 (<i>m</i>)
	2.75 (m)	b: 2.48 (<i>d</i> , 13.0)	b: 2.30 (<i>m</i>)	b: 2.49 (<i>m</i>)	b: 3.82 (<i>m</i>)	b: 3.60 (<i>m</i>)
6a	3.45 (m)	2.94 (<i>m</i>)	2.94 (<i>m</i>)	3.05 (<i>m</i>)	4.47 (<i>dd</i> , 13.0, 3.5)	4.35 (<i>dd</i> , 13.5, 3.0)
7	3.08 (m)	a: 3.05 (<i>t</i> , 3.6)	a: 2.94 (<i>m</i>)	a: 2.91 (<i>m</i>)	a: 3.53 (<i>dd</i> , 12.5, 3.5)	a: 3.17 (<i>m</i>)
	2.37 (m)	b: 2.40 (<i>m</i>)	b: 2.30 (<i>m</i>)	b: 2.51 (<i>m</i>)	b: 2.63 (<i>ddd</i> , 13.0, 12.5, 1.0)	b: 3.00 (<i>m</i>)
7a	-	-	-	-	-	-
8	7.05 (<i>d</i> , 7.2)	7.09 (<i>d</i> , 9.0)	6.72 (s)	6.72 (s)	7.12 (<i>dd</i> , 8.0, 1.0)	7.23 (<i>d</i> , 8.0)
9	6.85 (<i>d</i> , 7.2)	6.88 (<i>d</i> , 9.0)	-	-	6.86 (<i>d</i> , 8)	7.05 (<i>d</i> , 8.0)
10	-	-	-	-	-	-
11	-	-	7.99 (s)	7.98 (s)	-	-
11a	-	-	-	-	-	-
2-OCH ₃	3.87 (s)	3.91 (s)	3.79 (s)	3.85 (s)	3.85 (s)	3.88 (s)
10-OCH ₃	3.87 (s)	3.91 (s)	3.75 (s)	3.87 (s)	3.85 (s)	3.90 (s)
11-OCH ₃	3.71 (s)	3.73 (s)	-	-	3.66 (s)	3.67 (s)
1-OH	8.71 (s)	8.70 (s)	-	-	-	-
N-CH ₃	2.90 (s)	2.54 (s)	2.45 (s)	2.50 (s)	3.14 (s)	3.38 (s)

Table 3. ^{13}C NMR data of compounds (1-3) compared with corydine, isoboldine and corydine-*N*-oxide

Position	Corydine ⁶	1	Isoboldine ⁸	2	Corydine- <i>N</i> -oxide ⁹	3
	δc	δc	δc	δc	δc	δc
1	142.2 (C)	142.4 (C)	141.4 (C)	140.7 (C)	143.9 (C)	144.0 (C)
1a	119.1 (C)	119.4 (C)	120.4 (C)	119.8 (C)	125.6 (C)	120.8 (C)
1b	127.8 (C)	128.4 (C)	123.4 (C)	127.0 (C)	119.3 (C)	123.8 (C)
2	149.0 (C)	149.3 (C)	147.3 (C)	146.0 (C)	151.1 (C)	151.2 (C)
3	111.2 (CH)	111.5 (CH)	109.9 (CH)	108.8 (CH)	110.5 (CH)	112.5 (CH)
3a	123.7 (C)	124.2 (C)	126.7 (C)	123.9 (C)	122.5 (C)	123.5 (C)
4	28.8 (CH ₂)	29.3 (CH ₂)	28.7 (CH ₂)	28.8 (CH ₂)	27.0 (CH ₂)	25.2 (CH ₂)
5	52.6 (CH ₂)	53.0 (CH ₂)	53.4 (CH ₂)	53.5 (CH ₂)	65.6 (CH ₂)	65.0 (CH ₂)
6a	62.6 (CH)	63.0 (CH)	62.9 (CH)	62.7 (CH)	74.5 (CH)	72.3 (CH)
7	35.3 (CH ₂)	35.8 (CH ₂)	33.9 (CH ₂)	34.1 (CH ₂)	29.8 (CH ₂)	31.6 (CH ₂)
7a	130.5 (C)	131.1 (C)	129.5 (C)	129.5 (C)	129.3 (C)	129.3 (C)
8	124.2 (CH)	124.5 (CH)	115.6 (CH)	114.2 (CH)	126.1 (CH)	125.9 (CH)
9	110.8 (CH)	111.0 (CH)	145.9 (C)	144.7 (C)	111.9 (CH)	113.3 (CH)
10	151.7 (C)	152.0 (C)	146.0 (C)	145.3 (C)	152.3 (C)	153.8 (C)
11	143.7 (C)	144.0 (C)	114.2 (CH)	112.0 (CH)	144.0 (C)	145.7 (C)
11a	126.3 (C)	126.7 (C)	124.0 (C)	124.2 (C)	126.5 (C)	126.5 (C)
2-OCH ₃	56.3 (CH ₃)	56.2 (CH ₃)	56.4 (CH ₃)	56.2 (CH ₃)	56.1 (CH ₃)	56.7 (CH ₃)
10-OCH ₃	56.3 (CH ₃)	56.2 (CH ₃)	56.4 (CH ₃)	56.2 (CH ₃)	56.1 (CH ₃)	56.7 (CH ₃)
11-OCH ₃	61.7 (CH ₃)	62.1 (CH ₃)	-	-	62.1 (CH ₃)	62.2 (CH ₃)
1-OH	-	-	-	-	-	-
N-CH ₃	41.2 (CH ₃)	44.2 (CH ₃)	43.9 (CH ₃)	43.8 (CH ₃)	48.3 (CH ₃)	58.4 (CH ₃)

The kinetic growth curve of compound **1** against various bacterial pathogens including *S. aureus*, *S. epidermidis*, and methicillin-resistant *S. epidermidis* was shown in Figure 2. The pathogen growths treated with compound **1** at the concentration of 2,048 $\mu\text{g/mL}$ displayed a normal growth curve, comparable to the negative control. As a result, the antimicrobial activity of **1** exceeded 2,048 $\mu\text{g/mL}$. Consequently, the concentration of **1** that exhibited antibacterial activity needed to be greater than 2,048 $\mu\text{g/mL}$.

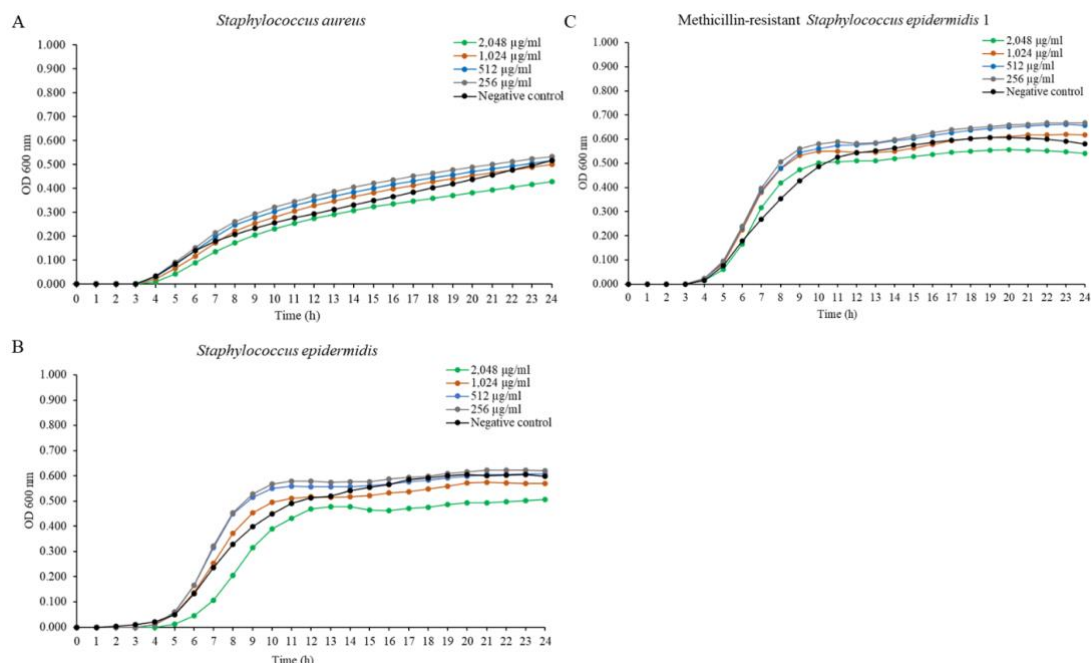


Figure 2. Growth curves of *Staphylococcus aureus* (A), *S. epidermidis* (B) and Methicillin-resistant *S. epidermidis* (C) treated with **1** at different concentrations.

Conclusion:

Corydine (**1**), isoboldine (**2**), and corydine-*N*-oxide (**3**) were obtained from the crude extract from the leaves of *Alphonsea elliptica*. Compound **1** displayed comparable antibacterial activity against *S. aureus*, *S. epidermidis*, and methicillin-resistant *S. epidermidis* to the negative control at the concentration of 2,048 µg/mL. Furthermore, compounds **1**, **2** and **3** were isolated from *Alphonsea elliptica* for the first time.

Acknowledgements:

The Faculty of Science, Prince of Songkla University for the research assistant scholarship, the Center of Excellence for Innovation in Chemistry (PERCH-CIC) and the Graduate School, Prince of Songkla University.

References:

1. Leeratiwong C, Chalermglin P, Johnson D. Thai For Bull (Bot). 2020;48(1):24-33.
2. Obaid A, Saripah S, Mhd BY, Nafiah M, Awang K, Aowda S, Litaudon M, Mohd HN, Naz H, Abbas P, Zuhani Y, Hashim Y, Majhool A. J Glob Pharma Technol. 2018;10:270-275.
3. Taheur FB, Kouidhi B, Fdhila K, Elabed H, Slama RB, Mahdouani K, Bakhrouf A, Chaieb K. Microb Pathog. 2016;97:213-220.
4. Chen JJ, Tsai IL, Ishikawa T, Wang CJ, Chen IS. Phytochemistry. 1996;42(5):1479-1484.
5. Singh D, Chaudhuri KP. Asian J. Chem. 2015;27(4):1567-1568.
6. Ravanelli N, Santos KP, Motta LB, Lago JHG, Furlan CM. S Afr J Bot. 2016;102:153-156.
7. Chang YC, Chung YC, Chang FR, Wu YCJ. J Chin Chem Soc. 2001;48:811-815.
8. Sun C, Li J, Wang D, Yu J, Wang X, Huang L. RSC Adv. 2015;5:75831-75837.
9. Ji Y, Wang C, Zhang Y, Zhang C, Cui D, Zhang X. Rec Nat Prod. 2019;13(4):363-366.
10. Ferreira MLR, Pascoli IC, Nascimento IR, Zukerman-Schpector J, Lopes Lucia MX. Phytochemistry. 2010;71:469-478.

COUMARIN AND ACRIDONE ALKALOID DERIVATIVES FROM THE STEMS OF *Citrus hystrix*

Kanda Panthong,^{1,2,*} Rakson Bunpetch,¹

¹Division of Physical Science and Center of Excellence for Innovation in Chemistry, Faculty of Science, Prince of Songkla University, Hat Yai, Songkhla 90110, Thailand

²Natural Product Research Center of Excellence, Faculty of Science, Prince of Songkla University, Hat Yai, Songkhla 90110, Thailand

*e-mail: kanda.p@psu.ac.th

Abstract:

One known coumarin derivative, scoparone (**1**), and three acridone alkaloids, baiyumine-A (**2**), citracridone-I (**3**) and citropone-A (**4**), were isolated from the acetone extract of the stems of *Citrus hystrix*. Their structures were determined by analysis of 1D and 2D NMR spectroscopic data and comparison of these data with those reported in the literatures. Compounds **1-4** were isolated for the first time from the stems of *Citrus hystrix*. The isolated compounds were evaluated for antioxidant, anti-HIV and antibacterial activities. Unfortunately, all isolated compounds displayed no activities against antioxidant, anti-HIV and antibacterial activities.

Introduction:

Citrus hystrix locally known as “magrood”, is a plant belonging to the Rutaceae family. It is a small size tree about 3-5 m tall with very distinctive leaves. It is found in Thailand and Southeast Asia. The biological activity from many parts of *C. hystrix* has been reported. The leaves showed cytotoxic,¹ antioxidant,^{2,3} antitumor promoter,^{4,5} and antibacterial⁶ activities. The fruit peels displayed antifertility activity⁷ and cholinesterase inhibitory.⁸ Our previous investigation of the roots of *C. hystrix* exhibited anti-HIV, antioxidant and antibacterial activities.⁹ However, a phytochemical examination and biological activity on the stems of *C. hystrix* have not yet been reported.

Methodology:

General material

Ultraviolet (UV) absorption spectra were recorded in methanol solution on a UV-visible spectrophotometer (Shimadzu, UV 1800). Infrared spectra (IR) were recorded using a FT-IR spectrometer (Thermo Scientific, Nicolet is5). ¹H and ¹³C NMR were recorded on a Bruker FTNMR Ultra Shield™ 300 and 500 MHz spectrometers with tetramethylsilane (TMS) as an internal standard. Thin layer chromatography (TLC) was performed on silica gel 60 GF₂₅₄ (Merck). Dry column vacuum chromatography (DCVC) and column chromatography (CC) were carried out on silica gel (Merck) types 60 and 100 (70-230 mesh ASTM), respectively, or on Sephadex LH-20 (GE-Healthcare).

Plant material

The stems of *C. hystrix* were collected in Songkhla province, in the Southern part of Thailand, in March 2008. A voucher specimen (Yuranan 01) was deposited at the Herbarium of Division of Biological Science, Faculty of Science, Prince of Songkla University, Hat Yai, Thailand.

Extraction and isolation

Air-dried and chopped stems of *C. hystrix* (2.20 kg) were extracted with acetone (3 × 10 L) for 7 days at room temperature to afford a dark brown gum (106.90 g) after evaporation of

the solvent under vacuum. Then 16.90 g of crude extract was subjected to DCVC, eluting with hexane, acetone and methanol in a polarity gradient manner to obtain 12 fractions (A1-A12). Fraction A4 (975.9 mg) was separated by repeated CC, CC over Sephadex LH-20 followed by recrystallization from CH₂Cl₂-hexane to give **1** (1.8 mg), **2** (34.7 mg), **3** (3.6 mg) and **4** (1.5 mg).

Free radical scavenging, anti-HIV and antibacterial assays

These assays were performed as previously described.⁹

Results and Discussion:

The acetone extract from the stems of *C. hystrix* exhibited the antioxidant, anti-HIV and antibacterial activities. These activities prompted us to further investigate its chemical constituents. The acetone extract of the stems of *C. hystrix* was subjected to chromatographic purification to give four known compounds [one coumarin derivative: scoparone (**1**),¹⁰ and three alkaloid derivatives: baiyumine-A (**2**),¹¹ citracridone-I (**3**)¹² and citropone-A (**4**)¹³] (Figure 1). Their structures were elucidated by spectroscopic method. ¹H NMR spectroscopic data were compared with those previously reported.

Compound **1** was obtained as a colourless solid and melted at 143.8-144.9 °C. Its NMR spectroscopic data (Table 1) were similar to those of scoparone. Then, **1** was assigned as 1,7-dimethoxycoumarin (scoparone) previously isolated from *Skimmia laureola*.¹⁰

Compound **2** was obtained as a yellow solid and melted at 155.4-155.9 °C. Its NMR spectroscopic data (Table 2) were similar to those of baiyumine-A. Therefore, **2** was assigned as 1-hydroxy-5-methoxy-6',6'-dimethylpyrano(2',3':3,4)acridone (baiyumine-A) which was previously isolated from *C. grandis f. hakunikuyu*.¹¹

Compound **3** was obtained as orange crystals and melted at 258.2-259.5 °C. Its NMR spectroscopic data (Table 2) were similar to those of **2** except that signals for three ABC pattern aromatic protons [δ_{H} 7.19 (1H, *dd*, *J* = 7.8, 1.5 Hz, H-6), 7.27 (1H, *t*, *J* = 7.8 Hz, H-7) and 7.95 (1H, *dd*, *J* = 7.8, 1.5 Hz, H-8)] of **2** were replaced by signals for two *ortho*-coupled aromatic protons [δ_{H} 6.98 (1H, *d*, *J* = 8.7 Hz, H-7) and 8.05 (1H, *d*, *J* = 8.7 Hz, H-8)]. HMBC correlations of both *ortho*-coupled aromatic protons with C-6 (δ_{C} 154.6) together with the chemical shift of C-6 indicated that a hydroxyl group was attached at C-6. Thus, **3** was assigned as 1,6-dihydroxy-5-methoxy-6',6'-dimethylpyrano(2',3':3,4)acridone (citracridone-I) which was previously isolated from *C. depressa*.¹²

Compound **4** was obtained as an orange solid and melted at 262.7-263.2 °C. Its NMR spectroscopic data (Table 2) were similar to those of citropone-A. Thus, **4** was assigned as citropone-A which was previously isolated from *C. natsudaoidai*.¹³

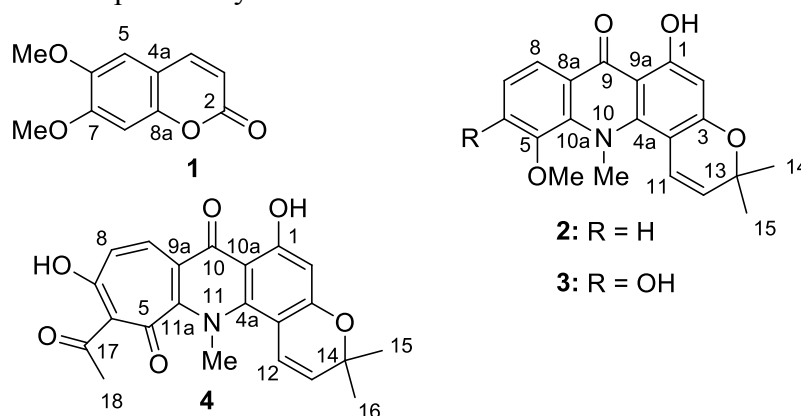


Figure 1. Structures of compounds **1-4**.

Table 1. The NMR data of **1** in CDCl₃

Position	δ_{H} (mult, J in Hz) ^a	δ_{C} (C-type) ^a
2	-	161.3 (C)
3	6.31 (<i>d</i> , 9.6)	113.6 (CH)
4	7.65 (<i>d</i> , 9.6)	143.2 (CH)
4a	-	111.4 (C)
5	6.87 (<i>s</i>)	108.1 (CH)
6	-	150.1 (C)
6-OMe	3.97 (<i>s</i>)	56.4 (CH ₃)
7	-	146.4 (C)
7-OMe	3.94 (<i>s</i>)	56.4 (CH ₃)
8	6.86 (<i>s</i>)	100.1 (CH)
8a	-	152.9 (C)

^a¹H NMR 300 MHz and ¹³C NMR 75 MHz**Table 2.** The NMR data of **2**, **3** and **4** in CDCl₃

Position	2^a		3^a		4^b	
	δ_{H} (mult, J in Hz)	δ_{C} (C-type)	δ_{H} (mult, J in Hz)	δ_{C} (C-type)	δ_{H} (mult, J in Hz)	δ_{C} (C-type)
1	-	164.7 (C)	-	164.8 (C)	-	164.3 (C)
1-OH	14.25 (<i>s</i>)	-	14.26 (<i>s</i>)	-	14.05 (<i>s</i>)	-
2	6.25 (<i>s</i>)	98.4 (CH)	6.25 (<i>s</i>)	98.8 (CH)	6.29 (<i>s</i>)	100.3 (CH)
3	-	161.5 (C)	-	161.2 (C)	-	161.9 (C)
4	-	102.6 (C)	-	102.7 (C)	-	101.9 (C)
4a	-	148.0 (C)	-	147.4 (C)	-	143.9 (C)
5	-	150.7 (C)	-	136.0 (C)	-	185.8 (C)
5-OMe	4.00 (<i>s</i>)	56.3 (CH ₃)	3.90 (<i>s</i>)	60.2 (CH ₃)	-	-
6	7.19 (<i>dd</i> , 7.8, 1.5)	115.6 (CH)	-	154.6 (C)	-	117.4 (C)
6-OH	-	-	-	-	-	-
7	7.27 (<i>t</i> , 7.8)	123.3 (CH)	6.98 (<i>d</i> , 8.7)	112.2 (CH)	-	176.7 (C)
7-OH	-	-	-	-	16.51 (<i>s</i>)	-
8	7.95 (<i>dd</i> , 7.8, 1.5)	118.0 (CH)	8.05 (<i>d</i> , 8.7)	123.5 (CH)	6.61 (<i>d</i> , 12.5)	124.0 (CH)
8a	-	125.2 (C)	-	118.6 (C)	-	-
9	-	182.1	-	181.6 (C)	7.91 (<i>d</i> , 12.5)	133.4



9a	-	(C) 107.6	-	106.9 (C)	-	(CH) 117.4
10	-	(C) -	-	-	-	(C) 180.0
10-NMe	3.73 (s)	49.2 (CH ₃)	3.70 (s)	48.1 (CH ₃)	-	(C) -
10a	-	138.4 (C)	-	141.7 (C)	-	108.5 (C)
11	6.64 (d, 9.6)	121.2 (CH)	6.54 (d, 9.6)	120.5 (CH)	-	-
11-NMe	-	-	-	-	3.69 (s)	47.0 (CH ₃)
11a	-	-	-	-	-	153.8 (C)
12	5.54 (d, 9.6)	124.0 (CH)	5.57 (d, 9.6)	124.8 (CH)	6.55 (d, 10.0)	120.5 (CH)
13	-	77.4 (C)	-	77.4 (C)	5.51 (d, 10.0)	124.6 (CH)
14	1.51 (s)	27.3 (CH ₃)	1.51 (s)	27.3 (CH ₃)	-	77.0 (C)
15	1.51 (s)	27.3 (CH ₃)	1.51 (s)	27.3 (CH ₃)	1.44 (s)	26.9 (CH ₃)
16	-	-	-	-	1.44 (s)	26.9 (CH ₃)
17	-	-	-	-	-	203.5 (C)
18	-	-	-	-	2.50 (s)	28.4 (CH ₃)

^a¹H NMR 300 MHz and ¹³C NMR 75 MHz

^b¹H NMR 500 MHz and ¹³C NMR 125 MHz

The crude extract of this plant displayed the antioxidant, anti-HIV and antibacterial activities. The isolated compounds were assayed for their biological activities in our previous report.⁹ Unfortunately, their biological activities of all isolated compounds showed no activities against antioxidant, anti-HIV and antibacterial activities⁹ possibly due to a synergistic effect in the crude extract.

Conclusion:

This is the first report on chemical constituents from the stems of *C. hystrix*. One known coumarin derivative, scoparone (**1**), and three alkaloid derivatives, baiyumine-A (**2**), citracridone-I (**3**) and citropone-A (**4**), were isolated by chromatographic techniques. These compounds showed no activities against antioxidant, anti-HIV and antibacterial activities.

Acknowledgements:

This work was supported by Faculty of Science, Prince of Songkla University.

References:

1. Ong CY, Ling SK, Ali RM, Chee CF, Samah ZA, Ho ASH, Teo SH, Lee HB. *Photobiol.* 2009;96:216–222.
2. Hutadilok-Towatana N, Chaiyamutti P, Panthong K, Mahabusarakam W, Rukachaisirikul V. *Pharm Biol.* 2006;44:221–228.
3. Wong SP, Leong LP, Koh JHW. *Food Chem.* 2006;99:775–783.
4. Murakami A, Nakamura Y, Koshimizu K, Ohigashi H. *J Agric Food Chem.* 1995;43:2779–2783.
5. Tiwawech D, Hirose M, Futakuchi M, Lin C, Thamavit W, Ito N, Shirai T. *Cancer Lett.* 2000;158:195–201.
6. Wannissorn B, Jarikasem S, Siriwangchai T, Thubthimthed S. *Fitoterapia.* 2005;76:233–236.
7. Piyachaturawat P, Glinsukon T, Chanjarunee A. *J Ethnopharmacol.* 1985;13:105–110.
8. Youkwan J, Sutthivaiyakit S, Sutthivaiyakit P. *J Nat Prod.* 2010;73:1879–1883.
9. Panthong K, Srisud Y, Rukachaisirikul V, Hutadilok-Towatana N, Piyawan Voravuthikunchai S, Tewtrakul S. *Phytochemistry.* 2013;88:79–84.
10. Razdan TK, Qadri B, Harkar S, Waight ES. *Phytochemistry.* 1987;26:2063–2069.
11. Wu TS. *Phytochemistry.* 1987;26:871–872.
12. Wu TS, Kuoh LS, Furukawa H. *Chem Pharm Bull.* 1983;31:895–900.
13. Ito C, Tanahashi S, Fujiwara K, Nakagawa M, McPhall AT, Wu TS, Kajiura I, Omura M, Furukawa H. *Chem Pharm Bull.* 1990;38:1881–1885.

ONE-POT SYNTHESIS OF 4-ARYL-1,2-NAPHTHOQUINONES AND 2-ARYL-1,4-NAPHTHOQUINONES

Pipat Pobpimai,^{1,2} Torsak Luanphaisarnnont^{1,2,*}

¹Department of Chemistry, Faculty of Science, Mahidol University, Bangkok 10400, Thailand

²Center of Excellence for Innovation in Chemistry (PERCH-CIC), Faculty of Science, Mahidol University, Bangkok 10400, Thailand

*e-mail: torsak.lua@mahidol.ac.th

Abstract:

Development of green and efficient synthetic methods is an ongoing challenge in synthetic chemistry. One approach to solve this problem is one-pot reactions wherein multiple transformations are achieved in one reaction vessel. Although many synthetic methods for 4-aryl-1,2-naphthoquinones and 2-aryl-1,4-naphthoquinones—important and useful structures—have been reported, one-pot methods directly from 1-naphthols are limited. This work focused on the development of a one-pot synthesis of 4-aryl-1,2-naphthoquinones and 2-aryl-1,4-naphthoquinones from 1-naphthols. Investigation of electronic requirement in the reaction was also reported.

Introduction:

Chemical synthesis is an important area in chemistry to access a variety of compounds with useful applications. Green chemistry is a strategy to make synthetic methods more environmentally and economically friendly. A one-pot reaction allows multi-step chemical transformations in one reaction vessel. Therefore, it can minimize chemical waste and increase time-efficiency. A one-pot synthesis is also convenient to operate, avoiding labor-consuming purification steps of intermediates in the synthesis. Despite these advantages, one-pot reactions are not widely used, possibly due to the complex compatibility among different substrates in the reaction.

4-Aryl-1,2-naphthoquinones and 2-aryl-1,4-naphthoquinones are sub-structures of many organic compounds with useful biological activities such as anti-angiogenesis,¹ anti-oxidant,² and anti-cancer properties.^{3,4} These motifs have also been found in many natural products.^{1,5} In addition, these compounds have been used as a photochromic dye.⁶

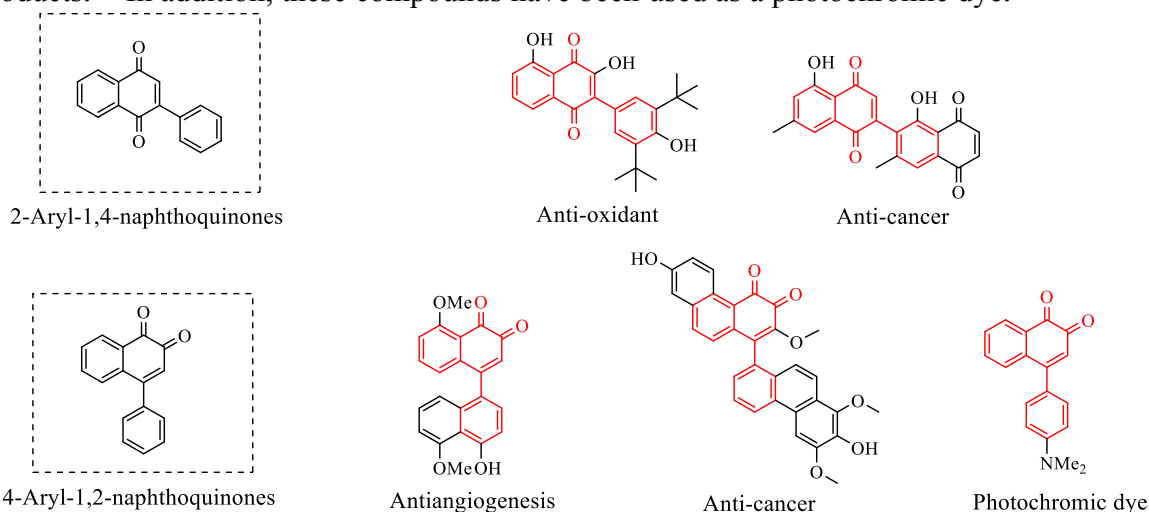
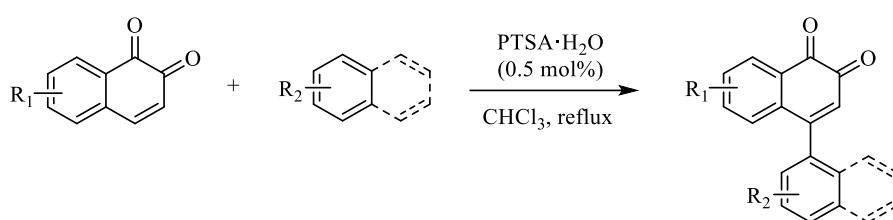


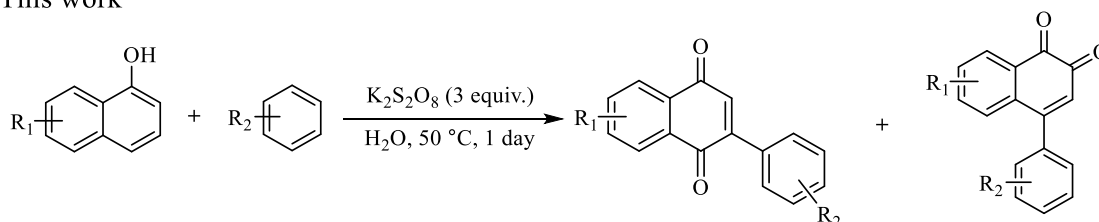
Figure 1. Examples of 2-aryl-1,4-naphthoquinone and 4-aryl-1,2-naphthoquinone derivatives

Previous syntheses of 2-aryl-1,4-naphthoquinones have been reported using diverse methods, including cross-coupling reactions,^{7–9} oxidative arylation,¹⁰ intramolecular cyclization,^{11,12} and oxidative dearomatization.¹³ For the synthesis of 4-aryl-1,2-naphthoquinones, various approaches have been explored, such as the oxidation of 2-naphthols,¹⁴ vinylogous Michael reactions,¹⁵ oxidative annulation of aryl glyoxal with alkynes,¹⁶ homo-coupling reactions,¹⁷ cross-coupling reactions,¹⁸ and conjugate addition.^{19–21} A one-pot approach to these derivatives has not been thoroughly investigated. Even though it potentially offers a more environmentally friendly route to the compounds. This work reported a one-pot method for the efficient synthesis of 4-aryl-1,2-naphthoquinones and 2-aryl-1,4-naphthoquinones using 1-naphthols and arenes as starting materials.

Previous work²¹



This work



Methodology:

General procedures: ¹H-NMR and ¹³C-NMR spectra were obtained from Bruker Advance 400 MHz NMR spectrometers. Chemical shifts are reported in ppm from tetramethylsilane (TMS) with the residual solvent resonance as an internal standard (CDCl₃ at δ_H 7.26 and δ_C 77.0). Data are reported as follows: s = singlet, d = doublet, t = triplet, m = multiplet; coupling constant(s) in Hz, the number of corresponding H atoms. Thin layer chromatography was performed on aluminum sheet with Merck silica gel 60 (0.063–0.200 nm) as a stationary phase.

Material: Commercial reagents and organic solvents were purchased from TCI, Merck, and Sigma-Aldrich. They were used without further purification unless otherwise noted.

General procedure for the synthesis of aryl naphthoquinones: To a mixture of 1-naphthol derivatives (0.2 mmol, 1 equiv) and potassium persulfate (K₂S₂O₈, 0.6 mmol, 3 equiv) in water (500 μL), arene (0.2 mmol, 1 equiv) was added. The reaction was heated to 50 °C for 24 h. The reaction mixture was cooled to room temperature, extracted with dichloromethane (3 x 30 mL), washed with saturated NaCl solution (50 mL), and dried with anhydrous Na₂SO₄. The solvent was removed under *vacuo*. The crude product was purified by column chromatography to give the desired product(s).

Synthesis of 2-(2,4,6-trimethoxyphenyl)naphthalene-1,4-dione (3aa) and 4-(2,4,6-trimethoxyphenyl)naphthalene-1,2-dione (4aa): The compounds were synthesized according to the general procedure. 1-Naphthol (28.8 mg, 0.2 mmol) and 1,3,5-trimethoxybenzene (28.8 mg, 0.2 mmol) were used as starting materials. The crude product

was purified by column chromatography (silica gel: EtOAc/hexane, 1/5, v/v). The products **3aa** and **4aa** were obtained as an orange solid (16.2 mg, 25%) and a red solid (23.6 mg, 36%), respectively. The NMR spectra of compounds **3aa** and **4aa** were identical to those reported in the literatures.^{21,22}

2-(2,4,6-Trimethoxyphenyl)naphthalene-1,4-dione (3aa): ¹H NMR (400 MHz, CDCl₃) δ_H 8.15–8.08 (m, 2H), 7.77–7.69 (m, 2H), 6.95 (s, 1H), 6.20 (s, 2H), 3.86 (s, 3H), 3.73 (s, 6H). ¹³C NMR (100 MHz, CDCl₃) δ_C 185.5, 183.8, 162.4, 158.8, 144.9, 138.7, 133.4, 133.3, 132.9, 132.3, 126.8, 125.9, 104.7, 90.9, 55.8(x2), 55.4.

4-(2,4,6-Trimethoxyphenyl)naphthalene-1,2-dione (4aa): ¹H NMR (400 MHz, CDCl₃) δ_H 8.13 (d, *J* = 7.2 Hz, 1H), 7.63–7.35 (m, 2H), 6.98 (d, *J* = 7.4 Hz, 1H), 6.35 (s, 1H), 6.23 (s, 2H), 3.89 (s, 3H), 3.71 (s, 6H). ¹³C NMR (100 MHz, CDCl₃) δ_C 180.8, 180.1, 162.3, 158.4, 151.7, 136.1, 135.1, 131.5, 130.1, 130.0, 129.6, 128.5, 106.4, 90.7, 55.8(x2), 55.5.

Synthesis of 2-(2,4-dimethoxyphenyl)naphthalene-1,4-dione (3ab) and 4-(2,4-dimethoxyphenyl)naphthalene-1,2-dione (4ab): The compounds were synthesized according to the general procedure. 1-Naphthol (28.8 mg, 0.2 mmol) was used and 1,3-dimethoxybenzene (27.6 μL, 0.2 mmol) was used as starting materials. The crude product was purified by column chromatography (silica gel: EtOAc/hexane, 1/5, v/v). The products **3ab** and **4ba** were obtained as an orange solid (2.3 mg, 4%) and a red solid (11.2 mg, 19%), respectively. The NMR spectra of compounds **3ab** and **4ab** were identical to those reported in the literatures.^{21,22}

2-(2,4-Dimethoxyphenyl)naphthalene-1,4-dione (3ab): ¹H NMR (400 MHz, CDCl₃) δ_H 8.21–8.05 (m, 2H), 7.81–7.69 (m, 2H), 7.20 (d, *J* = 8.3 Hz, 1H), 7.03 (s, 1H), 6.64–6.52 (m, 2H), 3.86 (s, 3H), 3.78 (s, 3H). ¹³C NMR (100 MHz, CDCl₃) δ_C 185.4, 184.0, 162.3, 158.6, 147.4, 136.3, 133.8, 133.6, 133.5, 132.7, 132.2, 131.6, 126.9, 125.9, 115.9, 104.7, 99.1, 96.9, 55.7, 55.5.

4-(2,4-Dimethoxyphenyl)naphthalene-1,2-dione (4ab): ¹H NMR (400 MHz, CDCl₃) δ_H 8.15 (dd, *J* = 7.2, 1.7 Hz, 1H), 7.57–7.41 (m, 2H), 7.18 (d, *J* = 8.3 Hz, 1H), 7.07 (dd, *J* = 7.5, 1.4 Hz, 1H), 6.65–6.54 (m, 2H), 6.39 (s, 1H), 3.89 (s, 3H), 3.74 (s, 3H). ¹³C NMR (100 MHz, CDCl₃) δ_C 180.8, 179.9, 162.3, 157.8, 155.3, 135.7, 135.0, 131.4, 130.4, 130.3, 129.8, 129.40, 128.4, 118.3, 104.9, 99.0, 55.6, 55.5.

Synthesis of 4'-methoxy-[1,1'-binaphthalene]-3,4-dione (4ad): Compound **4ad** was synthesized according to the general procedure. 1-Naphthol (28.8 mg, 0.2 mmol) was used as the 1-naphthol derivative and 1-methoxynaphthalene (31.6 μL, 0.2 mmol) was used as starting materials. The crude product was purified by column chromatography (silica gel: EtOAc/hexane, 1/3, v/v). Compound **4ad** was obtained as red solid (2.5 mg, 4%). The NMR spectra of compound **4ad** were identical to that reported in the literature.²¹

4'-Methoxy-[1,1'-binaphthalene]-3,4-dione (4ad): ¹H NMR (400 MHz, CDCl₃) δ_H 8.37 (d, *J* = 8.4 Hz, 1H), 8.22 (dd, *J* = 7.6, 1.5 Hz, 1H), 7.64 (d, *J* = 8.4 Hz, 1H), 7.57–7.36 (m, 5H), 6.91 (t, *J* = 8.3 Hz, 2H), 6.54 (s, 1H), 4.09 (s, 3H). ¹³C NMR (101 MHz, CDCl₃) δ_C 180.8, 179.7, 156.9, 156.7, 136.2, 135.3, 131.9, 131.4, 130.7, 130.2, 130.0, 129.1, 127.4, 126.5, 126.4, 125.9, 125.6, 125.4, 122.7, 103.2, 55.7.

Results and Discussion:

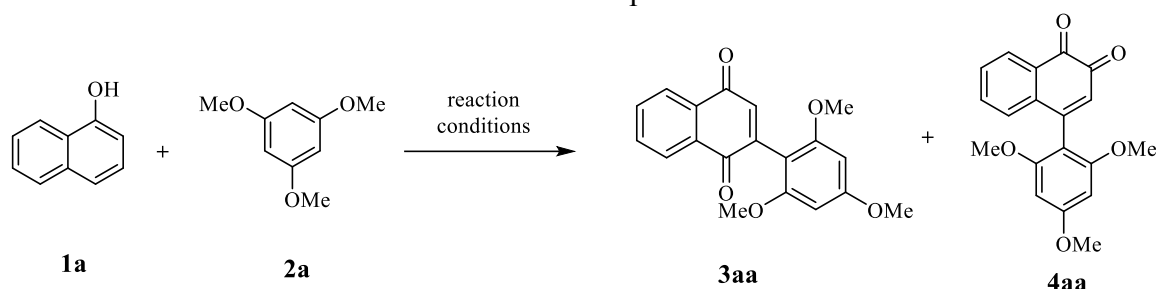
To investigate the one-pot reaction between 1-naphthol and arene, 1-naphthol (**1a**) and 1,3,5-trimethoxybenzene (**2a**) were selected as model substrates for reaction optimization (Table 1). The effect of oxidants was investigated. Persulfate oxidants were screened. Oxone[®], Na₂S₂O₈, K₂S₂O₈, and (NH₄)₂S₂O₈ gave the aryl naphthoquinone products in 9%,

22%, 40%, and 0%, respectively (entries 1–4). Peroxide oxidants, H_2O_2 and *m*-CPBA, were also screened but they did not give any desired products (entries 5 and 6). NaIO_4 and MnO_2 did not give any product either (entries 7 and 8). DDQ gave aryl-naphthoquinone products in 20% (entry 9). From these results, $\text{K}_2\text{S}_2\text{O}_8$ was chosen for further optimization.

Next, the solvent effect was investigated. Various solvents such as polar protic solvents (H_2O and MeOH, entries 1–10 and 15–18), polar aprotic solvents (MeCN and DCM, entries 11–12), and non-polar solvents (toluene and hexane, entries 13–14) were screened. From the results, only H_2O gave the products. Accordingly, the optimal solvent was H_2O .

The effect of the reaction temperature was screened. When the reaction temperature was lower to 5 °C (entry 15), the desired products were not observed. When the reaction temperature was increased to 50 °C (entry 16), the yield was improved to 58% with a 1:1.6 ratio of 2-aryl-1,4-naphthoquinone (**3aa**) and 4-aryl-1,2-naphthoquinone (**4aa**). The yields of the products were decreased when the reaction was heated to 70 °C and 100 °C (entries 17 and 18). Therefore, 50 °C was selected as the optimal reaction temperature.

Table 1 Reaction optimization^a



Entry	Oxidant	Solvent	Temperature (°C)	Yield (%) ^b (3aa : 4aa)
1	Oxone [®]	H_2O	rt	9 (1:1.3)
2	$\text{Na}_2\text{S}_2\text{O}_8$	H_2O	rt	22 (1:3.4)
3	$\text{K}_2\text{S}_2\text{O}_8$	H_2O	rt	40 (1:2.3)
4	$(\text{NH}_4)_2\text{S}_2\text{O}_8$	H_2O	rt	0
5	H_2O_2	H_2O	rt	0
6	<i>m</i> -CPBA	H_2O	rt	0
7	NaIO_4	H_2O	rt	0
8	MnO_2	H_2O	rt	0
9	DDQ	H_2O	rt	20 (1:1.2)
10	$\text{K}_2\text{S}_2\text{O}_8$	MeOH	rt	0
11	$\text{K}_2\text{S}_2\text{O}_8$	MeCN	rt	0
12	$\text{K}_2\text{S}_2\text{O}_8$	DCM	rt	0
13	$\text{K}_2\text{S}_2\text{O}_8$	Toluene	rt	0
14	$\text{K}_2\text{S}_2\text{O}_8$	Hexane	rt	0
15	$\text{K}_2\text{S}_2\text{O}_8$	H_2O	5	0
16	$\text{K}_2\text{S}_2\text{O}_8$	H_2O	50	58 (1:1.6) [21, 36] ^c
17	$\text{K}_2\text{S}_2\text{O}_8$	H_2O	70	46 (1:1.3)
18	$\text{K}_2\text{S}_2\text{O}_8$	H_2O	100	29 (1:1.4)

^aReaction conditions: 1-naphthol (**1a**) (14.4 mg, 0.1 mmol, 1 equiv), 1,3,5-trimethoxybenzene (**2a**) (16.8 mg, 0.1 mmol, 1 equiv), oxidant (0.3 mmol, 3 equiv), solvent (250 μL), temperature, 24 h.

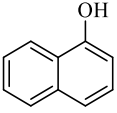
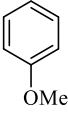
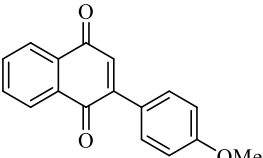
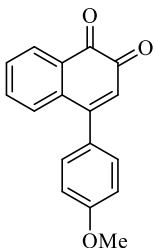
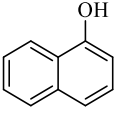
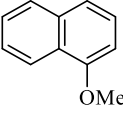
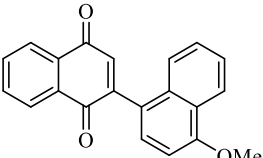
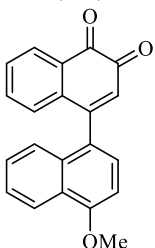
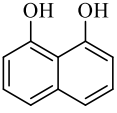
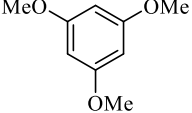
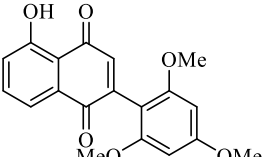
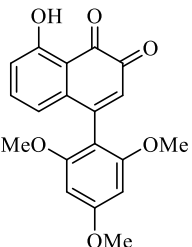
^bNMR yields were determined by using dimethyl sulfone as an internal standard.

^cIsolated yields of **3aa** and **4aa**, respectively.

With the optimal reaction conditions in hand, the substrate scope was explored (Table 2). When we performed the reaction between 1-naphthol (**1a**) and 1,3,5-trimethoxybenzene (**2a**) at a larger scale, the combined yield of the products slightly increased to 61% (25% of **3aa** and 26% of **4aa**). The electronic effect of the arene was investigated. When a less electron-rich substrate, 1,3-dimethoxybenzene (**2b**), was used instead of 1,3,5-trimethoxybenzene (entry 2), the combined yield dropped to 23% (4% of the para product **3ab** and 19% of the ortho product **4ab**). Further decreasing the electron density of the arene by using anisole (**2c**) as a substrate led to no product formation (entry 3). These results suggested that an electrophilic aromatic substitution was likely one of the key mechanistic steps in the reaction, consistent with previous literature.²¹ When 1-methoxynaphthalene (**2d**) was used as a substrate (entry 4), the ortho product **4ad** was obtained in 4%. This result suggested that the aromatic stabilization also played an important role in the reaction. A naphthalene ring in **2d**, which has lower aromatic stabilization per ring, was more nucleophilic than a benzene ring in **2c**. Interestingly, when 1,8-dihydroxynaphthalene (**1b**) was used as a substrate instead of 1-naphthol (entry 5), no product formation was observed. The presence of an additional hydroxy group appeared to be detrimental to the reaction.

Table 2 Substrate scopes^a

<div><div><div><div><div></div><div>1a–b</div></div><div><div><div><div></div><div>2a–d</div></div><div><div><div><div><div>$\xrightarrow[\text{H}_2\text{O, 50 } ^\circ\text{C, 1 day}]{\text{K}_2\text{S}_2\text{O}_8 \text{ (3 equiv.)}}$</div><div><div><div><div><div></div><div>3aa–ab</div></div><div><div><div><div></div><div>4aa–ab</div></div></div></div></div></div></div></div></div></div></div></div></div></div></div></div>				
Entry	1-Naphthol derivative (1)	Arene (2)	Products (yield,%) ^b	
			2-Aryl-1,4-naphthoquinones (3)	4-Aryl-1,2-naphthoquinones (4)
1	<div><div><div><div></div><div>1a</div></div><div><div><div><div></div><div>2a</div></div><div><div><div><div><div></div><div>3aa</div><div>(25%)</div></div><div><div><div><div></div><div>4aa</div><div>(36%)</div></div></div></div></div></div></div></div></div></div></div>			
2	<div><div><div><div></div><div>1a</div></div><div><div><div><div></div><div>2b</div></div><div><div><div><div><div></div><div>3ab</div><div>(4%)</div></div><div><div><div><div></div><div>4ab</div><div>(19%)</div></div></div></div></div></div></div></div></div></div></div>			

Entry	1-Naphthol derivative (1)	Arene (2)	Products (yield, %) ^b	
			2-Aryl-1,4-naphthoquinones (3)	4-Aryl-1,2-naphthoquinones (4)
3	 1a	 2c	 3ac (0%)	 4ac (0%)
4	 1a	 2d	 3ad (0%)	 4ad (4%)
5	 1b	 2a	 3ba (0%)	 4ba (0%)

^aReaction conditions: 1-naphthol (**1**) (0.2 mmol, 1 equiv), arene (**2**) (0.2 mmol, 1 equiv), K₂S₂O₈ (162.2 mg, 0.6 mmol, 3 equiv), H₂O (500 μL), 50 °C, 24 h.

^bIsolated yields.

Although the substrate scopes of the reaction were still limited, this work provided a proof of concept that a one-pot synthesis of 4-aryl-1,2-naphthoquinones and 2-aryl-1,4-naphthoquinones directly from commercially available 1-naphthol derivatives was viable. Furthermore, compared to the previous work,²¹ this method was more environmentally friendly because it used water as the optimal solvent.

Conclusion:

A one-pot synthesis of 4-aryl-1,2-naphthoquinones and 2-aryl-1,4-naphthoquinones was successfully developed. The reaction conditions were simple to operate. Investigation of the electronic effect suggested that the reaction required highly electron-rich arenes as viable substrates. Further mechanistic investigation is ongoing and will be reported in due course.

Acknowledgements:

This research was supported by Mahidol University Fundamental Fund: fiscal year 2024. Support from the Center of Excellence for Innovation in Chemistry (PERCH-CIC), Ministry of Higher Education, Science, Research and Innovation, and the Department of Chemistry, Faculty of Science, Mahidol University was gratefully acknowledged. We also thank the Central Instrumental Facility (CIF) at the Faculty of Science, Mahidol University for research facilities.

References:

1. Kamauchi H, Shiraishi Y, Kojima A, Kawazoe N, Kinoshita K, Koyama K. *J Nat Prod.* 2018;81:1290-1294.
2. Wurglics M, Michelitsch A, Wurm G. *Monatsh Chem.* 2002;133:1225-1230.
3. Sagar S, Kaur M, Minneman KP, Bajic VB. *Eur J Med Chem.* 2010;45:3519-3530.
4. Sun A, Liu J, Pang S, Lin J, Xu RJB. *Bioorg Med Chem Lett.* 2016;26:2375-2379.
5. Bodo B, Tih R G, Davoust D, Jacquemin H. *Phytochemistry.* 1983;22:2579-2581.
6. Ros-Lis JV, Martínez-Máñez R, Benito A, Soto J. *Polyhedron.* 2006;25:1585-1591.
7. Dawood K. *Tetrahedron.* 2007;63:9642-9651.
8. Kalt M, Schuehly W, Saf R, Ochensberger S, Solnier J, Bucar F, Kaiser M, Presser A. *Eur J Med Chem.* 2020;207:112837.
9. Khodade V, Dharmaraja A, Chakrapani H. *Bioorg Med Chem Lett.* 2012;22:3766-3769.
10. Deb A, Agasti S, Saboo T, Maiti D. *Adv Synth Catal.* 2014;356:705-710.
11. Sepahvand H, Ghasemi E, Sharbati M, Mohammadi MS, Pirlar MA, Shahverdizadeh GH. *New J Chem.* 2019;43:16555-16565.
12. Zhou B, Liu Q, Wang H, Jin H, Liu Y. *Tetrahedron.* 2019;75:3815-3821.
13. Baker Dockrey SA, Lukowski AL, Becker MR, Narayan AR. *Nat Chem.* 2018;10:119-125.
14. Kim H, Takizawa S, Oh K. *Org Biomol Chem.* 2016;14:7191-7196.
15. Christoffers J, Mann A. *Eur J Org Chem.* 1999;1999:2511-2514.
16. Hung C-H, Gandeepan P, Cheng L-C, Chen L-Y, Cheng M-J, Cheng C-H. *J Am Chem Soc.* 2017;139:17015-17021.
17. Guo J, Xu Y, Li K, Xiao L, Chen S, Wu K, Chen X, Fan Y, Liu J, Su C. *Angew Chem.* 2017;129:3910-3914.
18. Fujiwara Y, Domingo V, Seiple I, Gianatassio R, Del Bel M, Baran PS. *J Am Chem Soc.* 2011;133:3292-3295.
19. Zhu S, Chen Y, Wang Y, Yu P, Li S, Xiang S, Wang J, Xiao J, Tan B. *Nat Commun.* 2019;10:1-10.
20. Krishna A, Pandaram S, Ilangovan A. *Org Chem Front.* 2019;6:3244-3251.
21. Prasitwatcharakorn W, Rujirasereesakul C, Luanphaisarnnont T. *Results Chem.* 2022;4:100319.
22. Ullah S, Akter J, Kim SJ, Yang J, Park Y, Chun P, Moon HR. *Med Chem Res.* 2019;28:95-103.



TOTAL PHENOLIC CONTENT, FREE RADICAL SCAVENGING ACTIVITIES AND CYTOTOXICITY OF A LEAF EXTRACT AND ITS FRACTIONS FROM *Chrysophyllum cainito*

Parichat Thepthong,^{1,*} Maliwan Nunmai,¹ Wipawee Boonsri,¹ Phongnarin Aonchat,¹ Lamai Maikew,² Nisakorn Saewan³

¹Department of Chemistry, Faculty of Science and Digital Innovation, Thaksin University, Phattalung 93210, Thailand

²Research and Development Group, Thailand Institute of Nuclear Technology (Public Organization), Nakhon Nayok 26120, Thailand

³School of Cosmetic Science, Mae Fah Luang University, Chiang Rai 57100, Thailand

*e-mail: tsu_parichat@hotmail.com

Abstract:

Chrysophyllum cainito or star apple is a tropical tree belonging to the Sapotaceae family, originally found in Central America and the West Indies. The fruits of the star apple closely resemble apples in both size and shape. The leaves are commonly utilized in traditional medicine to manage diabetes mellitus and to alleviate inflammation linked with laryngitis and pneumonia. Additionally, they are employed to address respiratory issues such as coughs and colds. Furthermore, the leaves are used to create remedies that have the potential to aid in controlling high blood pressure. Flavonoid antioxidants have been identified in the leaves. The ethanol extract from the leaves and its chromatographic fractions (CCE1-CCE7) were examined for their total phenolic content and subjected to assessments of their antioxidant, nitric oxide inhibition, and cytotoxicity properties through *in vitro* assays. The results revealed that the phenolic content of the ethanol extract is 0.89 mg GAE/mL of extract. At a concentration in the well of 125 µg/mL, the ethanol extract exhibited a DPPH radical scavenging activity with an inhibition percentage of 73.19, slightly lower than that of CCE4, CCE5, and CCE6 (77.84%, 79.80%, and 90.42%, respectively). At a concentration of 50 µg/mL, fraction CCE6 also exhibited the highest nitric oxide scavenging with a percentage of inhibition of 78.47%. This fraction did not exhibit toxicity towards human keratinocyte cells.

Introduction:

Free radicals are exceptionally reactive entities characterized by the presence of an unpaired electron. They originate from routine metabolic processes within living organisms or exposure to polluted environments.¹ These free radicals have the potential to engage with and inflict damage upon DNA, cellular membranes, and proteins, thereby contributing to the onset of various illnesses including cardiovascular disease, cancer, and the aging process.² In the realm of disease prevention, antioxidants emerge as crucial players by mitigating the surplus of free radicals. It is worth noting that synthetic antioxidants like Butylated hydroxytoluene (BHT) and Butylated hydroxyanisole (BHA) have raised concerns about their adverse effects on human health.³ Consequently, there has been a growing quest for natural non-toxic antioxidants in recent years. Natural antioxidants, such as vitamin C, vitamin E, carotenoids, phenolics, and flavonoids, have demonstrated their ability to efficiently scavenge free radicals.⁴ Moreover, some of these natural antioxidants have been applied to preserve the quality and extend the shelf life of both food and cosmetic products. The antioxidant or anti-free radical impact is attributed to phenolic constituents like flavonoids, phenolic acids, and phenolic diterpenes. The effectiveness of these phenolic compounds primarily arises from their ability to undergo redox reactions, thereby absorbing and counteracting free radicals.⁵



Chrysophyllum cainito, commonly known as star apple, is a tropical tree belonging to the Sapotaceae family. It was indigenous to Central America and the West Indies. It has been used as a traditional remedy for laryngitis with inflammation, pneumonia, and diabetes mellitus.⁶ The biological activity of *C. cainito* has been extensively investigated. It exhibits a wide range of associated health benefits and properties, including antioxidants, antidiabetic, anti-inflammatory, anticancer, and antihypertensive properties.⁷ The fruit closely resembles apples, complete with a tender endocarp, and exhibits a distinctive star-shaped pattern within its pulp. It is important to note that while the skin is latex-rich, the rind is inedible. The leaves of *C. cainito* are characterized by their dark green coloration and shiny surface, alternate, the underside shines with a golden color when seen from a distance. They are typically elliptical or ovate in shape and exhibit a leathery texture.

A thorough literature review of the leaves has gathered research findings emphasizing the presence of natural antioxidants, specifically flavonoids and tannins. In the literature review conducted by Luo in 2002, seven polyphenolic antioxidants were identified, namely gallic acid, galloyl myricitrin, rutin, quercetin, myrecetrin, myricetin, quercetin and two triterpenoids β -amyrin and lupeol,⁸ ursolic acid, β -sitosterol, lupeol, and gallic acid⁹ were reported in leaves. Additionally, *C. cainito* leaves contain triterpene antioxidants, include β -amyrin acetate and gentistic acid.¹⁰

These investigations have primarily emphasized the ability of leaves extract and its fractions to scavenge DPPH and nitric oxide radicals. However, there is a lack of information regarding its potential cytotoxic effects and inhibition of nitric oxide radical, areas that have been largely unexplored. The present study is aimed to evaluate the total phenolic content and anti-free radical activities of extract and its fractions. Moreover, cytotoxicity was estimated on human keratinocyte cells by using the MTT assay to estimate the safety for industry usage.

Methodology:

Materials

Quick column chromatography (QCC) was performed on silica gel 60H (230-400 Mesh ASTM, Merck). Solvents for extraction and chromatography were distilled at their boiling ranges prior to use. 2,2-Diphenyl-1-picrylhydrazyl (DPPH) and sulfanilamide were obtained from Fluka Chemie GmbH. Dimethyl sulfoxide, ascorbic acid, Folin-Ciocalteu's phenol reagent and *N*-(1-naphthyl)ethylene diamine dihydrochloride (NEDA) were acquired from Merck. Gallic acid, sodium nitrite, and lipopolysaccharide (LPS) were supplied by Sigma-Aldrich. Fetal bovine serum (FBS), whereas Dulbecco's Modified Eagle's Medium (DMEM), penicillin-streptomycin antibiotic solution, and 3-(4,5-dimethylthiazol-2-yl)-2,5-diphenyl tetrazolium bromide (MTT) were purchased from Gibco. Absorbances were determined on a microplate reader UVM 340 (Biochrom, USA).

Plant material

The leaves of *C. cainito* were collected in Nakorn Si Thammarat province, the southern part of Thailand, in November 2022. The plant was identified by Dr. Paveena Kaewubon, a plant taxonomist from Department of Biology, Thaksin University.

Preparation of crude extract and fractions

The leaves of *C. cainito* were cleaned, cut into small pieces, and air-dried until a constant weight was achieved. The dried samples were pulverized using a laboratory blender. One kilogram of powdered sample was macerated in dichloromethane for 30 min followed by ultrasound-assisted extraction for 30 min at room temperature and filtered. The residue was further macerated with 95% ethanol for 5 days followed by ultrasound-assisted extraction for 30 min at room temperature and filtered. The filtered extract was concentrated using a rotary

evaporator under vacuum at 40 °C to yield the dichloromethane extract and ethanol extract, respectively. The ethanol extract (CCE, 25.0 g) was subjected to quick column chromatography and eluted with a stepwise gradient of 15% ethanol in dichloromethane and finally 40% ethanol in dichloromethane. Based on their TLC characteristics, fractions containing identical major compounds were combined, resulting in a total of seven fractions (CCE1-CCE7). The extract and fractions were subjected to freeze-drying to ensure that no water remained. The resulting extracts were then stored in an amber bottle at 4 °C until further analysis.

Determination of total phenolic content

The total phenolic content (TPC) was analyzed using the Folin-Ciocalteu assay as described by Vichit and Saewan (2015)¹¹ with some modifications. Briefly, the extracts and fractions (5 mg/mL, 12.5 µL) were mixed with 50 µL of deionized water, 25 µL of Folin-Ciocalteu reagent and 125 µL of 7% w/v sodium carbonate. Samples were incubated for 60 min at room temperature. The absorbance was measured at 750 nm using a microplate reader. The TPC of samples was determined using a gallic acid standard solution and expressed as gallic acid equivalents (mg GAE/mL extract).

DPPH radical scavenging assay

The antioxidant activity of the extract and its fractions was assessed using the DPPH radical scavenging assay, following the method described by Vichit and Saewan (2015).¹¹ The crude extract (5 mg) was dissolved in 1 mL of dimethyl sulfoxide and thoroughly mixed using a vortex mixer. 5 µL of the extract solution and 195 µL of 0.1 mM DPPH solution were incubated for 30 min in dark conditions at room temperature. Ascorbic acid was used as a positive standard. Absorbance at 515 nm was measured using a microplate reader, and each sample was tested in triplicate. The scavenging activity of the samples is the ability to reduce the color intensity of DPPH. Inhibition (%) was calculated using the following equation.

$$\% \text{ inhibition} = [(A_{\text{control}} - A_{\text{sample}}) / A_{\text{control}}] \times 100$$

A_{control} is the absorbance of the control (without extract), and A_{sample} is the absorbance in the presence of the test sample.

Fibroblast cell culture

Human fibroblast cells were cultured in Dulbecco's Modified Eagle Medium (DMEM), which was complemented with 10 % fetal bovine serum (FBS) and 1% Penicillin/Streptomycin. Cells were plated in a 96-well plate at a density of 2,000 cells/well and incubated at 37 °C in a 5% CO₂ humidified incubator for 24 h prior to activity assessment.

Nitric oxide inhibitory assay

The nitric oxide inhibition assay was conducted following the method reported by Vichit and Saewan (2016)¹² with some modifications. The extract solution (5 mg/mL) was diluted in DMEM without FBS at the concentration of 2 mg/mL, filtered, and sterilized through a 0.22 µm filter for experimental usage. The cell was supplemented with 100 µL of the sample before being stimulated with 1 µg/mL lipopolysaccharide (LPS) and incubated for 24 h. Nitric oxide production was assessed using Griess reagent system (Promega, USA). In brief, 50 µL of the culture medium was mixed with 50 µL of sulfanilamide solution and 50 µL of 0.1% *N*-1-naphthylethylenediaminedi hydrochloride solution. Then, the mixture was incubated for 5 min at room temperature, and absorbance was measured at 540 nm using a microplate reader. Chlorogenic acid was used as a positive control. The percentage of nitric oxide inhibition was calculated as follows:



$$\% \text{ inhibition} = [(A_{\text{control}} - A_{\text{sample}}) / A_{\text{control}}] \times 100$$

A_{control} is the absorbance of the control without extract, and A_{sample} is the absorbance in the presence of the test sample.

Cytotoxicity assay

The cytotoxicity assessment was performed by MTT assay, following the method reported by Vichit and Saewan (2015)¹¹ with a slight modification. The cytotoxicity of the extracts was investigated on human primary epidermal keratinocyte cells. Cells were treated with diluted extracts (0, 10, 25, 50, 100, 250, 500, 1000 and 2000 $\mu\text{g/mL}$) for 24 h. Afterward, the culture medium was removed. The 50 μL of 0.1 mg/mL of MTT solution was added to each well and incubated for 4 h. DMSO (100 μL) was added to all wells and incubated for 30 min at room temperature. The absorbance of each sample was measured at 570 nm using the microplate reader. The percentage of cell viability was calculated using the formula,

$$\% \text{ Viable cell} = (A_{\text{treated group}} / A_{\text{untreated group}}) \times 100$$

The cytotoxic activity was calculated and expressed as the 50 % cytotoxic concentration (CC_{50}) of the extract.

Results and Discussion:

A kilogram of star apple leaf powder underwent extraction using dichloromethane and ethanol, respectively. The results indicated that the resulting crude dichloromethane (CCD) extract weighed 15.90 grams, comprising 1.59% of the total weight. Likewise, the crude ethanol extract (CCE) weighed 46.69 grams, accounting for 4.67%, as presented in Table 1.

Table 1. Weight and extraction percentage of crude dichloromethane and crude ethanol

Crude	Weight (g)	% Extraction
CCD	15.90	1.59
CCE	46.69	4.67

The crude ethanol extract (20 g) was subjected to quick column chromatography employing silica gel C60 as the stationary phase and developing with a solvent mixture of dichloromethane and ethanol (15%-40% $\text{EtOH}:\text{CH}_2\text{Cl}_2$), resulting in seven fractions (CCE1-CCE7).

Total phenolic content

Phenolic compounds are known for their antioxidative properties. The ability of extract or fractions to resist oxidation depends on the amount of phenolic compound content. Hence, analyzing the total phenolic content of the crude and fractionated extract served as an initial assessment for antioxidant potential of the extract. The results were compared with a gallic acid standard, expressed in milligrams equivalent of gallic acid per one milliliter of extract (mg GAE/ml extract). The results are shown in Table 2.

The results of total phenolic content in crude extracts of star apple leaves revealed that the crude dichloromethane extract contained a total phenolic content of 0.21 ± 0.01 mg GAE/ml extract, whereas the ethanol extract showed a phenolic content of 0.89 ± 0.01 mg GAE/ml extract ($= 178.01 \pm 2.0$ mg GAE/g extract). The result indicated a similarity in the phenolic content compared to the previous report by Ningsih et al. in 2016 (190.13 ± 2.0 mg GAE/g extract),¹³ even though different extraction methods were used. Furthermore, differences in the ages of the sample and cultivation areas lead to variations in the quantities

of phenolic compounds. However, it can still be concluded that star apple leaves cultivated in Thailand contain relatively high amounts of phenolic compounds.

Table 2. The total phenolic content and DPPH radical scavenging activity of extract and its fractions.

Sample	mg GAE/ml extract	% DPPH radical scavenging
CCD	0.21 ± 0.01	34.79 ± 1.25
CCE	0.89 ± 0.01	73.19 ± 1.61
CCE1	0.09 ± 0.01	14.89 ± 1.81
CCE2	0.10 ± 0.00	25.46 ± 1.45
CCE3	0.25 ± 0.01	45.09 ± 2.12
CCE4	0.53 ± 0.01	77.84 ± 1.16
CCE5	0.58 ± 0.00	79.80 ± 2.54
CCE6	0.99 ± 0.02	90.42 ± 0.87
CCE7	0.35 ± 0.01	54.71 ± 2.24
Ascorbic acid	-	97.32 ± 2.66

The phenolic content in the fractions from ethanol extract increases with the polarity of the mobile phase in the range of 0.09-0.99 mg GAE/ml extract. CCE6 was eluted with 40% ethanol in dichloromethane and exhibited the highest total phenolic content at 0.99 ± 0.02 mg GAE/ml extract. The total phenolic content of fraction CCE6 was very close to that of the crude extract. Fractions with slightly lower phenolic content were CCE5 and CCE4, respectively.

TLC chromatogram of active fractions

Fractions CCE4, CCE5, and CCE6 showed higher phenolic content. The TLC chromatogram of these fractions is illustrated in Figure 1.

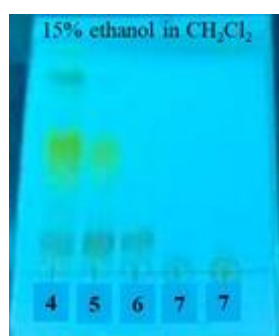


Figure 1. TLC chromatogram of high phenolic fractions from *C.cainito* leaves

DPPH radical scavenging activity

The DPPH radical scavenging method was used to evaluate the ability of the star apple leaves extracts and fractions from the ethanol extract in scavenging DPPH free radical, with ascorbic acid serving as the positive control. Compounds that have the ability to donate hydrogen radical species cause the conversion of DPPH radical to non-radical form, DPPH-H. This transformation is quantifiable through a reaction that can be measured at 515 nm.

At a concentration in the well of 125 $\mu\text{g/mL}$, the tested samples showed less activity than ascorbic acid. The dichloromethane and ethanol extracts displayed DPPH radical scavenging activity with the percentage of inhibition at 34.79 ± 1.25 and 73.19 ± 1.61 ,

respectively. The result was inconsistent with those reported by Kubola et al. (2011)¹⁴ due to different testing methods and samples (planting area and plant age).

The polar fractions (CCE4-CCE6) showed free radical inhibition with percentages of 77.84 ± 1.16 , 79.80 ± 2.54 , and 90.42 ± 0.87 , respectively. While the most polar CCE7 exhibited less activity with percentages of 54.71 ± 2.24 , as shown in Table 2. The DPPH radical scavenging activity results correspond to the phenolic content. Therefore, the active fractions CCE4, CCE5, and CCE6 were selected for further studies based on their DPPH radical scavenging activities.

Nitric oxide inhibitory activity

Nitric oxide is a free radical generated within biological tissues through specific nitric oxide synthases found in different types of inflammatory disorders.¹⁵ One approach to quantify nitric oxide entails utilizing the Griess diazotization reaction for spectrophotometric detection of nitrite, formed through the spontaneous oxidation of nitric oxide under physiological conditions. The process of diazotization occurs when nitrite reacts with sulphanilamide. This diazotized product subsequently combines with *N*-(1-naphthyl)ethylene diamine to form a pink diazo product, which is reduced by antioxidants. Antioxidants have the capability to impede the accumulation of nitrite ions. The intensity of the coloration serves as an indicator of the scavenging activity of antioxidants, particularly in terms of their hydrogen-donating ability.

Table 3. The nitric oxide inhibition of ethanol extract and high polar fractions.

Sample	% Nitric oxide inhibition
CCE	56.77 ± 1.49
CCE4	43.65 ± 1.42
CCE5	74.87 ± 2.66
CCE6	78.47 ± 1.17
Chlorogenic acid	91.29 ± 1.41

The most effective inhibition of nitric oxide synthesis was observed in the more polar fraction. At the stock concentration of 50 $\mu\text{g/mL}$, fractions CCE5 and CCE6 exhibited nitric oxide inhibition with percentages of 74.87 ± 2.66 and 78.47 ± 1.17 , respectively, which were lower than that of chlorogenic acid. While CCE4 exhibited less nitric oxide inhibitory activity than the ethanolic extract, as shown in Table 3. This is the first report of the nitric oxide inhibitory activity of the ethanol extract from star apple leaves.

The literature survey of *C. cainito* leaf extract revealed the existence of phenolic compounds like flavonoids, which possess either two *ortho*- or *para*-dihydroxy groups.¹⁶ Phenolic compounds are known for their antioxidative properties in biological systems, functioning as scavengers of free radicals. The nitric oxide scavenging activity of phenolic compounds has been reported previously.¹⁷ Based on the obtained results, phenolic compounds in polar fractions exhibited effective hydrogen transfer activity against nitric oxide radicals. These results support the antioxidant and anti-inflammatory activities of extracts of this plant species.

Cytotoxicity

The cytotoxic activity of ethanol extract and high polar fractions was investigated against human primary epidermal keratinocyte cells, using MTT assay. The advantages of this assay are its simplicity, rapidity, and precision.

The results indicated that all tested samples were not toxic to human keratinocyte cells, with DMSO serving as the negative control. The 50% cytotoxicity concentration (CC_{50}) values of crude extract and selected fractions range from 1207 ± 3.0 to 1288 ± 19.0 $\mu\text{g/mL}$, as shown in Table 4. The high CC_{50} values of all samples indicated that the ethanol extract of *C. cainito* leaves is a promising candidate for applications in food or cosmetic products.

Table 4. The cytotoxicity of ethanol extract and high polar fractions.

Sample	CC_{50} ($\mu\text{g/mL}$)
CCE	1213 ± 7.0
CCE4	1288 ± 19.0
CCE5	1276 ± 14.0
CCE6	1207 ± 3.0

Conclusion:

The results revealed that the ethanol extract and its polar chromatographic fractions derived from star apple leaves showed high phenolic content and displayed notable radical scavenging activities. Specifically, the highly polar fraction CCE6 exhibited substantial DPPH radical scavenging activity with a percentage of inhibition at $90.42 \pm 0.87\%$. Additionally, it demonstrated good inhibition of the nitric oxide radical, with a percentage of inhibition at $78.47 \pm 1.17\%$, in comparison to the positive control chlorogenic acid ($91.29 \pm 1.41\%$). Importantly, CCE6 was found to be non-toxic to human keratinocyte cells. Thus, CCE6 is an interesting fraction for further investigation into its chemical composition.

Acknowledgements:

This work was supported by the Thailand Science Research and Innovation Office of National Higher Education Science Research and Innovation Policy Council, Thaksin University (Fundamental Fund; TSU-66A105000011) Fiscal Year 2023.

References:

1. Prabha MR, Vasanth K. J Appl Pharm Sci. 2011;1(7):136–140.
2. Devasagayam TP, Tilak JC, Boloor KK, Sane KS, Ghaskadbi SS, Lele RD. J Assoc Physicians India. 2004;52:794–804.
3. Kahl R, Kappus HZ. Lebensm Unters Forsch. 1993;196:329–338.
4. Brewer MS. Compr. Rev. Food Sci Food Saf. 2011;10(4):221–247.
5. Panovska KT, Kulevanova S, Stefova M. Acta Pharm. 2005;55:207–214.
6. Morton JF. Morton, Miami, FL. Fruits of Warm Climates. 1987;pp 408–410.
7. Doan HV, Le TP. eCAM. 2020;Article ID 7259267.
8. Luo XD, Basile MJ, Kennely EJ. J Agric Food Chem. 2002;50(6):1379–1382.
9. Shailajan S, Gurjar D. Int J Pharm Sci Rev Res. 2014;26(1):106–111.
10. Lopez JA. Ing Cienc Quim. 1983;7:22–23.
11. Vichit W, Saewan N. Int J Pharm Pharm. 2015;7(7):329–334.
12. Vichit W, Saewan N. Int Food Res J. 2016;23(5):2006–2015.
13. Ningsih IY, Zulaikhah S, Hidayat MA, Kuswandi B. Agriculture and Agricultural Science Procedia. 2016;9:378–385.
14. Kubola J, Siriamornpun S, Meeso N. Food Chem. 2011;126(3):972–981.
15. Coleman JW. Int Immunopharmacol. 2001;1(8):1397–1406.
16. Luo, XD, Basile, MJ, Kennelly, EJ. J Agric Food Chem. 2002;50:1379–1382.
17. Panda BN, Raj AB, Shrivastava NR, Prathani AR. Asian J Res Chem. 2009;2(2):148–150.



UTILIZATION OF FRUIT PEEL EXTRACTS FROM *Punica granatum* AND *Nephelium lappaceum* FOR GREEN SYNTHESIS OF SILVER NANOPARTICLES AND THEIR IMPACT ON *Staphylococcus epidermidis* INHIBITION

Netnapa Chana,^{1,*} Supawadee Machuay,¹ Benjamas Nupan²

¹Department of Chemistry, Faculty of Science, Thaksin University, Phatthalung Campus, Phatthalung 93210, Thailand

²Department of Biology, Faculty of Science and Technology, Suratthani Rajabhat University, Suratthani 84100, Thailand

*e-mail:netnapa@tsu.ac.th

Abstract:

The green synthesis of silver nanoparticles has received great attention in the field of nanotechnology because of its high efficiency and minimal environmental impact. In the present study, the fruit peel extracts from five natural sources, namely *Garcinia mangostana* (mangosteen), *Nephelium lappaceum* (rambutan), *Punica granatum* (pomegranate), *Citrus reticulata* (mandarin orange), and *Citrus aurantifolia* (lime), were screened for their ability to inhibit *Staphylococcus epidermidis*. The results indicated that rambutan peel (RP) extract exhibited the most potent inhibitory effect with an inhibition zone of 30.33 ± 0.58 mm at a concentration of 50 mg/mL, followed by pomegranate peel (PP) at 24.67 ± 0.58 mm. Mangosteen peel (MP) extract displayed a relatively modest inhibitory effect with an inhibition zone of 8.33 ± 0.58 mm. The RP exhibited a minimum inhibitory concentration (MIC) equal to 0.78 mg/mL, and a minimum bactericidal concentration (MBC) equal to 12.5 mg/mL. While PP showed MIC of 12.5 mg/mL, and MBC more than 25 mg/mL. Subsequently, extracts from rambutan and pomegranate peel were employed as the reducing and stabilizing agents for the synthesis of silver nanoparticles (AgNPs), and the antimicrobial properties of these AgNPs against *S. epidermidis* were evaluated. UV-visible spectroscopy revealed characteristic peaks at 420 nm, along with the typical appearance of a dark brown color associated with AgNPs formation. The presence of hydroxyl (OH) and carbonyl (C=O) functional groups from plant secondary metabolites in AgNPs was confirmed by FTIR spectroscopy. The AgNPs produced from RP demonstrated significantly greater inhibitory efficacy against *S. epidermidis*, surpassing the inhibitory activity of PP extract by 15-fold in broth microdilution methods. As a result, this study highlights the simple synthesis of eco-friendly drug agents in the treatment of bacterial infectious diseases.

Introduction:

Gram-positive pathogen, *Staphylococcus epidermidis*, a bacterium inhabiting the skin, respiratory system, and human digestive tract, contributes to nosocomial infections. This species produces biofilm, a factor enhancing resistance to antibiotic therapy and host defense mechanisms.¹ Due to bacteria generating biofilm, there is a limited availability of effective antibacterial drugs. Therefore, the identification of new substances is an urgent need for neutralizing bacterial cells. Plant substances, such as monoterpenes, phenolic compounds, and flavonoids, have demonstrated activity in this regard.

Moreover, metallic nanoparticles derived from metals like Ag, Au, Ce, Pd, Pt, and Zn demonstrate antibacterial and antibiofilm formation activities. Nanoparticles have obtained great interest due to their multiple applications in diverse fields such as biomedicine, agriculture, pharmaceuticals, the textile industry, and food packaging. Among the metal



compounds exhibiting antimicrobial properties, silver compounds are the most prevalent. Silver nanoparticles (AgNPs) have been applied in various fields, including antifungal treatments, antioxidant formulations, anti-cancer therapies, anti-inflammatory agents, drug delivery systems, wound dressings, biosensors, and biocatalysts. They exhibited antibacterial and antibiofilm formation activity that depended on their size, shape, and concentration.²

Conventionally, various methods have been reported to the obtaining of AgNPs including chemical, physical, and biological or green methods. The disadvantages of physical and chemical methods are often costly, generating toxic by-products, use of expensive equipment, and low production efficiency. Recent studies have increasingly focused on the potential of AgNPs production through biological reducing agents, such as plant extracts and microbial filtrates. The presence of compounds such as terpenoids, flavonoids, or amino acids in extracts from different plant parts enables their use as agents for reducing silver ions. In addition to their efficacy, natural products are mostly non-toxic, and therefore, they can be used as safe therapeutic strategies.³

Noteworthy, fruit peels, commonly utilized in various applications such as cosmetic products, and for treating certain diseases, exhibit properties that accelerate wound healing, reduce inflammation, and combat bacteria. Our previous study demonstrated that fruit peels have a high level of antioxidant compounds capable of scavenging free radicals.⁴ Furthermore, agricultural waste, including leaf, flower, and peel extract has also been used as a source of green synthesis of metallic nanoparticles.⁵ Biologically synthesized nanoparticles are also less toxic and more environmentally friendly. Nanoparticles produced through green synthesis have demonstrated efficacy against different microbes, bacteria, and fungi, playing a role in the treatment of cancer and other ailments.

This study aimed to investigate the antimicrobial activity of a biowaste product comprising the peels of mangosteen, rambutan, pomegranate, orange, and lime. Additionally, it seeks to utilize a fruit peel extract to synthesize silver nanoparticles and assess their antibacterial activity against *S. epidermidis*. Furthermore, the present research may contribute to demonstrating that AgNPs synthesized from fruit peel is an eco-friendly and sustainable route for the development of new therapeutic drugs.

Methodology:

Materials

Fresh mangosteen, rambutan, pomegranate, orange, and lime were purchased from a local market in Pa phayom, Phatthalung province, Thailand. Silver nitrate and ethanol were purchased from Merck Chemicals. *S. epidermidis* (TISTR 518) strain was supplied by Dr. Benjamas Nupan, Department of Biology, Faculty of Science and Technology, Surathani Rajabhat University.

Preparation of fruit peel extract

The peels of mangosteen (MP), rambutan (RP), pomegranate (PP), orange (OP), and lime (LP) were washed with tap water to remove the dust and debris and then cut into small pieces. These peels were dried at 40 °C for 24 h. The twenty grams of each sample were then macerated in 200 mL of 95% ethanol for 5 days, and this extraction process was repeated twice. All extract obtained were then filtered using Whatman No. 1 filter paper. To obtain the crude fruit peel extract, the solvent was evaporated using a rotary evaporator. The extraction percentage was calculated by using the following formula:



$$\% \text{ Yield} = (\text{mass of the extract} / \text{mass of the dry plant sample}) \times 100$$

Finally, the extract should be stored at a temperature of 4 °C and tested for antimicrobial activity.

Antibacterial activity of fruit peel extract or AgNPs against S. epidermidis

Agar well diffusion assay

The fruit peel extract (MP, RP, PP, OP, LP) were tested for their antibacterial activity against *S. epidermidis* using the agar well diffusion method. *S. epidermidis* (TISTR 518) were cultured at 37 °C with nutrient broth (NB) until their growth stage reached a log-phase with optical density at 600 nm between 0.40-0.60. The bacterial suspensions were adjusted to 0.5 McFarland Standard (1×10^7 CFU/mL) with sterile NB after that swabbed to 20 mL NA plate. A hole with a 6 mm diameter was punched, and 50 μ L of the fruit peel extract solution (50 mg/mL in 10% DMSO) was introduced into the well. Gallic acid at 50 mg/mL concentration and 10% DMSO were used as positive and negative controls, respectively. Gallic acid, recognized as a natural polyphenolic compound found in plants, exhibits robust antibacterial properties that hinder the formation of bacterial biofilms through diverse mechanisms.⁶ The samples let to diffuse for some time. The plates were then incubated at 37 °C for 18-24 h. The diameter of the inhibition zone (mm) for each substance was observed and measured. The experiment was repeated thrice. AgNPs were also tested for the same method.

Minimum Inhibitory Concentration (MIC) and Minimum Bactericidal Concentration (MBC) evaluation

The resazurin-based turbidometric (TB) assay was adopted to demonstrate the minimum inhibitory concentration (MIC) of fruit peel extract and AgNPs against *S. epidermidis* according to the guidelines recommended by the CLSI (2012).⁷ The MIC is defined as the lowest concentration able to inhibit any visible bacterial growth. Briefly, 50 μ L of crude extracts or AgNPs (a two-fold serial dilution) was incubated in 96-well plates. The 50 μ L of bacterial suspension (1.5×10^6 cell/mL) was added into all wells. After an overnight incubation at 37 °C, 5 μ L resazurin (6.75 mg/mL) was added to all wells and incubated at 37 °C for another 4 h. Changes of color was observed and recorded. Resazurin has a midnight blue color, after entering the cell, in response to the metabolic activity of living cells, resazurin is reduced to resorufin, which has a pink color. The lowest concentration prior to color change was considered as MIC. The tests were performed in triplicate.

In order to elucidate the minimum bactericidal concentration (MBC) of fruit peel extracts or AgNPs, a loopful of aliquots from the MIC wells was transferred onto NA and incubated overnight. The lowest concentration with no visible growths on the plate was taken as MBC value.

Green synthesis of silver nanoparticles (AgNPs)

The aqueous AgNO₃ solution with a concentration of 10 mM was prepared in an Erlenmeyer flask. Then, 10 mL of 0.5 mg/mL fruit peel extract (RE and PP) was added to 200 mL of prepared silver nitrate to reduce the Ag⁺ ions. The mixture was stirred at room temperature and the color change was observed from colorless to yellowish and then to reddish brown. The synthesized AgNPs were then characterized using UV-vis spectroscopy, and FT-IR spectrophotometry.



AgNPs characterization techniques

UV-vis spectroscopy

UV-vis spectra were collected by using the instrument Shimadzu (UV-1800, Japan) at room temperature. The sample were recorded from 200 to 800 nm.

FT-IR analysis

To determine the bioactive substances, FT-IR measurements were conducted. This analysis utilized KBr pellets in diffuse reflectance mode with a resolution of 4 cm⁻¹.

Results and Discussion:

The utilization of chemicals in nanoparticle synthesis is environmentally unfriendly. An eco-conscious alternative known as green chemistry, involving the use of plant-mediated nanoparticle synthesis, has now become an intriguing approach. In this study, the effectiveness of fruit peel extract including the peel of mangosteen (MP), rambutan (RP), pomegranate (PP), orange (OP), and lime (LP) in antibacterial activity was observed and tested for AgNPs production.

Table 1.

Extraction yields and antimicrobial zone of inhibition (mm) obtained by agar well diffusion method of fruit peel ethanolic crude extract.

Samples	Scientific name	Sample code	Percentage yield (w/w)	Inhibition zone (mm)
pomegranate	<i>Punica granatum</i>	PP	42.33	24.67±0.58
rambutan	<i>Nephelium lappaceum</i>	RP	36.91	30.33±0.58
orange	<i>Citrus reticulata</i>	OP	29.58	NI
mangosteen	<i>Garcinia mangostana</i>	MP	23.95	8.33±0.58
lime	<i>Citrus aurantifolia</i>	LP	16.07	NI
Gallic acid	-	GA	-	11.8 ± 1.18

NI=No zone of inhibition

Percent yield of fruit peel extracts

The fruit peel was extracted using ethanol as the solvent, resulting in varying amounts of extracts. The highest yield of extract was achieved from pomegranate peel (PP), reaching a percentage yield of 42.33% (**Table 1**). This indicates that the majority of substances in pomegranate peel are highly polar and, therefore, are effectively extracted using solvents with high polarity. Rambutan peel (RP) followed with the next highest yield, registering a percentage yield of 36.91%. The percentage yield of OP, MP, and LP were 29.58%, 23.95%, and 16.07%, respectively.

Antibacterial activity of fruit peel extract

Molecules that hinder the growth of bacteria while minimizing damage to surrounding tissues are referred to as antibacterial compounds. The antibacterial activity of fruit peel extract including pomegranate, rambutan, orange, mangosteen, and lime was determined. Among the five extracts that were investigated for antibacterial activity against *S. epidermidis*, the findings indicated that RP extract had the highest antibacterial activity, with an inhibition zone measuring 30.33±0.58 mm, whereas PP and MP extract displayed inhibition zones of 24.67±0.58, and 8.33±0.58 mm, respectively (**Table 1** and **Figure 1**). On the other hand, LP and OP crude extracts did not demonstrate any zone of inhibition. The MIC and MBC of RP



and PP were determined by the resazurin-based TB assay (**Figure 1**). It was found that the MIC values of RP and PP extract were equal to 0.78 mg/mL, and 12.5 mg/mL, respectively. The MBC values were 12.5 mg/mL, and more than 25 mg/mL, respectively. The results indicated that types of fruit peel significantly impacted anti-*S. epidermidis* activities. The GC-MS analysis quantitatively identified 28 organic compounds from rambutan peel extract including inositol, and catechol with known antimicrobial activities.⁷ RP and PP extracts have been further used for the efficient synthesis of AgNPs.

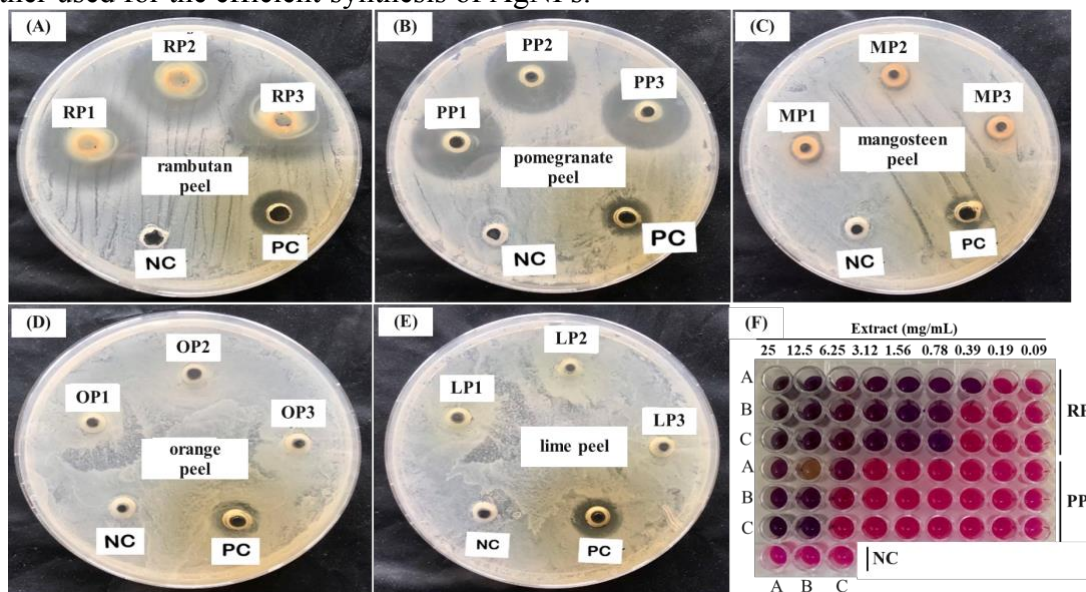


Figure 1.

A visible clear zone of the fruit peel: rambutan (A), pomegranate (B), mangosteen (C), orange (D), and lime (E) extract against *S. epidermidis*. Determination of the MIC (F) for RP and PP against *S. epidermidis*.

Preparation of silver nanoparticles

The formation of AgNPs is shown in **Figure 2A** and **B**. In the synthesis of AgNPs using RP and PP extract, the color of the solution changed to dark brown due to the reduction of Ag^+ in the solution. The chemical equation was:



The reaction of synthesized AgNPs from RP started with thirty minutes of incubation with silver nitrate (AgNO_3). It is well known that AgNPs exhibited a yellowish-brown color in aqueous solution.⁸ The reduction of Ag^+ ion occurred due to the phytochemicals present in the fruit peel extract such as polyphenol, flavonoids, tannin.

Characterization of AgNPs

To characterize the green-produced nanoparticles, Ultraviolet-visible Spectroscopy (UV-VIS), and Fourier Transform Infrared Spectroscopy (FT-IR) were employed.

UV-visible Spectrophotometry

Figure 3 shows the UV-visible spectra of RP extract, PP extract, and the synthesized AgNPs at different time points. The reduction procedure was easy and simply manageable, with UV-vis spectroscopy indicating the surface plasmon resonance (SPR) presence at 420 nm. The region of 350-550 nm is typical for the maximum absorption band of AgNPs.⁹



Furthermore, the highest production occurs at 1 hour after the reduction process begins for synthesized AgNPs from RP extract. The synthesis of AgNPs from PP decreases along with an increase in the time point caused by unstable AgNPs. Within the initial 30 minutes, AgNPs are rapidly generated from PP, leading to their condensation into larger particles and subsequent aggregation as the reaction time progresses. Various factors, such as the acidity or basicity of the reaction mixture, temperature, the reducing power of the plant extract, and the presence of secondary metabolites in the extract, influence the reaction time. Interestingly, even plants with fewer secondary metabolites demonstrate a rapid nanoparticle production.¹⁰ Consequently, the RP extract not only facilitates the reduction process but also serves as a capping and stabilizing agent, effectively preventing the aggregation of nanoparticles.

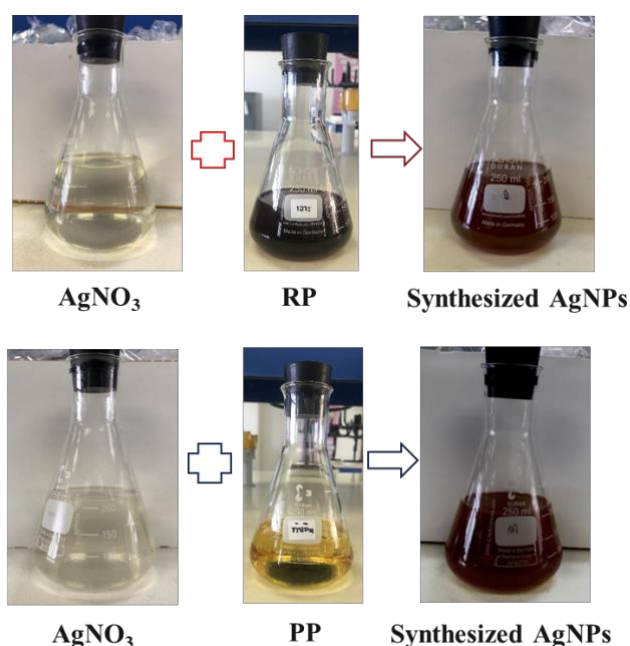


Figure 2.

Visual representation of synthesis of AgNPs with rambutan peel (A), pomegranate peel (B).

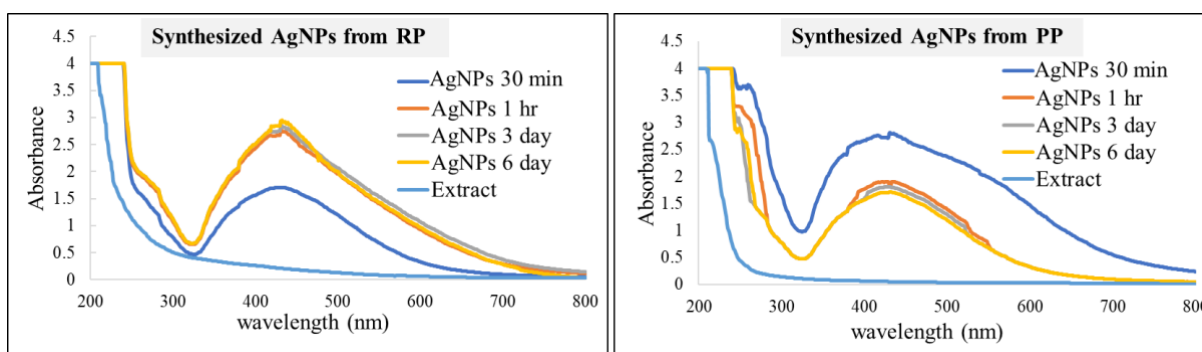


Figure 3.

UV-vis spectra recorded from the reaction mixture that show the production of AgNPs from: rambutan peel (A), pomegranate peel (B).



FTIR spectra

FTIR was utilized to identify active chemical groups in the fruit peel before and after reduction. FTIR spectra of RP and PP extract and their corresponding synthesized silver nanoparticle are depicted in **Figure 4**. RP and PP-derived AgNPs showed shifting in peaks along with the appearance and disappearance of absorption bands in the FTIR spectrum. The peaks show different stretches of bonds in biomolecules of the plant extract. The major shifts in band intensities were observed at 3600-3200 cm^{-1} . Exposure to IR leads to stretching of the O-H bond which is detected as a strong absorption band between 3000 and 3500 cm^{-1} . As mentioned earlier, the RP and PP used for the study have polyhydroxy groups, hence they show absorption bands between 3000 and 3500 cm^{-1} in the FTIR spectrum. By comparing the FTIR spectrum of the extract to its derived AgNPs, the presence of a weaker absorption band in the range of 3000-3500 cm^{-1} in the synthesized nanoparticles indicated the decrease in the concentration of O-H groups in the sample after the complete reaction. The decrease in O-H concentration can be attributed to its reaction with Ag^+ ions added to the solution for nanoparticle synthesis.¹¹ When Ag^+ ions come in contact with O-H groups, the white colloidal particles of AgOH are formed and turn to brown-colored Ag nanoparticles due to the surface plasmon resonance effect.¹² The signals at 3222, 3336, 3240, and 3320 cm^{-1} assigned to O-H stretching in polyphenol, sugar, and flavonoids, and C-H stretching around 2900 cm^{-1} arise from plant metabolites in RP and PP extract. For signals at 1609, and 1637 cm^{-1} corresponds to C=O in flavonoids. FTIR spectra of AgNPs exhibited the bands 1269, and 1266 cm^{-1} developed for the aromatic ring in AgNPs synthesized from RP and PP, respectively. AgNPs also showed the absorption bands of O-H and C=O in the particles. The results from FT-IR analyses confirm that the RP and PP extract have been successfully used for synthesizing AgNPs.

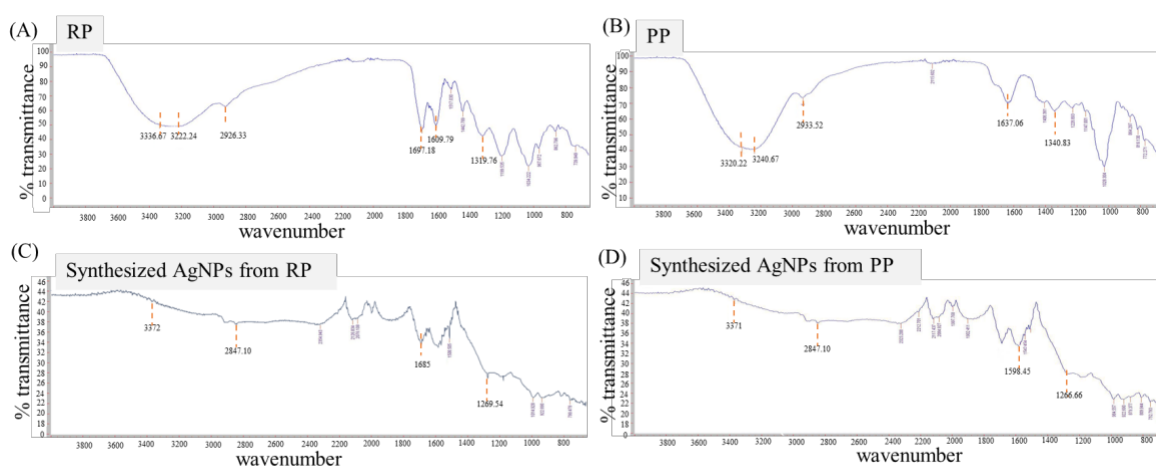


Figure 4.

FTIR spectra of rambutan peel (A) and pomegranate peel (B) and silver nanoparticles synthesized by the reduction of silver nitrate with the rambutan peel (C) and pomegranate peel (D) extract.



Antibacterial activity of AgNPs

The successful production of AgNPs was achieved through biological reduction. The bacterial effect of the formed AgNPs has been confirmed against the *S. epidermidis* strain. The present study revealed that *S. epidermidis* was sensitive to the synthesized AgNPs as shown in **Figure 5** and **Table 2**. The AgNPs synthesized using RP extract showed maximal inhibition with an inhibition zone of 20.67 ± 1.15 mm. Meanwhile, AgNPs synthesized using PP extract showed an inhibition zone of 17.67 ± 0.58 mm (**Figure 5A-5B**). The gallic acid (PC) and AgNO_3 showed a slightly less inhibitory effect than AgNPs from RP (**Table 2**). Li *et al.* observed comparable findings, illustrating the efficacy of AgNO_3 against bacteria. Specifically, Ag^+ penetrates the bacterial cell, leading to the degradation of essential proteins crucial for membrane gradients. Additionally, it intercalates between purine and pyrimidine base pairs, inducing DNA denaturation and subsequent bacterial inactivation.¹³ The results pertaining to the inhibition zone of AgNPs synthesized from RP at a concentration of $2.4 \mu\text{g/mL}$ were superior to those obtained with the RP extract.

Furthermore, MIC value of synthesized AgNPs from RP extracts was 15-fold lower than that of AgNPs from PP extract, implying its higher antibacterial activity than AgNPs from PP (**Figure 5C**). AgNPs synthesized from RP have higher antibacterial properties in comparison with silver ions and gallic acid due to their high surface area to volume ratio, and can easily penetrate bacterial cells.

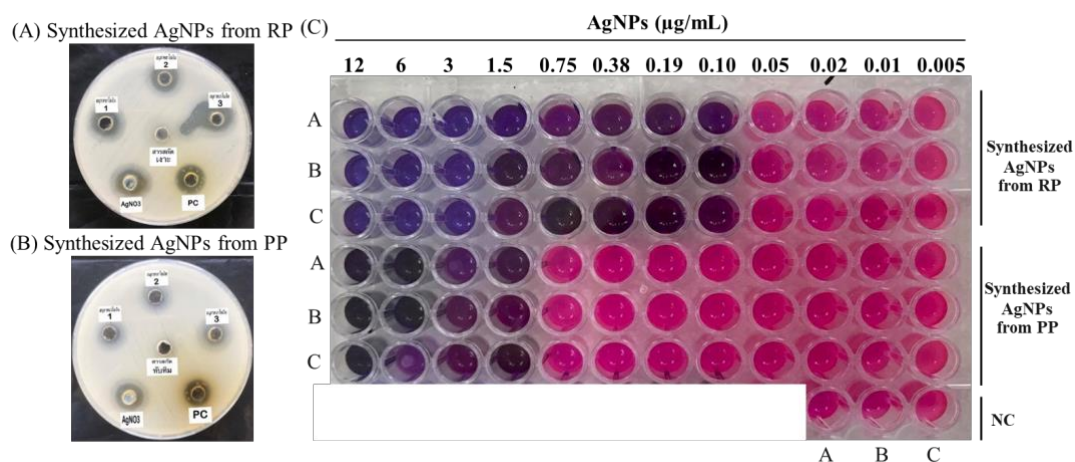


Figure 5.

Anti-*S. epidermidis* activity of synthesized AgNPs from rambutan peel (A) and pomegranate peel (B) using agar well diffusion method, (C) broth microdilution method.

The inhibitory activity of AgNPs against Gram-positive and Gram-negative bacteria is a controversial issue. Evidence reported that the inhibitory activity of AgNPs is more effective against Gram-negative bacteria.¹⁴ This study revealed that AgNPs are effective against Gram-positive bacteria. The hydroxyl group was the important redox-active functional group in RP that contributed to Ag^+ reduction. In addition, phenolics are well known to be important secondary metabolites in RP. Phenolics also have at least one aromatic ring with one or more hydroxyl groups. Pomegranate fruit contains tannins, phenolics, and flavonoids with antimicrobial activity.¹⁵ The inhibitory activity of synthesized AgNPs from RP has higher anti-*S. epidermidis* potential inhibition than AgNPs from PP due to more hydroxyl group of RP,



resulting in more Ag^+ ions reduction to metallic Ag^0 . AgNPs can readily infiltrate bacterial cell walls, disrupt cell membranes, generate reactive oxygen species, impede DNA replication, and interfere with protein synthesis, ultimately leading to cell death.¹⁶ Hence, this result provides the green and rapid synthesis of AgNPs using rambutan and pomegranate peel resources. Additionally, it provides the antibacterial efficacy of these AgNPs, suggesting their potential applications in medical and various other fields.

Table 2.

Anti-*S. epidermidis* activity of synthesized AgNPs from RP and PP obtained by agar well diffusion method.

Samples	Final concentrations of extract	Inhibition zone (mm± SD)
Synthesized AgNPs from RP	2.4 µg/mL	20.67±1.15
Synthesized AgNPs from PP	2.4 µg/mL	17.67±0.58
0.01 M AgNO_3	-	19±1.41
PC (Gallic acid)	-	16±1.41
NC (10% DMSO)	-	NI

NI=No zone of inhibition

Conclusions:

The study demonstrated that fruit peel extracts from rambutan and pomegranate contained antimicrobial compounds against *S. epidermidis*. These promising findings suggest the potential use of rambutan and pomegranate peel extracts in the synthesis of silver nanoparticles. The simple and eco-friendly synthesized AgNPs from this peel also displayed interesting *S. epidermidis* inhibition. Particularly, AgNPs synthesized with rambutan peel extract exhibited high efficiency, indicating its potential in application in antibacterial agents.

Acknowledgements:

This work was supported by National Higher Education, Science, Research and Innovation Policy Council, Thaksin University (Fundamental Research Fund; FF-2567A10512026) Fiscal Year 2024. The authors would like to thank the Department of Chemistry, Faculty of Science, Thaksin University, for providing research facilities, software packages, and computing times.

References:

- Swolana D, Wojtyczka RD. Int J Mol Sci. 2022;23:4298.
- Hamed AA, Kabary H, Khedr M, Emam AN. RSC Adv. 2020;10:10361-10367.
- Raj S, Sasidharan S, Balaji S, Dubey VK, Saudagar P. Protein J. 2020;11:135-158.
- Chana N, Muengpoon A, Pethkaew S, Kulsin N, Mahasuk A, Srirat S. SJST. 2022;44(4).
- Saratale RG, Saratale GD, Shin HS, et al. EPR. 2018;25:10164-10183.
- Keyvani-Ghamsari S, Rahimi M, Khorsandi K. Food Sci Nutr. 2023;11:5856-5872.
- Ansari M, Ahmed S, Abbasi A, Khan MT, Subhan M, Bukhari NA, Hatamleh AA, Abdelsalam NR. Sci Rep. 2023;13(1):18048.
- Yilmaz MT. Turk. J Med Sci. 2012;42:1423-1429.
- Antapaso H, Mittraparp-Arthorn P. Antioxidants (Basel). 2022;11(5):956.
- Singh R, Hano C, Tavanti F, Sharma B. Materials (Basel). 2021;14(22):6854.



11. Kadir A, Lakowicz JR, Geddes CD. J Phys Chem B. 2005;109:6247-6251.
12. Feng D, Chao Wu, Ai-Jun M, and Ke P. Environ Sci Nano. 2020;8:269-281.
13. Li R, Chen J, Cesario TC, Rentzepis PM. PNAS. 2016;113(48):13612-13617.
14. Wang H, Chen H, Wang Y, et al. Curr Nanosci. 2012;8:838-846.
15. Mohanty S, Mishra S, Jena P, Jacob B, Sarkar B, Sonawane A. Nanomedicine: NBM. 2012;8:916-924.
16. Maphetu N, Unuofin JO, Masuku NP, Olisah C, Lebelo SL. Biomed Pharmacother. 2022; 153:113256.



α -GLUCOSIDASE INHIBITORY ACTIVITY OF EXTRACTS FROM *Mitragyna speciosa* LEAVES

Wanrudee Hiranrat, Suttirot Sundang, Asadhawut Hiranrat*

Department of Chemistry, Faculty of Science, Thaksin University, Pa Phayom, Phatthalung 93210

*e-mail: hasadhawut@tsu.ac.th

Abstract:

The effects of *Mitragyna speciosa* leaves extracts against α -glucosidase enzyme were determined. Crude ethanol extracts of early mature leaf (EMLE) and mature leaf (MLE) were tested for α -glucosidase inhibitory activity. The results found that the EMLE showed better activity than MLE. Early mature leaves were further extracted with dichloromethane, ethyl acetate, and ethanol to give dichloromethane (EMLD), ethyl acetate (EMLT), and ethanol (EMLN) crude extracts, respectively. The results indicated that EMLN (IC_{50} 20.27 \pm 0.08 μ g/mL) displayed better activity than both EMLT (IC_{50} 21.09 \pm 0.43 μ g/mL) and EMLD (IC_{50} 22.62 \pm 0.15 μ g/mL). EMLN crude extract was separated using quick column chromatography to yield six subfractions, EMLN1-EMLN6. The result suggests that the major active principles for α -glucosidase inhibitory effects of *Mitragyna speciosa* extracts are EMLN6 (IC_{50} of 16.55 \pm 0.08 μ g/mL) and EMLN4 (IC_{50} of 12.49 \pm 5.12 μ g/mL). The subfractions separated from EMLN exhibited better activities than other crude extracts. However, all samples displayed lower α -glucosidase inhibitory activity than stand drug acarbose.

Introduction:

Diabetes mellitus (DM) is a metabolic disease associated with high blood sugar levels¹. Diabetes type I accounts for approximately 10% and occurs in patients whose pancreas is not able to produce enough insulin. Diabetes type II occurs when the body cannot use secreted insulin effectively and accounts for approximately 90%. Diabetes causes severe problems retinopathy, neuropathy, nephropathy, cardiovascular diseases, etc.². Over the last decade, the prevalence of DM has been rapidly increasing and is now regarded as one of the most important global health issues. Approximately 460 million people of the world population were affected by DM. Furthermore, DM was the top ten globally leading causes of death in 2019, predicted to reach more than 500 million deaths in the next twenty-five years. An effective approach to limit the amount of sugar entering the bloodstream is glucosidase inhibitors (AGIs). Current commercial AGI drugs represented by acarbose, miglitol, and voglibose are effective inhibitors of α -glucosidase. However, those drugs cause diarrhea, flatulence, abdominal pain, bloating, and discomfort³.

Synthetic drugs used to cure diabetes may have side effects. Research studies to find active ingredients from herbs, that can be used more safely, are another popular approach. According to the research report, there is the use of herbal substances in both extract and pure form. Herbs have been reported to have anti-diabetic effects. However, medicinal plants may need to be taken in large quantities in order to obtain active substances. Thus, the use of a good activity extract could be the disease-relief action. Therefore, we are interested in studying *Mitragyna speciosa* leaf extract. *Mitragyna speciosa* (also known as kratom) is a Southeast Asian medicinal plant belonging to the coffee family (Rubiaceae). Historically, kratom is used traditionally as a wound poultice, to treat fever, fatigue, pain and diabetes⁴⁻⁸. Since academic research has shown that mitragynine, an alkaloids from *Mitragyna speciosa*

leaves, has the effect of the transport of glucose in cells, swelling, relieves pain and anti-inflammatory action by inhibiting the secretion of prostaglandin E2 (PGE-2) and gene expression of cyclooxygenase 2 (COX-2) in lipopolysaccharide-treated macrophage cells¹⁰. Extracts containing alkaloids from *Mitragyna speciosa* leaves can be used to reduce drug withdrawal symptoms¹¹. Therefore, we are interested in obtaining extracts that inhibit α -glucosidase for further research on cell toxicity and to developing them into products to relieve diabetes.

Methodology:

Plant materials and extraction

The early mature and mature leaves of *Mitragyna speciosa* were collected from Pa Phayom district, Phatthalung province, Thailand. They were dried in a hot air oven at 60 °C, and then ground into fine powder with a blender. The dried early mature and mature leaves (50 g) were extracted with ethanol for 2 days at room temperature. The filtrate was collected through a filter paper and the residue was re-soaked in ethanol twice for 2 days per time. The combined filtrate was evaporated to dryness under reduced pressure to give ethanol extracts of early mature leaf (EMLE) and mature leaf (MLE).

α -Glucosidase inhibition assay of EMLE and MLE

Matsui, Yosimoto, Oki and Osajima method was used to examine the α -glucosidase inhibitory activity of extracts. Acarbose was used as the standard drug in this procedure. In this method, a sample solution of 25, 50, 100, 125, 250, 350, and 500 μ g/mL concentration was prepared in DMSO. 20 μ L of each concentration was added to 120 μ L of 0.2 M sodium phosphate buffer pH 6.8 in a 96-well microtiter plate. After that, 20 μ L of α -glucosidase enzyme solution (0.2 U/mL in buffer solution) was added. Positive control was prepared in a similar method but the extracted sample was replaced by 20 μ L of DMSO. The Blank was prepared same protocol, but the α -glucosidase enzyme solution was replaced with phosphate buffer, and 20 μ L of DMSO was added instead of the sample. The microplate was shaken for 10 min at room temperature, and then 20 μ L of 3.0 mM of 4-nitrophenyl β -D-glucopyranoside (PNPG) was filled to each well. The plate was shaken for 10 min at the same temperature and the absorbance was measured at 405 nm. The percentage of inhibition was calculated as Eq. 1.

$$\% \text{ Inhibition} = \left[\frac{(A-B) - (C-D)}{(A-B)} \right] \times 100 \quad \text{Eq.1}$$

A is the absorbance value when there is no test sample but enzymes, and B is the absorbance value when there is no test sample and enzymes. C is the absorbance value when the tested sample and enzymes are present. D is the absorbance value when there are no enzymes but a test sample.

Extraction in order of polarity

Early mature leaves of 500 g were extracted in order of increasing polarity with dichloromethane, ethyl acetate, and ethanol to give dichloromethane extract (EMLD), ethyl acetate extract (EMLT), and ethanol (EMLN) extract, respectively. All of these extracts were tested α -glucosidase inhibition.

Separation of the best activities extract to subfractions

EMLN showed better α -glucosidase inhibition activity than EMLD and EMLT. EMLN was separated into subfractions by quick column chromatography with 100%



dichloromethane and gradient solvent of methanol-dichloromethane until 100% methanol to afford 6 fractions based on TLC characteristics. All Fractions were tested α -glucosidase inhibitory activity.

Results and Discussion:

The early mature and mature leaves of *Mitragyna speciosa* were extracted with ethanol three times, 2 days each time. Each filtrate was evaporated to dryness under reduced pressure to give ethanol extracts of early mature leaves (EMLE) and mature leaves (MLE). The result of the α -glucosidase inhibition test shows that EMLE showed slightly better activity than MLE (Table 1). Therefore, the early mature leaves were extracted in order of increasing polarity with dichloromethane, ethyl acetate, and ethanol, respectively, to give EMLD, EMLT, and EMLN extracts. Weight, extract %yield, and physical appearance of all extracts are shown in Table 1. The result found that MLE had more yield extract than EMLE and EMLN>EMLT>EMLD, respectively. The result indicated that most compounds in *Mitragyna speciosa* leaves were polar compounds.

Table 1. Weight of extract, %yield, physical appearance and α -glucosidase inhibitory activity of extract from *Mitragyna speciosa*

Extract	Weight of extract	%Yield	Physical appearance	α -Glucosidase inhibitory activity
				IC ₅₀ (μ g/mL)
EMLE	1.8	3.6	green viscous oil	26.76 \pm 0.05
MLE	2.1	4.2	green viscous oil	28.23 \pm 0.03
EMLD	7.1	2.2	green viscous oil	22.62 \pm 0.15
EMLT	12.2	3.6	brown viscous oil	21.09 \pm 0.43
EMLN	18.5	5.7	brown viscous oil	20.27 \pm 0.08
acarbose				14 \pm 1.36

The α -glucosidase inhibitory activities of all extracts and acarbose, a positive standard drug, are shown in Table 1. The result shows that EMLE displayed better activity than MLE. The EMLN showed higher inhibitory activity against α -glucosidase than EMLT and EMLD. But all extracts exhibited lower inhibitory activity than the standard inhibitor acarbose.

EMLN showed the best α -glucosidase inhibitory activity, then EMLN was separated into subfractions by quick column chromatography to afford 6 subfractions. All Fractions were tested for α -glucosidase inhibitory. Weight of subfraction, physical appearance, α -glucosidase inhibitory activity of all subfractions were shown in Table 2. EMLN6 showed the best α -glucosidase inhibitory activity with IC₅₀ value 16.55 \pm 0.08 μ g/mL, while EMLN1-EMLN5 showed similar activity with IC₅₀ value 18.89 \pm 0.21, 18.89 \pm 0.21, 19.94 \pm 0.13, 18.78 \pm 0.03, 18.85 \pm 0.05 and 19.35 \pm 0.07 μ g/mL, respectively. However, all fractions showed lower α -glucosidase inhibitory activity than standard drug acarbose.

Conclusion:

Our findings suggest that the major active principles for α -glucosidase inhibitory effects of *Mitragyna speciosa* extracts might be present in EMLN (IC_{50} of $20.27 \pm 0.08 \mu\text{g/mL}$). Subfractions EMLN1-EMLN6, was separated from EMLN showed better activity than EMLN with IC_{50} between 16.55 ± 0.08 - $19.94 \pm 0.13 (\mu\text{g/mL})$. these results validate the potency of Kratom as an antidiabetic agent and suggests it could serve as an alternative remedy in the treatment of diabetes.

Table 2. Weight of subfractions, physical appearance, α -glucosidase inhibitory activity of subfractions EMLN1-EMLN6

Subfraction	Weight of subfraction	Physical appearance	α -Glucosidase inhibitory activity $IC_{50} (\mu\text{g/mL})$
EMLN1	1.184	green viscous oil	18.89 ± 0.21
EMLN2	1.102	dark green viscous oil	19.94 ± 0.13
EMLN3	1.126	dark green viscous oil	18.78 ± 0.03
EMLN4	2.055	dark green viscous oil	18.85 ± 0.05
EMLN5	2.344	dark green viscous oil	19.35 ± 0.07
EMLN6	3.531	brown viscous oil	16.55 ± 0.08

Acknowledgements:

This work was supported by Research and Innovation Policy Council, Thaksin University (Fundamental Fund; TSU-65A105000002) Fiscal Year 2022. The authors would like to thank the Department of Chemistry, Faculty of Science, Thaksin University, for providing research facilities.

References:

1. Mitra A, Dewanjee D, Dey B. World J. Diabetes. 2012;3:201 – 207.
2. DeFronzo RA, Ferrannini E, Groop L, Henry RR, Hermann WH, Holst JJ, Hu FB, Kahn CR, Raz I, Shulman GI, Simonson DC, Testa MA, Weiss R. Nat Rev Dis Primers. 2015;15019.
3. Derosa G, Maffioli P. Arch Med Sci. 2012;8:899 – 906.
4. Purintrapiban J, Kaewpradub N, Kansanalak S, Chittrakarn S, Janchawee B, Sawagjaroen K. Nat. Prod. Res. 2011;25:1379 – 1387.
5. Brown PN, Lund JA, Murch SJ. J. Ethnopharmacol. 2020;2017:302 – 325.
6. Halpenny GM. ACS Med. Chem. Lett. 2017;8:897 – 899.
7. Meireles V, Rosado T, Barroso M, Soares S, Goncalved J, Luis A, Caramelo D, Simao AY, Fernandez N, Duarte AP, Gallardo E. Medicine. 2019;6:35.
8. Chen L, Fei S, Olatunji OJ. Molecules. 2022;27:2208.



9. Purintrapiban J, kaewpradub N, Kansenalak S, Chittrakarn S, Janchawee B, Sawangaroen. Nat Prod Res. 2011;25(15):1379 – 1387.
10. Utar Z, Majid M, Adenan MI, Jamil M, Lan T. J.Ethnopharmacology. 2011;136(1):75 – 82.
11. Cheaha, D, Reakkamnuan, C, Nukitram, J, Chittrakam, S., Phukpattaranont, P, Keawpradub, N, Kumarnsit, E. J. Ethnopharmacology. 2017;208:129 – 137.



SESSION C-CHEMISTRY (PHYSICAL & THEORETICAL CHEMISTRY)



CRYSTAL VIOLET ADSORPTION BY MODIFIED SURFACE COFFEE GROUNDS ACTIVATED CARBON

Jarawee Chupiom¹, Piyaporn Pasitkul¹ and Panita Kongsune^{1,*}

¹Innovative Material Chemistry for Environment Center, Department of Chemistry, Faculty of Science and Digital Innovation, Thaksin University, Phattalung, 93210, Thailand

*e-mail: dpanita@tsu.ac.th, +66-74609600 ext 2362

Abstract:

Water pollution caused by organic dyes is a significant environmental concern due to their persistence, toxicity, and potential harm to aquatic ecosystems and human health. This study aims to assess the adsorption capacity of activated carbon derived from coffee grounds (CGAC) for removing Crystal Violet (CV). CGAC was prepared by combusting coffee grounds at 600 °C for 4 hours. The coffee grounds were subsequently activated with KOH. Further modification involved the surface doping of CGAC with EDTA, resulting in EDTA-CGAC, which exhibited enhanced CV removal efficiency. The adsorption of CV onto both CGAC and EDTA-CGAC is influenced by adsorbent dosage, initial CV concentration, adsorption temperature, and contact time. Maximum CV removal (99.92%) was attained with a CV concentration of 400 mg•L⁻¹, an adsorbent dose of 0.55 g, and a contact time of 60 minutes.

Introduction:

Industries like textiles, leather, and paper manufacturing often release synthetic dyes into water sources without proper treatment. These dyes pose significant risks to aquatic ecosystems and human health due to their persistence, toxicity, and potential disruption of aquatic life balance. Some synthetic dyes such as crystal violet (CV) contain chemicals harmful to humans, affecting the nervous system, skin, respiratory system, and internal organs. Prolonged or high-level exposure to such dyes can lead to health problems, including carcinogenic and allergic reactions. In the vicinity of Thaksin University at Phattalung campus and nearby districts of Phattalung province like Cha-uat District, Phapayom District, and Khuan Khanun District, the region boasts a rich cultural heritage, notably in the craft of "Krajood" (*Lepironia articulata*) basketry. This craft involves the use of dyes to enhance the beauty of woven textiles. The dyes employed for this purpose are primarily basic dyestuffs due to their strong affinity and rapid absorption. This research is centered on the absorption of crystal violet (CV), a commonly used basic dyestuff in dyeing. Moreover, crystal violet finds extensive applications beyond dyeing, including biology staining, disease treatment, and ink production.

Wastewater treatment encompasses various methods, including chemical precipitation, ion exchange, adsorption, or reverse osmosis [1]. However, these methods often come with high costs and operational expenses. Therefore, an intriguing approach involves researching and developing cost-effective, locally available natural adsorbent materials. Existing research in water treatment highlights the growing popularity of activated carbon as an adsorbent. Nonetheless, imported activated carbon remains costly. Hence, there is a pressing need to produce activated carbon from biomass to reduce expenses. For instance, coffee grounds, a byproduct of roasted coffee, possess a stable carbon content and small particle sizes, making them easily convertible into activated carbon.

Activated carbon is well-known for its remarkable adsorption properties due to its highly porous nature. Nevertheless, improving the surface modification of activated carbon to



create an excellent adsorbent remains an ongoing challenge. The introduction of oxygen and nitrogen atoms into activated carbon can enhance its adsorption capacity by influencing its surface chemistry [2]. One effective method for enhancing the adsorption properties of activated carbon involves modifying its surface with ethylenediaminetetraacetic acid (EDTA). EDTA, a chelating agent [3], can form complexes with various cationic ions, making it a valuable tool for functionalizing activated carbon surfaces and tailoring them for specific applications [4]. Several papers have reported on the modification adsorbent surface from different natural resources for use as metal ion adsorbents. Common metal ions that are studied include Pb, Cd, Cu, Zn, and Ni [5-7]. It was found that the adsorption efficiencies of these modified celluloses were clearly higher than those of the unmodified cellulose. EDTA's robust affinity for cationic ions is well-recognized, attributed to its abundant amine groups. The incorporation of EDTA into the hemicellulose structure of coffee grounds significantly enhances the adsorption capacity of crystal violet macromolecules.

Therefore, coffee grounds activated carbon (CGAC) and EDTA-doped coffee grounds activated carbon (EDTA-CGAC) were prepared and applied as absorbents to remove crystal violet dye from aqueous solutions in this study. The properties of both CGAC and EDTA-CGAC were analyzed using various experimental techniques, including scanning electron microscopy (SEM), energy-dispersive X-ray spectrometry (EDS), Fourier Transform Infrared spectroscopy (FT-IR), and Brunauer–Emmett–Teller (BET) analysis. For the adsorption of crystal violet dye onto both adsorbents, batch experiments were conducted. The effects of adsorbent dosage, contact time, pH, concentration of crystal violet dye, and temperature on the adsorption activity of CGAC and EDTA-CGAC were investigated.

Methodology:

Preparation of CGAC and EDTA-CGAC

Moisture was removed from coffee grounds by drying them at 105°C for 24 hours. Dried coffee grounds were mixed with 85% KOH and water in a 1:1 ratio by weight. The mixture was stirred well and allowed to soak at room temperature for 24 hours. The mixture was then placed into crucible and carbonized at 600°C for 4 hours. It was washed with distilled water, and the surface was adjusted to pH 7 with HCl. Subsequently, it was dried at 105°C for 24 hours. The resulting product, known as CGAC, was then taken, and 1 g of EDTA was added to it. The mixture was hydrothermally treated at 120°C for 48 hours. Finally, it was dried at 105°C for 24 hours, resulting in the product known as EDTA-CGAC.

Characterization of CGAC and EDTA-CGAC

The approximation properties CGAC and EDTA-CGAC were analyzed. The FT-IR spectra of CGAC and EDTA-CGAC was recorded in a range of 4000-400 cm⁻¹ (G8044AA, Agilent Technologies). The SEM in conjunction with EDS was applied for surface morphology and elemental analysis CGAC and EDTA-CGAC (Oxford, Merlin compact).

Surface acidity/basicity

The surface acidity was estimated by mixing 0.25 g of each adsorbent with 25 cm³ of 0.05 M NaOH solution in a conical flask for 48 hours at room temperature. After the mixtures separated the filtrates were titrated with 0.05 M HCl. The surface basicity was obtained by a similar procedure, while 0.05 M HCl solution was contacted with 0.25 g of adsorbents and the titration solution was 0.05 M NaOH.

Batch adsorption experiment

The adsorption capacity of CGAC and EDTA-CGAC was tested for the removal of Crystal violet from aqueous solution. The effects of absorbent dosage, pH of Crystal violet solution, contact time, and initial concentration of Crystal violet solution on absorption



equilibrium were studied and optimism, respectively. The CGAC and EDTA-CGAC of 0.25 – 0.65 g were soaked in 100 mL of 50-400 mg•L⁻¹ of Crystal violet solution for 180 min at 30-50 °C at the 240 rpm. The initial and final concentrations of Crystal violet were analyzed by UV-Visible spectrophotometer at 590 nm.

The removal percentages (R%) and equilibrium adsorption capacity (Q_e) of Crystal violet were calculated using the following Eqs. (1) and (2), respectively (Zare, Lakouraj, & Kasirian, 2018)

$$R\% = \frac{C_0 - C_e}{C_0} \times 100 \quad (1)$$

$$Q_e = \frac{C_0 - C_e}{m} \times V \quad (2)$$

where C₀ (mg/L) and C_e (mg/L) are the initial and final concentration of Crystal violet in the solution before and after adsorption, respectively. V (L) is the solution volume and m (g) is the weight of the adsorbent.

Results and Discussion:

FTIR spectra

To verify changes in the surface functional groups before and after carbonization and chelation of EDTA on the surface of CGAC, the FT-IR spectras of coffee grounds (CG), CGAC, and EDTA-CGAC were investigated. As shown in Fig. 1, the spectra of CG, which represents the adsorbent not subjected to heat treatment and thus containing especially volatile compounds, exhibited the richest variety of functional groups compared to the other CGAC and EDTA-CGAC adsorbents. However, the absorbance spectra of CGAC and EDTA-CGAC displayed very similar patterns. The absorbance band in the range of 2,850-2,950 cm⁻¹ corresponds to asymmetric and symmetric C–H stretching, while the range of 1,700-1,750 cm⁻¹ corresponds to C=O esters in hemicellulose, and 1,030 cm⁻¹ corresponds to C–OH. The main adsorption peaks of CGAC are located at 1,620, 1,250, 1,030, and 600-700 cm⁻¹, corresponding to C=C unsaturated compounds, asymmetric C–O–C stretching, C–OH stretching, and C–H bending, respectively [8-10], indicating that heat treatment can break down the cellulose or hemicellulose structure in coffee grounds. After EDTA modification, these peaks are still observed, similar to CGAC. However, a new absorption peak at 1,240-1,230 cm⁻¹, 3,500 cm⁻¹ and 3,560-3,854 cm⁻¹ appears in the spectrum of EDTA-CGAC, which can be assigned to the asymmetric stretching frequency of carboxyl groups[11], primary amine and O–H stretching vibration respectively, demonstrating the successful grafting of EDTA onto the CGAC surface. In addition, the absorbance spectra of CGAC and EDTA-CGAC before and after adsorption (CGAC_{CV} and EDTA-CGAC_{CV}) displayed very similar patterns. After CV adsorption, an absorption peak at 1,700 cm⁻¹, which corresponds to C=O stretching, appears with low intensity, demonstrating the successful adsorption of CV onto the CGAC and EDTA-CGAC surfaces.

SEM and EDS analysis

SEM images were used to characterize the morphology of CGAC (Fig. 2a) and EDTA-CGAC (Fig. 2b). The results indicate that the surface of CGAC and EDTA-CGAC exhibit fewer porous structures, channels, or voids. Element analysis of CGAC and EDTA-CGAC using EDS is presented in Fig. 2c and Fig. 2d, respectively. The EDS data suggests that CGAC has a higher carbon content, leading to increased graphitization and the removal of volatile compounds. EDS data for EDTA-CGAC reveals higher oxygen and nitrogen content, indicating that the successful doping of EDTA onto the CGAC surface.

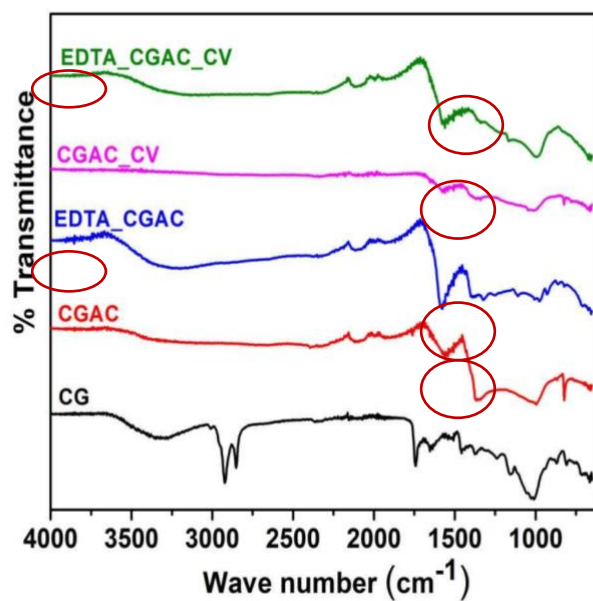


Fig. 1 The FTIR spectrum of CG, CGAC, EDTA_CGAC, CGAC_CV and EDTA_CGAC_CV adsorbents.

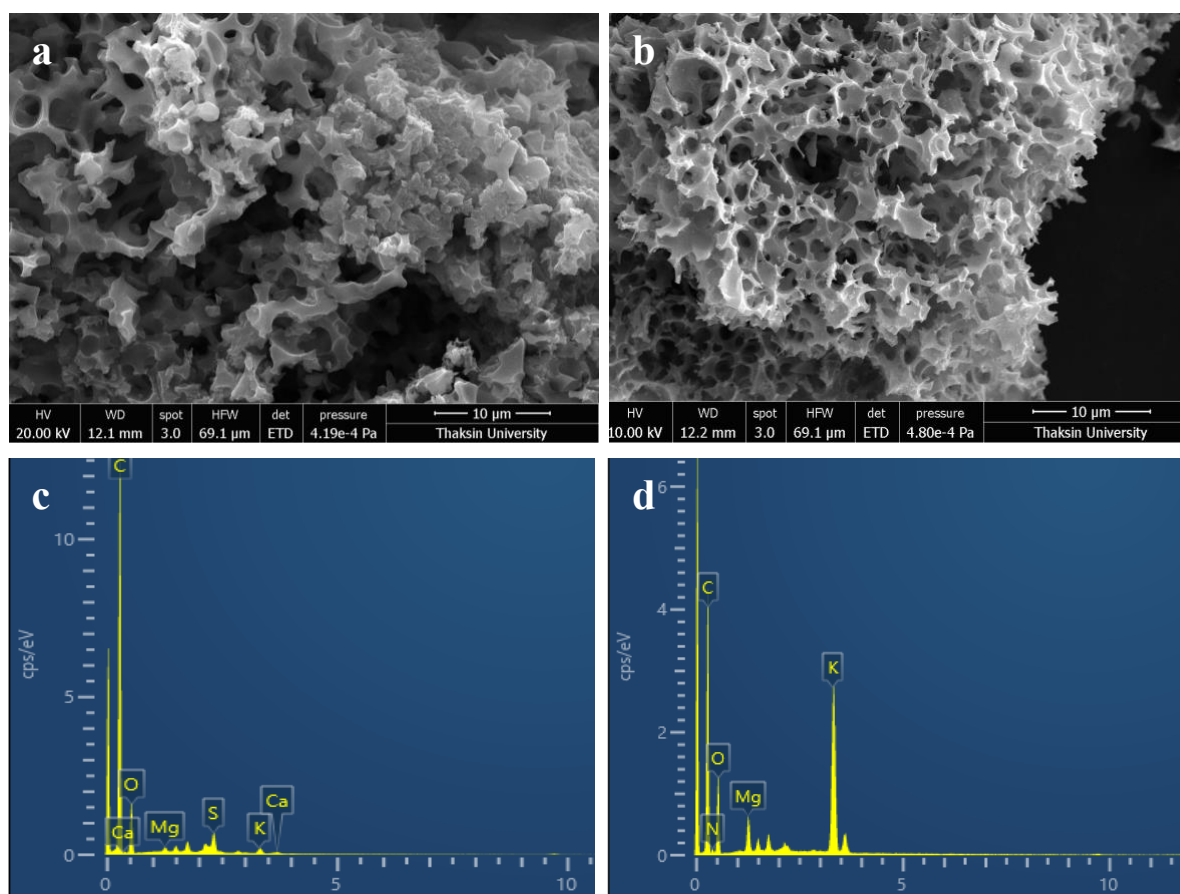


Fig. 2 The (a) SEM image of CGAC (b) image of EDTA-CGAC (c) EDS spectrum of CGAC adsorbent and (d) EDS spectrum of EDTA-CGAC adsorbent.

Boehm titration of the adsorbents

Oxygen and nitrogen atoms are important factors that affect the surface properties of activated carbon. Oxygen-containing functional groups, such as hydroxyl, and nitrogen-containing functional groups, such as amine, are commonly found on the surface. Higher oxygen content makes the surface more acidic, while higher nitrogen content makes it more basic. Acidic and basic surface functionalities are determined by Boehm titration and summarized in Table 1. The total surface area of CGAC and EDTA-CGAC was more basic than acidic due to their higher nitrogen content. Furthermore, the value of basic groups in the EDTA-CGAC sample was higher than in CGAC. Therefore, the activating agent influences the arrangement of surface functional groups.

Table 1 acidic and basic values of CGAC and EDTA-CGAC adsorbents

Adsorbent	Acidic site (mol/g)	Basic site (mol/g)
CGAC	0.75	1.27
EDTA-CGAC	0.10	1.70

The pH of Point of Zero Charge (pH_{PZC})

In this study, we measured the pH of CGAC and EDTA-CGAC to determine whether the activated carbon was acidic or basic in nature. Additionally, measuring the pH_{PZC} allowed us to understand whether the activated carbon contained positive, negative, or neutral charges. The pH_{PZC} values are plotted and observed in Fig. 3. The pH of the PZC for CGAC and EDTA-CGAC is 7.9 and 8.6, respectively. This indicates that when the pH_{PZC} is exceeded, the solution becomes negatively charged, promoting the absorption of cationic species. This effect may be attributed to the activation and carbonization procedure, which eliminates volatile components and significantly dries the material. It has been observed that an activated carbon content of 1–20% is suitable for effective pollution adsorption. This implies that the modification of EDTA changed the surface characteristics of CGAC. For the adsorbents used in this study (CGAC and EDTA-CGAC), the adsorption process is favored at $\text{pH} \leq \text{pH}_{\text{PZC}}$, which is 7.9 and 8.6, respectively.

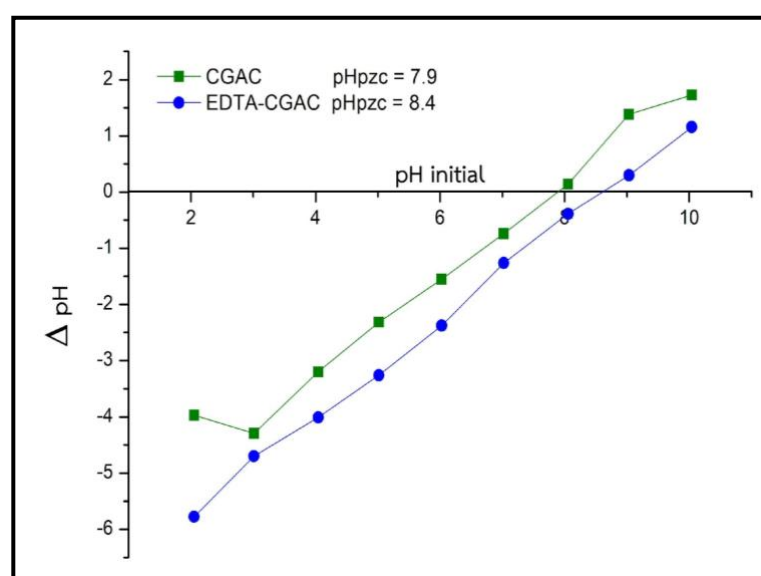


Fig. 3 pH_{PZC} of CGAC and EDTA-CGAC

Effects of parameters on CV adsorption

Results from the study of the effects of adsorbent dosage, CV initial concentration, adsorption temperature, and contact time on CV adsorption are displayed in Fig. 4a-4d, respectively. Fig. 4a presents the effect of adsorbent dose on CV adsorption, with varying adsorbent amounts from 0.25 to 0.75 g for both CGAC and EDTA-CGAC, at fixed times of 180 min, room temperature, and initial concentrations of 150 ppm. It was observed that the amount of CV adsorbed per unit weight of adsorbent (q) decreased with an increase in adsorbent dose, while the removal percentage of CV by CGAC and EDTA-CGAC slightly increased with an increase in adsorbent dose. This suggests that using 0.55 g of CGAC and EDTA-CGAC can yield a high value of q and CV removal.

The initial concentration of CV in the aqueous solution, one of the affecting parameters for adsorption, was investigated using a range of 50-400 $\text{mg}\cdot\text{L}^{-1}$ of CV solution (Fig.4b). The adsorption capacities increased when the initial concentration was increased from 50 to 400 $\text{mg}\cdot\text{L}^{-1}$.

The effect of adsorption temperature (Fig. 4c) shows that the adsorption capacity of CV onto CGAC and EDTA-CGAC increased at 30, 40, and 50 $^{\circ}\text{C}$, respectively, indicating that the adsorption process was endothermic.

The adsorption capacity curves of CGAC and EDTA-CGAC for CV at different time intervals are shown in Fig. 4d. The adsorption capacities increased sharply within 60 min for CGAC and EDTA-CGAC. In the initial stage of the adsorption process, the adsorption sites on the adsorbents for CV were adequate.

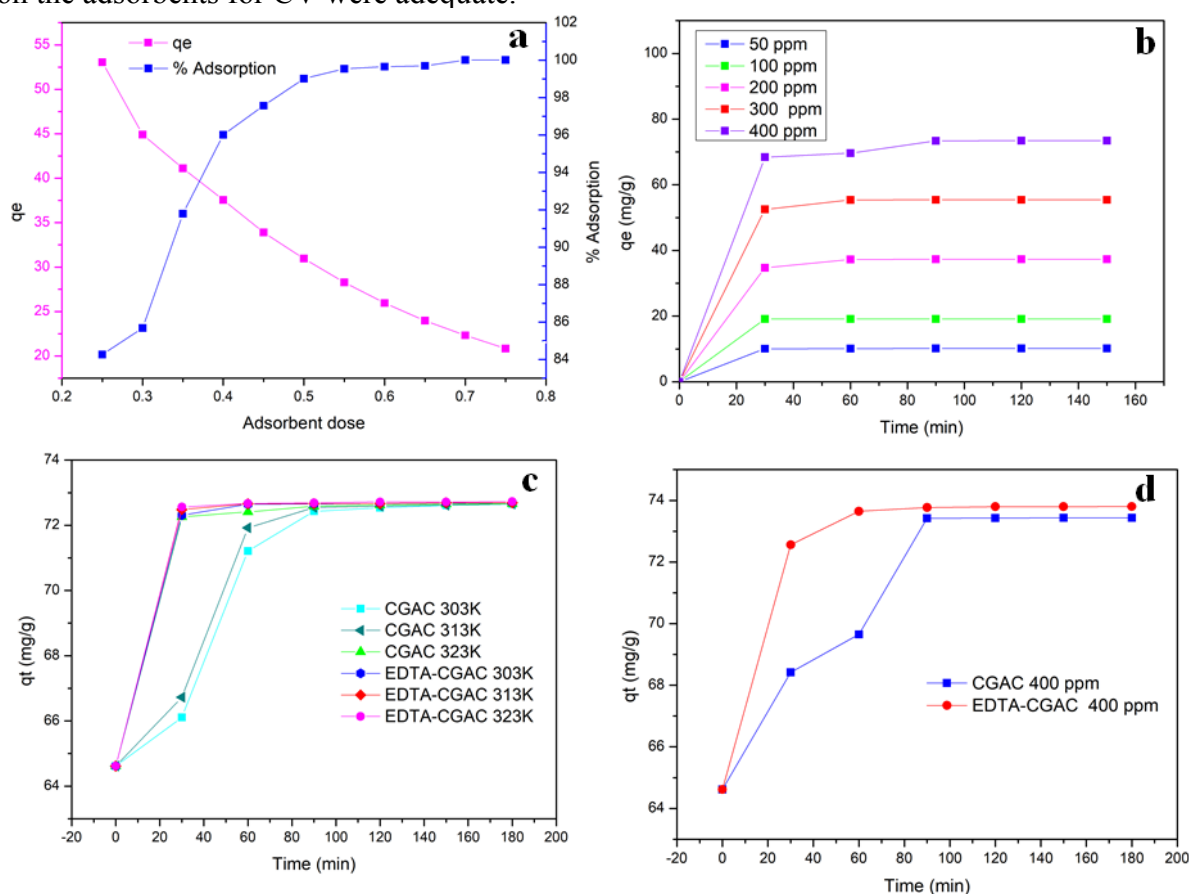


Fig. 4 The effects of (a) adsorbent dosage (b) initial CV concentration (c) Effect of adsorption temperature and (d) contact time on the adsorption capacity of CV onto the CGAC and EDTA-CGAC

As the adsorption proceeded, the available binding sites decreased, resulting in a decrease in the adsorption rate, and the adsorption capacity eventually reached saturation. Most adsorbents tended to reach adsorption equilibrium at 90 min, but the adsorption capacity of EDTA-CGAC reached equilibrium within only 60 min. This may be attributed to its larger specific surface area and porosity, allowing CV to migrate more quickly on the adsorbent surface. From the result can be found that the maximum adsorption capacity at equilibrium (q_e) of CV was $72.67 \text{ mg}\cdot\text{L}^{-1}$ and the percentage removal of CV is 99.92%.

Table 2 Adsorption capacity of CGAC and EDTA CGAC

Adsorbent	C_0 (mg/L)	C_t (mg/l)	q_e (mg/g)	% CV removal
CGAC	400	1.64	71.21	97.92
EDTA-CGAC	400	0.31	72.67	99.92

Conclusion:

In this study, CGAC was prepared by carbonizing coffee grounds and activating them with KOH. EDTA-CGAC was then synthesized by grafting EDTA onto the surface of CGAC, enhancing its CV removal ability. The results demonstrate that EDTA-CGAC exhibits higher adsorption efficiency than CGAC, suggesting that EDTA can effectively modify the surface of CGAC.

The adsorption of CV onto both CGAC and EDTA-CGAC depended on several factors, including adsorbent dosage, initial CV concentration, adsorption temperature, and contact time. The highest %removal of CV, reaching 99.92%, was achieved with a CV concentration of $400 \text{ mg}\cdot\text{L}^{-1}$, an adsorbent dose of 0.55 g, and a contact time of 60 min. Furthermore, the adsorption process was found to be endothermic.

Acknowledgements:

This work was supported by National Higher Education, Science, Research and Innovation Policy Council, Thaksin University (Fundamental Research Fund; TSU-66A105000013) Fiscal Year 2023. The authors would like to thank the Department of Chemistry, Faculty of Science, Thaksin University, for providing research facilities.

References:

1. Bilal, M., Rasheed, T., Iqbal, H.M.N., Hu, H., Wang, W., Zhang, X. International Journal of Biological Macromolecules. 2018;113: 983-90.
2. Lv, D., et al. Applied Surface Science. 2018;428: 648-658.
3. Y. Huang, A.A. Keller. Water Res. 2018;80: 159–168.
4. Pam, A. A., et al. BioResources. 2018;13: 215-221.
5. Pyrzynska, K. Chem. Eng. 2019;7: 102795- 102811.
6. d'Halluin, M. , et al. ACS Sustainable Chem. Eng. 2017;5: 1965–1973.
7. Abu-Danso, E. , Peraniemi, S. , Leiviska T. , Bhatnagar, A. Environ. Pollut. 2019;242: 1988–1997.
8. Wang, S., Zhang, F.-D., Huang, A.-M., Zhou, Q. Holzforschung. 2016;70: 503-510.
9. Balogun, A.O., Lasode, O., Li, H., McDonald, A. Waste and Biomass Valorization. 2014;6: 109-116.
10. D'souza, L., Devi, P.U.M., M.P., D.S., Naik, C.G. Analytical Chemistry Insights. 2008;3: 135 - 43.
11. Wang, X.-d., Li, Y., Dai, T.-t., He, X.-m., Chen, M.-s., Liu, C.-m., et al. Carbohydrate Polymers. 2021;260: 117811.



SCREENING POTENTIAL COMPOUNDS FROM *Mitragyna Speciosa* (Korth.) FOR INHIBITION ACETYLCHOLINESTERASE AND COX-2 BY MOLECULAR DOCKING TECHNIQUE

Panita Kongsune,^{1,*} Nootcharee Banditchon¹, Chuthamat Totang¹, Ajirawadee Hojaroenkul¹, Wisutta Decha¹, and Rattanaporn Pakee¹

¹Innovative Material Chemistry for Environment Center, Department of Chemistry, Faculty of Science and Digital Innovation, Thaksin University, Phattalung, 93210, Thailand

*e-mail: dpanita@tsu.ac.th, +66-74609600 ext 2362

Abstract:

Mitragyna speciosa, commonly known as kratom, is a plant native to Southeast Asia that has gained attention for its potential medicinal properties. Kratom contains a variety of alkaloids, which tend to produce stimulant-like effects, including increased energy, alertness, sociability, and pain relief. One major therapeutic strategy for treating Alzheimer's disease (AD) involves increasing brain acetylcholine (ACh) levels by inhibiting acetylcholinesterase (AChE) activity. Additionally, Cyclooxygenase-2 (COX-2) is an enzyme that plays a crucial role in the body's inflammatory response and sensitizes nerve endings, increasing their responsiveness to pain signals. It's important to note that the use of AChE and COX-2 inhibitors can lead to side effects, including cardiovascular risks and gastrointestinal disturbances, and they often have low bioavailability. Therefore, there is a need to discover and develop more effective AChE and COX-2 inhibitors, potentially sourced from natural compounds. The primary goal of this study is to conduct structure-based molecular docking to screen potential anti-AChE and COX-2 candidates of the 36 alkaloid structures and 8 flavonoid structures obtained from *Mitragyna speciosa* leaves. The results of the calculations indicate that several bioactive compounds exhibit a strong binding affinity with AChE compared to COX-2 protein. Notably, compounds from the alkaloid functional group, including Angustine and Isomitraphylline, displayed superior binding affinity (binding energy (BE) and dock score (% DS)) toward both AChE (BE = -10.028 kcal•mol⁻¹ and %DS = 100) and COX-2 (BE = -9.32 kcal•mol⁻¹ and %DS = 100). These findings suggest that compounds derived from *Mitragyna speciosa* (kratom) leaves have the potential to serve as therapeutic agents for further drug development targeting Alzheimer's disease by inhibiting AChE and for managing pain by targeting COX-2.

Keywords: Acetylcholinesterase, COX-2, *M. speciosa*, Alzheimer's disease, Docking

Introduction:

Alzheimer's disease (AD) is an irreversible neurodegenerative disease of brain neurons (1, 2). According to the World Health Organization (WHO), AD is one of the most common causes of dementia, and it affects approximately 50 million people worldwide (2). Many studies have found that AD is associated with decreased levels of neurotransmitter acetylcholine (ACh) in the brain (3). Acetylcholinesterase (AChE), an essential enzyme in the family of serine hydrolases, catalyzes the hydrolysis of ACh (4). Therefore, one of the major therapeutic strategies for the treatment of AD is to increase the ACh level in the brain by inhibiting the biological activity of AChE.

Cyclooxygenase-2 (COX-2) is an enzyme that plays a crucial role in the body's inflammatory response. It is part of a family of enzymes known as cyclooxygenases, which are involved in the production of prostaglandins. In addition to promoting inflammation, COX-2-derived prostaglandins also sensitize nerve endings, making them more responsive to



pain signals. This is why COX-2 inhibitors are often used as pain relievers. COX-2 inhibitors are a class of medications that specifically target and block the activity of the COX-2 enzyme. By doing so, they reduce the production of prostaglandins associated with inflammation and pain. This makes COX-2 inhibitors effective in treating conditions like osteoarthritis, rheumatoid arthritis, and acute pain.

There are currently four approved drugs targeting AChE used in patients with AD, *i.e.*, tacrine, dopenzial, galantamine, and rivastigmine (5-8). Unfortunately, these drugs are known to induce several side effects such as gastrointestinal disturbances, and they have low bioavailability. In addition, it's important to note that the use of COX-2 inhibitors can have side effects, including cardiovascular risks. Hence, it is needed to find and develop better AChE and COX-2 inhibitors for example from natural sources to treat AD and pain relievers without any side effects.

Mitragyna speciosa (kratom), commonly known as kratom, has a long history of traditional use in Southeast Asia, where it has been used for its stimulant and analgesic (pain-relieving) properties. It was often chewed or brewed into tea by laborers and farmers to combat fatigue and pain. Kratom is a tropical tree native to Southeast Asia, particularly in countries like Thailand, Malaysia, Indonesia, and Papua New Guinea. Kratom has gained popularity in recent years due to its potential medicinal properties and recreational use. Kratom contains a variety of alkaloids, these compounds tend to have stimulant-like effects, including increased energy, alertness and sociability interact. Kratom has gained attention for its potential medicinal applications, particularly in managing chronic pain and opioid withdrawal symptoms. Some individuals have used it as an alternative to prescription opioids or as a way to taper off opioids.

Many studies have isolated bioactive compounds from kratom leaves, but comprehensive studies are required to determine their molecular interactions. Molecular docking is an efficient tool for predicting the orientation of a ligand at the specific site of a receptor, and for exploring the receptor-ligand interactions. Recently, several studies have used the molecular docking method to study the interactions and conformations of ligand against AChE and COX-2 target. Herein, we aimed to explore the lead compound from kratom leaves for their medicinal potentials as therapeutic agents against AChE and COX-2 using structural modeling of molecular docking technique. The 36 alkaloid structures and 8 flavonoid structures molecules obtained from Kratom leaves were screened against AChE and COX-2 by molecular docking. A detailed understanding of ligand-protein interaction and its inhibitory activity against AChE and COX-2 could be helpful in further drug design and development for AD and pain relievers treatment.

Methodology:

Molecular docking technique was applied to study the binding orientation and affinity of the bioactive compounds from kratom toward the binding site of AChE and COX-2, utilizing AutoDock 4.2 (9). The three-dimensional (3D) structures of both targets were obtained from the Brookhaven Protein Data Bank (PDB) (10) are shown in Fig.1. The PDB IDs for AChE and COX-2 are 4EY6 (Resolution: 2.40 Å, R-Value Free: 0.206, R-Value Work: 0.167) (11) and 5KIR (Resolution: 2.70 Å, R-Value Free: 0.220, R-Value Work: 0.178) (12), respectively. The water molecules were removed, and missing hydrogen atoms were added to the protein structures.

The bioactive molecules from kratom leaves, including 36 alkaloid structures and 8 flavonoid structures, were drawn using Gauss View (13). Their three-dimensional (3D) structures were optimized at the Hartree-Fock level of theory with a 6-31G* basis set using

the Gaussian 03 program (14). Subsequently, the optimized structures were converted to .pdb format using GaussView (14) for molecular docking studies. Partial atomic charges for both the protein and ligands were assigned using the Gasteiger–Marsili method (15), which was implemented in AutoDock Tools (16). In the semiflexible docking protocol, the protein molecule was kept rigid, while flexibility of the ligands was allowed to account for torsional freedom. The protein and ligands were converted to .pdbqt format after initially adding hydrogen bonds and charges. These prepared molecules were used for docking analysis. A cubic grid box with dimensions of $50 \times 50 \times 50 \text{ \AA}$, with a grid spacing of 0.375 \AA , was positioned around the key residues of the protein. The cubical grid box of $50 \times 50 \times 50$ size with 0.375 \AA was fixed around the key residues of the AChE enzyme containing the catalytic triad (S203, H447 and E334), the anionic subsite (W86, Y133 and E202), the oxyanion subsite (G121, G122 and A204), the acyl-binding subsite (Trp236, Phe295, Phe297 and Phe338, the bottleneck region (Y124 and F338) and the peripheral anionic site (PAS, Y72, D74) [11]. Information from the crystal structure of COX-2 has revealed that key active residues (Tyr-385, Phe-381, Val-523, Glu-524 and Ser-530) [12] are found in the catalytic domain within the C-terminus and covered by cubical grid box of COX-2 system.

To assess binding affinity, galantamine and rofecoxib were re-docked into the AChE and COX-2 binding sites, respectively. Additionally, these two compounds served as control molecules for filtering other bioactive compounds. AutoGrid4 parameters were used to create a rigid grid box. Furthermore, AutoDock4, employing Lamarckian genetic algorithms, was employed to determine the best docking conformations. It's worth noting that AutoDock estimates free energies of binding based on typical molecular mechanics energy terms, including dispersion/repulsion, hydrogen bonding, electrostatic interactions (17), torsional entropy upon binding, and desolvation effects upon ligand binding, along with corresponding hydrophobic effects (18).

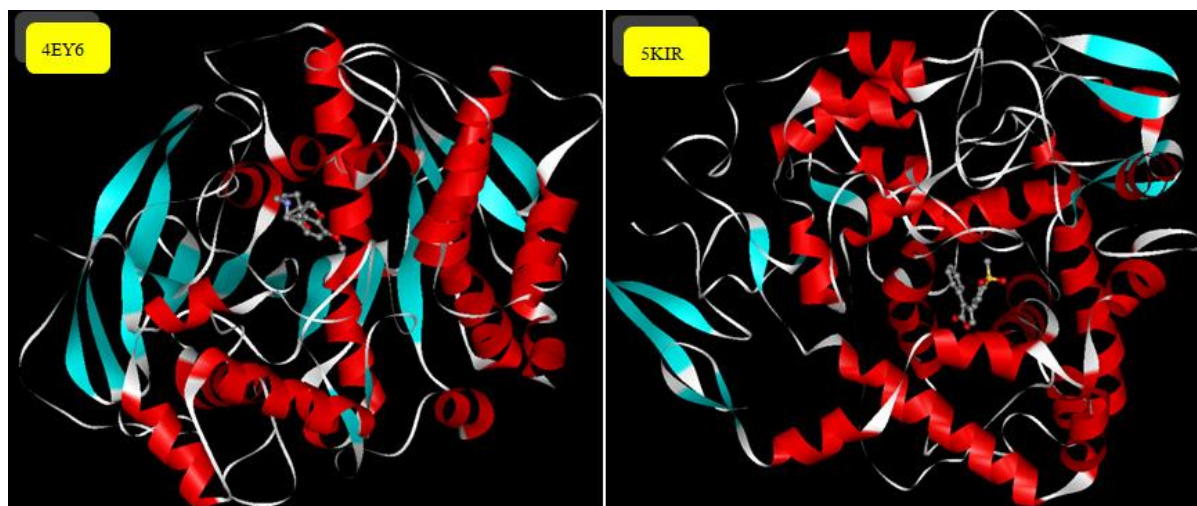


Fig. 1 The three-dimensional structures of AChE (4EY6) and COX-2 (5KIR) obtained from the Brookhaven Protein Data Bank (PDB).

Results and Discussion:

The molecular docking was performed using AutoDock program to screen the binding affinity of 36 alkaloid structures and 8 flavonoid structures from kratom leaves against the two targets of AChE and COX-2. The binding energy (BE, $\text{kcal}\cdot\text{mol}^{-1}$) and the percentage of

possible conformation or dock score (% DS) of all bioactive compounds against AChE were varying from -6.05 to -11.51 kcal•mol⁻¹ and 32 to 100 %, respectively. When the BE and % DS of these compounds against COX-2 were varying from -2.28 to -11.52 kcal•mol⁻¹ and 31 to 100 %. Galantamine (GAL) and Rofecoxib were used as control molecule were re-docked into the AChE and COX-2 binding sites for assessing binding affinity. The binding energy of galantamine and Rofecoxib were used as reference for filtering alkaloid and flavonoid compounds from the Kratom. The BE and %DS of top fourteen bioactive compounds against both targets are summarized in Table 1.

The docking program was verified by re-docking of galantamine back into the AChE binding site. The docking model of galantamine was well posed in the AChE binding site (Fig.2a) with the BE and %DS of -9.97 kcal•mol⁻¹ and 97%, suggesting that the setting parameters were suitable for this study. Rofecoxib was also redock back into the COX-2 binding site. The docking model of Rofecoxib was also well posed in the COX-2 binding site (Fig.2b) with the BE and %DS of -5.57 kcal•mol⁻¹ and 82%. The docking result shows that mostly bioactive compounds are good binding affinity in cavity of protein. Docking results indicated that alkaloid compounds from *Mitragyna speciosa* (kratom) exhibited higher binding affinities for AChE and COX-2 compared to flavonoid compounds. Specifically, indole and oxindole alkaloid compounds demonstrated superior binding affinities toward to the both targets when compared to other alkaloids. Notably, Angustine and Isomitraphylline exhibited excellently strong binding affinities to AChE, with values of -10.02 kcal•mol⁻¹ and -11.42 kcal•mol⁻¹, respectively. Furthermore, both Angustine and Isomitraphylline showed a 100% percentage of possible conformation (% DS), indicating favorable binding interactions between these compounds and AChE, a protein. Fig. 2(A) shows that the galanthamine was well occupied in the active site gorge of AChE in the orientation similar to those of Rofecoxib in the binding site of COX-2 (Fig.2(B)).

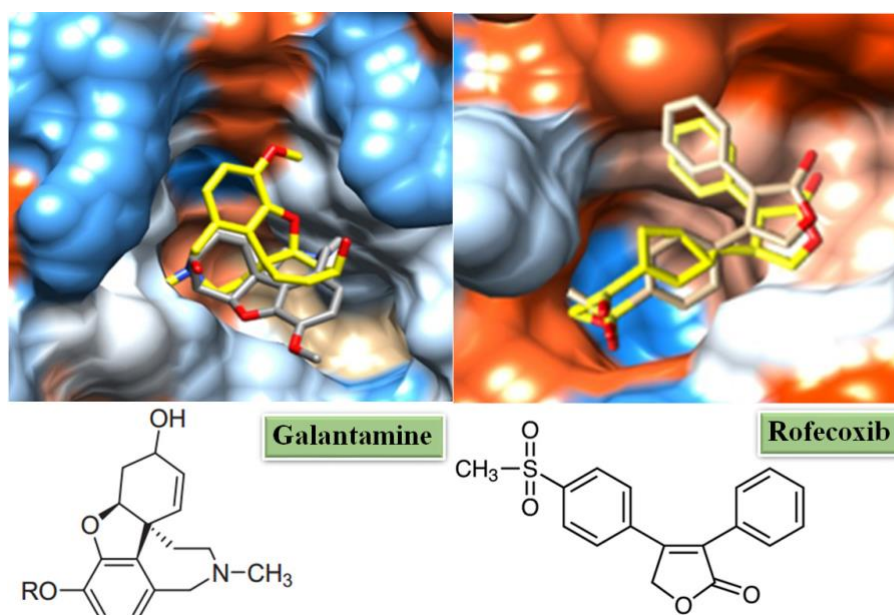
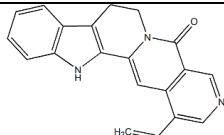
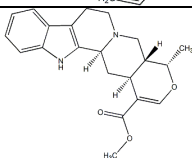
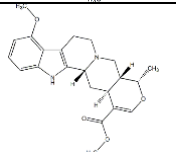
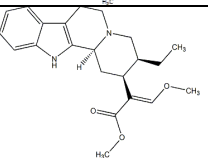
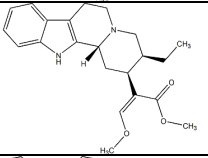
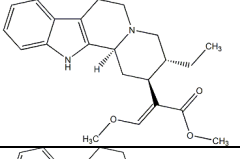
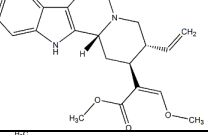
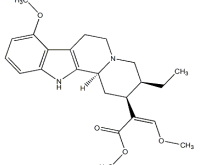
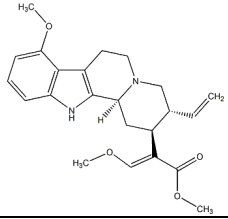
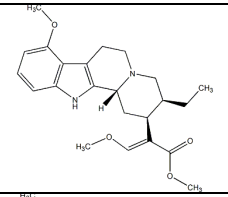
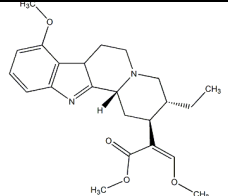
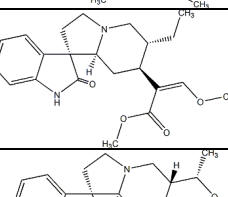
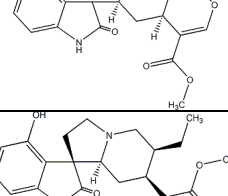
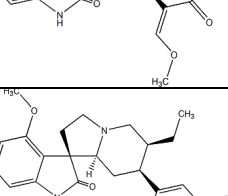
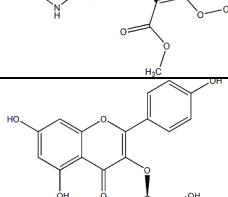
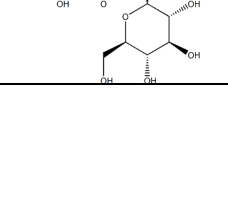
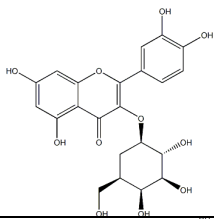
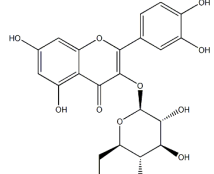


Fig.2 A close-up view of the superimposition of docking model (brown) and crystal structure (yellow) and 2D of (A) the galantamine in the binding site of human AChE, and (B) the Rofecoxib in the binding site of COX-2. The hydrophilic and hydrophobic surfaces are colored by blue and orange, respectively.

Table 1. The BE and %DS of commercial drugs and selected most favorable compounds in the binding pocket of AChE and COX-2.

Compounds	Structure	AChE		COX-2	
		BE (kcal•mol ⁻¹)	%DS	BE (kcal•mol ⁻¹)	%DS
		Galantamine		Rofecoxib	
		-9.97	97	-5.57	82
Angustine		-10.02	100	-9.32	100
Ajmalicine		-10.69	98	-8.42	95
Akuammigine		-9.43	97	-9.58	98
Corynantheidine		-10.26	86	-10.23	46
Isocorynantheidine		-10.05	73	-7.7	53
Hirsutine		-10.44	50	-10.31	58
Hirsuteine		-8.73	52	-11.4	55
Mitragynine		-10.38	64	-8.78	67

Paynantheine		-9.99	38	-9.61	51
Compounds	Structure	AChE		COX-2	
		BE (kcal•mol ⁻¹)	%DS	BE (kcal•mol ⁻¹)	%DS
Speciociliatine		-7.59	84	-10.19	55
7 α -Hydroxy-7H-mitragynine		-8.57	82	-7.81	41
Isorhynchophylline		-11.25	51	-2.62	53
Isomitraphylline		-11.42	100	-9.81	93
Isomitrafoline		-10.59	58	-3.93	35
Mitragynine oxidole B		-11.09	78	-6.58	65
Astragalin		-6.87	32	-11.25	62

Hyperoside		-7.9	47	-10.7	50
Isoquercitrin		-6.97	40	-11.52	67

4. Conclusion

In this study, the 36 alkaloid structures and 8 flavonoid structures molecules obtained from Kratom leaves were screened against AChE and COX-2 through molecular docking performed to screen the lead compounds for Alzheimer's disease pain relievers treatment. Docking results showed that compounds from the alkaloid functional group, including Angustine and Isomitraphylline, displayed superior binding affinity (BE and %DS) toward both AChE (BE = -10.028 kcal•mol⁻¹ and %DS = 100) and COX-2 (BE = -9.32 kcal•mol⁻¹ and %DS = 100). These findings suggest that compounds derived from *Mitragyna speciosa* (kratom) leaves have the potential to serve as therapeutic agents for further drug development targeting Alzheimer's disease by inhibiting AChE and for managing pain by targeting COX-2.

Acknowledgements:

This work was supported by National Science, Research and Innovation Fund (NSRF), Thaksin University (Research project grant FF-2567A10512017) Fiscal Year 2024. The authors would like to thank the Computational Chemistry Unit Cell, Faculty of Science, Chulalongkorn University, and the Department of Chemistry, Faculty of Science, Thaksin University, for providing research facilities, software packages and computing times.

References:

1. Parihar MS, Hemnani T. J. Clin. Neurosci. 2004;11(5):456-67.
2. World Health Organization and Alzheimer's disease International Report, Dementia. 2019.
3. Scarpini E, Schelterns P, Feldman H. The Lancet Neurol. 2003;2(9):539-47.
4. Pohanaka M. Expert Opin. Ther. Pat. . 2012;22:871-86.
5. Kelly CA, Harvey RJ, Cayton H. Med. J. 1997;314:693-4.
6. Whitehouse PJ. Acta Neurol. Scand. Suppl. 1999;149:42-5.
7. Gottwald MD, Rozanski RI, EOI. Drugs. 1999;8:1673-82.
8. Scott LJ, Goa KL. Drugs. 2000;60:1095-122
9. Morris GM, Goodsell DS, Halliday RS, Huey R, Hart WE, Belew RK, et al. J. Comput. Chem. 1998;19:1639-62.
10. Bernstein FC, Koetzle TF, Williams GJ, Meyer EFJ, Brice MD, Rodgers JR, et al. J. Mol. Biol. 1977;112:535-42.
11. Cheung J, Rudolph MJ, Burshteyn F, Cassidy MS, Gary EN, Love J, et al. J Med. Chem. 2012;55(22):10282-6.
12. Orlando BJ, Malkowski MG. Acta Crystallogr. F:Struct. Biol. 2016;72(Pt 10):772-6.



13. Dennington R, Keith T, Millam J. GaussView Semichem Inc., Shawnee Mission KS. 2009.
14. Frisch MJ, Trucks GW, Schlegel HB, Scuseria GE, Robb MA, Cheeseman JR, et al. Gaussian 03, Revision C.02: Gaussian, Inc., Wallingford CT.; 2004.
15. Gasteiger J, Marsili M. Tetrahedron. 1980;36:3219-28.
16. Morris GM, Huey R, Lindstrom W, Sanner MF, Belew RK, Goodsell DS, et al. J. Comput. Chem. 2009;30:2785-91.
17. Huey R, Morris GM, Olson AJ, Goodsel DS. J. Comput. Chem. 2007;28: 1145–52.
18. Ermakova E. Comput. Biol. Chem. 2016;64:281-96.



SESSION D-MATHEMATICS / STATISTICS / COMPUTER SCIENCE / DATA SCIENCE / AI

GRACEFUL LABELING OF SOME THE RING SUM GRAPHS AND THE BISTAR RELATED GRAPHS

Hakeemee sadeeyamu,¹ Napatsawan prombut,¹ Siwaporn Saewan^{2,*}

¹Students, Department of Mathematics and Statistics, Faculty of Science and Digital Innovation, Thaksin University, Phatthalung, 93210, Thailand

²Assoc. Prof. Dr., Department of Mathematics and Statistics, Faculty of Science and Digital Innovation, Thaksin University, Phatthalung, 93210, Thailand

*e-mail: siwaporn@tsu.ac.th

Abstract:

A graceful labeling of a simple connected graph $G = (V(G), E(G))$ with $|E(G)|$ edges is an injective function $f: V(G) \rightarrow \{0, 1, \dots, |E(G)|\}$ such that for each edge $uv \in E(G)$ is label $|f(u) - f(v)|$ then the results of edge labels are distinct. In this paper contains some results on graceful labeling of the bistar graph, the graph obtained by the duplication a vertex of the bistar graph by an edge, and the graph obtained by the ring sum of the path P_n and the complete bipartite graph $K_{2,m}$.

Introduction:

Let G be a simple graph with a vertex set $V(G)$ and edge set $E(G)$. Let $q = |E(G)|$ be the number of the edges of G . The **endpoints** of an edge is a set of two vertices connects to each edge. The vertices are in the endpoint of each edge are called **incident** with the edge. The vertices which are incident with a common edge are **adjacent**. A **simple graph** G is a graph with each edge in $E(G)$ connects two distinct vertices in $V(G)$. The **Neighbourhood** of a vertex v in a graph G is the set of all vertices which are adjacent to v . The set of neighbours of a vertex v is denoted by $N(v)$. For more detail, the reader can see in, Gross and Yellen¹ and Bondy and Murty³. A labeling of a graph G is a function f such that carries a set of graph elements into the set of integers. Rosa⁹ introduced a labeling called β -valuation, later Golomb⁷ called as graceful labeling.

Definition 1 A function f is called a **graceful labeling** of a simple graph G with $|E(G)| = q$ edges if $f: V(G) \rightarrow \{0, 1, 2, \dots, q\}$ is injective and the induced function $f^*: E(G) \rightarrow \{1, 2, \dots, q\}$ defined by

$$f^*(uv) = |f(u) - f(v)|$$

is bijective. A graph which has a graceful labeling is called a graceful graph.

Many papers published in the graceful labeling of graphs see Biatch et al.² Makadia et al.⁸ Boxwala and Vashishta⁴ and Sethuraman and Murugan¹⁰. See Gallian⁵ for a dynamic survey of graph labeling.

Definition 2 The **bistar graph** is the graph obtained by joining the centre (apex) vertices of two copies of the star $K_{1,n}$ by an edge and it is denoted by $B_{n,n}$. See Ghodasara and Patel⁶ for more details.

Definition 3 The duplication of a vertex v_k of a graph G produces a new graph by adding a new edge $e = v'_k v''_k$ such that

$$N(v''_k) = \{v_k, v'_k\} \text{ and } N(v'_k) = \{v_k, v''_k\},$$

where $N(u^*)$ denotes the set of neighborhood of a vertices u^* .

The duplication of a vertex u_2 of a bistar graph $B_{4,4}$ by a new edge $e = u'_2 u''_2$ shown in Figure 1.

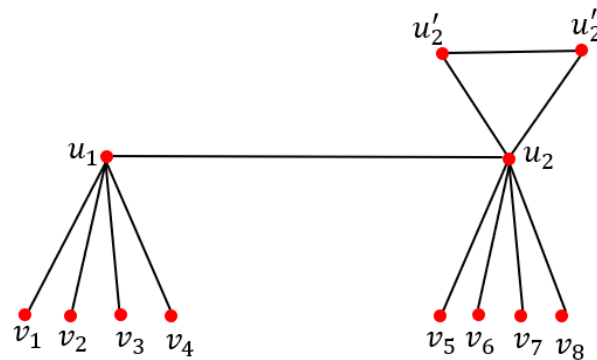


Figure 1.

Definition 4 Given two graphs $G_1 = (V(G_1), E(G_1))$ and $G_2 = (V(G_2), E(G_2))$ the ring sum of G_1 and G_2 denote by $G_1 \oplus G_2$ such that

$$G_1 \oplus G_2 = (V(G_1) \cup V(G_2), E(G_1) \cup E(G_2) - E(G_1) \cap E(G_2)).$$

Makadia et al⁴. proved some results on the ring sum of two graphs for their graceful. In this paper, we consider the ring sum of the path P_n and the complete bipartite graph $K_{2,m}$ with two common vertices v_1 and v_2 . The ring sum graph $P_4 \oplus K_{2,3}$ shown in Figure 2.

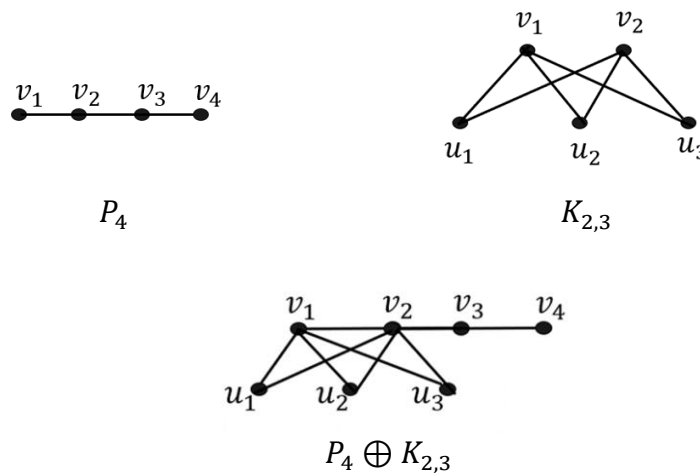


Figure 2.

In this paper we show the graceful labeling of the bistar graph, the graph obtained by the duplication a vertex of the bistar graph $B_{n,n}$ by a new edge and the graph obtained by the ring sum of the path P_n and the complete bipartite graph $K_{2,m}$.

Methodology:

1. Studying on the graceful labeling.
2. Studying on the graph operations.
3. Finding the graceful labeling of the bistar graph, the graph obtained by duplication a vertex by an edge of the bistar graph $B_{n,n}$ and the graph obtained by the ring sum of the path P_n and the complete bipartite graph $K_{2,m}$.
4. Establishing the new theorems of the graceful labeling.

Results and Discussion:

Theorem 1 $B_{n,n}$ is the graceful graph.

Proof Let $B_{n,n}$ be the bistar with the vertex set $M = \{u_1, u_2\}$ and $N = \{v_1, v_2, v_3, \dots, v_{2n}\}$.

Hence, we have $q = |E(B_{n,n})| = 2n + 1$.

Define $f: V(B_{n,n}) \rightarrow \{0, 1, 2, \dots, q = 2n + 1\}$ as follows.

$$f(v_{n+1}) = 0.$$

$$f(u_1) = 1.$$

$$f(v_i) = 2i \quad i = 1, 2, 3, \dots, n.$$

$$f(v_i) = 2i - 2n - 1, \quad i = n + 2, n + 3, \dots, 2n.$$

$$f(u_2) = 2n + 1.$$

Clearly f is an injective.

Next consider the induced function $f^*: E(G) \rightarrow \{1, 2, 3, \dots, q = 2n + 1\}$.

$$f^*(u_2 v_{n+1}) = 2n + 1.$$

$$f^*(u_2 u_1) = 2n.$$

$$f^*(u_1 v_i) = 2i - 1, \quad i = 1, 2, 3, \dots, n.$$

$$\{f^*(u_1 v_i) | i = 1, 2, 3, \dots, n\} = \{1, 3, 5, \dots, 2n - 1\}.$$

$$f^*(u_2 v_i) = 4n - 2i + 2, \quad i = n + 2, n + 3, \dots, 2n.$$

$$\{f^*(u_2 v_i) | i = 1, 2, 3, \dots, n\} = \{2, 4, 6, \dots, 2n - 2\}.$$

Thus

$$\begin{aligned} \{f^*(E(G))\} &= \{f^*(u_1 v_i) | i = 1, 2, 3, \dots, n\} \cup \{f^*(u_2 v_i) | i = n + 2, n + 3, \dots, 2n\} \\ &\quad \cup \{f^*(u_1 v_i)\} \cup \{f^*(u_2 u_1)\} \cup \{f^*(u_2 v_{n+1})\} \\ &= \{1, 2, 3, \dots, 2n + 1\}. \end{aligned}$$

It is obvious that f^* is a bijective. Then $B_{n,n}$ is the graceful graph. \square

The graceful graph $B_{3,3}$ shown in Figure 3.



Figure 3.

The caterpillar is a tree with the property that all the vertices are within distance 1 from a central path. The bistar are the caterpillar. Rosa⁹ have shown that all caterpillars are graceful. However, the graceful labeling f in Theorem 1 is easy and convenient for $B_{n,n}$.

Theorem 2 Let $B_{n,n}$ be the bistar graph with $M = \{u_1, u_2\}$ and $N = \{v_1, v_2, v_3, \dots, v_{2n}\}$. The graph G obtained by duplication of a vertex in M is the graceful graph.

Proof Let $B_{n,n}$ be the bistar graph with $M = \{u_1, u_2\}$ and $N = \{v_1, v_2, v_3, \dots, v_{2n}\}$. Let G be the graph obtained by duplication a vertex in M of $B_{n,n}$. Without loss of generality, duplication a vertex u_2 in M by a new edge $e = u'_2 u''_2$. Hence, we have $q = |E(G)| = 2n + 4$.

Define $f: V(G) \rightarrow \{0, 1, 2, \dots, 2n + 4\}$ as follows.

$$f(u_1) = 2.$$

$$f(u_2) = 2n + 4.$$

$$f(u'_2) = 1.$$

$$f(u_2'') = 0.$$

$$f(v_i) = 2i + 2, \quad i = 1, 2, 3, \dots, n.$$

$$f(v_i) = 2i - n - 2, \quad i = n + 1, n + 2, n + 3, \dots, 2n.$$

Clearly f is an injective.

Next consider the induced function $f^*: E(G) \rightarrow \{1, 2, 3, \dots, q = 2n + 4\}$.

$$f^*(u_2'u_2'') = 1.$$

$$f^*(u_1v_i) = 2i, \quad i = 1, 2, 3, \dots, n.$$

$$\{f^*(u_1v_i), i = 1, 2, 3, \dots, n\} = \{2, 4, 6, \dots, 2n\}.$$

$$f^*(u_2v_i) = 3n - 2i + 6, \quad i = n + 1, n + 2, n + 3, \dots, 2n.$$

$$\{f^*(u_2v_i), i = n + 1, n + 2, n + 3, \dots, n\} = \{3, 5, \dots, 2n + 1\}.$$

$$f^*(u_1u_2) = 2n + 2.$$

$$f^*(u_2u_2') = 2n + 3.$$

$$f^*(u_2u_2'') = 2n + 4.$$

Thus

$$\begin{aligned} \{f^*(E(G))\} &= \{f^*(u_2'u_2'')\} \cup \{f^*(u_1v_i) | i = 1, 2, 3, \dots, n\} \cup \{f^*(u_2v_i) | i = 1, 2, 3, \dots, n\} \\ &\quad \cup \{f^*(u_1u_2) = 2n + 2\} \\ &\quad \cup \{f^*(u_2u_2')\} \cup \{f^*(u_2u_2'')\} \\ &= \{1, 2, 3, \dots, 2n + 4\}. \end{aligned}$$

It is obvious that f^* is a bijective. Then G is the graceful graph. □

The graceful graph G shown in Figure 4.

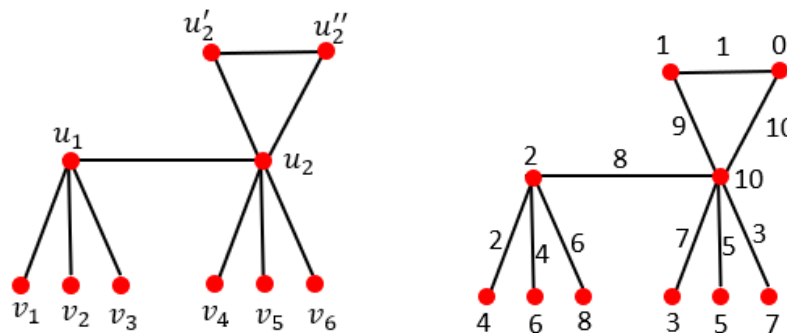


Figure 4.

Theorem 3 Let P_n be the path with n vertices and $K_{2,m}$ be the complete bipartite graph. Then $P_n \oplus K_{2,m}$ is the graceful graph.

Proof Let $v_1, v_2, v_3, \dots, v_n$ be the successive vertices of P_n and $N = \{v_1, v_2\}$ and $M = \{u_1, u_2, u_3, \dots, u_m\}$ be the bipartition of $K_{2,m}$. Let v_1 and v_2 be two common vertices of P_n and $K_{2,m}$. Let $P_n \oplus K_{2,m}$ be a ring sum graph of P_n and $K_{2,m}$. Thus $q = |E(P_n \oplus K_{2,m})| = 2m + n - 1$. Define $f: V(P_n \oplus K_{2,m}) \rightarrow \{0, 1, 2, \dots, 2m + n - 1\}$ as follows.

Case 1: If n is odd, then

$$f(v_i) = \begin{cases} \frac{i-1}{2}, & i = 1, 3, 5, \dots, n \\ \frac{2m+2n-i}{2}, & i = 2, 4, 6, \dots, n-1. \end{cases}$$

$$f(u_j) = q - (j - 1), j = 1, 2, 3, \dots, m.$$

Case 2: If n is even, then

$$f(v_i) = \begin{cases} \frac{i-1}{2}, & i = 1, 3, 5, \dots, n-1 \\ \frac{2m+2n-i}{2}, & i = 2, 4, 6, \dots, n. \end{cases}$$

$$f(u_j) = q - (j-1), j = 1, 2, 3, \dots, m.$$

Clearly f is an injective.

Next consider the induced function $f^*: E(P_n \oplus K_{2,m}) \rightarrow \{1, 2, 3, \dots, 2m+n-1\}$.

$$f^*(v_1 u_j) = q - (j-1), j = 1, 2, 3, \dots, m.$$

$$\{f^*(v_1 u_j) | j = 1, 2, 3, \dots, m\} = \{2m+n-1, 2m+n-2, \dots, m+n\}.$$

$$f^*(v_2 u_j) = m - (j-1), j = 1, 2, 3, \dots, m.$$

$$\{f^*(v_2 u_j) | j = 1, 2, 3, \dots, m\} = \{m, m-1, m-2, \dots, 1\}.$$

$$f^*(v_i v_{i+1}) = m+n-i, i = 1, 2, 3, \dots, n-1.$$

$$\{f^*(v_i v_{i+1}) | i = 1, 2, 3, \dots, n-1\} = \{m+n-1, m+n-2, \dots, m+1\}.$$

Thus

$$\begin{aligned} \{f^*(E(P_n \oplus K_{2,m}))\} &= \{f^*(v_2 u_j) | j = 1, 2, 3, \dots, m\} \\ &\cup \{f^*(v_i v_{i+1}) | i = 1, 2, 3, \dots, n-1\} \\ &\cup \{f^*(v_1 u_j) | j = 1, 2, 3, \dots, m\} \\ &= \{1, 2, 3, \dots, 2m+n-1\}. \end{aligned}$$

It is obvious that f^* is a bijective. Then $P_n \oplus K_{2,m}$ is the graceful graph. □

The graceful graph $P_4 \oplus K_{2,2}$ shown in Figure 5.

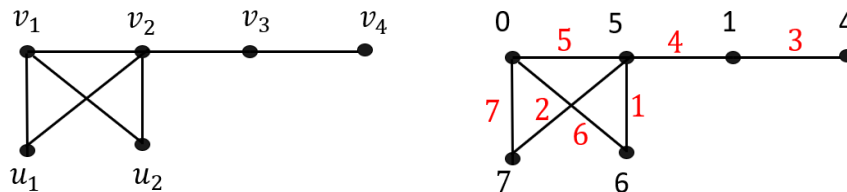


Figure 5.

Conclusion:

Motivated by the recent work of graceful labeling, we introduced the graceful labeling of the bistar graph, the graph obtained by duplication a vertex of a bistar graph $B_{n,n}$ by a new edge and the graph obtained by the ring sum of the path P_n and the complete bipartite graph $K_{2,m}$.

References:

1. Gross JL, Yellen J. Graph theory and Its Applications. Chapman & Hall/CRC Taylor & Francis Group. 2006.
2. Biatch MP, Baggab JS, Arumugam S. AKCE Int. J. Graphs Comb. 2020;2:673–678.
3. Bondy JA, Murty USR. Graph theory with applications. Elsevier Science Publishing Co., Inc. 1979.
4. Boxwala SA, Vashishta P. Electron. Notes Discrete Math. 2015; 48:127-133.
5. Gallian JA. Electron. J. Combin. 2019;1-79.
6. Ghodasara GV, Patel MJ. IJMTT. 2017; 172-177.
7. Golomb SW. Graph Theory and Computing. 1972;23-37.



8. Makadia HM, Karavadiya HM, and Kaneria VJ. *Proyecciones Journal of Mathematics*. 2019;2:305-314.
9. Rosa A. *Theory of Graphs*. 1966.
10. Sethuraman G, Murugan V. *AKCE Int. J. Graphs Comb.* 2020;17:592–605.



RECORDING WATER CONSUMPTION AND DENTAL FLUOROSIS AMONG CHILDREN IN HIGH FLUORIDE AREAS IN NORTHERN PART OF THAILAND BY GEOGRAPHIC INFORMATION TECHNOLOGY

Supoj Chamnanprai, Patcharaporn Kavila, Mansuang Wongsapai, Thawatchai Suthachai, Wisapen Kijtaned

Intercountry Centre for Oral Health

e-mail : supoj.chp@gmail.com

Abstract :

A policy of water provision for the rural population in Thailand has effected in dental fluorosis all over the country. The 14% of the total deep wells dug to serve as new water sources has exceeded fluoride concentration in drinking water. Fluoride excessive intake may result in several adverse health effects. The first sign of fluoride toxicity is dental fluorosis. Some areas in northern part of Thailand, fluoride concentrations in public water sources are higher than 10.0 mg/l. The objective of this study was to record water consumption and dental fluorosis among children who live in high fluoride areas in northern part of Thailand by geographic information technology. This study was carried out in 2021-2022. The subjects (n=537) were all the school children in aged 6–12 years that high fluoride areas in Chiangmai, Lamphun, Lampang and Phayao provinces. Samples of drinking water were collected and their fluoride concentration determined using the standard method. The results showed that 77.7% of the subjects consume bottled water and 13.6% from piped water. Unsafe water was drunk by 27.9% of the subjects. The village waterworks at Muang district, Lamphun province had the highest fluoride concentration of 14.0 mg/l. The prevalence of dental fluorosis (moderate-severe) in the children was 11.3% also in Lamphun province. Fluoride mapping is <https://sites.google.com/view/fluoridemapping/home>. There are many approaches or methods to solve the problem of high fluoride in drinking water, such as reverse osmosis technology, replacement of water sources with new ones and join another water system in other town or region. When piped water was provided by the government, people always considered it to be safe. Piped water is convenient to use clean and clear. However, it must be safe and not contain excessive fluoride concentration. Thailand needs a law to ensure that only safe water can enter the piped water system. In addition, the routine surveillance of water quality is also important.

Introduction :

Naturally occurring high fluoride levels in groundwater is a complicated issue for drinking water providers in many regions of the world¹. Fluorides in small quantities have a practical role in the protection against dental caries. However, its excessive intake may result in several adverse health effects. The first sign of fluoride toxicity is dental fluorosis. The risk of dental fluorosis is mainly related to the systemic consumption of fluorides during the first six years of age². Enamel fluorosis is a mottling of the tooth surface that is attributed to fluoride exposure during tooth formation. The process of enamel maturation consists of an increase in mineralization within the developing tooth and concurrent loss of early-secreted matrix proteins. Exposure to fluoride during maturation causes a dose-related disruption of enamel mineralization resulting in widening gaps in its crystalline structure, excessive retention of enamel proteins, and increased porosity³.



The severity of dental fluorosis is also dependent upon fluoride dose and the timing and duration of fluoride exposure. Besides dental fluorosis, chronic excessive consumption of fluoride may lead to skeletal fluorosis and hip fractures among the elderly⁴.

A well-intentioned policy of water provision for the rural population in Thailand has resulted in bringing a developmental disturbance of dental enamel, dental fluorosis, to over 8,500 communities all over the country. This has involved approximately 14% of the total deep wells dug to serve as new water sources during 1981–1990, a period known as the International Drinking Water Supply and Sanitation Decade.

Dental Fluorosis in Thailand occurs in specific locations scattered from north to south. People who live in these locations have lived with the fluorosis problem for generations. The nature of this problem differs from one locality to another in terms of severity, geographic location, fluoride concentration, socio-economic and culture dimensions. There are several regions in Thailand with fluoride concentration in public water supplies higher than 10.0 mg/l. The objective of this study was to record water consumption and dental fluorosis among children who live in high fluoride areas in northern part of Thailand by geographic information technology.

Methodology :

This study was conducted in 2021-2022. This study used purposive sampling. The subjects (n=537) were all the school children in aged 6–12 years who live in areas with fluoride concentration higher than 0.70 mg/l in Chiangmai, Lamphun, Lampang and Phayao provinces. Samples of drinking water were collected and their fluoride concentration. They were collected and their fluoride concentration determined using the standard method and analyzed the concentration of fluoride with the Ion Selective Electrode (ISE) method and using an ORION model 4 star at laboratory of ICOH.

A total of 537 school children were screened for dental fluorosis. Classification and was carried out by a dentist. The presence and severity of dental fluorosis was recorded using Dean's Index in affected and non-affected area school children. Based on the symptoms, dental fluorosis was classified into 6 categories.

Dean's Index Criteria⁵

Criteria	Definition
0 = Normal	Enamel surface is smooth, glossy and usually a pale creamy white color.
1 = Questionable	The enamel shows slight aberrations in the translucent normal enamel and which may range from a few white flecks to occasional spots
2 = Very Mild	Small, opaque, paper-white areas scattered irregularly over the tooth but involving less than 25% of the labial tooth surface
3 = Mild	White opacities of the enamel involving more than 25% but less than 50% of the tooth surface
4 = Moderate	The enamel surfaces show marked wear, and brown staining is frequently a disfiguring feature
5 = Severe	The enamel surfaces are severely affected and the hypoplasia is so marked that the general form of the tooth may be affected. There are pitted or worn areas and brown stains are widespread; the teeth often have a corroded appearance



Inclusion Criteria :

- Children aged 6-12 years who were born and live in this areas
- Without ever moving in or moving out of the area
- Thai Nationality
- Volunteered to participate in the research

Exclusion Criteria :

- A congenital disability and wearers of prosthetic limbs
- People with neurological problems

Statistical analysis :

All statistical analysis will be performed by using computer program. The data were analyzed statistically; number, percentage, mean, standard deviation.

Results and Discussion :

Table1 Number and percentage of drinking water by province and source of water

Source of water	Province			
	Lamphun	Chiangmai	Lampang	Phayao
bottled water	150(73.9)	142(85.0)	67(74.4)	59(77.6)
pipd water	32(15.8)	16(9.6)	19(21.1)	6(7.9)
vending machine	12(5.9)	9(5.4)	-	-
rain water	6(3.0)	-	-	10(13.2)
shallow well water	-	-	2(2.2)	-
ground water	3(1.5)	-	2(2.2)	1(1.3)
Total	203	167	90	76

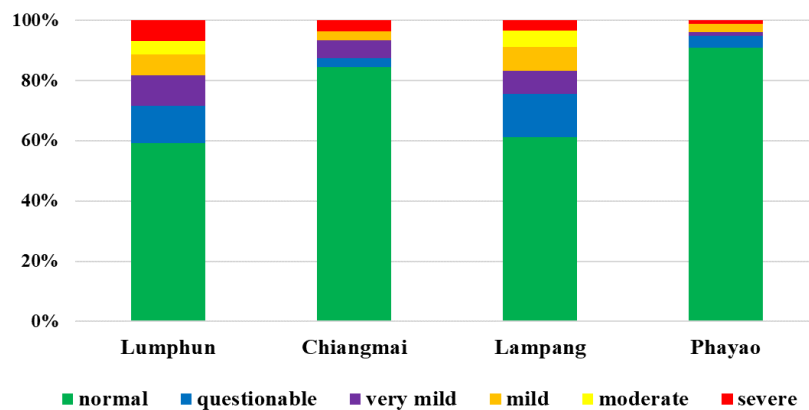
Table2 Number and percentage of drinking water and fluoride concentration(mg/l)

Province	Drinking water		
	F≤0.70 (mg/l)	F>0.70 (mg/l)	min-max (mg/l)
Lumphun	144(75.4)	47(24.6)	0.10-14.0
Chiangmai	104(62.3)	63(37.7)	0.10-6.74
Lampang	54(60.0)	36(40.0)	0.10-10.8
Phayao	76(100)	-	0.10-0.70
Total	378(72.1)	146(27.9)	0.10-14.0

The results showed that 77.7% of the subjects consume bottled water and 13.6% from piped water. Unsafe water was drunk by 27.9% of the subjects. The main sources of public water were from village tap water and waterworks, and fluoride concentration were between 0.10-14.0 mg/l. Lamphun province had the highest fluoride concentration of 14.0 mg/l.

**Table 3** Number and percentage of severity of dental fluorosis by province

province	N	number of normal teeth	questionable	very mild	mild	moderate	severe
Lumphun	204	121(59.3)	25(12.3)	21(10.3)	14(6.9)	9(4.4)	14(6.9)
Chiangmai	167	141(84.4)	5(3.0)	10(6.0)	5(3.0)	-	6(3.6)
Lampang	90	55(61.1)	13(14.4)	7(7.8)	7(7.8)	5(5.6)	3(3.3)
Phayao	76	69(90.8)	3(3.9)	1(1.3)	2(2.6)	-	1(1.3)
Total	537	386(71.9)	46(8.6)	39(7.3)	28(5.2)	14(2.6)	24(4.5)

**Figure1.** Percentage of severity of dental fluorosis by province

The prevalence of dental fluorosis in children was 28.1%. The distribution of these severity in the province of Lamphun, Lampang, Chiangmai, Phayao was 40.7%, 38.9%, 15.6% and 9.2% respectively. When classified by severity, it was found that Lamphun had the most severe level of dental fluorosis at 6.9%. The enamel surfaces are affected and hypoplasia is so marked that the general form of the tooth may be affected. The major diagnostic sign of this classification is discrete or confluent pitting. Brown stains are widespread and teeth often present a corroded-like appearance.

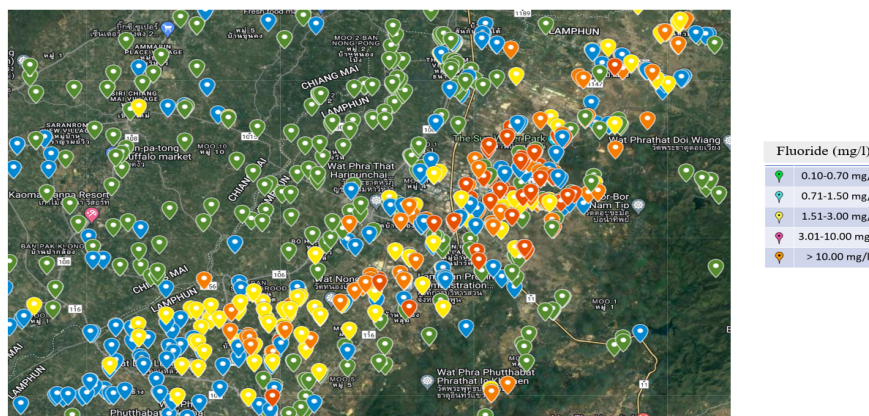


Figure2. Fluoride Mapping (<https://sites.google.com/view/fluoridemapping/home>)

Conclusion :

This study suggests that dental fluorosis is a public health problem. Excessive intake of fluoride during enamel development can lead to enamel fluorosis, a condition of the dental hard tissues in which the enamel covering of the teeth fails to crystallize properly, leading to defects that range from barely discernable markings to brown stains and surface pitting.

The villages water contained fluoride concentration more than standard (fluoride standard in Thailand ≤ 0.70 mg/l) and need to be removed fluoride or else alternative sources of drinking water provided for the community. A sustainable solution to the problem of fluoride contamination in drinking water is to change the drinking water source is as follow ; reverse osmosis technology, replacement of water sources with new ones and join another water system in other town or region.

Although drinking water is the main source of fluoride intake, fluoride intake from foods could also be high, depending on cooking methods. Soaking and boiling foods in fluoride containing water increases fluoride intake. Therefore, it is necessary to re-evaluate the fluoride intake from food and drinking water considering the methods used for cooking food in each country and region⁶.

When piped water was provided by the government, people always considered it to be safe. It is convenient to use, clean, clear, and never causes diarrhea. However, it must be safe and not contain excessive fluoride concentration. Thailand needs a law to ensure that only safe water can enter the piped water system. Adequate information and recommendations help people themselves to make informed decisions and regulate health risks from drinking water. Strategic plans and public awareness campaigns on fluorides in drinking water and health impact should be implemented. In addition, the routine surveillance of water quality is also important.

References :

- 1.Ene Indermitte, Astrid Saava and Enn Karro. Exposure to High Fluoride Drinking Water and Risk of Dental Fluorosis in Estonia. *Int. J. Environ. Res. Public Health* 2009, 6 , 710-721.



2. Toumba KJ, Twetman S, Splieth C, Parnell C, van Loveren C, Lygidakis NA. Guidelines on the use of fluoride for caries prevention in children: an updated EAPD policy document. *Eur Arch Paediatr Dent*. 2019 Dec;20(6):507-516.
3. Nation Research Council of the National Academies.(2006) Fluoride in Drinking Water: A Scientific Review of EPA's Standard.
4. Everett ET. Fluoride's effects on the formation of teeth and bones, and the influence of genetics. *J Dent Res*. 2011 May;90(5):552-60.
5. Petersen, P.E.; Baez, R.J.; World Health Organization. Oral Health Surveys: Basic Methods, 5th ed.; World Health Organization: Geneva, Switzerland, 2013.
6. Benyapa Sawangjang, Satoshi Takizawa, Re-evaluating fluoride intake from food and drinking water: Effect of boiling and fluoride adsorption on food, *Journal of Hazardous Materials*, Volume 443, Part A, 2023.

THE CENTER COLORING OF CORONA PRODUCT OF PATHS

Maripen Thesa,¹ Siwaporn Saewan^{2,*}

¹Students, Department of Mathematics and Statistics, Faculty of Science and Digital Innovation, Thaksin University, Phatthalung, 93210, Thailand

²Assoc. Prof. Dr., Department of Mathematics and Statistics, Faculty of Science and Digital Innovation, Thaksin University, Phatthalung, 93210, Thailand

*e-mail: si_wa_pon@hotmail.com

Abstract:

Let G be the simple connected graph. The center coloring of the graph G is an assignment of colors to each vertex of G , such that different distance vertices from the center are assigned different colors. The center coloring number of the graph G , denote $C_c(G)$, is the minimum number of colors required for the center coloring of G . In this paper we investigate on the center coloring number of the new graph obtained by the corona product operation of the path P_n and the path P_m .

Introduction:

Let G be the graph with a nonempty vertex set $V(G)$ and an edge set $E(G)$. The elements of $V(G)$ are called vertices and the elements of $E(G)$ are called edges. The **endpoints** of an edge is the set of two vertices connects to each edge. The vertices are in the endpoint of each edge are called **incident** with the edge. The vertices which are incident with a common edge are **adjacent**. A **simple graph** G is a graph with each edge in $E(G)$ connects two distinct vertices in $V(G)$. A **path** $v_0 - v_k$ in a graph G is an alternating sequence of vertices and edges

$$v_0 e_1 v_1 e_2 \dots e_k v_k,$$

such that $e_i = v_{i-1} v_i$ and the vertices in a sequence are distinct. The graph G is **connected** if for every pair of a vertex u and a vertex v , there is a path from a vertex u to a vertex v . The **length** of the path in the graph G is the number of edge-steps in the path. The **distance** $d(u, v)$ from a vertex u to a vertex v in the graph G is the length of the shortest $u - v$ path. The **eccentricity** of a vertex v in the graph G , denote by $e(v)$, is the distance from v to a vertex farthest from v . That is

$$e(v) = \max_{u \in V(G)} \{d(u, v)\}.$$

The graph G with the eccentricity of every vertices shown in Figure 1.

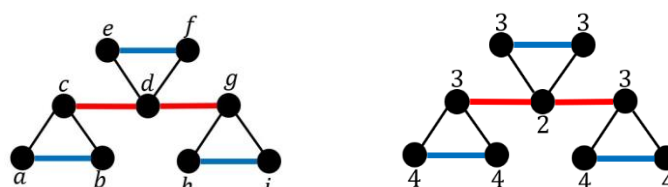


Figure 1.

The **radius** of the graph G , denoted $rad(G)$, is the minimum of the vertex eccentricities. That is

$$rad(G) = \min_{v \in V(G)} \{e(v)\}.$$

A **central vertex** v of the graph G is a vertex with minimum eccentricity. Thus, $e(v) = \text{rad}(G)$. A central vertex of a graph G in Figure 1 is a vertex d , shown in Figure 2.

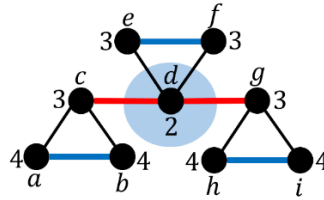


Figure 2.

The **center** of the graph G is the subgraph induced by the set of central vertices of G . The graph is **self-centered** if every vertex is in the center. For more detail, the reader can see in Buckley and Harary¹, Gross and Yellen² and Bondy and Murty³. In 2015 Yorgancioglu et al.⁴ was introduced the **center coloring** of the graph G . The center coloring of the graph G is an assignment of colors to each vertex of G , such that different distance vertices from the center are assigned different colors. The **center coloring number** of a graph G , denote $C_c(G)$, is the minimum number of colors required for the center coloring of G . In 2018 Yorgancioglu et al.⁵ has shown the relation between the center coloring and the other colorings. Yorgancioglu and Dündar⁶ observed the behavior of the center coloring of the graph obtained by some graph operations. The **Corona Product** graph $G \circ H$ is defined as the graph obtained from the graph G and the graph H by taking one copy of G and $|V(G)|$ copies of H and then joining by an edge such that each vertex of the i^{th} vertex of G to every vertex in the i^{th} copy of H . The corona product graph $P_3 \circ P_2$ and $P_2 \circ P_3$ shown in Figure 3.

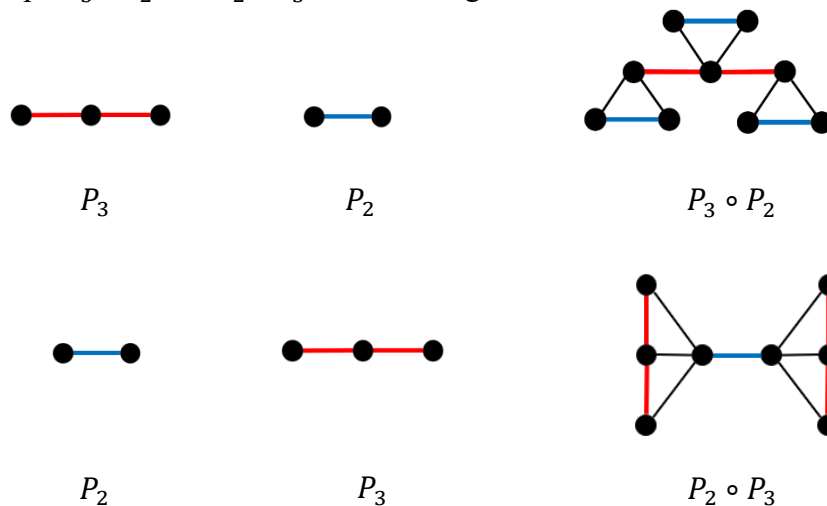


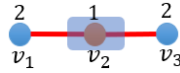
Figure 3.

In this study, we consider the center coloring of the corona product graph $P_n \circ P_m$ and we get center coloring number of the new graph $C_c(P_n \circ P_m)$.

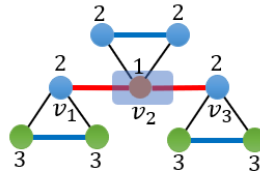
Methodology:

Studying on the center coloring of the new simple connected graph. The new graph $P_n \circ P_m$ obtained by the corona product of the path P_n and n copy of the path P_m . Finding the center

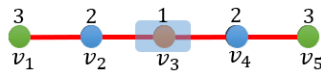
coloring number of the new graph $P_n \circ P_m$. Establishing the new theorem of the center coloring number. Figure 4. shows the center coloring number of P_n and $P_n \circ P_2$ where $n = 3, 5, 7$.



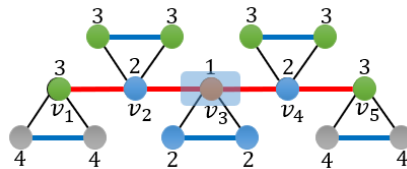
$$C_c(P_3) = 2$$



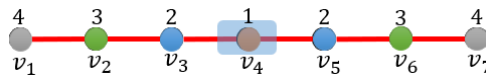
$$C_c(P_3 \circ P_2) = 3$$



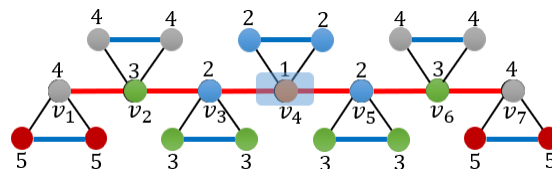
$$C_c(P_5) = 3$$



$$C_c(P_5 \circ P_2) = 4$$



$$C_c(P_7) = 4$$



$$C_c(P_7 \circ P_2) = 5$$

Figure 4.

Figure 5. shows the center coloring number of $P_n \circ P_2$ where $n = 4, 6, 8$.

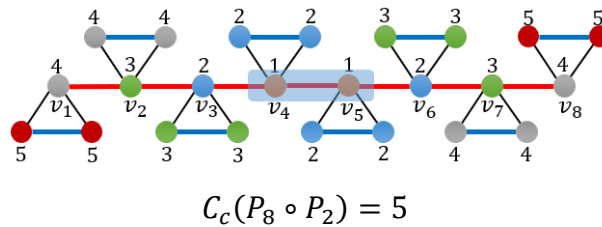
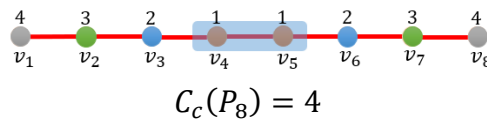
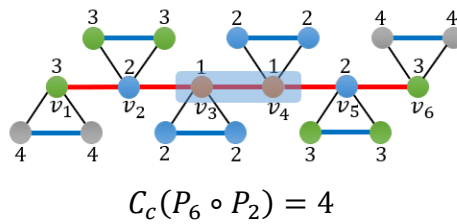
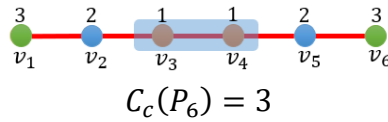
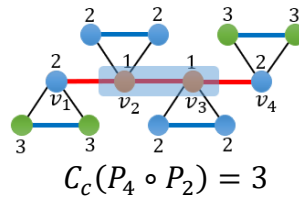
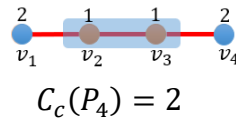


Figure 5.

Figure 6. shows the center coloring number of P_2 and $P_2 \circ P_n$ where $n = 2, 3, 4, 5$.

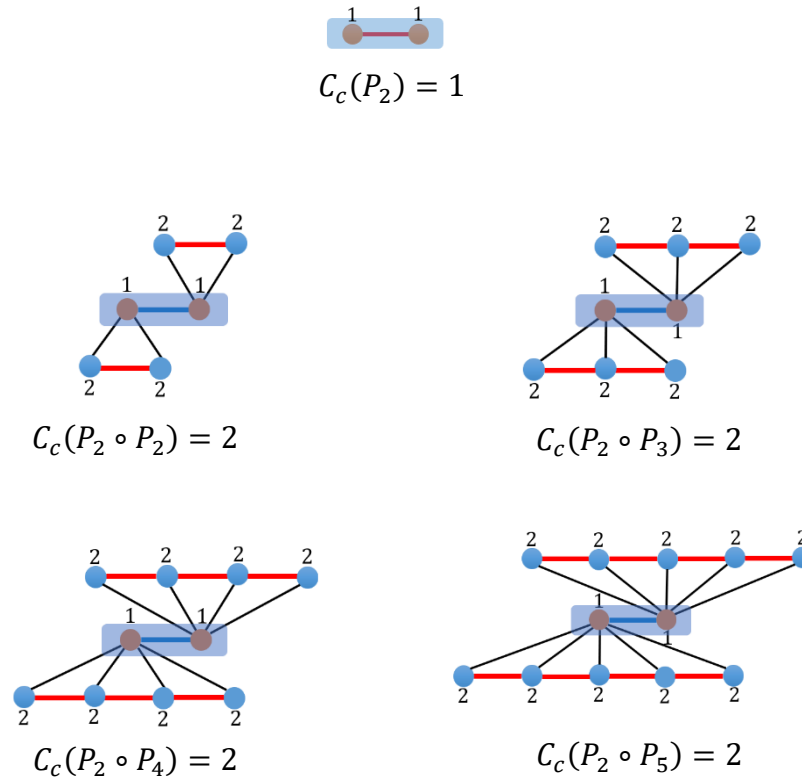


Figure 6.

Results and Discussion:

Theorem Let P_n be the path with n vertices and P_m be the path with m vertices. The center coloring number of the corona product graph $P_n \circ P_m$ is

$$C_c(P_n \circ P_m) = \left\lceil \frac{n}{2} \right\rceil + 1.$$

Proof. Let P_n be the path with n vertices and P_m be the path with m vertices. Let $v_1, v_2, v_3, \dots, v_n$ be the successive vertices of P_n and $u_1^i, u_2^i, u_3^i, \dots, u_m^i$ be the successive vertices of the i^{th} copy of P_m . Let $P_n \circ P_m$ be the corona product graph with $n + mn$ vertices.

If n is odd, then the center of the path P_n is a single vertex $v_{\frac{n+1}{2}}$ and $e(v_{\frac{n+1}{2}}) = \frac{n-1}{2}$.

So

$$d\left(v_{\frac{n+1}{2}}, v_1\right) = d\left(v_{\frac{n+1}{2}}, v_n\right) = \frac{n-1}{2},$$

where v_1 and v_n are vertices in P_n . The distance $d\left(v_{\frac{n+1}{2}}, v_1\right)$ and $d\left(v_{\frac{n+1}{2}}, v_n\right)$ are the maximum distance from the center to any vertices in a path P_n . Hence, $\frac{n-1}{2}$ colors are needed for $n-1$ vertices: $v_1, v_2, v_3, \dots, v_{\frac{n+1}{2}-1}, v_{\frac{n+1}{2}+1}, \dots, v_n$ and one color is needed for central vertex $v_{\frac{n+1}{2}}$.

Then $C_c(P_n) = \frac{n-1}{2} + 1 = \left\lceil \frac{n}{2} \right\rceil$.

Consider the corona product graph $P_n \circ P_m$. We have the center vertex of the corona product graph $P_n \circ P_m$ is a single vertex $v_{\frac{n+1}{2}}$.

So

$$d\left(v_{\frac{n+1}{2}}, v_1\right) = d\left(v_{\frac{n+1}{2}}, v_n\right) = \frac{n-1}{2},$$

where v_1 and v_n are vertices in $P_n \circ P_m$. For the vertices $u_1^1, u_2^1, u_3^1, \dots, u_m^1$ adjacent to v_1 and the vertices $u_1^n, u_2^n, u_3^n, \dots, u_m^n$ are adjacent to v_n . We have

$$d\left(v_{\frac{n+1}{2}}, u_1^1\right) = d\left(v_{\frac{n+1}{2}}, u_2^1\right) = \dots = d\left(v_{\frac{n+1}{2}}, u_m^1\right) = \frac{n-1}{2} + 1 = \left\lceil \frac{n}{2} \right\rceil,$$

and

$$d\left(v_{\frac{n+1}{2}}, u_1^n\right) = d\left(v_{\frac{n+1}{2}}, u_2^n\right) = \dots = d\left(v_{\frac{n+1}{2}}, u_m^n\right) = \frac{n-1}{2} + 1 = \left\lceil \frac{n}{2} \right\rceil.$$

The distance $d\left(v_{\frac{n+1}{2}}, u_j^1\right)$, $j = 1, 2, 3, \dots, m$ and $d\left(v_{\frac{n+1}{2}}, u_j^n\right)$, $j = 1, 2, 3, \dots, m$ are the maximum distance from the center to any vertices in the corona product graph $P_n \circ P_m$. Hence, $\frac{n-1}{2} + 1$ colors are needed for $n + mn - 1$ vertices and one color is needed for central vertex $v_{\frac{n+1}{2}}$. Then

$$C_c(P_n \circ P_2) = \frac{n-1}{2} + 1 + 1 = \left\lceil \frac{n}{2} \right\rceil + 1.$$

If n is even, then the center of the path P_n are two vertices $v_{\frac{n}{2}}$ and $v_{\frac{n}{2}+1}$. Since

$$e(v_{\frac{n}{2}}) = e(v_{\frac{n}{2}+1}) = \frac{n}{2}.$$

So

$$d\left(v_{\frac{n}{2}}, v_1\right) = d\left(v_{\frac{n}{2}+1}, v_n\right) = \frac{n}{2} - 1,$$

where v_1 and v_n are vertices in P_n . The distance $d\left(v_{\frac{n}{2}}, v_1\right)$ and $d\left(v_{\frac{n}{2}+1}, v_n\right)$ are the maximum distance from the center to any vertices in a path P_n . Hence, $\frac{n}{2} - 1$ colors are needed for $n - 2$ vertices: $v_1, v_2, v_3, \dots, v_{\frac{n}{2}-1}, v_{\frac{n}{2}+2}, \dots, v_n$ and one color is needed for the central vertices $v_{\frac{n}{2}}$ and $v_{\frac{n}{2}+1}$. Then $C_c(P_n) = \frac{n}{2} - 1 + 1 = \frac{n}{2} = \left\lceil \frac{n}{2} \right\rceil$.

Consider the corona product graph $P_n \circ P_m$. We have the center of the corona product graph $P_n \circ P_m$ are two vertices $v_{\frac{n}{2}}$ and $v_{\frac{n}{2}+1}$.

So

$$d\left(v_{\frac{n}{2}}, v_1\right) = d\left(v_{\frac{n}{2}+1}, v_n\right) = \frac{n}{2} - 1,$$

where v_1 and v_n are vertices in $P_n \circ P_m$. For the vertices $u_1^1, u_2^1, u_3^1, \dots, u_m^1$ adjacent to v_1 and the vertices $u_1^n, u_2^n, u_3^n, \dots, u_m^n$ are adjacent to v_n . We have

$$d\left(v_{\frac{n}{2}}, u_1^1\right) = d\left(v_{\frac{n}{2}}, u_2^1\right) = \dots = d\left(v_{\frac{n}{2}}, u_m^1\right) = \frac{n}{2} - 1 + 1 = \frac{n}{2},$$

and

$$d\left(v_{\frac{n}{2}+1}, u_1^n\right) = d\left(v_{\frac{n}{2}+1}, u_2^n\right) = \dots = d\left(v_{\frac{n}{2}+1}, u_m^n\right) = \frac{n}{2} - 1 + 1 = \frac{n}{2}.$$

Hence $\frac{n}{2}$ colors are needed for $n + mn - 2$ vertices and one color is needed for the central vertices $v_{\frac{n}{2}}$ and $v_{\frac{n}{2}+1}$. Then



$$C_c(P_n \circ P_m) = \frac{n}{2} + 1 = \left\lceil \frac{n}{2} \right\rceil + 1.$$

Conclusion:

In the paper, we have proved the center coloring number of the graph $P_n \circ P_m$ obtained by the corona product of the path P_n and n copy of the paths P_m .

References:

1. Buckley, F. and Harary, F. Addison-Wesley, California. 1989.
2. Gross, J. L. and Yellen, J. Chapman & Hall/CRC Taylor & Francis Group. 2006.
3. Bondy, J.A. and Murty, U.S.R. Elsevier Science Publishing Co., Inc. 1979.
4. Yorgancioglu, Z., Dundar, P. and Berberler, M. E. Journal of Discrete Mathematical Sciences, 18, 531-540.
5. Yorgancioglu, Z. O., Dündar, P. and Gursoy, M. U. NESciences, 2018; 3(1):28-37.
6. Yorgancioglu, Z.O. and Dündar, P. Open Access Library Journal, 8: e7318.



SESSION E-ENERGY / ENVIRONMENTAL & EARTH SCIENCE / MATERIALS SCIENCE / CHEMICAL TECHNOLOGY

Adsorption of hydrogen sulfide contained in biogas using biomass power plant ash as an adsorbent

Niramol Juntarachat^{1*}, Nattiya Khongkuea¹, Sirilak Chuaypanang², Yakoh Kalemdebh³

¹Innovative Materials Chemistry for Environment Center, Department of Chemistry, Faculty of Science, Thaksin University, Phattalung 93210, Thailand

²Department of environmental science, Faculty of Science, Thaksin University, Phattalung 93210, Thailand

³Department of Teaching Chemistry, Faculty of Education, Fatoni University, Pattani 94160, Thailand

*e-mail: niramol@tsu.ac.th

Abstract:

The removal of H₂S contained in biogas was studied using biomass power plant ash as an adsorbent. Firstly, the physiochemical properties of adsorbents were determined. The moisture content was found to be $3.25 \pm 0.06\%$. The pH value was 9.19 ± 0.72 . The iodine adsorption was 271.25 ± 2.54 mg/g. The BET surface was estimated to be 10.9 m²/g. Secondly, the adsorption efficiency of biomass power plant ash adsorbent for removing H₂S from biogas was investigated at different pallet sizes: 1.00 cm and 1.50 cm of diameter. The experiment was performed in a pack-column at the initial concentration of H₂S of 1000 ppm, 10 g of adsorbent and flowrate of biogas of 500 mL/min. The breakthrough capacity of adsorbent was estimated to be 7.57 mg/g and 6.05 mg/g for 1.00 cm and 1.50 cm of diameter, respectively. Biomass power plant ash could be a good alternative adsorbent for removing H₂S contained in biogas and further treatment of biomass power plant ash could increase its adsorption capacity.

Introduction:

Biogas, one of promising alternative energies, mainly consists of methane (CH₄), carbon dioxide (CO₂) and trace amounts of other gases such as hydrogen sulfide (H₂S), ammonia (NH₃) and carbon monoxide (CO). The presence of elevated concentrations of H₂S in biogas is problematic because of its highly corrosiveness and toxicity as well as its serious environmental concerns. Many processes have been studied and applied in order to remove H₂S from biogas. The adsorption process¹ is a one promising technology owing to its low cost operation and uncomplicated utilization and maintenance. Adsorbent type is an important factor affecting on the efficiency of process. Many works focused on agricultural and industrial wastes or by-products²⁻⁵.

According to the current situation of biomass power plants in Thailand, most biomass power plants use natural rubber woods as feedstocks, which produces a large amount of biomass ash in the process of power generation. Biomass ashes are landfilled so their recycling is important from environmental and economic viewpoints. One innovative and environmentally friendly application for biomass ashes is its use as an alternative adsorbent. Many researches focused on the development of biomass ash for the water pollution treatments such as for removing methylene blue⁶, phosphate⁷, zinc⁸ and Cadmium⁹. Few works in the open literature focused on the application of biomass ash for the biogas cleaning¹⁰. However, no works investigated the removal of hydrogen sulfide from real biogas.

In this work, the adsorption capacity of biomass power plant ash adsorbent was studied in order to remove H₂S from biogas. Firstly, physical and chemical properties of adsorbent were investigated for evaluating its adsorption ability. Secondly, the adsorption

efficiency of adsorbent was studied. Finally, morphological characteristics of adsorbent before and after adsorption were compared for assuring the H_2S adsorption.

Methodology:

1. Materials

Biomass power plant ash used in this study was collected from APK green engineering company, Hat-Yai district, Songkhla province, Thailand. Ash sample was dried at 105°C for 24 hours in an oven. Then it was extruded in a spherical form of 0.5, 1.0 cm and 1.5 cm of diameter using starch paste as a binder. A ratio between ash sample and starch paste was 10:1. Raw biogas used in this work was produced by anaerobic digestion of organic domestic wastes using an anaerobic digestion system. Composition of raw biogas was strictly controlled at 59.4% of CH_4 , 36.5% of CO_2 and 1000 ppm H_2S .

2. Physicochemical properties of adsorbents

The determination of physicochemical properties of ash adsorbent was performed using standard procedures. Moisture content was determined by heating 1 gram of sample at 105°C for 2 hours. pH value was determined by mixing 1 gram of dry biochar powder and 10 ml of deionized water. The suspension was then stirred to reach equilibrium using a magnetic stirrer for 30 min and was then filtered. Finally, the pH value of the solution was measured using a AS218 digital pH meter. The iodine number is the mass of iodine in grams that is consumed by 100 grams of a substance. The iodine number was determined according to the ASTM-D 4607-94 standard procedure.

3. Adsorption experiments

The removal efficiency of ash adsorbents was carried out by packing 10 gram of adsorbent material in an acrylic column (an internal diameter of 2.50 cm and the length of 40.00 cm). Two different pallet sizes of adsorbent were studied (1.00 cm and 1.50 cm of diameter). The configuration consists of a gas inlet, gas inlet sampling, gas outlet and gas outlet sampling. The gas inlet of packed-column was connected to the biogas production system. The experimental setup was presented in Fig. 1.

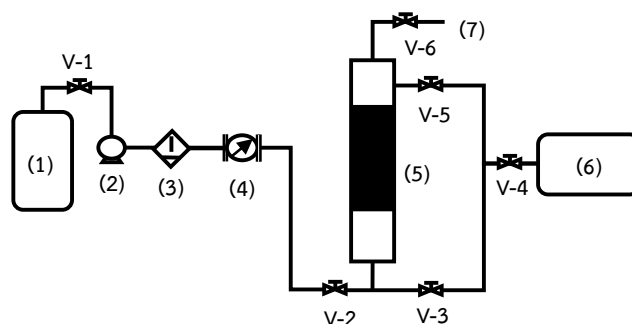


Figure 1 The experimental set-up for hydrogen sulfide removal: (1), biogas; (2), pump; (3), moisture filter; (4), flowmeter; (5), biochar columns; (6), gas chromatography mobile; (7), Biogas outlet; V, valve.

The adsorption process was carried out at room temperature and pressure. The biogas flowrate was kept at 500 mL/min. The biogas composition was analyzed before and after adsorption process using gas chromatography (Gas data FM130) every 5 minutes for 1 hour. The adsorption percentage was calculated using the following equation (1).

$$\text{adsorption percentage (\%)} = \frac{(C_0 - C_t)}{C_0} \times 100 \quad (1)$$

Where C_t is the concentration of adsorbate at time t and C_0 is the initial concentration of the adsorbate. A breakthrough curve was established from C/C_0 and time. A comparison of H_2S breakthrough curve (C/C_0 versus time) at different conditions of adsorption provides information about the optimal adsorption condition. The breakthrough capacity at 5% was calculated using the following equation (2).

$$q_t = \left(1 - \frac{C_t}{C_0}\right) \frac{Q_f t_f y_f}{m_c} \quad (2)$$

Where C_t is the concentration of adsorbate at time t and C_0 is the initial concentration of the adsorbate, t is time, Q_f is flowrate of biogas and m_c is mass of ash adsorbent.

Results and Discussion:

1. Physical and chemical properties of adsorbents

In order to evaluate the adsorption ability of power plant biomass ash, its physical and chemical properties were determined and are listed in Table 1. The moisture content of ash adsorbent found in this work ($3.25 \pm 0.06\%$) was lower than that investigated by Gorbounov et al.¹¹ (9%). The moisture content indicates an affinity between the adsorbent surface and water. An appropriated amount of moisture promotes the ionization of H_2S to produce HS^- on the surface of the adsorbent. But high moisture content can reduce the adsorption efficiency of the adsorbent by forming a water film on its surface.

Iodine number is a fundamental parameter used to characterize the adsorbent performance. Iodine number of biomass ash was observed to be 271.25 ± 2.54 mg/g. According to the investigation of Ekpote et al.¹², the higher the iodine number, the greater is the sorption capacity. For activated carbons, the iodine number value varies in the range of 500.00 – 1200.00 mg/g.

Table 1 Physical and chemical properties of power plant biomass ash studied in this work.

Physical and chemical properties	Ash adsorbent
Moisture content (%)	3.25 ± 0.06
pH	9.19 ± 0.72
BET Surface (m^2/g)	10.9
Iodine number (mg/g)	271.25 ± 2.54

The pH is another important parameter which influences the H_2S adsorption efficiency. The pH value of biomass ash was found to be 9.19 ± 0.72 . According to Shang et al.¹³, the pH values greater than 7.0 make the alkaline surface which is conducive to H_2S adsorption since H_2S is an acidic gas. Therefore, a highly basic adsorbent provides high adsorption capacity.

The BET surface of biomass ash was found to be $10.9 m^2/g$. Generally, adsorbent with high BET surface provide high adsorption efficiency. The relatively low surface areas observed for our sample were probably due to the nature of biomass ash, making it

unconducive for removing H_2S . For increasing the BET surface area of such an adsorbent, the modification of some functional group on the surface could be a promising method.

2. Adsorption capacity

The adsorption capacity of biomass power plant ash adsorbent was studied in order to evaluate its potential to remove H_2S from biogas, at 2 different pellet sizes: 1.00 cm and 1.50 cm of diameter. The biogas composition analysis was carried out using the GM 406 biogas analyzer every 5 min for 2 h. The H_2S breakthrough curves of ash adsorbent with pellet sizes of 1.00 cm and 1.50 cm of diameter are presented in Figure 2.

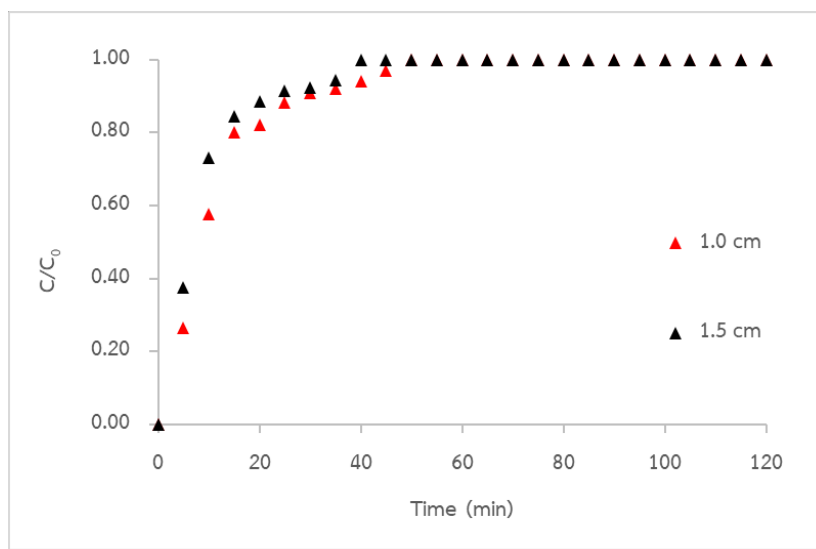


Figure 2 H_2S breakthrough curves for biomass power plant ash adsorbents of different pellet sizes : (Δ) : 1.00 cm of diameter and (\blacktriangle) : 1.50 cm of diameter

Breakthrough curves represent the time profile for saturation of a given amount of adsorbent. The smaller pellet size adsorbent (1.00 cm) showed slowly higher removal efficiency than the larger pellet size adsorbent (1.50 cm). The results found in this work agree well with the investigation of Thanakulpisit et al. who investigated efficiency of soy-bean based ink for removing H_2S from biogas. The breakthrough capacity of 1.00 cm and 1.50 cm of diameter were calculated to be 7.57 mg/g and 6.05 mg/g, respectively. Breakthrough capacity found in this study were slowly lower when compared to the breakthrough capacity of commercial activated carbon (13.76 mg/g) reported in the open literature¹⁵. A decrease in the pellet size leads to an increase in the surface area, therefore, increasing adsorptive site of the adsorbent and providing a greater number of adsorption sites for H_2S .

Conclusion:

In this work, the adsorption capacity of biomass power plant ash adsorbent was studied in order to remove H_2S from biogas. Physical and chemical properties of adsorbents were determined. The biomass ash adsorbent shown moisture content of $3.25 \pm 0.06\%$, pH value of 9.19 ± 0.72 , BET surface of $10.9 \text{ m}^2/\text{g}$ and iodine number of $271.25 \pm 2.54 \text{ mg/g}$. The H_2S adsorption efficiency of biomass ash was investigated at 2 different pellet sizes (1.00 cm and 1.50 cm of diameter). The smaller pellet size shown slightly higher adsorption capacity owing to its larger surface. The breakthrough capacity of ash adsorbents of 1.00 cm and 1.50 cm of diameter were estimated to be 7.57 mg/g and 6.05 mg/g, respectively. This

could assure the ability of biomass power plant ash adsorbent for removing H₂S contained in biogas.

Acknowledgements:

The authors would like to acknowledge the financial supports from national research council of Thailand (NRCT) and Thaksin University.

References:

1. Mitomo A., Sato T., Kobayashi N., Hatano S., Itaya Y., Mori S.. J. Chem. Eng. Jpn., 2003, 36, 1050–1056.
2. Ros A., Lillo-Ródenas M.A., Fuente E., Montes-Morán M.A., Martín M.J., Linares-Solano A. Chemosphere, 2006, 65, 132–140.
3. Gil-Lalaguna N., Sánchez J.L., Murillo M.B., Gea G. Fuel, 2015, 141, 99 -108.
4. MohamadNor N., Chung L.L., Teong L.K., Mohamed A.R. J. Environ. Chem. Eng., 2013, 1, 658-666.
5. Xu G., Yang X., Spinoso L. J. Environ. Manag., 2015, 151, 221-232.
6. Capela MN, Cesconeto FR, Pinto PC, Tarelho LAC, Seabra MP, Labrincha JA. Appl. Sci. 2022; 12:5134.
7. Park J-H, Hwang S-W, Lee S-L, Lee J-H, Seo D-C. Appl. Biol. Chem. 2021; 64:43.
8. Xu L, Xing X, Peng J. Int. J. Environ. Res. Public Health. 2022; 19: 9006.
9. Xu L, Zheng X, Cui H, Zhu Z, Liang J, Zhou J. Bioinorganic Chemistry and Applications. 2017; 9
10. Zhu HL, Papurello D, Gandiglio M, Lanzini A, Akpınar I, Shearing PR, Manos G, Brett DJL, Zhang YS. Processes. 2020; 8:1030.
11. Gorbounov M, Petrovic B, Ozmen S, Clough P, Soltani SM. Chemical Engineering Research and Design 194; 2023: 325–343.
12. Ekpote OA, Horsfall MJr, Tarawou T. Int. J. Biol. Chem. Sci. 2011; 5(3):1143 – 1152.
13. Shang G, Li Q, Liu L, Chen P, Huang, Journal of the Air & Waste Management Association. 2016; 66: 8–16.
14. Thanakunpaisit N, Jantarachat N, Onthong U, Energy Procedia, 2019: 38: 1134–1139.
15. Sitthikhankaew R, Predapitakkun S, Kiattikomol R, Pumhiran S. Assabumrungrat S, Laosiripojana N. 2011 IEEE First Conference on Clean Energy and Technology CET, pp 135 – 139.



ADSORPTION STUDY OF AMOXYCILLIN BY SURFACE MODIFICATION OF GRANULAR ACTIVATED CARBON

Chayanin Hanwarinroj,¹ Attajaree Smata,¹ Areerat Kanarat,¹ Eknarin Thanayupong,¹ Sineenat Thaiboonrod,¹ Peerakarn Banjerdkiij,² Saowaluk Chaleawlert-umpon,^{1,*} and Nuttaporn Pimpha^{1,*}

¹National Nanotechnology Center, National Science and Technology Development Agency, Thailand Science Park, Pathum Thani 12120, Thailand

²Department of Environmental Engineering, Faculty of Engineering, Kasetsart University, Bangkok 10900, Thailand

*e-mail: saowaluk@nanotec.or.th and nuttaporn@nanotec.or.th

Abstract:

Antibiotic pollution in water is an urgent environmental issue, particularly antimicrobial resistance concerning. One of the important sources of antibiotic contamination is hospital wastewater. Amoxycillin (AMX) is one of the most detected in effluent treatment plants due to a typically consumed antibiotic in medical treatments. Among treatment technologies, adsorption is considered a simple operation, relatively inexpensive cost, and highly efficient process. In this study, we were concerned about ecologically scalable and real practical uses so a simple modification of granular activated carbon with NaOH was proposed. The NaOH-modified GAC (GAC-N) presented a change in surface porosity and increasing small micropore structure. A more negatively charged surface of GAC-N over a wider pH range as compared to GAC was observed resulting from the addition of carbonyl and hydroxyl groups on the aromatic skeleton. The AMX adsorption capacity was investigated by batch experiments indicating a match well with the Langmuir isotherm and the pseudo-second-order kinetic model. The maximum AMX adsorption capacity of GAC-N was 121 mg g⁻¹. Several mechanisms including hydrogen bonding, π - π interaction, and electrostatic interaction involved in AMX adsorption on GAC-N. This work provided a simple and practical process for an improvement of AMX adsorption capacity by surface functionalization of GAC.

Introduction:

Antibiotics are one of the most important medicines used for the treatment and prevention of bacterial infections. A large amount of antibiotics is consumed in hospitals and their residues may be released into the environment through incomplete wastewater systems, leading to the development of antibiotic-resistant bacteria. Amoxicillin (AMX) is a broad-spectrum β -lactam antibiotic that belongs to the penicillin class. It is also commonly used for human prescription drugs against bacterial infections.¹ Some studies have reported antibiotic removal efficiencies in different hospital wastewater treatment processes in Thailand. AMX was one of the most detected effluents of hospital treatment plants.²⁻³ To date, numerous wastewater treatment technologies have been explored such as biodegradation, catalytic oxidation, membrane separation, and so on. Among them, adsorption is considered a simple operation, relatively inexpensive cost, and highly efficient process. To enhance the removal efficiency, most adsorbents basically should have a high surface area and a suitable pore size. Generally, carbon-based adsorbents are the most preferred choice due to their cost-effective material and easy modification with abundant functional groups.⁴⁻⁷ Concerning ecologically scalable and real practical uses in wastewater treatment plants, we aimed to study a simple surface modification way of granular activated carbon (GAC) with NaOH for AMX



adsorption enhancement. Batch experiments were carried out to investigate AMX adsorption performance in terms of adsorption kinetics and adsorption isotherms. Finally, the plausible mechanisms were proposed based on experiment adsorption information.

Methodology:

Chemicals

Coconut shell granular activated carbon (GAC) was obtained from Carbokarn Co., Ltd. Sodium hydroxide (NaOH) and amoxycillin (AMX) were purchased from Aldrich.

NaOH-modified GAC (GAC-N) preparation

5 g of unmodified GAC was stirred in a solution of 0.1 M NaOH for 24 hours at room temperature then it was incubated at 150°C for 3 h in a hot air oven. GAC-N was washed with deionized water until neutral pH and dried at 60°C for 18 h.

Characterization

The surface morphology of GAC-N was investigated by scanning electron microscope coupled with an energy dispersive X-ray spectroscopy (SEM-EDX, SU8230, Hitachi). The specific surface area was determined by nitrogen adsorption/desorption using a surface analyzer (3-Flex 3500, Micrometric) applying the Brunauer-Emmett-Teller (BET) method. The chemical surface was analyzed by Fourier transform infrared spectroscopy (FTIR, Nicolet iS50 FT-IR, Thermo Scientific) using KBr method. The zeta potential of GAC-N was determined using a nanoparticle analyzer (Zetasizer ultra, Malvern) at different pH aqueous mediums from 3 to 12. The elemental compositions of GAC-N were measured using an elemental analyzer (628 series, Leco).

Adsorption procedure

Batch adsorption experiments were conducted with 0.5 g of adsorbents (GAC and GAC-N) in 100 mL of AMX solution (a concentration range of 1,000 ng L⁻¹ to 350 mg L⁻¹) at room temperature under stirring at 300 rpm in darkness. 1.5 mL samples were withdrawn from the experimental AMX solution at various adsorption time intervals from 5 to 2,880 min and filtered through a 0.22 µm nylon filter. The concentrations of AMX in the solution were determined by liquid chromatography tandem mass spectrometer (LC-MS/MS, 1290 infinity/6495 Triple quad, Agilent). The adsorption capacity (q_t , mg g⁻¹) was calculated by eq (1):

$$q_t = \frac{(C_0 - C_t)V}{m} \quad (1)$$

where C_0 is the initial concentration (mg L⁻¹) of AMX in solution, C_t is the residual concentration of AMX at time (mg L⁻¹) of antibiotic in solution, V is the volume of AMX solution (L), and m is the mass of adsorbent (g).

Results and Discussion:

Characteristics of GAC-N

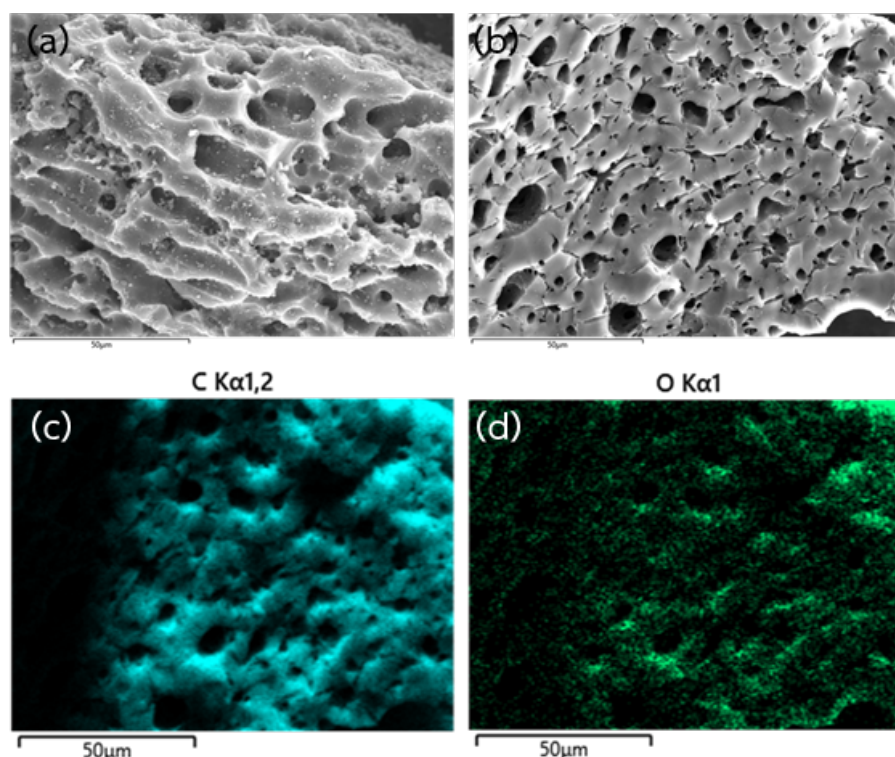


Figure 1. SEM images of (a) GAC and (b) GAC-N and the EDX mapping images of GAC-N with (c) C and (d) O elements.

SEM images (Figure 1a-b) present the surface morphology of GAC and GAC-N, respectively. Both surfaces were similar, containing a macroscopic roughness with an irregular porous structure. The EDX mapping results of GAC-N (Figure 1c-d) show that carbon and oxygen elements existed on the surface of GAC-N. The elemental analysis was used to determine the composition of GAC and GAC-N. The results (Table 1) showed that GAC-N had a higher O element containing than that of GAC.

Table 1. Chemical and textural parameters of GAC and GAC-N.

Sample	Element (%)				S_{BET} ($m^2 g^{-1}$)	V_t ($cm^3 g^{-1}$)	pH_{PZC}
	C	H	N	O			
GAC	73.9	0.1	0.7	25.4	1,146	0.469	4.3
GAC-N	68.7	0.1	0.8	30.4	1,112	0.425	<3

Figure 2a presents the nitrogen adsorption/desorption isotherms of all adsorbents indicating micropore dominant structural features. The BET surface area (S_{BET}) and total pore volume (V_t) of GAC-N were $1,112 m^2 g^{-1}$ and $0.457 cm^3 g^{-1}$, respectively which were almost not different as compared to GAC ($1,146 m^2 g^{-1}$ and $0.439 cm^3 g^{-1}$). It was suggested that the surface porous structure had no significant difference after surface modification of GAC with NaOH. However, in pore size distribution detail, the small micropore range ($<0.6 nm$) of GAC-N was higher than that of GAC. FTIR spectroscopy is presented in Figure 2c to provide some valuable information about the chemical characterization of adsorbents. A change of surface functional groups of GAC-N as compared to GAC was observed: the higher intensity and broader band in a range of $3700-3100 cm^{-1}$ (OH groups), the increased intensity of the peak at $1700 cm^{-1}$ (C=O groups), the shift of the peak at $1500 cm^{-1}$ to $1547 cm^{-1}$ (C=C

aromatic structure), and the additional peak at 1350 cm^{-1} and the broader peak at 1100 cm^{-1} (C-O groups). The FTIR results indicated that the oxygen-containing functional groups such as carboxyl and hydroxyl groups were successfully functionalized on the surface of GAC. Figure 3d presents the zeta potential of adsorbents within the solution pH range 3-12, indicating the adsorbent surface charge behavior. The point of zero charge (pH_{PZC}) is defined as the pH at which the net charge of the surface adsorbent is zero. As shown in Figure 3d and Table 1, the pH_{PZC} value of GAC-N ($\text{pH}_{\text{PZC}} < 3$) was lower than that of GAC ($\text{pH}_{\text{PZC}} 4.2$). It suggested the predominant negatively charged surface of GAC-N due to the significant introducing of carboxyl groups after the surface modification process.

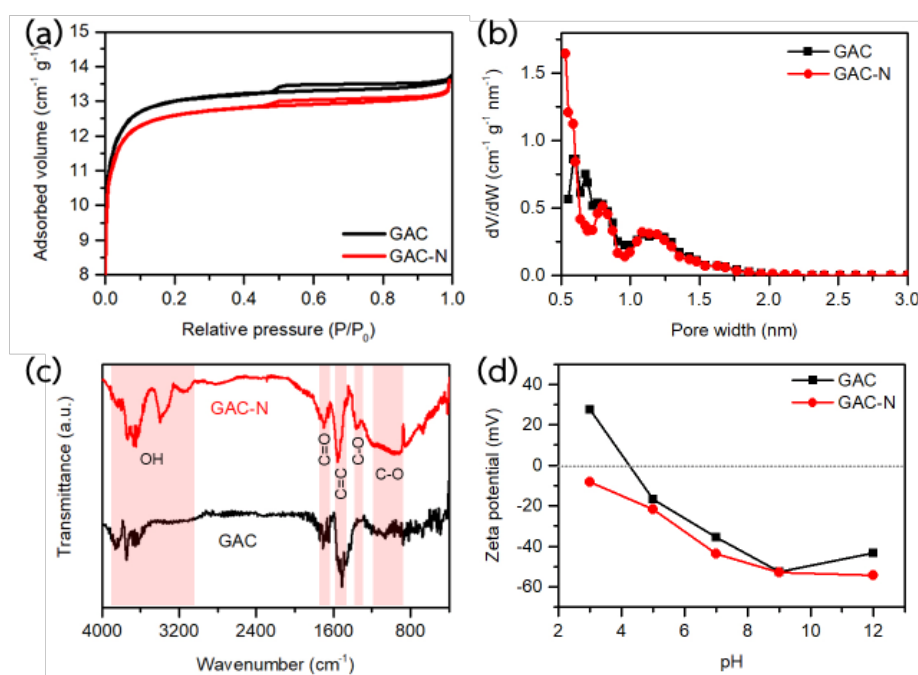


Figure 2. (a) Nitrogen adsorption/desorption isotherms, (b) pore size distribution, (c) FTIR spectra, and (d) zeta potential at different pH solutions of GAC and GAC-N.

Adsorption isotherms

The adsorption isotherms are investigated to describe the interaction between the adsorbate molecules with the surface adsorption sites of the adsorbent. Figure 3a presents the AMX adsorption profile of GAC and GAC-N. It revealed that AMX was quickly adsorbed within 5-60 min by both adsorbents and then slowly adsorbed until reaching equilibrium. However, GAC-N had a higher AMX adsorption capacity as compared to GAC. The effect of initial concentrations of AMX on the adsorption capacity was studied as shown in Figure 3b. When the initial concentration of AMX increased, a higher AMX adsorption capacity increased. The result adsorption data were fitted using the Langmuir and the Freundlich isotherm models,⁴ presenting the fit curves in Figure 3c and the calculated values in Table 2. Both adsorbents were better fit with the Langmuir model (R^2 0.980-1) than those of the Freundlich model (R^2 0.873-0.885). The better fit of the Langmuir model indicated that the AMX adsorption on the GAC and GAC-N was predominantly a controlled monolayer adsorption process. The K_L value of GAC-N was less than 1 (0.2) implying the favorable affinity of AMX on GAC-N whereas GAC had K_L 2.9 indicating the adsorption of AMX was unfavorable under the conditions used. Furthermore, the calculated maximum adsorption

capacity (q_m) by the Langmuir model was good consistent with those values from experiments. The experimental results revealed that GAC-N had a higher maximum adsorption capacity (121 mg g^{-1}) than that of GAC (110.7 mg g^{-1}).

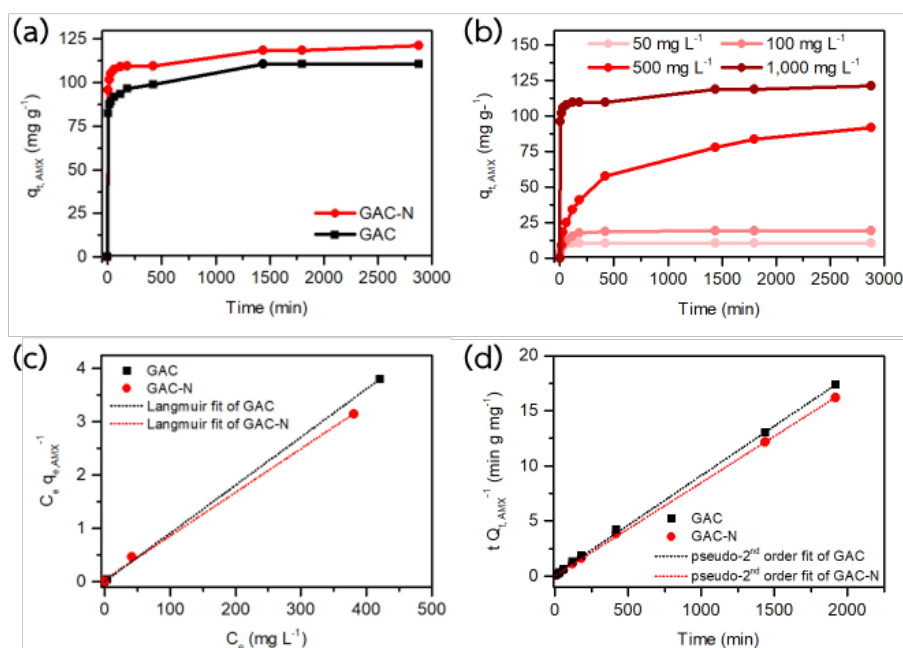


Figure 3. (a) Adsorption profiles of GAC and GAC-N at $1,000 \text{ mg L}^{-1}$ AMX and (b) adsorption capacity of GAC-N as a function of time at different initial concentrations of AMX. The AMX adsorption fit models: (c) the Langmuir adsorption isotherm and (d) the pseudo-second order kinetic fit curves (condition: AMX concentration $1,000 \text{ mg L}^{-1}$, adsorbent dosage 5 g L^{-1} , pH 6.2).

Table 2. Isotherm parameters for AMX adsorption on GAC and GAC-N.

Sample	$q_{t,exp}$ mg g^{-1}	Isotherm model					
		Langmuir			Freundlich		
		q_m mg g^{-1}	K_L L mg^{-1}	R^2	n	K_F L mg^{-1}	R^2
GAC	110.7	111.1	2.9	1	4.7	40.4	0.873
GAC-N	121.0	122.0	0.2	0.980	4.4	33.2	0.885

Adsorption kinetics

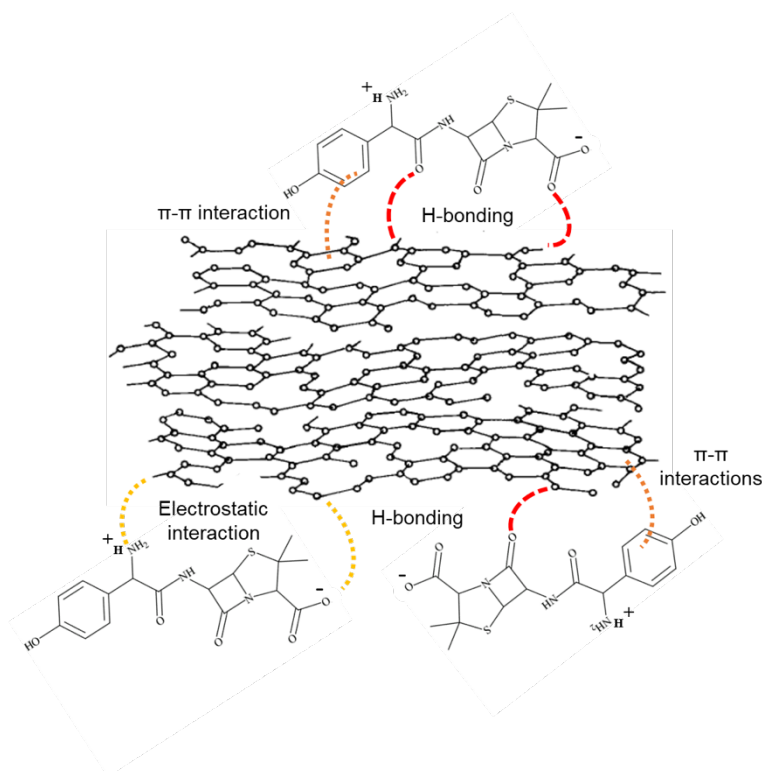
Kinetic studies are an important factor in the order of the rate constant. The adsorption data were analyzed by the pseudo-first order and the pseudo-second order model.⁴ The linearized form adsorption kinetic models were fit (only the pseudo-second order model fit curves are shown in Figure 3d) and the fitting parameters are listed in Table 3. The pseudo-second order model was better suitable to describe the experimental data of both adsorbents due to the highest correlation coefficient R^2 (0.999). It indicated that AMX adsorption rate was controlled by the chemisorption process. The rate constant (K_2) value of GAC-N was higher than GAC implying that AMX was adsorbed by GAC-N faster than GAC.

Table 3. Kinetic parameters for AMX adsorption on GAC and GAC-N.

Sample	Kinetic model					
	Pseudo-first order			Pseudo-second order		
	$q_{e,cal}$ $mg\ g^{-1}$	K_1 $1\ min^{-1}$	R^2	$q_{e,cal}$ $mg\ g^{-1}$	K_2 $g\ mg^{-1}\ min^{-1}$	R^2
GAC	1.7	0.0070	0.510	27.7	0.0584	0.999
GAC-N	7.0	0.0039	0.929	46.3	0.0798	0.999

Adsorption mechanisms

AMX is normally sensitive to aqueous pH owing to its functional groups containing carboxyl ($pK_{a1} = 2.4$), amine ($pK_{a2} = 7.4$), and phenol ($pK_{a3} = 9.6$).⁸⁻⁹ Our adsorption condition was almost neutral pH 6.2) based on the wastewater information of Pranangklaao hospital, Thailand. At pH 6.2, the zwitterion of AMX will be presented (AMX^{\pm}) with $-COO^-/-NH_3^+/-OH$ functional groups. Based on the experimental results on the isotherm and kinetic adsorptions, it was possible to propose involved mechanisms of AMX adsorption on GAC-N: hydrogen bonding, π - π interactions, and electrostatic interactions^{5,8} as shown in Figure 4. However, the electrostatic interactions might not be the dominant interaction between AMX and GAC-N due to presenting the zwitterion form of AMX in aqueous solution at pH 6. The main adsorption mechanisms could be hydrogen bonding and π - π interactions which were promoted by the enhanced surface functional groups on the GAC-N.

**Figure 4.** The possible adsorption mechanisms of AMX by GAC-N.



Conclusion:

The NaOH modified GAC (GAC-N) was successfully enhanced functionalization with carboxyl and hydroxyl groups on the surface. So, the negatively charged surface of GAC-N was demonstrated in the aqueous solution ($\text{pH}_{\text{PZC}} < 3$). Even though the specific surface area of GAC-N was not significantly changed as compared to GAC, increasing small micropores were observed. The AMX adsorption studies indicated that the kinetic data were well consistent with the pseudo-second-order model. The equilibrium data agreed well with the Langmuir isotherm. The adsorption process of the AMX was promoted by chemisorption such as hydrogen bonding, π - π interactions, and electrostatic attractions with surface functional groups of GAC-N. Therefore, AMX adsorption capacity of GAC-N was significantly enhanced mainly resulting from surface functionalization.

Acknowledgements:

This work was funded by National Research Council of Thailand (NRCT, grant number N25A660471, 2023) and National Nanotechnology Center (Project number P2351315), National Science and Technology Development Agency (NSTDA), Thailand.

References:

1. Homem V, Alves A, Santos L. *Int. J Environ Anal Chem.* 2010;90:1063-1084.
2. Chiemchaisri W, Chiemchaisri C, Hamjinda NS, Jeensalute C, Buranapakdee P, Thamlikitkul V. *Emerg Contam.* 2022;8:329-339.
3. Sinthuchai D, Boontanon SK, Piyaviriyakul P, Boontanon N, Jindal R, Polprasert C. *J Water, Sanit Hyg Dev.* 2021;11(6):959-971.
4. Yu J, Kang Y, Yin W, Fan J, Guo Z. *ACS Omega.* 2020;5(30):19187-19193.
5. Shi P, Chen C, Lu X, Wang P, Mi S, Lu J, Tong Z. *Ind Crops Prod.* 2023;203:117122.
6. Wang B, Xu X, Tang H, Mao Y, Chen H, Ji F. *Appl Surf Sci.* 2020;528:147048.
7. Mangla D, Sharma A, Ikram S. *J Hazard Mater.* 2022;425:127946.
8. Liu L, Cui W, Lu C, Zain A, Zhang W, Shen G, Qian X. *J Environ Manag.* 2020;268:110630.
9. Pezoti O, Cazetta AL, Bedin KC, Souza LS, Martins AC, Silva TL, Almeida VC. *Chem Eng J.* 2016;288:778-788.



CaCu₃Ti₄O₁₂ CERAMIC: HIGH DIELECTRIC PERMITTIVITY AND EXTRINSIC AND INTRINSIC ORIGINS

Prachit Khongrattana,¹ Atittaya Changchuea,² Pawin Sangthong,² Pariwat Dumnui,²

Natwara Tansungnern,² Jakkree Boonlakhorn³, *

¹Department of Teaching Science and Mathematics, Faculty of Education, Thaksin University, Songkhla Campus, Songkhla 90000, Thailand

²Bachelor of Education Program in Physics, Faculty of Education, Thaksin University, Songkhla Campus, Songkhla 90000, Thailand

³Department of Basic Science and Mathematics, Faculty of Science and Digital Innovation, Thaksin University, Songkhla Campus, Songkhla 90000, Thailand

*e-mail: jakkree.b@tsu.ac.th

Abstract:

The CCTO perovskite ceramic belongs to the class of colossal dielectric materials. It is worth noting that despite its remarkable dielectric properties, no ferroelectric behavior has been observed in this material. In this particular study, it has been observed that the CCTO ceramic, which has been prepared utilizing a solid-state reaction method, demonstrates a remarkably high dielectric permittivity of approximately 5.70×10^4 , accompanied by a loss tangent of approximately 0.187. The result of the impedance spectroscopy analysis reveals the presence of a heterogeneous microstructure characterized by the coexistence of *n*-type semiconducting grains and insulating grain boundaries. The conduction activation energies relating to both the grain and grain boundary have been successfully ascertained, yielding values of 0.086 and 0.552 eV, respectively. The impedance spectroscopy and conduction activation energies provide valuable insights into the main origin of the high dielectric permittivity observed in CCTO, which can be attributed to the internal barrier layer capacitor model. The determination of the relaxation activation energy provides evidence for the presence of an oxygen vacancy (V_O) within the grain, specifically of the bivalent type. Henceforth, it can be postulated that the formation of the semiconductive state within the grain of CCTO may be attributed to the charge compensation mechanism.

Introduction:

The compound known as CaCu₃Ti₄O₁₂ (CCTO) is a highly intriguing ternary oxide material that is notably devoid of ferroelectric properties¹. The unit cell of CCTO exhibits a doubled simple perovskite structure and is conventionally denoted as body-centered cubic of the *Im3* space group¹. The CCTO has garnered significant attention in the scientific community owing to its remarkably high dielectric permittivity value ($\epsilon' < 10^3$)¹⁻⁸. To date, a substantial amount of scholarly attention has been devoted to the investigation and clarification of the basic variables that give rise to the distinctive dielectric properties displayed by CCTO. The attribution of dielectric behavior in typical ceramics, such as CCTO, to extrinsic factors is widely acknowledged in scientific debate⁹. Of all the hypotheses posited, it is the internal barrier layer capacitor (IBLC) that stands out as the most prominent^{6, 10-11}. The widely recognized concept posits that during the sintering process, there occurs the formation of an insulating layer that covers the semiconducting grains. According to the IBLC model, this microstructure induces electrical charge trapping at grain boundaries. Hence, the number of boundary barrier layers might potentially account for the substantial ϵ' reported in CCTO¹². The induction of a giant dielectric behavior in CCTO can



be attributed to the influence of an IBLC, specifically through the phenomenon known as Maxwell-Wagner polarization ⁹.

Based on prior research, it has been observed that in certain instances, the utilization of an IBLC model proves inadequate in providing a comprehensive elucidation of a dielectric phenomenon occurring in CCTO ¹³. The dielectric behavior exhibited by CCTO is found to vary significantly under different testing temperatures and DC bias. The significance of specific variables, namely total capacitance, total resistance, and others, undergoes alteration in response to temperature variations. According to Wu's findings, the application of a DC bias to a CCTO sample during dielectric testing results in a reduction of the potential barrier height at the grain boundaries. This reduction subsequently leads to a change in the grain boundary capacitance (C_{gb}) of the CCTO material ¹⁴. Furthermore, the influence of electrode polarization resulting from the contact between the sample and electrode is more pronounced compared to an IBLC effect while conducting experiments at high temperatures ¹⁵⁻¹⁶. In addition to referencing antecedent research, it is worth noting that the dielectric behavior of CCTO can be altered through the process of sintering or annealing under varying atmospheric conditions ¹⁷⁻¹⁸. It has been observed in prior studies that the underlying cause of the high ϵ' exhibited by CCTO ceramic is dependent upon the specificities of the preparation process and the conditions under which the testing is conducted. Therefore, from an academic standpoint, the investigation of factors affecting the dielectric behavior of this ceramic is of great interest. Thus, the purpose of this research is to investigate all environmental influences on the dielectric properties of CCTO polycrystalline ceramic.

In this study, CCTO ceramic was produced via solid-state reaction (SSR). Temperature and frequency are the environmental testing controls. In the test, various electrical parameters, including grain resistance (R_g), grain boundary resistance (R_{gb}), and C_{gb} , were thoroughly considered across different testing conditions. In addition, intrinsic factors such as the presence of V_O and the mechanism of charge compensation are also examined. Methodology, results, and discussion are described in the following sections.

Methodology:

Ceramic preparation

The present study employed an SSR technique for the synthesis of CCTO ceramic. The materials employed in the preparation procedure consisted of CaCO_3 with a purity of 99.0%, CuO with a purity of 99.0%, and TiO_2 with a purity of 99.9%. The specifics of powder preparation are provided elsewhere¹⁹. The CCTO powder was compacted into a pellet measuring 9.5 mm in diameter and 2 mm in thickness. The CCTO pellet was sintered at 1090 °C for 3 h.

Characterizations

Using X-ray diffractometry (XRD, PANalytical, EMPYREAN) coupled with HighScore Plus Software Version 3.0e, the crystal structure and phase structures of the sintered CCTO sample were determined. The XRD pattern was collected using a 0.01°-step increase over the 2θ range of 20° – 80°. Rietveld refinement was utilized to analyze the XRD data. To analyze the morphology of our manufactured ceramics, a desktop scanning electron microscope (MiniSEM, SNE-4500M) was utilized.

Dielectric and electrical tests

The electrical and dielectric characteristics of sintered CCTO ceramic were evaluated utilizing a Keysight model E4990A instrument, operating at an oscillation voltage (V_{rms}) of 0.5 V. The study was centered around the analysis of dielectric properties within specific frequency and temperature ranges, specifically 40 to 10^7 Hz and -60 to 210 °C, respectively.

Results and Discussion:

Phase formation, crystal structure, and microstructure

The Rietveld profile fit acquired from sintered CCTO, as depicted in **Figure 1(a)**, demonstrates a prevailing phase that corresponds to CCTO. This phase has been indexed in the JCPDS No. 75-2188. The XRD analysis conducted in this study reveals the presence of a body-centered cubic (*bcc*) crystal structure belonging to the *Im3* space group. There is an absence of impurity phases observed in the XRD pattern. The Rietveld refinement technique can be utilized to determine the lattice parameter (*a*). The value of the parameter *a* for CCTO is measured to be 7.393 Å. The XRD results obtained in this study demonstrate a notable similarity to the findings reported in previous research on CCTO¹⁻³.

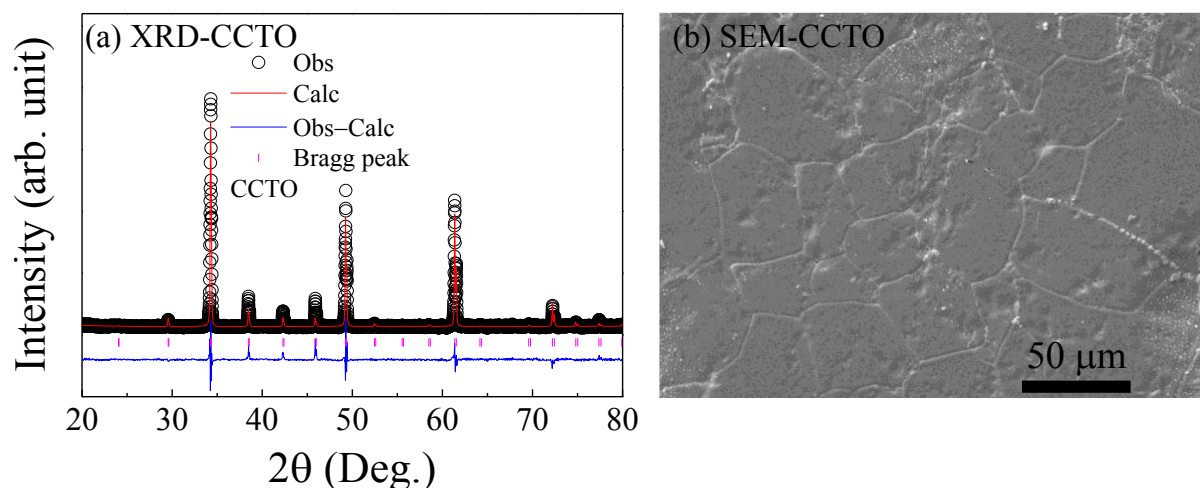


Figure 1.

(a) Rietveld profile fit of sintered CCTO ceramic (b) Surface microstructure.

The microstructural data of ceramic samples was obtained and analyzed using SEM and ImageJ software. The accomplishment of a dense ceramic structure of CCTO is demonstrated in **Figure 1(b)**. The size distribution of the CCTO sample, as determined from the analysis of the SEM image, covers a range of 16.89 to 74.34 μm . The calculated average grain size is $39.56 \pm 12.84 \mu\text{m}$.

Dielectric and electrical properties

A systematic evaluation was conducted to assess the dielectric property of the CCTO sample. The frequency dependencies of ϵ' and $\tan\delta$ values at a temperature of 20 °C are depicted in **Figure 2(a)**. The graph illustrates the remarkable stability of the ϵ' value within the frequency range of 10^2 to 10^5 Hz. Evidently, an enormous dielectric response can be discovered. Within this frequency range, it is worth noting that the grain boundary response and DC conduction exhibit a notably higher level of prominence compared to other mechanisms²⁰⁻²¹. At a temperature of 20 °C, the behavior of grain boundaries becomes more prominent. The ϵ' value of the CCTO sample quickly dropped at frequencies larger than 10^5 Hz, correlating to a significant rise in loss tangent ($\tan\delta$) at the same frequency. This

dielectric behavior is induced by V_O , which produces dielectric relaxation inside the grains²². The ϵ' and $\tan\delta$ values of the CCTO sample at a frequency of 1 kHz are measured to be 5.70×10^4 and 0.187, respectively. The ϵ' value obtained in this investigation exhibits comparability to the values published in prior literature^{1-3, 6, 11}.

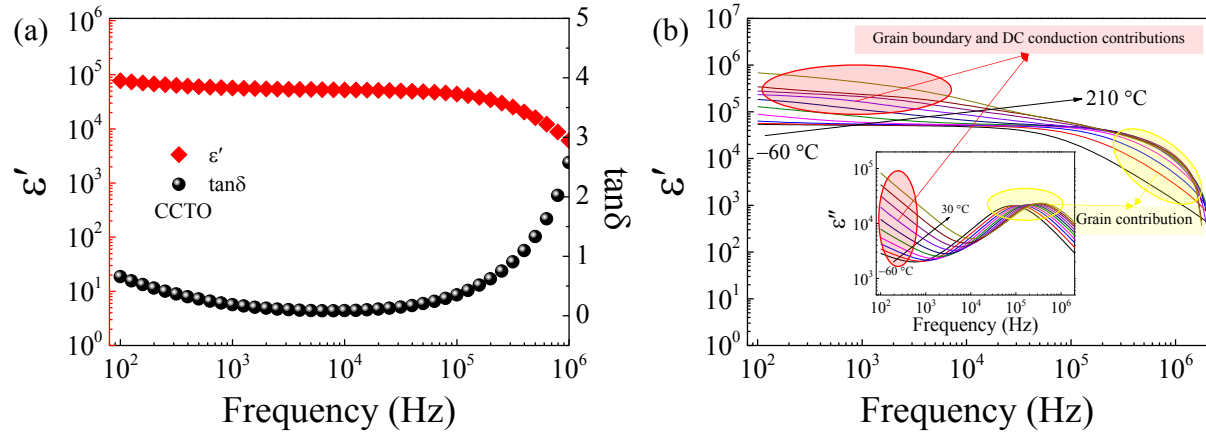


Figure 2.

(a) Frequency dependences of ϵ' and $\tan\delta$ at 20 °C of CCTO ceramic (b) Frequency dependence of ϵ' at various temperatures; its inset shows the frequency dependence of ϵ'' in the same temperature range.

Figure 2(b) and its inset show the frequency dependencies of ϵ' and total loss factor ($\epsilon'' = \epsilon' \tan\delta$) values across different temperatures. The observed trend indicates that the values of ϵ' and ϵ'' exhibit a substantial increase as the temperature rises, particularly in a frequency range lower than 10^4 Hz. The observed increments could potentially be influenced by the contributions of grain boundary and DC conduction in a low-frequency range, according to the relationship $\epsilon'' = \sigma_{dc} / \epsilon_0 \omega$, where ϵ_0 , σ_{dc} , and ω are the permittivity of free space ($\epsilon_0 = 8.854 \times 10^{-12}$ F/m), DC conductivity, and angular frequency ($\omega = 2\pi f$), respectively²². As seen in the inset of **Figure (b)**, in a higher frequency range than 10^4 Hz, it can be observed that a single ϵ'' peak undergoes a displacement towards higher frequencies with an increase in temperature. The observed phenomenon demonstrates the occurrence of dielectric relaxation in CCTO²², in which a single component of the dielectric response may originate from within the grains. The observed phenomenon of a significant decline in ϵ' is directly associated with a notable rise in $\tan\delta$. This shift towards higher frequencies occurred concurrently with an increase in temperature. The dielectric response observed in CCTO ceramics can be described as a thermally activated dielectric relaxation behavior²², which is a distinctive characteristic of this material. The calculation of the activation energy (E_a) for high-frequency relaxation was performed. The relationship between temperature and the frequency at the maximum- ϵ'' peak (f_{max}) can be characterized as follows:

$$f_{max} = f_0 \exp\left(\frac{-E_a}{k_B T}\right) \quad (1)$$

where f_0 represents a fixed value. The Boltzmann constant and absolute temperature are represented by the symbols k_B and T , respectively. The slope of the fitted line (data not present) is used to calculate the E_a of the CCTO sample, which is then found to be 0.90 eV. The E_a value presented exhibits a remarkable level of concurrence with the findings of Li et al.²³, approximately 0.1 eV. The generation of monovalent (V_O^+) and bivalent (V_O^{++}) oxygen

vacancies is a widely recognized phenomenon that occurs during the preparation process, particularly through techniques like sintering at elevated temperatures. The formation of donor energy levels at approximately 0.01 – 0.07 eV and 0.10 – 0.20 eV is attributed to the existence of intrinsic defects of V_O^+ and V_O^{++} , respectively. As a consequence of this, an E_a value of 0.09 eV may have been produced as a result of an electrical response occurring within the grains of CCTO ceramic as a direct result of the presence of V_O^{++} . The presence of V_O can trigger the charge compensation mechanism as a result of its ability to maintain charge equilibrium. Hence, it is possible to induce n -type semiconducting behavior in CCTO ceramic through the process of electronic charge carrier hopping between $Cu^+ \leftrightarrow Cu^{2+}$ and $Ti^{3+} \leftrightarrow Ti^{4+}$ ions^{13, 22}. Thus, the role of intrinsic factors, such as charge carrier densities, should not be overlooked when considering the giant dielectric response of CCTO ceramic. These factors, along with the impact of an IBLC structure, play a significant role in determining the overall giant dielectric behavior of the material¹³. The dielectric response of grain boundaries can be observed through a significant decrease in ϵ' and ϵ'' values in a low-frequency range. The dielectric responses observed at both low and high frequencies in CCTO are indicative of the influence of Maxwell-Wagner polarization, which serves as the primary mechanism underlying the remarkable giant dielectric properties exhibited by this material^{1-3, 6, 11}.

The electrical properties of grain and grain boundary were investigated using impedance spectroscopy. A complex impedance plot, denoted as Z^* , was constructed based on the given relationship:

$$Z^* = Z' - jZ'' = \frac{1}{j\omega C_0 \epsilon^*} \quad (2)$$

In the context of a Z^* plot, the real and imaginary components are typically represented as Z' and Z'' , respectively. The equation $C_0 = \epsilon_0 A/d$ represents the capacitance of free space. The expression $\epsilon^* = \epsilon' - j\epsilon''$ represents the complex dielectric permittivity.

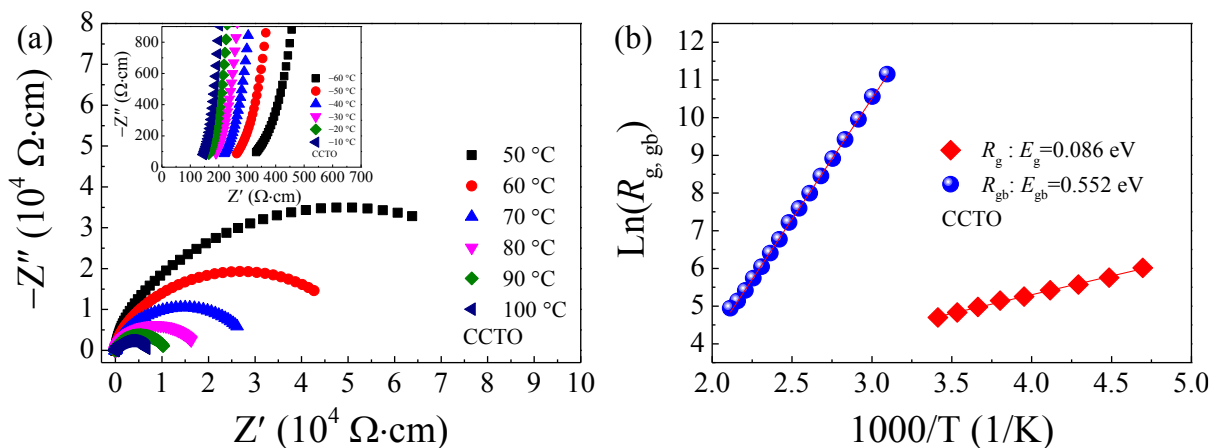


Figure 3.

(a) The Z^* plots of CCTO ceramic at the high-temperature range: its inset shows a high-frequency Z^* plot at a low-temperature range. (b) Arrhenius plots of R_g and R_{gb} for the CCTO sample.

As shown in **Figure 3(a)**, the microstructure of CCTO ceramic has been observed to comprise two distinct electrical components. The electrical response of the grain boundary is



represented by the prominent semicircular arc, while the inset displays the electrical properties of the grains through a nonzero intercept, indicating a semiconductive component within the grain. As mentioned previously, the presence of V_o may impact the small conductivity within the grain of CCTO due to a charge compensation mechanism resulting from charge balance. Inducing electronic charge carrier hopping between transition ions may induce a small conductivity within the grain of CCTO ceramic. Consequently, the high ϵ' value observed in CCTO samples may be primarily attributable to the formation of IBLC structure. Interestingly, the diameter of a large semicircle arc decreases with increasing temperature. Similarly, the nonzero intercept shifts to a lower value of Z' -axis as the temperature increases. These electrical characteristics demonstrate the correlation between R_g/R_{gb} and temperature. R_g and R_{gb} decrease as the temperature rises. This result is comparable to those found in the scientific literature^{13,22}.

The calculation of E_g and E_{gb} can be derived based on the values of R_g and R_{gb} obtained at various temperatures. The Arrhenius law can be conceptualized as follows:

$$R_{g,gb} = R_0 \exp\left(\frac{E_{g,gb}}{k_B T}\right) \quad (3)$$

where R_0 is the pre-exponential term. The temperature dependencies of R_g and R_{gb} for the CCTO ceramic are presented in **Figure 3(b)**. The temperature dependencies of R_g and R_{gb} were accurately modeled using the Arrhenius equation. The estimation of E_g and E_{gb} was conducted by utilizing the slopes of fitting lines. The values of E_g and E_{gb} for the CCTO ceramic were determined to be 0.086 and 0.552 eV, respectively. The value difference between E_g and E_{gb} is 0.466 eV. Based on the research conducted by Sinclair et al., the substantial disparity in value observed between E_g and E_{gb} provides insights into the underlying structural characteristics of the IBLC in CCTO ceramic.

Conclusion:

The dielectric properties of the massive CCTO perovskite ceramic have been studied. A high dielectric permittivity of 5.70×10^4 and a loss tangent of 0.187 were observed. A study found heterogeneous microstructure with n -type semiconducting grains and insulating grain boundaries. Grain and grain boundary conduction activation energies differ by 0.466 eV. High dielectric permittivity is due to the internal barrier layer capacitor model. The charge compensation mechanism causes CCTO grain semiconductivity.

Acknowledgements:

This work was supported by the Faculty of Science and Digital Innovation, Thaksin University. Also, the Faculty of Education, Thaksin University, supported this work.

References:

1. Subramanian, M. A.; Li, D.; Duan, N.; Reisner, B. A.; Sleight, A. W., J. Solid State Chem. 2000; 151 (2): 323-325.
2. Zu, H.; Wang, C.; He, X.; Wang, B.; Liu, H.; Huang, H.; Bian, J.; Cao, G., Ceram. Int. 2023; 49 (12): 20870-20877.
3. Chinnathambi, M.; Robert, R.; Jose, M., J. Mater. Sci.: Mater. Electron. 2023; 34 (20): 1561.
4. Evangeline T, G.; Annamalai, A, R.; Ctibor, P., Molecules 2023; 28 (4): 1649.
5. Hao, W.; Xu, P.; Han, P.; Wang, M., J. Eur. Ceram. Soc. 2023; 43 (3): 986-992.



6. Mao, P.; Zeng, C.; Guo, Y.; Lu, G.; Yan, Q.; Liu, Z.; Xie, B.; Zhao, Y.; Guo, K.; Zhang, L., *Mater. Res. Bull.* 2023; 164: 112276.
7. Shukla, A., *J. Solid State Chem.* 2023; 325: 124182.
8. Wu, R.; Li, H.; Liu, Y.; Chang, A.; Zhang, B., *J. Mater. Chem. C* 2023; 11 (35): 12037-12047.
9. Schmidt, R.; Stennett, M. C.; Hyatt, N. C.; Pokorny, J.; Prado-Gonjal, J.; Li, M.; Sinclair, D. C., *J. Eur. Ceram. Soc.* 2012; 32 (12): 3313-3323.
10. Jesus, L. M.; Barbosa, L. B.; Ardila, D. R.; Silva, R. S.; M'Peko, J. C., *Ceram. Int.* 2023; 49 (15): 25594-25601.
11. Merad, S.; Autret-Lambert, C.; Zaghrioui, M.; Neacsu, D.; Motret, O.; Gervais, F., *J. Solid State Chem.* 2023: 124339.
12. Xu, D.; Wang, B.; Lin, Y.; Jiao, L.; Yuan, H.; Zhao, G.; Cheng, X., *Physica B Condens. Matter* 2012; 407 (13): 2385-2389.
13. Ni, L.; Chen, X. M., *J. Am. Ceram. Soc.* 2010; 93 (1): 184-189.
14. Wu, K.; Huang, Y.; Hou, L.; Tang, Z.; Li, J.; Li, S., *J. Mater. Sci.: Mater. Electron.* 2018; 29 (6): 4488-4494.
15. Prasertsopha, N.; Pinitsoontorn, S.; Thongbai, P.; Yamwong, T., *Electron. Mater. Lett.* 2013; 9 (3): 347-351.
16. Boonlakhorn, J.; Suksangrat, P.; Sarakorn, W.; Kongsuk, S.; Thongbai, P.; Srepusharawoot, P., *Sci. Rep.* 2023; 13 (1): 4638.
17. Boonlakhorn, J.; Thongbai, P., *J. Electron. Mater.* 2015; 44 (10): 3687-3695.
18. Adams, T. B.; Sinclair, D. C.; West, A. R., *J. Am. Ceram. Soc.* 2006; 89 (10): 3129-3135.
19. Boonlakhorn, J.; Manyam, J.; Kongsuk, S.; Thongbai, P.; Srepusharawoot, P., *RSC Adv.* 2021; 11 (40): 25038-25046.
20. Boonlakhorn, J.; Prachamon, J.; Manyam, J.; Thongbai, P.; Srepusharawoot, P., *Ceram. Int.* 2021; 47 (10, Part A): 13415-13422.
21. Ahmad, M. M.; Kotb, H. M.; Joseph, C.; Kumar, S.; Alshoaibi, A., *Crystals* 2021; 11 (3): 313.
22. Ni, L.; Fu, M.; Zhang, Y., *J. Mater. Sci.: Mater. Electron.* 2018; 29 (20): 17737-17742.
23. Li, J. Y.; Zhao, X. T.; Li, S. T.; Alim, M. A., *J. Appl. Phys.* 2010; 108 (10): 104104.



DAM LEAKAGE DETECTION USING ELECTRICAL RESISTIVITY SURVEY AT HUAI FANG NOI RESERVOIR, CHOM THONG, CHIANG MAI, THAILAND

Thanaphon Boonsung, Adul Yawichai, Mingkhwan Kruachanta *

Chiang Mai University, Thailand

*e-mail: mingkhwan.kruachanta@cmu.ac.th

Abstract:

Huai Fang Noi Reservoir is located at Ban Mai Saraphi, Mae Soi Subdistrict, Chom Thong District, Chiang Mai Province. It has been reported to have water retention problems during the dry season. An electrical resistivity survey was conducted to detect the leakage positions along the dam ridge. The survey utilized a 2D dipole-dipole configuration with a minimum electrode spacing of 2 meters. Each survey line spanned a length of 160 meters and utilized 81 electrodes. There were a total of 4 survey lines: one on the slope of the upstream section and three on the crest of the dam ridge. The acquired data were processed to obtain inverted resistivity profiles. The interpretation combined the resistivity with the borehole data, interpreted in terms of the risk of leakage positions of the dam ridge. The areas with a very high risk of leakage exhibit anomalous low resistivity compared to the surrounding areas, which were found below the water level in both the compacted soil layer and rock foundation, covering a large area. The positions indicating a high risk of leakage suggest a possibility of leakage from upstream to downstream sections. The results of this survey provide valuable information for planning the upcoming maintenance of Huai Fang Noi Reservoir.

Introduction:

Huai Fang Noi Reservoir, formerly known as Huai Ta Lek Reservoir, is a small irrigation project located at Ban Mai Saraphi, Mae Soi Subdistrict, Chom Thong District, Chiang Mai Province (**Figure 1**). It was constructed to mitigate water insufficiency problems. The dam ridge was built in 1993 across Huai Ta Lek Creek to store natural water and supply it for agriculture year-round.¹ Huai Fang Noi Reservoir is an earth dam with an estimated storage capacity of 0.105 million cubic meters.^{1,2} The dam is approximately 133 meters long, 10 meters high, and 6 meters wide.^{1,2} The ridge crest is at an elevation of 351.0 meters, and the maximum and minimum water storage levels are at an elevation of 349.5 and 344.5 meters, respectively.¹ Generally, the reservoir area is relatively flat, with the lowest elevation point at approximately 343 meters, surrounded by low hills peaking at about 360 meters. According to geological observation, the reservoir area is situated on unconsolidated and semi-consolidated sediments formed by the weathered parent rocks from neighboring areas, transported and deposited in this location. The geological map (**Figure 2**) also displays two geological units: unconsolidated to semi-consolidated terrace deposits (Qt) and Silurian-Devonian age rocks (SD) in the study site and adjacent areas.³ The Qt sedimentary unit beneath the reservoir consists of quaternary age materials, including terrace deposits, gravel, sand, silt, clay, and laterite. These unconsolidated to semi-consolidated sediments are uncompacted materials with high porosity; therefore, the reservoir's water storage efficiency is relatively low. However, a liner has been placed on the reservoir floor to enhance water retention efficiency.

Recently, there have been reported that the reservoir is unable to retain water. It is suspected that there are leakages at the dam ridge. Three boreholes were drilled on the dam

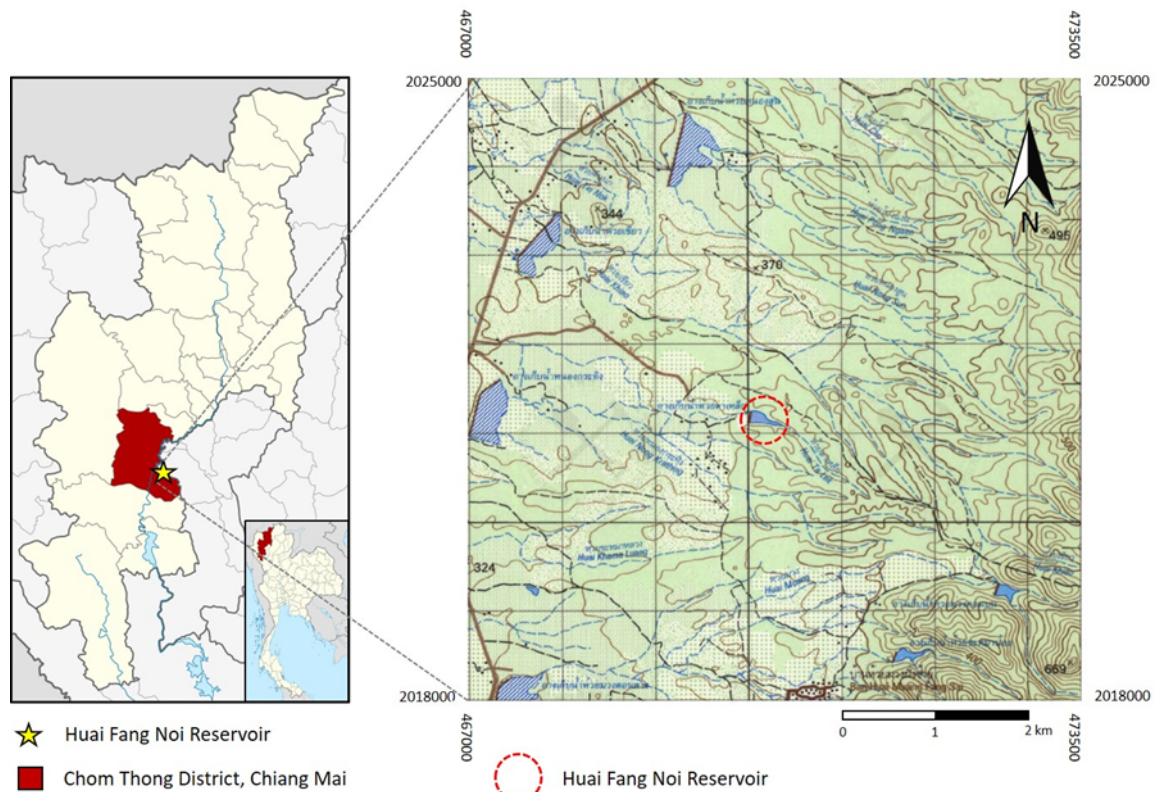


Figure 1. Huai Fang Noi Reservoir is located at Ban Mai Saraphi, Mae Soi Subdistrict, Chom Thong District, Chiang Mai Province.^{4, 5, 6}

Geological Map of Huai Fang Noi Reservoir, Chom Thong District, Chiang Mai Province

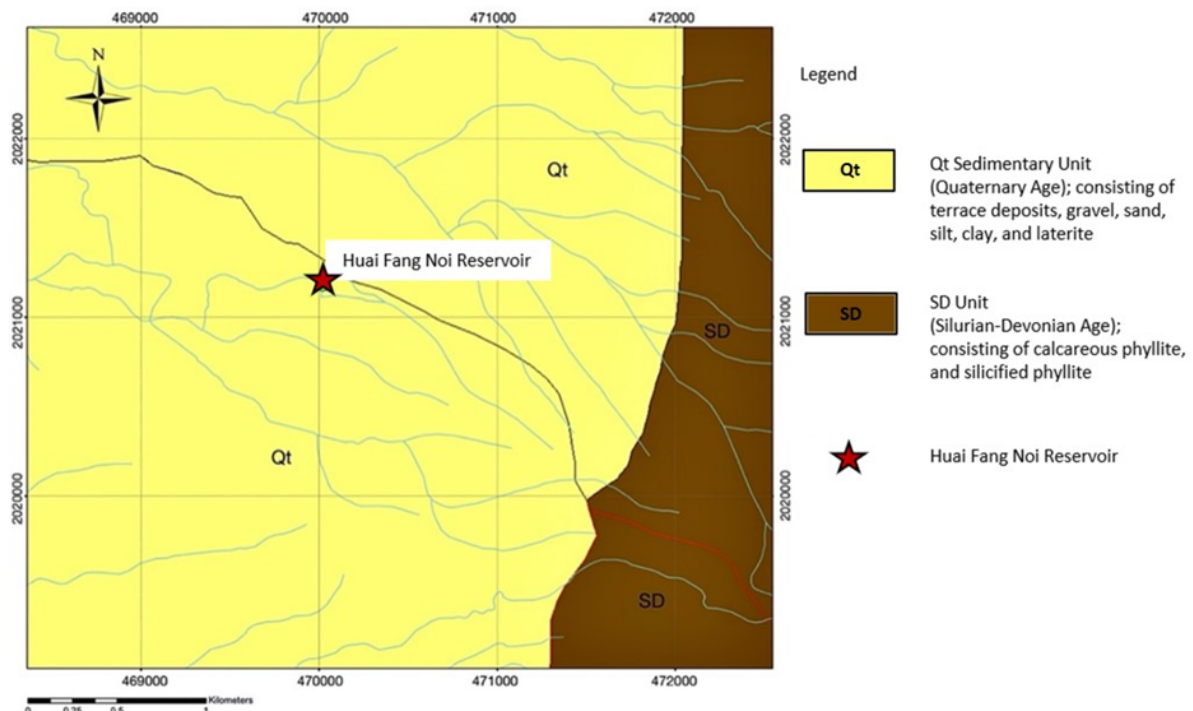


Figure 2. The geologic map of Huai Fang Noi Reservoir and adjacent area, modified from Bureau of Geology (1982).³



ridge to conduct geotechnical and geological investigations. It was found that the compacted soil layer of the ridge and its foundation had a high to very high level of permeability.¹ To pinpoint the leakage positions, a 2D electrical resistivity survey was designed. The electrical resistivity method measures the apparent resistivity of the subsurface geological materials by injecting direct current (DC) electricity via a current electrode into the ground and measuring the potential difference at a pair of potential electrodes. Electrical resistivity depends on the physical properties of the soil or rock layers, which consist of different minerals and pore fluids. When electric currents are injected into the ground, the subsurface material acts as a conductor because there are pores in the rocks or soils containing pore fluids that allow the current to flow through, enabling the measurement of the potential difference resulting from the flowing current. In contrast, the soil or rock matrix acts as an insulator, prohibiting the current from flowing through. The material's electrical resistivity is a value that represents one of the material's electrical properties, indicating how much the material resists electricity or allows electric current to flow through.⁷ The measured apparent resistivity can be inverted into true resistivity that can be used for the interpretation.

Electric resistivity is one of the most sensitive geophysical methods for detecting changes in rock or soil moisture. It has been proven to be highly effective in determining water-saturated zones and groundwater flow patterns. The resistivity of rocks or soils depends on various factors such as porosity, water saturation, permeability, ionic pore fluid content, and clay content. Water leakage through a dam manifests as low resistivity.⁸ Using an electrical resistivity survey to pinpoint the leakage positions of the dam has been successfully applied in various studies. For example, Aal and others (2004) combined electrical resistivity and self-potential methods to investigate seepage in the earth-fill Crystal Lake Dam in Washington County, Missouri, which could successfully detect internal erosion and anomalous seepage at an early stage.⁸ Chinedu and Ogah (2013) utilized electrical resistivity to image suspected seepage channels in an earth dam in Zaria, North-Western Nigeria.⁹ Michalis and others (2016) employed a combination of electrical resistivity tomography and electromagnetic sensing to assess the Mugdock reservoir dam infrastructure in central Scotland.¹⁰ Camarero and Moreira (2017) utilized 2D and pseudo-3D electrical resistivity tomography techniques to investigate water seepage in an earth dam in the rural municipality of Cordeirópolis in the State of São Paulo.¹¹ Nwokebuihe and others (2017) combined electrical resistivity tomography, induced polarization, and self-potential data to investigate the seepage in an earth-fill dam in Warren County, Missouri.¹² Raji and Adedoyin (2020) used 2D electrical resistivity geophysical survey and geological mapping to investigate the Unilorin Dam in Nigeria for structural anomalies that could compromise the dam's safety.¹³

Methodology:

To detect the leakage position at Huai Fang Noi Reservoir, the 2D electrical resistivity survey was performed. The method involves field data acquisition, data processing, and interpretation as follows.

Field Data Acquisition

To acquire the 2D electrical resistivity data, four survey lines were deployed, one on the slope of the upstream section (Line A) and the other three on the crest of the ridge (Line B, C, and D). The survey lines were arranged from upstream to downstream with parallel orientations. The line spacing between B and C, as well as C and D, is 2 meters. The spacing between lines A and B is 9 meters (**Figure 3**). The electrical resistivity survey used the 2D



Figure 3. Electrical resistivity survey lines at Huai Fang Noi Reservoir, modified from Google Earth.

surveys to acquire the cross-sections of subsurface resistivity distributions. A dipole-dipole configuration with a 2-meter minimum electrode spacing was chosen. In this configuration, 81 electrodes were utilized for each survey line. Each survey line spanned a length of 160 meters. After deploying and installing all the equipment, precise measurements of electrode positions and elevations were conducted using DGPS equipment.

Data Processing

The acquired field data, apparent resistivity, were exported from the resistivity meter. The exported data were quality-checked by removing the data points with negative resistivity values and those with a high standard deviation of measurements. After that, the quality-checked apparent resistivity data and topographic data were imported into the processing software to perform the inversion in order to get the true resistivity value. The 2D pseudosection was inverted into an inverted resistivity profile representing the true resistivity section of the subsurface at the survey line. The inversion process ran iteratively until reaching the acceptable RMS errors, set at 10% for this study.¹⁴ The processing of the data was performed individually for each survey line. The final inverted sections of each survey line were combined and interpreted in the next step.

Data Interpretation

The inverted resistivity section illustrates the resistivity distribution across the profile which was used to interpret the leakage positions. Generally, the leakage locations usually exhibit anomalous low resistivity than the surrounding area due to the water filling in pore space. The measured resistivity values are the result of the average resistivity of both the matrix and pore fluids. According to a study by Abidin and others in 2011¹⁵, the suspected leakage zones in this study were defined by resistivity values lower than 50 ohm-m.

Results and Discussion:

The inverted resistivity sections display resistivity values ranging from 5 to 6,500 ohm-m (**Figure 4**). The resistivity distribution patterns in all profiles cannot distinguish between the dam ridge and the rock foundation. Therefore, the geologic logs from three boreholes, drilled on the crest of the dam ridge approximately along Line B survey in 2022, were utilized to differentiate the dam ridge and the foundation.¹

According to the borehole data, the top layer is a compacted soil layer of the dam ridge, comprising silty gravel with sand and silt to sand, situated at the elevation of 338 to 348.6 meters above mean sea level. The second layer is a rock foundation, which is the weathered semi-consolidated sandstone. Additionally, the reservoir's water level on the survey date was 345.445 meters above the mean sea level. Thus, the contact between a compacted soil and a rock foundation, as well as the water level were overlaid on the resistivity sections to serve as a guideline for interpretation. The leakage locations generally exhibit anomalous low resistivity compared to the surrounding area. The zones below the water level presenting resistivity values lower than 50 ohm-m were suspected to be leakage zones, interpreted as a very high risk of leakage.

In the compacted soil layer, the laterally continuous anomalous low resistivity is observed both above and below the water level. The low resistivity of compacted soil above the water level can be attributed to the clay core of the dam ridge. Whereas the low resistivity of the compacted soil layer below the water level can be interpreted as the position of a very high risk of leakage (**Figure 4**). In the rock foundation, the anomalous low resistivity indicates that the rock is saturated with water. The locations with anomalous low resistivity are interpreted as a wide area of very high risk of leakage (**Figure 4**). The positions of very high risk of leakage are summarized in **Table 1**.

After interpreting the leakage positions for each line individually, all four interpreted resistivity profiles were combined to find the possible leakage paths. The combined profiles reveal two main leakage paths in the rock foundation. One is located approximately beneath the outlet pipe, and the other one is on the right side of the dam ridge near the spillway, where the leakage connects to the leakage position of the compacted soil layer (**Figure 5**).

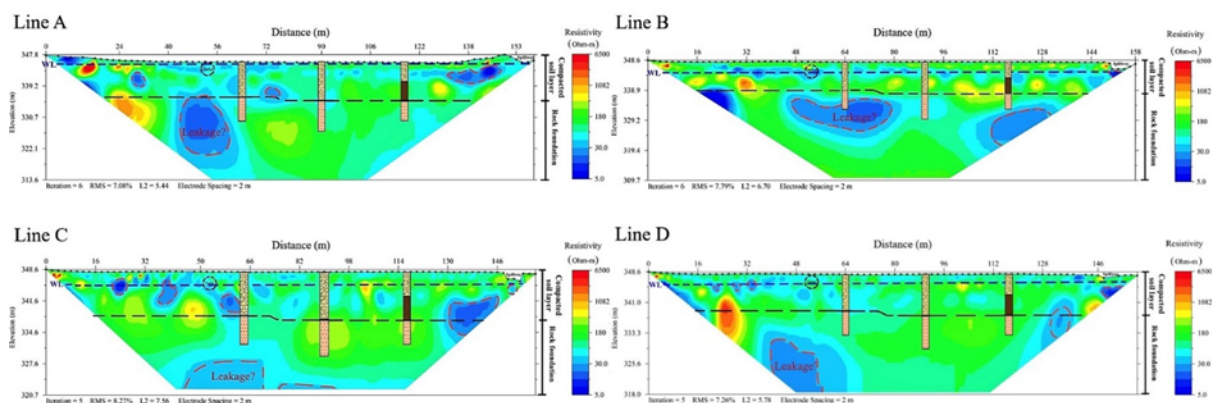


Figure 4. Inverted resistivity section of the survey lines on the dam ridge.

Table 1. The summary of very high-risk leakage positions.

Leakage position	Compact soil layer		Rock foundation	
	Distance (m)	Depth (m)	Distance (m)	Depth (m)
Line A	28-32	4.3	44.60	11.6
	72-76	10	-	-
	130-148	2.3	-	-
Line B	152-156	4	46-80	11.7
	-	-	112-130	14.6
Line C	22-26	3	46-94	21
	36-42	3.5	130-146	4
	56-62	5	-	-
	150-154	3.4	-	-
Line D	18-34	3.7	40-54	17
	148-154	3.8	132-138	9.7

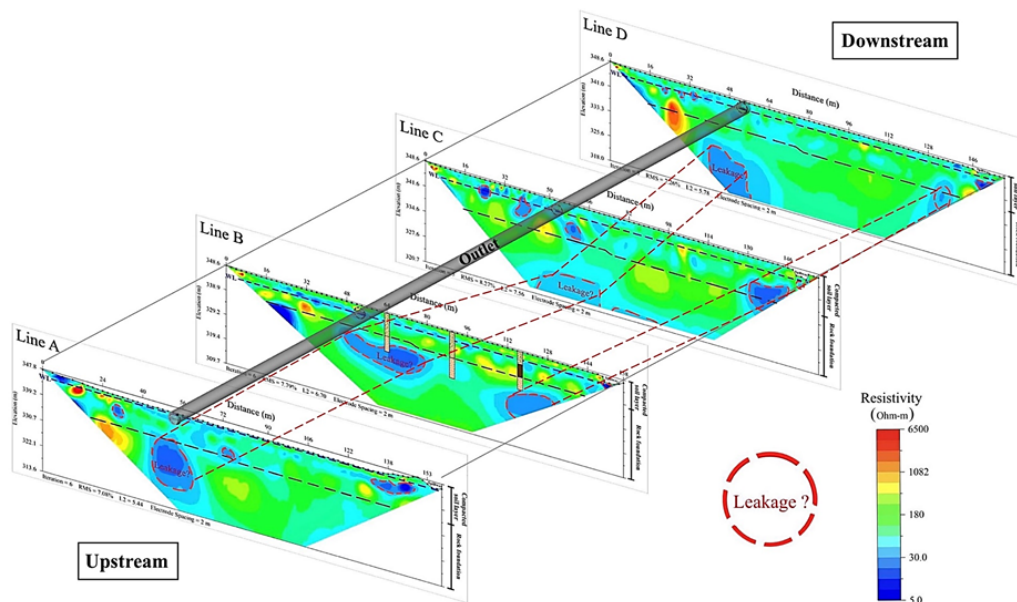


Figure 5. The interpretation of the combined inverted resistivity profiles of four survey lines shows a possibility of the leakage path from upstream to downstream sections.

Conclusion:

The leakage positions at Huai Fang Noi Reservoir were successfully identified using 2D electrical resistivity data. Areas at very high risk of leakage exhibit anomalous lower resistivity than the surrounding areas, observed in both compacted soil layer and rock foundation. However, in the compact soil layer, only the anomalous low resistivity below the water level was interpreted.

Identifying the leakage paths requires combining the parallel resistivity profiles to analyze the possible connecting leakage positions between lines from upstream to downstream sections. The result of this survey can serve as valuable information for planning the forthcoming maintenance of the reservoir.



Acknowledgements:

We would like to extend our sincere gratitude to Mr. Anuwat Rattanasathien for providing valuable information about Huai Fang Noi Reservoir, and to Associate Professor Dr. Pisanu Wongpornchai for his invaluable guidance and advice throughout this study.

References:

1. Engineering Management Division, Regional Irrigation Office1, Foundation Geological Survey Report of Huai Fang Noi Reservoir Project, Mae Soi Subdistrict, Chom Thong District, Chiang Mai Province, Internal Report, Royal Irrigation Department, 2022; 40.
2. Boonsung T. Electrical Resistivity Surveys for Dam Leakage Detection at Huai Fang Noi Reservoir, Ban Mai Saraphi, Mae Soi Subdistrict, Chom Thong District, Chiang Mai Province, BS Independent Study, Chiang Mai University, 2023; 54.
3. Bureau of Geology, The geologic map of Chiang Mai, scale 1:50,000, Department of Mineral Resources, 1982.
4. Wikipedia, Chiang Mai province; Available at: https://en.wikipedia.org/wiki/Chiang_Mai_province.
5. Wikipedia, Chom Thong district, Chiang Mai; Available at: https://en.wikipedia.org/wiki/Chom_Thong_district,_Chiang_Mai
6. National Imagery and Mapping Agency and Royal Thai Survey Department, Topographic map, L7018S, sheet 4745-IV, Amphoe Chom Tong, scale 1:50,000, Royal Thai Survey Department, 1999.
7. Asia Testing Equipment Co., Ltd., Resistivity Imaging Geophysical Survey Instrument; Available at: <https://www.asiatest.co.th/resistivity-imaging>.
8. Aal GZA, Ismail AM, Anderson NL, Atekwana EA. Journal of Applied Geophysics Geophysics. 2004; 44: 167-180.
9. Chinedu AD, Ogah AJ. Journal of Applied Sciences. 2013; 3: 145-154.
10. Michalis P, Sentence P, MacBrayne D. 3rd Joint International Symposium on Deformation Monitoring, Vienna, Austria. 30 March - 1 April 2016: 1-6.
11. Camarero PL, Moreira CA. REM-International Engineering Journal. 2017; 70: 47-52.
12. Nwokebuihe S., Alotaibi AM, Elkrry A, Torgashov EV, Anderson NL. AIMS Geosciences. 2017; 3: 1-13.
13. Raji WO, Adedoyin AD. Journal of King Saud University-Science. 2020; 32: 1123-1129.
14. Loke M H. Tutorial: 2-D and 3-D electrical imaging survey; Available at: <https://www.geotomosoft.com/downloads.php>.
15. Abidin MHZ, Saad R, Ahmad F, Wijeyesekera D, Baharuddin MFT. Malaysian Technical Universities International Conference on Engineering & Technology, Johor, Malaysia. 13-15 November 2011; 1-12.



EXPERIMENTAL HEAT TREATING OF AMETHYST FROM URUGUAY

Treeraphat Wangyo, Kanyarat Kwansirikul,* Phisit Limtrakun

Department of Geological Sciences, Faculty of Science, Chiang Mai University, Chiang Mai, Thailand 50200

*e-mail: kanyarat.k@cmu.ac.th

Abstract:

Amethyst has been one of the popular gemstones in the gems and jewelry trade because of its distinct color. In this study, thirty natural rough amethysts from Uruguay were experimentally heat treated to change their color and characterized gemological properties using gemological standard methods, and some advanced techniques. Specific gravities of the samples were in the range of 2.65 to 2.66. The refractive indices for n_e was 1.541 to 1.548 and n_o was 1.549 to 1.557 with birefringence between 0.007 to 0.009. They were inert under short-wave and long-wave UV radiation. Uneven color distribution and fractures or healed fractures were found in every sample when viewed under microscope. Some samples showed brown stains along healed fractures, zebra stripe, black inclusions, and goethite. The samples were heated at a maximum temperature of 250, 350, and 450°C in reducing conditions and soaking time for 1 hour at each maximum temperature. The result of the heating experiments revealed that the temperature over 450°C could change the violet color of amethysts to yellow color without transparency decreasing. Chemical composition analysis using SEM-EDS revealed major elements of silicon and oxygen. The only trace element detected was iron. The UV-Visible-NIR absorption spectra exhibited a broad absorption between 340-350, 500-600, and 850-1050 nm related to iron element and trace of water in the crystals. After heating at the temperature reached 450 °C, the intensity of absorption band between 500-600 nm decreased while the band between 340-350 nm intensified corresponding to the change of the violet color of amethyst turned to yellow.

Introduction:

Amethyst is a variety of α -quartz (SiO_2) which exhibits violet to lavender color shades. They can occur in very different geological environments, such as hydrothermal veins, alpine clefts, miaroles in granitic rocks and geodes in basaltic lavas.¹ Although, amethyst is widely distributed in many localities, such as Brazil, Uruguay, Canada, Sri Lanka, Rwanda, Morocco and Arizona, etc.,² Brazil and Uruguay localities are the world leaders in the production of amethyst and agate from geodes. The most important amethyst mineralization and amethyst mining is located in the areas of Rio Grande do Sul, Brazil and Artigas, Uruguay.¹

When quartz contains some impurities such as iron, aluminum and titanium, it will make quartz appear color.³ The colors of amethyst, citrine and prasiolite are all related to iron.³ Amethyst has been known that can be produced through the heating and gamma irradiation of amethyst from a mine called Montezuma in Brazil. This deposit initially became famous during the 1960s for amethyst that could be turned green by heating, known today as prasiolite or greened amethyst in the gems trade. It is well known that heat may reduce the oxidation state of iron in amethyst, and at about 300-500 °C the purple color will change to colorless or yellow or green. The resulting green quartz is quite stable to heat, unlike the pale green quartz that has been produced with gamma irradiation (but no heat treatment) from colorless to very slightly green quartz from Rio Grande do Sul State. This latter quartz loses much of its green color when heated to about 150-200 °C or exposed to strong sunlight.⁴ It is postulated that color of amethyst can be related to the replacing Si^{4+} with Fe^{3+} , and alkali metal ions, such as Li^+ , Na^+ or H^+ , are introduced to maintain the charge



balance.⁵ In addition, holes created during quartz irradiation can also act as charge compensations.⁶ However, the Fe oxidation state in purple-quartz was questioned between Fe^{3+} probed by electron paramagnetic technique as well as Mössbauer spectroscopy and Fe^{4+} derived by geochemical calculation.⁷ X-ray absorption spectroscopy (XAS) especially a region of X-ray absorption near edge structure (XANES) revealed that the cause of color in both purple and yellow quartz was affected by the Fe^{3+} donor states at 3.59 eV and 2.28 eV probed by the XAS technique.⁷

Several previous works have been studied the treatment methods, especially heat treatment and irradiation, of amethyst to discuss the mechanism of the coloration.² The obtained data indicate that the color change of amethyst after heating and irradiation is related to the color center activated by iron.^{2,8} The color center formation of amethyst could be related to the iron substitution for silicon in the quartz lattice. The alkali ion released in this mechanism may eventually react with an electron, leading to the creation of an interstitial neutral atom.⁹ The study of UV-Visible spectroscopy of amethyst also provide support for the existing form of iron element in amethyst. This technique is useful for finding the energy state of the ionic absorption relating to the color of the minerals. The combination of the oxidation state and the energy state has been applied to describe the color mechanism of gemstone. The main absorption bands of amethyst in UV-Vis-NIR spectra are located at 950 nm, 540 nm and 360 nm, which is considered to be related to the transition of Fe^{4+} in tetrahedral coordination, and these absorption bands show different degrees of changes after irradiation or heating.^{2,6} The absorption bands at different wavelength of amethyst UV-Vis spectra are also considered to correspond to the relevant color center.^{2,6} The UV-Vis-NIR spectra of some studies of amethyst coloration show a broad absorption bands at 545 nm and 345 nm. The absorption band at 545 nm (which is related to a charge-transfer transition of Fe^{3+} and O^{2-}) has a significant relationship with the color of amethyst.² Amethyst coloration was also reported that the violet coloration was observed only in samples where specific sites were occupied by Fe^{3+} ions.⁵ Mössbauer spectroscopic result measured on quartz with radiation and heat treatment showed that only Fe^{3+} was found in the prasiolite (green quartz) and amethyst.⁸ The UV-Vis spectrometer, X-ray diffraction (XRD), X-ray photoelectron spectrometer (XPS) and Electron paramagnetic resonance (EPR) spectrometer were used to analyze the visible absorption spectrum, crystal structure, iron ions valence state and oxygen type of amethyst. Based on the findings of the experiment, the energy band structure, density of states and optical absorption of Fe-doped $\alpha\text{-SiO}_2$ with different states were evaluated by the first-principles method to analyze the reason for the color change of amethyst theoretically. The study found that the color change of amethyst is related to the valence transition of iron ions and the existence of Fe^{4+} has an important effect in imparting purple color to the quartz.¹⁰

Citrine can be obtained by heating amethyst at a temperature of about 500 °C. During the heat treatment, the transformation of amethyst to citrine is related to the increase in the concentration of interstitial Fe^{3+} related defects and precipitation of iron particles in the quartz lattice.¹¹ The brown color is partly due to these inclusions and partly due to a shift of the charge-transfer band into the visible as S1 centers ($[\text{Fe}^{3+}\text{O}_4/\text{M}_i^+]$) are converted to less constricted I centers (Fe^{3+} in an interstitial site).¹¹ Therefore, the temperature of heat treatment has a great effect on amethyst color. The color of amethyst is stable and will not change obviously in dark condition after heat treatment.²

Although, amethyst is a popular gemstone, it is cheaper in the gems and jewelry trade when compare to citrine. One factor affecting their values is rarity. Citrine is rarer than amethyst although they can be found in the same deposits. Therefore, some amethysts will be



treated to turn their colors to citrine resulting in value increasing in the trade. However, not every amethyst locality can be changed the violet to intense yellow colors. The amethyst localities, and ranges of heating temperatures are considered to be the important factors of color-change succession. Thus, this study aims to experimentally heat amethyst from Uruguay, which is one of the most important localities for amethyst production, under reducing conditions to observe and study the effect of heat on the change of color after heating. The study also characterizes the gemological properties of the studied samples.

Methodology:

Thirty samples of natural rough amethyst from Uruguay ranging from 0.69 to 2.00 ct. were used in this study. Their colors displayed from light to dark violet with uneven color distribution. To get the color comparison effectively, all of them were polished on one side from different crystallographic orientations. In order to investigate whether the degree of color change of amethyst after heat treatment was related to its initial color, the amethyst samples were divided into three groups according to the initial color including light violet, medium violet, and dark violet groups. The samples were heated three times in reducing atmosphere and analyzed for the gemological properties, chemical compositions, and spectroscopic features. The analytical gemological techniques included specific gravity, refractive index, fluorescence, and internal features using standard gemological instruments. Some samples were selected for chemical composition analysis by Scanning Electron Microscope equipped with Energy Dispersive Spectrometer (SEM-EDS). Ultraviolet-visible-near infrared (UV-Vis-NIR) absorption spectra for all thirty samples were recorded throughout of 250 - 1500 nm before and after heat treatment using a Hitachi U4001 spectrophotometer, with a slit width of 2 mm and a scan speed of 300 nm/min. The Ultraviolet-Visible-Near infrared absorption spectra can give information related to electron transitions of trace elements or other structural defects. Heat treating experiments were carried out with a SANTE electric furnace. The samples were heated under reducing conditions at 250, 350, and 450°C with heating rate at 5°C/minute and soaked for 1 hour at each temperature. The furnace was slowly cooled down to room temperature before samples removing. All experiments and analysis methods were done at Faculty of Science, Chiang Mai University, Chiang Mai, Thailand.

Results and Discussion:

The thirty natural rough amethysts from Uruguay were light to dark violet with uneven color distribution and transparent to semi-transparent (Figure 1). The studied samples were classified into three groups depending on their initial color appearance viewed under a daylight fluorescence lamp. They consisted of light purple, medium purple, and dark purple groups. The specific gravity of all samples ranged from 2.65 to 2.66. The refractive indices for n_e was 1.541 to 1.548 (average 1.544) and n_o was 1.549 to 1.557 (average 1.552) with birefringence between 0.007 to 0.009. Those values were consistent with natural amethyst from other localities worldwide. The samples were inert under short-wave and long-wave ultraviolet radiation before heat treatment. For internal features observed under a gemological microscope, uneven color distribution and fractures or healed fractures were found in every sample. Some samples showed brown stains along fractures, zebra stripe related to twinning in the crystal, black inclusions, and goethite (iron hydroxide mineral).

Four samples were selected from the three groups for chemical analysis. The chemical data of the studied samples were summarized in Table 1. The selected samples revealed major weight percentage of elements of silicon (61.90-81.78 wt%) and oxygen (17.26-30.06 wt%).

The only trace element detected was iron (0.75-20.84wt%). The concentration of iron 20.84 wt% derived from the goethite inclusion (FeO(OH)) in one sample which was polished until the inclusion reached the sample surface before analyzing. The obtained chemical compositions corresponded to the general chemical formula of α -quartz; SiO₂. Iron (Fe) was the main coloring element affecting the color of amethyst.

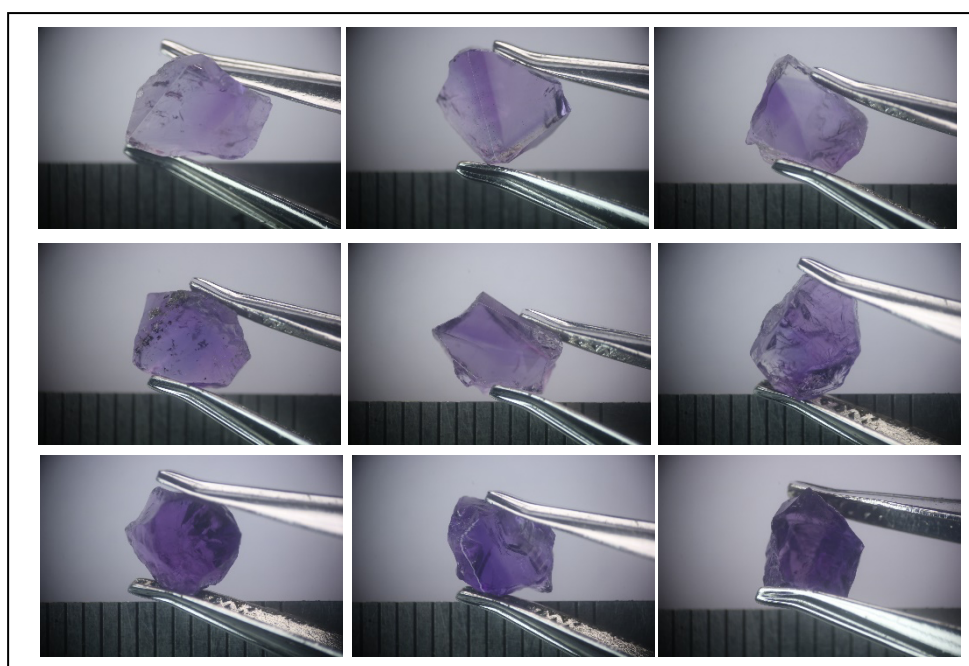


Figure 1.

A set of representative samples in three groups including light violet (upper row), medium violet (middle row), and dark violet (lower row), respectively.

Table 1.

Average chemical compositions in weight percentage of elements of the studied natural amethysts from Uruguay determined by SEM-EDS.



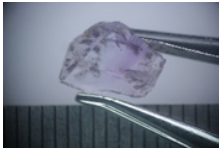
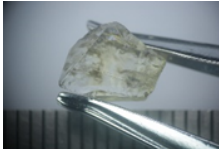

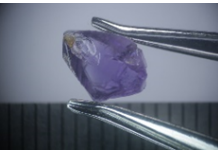
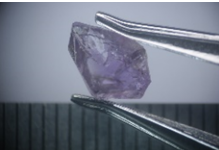


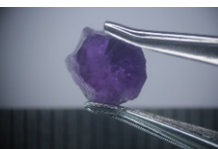

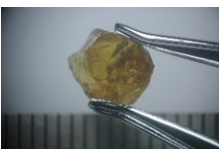
Average Chemical composition (wt.%)	Light violet group	Medium violet group	Dark violet group
Si	76.03	73.24	77.03
O	23.27	19.81	22.59
Fe	0.75	20.84	0.57

The 30 amethyst samples were heated under reducing conditions at 250, 350, and 450°C with soaking time for 1 hour at each maximum temperature. Change of the colors of the samples were compared before and after heat treatment (Table 2). The heating experiment showed that the initial colors and transparency of all samples remained unchanged after heating at 250°C. After heating at 350°C, the violet color intensity of most samples was faded. They showed very light violet to nearly colorless. After heating at 450°C, the very light violet samples from the previous heating stage turned into yellow color which varied in color intensities. After heat treatment, all samples were still inert under long-wave and short-

wave ultraviolet radiation. There was no change in the specific gravity and refractive indices significantly. The fractures, healed fractures, and zebra stripe in the heated stones were more developed (Figure 2). The brown stains and black inclusions turned to yellowish brown and brown or reddish brown colors, respectively, while the brown color of goethite mineral turned to reddish brown after heating at the last maximum temperature (Figure 3).

Table 2.

Representative of color changing of natural amethyst samples from Uruguay before and after heat treatment at different temperatures.

Initial color	Unheated	250 °C	350 °C	450 °C
Light violet				
Medium violet				
Dark violet				

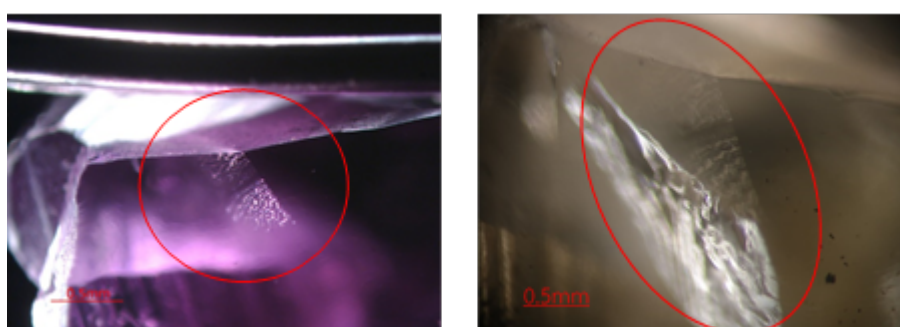


Figure 2. Comparison between the zebra stripe (red circle) in the representative amethyst sample before (left) and after heat treatment (right).

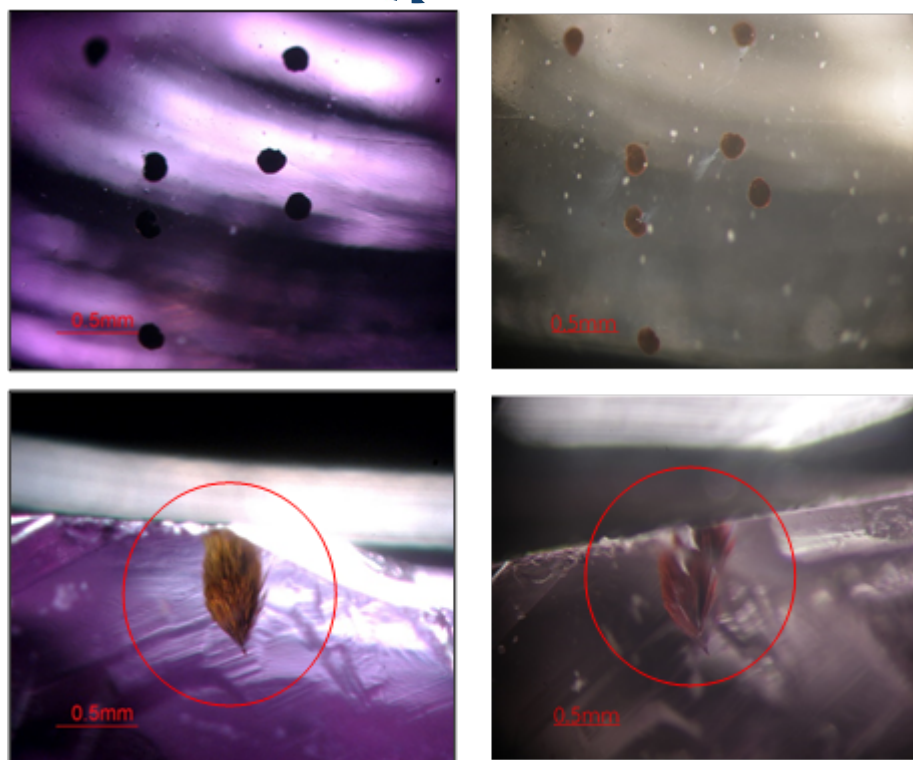


Figure 3. Comparison between the black inclusions (upper row) and goethite inclusion (lower row) in the representative amethyst samples before (left column) and after heat treatment (right column).

Yellow color in quartz can be obtained by heating amethyst at a temperature of about 500 °C. During the heat treatment, the transformation of amethyst to citrine is related to the increase in the concentration of interstitial Fe^{3+} associated with defects and precipitation of iron particles in the quartz lattice.¹¹ The yellow or brown color is partly due to these inclusions and partly due to a shift of the charge-transfer band into the visible region as S1 centers ($[\text{Fe}^{3+}\text{O}_4/\text{M}_i^{+}]$) which are converted to less constricted I centers (Fe^{3+} in an interstitial site).¹¹ After heat treatment, the color of amethyst is stable and will not change obviously in dark condition.² In some previous studies, when the temperature rises to 380 °C, the violet color begins to fade out and gradually becomes colorless. The absorption peaks at 348 and 545 nm disappeared when the color of amethyst lightened. Then it changes to light green at 420-440 °C. Therefore, prasiolite or green quartz can be obtained by heating amethyst from 420-440 °C. As the temperature continues to rise above 440 °C, it slowly changes to yellow and gradually deepens. The absorption band appeared around 340 nm.^{2,10,11} These results are correlated with the experimental heat treatment of amethyst samples from Uruguay in this study. When the temperature is over 600 °C, it may appear milky white. The suddenly increase of color difference at 580 °C, which is the temperature above the phase transition temperature (573 °C) of amethyst, can be related to the irreversible destruction of color center.^{2,11} The appropriate heating temperature to obtain citrine is suggested at approximately 560 °C.²

The UV-Vis-NIR absorption spectra of the thirty unheated amethyst samples showed a broad absorption between 340-350 nm, 500-600 nm, and 850-1050 nm. After heating under reducing conditions, when the temperature reached 450 °C, the intensity of absorption band

between 500-600 nm decreased while the band between 340-350 nm intensified (Figure 4), at which time the color of amethyst turned to yellow. This was consistent with the obtained absorption band which examined the cause of yellow color in the previous works.^{2,6,10,11} Those absorption bands obtained from some previous researches are considered to be related to the transition of Fe^{4+} in tetrahedral coordination and also considered to correspond to the relevant color center^{2,6} while another research considered those bands are related to a charge-transfer transition of Fe^{3+} and O^{2-} and has a significant relationship with the color of amethyst.² The absorption band at 545 nm was considered to be the color of amethyst while the yellow color is related to the band at 345 nm. Thus, the color change during heat treatment is related to the Fe charge state and not to oxygen vacancies.¹⁰

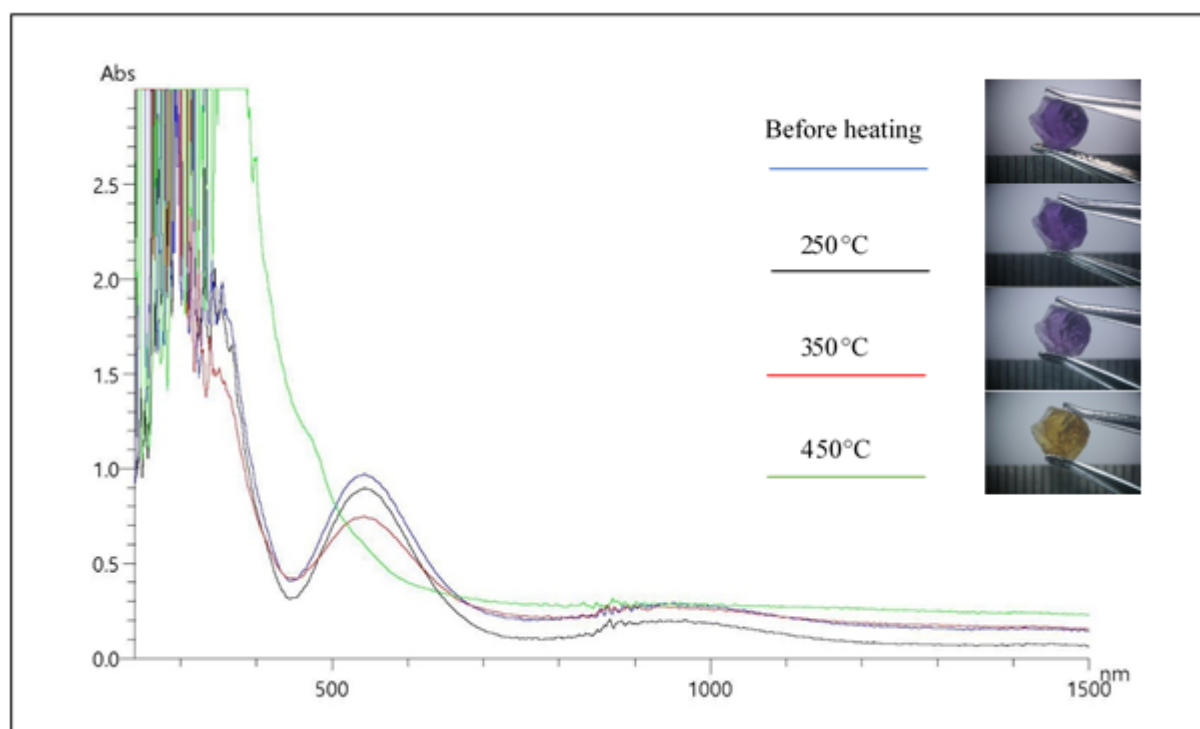


Figure 4. The UV-Vis-NIR absorption spectra of the amethyst samples from Uruguay before and after heat treatment under reducing conditions at different temperatures.

Conclusion:

The gemological properties of the studied amethyst samples from Uruguay indicated that they were consistent with natural amethyst from other localities worldwide. Chemical compositions showed silicon and oxygen as major elements, and iron as trace element. From this heating experiment showed that the temperature of heat treatment has a great effect on amethyst color. The initial colors and transparency of all samples remained unchanged after heating at 250°C. After heating at 350°C, the violet color intensity of most samples was faded and the optimum temperature to change violet to yellow colors was over 450 °C with no impact on the clarity of the samples. The UV-Vis-NIR absorption spectra of all samples indicated that the cause of color of the amethyst (violet color) and citrine (yellow color) was related to presence of iron in the crystal structure.



Acknowledgements:

The authors would like to thank the 50th Geological Anniversary Chiang Mai University and Faculty of Science, Chiang Mai University for providing financial support for this research. Thanks are extended to Mr. Siwakon Chimnakphant and staffs at the Department of Geological Sciences, Faculty of Science, Chiang Mai University for providing the facilities.

References:

1. Morteani G, Kostitsyn Y, Preinfalk C, Gilg HA. *Int J Earth Sci (Geol Rundsch)*. 2010;99:927-947.
2. Cheng R, Guo Y. *Nature (Scientific reports)*. 2020;10:14927.
3. Hatipoğlu M, Kibar R, Çetin A, Can N, Helvacı C, Derin H. *Radiant Eff Defects Solids*. 2011;166:537-548.
4. Gütter RS, Kohigashi HC. *Gems Gemol*. 2006;42(4):285-286.
5. Rossman GR. *Rev Miner Geochem*. 1994;29:433-467.
6. Nunes EHM, Lameiras FS, Houmard M, Vasconcelos, WL. *Radiant Phys Chem*. 2013;90(1):79-86.
7. Monarumit N, Sakkaravej S, Wanthanachaisaeng B, Saiyasombat C, Wongkokua W. *J Phys (Conference Series)*. 2020;1719:012001.
8. Czaja M, Kądziołka-Gaweł M, Konefał A, Sitko R, Teper E, Mazurak Z, Sachanbiński M. *Phys Chem Miner*. 2017;44:65-375.
9. Cohen AJ. *Am Miner*. 1985;70:1180-1185.
10. Chen R, Liu Y, Lin J, Cui X, Tian G, Yu J. *Appl Phys A*. 2022;128:914.
11. Lehmann G, Moore WJ. *J Chem Phys*. 1966;44:1741-1745.



GEOLOGY AND GEOCHEMISTRY OF THE BAN NONG KHROK HOT SPRING TOURISTIC ATTRACTION, PHRAO DISTRICT, CHIANG MAI PROVINCE FOR SUSTAINABLE GEOTOURISM POTENTIAL EVALUATION

Patcharin Kosuwan Jundee,^{1,*} Yupa Thasod,¹ Juntanee Duangkhamasawad², Pawintana Charoenboon³, Mayuree Phomphutha¹, Prachun Oopkamdang⁴

¹Department of Geological Science, Faculty of Science, Chiang Mai University, Chiang Mai, Thailand

² Mineral Resources Regional Office 1, Department of Mineral Resources, Ministry of Natural Resources and Environment, Lampang, Thailand

³Business Administration, School of Interdisciplinary Studies, Mahidol University, Kanchanaburi Campus, Kanchanaburi, Thailand

⁴Nong Khrok Village Headman Office, Phrao District, Chiang Mai, Thailand

*e-mail: patcharinkosuwan.j@cmu.ac.th

Abstract:

The Ban Nong Khrok Hot Springs Attraction is a part of the Ban Nong Khrok village, San Sai Sub-district, Phrao District, Chiang Mai Province. The methodology in this research is a geological investigation, geochemistry investigation, Thailand's geosite assessment model evaluation, and SWOT analysis. The geological investigation found that the hot springs occurred due to the movement of the Nong Khrok fault in lower Carboniferous rock. The physical characteristics study found that the surface temperature is 67-73 °C. These hot springs were high-temperature hot springs or hyperthermal springs. The hot springs are 12 litres per minute and have continuous flow, which is suitable for the spa business. The hot springs and the hot water supply in the Sai Nam Oon village tourism community and the Bamboo spa are mixing of infiltrating water and groundwater. The pH value is neutral to weakly alkaline, suitable for health spa tourism or hydrotherapy. The geosite potential assessment has low academic geological values but a high potential value for management and development values. SWOT analysis indicated that the strengths and sustainable competitive advantage are the Sai Nam Oon hot spring community homestay and the Bamboo spa. The weakness of geosite was the lack of academic knowledge dissemination in geological and health sciences. This research is a model for geosite attractions developing in low potential academic values by the local community. The community members realize and conserved the local resources. In addition, the government supports for safety and facilities management such as restrooms, shops, public relations, and community cooperation such as local geologic guides, community products, and community tourism activities can make geological tourist attractions become tourist attractions that promote sustainable income.

Introduction:

The Ban Nong Khrok hot springs are located at Nong Khrok village, San Sai sub-district, Phrao District, Chiang Mai Province, and have been developed into a tourist attraction by the Nong Khrok village community. This research aims to evaluate the geosite and promote the geotourism in the Ban Nong Khrok hot springs. The Ban Nong Khrok geosite potential evaluation is assessed by the geo-expert researchers. Geotourism is natural tourism and focuses on the geologic landscape (landforms, rock outcrops, rock types, sediments, soils and crystals) and geologic processes (volcanism, erosion, and glaciation)¹. Geotourism is tourism that sustains or enhances the distinctive geographical character of a place's environment, heritage, aesthetics, culture, and the well-being of its residents. Geotourism is consistent with



the sustainable development goals (SDGs) in inclusive and equitable quality education and promotes lifelong learning opportunities for all and healthy lives and well-being for all ages. The geosite is the geological resource that is suitable for geotourism attraction development. Geosite was carried out based on geoheritage values of international significance. The qualitative and quantitative assessments for geoconservation efforts should be made in all these geosites for many reasons, such as valorization of academic research, preservation of natural resources, and promotion of geotourism². In Thailand, the geosites were evaluated based on the Department of Minerals Resources (DMR) with DMR geosite assessment form. The DMR geosite assessment form assessed the Main values (scientific and specific type values) and the additional values (management and development). The DMR identified the geosites into seven types-typical minerals, typical rocks, geological structures, geomorphology, hot spring, type section, and fossil. The Ban Nong Khrok hot spring is classified as the hot spring geosite and assessed based on scientific values such as geological significance, geodiversity, rarity, and geological history and specific type values such as water flow volume and continuity, temperature, and geologic reference. The additional values are advantageous for sustainable development and tourism promotion management. The Additional value indicators are the suitability of size and boundary, accessibility, tourism infrastructure, security, community involvement, economic importance, knowledge transferring, zoning, protection from destruction, developing potential, and additional attractions. This study aims to analyze the characteristics of hot springs in terms of geology, geochemistry, and the potential for a geosite development. The scientific values are knowledge transferred to the Nong Khrok village community for development and management planning.

Methodology:

The geologic and hot spring investigation and geotourism evaluation were done in the Ban Nong Khrok Hot Springs Attraction, the Bamboo Spa, and the Nong Khrok village in May 2023. The sampling locations were located by handheld GPS device. The hot spring investigations aimed to in-situ physical properties parameters measuring and the hot water samples collecting for chemical analysis in the laboratory. The in-situ parameters measuring used the electrometric method with the portable waterproof, HANNA brand, model HI9125 for pH and temperature (°C) values and the electric conductivity (EC) meter, HANNA brand, model HI8733 for conductivity (µs/cm) value. The electrometric probes were washed with distilled water before being placed in the hot spring water source for the in-situ measurements. The four hot spring samples from the hot spring and Bamboo spa supply water were collected into the sampling water bottles for chemical analysis in the laboratory. The water sampling bottles were washed with 10% HCL acid (diluted) before placing the water samples. Each water samples were placed 500 ml hot water and 0.5 ml HNO₃ in the bottles for major cation (Ca, Mg, Na, K, Fe, Mn) analysis and 1,000 ml hot water in the bottles for major anion (Cl, HCO₃, CO₃, SO₄) analysis. The water samples were transferred into a cooling box and stored in a refrigerator at 20°C.

The total dissolved solid (TDS), cation (Na, K, Ca, Mg, Fe, and Mn) concentrations, and anion (Na, K, Ca, Mg, Fe, and Mn) concentrations were analyzed at the Geochemical Laboratory of Geological Science, Faculty of Science, Chiang Mai University. The TDS analysis used the dried method at 180 °C. The cation concentrations were analyzing by the PerkinElmer AAnalyst 200 Atomic Absorption Spectroscopy (AAS) with an accuracy of up to mg/l. The anion concentrations as the chloride (Cl) concentration were analyzed by the argentometric titration method with an accuracy of up to mg/l, the carbonate (CO₃) and



bicarbonate (HCO_3) concentrations were analyzed by titration method, and the SO_4 concentration was analyzed by turbidimeter (waterproof infra-red turbidimeter of Eutech Instruments model TN-100) with 0 to 1000 NTU.

The geosite potential evaluation used the geosite assessments model based on Thailand's DMR manual. Thailand's geosite assessments model (TH-GAM) indicators are composed of the Main Values (*MV*) and the additional values (*AV*). The *MV* indicators are dependent on the geosite's natural characteristics, and the *AV* indicators are human-induced that generated by modifications for use by visitors. The *MV* is composed of a group of scientific/educational (*VES*) indicators, and the *AV* consist of groups of functional values (*VFn*), protection values (*VPr*), and tourism values (*VTr*) indicators.

The geosite potential evaluation relied upon the weighted score method that evaluates following the equation (1). The sum of the weight of indicators is the multiple of the indicator's weight relative to others and the indicator's significance, which ranged from 1 to 5 in this case.

$$V_j = \sum W_k S_{jk} \quad (1)$$

V_j : Sum of the indicator's weight

W_k : Weight of indicators relative to other indicators

S_{jk} : Indicator's significance, ranging from 1 to 5 in this case

The assessment criteria in this research are the high potential scores ranging from 75 to 100, the moderate potential scores ranging from 50-74, and the low potential scores ranging from 0 to 49. Thailand's geosite assessment model (TH-GAM) and the indicator's weight for hot springs are shown in Table 1. The TH-GAM for the hot spring type was used for the Nong Khrok Hot Spring Attraction and was done in November 2022 and August 2023 by geo-experts. In addition, the SWOT analysis in the internal and external factors assessments. The SWOT analysis also included extensive observations of developments after the COVID-19 pandemic.

Results and Discussion:

Geological investigation for Ban Nong Khrok hot spring attraction area and vicinity is composed of six rock units (Figure 1) the lower Carboniferous sedimentary rock unit (C1), the upper Carboniferous sedimentary rock unit (C2), the Permian limestone unite (Pm), the Triassic granite (Trgr), Quaternary sedimentary rock unit (Qt), and Quaternary sediments unit (Qa). The Ban Nong Khrok hot spring attraction has found a geothermal water spring out by the Nong Khrok fault in the lower Carboniferous rock unit. The hotspring investigation found that the geothermal water springs out of several holes. The flow rate of a hot spring is 12 liters per minute, which is suitable for the spa business. The local community zoned the area and built up the hot spring pond and its facilities (Figure 2). There are four hot spring ponds (nos. 1, 2, 3, and 4), the rest pond (decreasing temperature pond) (no. 5), and the supply water in the Sai Nam Oon community homestay and the Bamboo spa through a PVC tube from the hot spring (no. 6). The landscape is suitable for use and has a geothermal water supply system by PVC tube to the Ban Nong Khrok village and the Bamboo spa.

Table 1. Thailand's Geosite Assessment Model (TH-GAM) and the weight of indicators (W_k) for hot springs.

TH-GAM Indicators	1	2	3	4	5	W_k
Main Values (MV)						
Scientific/Educational Value (VSE)						
1. Geoscientific issues outstanding	none	province	regional	national	international	15
2. Geodiversity (types of geosites)	none	> 1 type	> 2 types	> 3 types	> 4 types	10
3. Rarity	none	province	regional	national	international	20
4. Representativeness of geologic history	none	paleoenvironment	geologic time, geologic event	Paleoenvironment, geologic event	Paleoenvironment, geologic time, geologic event	15
The geosite's natural characteristics of Hot Spring						
5. Flow rate and characterizing flow	<<50 l/min., discontinuous flow	<50 l/min., discontinuous flow	<50 l/min., continuous flow	>50 l/min., discontinuous flow	>50 l/min., continuous flow	20
6. Temperature	<40°C	40-80°C	80-90°C	90-100°C	>100°C	10
7. Geoscientific references	none	province	regional	national	international	10
Additional Values (AV)						
Functional values (VFn), Touristic Value (VTr), and Protection (VPr)						
1. Suitability of the size and boundary of the area	<500 m ² , not clear boundaries	<500 m ² , clear boundaries	500-1,000 m ² , not clear boundaries	500-1,000 m ² , clear boundaries	>1,000 m ² , clear boundaries	10
2. Accessibility: Possibilities of approaching to the site (convenient to accessibility, good direction signs, and no environmental change)	inconvenient to accessibility, no direction signs, and environmental change	convenient to accessibility, poor direction signs, and environmental change	convenient to accessibility, good direction signs, but environmental change	convenient to accessibility and no environmental change but poor direction signs	convenient to accessibility, good direction signs, and no environmental change	10
3. Tourism infrastructure: Level of additional infrastructure for tourist (1. pedestrian pathways, 2. toilets, and 3. parking lots)	none	1 infrastructure	2 infrastructures	3 fair infrastructures	3 good infrastructures	10
4. Security measures: safety for tourists in geosite and vicinity, having a safety officer	none	low	medium	high	high with security grads	10
5. Community Involvement in area management and conservation	none	low with no geoscientific knowledge	medium with low geoscientific knowledge	high with moderate geoscientific knowledge	high with high geoscientific knowledge	10
6. Economic significance: New business from geosite, local guides employment, sustainable community management	none	new business, non-local guides employment	no new business, local guides employment	new business, local guides employment	new business, local guides employment, sustainable community management	10
7. Geoscientific information panels, promotion and local guides	none	information signs/ fair local guides	information signs and local guides	information signs and good local guides	information signs and expert local guides	5
8. Area zoning: good area zoning and good information sign, geosite staff	none	no zoning, no sign, geosite staff	zoning, no sign, geosite staff	zoning, sign, no geosite staff	zoning, sign, geosite staff	5
9. Invulnerability (the need for protection from destroy)	none	low (destroy within 100 years)	medium (destroy within 10 years)	high (destroy within 5 years)	Very high (destroy within 3 years)	15
10. Acceptable changes (development potential)	none	low	medium	high	very high	10
11. Additional natural values	none	1-2 sites	3 sites	4 sites	>5 sites	5

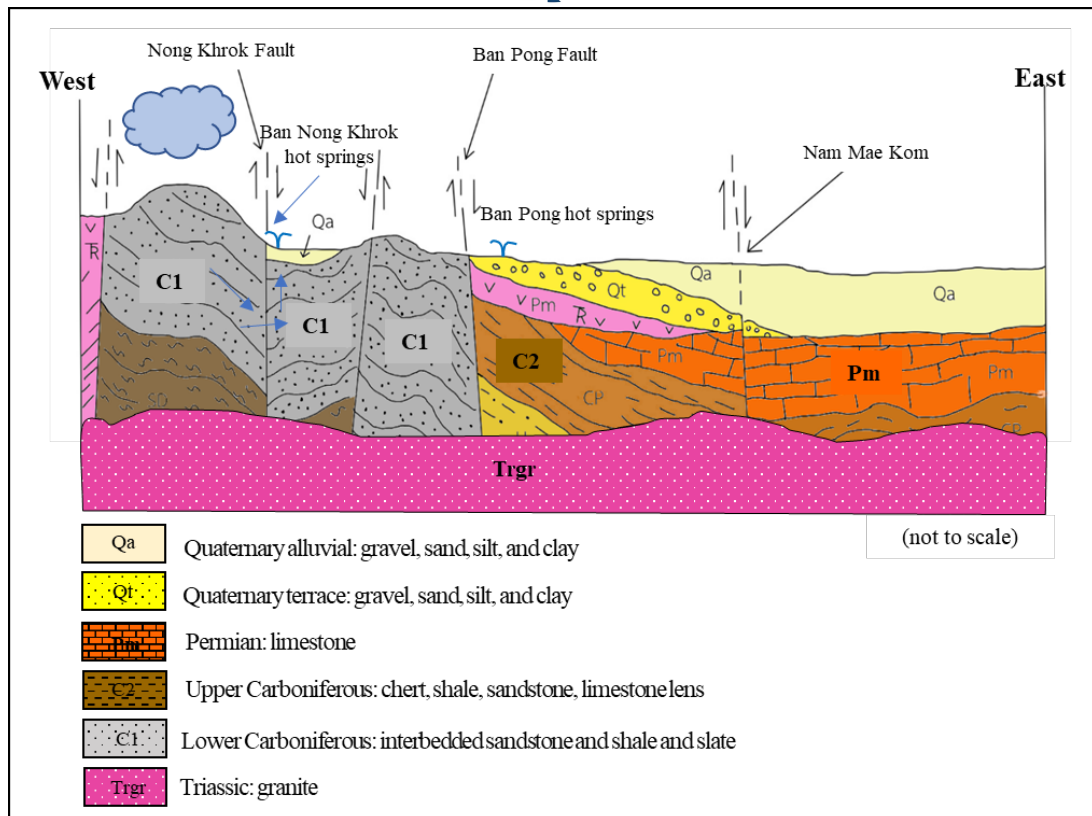


Figure 1. Geologic cross section and hot spring formation model of the Ban Nong Krok hot spring Tourist Attraction, Phrao District, Chiang Mai Province.

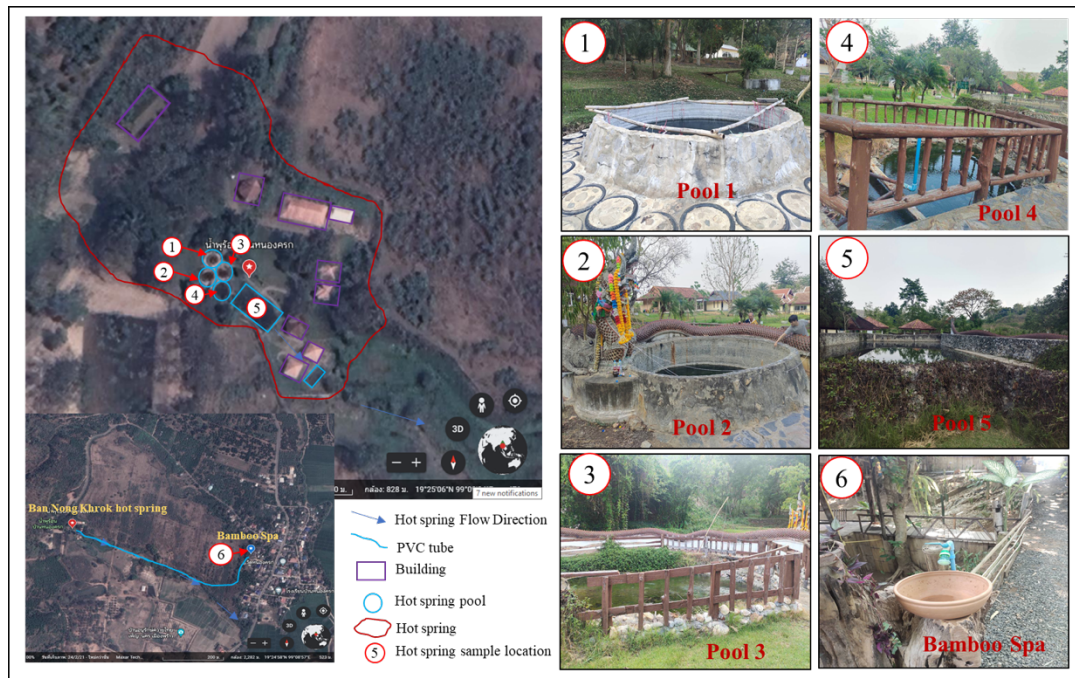


Figure 2. Hot spring water sample location of the Ban Nong Khrok Hot Springs Tourist Attraction and Bamboo Spa, Phrao District, Chiang Mai Province.

The physical properties are the in-situ parameters that are analyzed in the field as surface temperature (T), pH, and electric conductivity (EC) (Table 2). The surface of the hot springs ranges from 56 - 68.1 °C. The maximum surface temperature of pond number 1 is 68.1 °C, suitable for egg boiling. The temperatures of the pond are ranging from 64.70 to 67.70 °C. The other rest pond has lower temperatures to keep the water warm so that it is suitable for use, such as pond no. 5. The surface temperature of the Ban Nong Khrok Attraction is hyperthermal springs, based on the Thailand geothermal springs classification. The temperatures of the Sai Nam Oon community homestay and the Bamboo spa supply water are 38.5 °C, classified as a thermal spring suitable for hydrotherapy. The pH values of the hot spring samples range from 7.11 - 7.93, classified as a weak alkaline hot spring and bicarbonate alkalinity. Geochemistry of four hot spring water samples was done on two hot spring water samples (nos. 1 and 2), a rest pond sample (no. 5), and a supply of water samples in a Bamboo spa through a PVC tube from the hot spring (no. 6) (Figure 2). The EC in geothermal water refers to the ability of water to conduct an electric current that is determined by the ionic content of dissolved solid concentration. Sample no. 2 has the highest conductivity, while sample no.6 has the lowest TDS values.

The chemical concentration of total dissolved solids (TDS) and the major ions (Na, K, Ca, Mg, Fe, Mn, Cl, F, HCO₃, CO₃, and SO₄) was analyzed in a laboratory and shown in Table 3. The TDS of geothermal water samples ranged from 553 (sample no. 6) to 586 mg/l (sample no. 1), with 572.50 mg/l on average. All water samples are freshwater based on TDS classifications. The total hardness calculated from the 2.497 Ca + 4.115 Mg equation ranged from 75.07 to 88.24 mg/l with an average of 82.67 mg/l. The geothermal water samples were moderately in hardness. The Na content of geothermal water ranges from 166.60 to 185.00 mg/l with an average of 174.05 mg/l. The K content of geothermal water ranges from 13.17 to 17.80 mg/l, with an average of 15.16 mg/l. The Ca content of geothermal water ranges from 22.07 to 27.14 mg/l, with an average of 25.22 mg/l. The Mg content of geothermal water ranges from 4.69 to 7.85 mg/l, with an average of 4.79 mg/l. The Fe content of geothermal water ranges from 0.12 to 2.86 mg/l, with an average of 0.82 mg/l. Fe content of less than 1.0 mg/l (the standard drinking water of the Groundwater Act in 1991) except pond number 1 is thermal water samples. The Mn content of geothermal water ranges from 0.08 to 0.16 mg/l, with an average of 0.01 mg/l. The Cl content of geothermal water ranges from 0.72 to 6.51 mg/l, with an average of 3.41 mg/l. The sulfate (SO₄) content of geothermal water ranges from 13.75 to 20.13 mg/l, with an average of 16.86 mg/l. Bicarbonate (HCO₃) geothermal water content ranges from 465.47 to 497.83 mg/l, with an average of 484.76 mg/l. Hot springs have HCO₃ content higher than the average of Thailand's thermal water. The chemical reaction of geothermal water flows through wall rocks, such as limestone and dolomite. The CO₃ content of geothermal water ranges from 20.81 to 26.52 mg/l, with an average of 22.65 mg/l.

Table 2. The in-situ parameters (conductivity, temperature, and pH) of the research area.

Sample Number	Conductivity (ms/cm)	Temp. °C	Classification	pH	Classification
1. hot spring pond 1	1285	68.10	Hyper thermal	7.11	Neutral spring
2. hot spring pond 2	1307	67.60	Hyper thermal	7.23	Neutral spring
3. hot spring pond 3	1285	66.20	Hyper thermal	7.25	Neutral spring
4. hot spring pond 4	1258	64.70	Hyper thermal	7.43	Neutral spring
5. hot spring pond 5	1190	56.30	Hyper thermal	7.93	Weak alkaline spring
6. Bamboo spa	1031	38.50	Thermal	7.91	Weak alkaline spring

Table 3. The concentration of major ions (mg/l) in the Ban Nong Khrok hot springs.

Sample Number	1	2	5	6	Average
TDS	586	578	553	573	572.50
Total hardness	83.75	88.24	83.64	75.07	82.67
Na	178.0	166.6	166.6	185.0	174.05
K	17.80	15.03	14.63	13.17	15.16
Ca	25.81	27.41	25.57	22.07	25.22
Mg	4.69	4.81	4.81	4.85	4.79
Fe	2.86	0.15	0.16	0.12	0.823
Mn	0.08	0.16	0.09	0.08	0.103
Cl	0.85	0.72	5.54	6.51	3.41
HCO ₃	494.50	497.83	465.47	481.24	484.76
CO ₃	21.22	20.81	26.52	22.03	22.65
SO ₄	13.75	13.81	20.13	19.73	16.86

The Piper diagram⁴, Cl-SO₄-HCO₃ ternary diagram⁵, and K-Na-Mg ternary geothermometer diagram⁶ (Figure 3a) were used to classify the geothermal spring water samples. The hydrochemical facies were classified by Piper diagram⁴, which shows the bicarbonate geothermal water. The Cl-SO₄-HCO₃ ternary diagram⁵ used for the types of water classification by major anion that all geothermal spring water samples plot in the bicarbonate water field (Figure 3b), indicating a process of mixing with the near-surface groundwater during their ascent to the surface. All geothermal spring water samples are plotted in the immature area of the Mg-Na-K ternary diagram⁶ (Figure 3c), which means they are chemically not in equilibrium (the water mixed with meteoric water and groundwater).

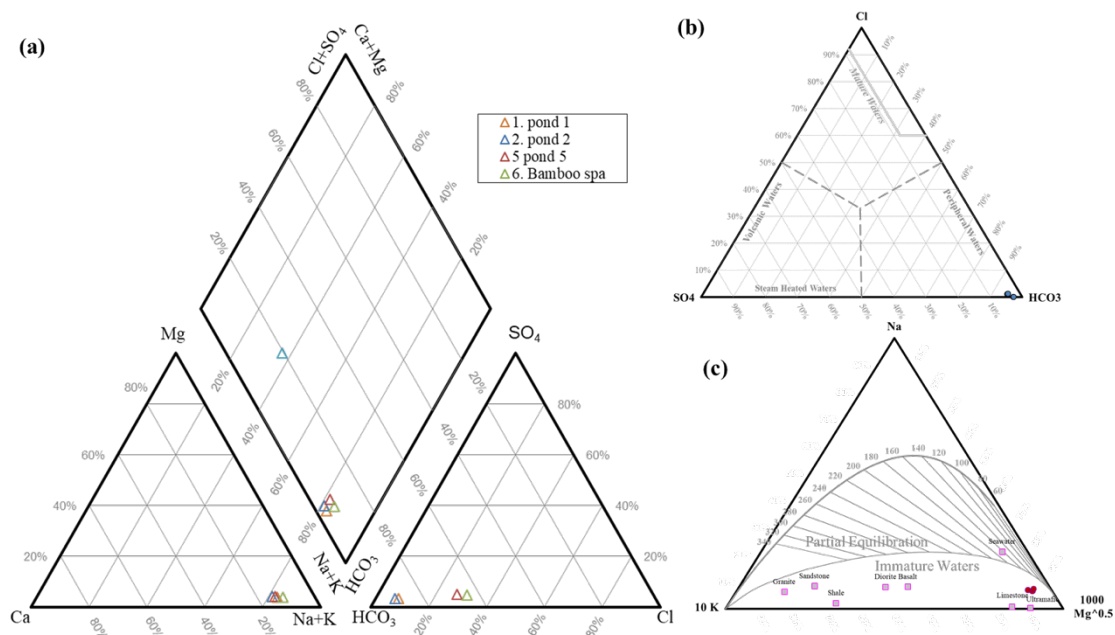


Figure 3. Geochemical diagram classification of hot spring water samples of the Ban Nong Khrok Hot Springs (a) Piper diagram⁴ (b) Cl-SO₄-HCO₃ ternary diagram⁵ and (c) Na-K-Mg ternary geothermometer diagram⁶.

Hot springs are a geothermal resource that add value to tourist destinations and attract visitors^{7,8}. The potential evaluation of geotourism is shown in Table 4. The weighting score for the main values of hot springs is divided into 60% scientific values and 40% special values. The assessment of the Ban Nong Khrok hot springs following the TH-GAM and the sum of weight score method is 36% of main values (18% scientific values and 18% special values for hot springs), which are low potential values. The additional values are functional, tourist values, and protection values. The assessment shows 90% additional values, which are high potential values. The potential assessment of the geosite in the Ban Nong Khrok Attraction shows low-potential academic values and high-potential additional values. This research is knowledge transfer to the local community by hot spring scientific sign panel and continuous monitoring of the tourist behaviour by QR code on sign panel. The advantages of this research are increasing the score of additional values, the local community sustainable development plans and the sustainable natural resources management.

In addition, the SWOT Analysis indicated that the strength is the Sai Nam Oon community homestay and the Bamboo spa are managed by the local community, the tourism activities of the Sai Nam Oon Village (the local way of life experience), and the support by the Northern Science Park to be an agricultural and health tourism community. The weakness

Table 4. Thailand's Geosite Assessment Model of the Ban Nong Khrok Hot Springs Attraction.

TH-GAM Indicators	W _k	S _{jk}	W _k S _{jk}	Remark
Main Values (MV)				
Scientific/Educational Value (VSE)				
1. Knowledge of geoscientific issues	15	1	3	not outstanding
2. Geodiversity	10	1	2	1 type of geosite within 3 km
3. Rarity	20	1	4	not outstanding
4. Representativeness	15	3	9	Nong Khrok fault (only special geologic event)
The geosite's natural characteristics of Hot Spring				
5. Flow rate and characterizing flow	20	3	12	12 lite/minute (less than 50 liter/minute)/ continuous (suitable for spa)
6. Temperature	10	2	4	66-69 °C (temperature between 40-80 °C)
7. Geoscientific references	10	1	2	not outstanding
ΣW_k(%)	100	V_j	36	Assessment Criteria: low-potential
Additional Values (AV)				
Functional Values (VFn), Touristic Values (VTr), and Protection Values (VPr)				
1. Suitability of the scope and size of the area	10	5	10	3,500 m ² (more than 1,000 m ²)
2. Accessibility	10	5	10	convenient to accessibility, good direction signs, and no environmental change
3. Tourism infrastructure	10	4	8	convenient to accessibility in geosite, toilets, more parking
4. Security measures	10	4	8	safety for tourists in geosite and vicinity, not having a safety officer
5. Community Involvement in area management and conservation	10	5	10	high community involvement in area management and conservation
6. Economic significance	10	4	8	hot water supply through PVC tube for Bamboo spa and Sai Nam Oon community homestay (not sustainable)
7. Geoscientific information panels, promotion, and local guides	5	2	2	the level rises up from 1 to 2 after this research and should be promoted by the local guides
8. Area zoning	5	4	4	good area zoning and good information sign but non-officer
9. Invulnerability (the need for protection from destroy)	15	5	15	may be destroyed within 3 years
10. Acceptable changes (development potential)	10	5	10	high development potential
11. Additional natural values	5	5	5	Bamboo spa, Thai Buffalo Conservation home, Ban Pong hot spring, organic mango farm, local activity, local food cooking (more than 5 attractions)
	100	V_j	90	Assessment Criteria: high-potential



is no dissemination of academic knowledge in geology and health sciences, and the currently renovated for the convenience of tourists. The opportunities are a part of the Phrao Model project that aims to develop the community through the local wisdom to develop community-based health and agricultural tourism after recovering from the COVID-19 pandemic. The threats are several well-known hot spring attractions for tourists in Chiang Mai province and in the process of re-opening services after the COVID-19 pandemic.

Table 5. SWOT analysis of geotourism in the Ban Nong Khrok hot springs attraction.

Strengths	Opportunities
<ul style="list-style-type: none"> • The Sai Nam Oon community homestay and the Bamboo spa are managed by the local community. • Tourism activities of the Sai Nam Oon Village (the local way of life experience) • The Ban Nong Khrok tourism community has been supported by the Northern Science Park to be an agricultural and health tourism community. 	<ul style="list-style-type: none"> • This geosite is in the area of the Phrao Model project that was established from the needs of the community and searching for wisdom to develop community-based health tourism. • Promoting agricultural and health tourism after recovering from the COVID-19 pandemic.
Weaknesses	Threats
<ul style="list-style-type: none"> • There is no dissemination of academic knowledge in geology and health sciences. • The attraction is currently being renovated for the convenience of tourists. 	<ul style="list-style-type: none"> • Chiang Mai province has a number of well-known hot spring attractions for tourists. • Currently in the process of opening services after the COVID-19 pandemic.

Conclusion:

The geotourism is a way to integrate the geological significant value and sustainable resource management. Therefore, scientific research for the geological resource is necessary for geosite assessment. The Ban Nong Khrok Hot Springs attraction is a part of the Ban Nong Khrok village area, Phrao District, Chiang Mai Province and is the hot spring geosite. The Ban Nong Khrok hot spring attraction has found a geothermal water spring out by the Nong Khrok fault in the lower Carboniferous rock unit. The physical characteristic of the hot spring is high-temperature hot springs (hyperthermal) with low quantity and continuous water flow that are suitable for spa business. The hot water supply of the hot spring and the Sai Nam Oon village tourism community and Bamboo spa hot water supply is the mixing of infiltrating water from rainwater and surface water and groundwater. The groundwater percolates deeply enough into the crust by the Nong Khrok fault, and it comes into contact with hot rock and circulates to the ground surface. The Ban Nong Khrok Hot Spring is a general hot spring based on chemical concentration. The pH value is neutral to weakly alkaline, suitable for health spa tourism or hydrotherapy. The geosite potential assessment of the Ban Nong Khrok hot springs attraction has low academic geological values but high management and development values. The SWOT analysis indicated that the strengths and sustainable competitive advantage are the Sai Nam Oon hot spring community homestay and the Bamboo spa. The weakness of geosite was the lack of academic knowledge dissemination in geological and health sciences. This scientific research on hot springs and geological knowledge transferring increased the TH-GAM scores and reduced the weaknesses. This research is a model for geological attractions developing in low academic value geosite by the local community.



Acknowledgements:

The authors would like to thank the Ban Nong Khrok village community and the San Sai Subdistrict Administrative Organization. The authors are grateful for the research funding provided by the Faculty of Science, Chiang Mai University.

References:

1. Dowling RK, Geotourism's Global Growth, *Geoheritage*, 2010;doi:10.1007/s12371-010-0024-7
2. Mirari S, Aoulad-Sidi-Mhend A, Benmlih A, Geosites for Geotourism, *Geoheritage*, and Geoconservation of the Khnefiss National Park, Southern Morocco Sustainability 2020, 12(17), 7109;https://doi.org/10.3390/su12177109
3. Subtavewung P, Raksaskulwong M, Tulyatid J, The Characteristic and Classification of Hot Springs in Thailand. *Proceedings World Geothermal Congress Antalya Turkey*. 2005:1-7
4. Piper AM. A graphic procedure in the geochemical interpretation of water-analyses. *Eos, Transactions American Geophysical Union*. 1944;25:914-928.
5. Giggenbach WF, Chemical techniques. In *Application of geochemistry in geothermal reservoir development*, (Ed) D'Amore, United Nation Institute for Training and Research, USA. 1991;119-144.
6. Giggenbach WF. Geothermal solute equilibria. Derivation of Na-K-Mg-Ca geoindicators. *Geochim. Cosmochim. Acta*. 1988;52:2749-65.
7. Erfurt-Cooper P. The importance of natural geothermal resources in tourism. *Proceedings World Geothermal Congress 2010 Bali, Indonesia*, 25-29 April. 2010;1-10.
8. Ngansom W and Duerrast H. Assessment and Ranking of Hot Springs Sites Representing Geothermal Resources in Southern Thailand using Positive Attitude Factors. *Chiang Mai J. Sci*. 2019;46(3):592-608.

GROUNDWATER CHARACTERISTICS AND CHEMISTRY OF THE SALINE AREA IN BAN THUM, KHON KAEN PROVINCE

Sutthipong Taweelarp*, Munlika Srichalee, Thanakrit Klungudom, Potpreecha Pondthai
Department of Geotechnology, Faculty of Technology, Khon Kaen University, Thailand
*e-mail: sutthita@kku.ac.th

Abstract:

Rapid urbanization in Ban Thum subdistrict, Mueang Khon Kaen district has increased the risk of widespread groundwater and soil salinity problems. The goal of this study is to evaluate the hydrogeological characteristics and groundwater chemistry of Ban Thum, in order to develop plans for sustainable groundwater use and address contamination issues. Hydrogeological data and twenty groundwater samples were collected and analyzed to determine the physico-chemical parameters, total dissolved solids, major cations, major anions, and trace metal ions. The results showed that the primary groundwater flow was from the northeastern to the southwestern part of the study area. Nevertheless, the presence of multiple cones of depression in the central region and a high hydraulic head area in the south resulted in groundwater movement from the south towards the central region. Based on TDS measurements, most of the groundwater samples fell into the fresh category, while some samples fell within the brackish water category. A comprehensive analysis of groundwater chemistry revealed multiple processes, including inflowing water recharging the aquifer, saltwater mixing, ion exchange along the flow path, and the influence of geological, mineralogical, and various geochemical environments. The predominance of the sodium-chloride facies in the hydrochemical distribution suggests the impact of halite dissolution within the groundwater system. Additionally, the Durov diagram shows potential processes, including dissolution or mixing, while the Gibbs diagram indicates that rock weathering is the primary influencer of groundwater composition.

Introduction:

Groundwater is a significant source of water for domestic, industrial, and agricultural usage. In numerous parts of Thailand where the supply of surface water is constrained, population growth, urbanization, industrialization, and agricultural expansion have increased the demand for groundwater resources. This trend is particularly pronounced in the northeastern Thailand. In addition to a high demand for water, this area encounters issues associated with water quality problems.

In northeastern Thailand, salinity stands out as a major challenge¹, arising from both natural processes and human activities. Natural factors include the presence of rock salt deposits, saline water, and groundwater flow, while human actions, such as deforestation, groundwater extraction, local salt production, and extensive irrigation, contribute to the issue.^{2,3,4,5} Due to its fast urbanization, Ban Thum subdistrict, Mueang Khon Kaen district in particular faces these significant issues. Additionally, some places in this region experience problems with soil salinity that obstruct common agricultural activity. The region has seen an increase in water demand over time, which has increased the risk of widespread soil salinity, saline groundwater, and groundwater contamination. The growth of residential communities and industrial facilities is closely related to these difficulties. This study aims to investigate the hydrogeological characteristics and assess the groundwater chemistry in the Ban Thum area, with the goal of planning for groundwater utilization and addressing future groundwater contamination issues in the local community.

Methodology:

Study Area

The study area (**Figure 1**) is located in the southern part of Ban Thum subdistrict, Mueang Khon Kaen district, Khon Kaen province. This region is rapidly urbanizing, with several new communities and numerous industrial industries present. The surficial layer of the study area consists of unconsolidated materials, specifically Quaternary alluvial and terrace soils, which vary in thickness from a few meters to over 5 m. The Quaternary sediments overlie mudstone, siltstone, and rock salt of the Maha Sarakham formation. This formation comprises four distinct salt units, primarily composed of basal anhydrite, lower salt, potash zone, a variegated salt unit, lower clastic, middle salt, middle clastic, upper salt, and upper clastic. Their thicknesses vary from 10 m. to over 200 m., contingent upon the local geological structure's association with rock salt deposition.⁵ In this area, shallow groundwater is found within the unconsolidated aquifer, which can be classified as either unconfined or semi-confined aquifer.⁶ The semi-confined aquifer is composed of fracture zones that have developed within the clastic sedimentary rocks.

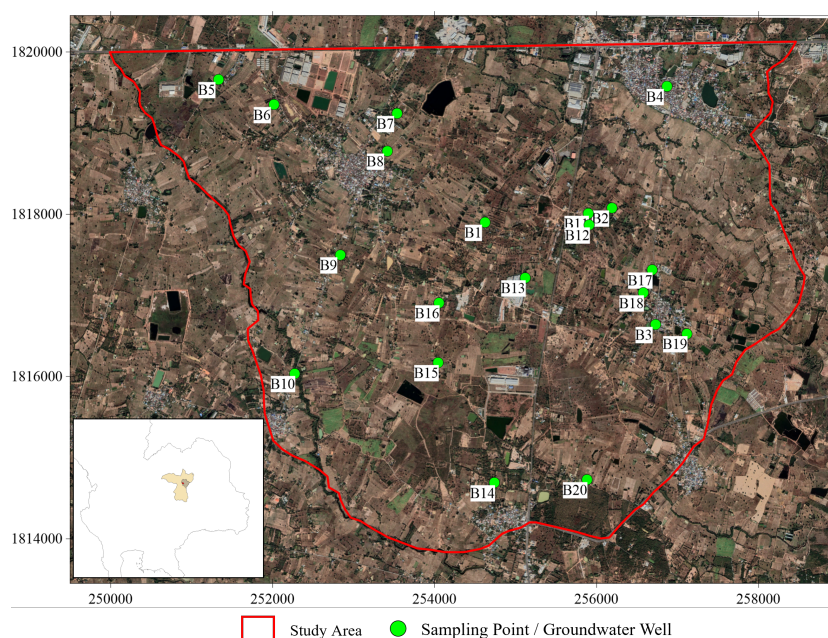


Figure 1. The location of the study area and the distribution of sampling points.

Groundwater Sampling

Twenty groundwater samples were collected from the study area in January 2023 at the well locations shown in **Figure 1**, using high-density polyethylene plastic containers. The well locations were established using RTK GNSS positioning systems. In-field measurements were conducted in order to determine the depth to the water table and assess certain properties of water samples, which comprised pH, electrical conductivity (EC), and temperature. Additionally, water samples were stored and preserved in both acidified and non-acidified bottles.

Analytical methods

The chemical analyses of water samples were carried out at the Geochemical Laboratory of the Department of Geotechnology, Faculty of Technology, Khon Kaen University, following the standard methods for the examination of water and wastewater outlined by the American Public Health Association. In the laboratory, the total dissolved solids (TDS) of water

samples were analyzed by drying them at 180°C. Major anions, including Cl^- , CO_3^{2-} , and HCO_3^- , and total hardness were determined through titration, while NO_3^- and SO_4^{2-} were analyzed using a UV-Visible Spectrophotometer. Major cations (Ca^{2+} , Mg^{2+} , K^+ , and Na^+) and trace metals, including Cd^{2+} , Cu^{2+} , Fe^{2+} , Mn^{2+} , Pb^{2+} , and Zn^{2+} , were determined using an Atomic Absorption Spectrometer. The accuracy of the chemical analyses for the cation-anion balance was verified using the ion balance equation. The ion balance errors for the analyzed samples were found to be below 5%, which is acceptable.

Results and Discussion:

Hydrogeological Characteristics

The data collected during the fieldwork can be used to calculate the hydraulic heads in the study area, as depicted in **Figure 2**. The hydraulic head in this area ranges from 130.94 to 205.90 meters above mean sea level. The primary direction of groundwater flow is from the northeastern part to the southwestern part of the study area, towards the Khong Yai and Khong Nam Chan. However, it exhibits several cones of depressions in the central region, and there is a high hydraulic head area in the southern part. This leads to the groundwater flowing from the south to the central part of the study area. The areas with lower hydraulic heads (Ban Lao Kwian Hak and Ban Daeng Noi) are associated with communities that have a high rate of groundwater extraction. In areas with high hydraulic heads, which are also affected by salinity issues in both soil and groundwater, the local population is unable to use the groundwater for domestic consumption or agricultural purposes. This situation results in higher groundwater levels compared to other areas.

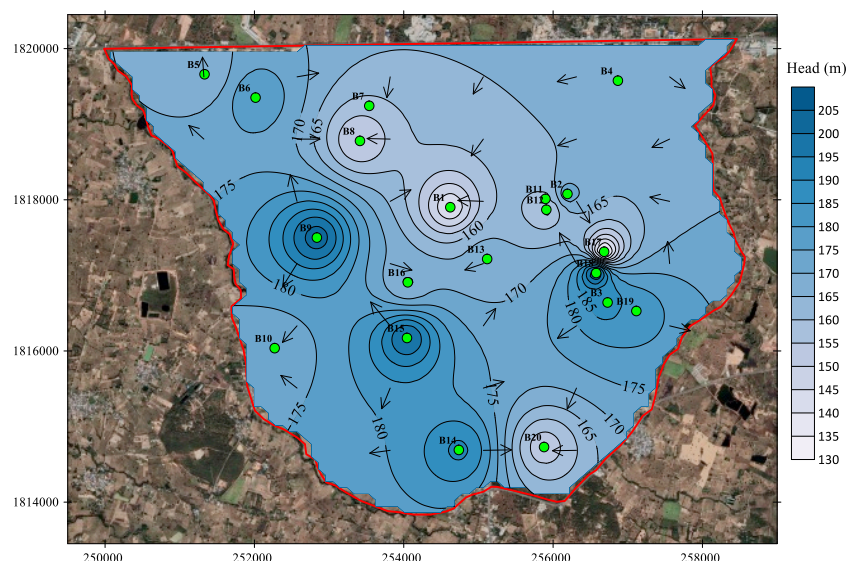


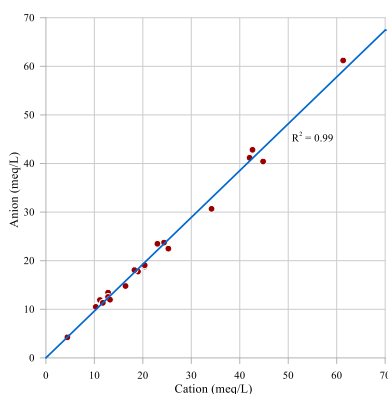
Figure 2. Groundwater contour map and groundwater flow directions of the study area

Groundwater Chemistry

Water chemistry parameters of groundwater samples and their basic statistical summaries are presented in **Table 1**. The results from a plot comparing ionic charges between cations and anions (**Figure 3**) demonstrate the accuracy and reliability of the analytical datasets. The correlation matrix in **Table 2** was used to understand the interrelationships among physicochemical parameters, different ions, their species, and to trace the source of origin.

Table 1. Chemical analysis for major ion concentrations of groundwater samples.

Sample	EC ($\mu\text{S}/\text{cm}$)	pH	Concentration (mg/L)												
			TDS	CO_3^{2-}	HCO_3^-	SO_4^{2-}	Cl^-	NO_3^-	Ca^{2+}	Na^+	K^+	Mg^{2+}	Fe^{2+}	Mn^{2+}	Zn^{2+}
B1	2,202	5.78	948	0	462	5.71	355.7	2.44	165.9	207.5	3.83	19.45	< 0.04	0.086	< 0.006
B2	1,926	6.99	928	0	494	8.40	345.9	2.26	131.4	212.6	3.78	28.75	< 0.04	< 0.016	< 0.006
B3	4,493	6.95	3,740	0	260	32.69	1,992.4	3.81	591.4	525	7.68	99.30	9.15	< 0.016	4.454
B4	2,066	7.47	1,204	0	364	111.43	338.09	59.76	84.91	215.8	159.9	32.15	< 0.04	< 0.016	< 0.006
B5	2,394	7.35	1,204	0	520	10.08	530.27	2.52	136.2	354.4	4.35	24.82	0.11	< 0.016	< 0.006
B6	1,171	7.71	600	40	594	7.31	124.96	2.79	39.58	310.9	4.30	10.01	< 0.04	< 0.016	< 0.006
B7	2,328	7.38	1,120	0	506	12.94	527.58	2.35	161	284.2	3.01	30.68	0.38	< 0.016	< 0.006
B8	3,118	7.08	2,256	0	334	12.10	1,224.62	9.03	170.3	772	5.15	30.60	2.43	< 0.016	< 0.006
B9	1,009	7.43	508	0	552	5.88	149.95	2.13	85.57	153.8	3.47	21.68	< 0.04	< 0.016	< 0.006
B10	475.1	6.83	244	0	162	6.30	50.434	1.95	45.06	31.51	1.20	9.58	< 0.04	< 0.016	< 0.006
B11	3,119	6.67	2,724	0	400	8.15	847.11	2.92	445.7	80.9	2.46	97.75	8.63	< 0.016	0.036
B12	1,910	6.99	904	0	414	5.71	429.62	2.26	101.2	305	3.87	23.91	< 0.04	< 0.016	< 0.006
B13	854.1	7.64	432	36	386	5.38	149.95	2.35	69.9	154.6	3.11	10.46	< 0.04	< 0.016	< 0.006
B14	859.2	7.40	440	0	458	4.96	130.38	2.48	53.01	188.4	3.24	9.94	< 0.04	< 0.016	< 0.006
B15	916.9	7.90	524	40	480	5.04	113.38	2.26	31.36	250	4.51	3.26	0.05	< 0.016	< 0.006
B16	803.8	7.58	416	0	450	4.62	105.83	2.26	65.2	133.7	4.27	13.46	< 0.04	< 0.016	< 0.006
B17	1,944	6.97	968	0	372	5.55	574.82	3.41	185	307.5	5.30	30.72	< 0.04	< 0.016	< 0.006
B18	4,240	6.69	2,816	0	410	12.52	1,203.20	15.85	301.1	502.1	5.99	60.86	< 0.04	< 0.016	< 0.006
B19	3,740	6.58	2,944	0	380	7.56	1,280.30	19.43	372.7	406.3	7.19	75.01	< 0.04	< 0.016	< 0.006
B20	939.3	7.09	540	0	502	6.72	124.96	5.27	88.19	162.4	3.14	20.17	0.59	< 0.016	< 0.006
Min	475.1	5.78	244	0	162	4.62	50.43	1.95	31.36	31.51	1.20	3.26	0.05	0.086	0.036
Max	4,493.0	7.90	3,740	40	594	111.43	1,992.4	59.76	591.4	772.0	159.9	99.30	9.15	0.086	4.454
Mean	2,025.4	7.12	1,273	5.8	425	13.95	529.97	7.38	166.23	277.93	11.99	32.63	3.05	0.086	2.245
S.D.	1,170.7	0.47	1,003.7	13.83	98.18	23.16	510.45	12.89	146.09	168.32	33.97	27.54	3.77	0.0	2.209

**Figure 3.** Comparison between sum of anions (meq/L) and sum of cations (meq/L)**Table 2.** Correlation coefficient matrix of chemical data of groundwater samples.

	EC	pH	TDS	HCO_3^-	SO_4^{2-}	Cl^-	NO_3^-	Ca^{2+}	Na^+	K^+	Mg^{2+}	TH
EC	1											
pH	-0.50	1										
TDS	0.96	-0.44	1									
HCO_3^-	-0.27	0.32	-0.36	1								
SO_4^{2-}	0.19	0.13	0.17	-0.23	1							
Cl^-	0.94	-0.40	0.96	-0.42	0.13	1						
NO_3^-	0.23	0.03	0.21	-0.20	0.91	0.13	1					
Ca^{2+}	0.87	-0.50	0.94	-0.37	0.07	0.90	0.03	1				
Na^+	0.69	-0.11	0.63	-0.14	0.06	0.74	0.12	0.40	1			
K^+	0.04	0.16	0.01	-0.15	0.97	-0.05	0.94	-0.10	-0.05	1		
Mg^{2+}	0.86	-0.45	0.93	-0.34	0.17	0.85	0.16	0.97	0.33	0.02	1	
TH	0.91	-0.49	0.97	-0.37	0.08	0.92	0.14	0.95	0.51	-0.06	0.96	1

The pH in the groundwater samples ranging from 5.78 to 7.90, with an average of 7.12, indicate a slightly acidic to alkaline nature of the groundwater. Furthermore, there is a negative correlation between pH and the major ions. Electrical Conductivity (EC) measured in the field serves as an indicator of ion presence and the concentrations of dissolved components. It exhibits a direct correlation with both total dissolved solids and chloride concentration, which are parameters used in groundwater classification. Electrical conductivity and total dissolved solids distribution are high in the southeastern part of the study area and decrease towards the west, as shown in **Figure 4**. The electrical conductivity of groundwaters in the study area varies between 475.1 and 4,493.0 microsiemens per centimeter ($\mu\text{S}/\text{cm}$), with an average of 2,025.4 $\mu\text{S}/\text{cm}$, showing a broad range of variations and standard deviations. TDS in groundwaters from the study area ranges from 244 to 3740 mg/L. Based on TDS, approximately 60% of groundwater samples fall into the fresh category (250-1000 mg/L), while over 40% fall within the brackish water category (1,000-10,000 mg/L). Variations in EC and TDS values are attributed to multiple processes, encompassing inflowing water recharging the aquifer, saltwater mixing, ion exchange along the flow path, and the influence of geological, mineralogical, and various geochemical environments.

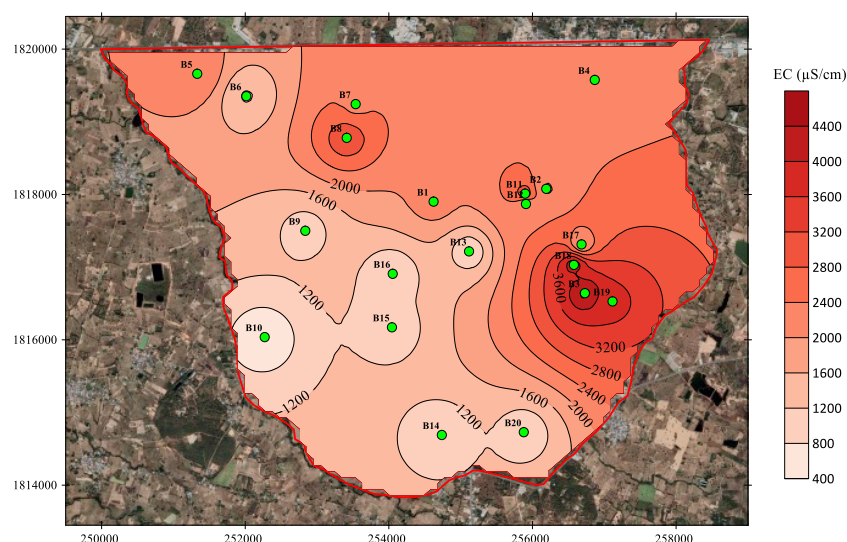


Figure 4. Spatial distribution of electrical conductivity in the study area

Total Hardness (TH) is another parameter that demonstrates a strong correlation with electrical conductivity and total dissolved solids. It is defined as the combined concentration of calcium and magnesium, expressed in milligrams per liter as calcium carbonate. The distribution of calcium and magnesium ions in groundwater from the study area is illustrated in **Figure 5**. Calcium ions exhibit concentrations ranging from 31.35 to 591.40 mg/l, whereas magnesium ions vary from 3.26 to 99.30 mg/l. Elevated concentrations of calcium and magnesium are concentrated in the southeastern part, while lower levels are evident in the western part, similar to the EC and TDS distribution. Calcium and magnesium primarily originate from the dissolution of carbonate minerals, notably calcite and dolomite, which are abundant in limestone terrains and serve as common cementing phases in many sandstones. In certain sedimentary sequences, layers containing highly soluble minerals like gypsum and anhydrite can also serve as significant sources of dissolved calcium.

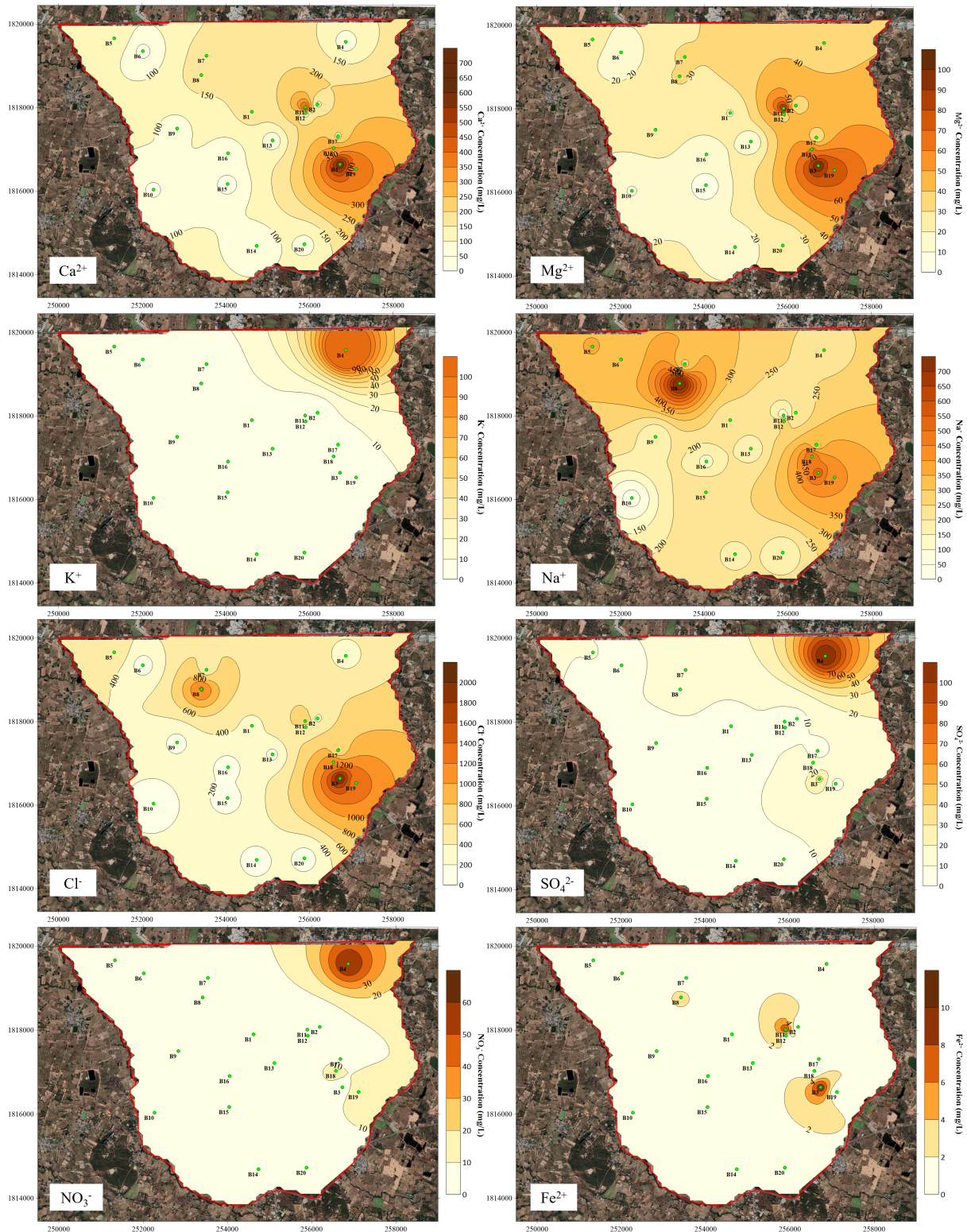


Figure 5. Spatial distribution of major ion concentrations (mg/L) in the study area.

Other significant cations in the groundwater are potassium and sodium. The concentration of potassium ions in the groundwater within the study area varies from 1.20 to 159.9 mg/L, with the highest levels detected in groundwater from the open shallow dug well, potentially indicating contamination from anthropogenic activities. The concentration of sodium ions ranged from 31.51 to 772.0 mg/L, correlating with the concentration of chloride ions, which ranged from 50.43 to 1,992.4 mg/L. The concentration of sodium ions ranged



from 31.51 to 772.0 mg/L, correlating with the concentration of chloride ions, which ranged from 50.43 to 1,992.4 mg/L. Both sodium and chloride concentrations are highest in the southwestern part of the study area, with one location in the northern part also exhibiting elevated levels as shown in **Figure 5**. Silicate weathering serves as a prevalent origin of dissolved sodium and potassium ions. Furthermore, sodium, potassium, and chloride are readily found in halite and sylvite, which are frequent components of ancient evaporite deposits. When these minerals encounter groundwater, they dissolve with such intensity that they contribute significantly to concentration levels.

Sulfate concentrations in groundwaters generally range from 4.62 to 111.43, as depicted in **Figure 5**, indicating relatively low concentration levels. However, there is one location where the sulfate concentration is at its highest, aligning with the highest potassium and nitrate concentrations. While sulfate ions are typically attributed to the dissolution of gypsum and anhydrite, the strong correlation between sulfate and nitrate concentrations suggests contamination from anthropogenic sources.⁷ The analyzed groundwater samples have exhibited high concentrations of trace metals, including iron, manganese, and zinc, which were observed in the water from a shallow dug well, potentially originating from anthropogenic sources. In particular, iron ions in certain areas, as shown in **Figure 5**, were found to exceed the recommended limit of 1 mg/L.

Hydrochemical Facies and Processes

The Piper trilinear diagram⁸ constitutes a significant tool employed for the interpretation of hydrogeochemical facies. By plotting the geochemical data on a Piper trilinear diagram, as depicted in **Figure 6a**, that can gain insight into the geochemical evolution of groundwater and its relationship with various dissolved ions. Groundwater falls within all zones of the diamond diagram, with 40 percent in the Sodium-Chloride type and 25 percent in the mixed Calcium-Sodium-Bicarbonate type, as shown in the hydrochemical facies distribution in **Figure 7**. The Piper Diagram shows a trend of increasing sodium and chloride concentrations from the recharge area to the discharge area, which is a result of the halite dissolution process. The Durov diagram⁹ (**Figure 6b**) provides an alternative way of illustrating potential geochemical processes that could influence the formation of water. It is one of the most frequently used diagrams for improving the characterization of hydrochemical water types and identifying potential hydrochemical processes.¹⁰ According to Lloyd and Heathcoat's classification (1985)^{11,12,13,14}, most groundwater samples fall within a field where neither cations nor anions dominate, suggesting dissolution or mixing in the groundwater. Some samples are also located in the sodium and chloride-dominant field, indicating a possible reverse ion exchange of sodium and chloride in the water. Meanwhile, a few samples fall within the bicarbonate and sodium field, which indicates ion exchange in the water.

The chemistry of groundwater is influenced by various factors, including the physical characteristics of the aquifer and the mineral composition of the water-bearing rocks. To depict the significant hydrogeochemical processes governing the chemical composition of groundwater as it flows, the Gibbs diagram¹⁵ should be employed. **Figure 8** shows that most samples are situated in the central part of the diagrams, suggesting that rock weathering is the primary factor influencing groundwater evolution. However, an observed trend towards the upper zone may indicate the influence of mixing between fresh and saline groundwater with elevated sodium and TDS levels.^{16,17,18} Moreover, specific groundwater samples are affected by the evaporation-fractional crystallization process. The increase in sodium ratios may be attributed to the presence of halite mineral^{19,20,21} in the Maha Sarakam Formation. Furthermore, evaporation, which is also influenced by climate factors, occurs in surface water

and moisture in the unsaturated zone, leading to the concentration of ions in that zone. Subsequently, when leaching processes take place in the area, water infiltrates toward the saturated zone.¹⁴

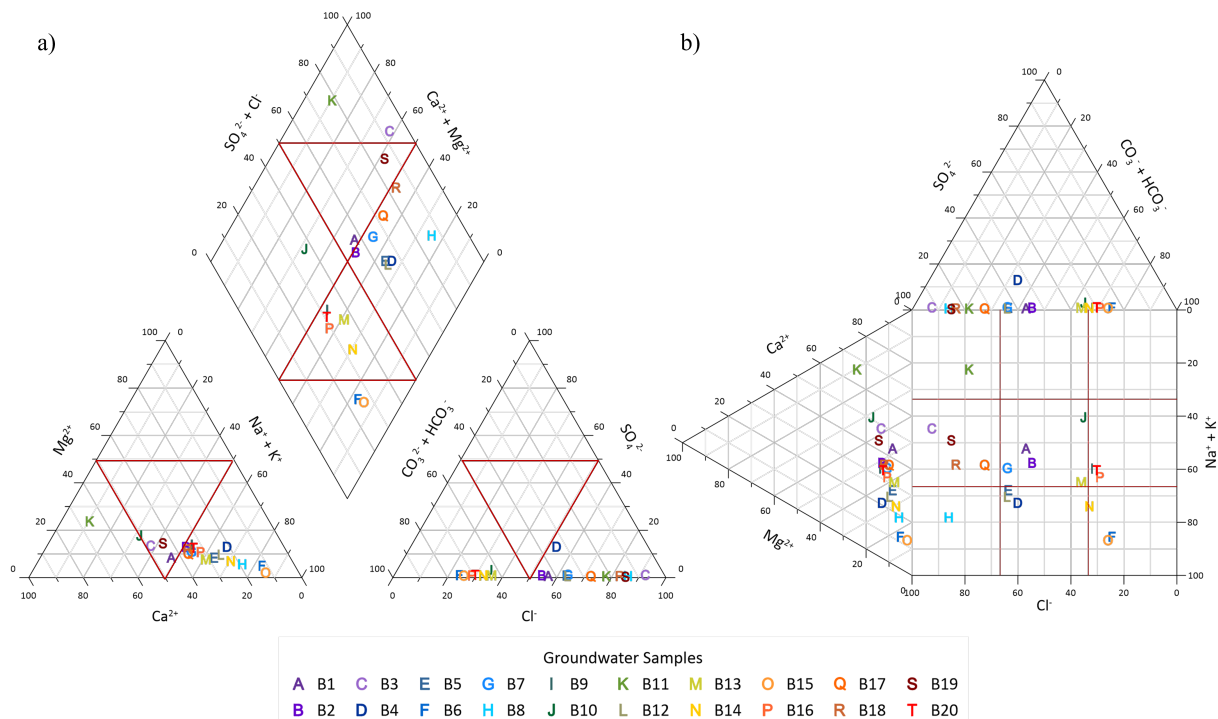


Figure 6. a) Piper trilinear b) Durov diagrams describing the hydrochemical facies classification in the study area.

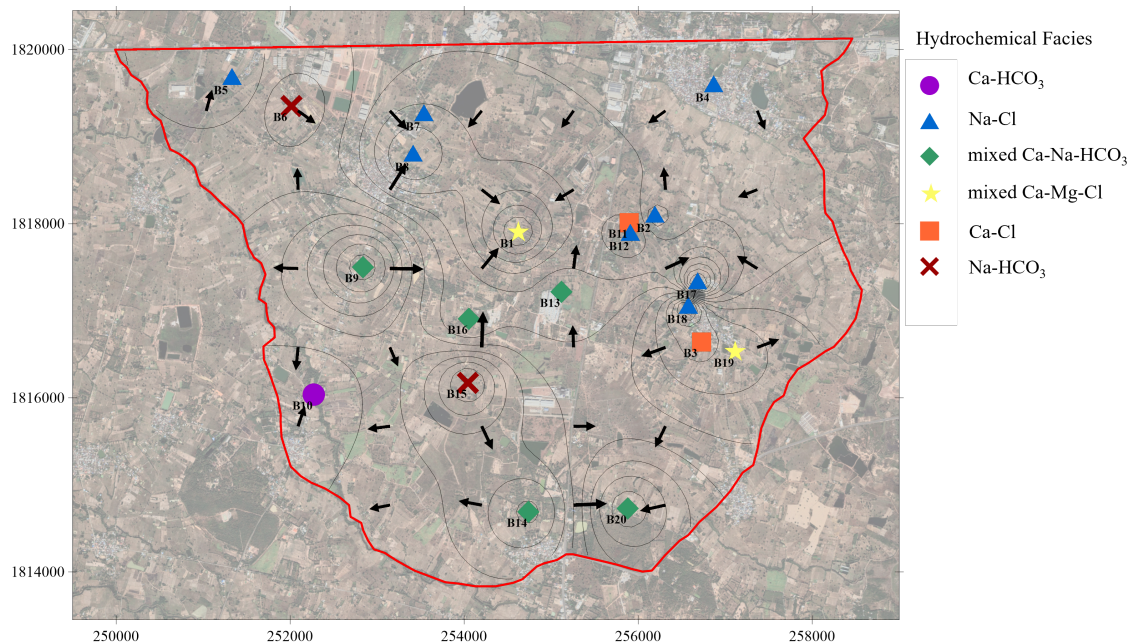


Figure 7. The distribution of hydrochemical facies in the study area compared with groundwater flow.

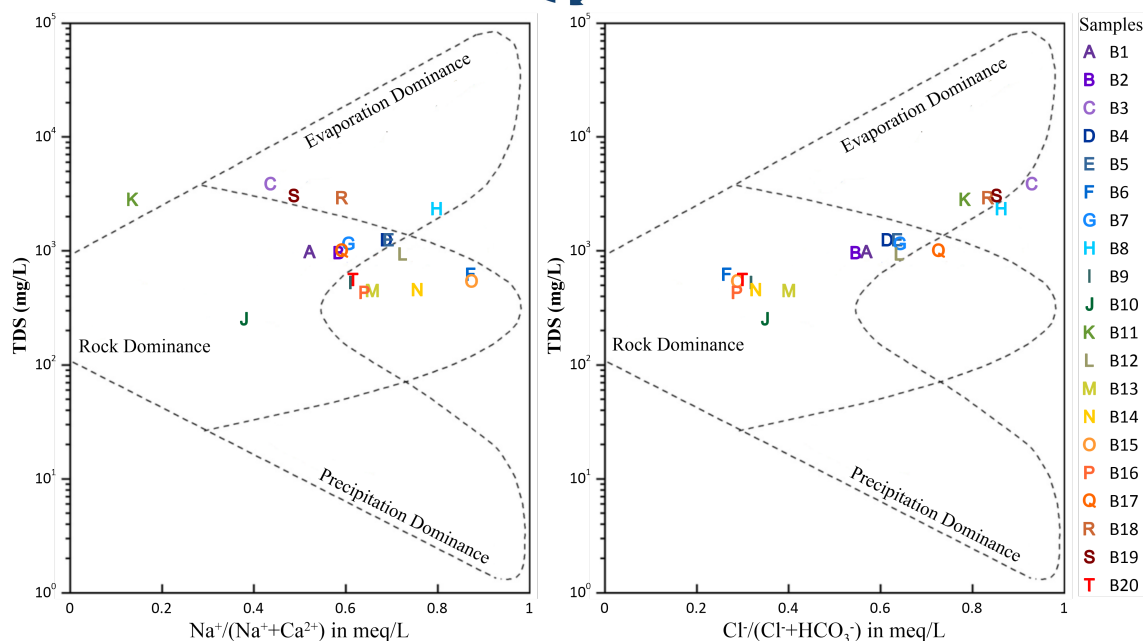


Figure 8. Gibbs diagram depicting the mechanism controlling the groundwater chemistry of the study area.

Conclusion:

To assess the hydrogeological characteristics and groundwater chemistry in the Ban Thum area, twenty groundwater samples and hydrogeological data were collected and analyzed. Groundwater primarily flowed from the northeastern to the southwestern part of the study area. However, the presence of multiple cones of depression in the central region and a high hydraulic head area in the south led to groundwater movement from the south towards the central region. These spatial variations in hydraulic head were associated with local groundwater extraction rates, ultimately affecting the availability of groundwater for domestic and agricultural use. A comprehensive analysis of groundwater chemistry revealed multiple factors influencing the water quality in the study area. The application of hydrochemical diagrams, including the Piper trilinear diagram, Durov diagram, and Gibbs diagram, provided valuable insights into the hydrogeochemical facies and processes that impact the groundwater in this area. The predominance of the sodium-chloride facies in the hydrochemical distribution suggests the impact of halite dissolution within the groundwater system. Additionally, the Durov diagram shows potential processes, including dissolution or mixing, while the Gibbs diagram indicates that rock weathering is the primary influencer of groundwater composition. Furthermore, there is clear evidence of interactions between fresh and saline groundwater, resulting in high sodium-chloride and total dissolved solids content in the groundwater.

This study offers a comprehensive understanding of the physical and chemical properties of groundwater in the study area. The information gathered is essential for determining the quantity and quality of groundwater, which can then help with sustainable management in the area. In the future, we may conduct more in-depth investigations into the precise mechanisms that influence groundwater chemistry and their consequences on local communities and ecosystems. Furthermore, the results establish a strong foundation for addressing salinity issues, enhancing groundwater utilization, and designing protective measures, all of which will contribute to ensuring the long-term sustainability of this essential resource.

Acknowledgements:

The authors would like to thank the Department of Geotechnology, Faculty of Technology, Khon Kaen University, for their support in providing access to laboratories and facilities.

References:

1. Ramnarong V, Buapeng S. *Jour. Geol. Soc. Thailand*. 1985;8:37-42
2. Wongsomsak S. *Southeast Asian Stud*. 1986;24(2):133-153
3. Saraphirom P, Wirojanagud W, Srisuk K. *Environ Earth Sci*. 2013;70:887-900
4. Arunin S, Pongwichian P. *Bull. Soc. Sea Water Sci. Jpn*. 2015;69:319-325
5. Arjwech R, Everett ME, Wanakao P. *Songklanakarin J. Sci. Technol*. 2019;41(5):974-983
6. Lertsirivorakul R, Milne-Home WA, Knight MJ. *Proc. Geo-Indo Conf*. 1995:665-673
7. Torres-Martínez JA, Mora A, Knappett PSK, Ornelas-Soto N, Mahlknecht J. *Water Res*. 2020;182:115962
8. Piper AM. *Trans. Am. Geophys. Union*. 1944;25(6):914-928
9. Durov SA. *Dokl Akad Nauk SSSR*. 1948;59(3):87-90
10. Besser H, Mokadem N, Redhaounia B, Hadji R, Hamad A, Hamed Y. *Euro-Mediterr. j. environ. integr*. 2018;3(16):1-15
11. Salman SA, Melegy AA, Shaban AM, Hassaan MM. *J. Appl. Sci. Res*. 2013;9(1):758-769
12. Ravikumar P, Somashekar RK, Prakash KL. *Elixir Earth Sci*. 2015;80:31073-31077
13. Li P, Wu J, Qian H, Zhang Y, Yang N, Jing L, Yu P. *Expo Health*. 2016;8:331-348
14. Al-Mutawqi KG, Ewaid SH, Abed SA, Al-Ansari N, Salim NA, Kadhim AJ. *J. Water Land Dev*. 2021;50(VI-IX):220-228
15. Gibbs RJ. *Science*. 1970;170:1088-1090
16. Srinivasamoorthy K, Gopinath M, Chidambaram S, Vasanthavigar M, Sarma VS. *J King Saud Univ Sci*. 2014;26:37-52
17. Mohanty AK, Gurunadha Rao VVS. *Catena*. 2019;172:558-571
18. Mohamed A, Asmoay A, Abdelrady F, Othman A. *Appl. Sci*. 2022;12:6340
19. Zhang B, Zhao D, Zhou P, Qu S, Liao F, Wang G. *Water*. 2020;12(3):836
20. Eamrat R, Lapkratok S, Mingyai S, Shakya BM. *Int. J. GEOMATE*. 2022;23(97):106-114
21. Gugulothu S, Subbarao N, Das R, Dhakate R. *Appl. Water Sci*. 2022;12(6):142

Hydrogen Sulfide Removal of Durian Peel Biochar for biogas cleaning

Surarat Siri-in, Niramol Juntarachat*

Innovative Materials Chemistry for Environment Center, Department of Chemistry,
Faculty of Science, Thaksin University, Phattalung 93210, Thailand

*e-mail: niramol@tsu.ac.th

Abstract:

In this work, the removal efficiency of hydrogen sulfide from biogas using durian peel biochar as an adsorbent was studied. Physical and chemical properties of durian peel biochar were determined. Moisture content, volatile matter content, ash content, and fixed carbon were found to be $8.31 \pm 1.67\%$, $41.87 \pm 0.59\%$, $18.98 \pm 1.92\%$, and $30.57 \pm 1.02\%$, respectively. The pH value of biochar was 8.62. FTIR results of durian peel biochar showed the carboxylic and hydroxide radical groups, being most likely responsible for H_2S adsorption. Then, the effect of pellet size (1.0 cm and 1.5 cm) and initial concentration of H_2S (500 ppm and 1000 ppm) on the adsorption capacity were investigated. The results showed that a smaller pellet size increase of the adsorption capacity owing to increasing of surface area of adsorbent. The lower initial concentration of H_2S of 500 ppm had higher adsorption capacity compared to 1000 ppm. Finally, the elemental and morphological changes before and after adsorption can assure the adsorption efficiency of such an adsorbent. Therefore, durian peel biochar could be used as an alternative adsorbent for removing H_2S contained in biogas.

Keywords: Biogas, Hydrogen sulfide, Adsorbent, Durian peels biochar.

Introduction:

Alternative renewable sources of energy are today seen as potential solutions to the problems of growing energy demand, progressive depletion, and negative environmental impact of fossil fuel resources. Biogas, one of potential renewable energies, is a mixture of different gases produced by the biological decomposition of organic matters in the absence of oxygen. Biogas mainly consist of methane (CH_4), carbon dioxide (CO_2), and trace amounts of other gases such as hydrogen sulfide (H_2S), ammonia (NH_3), hydrogen (H_2), nitrogen (N_2), and carbon monoxide (CO). The composition of the biogas varies based on the substrate feedstock, temperature, and pressure of each process¹. The presence of elevated concentrations of H_2S in biogas is problematic because of its highly corrosiveness and toxicity², and serious environmental concerns due to their oxidation to sulfur dioxide (SO_2) and sulfuric acid (H_2SO_4)³. Several physicochemical processes have been studied in order to remove H_2S from biogas such as the adsorption process⁴, catalytic process⁵, biological process⁶, and hydrate formation⁷. However, these technologies required a high-cost operation as well as technical complication, preventing its application for small-scale users.

The adsorption process is a promising technology to remove H_2S contained in biogas for small-scale users, especially in household owing to its low-cost operation and uncomplicated utilization and maintenance. Adsorbent type is an important factor effecting on the efficiency of such a process. Activated carbon is one of the most suitable adsorbent materials. But, its cost acts as a barrier to the take up of biogas technology. Biochar, a carbon-rich material obtained by a thermal decomposition of biomass under oxygen limiting conditions, is currently attractive for the new low-cost alternative adsorbents. In comparison with an activated carbon, the manufacturing of biochar required less energy and no pre- and post-activation processes.

In this research, we are interested in developing durian peels, into biochar to be used as an adsorbent for removing hydrogen sulfide from biogas. Durian peels are considered a large amount of residual waste, especially during the fruit season. They cause pollution problems for environment because they are generally eliminated by burning which has a negative effect on the environment. To reduce environmental pollution problems, this research has improved the efficiency of durian peels as durian biochar to be used as a good adsorbent.

Methodology

1. Preparation of biochar

Durian peel sample was collected from Pa Phayom District, Phatthalung Province and dried in the sun for a period of 24 hours. Sample was passed through a pyrolysis process at the temperature of 350 °C for 4 hours. Biochar was stored in a heat-proof jar for further analysis of physical and chemical properties and adsorption efficiency.

2. Chemical and physical properties of adsorbent

The physical and chemical properties of durian peel studied in this work were moisture content, volatile compound content, ash content, fixed carbon content, pH and BET surface. Moisture content analysis was performed according to ASTM D 3173 standard by heating 1 g of biochar at 105-110 °C for 180 minutes. Volatile matter content was determined according to ASTM D 3175 standard by heating 1 gram of charcoal at 900 °C for 30 minutes. The percentage of ash content was determined, according to ASTM-D 2866-94 standard procedure, Three experiments were performed for each property, Fixed carbon content (%) was calculated by $100 - (\text{moisture content (\%)} + \text{volatile matter content (\%)} + \text{ash content (\%)})$.

pH measurement was performed by taking 1 gram of biochar and mixed with 10 ml of distilled water. A mixture was agitated during 30 minutes for equilibrium and filtrated to separate biochar and solution. solution was taken to measure the pH using a pH meter. The experiment was repeated 3 times.

The functional group of selected biochar durian peel was analyzed before adsorption process, through FTIR transmission spectra. It was recorded using a PERKIN ELMER Spectrum One FTIR spectrophotometer in the wave number range of 4000–450 cm^{-1} . Durian peel biochar was ground with KBr (AR grade) at a ratio of roughly 1:999. 5 mg of fine powder (oven dried at 110 °C for 12 h) was made in to a pellet by continuously pressing at 5 ton.cm^2 for 1 min

3. Adsorption efficiency.

The efficiency adsorption of hydrogen sulfide contaminants in biogas was studied using durian peel biochar as an adsorbent. In the first step, the effect of pallet sizes (1.0 cm and 1.5 cm of diameter) of adsorbent on adsorption capacity was studied. Experiment was carried out using 10 g of durian peels biochar in the packed-column with an internal diameter of 2.50 cm and the length of 40.00 cm, initial concentration of hydrogen sulfide of 500 ppm and a flowrate of 500 mL/min. In the second step, the effect of initial concentration of hydrogen sulfide (500 ppm and 1000 ppm) on the adsorption capacity was investigated using durian peel biochar with the pallet size of 1.0 cm of diameter. The adsorption system is installed with the biogas production system. As shown in Figure 1. Composition to biogas was analyzed by GC every 5 min for 120 minutes.

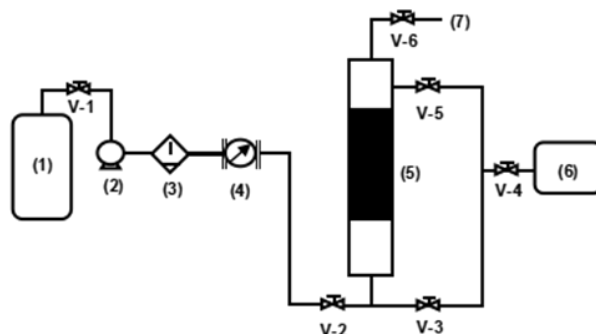


Figure 1 Schematic diagram of the adsorption system experiment

The adsorption percentage was calculated using the following equation (1).

$$\text{adsorption percentage (\%)} = \frac{(C_0 - C_t)}{C_0} \times 100 \quad (1)$$

Where C_t is the concentration of adsorbate at time t , C_0 is the initial concentration of the adsorbate, t is time, Q_f is flowrate of biogas and m_c is mass of ash adsorbent. A breakthrough curve was established from C/C_0 and time. A comparison of H_2S breakthrough curve (C/C_0 versus time) at different conditions of adsorption provides information about the optimal adsorption condition. The breakthrough capacity at 5% was calculated using the following equation (2).

$$q_t = \left(1 - \frac{c_t}{c_0}\right) \frac{Q_f t_f y_f}{m_c} \quad (2)$$

4. Morphological properties

The morphological analysis of coconut shell biochar before and after adsorption process was determined using a Scanning Electron Microscopy (SEM) in order to obtain the sorbent surface morphologies as well as to determine localized chemical composition.

Research and Discussion

1. Chemical properties and physical properties of biochar adsorbent

Physical and chemical properties of durian peel biochar was determined and are shown in Table 1.

Table 1 physical and chemical properties durian peel biochar

Feature	durian peel biochar
Moisture content (%)	8.57 ± 1.06
Volatile compound content (%)	41.87 ± 0.59
Ash content (%)	18.98 ± 1.92
Fixed carbon content (%)	30.57 ± 1.02
pH	8.62

The moisture content in durian peel biochar was found to be $8.57 \pm 1.06\%$ which was consistent with that found in the investigation of Manmeen et al.⁸ who study of H_2S removal with biochar, sewage sediment and pig biochar. They reported that increasing moisture content increases the ability to eliminate H_2S of biochar. Volatile compound content was found to be $41.87 \pm 0.59\%$. Biochar with low volatile compounds provides higher adsorption capacity¹². Ash content is equal to $18.98 \pm 1.92\%$. The fixed carbon content of biochar from the durian peel was $30.57 \pm 1.02\%$. Biochar with higher fixed carbon will have higher adsorption capacity. According to Juntarachat et al.¹² The pH value of durian peel biochar was

8.62. According to Shang et al.¹², the pH values greater than 7.0 make the alkaline surface which is conducive to H₂S adsorption since H₂S is an acidic gas.

2. FTIR analysis and morphological properties

Figure 2 shows the FTIR spectra of durian peel biochar in the range of 4000–450 cm⁻¹.

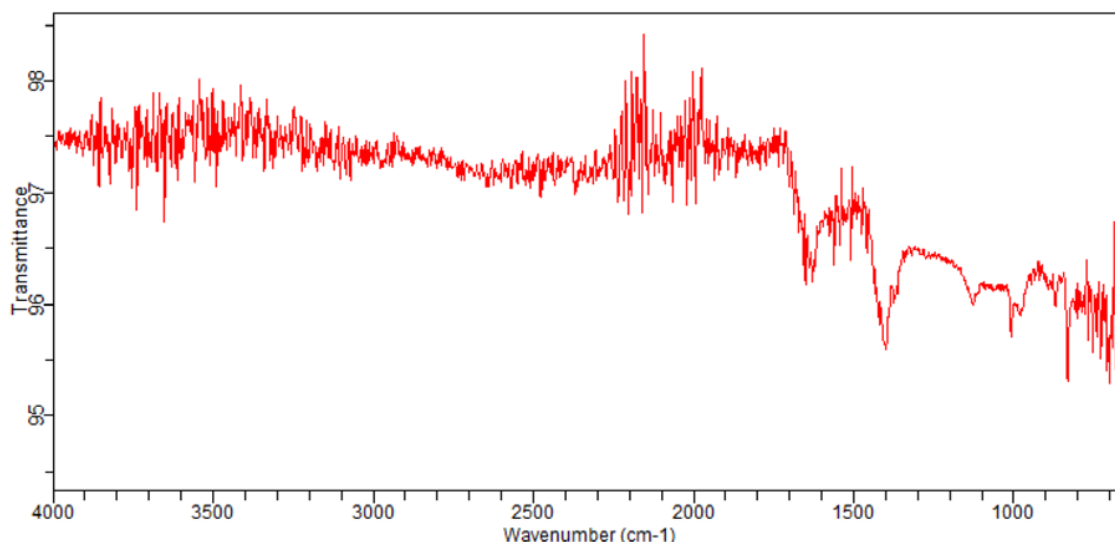


Figure 2 FTIR spectra of the durian peel biochar before the adsorption process

The important peaks were characterized. The peak at 700–690 cm⁻¹ was associated with C–H stretching vibration. The strong band at 1410 cm⁻¹ was attributed to C–O stretching vibration in the carboxylate group. The peak at 1710 cm⁻¹ corresponded to C = O stretching vibration in aromatic ring. The spectra between 3,500 and 3,200 cm⁻¹ broad characteristics revealed O–H stretching induced by hydrogen bonding. FTIR spectra pattern of durian peel biochar studied in this work agrees well with those investigated by Manmeen et al.⁸. FTIR analysis results showed that carboxylic and hydroxide radical groups which were most likely responsible for H₂S adsorption.

3. Hydrogen sulfide (H₂S) adsorption.

Efficiency adsorption of H₂S was studied using durian peel biochar as the adsorbent. In the first step, the effect of pallet sizes of adsorbent on the adsorption capacity as evaluated using initial concentration of H₂S of 500 ppm. Figure 3 represents H₂S breakthrough curves of adsorbent with diameters of 1.0 cm and 1.5 cm. It can be seen that durian peel biochar with the pallet size of 1 cm. had better adsorption efficiency than that with the pallet size of 1.5 cm. This can be explained by a greater adsorption area of adsorbent. Our experimental results agree well with the investigations of Shang et al.¹³

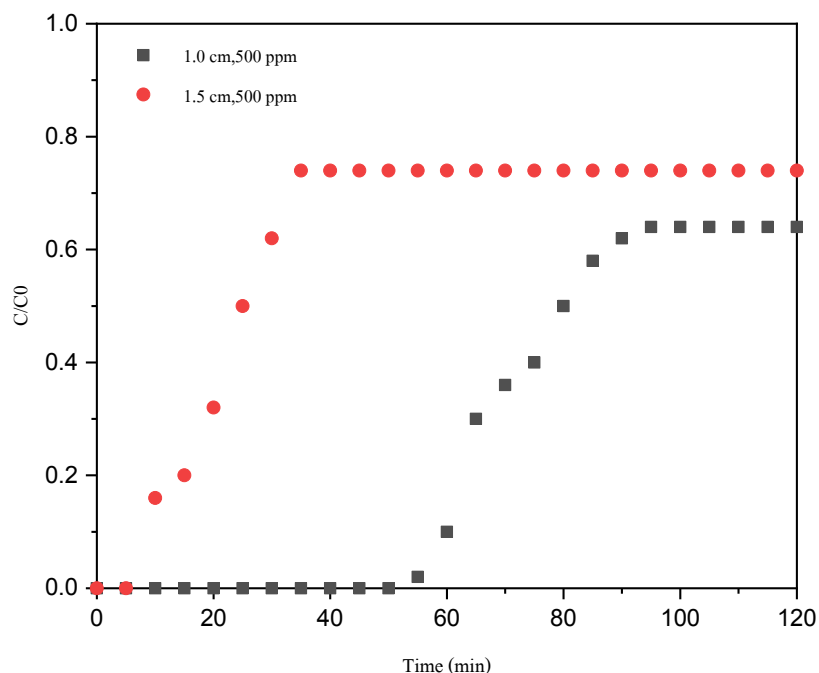


Figure 3 H₂S breakthrough curves of adsorbent with diameters of 1.0 cm and 1.5 cm

In the second step, the effect of initial concentration of H₂S on the capacity adsorption was investigated using adsorbent with 1.0 cm of diameter. Figure 4 represents H₂S breakthrough curves for the initial concentration of 500 ppm and 1000 ppm. It can be seen that the initial H₂S concentration of 500 ppm showed better adsorption efficiency compared to the initial concentration of H₂S of 1,000 ppm. Breakthrough time at 500 ppm and 1000 ppm were observed at 90 minutes and 50 minutes, respectively. A higher concentration of H₂S making higher volume of total molecules causes adsorptive site on the surface area of the adsorbent to saturate faster.

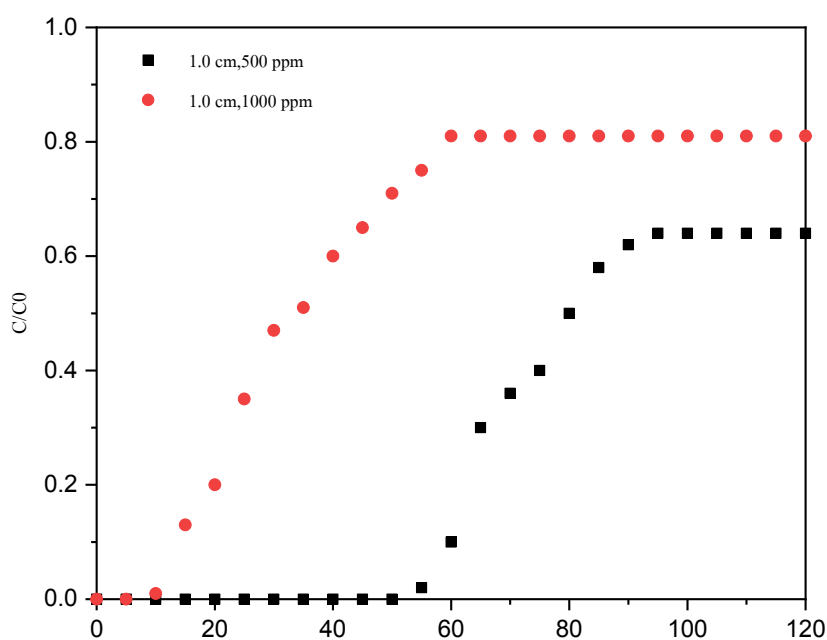


Figure 4 H₂S breakthrough curves for the initial concentration of 500 ppm and 1000 ppm

3. Morphological and elemental characteristics

SEM analysis of biochar derived from the durian peel before and after adsorption process were presented in Figure 5.

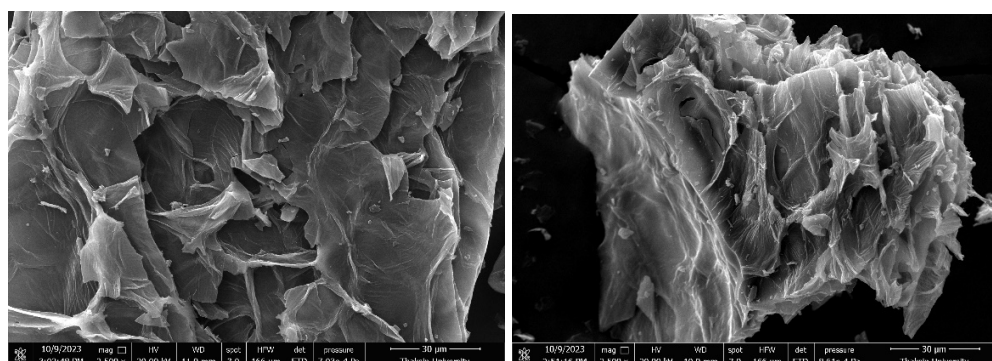


Figure 5 SEM micrograph of durian peel biochar at a magnification of 2500X:
(a): Durian peel biochar before the adsorption process and (b): Durian peel biochar after the adsorption process

Before the adsorption, the surface of adsorbent material was observed to be smooth at the magnification of 2500 X and it was found to possess cratered and rough cavities distributed over the surface at the same magnification after the adsorption. Table 2 presents EDX results before and after adsorption. Before the adsorption process, durian peel biochar contained 85.26 % carbon (C), 13.61 % oxygen (O), 1.01% potassium (K), and small trace of other elements.

Table 2 Elemental composition of durian peel biochar before and after the adsorption process

Elements (w%)		C	O	Mg	K	P	S
durian peel biochar	Before adsorption	85.26	13.61	0.12	1.01	-	-
	After adsorption	82.63	13.5	0.34	2.97	0.25	0.31

The concentration of sulfur (S) increased from 0% before the adsorption process to 0.31% after adsorption. The percentage of sulfur on durian peel biochar assuring its H₂S adsorption. Such elemental changes were observed in the investigation of Kanjanarong et al.¹¹

Conclusion

The removal efficiency of H₂S from biogas using durian peel biochar as an adsorbent was studied. Physical and chemical properties of biochar: moisture content, volatile matter content, ash content, and fixed carbon content were determined and found to be $8.57 \pm 1.06\%$, $41.87 \pm 0.59\%$, $18.98 \pm 1.92\%$ and $30.57 \pm 1.02\%$, respectively. An appropriate amount of moisture can increase the adsorption capacity of adsorbent but the high ash content can decrease such a capacity. The pH value of biochar was 8.62, making the alkaline surface of adsorbent and leading to be conducive for removing H₂S. Then, the H₂S removal efficiency of durian peel biochar adsorbent was investigated at different pellet sizes: 1.0 and 1.5 cm with initial concentration of H₂S at 500 ppm and 1000 ppm. The results showed that a small pellet size increases surface area of adsorbent, allowing the increase of the adsorption capacity and the lower initial concentration of H₂S increased the adsorption capacity of adsorbent.

The elemental and morphological change before and after adsorption can assure the ability of durian peel biochar for the biogas cleaning.

Acknowledgements:

The authors would like to acknowledge all supports from Thaksin University.

References

1. Moset V, Fontaine D, Møller HB. *Energy*. 2017;141:451–460.
2. Heubeck S, Craggs R. *Int. Asso. Water Pol. Res.* 2010; 61: 1019–26, 2010.
3. Corro G, Paniagua L, Pal U, Bañuelos F, Rosas M. *Energy Conversion and Management*. 2013; 74: 471–481.
4. Horikawa MS, Rossi F, Gimenes ML, Costa CMM, Silva MGC. *Brazilian Journal of Chemical Engineering*, 2004; 21.
5. Wang J, Zhang Y, Han L, Chang L, Bao W. *Fuel*. 2011; 103:73–79
6. Omri I, Bouallagui H, Aouidi F, Godon JJ, Hamdi M, Biores. *Tech.* 2011;102: 10202 – 10209.
7. Sun Q, Li H, Yan J, Liu L, Yu Z, Yu X. *Renewable and Sustainable Energy Reviews*. 2015; 51: 521–532.
8. Manmeen A, Kongjan P, Palamanit A, Jariyaboon R, *Biomass and Bioenergy*, 2023; 174. doi:10.1016/j.biombioe.2023.106816.
9. Manmeen A, Jariyaboon R, *Doctor of Philosophy (Energy Technology)*, 2023; 219.
10. Sahota S, Vijay VK, Subbarao PMV, Chandra R, Ghosh P, Shah G, Kapoor R, Vijay V, Koutu V, Thakur IS. *Biores. Tech.* 2018; 250: 635–641.
11. Kanjanarong J, Giri BS, Jaisi DP, Oliveira FR, Boonsawang P, Chaiprapat S, Singh RS, Balakrishna A, Khanal SK. *Biores Technol.* 2016; 234:115–121
12. Juntarachat, N, Onthong U. *Biomass Conversion and Biorefinery*. 2022 doi.org/10.1007/s13399-022-03430-z
13. Shang G, Shen G, Liu L, Chen Q, Xu Z, *Biores. Tech.* 2016; 133: 495–499,

MINERALOGY AND ALTERATION OF PAK PAT VOLCANIC ROCKS IN NAM PAT DISTRICT, UTTARADIT PROVINCE, NORTHERN THAILAND

Burapha Phajuy¹, Vimoltip Singtuen^{2,*}, Watcharapong Piewmoh¹ and Pheeraphon Phonboon¹

¹ Department of Geological Sciences, Faculty of Science, Chiang Mai University, Chiang Mai, Thailand

² Department of Geotechnology, Faculty of Technology, Khon Kaen University, Khon Kaen, Thailand

*e-mail: vimoltipst@gmail.com

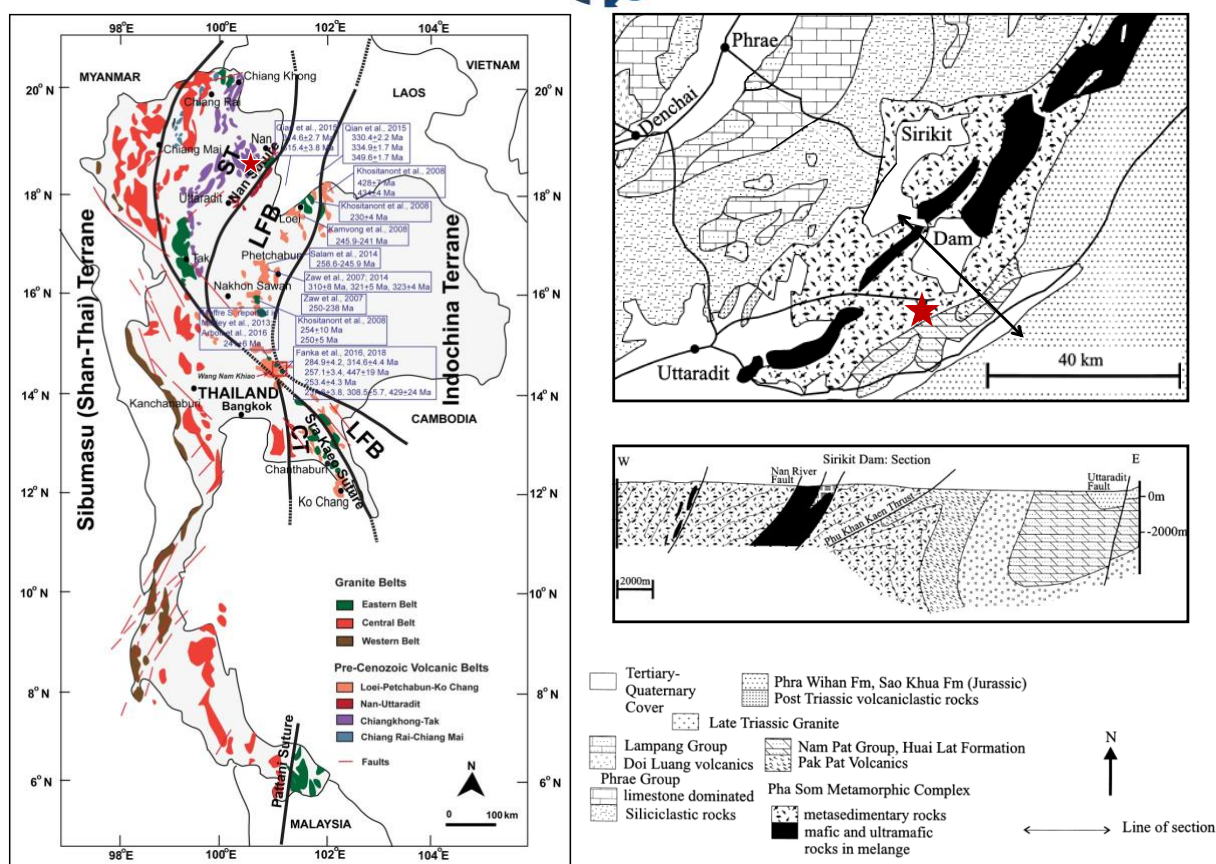
Abstract:

Pak Pat volcanic rocks are scattered around the Nam Pat District of Uttaradit Province and are part of the Nan-Uttaradit volcanic Belts. This study aims to classify the eruption pattern, mineral components, rock name, and alteration processes based on field investigation, lithology, petrography, and geochemistry of both major oxides and trace elements. According to macroscopic and microscopic studies, the studied rocks can be classified into three types, consisting of (1) porphyritic andesite with plagioclase phenocryst, (2) seriated andesite with plagioclase phenocryst, and (3) plagioclase-rich poor-sorted crystal tuff. In addition, volcanic facies of appearance can be distinguished, consisting of homogenous volcanic facies formed by cooling lava with intermediate composition (andesite) and pyroclastic facies formed by deposits of volcanic ash and volcanic fragments (crystal tuff) exploded in an explosion type. Based on its chemical composition, the rocks can be classified as andesite/basalt and andesite as well as dacite based on major oxides. The high molar $(K+Na+2Ca)/Al$ and very low molar K/Al suggest that andesites gained K^+ and loss of Na^+ and Ca^{2+} . Furthermore, the alteration index (AI) and Chlorite-Carbonate-Pyrite Index (CCPI) ratios are interpreted as the rocks related to the sericitization of plagioclase and alteration of alkaline feldspars.

Introduction:

The geology of northern Thailand is very irregular, diverse, and obscure. Even though tectonic models which may explain the geological history of this region have been proposed for decades, this idea is still controversial. The evolution of volcanic rocks before the collision of the SIBUMASU Block and the Indochina Block, until they collided in the late Triassic period¹⁻⁴, resulted in volcanic rock formations spreading in Thailand in 4 directions from west to east as follows: 1) Chiang Rai-Chiang Mai volcanic belt, 2) Chiang Khong-Tak volcanic belt, 3) Nan-Uttaradit volcanic belt, and 4) Loei-Phetchabun volcanic rock belt (Figure 1).

The volcanic rock in this study is part of the Nan-Uttaradit volcanic rock line distributed in the area of Ban Pak Pat, Saen Tor Sub-district, Nam Pat District, Uttaradit Province. Singharajwarapan and Berry⁵ suggest that the Pak Pat volcanic rocks have composition ranges from intermediate to acid, consisting of greyish to greenish volcanic rocks with chemical compositions similar to rhyolite to dacite associated with greenish to purple-red pyroclastic rocks. The Pak Pat volcanic rocks occurred during the Permian period to the Triassic period as a barrier between the Nan River in the west and the Nam Pat group in the east. These volcanic rocks discontinue contact with the metagreywacke and phyllites of the Pha Som Group (Silurian-Devonian) in the western boulders by the Phu Khon Kaen thrust fault line. In addition, the eastern flank borders the Middle Triassic Huai Lat Formation⁶ by unconformity (Figure 1).



The volcanic rocks in this area are not clearly classified and studied in mineralogy and alteration. The purpose of this study is to classify rock names and volcanic facies according to mineral composition and texture based on petrographic data. In addition, this work studies the geochemical composition of both major oxides and trace elements that can be used to interpret the alteration conditions and to draw conclusions about the formation of igneous rocks in this area. Furthermore, the usefulness of this study can be used to compare with the data in the nearby areas that have been studied which may be used to improve the theory of tectonic evolution in Thailand to be accurate.

Methodology:

The method of this study included a field investigation, a petrographic study, and a chemical analysis of least-altered rock samples. The names and alteration processes of these rocks could be interpreted based on their mineralogical and geochemical characteristics.

Eighteen standard thin sections, nine geochemical samples, loss on ignition (LOI), trace elements and major oxides analyses were prepared and analyzed at the Department of Geological Sciences, Faculty of Science, Chiang Mai University. Determination of major oxides (SiO_2 , TiO_2 , Al_2O_3 , MnO , MgO , CaO , Na_2O , K_2O , P_2O_5 , and total iron oxides in the form Fe_2O_3) and trace elements (Ba, Sr, Rb, Zr, T, Nb, Cr, Ni, Sc, and V) are performed by X-ray fluorescence Spectrometer (XRF).

The determination of parental oxides is in the form of a fusion disc. This was done by mixing 0.7 g of the sample powder with 0.06 g of lithium bromide and 3 g of dilithium

tetraborate. The mixture was mixed and placed in a platinum crucible, melted using a gas burner for about 20 minutes, and then poured into a platinum crucible and placed on a hot plate. Trace Element Quantification Analysis is in the form of a pressed powder. Sample preparation was performed by mixing 5 g of sample powder with 0.3 g of XRF MULTI-MIX PXR-200, which was then placed in a mould containing 3 g of boric acid as a retainer and compressed by a hydraulic press with a force of 180 kN for 1 min. LOI was analysed by heating a platinum crucible containing a 1.0 g sample in a furnace at 1000°C for 12 h.

Results and Discussion:

The topography of the study area is mostly gentle slope mountains and heights 248–307 m. above sea level. The study area is an old quarry, located at the foot of the Phu Huai Muang mountain range (Figure 2). Field observation divides rocks into two types that consist of (1) greyish-green porphyritic rocks presented with opaque minerals and (2) greyish-green pyroclastic rocks presented with rock fragments and pyrite. There are opaque minerals scattered in the grey-green fine-grained rock. There are many directions of veins cutting through. The samples do not show magnetism.



Figure 2. Outcrops of Pak Pat volcanic rocks in Nam Pat District, Uttaradit Province (a) old quarry, (b) porphyritic rocks, and (c) pyroclastic rocks.

The petrographic study suggests that the rock samples taken in this project were separated into three groups. There are five samples of andesite exhibited a porphyritic texture, three samples of andesite exhibited a seriate texture according to the Streckeisen classification⁷, and ten samples of crystal tuff presented volcanic fragments according to the Schmid classification⁸.

Porphyritic andesites are sample numbers PP2, PP11, PP14, PP15 and PP18. The samples are greyish green, and the weathered surface presents yellowish brown. Some samples react with dilute hydrochloric acid (PP11, PP15 and PP18) and some do not react with dilute hydrochloric acid (PP2 and PP14). According to petrography, the studied rocks were classified as porphyritic andesite exhibiting plagioclase phenocrysts and a small amount of quartz between the plagioclase crystals (Figure 3a). Plagioclase crystals (size 0.25-2 mm across) are dispersed about 30% by volume of the rock and moderately alter to sericite and epidote (Figure 3b-c). Some plagioclase glomerocrysts have been replaced by hematite and calcite. The groundmass is fine-grained plagioclase crystals with small amounts of quartz and partly replaced by epidote, chlorite, calcite, pyrite and a small amount of quartz.

Seriated andesites are samples numbered PP1, PP5 and PP17. The specimens are grey-green, and the weathered surface presents yellowish brown. Some samples react with dilute hydrochloric acid (PP5) and others do not react with dilute hydrochloric acid (PP1 and PP17).

In addition, the seriated andesites exhibit a seriated texture (Figure 3d), with plagioclase crystals embedded in the ground minerals that present a uniform alignment (Figure 3e). Phenocrysts have different sizes up to 2 mm across, showing anhedral to subhedral shapes. Plagioclase moderately altered to sericite and epidote as well as some crystals were replaced by calcite. Some of the rocks were replaced by epidote, chlorite, and pyrite as well as epidote and calcite veins.

Pyroclastic rocks are samples numbered PP3, PP4, PP7, PP8, PP9, PP10, PP12, PP3, PP16 and PP19. The specimens are greyish-green, and the weathered surface presents yellowish brown color. Some samples react with dilute hydrochloride (PP3, PP4, PP8, PP9 and PP13) and some did not react with dilute hydrochloride (PP7, PP10, PP12, PP16 and PP19). Petrography classifies the rock as crystal tuff showing pyroclastic texture and volcanic fragments (Figure 3f). The samples present poor sorting and are composed of various sizes of plagioclase in fine volcanic ash that highly altered to clay minerals. The plagioclase is smallest at about 0.15 mm, and largest at about 3 mm, showing anhedral to subhedral shapes. Plagioclase moderately altered to sericite and epidote, some of which have been replaced by iron oxide, epidote, chlorite, pyrite, quartz, and calcite and also present as veins.

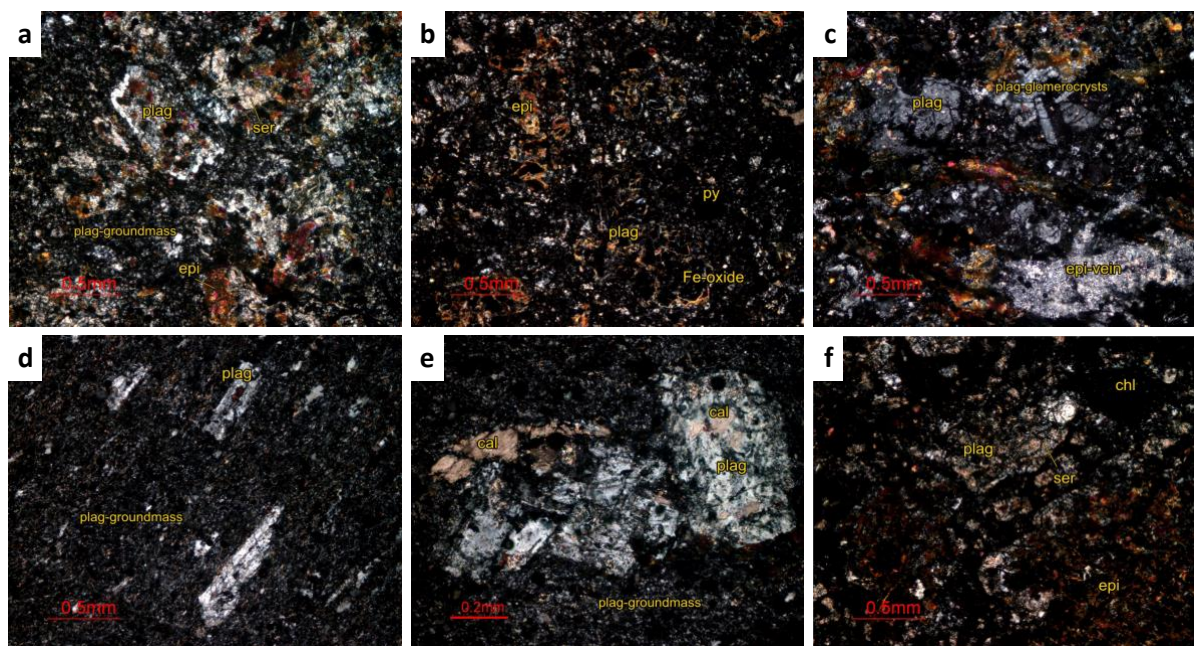


Figure 3. Photomicrographs in cross-polarized light of Pak Pat volcanic rocks in Nam Pat District, Uttaradit Province (a), (b), (c) porphyritic andesite with plagioclase phenocrysts, (d), (e) seriated andesite, and (f) crystal tuff.

According to geochemical analysis, the studied rocks have the following major oxide contents: 53.31-68.68 wt% SiO₂, 0.45-0.90 wt% TiO₂, 17.21-23.21 wt%; Al₂O₃, 4.98-10.02 wt% FeO, 0.05-0.14 wt% MnO, 3.31-7.71 wt% CaO, 1.06-4.43 wt% MgO, 0.28-1.01 wt% K₂O, 2.52-3.73 wt% Na₂O, and 0.11-0.25 wt% P₂O₅ as present in Table 1. In addition, the amounts of trace elements are as follows: Ba 469.53-697.17 ppm, Rb 7.36-27.27 ppm, Sr 217.90-405.55 ppm, Y 17.06-18.26 ppm, Zr 74.80-150.66 ppm; Nb 1.42-2.51 ppm, Ni 15.02-20.26 ppm, Cr 9.50-17.17 ppm, V 69.79-148.02 ppm, Sc 9.16-23.99 ppm, and Th 0.01-10.42 ppm.

The chemical variation diagram of major oxides and zirconium (Zr) classifies that TiO_2 , FeO and MgO tended to decrease with increasing Zr content indicating magnetite, ilmenite and titanite crystallization. The Cr and Ni tended to decrease with increasing Zr content indicating olivine and pyroxene crystallization, while Al_2O_3 tended to decrease and CaO tended to increase and decrease with increasing Zr content indicating plagioclase crystallization.

Table 1 Geochemical analysis presents major oxides and trace elements of the Pak Pat Volcanic Rocks

Sample no.	PP1	PP2	PP3	PP4	PP5	PP9	PP12	PP14	PP15
Major oxide (wt%)									
SiO_2	66.29	55.09	56.70	54.97	68.68	53.31	54.47	57.28	55.44
TiO_2	0.49	0.87	0.90	0.84	0.45	0.90	0.87	0.81	0.85
Al_2O_3	18.56	23.21	20.59	22.28	17.21	23.04	22.68	21.55	22.36
FeO*	5.28	8.55	10.02	8.67	4.98	9.54	8.77	8.52	8.60
MnO	0.09	0.08	0.10	0.12	0.05	0.13	0.14	0.09	0.11
CaO	3.47	6.40	4.57	7.36	3.31	6.15	6.97	5.10	7.71
MgO	1.34	2.79	4.43	3.21	1.06	4.06	3.94	3.48	2.84
K_2O	1.01	0.36	0.68	0.28	0.72	0.49	0.35	0.71	0.14
Na_2O	3.73	3.36	2.89	2.97	3.81	3.17	2.52	3.21	2.65
P_2O_5	0.25	0.15	0.13	0.16	0.24	0.16	0.17	0.11	0.16
sum.	100.53	100.86	101.00	100.87	100.50	100.96	100.88	100.85	100.86
LOI	2.62	3.77	4.60	3.81	2.40	4.29	3.84	4.06	3.89
Trace elements (ppm)									
Ba	697.17	503.84	525.98	492.32	657.82	505.52	494.23	562.51	469.53
Rb	27.27	12.2	24.14	7.36	23.33	13.39	13.06	20.5	8.98
Sr	348.01	370.7	217.9	405.55	355.66	323.7	380.1	278.06	403.88
Y	18.26	17.27	17.84	17.33	17.81	17.38	17.08	17.5	17.06
Zr	150.66	80.15	76.98	95.91	143.45	90.22	96.06	74.8	94.34
Nb	2.32	3.01	2.51	1.95	1.55	2.14	1.42	1.73	1.58
Ni	15.02	16.17	20.26	19.94	16.76	19.86	21.1	18.49	18.67
Cr	10.63	9.5	17.5	15.99	10.01	12.46	17.19	10.05	9.64
V	75.68	136.51	148.05	128.97	69.79	143.78	139.1	133.03	137.19
Sc	9.16	18.15	14.81	23.99	11.91	19.08	22.83	18.55	24.05
Th	0.17	5.1	10.42	2.52	<1.00	5.28	<1.00	1.74	<1.00
Select element ratios									
Zr/ TiO_2	310.15	92.61	85.76	113.58	320.77	100.68	110.01	92.91	110.80
Nb/Y	0.13	0.17	0.14	0.11	0.09	0.12	0.08	0.10	0.09
Nb/Zr	0.02	0.04	0.03	0.02	0.01	0.02	0.01	0.02	0.02

The chemical composition of the studied rocks can be considered in conjunction with the classification scheme of Le Bas et al.⁹, shown in Figure 4a, using $\text{Na}_2\text{O}+\text{K}_2\text{O}/\text{SiO}_2$ content, consisting of basaltic andesite (sample PP2, PP4, PP9, PP12 and PP15), andesite (sample PP3 and PP14) and dacite (sample PP1 and PP5), which is similar to the classification scheme of Winchester and Floyd¹⁰ shown in Figure 4b using the amount of $\text{Zr}/\text{Ti} \times 0.0001$ content. It consists of andesite/basalt (for example PP2, PP3, PP4, PP9, PP12, PP14 and PP15) and andesite (sample PP1 and PP5).

Alteration indices, such as the Ishikawa alteration index (AI) and the chlorite-carbonate-pyrite index (CCPI), have been developed to measure sericite intensity, chlorite, carbonate, and pyrite replacement of sodic feldspars associated with hydrothermal alteration proximal to the orebodies. In addition, silica will be formed as cryptocrystalline quartz and microcrystalline quartz during the hydrothermal alteration.

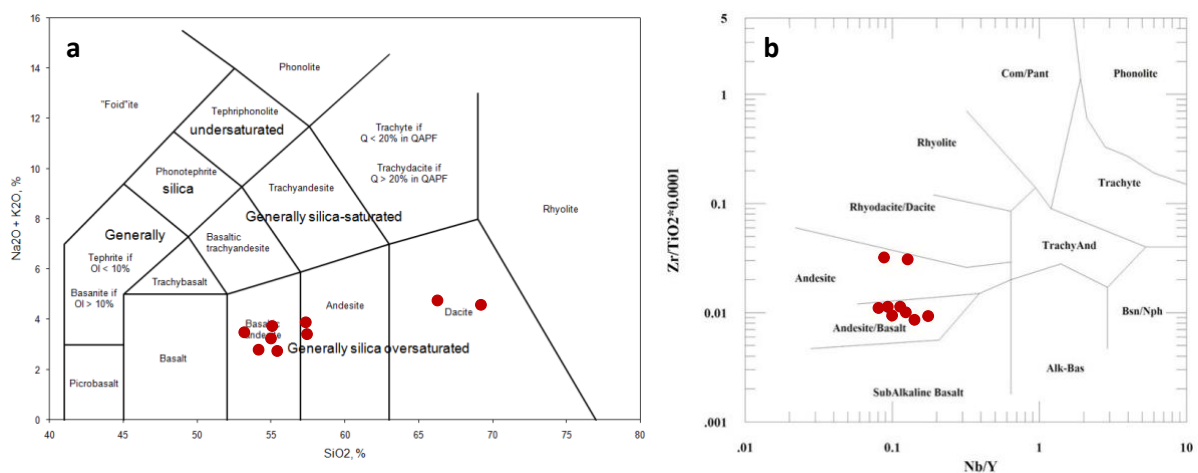


Figure 4. Volcanic rocks classification by geochemical composition (a) $\text{Na}_2\text{O}+\text{K}_2\text{O}/\text{SiO}_2$ ¹⁰ and (b) $\text{Zr}/\text{Ti} \times 0.0001$ - Nb/Y ¹¹.

The studied andesites were plotted close to the plagioclase area with a high molar $(\text{K}+\text{Na}+2\text{Ca})/\text{Al}$ value and very low molar K/Al on the diagram¹¹⁻¹². Potassium metasomatism decreases molar $(\text{K}+\text{Na}+2\text{Ca})/\text{Al}$ and increases molar K/Al values, partly observed for the studied rocks (Figure 5a). This diagram can assume as the andesite gained K^+ as well as loss Na^+ and Ca^{2+} similarly to CCPI. This result is relatively consistent with some plagioclases' petrography altered to sericite, and alkali-feldspars were replaced by clay minerals in the selected volcanic rocks. According to the verses of AI and CCPI, andesitic samples are interpreted as related to plagioclase alteration or sericitization and alteration of alkaline feldspar (Figure 5b).

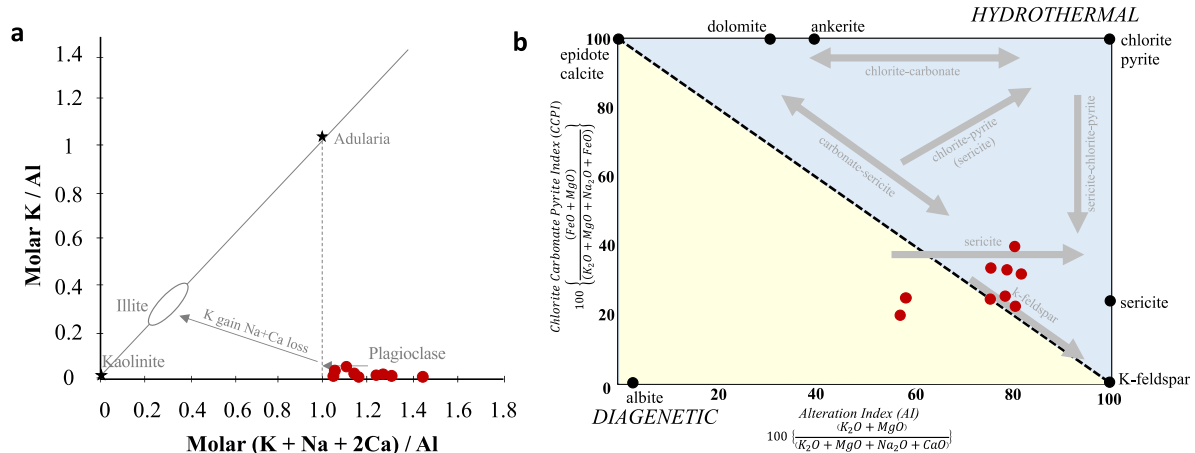


Figure 5. (a) Plots of K/Al vs. (K+Na+2Ca)/Al¹¹⁻¹² by the alteration minerals kaolinite, illite, and adularia plot on a line of slope 1. Unaltered rocks typically have (K+Na+2Ca)/Al >1. Potassium metasomatism leads to decreasing (K+Na+2Ca)/Al and increasing K/Al values. (b) Plots of the Chlorite-Carbonate-Pyrite Index versus Alteration Index of studied volcanic rocks on the alteration box plot¹³ showing the relative degree of alteration and general alteration mineralogy.

Conclusion:

Field studies have shown that the Pak Pat Volcanic Rocks at Nam Pat District, Uttaradit Province, Northern Thailand are composed of volcanic rocks cooled from intermediate lava and pyroclastic rocks formed by explosion. The petrographical study classified rocks into 3 groups, which consist of (1) porphyritic andesite with plagioclase glomerocysts, (2) Seriated andesite exhibits plagioclase phenocrysts and groundmass alignment, and (3) plagioclase-rich crystal tuff presents pyroclastic poor-sorted. Plagioclase phenocrysts always present anhedral to subhedral crystals. All of these rocks illustrate moderate to high alteration i.e., plagioclase alters to sericite, epidote, and clay minerals. There are many directions of epidote, calcite, chlorite, and iron-rich veins. In addition, some of the rock has been replaced by epidote, chlorite, calcite, pyrite and small amounts of quartz.

The results of the study can be concluded that the volcanic rocks in Ban Pak Pat, Saen Tor Sub-district, Nam Pat District, Uttaradit Province had an explosive eruption, which is hypothesised to have caused a lava flow, volcanic fragments, and volcanic ash before the lava cools and crystallizes to volcanic rocks. These volcanic fragments and volcanic ash are also deposited in this lava bundle, which produces pieces of pyroclastic rocks. The volcanic rocks in this area can be classified into two volcanic facies that comprise (1) volcanic rocks formed by cooling lava with intermediate composition (andesite) and (2) pyroclastic rocks formed by deposits of volcanic ash and volcanic fragments (crystal tuff).

Intermediate-mafic volcanic rocks in this study area can be classified according to their chemical composition as basaltic andesite, andesite, and dacite (based on major oxides), as well as andesite and andesite/basalt (based on trace elements). According to high molar (K+Na+2Ca)/Al and very low molar K/Al, the andesite gained K⁺ as well as loss Na⁺ and Ca²⁺ by alteration process. In addition, the AI and CCPI ratios of andesites are interpreted as related to the sericitization of plagioclase and alteration of alkaline feldspars.

Further study of the chemical composition is required because the rock samples taken in the study are probably different from their origin because these rocks have altered a lot. As a result, the geochemical data is inappropriate for tectonics interpretation. Therefore, a rare



earth elements (REEs) analysis should be conducted for more in-depth details to describe the tectonic setting and the eruption environment of the area.

Acknowledgements:

The authors would like to acknowledge the Department of Geological Sciences, Faculty of Science, Chiang Mai University for laboratory study.

References:

1. Charusiri P, Daorerk V, Archibald D, Hisada K, Am-paiwan T. J Geo Soc Thailand. 2002;1:1–20.
2. Metcalfe I. J Asian Earth Sci. 2013;66:1-33.
3. Sone M, Metcalfe I. Tectonics. 2008;340:166-179.
4. Zaw K, Meffre S, Lai CK, Santosh M, Burrett C, Graham IT. Gondwana Res. 2014;26:5-30.
5. Singharajwarapan S, Berry R. J Asian Earth Sci. 2000;18:663-673.
6. Lüddecke S, Chonglakmani C, Helmcke D. J Geo Soc Thailand. 1991;2:91-101.
7. Streckeisen AL. Neues Jahrbuch für Mineralogie, Abhandlungen. 1978;141:1-14.
8. Schmid R. J Geo Soc America. 1981;9:41-43.
9. Le Bas MJ, Le Maitre RW, Streckheisen A, Zanettin B.A. J Petro. 1986;27:745–750.
10. Winchester JA, Floyd PA. Chem Geol. 1977;20:325–343.
11. Booden MA, Smith IEM, Mauk JL, Black PM. J Volc Geotherm Res. 2010;195:83-96.
12. Madeisky HE. Geology and ore deposits of American Cordillera. 1996;3:153-185.
13. Large RR, Gemmell JB, Paulick H, Huston DL. Economic Geol. 2001;96:957-971.



ONE-STEP SYNTHESIS OF SUGARCANE BAGASSE GROUND-BASED MICROPOROUS CARBON USING KOH AS AN ACTIVATION AGENT FOR CO₂ ADSORPTION.

Ratchadaporn Kueasook, Liqing Li*

School of Energy Science and Engineering, Central South University, Changsha Hunan, 410082, China.

*e-mail: liqingli@hotmail.com

Abstract:

Microporous carbon materials were successfully prepared from sugarcane bagasse via solid-state potassium hydroxide (KOH) activation. The preparation procedures were proposed in this study; and could be considered as an easy and solvent-free for the synthesis of materials. Sugarcane bagasse was used as carbon precursor, melamine as a nitrogen source, and KOH as an activation agent. The microporous carbon material was then obtained by pyrolysis at 600 °C for 1 h under nitrogen atmosphere. The effects of with-/without activation agent were studied. Evidently, various techniques were employed to investigate the physicochemical properties of the micropore carbons. The BET surface area and pore volume of the microporous carbon materials were estimated from the N₂ adsorption isotherms at 77 K, up to 787.972 m²/g and 0.463 cm³/g respectively. The narrow pore size distribution showed an average supermicropore size of about 0.53 nm. The chemical activation using KOH provided microporosity. The microporous carbon material (BMOH) showed the carbon dioxide adsorption at 1 bar of 4.36 and 2.96 mmol/g at 0, 25 °C respectively. The adsorption capacity of carbon dioxide for KOH-activated microporous carbon material is higher than carbon material (without KOH activation). Apparently, this showed that microporosity is considered as the crucial factor for carbon dioxide adsorption performance.

Introduction:

Increasing levels of greenhouse gases such as methane, CO₂, chlorofluorocarbons, and nitrous oxide have contributed the global climate change. CO₂ is one of the most important greenhouse gases because it causes about 65% of the total greenhouse effect such as global warming, sea levels rising and extreme weather(1). For this reason, the development of efficient and economical CO₂ capture technologies is necessary. Different technologies have been used to capture CO₂ such as physical, chemical adsorption and membrane separation. Adsorption is considered one of the most suitable and effective choices because of simplicity, consumes low energy, and easy to regeneration. Many porous materials such as metal-organic frameworks (MOFs)(2), covalent organic frameworks (COFs), zeolite(3), and carbon material(4–6) are used as adsorbents. Activated carbon materials is the most widely used and effective adsorbent because of its high specific surface, large pore volume and high physical and thermal stability. This makes activated carbon a good material for CO₂ adsorption. Biomass is a considered resource for preparing activated carbon materials because of its abundant, renewable, low-pollution and low-cost materials. Sugarcane bagasse is consisted of three main components which are hemicellulose, lignin, and pectin. indicating that it can be pyrolyzed to produce carbon compounds with functional groups(7). Sugarcane bagasse, the main waste product of the sugar industry was selected as the carbon source in this study. In addition to activation treatment, the presence of numerous active functional

groups is a crucial factor in improving the efficacy of carbon materials in various applications via using of surface modification techniques. The process of doping nitrogen has garnered significant attention in studies due to its abilities as an effective means of enhancing the capacity for CO₂ adsorption. The N atom's amount of protons plays in determining how reactive an amine will be to acidic CO₂ molecules(8,9). It is the common knowledge that CO₂ molecules have an acidic character, which causes them to interact with the amine functional groups in an acid-base manner. From the previous research, the synthesis of activated carbon from biomass requires a two-step process. Firstly, the carbonization of the biomass in an oxygen-free environment at a temperature below 800°C. Secondly, the activation of the resulting carbon enhances its microstructural characteristics including surface area, porosity, pore volume, pore diameter, and surface modification(10,11).

Therefore, this study proposes a unique, simple approach for fabricating microporous carbon in one step by using a carbonization process coupled with doping melamine and activation with KOH where the carbon precursor is mixed with a nitrogen source and activation agent before carbonization. Bagasse was used as a carbon precursor, potassium carbonate as an activation agent, and melamine as the additional N source.

Methodology:

The microporous carbon materials (BMOH) from sugarcane bagasse via solid-state potassium hydroxide (KOH) activation was synthesized by the following procedure (**Figure 1.**). First, sugarcane bagasse was washed with distilled water several times to remove impurities. After that, the resulting was dried in an oven at 100°C for 48 h, and then the dried bagasse was grounded. For a typical preparation method of the microporous carbon materials, bagasse grounds (1g), melamine (0.25g), and KOH (1g) were mixed in a mortar for 15 minutes. The obtained materials were placed in a tube furnace at a 600°C rate of 5°C/min under N₂ flow of 200 mL/min for 1h. After carbonization, the resulting materials were cooled down to room temperature. The next steps are to wash with 5% HCl and then wash with DI water several times until pH neutral removes the remaining impurities. Finally, the microporous carbon material was obtained. As a control experiment, bagasse grounds mixed with KOH was carbonized without melamine labeled name “BK”.

The pore structure characteristics of BMOH and BM were characterized by N₂ adsorption-desorption isotherms at -196°C. Based on isotherm, the Brunauer-Emmett-Teller (BET) and 2D non-local density functional theory (2D-NLDFT) methods were used to calculate the specific surface area (S_{BET}) and pore size distribution. The surface property of BMOH was studied by X-ray photoelectron spectroscopy (XPS). To investigate the adsorption efficiency of BMOH and BM towards CO₂, adsorption isotherm experiments were performed by using Surface Area and Porosimetry Analyzer (JW-ZQ200). The sample was pretreated at 150°C in a vacuum environment for 3h before measurements. The CO₂ adsorption experiments were measured at 0 and 25 °C under 1 bar pressure.

Results and Discussion:

The preparation method that proposed in this study can be considered to be easy and solvent-free for the synthesis of materials. Moreover, multiple steps usually used for chemical activation can be avoided. Melamine served as the N-dope during the carbonization process. Moreover, KOH was easily combined with bagasse grounds and then the resulting mixture was treated for carbonization and activation without any adding steps (**Figure 1.**). The morphology of synthesized materials was studied by using scanning electron microscopy (SEM). **Figure 2.** shows macropores originated from the natural phloem and xylem of BG.

This confirms that the macropores in the raw sugarcane bagasse can be reserved even after high-temperature treatment in the preparation process. The activated sample reveals a small pore in the surface due to the chemical activation with KOH. The nitrogen adsorption-desorption isotherms and 2D-NLDFT pore distributions of synthesized materials are shown in **Figure 3**. Both samples exhibit a type I isotherm, as classified by the IUPAC, indicating that the microporosity is mainly present. For the BMOH (KOH-activated), The BET surface area is $787.972 \text{ m}^2/\text{g}$, and the pore volume is calculated to be $0.463 \text{ cm}^3/\text{g}$. The pore size distribution using the 2D-NLDFT model indicates the existence of micropore size with an average diameter of 0.560 nm . Supermicropores, which have dimensions ranging from less than 0.7 to 0.9 nm , are known to have a considerable impact on physical adsorption. In comparison, the non-activated sample (BM) demonstrates an absence of porosity in the micropore region (**Figure 3b.**). According to the results from the N_2 sorption analysis, it is indicated that the microporosity was generated from the activation agent (KOH) on the BG surfaces. Therefore, the KOH activation strongly influences the BET surface and amount of micropore.

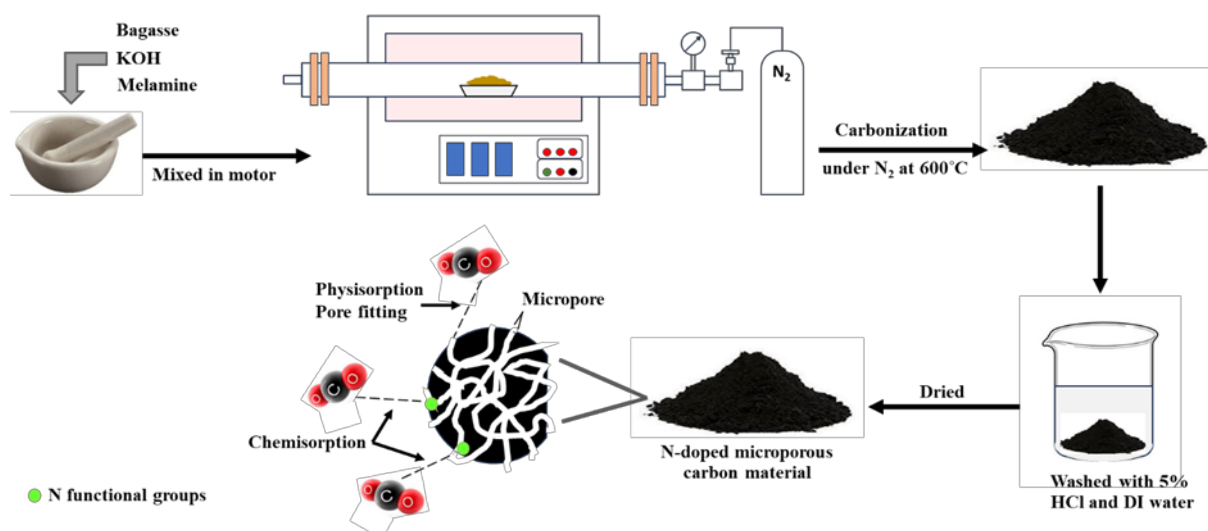


Figure 1. Schematic Illustration of the preparation steps for BMOH for CO_2 adsorption.

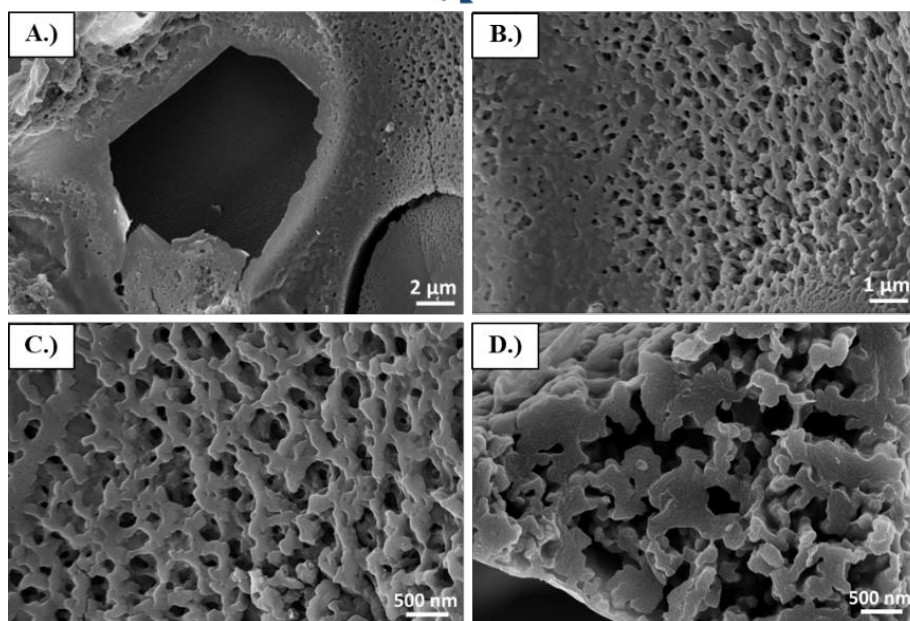


Figure 2. SEM image of BMOH.

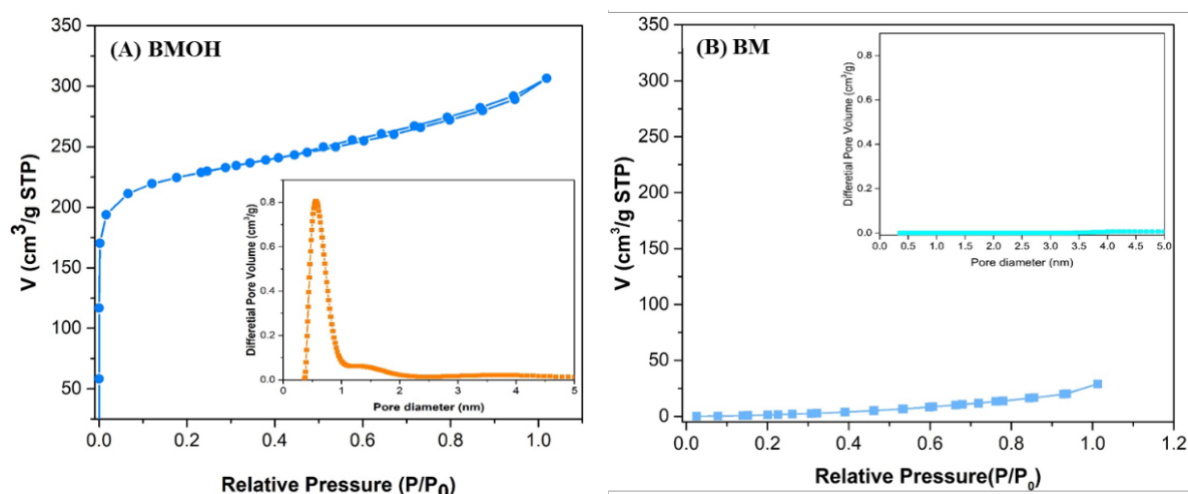


Figure 3. N₂ adsorption-desorption isotherms at -196°C and pore size distributions using 2D-NLDFT model.

The elemental compositions and functionality assignments on the BMOH surface were determined by using X-ray photoelectron spectroscopy (XPS). The wide scan presented in **Figure 4a**, reveals that the BMOH sample exhibited carbon, nitrogen, and oxygen levels within the ranges of 85.32 wt%, 8.02 wt%, and 6.67 wt%, respectively. The deconvoluted spectra for C1S (**Figure 4b**) for BMOH show patterns at binding energies of 284.2 and 285.5 eV corresponding to graphitic C=C and C-O respectively. In N1S spectra **Figure 4c**, the main nitrogen functional group for BMOH was found to be pyrrolic nitrogen (400 eV) and pyridinic nitrogen (397.8 eV) with the absence of quaternary nitrogen. This showed that the N atom was successfully added to the carbon material.

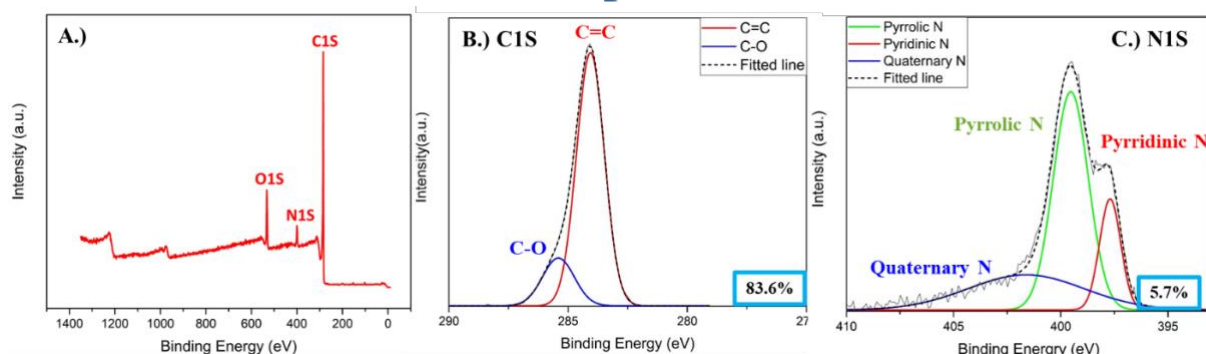


Figure 4. X-ray photoelectron spectroscopy (XPS) spectra of BMOH: (a) wide scan, (b) C 1s high-resolution spectra, and (c) N 1s high-resolution spectra.

The carbon dioxide adsorption isotherm at 0°C and 25°C under 1 bar for BMOH and BM are shown in **Figure 5**. The BMOH showed the carbon dioxide adsorption of 4.36 and 2.96 mmol/g at 0, 25°C respectively. Supermicropores which contain dimensions less than 1 nm are known to have a considerable impact on physical adsorption. While BM has no surface area according to the BET method, the CO₂ adsorption capacity of BG was 1.08 mmol/g at 25°C. This result suggests that the CO₂ adsorption capacity was not influenced only by microporosity but the nitrogen content of the sample affected the CO₂ adsorption capacity. The nitrogen functional group on sample surfaces interacts with carbon dioxide. Evidently, pyrrolic, pyridinic, amines, or amide groups are seen and considered as improving the adsorption ability of carbon materials for CO₂. According to previous reports, pyridinic nitrogen has provided a positive effect on the uptake of CO₂. This is attributed to the introduction of Lewis base sites and improved wettability, resulting in a stronger binding between pyridinic nitrogen and CO₂ molecules (12). Pyrrolic nitrogen groups are known to establish covalent bonds with CO₂ molecules through the hydrogen atom, which can be attributed to the high electronegativity of oxygen atoms in CO₂(13). Therefore, the main adsorption mechanisms of CO₂ on micropore material (BMOH) were pore filling, Lewis acid-base, and covalent bond(14,15).

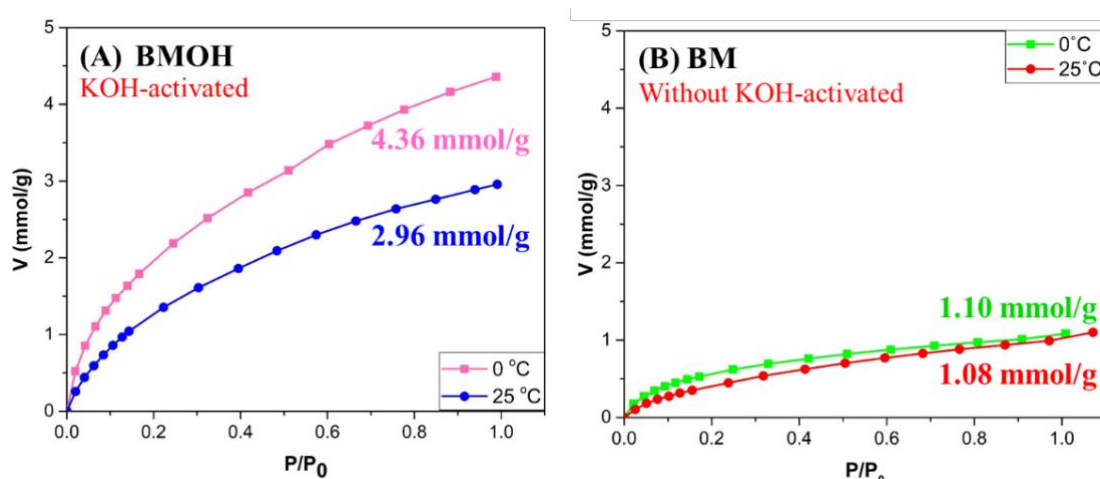


Figure 5. CO₂ adsorption isotherms of the synthesized samples.

Table 1. Pore texture properties were measured by nitrogen sorption at 77 K and CO₂ adsorption performance.

Samples	Weight of KOH (g)	S _{BET} (m ² /g)	Pore size (nm)	Pore volume (cm ³ /g)		CO ₂ adsorption (mmol/g)	
				V _T ^a	V _{Supermicro} ^b	25°C	0°C
BMOH	0.25	787.972	0.560	0.463	0.269	2.957	4.359
BM	-	4.360	4.479	0.041	-	1.101	1.084

^a Total pore volume

^b 2D-NLDFT Supermicropore volume (<1nm)

Conclusion:

The preparation material (BMOH) was successfully prepared from sugarcane bagasse via solid-state potassium hydroxide (KOH) activation. Sugarcane bagasse was used as a carbon precursor, melamine as a nitrogen source, and KOH as an activation agent., followed by pyrolysis under a nitrogen atmosphere. Various techniques were used for the investigation of chemical and physical properties. The resulting material showed a supermicropore structure and N-content. The doping of N was beneficial to the improvement of CO₂ adsorption efficiency. BMOH showed good adsorption performance of carbon dioxide. It can be concluded that the adsorbent's narrow micropores and N content played a crucial role in the process of CO₂ adsorption.

References:

1. Quan C, Zhou Y, Wang J, Wu C, Gao N. Journal of CO₂ Utilization. 2023;68:102373.
2. Gaikwad S, Kim Y, Gaikwad R, Han S. J Environ Chem Eng. 2021;9(4):105523.
3. Bae TH, Hudson MR, Mason JA, Queen WL, Dutton JJ, Sumida K, et al. Energy Environ Sci. 2013;6(1):128–38.
4. Khosrowshahi MS, Mashhadimoslem H, Emrooz HBM, Ghaemi A, Hosseini MS. Diam Relat Mater. 2022;127:109204.
5. Staciwa P, Sibera D, Pelech I, Narkiewicz U, Łojkowski W, Dąbrowska S, et al. Microporous and Mesoporous Materials. 2021;314:110829.
6. Liu X, Zhou Y, Wang CL, Liu Y, Tao DJ. Chemical Engineering Journal. 2022;427:130878.
7. Guo Y, Tan C, Sun J, Li W, Zhang J, Zhao C. Chemical Engineering Journal. 2020;381:122736.
8. Shi J, Cui H, Xu J, Yan N, You S. Journal of CO₂ Utilization. 2022;62(June):102081.
9. Chang B, Shi W, Yin H, Zhang S, Yang B. Chemical Engineering Journal. 2019;358:1507–18.
10. Luo S, Chen S, Chen S, Zhuang L, Ma N, Xu T, et al. J Environ Manage. 2016;168:142–8.
11. Han J, Zhang L, Zhao B, Qin L, Wang Y, Xing F. Ind Crops Prod. 2019;128:290–7.
12. Cruz OF, Gómez IC, Rodríguez-Reinoso F, Silvestre-Albero J, Rambo CR, Martínez-Escandell M. Chem Eng Sci. 2023;273:118671.
13. Wu Y, Wang J, Muhammad Y, Subhan S, Zhang Y, Ling Y, et al. Chemical Engineering Journal. 2018;349:92–100.



14. Rouzitalab Z, Mohammady Maklavany D, Rashidi A, Jafarinejad S. J Environ Chem Eng. 2018;6(5):6653–63.
15. Zhao J, Shan W, Zhang P, Dai S. Chemical Engineering Journal. 2020;381:122579.



SESSION F-FOOD SCIENCE AND TECHNOLOGY/AGRICULTURAL SCIENCE



CHARACTERIZATION OF PECTIN FROM DURIAN RIND USING STEAM EXPOSITION

Suthipat Chookan,¹ Kesini Chaykat,¹ Nantharat Phruksaphithak^{2,*}

¹Scientific Classroom in the University-Affiliated School Project, Faculty of Science, Thaksin University, Phatthalung, Thailand

²Department of Chemistry, Faculty of Science, Thaksin University, Phatthalung, Thailand

*e-mail: nantharat@tsu.ac.th

Abstract:

Durian is a famous fruit of Thailand and Southeast Asia. Due to Thailand's high yearly durian production volume of over 599.6 thousand metric tons, there is an abundance of durian biomass waste, which is becoming more and more popular around the world. Characteristics of durian pectin which was extracted from a steam explosion technique at 121°C for 30 minutes were studied. The results show that the durian pectin had a brown color. The yield, moisture content, and ash of durian pectin are $6.78 \pm 0.48\%$, $9.31 \pm 0.57\%$, and $9.33 \pm 0.31\%$, respectively. Fourier transform infrared spectroscopy (FT-IR) and X-ray diffraction (XRD) analysis confirmed the durian pectin structure in terms of functional groups of polysaccharides and crystalline, respectively. The thermal stabilities of durian pectin were investigated using thermogravimetric analysis (TGA). The findings demonstrate that durian rind can be a suitable alternate source for pectin extraction, acquiring potential advantages for industrial pectin extraction economically and environmentally.

Introduction:

Pectin, a biopolymer comprising a blend of naturally occurring polysaccharides, is commonly found in the primary cell walls of many plant cells. Its applications have been expanding rapidly in the pharmaceutical and biotechnology sectors. Traditionally, pectin has been utilized for making jams due to its exceptional gelling and thickening properties. More recently, it has found its way into drug delivery systems and various other biotechnological applications. Pectin also serves as a matrix material for encapsulating drugs, proteins, and cells. Beyond these applications, numerous studies have indicated that incorporating pectin into one's diet can lead to reductions in serum total cholesterol and low-density lipoprotein cholesterol levels, as well as the moderation of glucose responses¹.

Steam explosion (SE) is an efficient heat treatment technology. The principle of SE is that biomass undergoes high-pressure steam and then instantaneously depressurizes, opening the biomass structure and releasing small molecular substance. Studies have shown that SE has a high extraction yield in the extraction of bioactive components, such as phenols, flavonoids, and monosaccharides².

The durian fruit, a renowned Thai delicacy, enjoys global popularity. It is characterized by its substantial size, typically round or oval shape, and a green hue that turns brownish when ripe. Encased in a thick, hard outer shell adorned with pyramid-shaped thorns, the durian's distinctive appearance sets it apart. However, it's worth noting that a significant portion of the durian's total weight, approximately 65-70%, comprises inedible durian rinds³. This surplus waste poses a notable environmental challenge, often ending up in landfills or being incinerated, thereby contributing to air, land, and water pollution. Consequently, harnessing the potential of durian rinds as a source of pectin holds both economic and environmental

promise. The purpose of this research is to determine pectin content in durian rinds using steam explosion extraction and to partially characterize the properties of pectin from durian rinds

Methodology:

Materials

Ethanol used in this work was food grade. The durian huk of Durian Monthong was obtained on the same day from the local market at Paphayom, Phthalung. The durian rind (white part) was separated from the fruit, cut into pieces, washed, and dried in a vacuum oven at 45°C for 48 h. The dried durian rind was ground in a mesh size of 100 µm and packed in a polyethylene bag at ambient temperature in addition to that stored for the extraction process.

Pectin extraction

Pectin was extracted from the durian rind under the optimal conditions⁴. Deionized water (DI) and dried durian rind were combined in a 1:12 w/v solid to liquid ratio. After that, the mixture was extracted for 30 minutes at 121°C using an autoclave. After being allowed to cool to room temperature at 25°C, the slurries were filtered through cheesecloth. Two rewashes of the solutions were performed using 80% ethanol at a clear solution to ethanol ratio of 1:2 v/v. After collecting the precipitate, acetone was used to wash it. After the wet pectin was dried for 12 hours at 65°C, its weight remained constant. Lastly, the dehydrated pectin was sieved and powdered in a grinder in preparation for additional research.

Characterization

The yield percentage of pectin was computed and reported as yield (%)¹.

$$\text{Yield(\%)} = \frac{\text{Weight (g) of pectin}}{\text{Weight (g) of dried durian power}} \times 100$$

The technique used to calculate the moisture content was as follows⁴. Equation following was used to compute the moisture content.

$$\text{Moisture(\%)} = \frac{\text{Weight (g) of sample before drying} - \text{weight(g) of sample after drying}}{\text{Weight (g) of sample before drying}} \times 100$$

Ash contents of the durian rind, pectin and commercial pectin were determined using the method⁵. The ash content of pectin samples was calculated according to equation

$$\text{Ash content(\%)} = \frac{\text{Weight (g) of ash}}{\text{Weight (g) of sample}} \times 100$$

The Fourier-transform infrared spectroscopy (FTIR) spectrum of the dried durian rind and the pectin was recorded with Agilent Cary 630 FTIR spectrometer. The scanning range was 4000 to 650 cm⁻¹, and the resolution was 4 cm⁻¹.

X-ray diffraction (XRD) (D2 Phaser, Bruker) was used to determine the crystallinity of the durian pectin.

The dried durian rind and the pectin were then observed by a scanning electron microscope (SEM) (FEI Quanta 450 FEG). All samples were sputter coated with gold before shooting. A thermogravimetric analyzer (TGA 8000, PerkinElmer) was used to analyze the thermographic properties of durian pectin.



Results and Discussion:

Pectin

The durian rind is a solid that present a light yellow-brown color. Using steam explosion, pectin from durian peels is a solid that is a dark brown color. While commercial pectin appears as a solid or fine powder that is white-to-light-brown powder, in color. The durian pectin extracted from durian rind using the steam explosion method has a darker color than commercial pectin. The pH of durian pectin is approximately 3.58 ± 0.04 which higher than commercial pectin (2.92 ± 0.02).



Figure 1.
Pectin photograph

Pectin yield

The results for physicochemical characteristics of pectin from different sources are displayed in Table 1. The yield of extracted pectin from durian rinds has the least yield 6.78 ± 0.48 % while the pectin yield of other varieties does not differ distinctly with durian in Malaysia such as Musang King (7.73 ± 0.23), Hajjah Hasmah (5.60 ± 0.20)⁶, which is lower than the values reported for other papaya peel (19.32 ± 2.08)⁷. The amount, chemical structure and chemical composition of pectin could differ relying on plant species and varieties due to genetic factors (e.g., gene expression) or development factors (e.g., climate) of the plants⁶ and the extraction methods⁷

Table 1.
Physiochemical properties of durian rind, durian pectin, and commercial pectin

Characteristics	Value obtained		
	Durian rind	Pectin	Commercial pectin
Yield (%)	-	6.78 ± 0.48	-
Moisture content (%)	9.11 ± 0.11	9.31 ± 0.57	5.76 ± 0.13
Ash content (%)	3.51 ± 0.26	9.33 ± 0.31	2.23 ± 0.48

Moisture content

Moisture content is very crucial in determining the quality of food products and needs to be emphasized for preserving of the materials when stored. This is to avoid enzymatic degradation and also prevent from the microbial growth. From the results in Table 1, it

exhibited that the moisture content of durian pectin was 8.31 ± 0.57 %. This means that the moisture content of durian pectin was in the acceptable range which is lower than 12%^{4,8}

Ash content

Parameter of ash content revealed the inorganic impurities found in the pectin. Pectin may indicate as pure, good quality and have ability for better gel-forming when it contains low value of ash content. The result obtained for ash content of durian pectin as shown in Table 1 was found to be 9.33 ± 0.31 %. It is observed that the value of ash content in durian pectin is lower. The maximum limit of ash content in pectin must be 10% which indicates a good quality of gel formation. Thus, the lower ash content presents in this study shows the purity of pectin and also considered as a good pectin quality [5] [10].

Characterization of pectin

The amorphous or crystalline durian pectin structure was examined using X-ray diffraction (XRD) investigations, as shown in Figure 2. Sharp signals at 14.05, 21.18, and 31.98 (2θ) in the durian pectin's XRD pattern, which represent the crystal structure and molecular arrangement of pectin, are visible. It is generally acknowledged that pectin is always present, although, less crystalline or amorphous. Similar findings for pectin from various sources were reported in earlier investigations¹⁰. It's possible that one of the extract's components is pectin.

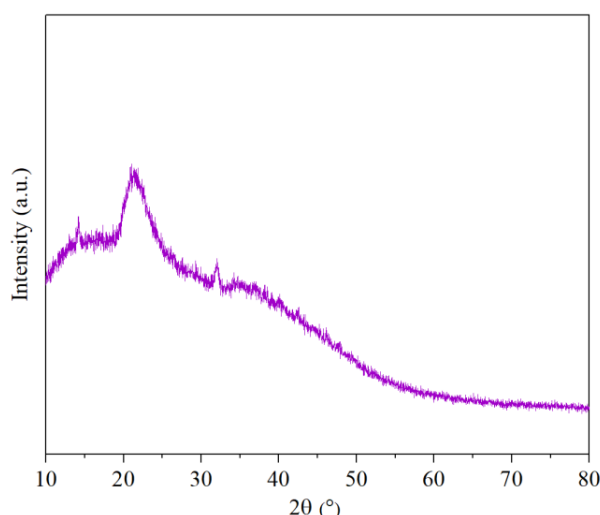


Figure 2.
XRD of the extracted pectin

Further FT-IR research was required to confirm pectin's status as a constituent based on the results of the original XRD analysis. Figure 3 illustrates that pectin is composed of various functional groups, such as hydroxyl (-OH), ester (-COO-), and carboxyl (-COOH) groups. The FTIR spectra of samples of durian pectin show characteristic peaks at 3357, 2930, 1739, and 1010 cm^{-1} , which correspond to -OH, -CH, C=O of ester, and C-O of galacturonic acid, respectively⁸. The low intensity bands at 1230 cm^{-1} show that the pectin samples were acetylated. The region of 1200-1000 cm^{-1} is where glycosidic bond skeletal C-O and C-C vibration bands are located. Consequently, we are able to confirm that the extract's FT-IR spectra include pectin. The peaks in the durian pectin are more noticeable than they are in the dried durian rind. This is because the FTIR functional group and other durian rind components are enhanced during the extraction process, resulting in a concentration of pectin.

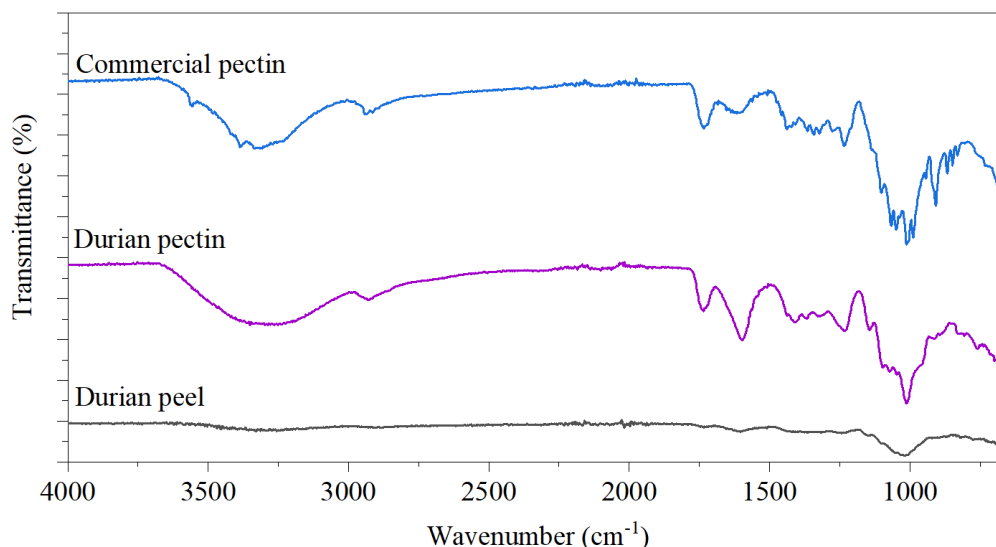


Figure 3.
FTIR spectrum of dried durian and extracted pectin.



Figure 4.
SEM of dried durian rind power, durian pectin and commercial pectin.

SEM of dried durian rind powder, durian pectin and commercial grade are presented in Fig.4. The micrograph of initial dried durian powder was compact and smooth in shape. Meanwhile, the SEM of durian pectin was illustrated in Fig. 4. The micrographs demonstrate the uneven forms, rough surface, and tactile sensitivity of durian pectin. The fingers' moisture moistens the surface, smooths it, and improves the pectin's ability to bond with other particles¹². A prior investigation on the pectin from mango and apple pomace revealed uneven and rough surfaces as well. Because of its small particle size, commercial pectin also produced comparable results.

Thermal properties of pectin

Thermogravimetric analysis was utilized to examine the thermal stabilities of durian pectin, as illustrated in Figure 5. According to the results of the thermogravimetric analysis (TGA), durian pectin's weight can be split into three zones, which has also been noted in earlier research⁸. The first zone (50 - 170 °C) shown a slight mass loss (around 15%) as a result of absorbed water in the pectin evaporating. The second zone (170 - 400 °C) demonstrated a considerable drop in weight (about 45%) as a result of the breakdown of the pyrolytic

polysaccharide. At this point, the pectin's galacturonic acid chain underwent significant heat breakdown, the acid side chains and carbon in the ring underwent decarboxylation, and solid char and gaseous products started to form¹². Lastly, the third zone (400 - 600 °C) symbolized the weight loss that occurred gradually (about 40%) as a result of the char's thermal breakdown. Additionally, the quantitative values derived from the DP TGA curves are presented in Figure 5.

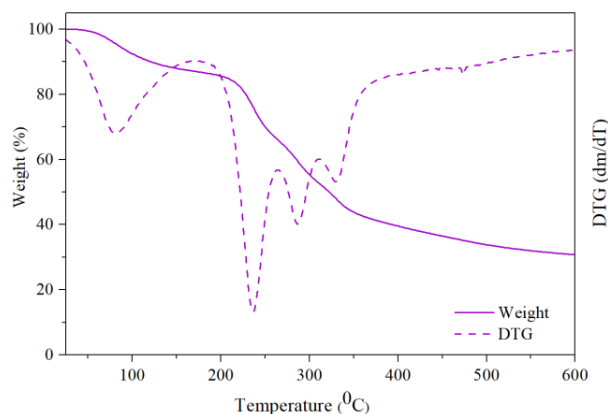


Figure 5.
Thermogravimetric analyses of durian pectin

T_{50%} represented the temperature at which 50% mass loss happens, whereas DTG_{max} showed the maximum decomposition rate temperature. T_{50%} and DTG_{max} values for DP were 321.93°C and 237.93°C, in that order. Conversely, at 600°C, the total mass loss of DP was 60%. The results are much higher than those of the melon rind and similar to those of the kiwifruit [14]. In conclusion, it seemed that the DP had a fair amount of thermal stability. Good thermal stability pectin is advantageous to the food industry since it may be utilized as a food additive in foods that are prepared at high temperatures, such as pastries, cakes, and bread.

Conclusion:

In this study, steam extraction was used to successfully extract pectin from dry durian rind. The morphological and chemical properties of pectin were described. The findings demonstrated that, in comparison to other fruit peels, durian pectin yields a lower amount of pectin. However, it's to note that high moisture and ash contents were discovered in the extracted durian pectin. While, the industrial waste's high degree of purity was shown by its lower ash concentration. In light of these findings, durian rinds appear to be a one promising source of pectin. This has the potential to facilitate the mass manufacturing of different polysaccharides, such as pectin and its derivatives, from agro-industrial waste in a more sustainable manner.

Acknowledgements:

Our team of reseachers would like to thank the Science Classroom in the University-Affiliated School Project (SciUS), under the direcrion and support of the Ministry of Higher Education, Science, Research. and Innovation, for finacial support. We would also like to thank the Department of Chemistry, Faculty of Science, Thaksin University, Phatthalung campus for the chemical suggestions and their great support too.



References:

- [1] Freitas CMP, Coimbra JSR, Souza VGL, Sousa RCS. Coatings. 2021;11(8): 922.
- [2] Liang Y, Yang Y, Zheng L, Zheng X, Xiao D, Wang S, Ai B, Sheng Z. Foods. 2022; 11(24): 3995.
- [3] Jong SH, Abdullah N, Muhammad N. Carbohydr. Polym. Technol. Appl. 2023;5: 100263.
- [4] Suwannar Y, Sawasdika J, Suwannara R. Rajabpat Rambhai Barni Research Journal, 2021; 13(2): 25-37.
- [5] Hasem NH, Mohamad Fuzi SFZ, Kormin F, Abu Bakar MF, Sabran SF. Earth Environ. Sci. 2019;269(1):012019.
- [6] Ceylan C, Bayraktar O, Atci E, Sarrafi S, GIDA. 2017;42(5):568-576.
- [7] Jong SH, Abdullah N, Muhammad N. IOP Conf. Ser.: Earth Environ. Sci. 2021;736(1):012029
- [8] Carinna Ruth Darmawan YH. Reaktor. 2021;21(3):116-123
- [9] Mamiru D, Gonfa G. Heliyon. 2023;9(2):13525
- [10] Daud NZA, Said BNM, Ja'afar F, Yasin HM, Kusrini E, Usman A. IJTech. 2019;10(6): 1131
- [11] De Oliveira Junior SD, De Araujo JS, De Asevedo EA, De Medeiros FGM, Dos Santos VS, De Sousa Junio FC, De Araujo NK, Dos Santos ES. Biomass Conv. Bioref. 2023; 13(3):1565-1579.
- [12] Fracasso AF, Perussello CA, Carpine D, Petkowicz CLDO, Haminiuk CWI. Int. J. Biol. Macromol. 2018;109:784-792.
- [13] Wang W, Ma X, Jiang P, Hu L, Zhi Z, Chen J, Ding T, Ye X, Liu D. Food Hydrocoll. 2016;61:730-739.
- [14] Guzel M, Akpinar O. Food Bioprod. Process. 2019;115: 126–133.



MICROWAVE-ASSISTED EXTRACTION OF CAROTENOIDS IN PALMYRA PALM MEAT BY ADDING DIFFERENT VEGETABLE OILS AS SOLVENT

Dusida Noothong, Suhaimee Mattha, Bhudsawan Hiranvarachat*, Punnanee Sumpavapol and Karnjapan Janthawornpong

Faculty of Agro-Industry, Prince of Songkla University, Hat Yai Campus, Songkhla, Thailand

*e-mail: bhudsawan.h@psu.ac.th

Abstract:

The aim of this study was to study the effects of selected edible solvent by adding vegetable oil i.e., soybean oil and palm oil on the extraction of bioactive compounds from ripening meat of palmyra palm fruit by using microwave-assisted extraction (MAE). Solvent concentration of 10% (v/v) with a microwave power of 450 watts (W) during the extraction period of 0-35 min was investigated. Extracting by adding palm oil as solvent resulted in the highest β -carotene content, which was approximately 8 mg/100 g (d.b.). On the other hand, in the case of total carotenoids content, adding 10% of either palm oil or soybean oil resulted in the similar trend. Extracting carotenoids for 25-35 min resulted total carotenoids content in the range of 9.6-10 mg/100 g (d.b.). However, the antioxidant activities of the extracts under various extraction conditions did not exhibit significant variation.

Keywords: Vegetable oil, β -Carotene content, Antioxidant activities, palmyra palm meat, green extraction solvent

Introduction:

Asian palmyra palm (*Borassus flabellifer* L.) is one of the important crops in Thailand as it is known for its high economic and nutritional content. Ripen palmyra palm meat is the product that come from the part that connected to mesocarp of the ripe palm. Only ripen palmyra palm fruit can be harvested and utilized as a palm meat. Palmyra palm meat can used as an ingredient in many food dishes since it contains carotenoids and sweet-smelling. However, the fruit has a short shelf-life since it has a rich source of sugar, which resulted in easily deteriorated. Thus, in harvest season, many palmyra palm fruit is abandoned. Extraction the carotenoids in palmyra palm meat is one of the choices for adding value.

Many extraction techniques could be used in food industry. Microwave-assisted extraction (MAE) is one of the interesting techniques that operate a short time and enhance the higher extraction yields. Generally, microwave heats up food by directly radiate to polar compounds, such as water containing in food matrix. To extract carotenoids, which is a non-polar compound, the non-polar solvent should be added to get higher extraction yields. MAE involves the use of a solvent to extract the desired compounds in the form of an extract.^{1,2,3} The choice of solvent to extract carotenoids was focused in the study.

The traditional extraction method to extract carotenoids was the use of hexane or acetone or ethanol, which was not an environmentally friendly solvent. The utilization of environmentally solvents, such as water or vegetable oil, in green extraction processes is now interesting. Vegetable oils were selected for carotenoids extraction due to their lipophilic properties.



The aim of this work is to study the effects of vegetable oil on the extraction of carotenoids content, β -carotene content and antioxidant activities assessed by ABTS and FRAP assays in palmyra palm meat by using microwave-assisted extraction.

Methodology:

Sample preparation

The ripe palmyra palm fruit was collected around Songkhla city, Thailand. Only soften and yellowish fruit was used in the study. The palmyra palm meat was extracted from the mesocarp by pressing the detached mesocarp using hands with addition of some tap water. The excessive water was removed using filter cloth to get the palmyra palm meat. The palmyra palm meat was kept at 4°C.

The palmyra palm meat was dried by hot air drying at the temperature of 70°C until it reached the final moisture content of 10% (d.b.). Dried sample was milled and sieved with 80 mesh sieved. The powder dried sample was kept in the aluminum foil at -18°C prior to further analysis.

Preliminary experiments to determine rehydration ability

Since microwave generate heat by directing radiated to polar compounds. Dried palmyra palm meat was first rehydrated prior to extracting in the next step. Suitable condition to obtain rehydrated palmyra palm meat was conducted. The rehydration ability (R) of a dried sample was determined by immersing it in water at the proportion of sample and water in 3 samples were 1:10, 1:15, 1:20 for 10-60 min. Its weight of the sample was recorded. The rehydration ability was calculated by:

$$R = W_{after}/W$$

where W_{after} (g) is the rehydrated sample weight and W (g) is the weight of dried sample. The average values of five samples were reported.

Microwave-assisted extraction (MAE)

A domestic microwave oven at a frequency of 2450 MHz with the turn-table removed was modified for MAE. A 1000-mL round-bottom flask containing sample was placed inside the microwave oven cavity. The flask was fitted with an external condenser to condense the vaporized extract, which was then collected in a graduated cylinder. Cold water (~4 °C) was used as a condensing medium. 10 g of rehydrated sample at the suitable rehydration ability condition was mixed with 2 vegetable oils: soybean oil and palm oil at 10 % (w/v). Rehydrated sample without adding vegetable oils was used as a control. After MAE the condensed extract was mixed with the remaining extract in the flask. The whole content was filtered through Whatman No. 1 filter paper. A separation funnel was used to enhance the separation between the aqueous and organic phases. The organic phase, containing carotenoids, was stored in a dark tube prior to further analysis.

Total carotenoids analysis

Total carotenoids content was performed according to the method of Hiranvarachet et al.⁴ It was determined at 450 nm using a spectrophotometer. Quantification of the total carotenoids content was carried out by using β -carotene as a standard.

β -carotene analysis

β -carotene was quantified based on the suggested method of Hiranvarachet et al.⁴ The analysis system consists of an HPLC equipped with a photodiode array detector. A mixture of



methanol and tetrahydrofuran (THF) (80:20% (v/v)) was used as the mobile phase at a flow rate of 1.5 mL/min. Symmetry® C₃₀ 5 µm (4.6 × 250 mm) HPLC column (YMC, Japan) was used for the analysis of β -carotene. An extract was filtered through a 0.2-µm filter before injection. Detection of β -carotene was made at a wavelength of 450 nm.

ABTS assay

The antioxidant activities as assessed by ABTS assay was performed according to the methods of Hiranvarachat et al.⁵ with some modifications. ABTS^{•+} radical cation was prepared by mixing ABTS stock solution (7 mM) with 2.45 mM potassium persulphate (at a ratio of 2:1). The mixture was kept in dark at room temperature for 16 h. The solution was diluted with ethanol until its absorbance reached 0.70 ± 0.02 at 734 nm. Trolox was used as an antioxidant standard. 1 mL of ABTS^{•+} solution was mixed with 100 µL of Trolox solution. The absorbance was then measured at 734 nm using the spectrophotometer at exactly 1 min after mixing.

FRAP assay

The antioxidant activities as assessed by FRAP assay was performed according to the methods of Hiranvarachat et al.⁵. 300 mM acetate buffer at pH 3.6, which contained 16 mL of acetic acid per liter of the buffer solution; 10 mM TPTZ in 40 mM HCl solution and 20 mM ferric chloride solution were prepared. FRAP reagent was prepared by mixing 25 mL of the acetate buffer, 2.5 mL of the TPTZ solution and 2.5 mL of the ferric chloride solution. Trolox was used as an antioxidant standard. The prepared FRAP reagent was warmed to 37 °C. Three mL of the reagent was mixed with 100 µL of the Trolox solution. The absorbance was then measured at 593 nm using the spectrophotometer at exactly 4 min after mixing.

Statistical analysis

The data are presented as mean values with standard deviations. All data were subject to one-way analysis of variance (ANOVA) using SPSS® software. Differences between mean values were established using Duncan's multiple range tests at a confidence level of 95%. All experiments were performed in duplicate unless specified otherwise.

Results and Discussion:

Preliminary experiment to determine rehydration ability

Moisture content and rehydration ability of rehydrated palmyra palm meat at different proportion conditions was investigated (Table 1). The moisture content of the samples in all conditions were in the range of 88-90 kg/kg (d.b.). Regarding the rehydration ability, the more rehydration time resulted in the more rehydration ability. When more water was added to dried sample (at the proportion of 1:20), the higher rehydration ability of sample was recorded. the proportion of sample and water 1:20 for 50 min resulted in the highest rehydration ability.

**Table 1.** Rehydration ability of dried palmyra palm meat

Proportion of sample and water (w/v)	Time (min)	Moisture content (kg/kg, d.b.)	Rehydration ability
1:10	10	88.65±0.22 ^I	6.99±0.05 ^H
	20	88.96±0.14 ^{HI}	7.17±0.13 ^{GH}
	30	88.63±0.14 ^I	7.21±0.15 ^{FGH}
	40	88.93±0.24 ^{HI}	7.47±0.04 ^{DEF}
	50	89.30±0.24 ^{GH}	7.43±0.02 ^{DEFG}
	60	89.32±0.04 ^{GH}	7.49±0.02 ^{CDE}
1:15	10	89.49±0.03 ^{FG}	7.35±0.01 ^{EFG}
	20	89.95±0.17 ^{DEF}	7.63±0.01 ^{ABCD}
	30	90.00±0.15 ^{DEF}	7.67±0.01 ^{ABCD}
	40	90.15±0.25 ^{CDF}	7.76±0.12 ^{ABC}
	50	90.23±0.04 ^{BCDF}	7.70±0.13 ^{ABCD}
	60	89.80±0.02 ^{EFG}	7.80±0.15 ^{AB}
1:20	10	90.58±0.09 ^{ABC}	7.33±0.03 ^{EFG}
	20	90.74±0.21 ^{AB}	7.49±0.02 ^{CDE}
	30	90.39±0.02 ^{ABCD}	7.48±0.02 ^{DEF}
	40	90.59±0.20 ^{ABC}	7.55±0.09 ^{BCDE}
	50	90.60±0.27 ^{ABC}	7.86±0.04 ^A
	60	90.82±0.03 ^A	7.89±0.10 ^A

*Different letters in the same column indicate that values are significantly different ($p < 0.05$)

Total carotenoids and β -carotene contents of the extracts

Total carotenoids and β -carotene contents of the extracts by adding different vegetable oil were exhibited in Figures 1 and 2, respectively. In the case of total carotenoids content, the extract containing vegetable oil continuously increased in the first 20 min and started slightly constant. The trend depicted in the extraction line of both types of vegetable oils indicates a consistent direction. The observed trend indicates that the extracts containing vegetable oil exhibited higher concentrations compared to the control.

However, in the case of β -carotene content, the curve of the extract containing edible are continuously increased in the first 30 minute and start significantly dropped. These finding were in agreement with the study by Baria et al.⁶, which investigated the extraction of carotenoids in mango flesh using a microwave. Three types of vegetable oil: peanut oil, sunflower oil and flaxseed oil were conducted. The study revealed that the extraction time has an impact on carotenoids content due to the increased heat, leading to the degradation of carotenoids. The trend of extract containing palm oil seems to be higher than other samples. The β -carotene extracted within the duration of 25-35 min obtained a value within the range of 9.6-10 mg/100 g (d.b.).

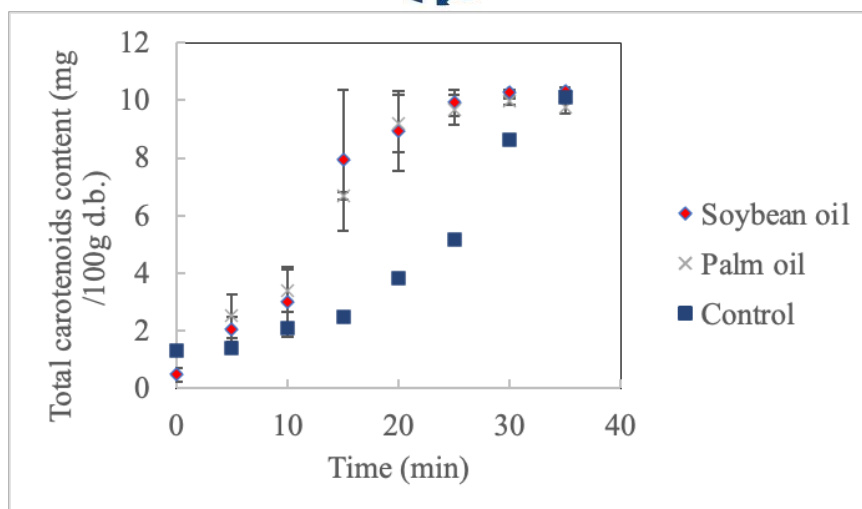


Figure 1.

Total carotenoids content of the extracts by adding different vegetable oil

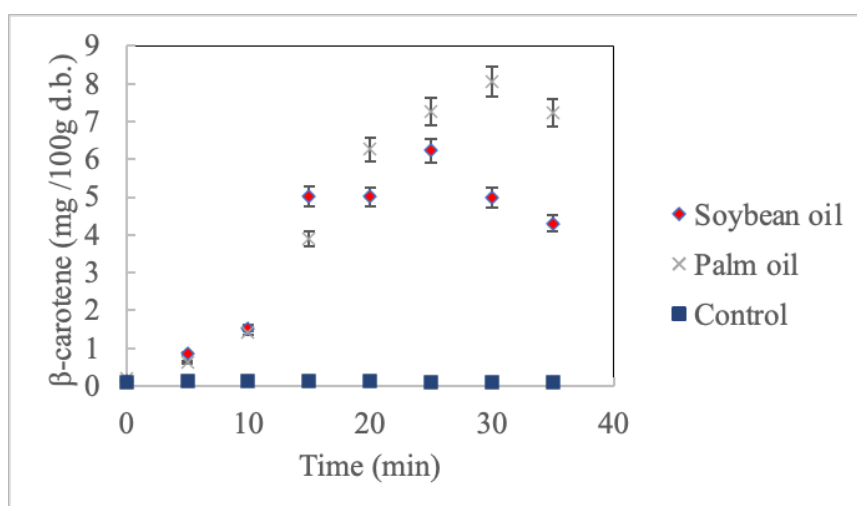


Figure 2.

β-carotene of the extracts by adding different vegetable oil

Antioxidant activities as assessed by ABTS and FRAP assays

The antioxidant activities as assessed by ABTS and FRAP assays were shown in Figures 3 and 4, respectively. In the case of ABTS assay, the trend of extract containing vegetable oils seemed to be unchanged. A slight difference in antioxidant activities was observed among the control and the extract using vegetable oil. Although the total carotenoids, as well as β-carotene content tended to increase during extraction, a slightly different in antioxidant activity as assessed by ABTS assay was observed during extraction process. The maximum antioxidant activities as assessed by ABTS was in the range of 0.13-0.14 mM Trolox/100 g (d.b.) in all types of vegetable oil. A similar trend was observed in the case of antioxidant activities as assessed by FRAP assay. This agreed with the research of Chuyen et al.⁷, which investigated the microwave-assisted extraction of rice bran using MAE and ultrasonic. They studied the use of microwaves power of 120, 240 and 360 W and extraction times in the range of 0 to 30 minutes. Carotenoids content and antioxidant activities were evaluated. The study



found that the levels of antioxidant compounds extracted were closely related to the total carotenoid content. Higher carotenoid content resulted in higher levels of antioxidant compounds.

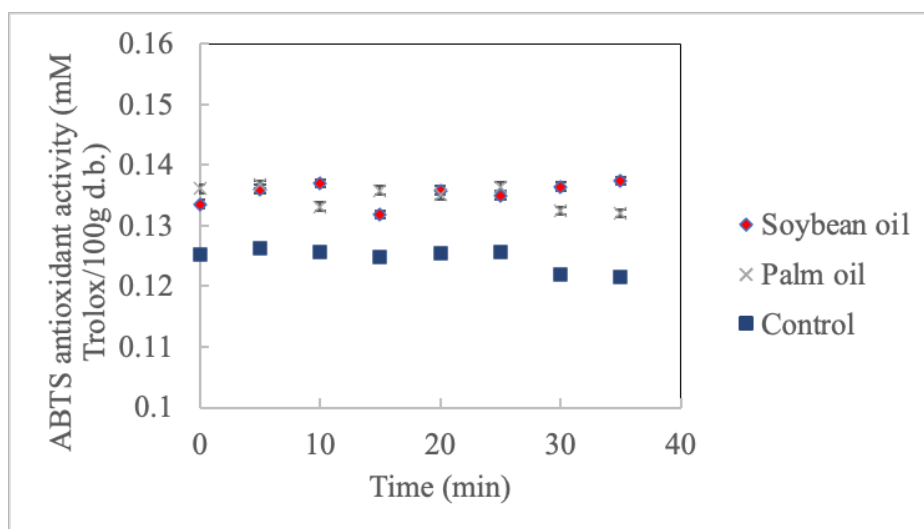


Figure 3.

ABTS antioxidant activity of the extracts by adding different vegetable oil

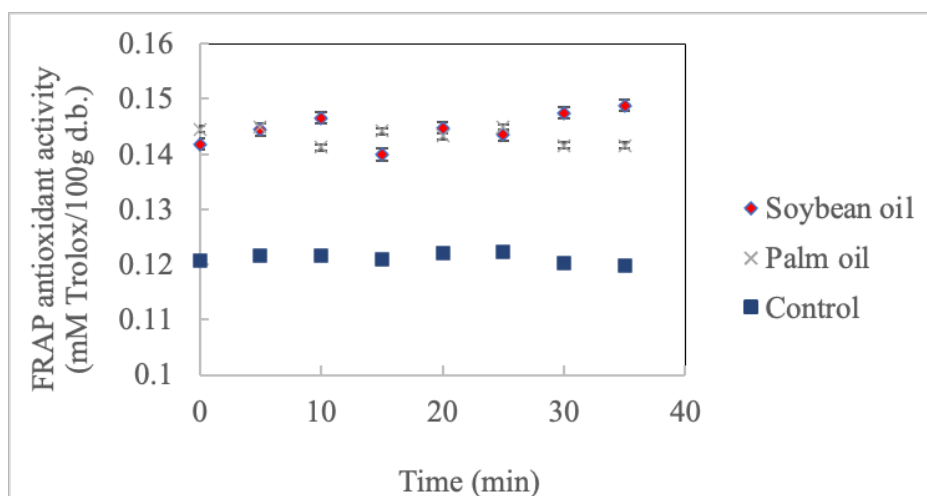


Figure 4.

FRAP antioxidant activity of the extracts by adding different vegetable oil

Conclusion:

Based on the study, two types of vegetable oils consisting of soybean oil and palm oil at the concentration of 10 (w/v) were used in the study. While extracting β -carotene at a microwave power of 450 W, adding 10% of palm oil yielded the highest β -carotene extraction at 8 mg/100 g (d.b.). On the other hand, in the case of total carotenoids content, adding 10% of either palm oil or soybean oil resulted in the similar trend. However, the antioxidant activities of the extracts in different extracting conditions were not much different.



Acknowledgements:

This research was supported by National Science, Research and Innovation Fund (NSRF) and Prince of Songkla University (Grant No. AGR6505153b).

References:

1. Hiranvarachat B, Devahastin S and Chiewchan N. *Int J Food Sci Nutr*. 2012; 47(3): 535-541.
2. Ying SW, Khoo HE, Kong KW and Ismail A. *Int J Food Prop*. 2013; 16: 826–837.
3. Tiwari S, Upadhyay N, Singh AK, Meena GS and Arora S. *J Food Sci Tech*. 2019; 56: 4678–4687.
4. Hiranvarachat B, Devahastin S and Chiewchan N. *Food Bioprod Process*. 2011; 89(2), 116-127.
5. Hiranvarachat B. and Devahastin S. *J Food Eng*. 2014; 126: 17-26.
6. Baria B, Upadhyay N, Singh AK and Malhotra RK. *LWT - Food Sci Technol*. 2019; 104: 186–194.
7. Chuyen HV, Nguyen MH, Roach PD, Golding JB and Parks SP. *Food Sci Nutr*. 2018; 6: 189–196.



SESSION SP2-2: THAI TRADITIONAL MEDICINE:
FROM TRADITIONAL USE TO
COMMERCIALIZATION RHODOMYRTUS
TOMENTOSA (AITON) HASSK AND
MITRAGYNA SPECIOSA (KORTH) HAVIL



EVALUATION OF ANTIOXIDANT ACTIVITY AND TOTAL PHENOLIC CONTENT OF DIFFERENT *Mitragyna speciosa* STRAINS IN THAILAND

Sirirat Srirat,¹ Wipawee Boonsri,¹ Netnapa Chana^{1,*}

¹Department of Chemistry, Faculty of Science, Thaksin University, Phatthalung Campus, Phatthalung, 93210 Thailand

*e-mail:netnapa@tsu.ac.th

Abstract:

Nowadays, *Mitragyna speciosa* commonly known as kratom has been a growing interest due to its numerous health benefits. Kratom, a medicinal plant native to Southeast Asia and indigenous to Thailand, is gaining popularity. In the southern region of Thailand, there are three types of kratom with morphological variations of leaf including red vein KanDang (KD), green vein TangGua (TG), and leaf with a pair of very small teeth near the apex known as YakYai (YY). This study focused on examining the total phenolic content (TPC) and antioxidant effects of these three kratom strains using DPPH, ABST, and FRAP assays. Plant leaves and petioles were extracted in ethanol. Among the strains, the YY strain exhibited the highest antioxidant activity and also displayed high TPC. Specifically, the TPC of YY was 47.02 ± 0.79 mg GAE/g extract, while the antioxidant activity of YY leaves (IC_{50} value) in the DPPH, and ABTS assays were 24.08 ± 1.67 μ g/mL, and 9.36 ± 1.39 μ g/mL, respectively. Additionally, the FRAP values also showed the highest (270.58 ± 3.18 mgFe²⁺/g extract), when compared to the other strains. Furthermore, the YY petiole displayed good antioxidant activities with an IC_{50} value in the DPPH, ABTS, and FRAP assays were 18.10 ± 1.27 μ g/mL, 11.48 ± 0.17 μ g/mL, and 184.31 ± 16.38 mgFe²⁺/g extract, respectively. The amount of TPC in YY petiole was 47.41 ± 0.15 mgGAE/g extract, with no significant difference in comparison to the leaf extract. Overall, all strains exhibited potent activity, with IC_{50} values below 38.50 μ g/mL. These findings demonstrated that the YY strain extract of kratom possesses a significant antioxidant activity in *in vitro* tests.

Introduction:

Free radicals are reactive oxygen species produced from cellular metabolism. Various pollutants such as ozone, heavy metals, smoke, and cigarettes cause free radical production. An excess of these radicals results in extensive oxidation and destroying the structure and function of biomolecules leading to cellular death. These radicals, possessing unpaired electrons in their atomic orbitals, are unstable and reactive. They can either donate or accept an electron, acting as oxidants and reductants.¹ Free radical damage appears to be common in many diseases such as neurological diseases, cardiovascular diseases, aging, cancer, diabetes, and high blood pressure disorders.² Under normal conditions, free radicals are removed from the body through antioxidant processes. However, an imbalance in their production and protection of free radicals can be harmful to health.

Many exogenous small molecule antioxidants, like polyphenols, are commonly isolated from various plants to combat free radicals.³ Due to the health benefits of antioxidants, food products rich in antioxidants are often called “superfoods”. Additionally, pharmaceutical therapies employing antioxidants to treat diverse diseases are established. The antioxidants work by preventing or delaying the oxidation of chemicals. Synthetic antioxidants are provided to supplement the antioxidant mechanism from external sources. Medicinal plants, due to their therapeutic potential and natural origin, are a primary source of natural antioxidants.⁴ Some non-enzymatic elements such as flavonoids, polyphenols, glutathione, and certain vitamins have been reported to possess strong antioxidant activities

in both *in vivo* and *in vitro* studies. Hence, natural products are one of the options for disease treatment because they have a variety of properties and biological activities.

Mitragyna speciosa (kratom) is one of the medicinal plants harnessed for its various medicinal properties and biological activities. Pharmacological studies have found that the substances most commonly found in kratom are alkaloids, notably Mitragynine, which is the main alkaloid with impact on pain relief, anti-inflammatory, antidepressant, antimicrobial, antioxidant, and antibacterial effects.⁵ In addition, flavonoids, tannins, lignans, and terpenoids, were found in kratom leaves. The natural phytochemicals present in leaves, flowers, rhizome, and petioles of medicinal plants include phenolic compounds, leading to their therapeutic use in the treatment of different diseases. In southern Thailand, there are three main categories for the different kratom strains with morphological variations of leaves: red vein (KanDang, KD), white vein (TangGua, TG), and leaves with a pair of very small teeth exerted near the apex (YakYai, YY) (**Figure 1**). However, the antioxidant activity of kratom has been studied, but the phytochemical composition and antioxidant activity depend on its variety and environmental conditions. The objective of the present study was to assess and compare the total phenolic content (TPC) and antioxidant activity of different *M. speciosa* strains prevalent in Thailand, to determine their potential in kratom-containing nutraceutical, and medicinal formulations.

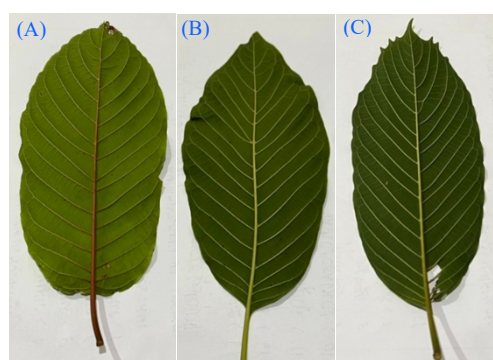


Figure 1.

The leaf shape and vein of plants in *Mitragyna speciosa* in Thailand. KanDang (A), TangGua (B), and YakYai (C).

Methodology:

Materials

The fresh leaves of three strains of *M. speciosa* (KanDang, TangGua, and YakYai types) were harvested in May 2022, all at the same phenological stage, which consisted of the top mature leaves. These leaves were collected from Krabi province, Thailand. Gallic acid, sodium carbonate (Na_2CO_3), absolute ethanol, hydrochloric acid (HCl), 2,4,6-tris(2-pyridyl)-s-triazine (TPTZ) were purchased from Sigma-Aldrich. Folin-Ciocalteu reagent was obtained from Fisher Scientific. Ascorbic acid, 2,2-diphenyl-1-picrylhydrazyl (DPPH), 2,2'-azino-bis(3-ethylbenzothiazoline-6-sulphonic acid) diammonium salt (ABTS) were purchased from Merck. Potassium persulphate and sodium acetate trihydrate were acquired from LobaChemie Pvt. Ltd. Iron (III) chloride hexahydrate ($\text{FeCl}_3 \cdot 6\text{H}_2\text{O}$) and glacial acetic acid (CH_3COOH) were purchased from QRc New Zealand.

Plant extractions

All three strains of kratom leaves were gathered, dried, and finely ground into powder. The leaves and petiole were then separated. Subsequently, 100 grams of the sample were subjected to extraction using 500 mL of 95% ethanol via the conventional maceration



method over a 5-day period. The resulting solution was filtered through Whatman No. 1 paper, and this extraction process was repeated twice. The solvent was evaporated using a rotary evaporator. The extraction percentage was calculated by using the following formula:

$$\% \text{ Yield} = (\text{mass of the extract} / \text{mass of the dry plant sample}) \times 100 \quad (1)$$

Finally, the extract should be stored at a temperature of 4 °C.

Determination of total phenolic content

The total phenolic content (TPC) of the kratom samples was assessed using a modified Folin-Ciocalteu colorimetric method.⁶ A 30 µL aliquot of the extract solution (0.1 mg/mL) was introduced into 96-well plates and thoroughly mixed with a diluted Folin-Ciocalteu reagent (110 µL). The samples were then vigorously shaken. After a 3-minute incubation, a 110 µL portion of 7.5% Na₂CO₃ solution was added, followed by thorough mixing, and the mixture was left at room temperature for 30 minutes. Subsequently, the absorbance at 765 nm was determined using a spectrophotometer plate reader. The TPC was quantified by comparing it with the standard calibration curve of Gallic acid. The results for TPC are expressed in milligrams of Gallic acid equivalent per gram of dry extract (mgGAE/g extract).

Determination of antioxidant capacity

The antioxidant capacity was determined with three different methods: DPPH (2, 2-diphenyl-1-picrylhydrazyl) radical scavenging activity, FRAP (Ferric ion reducing antioxidant power) and ABTS (2,2'-azinobis-3-ethylbenzothiazoline-6-sulfonic acid) procedures.

DPPH assay

The DPPH radical scavenging capacity of each extract was determined according to the modifications of the method by Brand-Williams.⁷ Each extract was prepared in various concentrations. Sample 100 µL mixed with DPPH (2,2-diphenyl-1-picrylhydrazyl radical) solution with a concentration of 0.2 mM in a volume of 150 µL in a 96 well plate, and leave in a dark place at room temperature for 30 minutes. The absorbances was recorded at a wavelength of 517 nm, and converted into the percentage of radical scavenging activity using the following equation (2):

$$\text{Radical scavenging activity (\%)} = [(Abs_{\text{control}} - Abs_{\text{sample}}) / Abs_{\text{control}}] \times 100 \quad (2)$$

Where: Abs_{control} is the absorbance of the control.

Abs_{sample} is the absorbance in the presence of the extract.

Ascorbic acid was used as a reference standard. All tests were performed in triplicate. The half-maximal inhibitory concentration (IC₅₀) values were calculated by linear regression of plots, where the x-axis represents the concentration of the tested plant extracts, and the y-axis represents the average percent of scavenging capacity. The concentration of the sample required to scavenge 50% of DPPH (IC₅₀) was determined.

ABTS radical-scavenging activity

The ABTS radical scavenging test was adapted from the generation of ABTS radical cation (ABTS⁺), achieved by mixing a 7 mM ABTS solution with a 2.45 mM potassium persulfate solution at a volumetric ratio of 1:0.5. This mixture was allowed to stand in darkness at room temperature for 12-16 hours before use. The ABTS⁺ solution was diluted in ethanol until it reached an absorbance of 0.7 ± 0.02 at 734 nm. Subsequently, 270 µL of the ABTS⁺ solution was combined with 30 µL of the ethanolic plant extract at varying concentrations. The mixture was then kept in darkness at room temperature for 30 minutes, and the absorbance was measured at 734 nm using a microplate reader. Ascorbic acid was

employed as a positive control. The percentage of ABTS inhibition was determined using equation (3):

$$\text{ABTS inhibition (\%)} = [(\text{Abs}_{\text{control}} - \text{Abs}_{\text{sample}}) / \text{Abs}_{\text{control}}] \times 100 \quad (3)$$

Where: $\text{Abs}_{\text{control}}$ is the absorbance of the control.

$\text{Abs}_{\text{sample}}$ is the absorbance in the presence of the extract.

The results are presented as the half-maximal inhibitory concentration (IC_{50}). All tests were conducted in triplicate.

Ferric reducing antioxidant power (FRAP) assay

The ferric ion-reducing antioxidant power (FRAP) test was conducted according to the method described by Benzie and Strain.⁸ The FRAP reagent was prepared by combining three solutions (300 mM sodium acetate buffer, pH = 3.6, 10 mM TPTZ solution in 40 mM HCl, and 20 mM $\text{FeCl}_3 \cdot 6\text{H}_2\text{O}$) in a volumetric ratio of 10:1:1. Next, 270 μL of the FRAP reagent was blended with 30 μL of the ethanolic plant extract within 96-well plates. The plate was then placed in darkness at room temperature for 5 minutes to facilitate the reduction reaction. Subsequently, the absorbance was measured at 593 nm using a microplate spectrophotometer. The antioxidant capacity was calculated using a linear calibration curve and expressed as mgFe^{2+} per gram of the extract.

Statistical analysis

SPSS statistics version 17.0 was used for data analysis. The data were presented as the mean \pm standard deviation. One-way analysis of variance (ANOVA) followed by the Tukey multiple-range test were performed. Significance was established at a p -value below 0.05.

Results and Discussion:

Free radicals are reactive molecules that play a role in numerous physiological processes and have been linked to various diseases. They can cause extensive damage to biomolecules and tissues. While synthetic drugs are often used to counteract oxidative damage, they are associated with undesirable side effects. As a result, there is a growing interest in investigating natural substances with the ability to scavenge free radicals and exhibit antioxidant properties. *M. speciosa*, or kratom, is a rich source of substances that have been reported to have psychoactive and analgesic properties.⁹ However, reports on the properties of different strains obtained are still limited. The three types of kratom, as shown in **Figure 1.**, were extracted with ethanol which is known as a suitable solvent for polyphenol extraction and is safe for human consumption.¹⁰ The yields of the extraction were measured between the part used and varieties, ranging from 4.63% to 12.97% (w/w) (**Table 1.**). The maximum extract yield was obtained from the YakYai leaves (ELYY) with a percentage yield of 12.97%. This indicates that most of the substances in YakYai leaves are highly polar such as polyphenol compounds and therefore can be extracted well with high-polarity solvents.

Table 1.

Extraction yields and total phenolic content (TPC) of ethanolic crude extract in different strains of kratom.

Part used	Strains	Sample code	Percentage yield (w/w)	Total phenolic content (mgGAE/g extract)
Petiole	YakYai	EPYY	4.63	47.41 ± 0.15^a
	TangGua	EPTG	7.44	44.14 ± 0.30^b
	KanDang	EPKD	8.18	43.73 ± 0.98^b
Leaves	YakYai	ELYY	12.97	47.02 ± 0.79^a
	TangGua	ELTG	11.19	43.95 ± 0.44^b
	KanDang	ELKD	11.87	46.20 ± 0.32^a

Total phenolic content (TPC) of kratom extracts

Brown *et al.* have reported on the presence of alkaloids and other substances, within the *Mitragyna* plant, such as flavonoids, polyphenolic compounds, triterpenoids, saponins, monoterpenes, and secoiridoids.¹¹ Phenolic compounds are well known for their antioxidant activity which can reduce the production of free radicals and lower oxidative stress. The amount of total phenolic compounds in the leaves and petiole of three strains of kratom can be calculated from the equation of the standard curve of Gallic acid solution. The resulting equation, $y = 0.0663x + 0.0648$, exhibits a high coefficient of correlation, $R^2 = 0.9982$. As can be observed, TPC levels varied among the different strains, as indicated in **Table 1**. In comparison to all types, YakYai displayed the highest TPC value. Specifically, the TPC content in YakYai petiole (EPYY) was 47.41 ± 0.15 mgGAE/g extract, showing no significant difference in comparison to the leaf extract (ELY) at 47.02 ± 0.79 mgGAE/g extract. Among the kratom leaves, the strain with the lowest TPC was TangGua, with a TPC of 43.95 ± 0.44 mgGAE/g extract. Phenolic compounds, being a diverse group of secondary metabolites, exhibit variations in distribution and content among plant species. The amount of TPC depends not only on the variety but also on geographic origin, maturity stage, and ecotype.¹² These findings are consistent with those described by Doloh *et al* for different kratom-containing formulations.¹³

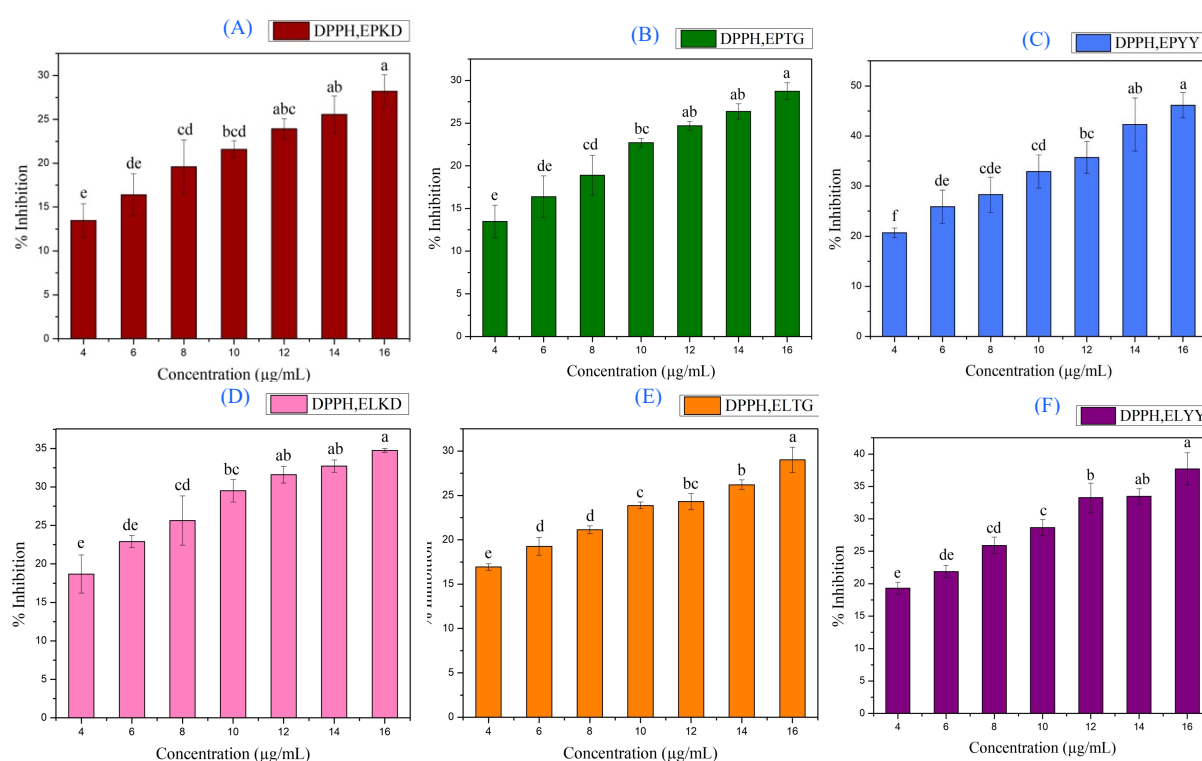


Figure 2.

The effect of ethanol extract concentration on DPPH inhibition in the (A) petiole from KanDang (EPKD), (B) petiole from TangGua (EPTG), (C) petiole from YakYai (EPYY), (D) leave from KanDang (ELKD), (E) leave from TangGua (ELTG), (F) leave from YakYai (ELYY). Data are mean values of three measurements with standard errors.

Antioxidant activity of kratom extracts

Phenolic compounds are a group of secondary metabolites present in a wide array of medicinal plants, and they have been associated with their antioxidant properties. To facilitate the comparison between methods, DPPH, ABTS, and FRAP assays have been developed to estimate the antioxidant activity of three types of kratom. As illustrated in **Figure 2-3**, the effects of kratom extract concentration on antioxidant activity are depicted using DPPH and ABTS assays, respectively. Notably, the percentage of radical inhibition displayed a concentration-dependent pattern with the plant extracts. The reason might be that increasing the concentration of the extracts leads to higher antioxidant content of the material, causing the donation of electrons to neutralize free radicals.

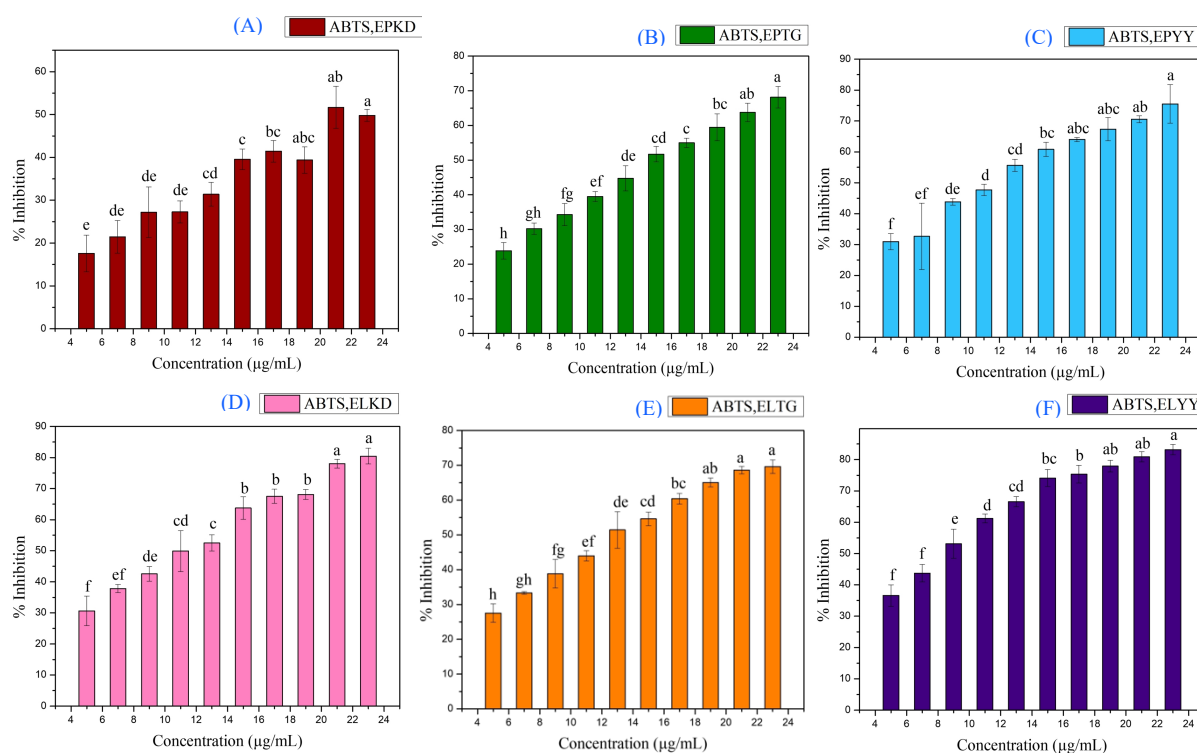


Figure 3.

ABTS radical scavenging activities of all ethanolic kratom extract from various sources, including: (A) petiole from KanDang (EPKD), (B) petiole from TangGua (EPTG), (C) petiole from YakYai (EPYY), (D) leave from KanDang (ELKD), (E) leave from TangGua (ELTG), (F) leave from YakYai (ELYY). Data represent the mean values obtained from three measurements.

The results obtained for DPPH and ABTS assays were plotted as percentage inhibition versus sample concentration. The correlation obtained by the linear regression for various kratom strains is illustrated in **Figure 4**. Consequently, 50% inhibitory concentration of free radicals (IC_{50}) values was determined based on their linear regression. In **Figure 5**, the antioxidant capacity values obtained using the three methods in the diverse kratom varieties analyzed are presented. **Figure 5** highlights the variability in antioxidant activities among different kratom varieties. In the DPPH assay, the strongest antioxidant activity was observed in the YakYai strain. The petiole (EPYY) and leaf of YakYai (ELYY) exhibited IC_{50} value of 18.10 ± 1.27 and 24.08 ± 1.67 $\mu\text{g/mL}$, respectively, while TangGua leaves (ELTG) displayed the lowest antioxidant capacity with IC_{50} values of 38.50 ± 2.16 $\mu\text{g/mL}$.

The results from the ABTS assay established that YakYai leaf (ELYY) exhibited the highest antioxidant capacity ($IC_{50} = 9.36 \pm 1.39$ $\mu\text{g/mL}$), while TangGua leaf (ELTG) showed

the lowest results ($IC_{50} = 13.57 \pm 0.24 \mu\text{g/mL}$). The assay was compared with the trapping potential of ascorbic acid. Although the radical scavenging abilities of kratom extracts were significantly lower than that of ascorbic acid, they still exhibited a good antioxidant capacity for all kratom varieties studied with IC_{50} values below $38.50 \mu\text{g/mL}$. The scavenging of the DPPH radical by the extracts was found to be less potent than that of $ABTS^{+}$ radicals. The stereo selectivity of the radicals and the solubility of extracts in various solvent systems are among the factors reported to affect the capacity of extracts to react and quench different radicals.¹⁴

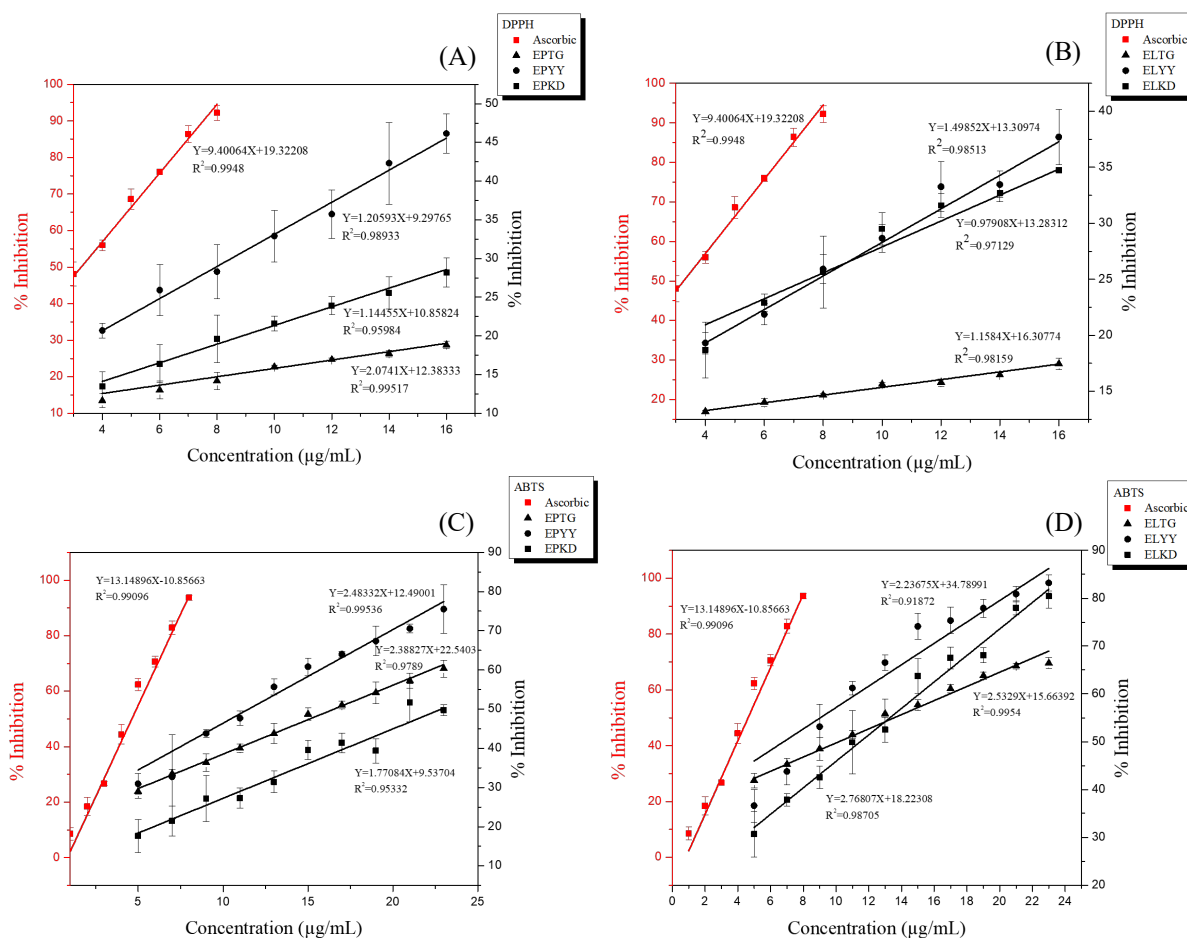


Figure 4.

Effect of kratom extract concentrations in antioxidant assays. (A-B) DPPH radical dot and (C-D) ABTS dot methods for petiole and leaves of different strain of kratom extract: petiole from KanDang (EPKD), petiole from TangGua (EPTG), petiole from YakYai (EPYY), leave from KanDang (ELKD), leave from TangGua (ELTG), and leave from YakYai (ELYY). XY curves fitted with linear model using OriginLab.

The FRAP assay is an important antioxidant method for assessing antioxidant capacity by measuring the ability to convert ferric iron into ferrous cations. It was found that ELYY is high potential effectiveness with a FRAP value equal to $270.58 \pm 3.18 \text{ mgFe}^{2+}/\text{g}$ extract. The sequence of FRAP values was ELKD, EPYY, ELTG, EPTG, and EPKD.

This study suggests that phenolic compounds are responsible for the measured antioxidant activity. The TPC and antioxidant activity obtained with the three antioxidant assays in the YakYai strain were relatively high suggesting the YakYai showed good biological polyphenolic compounds better than the other strains. This is supported by

previous studies indicating that kratom from different sources is a reservoir of polyphenolic constituents, notably flavonoids and phenolic glycosides.¹⁵ Similar results reported in **Table 2**, also revealed that *M. speciosa* extract showed a high content of phenolic compounds with excellent antioxidant activity.¹⁶⁻²² The hydroxyl groups in phenolic compounds confer scavenging or chelation ability, and also act on membrane-bound enzymes. The results can provide valuable information for the selection of the strain of kratom, in order to obtain products with high TPC and antioxidant characteristics. Future studies are needed to characterize extracts for specific phytochemicals related to antioxidant activity in the YakYai strain.

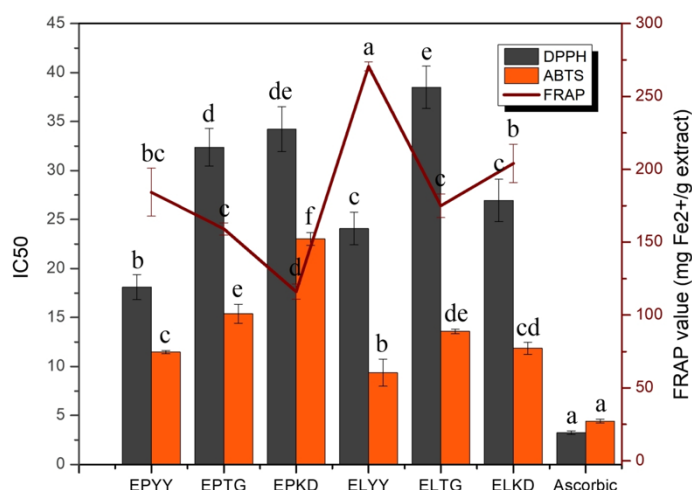


Figure 5.

The antioxidant capacities of the ethanolic extracts of leaves and petiole of three types of kratom were measured by the DPPH (IC₅₀), ABTS (IC₅₀), and FRAP assays. Mean values that do not share a letter indicate significant differences (Tukey's test, $p < 0.05$).

Table 2.

Comparison between *M. speciosa* extract from different sources for antioxidant activities.

Strains	Extract	DPPH (IC ₅₀)	ABTS (IC ₅₀)	FRAP	References
Green veined	Ethanol	1.04±0.01 mg/mL	-	39.87±0.26 mg CE/g dry weight	17
Red veined	Methanol	0.11mg/ml	-	-	18
Malaysian kratom	Hexane	>1mg/mL	20.84±0.92mg/mL	11.45±0.99µg/mL	19
	Dichloro-methane	>1mg/mL	20.84±0.92mg/mL	7.94±0.96µg/mL	
Malaysian kratom	Methanol	0.0397±0.0035mg/mL	-	-	20
Malaysian kratom	Methanol	213.45±31.31µg/mL	-	-	16
	Aqueous	104.81±5.77µg/mL	-	-	
-	Ethanol	0.35±0.01mg/mL	-	115.46±1.51 mgGAE/g extract	13
-	Ethanol	21.61±0.01µg/mL	9.33±0.01µg/mL	89.31±1.44 quercetin/g extract	21
-	Methanol	4.34±1.79µg/mL.	4.25±1.59µg/mL	-	22



Conclusion:

The antioxidant activity of three kratom strains, assessed using various testing methods, revealed that each strain of plant has variations in their antioxidant activity and constituent substances. Among the study findings, YakYai kratom exhibited the most promising results in tests of antioxidant activity and phenolic content, making it a prime candidate for further research and development.

Acknowledgements:

This work was supported by National Higher Education, Science, Research and Innovation Policy Council, Thaksin University (Fundamental Research Fund; 66A105000014) Fiscal Year 2023). The authors would like to thank the Department of Chemistry, Faculty of Science, Thaksin University, for providing research facilities, software packages and computing times.

References:

1. Cornelli U. Clin. Dermatol. 2009;27:175-194.
2. Lobo V, Patil A, Phatak A, Chandra N. Phcog Rev. 2010;4:118–126.
3. Charlton NC, Mastuygin M, Török B, Török M. Molecules. 2023;28:1057.
4. Hoang HT, Moon JY, Lee YC. Cosmetics. 2021;8:106.
5. Luliana S, Robiyanto R, Islamy MR. Pharm. Sci. Res. 2018;5:58 - 64.
6. Nikolaeva T, Lapshin P, Zagorskina N. Russ. J. Bioorganic Chem. 2022;48:1519-1525.
7. Bondet V, Brand-Williams W, Berset C. LWT. 1997;30:609-615.
8. Aydın Kurç M, Orak H, Gülen D, Caliskan H, Argon M, Sabudak T. Molecules. 2023;28:7177.
9. Firmansyah A, Sundalian M, Taufiq M. Biointerface Res. Appl. Chem. 2021;11:9704 - 9718.
10. Meireles V, Rosado T, Barroso M, et al. Medicines. 2019;6:35.
11. Brown PN, Lund JA, Murch SJ. J Ethnopharmacol. 2017;202:302-325.
12. Elisa DH, Marcela GM, Alejandra GUJ, Elena DHM. J. Cereal Sci. 2022;103:103399.
13. Suhaila D, Boonsong W, Juraithip W. JHSMR. Published online 2023.
14. Yu L, Perret J, Davy B, Wilson J, Melby C. J. Food Sci. 2002;67:2600-2603.
15. Chen L, Fei S, Olatunji OJ. Molecules. 2022;27:2208.
16. Parthasarathy S, Azizi JB, Ramanathan S, et al. Molecules. 2009;14:3964-3974.
17. Piyawat S, Natcha P, Juraithip W, et al. Khon Kaen Agr. J. 2564;49:332-338.
18. Thamonwan M, Piyanadda S. Presented at: 2021; Surattthani Rajabhat University.
19. Rahman M, Nafiah M, Wan W, Salleh S, Hashim N, Zamakshshari N. MJChem. 2022; 24:191-198.
20. Azhar S, Ashari S, Tan J, et al. Ind Crops Prod. 2023;198:116668.
21. Zhang P, Wei W, Zhang X, Wen C, Ovatlarnporn C, Olatunji OJ. Biomed. Pharmacother. 2023;162:114689.
22. Zailan N Sarchio S, Hassan M. MJMHS. 2022;18: 92-99.

AUTHOR INDEX

Areeya Tohteb	330	Piyakorn Preedeesanith	294
Bhudsawan Hiranvarachat	708	Ploy Nantapisit	149
Bhuvit Charoenpanich	95	Poramat Chianvichai	61
Burapha Phajuy	686	Praepan Lapphaisal	509
Charin Chandit	385	Prant Chotiphantawanon	403
Chayanook Seetha	477	Prarinwaris Pangprasertgul	221
Chonticha Suwan	302	Prasong Kessaratikoon	363
Dawn Cook	156	Ratchadaporn Kueasook	694
Felicitas Ene	188	Rawiporn Promsung	339
Gregorius Nico Setiawan	164	Rosmamuhamadani Ramli	89
Gunn Tangkanont	504	Rukchart Prasertpong	195
Hakeemee Sadeeyamu	606	Sathit Prasomphan	248
Jakkree Boonlakhorn	637	Suwit Khongpakdee	348
Jarawee Chupirom	591	Sanya Meesim	428
Jeerasak Phu-arphit	55	Saowaluk Chaleawlwert-umpon	630
Jidapa Lumpapiwat	15	Saowapa Chotisuwan	537
Jidapar Wathanaphol	443	Sara Shoaib	121
Joewono Widjaja	30	Sasiprapa Radchatawin	275
Khanittha Sawaddee	1	Sawanya Suwannawong	241
Kamonpan Junlat	230	Sirirat Srirat	715
Kanda Panthong	557	Sitapun Jethanajun	468
Kanok-orn Mayer	113	Somrudee Jitpraphai	282
Kanokpon Suriyamorn	269	Sopon Nuchpun	139
Kanokwan Homdee	6	Sorawit Tongyib	105
Kantima Rattana	528	Supoj Chamnanprai	612
Kanyarat Kwansirikul	651	Surarat Siri-in	679
Kedsirin Ruttajorn	492	Sutthipong Taweelarp	669
Kittimasak Naijit	258	Teerapat Onyala	379
Maripen Thesa	618	Tamonwan Lotangchanintra	372
Mingkhwan Kruachanta	644	Thammarat Taengtang	357
Nantharat Phruksaphithak	701	Thanapat Phenvongsakul	81
Narongrid Rorsena	215	Thanapon Chakarothai	543
Narongsak Sriwiran	417	Thanaporn Maswanna	452
Natchapong Chuangsom	550	Thanchanok Lincharoen	21
Netnapa Chana	576	Thanyanan Somnam	71
Niramol Juntarachat	625	Thitiporn Promnil	434
Oranit Sriwichian	497	Thunchanok Khammanee	460
Ou-aukwan Charoenkul	45	Toyin Ayandokun	180
Pakin Tasee	36	Wanrudee Hiranrat	586
Panita Kongsune	598	Weeraya Treewanjutha	519
Panyawut Rattanaarom	392	Wikanda Thongnueakhaeng	311
Parichat Thepthong	569	Wimonsiri Puegsa	410
Patcharin Jundee	659	Yanika Chantachot	484
Patitta Suksomboon	206		
Pattaree Payomhom	131		
Peeraporn Pakakaew	319		
Pichamon Masnguluem	174		
Pipat Pobpimai	562		

